



T. Pradeep  
Publications 2022

# Chemical Science

Volume 13  
Number 45  
7 December 2022  
Pages 13251-13634

[rsc.li/chemical-science](https://rsc.li/chemical-science)



ISSN 2041-6539



**EDGE ARTICLE**

Thalappil Pradeep *et al.*  
Spatial reorganization of analytes in charged aqueous  
microdroplets

# Contents

1. Publications	5-633
2. Editorials	634-636
3. Book Chapter	637-670
4. Patents/Technology	671-673
5. Selected media reports	674-680

# Journal Papers Published in 2022\*

## Publications from our group

- (1) Islam, M. R.; Gupta, S. S.; Jana, S. K.; Pradeep, T. Industrial Utilization of Capacitive Deionization Technology for the Removal of Fluoride and Toxic Metal Ions ( $\text{As}^{3+/5+}$  and  $\text{Pb}^{2+}$ ). *Glob. Chall.* **2022**, *6* (4), 2100129. (DOI: 10.1002/gch2.202100129).
- (2) Chakraborty, A.; Dave, H.; Mondal, B.; Nonappa; Khatun, E.; Pradeep, T. Shell-Isolated Assembly of Atomically Precise Nanoclusters on Gold Nanorods for Integrated Plasmonic-Luminescent Nanocomposites. *J. Phys. Chem. B.* **2022**, *126* (8), 1842–1851. (DOI: 10.1021/acs.jpccb.1c10207).
- (3) Paulthangam, K. M.; Som, A.; Ahuja, T.; Srikrishnarka, P.; Nair, A. S.; Pradeep, T. Role of Zinc Oxide in the Compounding Formulation on the Growth of Nonstoichiometric Copper Sulfide Nanostructures at the Brass–Rubber Interface. *ACS Omega* **2022**, *7*(11), 9573–9581. (DOI: 10.1021/acsomega.1c06207).
- (4) Dar, W. A.; Jana, A.; Sugi, K. S.; Paramasivam, G.; Bodiuzzaman, M.; Khatun, E.; Som, A.; Mahendranath, A.; Chakraborty, A.; Pradeep, T. Molecular Engineering of Atomically Precise Silver Clusters into 2D and 3D Framework Solids. *Chem. Mater.* **2022**, *34*(10), 4703–4711. (DOI: 10.1021/acs.chemmater.2c00647).
- (5) Jana, A.; Unnikrishnan, P. M.; Poonia, A. K.; Roy, J.; Jash, M.; Paramasivam, G.; Machacek, J.; Adarsh, K. N. V. D.; Base, T.; Pradeep, T. Carboranethiol-Protected Propeller-Shaped Photoresponsive Silver Nanomolecule. *Inorg. Chem.* **2022**, *61* (23), 8593–8603. (DOI: 10.1021/acs.inorgchem.2c00186).
- (6) Basuri, P.; Kumar, J. S.; Das, S.; Pradeep, T. Accelerated Non-Enzymatic Fatty Acid Esterification during Microdroplet Collision: A Method for Enhanced



Sustainability. *ACS Sustain. Chem. Eng.* **2022**, *10* (26), 8577–8587. (DOI: 10.1021/acssuschemeng.2c02070).

(7) Jana, S. K.; Chaudhari, K.; Islam, M. R.; Natarajan, G.; Ahuja, T.; Som, A.; Paramasivam, G.; Raghavendra, A.; Sudhakar, C.; Pradeep, T. Selective and Practical Graphene-Based Arsenite Sensor at 10 Ppb. *ACS Appl. Nano Mater.* **2022**, *5* (8), 11876–11888. (DOI: 10.1021/acsanm.2c02860).

(8) Srikrishnarka, P.; Dasi, R. M.; Jana, S. K.; Ahuja, T.; Kumar, J. S.; Nagar, A.; Kini, A. R.; George, B.; Pradeep, T. Toward Continuous Breath Monitoring on a Mobile Phone Using a Frugal Conducting Cloth-Based Smart Mask. *ACS Omega* **2022**, *7* (47), 42926–42938. (DOI: 10.1021/acsomega.2c05017).

(9) Basuri, P.; Shantha Kumar, J.; Unni, K.; Manna, S.; Pradeep, T. Aggregation of Molecules Is Controlled in Microdroplets. *Chem. Commun.* **2022**, *58* (91), 12657–12660. (DOI: 10.1039/D2CC04587G).

(10) Malla, B. K.; Vishwakarma, G.; Chowdhury, S.; Selvarajan, P.; Pradeep, T. Formation of Ethane Clathrate Hydrate in Ultrahigh Vacuum by Thermal Annealing. *J. Phys. Chem. C* **2022**, *126* (42), 17983–17989. (DOI: 10.1021/acs.jpcc.2c06264).

(11) Basuri, P.; Chakraborty, A.; Ahuja, T.; Mondal, B.; Kumar, J. S.; Pradeep, T. Spatial Reorganization of Analytes in Charged Aqueous Microdroplets. *Chem. Sci.* **2022**, *13* (45), 13321–13329. (DOI: 10.1039/D2SC04589C).

(12) Vishwakarma, G.; Malla, B. K.; Methikkalam, R. R. J.; Pradeep, T. Rapid Crystallization of Amorphous Solid Water by Porosity Induction. *Phys. Chem. Chem. Phys.* **2022**, *24* (42), 26200–26210. (DOI: 10.1039/D2CP02640F).

(13) Nagar, A.; Islam, M. R.; Joshua, K.; Gupte, T.; Jana, S. K.; Manna, S.; Thomas, T.; Pradeep, T. Ion-Exchanging Graphenic Nanochannels for Macroscopic Osmotic Energy Harvesting. *ACS Sustain. Chem. Eng.* **2022**, *10* (46), 15082–15093. (DOI: 10.1021/acssuschemeng.2c04138).

(14) Gupte, T.; Pandurangan, S.; Islam, M. R.; Srikrishnarka, P.; Nagar, A.; Ayyadurai, N.; Thomas, T.; Pradeep, T. Human Skin-Cell-Based Sensor for Environmental Arsenic Detection and for Creating Social Awareness. *ACS Sustain. Chem. Eng.* **2022**, *10* (51), 17124–17133. (DOI: 10.1021/acssuschemeng.2c04586).

(15) Jash, M.; Jana, A.; Poonia, A. K.; Khatun, E.; Chakraborty, P.; Nagar, A.; Ahuja, T.; Adarsh, K. V.; Pradeep, T. Phosphine-Protected Atomically Precise Silver–Gold Alloy Nanoclusters and Their Luminescent Superstructures. *Chem. Mater.* **2022**, acs.chemmater.2c03222. (DOI: 10.1021/acs.chemmater.2c03222).

(16) Jana, A.; Jash, M.; Dar, W. A.; Roy, J.; Chakraborty, P.; Paramasivam, G.; Lebedkin, S.; Kirakci, K.; Manna, S.; Antharjanam, S.; Machacek, J.; Kucerakova, M.; Ghosh, S.; Lang, K.; Kappes, M. M.; Base T and Pradeep T. Carborane-thiol protected copper nanoclusters: Stimuli-responsive materials with tunable phosphorescence, *Chem. Sci.* **2022**. (DOI:10.1039/D2SC06578A).

## Publications with other groups

(1) Som, A.; Griffo, A.; Chakraborty, I.; Hähl, H.; Mondal, B.; Chakraborty, A.; Jacobs, K.; Laaksonen, P.; Ikkala, O.; Pradeep, T and Nonappa. Strong and elastic membranes via hydrogen bonding directed self-assembly of atomically precise nanoparticles. *Small.* **2022**, 2201707. (DOI: 10.1002/sml.202201707).

Some of these papers will appear in 2023. Some were listed in publications of 2021 without page numbers, but appeared in 2022.

# Editorials

(1) Allen, D. T.; Licence, P.; Subramaniam, B.; Anastas, P. T.; Carrier, D. J.; Chen, J.; Gathergood, N.; Garcia, J. M.; Gong, J.; Han, H.; Kuok (Mimi) Hii, K.; Hwang, B.-J.; Marr, A.; Meier, M.; Moores, A.; Nakamura, R.; Pradeep, T.; Rossi, L.; Sels, B.; Tam, M. K. C.; Zhuang, L.; Serrano, J. F. Building Pathways to a Sustainable Planet. *ACS Sustain. Chem. Eng.* **2022**, *10* (1), 1–2. (DOI: 10.1021/acssuschemeng.1c08512).

# Books/Book chapters

- (1) Atomically precise metal nanoclusters, edited by Thalappil Pradeep, Elsevier, Amsterdam, 2023.
- (2) Concepts of sustainability in clean water technologies, Sritama Mukherjee, Jenifer Shantha Kumar, Ankit Nagar, and Thalappil Pradeep in Peter Boul (Ed.), Energy Transition: Climate Action and Circularity, ACS Symposium Series; American Chemical Society: Washington, DC, 2022.

# Journal Papers

Publications from  
our group

# Industrial Utilization of Capacitive Deionization Technology for the Removal of Fluoride and Toxic Metal Ions ( $\text{As}^{3+/5+}$ and $\text{Pb}^{2+}$ )

Md Rabiul Islam, Soujit Sen Gupta, Sourav Kanti Jana, and Thalappil Pradeep\*

Capacitive deionization (CDI) is an emerging desalination technology, particularly useful for removing ionic and polarizable species from water. In this context, the desalination performance of fluoride and other toxic species (lead and arsenic) present in brackish water at an industrial scale of a few kiloliters using a CDI prototype built by InnoDI Private Limited is demonstrated. The prototype is highly efficient in removing ionic contaminants from water, including toxic and heavy metal ions. It can remove fluoride ions below the World Health Organization (WHO) limit (1.5 ppm) at an initial concentration of 7 ppm in the input feed water. The fluoride removal efficiency of the electrodes (at a feed concentration of 6 ppm) deteriorates by  $\approx 4\text{--}6\%$  in the presence of bicarbonate and phosphate ions at concentrations of 100 ppm each. The removal efficiency depends on flow rate, initial total dissolved solids, and other co-ions present in the feed water. Interestingly, toxic species ( $\text{As}^{3+/5+}$  and  $\text{Pb}^{2+}$ ) are also removed efficiently (removal efficiency  $> 90\%$ ) by this technology. The electrodes are characterized extensively before and after adsorption to understand the mechanism of adsorption at the electrode.

such as arsenic (As), lead (Pb), fluoride ( $\text{F}^-$ ), nitrate, and uranium, along with the presence of anthropogenic contaminants such as pesticides, perchlorates, and dyes, thus rendering the water unfit for drinking. Toxic elements such as As and Pb exist in different forms in nature. Exposure to all these contaminants above a specific limit can cause serious health hazards, even carcinogenicity in humans. Among these, fluoride and arsenic are major threats to the Indian population; more than 20 states are severely affected by fluoride and over 12 states by arsenic.<sup>[3,4]</sup> Arsenic contamination in groundwater occurs due to the erosion of natural minerals into aquifers, as a result of complex geochemistry and hydrochemistry.<sup>[5–7]</sup> According to the World Health Organization (WHO), over 137 million people in more than 70 countries, and  $\approx 57$  million people in 30 countries consume


water containing more than 1.5 ppm fluoride and 50 ppb of arsenic, respectively.<sup>[8–10]</sup> The standard acceptable limits set by WHO for  $\text{F}^-$  and As are 1.5 ppm and 10 ppb, respectively. Major health effects due to  $\text{F}^-$  intake include dental and skeletal fluorosis. As per reports, excess  $\text{F}^-$  intake can affect the kidney, liver, and reproductive system and cause arthritis, thyroid malfunction, and brain damage.<sup>[11]</sup> On the other hand, long-term exposure to As through drinking water and food can lead to cancer, cardiovascular diseases, skin lesions, and diabetes.<sup>[12]</sup>

In the recent past, researchers have found many efficient solutions for removing As by adsorption using diverse materials.<sup>[7,13]</sup> However, adsorption is not an effective solution to remove  $\text{F}^-$ , as its concentration is as high as 2–10 ppm in some parts of the country.<sup>[14,15]</sup> Efforts have been made to remove  $\text{F}^-$  from drinking water using activated alumina, but it is ineffective due to low adsorption capacity and lack of regeneration and reusability without side effects. Activated alumina,<sup>[16]</sup> hybrid graphene oxide (GO)-ferric hydroxide composite,<sup>[17]</sup> magnetite-reduced graphene oxide (M-rGO) composite,<sup>[18]</sup> iron oxide,<sup>[19]</sup> functionalized graphene nanosheets,<sup>[20]</sup> 3D hybrid graphene-carbon nanotube-iron oxide composite,<sup>[21]</sup> iron oxyhydroxide-chitosan composite,<sup>[22]</sup> activated carbon,<sup>[23]</sup> silicon dioxide,<sup>[24]</sup> and cellulose-based materials<sup>[6]</sup> have been used to remove arsenic from water in the recent past. Among the different heavy metals, Pb has also been widely found in drinking water, which is also highly toxic to human health. Presence of lead, even in trace amounts, can affect nervous, digestive,

## 1. Introduction

Availability of clean drinking water is one of the major challenges of 21st century. According to the United Nations, more than two-thirds of the human population will be under water scarcity by 2025.<sup>[1,2]</sup> This is because existing fresh water is getting increasingly contaminated due to a) increased industrialization, b) excessive use of chemical fertilizers in agriculture, c) unprocessed industrial, human, and animal waste, and d) climate change. Groundwater contamination has been gradually increasing with the presence of several toxic contaminants,

M. R. Islam, S. S. Gupta, S. K. Jana, T. Pradeep  
DST Unit of Nanoscience (DST UNS),  
and Thematic Unit of Excellence (TUE)  
Department of Chemistry  
Indian Institute of Technology Madras  
Chennai 600 036, India  
E-mail: pradeep@iitm.ac.in

 The ORCID identification number(s) for the author(s) of this article can be found under <https://doi.org/10.1002/gch2.202100129>.

© 2022 The Authors. Global Challenges published by Wiley-VCH GmbH. This is an open access article under the terms of the Creative Commons Attribution License, which permits use, distribution and reproduction in any medium, provided the original work is properly cited.

DOI: 10.1002/gch2.202100129

and skeletal systems, and therefore, must be removed from the water. It has a tendency to accumulate in tissues of living organisms. Major industrial sources of Pb contamination in the environment are battery manufacturing, acid metal plating, and finishing, ammunition, tetraethyl lead manufacturing, ceramic and glass industries, and printing, painting, and dyeing industries. According to the US Environmental Protection Agency (USEPA), the maximum acceptable level for Pb is 15 ppb (WHO limit: 10 ppb). To achieve this goal, several methods have been applied for the removal of lead from wastewaters, such as precipitation, solvent extraction, ion exchange, coagulation, and floatation, and different materials used for lead removal are fly ash, activated carbon, ion-exchange resins (IERS), nanosized zero-valent iron (nZVI)-based materials, and different graphenic materials.<sup>[25,26]</sup>

To meet the demands of safe drinking water globally, several methods were extensively reported for brackish and seawater desalination.<sup>[27]</sup> In the past few decades, desalination techniques including 1) distillation, 2) thermal desalination (multistage flash distillation, multieffect evaporation, vapor compression evaporation, etc.), 3) membrane desalination (reverse osmosis (RO), electrodialysis, membrane distillation, etc.), and 4) ion-exchange have been developed. However, major disadvantages of these existing techniques are that they are neither cost-effective nor energy-efficient. In this context, capacitive deionization (CDI) is emerging as an alternative desalination technology as it is capable of desalination of ionic and polarizable pollutants from brackish water at an affordable cost.<sup>[28]</sup> CDI works on the principle of electroadsorption of ions on porous carbon electrodes when a small potential difference (0.8–2.0 V) is applied across them.<sup>[29]</sup> A CDI cell consists of a pair of porous electrodes (mainly made of carbon), separated by a nonconducting membrane called as separator. When a potential difference is applied across the electrodes, the electrodes get charged, which drives oppositely charged ions toward them by electrostatic attraction. The electrostatic migration continues until an equilibrium is reached, forming an electrical double layer at the interface of the respective electrode. This step is known as electroadsorption, and subsequently, desorption happens when the potential is reversed or the external power supply is shorted. However, the limitation of this technology lies in the availability of sustainable electrode materials with high electroadsorption capacity. The electrode material has a significant role in faster adsorption and desorption kinetics for a perfect CDI process. The electrode material should have the following characteristics: i) large surface area, ii) high porosity, iii) high electrical conductivity, iv) electrochemical stability, v) bio-inertness, vi) fast adsorption–desorption kinetics, vii) good wetting behavior, viii) low cost, and ix) scalability. Generally, electrode materials used for CDI are mostly carbon-based materials such as activated carbon, carbon cloth, ordered mesoporous carbon, carbon nanofibers, carbon nanotubes/multiwalled carbon nanotubes (CNTs/MWCNTs), and graphene and graphene-based composites.<sup>[30]</sup>

CDI has numerous advantages. i) It is highly energy-efficient, as it does not require use of any high-pressure pumps. ii) The device module works at a lower DC potential  $\approx 0.8$ –2.0 V. Thus, it can be energized with solar/wind power. More importantly, it can work in rural areas where the availability of grid

power is a concern. iii) Water rejection by this technique is significantly less compared to other techniques such as RO. iv) Carbon particles, which are usually used to make active electrodes for CDI, can withstand much higher temperatures than membranes, and therefore can be used for wider applications. Uniqueness of CDI technology over other water purification technologies may be summarized as low operating cost, energy-efficiency, low wastage, and retention of essential minerals by varying the operating potentials.

In the present work,  $F^-$  along with other toxic species ( $As^{3+/5+}$  and  $Pb^{2+}$ ) containing water was purified efficiently using CDI technology at a scale of relevance for practical applications. This prototype efficiently removed  $F^-$  below the WHO limit (1.5 ppm) when the concentration of fluoride in feed water was nearly 7 ppm. The same prototype also removed As from 40 to 5.6 ppb and Pb from 200 to 7 ppb, thus bringing output concentrations below acceptable limits. Different experimental conditions, such as flow rate, initial total dissolved solids (TDS), and presence of co-ions, were optimized to achieve better desalination. Moreover, spectroscopy and microscopy were performed to characterize the electrode surface before and after desalination. The present results show that this CDI prototype is an efficient, cost-effective, and alternative technology to remove toxic species such as  $F^-$  along with  $As^{3+/5+}$  and  $Pb^{2+}$  from contaminated water.

## 2. Result and Discussion

### 2.1. Experimental Set-Up and Characterization of the Carbon Electrode

Detailed illustration of the CDI experimental set-up is provided in Figure S1 in the Supporting Information. The set-up is composed of several units, each of the units is shown separately. Figure S2 in the Supporting Information shows a photograph of the CDI experimental set-up. A schematic representation of the CDI phenomenon is demonstrated in **Figure 1A**, where cathodes and anodes are alternatively stacked, and a DC voltage is applied across the stack. The photograph of CDI electrode cell is shown in **Figure 1B**. The surface morphology of the electrode material was investigated by high-resolution scanning electron microscopy (HRSEM), and the corresponding micrograph is shown in **Figure 1C**. The HRSEM image of the carbon material revealed the highly porous nature of the carbon electrode, which was assembled with porous graphene nanosheets (**Figure 1C**). We present HRSEM of the electrode materials with 650 000 $\times$  magnification highlighting the pores present in the electrode materials. From this image, we observed that the electrode materials are highly porous in nature.

Cross-sectional views of electrodes were also examined through HRSEM images shown in **Figure 1D–F**. Thickness of the ion-exchange membrane, which was coated on the electrode material, was found to be  $\approx 15$ –20  $\mu m$  (**Figure 1D**). Additionally, the HRSEM images showed that the thickness of the current collector (i.e., the graphite sheet) of the electrode was around 250  $\mu m$ , and the graphenic material coated on the current collector had a thickness of about  $120 \pm 10 \mu m$  for both electrodes (**Figure 1E,F**). The SEM energy-dispersive X-ray spectroscopy



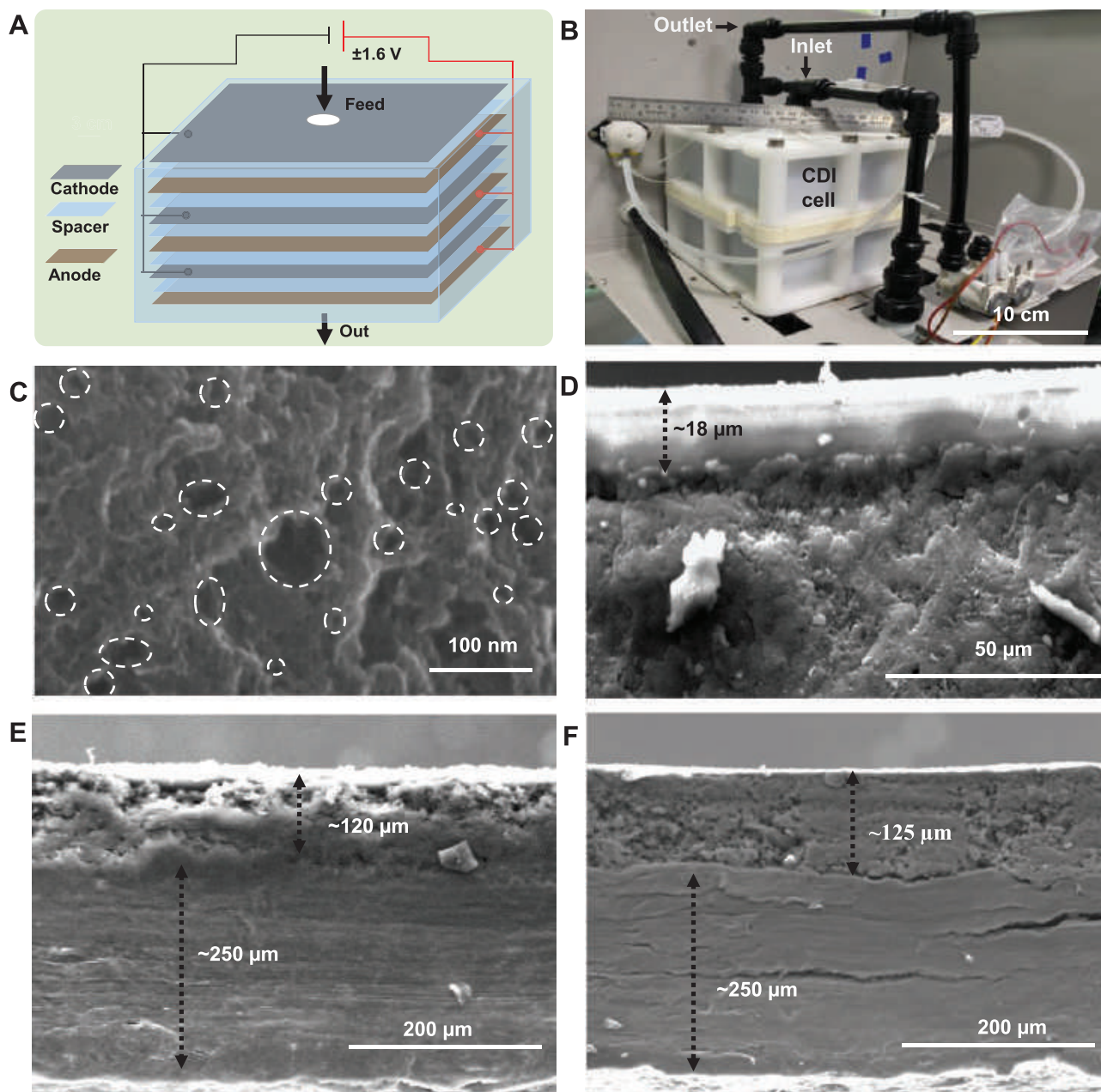


**Figure 1.** A) Schematic of CDI phenomenon where cathodes and anodes are alternatively stacked, and a DC voltage is applied across the stack B) photograph of the CDI electrode cell. C) HRSEM image of carbon material and HRSEM of the carbon material highlighting the pores present in the nanoscale regime. Cross-sectional HRSEM images of D) ion-exchange resins (IERS), E) cathode, and F) anode.

(EDS) was performed to analyze the distribution of elements in the graphenic carbon electrode. The SEM EDS spectrum of active materials (carbon) of the electrode confirmed the presence of a small amount of oxygen along with carbon, which are the major elements of the electrode material (Figure S3, Supporting Information). The SEM images of the carbon electrodes at different magnifications shown in the inset of the same figure confirm the hierarchical morphology of the active electrodes. The carbon to oxygen ratio was identified as 10.5:1, as per the SEM EDS analysis. The particle size was observed to be  $15 \pm 5 \mu\text{m}$  (Figure S3, Supporting Information). Furthermore, surface morphology and

elemental mapping of electrodes (cathode and anode) are shown in Figures S4 and S5 in the Supporting Information, respectively. Insets of Figures S4 and S5 in the Supporting Information correspond to EDS mapping of each element. The nanosheets-like structure of the electrode material masked by an ion-exchange resin was observed in the SEM image, and smooth surface of the resin was also evident on the electrode surfaces (Figure 1E,F). EDS spectrum of the cathode (Figure S4, Supporting Information) revealed the presence of calcium (Ca), which could be attributed to cation-exchange resin. Other elements such as carbon and oxygen were also present. However, the presence of



$\text{Cl}^-$  ions at the anodic surface confirms the chemical composition of the anion-exchange resin (Figure S5, Supporting Information). Figure S6 in the Supporting Information represents the Raman spectrum of the carbon material. The graphenic nature of the material was confirmed by the presence of G- and D-bands at 1604 and 1345  $\text{cm}^{-1}$ , respectively. Usually, G- and D-bands signify  $\text{sp}^2$  hybridization (graphitic signature of carbon) and disorder of the  $\text{sp}^2$  hybridized hexagonal sheet of graphenic carbon, respectively. The peak intensity and line-width of the D-band are larger than the G-band in carbon materials, indicating higher disorder/defects, which could be attributed to intense chemical treatments and/or increased amorphous carbon content (unreacted graphite powder). Thus, the Raman spectrum confirms the presence of a graphitic signature of carbon (in-plane  $\text{sp}^2$  carbon) and defects present in carbon particles ( $\text{sp}^3$  carbon).

## 2.2. Electrochemical Characterization of both Anode and Cathode Materials

Cyclic voltammetry (CV) was carried out in 1 M NaCl solution to understand the adsorption–desorption and capacitive behavior of the electrodes (anode and cathode). Voltammograms of both electrodes at different scan rates, from 1 to 100  $\text{mV s}^{-1}$ , are shown in Figure S7A,B in the Supporting Information. The voltammograms revealed that both anode and cathode are perfectly reversible at lower scan rates. These attributes to anodic and cathodic currents (or capacitive currents) are the mirror images, indicating that both adsorption and desorption processes occur almost at the same kinetic rate. However, at higher scan rates (beyond 50  $\text{mV s}^{-1}$ ), alteration in the shape of the CV profile of each electrode was monitored, implying that less amount of ions was adsorbed at electrodes. This result suggests that ions do not have enough time to access the entire electrochemical surface of the electrode material. Thus, at higher scan rates, adsorption and desorption of ions are limited by ionic resistance. Specific capacitance ( $C_{\text{sp}}$ ) of both the electrodes at each scan rate was calculated and plotted as a function of scan rate (Figure S7C,D, Supporting Information). Exponential decay of the specific capacitance exhibits a higher value ( $\approx 68 \text{ F g}^{-1}$ ) of  $C_{\text{sp}}$  at a lower scan rate and gets constant at a higher scan rate. This could be explained as the adsorption and desorption are faster at a lower scan rate as ions have enough time to get adsorbed on the oppositely charged electrode surfaces. This phenomenon is similar to the charge storage mechanism of an electrochemical capacitor. However, at a higher scan rate, the diffusion-controlled process dominates; therefore, adsorption and desorption rates are lower. Also, high salt adsorption capacity of the electrode material was observed, as seen in the electrochemical study (Figure S7, Supporting Information), which further confirms the porous nature of the electrode materials.

Scan rates-dependent adsorption–desorption characteristics were studied for anode and cathode in 1 M of NaCl and NaF solutions. At a lower scan rate (1  $\text{mV s}^{-1}$ ), the charge storage capacities (area under the curve of the voltammograms) of both the electrodes were found to be the same (Figure S8A, Supporting Information). However, at a higher scan rate (100  $\text{mV s}^{-1}$ ), CV of both anode and cathode was performed in 1 M NaCl solution, and the corresponding voltammogram showed the difference

in charge storage capacities (Figure S8B, Supporting Information). As the ionic mobility of  $\text{Na}^+$  and  $\text{Cl}^-$  are different (5.19 and 7.92  $\text{m}^2 \text{ s}^{-1} \text{ V}^{-1}$ , respectively), and diffusion of ions is controlled by the ionic mobilities of the counter-ions (cations for cathode or anions for anode). Therefore, the cathode shows a significantly higher charge storage capacity than the anode. The same experiment was carried out in 1 M NaF solution, which does not show any significant change in the charge storage capacity. However, ionic mobilities of both  $\text{Na}^+$  and  $\text{F}^-$  are almost the same (5.19 and 5.74  $\text{m}^2 \text{ s}^{-1} \text{ V}^{-1}$ , respectively). Thus, CV of both the electrodes, which were performed in 1 M NaF solution, showed the same charge storage capacity at the same scan rate. Interestingly, at a lower and higher scan rate (1 and 100  $\text{mV s}^{-1}$ , respectively), voltammograms of both the electrodes are almost similar (Figure S8C,D, Supporting Information). This indicates that the capacitive currents of the electrodes are equal for both scan rates.

In order to understand charge transport at the electrode–electrolyte interface and its effect on capacitive desalination, electrochemical impedance spectroscopy (EIS) measurement was carried out for both anode and cathode. EIS was performed in 1 M NaCl solution by applying 10 mV sinusoidal AC signal to the working electrode (here, graphite electrode coated with carbon material), and the frequency of the input signal was varied from 5 MHz to 1 mHz. The total impedance of the electrochemical cell was recorded at 10 dB per decade of the applied frequency, and the Nyquist plots of both cathode and anode are shown in Figure S9A,B in the Supporting Information. The Nyquist plot represents the impedance of the working electrode at each frequency. An equivalent circuit was deduced by fitting the impedance data with the experimental Nyquist profile of the individual electrode. Fitting values of an equivalent circuit of both cathode and anode are shown in Table S1 in the Supporting Information. Each circuit element, which is discussed in the caption of Figure S9C in the Supporting Information, is analogous to different interfacial electrochemical phenomena. These phenomena are involved with i) diffusion of bulk ions to the electrode–electrolyte interface, ii) charge transfer through adsorption and desorption of ions at the electrode surface ( $R_{\text{ct}}$ ), and iii) charge transport through the active carbon material to the graphite electrode (current collector, R1). Analysis of Nyquist plots and corresponding equivalent circuits revealed internal resistance of the anode ( $\approx 38.3 \Omega$ ) to be higher than the cathode ( $\approx 12.5 \Omega$ ). This signifies that the electronic conductivity of the cathode material is higher than the anode material. Therefore, at the same scan rate, the capacitive current is lower for the anode compared to the cathode (Figure S8, Supporting Information). However, charge transfer resistance is almost the same for the two electrodes (for cathode  $\approx 7.1 \Omega$  and anode 9.8  $\Omega$ ), which is attributed to the same adsorption and desorption rate of ions on the electrodes. CDI works on the principle of physical adsorption/desorption of ions. However, there was no significant difference in adsorption (charge) and desorption (discharge) rates. Even after 3 h of continuous adsorption and desorption cycles, electrode surface was usually regenerated in CDI technology to recover the active sites of the electrode for further adsorption and desorption processes. However, there is a difference in diffusion impedance [ $Z_{\text{D}} = C3 \parallel R3$ ] between anode and cathode, i.e., R3 of the anode is three times higher

than the cathode, attributed to the slightly lower adsorption rate at the surface of the anode (Table S1, Supporting Information).

### 2.3. Adsorption–Desorption Experiment of the Electrode

Adsorption–desorption measurement was performed in batch mode with single electrode pair (cathode and anode, each of the dimensions  $3 \times 5 \text{ cm}^2$ ) immersed in 1000 ppm of 80 mL.

NaCl solution and a DC potential of  $\pm 1.6 \text{ V}$  was applied across them. After 360 s, a decrease in the concentration of the solution to 970 ppm during the adsorption cycle was noticed. After reversing the terminal, complete desorption was noticed at 200 s to reach the initial concentration (1000 ppm), as shown in Figure 2A.

To get insights into the adsorption and desorption kinetics, both adsorption and desorption profiles were analyzed at different time segments. A similar experiment was reported in

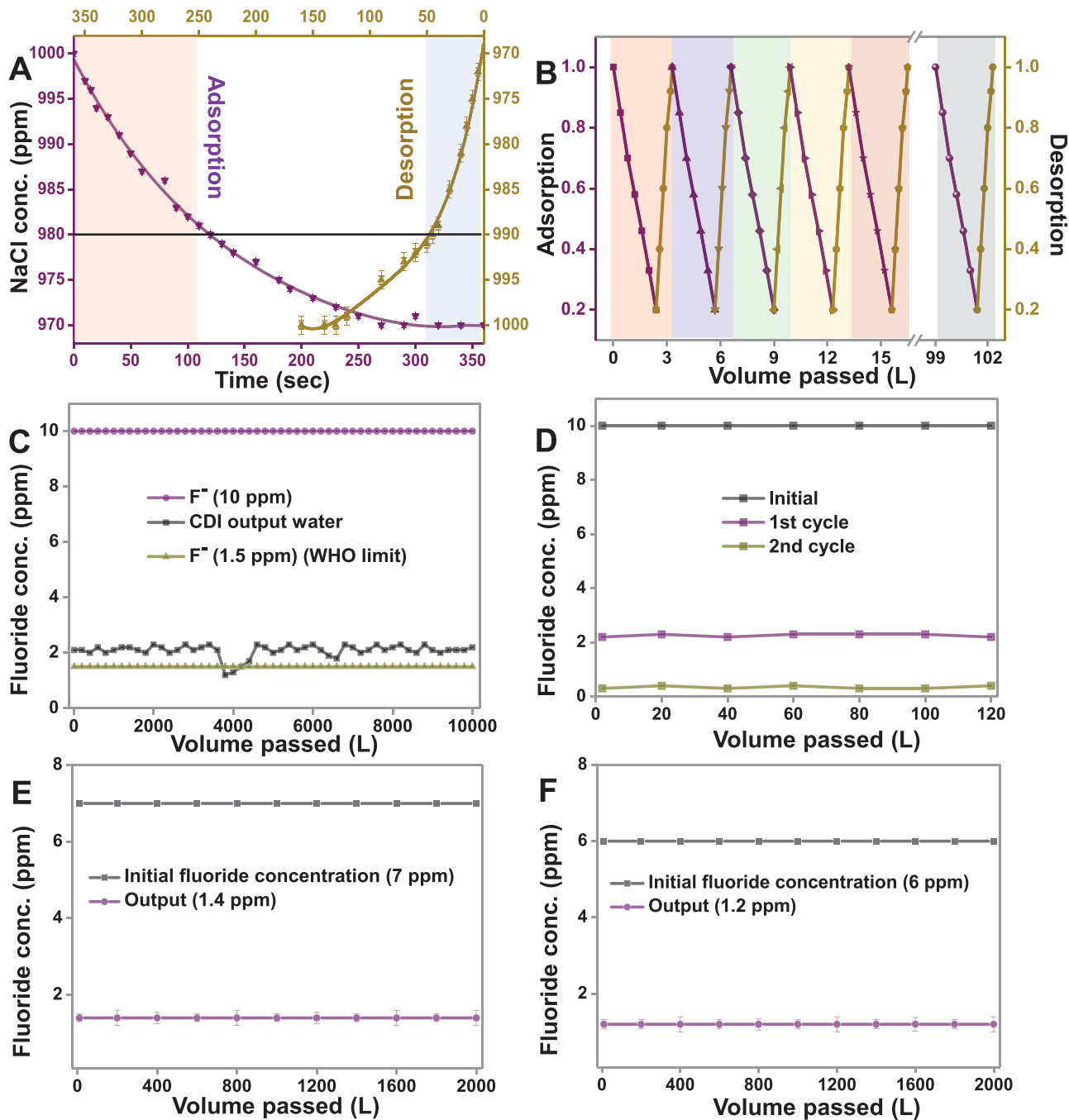


**Figure 2.** A) Single adsorption–desorption cycle containing 1000 ppm of NaCl in batch mode and B) adsorption–desorption performance in a continuous flow-through mode for multiple cycles, CDI performance for the removal of fluoride ion in tap water with initial concentration C) 10 ppm for 10 000 L, D) 10 ppm for a double pass for 120 L, E) 7 ppm for 2000 L, and F) 6 ppm for 2000 L.

our previous work.<sup>[31]</sup> In this work, fast adsorption kinetics was observed for 20 ppm in the first 125 s, while desorption of the same concentration of ions was seen in 45 s. Therefore, in flow-through experiments (when NaCl solution was passed through the cell), the time of adsorption/desorption was kept at 120/45 s to achieve maximum desalination efficiency. Figure 2B shows the efficiency of CDI electrodes in a flow-through experiment for multiple cycles (for 30 cycles). The initial concentration was kept at 1000 ppm, and the output concentration was found to be 200 ppm after 120 s of adsorption. After desorption, the concentration in the rejected water was measured to be 3140 ppm after 45 s at a flow rate of 120 L h<sup>-1</sup>.

Different experiments were carried out to evaluate the CDI performance for the removal of F<sup>-</sup> from input feed water. Different concentrations of F<sup>-</sup> were spiked in tap water, and the removal efficiency was measured. The initial TDS of tap water was ≈950 ppm, and the quantitative analysis of ions was measured by ion chromatography (IC). When the initial concentration of F<sup>-</sup> was 10 ppm, the output concentration of the same was found to be 2–2.1 ppm, after passing 10 000 L of water through the electrochemical cell during capacitive desalination (Figure 2C). The reduction of TDS was around 80%, i.e., from ≈1000 to ≈200 ppm. However, a sudden decrease in fluoride concentration below 2 ppm was witnessed (black trace of Figure 2C) when 4000 L of tap water was passed during the experiment. This fluctuation might be because of lower TDS of input tap water below a certain value. The output water having F<sup>-</sup> concentration of 2–2.1 ppm was then passed through the CDI cell for the second cycle (i.e., double pass), and the concentration of F<sup>-</sup> reduced to 0.4 ppm, which is below the acceptable limit in drinking water as per WHO's standard (Figure 2D). Therefore, for a higher concentration of F<sup>-</sup>, a double pass is required to bring the F<sup>-</sup> concentration below 1.5 ppm. However, the removal efficiency depends on the flow rate, initial TDS, and the presence of co-ions.

The typical concentration of F<sup>-</sup> in groundwater and surface water bodies of fluoride-affected areas in India was reported to be 0.5–6 ppm (Table 1). Few places had fluoride ion concentrations higher than 10 ppm, as in Prakasham district in Andhra Pradesh, Unnao district in Uttar Pradesh, and Karbianglong district in Assam. When F<sup>-</sup> concentrations of 7 and 6 ppm were spiked into the input tap water, output concentrations of F<sup>-</sup> were observed to be 1.4 and 1.2 ppm, respectively (Figure 2E,F). The observed result suggests that the CDI module could efficiently remove F<sup>-</sup> (below WHO limit) from water with an input F<sup>-</sup> concentration of ≈7 ppm or lower. For higher concentrations (above 7 ppm), a double pass methodology is required. Additionally, CDI performance using different concentrations of F<sup>-</sup> was also studied, in which the initial concentration of the F<sup>-</sup> was maintained as 100, 50, 10 ppm (Figure S10A–C, Supporting Information). Moreover, the effect of different TDS and flow rates were also studied with an input concentration of 10 ppm of F<sup>-</sup> (Figure S10D, Supporting Information).

Effect of removal efficiency of F<sup>-</sup> at an input concentration of 6 ppm was also examined with variation in TDS and flow rate. Initially, TDS of tap water was measured to be 1050 ppm, which, upon passing through the CDI module, reduced to 210 ppm in the output water. Similarly, when 210 and 50 ppm of water were passed through the CDI module, the output water was at

**Table 1.** Typical concentration of fluoride ions found at fluoride-affected areas in India.

S. no.	First author(ref.)	Year	State/location	Fluoride conc. [ppm]
1	N. Subba Rao <sup>[32]</sup>	2003	Andhra Pradesh/Guntur	0.60–2.30
2	N. Subba Rao <sup>[33]</sup>	2003	Andhra Pradesh/ Anantapur	0.56–5.80
3	P. D. Sreedevi <sup>[34]</sup>	2006	Andhra Pradesh	0.38–4.00
4	D. Sujatha <sup>[35]</sup>	2003	Andhra Pradesh/Ranga Reddy	0.40–4.80
5	J. Dutta <sup>[36]</sup>	2010	Assam/Sonitpur	0.17–5.60
6	N. J. Raju <sup>[37]</sup>	2009	Uttar Pradesh/ Sonbhadra	0.48–6.70
7	P. Sharma <sup>[38]</sup>	2012	Assam/Nalbari	0.02–1.56
8	S. Ramanaiah <sup>[39]</sup>	2006	Andhra Pradesh/ Prakasam	0.50–9.0
9	S. Gupta <sup>[40]</sup>	2006	West Bengal/Birbhum	0.01–1.95
10	Meenakshi <sup>[41]</sup>	2004	Haryana/Jind	0.3–6.9
11	G. Karthikeyan <sup>[42]</sup>	2000	Tamil Nadu/ Dharmapuri	0.98–5.60
12	P. Kotecha <sup>[43]</sup>	2012	Gujarat/Vadodara	0.02–4.17
13	N. Sankaramakrishnan <sup>[44]</sup>	2008	Uttar Pradesh/Kanpur	>1.5
14	C. R. Ramakrishnaiah <sup>[45]</sup>	2009	Karnataka/Tumkur	0.02–3.2
15	A. Shivashankara <sup>[46]</sup>	2000	Karnataka/Gulbarga	0.6–13.4
16	G. Viswanathan <sup>[47]</sup>	2010	Tamil Nadu/Dindigul	0.76–3.17
17	M. Bishnoi <sup>[48]</sup>	2007	Haryana/Rohtak	0.03–2.09
18	D. V. Reddy <sup>[49]</sup>	2010	Telangana/Nalgonda	0.50–7.00
19	D. R. R. Sarma <sup>[50]</sup>	1997	Andhra Pradesh/ Visakhapatnam	0.24–8.10
20	S. K. Jha <sup>[51]</sup>	2010	Uttar Pradesh/Unnao	0.8–13.9
21	M. Arif <sup>[52]</sup>	2012	Rajasthan/Nagaur	0.4–6.6
22	S. Yadav <sup>[53]</sup>	2011	Uttar Pradesh/Rampur	0.32–1.80
23	P. Kotoky <sup>[54]</sup>	2010	Assam/Karbi Anglong	0.95–20.60
24	A. C. Samal <sup>[55]</sup>	2015	West Bengal/Purulia	0.01–1.6
25	H. Pauwels <sup>[56]</sup>	2015	Andhra Pradesh/ Maheshwaram	0.26–3.73
26	K. S. Patel <sup>[57]</sup>	2017	Chhattisgarh/ Rajnandgaon	3.7–27
27	S. Manikandan <sup>[58]</sup>	2014	Tamil Nadu/Krishnagiri	0.50–5.45

50 and 20 ppm, respectively. Water samples of different TDS, each of 120 L volume, were collected from the IITM tap water, and further, F<sup>-</sup> was spiked in each water sample in such a way that the final concentration of F<sup>-</sup> was maintained at 6 ppm. After performing desalination through CDI, the output concentrations of fluoride were found to be 1.2, 0.8, 0.5 ppm for input TDS of 1050, 210, and 50 ppm, respectively (Figure 3A). Even when the TDS of input water was reduced to below 50 ppm, and the F<sup>-</sup> concentration was kept fixed at 6 ppm, the output F<sup>-</sup> concentration was found to be 0.5 ppm. The flow rate was kept fixed at 120 L h<sup>-1</sup> for the above experiments.

F<sup>-</sup> removal efficiency was also checked as a function of flow rate (Figure 3B). With input concentrations of F<sup>-</sup> and TDS at 6 and 1050 ppm, respectively, the output concentrations of F<sup>-</sup>

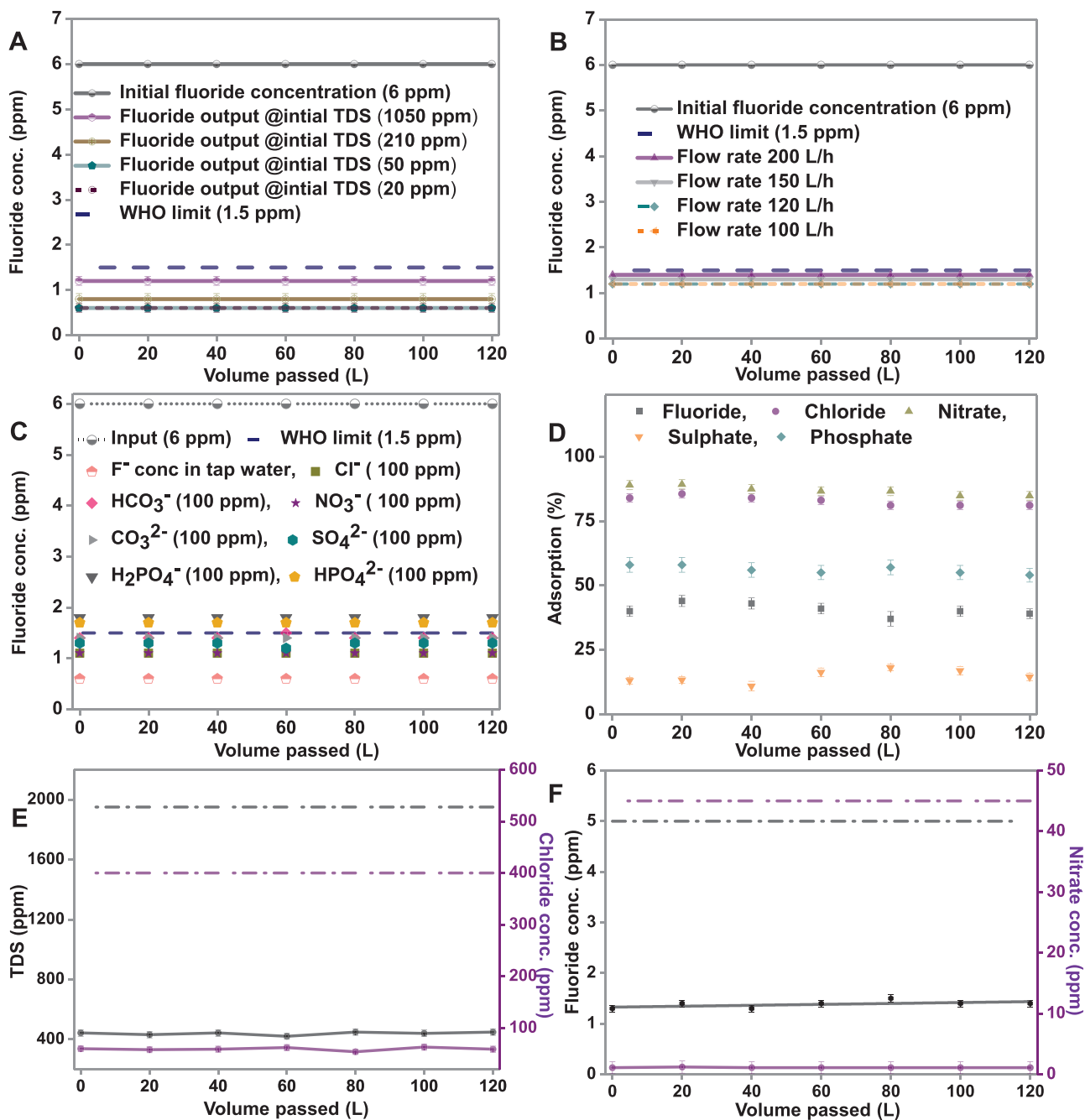


**Figure 3.** CDI performance for removing  $F^-$  at an initial concentration of 6 ppm at A) different initial TDS and B) different flow rates, C) different co-ions spiked in tap water, and D) adsorption efficiency for anions in a mixture. Effect of E) TDS and  $Cl^-$ , and F)  $F^-$  and  $NO_3^-$  were studied on the CDI performance.

were observed as 1.4, 1.3, and 1.2 ppm with flow rates of 200, 150, and 120  $L h^{-1}$ , respectively. The limit of removal efficiency is attributed to the constraint of flow rate, as the ions do not have enough time to get adsorbed onto the electrodes. The fluoride removal efficiency of CDI in the presence of co-ions was also investigated. At a constant concentration of 6 ppm of  $F^-$ , CDI experiments were performed in the presence of  $Cl^-$ ,  $NO_3^-$ ,  $HPO_4^{2-}$ ,  $H_2PO_4^-$ ,  $SO_4^{2-}$ ,  $HCO_3^-$ , and  $CO_3^{2-}$ , each at 100 ppm. The removal efficiency of  $F^-$  exhibited a negligible effect for

100 ppm  $Cl^-$ ,  $NO_3^-$ , or  $SO_4^{2-}$  (Figure 3C). However, the adsorption efficiency of the electrode decreased drastically when phosphates ( $HPO_4^{2-}$  and  $H_2PO_4^-$ ) or bicarbonate ( $HCO_3^-$ ) were added to the input solution (Figure 3C).

Selectivity and the removal efficiency of  $F^-$  were also studied in the presence of a mixture of  $Cl^-$ ,  $NO_3^-$ ,  $SO_4^{2-}$ ,  $F^-$ , and  $PO_4^{3-}$ , each at 100 ppm (Figure 3D). The data suggested that ion adsorption kinetics follows the following order:  $NO_3^- \geq Cl^- > PO_4^{3-} > F^- > SO_4^{2-}$ . Figure 3E,F demonstrates

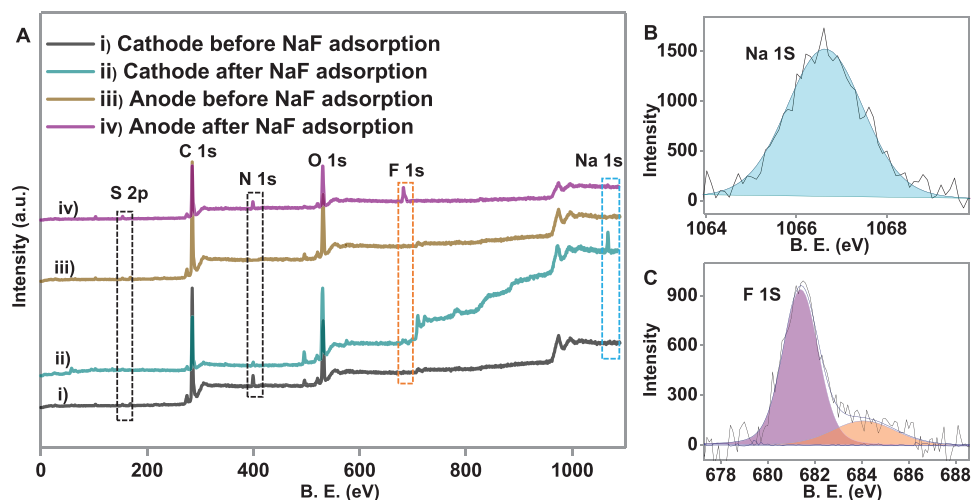


**Figure 4.** A) XPS survey spectra of the material after single-stage adsorption on i) cathode and iii) anode (before adsorption); ii) cathode and iv) anode (after NaF adsorption), B) and C) are the deconvoluted XPS spectra of Na 1s (light blue) and F 1s (pink@681.4 eV and orange color@684.5 eV) for cathode and anode, respectively after NaF adsorption.

the effect of TDS,  $\text{Cl}^-$ , and  $\text{NO}_3^-$  on the adsorption of  $\text{F}^-$ . When synthetic water (TDS maintained at  $\approx 1957$ ) containing 5 ppm of  $\text{F}^-$ , along with 400 ppm of  $\text{Cl}^-$  and 45 ppm of  $\text{NO}_3^-$ , was passed through the CDI system, the output concentration of  $\text{F}^-$  was 1.2 ppm, and a significant reduction in TDS (from  $\approx 1957$  to  $\approx 415$  ppm) was also observed (after one cycle). Our results show that  $\text{F}^-$ -contaminated real water could be purified efficiently using this technique.

Post adsorption, electrodes were characterized thoroughly using both SEM EDS and X-ray photoelectron spectroscopy (XPS) to confirm the adsorption of  $\text{F}^-$ . Figure S11 in the Supporting Information shows the SEM EDS spectrum of the electrodes after the adsorption of NaF onto them. Figure S11A in the Supporting Information shows that cations ( $\text{Na}^+$  ions) were adsorbed on the cathode, confirmed by elemental mapping (shown in the inset). Similarly, Figure S11B in the Supporting Information confirmed that counter ions ( $\text{F}^-$  ions) were adsorbed on the anode surface. **Figure 4A** shows the XPS survey spectra of both anode and cathode before and after the adsorption of NaF solution. In the XPS survey spectra, no significant changes were observed in the binding energies of carbon, nitrogen, oxygen, and sulfur of both cathode and anode, even after electrochemical adsorption, which justifies that adsorption is physical in nature. The XPS survey spectra (Figure 4A) and deconvoluted XPS spectra (Figure 4B,C) revealed the adsorption of  $\text{Na}^+$  and  $\text{F}^-$  ions at cathode and anode, respectively. The XPS data also suggest that only  $\text{Na}^+$  and  $\text{F}^-$  ions were adsorbed on cathode and anode, respectively. Moreover, deconvoluted XPS spectra of C 1s at both electrodes before and after NaF adsorption revealed no significant changes in binding energy, which validates that electroadsorption is physical in nature (Figure S12, Supporting Information).

**Figure 5A,B** shows that CDI can efficiently remove other common toxic metal ions such as  $\text{As}^{3+/5+}$  and  $\text{Pb}^{2+}$  from water. To investigate the desalination performance of CDI for  $\text{As}^{3+/5+}$  removal, the input concentration of As was maintained at 40 ppb ( $\text{As}^{3+}:\text{As}^{5+} = 1:1$ ), and it was spiked into tap

water. The concentration of As in the permeate water (production water) was reduced to  $\approx 5.6$  ppb when the spiked water was run through the CDI unit, which is below the acceptable limit set by WHO (Figure 5A). Thus, permeate water after desalination is fit for drinking purposes. Moreover, 200 ppb of  $\text{Pb}^{2+}$  was also spiked into the tap water and was run through the CDI cell; the permeate water concentration of  $\approx 7$  ppb was obtained, which is below the Environmental Protection Agency (EPA) and WHO limits (Figure 5B). To check the repeatability, the adsorption experiments for Pb and As were performed five times ( $\approx 1100$  L of water was tested for both ions). The detailed adsorption mechanisms are shown in Figures S13–S16 in the Supporting Information. SEM EDS data confirmed that only cations were adsorbed on the cathode and anions on the anode. Figure 5C,D displays the XPS survey spectra of the cathode after adsorption of As and Pb, which revealed that both As and Pb could be removed. Insets of both Figure 5C,D show deconvoluted spectra of As and Pb on the cathode. XPS data confirm that cations are removed at the cathode and anions at the anode. XPS data also indicate that ions are almost completely removed from both the electrodes, and adsorption sites at the electrode surfaces are regenerated.

### 3. Conclusion

The present work demonstrates the desalination performance of a CDI prototype against brackish water containing  $\text{F}^-$  along with other toxic species ( $\text{As}^{3+/5+}$  and  $\text{Pb}^{2+}$ ), at an industrial scale. The CDI technology efficiently removes  $\text{F}^-$  concentration below the WHO limit when the concentration of fluoride in feed water is  $\approx 7$  ppm. For higher input  $\text{F}^-$  concentration, a double pass is required to bring the  $\text{F}^-$  concentration below the prescribed limit. The fluoride removal efficiency of the electrodes depends on flow rate, initial TDS, and co-ions present in the water. Moreover, the removal efficiency is reduced in the presence of phosphates and bicarbonates



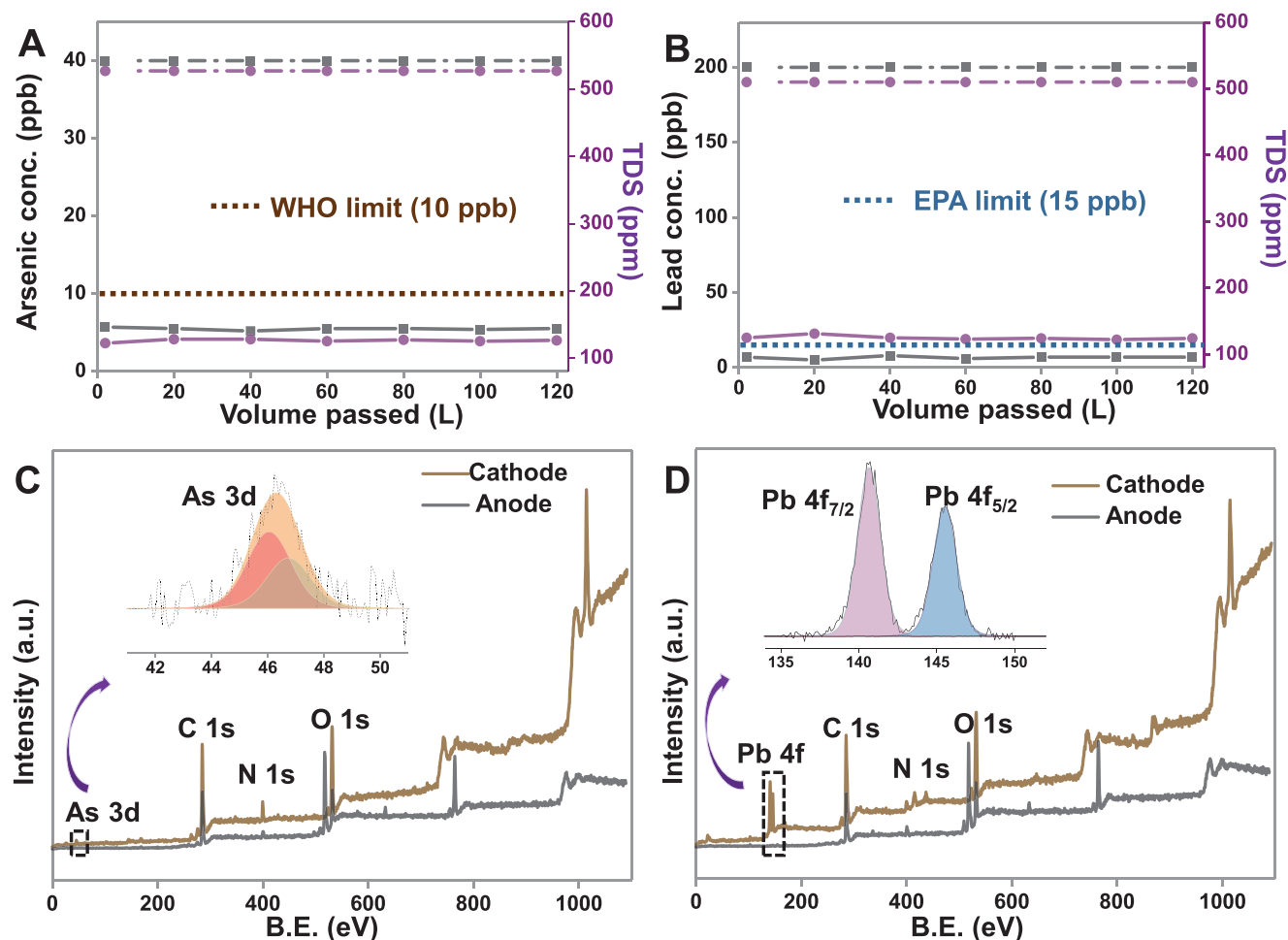


**Figure 5.** CDI performance for the removal of toxic ions (arsenic and lead) in tap water with initial concentration: A) 40 ppb of As (as  $\text{As}^{3+/5+}$ ) and B) 200 ppb of Pb (as  $\text{Pb}^{2+}$ ); XPS survey spectra of the material after single-stage adsorption on cathode and anode C) after arsenic adsorption, and D) after lead adsorption. Deconvoluted XPS spectra of As 3d Pb 4f regions are shown in the inset.

in the water. Additionally, the CDI prototype was utilized to remove other toxic species such as  $\text{As}^{3+/5+}$  and  $\text{Pb}^{2+}$  from contaminated water. The electrodes were characterized extensively before and after adsorption to check the adsorption mechanism, which revealed that the process (adsorption/desorption) is physical in nature. Electrodes also exhibited high electroadsorption performance, fast deionization rate, and good regeneration capability. The CDI technology could thus be an efficient and alternate way to remove toxic ions from brackish water.

#### 4. Experimental Section

**Materials:** Sodium chloride (NaCl) and glacial acetic acid were purchased from RANKEM, India. Sodium hydroxide (NaOH) was purchased from Merck. Sodium dihydrogen ortho-phosphate ( $\text{NaH}_2\text{PO}_4$ ), disodium phosphate ( $\text{Na}_2\text{HPO}_4$ ), and sodium fluoride (NaF) were purchased from Fisher Scientific, India. Sodium sulfate ( $\text{Na}_2\text{SO}_4$ ), sodium nitrate ( $\text{NaNO}_3$ ), sodium nitrite ( $\text{NaNO}_2$ ), sodium carbonate ( $\text{Na}_2\text{CO}_3$ ), sodium bicarbonate ( $\text{NaHCO}_3$ ), and potassium chloride (KCl) were purchased from RANKEM, India. All chemicals were of analytical grade and were used as received without further purification.

**Instrumentation:** SEM equipped with EDAX (FEI Quanta 200, Czechoslovakia) was used to record the surface morphology, elemental composition, and elemental mapping of the samples. Also, HRSEM images of the electrode materials were obtained through Thermo Scientific Verios G4 UC SEM. XPS measurements were done with an Omicron ESCA Probe spectrometer with polychromatic Mg  $K\alpha$  X-rays. Most of the spectra were deconvoluted to their component peaks using the Casa XPS software. The energy resolution of the spectrometer was set at 0.1 eV at pass energy of 20 eV. Binding energy was corrected with respect to C 1s at 284.5 eV. Raman spectra were obtained with a WITec GmbH, Alpha-SNOM alpha 300 S confocal Raman microscope having a 532 nm laser as the excitation source. The Eutech Cyber scan PC650 multiparameter monitor supplied by Thermo Scientific, India, was used for measuring conductivity, pH, and fluoride concentration. Ion-exchange chromatography or Ion chromatography (883 Basic IC plus model) was used for quantitative analysis of common anions (such as fluoride, chloride, nitrate, nitrite, and sulfate) in an aqueous solution. Metrosep A Supp 5 – 250/4.0 column (Order number: 6.1006.530) was used, and polyvinyl alcohol with quaternary ammonium groups was used as carrier materials for anion detection. Sodium carbonate ( $3.2 \times 10^{-3}$  M) and sodium bicarbonate ( $1 \times 10^{-3}$  M) mixture were used in 1:1 ratio for anion sample detection. In addition,  $100 \times 10^{-3}$  M  $\text{H}_2\text{SO}_4$  and deionized water (DI) were used as suppressor eluents for cleaning the column.

The electrochemical capacitive behavior of carbon electrodes was determined by CV using a CH Electrochemical Analyzer (CH 600A). The

CV was performed at various scan rates (1–100 mV s<sup>-1</sup>) in a potential range of -1.0 to +1.0 V. The specific capacitance was calculated from the CV curve based on the following equation

$$C_s = \left( \frac{1}{mR\Delta V} \right) \times \int I(V) dV \quad (1)$$

where  $C_s$  is the specific capacitance,  $m$  is the mass of the active material,  $R$  is the scan rate,  $dV$  is the potential window of scanning and  $\int I(V) dV$  is the integral area under the CV curve. The electrochemical capacitive behavior of the electrode materials was determined by CV.

All electrochemical experiments were carried out at room temperature using 1 M NaCl and 1 M NaF electrolytes solution in a three-electrode cell adopted with a carbon electrode as the working electrode, a platinum electrode as the counter electrode, and Ag/AgCl (3 M KCl) as the reference electrode. The Eutech Cyber scan PC650 multiparameter monitor supplied by Thermo Scientific, India, was used for ionic conductivity and fluoride ion measurement.

**Fabrication of CDI Electrodes:** Normally polyvinyl fluoride (PVDF) and polyvinyl alcohol (PVA) are used as binders for CDI electrodes. Here, for preparation of anode and cathode materials, PVDF and carbon material were taken in different ratios in dimethylformamide, and different optimizations were done. Best electrode material was obtained after wet grinding for 4 h (using a normal grinder). The optimized electrode slurry was coated on both sides of graphite sheets (thickness ≈350 μm). Both coating was performed by doctor blade technique and curing of the coated electrode was done at 120 °C for 1.5 h. The coating thickness of carbon materials was about ≈125 μm in both sides (Figure 1E,F). Further, optimized electrodes were coated with ion exchange resins (IERS) using a spray gun and dried with an IR heater at 340 °C for 1–2 min. Dried electrodes were kept under water until further use (Figure 1D). Finally, the dimension of the CDI electrodes was maintained as ≈10 × 10 cm<sup>2</sup> for desalination purpose. The CDI module was designed with an assembly of hundred pairs of electrodes.

It was known that thickness of the electrode materials would play an important role in the performance of the cell. It was well known that the adsorption capacity of the electrode would be increased with increasing the material loading on the substrate. But, the optimized thickness of the active electrode material (both carbon material and ion-exchange resins (IERS)) on the substrate was the utmost criterion for the CDI electrode design. Moreover, the physical stability of the electrode would be lost with higher loading of the electrode material, and eventually, electrodes would also lose their adsorption efficiency. Therefore, the optimum thickness of the electrode material was taken care of for higher removal efficiency. In this case, the optimum thickness of ≈120–140 μm of carbon material coating with IERS thickness of 20–30 μm was maintained, on top of the active material. It was shown (Figure 2C) that there was no change of adsorption capacity observed even after passing 10 000 L of water continuously through the CDI cell. Therefore, it was concluded that this electrode material with optimum thickness was stable for the process of desalination.

**Fluoride Removal Experimental Set-Up for CDI:** CDI unit was built, as shown in the schematic in the Supporting Information (Figure S1, Supporting Information). A 0.5 HP pump was used in the unit. The flow rate of water was controlled by a valve from 100 to 200 L h<sup>-1</sup>. The unit consisted of three pre-filtration stages, a 50 μm cartridge for unsuspended particles, a carbon filter for organics, color, and odor, and 10 μm cartage for any smaller unsuspended particle. Before performing the desalination study using CDI cells, the raw water (DI) was passed through a UV chamber for bacterial remediation. The CDI cell consisted of 100 pairs of electrodes (each of the dimensions 10 × 10 cm<sup>2</sup>), and water was passed in flow-through mode. An interelectrode spacing of ≈0.2 mm was maintained with a nylon membrane for the electrode cell assembly. The electrochemical performance of the CDI cell was automated by electronic circuitry such that the adsorption cycle lasted for 120 s, and the desorption cycle for 45 s. The cells were connected to a DC power source, with voltage ranging from 0.8 to 2 V. The flow rate for all adsorption and desorption cycles was maintained at 120 L h<sup>-1</sup>.

The CDI modules generally were expressed as electrode pairs; if the number of CDI electrode pairs were increased, the adsorption efficiency would be increased. Consequently, the removal efficiency would be increased. In the CDI module with 100 electrode pairs, ion adsorption capacity or salt removal capacity was 80% with an input TDS of 1000–3000 ppm of NaCl solution. The production capacity of the CDI module was 2000 L per day (LPD). It was seen that maximum water rejection in this prototype was ≈18% for all the contaminants.

CDI was explored extensively for brackish water desalination under the premise of being energetically competitive with RO. It was seen that quanta of energy consumed by different CDI and RO were comparable in identical conditions. However, the energy expenditure of experiments was not reported which were carried out using membrane capacitive deionization (MCDI) prototype. However, it was reported that the energy requirement of MCDI was two to three times higher than RO for brackish water desalination (using the same condition such as water recovery (WR) = 80%, salt rejection ( $R_{\text{salt}}$ ) = 80%, flux ( $J_w$ ) = 10.0 L m<sup>-2</sup> h<sup>-1</sup>, and feed salinity of 34.22 × 10<sup>-3</sup> M (2 g L<sup>-1</sup>)).<sup>[59]</sup> It was also shown that in the same condition, energy consumption of MCDI (≈0.4 kWh m<sup>-3</sup>) was less than CDI (≈2.5 kWh m<sup>-3</sup>).<sup>[59]</sup> Furthermore, it was seen that for these desalination conditions (water recovery (WR) = 93.5%, salt rejection ( $R_{\text{salt}}$ ) = 80%, flux ( $J_w$ ) = 11.9 L m<sup>-2</sup> h<sup>-1</sup>, and a feed salinity of 40 × 10<sup>-3</sup> M), the energy consumption of RO (≈0.5 kWh m<sup>-3</sup>) was higher than of MCDI (≈0.4 kWh m<sup>-3</sup>).<sup>[59]</sup> As similar desalination conditions were maintained for brackish water using this prototype, it was believed that energy consumption of this prototype was similar during desalination. The cost of desalination was also calculated using this CDI prototype, which was ≈3–4 paisa (US\$0.00040 to 0.00054) per liter.

**TISAB (Total Ionic Strength Adjustment Buffer) II Preparation:** First, 500 mL DI water was taken in 1 L beaker, and 57 mL of glacial acetic acid was added to it; the solution mixture was then allowed to stir for 10 min. Subsequently, 58 g of sodium chloride (NaCl) was added to the prepared solution and stirred for another 1 h at room temperature. Further, 5 M sodium hydroxide (NaOH) was slowly added into the solution until a pH of 5.3–5.4 was achieved. Later, the solution was shaken vigorously, cooled to room temperature, and kept in a 1 L conical flask. The solution was aged overnight before use. For the fluoride concentration measurement, both sample and TISAB mixture were taken in 1:1 ratio.

## Supporting Information

Supporting Information is available from the Wiley Online Library or from the author.

## Acknowledgements

M.R.I. and S.S.G. contributed equally to this work. The authors thank the Department of Science and Technology (DST) and its Water Technology Initiative (WTI) for constantly supporting this research program. M.R.I. thanks the Council of Scientific & Industrial Research (CSIR) for his SRF fellowships. S.S.G. and S.K.J. thank IIT Madras for their research fellowships.

## Conflict of Interest

The authors declare no conflict of interest.

## Data Availability Statement

The data that support the findings of this study are available on request from the corresponding author.

## Keywords

arsenic, capacitive deionization, desalination, fluoride, lead, water purification

Received: November 16, 2021

Revised: January 6, 2022

Published online: January 27, 2022

- [1] J. Schewe, J. Heinke, D. Gerten, I. Haddeland, N. W. Arnell, D. B. Clark, R. Dankers, S. Eisner, B. M. Fekete, F. J. Colón-González, S. N. Gosling, H. Kim, X. Liu, Y. Masaki, F. T. Portmann, Y. Satoh, T. Stacke, Q. Tang, Y. Wada, D. Wisser, T. Albrecht, K. Frieler, F. Piontek, L. Warszawski, P. Kabat, *Proc. Natl. Acad. Sci. USA* **2014**, *111*, 3245.
- [2] M. A. Shannon, P. W. Bohn, M. Elimelech, J. G. Georgiadis, B. J. Mariñas, A. M. Mayes, *Nature* **2008**, *452*, 301.
- [3] P. Bhattacharya, A. C. Samal, S. Banerjee, J. Pyne, S. C. Santra, *Environ. Sci. Pollut. Res. Int.* **2017**, *24*, 20300.
- [4] S. Mukherjee, M. Shah, K. Chaudhari, A. Jana, C. Sudhakar, P. Srikrishnarka, M. R. Islam, L. Philip, T. Pradeep, *ACS Omega* **2020**, *5*, 25253.
- [5] R. Liu, J. Qu, *J. Environ. Sci.* **2021**, *110*, 178.
- [6] S. Mukherjee, A. A. Kumar, C. Sudhakar, R. Kumar, T. Ahuja, B. Mondal, P. Srikrishnarka, L. Philip, T. Pradeep, *ACS Sustainable Chem. Eng.* **2019**, *7*, 3222.
- [7] L. Weerasundara, Y. S. Ok, J. Bundschuh, *Environ. Pollut.* **2021**, *268*, 115668.
- [8] S. V. Flanagan, R. B. Johnston, Y. Zheng, *Bull. W. H. O.* **2012**, *90*, 839.
- [9] WHO, *World Health Organization Expert Committee on Oral Health Status and Fluoride Use: Fluorides and Oral Health*, World Health Organization, Geneva **1994**.
- [10] E. Shaji, M. Santosh, K. V. Sarath, P. Prakash, V. Deepchand, B. V. Divya, *Geosci. Front.* **2021**, *12*, 101079.
- [11] M. Mohapatra, S. Anand, B. K. Mishra, D. E. Giles, P. Singh, *J. Environ. Manage.* **2009**, *91*, 67.
- [12] M. M. El-Masri, *Can. Nurse* **2014**, *110*, 14.
- [13] B. S. Bajwa, S. Kumar, S. Singh, S. K. Sahoo, R. M. Tripathi, *J. Radiat. Res. Appl. Sci.* **2017**, *10*, 13.
- [14] N. Radha, T. B. Pushpa, *Int. J. Eng. Res. Technol.* **2019**, *08*, 303.
- [15] S. S. Waghmare, T. Arfin, *Int. J. Innovative Sci. Eng. Technol.* **2015**, *2*, 560.
- [16] T. F. Lin, J. K. Wu, *Water Res.* **2001**, *35*, 2049.
- [17] K. Zhang, V. Dwivedi, C. Chi, J. Wu, *J. Hazard. Mater.* **2010**, *182*, 162.
- [18] V. Chandra, J. Park, Y. Chun, J. W. Lee, I.-C. Hwang, K. S. Kim, *ACS Nano* **2010**, *4*, 3979.
- [19] S. Yao, Z. Liu, Z. Shi, *J. Environ. Health Sci. Eng.* **2014**, *12*, 58.
- [20] A. K. Mishra, S. Ramaprabhu, *Desalination* **2011**, *282*, 39.
- [21] S. Vadahanambi, S.-H. Lee, W.-J. Kim, I.-K. Oh, *Environ. Sci. Technol.* **2013**, *47*, 10510.
- [22] A. A. Kumar, A. Som, P. Longo, C. Sudhakar, R. G. Bhui, S. S. Gupta, M. U. S. Anshup, A. Chaudhary, R. Kumar, T. Pradeep, *Adv. Mater.* **2017**, *29*, 1604260.
- [23] W. Chen, R. Parette, J. Zou, F. S. Cannon, B. A. Dempsey, *Water Res.* **2007**, *41*, 1851.
- [24] H.-T. Fan, X. Fan, J. Li, M. Guo, D. Zhang, F. Yan, T. Sun, *Ind. Eng. Chem. Res.* **2012**, *51*, 5216.
- [25] Q. Du, G. Li, S. Zhang, J. Song, Y. Zhao, F. Yang, *J. Hazard. Mater.* **2020**, *383*, 121170.
- [26] N. Selvanantharajah, P. Iyngaran, P. Abiman, N. Kuganathan, *C* **2021**, *7*, 23.
- [27] M. R. Islam, P. Khurana, P. Srikrishnarka, A. Nagar, M. Jash, S. K. Jennifer, M. A. Ganayee, M. Kumar, T. Pradeep, *Adv. Mater. Interfaces* **2021**, *8*, 2100533.
- [28] M. R. Islam, S. Sen Gupta, S. K. Jana, P. Srikrishnarka, B. Mondal, S. Chennu, T. Ahuja, A. Chakraborty, T. Pradeep, *Adv. Mater. Interfaces* **2021**, *8*, 2001998.
- [29] S. Sen Gupta, M. R. Islam, T. Pradeep, in *Advances in Water Purification Techniques*, (Ed: S. Ahuja), Elsevier, New York **2019**, pp. 165–202.
- [30] S. Porada, R. Zhao, A. van der Wal, V. Presser, P. M. Biesheuvel, *Prog. Mater. Sci.* **2013**, *58*, 1388.
- [31] R. Kumar, S. Sen Gupta, S. Katiyar, V. K. Raman, S. K. Varigala, T. Pradeep, A. Sharma, *Carbon* **2016**, *99*, 375.
- [32] N. S. Rao, *Hydrol. Sci. J.* **2003**, *48*, 835.
- [33] N. Subba Rao, D. John Devadas, *Environ. Geol.* **2003**, *45*, 243.
- [34] P. D. Sreedevi, S. Ahmed, B. Made, E. Ledoux, J. M. Gandolfi, *Environ. Geol.* **2006**, *50*, 1.
- [35] D. Sujatha, *Environ. Geol.* **2003**, *44*, 587.
- [36] D. Joydev, N. Manoranjan, C. Mridual, A. K. Misra, *Int. J. ChemTech Res.* **2010**, *2*, 1199.
- [37] N. J. Raju, S. Dey, K. Das, *Curr. Sci.* **2009**, *96*, 979.
- [38] P. Sharma, H. P. Sarma, C. Mahanta, *Environ. Earth Sci.* **2012**, *65*, 2147.
- [39] S. V. Ramanaiah, S. Venkata Mohan, B. Rajkumar, P. N. Sarma, *J. Environ. Sci. Eng.* **2006**, *48*, 129.
- [40] S. Gupta, S. Banerjee, *Fluoride* **2009**, *42*, 224.
- [41] V. K. G. Meenakshi, R. Kavita, A. Malik, *J. Hazard. Mater.* **2004**, *106*, 85.
- [42] G. Karthikeyan, A. Shunmugasundarraaj, *Fluoride* **2000**, *33*, 121.
- [43] P. V. Kotecha, S. V. Patel, K. D. Bhalani, D. Shah, V. S. Shah, K. G. Mehta, *Indian J. Med. Res.* **2012**, *135*, 873.
- [44] N. Sankaramakrishnan, A. K. Sharma, L. Iyengar, *Environ. Monit. Assess.* **2008**, *146*, 375.
- [45] C. R. Ramakrishnaiah, C. Sadashivaiah, G. Ranganna, *E-J. Chem.* **2009**, *6*, 523.
- [46] A. Shivashankara, Y. Shivarajashankara, H. Rao, G. Bhat, *Fluoride* **2000**, *33*, 66.
- [47] G. Viswanathan, S. Gopalakrishnan, S. Siva Ilango, *Water Res.* **2010**, *44*, 6186.
- [48] M. Bishnoi, S. Arora, *J. Environ. Biol.* **2007**, *28*, 291.
- [49] D. V. Reddy, P. Nagabhushanam, B. S. Sukhija, A. G. S. Reddy, P. L. Smedley, *Chem. Geol.* **2010**, *269*, 278.
- [50] D. R. Sarma, S. L. N. Rao, *Bull. Environ. Contam. Toxicol.* **1997**, *58*, 241.
- [51] S. K. Jha, A. K. Nayak, Y. K. Sharma, *Environ. Geochem. Health* **2010**, *32*, 217.
- [52] M. Arif, I. Hussain, J. Hussain, S. Sharma, S. Kumar, *Bull. Environ. Contam. Toxicol.* **2012**, *88*, 870.
- [53] S. Yadav, K. Rajesh, *Adv. Appl. Sci. Res.* **2011**, *2*, 197.
- [54] P. Kotoky, U. K. Tamuli, G. C. Borah, M. K. Baruah, B. K. Sarmah, A. B. Paul, K. G. Bhattacharyya, *Fluoride* **2010**, *43*, 157.
- [55] A. C. Samal, P. Bhattacharya, A. Mallick, M. M. Ali, J. Pyne, S. C. Santra, *Environ. Sci. Pollut. Res.* **2015**, *22*, 6220.
- [56] H. Pauwels, P. Négrel, B. Dewandel, J. Perrin, C. Mascré, S. Roy, S. Ahmed, *J. Hydrol.* **2015**, *525*, 302.
- [57] K. S. Patel, B. L. Sahu, N. S. Dahariya, A. Bhatia, R. K. Patel, L. Matini, O. Sracek, P. Bhattacharya, *Appl. Water Sci.* **2017**, *7*, 1817.
- [58] S. Manikandan, S. Chidambaram, A. L. Ramanathan, M. V. Prasanna, U. Karmegam, C. Singaraja, P. Paramaguru, I. Jainab, *Arabian J. Geosci.* **2014**, *7*, 273.
- [59] S. Porada, L. Zhang, J. E. Dykstra, *Desalination* **2020**, *488*, 114383.



## Supporting Information

for *Global Challenges*, DOI: 10.1002/gch2.202100129

Industrial Utilization of Capacitive Deionization  
Technology for the Removal of Fluoride and Toxic Metal  
Ions ( $\text{As}^{3+/5+}$  and  $\text{Pb}^{2+}$ )

*Md Rabiul Islam, Soujit Sen Gupta, Sourav Kanti Jana,  
and Thalappil Pradeep\**

## Supporting Information

**Industrial Utilization of CDI Technology for Removal of Fluoride and Toxic Species (As<sup>3+</sup>/<sup>5+</sup> and Pb<sup>2+</sup>)***Md Rabiul Islam,<sup>1#</sup> Soujit Sen Gupta,<sup>1#</sup> Sourav Kanti Jana<sup>1</sup> and Thalappil Pradeep<sup>1\*</sup>*

<sup>1</sup>*DST Unit of Nanoscience and Thematic Unit of Excellence, Department of Chemistry, Indian Institute of Technology Madras, Chennai-600036, India*

<sup>#</sup> *These authors are contributed equally to this work*

***Corresponding Author***

*\*E-mail: [pradeep@iitm.ac.in](mailto:pradeep@iitm.ac.in)*

**Thalappil Pradeep, DST Unit of Nanoscience (DST UNS) and Thematic Unit of Excellence (TUE), Department of Chemistry, Indian Institute of Technology Madras, Chennai 600036, India.**

**Tel.: +91-44 2257 4208; Fax: +91-44 2257 0545/0509**

## Table of Contents

S. No	Description	Page
1	Schematic of CDI experimental set-up	S-3
2	Photograph of CDI experimental set-up	S-4
3	SEM EDS and SEM images of carbon materials	S-5
4	SEM images and SEM EDS of cathode	S-6
5	SEM SEM images and SEM EDS of anode	S-7
6	Raman spectra of carbon materials	S-8
7	Cyclic voltammetry (CV) with varying scan rate and specific capacitance vs. scan rate for both electrodes	S-9
8	Cyclic voltammetry (CV) of both cathode and anode in different scan rates in 1 M NaCl and 1 M NaF electrolyte	S-10
9	Nyquist Plot of cathode, anode, and circuit for both electrodes.	S-11
10	CDI performance for removing of F <sup>-</sup> with different concentrations (100, 50, and 10 ppm) and the flow rate effect on 10 ppm input F <sup>-</sup> solution.	S-12
11	SEM EDS of NaF adsorption after single adsorption on cathode and anode.	S-13
12	Deconvoluted XPS spectra of C 1s of electrodes before and after NaF adsorption.	S-14
13	SEM EDS of cathode after Pb(NO <sub>3</sub> ) <sub>2</sub> adsorption.	S-15
14	SEM EDS of anode after Pb(NO <sub>3</sub> ) <sub>2</sub> adsorption.	S-16
15	SEM EDS of cathode after arsenic adsorption.	S-17
16	SEM EDS of anode after arsenic adsorption.	S-18
17	Fitting vales of an equivalent circuit of both electrodes	S-19

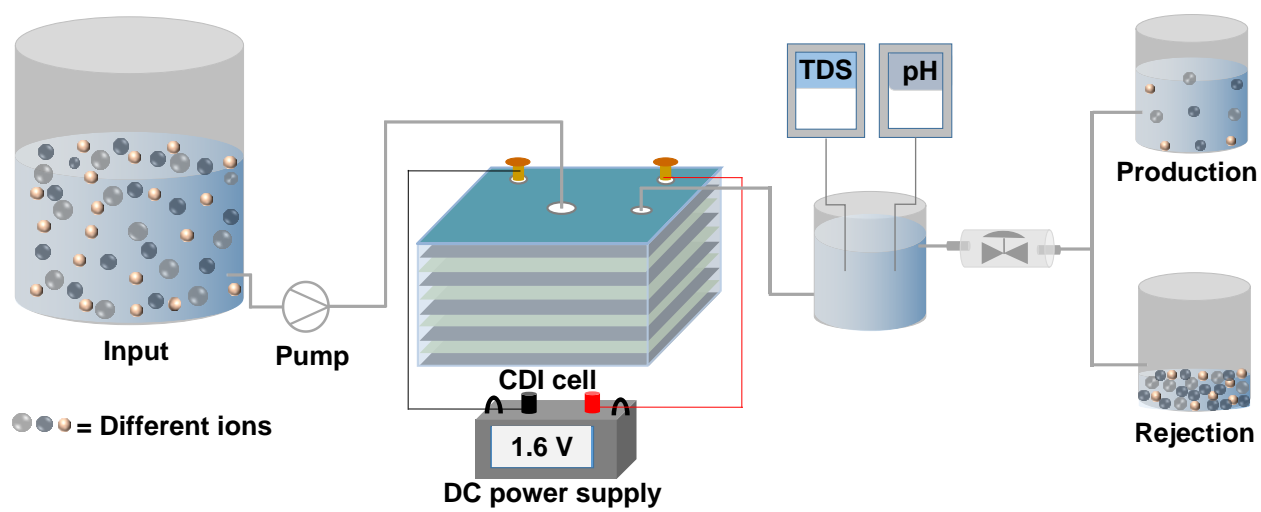


**Figure S1.** Schematic of CDI experimental set-up.

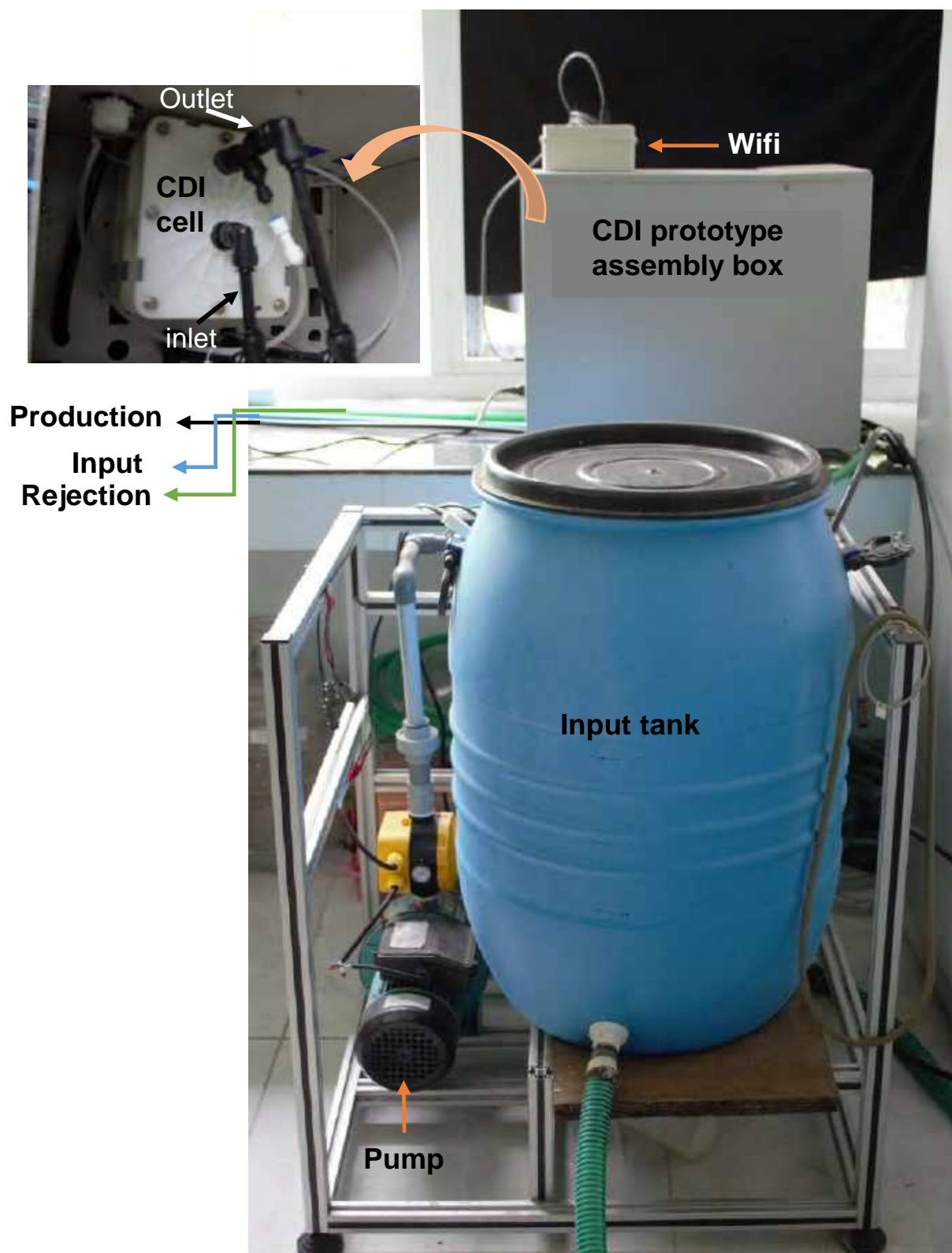


**Figure S2.** Photograph of the prototype of CDI experimental set-up. CDI box contains CDI cell and controlling electronic boards.

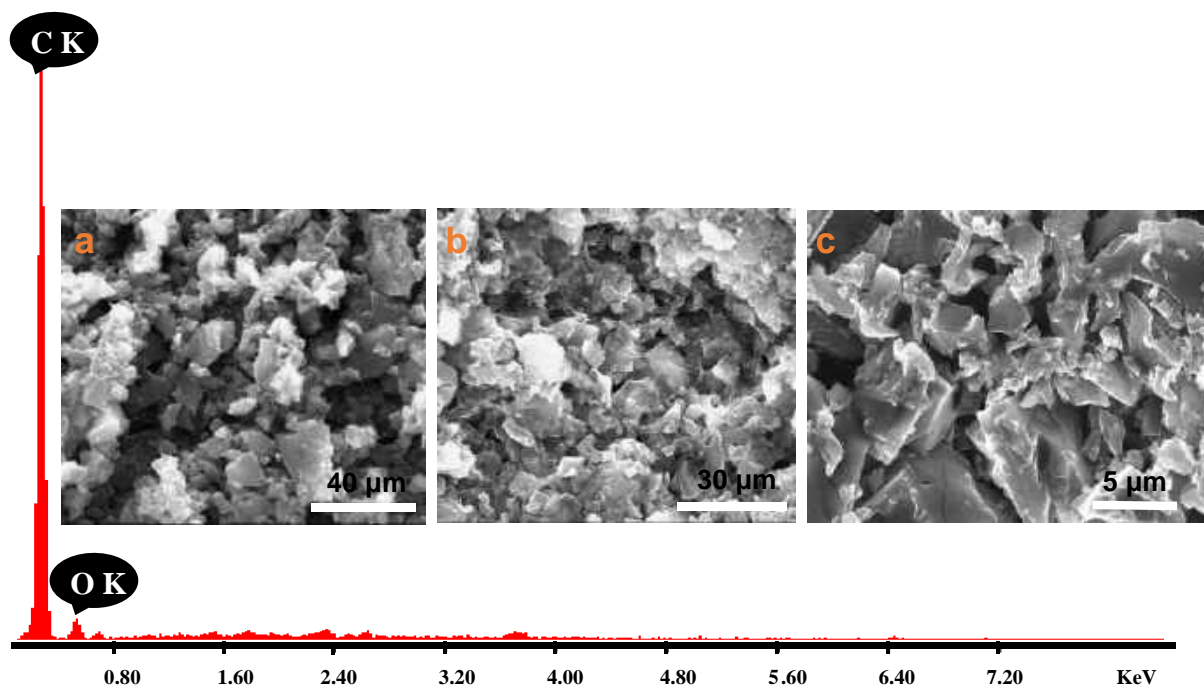


**Figure S3.** SEM EDS of carbon materials and SEM images are shown in the insets. (Scale bar is 40, 30, 5  $\mu\text{m}$  for a, b, c, respectively)

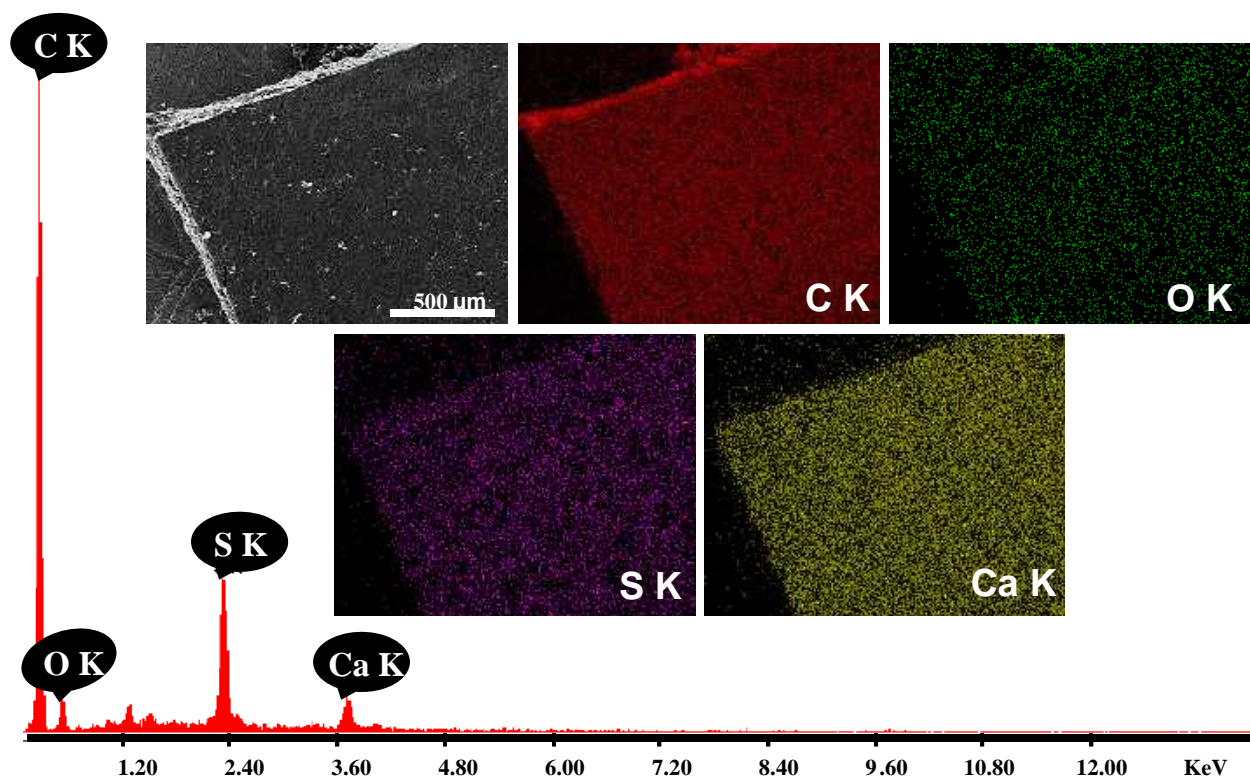


**Figure S4.** SEM EDS of the cation-exchange resin-coated electrode (cathode). The SEM image and the corresponding elemental mapping images are shown in the insets.

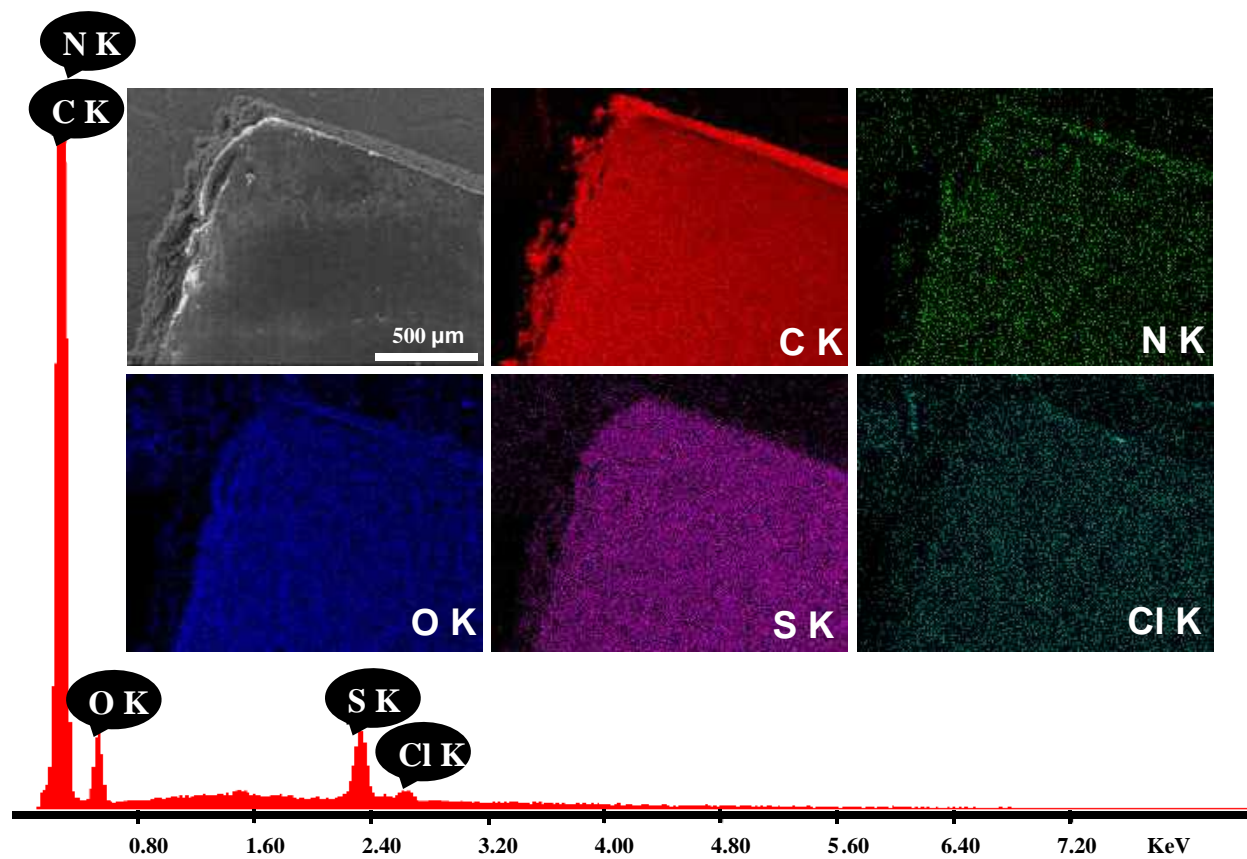


**Figure S5.** SEM EDS of the anion-exchange resin-coated electrode (anode). The SEM image and the corresponding elemental mapping images are shown in the insets.



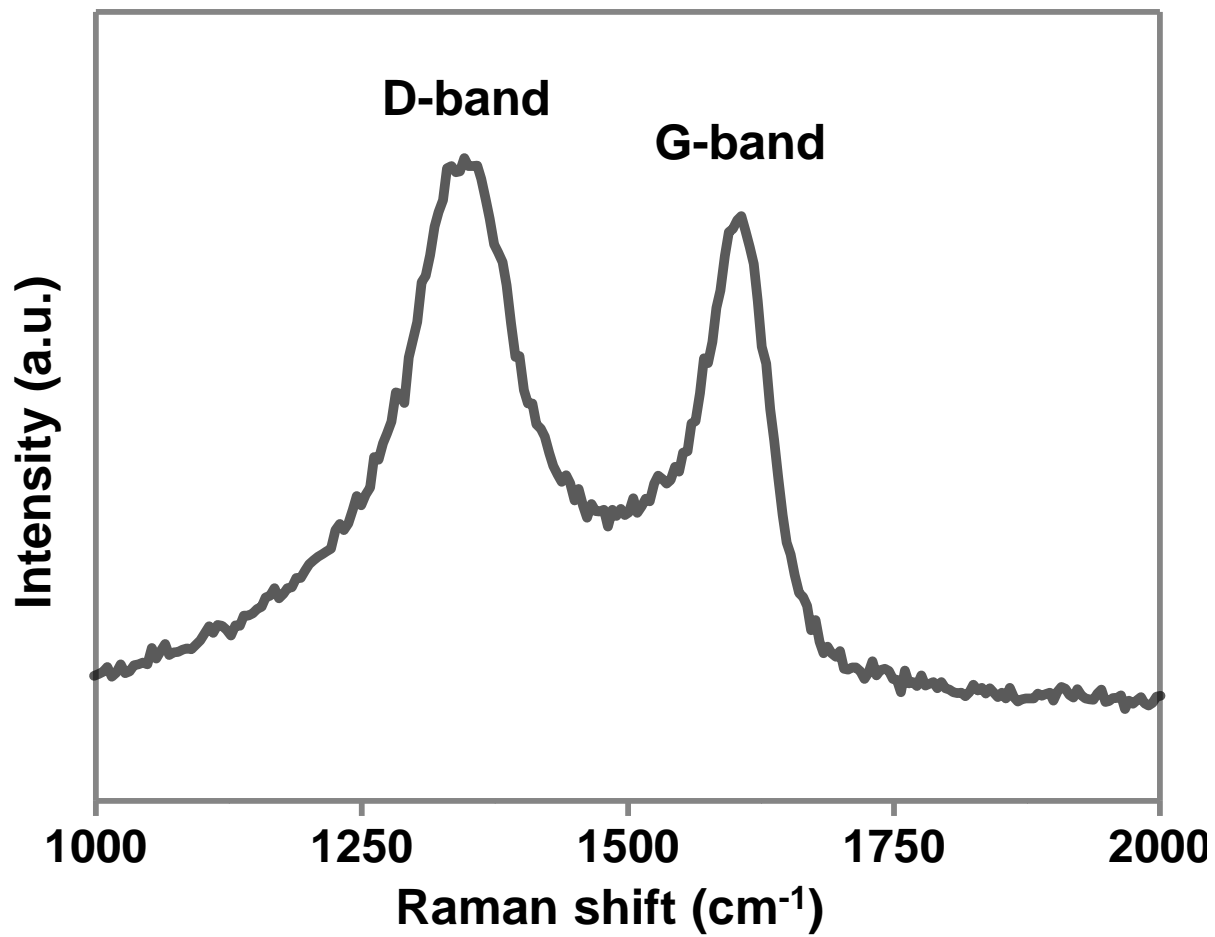
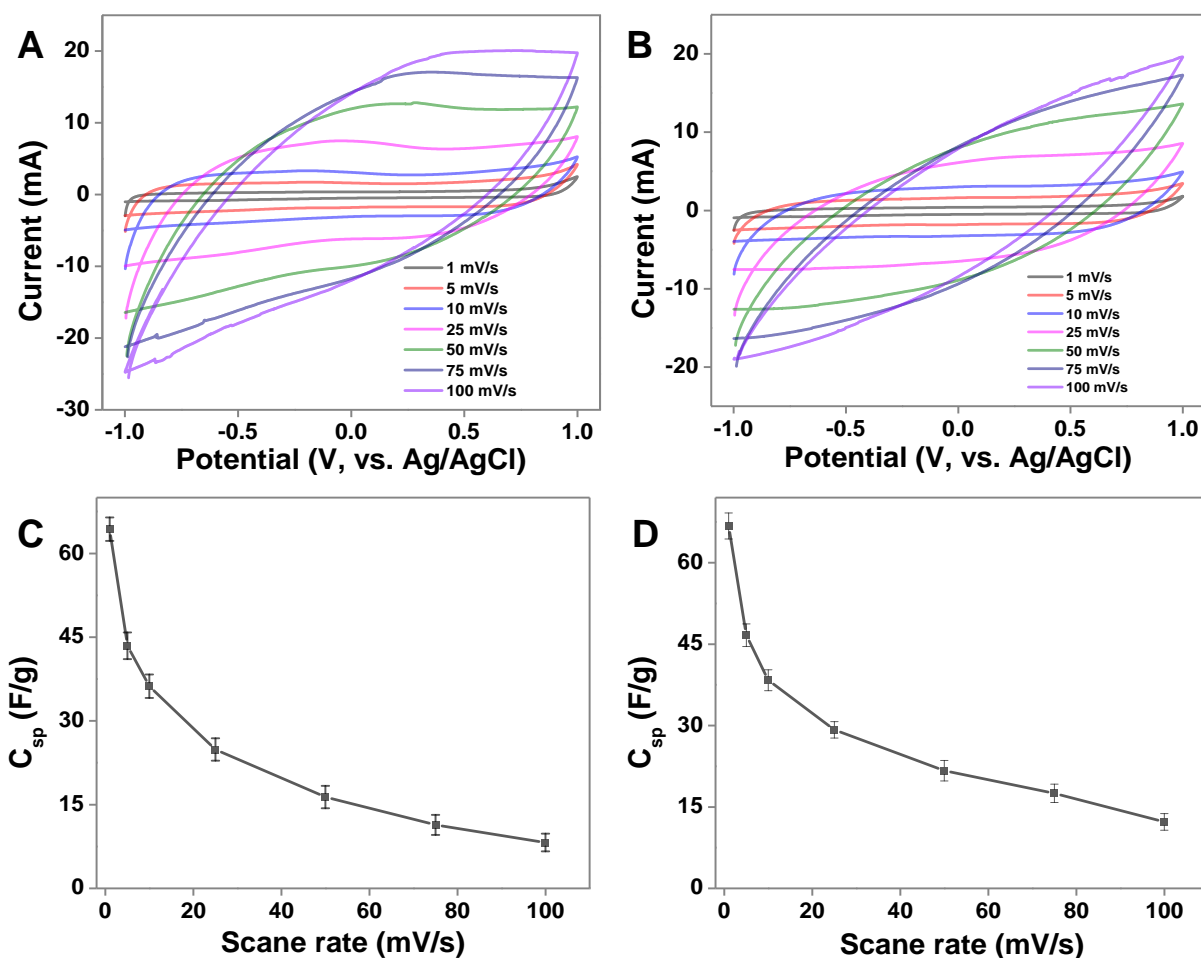
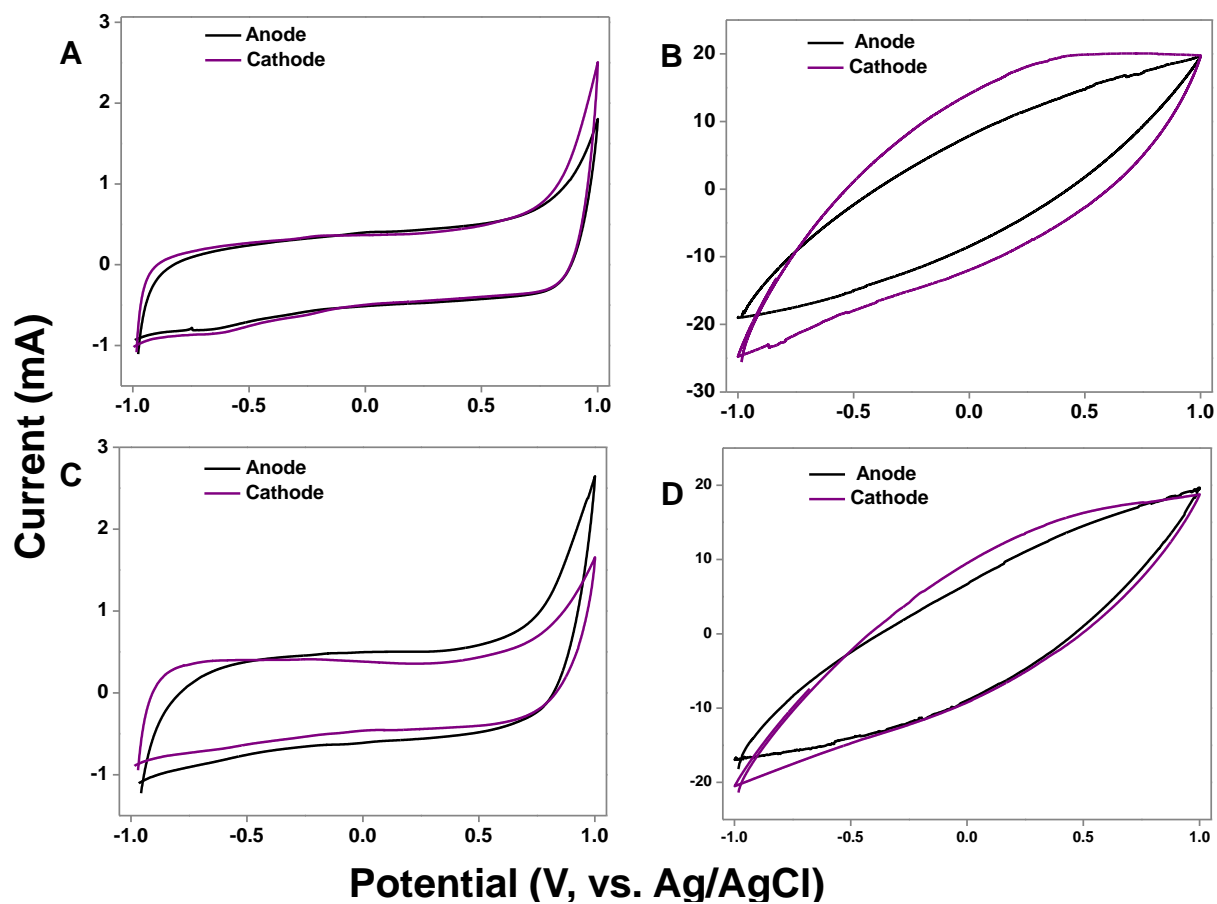


Figure S6. Raman spectrum of carbon materials.



**Figure S7.** Cyclic voltammetry (CV) with varying scan rates A) cathode and B) anode; C) and D) are specific capacitance vs. scan rates for both cathode and anode materials, respectively. CV potential was varied with respect to Ag/AgCl electrodes using 1 M NaCl solution as an electrolyte.



**Figure S8.** Cyclic voltammetry (CV) of A) cathode and anode both @1 mV/s in 1 M NaCl electrolyte, B) cathode and anode both @100 mV/s in 1 M NaCl electrolyte, C) cathode and anode both @1 mV/s in 1 M NaF electrolyte and D) cathode and anode both @100 mV/s in 1 M NaF electrolyte.

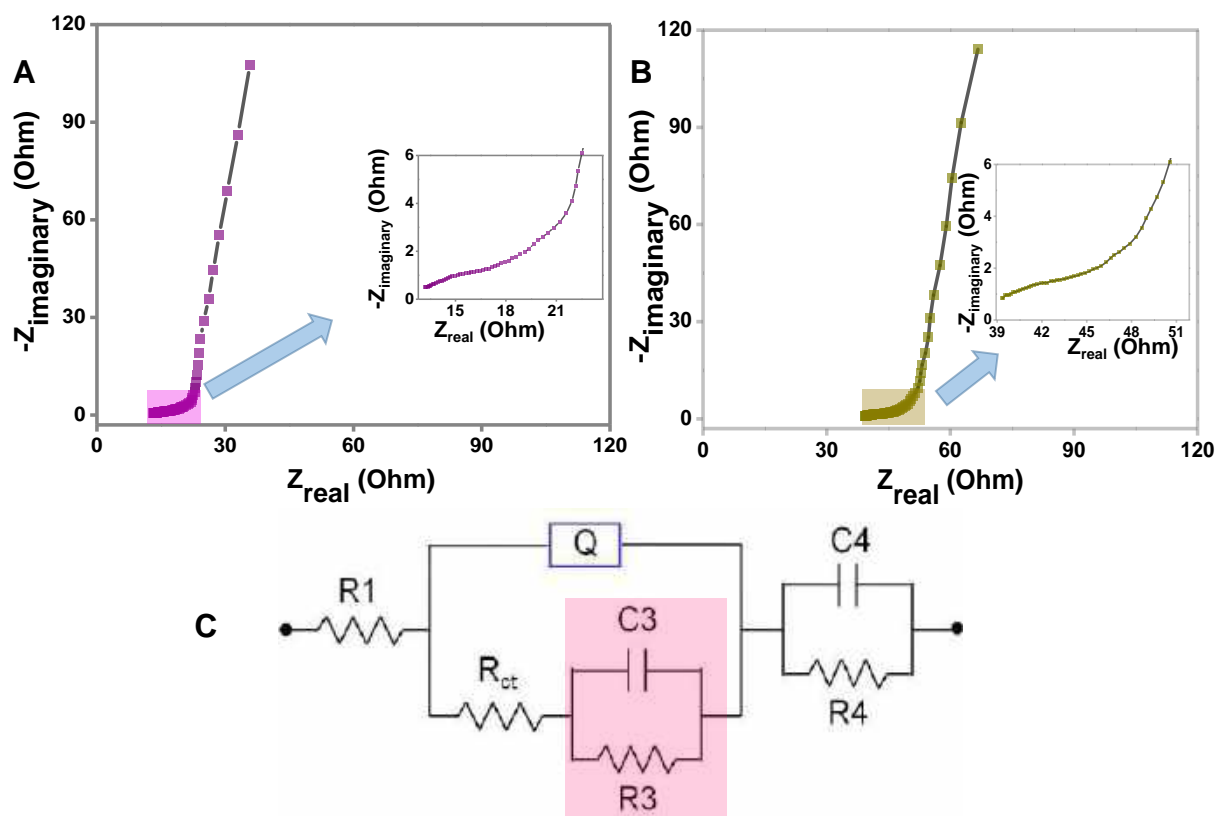


**Figure S9.** Nyquist Plot of A) cathode (the inset chart shows the magnified high-frequency region), B) anode (the inset chart shows the magnified high-frequency part), C) circuit for cathode and anode.

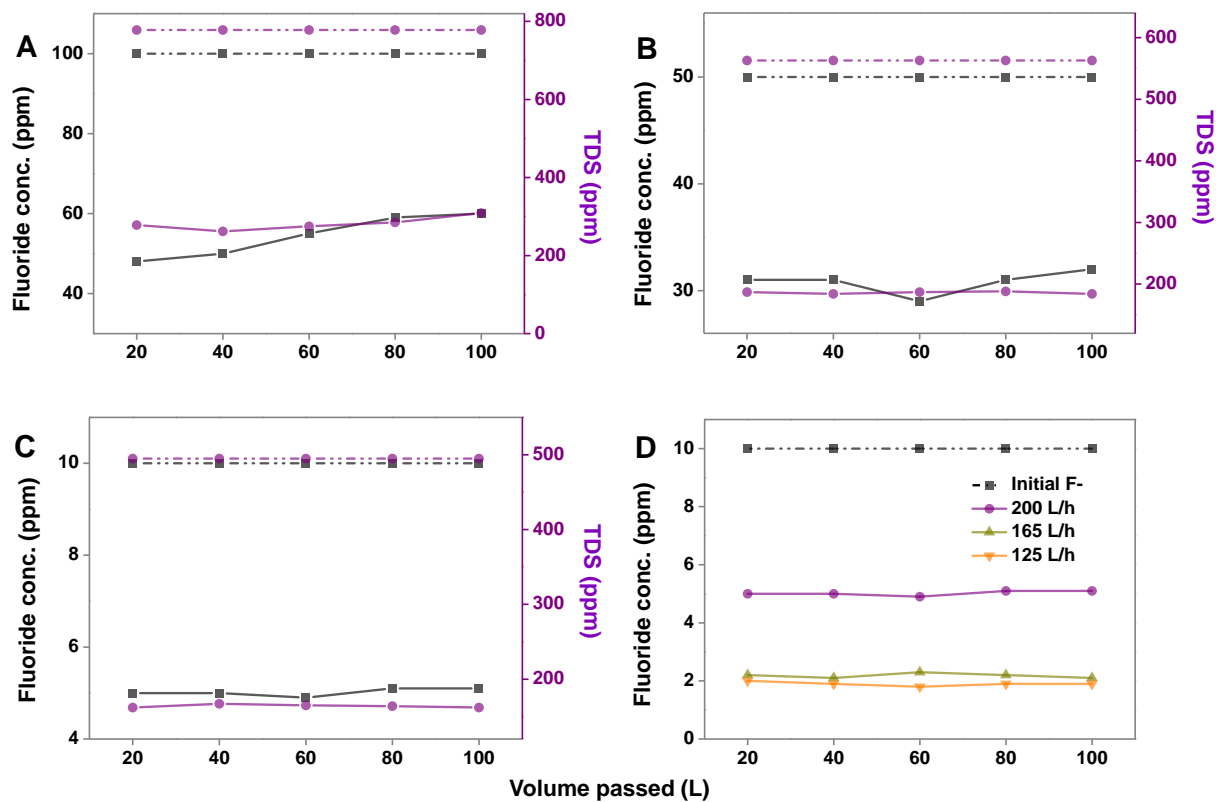


**Figure S10.** CDI performance for the removal of fluoride ion in tap water with initial concentration A) 100 ppm B) 50 ppm, C) 10 ppm with different TDS, and D) effect of flow rate with 10 ppm input fluoride concentration.

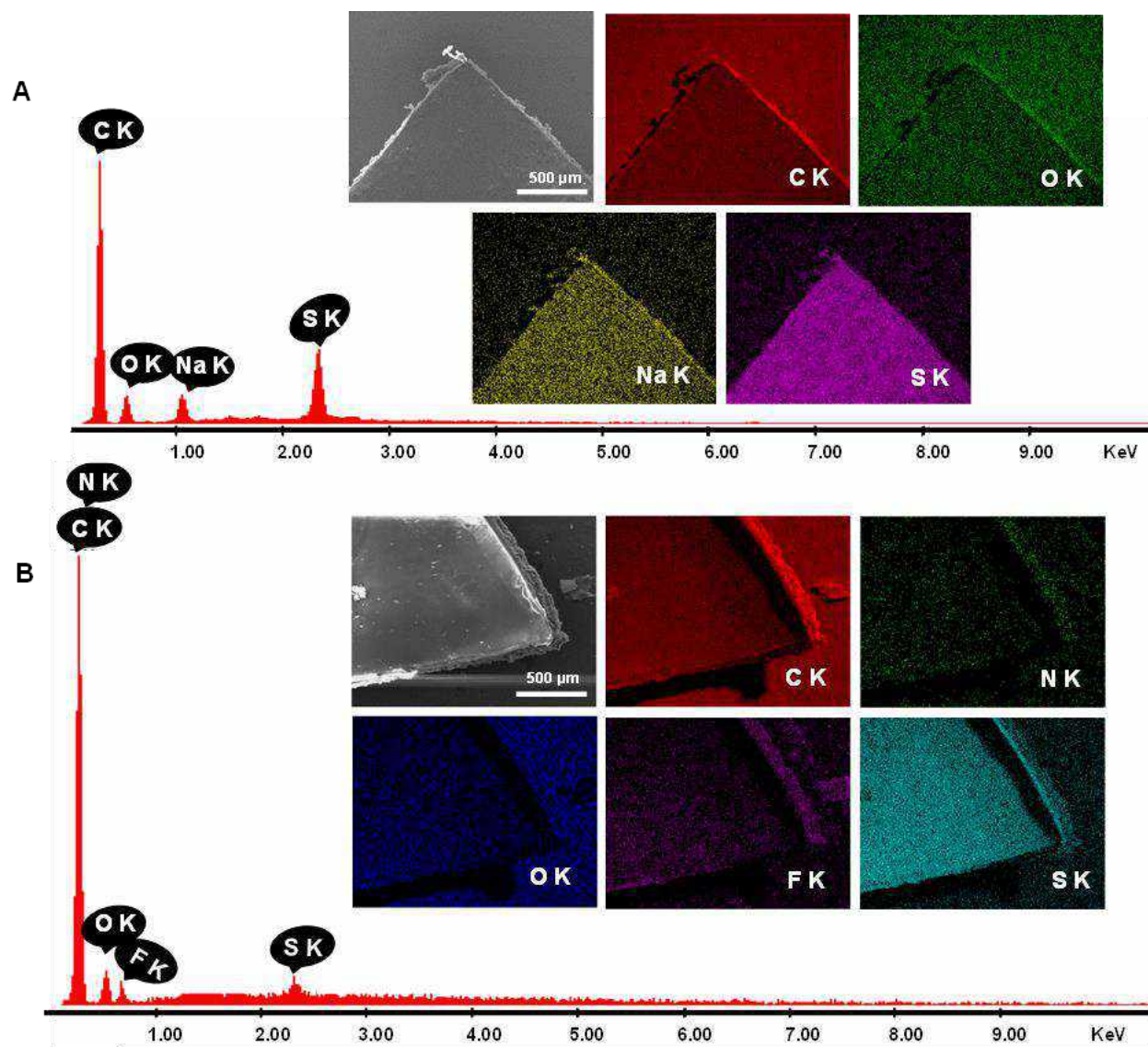


**Figure S11.** SEM EDS of NaF adsorption after single adsorption on A) cathode and B) anode. The corresponding SEM and elemental mapping images are shown in the inset.

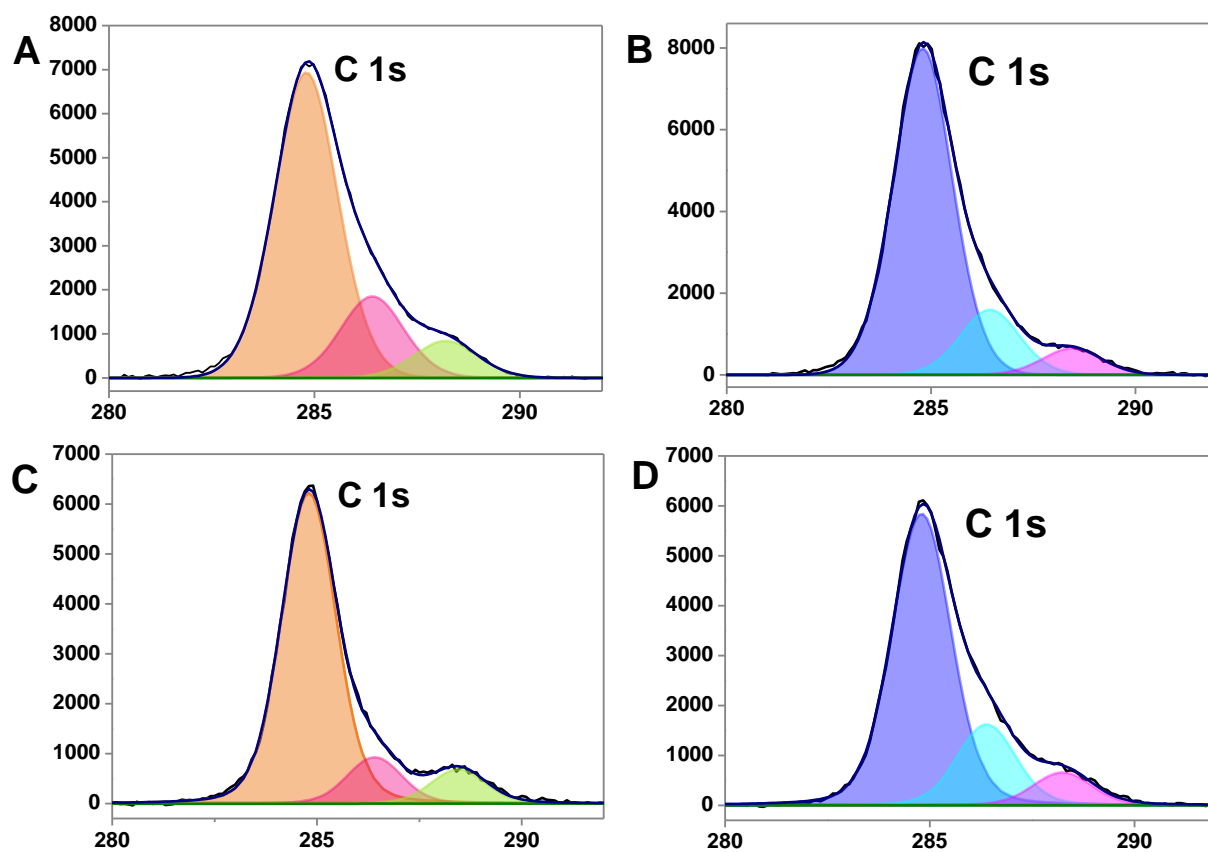


**Figure S12.** Deconvoluted XPS spectra of C 1s in A) cathode and B) anode before NaF adsorption; C) cathode and D) anode after NaF adsorption.

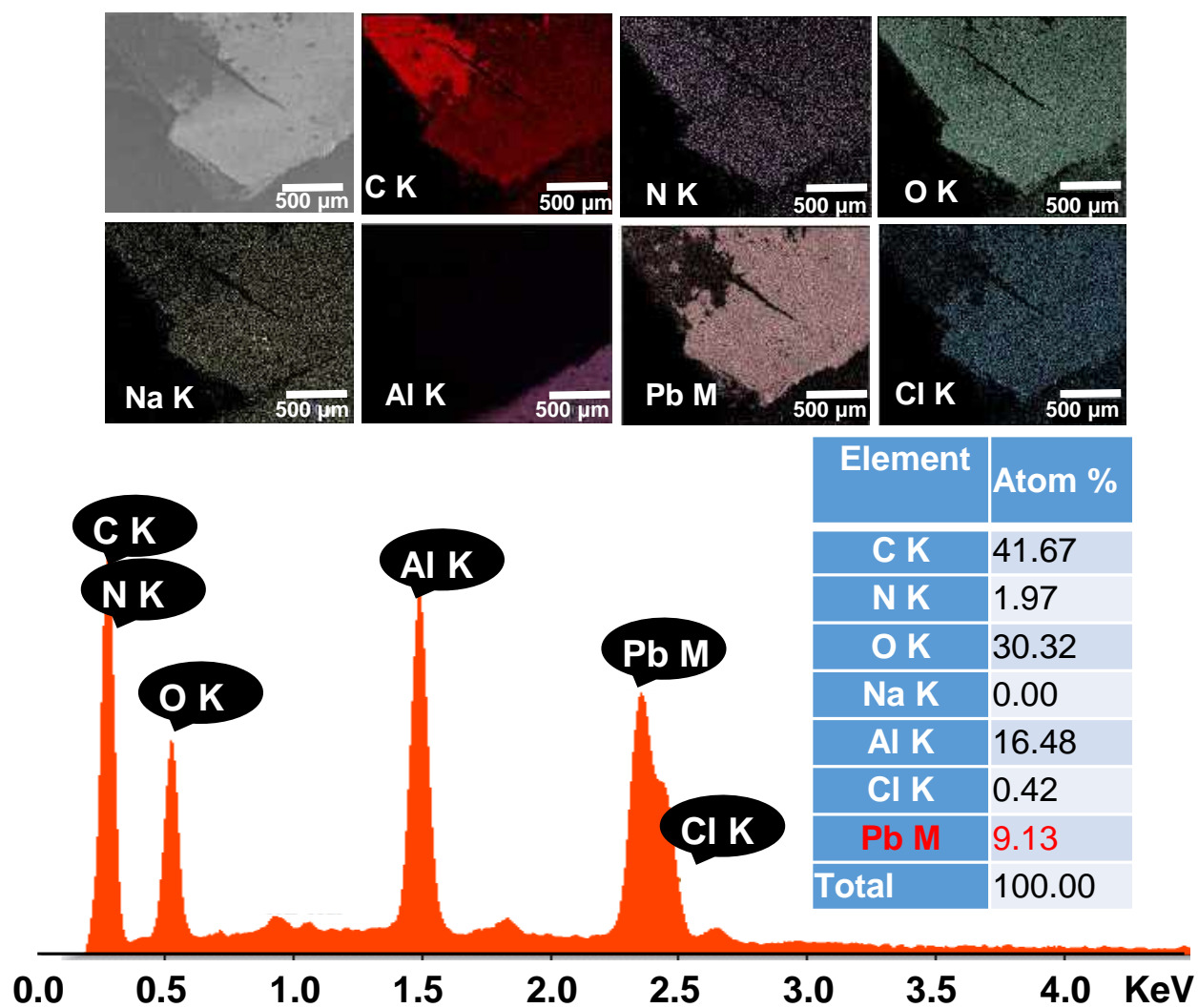


**Figure S13.** SEM EDS of  $\text{Pb}(\text{NO}_3)_2$  adsorption after single adsorption on the cathode. The corresponding SEM and elemental mapping images are shown in the inset.



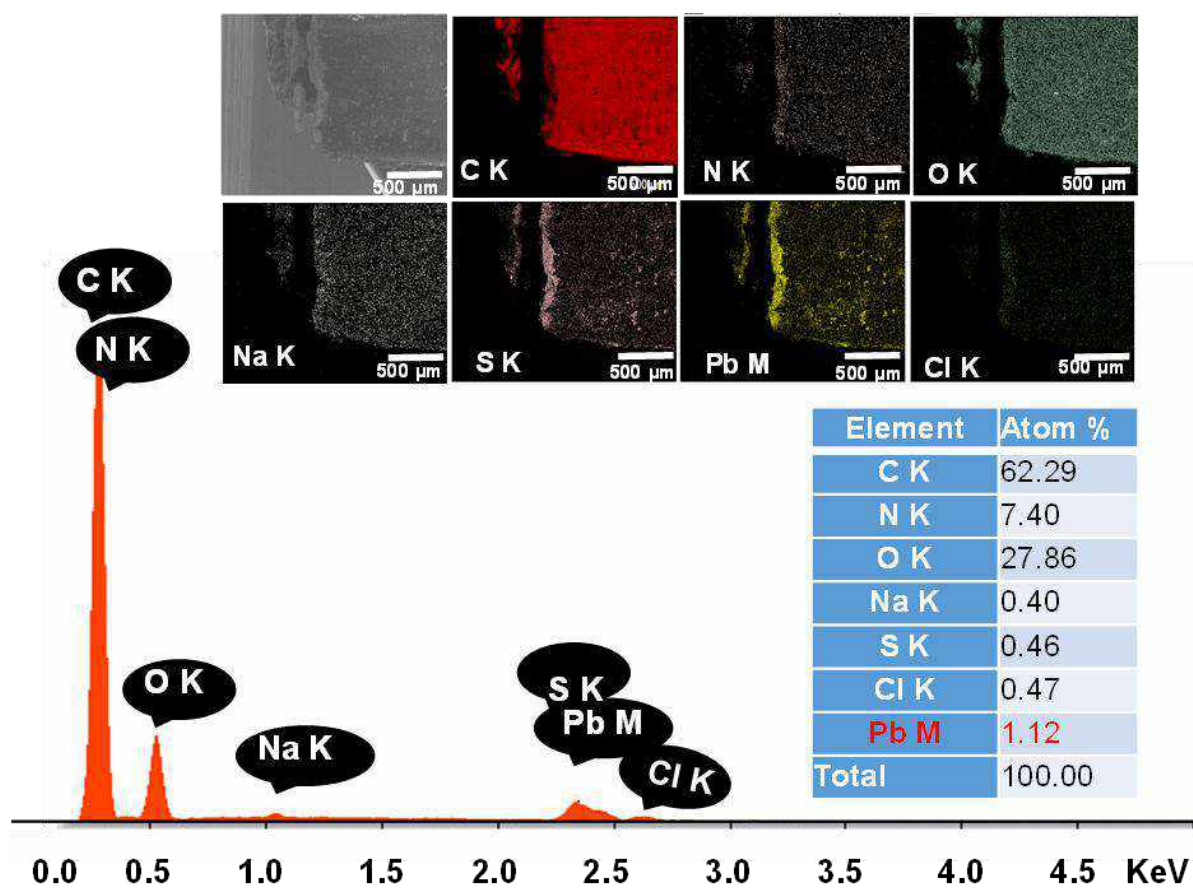


**Figure S14.** SEM EDS of  $\text{Pb}(\text{NO}_3)_2$  adsorption after single adsorption on the anode. The corresponding SEM and elemental mapping images are shown in the inset.

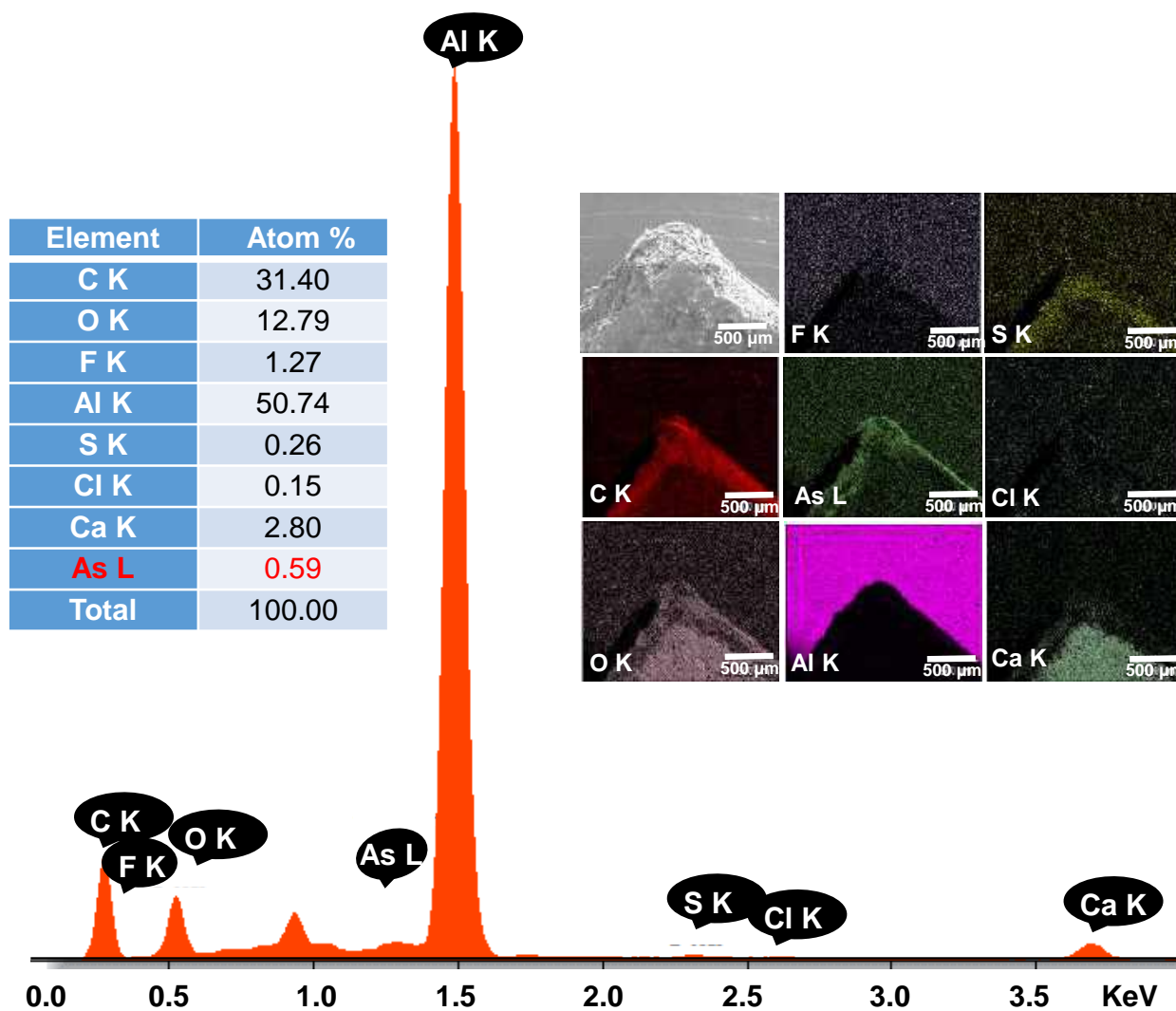


**Figure S15.** SEM EDS of arsenic adsorption after single adsorption on the cathode. The corresponding SEM and elemental mapping images are shown in the inset.

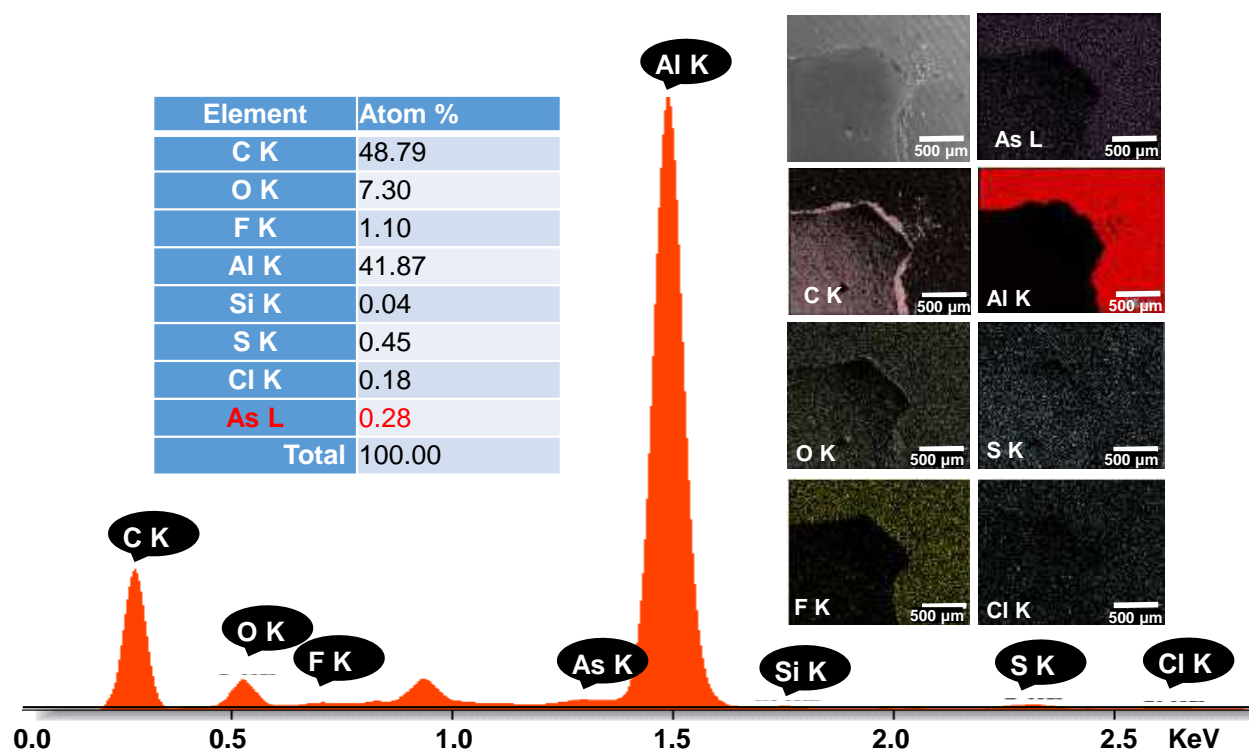


**Figure S16.** SEM EDS of arsenic adsorption after single adsorption on the anode. The corresponding SEM and elemental mapping images are shown in the inset.

**Table S1.** Fitting vales of an equivalent circuit of both cathode and anode

Cathode		Anode	
R1	12.5 Ohm	R1	38.23 Ohm
Q1	0.06 F.s <sup>^(a-1)</sup>	Q1	0.04 F.s <sup>^(a-1)</sup>
a1	0.055	a1	0.049
R <sub>ct</sub>	7.1 Ohm	R <sub>ct</sub>	9.8 Ohm
C3	16.15e-9 F	C3	16.5e-9 F
R3	1.8 MOhm	R3	5.9 MOhm
C4	0.2905 F	C4	0.275 F
R4	794.3 Ohm	R4	831.4 Ohm

# Shell-Isolated Assembly of Atomically Precise Nanoclusters on Gold Nanorods for Integrated Plasmonic-Luminescent Nanocomposites

Published as part of *The Journal of Physical Chemistry virtual special issue "Kankan Bhattacharyya Festschrift"*.

Amrita Chakraborty, Harsh Dave, Biswajit Mondal, Nonappa, Esma Khatun, and Thalappil Pradeep\*



Cite This: *J. Phys. Chem. B* 2022, 126, 1842–1851



Read Online

ACCESS |



Metrics & More

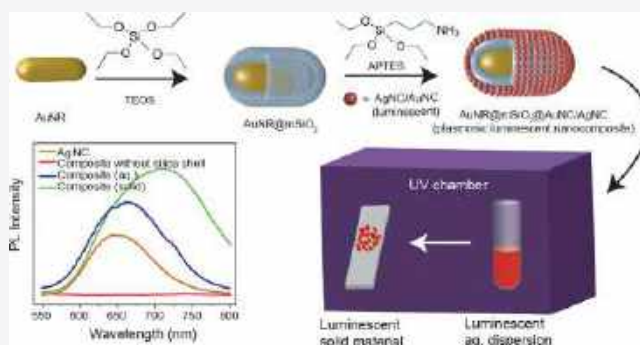


Article Recommendations



Supporting Information

**ABSTRACT:** In this work, we integrate atomically precise noble metal nanoclusters (NCs) on gold nanorods (AuNRs) to create hybrid plasmonic-luminescent nanomaterials. Initially, we assemble luminescent  $\text{Ag}_{29}(\text{LA})_{12}$  NC (LA = lipoic acid) to silica shell-encapsulated AuNRs. The resulting nanostructure shows plasmon-enhanced luminescence in aqueous medium as well as in the solid state. Atomic precision of the fluorophores used in this case allows detailed characterization of individual nanocomposites by diverse techniques, including transmission electron microscopy (TEM) and 3D electron tomographic reconstruction. We extend this strategy to prepare similar structures with gold NC protected with bovine serum albumin ( $\text{Au}_{30}\text{BSA}$ ). These two examples demonstrate the generic nature of the present strategy in preparing plasmonic-luminescent hybrid nanostructures using atomically precise NCs.



## INTRODUCTION

The size- and shape-dependent optoelectronic, mechanical, and chemical properties of nanoscale materials make them important in numerous fields such as water purification,<sup>1</sup> renewable energy,<sup>2</sup> catalysis,<sup>3</sup> sensing,<sup>4</sup> and therapy.<sup>5</sup> Metallic nanoparticles (NPs) of <2 nm diameter are termed as nanoclusters (NCs). They are atomically precise and therefore have molecule-like absorption features. NCs show unusual optoelectronic properties compared to larger plasmonic NPs. For example, some of them exhibit bright luminescence, which has found applications in bioimaging, biolabeling, and diagnostics.<sup>6,7</sup> Among the imaging-based diagnosis techniques, fluorescence imaging is immensely popular for early cancer detection due to its low cost, high sensitivity, and high spatial resolution. However, conventional dyes like rhodamine 6G show ultrabright fluorescence and a quantum yield (QY) as high as 80%, but they undergo photobleaching.<sup>8</sup> Also, molecular dyes are cytotoxic; they often drip out of the cytoplasm during fluorescence microscopy in the case of live-cell imaging. Bright photoluminescence, high quantum yield, significant photostability, and large Stokes shifts are typical of a good contrast agent. Semiconductor QDs like CdSe, CdTe, CdS, ZnS, ZnSe, PbS, and PbSe show high luminescence intensity and quantum yield, significant stability against photobleaching, and narrow and symmetric emission spectra that are tunable over a broad range of wavelengths from UV to NIR region.<sup>9</sup> However, with a few exceptions like silicon QDs<sup>10</sup> and carbon dots,<sup>11</sup> most of the QDs cause cytotoxicity

due to the presence of heavy metal ions and tend to aggregate inside the cell, which prevents their extensive use in therapeutic applications.<sup>12</sup> On the contrary, a number of luminescent noble metal NCs display relatively low cytotoxicity and high biocompatibility. In the case of protein-protected NCs, complex 3D structures of proteins can withstand a wide range of pH.<sup>13</sup> Besides, their ultrafine sizes help the cells to retain their regular biophysical functions in their unaltered state.<sup>14</sup> Size uniformity and good mechanical strength of atomically precise NCs make them better candidates as multifunctional fluorophores compared to most semiconductor QDs, owing to the difficulty in precise size control. Therefore, efforts are being made to improve the luminescence and photostability of NCs in the recent past.<sup>15,16</sup> A straightforward approach in this direction is to conjugate luminescent Au and Ag NCs to plasmonic NPs, as they enhance the local electric field in the surroundings. Any fluorophore is greatly affected by the surface plasmon of the NPs in close proximity.<sup>17</sup> However, depending on the distance between them, this interaction is known to either enhance (by

Received: December 1, 2021

Revised: January 30, 2022

Published: February 18, 2022





far-field energy transfer) or quench (due to nonradiative decay) the photoluminescence (PL) intensity of the fluorophore. As a result, assembling dye molecules or QDs with a central plasmonic NP, surrounded by a nonmetallic oxide or polymer shell, has been tried.<sup>18</sup> Use of noble metal NCs in this context is promising, yet limited. Plasmonic noble metal NPs of nonspherical shape exhibit shape-dependent physicochemical properties. For example, gold nanorods (AuNRs) exhibit strong absorption and scattering in the near-infrared (NIR) region, where most human tissues, intrinsic chromophores, hemoglobin, and water show very poor absorbance, making it an efficient nanoprobe for *in vivo* biomedical imaging, drug delivery, and phototherapy.<sup>19</sup> Since a combination of multiple imaging modalities offers synergistic advantages over single techniques, recent emphasis has been to develop hybrid nanomaterials where different NPs of various properties are integrated into a single nanostructure. These structures exhibit combined qualities of their components leading to efficient multimodal nanoprobos.<sup>20–23</sup> Importantly, mesoporous silica-coated AuNRs, when loaded with indocyanine green, act as a contrast agent for computed tomography (CT) scan and fluorescence dual mode imaging.<sup>24</sup> Conjugation of Gd(III) ions with AuNRs has resulted in a single nanoprobe for simultaneous magnetic resonance imaging (MRI) and CT imaging.<sup>25</sup> Anisotropic NPs are also attractive as building blocks of plasmonically engineered metamaterials as they induce directional interaction.<sup>26</sup> Recent studies have shown that NCs can take part in the colloidal assembly within themselves,<sup>27</sup> as well as with 1D plasmonic NPs, producing precision assemblies.<sup>28,29</sup> Therefore, it is interesting to create a binary assembly of anisotropic noble metal NPs and luminescent NCs and investigate the effect of surface plasmons on the photophysical properties of the NCs.

Herein, we introduce a multimodal imaging probe by loading luminescent noble metal NCs onto AuNRs protected by a silica shell of uniform thickness, and study the structures and photophysical properties of the composite nanostructures. Lipoic acid (LA)-protected Ag NC, Ag<sub>29</sub>(LA)<sub>12</sub> (abbreviated as Ag<sub>29</sub>), is chosen as the luminescent component, which is ultrasmall in size, atomically precise, and distinctly visible using transmission electron microscopy. This is conjugated to AuNRs through a mesoporous silica shell, leading to a nanocomposite where the luminescence of Ag<sub>29</sub> is enhanced due to plasmonic coupling. Using 3D tomographic reconstruction of the transmission electron micrographs, we study the growth of silica shells on AuNR surface facets and the attachment of Ag<sub>29</sub> NCs to the mesoporous shell. We have also conjugated Au<sub>30</sub>BSA (BSA = bovine serum albumin), one of the extensively studied luminescent NCs for live-cell imaging with silica-coated AuNR, in a similar approach. In both cases, the PL intensity of the NC was enhanced due to plasmonic coupling, demonstrating the generic nature of the strategy. We believe that the precise structural insights presented will encourage the community to explore NCs with diverse functionality and rich surface chemistry to design composite nanomaterials that may be useful for applications beyond multimodal bioimaging, such as targeted drug delivery and biosensing.

## EXPERIMENTAL METHODS

**Chemicals.** Gold(III) chloride trihydrate (HAuCl<sub>4</sub>·3H<sub>2</sub>O), cetyltrimethylammonium bromide (CTAB), sodium borohydride (NaBH<sub>4</sub>), tetraethyl orthosilicate (TEOS), and (3-

aminopropyl) triethoxysilane (APTES) were purchased from Sigma-Aldrich, USA. Lipoic acid (LA), silver nitrate (AgNO<sub>3</sub>), ascorbic acid, and sodium hydroxide (NaOH) were purchased from Rankem India Pvt., Ltd. BSA was purchased from HiMedia Pvt., Ltd. Deionized (DI) water was used for all syntheses.

**Methods. Synthesis of AuNRs.** The synthesis of AuNRs was carried out using the protocol proposed by Samal et al.<sup>30</sup> In this wet chemical synthesis method, 20 mL of 100 mM CTAB was added to a conical flask to which, sequentially, 1 mL of 10 mM HAuCl<sub>4</sub>·3H<sub>2</sub>O, 130 μL of 10 mM AgNO<sub>3</sub>, and 140 μL of 100 mM ascorbic acid were added with mild stirring. Then, 200 μL of a freshly prepared ice-cold NaBH<sub>4</sub> solution (1.67 mM) was quickly injected into the reaction mixture and stirring was stopped immediately. Although the dark brown color, characteristic of AuNRs, appeared within 0.5 h, this growth medium was kept still for at least 4 h to ensure a high yield of the AuNRs. The temperature was maintained at 28 °C throughout the synthesis. Finally, the mixture was centrifuged twice at 13 000 rpm for 12 min. Each time the supernatant was discarded by decanting, and the pellet was redispersed in DI water.

**Synthesis of AuNR@mSiO<sub>2</sub> (Where m = Thickness of Silica Shell).** To grow a mesoporous silica shell encapsulating the AuNRs, we followed the previously reported method.<sup>31</sup> However, for different shell thicknesses, the protocol was slightly modified to achieve the best result.

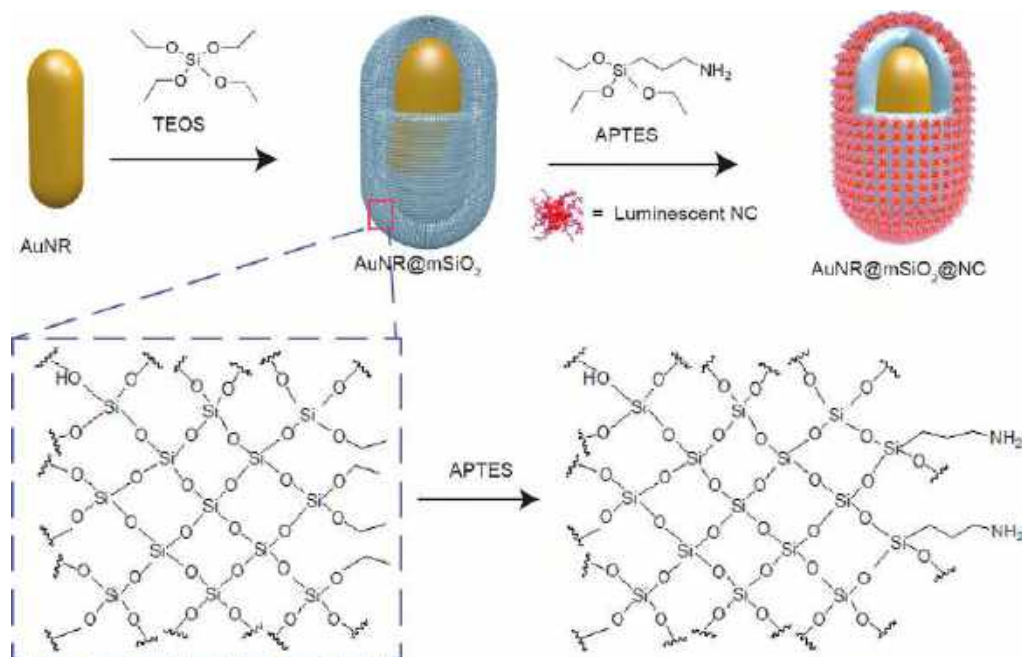
**Silica Shell of 8 ± 0.76 nm Thickness, Denoted as AuNR@8SiO<sub>2</sub>.** First, 10 mL of purity AuNRs (optical density, i.e., O.D. = 1.2 at 780 nm) was taken in a 30 mL glass vial. The pH was adjusted to 10–10.4 by slowly adding 100 μL of 100 mM NaOH upon continuous stirring until the pH was stable. To the reaction mixture, 90 μL of 20% TEOS (v/v in methanol) was added in three portions of 30 μL each with 30 min interval between each addition. The reaction was continued for 24 h, and then the product was precipitated by centrifugation at 11 000 rpm for 12 min. DI water was used to remove excess silica.

**Silica Shell of 12 ± 0.95 nm Thickness, Denoted as AuNR@12SiO<sub>2</sub>.** The synthesis was performed as described for AuNR@8SiO<sub>2</sub>. In brief, 8 mL of the AuNR batch (OD = 1.2 at 780 nm) was used and the pH was adjusted to 10–10.4. 15 μL of 20% TEOS was added in 3 steps and the reaction was continued for 12 h. The product was precipitated using centrifugation and purified by washing with DI water, as described before.

**Silica Shell of 16 ± 0.84 nm Thickness, Denoted as AuNR@16SiO<sub>2</sub>.** This was a two-step process. The first step was similar to that of AuNR@12SiO<sub>2</sub>. After the unbound silica was removed from the product by decanting the supernatant, the pellet of AuNR@12SiO<sub>2</sub> was dispersed in 8 mL of DI water. By adding 100 mM NaOH under stirring conditions, we adjusted the pH of the solution and the same protocol was repeated. Finally, the product was washed in a similar fashion by centrifugation at 11 000 rpm for 12 min.

**Amine-Functionalization of AuNR@mSiO<sub>2</sub>.** The silica shell was modified by adding an end-functional group according to a previous report with some customization.<sup>32</sup> Briefly, 12.5 μL of APTES was added to 10 mL of clean AuNR@mSiO<sub>2</sub> of any silica shell thickness (O.D. 1.2 at 780 nm) under vigorous stirring. Stirring was continued for 2–3 h at room temperature, and the synthesized product was centrifuged at 11 000 rpm for 10 min. The supernatant containing unreacted APTES was

**Scheme 1. Schematic of the Growth of Mesoporous Silica Shell on AuNR and Subsequent Addition of  $-\text{NH}_2$  Functional Group to Finally Attach Luminescent NC**



decanted and the precipitate, named  $\text{AuNR@mSiO}_2-\text{NH}_2$ , was dispersed in DI water.

**Synthesis of  $\text{Ag}_{29}(\text{LA})_{12}$  NCs.** The LA-protected Ag NC was synthesized using a previous report.<sup>33</sup> Precisely, 19 mg of LA (92  $\mu\text{mol}$ ) and 7 mg of  $\text{NaBH}_4$  (0.19 mmol) were added to a 30 mL glass vial containing 14 mL of water. The reaction mixture was stirred until all LA had dissolved, and then 700  $\mu\text{L}$  of 25 mM  $\text{AgNO}_3$  (17.5  $\mu\text{mol}$ ) was added, which turned the solution turbid. This was followed by the addition of 10 mg of  $\text{NaBH}_4$  (0.26 mmol) dissolved in 2 mL of water. The cluster took 3–5 h to form. The reaction vial was wrapped in an aluminum foil to avoid the exposure of the clusters to light. The synthesis was carried out at room temperature. Samples were stored in the dark at 4  $^\circ\text{C}$ .

**Synthesis of  $\text{Au}_{30}\text{BSA}$  NCs.** BSA-protected gold NCs were synthesized as reported previously by Mohanty et al.,<sup>34</sup> where the cluster was assigned as  $\text{Au}_{30}\text{BSA}$  based on the MALDI MS. For this, 125 mg of BSA was added to 5 mL of DI water, and the mixture was sonicated until it was fully dissolved. Then, 5 mL of 6 mM  $\text{HAuCl}_4$  solution was added under mild stirring. After 1 min, 500  $\mu\text{L}$  of freshly prepared 1 M  $\text{NaOH}$  solution was added. The reaction was allowed to be stirred for 12 h.

**Synthesis of  $\text{AuNR@mSiO}_2@\text{Ag}_{29}$ .** According to Beer–Lamberts Law, for a dilute colloidal solution

$$A = \epsilon \cdot c \cdot l$$

where  $A$  = absorbance,  $\epsilon$  = molar extinction coefficient,  $c$  = concentration, and  $l$  = path length. For a given nanosystem (AuNRs or the NCs), since  $\epsilon$  and  $l$  are constants,  $A \propto c$ .

We have maintained the concentration of AuNRs and  $\text{Ag}_{29}$  by keeping their O.D. value fixed throughout. Precisely, 1.5  $\mu\text{L}$  of as-synthesized  $\text{Ag}_{29}$  NC (O.D. = 2.8 at 328 nm) was taken in a 5 mL glass vial which was kept in dark. To this, 500  $\mu\text{L}$  of freshly synthesized  $\text{AuNR@mSiO}_2-\text{NH}_2$  (O.D. = 1 at 780 nm) was added dropwise under moderate stirring (300 rpm). The stirring was stopped after 30 min. The solution was centrifuged at 8000 rpm for 10 min and the supernatant

containing unbound NCs was discarded. The precipitate containing  $\text{AuNR@mSiO}_2@\text{Ag}_{29}$  was dispersed in 1 mL of DI water and was kept in dark throughout.

**Synthesis of  $\text{AuNR@mSiO}_2@\text{Au}_{30}\text{BSA}$ .** The procedure was same as that described in the case of  $\text{Ag}_{29}$ . Here, the concentration of  $\text{Au}_{30}\text{BSA}$  was maintained such that O.D. = 3 at 365 nm.

**UV–Vis Spectroscopy.** Optical absorption spectra of the samples were recorded using a PerkinElmer Lambda 25 UV–visible spectrometer. We used Milli-Q water for the baseline sample as well as for diluting the samples. A quartz cuvette of 1 cm path length has been used for all the measurements.

**PL Spectroscopy.** The PL spectra were measured on a HORIBA JOBIN YVON Nano Log instrument. The slit of the bandpass filters for excitation and emission was set at 3 nm.

**High-Resolution Transmission Electron Microscopy.** A 3  $\mu\text{L}$  aliquot of each sample was drop-cast on a TEM grid (made of copper, 300 mesh) and allowed to dry under ambient conditions. The images were then collected using a JEOL 3010 transmission electron microscope with an accelerating voltage of 200 kV.

**Serial EM and Electron Tomography Reconstruction.** Copper grids (300 mesh) with an ultrathin carbon support film were used to prepare specimen for electron tomography reconstruction. The specimen preparation was carried out by adding 3  $\mu\text{L}$  of the sample on a plasma-cleaned TEM grid and allowed to dry under ambient conditions. The images acquisition was carried out using a JEOL JEM-3200FSC field-emission TEM operated at 300 kV with an Omega-type zero-loss filter. The tilt series of 2D projections (between  $\pm 69^\circ$  angles with  $2^\circ$  increment steps) were recorded using SerialEM software.<sup>35–37</sup> The relignment and final alignment were carried out using IMOD software.<sup>38</sup> Finally, the maximum entropy method (MEM) was used with a custom-made program for reconstruction and colored tomograms were prepared using Chimera software.<sup>37</sup>



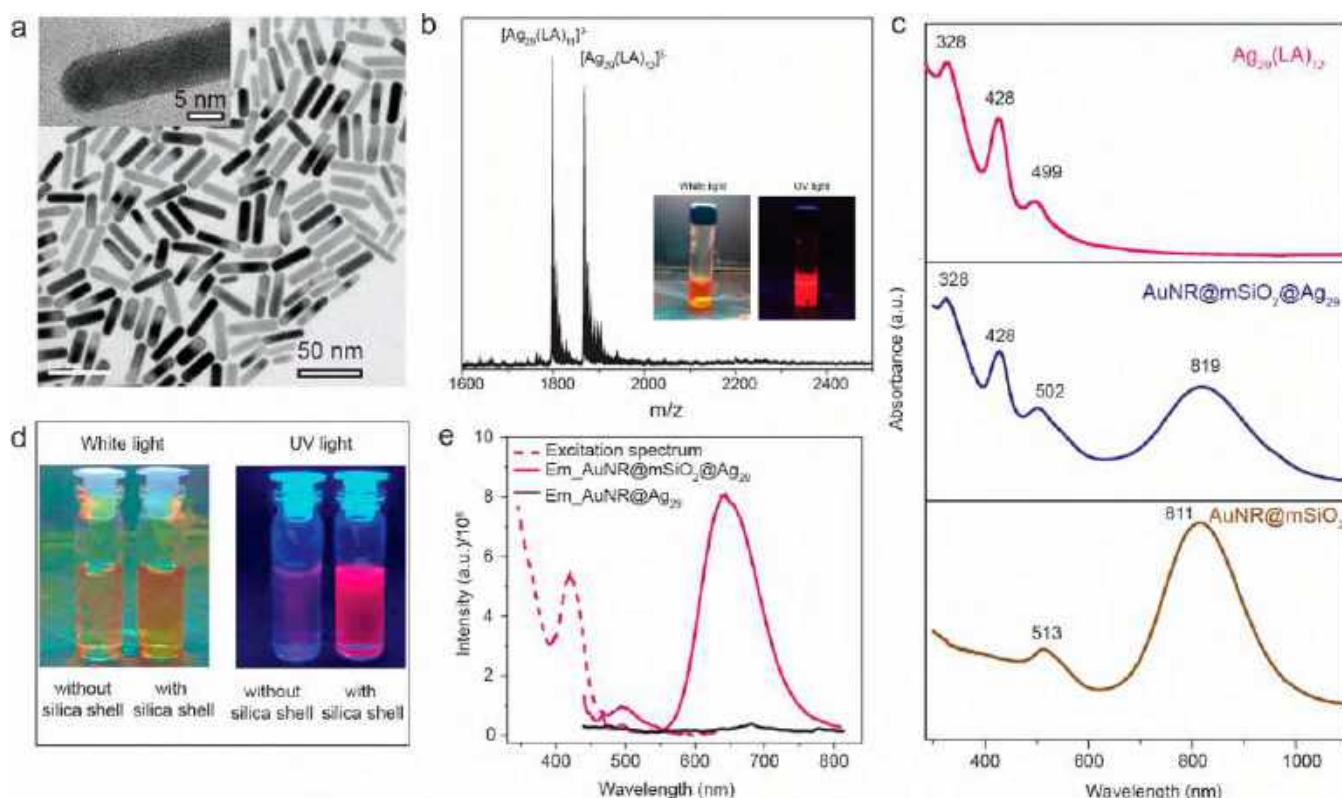


**Figure 1.** (a) TEM image of AuNRs (HRTEM image of a single AuNR in the inset shows surface facets). (b) ESI MS of  $\text{Ag}_{29}$  showing a molecular ion peak at  $m/z \sim 1868$  along with a peak corresponding to  $[\text{Ag}_{29}(\text{LA})_{11}]^{-3}$ , formed as a byproduct; the inset showing photographs of bright red luminescent  $\text{Ag}_{29}$  under UV light. (c) Absorption spectra of  $\text{Ag}_{29}$ ,  $\text{AuNR@mSiO}_2$ , and  $\text{AuNR@mSiO}_2@\text{Ag}_{29}$  along with peak positions for comparison. (d) Photograph of  $\text{AuNR@Ag}_{29}$  (left) and  $\text{AuNR@mSiO}_2@\text{Ag}_{29}$  (right) solutions under white light and UV light. (e) Excitation and emission spectra of  $\text{AuNR@mSiO}_2@\text{Ag}_{29}$  along with the emission spectra of  $\text{AuNR@Ag}_{29}$  (excitation wavelength = 425 nm for both).

## RESULTS AND DISCUSSION

**Synthesis Strategy and Properties of the Composite Material.** Previous studies have shown that direct attachment of fluorophores to a plasmonic core often quenches the PL of the latter, due to near-field damping.<sup>39,40</sup> To retain the PL, lipids, polymers, or amorphous silica shells have been grown on the intrinsic AuNRs. These give enhanced chemical and physical stability to the AuNRs in cellular environment and upon laser exposure and act as spacers between the plasmonic NP and the fluorophores, preventing PL quenching.<sup>41</sup> Owing to their inexpensive nature, biocompatibility, easy functionalization on the AuNR surface, and further conjugation with a range of fluorophores, we grew amorphous silica encapsulating the AuNRs prior to assembling luminescent NCs, as shown in Scheme 1. Many seedless and seed-mediated methods are known for synthesizing AuNRs of various aspect ratios with high size and shape uniformity. In this work, we synthesized ultrasmall AuNRs following a simple one-pot synthetic procedure using CTAB as described in the Experimental Section.<sup>30</sup> TEM image of the particles in Figure 1a shows their size and shape uniformity, while the HRTEM in the inset shows the faceted structure of each AuNR.

For growing a silica shell on AuNR, a well-established method developed by Gorelikov et al. was followed with slight modifications, as described in the “Experimental Methods” section.<sup>31</sup> The resulting composite is abbreviated here as  $\text{AuNR@mSiO}_2$ . The growth of silica shell was initially confirmed from the red shift of the LSPR of parent AuNRs and a change in its zeta potential from  $+30.4 \pm 3$  eV to  $-31 \pm$

$3.5$  eV (Figure S1). Subsequently, as depicted in Scheme 1, the  $\text{AuNR@mSiO}_2$  was treated with APTES that introduced an amine functional group to the silica shell, and the entity is denoted as  $\text{AuNR@mSiO}_2\text{-NH}_2$ . This step is typically followed to make it interact with the desired fluorophore.<sup>42,43</sup> As the fluorescent component, we chose NCs that show steady and bright PL. LA is a small dithiol that has been used to prepare both Au and Ag NCs.<sup>33,44–46</sup> LA and LA-protected NCs are water-soluble, and their carboxylate ends offer the desired functionality. Therefore, we synthesized LA-protected  $\text{Ag}_{29}$  NC, namely  $\text{Ag}_{29}(\text{LA})_{12}$  (abbreviated as  $\text{Ag}_{29}$ ) based on the procedure reported by Linden et al.<sup>33</sup> Formation of  $\text{Ag}_{29}$  was confirmed from its bright red luminescence, characteristic UV–vis absorption spectrum, and ESI MS spectrum (Figure 1b,c). Freshly prepared  $\text{AuNR@mSiO}_2\text{-NH}_2$  was immediately added to  $\text{Ag}_{29}$  NC under mild stirring condition. After 3–4 h of mixing at room temperature, the material was purified by centrifugation to remove unbound NCs, if any were present. The resulting NC conjugated nanocomposite, denoted as  $\text{AuNR@mSiO}_2@\text{Ag}_{29}$ , was thoroughly characterized.

The absorption spectrum of  $\text{Ag}_{29}$  typically shows sharp bands with maxima around 328, 428, and 499 nm.<sup>33</sup> In contrast,  $\text{AuNR@mSiO}_2$  exhibits two plasmonic bands: longitudinal surface plasmon resonance (LSPR) at 811 nm and transverse surface plasmon resonance (TSPR) band around 513 nm. Figure 1c shows the comparative absorption spectra of as-synthesized AuNRs,  $\text{Ag}_{29}$ , and  $\text{AuNR@mSiO}_2@\text{Ag}_{29}$ , which reveal that the signature electronic transition bands of  $\text{Ag}_{29}$  and plasmonic transition band of AuNR were

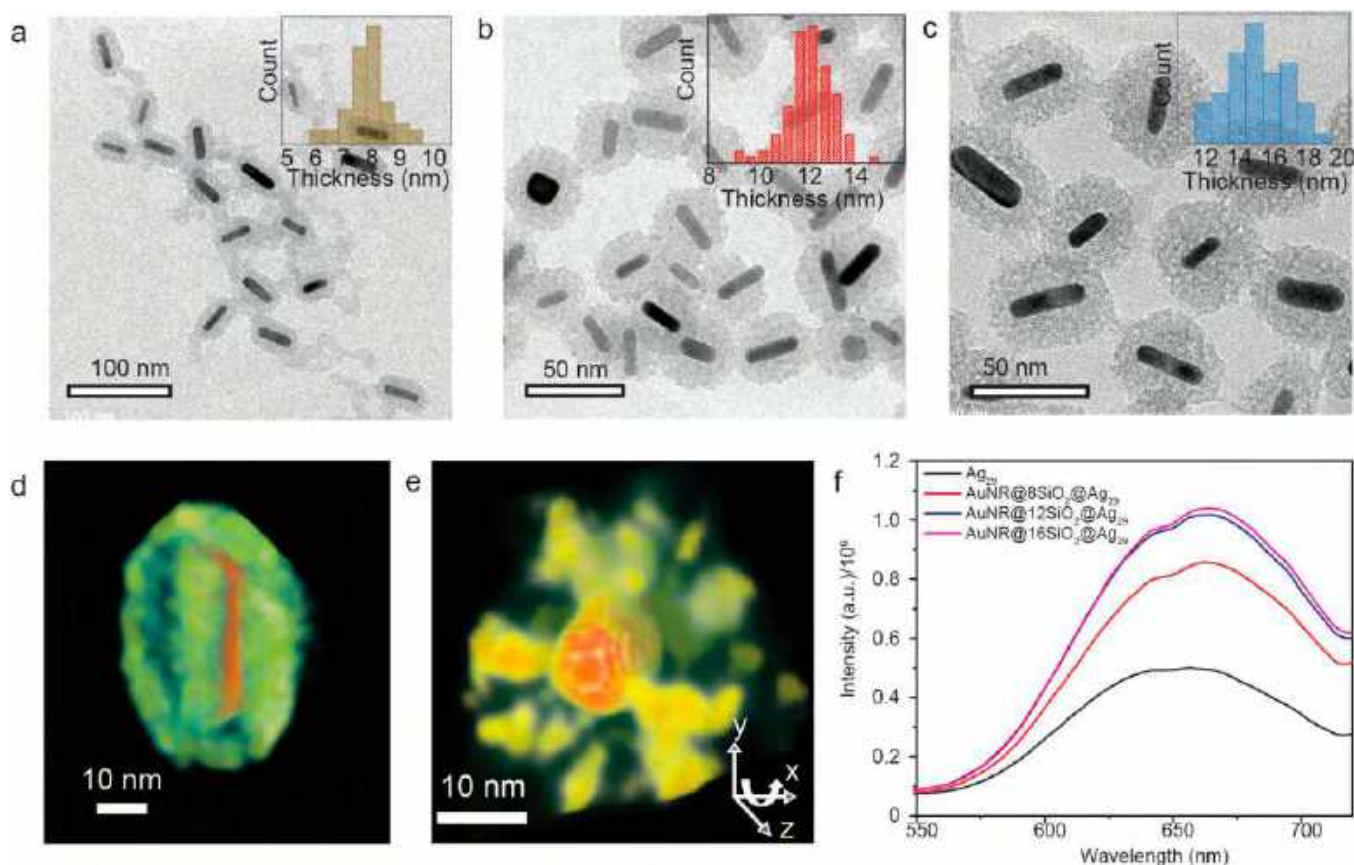


**Figure 2.** TEM images of AuNR@mSiO<sub>2</sub> with (a)  $8 \pm 0.76$  nm, (b)  $12 \pm 0.95$  nm, and (c)  $16 \pm 0.84$  nm thick silica shells, respectively, along with the distribution of shell thickness in insets. 3D reconstructed TEM tomograms of the (d) side view and (e) top view of AuNR@12SiO<sub>2</sub>, (f) comparative emission spectra of AuNR@mSiO<sub>2</sub>@Ag<sub>29</sub> at different shell thickness and that of blank Ag<sub>29</sub> (all excited at 425 nm).

retained in the resulting composite. As presented in Figure 1d, AuNR@mSiO<sub>2</sub>@Ag<sub>29</sub> showed bright red luminescence under UV light. On the contrary, when we functionalized AuNRs directly by APTES (i.e., without growing any silica shell on them) and made them interact with Ag<sub>29</sub> in a fashion similar to that used for the control (abbreviated as AuNR@Ag<sub>29</sub>), no such red luminescence was observed. The PL excitation spectrum of AuNR@mSiO<sub>2</sub>@Ag<sub>29</sub> showed a maximum at 425 nm. When excited at this wavelength, it showed intense PL emission with a maximum at  $\sim 650$  nm, as depicted in Figure 1e. However, the emission spectrum of AuNR@Ag<sub>29</sub> showed near-zero intensity throughout the range of visible wavelength. The TEM image of AuNR@Ag<sub>29</sub> is shown in Figure S2 and suggests that NCs were directly conjugated to AuNRs.

**Effect of Silica Shell Thickness.** In the case of plasmon-enhanced fluorescence, depending on its distance from the plasmonic NP, luminescence intensity of a fluorophore (both molecular dyes as well as QDs) can either be enhanced or quenched.<sup>47,48</sup> Precisely, the shell thickness plays a crucial role in determining the overall luminescence of the composite in the case of shell-isolated plasmonic-luminescent composites.<sup>41</sup> Here, AuNRs with three different silica shell thicknesses were obtained by optimizing the synthetic protocol (see the “Experimental Methods” section). TEM images along with statistical analyses of silica shell thicknesses are shown in Figure 2a–c, which revealed highly uniform silica shells of thickness  $8 \pm 0.76$  nm,  $12 \pm 0.95$  nm, and  $16 \pm 0.84$  nm, respectively. Although silica coating around AuNR and other NPs has been studied before, their characterization was mostly

limited to TEM imaging and optical absorption spectroscopy. However, conventional TEM images show the 2D projection of a 3D object, providing limited information about its true morphology. Hence, we reconstructed the 3D images of individual AuNR@mSiO<sub>2</sub> using a series of 2D projections (Video S1). Figure 2d shows 3D views of a single AuNR@mSiO<sub>2</sub> particle from the side, while Figure 2e shows the view from the tip of the AuNR (90° rotation along the *x*-axis). Unlike in their TEM images, the 3D tomographs of AuNR@mSiO<sub>2</sub> clearly show that the silica shell was not uniformly distributed on the AuNR surface, rather the surface facets of AuNRs were protected alternately. This was true for each AuNR@mSiO<sub>2</sub> particle, irrespective of the thickness of the silica shell. This periodic growth of silica can be explained in terms of differential surface energy of different sets of planes that AuNRs are made of. In our previous studies, 3D images of a single CTAB-coated AuNRs, synthesized in a similar method, revealed its octagonal morphology.<sup>28</sup> According to the literature, these eight planes of AuNRs are made of four (110) and four (100) surface facets arranged alternately.<sup>49</sup> Due to differential surface energies of these facets, metallic Pd,<sup>50</sup> Ag,<sup>51</sup> and Ag NC<sup>28</sup> are known to be deposited preferentially on one of these facets. This finding is important as the plasmonic NPs of different morphologies (e.g., sphere, triangle, cubes, etc.) are made of different sets of surface facets, depending on the synthesis protocol.<sup>52</sup> Thus, the distribution of silica shell encapsulating these structures is likely to differ from one another, which might have a profound effect on their photophysical properties. Here, when the three batches of



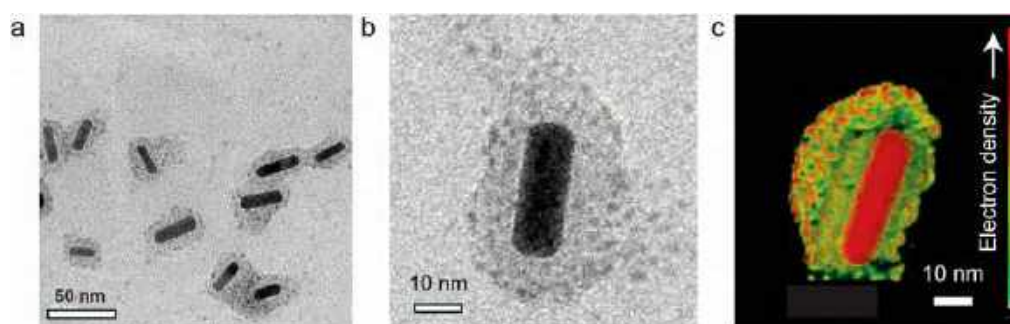


**Figure 3.** TEM images of (a) AuNR@mSiO<sub>2</sub>@Ag<sub>29</sub>, (b) single AuNR@mSiO<sub>2</sub>@Ag<sub>29</sub>, and (c) 3D reconstructed image of (b), where some of the atoms from the front part are omitted to give a clear core–shell view.

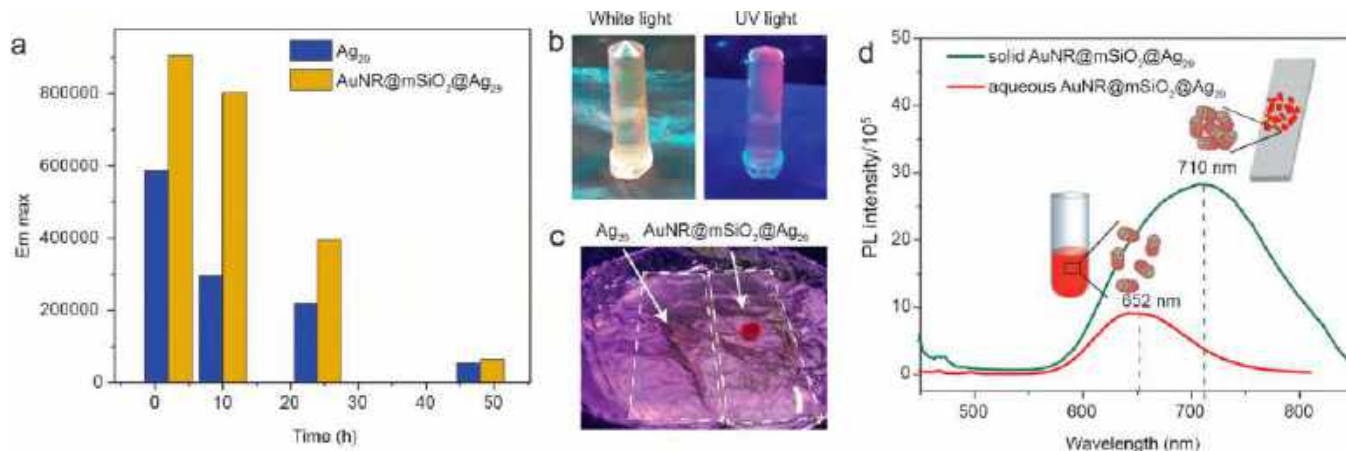


**Figure 4.** (a) Emission maxima of AuNR@mSiO<sub>2</sub>@Ag<sub>29</sub> and blank Ag<sub>29</sub> plotted against time. (b) Photograph of luminescent AuNR@mSiO<sub>2</sub>@Ag<sub>29</sub> spun down from the aqueous dispersion. (c) Photograph under UV light showing comparative luminescence of solid AuNR@mSiO<sub>2</sub>@Ag<sub>29</sub> and solid Ag<sub>29</sub> (the glass slides are marked by white dashed lines for clear visibility). (d) Comparative PL spectra of AuNR@mSiO<sub>2</sub>@Ag<sub>29</sub> in aqueous solution and solid phases; schematic showing the aggregation causing the red shift of the spectrum.

AuNR@mSiO<sub>2</sub> were functionalized with APTES and subsequently treated with Ag<sub>29</sub> under the same conditions, AuNR@mSiO<sub>2</sub>@Ag<sub>29</sub> showed enhanced luminescence compared to the blank cluster (Figure 2f). In the case of AuNR@mSiO<sub>2</sub>@Ag<sub>29</sub>, the enhancement was even greater, but upon going to 16 nm thick silica shell, we found no significant change in the PL intensity. Therefore, we carried out all the subsequent experiments with AuNR@mSiO<sub>2</sub>@Ag<sub>29</sub>.

**Structural Insight into the Nanocomposite.** Silica NPs and silica-coated metallic NPs conjugated with fluorophores such as QDs and organic dyes have proved their utility in diverse ways.<sup>24,53</sup> However, these studies were focused on the performance of the material as a nanoprobe in respective fields, rather than their detailed characterization. Besides, most of these often lead to aggregated nanocomposites with poor colloidal stability, making it difficult to study their structural details. The strictly monodisperse size and shape of NCs make them much more favorable for colloidal assembly compared to QDs, which usually suffer from significant polydispersity. However, due to their metallic core, most NCs can be imaged under high-resolution transmission electron microscopy (HRTEM), unlike the molecular dyes. Here, AuNR@mSiO<sub>2</sub>@Ag<sub>29</sub> was thoroughly characterized using TEM and corresponding 3D images.

Figure 3a includes TEM image of AuNR@mSiO<sub>2</sub>@Ag<sub>29</sub>, which reveals their structural uniformity. An image of a single nanocomposite particle (Figure 3b) shows that the Ag<sub>29</sub> NC moieties were attached to the silica shell encapsulating

individual AuNRs such that the size and shape of the resulting nanocomposite were guided by that of the AuNR and the thickness of the silica shell. This indicates that by choosing the right morphology of the template nanoparticle, we can obtain plasmonic luminescent nanocomposites of desired size and shape that may act as building blocks for advanced hierarchical metamaterials. A 3D image of a single AuNR@mSiO<sub>2</sub>@Ag<sub>29</sub> is presented in Figure 3c (Video S2 contains the corresponding tilt series), where the red color denotes high electron density. For a better understanding of the core–shell structure, some of the atoms were deliberately removed during reconstruction. The underlying AuNR and Ag<sub>29</sub> NCs on the surface appear in red, making the visualization easier. Since Ag NCs are photosensitive, the PL intensity of the nanocomposite decreased with time as that of the parent Ag<sub>29</sub> decreased (Figure S3a–c). Figure 4a shows the emission maxima of AuNR@mSiO<sub>2</sub>@Ag<sub>29</sub> and that of parent Ag<sub>29</sub> as a function of time. The results suggest that AuNR@mSiO<sub>2</sub>@Ag<sub>29</sub> showed enhanced PL at any point of time as compared to Ag<sub>29</sub> until their PL was quenched after 2 days. The TEM image of the composite after 48 h (Figure S3d) reveals that the NCs aggregated to form Ag NPs, which explains the quenching of their luminescence. Noble metal NCs show weak PL quantum yield in an aqueous solution mostly due to nonradiative relaxation through surface–ligand motion.<sup>54</sup> However, using poor solvent or electrostatic attraction, they can be aggregated, which leads to significant enhancement of their PL QY.<sup>55,56</sup> Fluorescent NCs and QDs often suffer from aggregation–

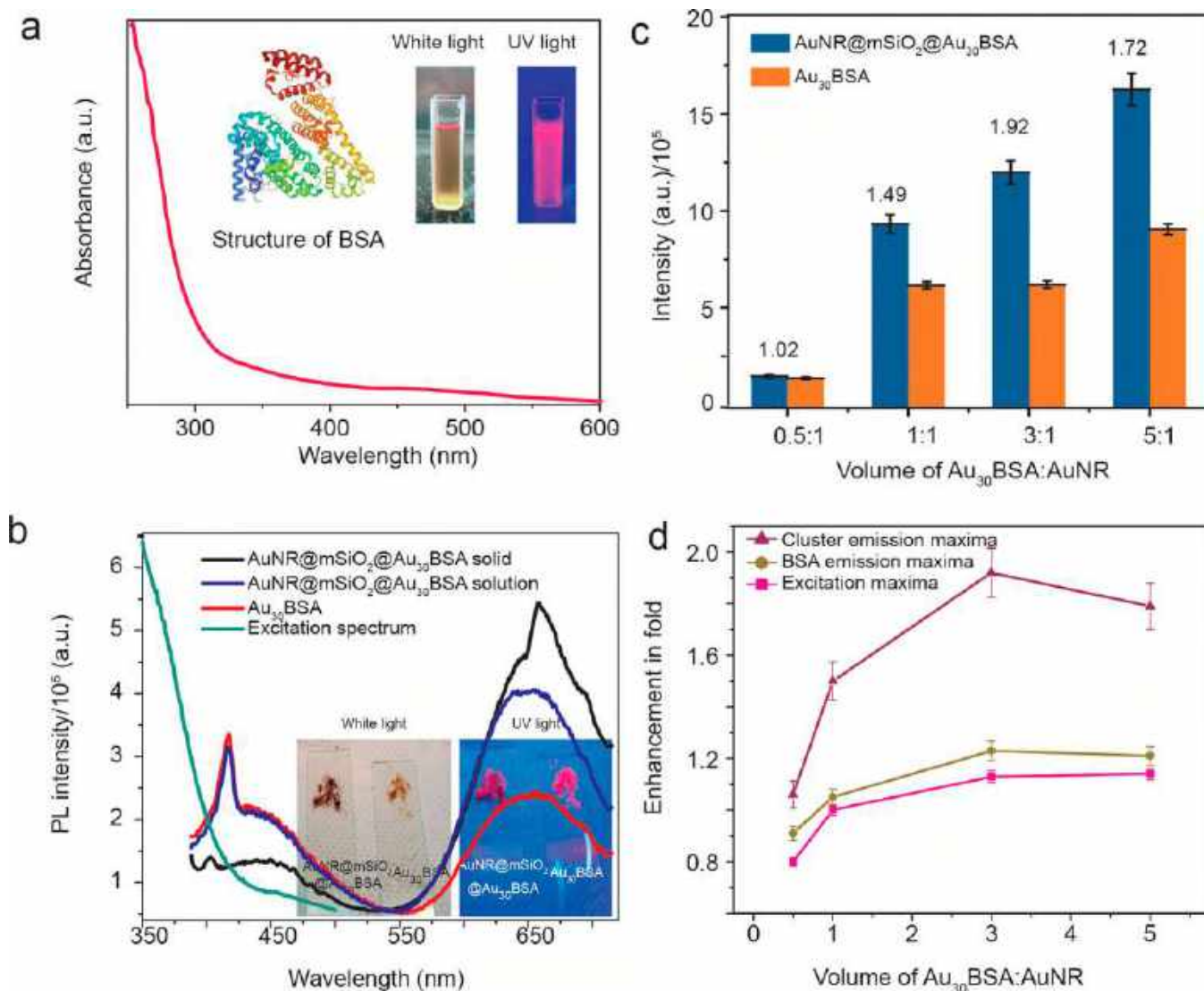


**Figure 5.** (a) UV-vis absorption spectrum of Au<sub>30</sub>BSA with the crystal structure of BSA and photographs of Au<sub>30</sub>BSA NC under white light and UV light (inset). (b) PL emission spectra of AuNR@mSiO<sub>2</sub>@Au<sub>30</sub>BSA in both solution and in solid phases, and blank Au<sub>30</sub>BSA along with the excitation spectrum; inset shows photographs of luminescent solid AuNR@mSiO<sub>2</sub>@Au<sub>30</sub>BSA and solid Au<sub>30</sub>BSA. (c) Ratio of PL enhancement compared to free Au<sub>30</sub>BSA at gradually higher Au<sub>30</sub>BSA to AuNR concentration ratio. (d) Change in the excitation, protein emission, and cluster emission maximum with increasing Au<sub>30</sub>BSA concentration.

induced photon reabsorption, nonradiative resonant energy transfer, and/or direct  $\pi$ - $\pi$  interactions, and so on, leading to fluorescence quenching during solidification.<sup>57–59</sup> Therefore, efforts are being made to achieve luminescent NCs in the solid state with improved PL properties, which would lead to potential applications in making ecofriendly alternatives for conventional toxic nanophosphores.<sup>60</sup> Here, APTES was added to the aqueous dispersion of AuNR@mSiO<sub>2</sub>@Ag<sub>29</sub> in order to screen electrostatic repulsion between surface NCs, allowing them to aggregate. This aggregated AuNR@mSiO<sub>2</sub>@Ag<sub>29</sub> was precipitated upon centrifugation. As shown in Figure 4b, the pellet thus obtained showed red luminescence under UV light, leaving the supernatant nonluminescent. This pellet was dried under ambient condition in dark to obtain solid AuNR@mSiO<sub>2</sub>@Ag<sub>29</sub>. The parent Ag<sub>29</sub> NC was also solidified following a similar procedure.

Figure 4c shows photographs of solid Ag<sub>29</sub> and solid AuNR@mSiO<sub>2</sub>@Ag<sub>29</sub> made from the same amount of NC under UV light, where the latter shows bright red

luminescence. The PL of solid Ag<sub>29</sub> was almost completely quenched. The PL spectra of solid AuNR@mSiO<sub>2</sub>@Ag<sub>29</sub> and aqueous AuNR@mSiO<sub>2</sub>@Ag<sub>29</sub> are presented in Figure 4d. In the solid phase, the nanocomposite showed significantly enhanced luminescence along with a dramatic red shift in its emission maximum. Such increase in Stokes shift in the solid state is commonly known due to the greater intermolecular interaction in solid state as compared to in solution. Thus, the resulting nanocomposite has potential in diverse fields as a more efficient fluorophore compared to its constituent NC.

**Generalization of the Strategy.** A large number of luminescent Au NCs reported in the past decade exhibit unique physicochemical properties depending on the composition of their metallic core and surface ligands. Among these, protein-protected Au NCs are studied extensively for live-cell imaging and diagnostics as well as chemical<sup>61</sup> and biosensing<sup>62</sup> due to their biocompatibility, exceptional stability, and water solubility. We synthesized BSA-protected Au NC, namely, Au<sub>30</sub>BSA, following a reported procedure.<sup>63</sup> Figure 5a shows

the characteristic UV–vis absorption spectrum and inset includes photographs of the NC under visible and UV light, showing bright red luminescence. Following the procedure described in the case of Ag<sub>29</sub>, Au<sub>30</sub>BSA was anchored to AuNR@mSiO<sub>2</sub>-NH<sub>2</sub> to synthesize a AuNR@mSiO<sub>2</sub>@Au<sub>30</sub>BSA nanocomposite. In the case of protein-protected NCs, the tiny metallic cores are almost fully buried within the bulky protein structures, making them difficult to visualize under TEM. However, the attachment of Au<sub>30</sub>BSA to the silica shell of AuNR@mSiO<sub>2</sub> can be inferred from TEM images of AuNR@mSiO<sub>2</sub>@Au<sub>30</sub>BSA (Figure S4a). Similar to parent Au<sub>30</sub>BSA, upon excitation at 365 nm, the resulting nanocomposite also showed two maxima in its emission spectrum, one at ~425 nm due to BSA and another at ~650 nm due to the core of the NC (Figure 5b). In this case, the PL of the NC was also enhanced in its composite form, as shown in Figure 5b. Owing to the photostability of Au<sub>30</sub>BSA, AuNR@mSiO<sub>2</sub>@Au<sub>30</sub>BSA showed intense luminescence for more than a month suggesting high colloidal stability of the nanocomposite. Both the blank NC and the composite also showed bright red PL in their solid form (inset of Figure 5b). In this case, the emission maximum of the solid nanocomposite was red-shifted compared to the aqueous dispersion. Maximum loading of Au<sub>30</sub>BSA to the individual AuNR@mSiO<sub>2</sub> structures was ensured by adding gradually higher amount of Au<sub>30</sub>BSA to a fixed amount of AuNR@mSiO<sub>2</sub> and comparing their PL spectra with the same concentration of Au<sub>30</sub>BSA as blank in each case. As shown in Figure 5c, the highest PL enhancement factor of 1.92 was obtained when the AuNR/Au<sub>30</sub>BSA volume ratio was 1:3. In order to prove that this enhancement was due to plasmonic coupling and not the confinement effect of silica,<sup>64</sup> we measured the enhancement of the excitation and emission spectra of the composite with gradually higher NC concentration and plotted the excitation maximum and the two emission maxima (at ~420 nm due to the BSA protein and ~650 nm due to the Au<sub>30</sub> core) in Figure 5d. With increasing Au<sub>30</sub>BSA concentration, the change in protein emission maxima followed the trend of the excitation maxima, which is a direct consequence of the change in NC concentration, but the change in emission maximum around 650 nm was much more profound. Since AuNRs primarily scatter at this silica shell thickness, presumably the Purcell effect predominates over FRET.<sup>65</sup> Hence, emission due to the Au<sub>30</sub> core that overlaps with the LSPR band of AuNRs gets enhanced, but the protein emission is not enhanced. Hence, this observation confirms that the greater PL intensity of the composite than the parent NC is due to plasmon-induced enhancement. Thus, both the luminescent NCs of very different compositions form brighter plasmonic luminescent nanocomposites encapsulating individual AuNRs, using this approach.

## CONCLUSIONS

In conclusion, we assembled fluorescent Ag<sub>29</sub> NCs on a versatile anisotropic plasmonic nanoprobe, namely, AuNR, through a mesoporous silica shell. The resulting nanocomposite is structurally precise and well-dispersed in aqueous medium, and it shows enhanced PL in both dispersed and solid phases. The size and shape of the composite are guided by the encapsulated AuNR and therefore are tunable, depending on the AuNR chosen. Using Au<sub>30</sub>BSA NC, we showed that the proposed approach is not only straightforward but also generic for water-soluble luminescent NCs, irrespective of their composition. Thus, by taking the right pair of NCs and NPs

as starting materials for the proposed strategy, one can obtain an attractive nanoprobe for dual-mode bioimaging, targeted drug delivery, therapeutics, or any PL-based sensing application. Structural investigations of such plasmonic luminescent nanocomposites in great detail show their potential to act as luminescent building blocks of defined geometry for engineering advanced nanomaterials.

## ASSOCIATED CONTENT

### Supporting Information

The Supporting Information is available free of charge at <https://pubs.acs.org/doi/10.1021/acs.jpbc.1c10207>.

Confirmation of silica growth on AuNRs, TEM image of AuNR@Ag<sub>29</sub>, change in AuNR@mSiO<sub>2</sub>@Ag<sub>29</sub> with time, TEM image of AuNR@mSiO<sub>2</sub>@Au<sub>30</sub>BSA, and its PL excitation and emission at various Au<sub>30</sub>BSA concentration (PDF)

Tomographic reconstruction of AuNR@mSiO<sub>2</sub> (AVI)

Tomographic reconstruction of AuNR@mSiO<sub>2</sub>@Ag<sub>29</sub> (AVI)

## AUTHOR INFORMATION

### Corresponding Author

Thalappil Pradeep – DST Unit of Nanoscience and Thematic Unit of Excellence, Department of Chemistry, Indian Institute of Technology Madras, Chennai 600036, India;  
orcid.org/0000-0003-3174-534X; Email: [pradeep@iitm.ac.in](mailto:pradeep@iitm.ac.in)

### Authors

Amrita Chakraborty – DST Unit of Nanoscience and Thematic Unit of Excellence, Department of Chemistry, Indian Institute of Technology Madras, Chennai 600036, India

Harsh Dave – DST Unit of Nanoscience and Thematic Unit of Excellence, Department of Chemistry, Indian Institute of Technology Madras, Chennai 600036, India; Present Address: Department of Bioengineering, University of Texas at Dallas, Richardson, Texas 75080, USA

Biswajit Mondal – DST Unit of Nanoscience and Thematic Unit of Excellence, Department of Chemistry, Indian Institute of Technology Madras, Chennai 600036, India

Nonappa – Faculty of Engineering and Natural Sciences, Tampere University, FI-33720 Tampere, Finland;  
orcid.org/0000-0002-6804-4128

Esma Khatun – DST Unit of Nanoscience and Thematic Unit of Excellence, Department of Chemistry, Indian Institute of Technology Madras, Chennai 600036, India

Complete contact information is available at: <https://pubs.acs.org/doi/10.1021/acs.jpbc.1c10207>

### Author Contributions

A.C. designed the experiments and carried out samples' preparation. H.D. carried out UV–vis spectroscopy and PL studies. B.M. collected TEM images. N. carried out imaging and electron tomography reconstruction measurements. E.K. synthesized Ag<sub>29</sub> and Au<sub>30</sub>BSA NC. The manuscript was written through contributions of all authors.

### Notes

The authors declare no competing financial interest.



## ACKNOWLEDGMENTS

We thank the Department of Science and Technology, Government of India for supporting our research. A.C. thanks the Council of Scientific and Industrial Research and B.M. and E.K. thank IIT Madras for their research fellowships. T.P. acknowledges funding for the Centre of Excellence on Molecular Materials and Functions under the Institution of Eminence scheme of IIT Madras. We acknowledge the support from the Ministry of Education and Culture (FICORE-2021 through MEC Global pilot program) and the Photonics Research and Innovation (PREIN) flagship and facilities at the OtaNano-Nanoscience Center (Aalto-NMC).

## REFERENCES

- (1) Simeonidis, K.; Martinez-Boubeta, C.; Zamora-Pérez, P.; Riveral-Gil, P.; Kaprara, E.; Kokkinos, E.; Mitrakas, M. Implementing nanoparticles for competitive drinking water purification. *Environ. Chem. Lett.* **2019**, *17*, 705–719.
- (2) Rani, A.; Reddy, R.; Sharma, U.; Mukherjee, P.; Mishra, P.; Kuila, A.; Sim, L. C.; Saravanan, P. A review on the progress of nanostructure materials for energy harnessing and environmental remediation. *J. Nanostructure Chem.* **2018**, *8*, 255–291.
- (3) Tyo, E. C.; Vajda, S. Catalysis by clusters with precise numbers of atoms. *Nat. Nanotechnol.* **2015**, *10*, 577–588.
- (4) Wang, Y.; Zhou, X.; Xu, C.; Jin, Y.; Li, B. Gold Nanorods as Visual Sensing Platform for Chiral Recognition with Naked Eyes. *Sci. Rep.* **2018**, *8*, 5296.
- (5) Wolfbeis, O. S. An overview of nanoparticles commonly used in fluorescent bioimaging. *Chem. Soc. Rev.* **2015**, *44*, 4743–4768.
- (6) Chakraborty, I.; Pradeep, T. Atomically Precise Clusters of Noble Metals: Emerging Link between Atoms and Nanoparticles. *Chem. Rev.* **2017**, *117*, 8208–8271.
- (7) Tan, X.; Jin, R. Ultrasmall metal nanoclusters for bio-related applications. *WIREs Nanomed. Nanobiotechnol.* **2013**, *5*, 569–581.
- (8) Eggeling, C.; Widengren, J.; Rigler, R.; Seidel, C. A. M. Photobleaching of Fluorescent Dyes under Conditions Used for Single-Molecule Detection: Evidence of Two-Step Photolysis. *Anal. Chem.* **1998**, *70*, 2651–2659.
- (9) Kairdolf, B. A.; Smith, A. M.; Stokes, T. H.; Wang, M. D.; Young, A. N.; Nie, S. Semiconductor Quantum Dots for Bioimaging and Biodiagnostic Applications. *Annu. Rev. of Anal. Chem.* **2013**, *6*, 143–162.
- (10) Montalti, M.; Cantelli, A.; Battistelli, G. Nanodiamonds and silicon quantum dots: ultrastable and biocompatible luminescent nanoprobe for long-term bioimaging. *Chem. Soc. Rev.* **2015**, *44*, 4853–4921.
- (11) Wang, Y.; Hu, A. Carbon quantum dots: synthesis, properties and applications. *J. Mater. Chem. C* **2014**, *2*, 6921–6939.
- (12) Weng, J.; Ren, J. Luminescent Quantum Dots: A Very Attractive and Promising Tool in Biomedicine. *Curr. Med. Chem.* **2006**, *13*, 897–909.
- (13) Retnakumari, A.; Setua, S.; Menon, D.; Ravindran, P.; Muhammed, H.; Pradeep, T.; Nair, S.; Koyakutty, M. Molecular-receptor-specific, non-toxic, near-infrared-emitting Au cluster-protein nanoclusters for targeted cancer imaging. *Nanotechnology* **2010**, *21*, 055103.
- (14) Nonappa. Luminescent gold nanoclusters for bioimaging applications. *Beilstein J. Nanotechnol.* **2020**, *11*, 533–546.
- (15) Hynninen, V.; Chandra, S.; Das, S.; Amini, M.; Dai, Y.; Lepikko, S.; Mohammadi, P.; Hietala, S.; Ras, R. H. A.; Sun, Z.; et al. Luminescent Gold Nanocluster-Methylcellulose Composite Optical Fibers with Low Attenuation Coefficient and High Photostability. *Small* **2021**, *17*, 2005205.
- (16) Chandra, S.; Nonappa; Beaune, G.; Som, A.; Zhou, S.; Lahtinen, J.; Jiang, H.; Timonen, J. V. I.; Ikkala, O.; Ras, R. H. A. Highly Luminescent Gold Nanocluster Frameworks. *Adv. Opt. Mater.* **2019**, *7*, 1900620.
- (17) Yu, H.; Peng, Y.; Yang, Y.; Li, Z.-Y. Plasmon-enhanced light–matter interactions and applications. *npj Comput. Mater.* **2019**, *5*, 45.
- (18) Xia, H.-X.; Yang, X.-Q.; Song, J.-T.; Chen, J.; Zhang, M.-Z.; Yan, D.-M.; Zhang, L.; Qin, M.-Y.; Bai, L.-Y.; Zhao, Y.-D.; et al. Folic acid-conjugated silica-coated gold nanorods and quantum dots for dual-modality CT and fluorescence imaging and photothermal therapy. *J. Mater. Chem. B* **2014**, *2*, 1945–1953.
- (19) Alkilany, A. M.; Thompson, L. B.; Boulos, S. P.; Sisco, P. N.; Murphy, C. J. Gold nanorods: their potential for photothermal therapeutics and drug delivery, tempered by the complexity of their biological interactions. *Adv. Drug Delivery Rev.* **2012**, *64*, 190–9.
- (20) Drisko, G. L.; Sanchez, C. Hybridization in Materials Science – Evolution, Current State, and Future Aspirations. *Eur. J. Inorg. Chem.* **2012**, *2012*, 5097–5105.
- (21) Sanchez, C.; Belleville, P.; Popall, M.; Nicole, L. Applications of advanced hybrid organic–inorganic nanomaterials: from laboratory to market. *Chem. Soc. Rev.* **2011**, *40*, 696–753.
- (22) Sailor, M. J.; Park, J. H. Hybrid nanoparticles for detection and treatment of cancer. *Adv. Mater. (Deerfield Beach, Fla.)* **2012**, *24*, 3779–802.
- (23) Melancon, M. P.; Zhou, M.; Li, C. Cancer Theranostics with Near-Infrared Light-Activatable Multimodal Nanoparticles. *Acc. Chem. Res.* **2011**, *44*, 947–956.
- (24) Luo, T.; Huang, P.; Gao, G.; Shen, G.; Fu, S.; Cui, D.; Zhou, C.; Ren, Q. Mesoporous silica-coated gold nanorods with embedded indocyanine green for dual mode X-ray CT and NIR fluorescence imaging. *Opt. Express* **2011**, *19*, 17030–9.
- (25) Sun, H.; Yuan, Q.; Zhang, B.; Ai, K.; Zhang, P.; Lu, L. GdIII functionalized gold nanorods for multimodal imaging applications. *Nanoscale* **2011**, *3*, 1990–1996.
- (26) Lee, S.; Sim, K.; Moon, S. Y.; Choi, J.; Jeon, Y.; Nam, J.-M.; Park, S.-J. Controlled Assembly of Plasmonic Nanoparticles: From Static to Dynamic Nanostructures. *Adv. Mater.* **2021**, *33*, 2007668.
- (27) Nonappa; Lahtinen, T.; Haataja, J. S.; Tero, T.-R.; Häkkinen, H.; Ikkala, O. Template-Free Supracolloidal Self-Assembly of Atomically Precise Gold Nanoclusters: From 2D Colloidal Crystals to Spherical Capsids. *Angew. Chem., Int. Ed.* **2016**, *55*, 16035–16038.
- (28) Chakraborty, A.; Fernandez, A. C.; Som, A.; Mondal, B.; Natarajan, G.; Paramasivam, G.; Lahtinen, T.; Häkkinen, H.; Nonappa; Pradeep, T. Atomically Precise Nanocluster Assemblies Encapsulating Plasmonic Gold Nanorods. *Angew. Chem., Int. Ed.* **2018**, *57*, 6522–6526.
- (29) Som, A.; Chakraborty, I.; Maark, T. A.; Bhat, S.; Pradeep, T. Cluster-Mediated Crossed Bilayer Precision Assemblies of 1D Nanowires. *Adv. Mater.* **2016**, *28*, 2827–2833.
- (30) Samal, A. K.; Sreeprasad, T. S.; Pradeep, T. Investigation of the role of NaBH<sub>4</sub> in the chemical synthesis of gold nanorods. *J. Nanopart. Res.* **2010**, *12*, 1777–1786.
- (31) Gorelikov, I.; Matsuura, N. Single-Step Coating of Mesoporous Silica on Cetyltrimethyl Ammonium Bromide-Capped Nanoparticles. *Nano Lett.* **2008**, *8*, 369–373.
- (32) Liu, J.; Detrembleur, C.; De Pauw-Gillet, M.-C.; Mornet, S.; Jérôme, C.; Duguet, E. Gold Nanorods Coated with Mesoporous Silica Shell as Drug Delivery System for Remote Near Infrared Light-Activated Release and Potential Phototherapy. *Small* **2015**, *11*, 2323–2332.
- (33) van der Linden, M.; Barendregt, A.; van Bunningen, A.; Chin, P.; Thies-Weesie, D.; De Groot, F.; Meijerink, A. Characterisation, degradation and regeneration of luminescent Ag<sub>29</sub> clusters in solution. *Nanoscale* **2016**, *8*, 19901–19909.
- (34) Mohanty, J. S.; Baksi, A.; Lee, H.; Pradeep, T. Noble metal clusters protected with mixed proteins exhibit intense photoluminescence. *RSC Adv.* **2015**, *5*, 48039–48045.
- (35) Mastronarde, D. N. SerialEM: A Program for Automated Tilt Series Acquisition on Tecnai Microscopes Using Prediction of Specimen Position. *Microsc. Microanal.* **2003**, *9*, 1182–1183.
- (36) Mastronarde, D. N. Automated electron microscope tomography using robust prediction of specimen movements. *J. Struct. Biol.* **2005**, *152*, 36–51.

- (37) Nonappa; Engelhardt, P. Electron Tomography of Whole Mounts. *Wiley Anal. Sci.* **2019**, *21*, 22–24.
- (38) Kremer, J. R.; Mastrorarde, D. N.; McIntosh, J. R. Computer Visualization of Three-Dimensional Image Data Using IMOD. *J. Struct. Biol.* **1996**, *116*, 71–76.
- (39) Dulkeith, E.; Morteani, A. C.; Niedereichholz, T.; Klar, T. A.; Feldmann, J.; Levi, S. A.; van Veggel, F. C.; Reinhoudt, D. N.; Möller, M.; Gittins, D. I. Fluorescence quenching of dye molecules near gold nanoparticles: radiative and nonradiative effects. *Phys. Rev. Lett.* **2002**, *89*, 203002.
- (40) Li, S.; Zhang, T.; Zhu, Z.; Gao, N.; Xu, Q.-H. Lighting up the gold nanoparticles quenched fluorescence by silver nanoparticles: a separation distance study. *RSC Adv.* **2016**, *6*, 58566–58572.
- (41) Reineck, P.; Gómez, D.; Ng, S. H.; Karg, M.; Bell, T.; Mulvaney, P.; Bach, U. Distance and Wavelength Dependent Quenching of Molecular Fluorescence by Au@SiO<sub>2</sub> Core–Shell Nanoparticles. *ACS Nano* **2013**, *7*, 6636–6648.
- (42) Marques, M. E.; Mansur, A. A. P.; Mansur, H. S. Chemical functionalization of surfaces for building three-dimensional engineered biosensors. *Appl. Surf. Sci.* **2013**, *275*, 347–360.
- (43) Villa, S.; Riani, P.; Locardi, F.; Canepa, F. Functionalization of Fe<sub>3</sub>O<sub>4</sub> NPs by Silanization: Use of Amine (APTES) and Thiol (MPTMS) Silanes and Their Physical Characterization. *Materials (Basel)* **2016**, *9*, 826.
- (44) Shang, L.; Yang, L.; Stockmar, F.; Popescu, R.; Trouillet, V.; Bruns, M.; Gerthsen, D.; Nienhaus, G. U. Microwave-assisted rapid synthesis of luminescent gold nanoclusters for sensing Hg<sup>2+</sup> in living cells using fluorescence imaging. *Nanoscale* **2012**, *4*, 4155–4160.
- (45) Adhikari, B.; Banerjee, A. Facile Synthesis of Water-Soluble Fluorescent Silver Nanoclusters and HgII Sensing. *Chem. Mater.* **2010**, *22*, 4364–4371.
- (46) Shang, L.; Azadfar, N.; Stockmar, F.; Send, W.; Trouillet, V.; Bruns, M.; Gerthsen, D.; Nienhaus, G. U. One-Pot Synthesis of Near-Infrared Fluorescent Gold Clusters for Cellular Fluorescence Lifetime Imaging. *Small* **2011**, *7*, 2614–2620.
- (47) Jiang, R.; Li, B.; Fang, C.; Wang, J. Metal/Semiconductor Hybrid Nanostructures for Plasmon-Enhanced Applications. *Adv. Mater.* **2014**, *26*, 5274–5309.
- (48) Li, J.-F.; Li, C.-Y.; Aroca, R. F. Plasmon-enhanced fluorescence spectroscopy. *Chem. Soc. Rev.* **2017**, *46*, 3962–3979.
- (49) Goris, B.; Bals, S.; Van den Broek, W.; Carbó-Argibay, E.; Gómez-Graña, S.; Liz-Marzán, L. M.; Van Tendeloo, G. Atomic-scale determination of surface facets in gold nanorods. *Nat. Mater.* **2012**, *11*, 930–935.
- (50) Xiang, Y.; Wu, X.; Liu, D.; Jiang, X.; Chu, W.; Li, Z.; Ma, Y.; Zhou, W.; Xie, S. Formation of Rectangularly Shaped Pd/Au Bimetallic Nanorods: Evidence for Competing Growth of the Pd Shell between the {110} and {100} Side Facets of Au Nanorods. *Nano Lett.* **2006**, *6*, 2290–2294.
- (51) Cho, E. C.; Camargo, P. H. C.; Xia, Y. Synthesis and Characterization of Noble-Metal Nanostructures Containing Gold Nanorods in the Center. *Adv. Mater.* **2010**, *22*, 744–748.
- (52) Carbó-Argibay, E.; Rodríguez-González, B. Controlled Growth of Colloidal Gold Nanoparticles: Single-Crystalline versus Multiply-twinned Particles. *Isr. J. Chem.* **2016**, *56*, 214–226.
- (53) Zhu, J.; Chang, H.; Li, J. J.; Li, X.; Zhao, J. W. Using silicon-coated gold nanoparticles to enhance the fluorescence of CdTe quantum dot and improve the sensing ability of mercury (II). *Spectrochim. Acta A Mol. Biomol. Spectrosc.* **2018**, *188*, 170–178.
- (54) Wu, Z.; Jin, R. On the Ligand's Role in the Fluorescence of Gold Nanoclusters. *Nano Lett.* **2010**, *10*, 2568–2573.
- (55) Goswami, N.; Yao, Q.; Luo, Z.; Li, J.; Chen, T.; Xie, J. Luminescent Metal Nanoclusters with Aggregation-Induced Emission. *J. Phys. Chem. Lett.* **2016**, *7*, 962–975.
- (56) Goswami, N.; Lin, F.; Liu, Y.; Leong, D. T.; Xie, J. Highly Luminescent Thiolated Gold Nanoclusters Impregnated in Nanogel. *Chem. Mater.* **2016**, *28*, 4009–4016.
- (57) Chen, Y.; Zheng, M.; Xiao, Y.; Dong, H.; Zhang, H.; Zhuang, J.; Hu, H.; Lei, B.; Liu, Y. A Self-Quenching-Resistant Carbon-Dot Powder with Tunable Solid-State Fluorescence and Construction of Dual-Fluorescence Morphologies for White Light-Emission. *Adv. Mater. (Deerfield Beach, Fla.)* **2016**, *28*, 312–318.
- (58) Gan, Z.; Di, Y.; Huang, S.; Shen, J.; Yang, L.; Zhang, X. Modulating the fluorescent color of carbon nanodots via photon reabsorption and carbonization degree. *Appl. Phys. Lett.* **2017**, *111*, 241903.
- (59) Gan, Z.; Xu, H.; Fu, Y. Photon Reabsorption and Nonradiative Energy-Transfer-Induced Quenching of Blue Photoluminescence from Aggregated Graphene Quantum Dots. *J. Phys. Chem. C* **2016**, *120*, 29432–29438.
- (60) Huang, H.-Y.; Cai, K.-B.; Talite, M. J.; Chou, W.-C.; Chen, P.-W.; Yuan, C.-T. Coordination-induced emission enhancement in gold-nanoclusters with solid-state quantum yields up to 40% for eco-friendly, low-reabsorption nano-phosphors. *Sci. Rep.* **2019**, *9*, 4053.
- (61) Senthamizhan, A.; Celebioglu, A.; Uyar, T. Real-time selective visual monitoring of Hg<sup>2+</sup> detection at ppt level: An approach to lighting electrospun nanofibers using gold nanoclusters. *Sci. Rep.* **2015**, *5*, 10403.
- (62) Chen, Z.; Qian, S.; Chen, X.; Gao, W.; Lin, Y. Protein-templated gold nanoclusters as fluorescence probes for the detection of methotrexate. *Analyst* **2012**, *137*, 4356–4361.
- (63) Chevrier, D. M.; Thanthirige, V. D.; Luo, Z.; Driscoll, S.; Cho, P.; MacDonald, M. A.; Yao, Q.; Guda, R.; Xie, J.; Johnson, E. R.; Chatt, A.; et al. Structure and formation of highly luminescent protein-stabilized gold clusters. *Chem. Sci.* **2018**, *9*, 2782–2790.
- (64) Zhou, R.; Sun, S.; Li, C.; Wu, L.; Hou, X.; Wu, P. Enriching Mn-Doped ZnSe Quantum Dots onto Mesoporous Silica Nanoparticles for Enhanced Fluorescence/Magnetic Resonance Imaging Dual-Modal Bio-Imaging. *ACS Appl. Mater. Interfaces* **2018**, *10*, 34060–34067.
- (65) Li, M.; Cushing, S. K.; Wu, N. Plasmon-enhanced optical sensors: a review. *Analyst* **2015**, *140*, 386–406.



## Supporting Information

### Shell-Isolated Assembly of Atomically Precise Nanoclusters on Gold Nanorods for Integrated Plasmonic-Luminescent Nanocomposites

Amrita Chakraborty,<sup>1</sup> Harsh Dave,<sup>1,#</sup> Biswajit Mondal,<sup>1</sup> Nonappa,<sup>2</sup> Esma Khatun<sup>1</sup> and Thalappil Pradeep\*<sup>1</sup>

#### Affiliations

<sup>1</sup>DST Unit of Nanoscience and Thematic Unit of Excellence, Department of Chemistry, Indian Institute of Technology Madras, Chennai 600036, India. <sup>2</sup>Faculty of Engineering and Natural Sciences, Tampere University, FI-33101, Tampere, Finland.

#### Table of contents

No.	Title	Page No.
Figure S1	Confirmation of silica growth on AuNRs	2
Figure S2	TEM image of AuNR@Ag <sub>29</sub>	2
Figure S3	Change in AuNR@mSiO <sub>2</sub> @Ag <sub>29</sub> with time	3
Figure S4	TEM image of AuNR@mSiO <sub>2</sub> @Au <sub>30</sub> BSA, and its PL excitation and emission at various Au <sub>30</sub> BSA concentration	3
Video S1	Tomographic reconstruction of AuNR@mSiO <sub>2</sub>	Attached
Video S2	Tomographic reconstruction of AuNR@mSiO <sub>2</sub> @Ag <sub>29</sub>	Attached

## Supporting Figures

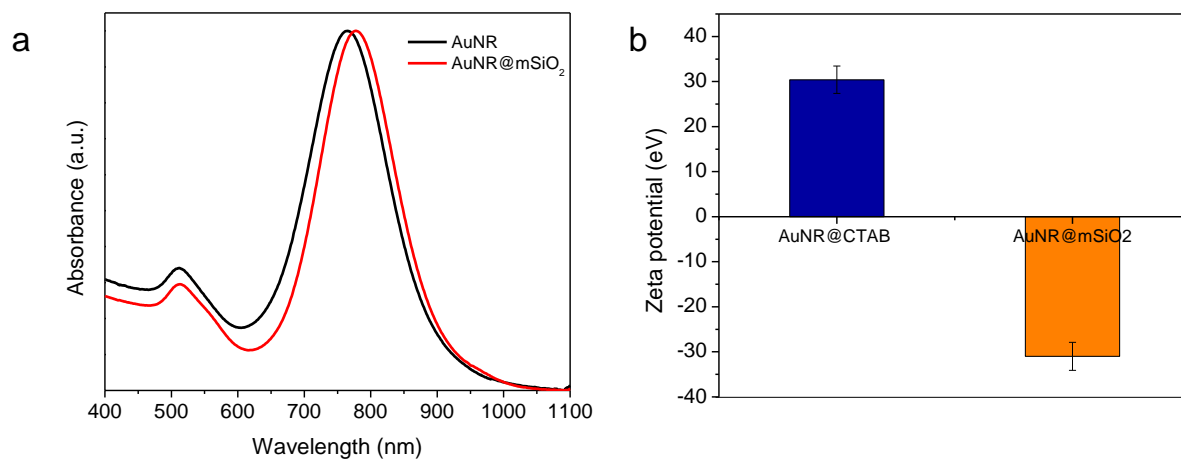


**Figure S1.** (a) Comparative absorption spectra of AuNR and AuNR@mSiO<sub>2</sub>, and (b) change in zeta potential value upon silica coating of AuNR.

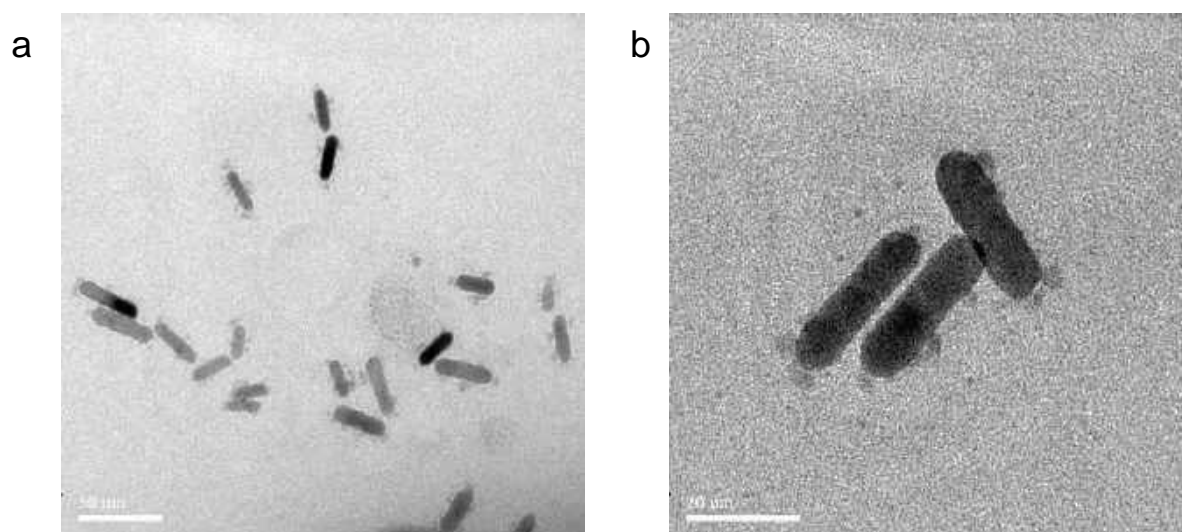


**Figure S2.** (a) TEM image of AuNR@Ag<sub>29</sub>, and b) that at higher magnification, showing direct attachment of NC to AuNR surface.

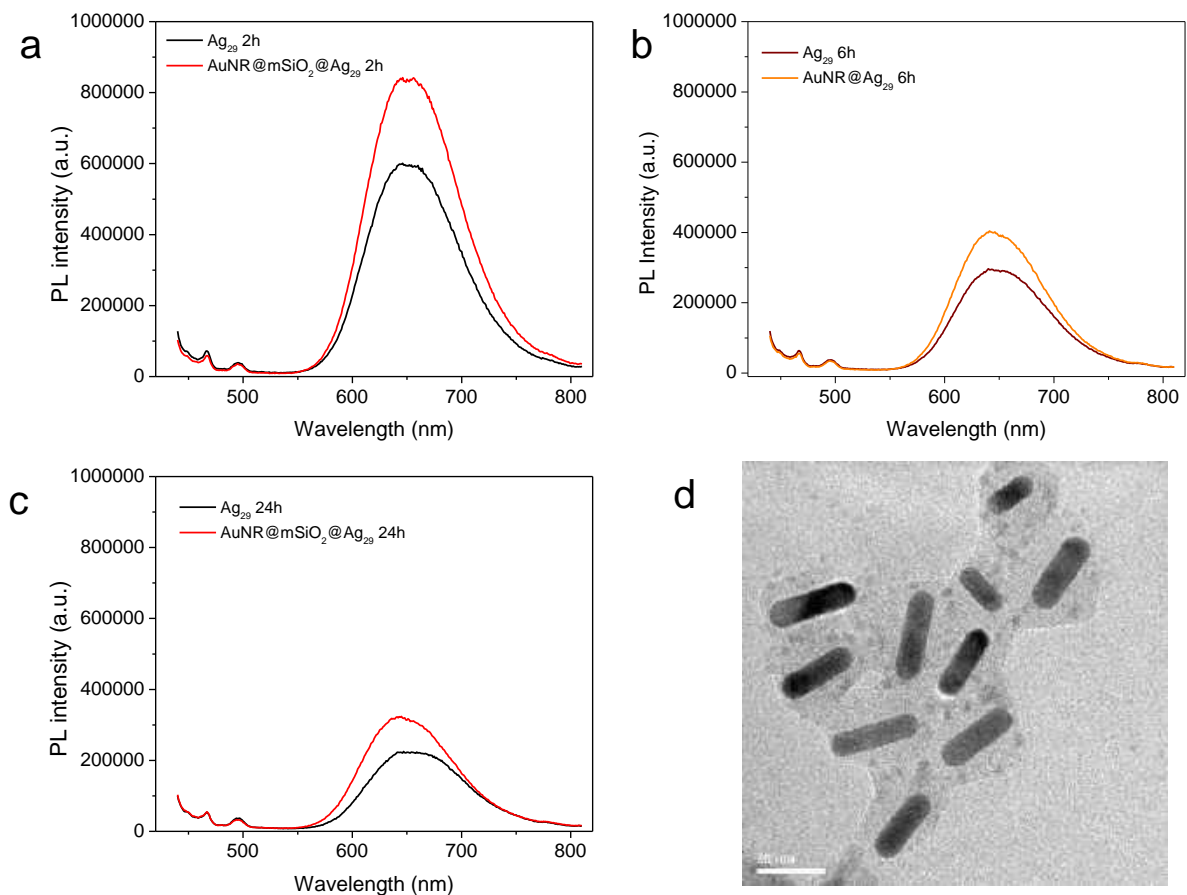


**Figure S3.** Comparative PL emission spectra of AuNR@mSiO<sub>2</sub>@Ag<sub>29</sub> and blank Ag<sub>29</sub> after (a) 2h, (b) 6h and (c) 24 h. (d) TEM image of AuNR@mSiO<sub>2</sub>@Ag<sub>29</sub> after 48 h.

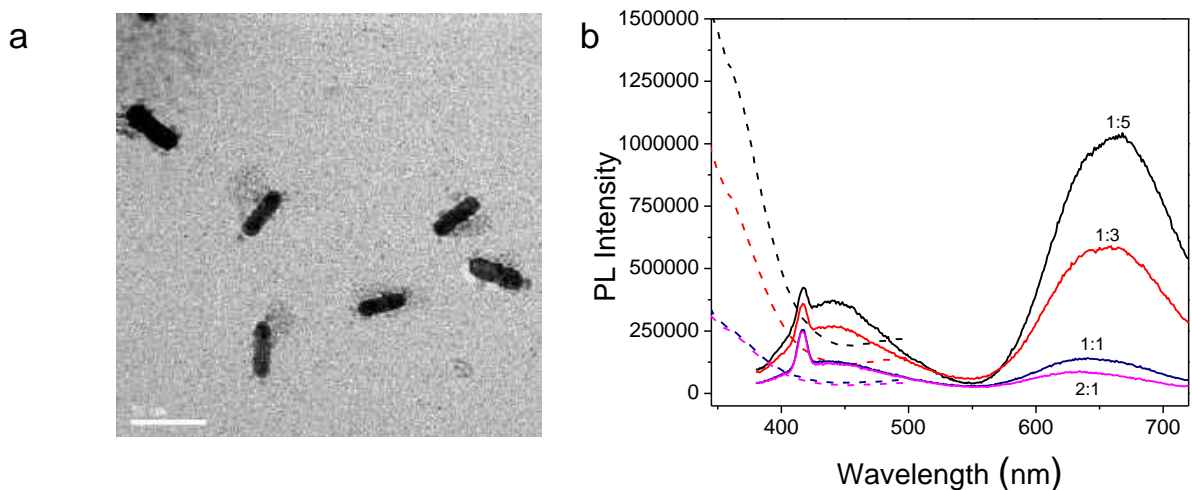


**Figure S4.** (a) TEM image of AuNR@mSiO<sub>2</sub>@Au<sub>30</sub>BSA, (b) comparative excitation spectra (dotted lines) and emission spectra (solid lines) corresponding to AuNR: Au<sub>30</sub>BSA volume ratios 2:1 (magenta), 1:1 (blue), 1:3 (red) and 1:5 (black) in AuNR@mSiO<sub>2</sub>@Au<sub>30</sub>BSA.

# Role of Zinc Oxide in the Compounding Formulation on the Growth of Nonstoichiometric Copper Sulfide Nanostructures at the Brass–Rubber Interface

Kannan Murugesan Paulthangam, Anirban Som, Tripti Ahuja, Pillalamarri Srikrishnarka, Appukuttan Sreekumaran Nair,\* and Thalappil Pradeep\*



Cite This: *ACS Omega* 2022, 7, 9573–9581



Read Online

ACCESS |



Metrics & More

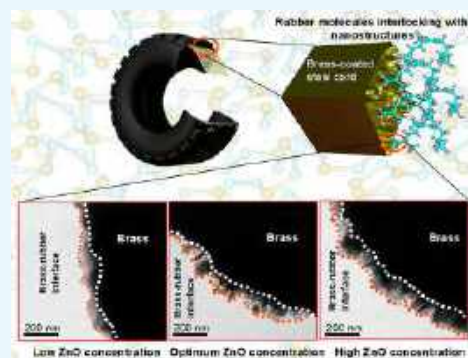


Article Recommendations



Supporting Information

**ABSTRACT:** Tire technology has evolved substantially by the introduction of brass-coated steel cords (BCSCs) in radial tires. The durability of radial tires is dependent on the integrity of the brass–rubber interface composed predominantly of nonstoichiometric copper sulfide ( $\text{Cu}_{2-x}\text{S}$ , where  $x = 1$  to 2) nanostructures whose morphology and characteristics are dependent upon the crucial rubber additive, ZnO. Its higher concentration impacts environmental sustainability, while at lower levels, there is insufficient bonding between steel and the rubber thus affecting tire's safety. This brings in the need for an optimum ZnO concentration to be used in radial tires and is thus the theme of the present work. The changes in the properties of interfacial nanostructures such as morphology, thickness, crystallinity, and chemical composition were studied at various ZnO concentrations. We adopted our previously reported methodology, the “brass mesh experiment”, to investigate the thickness of nanostructures at varied ZnO concentrations using transmission electron microscopy (TEM). Significant results were obtained from field-emission scanning electron microscopy (FESEM), X-ray diffraction (XRD), Raman imaging and X-ray photoelectron spectroscopy (XPS). In conjunction with a more practical experimental technique, namely the measurement of pull-out force (POF), it has been concluded that 9 parts per hundred rubber (PHR) ZnO is essential for the optimum growth of nanostructures and is considered to be the optimum for the composition studied. We believe that the scientific approach outlined in the manuscript would help the tire- and the material science communities to widen the knowledge of understanding sustainability in tire industries. It is estimated that the optimization presented here can save \$400–450 million for the tire industry and 2.4 million tons of ZnO per year.



## INTRODUCTION

Brass-coated steel cords (BCSCs) are widely used to construct the complex structure of radial tires (RTs) to enhance product durability and performance.<sup>1</sup> Conventionally, a ~200 nm thick brass coating on steel cords is, in fact, the adhesion promoter that remarkably improves the bonding between rubber and steel cords by building up a robust bonding interface resistant to high temperature and dynamic loading.<sup>2</sup> Of the many materials that are involved in the complex tire manufacturing processes,<sup>3</sup> zinc oxide (ZnO), the vulcanization activator, plays a vital role in adhesion between brass and rubber.<sup>4</sup> Because of the supreme physical and chemical properties of ZnO, the tire industry remains its largest market (~60%), estimated to be 120 million metric tons per year, accounting for 3.0 billion tires manufactured annually.<sup>5</sup> A typical tire contains 1–3% of ZnO by weight.<sup>6,7</sup> Zinc leaching from tires is known, and it is classified to be toxic for the aquatic environment above 2 ppm, according to a directive of the European Union.<sup>8–10</sup> The International Programme on Chemical Safety (IPCS) has recommended regulatory criteria for Zn, assessing an optimum ZnO level in rubber products vital for reducing harmful

environmental impact.<sup>11</sup> Also, higher ZnO concentrations (more than the optimum level) in the rubber compound increases the overall mass of the tire because of its higher specific gravity compared with other ingredients, which cause undesirable attributes such as high rolling resistance (RR) and consequently higher fuel consumption and associated negative contribution to the carbon footprint.<sup>12</sup>

Apart from ecological issues, an optimum concentration of ZnO is of significance in the tire industry for increased strength at operating conditions.<sup>13</sup> However, studies to arrive at an optimum concentration of ZnO require a thorough understanding of the morphology, interface thickness, and chemical composition for desired adhesion. There is a positive

Received: December 8, 2021

Accepted: February 25, 2022

Published: March 10, 2022



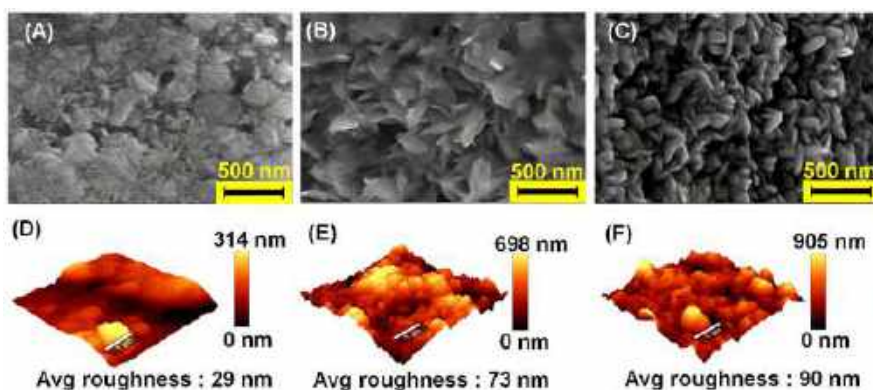


**Figure 1.** Morphology and thickness of the interface. FE-SEM images of vulcanized steel cords with (A) 6, (B) 9, and (C) 12 PHR ZnO loadings. AFM images portraying the interface roughness for (D) 6, (E) 9, and (F) 12 PHR ZnO.

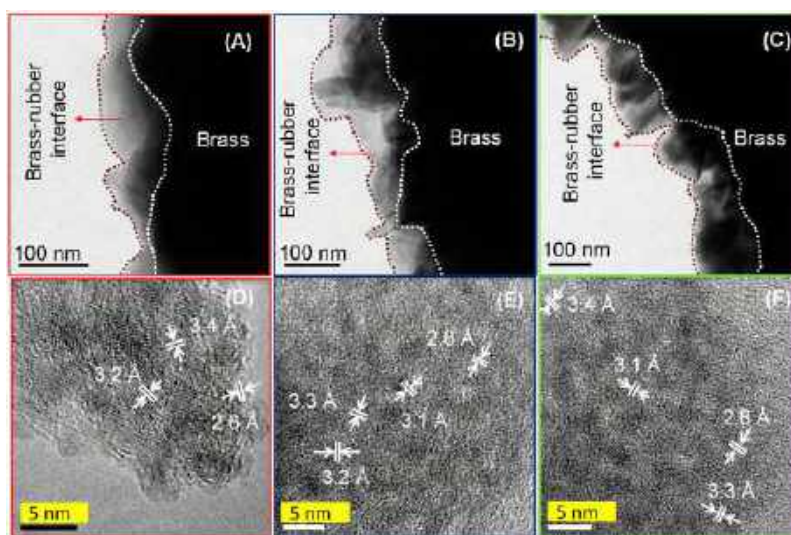


**Figure 2.** Bright-field TEM images of the nanostructures grown over brass mesh at (A) 6, (B) 9, and (C) 12 PHR ZnO. Corresponding high-resolution TEM images are in (D–F). Scale: 5 nm.

correlation between ZnO concentration and the cost incurred for tire production, that is, per unit increase in PHR (parts per hundred rubber, PHR - a measurement used by rubber chemists to denote weight), increases  $\sim$ \$400–450 million annually for tire industries globally. This is significant as many tire chemists are unaware of the impact of ZnO on the interfacial properties, contributing to increased tire manufacturing costs and reduced environmental sustainability.<sup>14</sup>

In recent years, there has been a growing interest in knowing how the two sources of ZnO (one from the rubber compound—a term referring to a mixture of rubbers, fillers, vulcanization activators, accelerators, promoters, etc.—and the other already present in the BCSCs) affect the formation of the bonding interface. Recent literature has highlighted how these different sources of ZnO affect the steel cord–rubber adhesion through the inclusion of isotopically labeled Zn (<sup>64</sup>Zn) in the rubber compound, using secondary ion mass spectrometry (SIMS).<sup>4</sup> The study was further advanced by interpreting the origin of ZnS from ZnO added to the rubber compound. It has been proved that the formation of ZnS at the interface is known to be disadvantageous as it weakens the interfacial bonding with rubber.<sup>2,15</sup> Interesting correlations between the microstructure changes (interfacial thickness) and the associated mechanical properties such as pull-out force

(POF), tensile strength, modulus, and elongation at break have been studied. It was found that with the increase in interfacial thickness, the POF decreases, corresponding to lower interfacial strength. However, only very little is known on how variations in the concentration of ZnO as a compounding ingredient affect the morphology, interface thickness, crystallinity, and chemical composition of nanostructures at the brass–rubber interface.

Most studies have focused on explaining the optimum concentration of ZnO in the adhesion interface based on pull-out force (POF) and physical properties of the rubber compound such as modulus, tensile strength, and Mooney viscosity.<sup>16</sup> Additionally, not many reports have highlighted the environmental concerns caused because of tire-related issues such as the tire weight and the associated fuel consumption based on desired ZnO concentration for better interfacial bonding.<sup>17</sup> To fill this knowledge gap, in this paper, we present a detailed study of improving the sustainability of the tire industry through understanding the changes in critical interfacial parameters such as morphology, interfacial thickness, and chemical composition of the adhesive interface to arrive at the optimum ZnO concentration in the rubber compound. We found that varying ZnO concentrations in rubber compounds can be used to control these parameters.



We observed that the average surface roughness of the interfacial nanostructures increased from  $\sim 29$  to  $\sim 90$  nm by varying the ZnO concentration. Therefore, we followed an alternative approach to enhance sustainability that is advantageous to the established methods by quantifying the nanoscale features of the interface at various ZnO concentrations and correlating them with the bulk properties of the tires. Additionally, the brass mesh experiment,<sup>2</sup> a new methodology reported by us recently, which is also a viable approach, was adopted in this study to measure the interfacial thickness. The correlation between the interfacial thickness and its bonding strength with rubber was established by a more practical methodology, namely the pull-out force (POF) measurements. We believe that the present findings would help the rubber compounders to choose the optimum ZnO concentration suited for the formulation, thus reduce manufacturing costs, and improve sustainability.

## RESULTS AND DISCUSSION

**Morphology and Measurement of the Thickness of the Brass–Rubber Interface.** Morphology and roughness of the nanostructures at the interface imaged at three different ZnO concentrations (6, 9, and 12 PHR) are shown in Figure 1. An increase in the density of nanostructures accompanied by a morphology change was noted with an increase in ZnO concentration (Figure 2A–C). As shown in Figure 1A, the nanostructures have started to grow at 6 PHR of ZnO loading. Interface formed at 6 PHR had a combination of flaky and circular structures, indicating that this kind of an interface was still in the process of growing. The interface transitioned to completely flaky/leafy structures at 9 PHR ZnO, as evident from Figure 1B. At 12 PHR ZnO loading, the flaky nanostructures were transformed into dense flower-shaped structures (Figure 1C). Figure S2 depicts large area SEM and EDS data corresponding to Figure 1A–C. One of the significant findings from the SEM-EDS data is the increase in the atomic% of Cu, S, O, and Zn of the nanostructures with an increase in the ZnO concentration. It was noted that the interface formed in Figure 1C had more Cu and S than in Figure 1A. Thus, an increase of ZnO in the rubber compound promotes an increased percentage of active sulfurating species to react with Cu and Zn to form copper- and zinc sulfides. Also, EDS analysis revealed significantly higher O and Zn atomic% changes as a function of the ZnO concentration.

The surface roughness of the nanostructures at different ZnO loadings was measured using Atomic Force Microscopy (AFM) (Figure 1D–F). As can be seen from Figure S3, the average surface roughness was high for the vulcanized interface compared to the unreacted state. Significantly, interface roughness with 6, 9, and 12 PHR of ZnO was 29, 73, and 90 nm, respectively. The present findings confirm a direct correlation between the surface roughness and morphology of the interfacial nanostructure with ZnO concentration.

The concentration of ZnO in the rubber compound, to a large extent, affects its interaction with the vulcanization accelerator.<sup>18</sup> For instance, a higher ZnO PHR increases the cross-linking of the rubber.<sup>16,19</sup> ZnO, along with stearic acid, increases the rubber cross-linking by forming S bridges. This leads to higher active sulphurating species available to the interface leading to a larger interface growth. A higher ZnO concentration in rubber compound leads to the formation of higher concentrations of  $\text{Cu}_{2-x}\text{S}$  and ZnS at the interface, leading to increased nanostructure size and roughness.

However, at lower concentrations, the accelerator devoid of sufficient ZnO for vulcanization extracts zinc from the brass. This leads to higher  $\text{CuS}/\text{Cu}_{2-x}\text{S}$  thickness as the brass becomes rich in Cu. Thus, both higher and lower ZnO concentration in rubber compounds lead to difficulties in forming the right interface, thereby drastically affecting the adhesion properties.

To understand the role of ZnO in controlling the interfacial thickness, we adopted a simple technique, the “brass-mesh” experiment.<sup>2</sup> Figure 2A–C portrays the nanostructures grown on the brass mesh with different concentrations of ZnO in the rubber compound. Multiple TEM images were taken from different regions of the brass-mesh. Figure 2A shows the nanostructures grown on the brass grid at 6 PHR ZnO. The nanostructures formed do not have a proper dendritic structure because of the insufficient amount of the active sulfurating species at the interface. The nanostructures grow denser, accompanied by a change in dendritic morphology from flaky/leafy to flower-shaped, from 9 PHR to 12 PHR ZnO (Figure 2B,C). In panels D–F, respectively, of Figure 2, we show high-resolution TEM images of the nanostructures formed on the brass mesh at 6, 9, and 12 PHR ZnO that were then correlated with XRD, Raman images, and XPS (Figures 3, 4, and 5),

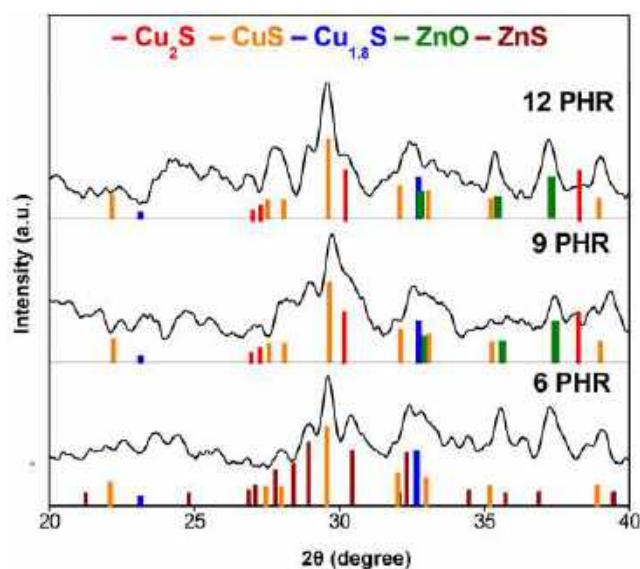


**Figure 3.** Crystallinity of the adhesion interface. XRD patterns of the vulcanized BCSCs at different ZnO concentrations, showing the various phases of nanoscale materials existing at the interface.

respectively, to confirm the chemical substances. The lattice spacings of 2.6, 3.2 and 3.4 Å at 6 PHR ZnO correspond to the presence of planes of CuS [(103)],  $\text{Cu}_{1.8}\text{S}$  [(101)], and ZnS [(111)] at the adhesion interface, which are consistent with the XRD results.<sup>20–22</sup> Thus, the interfacial nanostructures formed due to vulcanization with 6 PHR ZnO had the composition of a mixture of CuS,  $\text{Cu}_{1.8}\text{S}$ , and ZnS. At 9 and 12 PHR ZnO, analysis shows the presence of CuS [(103)],  $\text{Cu}_{1.8}\text{S}$  [(101)],  $\text{Cu}_2\text{S}$  [(101)], and ZnO [(100)] confirmed by the presence of 2.8, 3.1, 3.3, and 3.4 Å lattice spacings.<sup>23</sup>

As shown in Figure 2A–C, it is apparent that the nanostructures grew in size with the increase in ZnO concentration. Additionally, the crystallinity of the nanostructures changed from 6 PHR to 9 PHR ZnO. A higher ZnO concentration in rubber compound facilitates a higher

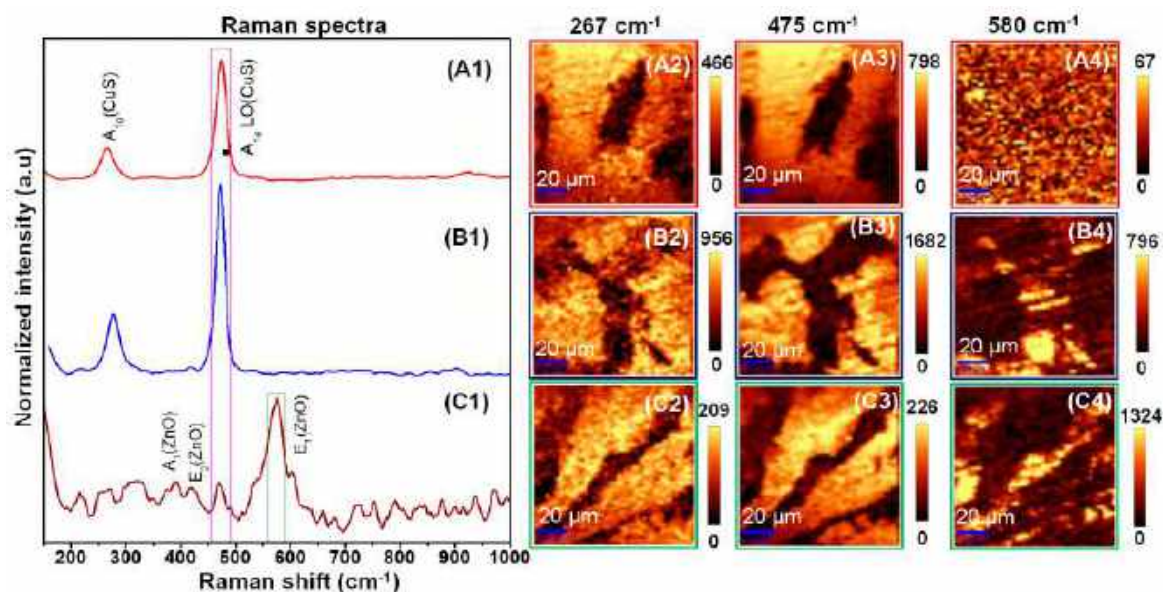


**Figure 4.** Raman spectra of BCSC at ZnO concentrations of (A1) 6, (B1) 9, and (C1) 12 PHR. Images A2, B2, and C2 correspond to confocal Raman maps at  $267\text{ cm}^{-1}$  (scale:  $20\text{ }\mu\text{m}$ ). A3, B3 and C3 are maps at  $475\text{ cm}^{-1}$  and A4, B4, and C4 are maps at  $580\text{ cm}^{-1}$ . Images A2–A4 correspond to 6 PHR, images B2–B4 correspond to 9 PHR, and images C2–C4 correspond to 12 PHR ZnO concentrations, respectively. The color bar on the right represents the CCD counts.

concentration of active sulphurating species and hence a higher concentration of  $\text{Cu}_{2-x}\text{S}/\text{ZnS}/\text{ZnO}$ , resulting in higher interfacial thickness.

From Figure S4A, it is also seen that the average interfacial thickness increased from  $\sim 65\text{ nm}$  to  $\sim 114\text{ nm}$  when the ZnO concentration was varied from 6 to 12 PHR. Upon comparing aged and unaged POF (Figure S4B–D), there was a steep increase in POF for the unaged. When the interface is aged, there was an initial rise in the POF for 6 PHR and 9 PHR followed by a drop at 12 PHR, which is predominantly attributed to two main reasons: the first being the catalytic activity of ZnO at higher concentrations, causing oxidative degradation of the interface; and the second being a change in the composition of the interface.<sup>24</sup> In addition, crystalline interfacial nanostructures in the aged interface also correspond to the reduction of POF.<sup>25</sup> Hence, it can be inferred that the addition of 9 PHR ZnO in the rubber compound formulation of the ply region of a tire is sufficient for a suitable interface thickness and excess ZnO can be avoided. We wish to point out that the POF values reported in the present manuscript are higher than those in the above-mentioned literature as the present experiments were conducted under realistic tire vulcanization conditions, and the formulation had a higher concentration of adhesion promoters than those reported in literature.<sup>26,27</sup>

Mooney viscosity (MV) of the compounds was measured to understand the processability of the rubber compounds and Figure S5A,C shows the MV and moment highest (MH) of the rubber compound at different ZnO concentrations. At a higher MV and MH, the rubber compound was difficult to be processed for vulcanization, while a lower MV would lead to air blisters in the vulcanized material. An increase in MV was noted with an increase in ZnO, inferring that the rubber compound would be hard to process for vulcanization. It was also noted that no air blisters were formed at 6 PHR. It is interesting to note from Table S2 that the cross-link density of rubber compounds increased with an increase in ZnO

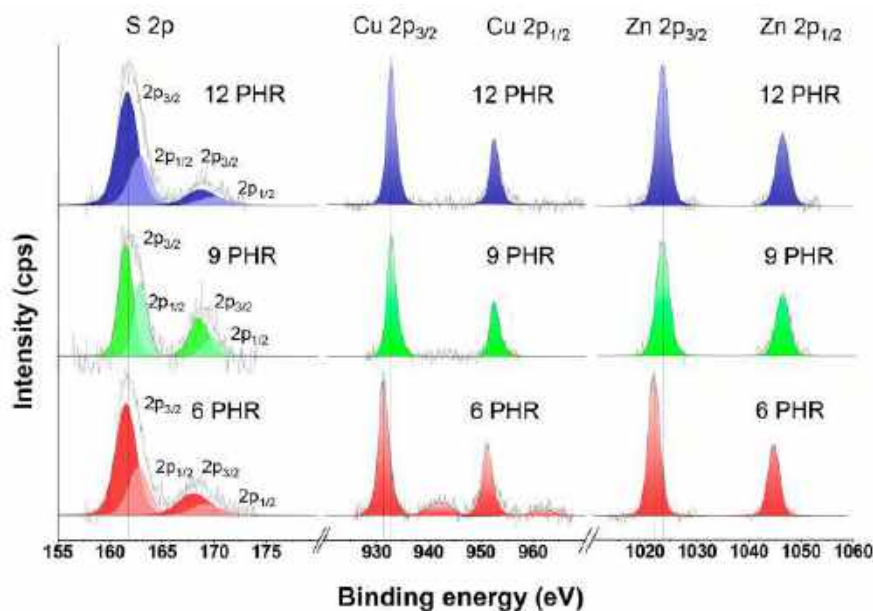
concentration. This result further corroborates with the fact that higher ZnO promotes higher active sulfurating agents for vulcanization. Figure S5B shows the tensile strength of the rubber compound as a function of ZnO concentration. Tensile strength signifies the stress that the rubber compound can tolerate before failure and is generally expressed in MPa.<sup>28,29</sup> The tensile strength decreased significantly with an increase in ZnO concentration, inferring an easy failure of the rubber compound at 12 PHR. Figure S5D shows that the modulus of rubber is lower at 9 PHR of ZnO addition, and this significant observation can be related to the flexibility of the rubber compound. In summary, physical properties such as tensile strength, modulus, and cross-linking density of rubber compound, along with corroboration of results obtained from POF and interfacial thickness measurements, suggested the optimum ZnO concentration as 9 PHR.

Fully crystalline nanostructures make the interface brittle, leading to interface failures.<sup>2,25</sup> Hence it is essential to understand the crystallinity of the different species formed under different ZnO loadings. For this, we carried out XRD measurements on vulcanized BCSCs with rubber compounds having different ZnO loadings to find the chemical identity and crystallinity of nanostructures. Figure S6 shows the XRD pattern of unvulcanized BCSC, and Figure 3 shows the XRD patterns of the interface after vulcanization with different loadings of ZnO in the rubber compound. We confirmed that the interface consists of a mixture of copper sulfides, ZnO and ZnS. Low ZnO concentration (6 PHR) in the rubber compound leads to the formation of CuS (ICSD code: 24586, confirmed by the presence of peaks at  $2\theta$  values of  $10.7$ ,  $21.6$ ,  $31.6$ ,  $32.6$ , and  $42.9$  degrees),  $\text{Cu}_{1.8}\text{S}$  (ICSD code: 69756, confirmed by the presence of peaks at  $2\theta$  values of  $19.5$ ,  $22.6$ ,  $32.2$ , and  $37.9$ ) and ZnS (ICSD code: 107133, confirmed by the presence of peaks at  $2\theta$  values of  $26.9$ ,  $27.1$ ,  $27.8$ ,  $28.5$ ,  $29.0$ ,  $30.5$ , and  $32.4$ ). At higher ZnO loadings (9 and 12 PHR), the interface consists of a mixture of CuS,  $\text{Cu}_{1.8}\text{S}$ ,  $\text{Cu}_2\text{S}$  (ICSD code: 200986, confirmed by the presence of peaks at  $2\theta$  values



**Table 1. Brass–Rubber Interface Thickness and Composition Found at Various ZnO Concentrations**

s. no.	ZnO concentration (PHR)	interface thickness (nm)	surface roughness (nm)	material composition	total cross-link density (mol/cc)
1	6	~65	29	CuS, Cu <sub>1.8</sub> S, and ZnS	$2.61 \times 10^{-5}$
2	9	~74	73	CuS, Cu <sub>1.8</sub> S, Cu <sub>2</sub> S, and ZnO	$3.09 \times 10^{-5}$
3	12	~114	90	CuS, Cu <sub>1.8</sub> S, Cu <sub>2</sub> S, and ZnO	$3.44 \times 10^{-5}$

**Figure 5.** High-resolution XPS spectra of the chemical species formed at the brass rubber interface at 6, 9, and 12 PHR ZnO. Dark lines represent the background, and the colored peaks portray peak fitting.

of 26.2, 29.1, and 37.2), and ZnO (ICSD code: 29272, confirmed by the presence of peaks corresponding to  $2\theta$  values of 31.8, 34.5, and 36.3). Table 1 summarizes the thickness, surface roughness, and chemical composition of the interface at various ZnO loadings. Since the chemical species formed at 9 and 12 PHR are the same, the results are corroborated with POF measurements, wherein beyond 9 PHR, a decrease in POF was noted. A detailed look at Raman mapping was expected to give conclusive information on the optimum ZnO concentration. Note that the Cu–S system forms several phases, and many are detected at the interface.<sup>25</sup>

Raman imaging and XPS provide qualitative information on the chemical state of the nanostructures formed on the surface of vulcanized BCSCs. Spectra, A1, B1, and C1, respectively, of Figure 4 represent the Raman spectra at 6 PHR, 9 PHR, and 12 PHR ZnO. At 6 PHR (Figure 4A1), vibrational modes at 475 ( $A_{1g}$  LO mode) and 267  $\text{cm}^{-1}$  ( $A_{1g}$  mode) are seen and are attributed to the presence of CuS. The most dominant modes seen at 9 PHR and 12 PHR (Figure 4B1,C1) of ZnO are 580, 437, and 475  $\text{cm}^{-1}$ , corresponding to the  $E_2$  and  $E_1$  LO modes of ZnO and  $A_{1g}$  LO mode of CuS.<sup>30,31</sup> The chalcocite ( $\text{Cu}_2\text{S}$ ) phases identified in TEM and XRD for 9 PHR and 12 PHR are unseen in Raman as  $\text{Cu}_2\text{S}$  is Raman inactive.<sup>30</sup> Confocal Raman image (Figure S7) shows the appearance of the BCSC with varying ZnO concentrations. It is interesting to note that there is a visible difference between reacted and unreacted BCSCs.<sup>24,25</sup> Raman imaging (Figure 4A2 to C4) of specific regions (i.e., using 267, 475 (specific to CuS) and 580  $\text{cm}^{-1}$  (specific to ZnO)) selected from confocal Raman image was performed to understand the distribution of chemical species at the interface. The bright regions in the

Raman heat maps in (Figure 4A2–C4) correspond to the presence of CuS and ZnO, and the color bar represents the CCD counts. Raman images corresponding to 267  $\text{cm}^{-1}$  are shown in Figure 4A2, B2, and C2, and those due to 475  $\text{cm}^{-1}$  are shown in Figure 4A3, B3, and C3. The concentration of CuS (as represented by the CCD values) along the vulcanized BCSCs decreased with an increase in ZnO concentration, and it is apparent that the concentration of CuS is higher at 9 PHR ZnO. Figure 4A4, B4, and C4, respectively, present Raman mapping of the 580  $\text{cm}^{-1}$  feature, where the concentration of ZnO along the vulcanized BCSC increased with an increase in the ZnO concentration. From the Raman imaging, the concentration of CuS and ZnO at the interface can be understood.

We have taken three different samples of brass cords with different ZnO concentrations with different areas for confocal Raman mapping. Thus, CCD count scales are different for the three samples. Moreover, it is evident from Raman spectra and confocal Raman images (Figure 4B2,B3) that the CuS concentration is higher at 9 PHR ZnO. Raman spectra from multiple locations were collected, and a similar trend in intensities of peaks at 280, 475, and 580  $\text{cm}^{-1}$  was observed. Based on the CCD counts (in Raman images), we can state that the concentration of CuS is higher in 9 PHR than 6 PHR. Additionally, in spectrum B1, it was seen that peaks at 280 and 475  $\text{cm}^{-1}$  were 20-fold intense than that at 580  $\text{cm}^{-1}$ , and it appeared submerged.

Our experiments corroborate with the aged-POF (Figure S4C,D) that higher ZnO concentration (12 PHR) in rubber compound results in the buildup of ZnO at the brass–rubber interface. These values correlate reasonably well with the

concept that the formation of ZnO at the interface reduces adhesion. At 9 PHR ZnO, aged- and unaged-POF showed maximum interfacial strength, and the results are in good agreement with the Raman heat maps in Figure 4B2,B3. This highlights the higher concentration of CuS at 9 PHR ZnO and demonstrates the advantage of using Raman heat maps in evaluating brass-rubber interface in RTs.

XPS analysis was carried out to determine the oxidation state of the species at the interface formed under different ZnO loadings. Figure 6 shows the XPS spectrum in the  $2p_{3/2}$  and  $2p_{1/2}$  region of S, Cu, and Zn. The binding energy (BE) values change at different ZnO concentrations, indicating varied chemical species at the interface. Figure 5 represents the formation of two types of S (copper sulfide and sulfate/sulfonate) at all ZnO concentrations at 161.2 and 169 eV, respectively. Sulfate/sulfonate species appear due to X-ray irradiation of sulfides on surfaces and need not be due to their presence on the native surface.<sup>32</sup> High-resolution XPS revealed the formation of CuS and ZnS (BE at 932.2 and 1021.8 eV, respectively) at 6 PHR ZnO.<sup>33,34</sup> As the concentration of ZnO increases (i.e., at 9 and 12 PHR), a change in the chemical state of the interface was noted. Composition of the interface at 9 and 12 PHR ZnO loading in the rubber compound showed the presence of  $Cu_2S$  (BE = 932.8 eV) and ZnO (BE = 1022.5 eV).<sup>2</sup> Due to minor difference in the binding energies between them, it has become difficult to distinguish between the species. Thus, a Wagner plot (Figure S8) was used to differentiate between CuS,  $Cu_2S$ , ZnO, and ZnS.<sup>35,36</sup>

The relative atomic percentages of Cu, Zn, S, and O present at the interface due to vulcanization at different ZnO loadings are presented in Table S1. Interestingly, the increase in atomic % of Zn and O accounts for the increase in ZnO accumulation at the interface and corroborates with the Raman heat maps. It was found that the atomic% of Cu and S on the surface increased from 6 to 12 PHR ZnO, which relates to the increasing POF in the unaged state (Figure S4 B). Accumulation of ZnO at the brass-rubber interface at 12 PHR (found through XPS) provides additional evidence for the decline in POF during aging. Furthermore, Figure S9 shows the ply region of a RT. An enlarged image of the ply region showing the nanostructure interlocking with the rubber compound resulting in better durability with optimum ZnO concentration is also shown. Thus, the XPS and Raman heat maps also conclude that the optimum dosage is 9 PHR in the studied formulation.

## CONCLUSIONS

This study highlights the importance of enhancing sustainability of the tire industries by optimizing the ZnO concentration and consequently reducing the manufacturing costs. Our work has led to a detailed study of the change in critical interfacial parameters such as morphology, interfacial thickness, and chemical composition of the adhesive interface to arrive at the optimum ZnO concentration needed in the rubber compound formulations. Various performance-enhancing properties of RTs, such as the morphology, interfacial thickness, and the chemical state of the interface have been studied at different PHR of ZnO (6, 9, and 12 PHR) using various analytical techniques. The morphology of the interface changed as a function of ZnO loading in the rubber compound formulation. A simple methodology, “the brass mesh experiment,” was adopted to measure the thickness of the nanostructures at the brass-rubber interface. The nanostructures

grew in thickness from ~65 nm to ~114 nm as the concentration of ZnO increased. The tires have to be run on the road or lab conditions (say an endurance test) at different operation times (12, 48, or 96 h) to simulate operating conditions in roads. However, using the filter paper method (which is a model study adopted for compound evaluation), the evolution of interfacial nanostructure with the above operating conditions cannot be studied as a real tire cannot be made with filter paper inside. Thus, understanding the evolution of nanostructures under aging conditions such as salt, heat, or humidity aging to understand them better was taken up for the present work. X-ray diffraction studies, Raman, and XPS confirmed varying chemical composition of the interface with the increase in ZnO concentration. From XRD, it was noted that the optimum ratios of CuS,  $Cu_{1.8}S$ ,  $Cu_2S$ , and ZnO were formed at 9 PHR ZnO concentration, which might be the reason for the retention of adhesion during aging. In addition, Raman imaging revealed a higher concentration of CuS at 9 PHR. A decrease in interfacial strength at 12 PHR was predicted due to a high concentration of ZnO at the interface. XPS results further confirmed the presence of ZnO at 12 PHR in the brass-rubber interface. Comparison of results from analytical studies with a more practical measurement, aged-POF (heat-aged POF: 124.8 kgF and salt-aged POF: 64.8 kgF) inferred that 9 PHR was the optimum. The cost-saving for tire industries globally in using an optimum ZnO concentration is estimated to be ~\$400–450 million per year. In addition, the tire manufacturers use ~12–15 PHR of ZnO in the belt and ply region of an RT. With the incorporation of 9 PHR ZnO in the belt and ply region, the usage can be reduced by 30%. This will bring relief for the growing environmental concerns of Zn release from end-of-life tires. Also, the present work will help the tire scientific community optimize ZnO content in their formulations, reduce the weight of RT, and bring down the manufacturing cost. We note that tests such as endurance, high-speed durability and strength at varying load, speed, and inflation pressure with 9 PHR ZnO will simulate tire performance closer to reality. From a futuristic perspective, the ZnO build-up mechanism at the interface at higher ZnO concentration could be studied using atom probe tomography (APT) and atomistic simulations.

## MATERIALS AND METHODS

Materials required for the preparation of the rubber mix were obtained from different manufacturers. The ZnO powder (99.9%) was obtained from J.G. Chemicals, Gujarat, and stearic acid (S.A) was purchased from Jocil, India. Silica (99.9%) and carbon black were purchased from Madhu Silica and Birla Carbon, India, respectively. Whatman No.42 filter paper was procured from GE Healthcare, Bangalore. BCSCs were obtained from Bekaert, Pune, and stored in optimum humidity conditions, and brass foil was procured from Krishna copper private limited, Gujarat. All the materials and chemicals were used as obtained from the suppliers.

**a. Preparation of Rubber Compound with Different Concentrations of ZnO.** A standard ASTM procedure was followed for preparing the rubber compound. First, rubber and other chemicals such as carbon black and ZnO were weighed using a Mettler Toledo weighing machine. The rubber compound preparation follows a two-step procedure to disperse the rubber additives with the polymer better, using an internal mixer. Stage 1 involves mixing natural rubber, S.A,

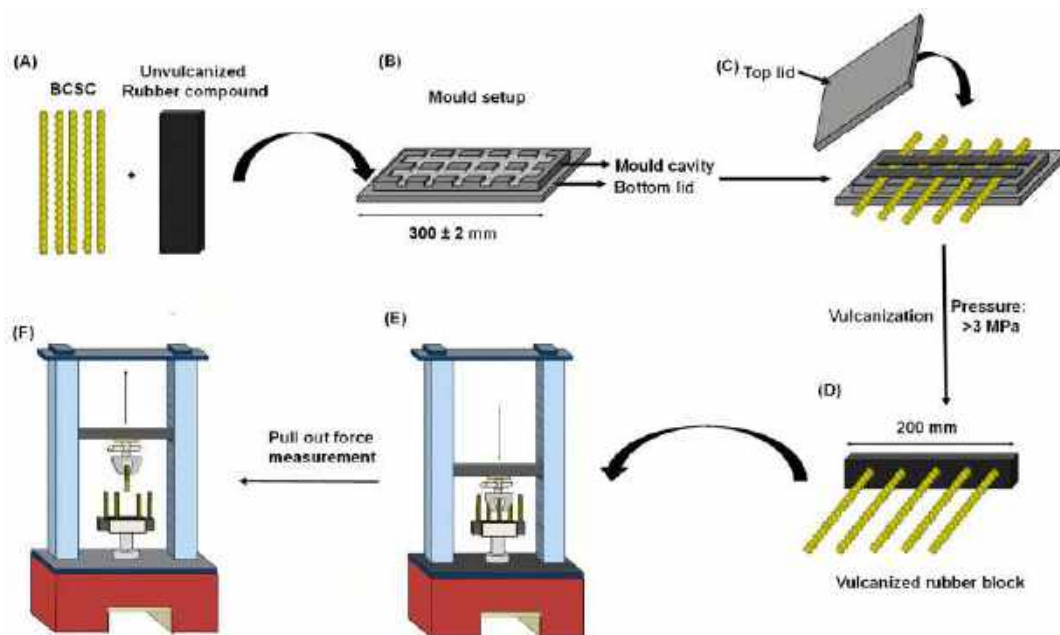


**Figure 6.** Schematic showing the preparation of the vulcanization setup for POF measurement of BCSC. (A) Unvulcanized rubber compound and BCSC before vulcanization. (B) Mold setup showing cavity and bottom lid. (C) Unvulcanized rubber compound and BCSC placed inside the mold cavity. (D) Rubber block with BCSC removed and trimmed after vulcanization. (E) Vulcanized rubber block placed in Instron 3300 instrument for POF measurement. (F) BCSC pulled out from vulcanized rubber block and POF is measured. Steps are in the sequence of A to F.

and carbon black along with different concentrations of ZnO. Then, each batch of the rubber mix was discharged from the internal mixer at 150 °C. In stage 2, the rubber batch from step 1 was cut into strips followed by the gradual addition of S and accelerator. Finally, the rubber mix was passed through a two-roll mill six times as per ASTM D2229.

**b. Vulcanization of the Rubber Mixture with BCSCs for POF Measurement.** This section deals with the preparation and determination of force needed to pull a BCSC from a block of vulcanized rubber. The BCSC and the rubber compound, cut to the desired dimensions, were kept ready for the molding process, as illustrated in Figure 6A. A mold (capable of producing four test blocks with 200 mm length and 12.5 mm thick samples) was chosen to vulcanize the BCSCs with the rubber mix (Figure 6B). The rubber compound was cut to the size of the mold cavity and placed on either side of BCSCs (Figure 6C). Later, the steel cords were placed over the rubber inside the mold. Another layer of rubber was carefully placed over the prepared base. This construction was gently pressed using a wooden dowel. The rubber blocks with BCSCs embedded between them were carefully removed from the block and stored at  $23 \pm 2$  °C until vulcanization.

Preheating of the mold was done in a press at 140 °C for 40 min, and the press chosen for vulcanization had a capacity of exerting pressure greater than 3.5 MPa on the mold during vulcanization. Later, the rubber-BCSC assembly was placed on the mold and closed using the top plate of the mold. Postvulcanization, the vulcanized rubber block with BCSC was taken out of the mold (Figure 6D). The POF of this rubber block was measured by an Instron 3300 series universal testing system. In the next step, the vulcanized rubber block was pushed into the lower fixture of the instrument, and the steel cords were clamped to the upper grip (Figure 6E). Finally, the equipment measured the maximum force required to extract the cord from the vulcanized rubber block (Figure 6F).

**Brass Mesh Experiment to Measure the Interfacial Thickness.** Brass foil (brass composition equivalent to that of industrial BCSCs) having a thickness of 0.3 mm was procured from Krishna Copper Private Limited, Gujarat. Later, the brass foil was cut to the dimension of a TEM grid with a YAG laser, Nd:YAG Laser Tech., India, operating at a power of 800 W (Figure S1). The laser-cut brass mesh was used for vulcanization and subsequent measurement of the interfacial thickness.

**Sample Preparation Technique Using Filter Paper Methodology.** A filter paper (Whatman grade 42 filter papers obtained from GE Healthcare Life Science, Bangalore) was placed between rubber and BCSCs to separate them after vulcanization. Filter paper allows sulfur, accelerator, and metal ions from the rubber compound to pass through it to react with the surface of BCSCs without the direct interaction of NR and carbon black with BCSCs. Samples vulcanized with the filter paper methodology gave a clean reacted surface that was used for spectroscopic and microscopic investigations.

**Aging of the Brass–Rubber Interface after Vulcanization for POF Measurements.** One way to quantify the durability of radial tires is to know the distance the tire has run in its lifetime without any failure issues such as ply separation, sidewall damage, and cracks. In order to study such failures, one has to wait for months to complete the field-level evaluations. However, in compound level, as in the present case, accelerated aging experiments were conducted in the laboratory to simulate field-level evaluations and verified by POF experiments to substantiate the durability of the ply region. Thus, aging experiments that resulted in faster adhesion interface degradation were conducted. Two types of aging experiments were carried on the vulcanized rubber blocks with BCSCs i.e., heat (or thermal) and salt aging. Heat aging was conducted at 100 °C for 1 week in an industrial lab oven, and salt aging was carried out by immersing the vulcanized blocks in a solution containing 20% sodium chloride (NaCl) for 1



week at room temperature. All the test blocks were used unaltered for POF measurements after aging.

**Characterization.** Scanning electron microscopy (SEM) was done with a Thermo Scientific Verios G4 UC FE-SEM at an acceleration voltage of 5 kV. Atomic force microscopy (AFM) of the interface was performed using Witec Alpha 300S operated in noncontact mode. High-resolution transmission electron microscopy (HR-TEM) was done with a JEOL 3010 instrument at an operating voltage of 200 kV. X-ray diffraction (XRD) patterns of vulcanized BCSCs were collected by Bruker D8 discovery diffractometer using Cu K $\alpha$  radiation (wavelength = 1.54 Å), and the results were analyzed using X'Pert HighScore software. XPS spectra of the vulcanized interface were collected using an Omicron ESCA probe spectrometer with a polychromatic Al K $\alpha$  X-ray source ( $h\nu = 1486.6$  eV).

## ■ ASSOCIATED CONTENT

### SI Supporting Information

The Supporting Information is available free of charge at <https://pubs.acs.org/doi/10.1021/acsomega.1c06207>.

Schematic of laser cut mesh from brass foil; large area SEM images and EDS data of vulcanized cords; AFM of BCSC showing surface roughness; graphical representation showing the brass-rubber interface thickness, unaged and aged pull out force; physical properties of rubber compound with different ZnO concentration; XRD pattern of unvulcanized brass-coated steel cord; LED white light image of unreacted and reacted BCSC; Wagner plots of Cu 2p<sub>3/2</sub> and Zn 2p<sub>3/2</sub> regions for compound identification at brass-rubber interface; schematic showing ply region of a radial tire and an enlarged image of the ply region showing the nanostructures interlocking with the rubber compound; relative atomic% obtained from XPS; total cross-link density of rubber compound at different ZnO concentrations (PDF)

## ■ AUTHOR INFORMATION

### Corresponding Authors

**Appukkuttan Sreekumaran Nair** – MRF Limited, R&D Centre, Chennai 600019, India; Email: [sreekumaran.nair@mrfmail.com](mailto:sreekumaran.nair@mrfmail.com)

**Thalappil Pradeep** – DST Unit of Nanoscience (DST UNS) and Thematic Unit of Excellence (TUE), Department of Chemistry, Indian Institute of Technology Madras, Chennai 600036, India; [orcid.org/0000-0003-3174-534X](https://orcid.org/0000-0003-3174-534X); Email: [pradeep@iitm.ac.in](mailto:pradeep@iitm.ac.in)

### Authors

**Kannan Murugesan Paulthangam** – MRF Limited, R&D Centre, Chennai 600019, India; DST Unit of Nanoscience (DST UNS) and Thematic Unit of Excellence (TUE), Department of Chemistry, Indian Institute of Technology Madras, Chennai 600036, India; [orcid.org/0000-0001-5526-2620](https://orcid.org/0000-0001-5526-2620)

**Anirban Som** – DST Unit of Nanoscience (DST UNS) and Thematic Unit of Excellence (TUE), Department of Chemistry, Indian Institute of Technology Madras, Chennai 600036, India; Present Address: A.S.: Department of Applied Physics, School of Science, Aalto University, 02150 Espoo, Finland; [orcid.org/0000-0002-6646-679X](https://orcid.org/0000-0002-6646-679X)

**Tripti Ahuja** – DST Unit of Nanoscience (DST UNS) and Thematic Unit of Excellence (TUE), Department of Chemistry, Indian Institute of Technology Madras, Chennai 600036, India

**Pillalamarri Srikrishnarka** – DST Unit of Nanoscience (DST UNS) and Thematic Unit of Excellence (TUE), Department of Chemistry, Indian Institute of Technology Madras, Chennai 600036, India; [orcid.org/0000-0001-5187-6879](https://orcid.org/0000-0001-5187-6879)

Complete contact information is available at: <https://pubs.acs.org/10.1021/acsomega.1c06207>

## Funding

MRF Ltd. financially supported this work through a research grant. Equipment used in this work was supported by the Department of Science and Technology.

## Notes

The authors declare no competing financial interest.

## ■ ACKNOWLEDGMENTS

M.P.K. and A.S.N. would like to thank the staff at Carl Zeiss, Bangalore, for accessing FESEM. In addition, M.P.K. and T.P. thank MRF Ltd. for financial support for conducting this work through a research grant. Finally, the authors thank the Department of Science and Technology, Government of India, for equipment support.

## ■ REFERENCES

- (1) Nah, C.; Sohn, B. Y.; Park, S.-J. Adhesion of brass/cobalt/copper-plated steel cord to a typical rubber compound. *J. Adhes. Sci. Technol.* **2002**, *16*, 653–667.
- (2) Kannan, M. P.; Som, A.; Ahuja, T.; Subramanian, V.; Nair, A. S.; Pradeep, T. Nonstoichiometric Copper Sulfide Nanostructures at the Brass-Rubber Interface: Implications for Rubber Vulcanization Temperature in the Tire Industry. *ACS Appl. Nano Mater.* **2020**, *3*, 7685–7694.
- (3) Vanooij, W. J.; Harakuni, P. B.; Buytaert, G. Adhesion of Steel Tire Cord to Rubber. *Rubber Chem. Technol.* **2009**, *82*, 315–339.
- (4) Fulton, W. S.; Sykes, D. E.; Smith, G. C. SIMS depth profiling of rubber-tyre cord bonding layers prepared using 64Zn depleted ZnO. *Appl. Surf. Sci.* **2006**, *252*, 7074–7077.
- (5) Mishra, Y. K.; Adelung, R. ZnO tetrapod materials for functional applications. *Mater. Today* **2018**, *21*, 631–651.
- (6) Milani, M.; Pucillo, F. P.; Ballerini, M.; Camatini, M.; Gualtieri, M.; Martino, S. First evidence of tyre debris characterization at the nanoscale by focused ion beam. *Mater. Charact.* **2004**, *52*, 283–288.
- (7) Dimkpa, C. O.; Latta, D. E.; McLean, J. E.; Britt, D. W.; Boyanov, M. I.; Anderson, A. J. Fate of CuO and ZnO Nano- and Microparticles in the Plant Environment. *Environ. Sci. Technol.* **2013**, *47*, 4734–4742.
- (8) Li, M.; Pokhrel, S.; Jin, X.; Mädler, L.; Damoiseaux, R.; Hoek, E. M. V. Stability, Bioavailability, and Bacterial Toxicity of ZnO and Iron-Doped ZnO Nanoparticles in Aquatic Media. *Environ. Sci. Technol.* **2011**, *45*, 755–761.
- (9) Tang, Y.; Xin, H.; Yang, S.; Guo, M.; Malkoske, T.; Yin, D.; Xia, S. Environmental risks of ZnO nanoparticle exposure on *Microcystis aeruginosa*: Toxic effects and environmental feedback. *Aquat. Toxicol.* **2018**, *204*, 19–26.
- (10) Skidmore, J. F. Toxicity of Zinc Compounds to Aquatic Animals, with Special Reference to Fish. *Q. Rev. Biol.* **1964**, *39*, 227–248.
- (11) Youssef, M. S.; Elamawi, R. M. Evaluation of phytotoxicity, cytotoxicity, and genotoxicity of ZnO nanoparticles in *Vicia faba*. *Environ. Sci. Pollut. R.* **2020**, *27*, 18972–18984.

- (12) Amari, T.; Themelis, N. J.; Wernick, I. K. Resource recovery from used rubber tires. *Resour. Policy* **1999**, *25*, 179–188.
- (13) van Ooij, W. J.; Kleinhesselink, A. Application of XPS to the study of polymer-metal interface phenomena. *Appl. Surf. Sci.* **1980**, *4*, 324–339.
- (14) Fulton, W. S. Tire-Cord Adhesion: How the Source of Zinc Can Influence the Structure of the Bonding Interface. *Rubber Chem. Technol.* **2006**, *79*, 790–805.
- (15) Ozawa, K.; Kakubo, T.; Amino, N.; Mase, K.; Ikenaga, E.; Nakamura, T. Angle-Resolved HAXPES Investigation on the Chemical Origin of Adhesion between Natural Rubber and Brass. *Langmuir* **2017**, *33*, 9582–9589.
- (16) van Ooij, W. J.; Weening, W. E.; Murray, P. F. Rubber Adhesion of Brass-Plated Steel Tire Cords: Fundamental Study of the Effects of Compound Formulation Variations on Adhesive Properties. *Rubber Chem. Technol.* **1981**, *54*, 227–254.
- (17) Jeon, G. S.; Han, M. H.; Seo, G. Effect of ZnO contents at the surface of brass-plated steel cord on the adhesion property to rubber compound. *Korean J. Chem. Eng.* **1999**, *16*, 248–252.
- (18) van Ooij, W. J. Mechanism and Theories of Rubber Adhesion to Steel Tire Cords—An Overview. *Rubber Chem. Technol.* **1984**, *57*, 421–456.
- (19) van Ooij, W. J. Mechanism of Rubber-To-Brass Adhesion: Effect of Rubber Composition on the Adhesion. *Rubber Chem. Technol.* **1978**, *51*, 52–71.
- (20) Liu, Y.; Zhu, G.; Yang, J.; Bao, C.; Wang, J.; Yuan, A. Phase purification of Cu-S system towards Cu<sub>1.8</sub>S and its catalytic properties for a clock reaction. *RSC Adv.* **2015**, *5*, 103458–103464.
- (21) Park, H.; Kwon, J.; Kim, J.; Park, K.; Song, T.; Paik, U. Facile Growth of Metal-Rich Cu<sub>1.75</sub>S and Cu<sub>1.8</sub>S Microspheres Assembled with Mesoporous Nanosheets and Their Application in Na-Ion Batteries. *Cryst. Growth Des.* **2020**, *20*, 3325–3333.
- (22) Patrick, R. A. D.; Mosselmans, J. F. W.; Charnock, J. M.; England, K. E. R.; Helz, G. R.; Garner, C. D.; Vaughan, D. J. The structure of amorphous copper sulfide precipitates: An X-ray absorption study. *Geochim.* **1997**, *61*, 2023–20366.
- (23) Peng, M.; Ma, L.-L.; Zhang, Y.-G.; Tan, M.; Wang, J.-B.; Yu, Y. Controllable synthesis of self-assembled Cu<sub>2</sub>S nanostructures through a template-free polyol process for the degradation of organic pollutant under visible light. *Mater. Res. Bull.* **2009**, *44*, 1834–1841.
- (24) Baldwin, J. M.; Bauer, D. R.; Ellwood, K. R. Rubber aging in tires. Part 1: Field results. *Polym. Degrad. Stab.* **2007**, *92*, 103–109.
- (25) Patil, P. Y.; van Ooij, W. J. Mechanistic Study of the Effect of Adhesion-Promoter Resins on the Crystal Structure of the Copper Sulfide Adhesion Layer at the Rubber-Brass Interface. *Rubber Chem. Technol.* **2006**, *79*, 82–93.
- (26) Jeon, G. S.; Seo, G. Influence of Cure Conditions on the Adhesion of Rubber Compound to Brass-plated Steel Cord. Part II. Cure Time. *J. Adhes.* **2001**, *76*, 223–244.
- (27) Jeon, G. S. Adhesion Between Rubber Compounds Containing Various Adhesion Promoters and Brass-Plated Steel Cords. Part I. Effect of Sulfur Loading in Rubber Compounds. *J. Adhes. Sci. Technol.* **2008**, *22*, 1223–1253.
- (28) Khan, I.; Poh, B. T. Natural Rubber-Based Pressure-Sensitive Adhesives: A Review. *J. Polym. Environ.* **2011**, *19*, 793–811.
- (29) Larsen, I. L.; Thorstensen, R. T. The influence of steel fibres on compressive and tensile strength of ultra high performance concrete: A review. *Constr. Build. Mater.* **2020**, *256*, 119459.
- (30) Baert, K.; Breugelmanns, T.; Buytaert, G.; Brabant, J. V.; Hubin, A. The combination of surface enhanced Raman spectroscopy and an ionic liquid as a model system to study the adhesion interface between sulfur and brass. *J. Raman Spectrosc.* **2013**, *44*, 377–381.
- (31) Shawky, A.; El-Sheikh, S. M.; Gaber, A.; El-Hout, S. I.; El-Sherbiny, I. M.; Ahmed, A. I. Urchin-like CuS nanostructures: simple synthesis and structural optimization with enhanced photocatalytic activity under direct sunlight. *Appl. Nanosci.* **2020**, *10*, 2153–2164.
- (32) Uhlig, S.; Möckel, R.; Pleßow, A. Quantitative analysis of sulphides and sulphates by WD-XRF: Capability and constraints. *Xray Spectrom.* **2016**, *45*, 133–137.
- (33) Biesinger, M. C. Advanced analysis of copper X-ray photoelectron spectra. *Surf. Interface Anal.* **2017**, *49*, 1325–1334.
- (34) Vdovenkova, T.; Vdovenkov, A.; Tornqvist, R. ZnS wide band gap semiconductor thin film electronic structure sensitivity to Mn impurity. *Thin Solid Films* **1999**, *343-344*, 332–334.
- (35) *NIST X-ray Photoelectron Spectroscopy Database, NIST Standard Reference Database Number 20*; National Institute of Standards and Technology: Gaithersburg, MD, 2000.
- (36) Wagner, C. D. Auger lines in x-ray photoelectron spectrometry. *Anal. Chem.* **1972**, *44*, 967–973.

## Supporting information

# Role of Zinc Oxide in the Compounding Formulation on the Growth of Non-stoichiometric Copper Sulfide Nanostructures at Brass-Rubber Interface

*Kannan Murugesan Paulthangam,<sup>‡</sup> Anirban Som,<sup>‡</sup> Tripti Ahuja,<sup>‡</sup> Pillalamarri Srikrishnarkū<sup>‡</sup>*

*Appukuttan Sreekumaran Nair,<sup>\*†</sup> Thalappil Pradeep<sup>\*</sup>*

<sup>‡</sup>DST Unit of Nanoscience (DST UNS) and Thematic Unit of Excellence (TUE), Department of Chemistry, Indian Institute of Technology Madras, Chennai 600036, India.

<sup>†</sup>MRF Limited, R&D Centre, Tiruvottiyur, Chennai 600019, India.

\*For correspondence, E-mail: [sreekumaran.nair@mrfmail.com](mailto:sreekumaran.nair@mrfmail.com), [pradeep@iitm.ac.in](mailto:pradeep@iitm.ac.in)

### Table of contents

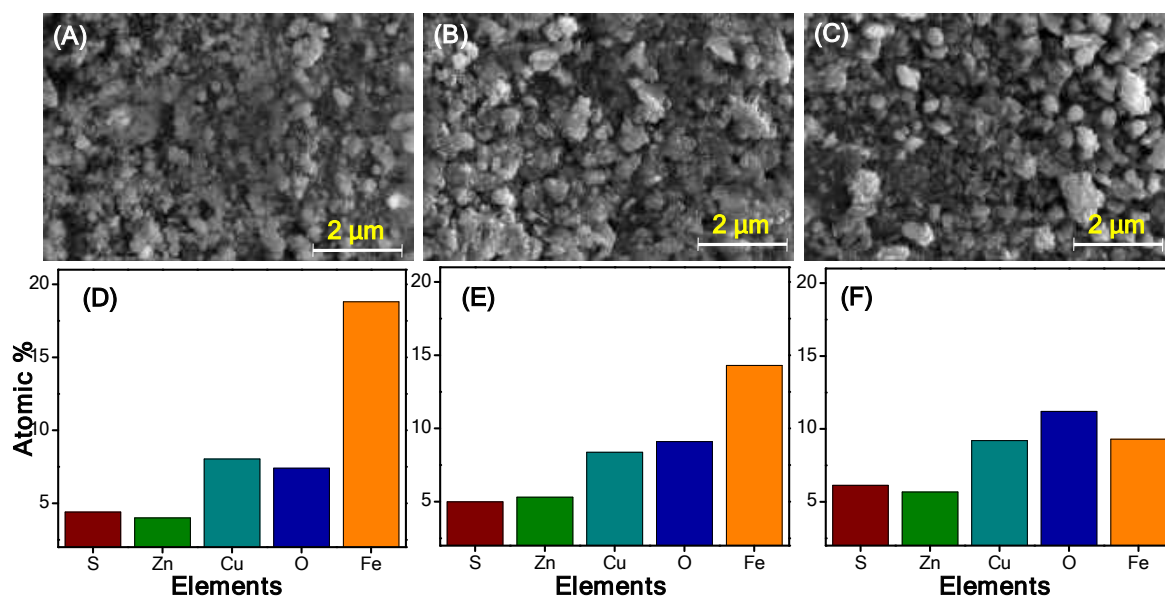
Figures	Title	Page no.
Figure S1	Schematic of laser cut mesh from brass foil	S-2
Figure S2	Large area SEM images and EDS data of vulcanized cords	S-2
Figure S3	AFM of BCSC showing surface roughness	S-3
Figure S4	Graphical representation showing the brass-rubber interface thickness, unaged and aged pull out force	S-3
Figure S5	Physical properties of rubber compound with different ZnO concentrations	S-4

Figure S6	XRD pattern of un-vulcanized brass-coated steel cord	S-5
Figure S7	LED white light image of unreacted and reacted BCSC	S-5
Figure S8	Wagner plots of Cu <sub>2p<sub>3/2</sub></sub> and Zn <sub>2p<sub>3/2</sub></sub> regions at brass-rubber interface for compound identification	S-6
Figure S9	Schematic showing ply region of a radial tire and an enlarged image of the ply region showing the nanostructures interlocking with the rubber compound.	S-7
Table S1	Relative atomic % obtained from XPS	S-7
Table S2	Total crosslink density of rubber compound at different ZnO concentrations	S-8



**Figure S1.** Schematic image of a laser cut mesh from brass foil that was used for interfacial thickness measurement.





**Figure S2.** Large area SEM images at (A) 6, (B) 9, (C) 12 PHR ZnO and their corresponding EDX spectra at (D) 6, (E) 9, (F) 12 PHR ZnO.

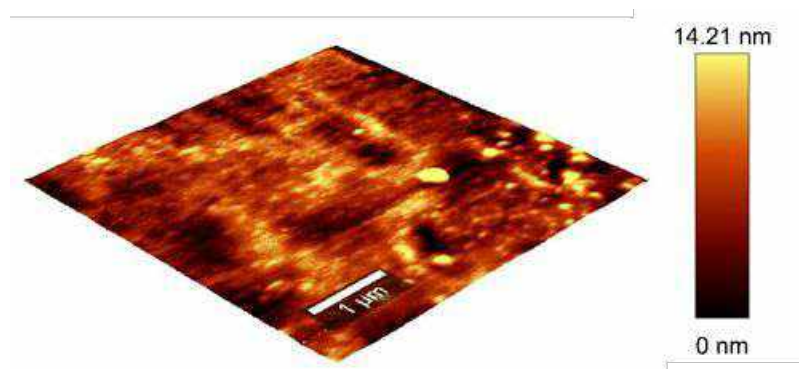


**Figure S3.** AFM of bare BCSC showing the surface roughness.

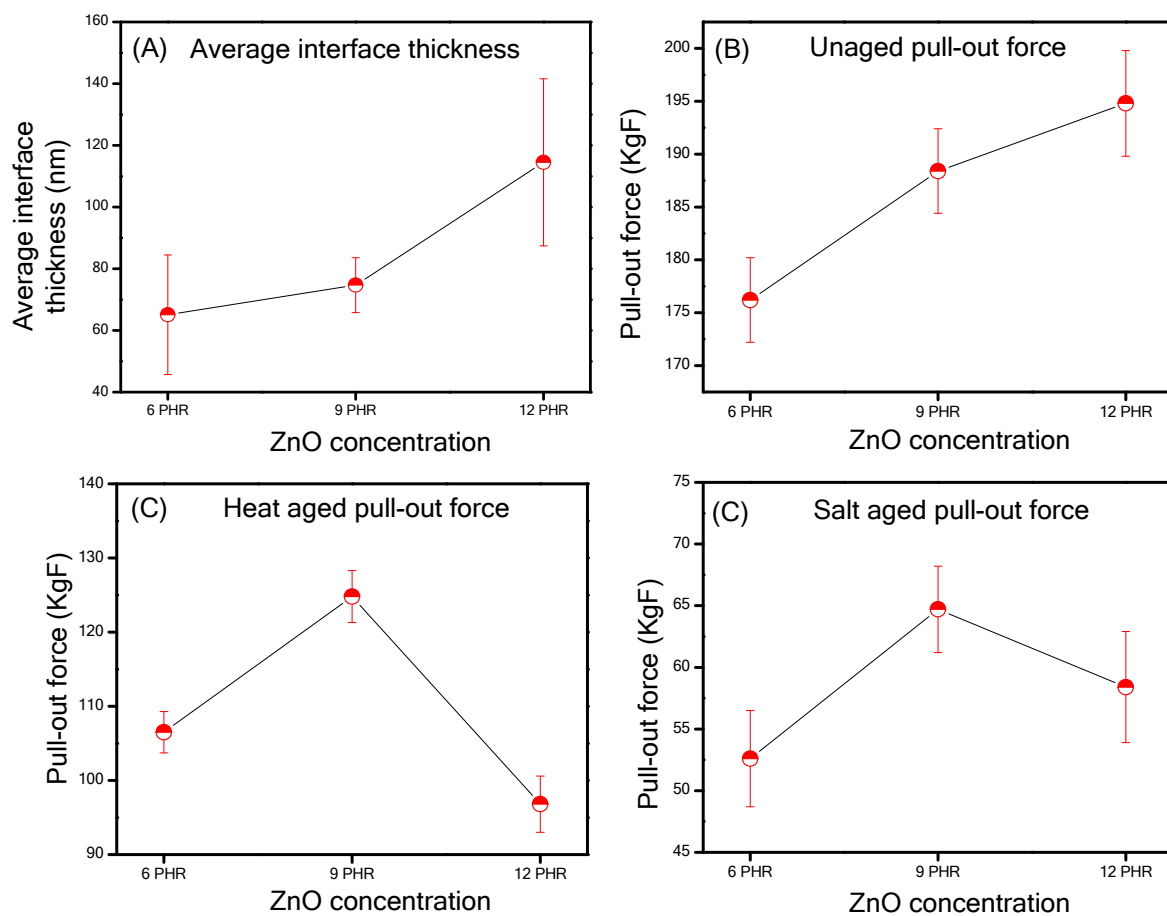


**Figure S4.** Graphical representation (A) showing the brass-rubber interface thickness with different ZnO concentrations, (B) un-aged, (C) salt-aged and (D) heat-aged pull-out force as a function of ZnO concentrations.

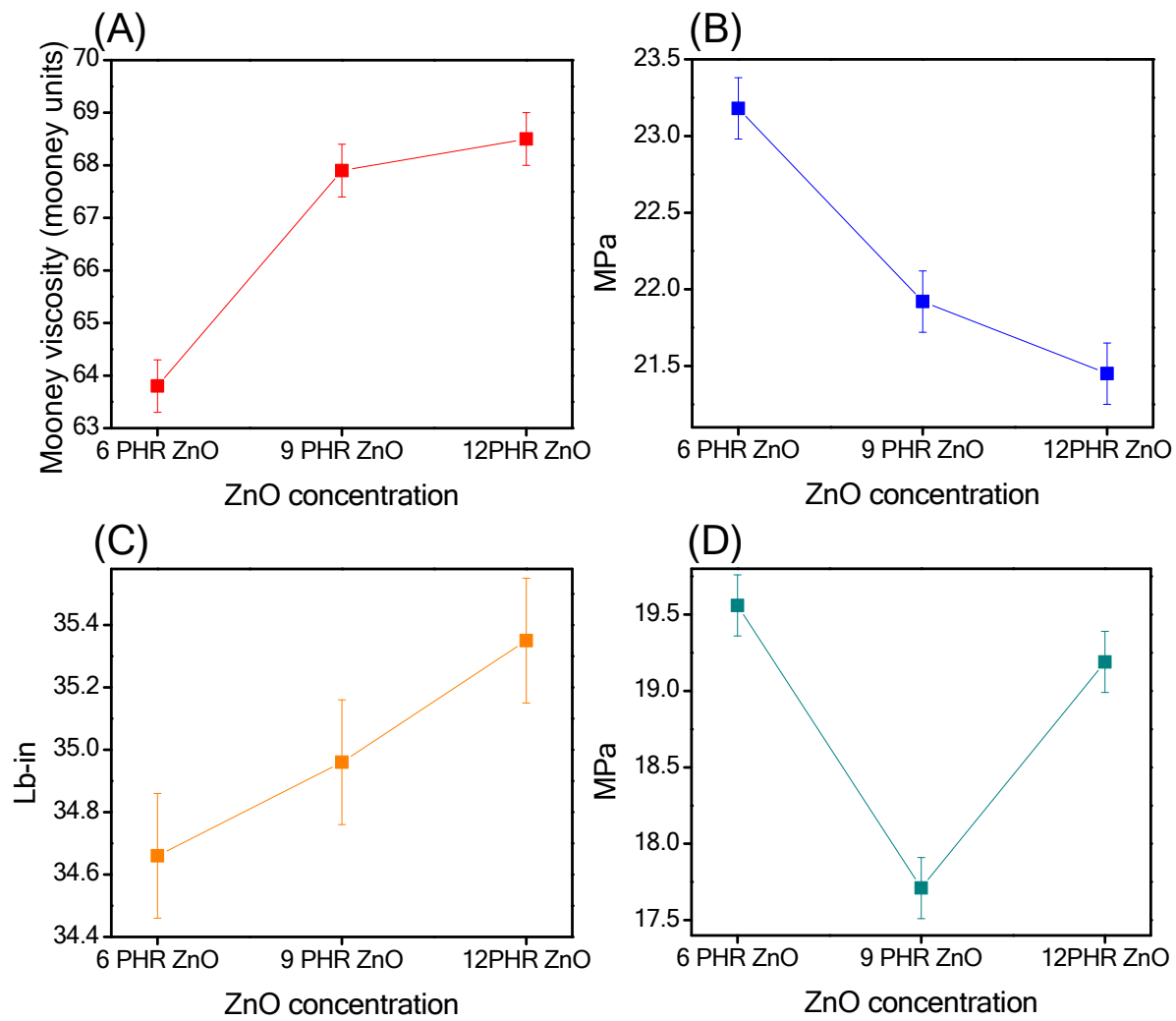


**Figure S5.** Physical properties of rubber compound with increasing ZnO concentration: (A) Mooney viscosity, (B) tensile strength, (C) moment highest (MH) and (D) 300 % modulus.

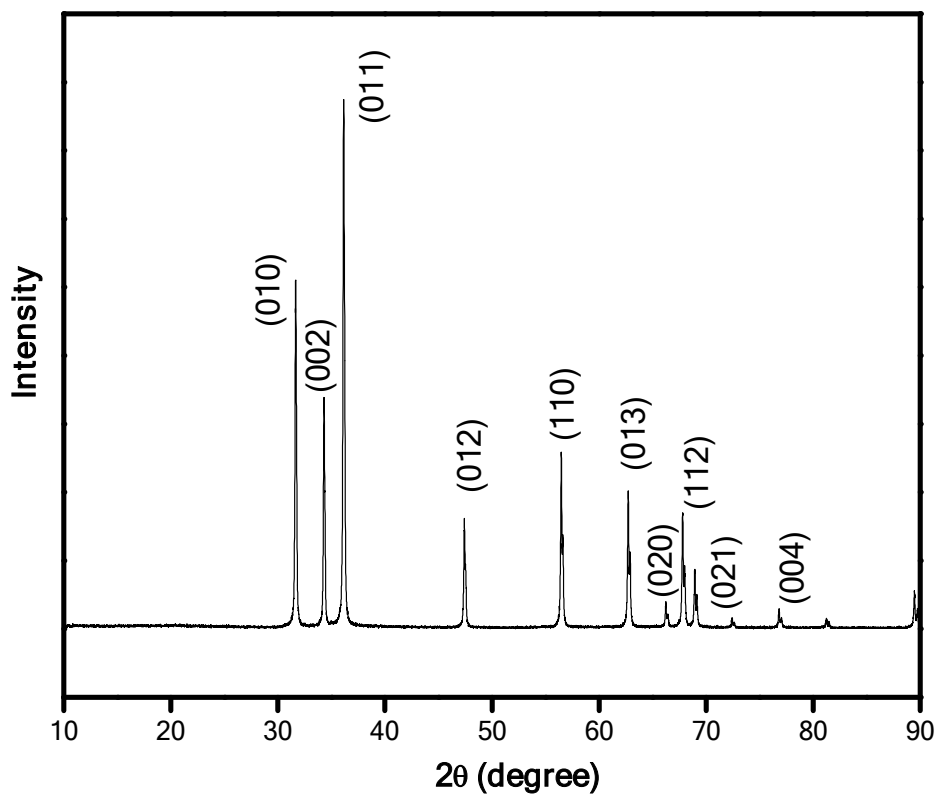


**Figure S6.** XRD pattern of the ZnO added to the rubber compound.

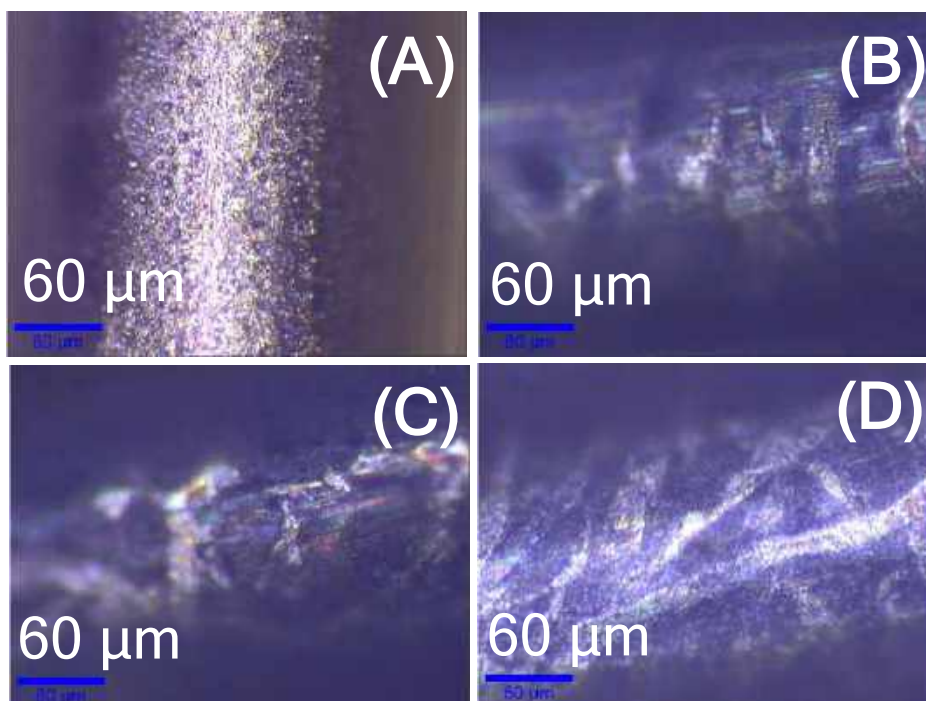


**Figure S7.** LED white light image of (A) unreacted (B), (C) and (D) vulcanized BCSC with 6, 9 and 12 phr ZnO.

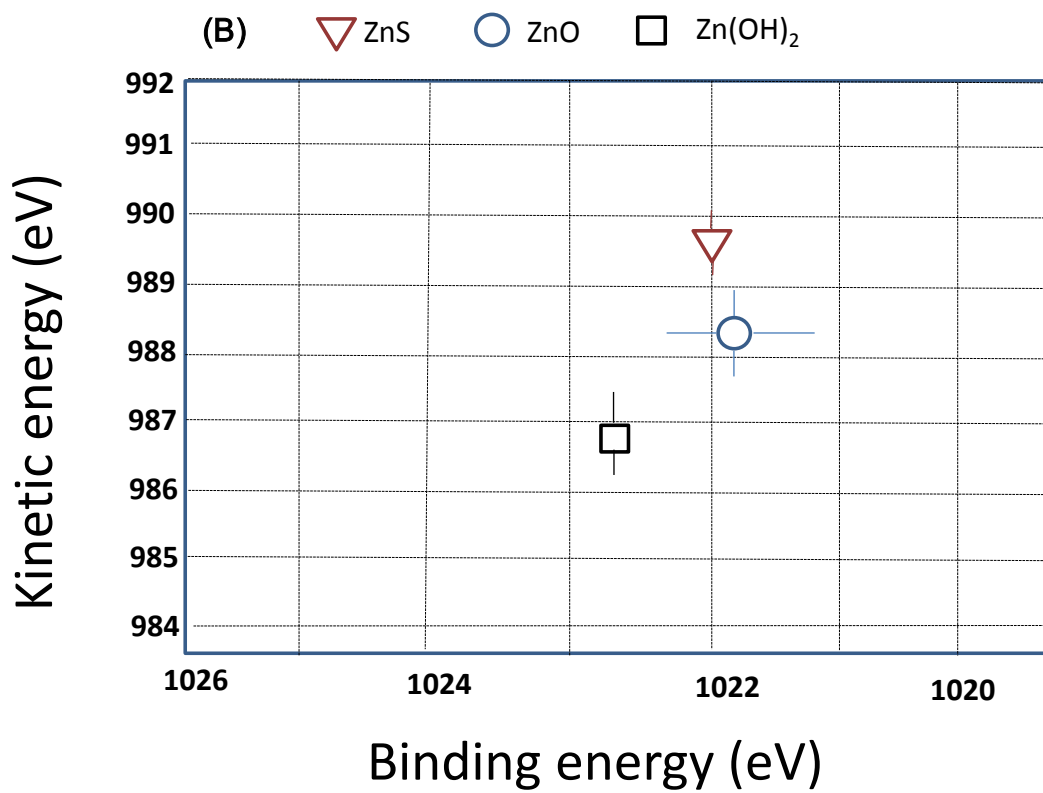
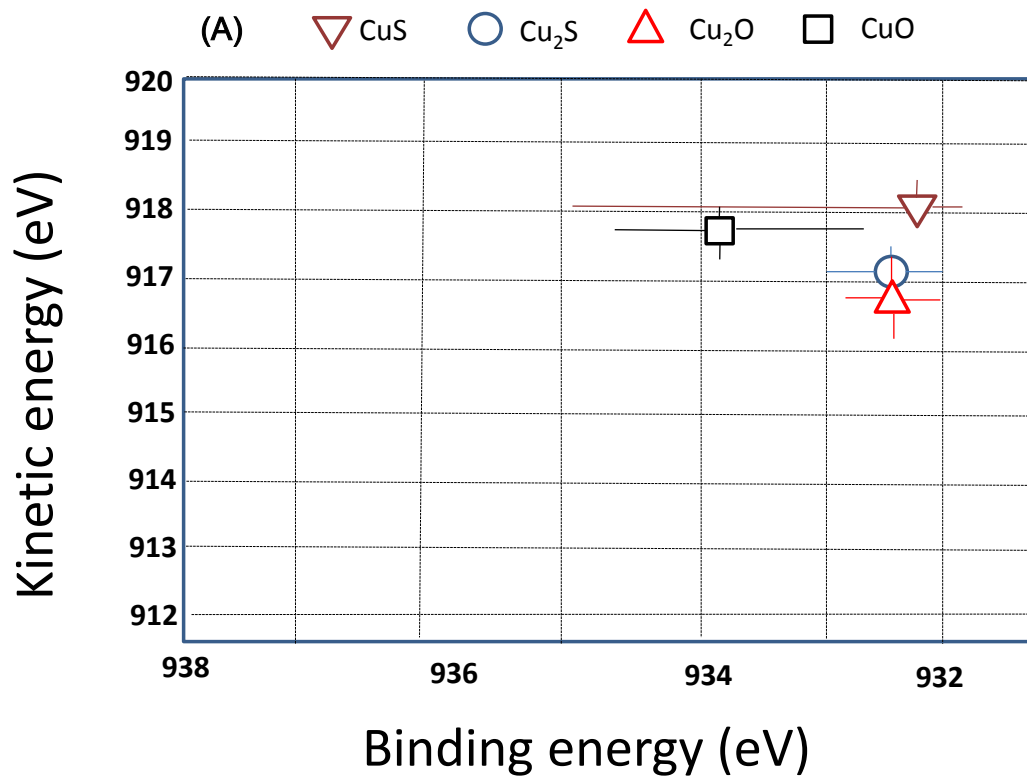




**Figure S8.** Wagner plots of (A)  $\text{Cu}2p_{3/2}$  and (B)  $\text{Zn}2p_{3/2}$  regions for compound identification at brass-rubber interface. Adapted from references 35 and 36 in the main text.

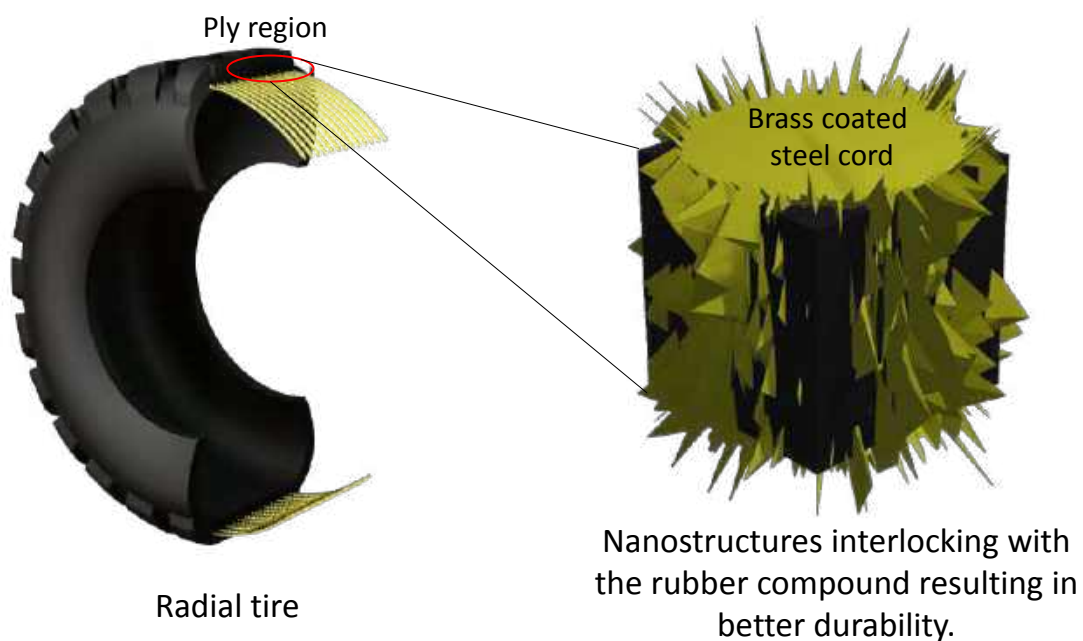


**Figure S9.** Schematic showing ply region of a radial tire and an enlarged image of the ply region showing the nanostructures interlocking with the rubber compound.

**Table S1.** Total crosslink density of rubber compound at different ZnO concentration.

<b>ZnO concentration (PHR)</b>	<b>Total crosslink density (mol/cc)</b>
6	2.61 E-5
9	3.09 E-5

12	3.44 E-5
----	----------

**Table S2.** Relative atomic % obtained from XPS.

Element	6PHR ZnO	9PHR ZnO	12PHR ZnO
Cu	1.43	1.46	1.77
Zn	1.92	2.15	2.93
S	1.64	1.68	1.87
O	9.27	12.25	13.33

# Molecular Engineering of Atomically Precise Silver Clusters into 2D and 3D Framework Solids

Wakeel Ahmed Dar, Arijit Jana, Korath Shivan Sugi, Ganesan Paramasivam, Mohammad Bodiuzzaman, Esma Khatun, Anirban Som, Ananthu Mahendranath, Amrita Chakraborty, and Thalappil Pradeep\*



Cite This: *Chem. Mater.* 2022, 34, 4703–4711



Read Online

ACCESS |



Metrics & More

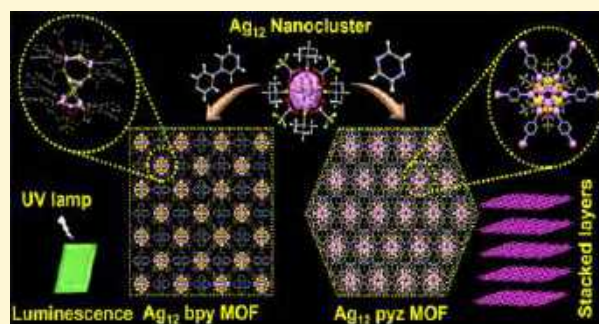


Article Recommendations



Supporting Information

**ABSTRACT:** Two- and three-dimensional (2D and 3D) atomically precise nanocluster (NC)-based metal–organic frameworks (MOFs) with properties richer than those of NCs themselves are emerging materials. However, fabricating such materials with good stability has not been easy. In this work, a facile synthetic strategy was employed for the creation of silver NC–MOFs starting from  $[\text{Ag}_{12}(\text{TBT})_7(\text{TFA})_4(\text{CH}_3\text{CN})_6]^+$ , facilitated by heterocyclic amines, 4,4'-bipyridine (bpy) and pyrazine (pyz), via metal–metal and metal–sulfide rearrangement reactions, where TBT and TFA are tertiarybutylthiolate and trifluoroacetate, respectively. In one of the reactions, the pyz ligand facilitates the formation of a 2D framework with a trigonal crystal system, which exhibits high stability and emits bright green luminescence at low temperatures. Owing to its facile synthesis, good stability, efficient luminescence, uniform porosity, and layered structure, the resultant hexagonal 2D nanosheets can be efficiently exfoliated from parent crystals. The 2D nanosheets are structurally similar to graphene. A top-down approach was employed for the exfoliation of stable 2D nanosheets with lateral dimensions in the range of 0.156  $\mu\text{m}$ . In another case, the bpy ligand induces the construction of a 3D framework with an orthorhombic crystal system. Owing to its interpenetrated AB $\cdots$ AB structure, robustness, and efficient green luminescence at room temperature, the resultant 3D MOF is capable of functioning as a high-performance luminescent sensor for selective detection of explosive analogues, 2-nitrotoluene and 2,4-dinitrotoluene, with excellent recyclability. However, in the absence of the heterocyclic amines, a pristine AgNC was formed. Time-dependent density functional theory calculations were employed to understand the mechanism of energy transfer in AgNC–MOFs. Our strategy offers an unprecedented approach in which heterocyclic amines facilitate intramolecular rearrangement reactions, resulting in 2D and 3D atomically precise NC framework materials. This work not only demonstrates the creation of 2D and 3D materials but also provides new insights into the critical surface coordination chemistry controlled by heterocyclic amines for defining the morphology and properties of cluster frameworks.



## INTRODUCTION

Synthetic methodologies for the design and engineering of atomically precise noble metal nanoclusters (NCs), especially those of gold and silver, have witnessed burgeoning research interest in the past decade because of their architectural diversity and precise tuning of physical properties.<sup>1,2</sup> NCs are stabilized by a variety of surface anchoring ligands such as thiolates,<sup>3–11</sup> imine thiolates,<sup>12</sup> phosphines,<sup>13–15</sup> alkynyls,<sup>16–18</sup> and so forth. The stabilizing ligands are critical not only for maintaining their structures with atomic precision but also for controlling many of their unique properties.<sup>1,7,10,11,19–23</sup> NCs have sizes between discrete atoms and plasmonic nanoparticles. The exceptional properties of NCs, such as their precise nuclearity, quantized electronic energy levels, spectroscopic signatures, intercluster reactions, and so forth, strongly support their molecular behavior.<sup>10</sup> Structural analyses of NCs confirm their precise atomic arrangements, which are indispensable for understanding their properties in great

detail.<sup>1,24</sup> Rich structural diversity among NCs was revealed by single-crystal X-ray diffraction (SCXRD).<sup>3,5,7,9,22,25–28</sup> Instability of many of the AgNCs has, however, hindered comprehensive studies including their luminescence and electronic absorption properties since they are susceptible to decomposition even under mild activation. To improve the applicability of AgNCs, organic linkers such as 4,4'-bipyridine (bpy) or 1,2-bis(4-pyridyl)ethane were introduced to connect the adjacent NCs, which resulted in silver NC-based metal–organic frameworks (AgNC–MOFs).<sup>29–32</sup> Investigations of AgNC–MOFs are still at an early stage.<sup>30–37</sup> Constructed from

Received: March 1, 2022

Revised: April 26, 2022

Published: May 11, 2022



the assembly of NCs, AgNC-MOFs represent a novel class of solids with metal-rich nodes, and they demonstrate efficient integration of properties of component NCs as well as linker molecules. Augmentation of rigid structures substantially increases the stability of NC-based frameworks as well as their characteristics, including stability, luminescence, and electronic properties, over pristine NCs.<sup>29</sup> These frameworks have uniform NC nodes, resulting in integrated structures, wide channels, and most significantly, unusual robustness.<sup>29–32</sup> These are favorable for catalysis also.<sup>33</sup> Zang et al. reported the first AgNC-MOF in which the adjacent NCs were coordinated via a bidentate connector, 4,4'-bipyridine.<sup>29</sup> After that, several AgNC-MOFs composed of Ag<sub>8</sub>, Ag<sub>10</sub>, Ag<sub>12</sub>, Ag<sub>14</sub>, Ag<sub>15</sub>, and Ag<sub>27</sub> have been synthesized with different organic linkers.<sup>30–37</sup> These materials are useful for various applications such as molecular sensors for detecting traces of ethanol in breath,<sup>29</sup> ratiometric sensing of oxygen,<sup>33</sup> sensing of chloromethanes,<sup>31</sup> carbon dioxide fixation,<sup>37</sup> and photocatalytic oxidation of the mustard gas simulant, namely 2-chloroethyl ethyl sulfide.<sup>38</sup> The number of metal atoms in a cluster, its structure, and the type of coordinating ligand modify the properties of the framework system. Understanding synthetic methodologies for the design and engineering of cluster-based frameworks with good stability and efficient luminescence at normal temperature and pressure (NTP) will be useful for designing new materials for specific applications, including explosive detection, energy storage, catalysis, and so forth.

2D materials beyond graphene have attracted intense research interest because of their unexpected physicochemical properties arising from their distinctive 2D morphology, precise thickness, quantum size effect, high electron mobility, and so forth.<sup>39</sup> Compared to the widely studied 2D nanosheets of transition metal dichalcogenides, graphene, hexagonal boron nitride, and others, 2D nanosheets of AgNC-MOFs with unique structural composition are a recent addition to the class of 2D nanomaterials. Thin and homogenous AgNC-MOF nanosheets with more intriguing structures and properties may be useful for prospective applications compared to their bulk counterparts. To create 2D AgNC-MOF nanosheets enriched with NC nodes, a top-down approach may be employed, in which bulk crystals could be delaminated or exfoliated into single layers using a solution-sonication technique. Such a top-down method may be effective in constructing stable AgNC-MOF nanosheets with rational shapes.

With this thought, we have prepared atomically precise 2D nanosheets using delamination or exfoliation of pristine AgNC-MOF crystals. The AgNC-MOF, with the chemical composition  $\{[Ag_{12}(TBT)_6(TFA)_6(pyZ)_6] \cdot 2CH_3CN\}_n$  (TBT = tertiarybutylthiolate, TFA = trifluoroacetate, and pyZ = pyrazine) denoted as (1), was synthesized by the reaction of silver thiolate and silver trifluoroacetate with pyrazine, and it showed exceptional stability for more than a year. The pristine MOF crystals were first physically and structurally analyzed and then delaminated or exfoliated using a top-down approach to yield 2D nanosheets. 2D sheets of (1) are similar to graphene and associated with metal-rich nodes. We also developed a 3D AgNC-MOF, denoted as (2), with a honeycomb-like structure with the chemical formula  $\{[Ag_{12}S_2(TBT)_8(TFA)_4(bpy)_8] \cdot bpy\}_n$  (bpy = 4,4'-bipyridine) using a similar reaction procedure, except that instead of pyz, bpy was employed. In addition to their stability, lamellar morphology, and luminescent properties, thin films of this framework with exceptional photostability can serve as efficient luminescent

sensors with sensitivity and selectivity for the detection of aromatic nitrotoluenes [2-nitrotoluene (NT) and 2,4-dinitrotoluene (DNT)], surrogates for explosives. Without heterocyclic amines, a pristine  $[Ag_{12}(TBT)_7(TFA)_4(CH_3CN)_6]^+$  NC, denoted as Ag<sub>12</sub>, was obtained. In all the cases, Ag<sub>12</sub> serves as the basic unit with different geometric arrangements and shows different bonding patterns in both frameworks. From the structural analysis, it is evident that pyz and bpy induce intramolecular metal–metal and metal–sulfide rearrangements in the Ag<sub>12</sub> NC to yield 2D (1) and 3D (2) frameworks, respectively. Both of these are different in geometry, structural composition, morphology, and physical properties.

## RESULTS AND DISCUSSION

### Synthesis and Characterization of AgNC-MOFs.

Synthetic approaches for AgNC-MOFs and pristine Ag<sub>12</sub> NC are schematically presented in Figure 1. In brief, the AgNC-

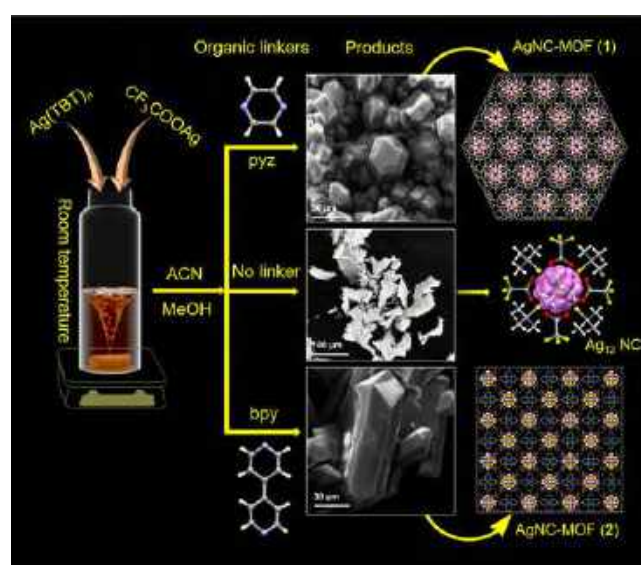


**Figure 1.** Schematic representation of the synthesis of AgNC-MOFs: (1) (top-right) and (2) (bottom-right) are crystal structures of the product, and without an organic linker, Ag<sub>12</sub> NC (middle) was obtained. ACN-acetonitrile; MeOH-methanol. Color codes: Ag light pink; S yellow; C gray; N magenta; F green; H white; and O red.

MOF (1) was synthesized by adding an equal amount of silver thiolate and silver trifluoroacetate precursors in a 1:1 solvent mixture of acetonitrile (ACN) and methanol. Subsequently, the pyz ligand was added to the reaction mixture, and stirring was continued for 2 h. The reaction product was filtered and kept for slow evaporation at a low temperature ( $10 \pm 5$  °C), and after one week, polyhedral-shaped crystals were obtained (Figure 1). AgNC-MOF (2) with rod-shaped crystals was obtained using the same reaction procedure, except that instead of pyz, bpy was used (Figure 1). However, when no heterocyclic amine was used, pristine Ag<sub>12</sub> NC was obtained, which was characterized by high-resolution electrospray ionization-mass spectrometry (HR ESI-MS) and UV–vis spectroscopy. AgNC-MOFs (1) and (2) were structurally characterized by SCXRD, and the phase purity of microcrystals was ascertained by powder X-ray diffraction (PXRD). Additional characterization used thermogravimetric analysis (TGA). Electronic properties were studied by UV–vis and



fluorescence spectroscopies. Experimental details are presented in the [Supporting Information](#)

**Structural Anatomy of AgNC-MOF (1).** Product (1) was obtained in good yield (~60% in terms of Ag). It crystallizes into a trigonal space group,  $P\bar{3}m$ . The total structure of (1) is shown in [Figure 2](#) and all other structural parameters are

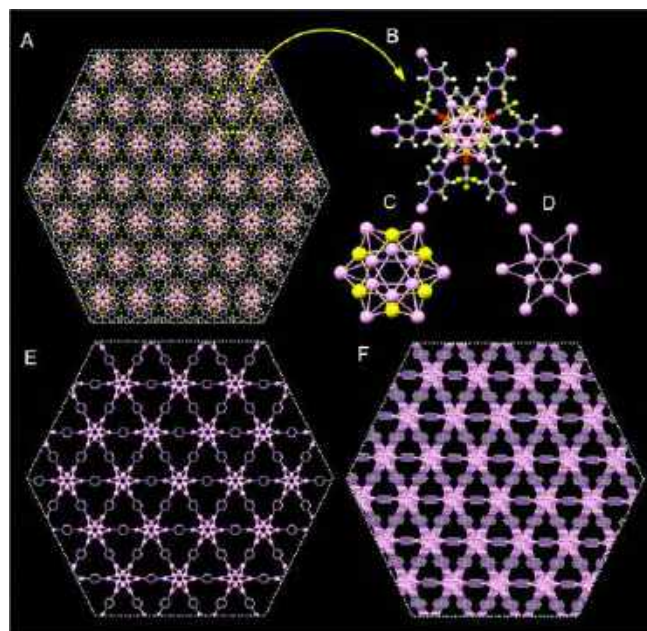


**Figure 2.** (A) Total crystal structure of (1). (B) Structure of the monomeric unit  $[\text{Ag}_{12}(\text{TBT})_6(\text{TFA})_6(\text{pyz})_6]$ . (C) Structure of the hollow cuboctahedron silver-sulfide  $\text{Ag}_{12}\text{S}_6$  core. (D) Structure of the  $\text{Ag}_{12}$  metallic core without ligands in the  $ab$ -plane. (E) Structure of (1) in the  $ab$ -plane appears similar to graphene (H atoms as well as *tert*-butyl and TFA groups have been removed for clarity). (F) Layered structure of (1). Color codes: Ag light pink; S yellow; C gray; N light blue; F green; and O red.

summarized in [Table S1](#). In the framework structure, metal-rich nodes corresponding to silver chalcogenide ( $\text{Ag}_{12}\text{S}_6$ ) clusters are interconnected by the bidentate pyz ligand. The geometrical framework holding  $\text{Ag}_{12}\text{S}_6$  at the center can be represented by a sheet connecting 12 Ag and six S atoms, resulting in a hollow cuboctahedron. Considering the arrangement of Ag atoms, the  $\text{Ag}_{12}$  core can be visualized as three hexagons bisecting each other ([Figure S3B](#)). Each  $\text{Ag}_{12}\text{S}_6$  is co-stabilized by six TBT and six TFA ligands. Each TFA ligand is coordinated through one of its O-atoms. Furthermore, each  $\text{Ag}_{12}\text{S}_6$  node is interconnected by six bidentate pyz ligands in a hexagonal planar pattern, forming an infinite 2D framework structure. Rearrangement across the  $\text{Ag}_{12}$  NC induced by pyz resulted in the formation of (1). During the reaction, one TBT unit was eliminated, and two additional TFA units from the reaction mixture were coordinated to the  $\text{Ag}_{12}\text{S}_6$  core to maintain the charge balance. The bond lengths of Ag–Ag, Ag–S, Ag–O, and Ag–N are 3.08, 2.54, 2.39, and 2.33 Å, respectively ([Figure S3F](#)). The total structure of this 2D framework in the  $ab$ -plane is shown in [Figures 2A](#) and [S4](#). A cross-section of the framework is shown in [Figures 2B](#) and [S4C](#). The structure of the hollow cuboctahedron silver-sulfide  $\text{Ag}_{12}\text{S}_6$  core and  $\text{Ag}_{12}$  metallic core without ligands is shown in [Figure 2C,D](#). Furthermore, the stacking pattern of the 2D framework layers demonstrates AA...AA parallel packing, with

$\text{Ag}_{12}$  cluster nodes in neighboring layers completely aligned one above the other ([Figure S5](#)). The distance between the adjacent layers considering the nearest Ag atoms of the  $\text{Ag}_{12}$  core is 7.53 Å. These layers are held together by weak van der Waals interactions and H...F hydrogen bonding between the neighboring layers (average H...F distance of 3.27 Å). ACN molecules occupy voids in the framework structure, which are alternatively positioned above and below the framework pores, with the  $\text{CH}_3$  group facing each void ([Figure S6](#)). Structural arrangements in different orientations are shown in [Figure S7](#). Along the  $bc$ -plane, the framework structure of (1) shows prominent spacing between the 2D framework layers ([Figure S5](#)). It is clear that (1) possesses a unique 2D structure, in which NCs joined together by pyz linkers in each layer are similar to graphene ([Figures 2E](#) and [S4](#)). [Figure 2F](#) represents the layered structure of (1). The framework structure of this material exhibits enhanced stability for over a year. Therefore, we believe that (1) could be an attractive choice for constructing 2D nanosheets.

Micrographs of crystals of (1) are shown in [Figures 3A–C](#) and [S1](#). The layered structure was visible in them ([Figures 3B,C](#), [S1C,D](#), and [S8](#)). It appeared possible to separate these layers. Traditional exfoliating treatments could be effective in terms of efficiency and control over morphology. We, therefore, proceeded with a top-down approach for the scalable fabrication of their nanosheets using the ultrasonication technique. A few crystals were dispersed in 1 mL of ACN in a 2 mL vial, and the mixture was vigorously sonicated for several hours in a 100 W ultrasonic bath, resulting in nanosheets. [Figure 3D](#) shows the HR transmission electron microscopy (TEM) image depicting a multilayer AgNC-MOF (1) with an interlayer spacing of ~0.72 nm (inset a). In the crystal structure of (1), the (010) lattice planes are separated by a distance of 1.13 nm. However, the NC cores from the adjacent layers are separated by 0.75 nm. This distance is seen as the layer with lighter contrast in the TEM image, while NC cores are responsible for a layer with darker contrast (inset a). A slightly smaller distance seen from the TEM image (0.72 nm) is likely due to electron beam-induced structural compaction during image acquisition. A schematic representation of the multilayer structure of AgNC-MOF (1) is shown in [Figure 3E](#), in which 2D sheets are stacked one on top of the other through weak interaction and so can be exfoliated easily. High-resolution cryo-TEM micrographs confirm the successful exfoliation of hexagonal 2D nanosheets with lateral dimensions in the micron range (0.156  $\mu\text{m}$ ) with structural and morphological features shown in [Figures 3D,F,G](#), [S9](#), and [S10](#). [Figure 3H](#) depicts a schematic illustration of a hexagonal cross-section of the total structure in the  $ab$ -plane, which resembles an exfoliated hexagonal 2D sheet. The creation of 2D nanosheets enriched with metal-rich NC nodes, similar to graphene, opens up a new possibility for the development of 2D functional materials. These findings suggest that the top-down approach is a simple and effective method for the scalable production of NC-based 2D nanosheets, which can be expanded to a wide range of layered cluster-based MOFs. Furthermore, TGA/DTG investigations of crystals of (1) under an inert ( $\text{N}_2$ ) atmosphere establish their stability up to 100 °C ([Figure S11](#)).

**Structural Anatomy of AgNC-MOF (2).** SCXRD analysis of (2) reveals the formation of a long polymeric or framework structure, namely  $\{[\text{Ag}_{12}\text{S}_2(\text{TBT})_8(\text{TFA})_4(\text{bpy})_8] \cdot \text{bpy}\}_n$ , which crystallizes in the orthorhombic space group  $I222$



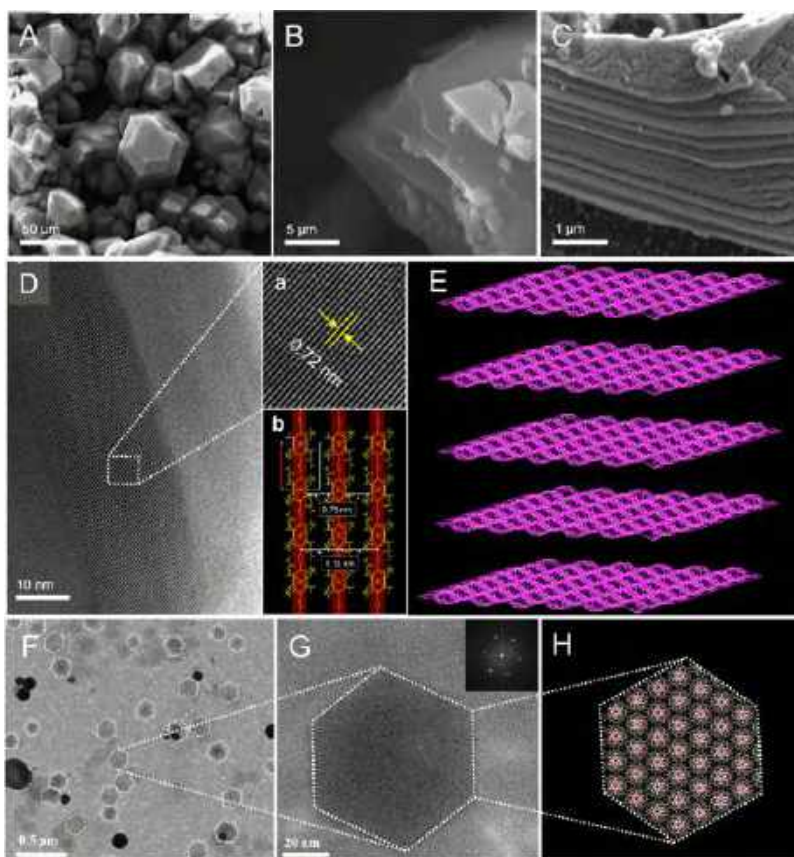


**Figure 3.** Morphology and structural features of AgNC-MOF (1): (A) SEM image of the crystals showing discrete polyhedra. (B,C) FESEM micrographs supporting the layered structure. (D) TEM image showing stacked 2D layers. Inset a: expanded image from the marked area showing an interlayer distance of 0.72 nm. Inset b: schematic showing NCs from adjacent layers separated by a distance of 0.75 nm. The spacing shown is due to the (010) plane of (1). (E) Schematic representation of the total crystal structure of (1) in which multiple 2D AgNC-MOF sheets are stacked consecutively. (F) HR TEM micrograph showing distinct hexagonal 2D sheets exfoliated from the crystal by sonication. (G) Expanded view of a hexagonal 2D sheet and its electron diffraction pattern (inset). (H) Crystal structure in the *ab*-plane in which the atomic arrangement appears comparable to an exfoliated hexagonal 2D sheet.

(Table S2). The structural details of (2) are shown in Figures 4A–D and S12–S16. In the framework structure, all the silver

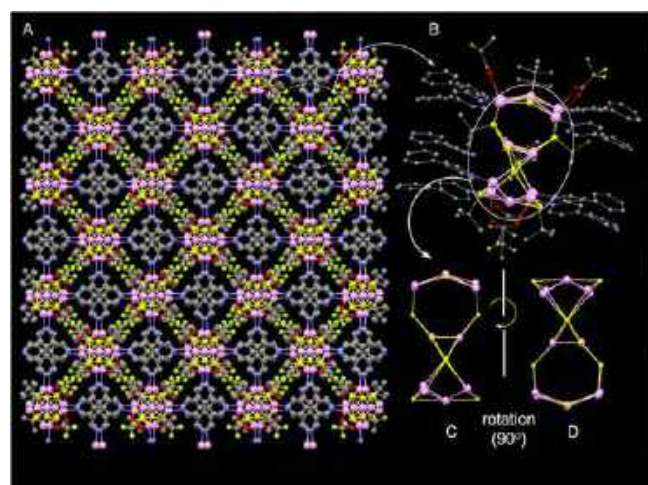


**Figure 4.** (A) Complete crystal structure of (2). (B) Crystal structure of the monomeric unit  $[\text{Ag}_{12}\text{S}_2(\text{TBT})_8(\text{TFA})_4(\text{bpy})_8]$ . (C,D) are inner silver-sulfide cores ( $\text{Ag}_{12}\text{S}_{10}$ ) without ligands having a  $C_4$  symmetry. Color codes: Ag pink; S yellow; C gray; N magenta; F green; and O red.

chalcogenide ( $\text{Ag}_{12}\text{S}_{10}$ ) clusters at the center adopt a dumb-bell-shape, which comprises  $\text{Ag}_5\text{S}_4$  moieties at the top and bottom and an  $\text{Ag}_2\text{S}_2$  moiety in the middle (Figure S12). This is an entirely new structure and has not been reported yet. The structural anatomy of  $\text{Ag}_5\text{S}_4$  and  $\text{Ag}_2\text{S}_2$  moieties is shown in Figures S12 and S13. Each  $\text{Ag}_{12}$  cluster node is co-stabilized by eight TBT and four TFA ligands. In addition, each NC node is interconnected by eight bidentate bpy ligands arranged in a square planar bilayer pattern, forming an infinite 3D polymeric honeycomb-like structure, with additional uncoordinated bpy ligands anchored in between the coordinated bpy ligands held together by  $\pi$ - $\pi$  interactions (Figures S14 and S15). The bond lengths of Ag–Ag, Ag–S, Ag–O, and Ag–N vary in the range of 2.93–2.97, 2.42–2.55, 2.44–2.57, and 2.35–2.36 Å, respectively (Figure S17). Moreover, these 3D framework layers appear to be interpenetrated with each other, showing an AB...AB packing arrangement. These adjacent 3D layers are held together by F...H interactions between the terminal F-atoms of TFA molecules of one layer and H atoms of bridging bpy units of another layer, which can be best viewed along the *ac*-plane (Figure S15). Thus, a similar rearrangement across the  $\text{Ag}_{12}$  NC brought about by the bpy ligand resulted in the formation of (2). In this case, one additional TBT unit from the solution was added to the NC core to maintain the charge balance. This material is stable for more than a year, and its

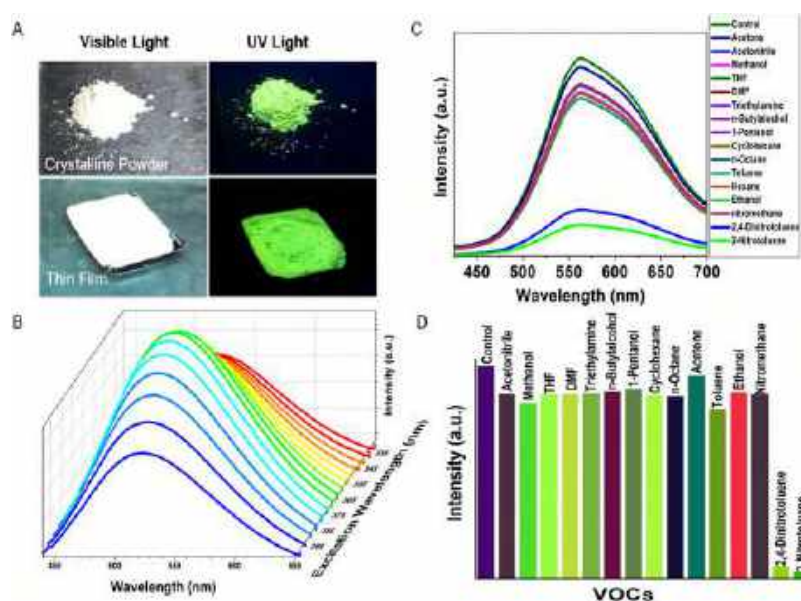


**Figure 5.** (A) Photograph of the crystalline powder and thin film of (2) under visible and UV light. (B) PL spectra of (2) crystalline powder at room temperature at various excitations ranging from 330 to 400 nm. (C) PL of thin films of (2) independently exposed to the vapors of various organic molecules, excited at 370 nm. (D) Bar graph showing the sensitivity of thin films of (2) exposed to the vapors of various organic solvents.

properties are insensitive to air/O<sub>2</sub>. From thermograms (Figure S18), it was observed that material (2) was thermally stable up to 145 °C. The phase purity of (1) and (2) was ascertained by PXRD (Figures S19 and S20). We attempted to separate the adjacent layers from each other in (2); however, we were unable to obtain the component layers, unlike in (1). This could be due to the strong  $\pi$ - $\pi$  stacking interactions between the bpy ligands and strong hydrogen bonding (H...F  $\sim$  2.49 Å) interactions between F-atoms of the CF<sub>3</sub> group and H atoms of the bpy ligand of adjacent layers in (2).

**Understanding the Ag<sub>12</sub> NC.** Ag<sub>12</sub> NC was obtained by a reaction between silver thiolate and silver trifluoroacetate in a solvent mixture of methanol and ACN without the use of any organic connectors (bpy and pyz). The obtained reaction product was initially analyzed by UV-vis spectroscopy and HR ESI-MS (Figures S21 and S22). The ESI-MS spectrum (shown in Figure S22) shows a peak at  $m/z$  2616, and it matches well with the molecular composition of [Ag<sub>12</sub>(TBT)<sub>7</sub>(TFA)<sub>4</sub>(CH<sub>3</sub>CN)<sub>6</sub>]<sup>+</sup>. To identify the counter ion, the IR (infrared) spectrum of a few crystals of Ag<sub>12</sub> NC was recorded. The IR spectrum revealed a distinct band at 1364 cm<sup>-1</sup> attributed to the N-O stretching of NO<sub>3</sub><sup>-</sup>, indicating it to be the counter ion in this case. NO<sub>3</sub><sup>-</sup> has its origin from AgNO<sub>3</sub> used during the synthesis of Ag(TBT)<sub>*n*</sub>. The product solution was kept for crystallization at room temperature; and after a few days, the crystalline product was obtained. The resulting crystals were unstable and showed no X-ray diffraction. The UV-vis spectrum and HR ESI-MS of this sample solution match well with those reported for Ag<sub>12</sub> NC.<sup>26</sup> We, therefore, suggest that the addition of organic connectors, that is, bpy or pyz, causes a major structural change in the NC system via intramolecular metal-metal and metal-sulfide rearrangements, which leads to the formation of stable 3D and 2D AgNC-MOFs. This suggests that organic connectors actively promote intramolecular rearrangement in Ag<sub>12</sub> NC. To the best of our knowledge, this is the first example of an intramolecular metal-metal and metal-sulfide

rearrangement reaction in AgNCs promoted by heterocyclic amines.

**Photoluminescence.** A variety of AgNCs have been reported so far. However, they show less stability and poor luminescence at room temperature. The structural modifications of AgNCs and their transformation into AgNC-MOFs using suitable organic connectors circumvent this problem.<sup>29-31</sup> The AgNC-MOFs (1) and (2) reported in this work exhibit enhanced stability and efficient photoluminescence (PL).

**PL of AgNC-MOF (2).** Freshly prepared crystals of (2) emit bright green luminescence upon UV light exposure at NTP (Figures 5A and S23). To our delight, this material does not show any sensitivity towards oxygen/air, moisture, or fluctuations in room temperature, in contrast to the previously reported framework structures.<sup>29</sup> The spectral profiles of this crystalline material show a single broad emission band in the green region recorded at various excitations shown in Figure 5B. The excitation at 370 nm favors high-energy green emission with a peak maximum at 520 nm. The emission maximum ( $\lambda_{em}$ ) changes with a change in the excitation wavelength (Figure S23D). The material remains stable for more than a year, and the structure and PL remain unaffected upon repeated exposure to air/O<sub>2</sub> or temperature fluctuations, ensuring the endurance and robustness of this material. The structure and geometry of Ag<sub>12</sub> NC nodes are entirely new in this framework structure. The occurrence of efficient PL from (2) could be attributed to the perfect alignment of bpy chromophores around atomically precise NCs as well as the framework's rigid structure. This efficiently prevents non-radiative energy loss by inhibiting vibronic coupling in the framework structure.<sup>29</sup> Density functional theory (DFT) calculations reveal that the emission from the excited states of this system arises due to ligand (bpy)-to-metal charge transfer (LMCT) transitions (discussed below). In this case, the fluorescence lifetime in microseconds ( $\tau_{em,NTP} = 0.138 \mu s$ ) implies that emission originates from triple excited states.<sup>29</sup> The PL lifetime measurements were calculated upon excitation



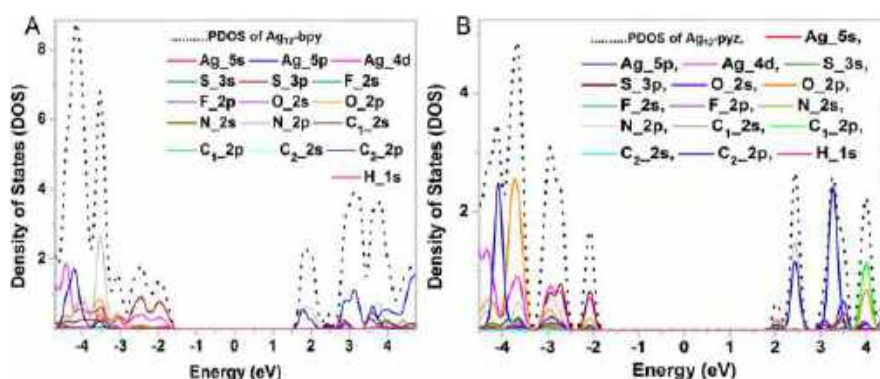


Figure 6. PDOS of (A) Ag<sub>12</sub>-bpy and (B) Ag<sub>12</sub>-pyz.

at 370 nm and the emission of 520 nm using a pulse-diode LED as an excitation source (Figure S24). In addition, we investigated the thin films of the same materials for PL studies. Thin films were prepared using the solution drop-casting method (details are presented in the Supporting Information). PL observed from a thin film of (2) was almost similar to that of its crystalline powder and was investigated for sensing properties (section on sensing of nitroaromatics) (Figures 5C and S23C). The origin of emission transitions is discussed in detail using DFT calculations (see below).

**Understanding of the Electronic Structure of AgNC-MOF (2).** Electronic energy levels and transitions of both the MOFs were calculated using time-dependent density functional theory (TD-DFT). To reduce computational complexity, monomeric units, namely [Ag<sub>12</sub>(S<sub>2</sub>)(TBT)<sub>8</sub>(TFA)<sub>4</sub>(bpy)<sub>10</sub>] abbreviated as Ag<sub>12</sub>-bpy, were used in this work. The optimized geometry of this system and the calculated emission spectrum are shown in Figure S25A,B. The total density of states (TDOS) and partial density of states (PDOS) were calculated for the Ag<sub>12</sub>-bpy unit, and the spectra are plotted in Figure S25C,D. The middle of the highest occupied molecular orbital–lowest unoccupied molecular orbital (HOMO–LUMO) gap was set to zero to correlate with the Fermi level. For the Ag<sub>12</sub>-bpy system, the contribution of 2p atomic orbitals (AOs) of C atoms has been extensively investigated in the PDOS spectra by separately grouping aliphatic Cs of TBT as C<sub>1</sub> and aromatic carbons of bpy as C<sub>2</sub>, as shown in Figure 6A. From the PDOS spectra, we see that the major contribution emerges from the 2p ( $\pi$  orbitals, C<sub>2</sub>) AOs of bpy ligands along with 2p AOs of N atoms. This indicates that the  $\pi$ -orbitals of bpy ligands play a substantial role in the emission transitions that emerge from the lowest LUMOs of the cluster system. Therefore, we believe that ligand (bpy)-to-metal charge transfer (LMCT) is primarily responsible for the emission transitions in the Ag<sub>12</sub>-bpy system.

**PL of AgNC-MOF (1).** The crystals of (1) under UV light do not show any detectable luminescence at room temperature; however, a bright green luminescence was observed at low temperatures (shown in Figure S27). The solid-state PL spectrum recorded under 365 nm excitation displays a brilliant green emission band with a peak maximum at 510 nm at a low temperature (80 K) (Figure S27). The optimized geometry of the monomeric unit, namely [Ag<sub>12</sub>(TBT)<sub>6</sub>(TFA)<sub>6</sub>(pyz)<sub>6</sub>] denoted as Ag<sub>12</sub>-pyz is shown in Figure S28A. TDOS and PDOS spectra of Ag<sub>12</sub>-pyz are plotted in Figures 6B and S28C,D. In the PDOS spectra, the contributions of 2p AOs of

C atoms were investigated in detail by separately grouping them into aliphatic (TBT) and aromatic (pyz) carbons, denoted as C<sub>1</sub> and C<sub>2</sub>, respectively. The PDOS spectra show that the contribution of 2p ( $\pi$  orbitals, C<sub>2</sub>) AOs of pyz ligands, as well as 2p AOs of nitrogen atoms, are shifted away from the LUMOs and are likely to be dominant at 3.1 eV, thereby minimizing their dominance in higher unoccupied MOs. This suggests that  $\pi$ -orbitals of the pyz ligand are not involved in emission transitions. Therefore, the emission from the Ag<sub>12</sub>-pyz system could be attributed to the metal-to-ligand charge transfer.

**UV–Vis Absorption Spectroscopy.** UV–vis absorption measurements were carried out for all the reaction products, namely Ag<sub>12</sub> NC and AgNC-MOFs (1) and (2) as ACN solutions. The absorption spectrum of Ag<sub>12</sub> NC was similar to that reported previously (Figure S21).<sup>26</sup> The UV–vis absorption spectrum of (1) and pristine pyz are nearly identical and display a broad absorption band in the window of 215–340 nm with a maximum at  $\lambda_{\text{max}}$  260 nm, followed by shoulder peaks (Figure S30). These peaks can be assigned to  $\pi$ - $\pi^*$  and  $n$ - $\pi^*$  (C=C and C=N) transitions of the pyz ligand. The calculated absorption spectrum of Ag<sub>12</sub>-pyz displays a broad absorption band between 209 and 355 nm. UV–vis spectra of (2) and the free bpy ligand show nearly identical absorption bands with maxima ( $\lambda_{\text{max}}$ ) at 237 nm (Figure S31). These peaks could be due to the  $\pi$ - $\pi^*$  and  $n$ - $\pi^*$  (C=C and C=N) transitions of the bpy ligand present in the system. The calculated spectrum displays a broad absorption band in the region between 220 and 450 nm with one intense peak at 234 nm followed by small shoulder peaks at 260 and 285 nm. The optimized structure of the Ag<sub>12</sub>-bpy system suggests that absorption peaks in (2) emerge from bpy ligands only. Therefore, all absorption transitions appearing in both the frameworks could be attributed to  $\pi$ - $\pi^*$  and  $n$ - $\pi^*$  transitions of C=C and C=N of linkers.

**Photostability of AgNC-MOF (2).** One of the major challenges for silver-based NCs is their sensitivity towards light, which restricts their use as photocatalysts. The interaction of silver-based NCs with photons generates electrons easily, allowing Ag<sup>+</sup> to be quickly converted to metallic Ag. As a result, obtaining photostable Ag-based NCs for photocatalytic activities remains a challenge. Thin films of (2) were exposed to UV and visible light to investigate their photostability. The integrated emission intensity ( $\lambda_{\text{em}}$  520 nm) was monitored separately under uninterrupted exposure of 370 and 500 nm radiations in the UV and visible regions, respectively, for 2000 s (Figure S32). Results show that

degradation has been greatly reduced compared to pristine Ag<sub>12</sub> NCs. The photostability of framework materials could be attributed to their rigid double-layer structure and the shielding of silver atoms by organic ligands. This could make them promising candidates for photocatalysis.

**Sensing of Nitroaromatics.** PL from thin films of (2) was studied for fluorescence sensing. Prior to exposure, thin films were first activated by passing dry air to remove traces of trapped solvents. In all cases, the PL spectra of thin films of (2) were recorded at  $\lambda_{\text{ex}}$  370 nm. The emission spectrum of a pristine thin film of (2) is shown in Figure 5C. The thin films were then exposed separately to various organic solvent vapors such as ACN (1), methanol (2), ethanol (3), tetrahydrofuran (4), DMF (5), triethylamine (6), *n*-butyl alcohol (7), 1-pentanol (8), cyclohexane (9), *n*-octane (10), acetone (11), toluene (12), nitromethane (13), NT (14), and DNT (15). Just after their exposure, PL was recorded (shown in Figure 5C,D). The emission intensity changed drastically upon exposure to NT and DNT vapors. Other solvents (1–13) did not induce any significant variation in the luminescence intensity of the thin films. This suggests the higher sensitivity of (2) towards NT and DNT. To demonstrate the sensitivity, thin films of (2) were exposed to the equilibrated vapors of NT (ca. 200 ppm at 25 °C) and DNT (ca. 0.0018 ppm at 25 °C) for different time intervals such as 15, 30, 50, 100, 150, and 200 s. After 15 s of analyte exposure, the emission intensities of thin films were drastically reduced by NT and DNT (Figure 5C,D). Exposure of thin films to analyte vapors beyond 30 s resulted in no further quenching, and the response time of (2) for each analyte appears to be 15 s. We measured the time-dependent fluorescence quenching for NT and DNT. The percentage quenching efficiencies  $[(I_0 - I)/I_0 \times 100]$ ;  $I_0$  being the luminescence intensity of the pristine thin film, while  $I$  is the luminescence intensity after exposure to a selected analyte of thin films of (2) upon exposure to the equilibrated vapors of NT and DNT at different time intervals are shown in Figure S33. The percentage quenching efficiencies of NT and DNT are 84 and 74%, respectively. The higher quenching efficiency of NT is likely due to its higher vapor pressure.<sup>40</sup> After being exposed to NT and DNT, thin films of (2) were kept in an oven at 45 °C for 20 min, and the emission was regained. The process could be repeated several times without any loss of efficiency, which establishes the reusability of the material. The quenching of PL could be due to the transfer of energy from the HOMOs of the excited (2) to the LUMOs of nitro-aromatic compounds (NT and DNT), which are strong  $\pi$ -acceptors (Figure S35).<sup>41</sup> When exposed to the vapors of aliphatic nitro compounds, the emission intensity does not show a considerable change. These findings suggest that this material can distinguish between aliphatic and aromatic nitro compounds and can serve as an efficient fluorescent sensor for the detection of explosives.

## CONCLUSIONS

In summary, a heterocyclic amine-assisted rearrangement approach can be adapted to construct 2D and 3D silver cluster-based metal–organic frameworks. The pyz and bpy organic connectors facilitate the construction of 2D  $\{[Ag_{12}(TBT)_6(TFA)_6(pyz)_6] \cdot 2CH_3CN\}_n$  (1) and 3D  $\{[Ag_{12}S_2(TBT)_8(TFA)_4(bpy)_8] \cdot bpy\}_n$  (2) frameworks, respectively, under similar reaction conditions. Each framework material exhibits different morphology, structure, and physical properties. The synthesized atomically precise NC-based 2D

framework material promoted by pyz is associated with its distinguishing characteristics such as a simple synthetic method, good yield, enhanced stability, uniform porosity, metal-rich nodes, brilliant luminescence, and a layered structure. Ultrasonication-assisted top-down exfoliation of the parent crystals of (1) results in nanosheets, and each layer appears structurally similar to graphene. Creating 2D nanosheets in the exotic class of atomically precise materials with metal-rich NC nodes and effectively separating those sheets could open up a new domain in the field of NC chemistry. The bpy ligand-induced 3D framework material has a unique interpenetrated AB $\cdots$ AB packing structure, robustness, good photostability, and displays efficient green luminescence at room temperature. The resulting 3D MOF (2) can function as a high-performance luminescence sensor for the selective recognition of explosives such as NT and DNT with recyclability. In the absence of the heterocyclic amine, a pristine  $[Ag_{12}(TBT)_7(TFA)_4(CH_3CN)_6]^+$  NC was obtained. Overall, this study presents an efficient synthetic approach for creating 2D and 3D AgNC-MOFs with rich architectural diversity, high-density metallic nodes, and concomitant properties, paving the way for making 2D and 3D framework structures of NCs for advanced applications.

## EXPERIMENTAL SECTION

**Chemicals.** Tertiarybutylthiol (TBT), silver trifluoroacetate (TFA), and silver nitrate (AgNO<sub>3</sub>) were purchased from Aldrich. All chemicals were used as received without further purification. All the solvents were purchased from Rankem chemicals and were of analytical grade. Silver thiolate  $[Ag(TBT)_n]$  used during the reaction was synthesized using the standard procedure.

**Synthesis of Silver Cluster-Based Metal–Organic Frameworks and Silver NC.** *Synthesis of  $\{[Ag_{12}(TBT)_6(TFA)_6(pyz)_6] \cdot 2CH_3CN\}_n$  (1) MOF.* The AgNC-MOF (1) was synthesized by adding 20 mg each of silver thiolate, Ag(TBT)<sub>n</sub>, and silver trifluoroacetate to a mixture of 2 mL each of ACN and methanol solution. To this was added 20 mg of pyz, and the reaction mixture was kept stirring for 2 h and subsequently filtered. The reaction mixture was kept for slow evaporation at a low temperature (10 ± 5 °C), and after one week, polyhedron-shaped crystals suitable for SCXRD were obtained. The analysis of SCXRD shows the formation of synthesis of  $\{[Ag_{12}(TBT)_6(TFA)_6(pyz)_6] \cdot 2CH_3CN\}_n$  (1).

*Synthesis of  $\{[Ag_{12}S_2(TBT)_8(TFA)_4(bpy)_8] \cdot bpy\}_n$  (2) MOF.* AgNC-MOF (2) was synthesized following a similar approach to that described above but with a different organic linker, such as bpy. AgNC-MOF (2) was synthesized by adding 20 mg each of silver thiolate, Ag(TBT)<sub>n</sub>, and silver trifluoroacetate to a mixture of 2 mL each of ACN and methanol solution. To this was added 20 mg of bpy, and the reaction mixture was kept stirring for 2 h and subsequently filtered. The filtrate was kept for slow evaporation at a low temperature (10 ± 5 °C) and after one week, rod-shaped crystals suitable for SCXRD were obtained. The analysis of SCXRD shows the formation of synthesis of  $\{[Ag_{12}S_2(TBT)_8(TFA)_4(bpy)_8] \cdot bpy\}_n$  (2).

*Synthesis of  $[Ag_{12}(TBT)_7(TFA)_4(CH_3CN)_6]^+$  NC.* 20 mg each of silver thiolate  $[Ag(TBT)_n]$  and silver trifluoroacetate were added to a solution of ACN and methanol (2 mL each). The reaction mixture was kept on stirring for 1 h, and after that, the reaction mixture was left for crystallization at a low temperature. In this method, no organic connector was employed. After a few days, a crystalline powder was obtained that was investigated by UV–vis and ESI-MS measurements, which showed the formation of the  $[Ag_{12}(TBT)_7(TFA)_4(CH_3CN)_6]^+$  NC, denoted as Ag<sub>12</sub>.

**Cryo-TEM Sample Preparation.** Samples used for TEM analysis were prepared by drop-casting from the ACN dispersions of the samples onto ultrathin (<10 nm thickness) carbon-coated copper grids. The grids were plasma cleaned on a Gatan Solarus (model 950) plasma cleaner for 30 s prior to the sample preparation. TEM images

were collected in a low-dose mode on a JEM-3200FSC field-emission cryo-electron microscope (JEOL Ltd.) with an Omega-type zero-loss energy filter operated at 300 kV. The images were acquired with Gatan DigitalMicrograph software, maintaining the specimen temperature at  $-187\text{ }^{\circ}\text{C}$  to minimize beam-induced damage.

**Thin-Film Preparation.** Quartz (or glass) slides with a dimension of  $16\text{ mm} \times 16\text{ mm}$  were rinsed with acetone and kept in an oven for 1 h at  $80\text{ }^{\circ}\text{C}$  to remove any traces of impurities. Thin films were prepared using a drop-casting method at room temperature. For this, a solution containing (2) was filtered to obtain a clear solution. A few droplets of this transparent solution were slowly dropped at the four vertices of the slide until the solution was spread to cover the entire slide. These were left for air drying to obtain a thin coating of AgNC-MOF, which was used to detect nitroaromatics.

## ASSOCIATED CONTENT

### Supporting Information

The Supporting Information is available free of charge at <https://pubs.acs.org/doi/10.1021/acs.chemmater.2c00647>.

Instrumentation, X-ray crystallographic parameters, HR TEM micrographs, general instrumental parameters used for ESI-MS measurements, additional experimental data, computational details, band gap calculations, and other details (PDF)

Crystallographic data for  $\{[\text{Ag}_{12}(\text{TBT})_6(\text{TFA})_6(\text{pyz})_6] \cdot 2\text{CH}_3\text{CN}\}_n$  (1) (CIF)

Crystallographic data for  $\{[\text{Ag}_{12}\text{S}_2(\text{TBT})_8(\text{TFA})_4(\text{bpy})_8] \cdot \text{bpy}\}_n$  (2) (CIF)

## AUTHOR INFORMATION

### Corresponding Author

**Thalappil Pradeep** – Department of Chemistry, DST Unit of Nanoscience and Thematic Unit of Excellence, Indian Institute of Technology Madras, Chennai 600036, India; [orcid.org/0000-0003-3174-534X](https://orcid.org/0000-0003-3174-534X); Email: [pradeep@iitm.ac.in](mailto:pradeep@iitm.ac.in)

### Authors

**Wakeel Ahmed Dar** – Department of Chemistry, DST Unit of Nanoscience and Thematic Unit of Excellence, Indian Institute of Technology Madras, Chennai 600036, India

**Arijit Jana** – Department of Chemistry, DST Unit of Nanoscience and Thematic Unit of Excellence, Indian Institute of Technology Madras, Chennai 600036, India

**Korath Shivan Sugi** – Department of Chemistry, DST Unit of Nanoscience and Thematic Unit of Excellence, Indian Institute of Technology Madras, Chennai 600036, India

**Ganesan Paramasivam** – Department of Chemistry, DST Unit of Nanoscience and Thematic Unit of Excellence, Indian Institute of Technology Madras, Chennai 600036, India

**Mohammad Bodiuzzaman** – Department of Chemistry, DST Unit of Nanoscience and Thematic Unit of Excellence, Indian Institute of Technology Madras, Chennai 600036, India

**Esma Khatun** – Department of Chemistry, DST Unit of Nanoscience and Thematic Unit of Excellence, Indian Institute of Technology Madras, Chennai 600036, India

**Anirban Som** – Department of Chemistry, DST Unit of Nanoscience and Thematic Unit of Excellence, Indian Institute of Technology Madras, Chennai 600036, India; [orcid.org/0000-0002-6646-679X](https://orcid.org/0000-0002-6646-679X)

**Ananthu Mahendranath** – Department of Chemistry, DST Unit of Nanoscience and Thematic Unit of Excellence, Indian Institute of Technology Madras, Chennai 600036, India

**Amrita Chakraborty** – Department of Chemistry, DST Unit of Nanoscience and Thematic Unit of Excellence, Indian Institute of Technology Madras, Chennai 600036, India

Complete contact information is available at:

<https://pubs.acs.org/doi/10.1021/acs.chemmater.2c00647>

## Notes

The authors declare no competing financial interest.

## ACKNOWLEDGMENTS

We thank the Department of Science and Technology for supporting our research program. We thank the Sophisticated Analytical Instruments Facility, Indian Institute of Technology, Madras, for SCXRD data collection.

## REFERENCES

- Chakraborty, I.; Pradeep, T. Atomically Precise Clusters of Noble Metals: Emerging Link between Atoms and Nanoparticles. *Chem. Rev.* **2017**, *117*, 8208–8271.
- Jin, R.; Zeng, C.; Zhou, M.; Chen, Y. Atomically Precise Colloidal Metal Nanoclusters and Nanoparticles: Fundamentals and Opportunities. *Chem. Rev.* **2016**, *116*, 10346–10413.
- Joshi, C. P.; Bootharaju, M. S.; Alhilaly, M. J.; Bakr, O. M.  $[\text{Ag}_{25}(\text{SR})_{18}]^-$ : The “Golden” Silver Nanoparticle. *J. Am. Chem. Soc.* **2015**, *137*, 11578–11581.
- Yang, H.; Wang, Y.; Huang, H.; Gell, L.; Lehtovaara, L.; Malola, S.; Häkkinen, H.; Zheng, N. All-Thiol-Stabilized  $\text{Ag}_{44}$  and  $\text{Au}_{12}\text{Ag}_{32}$  Nanoparticles with Single-Crystal Structures. *Nat. Commun.* **2013**, *4*, 2422.
- Khatun, E.; Bodiuzzaman, M.; Sugi, K. S.; Chakraborty, P.; Paramasivam, G.; Dar, W. A.; Ahuja, T.; Antharjanam, S.; Pradeep, T. Confining an  $\text{Ag}_{10}$  Core in an  $\text{Ag}_{12}$  Shell: A Four-Electron Superatom with Enhanced Photoluminescence upon Crystallization. *ACS Nano* **2019**, *13*, 5753–5759.
- Liu, J.-W.; Feng, L.; Su, H.-F.; Wang, Z.; Zhao, Q.-Q.; Wang, X.-P.; Tung, C.-H.; Sun, D.; Zheng, L.-S. Anisotropic Assembly of  $\text{Ag}_{52}$  and  $\text{Ag}_{76}$  Nanoclusters. *J. Am. Chem. Soc.* **2018**, *140*, 1600–1603.
- Fenske, D.; Anson, C. E.; Eichhöfer, A.; Fuhr, O.; Ingendoh, A.; Persau, C.; Richert, C. Syntheses and Crystal Structures of  $[\text{Ag}_{123}\text{S}_{35}(\text{S}^t\text{Bu})_{50}]$  and  $[\text{Ag}_{344}\text{S}_{124}(\text{S}^t\text{Bu})_{96}]$ . *Angew. Chem., Int. Ed.* **2005**, *44*, 5242–5246.
- Dass, A.; Theivendran, S.; Nimmala, P. R.; Kumara, C.; Jupally, V. R.; Fortunelli, A.; Sementa, L.; Barcaro, G.; Zuo, X.; Noll, B. C.  $\text{Au}_{133}(\text{SPh-TBu})_{52}$  Nanomolecules: X-Ray Crystallography, Optical, Electrochemical, and Theoretical Analysis. *J. Am. Chem. Soc.* **2015**, *137*, 4610–4613.
- Harkness, K. M.; Tang, Y.; Dass, A.; Pan, J.; Kothalawala, N.; Reddy, V. J.; Cliffl, D. E.; Demeler, B.; Stellacci, F.; Bakr, O. M.; McLean, J. A.  $\text{Ag}_{44}(\text{SR})_{304}^-$ : A Silver-Thiolate Superatom Complex. *Nanoscale* **2012**, *4*, 4269–4274.
- Du, Y.; Sheng, H.; Astruc, D.; Zhu, M. Atomically Precise Noble Metal Nanoclusters as Efficient Catalysts: A Bridge between Structure and Properties. *Chem. Rev.* **2020**, *120*, 526–622.
- Negishi, Y.; Arai, R.; Niihori, Y.; Tsukuda, T. Isolation and structural characterization of magic silver clusters protected by 4-(tert-butyl)benzyl mercaptan. *Chem. Commun.* **2011**, *47*, 5693–5695.
- Jana, A.; Chakraborty, P.; Dar, W. A.; Chandra, S.; Khatun, E.; Kannan, M. P.; Ras, R. H. A.; Pradeep, T. Dual Emitting  $\text{Ag}_{35}$ nanocluster Protected by 2-Pyrene Imine Thiol. *Chem. Commun.* **2020**, *56*, 12550–12553.
- Zhang, Q.-F.; Williard, P. G.; Wang, L.-S. Polymorphism of Phosphine-Protected Gold Nanoclusters: Synthesis and Characterization of a New 22-Gold-Atom Cluster. *Small* **2016**, *12*, 2518–2525.
- Sharma, S.; Chakraborty, K. K.; Saillard, J.-Y.; Liu, C. W. Structurally Precise Dichalcogenolate-Protected Copper and Silver Superatomic Nanoclusters and Their Alloys. *Acc. Chem. Res.* **2018**, *51*, 2475–2483.



- (15) Sugiuchi, M.; Shichibu, Y.; Konishi, K. An Inherently Chiral Au<sub>24</sub> Framework with Double-Helical Hexagold Strands. *Angew. Chem., Int. Ed.* **2018**, *57*, 7855–7859.
- (16) Wan, X.-K.; Guan, Z.-J.; Wang, Q.-M. Homoleptic Alkynyl-Protected Gold Nanoclusters: Au<sub>44</sub>(PhC≡C)<sub>28</sub> and Au<sub>36</sub>(PhC≡C)<sub>24</sub>. *Angew. Chem., Int. Ed.* **2017**, *56*, 11494–11497.
- (17) Lei, Z.; Li, J. J.; Wan, X. K.; Zhang, W. H.; Wang, Q. M. Isolation and Total Structure Determination of an All-Alkynyl-Protected Gold Nanocluster Au<sub>144</sub>. *Angew. Chem., Int. Ed.* **2018**, *57*, 8639–8643.
- (18) Lei, Z.; Wan, X.-K.; Yuan, S.-F.; Guan, Z.-J.; Wang, Q.-M. Alkynyl Approach toward the Protection of Metal Nanoclusters. *Acc. Chem. Res.* **2018**, *51*, 2465–2474.
- (19) Fenske, D.; Persau, C.; Dehnen, S.; Anson, C. E. Syntheses and Crystal Structures of the Ag-S Cluster Compounds [Ag<sub>70</sub>S<sub>20</sub>(SPh)<sub>28</sub>(Dppm)<sub>10</sub>](CF<sub>3</sub>CO<sub>2</sub>)<sub>2</sub> and [Ag<sub>262</sub>S<sub>100</sub>(S<sup>t</sup>Bu)<sub>62</sub>(Dppb)<sub>6</sub>]. *Angew. Chem., Int. Ed.* **2004**, *43*, 305–309.
- (20) Liu, X.; Chen, J.; Yuan, J.; Li, Y.; Li, J.; Zhou, S.; Yao, C.; Liao, L.; Zhuang, S.; Zhao, Y.; Deng, H.; Yang, J.; Wu, Z. A Silver Nanocluster Containing Interstitial Sulfur and Unprecedented Chemical Bonds. *Angew. Chem.* **2018**, *130*, 11443–11447.
- (21) Liu, J. W.; Wang, Z.; Chai, Y. M.; Kurmoo, M.; Zhao, Q. Q.; Wang, X. P.; Tung, C. H.; Sun, D. Core Modulation of 70-Nuclei Core-Shell Silver Nanoclusters. *Angew. Chem., Int. Ed.* **2019**, *58*, 6276–6279.
- (22) Li, B.; Huang, R.-W.; Qin, J.-H.; Zang, S.-Q.; Gao, G.-G.; Hou, H.-W.; Mak, T. C. W. Thermochromic Luminescent Nest-Like Silver Thiolate Cluster. *Chem.—Eur. J.* **2014**, *20*, 12416–12420.
- (23) Díez, I.; Pusa, M.; Kulmala, S.; Jiang, H.; Walther, A.; Goldmann, A. S.; Müller, A. H. E.; Ikkala, O.; Ras, R. H. A. Color Tunability and Electrochemiluminescence of Silver Nanoclusters. *Angew. Chem., Int. Ed.* **2009**, *48*, 2122–2125.
- (24) Yu, H.; Rao, B.; Jiang, W.; Yang, S.; Zhu, M. The Photoluminescent Metal Nanoclusters with Atomic Precision. *Coord. Chem. Rev.* **2019**, *378*, 595–617.
- (25) Wang, Z.-Y.; Wang, M.-Q.; Li, Y.-L.; Luo, P.; Jia, T.-T.; Huang, R.-W.; Zang, S.-Q.; Mak, T. C. W. Atomically Precise Site-Specific Tailoring and Directional Assembly of Superatomic Silver Nanoclusters. *J. Am. Chem. Soc.* **2018**, *140*, 1069–1076.
- (26) Dar, W. A.; Bodiuzzaman, M.; Ghosh, D.; Paramasivam, G.; Khatun, E.; Sugi, K. S.; Pradeep, T. Interparticle Reactions between Silver Nanoclusters Leading to Product Cocrystals by Selective Cocrystallization. *ACS Nano* **2019**, *13*, 13365–13373.
- (27) Bodiuzzaman, M.; Ghosh, A.; Sugi, K. S.; Nag, A.; Khatun, E.; Varghese, B.; Paramasivam, G.; Antharjanam, S.; Natarajan, G.; Pradeep, T. Camouflaging Structural Diversity: Co-Crystallization of Two Different Nanoparticles Having Different Cores But the Same Shell. *Angew. Chem., Int. Ed.* **2019**, *58*, 189–194.
- (28) Bi, Y.; Wang, Z.; Liu, T.; Sun, D.; Godbert, N.; Li, H.; Hao, J.; Xin, X. Supramolecular Chirality from Hierarchical Self-Assembly of Atomically Precise Silver Nanoclusters Induced by Secondary Metal Coordination. *ACS Nano* **2021**, *15*, 15910–15919.
- (29) Huang, R.-W.; Wei, Y.-S.; Dong, X.-Y.; Wu, X.-H.; Du, C.-X.; Zang, S.-Q.; Mak, T. C. W. Hypersensitive Dual-Function Luminescence Switching of a Silver-Chalcogenolate Cluster-Based Metal-Organic Framework. *Nat. Chem.* **2017**, *9*, 689–697.
- (30) Huang, R. W.; Dong, X. Y.; Yan, B. J.; Du, X. S.; Wei, D. H.; Zang, S. Q.; Mak, T. C. W. Tandem Silver Cluster Isomerism and Mixed Linkers to Modulate the Photoluminescence of Cluster-Assembled Materials. *Angew. Chem., Int. Ed.* **2018**, *57*, 8560–8566.
- (31) Dong, X.-Y.; Huang, H.-L.; Wang, J.-Y.; Li, H.-Y.; Zang, S.-Q. A Flexible Fluorescent SCC-MOF for Switchable Molecule Identification and Temperature Display. *Chem. Mater.* **2018**, *30*, 2160–2167.
- (32) Alhilal, M. J.; Huang, R.-W.; Naphade, R.; Alamer, B.; Hedhili, M. N.; Emwas, A.-H.; Maity, P.; Yin, J.; Shkurenko, A.; Mohammed, O. F.; Eddaoudi, M.; Bakr, O. M. Assembly of Atomically Precise Silver Nanoclusters into Nanocluster-Based Frameworks. *J. Am. Chem. Soc.* **2019**, *141*, 9585–9592.
- (33) Dong, X. Y.; Si, Y.; Yang, J. S.; Zhang, C.; Han, Z.; Luo, P.; Wang, Z. Y.; Zang, S. Q.; Mak, T. C. W. Ligand Engineering to Achieve Enhanced Ratiometric Oxygen Sensing in a Silver Cluster-Based Metal-Organic Framework. *Nat. Commun.* **2020**, *11*, 3678–3679.
- (34) Wu, X.-H.; Luo, P.; Wei, Z.; Li, Y.-Y.; Huang, R.-W.; Dong, X.-Y.; Li, K.; Zang, S.-Q.; Tang, B. Z. Guest-Triggered Aggregation-Induced Emission in Silver Chalcogenolate Cluster Metal-Organic Frameworks. *Adv. Sci.* **2019**, *6*, 1801304.
- (35) Wei, Z.; Wu, X. H.; Luo, P.; Wang, J. Y.; Li, K.; Zang, S. Q. Matrix Coordination Induced Emission in a Three-Dimensional Silver Cluster-Assembled Material. *Chem.—Eur. J.* **2019**, *25*, 2750–2756.
- (36) Wu, X.-H.; Wei, Z.; Yan, B.-J.; Huang, R.-W.; Liu, Y.-Y.; Li, K.; Zang, S.-Q.; Mak, T. C. W. Mesoporous Crystalline Silver-Chalcogenolate Cluster-Assembled Material with Tailored Photoluminescence Properties. *CCS Chem.* **2019**, *1*, 553–560.
- (37) Zhao, M.; Huang, S.; Fu, Q.; Li, W.; Guo, R.; Yao, Q.; Wang, F.; Cui, P.; Tung, C. H.; Sun, D. Ambient Chemical Fixation of CO<sub>2</sub> Using a Robust Ag<sub>27</sub> Cluster-Based Two-Dimensional Metal-Organic Framework. *Angew. Chem.* **2020**, *132*, 20206–20211.
- (38) Cao, M.; Pang, R.; Wang, Q.-Y.; Han, Z.; Wang, Z.-Y.; Dong, X.-Y.; Li, S.-F.; Zang, S.-Q.; Mak, T. C. W. Porphyrinic Silver Cluster Assembled Material for Simultaneous Capture and Photocatalysis of Mustard-Gas Simulant. *J. Am. Chem. Soc.* **2019**, *141*, 14505–14509.
- (39) Xu, M.; Liang, T.; Shi, M.; Chen, H. Graphene-Like Two-Dimensional Materials. *Chem. Rev.* **2013**, *113*, 3766–3798.
- (40) Banerjee, D.; Hu, Z.; Pramanik, S.; Zhang, X.; Wang, H.; Li, J. Vapor phase detection of nitroaromatic and nitroaliphatic explosives by fluorescence active metal-organic frameworks. *CrystEngComm* **2013**, *15*, 9745–9750.
- (41) Jurcic, M.; Peveler, W. J.; Savory, C. N.; Scanlon, D. O.; Kenyon, A. J.; Parkin, I. P. The Vapour Phase Detection of Explosive Markers and Derivatives Using Two Fluorescent Metal-Organic Frameworks. *J. Mater. Chem. A* **2015**, *3*, 6351–6359.

## Recommended by ACS

### Assembly of Atomically Precise Silver Nanoclusters into Nanocluster-Based Frameworks

Mohammad J. Alhilal, Osman M. Bakr, et al.

MAY 28, 2019  
JOURNAL OF THE AMERICAN CHEMICAL SOCIETY

READ 

### [Ag<sub>9</sub>(1,2-BDT)<sub>6</sub>]<sub>3</sub>—: How Square-Pyramidal Building Blocks Self-Assemble into the Smallest Silver Nanocluster

Badriah J. Alamer, Osman M. Bakr, et al.

MARCH 17, 2021  
INORGANIC CHEMISTRY

READ 

### [Cu<sub>36</sub>H<sub>10</sub>(PET)<sub>24</sub>(PPh<sub>3</sub>)<sub>6</sub>Cl<sub>2</sub>] Reveals Surface Vacancy Defects in Ligand-Stabilized Metal Nanoclusters

Chunwei Dong, Osman M. Bakr, et al.

JULY 13, 2021  
JOURNAL OF THE AMERICAN CHEMICAL SOCIETY

READ 

### Ag<sub>23</sub>Au<sub>2</sub> and Ag<sub>22</sub>Au<sub>3</sub>: A Model of Cocrystallization in Bimetal Nanoclusters

Lizhong He, Junhao Liang, et al.

JUNE 02, 2021  
INORGANIC CHEMISTRY

READ 

Get More Suggestions >

# Molecular Engineering of Atomically Precise Silver Clusters into 2D and 3D Framework Solids

Wakeel Ahmed Dar, Arijit Jana, Korath Shivan Sugi, Ganesan Paramasivam, Mohammad Bodiuzzaman, Esma Khatun, Anirban Som, Ananthu Mahendranath, Amrita Chakraborty and Thalappil Pradeep\*

Department of Chemistry, DST Unit of Nanoscience and Thematic Unit of Excellence, Indian Institute of Technology Madras, Chennai 600036, India.

<b>Item</b>	<b>Description</b>	<b>Page no.</b>
<b>Section 1</b>	Instrumentation	3
	General instrumental parameters used for ESI-MS measurements	4
	X-ray crystallography	5
	Single crystal X-ray diffraction (SCXRD) analysis	5
<b>Table S1</b>	Crystal data and structure refinement of AgNC-MOF (1)	6
<b>Table S2</b>	Crystal data and structure refinement of AgNC-MOF (2)	7
<b>Section S2</b>	Computational details of AgNC-MOF (1) and AgNC-MOF (2)	8
<b>Section S3</b>	Band gap calculations	8
<b>Figure S1</b>	SEM micrographs of AgNC-MOF (1)	10
<b>Figure S2</b>	SEM micrographs of AgNC-MOF (2)	11
<b>Figure S3</b>	Structural anatomy of Ag <sub>12</sub> S <sub>6</sub> core in (1)	11
<b>Figure S4</b>	Complete crystal structure of AgNC-MOF (1) in the <i>ab</i> -plane	12
<b>Figure S5</b>	Structural arrangement of layers in (1)	13
<b>Figure S6</b>	The arrangement of acetonitrile molecules in (1)	13

<b>Figure S7</b>	Perspective of (1) in different orientations	14
<b>Figure S8</b>	FESEM images of (1) crystal	15
<b>Figure S9</b>	Cryo-TEM micrographs of (1) crystals dispersed in acetonitrile solvent	16
<b>Figure S10</b>	TEM micrograph of the discrete hexagonal-sheet-like structure of (1) and perspective of single-crystal X-ray structure of (1) overlaid on TEM micrograph	16
<b>Figure S11</b>	TG and DTG plots of AgNC-MOF (1) crystals	17
<b>Figure S12</b>	Anatomy of Ag <sub>12</sub> S <sub>10</sub> core of AgNC-MOF (2)	17
<b>Figure S13</b>	Construction of Ag <sub>12</sub> -cluster node present in AgNC-MOF (2)	18
<b>Figure S14</b>	Complete crystal structure of the (2) along the <i>ab</i> -plane	18
<b>Figure S15</b>	The AB...AB packing of Ag <sub>12</sub> cluster nodes of (2)	19
<b>Figure S16</b>	Honeycomb structures of AgNC-MOF (2) in different orientations	19
<b>Figure S17</b>	Bond distances of a cross-section of (2)	20
<b>Figure S18</b>	TG and DTG plots of AgNC-MOF (2) crystals	20
<b>Figure S19</b>	PXRD pattern of AgNC-MOF (1)	21
<b>Figure S20</b>	PXRD patterns of AgNC-MOF (2)	21
<b>Figure S21</b>	UV-Vis absorption spectrum of Ag <sub>12</sub> nanocluster	22
<b>Figure S22</b>	ESI-MS of Ag <sub>12</sub> NC	22
<b>Figure S23</b>	Luminescence details of (2)	23
<b>Figure S24</b>	Luminescence lifetime of (2)	24
<b>Figure S25</b>	DFT calculations of Ag <sub>12</sub> -bpy	25

<b>Figure S26</b>	Frontier MO representations (HOMO and LUMO) of $[\text{Ag}_{12}\text{S}_2(\text{TBT})_8(\text{TFA})_4(\text{bpy})_{10}]$	26
<b>Figure S27</b>	Photoluminescence of AgNC-MOF ( <b>1</b> )	26
<b>Figure S28</b>	DFT calculations of Ag <sub>12</sub> -pyz	27
<b>Figure S29</b>	Calculated emission spectrum of Ag <sub>12</sub> -pyz	28
<b>Figure S30</b>	UV-Vis absorption spectra of AgNC-MOF ( <b>1</b> ): experimental and calculated	28
<b>Figure S31</b>	UV-Vis absorption spectra of AgNC-MOF ( <b>2</b> ): experimental and calculated	29
<b>Figure S32</b>	Photostability of AgNC-MOF ( <b>2</b> )	29
<b>Figure S33.</b>	Quenching efficiencies of thin films of ( <b>2</b> ) upon exposure to (A) NT and (B) DNT	30
<b>Figure S34</b>	Calculation of the band gap of AgNC-MOF ( <b>2</b> ) solution	30
<b>Figure S35</b>	Schematic representation of the molecular orbitals responsible for energy transfer	31
	References	31

## Section 1

### Instrumentation

UV-Vis spectra were measured using a PerkinElmer Lambda 25 instrument in the wavelength range of 200–1100 nm. Fourier-transform infrared spectra (FT IR) were recorded using a PerkinElmer spectrometer. Powder X-ray diffraction (XRD) was recorded using a Bruker D8 Advance X-ray diffractometer. Luminescence measurements were carried out on a Horiba Jobin Yvon NanoLog spectrofluorometer. The slit width for the excitation and emission was set as 2 nm. The fluorescence decay profile was measured using a time-correlated, single-photon counting (TCSPC) (Horiba Jobin Yvon) instrument. Diode laser source ( $\lambda_{\text{ex}}$  370 nm), having a pulse repetition rate of 1 MHz was used for the excitation. The decay curve was

collected at a wavelength near the emission maxima ( $\lambda_{em}$  520 nm) and spectrum fitting was performed using IBH DAS6 software. The morphological evaluation of the crystalline material was performed using FEI Quanta 200 environmental scanning electron microscope (ESEM) equipped with an EDAX EDS system. The internal morphology of the crystals was observed from the high resolution (FESEM) micrographs using Thermo Scientific Verios G4 scanning electron microscope (SEM), Verios G4 XHR SEM provides sub-nanometer resolution from 1 to 30 kV. Thermograms (TG/DTG) were recorded on the instrument NETZSCH STA 449 F3 Jupiter- equipped with a dual furnace made up of SiC to enhance the sample throughput equipped with a sensor made up of Pt-Rh wire.

### **General instrumental parameters used for ESI-MS measurements**

The cluster sample was analyzed by Waters Synapt G2Si High Definition Mass Spectrometer equipped with electrospray ionization (ESI) source, and ion mobility (IM) separation. The sample was measured in positive-ion mode. The optimized conditions for the measurement are given below:

Sample concentration: 10  $\mu\text{g/mL}$

Solvent:  $\text{CH}_3\text{CN}$

Flow rate: 30  $\mu\text{L/min}$

Capillary voltage: 2- 3 kV

Cone voltage: 30 V

Source offset: 20 V

Trap collision Energy: 0 V

Transfer collision Energy: 0 V

Source temperature: 100°C

Desolvation temperature: 200°C

Desolvation gas Flow: 400 L/h



Trap gas flow: 10 L/h

### **X-ray crystallography**

Single crystal data were measured using a Bruker Kappa APEX III CMOS diffractometer using MoK $\alpha$  ( $\lambda = 0.71073 \text{ \AA}$ ) radiation. Indexing was performed using APEX III. Data integration and reduction were performed using SAINT V8.37A. Absorption correction was performed by the multi-scan method implemented in SADABS (Bruker, 2016). The space group was determined using XPREP implemented in APEX III.

### **Single crystal X-ray diffraction (SCXRD) analysis**

The structure was solved using SHELXT-2017 and least-squares refined using SHELXL-2017 software packages. Crystal data and refinement conditions are shown in Table S1. Suitable restraints were applied during the least-squares (LS) refinement. The difference Fourier map towards the end showed the presence of acetonitrile molecules inside the lattice.

**Table S1. Crystal data and structure refinement of AgNC-MOF (1)**

Identification code	W164R
Empirical formula	$C_{48}H_{66}Ag_{12}F_{18}N_6O_{12}S_6 \cdot 2 (C_2H_3N)$
Formula weight	2829.97
Temperature	293(2) K
Wavelength	0.71073 Å
Crystal system	Trigonal
Space group	P-3m1
Unit cell dimensions	a = 15.0573(5) Å $\alpha = 90^\circ$ b = 15.0573(5) Å $\beta = 90^\circ$ c = 11.3014(4) Å $\gamma = 120^\circ$
Volume	2219.00(17) Å <sup>3</sup>
Z	1
Density (calculated)	2.118 Mg/m <sup>3</sup>
Absorption coefficient	2.813 mm <sup>-1</sup>
F(000)	1358
Crystal size	0.100 x 0.100 x 0.050 mm <sup>3</sup>
Theta range for data collection	3.606 to 26.988°
Index ranges	-19 ≤ h ≤ 19, -16 ≤ k ≤ 19, -14 ≤ l ≤ 14
Reflections collected	38878
Independent reflections	1809 [R(int) = 0.0336]
Completeness to theta = 25.242°	99.5 %
Absorption correction	Semi-empirical from equivalents
Max. and min. transmission	0.7462 and 0.5742
Refinement method	Full-matrix least-squares on F <sup>2</sup>
Data / restraints / parameters	1809 / 4 / 99
Goodness-of-fit on F <sup>2</sup>	1.203
Final R indices [I > 2σ(I)]	R1 = 0.0437, wR2 = 0.0862
R indices (all data)	R1 = 0.0561, wR2 = 0.0986
Extinction coefficient	0.0028(3)
Largest diff. peak and hole	1.229 and -0.745 e.Å <sup>-3</sup>

**Table S2. Crystal data and structure refinement of AgNC-MOF (2)**

Identification code	w160r
Empirical formula	C <sub>90</sub> H <sub>112</sub> Ag <sub>12</sub> F <sub>12</sub> N <sub>10</sub> O <sub>8</sub> S <sub>10</sub>
Formula weight	3304.93
Temperature	293(2) K
Wavelength	0.71073 Å
Crystal system	Orthorhombic
Space group	I222
Unit cell dimensions	a = 17.3070(9) Å      α = 90° b = 17.3297(9) Å      β = 90° c = 20.7178(10) Å     γ = 90°
Volume	6213.8(5) Å <sup>3</sup>
Z	2
Density (calculated)	1.766 Mg/m <sup>3</sup>
Absorption coefficient	2.080 mm <sup>-1</sup>
F(000)	3236
Crystal size	0.200 x 0.100 x 0.100 mm <sup>3</sup>
Theta range for data collection	3.065 to 24.742°
Index ranges	-20 ≤ h ≤ 20, -20 ≤ k ≤ 20, -24 ≤ l ≤ 24
Reflections collected	72335
Independent reflections	5325 [R(int) = 0.0878]
Completeness to theta = 24.742°	99.6 %
Absorption correction	Semi-empirical from equivalents
Max. and min. transmission	0.64 and 0.57
Refinement method	Full-matrix least-squares on F <sup>2</sup>
Data / restraints / parameters	5325 / 372 / 352
Goodness-of-fit on F <sup>2</sup>	1.159
Final R indices [I > 2 sigma(I)]	R1 = 0.0732, wR2 = 0.1971
R indices (all data)	R1 = 0.0942, wR2 = 0.2085
Absolute structure parameter	0.07(15)
Extinction coefficient	n/a
Largest diff. peak and hole	1.476 and -2.021 e.Å <sup>-3</sup>

## Section S2. Computational details of AgNC-MOF (1) and AgNC-MOF (2)

The geometric structures of Ag<sub>12</sub>bpy and Ag<sub>12</sub>pyz MOFs were optimized in real space having grid spacing of 0.2 Å for calculating electron density maps using density functional theory (DFT). Atomic coordinates obtained from single-crystal structures have been used to initiate the calculations. All the calculations were carried out in the GPAW software package. The valence electronic configuration of all the atoms was included in the calculation by PAW setups Ag(4d<sup>10</sup>5s<sup>1</sup>), S(3s<sup>2</sup>3p<sup>4</sup>), F(2s<sup>2</sup>2p<sup>5</sup>), O(2s<sup>2</sup>2p<sup>4</sup>), N(2s<sup>2</sup>2p<sup>3</sup>), C(2s<sup>2</sup>2p<sup>2</sup>) and H(1s<sup>1</sup>) along with the scalar-relativistic effects for Ag atoms. The atomic interactions were described by the hybrid Perdew, Burke and Ernzerhof (PBE) functional. The structure was relaxed until the residual forces become 0.05 eV/Å, without applying any symmetry constraints. The electronic properties such as molecular orbitals (MOs), the total density of states, and the partial density of states were calculated to gain some insights into the charge transfer of the clusters. The molecular orbitals (MOs) of the clusters were plotted for frontier and MOs responsible for their optical absorption and emission transitions. The TDOS and PDOS were calculated using G09 and Multiwfn software packages. The excited-state geometries of both clusters were optimized in the delta SCF method. The optical absorption and emission spectra of the MOFs were calculated using linear response TDDFT. Both the spectra were plotted with a Gaussian broadening of 0.085 eV.

## Section S3. Band gap calculations

The band gap was calculated using Kubelka-Munk (KM) equation given below

$$F(R_{\infty}) = \frac{(1-R_{\infty})^2}{2R_{\infty}} = \frac{K}{S} \quad (1)$$

Where,  $F(R_{\infty})$ ,  $R_{\infty}$ ,  $S$  and  $K$  represent the remission function, limiting reflectance, scattering function and absorption function, respectively.

For the materials scattering in a diffused manner perfectly, then scattering function ( $S$ ) becomes independent of wavelength, and the KM function then becomes proportional coefficient of absorption ( $\alpha$ ) as given below

$$F(R_{\infty}) \propto \alpha \propto \frac{(h\nu - E_g)^n}{h\nu} \quad (2)$$

Where, n value is equal to 2 and ½ for allowed indirect and allowed direct band gap transitions, respectively.<sup>1,2</sup>

The representation of the plot between  $[F(R_{\infty})h\nu]^2$  versus  $h\nu$  can be employed to calculate the allowed direct band gap. The extrapolation of the straight-line portion of the curve gives the band gap (E ) (Figure S34).



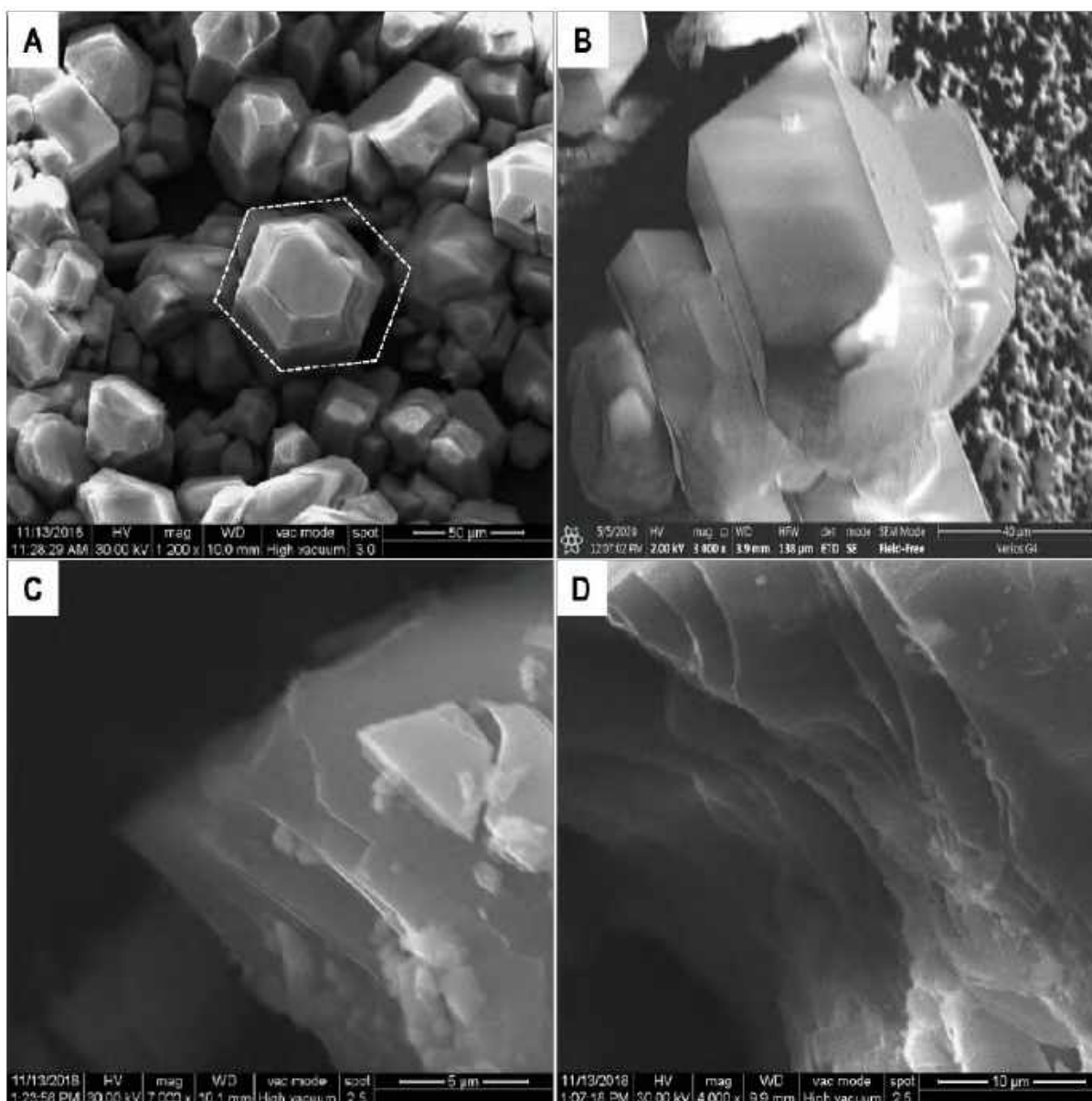


**Figure S1.** (A) and (B) are the SEM images showing the polyhedral crystals of AgNC-MOF (1). (C) and (D) are the SEM images of crushed crystals, indicating multiple layer-like planes inside the crystals.

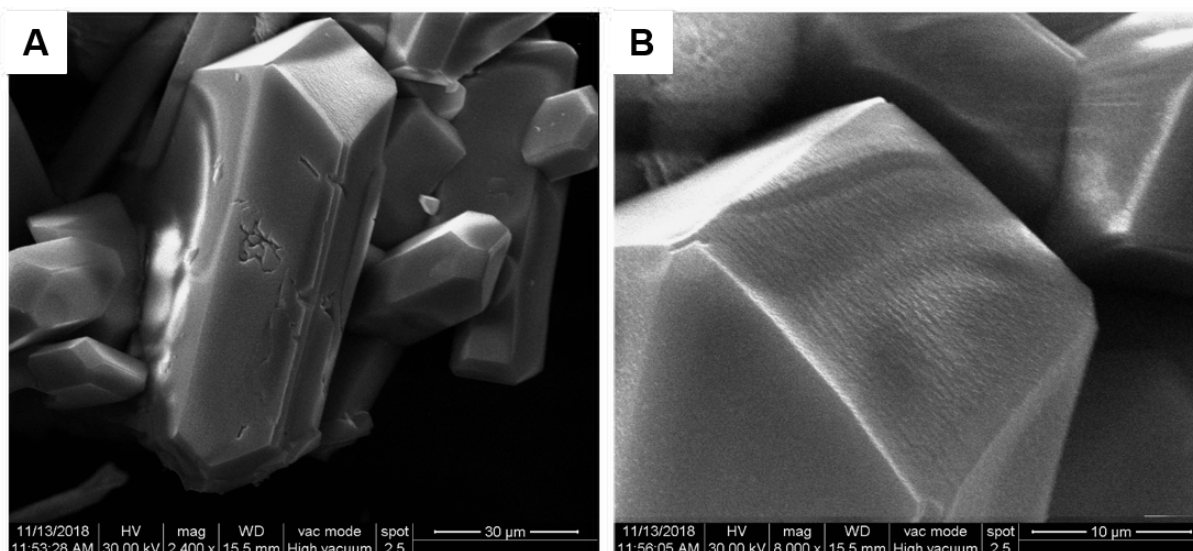


**Figure S2.** (A) and (B) are SEM micrographs of AgNC-MOF (**2**) crystals having rod shape.

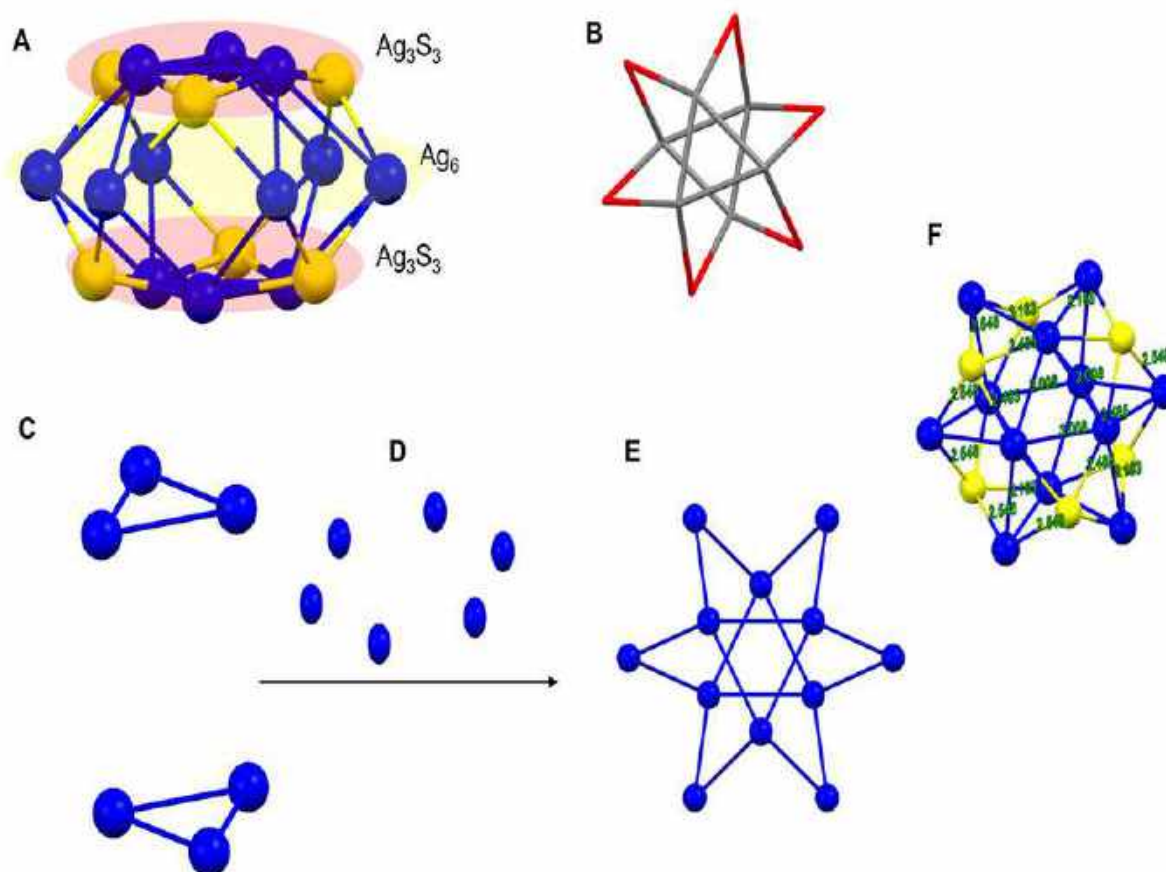


**Figure S3.** (A) Structure of  $\text{Ag}_{12}\text{S}_6$  core shows sandwich-like structure:  $\text{Ag}_3\text{S}_3\text{-Ag}_6\text{-Ag}_3\text{S}_3$ . (B) Arrangement of Ag-atoms in  $\text{Ag}_{12}$  core showing three hexagons bisecting each other. (C-E) Construction of  $\text{Ag}_{12}$  core structure. (F) Interatomic bond distances of  $\text{Ag}_{12}\text{S}_6$  core. Color codes: Ag blue, grey and red; S yellow.

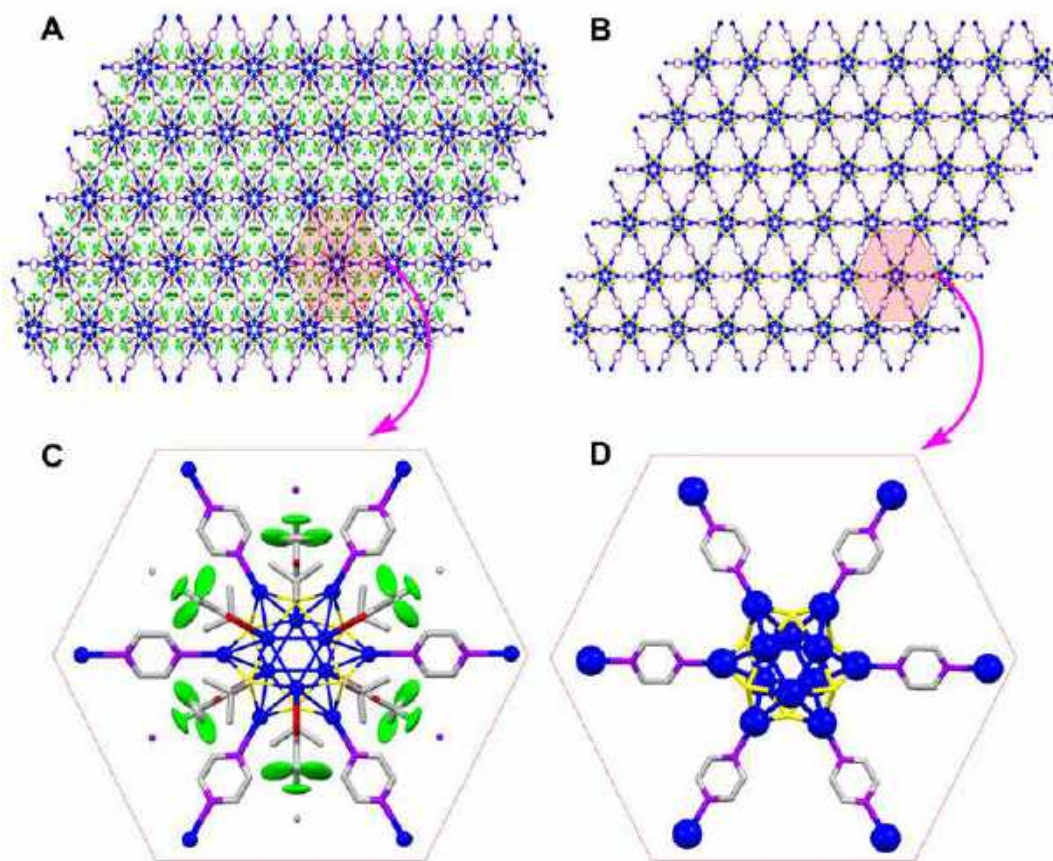


**Figure S4.** (A) Complete crystal structure of (**1**) in *ab*-plane (hydrogen atoms have been omitted for clarity). (B) Structure of (**1**) in *ab*-plane without tertiary butyl and trifluoroacetate groups and its appearance is analogous to inorganic graphene. (C) and (D) are monomer units. Color codes: Ag blue; S yellow; C grey; N magenta; F green and O red.



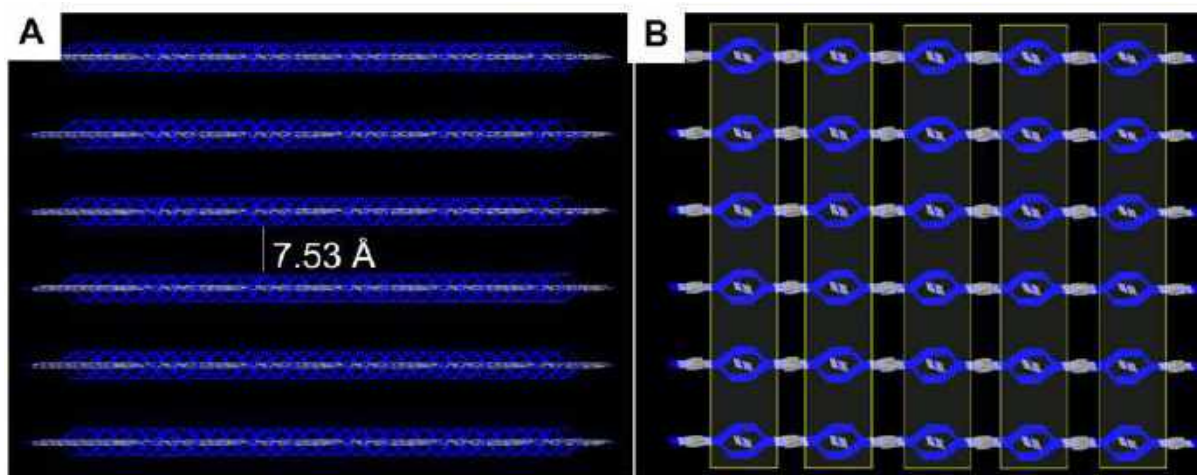


**Figure S5.** (A) Structures of **(1)** in the *bc*-plane by including only its Ag<sub>12</sub> core and pyz linker show that the separation between the neighbouring layers is prominent. (B) Symmetrical alignment of cluster nodes in each layer of **(1)**. Color codes: Ag blue; C grey.

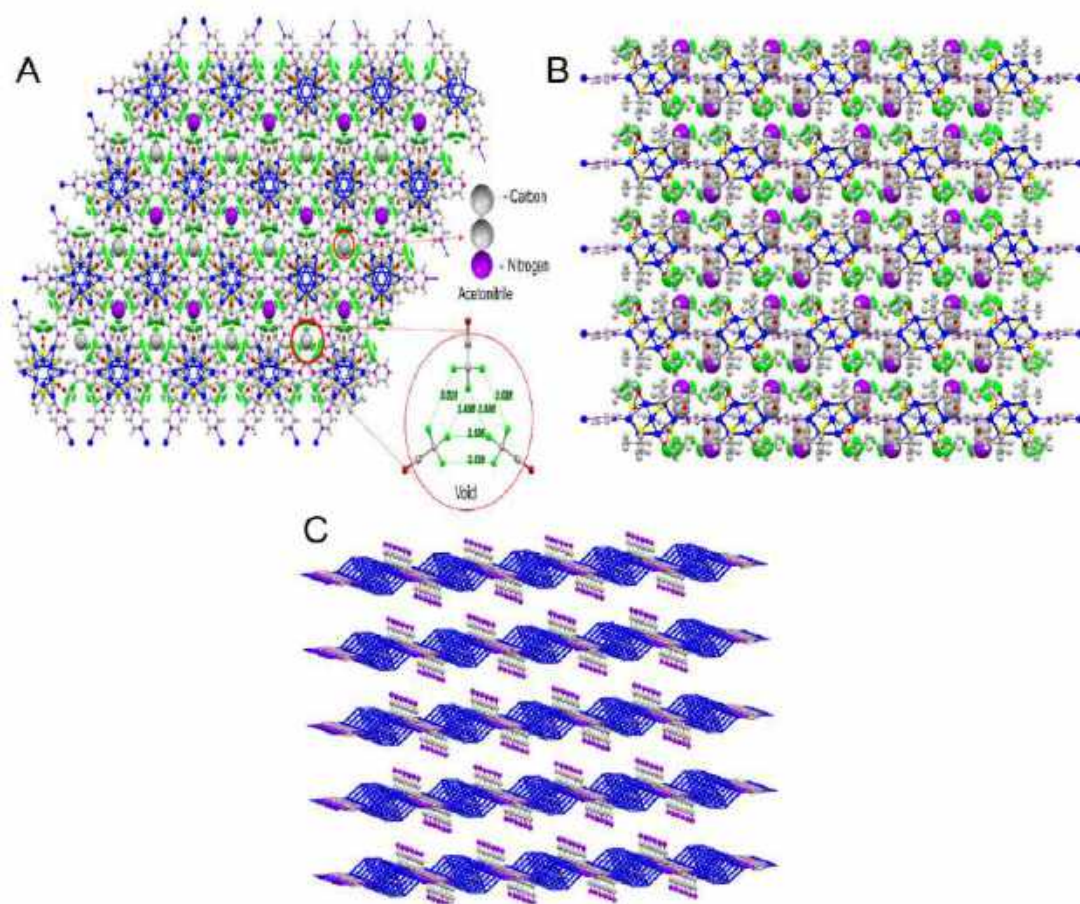


**Figure S6.** The arrangement of acetonitrile molecules in **(1)** along (A) *ab*-plane; (B) *bc*-plane and (C) *ac*-plane (TBT and TFA ligands are omitted for clarity). In each case, the –CH<sub>3</sub> group faces the void for H...F bonding and are alternatively placed around the cluster. Color codes: Ag blue; S yellow; C grey; N magenta; F green and O red.

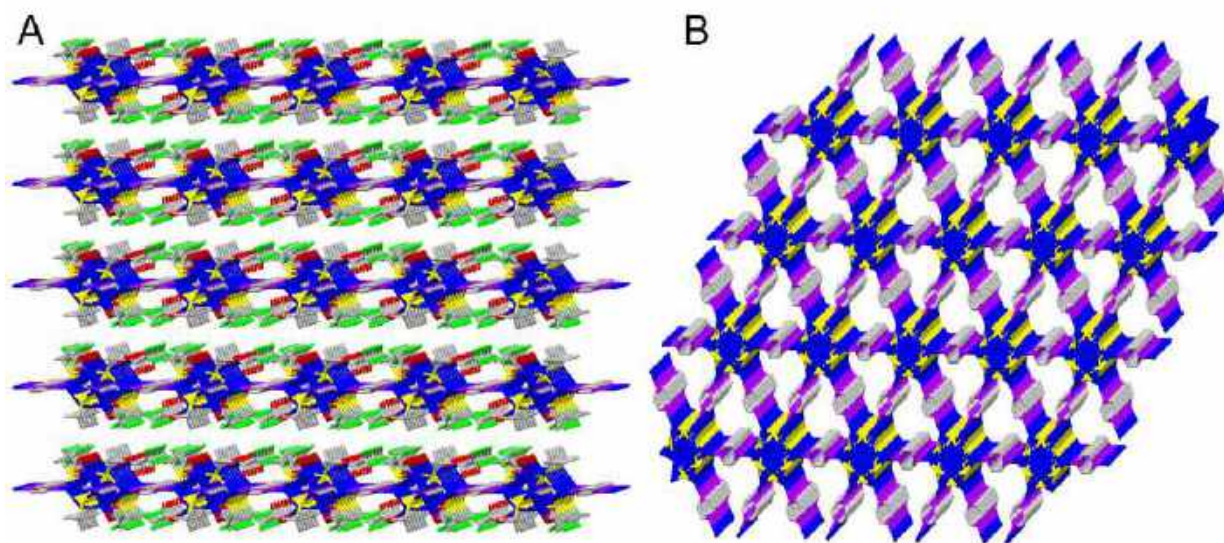


**Figure S7.** The perspective of (**1**) along (A) *bc*-plane and (B) *ac*-plane. Color codes: Ag blue; S yellow; C grey; N magenta; F green and O red.



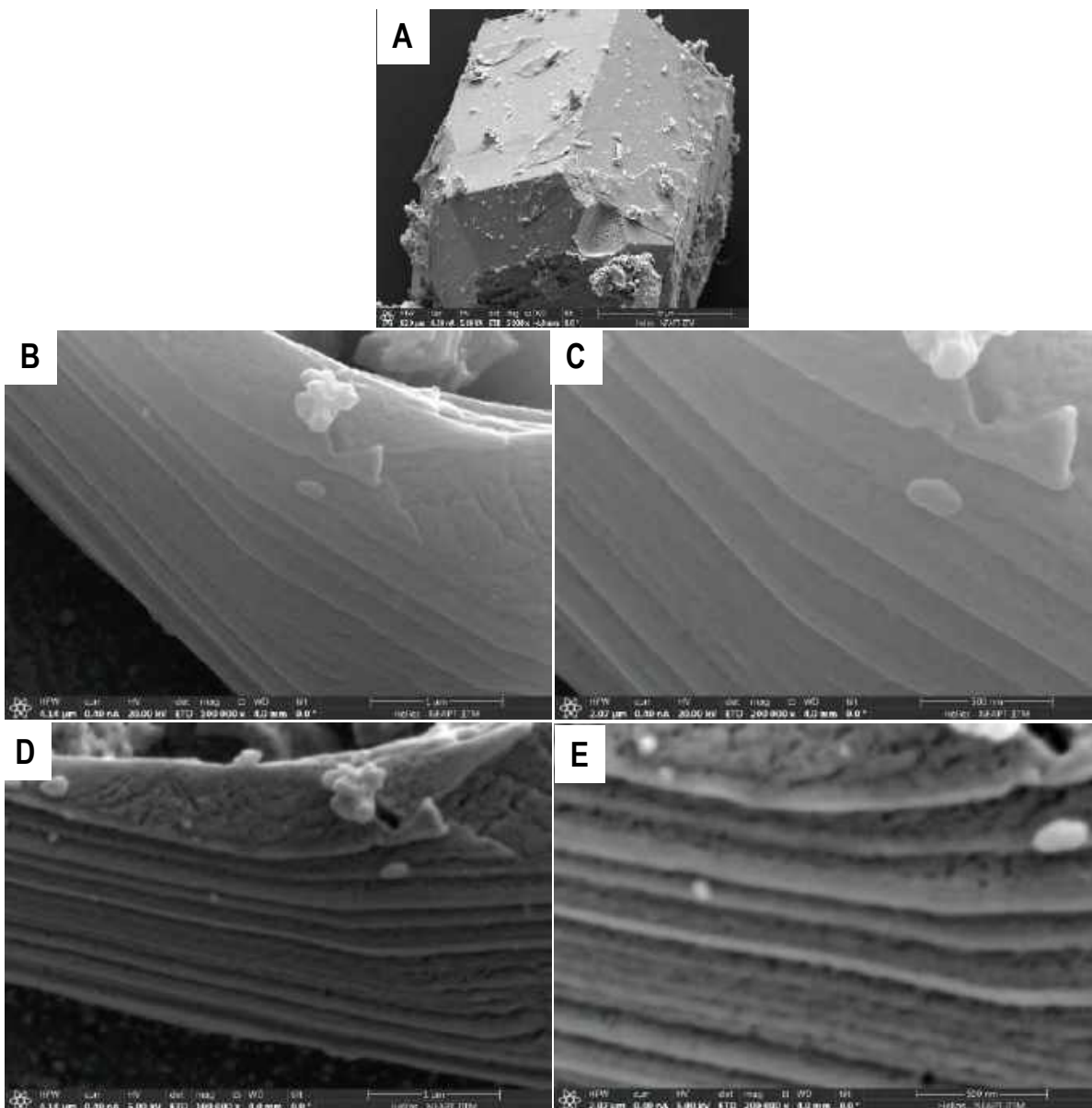


**Figure S8.** (A) FESEM image of AgNC-MOF (**1**) crystal. (B-E) are the FESEM images of the cross-section of the crystal in different orientations revealing the prominent layered-like structure within the crystals of (**1**).

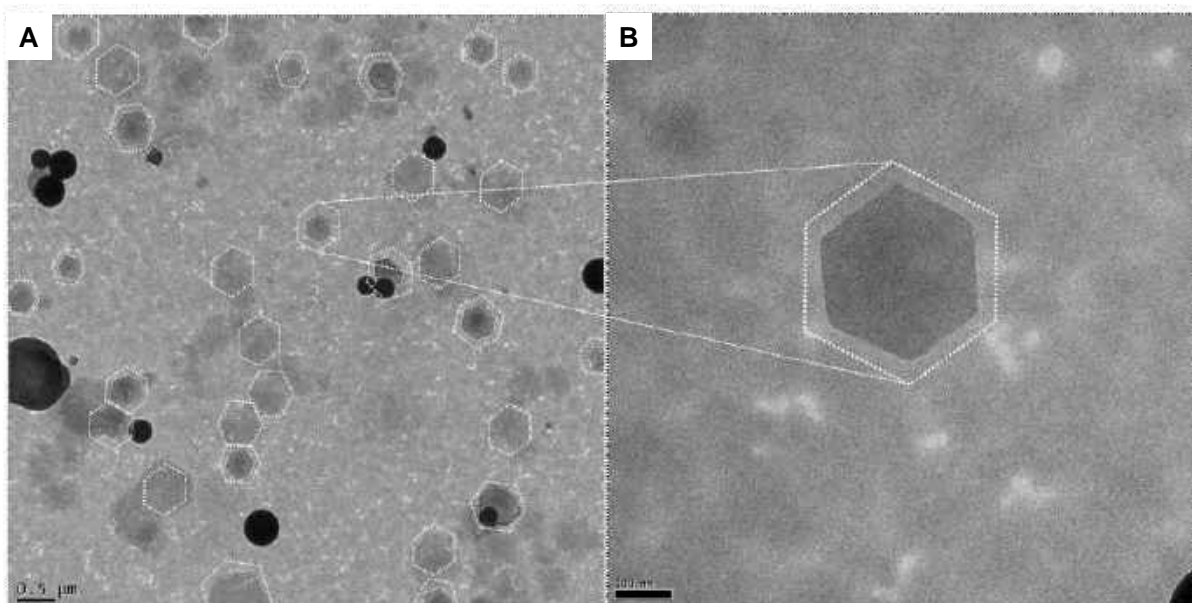


**Figure S9.** (A) HR TEM micrograph of (**1**) crystals dissolved in acetonitrile. The hexagonal-sheet like structures were successfully separated from each other. (B) TEM micrograph of discrete hexagonal sheet-like structure of (**1**) in micron range.

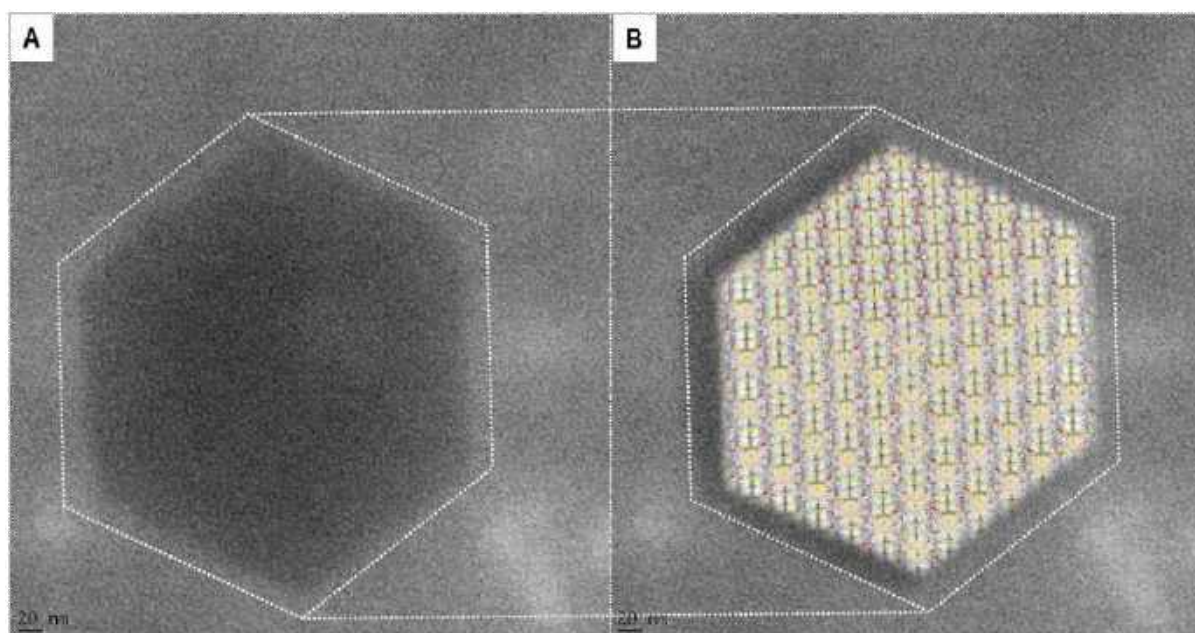


**Figure S10.** (A) HR TEM micrograph and (B) perspective of a single-crystal X-ray structure of (**1**) overlaid on a hexagonal sheet-like structure.

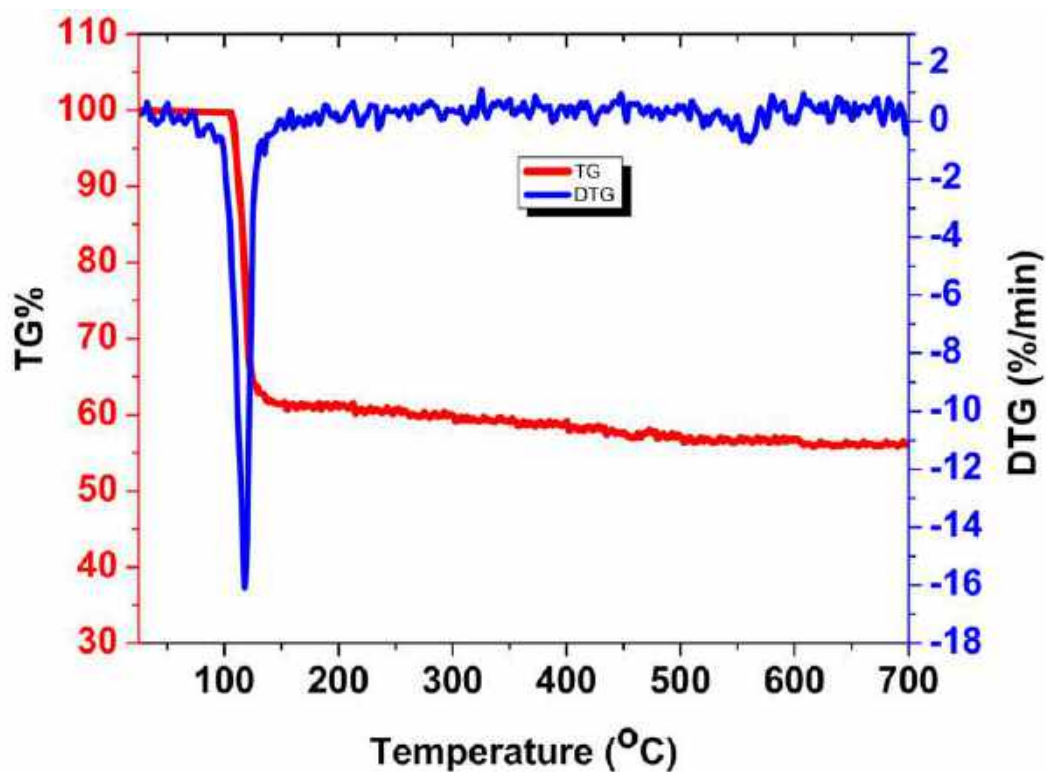


**Figure S11.** TG and DTG plots of AgNC-MOF (1) crystals.

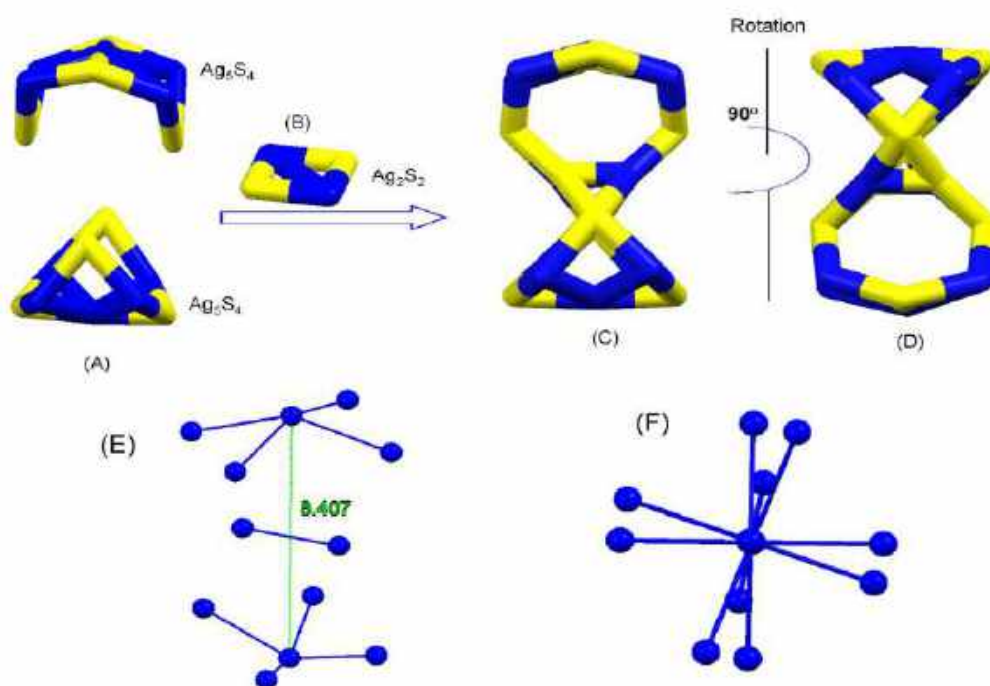


**Figure S12.** Anatomy of  $\text{Ag}_{12}\text{S}_{10}$  core of AgNC-MOF (2). (A) The perspectives of  $\text{Ag}_5\text{S}_4$  moieties at the top and bottom of the  $\text{Ag}_{12}$  core, (B) structure of  $\text{Ag}_2\text{S}_2$  moiety, which acts as a link between the  $\text{Ag}_5\text{S}_4$  moieties, (C) and (D) are dumbbell-shaped structures of  $\text{Ag}_{12}\text{S}_{10}$  core,



(E) arrangements of Ag-atoms only of Ag<sub>12</sub> core, and (F) represents the top view of the Ag<sub>12</sub> core.

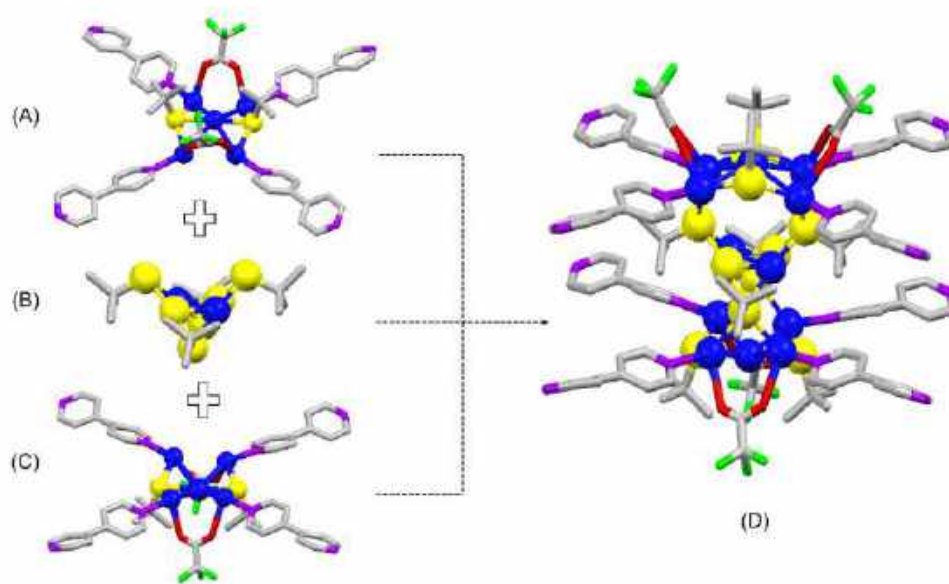


**Figure S13.** Construction of Ag<sub>12</sub>-cluster node present in AgNC-MOF (**2**).

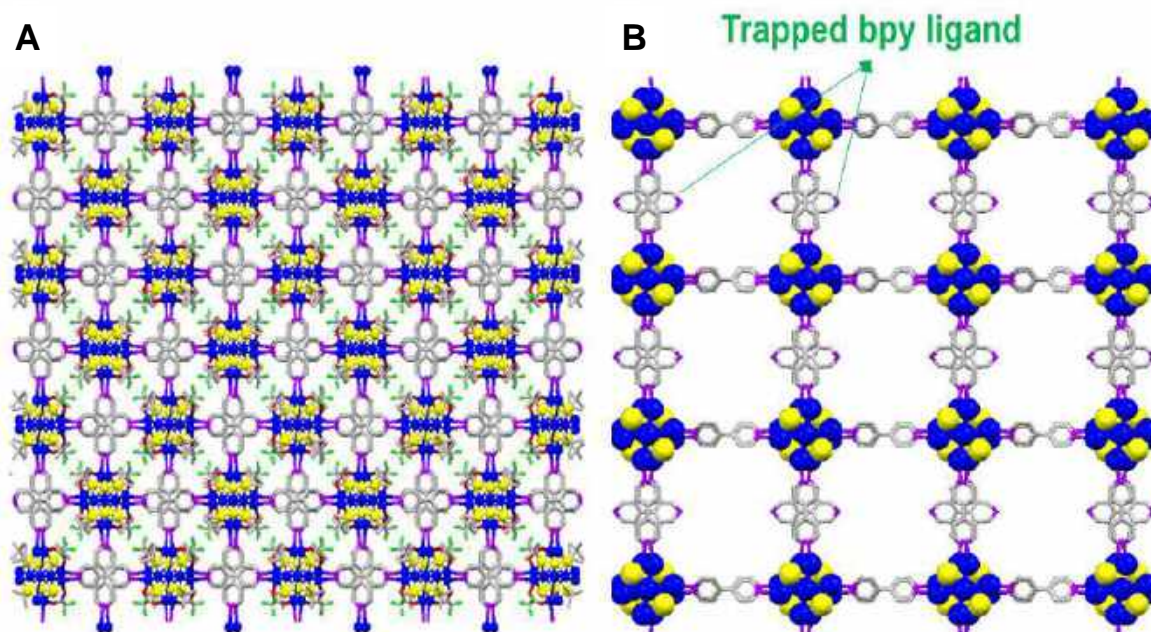


**Figure S14.** (A) Complete crystal structure of the **(2)** along the *ab*-plane showing the repeating units of Ag<sub>12</sub>-cluster nodes (hydrogen atoms have been omitted for clarity). (B) Structural representation of a single layer of **(2)** showing the prominent pores in the framework. The bpy ligand is also trapped in between the coordinated bpy units of the framework (other atoms have been omitted for clarity).

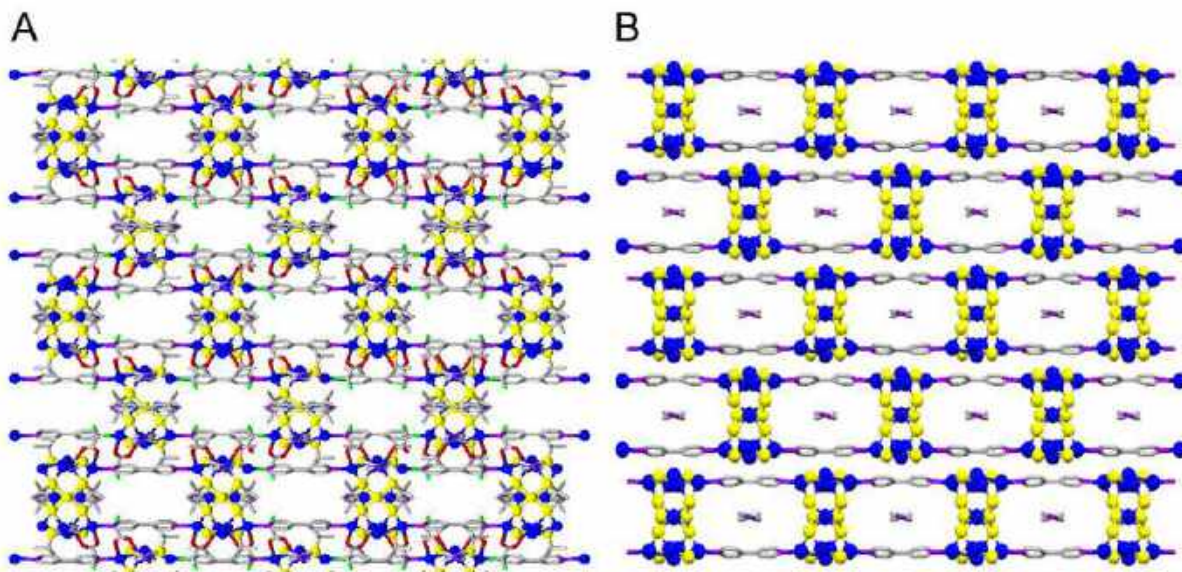


**Figure S15.** (A) The AB...AB packing of Ag<sub>12</sub> cluster nodes of (2). (B) The stacking of 3D layers in (2) and the position of bpy units in the lattice (other atoms of coordinated ligands have been omitted for clarity).

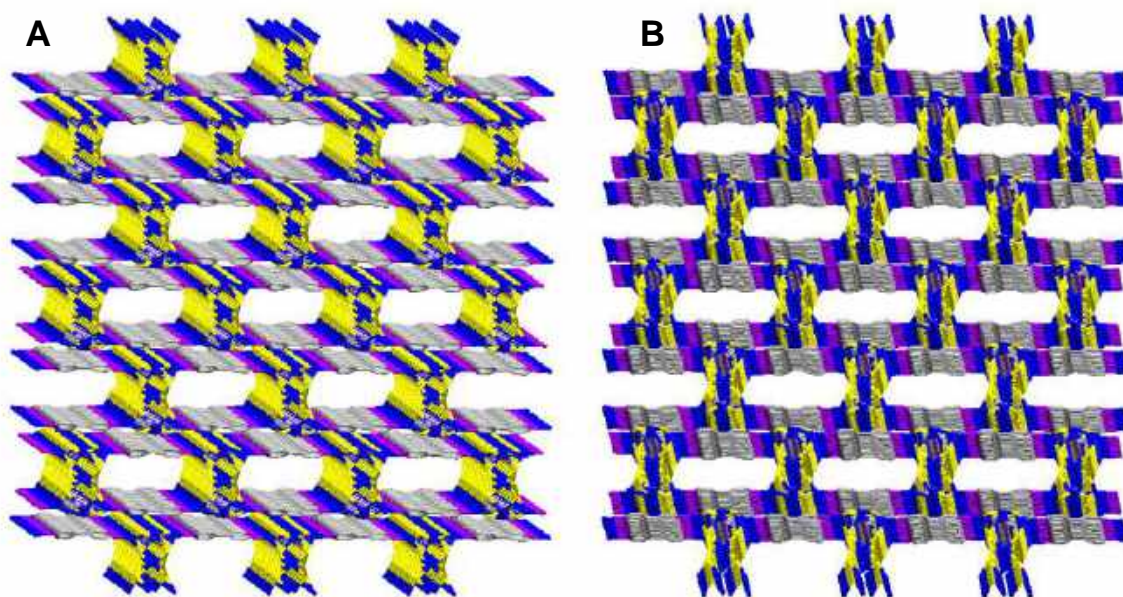


**Figure S16.** (A) and (B) represent the honeycomb structures of AgNC-MOF (2) in different orientations (other ligands have been omitted for clarity).



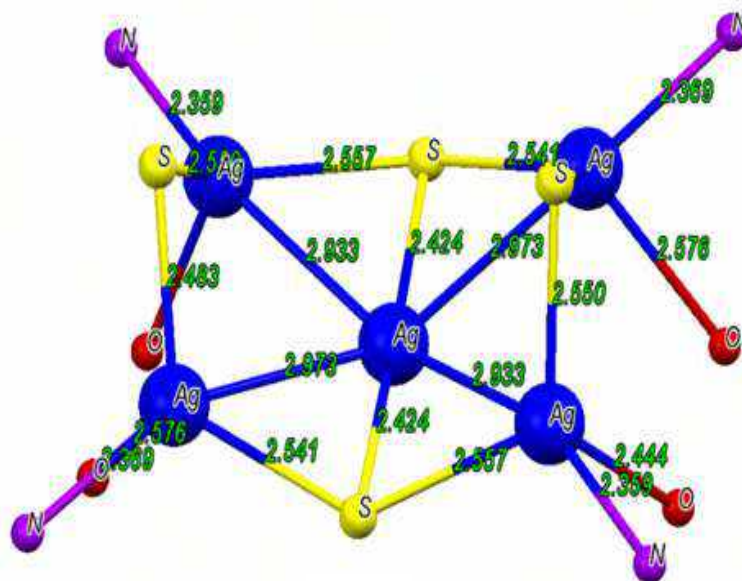


**Figure S17.** Bond distances between Ag-S, Ag-O, and Ag-N of the cross-section of (2).

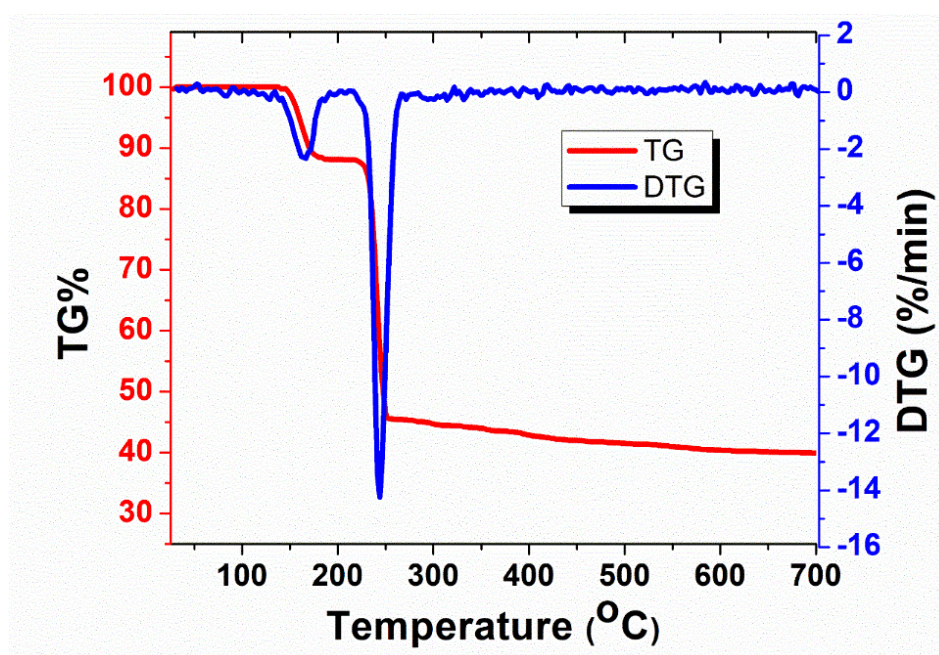


**Figure S18.** TG and DTG plots of AgNC-MOF (2) crystals.

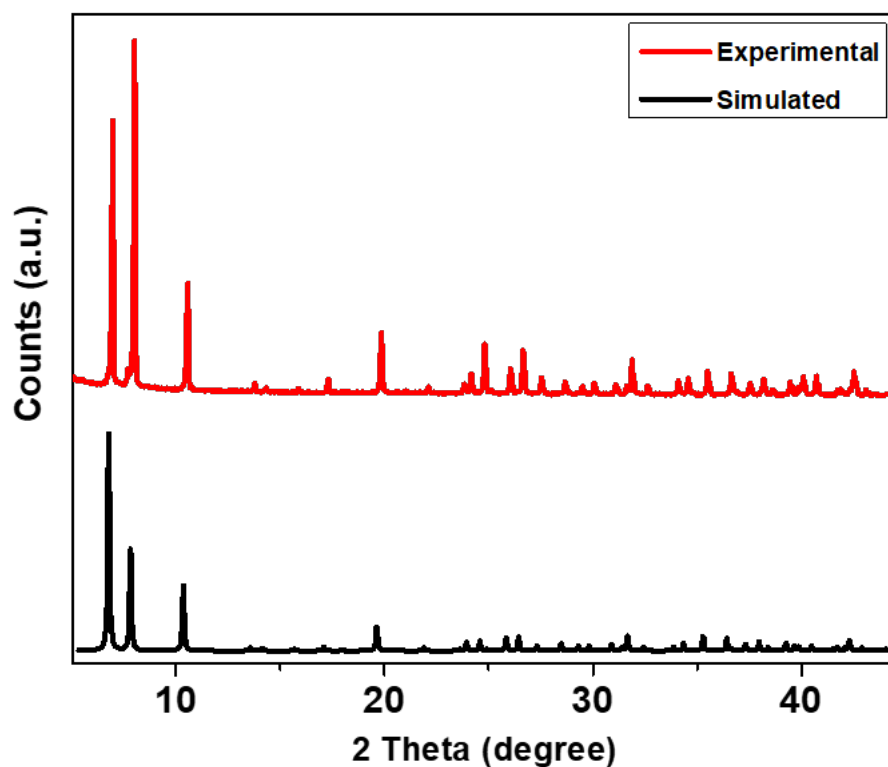


**Figure S19.** PXRD pattern of AgNC-MOF (1): experimental (redline) and simulated obtained from single-crystal data (black line).

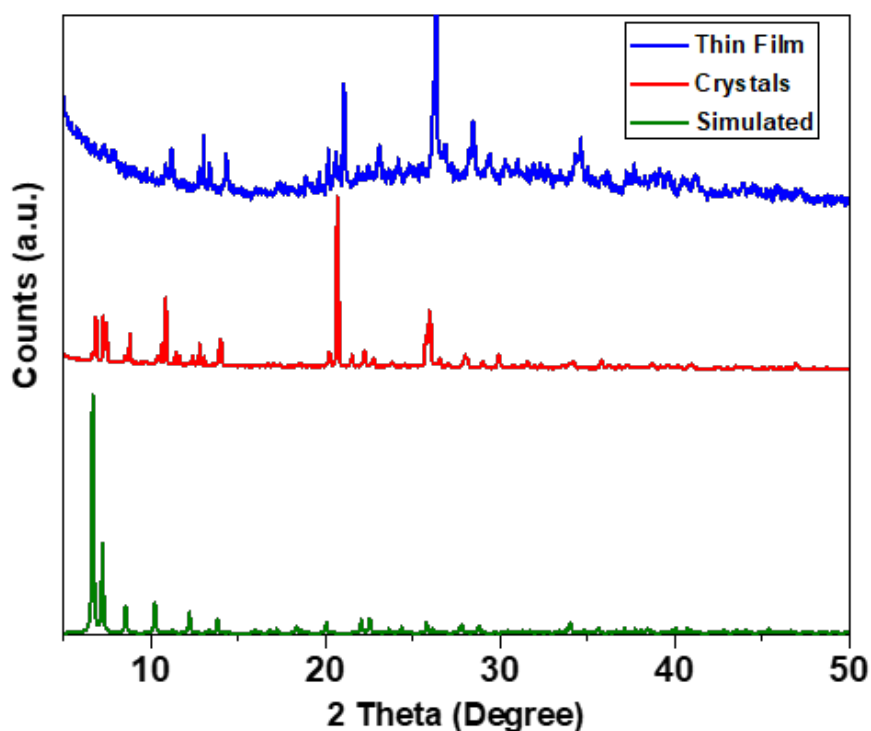


**Figure S20.** PXRD patterns of AgNC-MOF (2): thin-film (blue line), crystalline powder (red line), and the simulated obtained from single-crystal data (green line).

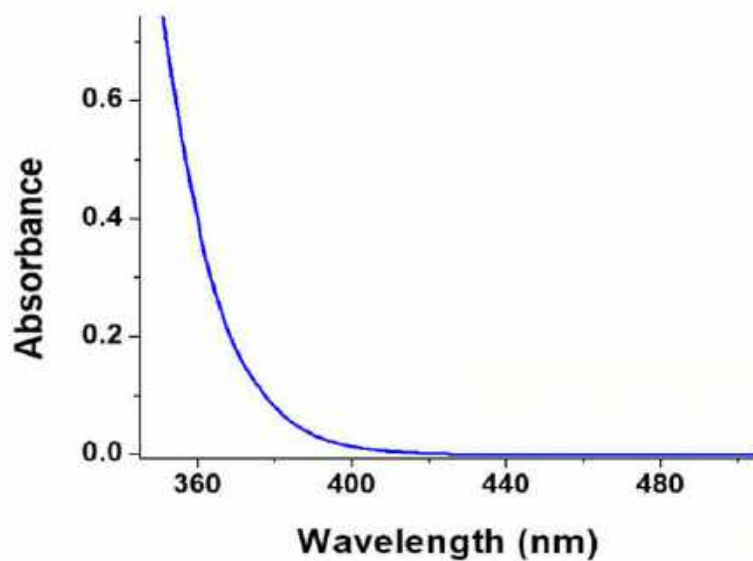


**Figure S21.** UV-Vis absorption spectrum of Ag<sub>12</sub> nanocluster solution.

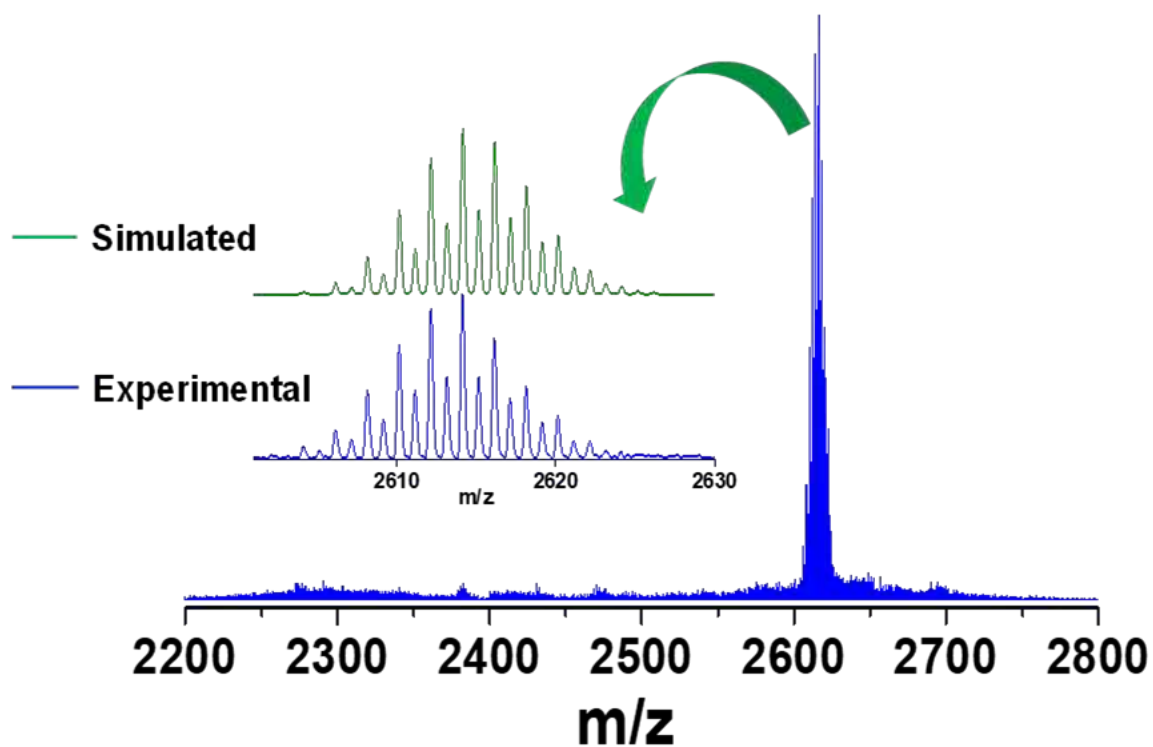


**Figure S22.** ESI-MS in positive ion mode. The main intense peak at  $m/z = 2616$  corresponds to  $[\text{Ag}_{12}(\text{TBT})_7(\text{CF}_3\text{COO})_4(\text{CH}_3\text{CN})_6]^+$  denoted as Ag<sub>12</sub> NC. Inset shows the comparison between experimental and simulated isotopic distribution patterns.

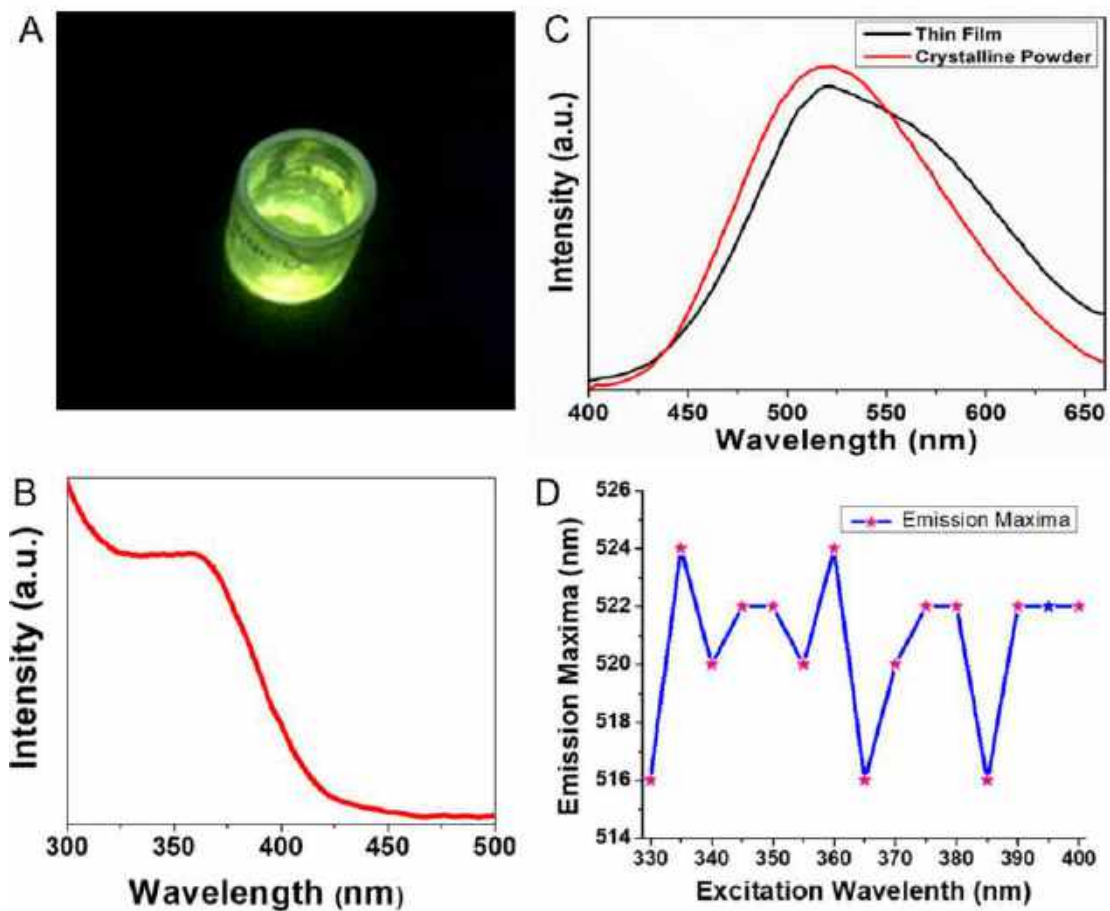


**Figure S23.** (A) Photograph showing bright green luminescence from the crystals of AgNC-MOF (2) under UV light. (B) Normalized excitation spectrum ( $\lambda_{em} = 520$  nm) of (2). (C) PL of crystalline powder and a thin film of (2) upon 370 nm excitation. (D) Emission maxima obtained at different excitations.

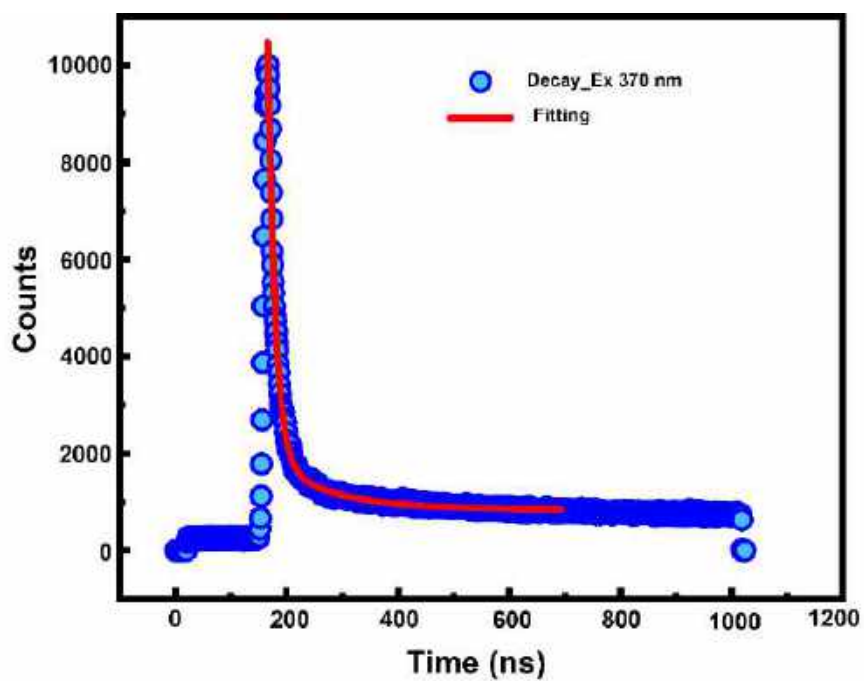


**Figure S24.** Luminescence decay curve of (2) in the air (blue color, at 520 nm) upon excitation at 370 nm, and the red line is the fitting curve.



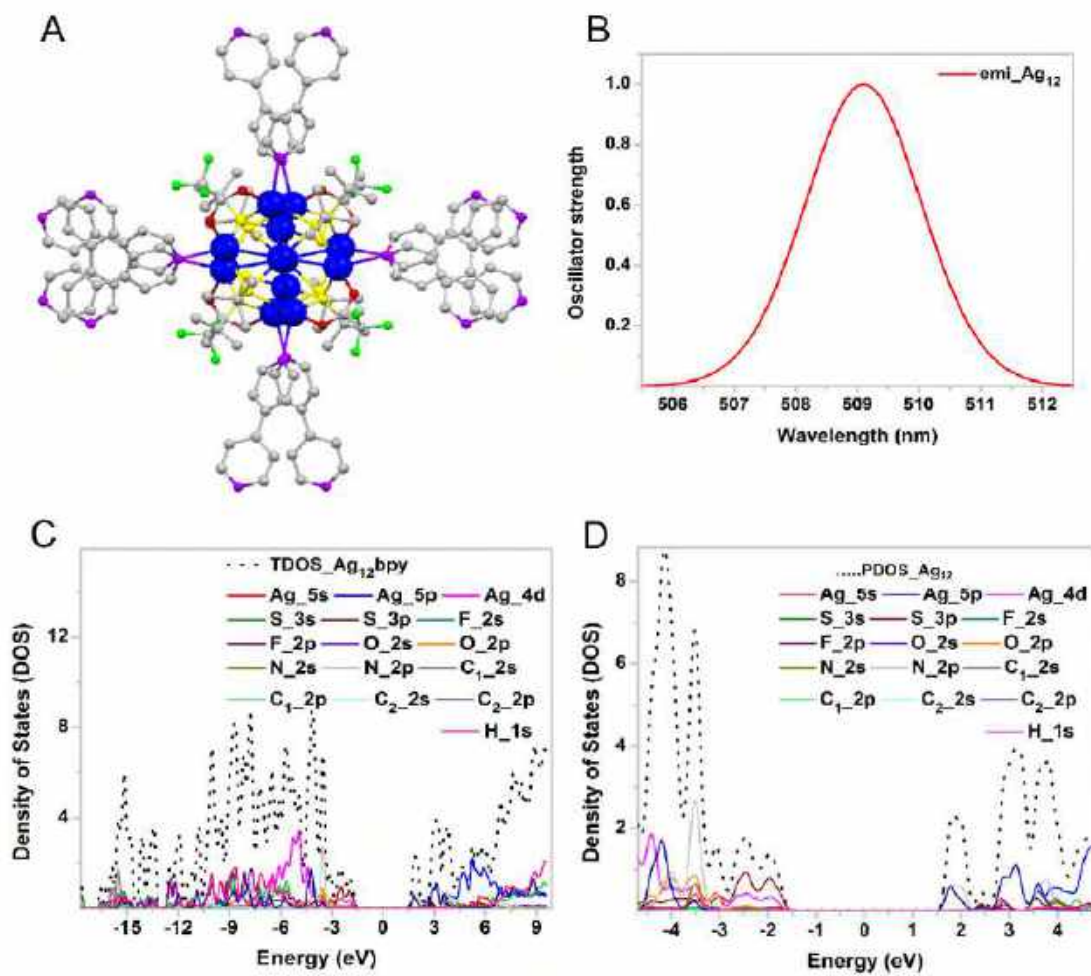


**Figure S25.** DFT calculations of Ag<sub>12</sub>-bpy: (A) optimized geometry, (B) calculated emission spectrum, (C) total density of states (TDOS), and (D) partial density of states (PDOS).

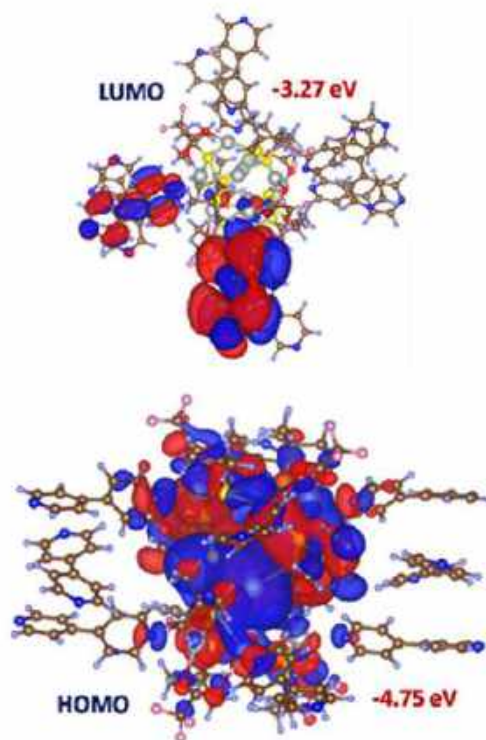


**Figure S26.** Frontier MO representations (HOMO and LUMO) of Ag<sub>12</sub>-bpy.

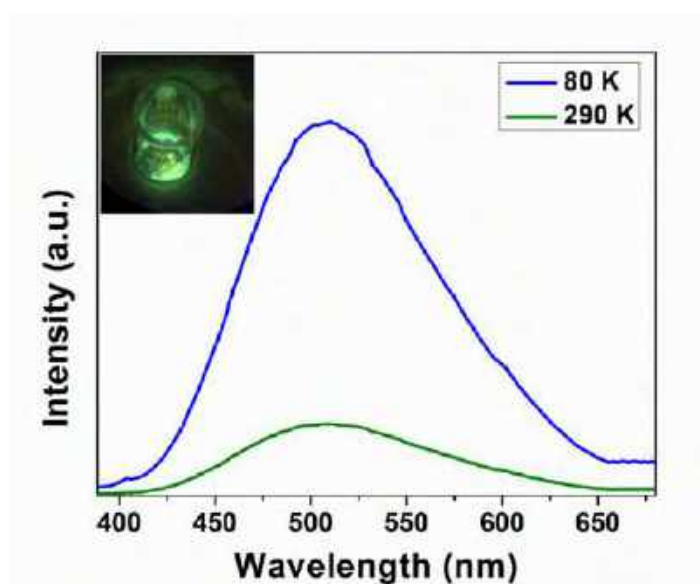


**Figure S27.** Temperature-dependent luminescence spectra of **(1)** excited at 365 nm in solid-state. *Inset:* Photograph showing the luminescence of as-synthesized crystals of AgNC-MOF **(1)** in a small beaker under UV light at low temperature.

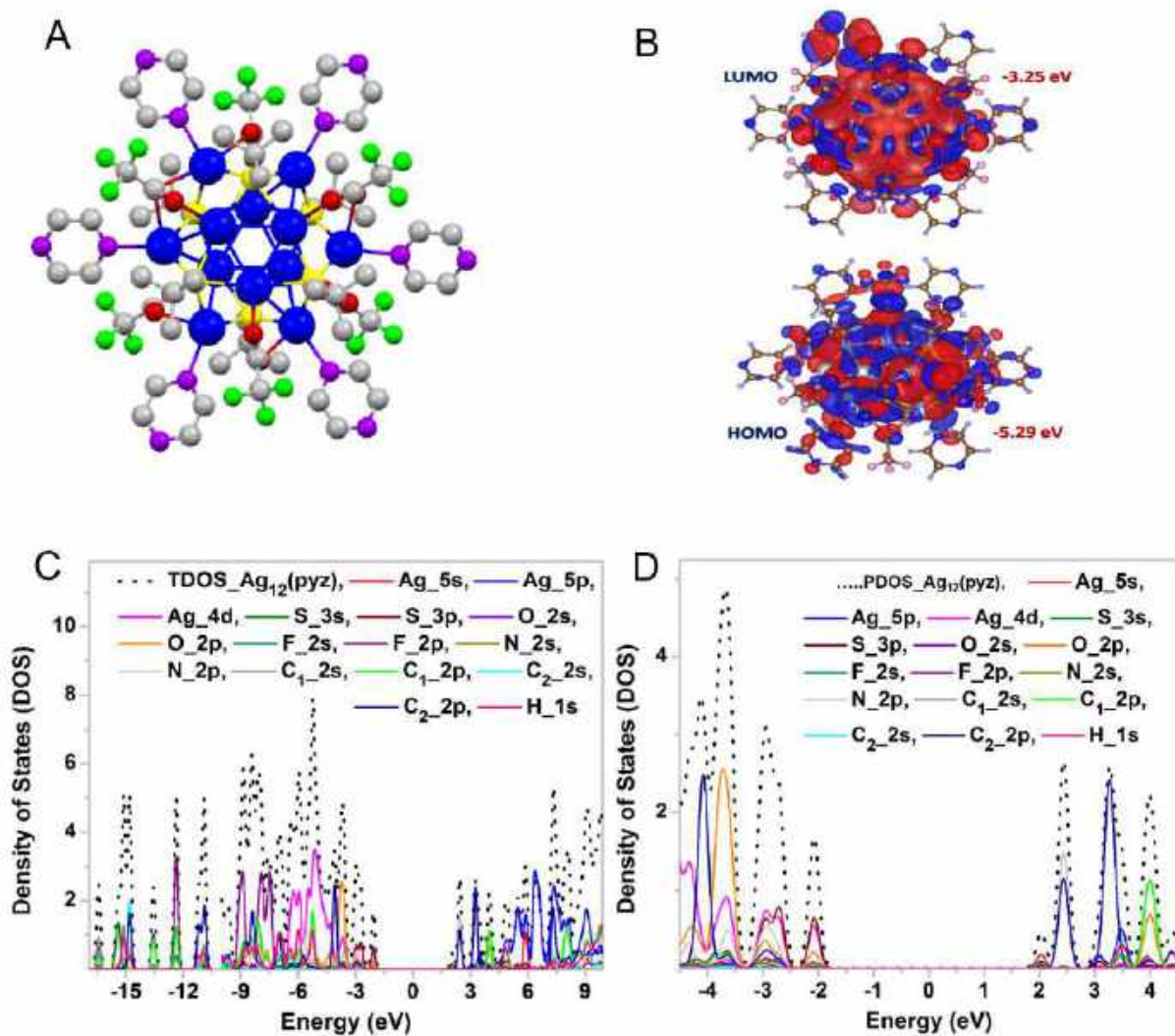


**Figure S28.** DFT calculations of Ag<sub>12</sub>-pyz: (A) optimized geometry, (B) frontier MO representations (HOMO and LUMO), (C) total density of states (DOS), and (D) partial density of states (PDOS).

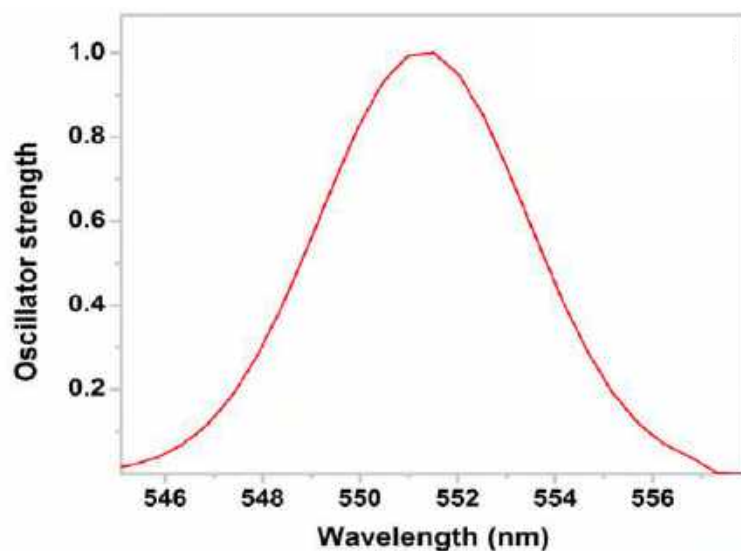


**Figure S29.** Calculated emission spectrum of Ag<sub>12</sub>-pyz.

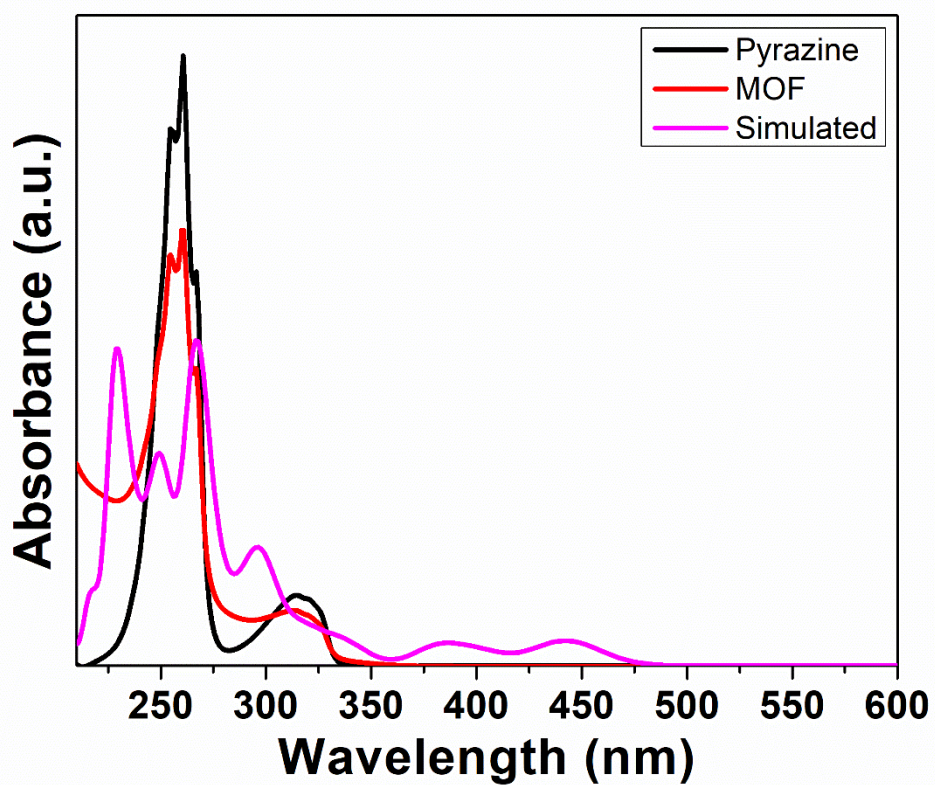


**Figure S30.** UV-Vis absorption spectra of pyrazine solution (black), AgNC-MOF (1) solution, (red) and calculated or simulated spectra of Ag<sub>12</sub>-pyz (pink).



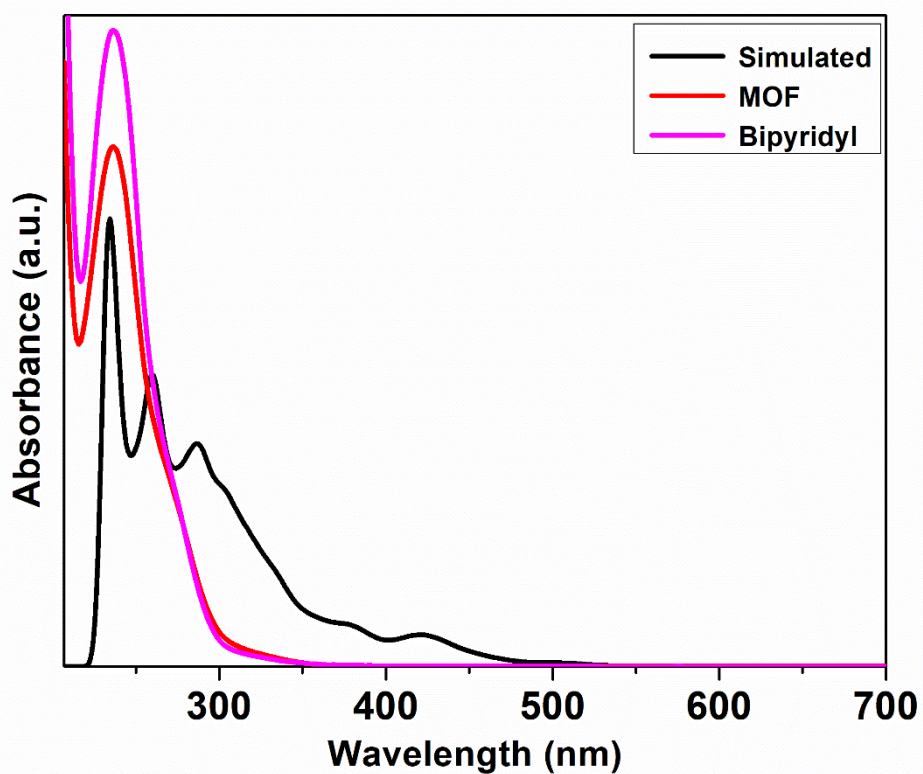


**Figure S31.** UV-Vis absorption spectra of AgNC-MOF (**2**) solution (red), 4, 4'-bipyridyl (bpy) solution (pink), and simulated or calculated spectra of Ag<sub>12</sub>-bpy (black).

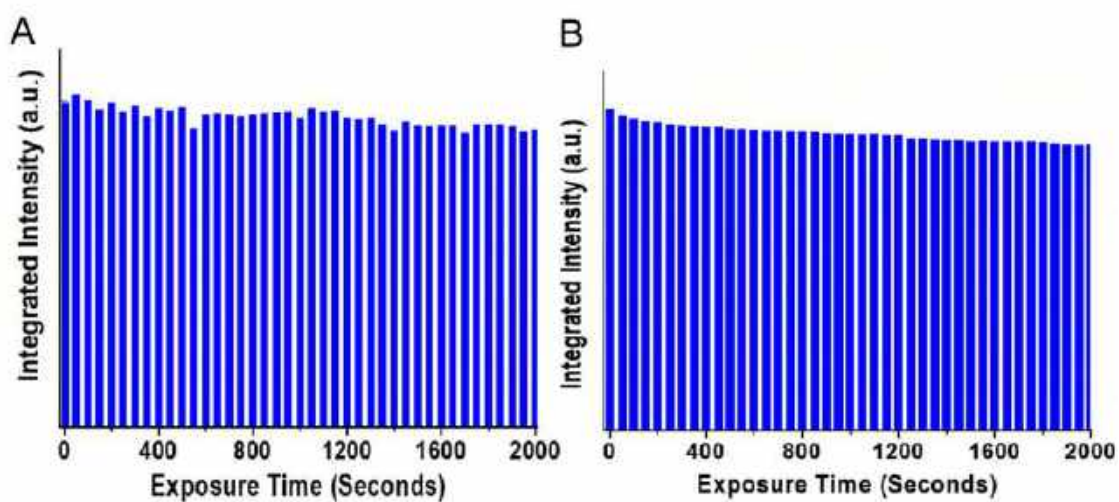


**Figure S32.** (A) Photostability of AgNC-MOF (**2**) under (A) UV and (B) visible light exposure for 2000 seconds.



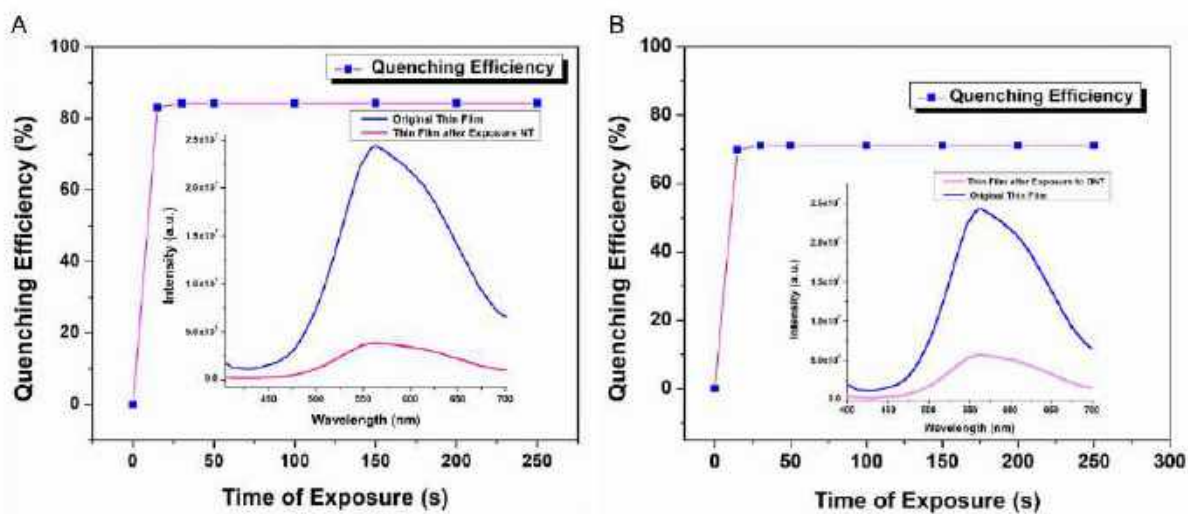


**Figure S33.** Quenching efficiencies of thin films of (2) upon exposure to (A) NT and (B) DNT.

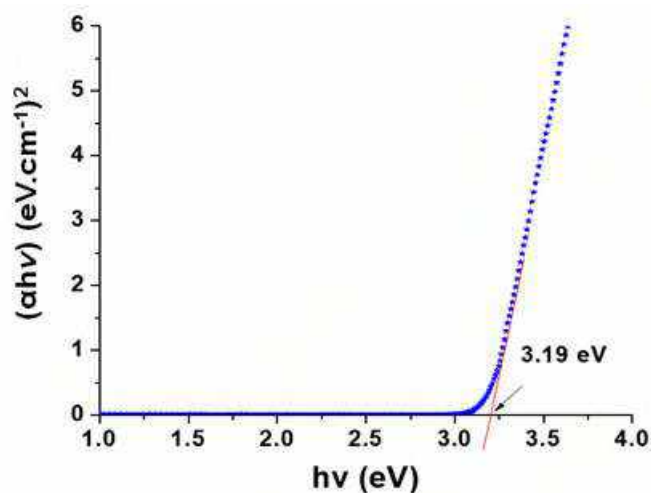


**Figure S34.** Calculation of the band gap by Kubelka–Munk function using UV-Vis spectrum of AgNC-MOF (2) solution.

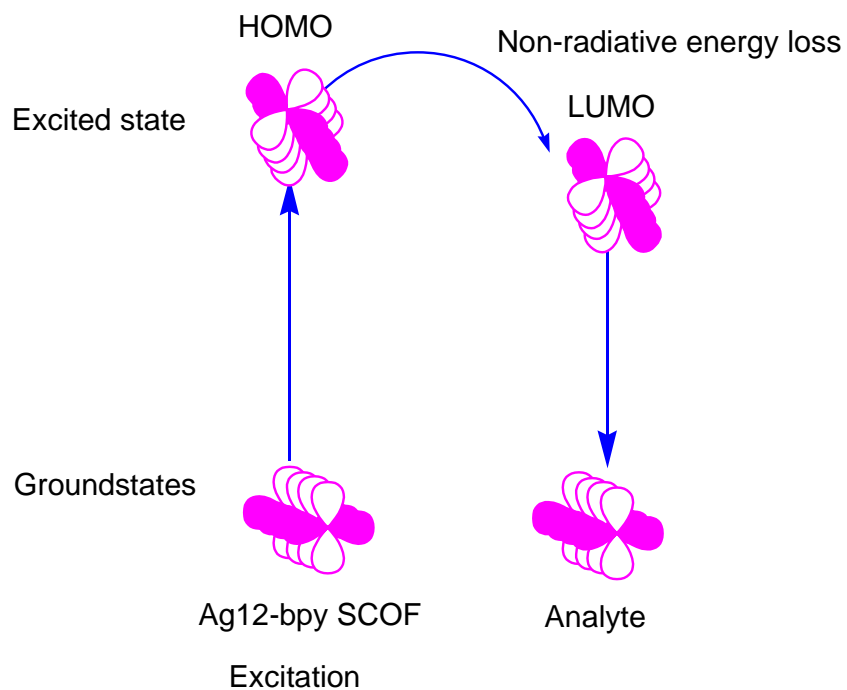


**Figure S35.** Schematic representation of the molecular orbitals responsible for energy transfer.

### References

- [1] N. Li, S. Jayaraman, S. Y. Tee, P. S. Kumar, C. J. J. Lee, S. L. Liew, D. Chi, T. S. A. Hor, S. Ramakrishna, and H. K. Luo, Effect of La-Doping on optical bandgap and photoelectrochemical performance of hematite nanostructures, *J. Mater. Chem. A*. **2014**, *2*, 19290-19297.
- [2] S. Li, J. Cai, Y. Mei, Y. Ren, and G. Qin, Thermal Oxidation Preparation of Doped Hematite Thin Films for Photoelectrochemical Water Splitting, *Int. J. Photoenergy*. **2014**, *14*, 794370.



# Carboranethiol-Protected Propeller-Shaped Photoresponsive Silver Nanomolecule

Arijit Jana, Parvathy M. Unnikrishnan, Ajay K. Poonia, Jayoti Roy, Madhuri Jash, Ganesan Paramasivam, Jan Machacek, Kumaran Nair Valsala Devi Adarsh,\* Tomas Base,\* and Thalappil Pradeep\*



Cite This: *Inorg. Chem.* 2022, 61, 8593–8603



Read Online

ACCESS |



Metrics & More

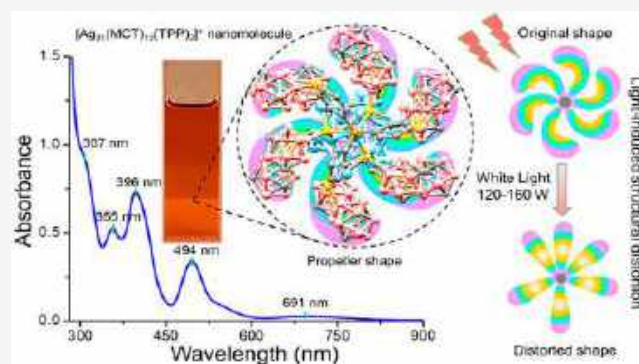


Article Recommendations



Supporting Information

**ABSTRACT:** We report the synthesis, structural characterization, and photophysical properties of a propeller-shaped  $\text{Ag}_{21}$  nanomolecule with six rotary arms, protected with *m*-carborane-9-thiol (MCT) and triphenylphosphine (TPP) ligands. Structural analysis reveals that the nanomolecule has an  $\text{Ag}_{13}$  central icosahedral core with six directly connected silver atoms and two more silver atoms connected through three Ag–S–Ag bridging motifs. While 12 MCT ligands protect the core through metal–thiolate bonds in a 3–6–3-layered fashion, two TPP ligands solely protect the two bridging silver atoms. Interestingly, the rotational orientation of a silver sulfide staple motif is opposite to the orientation of carborane ligands, resembling the existence of a bidirectional rotational orientation in the nanomolecule. Careful analysis reveals that the orientation of carborane ligands on the cluster's surface resembles an assembly of double rotors. The zero circular dichroism signal indicates its achiral nature in solution. There are multiple absorption peaks in its UV–vis absorption spectrum, characteristic of a quantized electronic structure. The spectrum appears as a fingerprint for the cluster. High-resolution electrospray ionization mass spectrometry proves the structure and composition of the nanocluster in solution, and systematic fragmentation of the molecular ion starts with the loss of surface-bound ligands with increasing collision energy. Its multiple optical absorption features are in good agreement with the theoretically calculated spectrum. The cluster shows a narrow near-IR emission at 814 nm. The  $\text{Ag}_{21}$  nanomolecule is thermally stable at ambient conditions up to 100 °C. However, white-light illumination (lamp power = 120–160 W) shows photosensitivity, and this induces structural distortion, as confirmed by changes in the Raman and electronic absorption spectra. Femtosecond and nanosecond transient absorption studies reveal an exceptionally stable excited state having a lifetime of  $3.26 \pm 0.02 \mu\text{s}$  for the carriers, spread over a broad wavelength region of 520–650 nm. The formation of core-centered long-lived carriers in the excited state is responsible for the observed light-activated structural distortion.



## INTRODUCTION

Atomically defined silver nanomolecules or nanoclusters with their core dimension below 3 nm, falling within the gap between atoms and nanoparticles, are a new class of nanomaterials with functional properties.<sup>1,2</sup> Ligands on the surface of these nanoclusters have a profound role in controlling their nuclearity, shape, size, and stability. Organic ligands such as thiols,<sup>3</sup> pyreneimethiols,<sup>4</sup> phosphines,<sup>5</sup> calixarenes,<sup>6</sup> alkynes,<sup>7</sup> carboxylic acids,<sup>8</sup> deoxyribonucleic acids (DNAs),<sup>9</sup> and organometallic ligands such as polyoxometalates<sup>10,11</sup> have been used for the synthesis of silver nanoclusters. The size confinement, closely packed electronic energy levels, and associated electronic nature lead to numerous applications in the fields of electroluminescence,<sup>12</sup> sensors,<sup>13</sup> catalysis,<sup>14</sup> bioimaging,<sup>15</sup> etc. Understanding the properties of nanoclusters depends on the determination of their atomic structures through single-crystal X-ray diffraction (SC-XRD) analysis. A handful of silver nanoclusters, including

$\text{Ag}_6$ ,<sup>16</sup>  $\text{Ag}_{14}$ ,<sup>17</sup>  $\text{Ag}_{22}$ ,<sup>18</sup>  $\text{Ag}_{25}$ ,<sup>19</sup>  $\text{Ag}_{29}$ ,<sup>20</sup>  $\text{Ag}_{44}$ ,<sup>21</sup>  $\text{Ag}_{146}$ ,<sup>22</sup> and several others,<sup>23,24</sup> with various ligands and charge states have been characterized structurally. Obviously, for a better understanding of these nanomolecules, both structurally and electronically, and to explore their potential toward applications, it is necessary to synthesize new silver nanoclusters and study their atom-specific functional properties.

Properties of the nanoclusters, such as optical absorption, photoluminescence (PL), chirality, and circularly polarized luminescence, depend on the atomic arrangements of the core and the chemical environments of the surface ligands.<sup>25–28</sup>

Received: January 22, 2022

Published: May 27, 2022



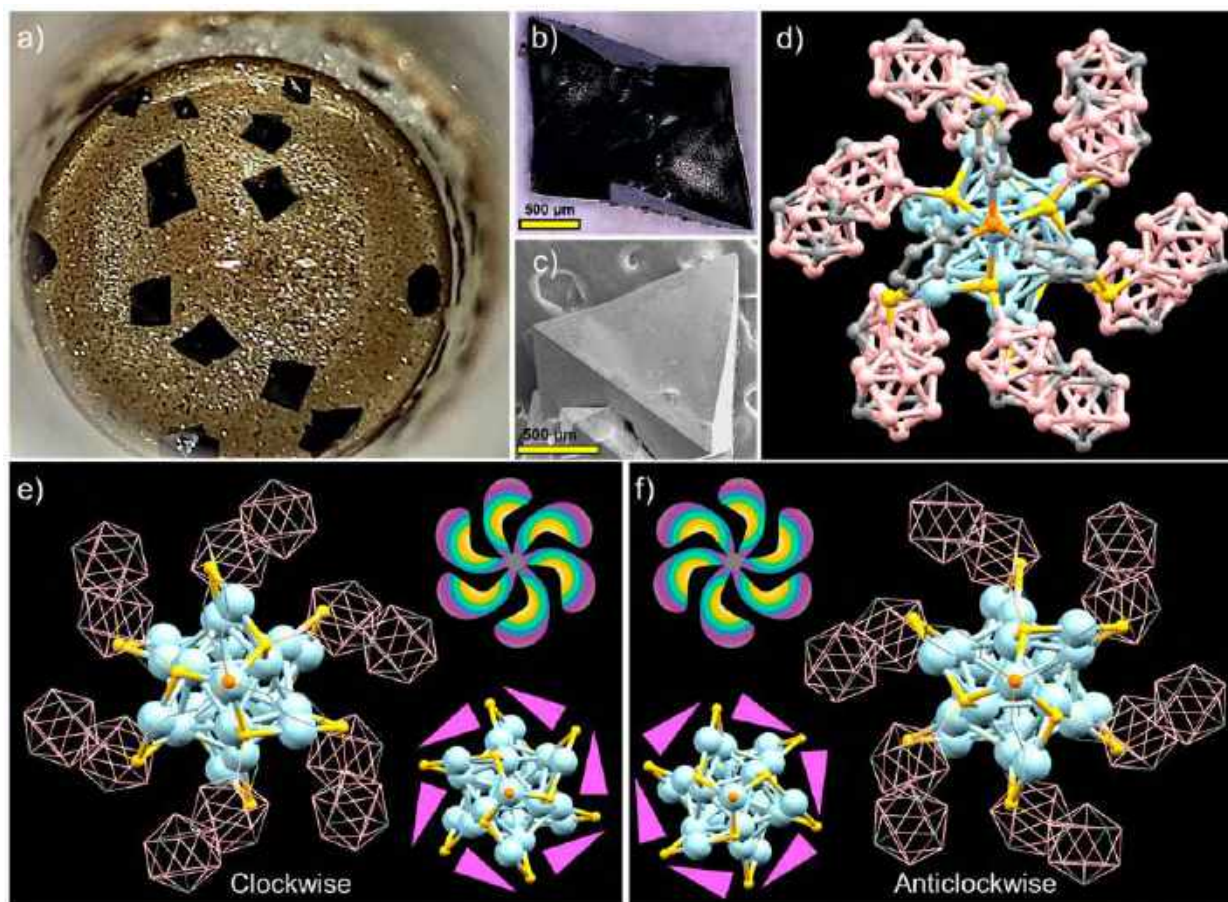


**Figure 1.** (a) Photograph of the bottom of the crystallization vial showing the growth of black pyramidal  $\text{Ag}_{21}$  crystals. (b) Optical microscopy and (c) FESEM images of a millimeter-sized single crystal. (d) Total structure of  $[\text{Ag}_{21}(\text{MCT})_{12}(\text{TPP})_2]$  showing a propeller shape having six rotary arms along one direction. (e) View of the propeller having a clockwise rotational orientation from the other side. (f) View of the same propeller with an anticlockwise rotational orientation from the other side. The top insets show schematic representations of the respective propellers, and the bottom insets show antiorientations of the respective silver sulfide core structures. Atomic color code: light blue, silver; yellow, sulfur; orange, phosphorus; pink, boron; gray, carbon. Hydrogen atoms have been removed for clarity.

Atomic arrangements in the metallic cores often determine the electronic structure. Previous studies show different types of inner-core architectures derived from pyramid,<sup>29</sup> cuboctahedron,<sup>30</sup> icosahedron,<sup>31</sup> and decahedron<sup>32</sup> with variable optical absorption features. Nanoclusters of lower atomicity (<200) are molecular in nature and exhibit multiple peaks in their respective absorption spectra, whereas an atomicity greater than 200 gives particles with plasmonic absorption features.<sup>33–35</sup> Not only the atomic structure but also the nearest chemical environments, such as the outer shell of the ligands,<sup>36</sup> temperature,<sup>37</sup> pressure,<sup>38</sup> solvents,<sup>39</sup> and coordinating ions,<sup>40</sup> have a profound effect on their absorption as well as emission properties.

The reactivity is a major concern for many silver nanoclusters. Recently, we showed light-activated conversion of the  $\text{Ag}_{42}$  nanocluster.<sup>41</sup> Another report showed that a bare  $\text{Ag}_{17}^+$  nanocluster reacts with carbon monoxide<sup>42</sup> and acetylene gases and forms different adduct species.<sup>43</sup> Ligand-exchange-induced structural conversion was also noticed for a few silver nanoclusters.<sup>44</sup> Atomic exchange between two nanoclusters in solution leads to a mixture of alloy nanoclusters through the formation of transient dimer species, following a concerted reaction pathway.<sup>45,46</sup> The use of a suitable surface ligand determines the stability of the nanoclusters. Among

different thiols, carboranethiols are gaining prominence because of their extraordinary thermal stability, robust 3D structure, and specific borane aromaticity with electron delocalization all over the icosahedral boron–carbon framework.<sup>47</sup> Recently, Zang et al. have synthesized carboranethiol-protected silver nanoclusters and nanocluster-assembled frameworks such as  $\text{Ag}_{14}$ ,<sup>48</sup>  $\text{Ag}_{17}$ ,<sup>49</sup> and  $\text{Ag}_{30}$ .<sup>50</sup> Among such clusters, *o*-carboranealkynyl-protected  $\text{Ag}_{14}$  and  $\text{Cu}_6\text{Ag}_8$  nanoclusters behave as efficient hypergolic materials, which ignite spontaneously upon their exposure to an oxidizer.<sup>51</sup>

## RESULTS AND DISCUSSION

In this work, we present the synthesis of a *m*-carborane-9-thiol (MCT)- and triphenylphosphine (TPP)-coprotected silver nanocluster of the formula  $[\text{Ag}_{21}(\text{MCT})_{12}(\text{TPP})_2]^+$  (abbreviated as  $\text{Ag}_{21}$ ) using ligand-exchange-induced structure transformation (LEIST) of  $[\text{Ag}_{18}(\text{TPP})_{10}\text{H}_{16}]^{2+}$  (abbreviated as  $\text{Ag}_{18}$ ). Details of the synthesis and characterization of  $\text{Ag}_{18}$  through UV–vis absorption and mass spectrometry studies are presented in Figure S1. During the synthesis of  $\text{Ag}_{21}$  through the LEIST reaction, 10 mg of purified  $\text{Ag}_{18}$  dissolved in methanol was reacted with 8 mg of the MCT ligand. After 2 h of exchange reaction, the initially green  $\text{Ag}_{18}$  solution gradually turned red, characteristic of  $\text{Ag}_{21}$ , through yellowish and



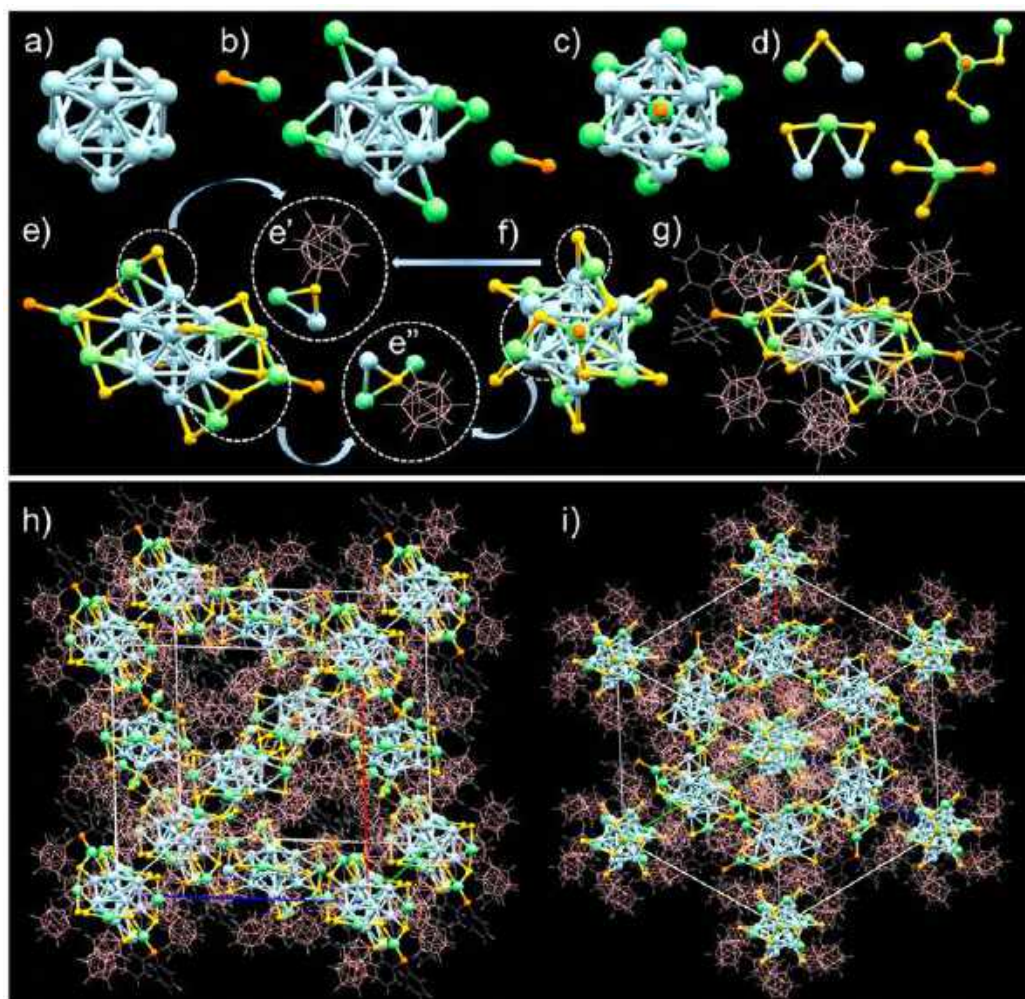


**Figure 2.** Structural anatomy of the  $\text{Ag}_{21}$  nanocluster: (a) central icosahedral  $\text{Ag}_{13}$  core; (b and c)  $\text{Ag}_{13}\text{-Ag}_6\text{-Ag}_2\text{P}_2$ -layered structure viewed from two different orientations; (d) different types of Ag-S motifs present in the cluster; (e and f) a silver sulfide skeleton structure without MCT and Ph ligands; (e' and e'') different types of carborane binding; (g) complete structure of  $[\text{Ag}_{21}(\text{MCT})_{12}(\text{TPP})_2]^+$  having MCT and TPP ligands; (h) face-centered-cubic unit cell molecular packing of the nanocluster viewed along the axial directions; (i) MOF-like packing viewed from a corner of the cube. Color code: light blue, inner core Ag; green, outer core Ag; yellow, sulfur; orange, phosphorus; pink, boron; gray, carbon; white, hydrogen.

brownish intermediate nanoclusters. Figure S2 shows the photographs of this color change. Time-dependent UV-vis absorption spectra (shown in Figure S3) measured during the reaction showed that the formation of  $\text{Ag}_{21}$  started after 30 min of an exchange reaction. Overnight size focusing in methanol led to the formation of monodispersed nanoclusters having sharp absorption features. Each aspect of compositional, structural, and charge-state characterization of  $[\text{Ag}_{21}(\text{MCT})_{12}(\text{TPP})_2]^+$  is presented consequently.

For diffraction analysis, suitable single crystals were obtained after 7 days of slow diffusion of hexane vapors into a concentrated nanocluster solution in dichloromethane (DCM; 30 mg/mL) at  $\sim 4^\circ\text{C}$ . Although the nanocluster is dark red in its DCM solution, millimeter-sized pyramidal black crystals formed upon crystallization. A photographic image of the as-grown crystals is shown in Figure 1a. The optical microscopy images shown in Figures 1b and S4 depict the pyramidal surfaces of the crystals, which were further verified by field-emission scanning electron microscopy (FESEM) images, as shown in Figures 1c and S5a,b. The energy-dispersive spectroscopy (EDS) spectrum and respective elemental

mapping (Figures S5c and S6) fit the nominal stoichiometry of the cluster, confirming the presence of boron, carbon, sulfur, phosphorus, and silver in the crystals. The as-grown crystals show well-defined diffraction spots (Figure S7) under the X-ray beam, which is indicative of good crystallinity. The powder X-ray diffraction (PXRD) patterns of the microcrystalline samples are in good agreement with the diffractogram generated from the SC-XRD data (Figure S8a). SC-XRD reveals that the nanocluster crystallizes in a cubic crystal system with the  $Pa\bar{3}$  space group and a cell volume of  $19130 \text{ \AA}^3$ .

Further details of the structural parameters are summarized in Tables S1 and S2. The complete molecular structure of the nanomolecule including its ligand shell, as shown in Figure 1d, resembles a propeller with six rotary arms, where the TPP centers represent the nodes. Although the nanomolecule does not have a 6-fold symmetry axis, the spatial orientation of the carborane ligands resembles a propeller in 2D projection. Careful analysis reveals that  $\text{Ag}_{21}$  looks like a left-handed propeller when viewed from a TPP at the head, while it is right-handed when viewed from the opposite direction (Figure



1e,f). The orientation of the silver sulfide structure is also opposite to that of the orientation of carboranes, similar to the bidirectional orientation in the nanomolecule. The inherent chirality of the cluster, as observed in its single crystal, was investigated using circular dichroism (CD) measurements. However, the CD spectrum shown in Figure S9 shows no chiral response in the wavelength range of 240–800 nm, suggesting an achiral nature of the cluster in the DCM solution. The symmetric character of the nanomolecule in solution is perhaps due to the dynamic nature of carborane ligands on the cluster surface. Another reason behind the lack of a CD signal is the intense absorption features of the nanomolecule in comparison to the local orientations of the pendant groups. Further analysis reveals the presence of a  $C_3$  rotational symmetry axis along the TPP node of the nanomolecule, and the orientation of carborane ligands on its surface looks like an assembly of double rotors (as shown in Figure S10).

Another independent view of the nanomolecule gives an oval-like shape with two TPP units at the head and tail positions of the cluster (Figure S11). The ORTEP image in Figure S12 shows the cluster's oval-like shape with specific packing of the ligands. The distance between the two phosphorus atoms at antipodal positions of the cluster is 17.139 Å. A total of 12 carborane ligands enclose the surface of the cluster through silver–thiolate bonds. The arrangement of the carboranes is in a 3:6:3 fashion on the outer surface of the cluster along the P–P axis (as shown in Figure S13). The three MCT ligands near the head are in a staggered conformation with three other MCT ligands near the tail (as shown in Figure S14). The staggered orientation of these carboranes determines the opposite orientation of the propeller.

The structural anatomy of  $Ag_{21}$  reveals a central icosahedral  $Ag_{13}$  core and a shell of eight silver atoms (Figure 2a–c). The average Ag–Ag bond distance in the  $Ag_{13}$  core is 2.795 Å, suggesting strong metallic bonding. Six out of the remaining eight silver atoms are directly connected to the  $Ag_{13}$  core through Ag–Ag bonds with a distance range of 2.924–3.076 Å, showing weaker Ag–Ag bonding compared to that in the core. The remaining two silver atoms are 4.305 Å away from the nearest  $Ag_3$  triangular facets and 6.168 Å from the central silver atom. These two silver atoms are connected with the cluster through three Ag–S–Ag bonds in a tripod fashion with an average Ag–S bond distance of 2.637 Å. Detailed analysis reveals that the 12 carboranes bind with the outer surface through different types of silver sulfide motifs (Figure 2d–f). Among them, six carboranes present on the body of the cluster are connected by six  $Ag_2S$  motifs, where each sulfur is bridged between one silver atom from the  $Ag_{13}$  core with an Ag–S bond distance of 2.527 Å and one silver from the outer shell with an Ag–S distance of 2.378 Å (Figure 2e'). The remaining six carboranes near the TPPs are connected by  $Ag_3S$  motifs, where one silver is isolated and the other two are from the  $Ag_{13}@Ag_6$  unit (Figure 2e''). A comparison between  $[Ag_{25}(SR)_{18}]^-$  and  $[Ag_{21}(MCT)_{12}(TPP)_2]^+$  (as shown in Figures S15 and S16) shows that both of them have central  $Ag_{13}$  icosahedra.<sup>19</sup> However, the remaining 12 silver atoms of  $[Ag_{25}(SR)_{18}]^-$  capped the triangular icosahedral facets through  $\mu_3$  and  $\mu_2$  capping modes with average bond distances of 2.858–3.189 Å, whereas in our  $Ag_{21}$ , only six silver atoms capped the triangular facets through  $\mu_2$  capping mode with average bond distances of 2.924–3.076 Å. Fewer atoms capping the central  $Ag_{13}$  icosahedron in  $Ag_{21}$  in comparison to

$Ag_{25}$  and also binding of the additional two silver atoms in  $Ag_{21}$  not being directly connected to the silver core can be attributed to the greater steric requirements of the bulky carborane ligands. There are other reports of the  $Ag_{21}$  nanocluster, protected by dithiophosphate<sup>52</sup> and diselenophosphate<sup>53</sup> ligands with a central icosahedral  $Ag_{13}$  core connected with eight  $\mu_3$ -capped silver atoms. Yet another perspective is that the bulkiness of the ligand has a proven effect on the structure of the metal part of the cluster, which could be potentially further investigated using narrower 10-vertex carboranes, dicarba-*closo*-decaboranes.

The molecular packing of the nanomolecule in the single crystal shown in Figure 2h presents a face-centered-cubic-type arrangement with eight clusters positioned in the corners of the cube, having an intercluster distance of 26.745 Å and the remaining six clusters centered on the faces of the cube. The packing density is  $4 [(8 \times 1/8) + (6 \times 1/2)]$  in the unit cell. Extended packing showed (Figure S17) A–B–A–B-type lamellar packing with oval shapes of the clusters along each (*a*, *b*, and *c*) axis. A view of the packing (as shown in Figures 2i and S18 and S19) through the corners of the cube showed a metal–organic framework (MOF)-like structure. Careful analysis reveals that a view of the intercluster packing through the corner of the cube shows that eight clusters have propeller orientations, whereas the remaining six clusters have oval shapes (Figure S19). Views along *a*, *b*, and *c* corners lead to two clusters each having propeller orientations, whereas the remaining 12 clusters have oval shapes (Figure S18). Multiple intercluster BH–BH and BH–CH van der Waals interactions among the carboranes are the reason behind their molecular packing (as shown in Figure S20). A recent study of double-helical DNA-like intercluster packing shows engineering design aspects of the metallic nanocluster.<sup>54</sup> In this direction, the propeller-like structure and MOF-like packing arrangements make the  $Ag_{21}$  nanomolecule interesting.

The UV–vis absorption spectrum of  $Ag_{21}$  (as shown in Figure 3a) in its DCM solution is characteristic and has bands at 691, 494, 396, 355, and 307 nm, which are typical for a confined electronic structure. Time-dependent absorption spectra showed the stability of the crystals up to 60 days (Figure S21) under ambient conditions. 3D carboranes present on the surface of the cluster may be the reason behind their

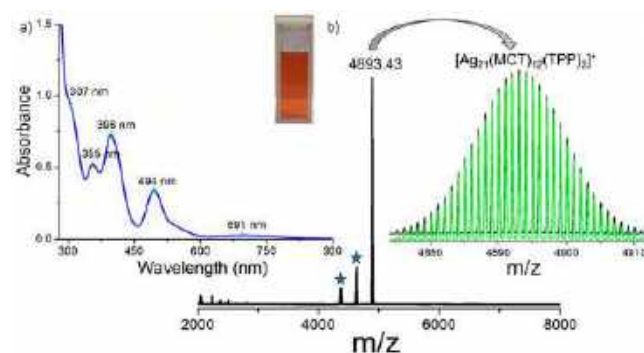


**Figure 3.** (a) UV–vis absorption spectrum of  $Ag_{21}$  in DCM (inset: photographic image of the cluster in DCM). (b) Full-range high-resolution ESI-MS spectrum of the cluster having a peak at  $m/z$  4893.43 in a monopositive charge state, assigned as  $[Ag_{21}(MCT)_{12}(TPP)_2]^+$  [right inset: exact matching of the experimental spectrum (black) with the theoretical spectrum (green)]. Each ★ indicates TPP loss from the parent peak.

superior stability. The absorption spectra of  $\text{Ag}_{21}$  in different solvents such as 1,2-dichlorobenzene, acetone, chloroform, DCM, methanol, ethanol, dimethylformamide (DMF), and dimethyl sulfoxide (DMSO) were measured (as shown in Figure S22). All of the spectra were identical except in DMF and DMSO. Broadening of the spectral bands, along with small shifts in their peak positions, indicate solvatochromism. The ligand-centered ground-state orbitals may be prone to interaction with these polar aprotic solvents, and this could explain the spectral broadening.

The molecular composition of  $\text{Ag}_{21}$  in solution was studied using high-resolution electrospray ionization mass spectrometry (ESI-MS). The sample preparation and instrumental conditions are specified in the Supporting Information. The full-range high-resolution ESI-MS spectrum shown in Figure 3b gave a major peak centered at  $m/z$  4893.43 in positive-ion mode. An expanded view of the peak shows a characteristic peak-to-peak separation of  $m/z$  1, which confirms the charge state as  $1+$ . The peak was assigned to  $[\text{Ag}_{21}(\text{MCT})_{12}(\text{TPP})_2]^+$ . The isotopic distribution of the experimental spectrum matches that of the theoretical spectrum. Two other fragment peaks at  $m/z$  4630.5 and 4368.35 are assigned to the sequential mass loss of 262 amu, suggesting two TPP losses from the parent nanocluster. The cluster did not show features in the negative-ion mode. However, the characteristic ion peak at  $m/z$  61.98 in negative-ion mode confirms the presence of  $\text{NO}_3^-$  as a counterion in the crystal (Figure S23).

We analyzed the free electron count of  $[\text{Ag}_{21}(\text{MCT})_{12}(\text{TPP})_2]^+$  to investigate its stability. For this nanomolecule, 21 silver atoms have one valence ( $5s^1$ ) electron each. Therefore, the total metal electron count is  $N_{\text{VA}} = 21$ . The 12 MCT ligands are electron-withdrawing, whereas the TPP ligands are neutral and so ligand electrons are involved in the binding, where  $M = 12$ . The cluster has a net charge of  $1+$ , so that  $Z = 1$ . This gives a valence electron count of  $8e$  ( $N_{\text{VA}} - M - Z = 21 - 12 - 1 = 8$ ), indicating a superatomic electronic configuration.<sup>55,56</sup> This  $8e$  superatomic cluster having a closed-shell electron distribution in  $1s^21p^6$  superatomic orbitals is the reason behind its electronic stability.

In order to gain additional insight into bonding and structure, we studied the MS/MS fragmentation of the molecular ion peak (Figure 4). Fragmentation studies were carried out by varying the collision energy (CE) by selecting the parent ion peak at  $m/z$  4893.43 with a charge state of  $1+$ . A sequential increase of CE from 2 to 20 (in instrumental units) resulted in two consecutive mass losses of 262 units, which correspond to two TPP fragments. The loss of TPP fragments at low CE is due to a weak Ag–P bond, having a bond length of 2.401 Å. At a CE of 25, the peak at  $m/z$  4368.25 displayed the loss of both TPPs. A further increase of the CE up to 70 led to no more fragmentation of the peak at  $m/z$  4368.25, revealing strong bonding of the carboranes within the cluster. At a CE of 75, new fragments are observed from  $m/z$  4368.25, careful analysis of which reveals a sequential mass loss of 283 units (Figure S24). The  $m/z$  283 mass loss fits the combined mass of one silver atom and one MCT ligand. So, this sequential loss is due to the systematic loss of Ag–MCT. A further increase of the CE up to 150 shows eight sequential losses of Ag–MCT fragments. Another series of mass fragments with the mass loss of MCT units ( $m/z$  175) was also present. The strong appearance of Ag–MCT loss peaks in comparison to MCT loss peaks indicate strong B–S bonds, which is different from the *o*-carborane-1,2-dithiol-protected  $\text{Ag}_{42}$

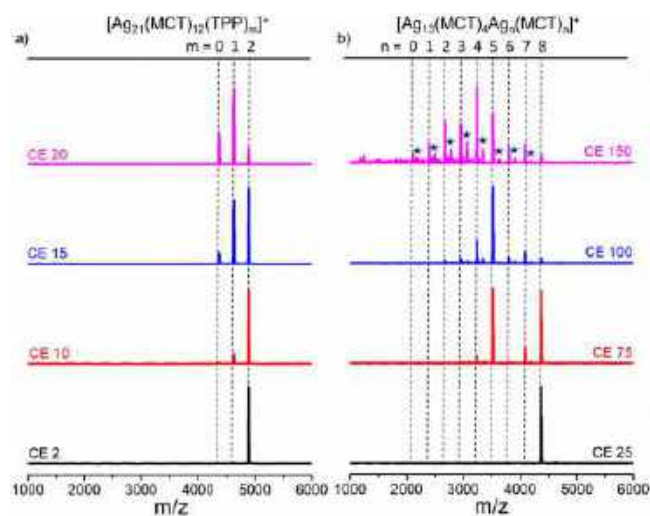


**Figure 4.** CE-dependent MS/MS pattern of the parent cluster (a) up to a CE of 20, showing only two TPP losses, and (b) a further increase in the CE up to 150, leading to eight Ag–MCT losses. Each ★ peak shows the sequential loss of MCT alone.

nanocluster.<sup>41</sup> To understand the stability of the fragmented peaks, we calculated the valence electrons of each fragmented clusters (Table S3).

The Ag–MCT loss peaks have eight valence electrons in comparison to nine valence electrons of fragments generated due to MCT losses. The closed-shell magic electronic configuration makes Ag–MCT fragments more stable than MCT loss fragments. This systematic fragmentation correlates very well with the structure of the nanocluster with eight silver atoms outside the  $\text{Ag}_{13}$  core. The CE-dependent fragmentation experiments correlate with the structural complexity and nature of bonding of the nanomolecule.

The size of  $\text{Ag}_{21}$  was characterized using transmission electron microscopy (TEM). TEM images (as shown in Figure S25) showed particles with an average diameter of  $1.91 \pm 0.2$  nm. The EDS elemental mapping confirms the elemental composition of the clusters consisting of silver, sulfur, phosphorus, carbon, and boron in the clusters. The atomic ratio of silver and sulfur is 1.47, which nearly correlates to the ratio of 21:12 (1.75). The presence of all of the elements has been further confirmed using X-ray photoelectron spectroscopy (XPS). XPS spectra (Figure S26) have signature features of the respective elements. The binding energies of 368.3 and 374.3 eV for Ag  $3d_{5/2}$  and  $3d_{3/2}$  are due to silver(0). A single peak at 189.8 eV for the B 1s region is characteristic of boron in carborane moieties, whereas three peaks at 283.6, 285.1, and 286.9 eV in the C 1s region of the spectra indicate different types of carbon atoms originating from carborane as well as TPP ligands. The peak at 131.4 eV is due to P 2p of TPP ligands. Along with other characteristic peaks, two peaks at 406.7 and 531.6 eV are due to N and O 1s, respectively, which exhibit the presence of nitrate ions in the crystals.

Multinuclear NMR spectra of a free MCT ligand and  $\text{Ag}_{21}$  were recorded to confirm the binding of the ligands. Free MCT ligands display characteristic sharp  $^{11}\text{B}$  NMR signals at  $-3.2$ ,  $-6.8$ ,  $-9.8$ ,  $-13.5$ ,  $-14.8$ ,  $-18.5$ , and  $-21.7$  ppm with an integration ratio of 1:2:1:2:2:1:1, respectively, for 10 boron atoms (Figures S27 and S28 and Table S4). Around 30 mg of purified clusters dissolved in 0.75 mL of  $\text{CDCl}_3$  was used to measure the NMR spectrum of  $\text{Ag}_{21}$ . The  $^{11}\text{B}$  NMR spectrum



in Figure S29 shows a set of seven sharp peaks at +2.22, +0.91, -5.40, -8.20, -12.05, -14.24, and -17.84 ppm due to the presence of a nonequivalent boron atom of 12 *m*-carborane ligands. The broadness of the peaks is due to the high electron density of the metallic silver core near the carborane. The proton-decoupled  $^{13}\text{C}$  NMR spectrum (Figure S30) showed the signature peaks of the carbon atom for carborane at 54.32 and 55.53 ppm. Along with the carborane peaks, a set of peaks in the region of 128.48–133.93 ppm appear because of the aromatic carbons of TPP ligands. A broad  $^{31}\text{P}$  NMR peak (as shown in Figure S31) at 8.67 ppm shows the binding of TPP. It may be noted that free TPP exhibits a sharp feature at -5.66 ppm. Furthermore, to explore the binding of the ligands, we measured the IR spectrum of the  $\text{Ag}_{21}$  crystals and compared it with that of the free MCT ligand (Figure S32). The appearance of similar vibrational peaks proves the presence of carboranes in the cluster. Along with the carborane features, we observed three new peaks at 1385, 1435, and 1480  $\text{cm}^{-1}$ , which are due to the antisymmetric N–O stretching of  $\text{NO}_3^-$  ions present in the crystal lattices.<sup>57</sup> Although we have not observed nitrate as a counterion in the single-crystal structure, the presence of a  $\text{NO}_3^-$  signature in the IR and ESI-MS spectrum, along with the characteristic N 1s of nitrate in XPS, confirming the positive charge of the cluster with nitrate as the counterion. We measured the Raman spectra of the clusters and compared the spectral features with those of the free MCT ligand (Figure S33 and Table S5). The assignments of the spectral features are similar to those in the literature.<sup>58</sup> Characteristic vibrational peaks of MCT in  $\text{Ag}_{21}$  are nearly similar to those of free MCT. The doublet peaks of C–H stretching (3051 and 3070  $\text{cm}^{-1}$ ) and B–H stretching (2618 and 2645  $\text{cm}^{-1}$ ) become singlet peaks at 3081 and 2652  $\text{cm}^{-1}$ , respectively. Similarly, red shifts of the C–H and B–H vibrational features were observed as a result of the effect of the chemical environment in  $\text{Ag}_{21}$ . Identical vibrational features of the icosahedral cage breathing mode at 760  $\text{cm}^{-1}$  indicate the indistinguishable chemical environment of the carborane cage. Raman studies show that the B–H and C–H chemical environments are more affected in comparison to the carborane cage.

Molecular absorption features of the nanomolecule were assigned on the basis of their comparison with the computationally simulated spectra using time-dependent density functional theory (TDDFT) calculations in a grid-based projector-augmented-wave method. To reduce the computational cost, we replaced  $\text{PPh}_3$  as  $\text{PH}_3$ . Linear-response TDDFT calculations were carried out to simulate the optical absorption spectra. A detailed discussion of the theoretical calculations is presented in the Supporting Information. The simulated absorption spectrum of the optimized structure in the gas phase matches well with the experimental spectrum (Figure 5a). Changes seen are also attributed to the effect of the solvents. To understand the effect of phosphines, we also optimized the structure with phosphines. The calculated absorption spectrum is almost similar to the earlier structure without phosphines (as shown in Figure S34). The values of the oscillator strength of all of these transitions are summarized in Table S6. Figures S35–S38 show the contribution of the molecular orbitals corresponding to the transition at 672, 565, 494, and 422 nm, respectively. The electronic transition at 672 nm (1.84 eV) originates as a result of the transition from HOMO-1 and HOMO-2 to LUMO and LUMO+1 (where HOMO = highest occupied molecular orbital and LUMO =

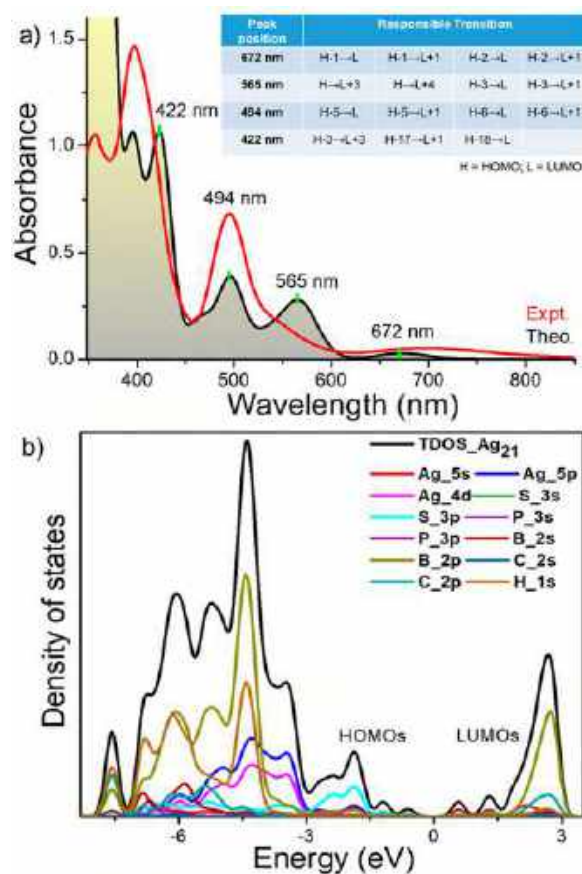


**Figure 5.** (a) Experimental absorption spectrum of the  $\text{Ag}_{21}$  nanocluster and correlation with the theoretical spectrum. The inset shows the molecular orbitals responsible for the features (H = HOMO and L = LUMO). (b) DOS analysis with respect to individual atomic orbitals.

lowest unoccupied molecular orbital). The electron density maps show that this peak is due to charge transfer within the metallic core. The next prominent peak at 494 nm (2.51 eV) is associated with the transition from HOMO-5 and HOMO-6 to LUMO and LUMO+1. Electron density maps show charge transfer from the delocalized HOMOs in the shell to the core-centered LUMOs.

Another prominent peak at 422 nm (2.94 eV) is associated with the transition from HOMO-3, HOMO-17, and HOMO-18 to LUMO+3, LUMO+1, and LUMO. This transition is associated with charge transfer from the ligand-shell-delocalized HOMO to the kernel-localized LUMO. For an additional assessment of the effect of hybridization on the formation of molecular orbitals, the density of states (DOS) was analyzed in the entire energy region (Figure S39). The middle of the plots was set to zero to indicate the Fermi level. Orbitals of negative energy are considered to be HOMOs, whereas orbitals with positive energy are considered to be LUMOs. Ag 5s and 5p orbitals and S 3p orbitals dominated the energy levels (i.e., HOMOs and LUMOs) near the Fermi level. The deeply occupied orbitals having energy of  $<-1.5$  eV are mostly dominated by the S 3p atomic orbitals, and deeply unoccupied orbitals having energy of  $>1.5$  eV are occupied by the 2p atomic orbitals of boron and carbon atoms. According to the DOS calculation, low-energy transitions are silver-core-centered, whereas higher energy transitions are mostly ligand-centered.

Furthermore, we studied the PL property of  $\text{Ag}_{21}$  in solution by dissolving a few crystals in DCM. We did not observe any emission from the solution under a 365 nm UV lamp (as shown in the inset of Figure 6). PL measurements show (Figure 6) a sharp emission centered at 814 nm in the near-IR (NIR) region. The asymmetry of the emission line shape may be contributed by the detector response in the NIR region. The sharpness of the emission spectrum exhibits their molecular nature. The sharp excitation maximum at 459 nm is near to the edge of the absorption maximum at 494 nm, which is ligand-shell-to-metal-core (LSMC) charge transfer. The apparent Stokes shift of  $2053\text{ cm}^{-1}$  was calculated from the energy gap between the absorption edge and the emission maximum (Figure S40). Such a modest Stokes shift also indicates closely spaced energy levels of the nanocluster.

We studied the thermal and light sensitivity of the cluster. The cluster shows thermal stability up to  $100\text{ }^{\circ}\text{C}$  at ambient conditions. Illumination with white light leads to structural distortion, even at room temperature ( $25\text{ }^{\circ}\text{C}$ ). Figure 7a shows a schematic representation of the structural stability upon heating and structural distortion upon light irradiation. Photographic images (Figure 7b) of reddish microcrystalline samples showed no visible color change upon heating at  $100\text{ }^{\circ}\text{C}$ . To investigate the thermal stability, we measured the UV–vis and Raman spectra after heating at different temperatures. About 8–10 mg of a microcrystalline powder was used for heating (exposure time, 4 h). Identical absorption features (Figure 7d) exhibit the structural stability of the clusters after  $100\text{ }^{\circ}\text{C}$  heating. Furthermore, Raman measurements (Figure 7e) showed identical spectral signatures until  $100\text{ }^{\circ}\text{C}$ , which further confirms the same. The sample heated at  $120\text{ }^{\circ}\text{C}$  showed signatures of changes with the emergence of new features at  $1346$  and  $1593\text{ cm}^{-1}$ . Thermogravimetric analysis (TGA) and differential thermogravimetric (DTG) studies (Figure 7f) showed no weight loss up to  $140\text{ }^{\circ}\text{C}$ . We performed a differential scanning calorimetry (DSC) study in a temperature range of  $-90$  to  $+750\text{ }^{\circ}\text{C}$ . Figures S41 and S42 show the DSC data of the cluster. The linear thermogram from

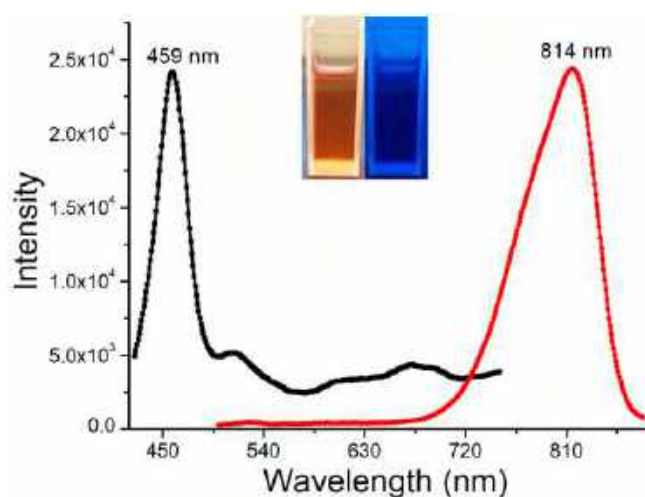


**Figure 6.** PL excitation (black) and emission (red) spectra of  $\text{Ag}_{21}$  were measured in its DCM solution. The emission spectrum was measured using 460 nm excitation. The excitation spectrum was measured for 814 nm emission. The inset shows optical images of the nanocluster under daylight (left) and under a 365 nm UV lamp (right).

$-90$  to  $+125\text{ }^{\circ}\text{C}$  confirms thermal stability. An exothermic peak observed at  $140\text{ }^{\circ}\text{C}$  is probably due to ligand ordering.

Interestingly, we observed spectral broadening of the UV–vis absorption features upon illumination of the microcrystalline samples using white light (xenon arc lamp). Lamp-power-dependent studies (exposure time 4 h) showed that up to  $\sim 100\text{ W}$  there was no variation of the absorption features. In the range of  $120$ – $160\text{ W}$ , spectral features become broad because of the formation of distorted clusters. Beyond  $160\text{ W}$ , even more drastic changes are seen. Spectra were measured after dissolving the irradiated samples in DCM. Raman studies of microcrystalline samples (as shown in Figure 7h) show that, up to  $100\text{ W}$ , there was no change in the vibrational features, whereas samples exposed at  $120$  and  $160\text{ W}$  had multiple new peaks. We also observed similar intensities of the BH ( $2652\text{ cm}^{-1}$ ) and CH ( $3081\text{ cm}^{-1}$ ) stretching vibrations after  $120$  and  $160\text{ W}$  light exposure, and the intensity of the cage breathing mode ( $760\text{ cm}^{-1}$ ) also reduced significantly, which implies a strain in the carborane moieties. The appearance of new peaks near  $1000$ – $1300\text{ cm}^{-1}$  (the CH and BH bending regions) also confirmed structural distortion. To explore the molecular stability, we measured ESI-MS of the samples, exposed to  $120\text{ W}$  light. The characteristic peak at  $m/z$  4893.43 confirms its stability. Therefore, light-illuminated changes in the crystalline state in the initial stages are attributed to possible molecular distortions in the structure, although more studies are necessary to understand the precise nature of the changes. An earlier investigation of the mechanical properties of cluster crystals using nanoindentation would suggest a flexible character for cluster crystals.<sup>59</sup> Upon further exposure, at  $180\text{ W}$  and above, it appears that additional changes are happening, as suggested by the emergence of new bands, at  $1346$  and  $1593\text{ cm}^{-1}$ . These bands are similar to those arising during thermal annealing, which suggests that both thermal and photochemical changes result in the same product eventually. However, more studies are necessary to confirm this.

To understand the electron dynamics responsible for the multiple absorption features and photoresponsivity, we performed femtosecond and nanosecond transient absorption (fs–ns-TA) spectroscopy. Experimental details of the measurements are given in the Supporting Information. Figure 8 shows the summarized fs–ns-TA data of  $\text{Ag}_{21}$  nanocluster, using a  $400\text{ nm}$ ,  $120\text{ fs}$  pump laser with a fluence of  $170\text{ }\mu\text{J}/\text{cm}^2$ . The contour plot of the obtained result is shown in Figure 8a. To better understand the excited-state features, the spectral profile of TA at selected time delays is plotted in Figure 8b. The figure shows that TA is primarily dominated by the two types of excited-state absorption (ESA) located in the region of  $\sim 465\text{ nm}$  and broad ESA beyond  $500\text{ nm}$ . A relatively weak negative signal (photobleach) is observed near  $490\text{ nm}$ . It is at the position of the peak observed in the optical absorption of nanocluster (Figure 3a) and arises as a result of phase space filling by pump excitation.

The weak ESA feature centered at  $\sim 465\text{ nm}$  is observed to have a short lifetime ( $<10\text{ ps}$ ) and disappear rapidly compared to the other ESA feature (Figure S43). Here, it is also noticed that photobleach growth accompanies the ESA decay. Such a behavior suggests that the ESA feature is possibly due to structural relaxation or charge transfer from the core to shell. Figure 8c shows the femtosecond-decay profiles associated with the broad ESA features. It offers a prolonged transient behavior and does not decay in the femtosecond window. To determine the kinetics of the long component, we measured



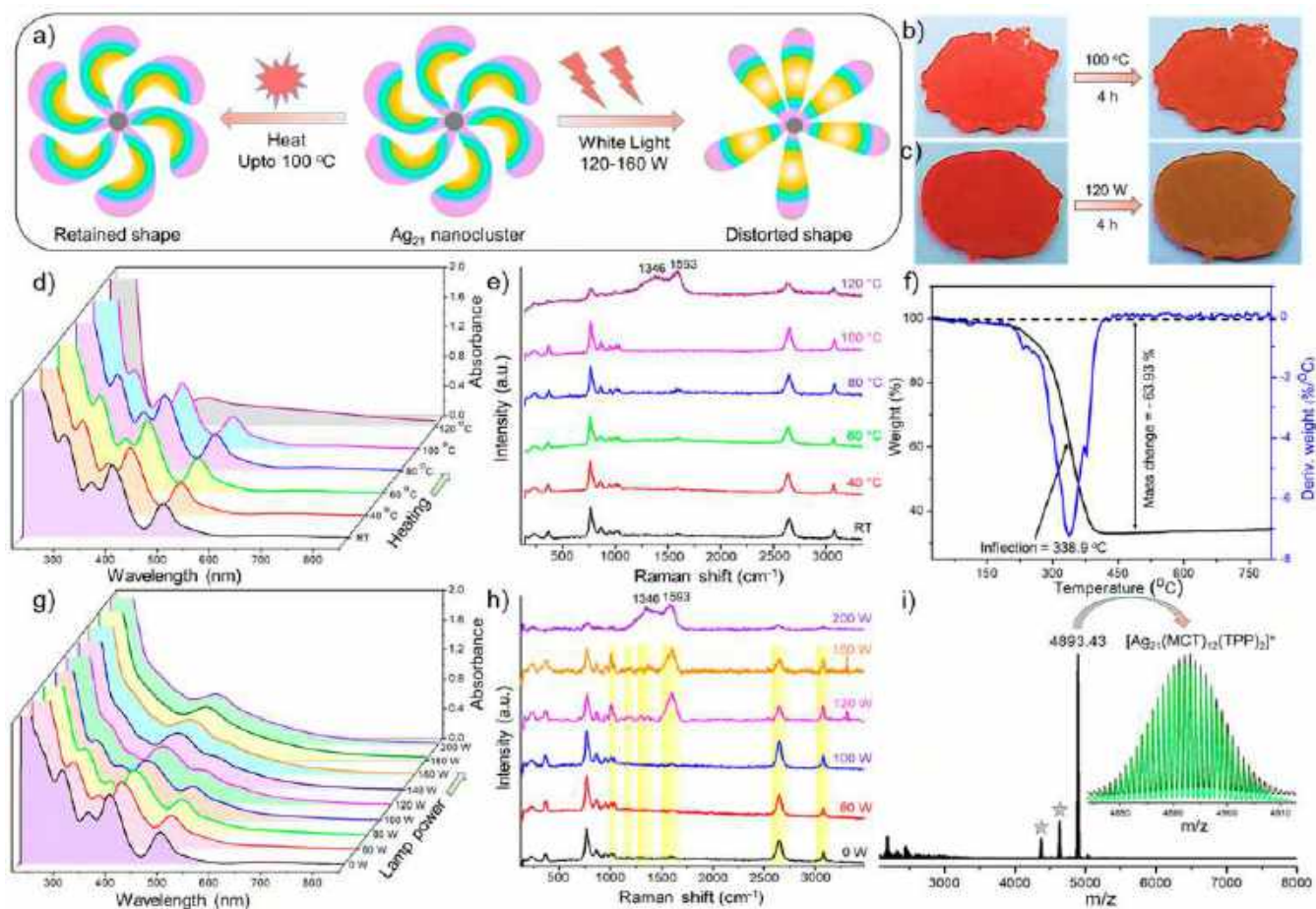


**Figure 7.** (a) Schematic representation showing the thermal and photo-illumination effects on  $\text{Ag}_{21}$  crystals. (b) Photographic images showing no visible color change after heating at  $100\text{ }^{\circ}\text{C}$ . (c) Photographic images showing a visible color change after  $120\text{ W}$  light illumination. (d) UV–vis absorption spectra after heating at different temperatures. Identical absorption spectra were observed up to  $100\text{ }^{\circ}\text{C}$ . (e) Raman spectra of  $\text{Ag}_{21}$  crystals after heating at different temperatures. (f) TGA and DTG analyses showing thermal stability of the cluster up to  $140\text{ }^{\circ}\text{C}$  with an inflection at  $338.9\text{ }^{\circ}\text{C}$ . (g) Sequential UV–vis absorption spectra after light exposure using different lamp powers (exposure time of  $4\text{ h}$  on each time). (h) Raman spectra showing the appearance of new vibrational peaks using lamp powers of  $120\text{--}160\text{ W}$ . Changes are highlighted. (i) Positive-ion-mode ESI-MS spectrum showing the presence of the cluster after  $120\text{ W}$  light exposure. The inset shows an exact matching of the experimental (black) and theoretical (green) spectra. The peaks labeled  $\star$  indicate TPP losses from the parent  $\text{Ag}_{21}$ .

ns-TA spectroscopy in Figure 8d, where it decays in the window of  $30\text{ }\mu\text{s}$ . The curve shown is fitted with a single-exponential function and renders a decay constant of  $3.26 \pm 0.02\text{ }\mu\text{s}$ . Such a long lifetime of carriers in the excited state is also observed in other gold and silver nanoclusters possibly because of ligand-to-metal charge transfer and the inherent geometry of the cluster.<sup>60</sup> The stable carriers predominantly center in the metallic core region of the excited state throughout the wavelength range of  $520\text{--}650\text{ nm}$ , which are likely to be the reason behind the photoresponsive nature.

## CONCLUSION

In conclusion, we synthesized a MCT- and TPP-coprotected silver nanocluster,  $[\text{Ag}_{21}(\text{MCT})_{12}(\text{TPP})_2]^+$ , starting from the  $\text{Ag}_{18}$  precursor cluster, protected with TPP and hydride. SC-XRD reveals that the nanocluster has an  $\text{Ag}_{13}$  central icosahedral core, which is connected with six silver atoms through direct Ag–Ag bonds and two other silver atoms connected via three Ag–S–Ag bonds in a tripodal fashion. Twelve carboranes surround the cluster as thiolates in a layered fashion, whereas two TPPs are connected at the head and tail positions of the oval-like cluster core through Ag–P bonds.

The MCT ligands assemble into an array resembling a propeller having six rotary arms when viewed along its TPP–TPP axis. A bidirectional rotational orientation of the silver sulfide core with the MCT ligand was observed in the nanomolecule. High-resolution mass spectrometry showed the systematic loss of two TPP ligands at low CEs and eight carborane ligands with silver atoms at high CEs, confirming strong bonds between the carborane ligands and the silver cluster. DFT has helped in the understanding of the experimental electronic absorption spectrum. The cluster showed a sharp NIR emission at  $814\text{ nm}$ . Although the  $\text{Ag}_{21}$  cluster shows an ambient thermal stability of up to  $100\text{ }^{\circ}\text{C}$  in its solid state, it manifests light-triggered structural distortion, as shown in UV–vis absorption and Raman spectroscopy studies. fs–ns-TA studies proved the formation of stable excited-state carriers with a lifetime of  $3.26 \pm 0.02\text{ }\mu\text{s}$  in the  $520\text{--}650\text{ nm}$  region, responsible for its photoresponsivity. Altogether, these studies suggest that thermally stable and photochemically active atomically precise silver clusters of unique structure and inherent beauty can be formed using carboranethiols as ligands.



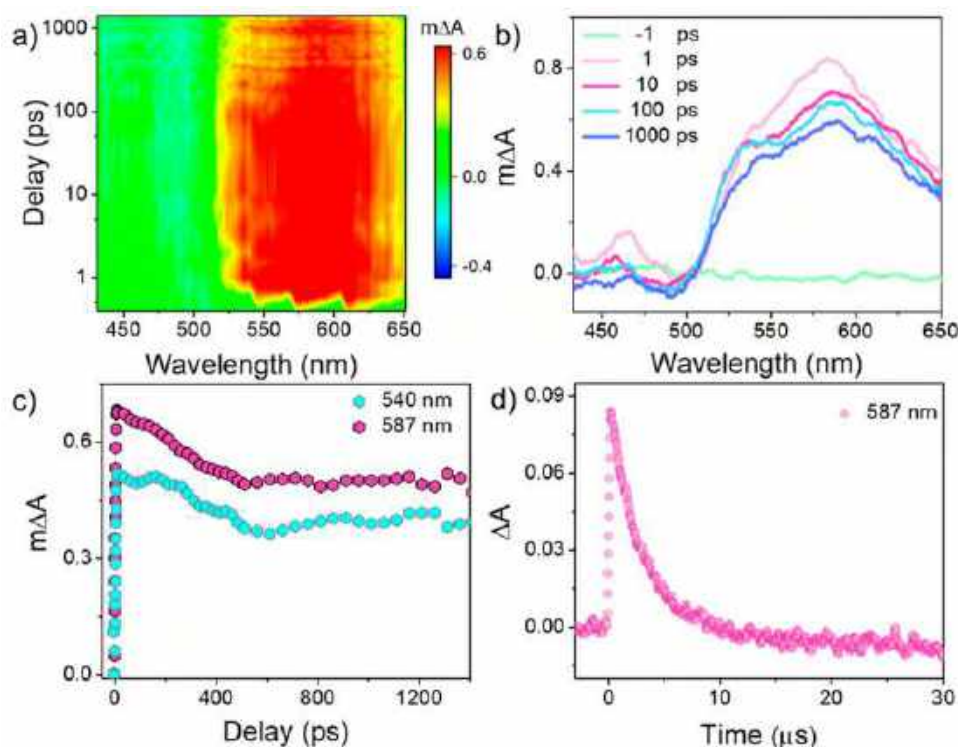


**Figure 8.** (a) Contour plot of the fs-TA spectrum of  $\text{Ag}_{21}$  showing broad ESA features from the 520–650 nm region. (b) Time evolution of the spectral profile of ESA features. (c) Femtosecond-decay spectra of ESA indicating higher stability of the excited-state carriers. (d) Nanosecond time evolution spectrum measured using nanosecond laser flash photolysis.

## ■ ASSOCIATED CONTENT

### SI Supporting Information

The Supporting Information is available free of charge at <https://pubs.acs.org/doi/10.1021/acs.inorgchem.2c00186>.

Experimental section, instrumentation, theoretical calculations, UV–vis, ESI-MS, CD, FESEM, EDS, PXRD, TEM, XPS, NMR, Fourier transform infrared, HOMO–LUMO, DSC, and associated figures (PDF)

### Accession Codes

CCDC 2094436 contains the supplementary crystallographic data for this paper. These data can be obtained free of charge via [www.ccdc.cam.ac.uk/data\\_request/cif](http://www.ccdc.cam.ac.uk/data_request/cif), or by emailing [data\\_request@ccdc.cam.ac.uk](mailto:data_request@ccdc.cam.ac.uk), or by contacting The Cambridge Crystallographic Data Centre, 12 Union Road, Cambridge CB2 1EZ, UK; fax: +44 1223 336033.

## ■ AUTHOR INFORMATION

### Corresponding Authors

**Thalappil Pradeep** – Department of Science and Technology (DST) Unit of Nanoscience and Thematic Unit of Excellence, Department of Chemistry, Indian Institute of Technology (IIT) Madras, Chennai 600036, India; [orcid.org/0000-0003-3174-534X](https://orcid.org/0000-0003-3174-534X); Email: [pradeep.iitm.ac.in](mailto:pradeep.iitm.ac.in)

**Tomas Base** – Department of Synthesis, Institute of Inorganic Chemistry, The Czech Academy of Science, Rez 25068, Czech Republic; [orcid.org/0000-0003-2533-8705](https://orcid.org/0000-0003-2533-8705); Email: [tbase@iic.acs.cz](mailto:tbase@iic.acs.cz)

**Kumaran Nair Valsala Devi Adarsh** – Department of Physics, Indian Institute of Science Education and Research Bhopal, Bhopal 462066, India; [orcid.org/0000-0002-6337-6545](https://orcid.org/0000-0002-6337-6545); Email: [adarsh@iiserb.ac.in](mailto:adarsh@iiserb.ac.in)

### Authors

**Arijit Jana** – Department of Science and Technology (DST) Unit of Nanoscience and Thematic Unit of Excellence, Department of Chemistry, Indian Institute of Technology (IIT) Madras, Chennai 600036, India

**Parvathy M. Unnikrishnan** – Department of Science and Technology (DST) Unit of Nanoscience and Thematic Unit of Excellence, Department of Chemistry, Indian Institute of Technology (IIT) Madras, Chennai 600036, India

**Ajay K. Poonia** – Department of Physics, Indian Institute of Science Education and Research Bhopal, Bhopal 462066, India; [orcid.org/0000-0002-5551-7299](https://orcid.org/0000-0002-5551-7299)

**Jayoti Roy** – Department of Science and Technology (DST) Unit of Nanoscience and Thematic Unit of Excellence, Department of Chemistry, Indian Institute of Technology (IIT) Madras, Chennai 600036, India

**Madhuri Jash** – Department of Science and Technology (DST) Unit of Nanoscience and Thematic Unit of Excellence, Department of Chemistry, Indian Institute of Technology (IIT) Madras, Chennai 600036, India

**Ganesan Paramasivam** – Department of Science and Technology (DST) Unit of Nanoscience and Thematic Unit of Excellence, Department of Chemistry, Indian Institute of Technology (IIT) Madras, Chennai 600036, India

**Jan Machacek** – Department of Synthesis, Institute of Inorganic Chemistry, The Czech Academy of Science, Rez 25068, Czech Republic; [orcid.org/0000-0003-4723-0789](https://orcid.org/0000-0003-4723-0789)

Complete contact information is available at:

<https://pubs.acs.org/doi/10.1021/acs.inorgchem.2c00186>

### Notes

The authors declare no competing financial interest.

## ACKNOWLEDGMENTS

The authors acknowledge DST, Government of India, and the Ministry of Education, Youth and Sports of Czech Republic for financial support to the bilateral research projects DST/INT/Czech/P-16/2020 and LTAIN19152, respectively. K.N.V.D.A. gratefully acknowledges the Science and Engineering Research Board for Grant CRG/2019/002808. We thank Sophisticated Analytical Instruments Facility, IIT Madras, for the SC-XRD measurements. We thank Sudhadevi Antharjanam and Sujana Manna for SC-XRD and Raman studies, respectively. A.J. thanks IIT Madras for his research fellowship. T.P. acknowledges funding from the Centre of Excellence on Molecular Materials and Functions under the Institution of Eminence scheme of IIT Madras. This work is part of an India–Czech Republic collaboration aimed at exploring the potential of atomically precise nanomaterials produced by combining metal and boron clusters, initiated by T.P. and T.B.

## REFERENCES

- (1) Jin, R.; Zeng, C.; Zhou, M.; Chen, Y. Atomically Precise Colloidal Metal Nanoclusters and Nanoparticles: Fundamentals and Opportunities. *Chem. Rev.* **2016**, *116*, 10346–10413.
- (2) Chakraborty, I.; Pradeep, T. Atomically Precise Clusters of Noble Metals: Emerging Link between Atoms and Nanoparticles. *Chem. Rev.* **2017**, *117*, 8208–8271.
- (3) Alhilaly, M. J.; Bootharaju, M. S.; Joshi, C. P.; Besong, T. M.; Emwas, A. H.; Juarez-Mosqueda, R.; Kaappa, S.; Malola, S.; Adil, K.; Shkurenko, A.; Häkkinen, H.; Eddaoudi, M.; Bakr, O. M.  $[\text{Ag}_{67}(\text{SPhMe}_2)_{32}(\text{PPh}_3)_8]^{3+}$ : Synthesis, Total Structure, and Optical Properties of a Large Box-Shaped Silver Nanocluster. *J. Am. Chem. Soc.* **2016**, *138*, 14727–14732.
- (4) Jana, A.; Chakraborty, P.; Dar, W. A.; Chandra, S.; Khatun, E.; Kannan, M. P.; Ras, R. H. A.; Pradeep, T. Dual Emitting  $\text{Ag}_{35}$  nanocluster Protected by 2-Pyrene Imine Thiol. *Chem. Commun.* **2020**, *56*, 12550–12553.
- (5) Bootharaju, M. S.; Dey, R.; Gevers, L. E.; Hedhili, M. N.; Basset, J. M.; Bakr, O. M. A New Class of Atomically Precise, Hydride-Rich Silver Nanoclusters Co-Protected by Phosphines. *J. Am. Chem. Soc.* **2016**, *138*, 13770–13773.
- (6) Guan, Z. J.; Zeng, J. L.; Nan, Z. A.; Wan, X. K.; Lin, Y. M.; Wang, Q. M. Thiacalix[4]Arene: New Protection for Metal Nanoclusters. *Sci. Adv.* **2016**, *2*, 1–8.
- (7) Lei, Z.; Wan, X.-K.; Yuan, S.-F.; Guan, Z.-J.; Wang, Q.-M. Alkynyl Approach toward the Protection of Metal Nanoclusters. *Acc. Chem. Res.* **2018**, *51* (10), 2465–2474.
- (8) Liu, K. G.; Hu, M. L.; Jiang, D. E.; Gao, X. M.; Liu, T. All-Carboxylate-Protected Superatomic Silver Nanocluster with an Unprecedented Rhombohedral  $\text{Ag}_8$  Core. *J. Am. Chem. Soc.* **2020**, *142*, 16905–16909.
- (9) Cerretani, C.; Kanazawa, H.; Vosch, T.; Kondo, J. Crystal Structure of a NIR-Emitting DNA-Stabilized  $\text{Ag}_{16}$  Nanocluster. *Angew. Chemie - Int. Ed.* **2019**, *58*, 17153–17157.
- (10) Liu, J. W.; Wang, Z.; Chai, Y. M.; Kurmoo, M.; Zhao, Q. Q.; Wang, X. P.; Tung, C. H.; Sun, D. Core Modulation of 70-Nuclei Core-Shell Silver Nanoclusters. *Angew. Chemie - Int. Ed.* **2019**, *58*, 6276–6279.
- (11) Wang, Z.; Su, H. F.; Kurmoo, M.; Tung, C. H.; Sun, D.; Zheng, L. S. Trapping an Octahedral  $\text{Ag}_6$  Kernel in a Seven-Fold Symmetric  $\text{Ag}_{56}$  Nanowheel. *Nat. Commun.* **2018**, *9* (1), 1–8.
- (12) Diez, I.; Pusa, M.; Kulmala, S.; Jiang, H.; Walther, A.; Goldmann, A. S.; Müller, A. H. E.; Ikkala, O.; Ras, R. H. A. Color Tunability and Electrochemiluminescence of Silver Nanoclusters. *Angew. Chemie - Int. Ed.* **2009**, *48*, 2122–2125.
- (13) Fan, C.; Lv, X.; Liu, F.; Feng, L.; Liu, M.; Cai, Y.; Liu, H.; Wang, J.; Yang, Y.; Wang, H. Silver Nanoclusters Encapsulated into Metal-Organic Frameworks with Enhanced Fluorescence and Specific Ion Accumulation toward the Microdot Array-Based Fluorimetric Analysis of Copper in Blood. *ACS Sensors* **2018**, *3*, 441–450.
- (14) Jin, R.; Li, G.; Sharma, S.; Li, Y.; Du, X. Toward Active-Site Tailoring in Heterogeneous Catalysis by Atomically Precise Metal Nanoclusters with Crystallographic Structures. *Chem. Rev.* **2021**, *121* (2), 567–648.
- (15) Luo, Z.; Zheng, K.; Xie, J. Engineering Ultrasmall Water-Soluble Gold and Silver Nanoclusters for Biomedical Applications. *Chem. Commun.* **2014**, *50*, 5143–5155.
- (16) Han, Z.; Dong, X.; Luo, P.; Li, S.; Wang, Z.; Zang, S.; Mak, T. C. W. Ultrastable Atomically Precise Chiral Silver Clusters with More than 95% Quantum Efficiency. *Sci. Adv.* **2020**, *6* (6), 1–8.
- (17) Yang, H.; Lei, J.; Wu, B.; Wang, Y.; Zhou, M.; Xia, A.; Zheng, L.; Zheng, N. Crystal Structure of a Luminescent Thiolated Ag Nanocluster with an Octahedral  $\text{Ag}_6^{4+}$  Core. *Chem. Commun.* **2013**, *49*, 300–302.
- (18) Khatun, E.; Bodiuzzaman, M.; Sugi, K. S.; Chakraborty, P.; Paramasivam, G.; Dar, W. A.; Ahuja, T.; Antharjanam, S.; Pradeep, T. Confining an  $\text{Ag}_{10}$  Core in an  $\text{Ag}_{12}$  Shell: A Four-Electron Superatom with Enhanced Photoluminescence upon Crystallization. *ACS Nano* **2019**, *13* (5), 5753–5759.
- (19) Joshi, C. P.; Bootharaju, M. S.; Alhilaly, M. J.; Bakr, O. M.  $[\text{Ag}_{25}(\text{SR})_{18}]^-$ : The “Golden” Silver Nanoparticle. *J. Am. Chem. Soc.* **2015**, *137*, 11578–11581.
- (20) AbdulHalim, L. G.; Bootharaju, M. S.; Tang, Q.; Del Gobbo, S.; AbdulHalim, R. G.; Eddaoudi, M.; Jiang, D. E.; Bakr, O. M.  $\text{Ag}_{29}(\text{BDT})_{12}(\text{TPP})_4$ : A Tetravalent Nanocluster. *J. Am. Chem. Soc.* **2015**, *137*, 11970–11975.
- (21) Desireddy, A.; Conn, B. E.; Guo, J.; Yoon, B.; Barnett, R. N.; Monahan, B. M.; Kirschbaum, K.; Griffith, W. P.; Whetten, R. L.; Landman, U.; Bigioni, T. P. Ultrastable Silver Nanoparticles. *Nature* **2013**, *501*, 399–402.
- (22) Song, Y.; Lambright, K.; Zhou, M.; Kirschbaum, K.; Xiang, J.; Xia, A.; Zhu, M.; Jin, R. Large-Scale Synthesis, Crystal Structure, and Optical Properties of the  $\text{Ag}_{146}\text{Br}_2(\text{SR})_{80}$  Nanocluster. *ACS Nano* **2018**, *12* (9), 9318–9325.
- (23) Bodiuzzaman, M.; Ghosh, A.; Sugi, K. S.; Nag, A.; Khatun, E.; et al. Camouflaging Structural Diversity: Co-Crystallization of Two Different Nanoparticles Having Different Cores but the Same Shell. *Angew. Chemie - Int. Ed.* **2019**, *58*, 189–194.
- (24) Dar, W. A.; Bodiuzzaman, M.; Ghosh, D.; Paramasivam, G.; Khatun, E.; Sugi, K. S.; Pradeep, T. Interparticle Reactions between Silver Nanoclusters Leading to Product Cocrystals by Selective Cocrystallization. *ACS Nano* **2019**, *13*, 13365–13373.
- (25) Deng, G.; Teo, B. K.; Zheng, N. Assembly of Chiral Cluster-Based Metal-Organic Frameworks and the Chirality Memory Effect during Their Disassembly. *J. Am. Chem. Soc.* **2021**, *143*, 10214–10220.
- (26) Yao, Q.; Xie, J. Pasteur-like Separation of Silver Nanocluster Racemates by Conglomerate Crystallization. *ACS Cent. Sci.* **2020**, *6*, 1862–1865.
- (27) Zhang, M. M.; Dong, X. Y.; Wang, Z. Y.; Luo, X. M.; Huang, J. H.; Zang, S. Q.; Mak, T. C. W. Alkynyl-Stabilized Superatomic Silver Clusters Showing Circularly Polarized Luminescence. *J. Am. Chem. Soc.* **2021**, *143*, 6048–6053.
- (28) Kang, X.; Zhu, M. Tailoring the Photoluminescence of Atomically Precise Nanoclusters. *Chem. Soc. Rev.* **2019**, *48*, 2422–2457.
- (29) Alamer, B. J.; Bootharaju, M. S.; Kozlov, S. M.; Cao, Z.; Shkurenko, A.; Nematulloev, S.; Maity, P.; Mohammed, O. F.; Eddaoudi, M.; Cavallo, L.; Basset, J. M.; Bakr, O. M.  $[\text{Ag}_9(1,2\text{-BDT})_6]^{3-}$ : How Square-Pyramidal Building Blocks Self-Assemble into the Smallest Silver Nanocluster. *Inorg. Chem.* **2021**, *60*, 4306–4312.
- (30) Das, A.; Li, T.; Nobusada, K.; Zeng, C.; Rosi, N. L.; Jin, R. Nonsuperatomic  $[\text{Au}_{23}(\text{SC}_6\text{H}_{11})_{16}]^-$  Nanocluster Featuring Bipyramidal  $\text{Au}_{15}$  Kernel and Trimeric  $\text{Au}_3(\text{SR})_4$  Motif. *J. Am. Chem. Soc.* **2013**, *135*, 18264–18267.

- (31) Zhu, M.; Aikens, C. M.; Hollander, F. J.; Schatz, G. C.; Jin, R. Correlating the Crystal Structure of A Thiol-Protected Au<sub>25</sub> Cluster and Optical Properties. *J. Am. Chem. Soc.* **2008**, *130*, 5883–5885.
- (32) Li, Y.; Zhou, M.; Jin, R. Programmable Metal Nanoclusters with Atomic Precision. *Adv. Mater.* **2021**, *33*, 2006591.
- (33) Liu, J. Y.; Alkan, F.; Wang, Z.; Zhang, Z. Y.; Kurmoo, M.; Yan, Z.; Zhao, Q. Q.; Aikens, C. M.; Tung, C. H.; Sun, D. Different Silver Nanoparticles in One Crystal: Ag<sub>210</sub>(<sup>1</sup>PrPhS)<sub>71</sub>(Ph<sub>3</sub>P)<sub>5</sub>Cl and Ag<sub>211</sub>(<sup>1</sup>PrPhS)<sub>71</sub>(Ph<sub>3</sub>P)<sub>6</sub>Cl. *Angew. Chemie - Int. Ed.* **2019**, *58*, 195–199.
- (34) Yang, H.; Wang, Y.; Chen, X.; Zhao, X.; Gu, L.; Huang, H.; Yan, J.; Xu, C.; Li, G.; Wu, J.; Edwards, A. J.; Dittrich, B.; Tang, Z.; Wang, D.; Lehtovaara, L.; Häkkinen, H.; Zheng, N. Plasmonic Twinned Silver Nanoparticles with Molecular Precision. *Nat. Commun.* **2016**, *7*, 1–8.
- (35) Ma, M. X.; Ma, X. L.; Liang, G. M.; Shen, X. T.; Ni, Q. L.; Gui, L. C.; Wang, X. J.; Huang, S. Y.; Li, S. M. A Nanocluster [Ag<sub>307</sub>Cl<sub>62</sub>(SPh'Bu)<sub>110</sub>]: Chloride Intercalation, Specific Electronic State, and Superstability. *J. Am. Chem. Soc.* **2021**, *143*, 13731–13737.
- (36) Kang, X.; Wang, S.; Zhu, M. Observation of a New Type of Aggregation-Induced Emission in Nanoclusters. *Chem. Sci.* **2018**, *9*, 3062–3068.
- (37) Sun, Q.-Q.; Li, Q.; Li, H.-Y.; Zhang, M.-M.; Sun, M.-E.; Li, S.; Quan, Z.; Zang, S.-Q. Thermochromism and Piezochromism of an Atomically Precise High-Nuclearity Silver Sulfide Nanocluster. *Chem. Commun.* **2021**, *57*, 2372–2375.
- (38) Li, Q.; Mosquera, M. A.; Jones, L. O.; Parakh, A.; Chai, J.; Jin, R.; Schatz, G. C.; Gu, X. W. Pressure-Induced Optical Transitions in Metal Nanoclusters. *ACS Nano* **2020**, *14*, 11888–11896.
- (39) Yuan, S. F.; Guan, Z. J.; Liu, W. Di; Wang, Q. M. Solvent-Triggered Reversible Interconversion of All-Nitrogen-Donor-Protected Silver Nanoclusters and Their Responsive Optical Properties. *Nat. Commun.* **2019**, *10*, 1–7.
- (40) Bi, Y.; Wang, Z.; Liu, T.; Sun, D.; Godbert, N.; Li, H.; Hao, J.; Xin, X. Supramolecular Chirality from Hierarchical Self-Assembly of Atomically Precise Silver Nanoclusters Induced by Secondary Metal Coordination. *ACS Nano* **2021**, *15* (10), 15910–15919.
- (41) Jana, A.; Jash, M.; Poonia, A. K.; Paramasivam, G.; Islam, M. R.; Chakraborty, P.; Antharjanam, S.; Machacek, J.; Ghosh, S.; Adarsh, K. N. V. D.; Base, T.; Pradeep, T. Light-Activated Intercluster Conversion of an Atomically Precise Silver Nanocluster. *ACS Nano* **2021**, *15* (10), 15781–15793.
- (42) Baksi, A.; Jash, M.; Bag, S.; Mudedla, S. K.; Bodiuzzaman, M.; Ghosh, D.; Paramasivam, G.; Subramanian, V.; Pradeep, T. Mechanistic Elucidation of the Structure and Reactivity of Bare and Hydride-Protected Ag<sub>17</sub><sup>+</sup> Clusters. *J. Phys. Chem. C* **2019**, *123*, 28494–28501.
- (43) Jash, M.; Methikkalam, R. R. J.; Bodiuzzaman, M.; Paramasivam, G.; Pradeep, T. Reaction between Ag<sub>17</sub><sup>+</sup> and Acetylene Outside the Mass Spectrometer: Dehydrogenation in the Gas Phase. *Chem. Commun.* **2020**, *56*, 15623–15626.
- (44) Bootharaju, M. S.; Burlakov, V. M.; Besong, T. M. D.; Joshi, C. P.; Abdulhalim, L. G.; Black, D. M.; Whetten, R. L.; Goriely, A.; Bakr, O. M. Reversible Size Control of Silver Nanoclusters via Ligand-Exchange. *Chem. Mater.* **2015**, *27*, 4289–4297.
- (45) Krishnadas, K. R.; Baksi, A.; Ghosh, A.; Natarajan, G.; Som, A.; Pradeep, T. Interparticle Reactions: An Emerging Direction in Nanomaterials Chemistry. *Acc. Chem. Res.* **2017**, *50*, 1988–1996.
- (46) Neumaier, M.; Baksi, A.; Weis, P.; Schneider, E. K.; Chakraborty, P.; Hahn, H.; Pradeep, T.; Kappes, M. M. Kinetics of Intercluster Reactions between Atomically Precise Noble Metal Clusters [Ag<sub>25</sub>(DMBT)<sub>18</sub>]<sup>-</sup> and [Au<sub>25</sub>(PET)<sub>18</sub>]<sup>-</sup> in Room Temperature Solutions. *J. Am. Chem. Soc.* **2021**, *143*, 6969–6980.
- (47) Poater, J.; Vinas, C.; Bennour, I.; Escayola, S.; Sola, M.; Teixidor, F. Too Persistent to Give Up: Aromaticity in Boron Clusters Survives Radical Structural Changes. *J. Am. Chem. Soc.* **2020**, *142*, 9396–9407.
- (48) Wang, Z.; Wang, M.; Li, Y.; Luo, P.; Jia, T.; Huang, R.; Zang, S.; Mak, T. C. W. Atomically Precise Site-Specific Tailoring and Directional Assembly of Superatomic Silver Nanoclusters. *J. Am. Chem. Soc.* **2018**, *140*, 1069–1076.
- (49) Li, Y.; Wang, Z.; Ma, X.; Luo, P.; Du, C.; Zang, S. Distinct Photophysical Properties in Atom-Precise Silver and Copper Nanocluster Analogues. *Nanoscale* **2019**, *11*, 5151–5157.
- (50) Huang, J.; Wang, Z.; Zang, S.; Mak, T. C. W. Spontaneous Resolution of Chiral Multi-Thiolate-Protected Ag<sub>30</sub> Nanoclusters. *ACS Cent. Sci.* **2020**, *6*, 1971–1976.
- (51) Wang, Q.; Wang, J.; Wang, S.; Wang, Z.; Cao, M.; He, C.; Yang, J.; Zang, S.; Mak, T. C. W. O-Carborane Based and Atomically-Precise Metal Clusters as Hypergolic Materials. *J. Am. Chem. Soc.* **2020**, *142* (28), 12010–12014.
- (52) Dhayal, R. S.; Liao, J. H.; Liu, Y. C.; Chiang, M. H.; Kahlal, S.; Saillard, J. Y.; Liu, C. W. Ag<sub>21</sub>{S<sub>2</sub>P(O<sup>1</sup>Pr)<sub>2</sub>}<sub>12</sub><sup>+</sup>: An Eight-Electron Superatom. *Angew. Chemie - Int. Ed.* **2015**, *54*, 3702–3706.
- (53) Chang, W. T.; Lee, P. Y.; Liao, J. H.; Chakrahari, K. K.; Kahlal, S.; Liu, Y. C.; Chiang, M. H.; Saillard, J. Y.; Liu, C. W. Eight-Electron Silver and Mixed Gold/Silver Nanoclusters Stabilized by Selenium Donor Ligands. *Angew. Chemie - Int. Ed.* **2017**, *56*, 10178–10182.
- (54) Li, Y.; Zhou, M.; Song, Y.; Higaki, T.; Wang, H.; Jin, R. Double-Helical Assembly of Heterodimeric Nanoclusters into Super-crystals. *Nature* **2021**, *594*, 380–384.
- (55) Walter, M.; Akola, J.; Lopez-Acevedo, O.; Jadzinsky, P. D.; Calero, G.; Ackerson, C. J.; Whetten, R. L.; Grönbeck, H.; Häkkinen, H. A Unified View of Ligand-Protected Gold Clusters as Superatom Complexes. *Proc. Natl. Acad. Sci. U. S. A.* **2008**, *105* (27), 9157–9162.
- (56) Weerawardene, K. L. D. M.; Häkkinen, H.; Aikens, C. M. Connections between Theory and Experiment for Gold and Silver Nanoclusters. *Annu. Rev. Phys. Chem.* **2018**, *69*, 205–229.
- (57) Goebbert, D. J.; Garand, E.; Wende, T.; Bergmann, R.; Meijer, G.; Asmis, K. R.; Neumark, D. M. Infrared Spectroscopy of the Microhydrated Nitrate Ions NO<sub>3</sub>(H<sub>2</sub>O). *J. Phys. Chem. A* **2009**, *113*, 7584–7592.
- (58) Leites, L. A. Vibrational Spectroscopy of Carboranes and Parent Boranes and Its Capabilities in Carborane Chemistry. *Chem. Rev.* **1992**, *92* (2), 279–323.
- (59) Sugi, K. S.; Bandyopadhyay, P.; Bodiuzzaman, M.; Nag, A.; Hridaya, M.; Dar, W. A.; Ghosh, P.; Pradeep, T. Manifestation of Structural Differences of Atomically Precise Cluster-Assembled Solids in Their Mechanical Properties. *Chem. Mater.* **2020**, *32*, 7973–7984.
- (60) Lin, X.; Cong, H.; Sun, K.; Fu, X.; Kang, W.; Wang, X.; Jin, S.; Wu, R.; Liu, C.; Huang, J. One-Step Rapid Synthesis, Crystal Structure and 3.3 Microseconds Long Excited-State Lifetime of Pd<sub>1</sub>Ag<sub>28</sub> Nanocluster. *Nano Res.* **2020**, *13* (2), 366–372.

## Supporting Information

# Carborane-thiol Protected Propeller-Shaped Photoresponsive Silver Nanomolecule

Arijit Jana,<sup>a</sup> Parvathy M. Unnikrishnan,<sup>a</sup> Ajay K. Poonia,<sup>b</sup> Jayoti Roy,<sup>a</sup> Madhuri Jash,<sup>a</sup> Ganesan Paramasivam,<sup>a</sup> Jan Machacek,<sup>c</sup> Kumaran Nair Valsala Devi Adarsh,<sup>b\*</sup> Tomas Base<sup>c\*</sup> and Thalappil Pradeep<sup>a\*</sup>

<sup>a</sup> DST Unit of Nanoscience (DST UNS) and Thematic Unit of Excellence (TUE), Department of Chemistry, Indian Institute of Technology Madras, Chennai – 600036, India

<sup>b</sup> Department of Physics, Indian Institute of Science Education and Research Bhopal, Bhopal – 462066, India

<sup>c</sup> Department of Synthesis, Institute of Inorganic Chemistry, The Czech Academy of Science, 1001 Husinec - Rez, 25068, Czech Republic

### Email:

\*T.P.- pradeep.iitm.ac.in

\*T.B. - tbase@iic.acs.cz

\*K.N.V.D.A. - adarsh@iiserb.ac.in

### Table of Contents

Items	Description	Page No
1.	Experimental procedures	S4, S5
2.	Instrumentation	S5-S7
3.	Theoretical calculations	S7
<b>Table S1</b>	Crystal data and structure refinement for Ag <sub>21</sub> nanocluster	S8
<b>Table S2</b>	Atomic coordinates and equivalent isotropic displacement parameters for Ag <sub>21</sub>	S9, S10
<b>Figure S1</b>	Characterization of Ag <sub>18</sub> through UV-vis spectrum and mass spectrometric studies	S10
<b>Figure S2</b>	Photographic images of Ag <sub>21</sub> cluster synthesis through LEIST reaction	S11
<b>Figure S3</b>	Time-dependent UV-vis absorption spectra during Ag <sub>21</sub> synthesis	S11
<b>Figure S4</b>	Optical microscopic images of single crystals	S12



<b>Figure S5</b>	FESEM images of the pyramidal Ag <sub>21</sub> crystal and the EDS collected from the same crystal	S13
<b>Figure S6</b>	EDS elemental mapping showing the presence of respective elements	S13
<b>Figure S7</b>	The patterned X-ray diffraction spots collected from the single crystal	S14
<b>Figure S8</b>	Comparative PXRD pattern of Ag <sub>21</sub> microcrystals along with a theoretical pattern	S14
<b>Figure S9</b>	Circular dichroism (CD) spectra of Ag <sub>21</sub> and MCT ligand in DCM solution	S15
<b>Figure S10</b>	The presence of C <sub>3</sub> rotational axis in the nanomolecule and double rotor orientation of carborane ligands present on the cluster surface	S15
<b>Figure S11</b>	Space filling model of Ag <sub>21</sub> showing an oval-like shape	S16
<b>Figure S12</b>	The ORTEP molecular structure of [Ag <sub>21</sub> (MCT) <sub>12</sub> (TPP) <sub>2</sub> ] nanocluster	S16
<b>Figure S13</b>	The arrangements of carboranes in the body of the cluster	S17
<b>Figure S14</b>	The staggered orientation of the six carboranes	S17
<b>Figure S15</b>	Atomic arrangements of silver skeleton of Ag <sub>25</sub> nanocluster	S18
<b>Figure S16</b>	Atomic arrangements of silver skeleton of Ag <sub>21</sub> nanocluster	S18
<b>Figure S17</b>	Extended views intercluster packing of Ag <sub>21</sub> along the axial directions	S19
<b>Figure S18</b>	Intercluster packing of Ag <sub>21</sub> along o-corner of the unit cell	S20
<b>Figure S19</b>	Intercluster packing of Ag <sub>21</sub> along a, b, c-corners of the unit cell	S21
<b>Figure S20</b>	Intercluster packing shows the presence of several BH-BH and BH-CH interactions	S21
<b>Figure S21</b>	Time-dependent UV-vis absorption spectrum of Ag <sub>21</sub> indicating its stability	S22
<b>Figure S22</b>	UV-vis absorption spectra of Ag <sub>21</sub> nanocluster in different solvents	S22
<b>Figure S23</b>	Lower range ESI-MS shows the presence of NO <sub>3</sub> <sup>-</sup> counter ions in the crystal	S23
<b>Figure S24</b>	Expanded view of MS/MS fragmentation pattern at CE 75	S24
<b>Table S3</b>	Correlations between peak intensity and electron counts of fragmented clusters	S24, S25
<b>Figure S25</b>	The TEM images of the Ag <sub>21</sub> nanocluster along with the EDS spectrum	S25
<b>Figure S26</b>	XPS spectra of Ag <sub>21</sub> nanocluster along with appropriate peak fitting	S26



<b>Figure S27</b>	$^{11}\text{B}$ NMR spectrum of MCT ligand in $\text{CDCl}_3$ solvent	S27
<b>Figure S28</b>	$^{11}\text{B}$ - $^{11}\text{B}$ COSY NMR spectrum of MCT ligand in $\text{CDCl}_3$ solvent	S28
<b>Table S4</b>	$^{11}\text{B}$ NMR chemical shift data for the MCT ligand	S28
<b>Figure S29</b>	$^{11}\text{B}$ NMR spectrum of $\text{Ag}_{21}$ nanocluster in $\text{CDCl}_3$ solvent	S29
<b>Figure S30</b>	$^{13}\text{C}\{^1\text{H}\}$ NMR spectrum of $\text{Ag}_{21}$ nanocluster in $\text{CDCl}_3$ solvent	S29
<b>Figure S31</b>	$^{31}\text{P}$ NMR spectrum of $\text{Ag}_{21}$ nanocluster in $\text{CDCl}_3$ solvent	S30
<b>Figure S32</b>	FT-IR spectrum of $\text{Ag}_{21}$ nanocluster and a comparison with MCT ligand	S30
<b>Figure S33</b>	Raman spectrum of $\text{Ag}_{21}$ microcrystals and a comparison with MCT ligands	S31
<b>Table S5</b>	Spectral assignments of vibrational Raman features of MCT ligand	S31
<b>Figure S34</b>	Theoretically optimized structure of $\text{Ag}_{21}$ nanomolecule along with two TPP ligands and corresponding calculated absorption spectrum	S32
<b>Table S6</b>	The calculated oscillator strengths ( $f$ ) of transitions	S32
<b>Figure S35</b>	The DOS plots of molecular orbitals with the energy contribution for the transition at 672 nm	S32
<b>Figure S36</b>	The DOS plots of molecular orbitals with the energy contribution for the transition at 565 nm	S33
<b>Figure S37</b>	The DOS plots of molecular orbitals with the energy contribution for the transition at 494 nm	S33
<b>Figure S38</b>	The DOS plots of molecular orbitals with the energy contribution for the transition at 422 nm	S33
<b>Figure S39</b>	The full range density of states (DOS) with contributions of atomic orbitals	S34
<b>Figure S40</b>	Absorption and emission spectra of $\text{Ag}_{21}$ in energy scale	S34
<b>Figure S41</b>	DSC data of $\text{Ag}_{21}$ crystals in the temperature range of -90 to 200 °C	S35
<b>Figure S42</b>	DSC data of $\text{Ag}_{21}$ crystals in the temperature range of 25 to 800 °C	S35
<b>Figure S43</b>	Spectral kinetics of the TA at the selected time scales	S36
<b>4.</b>	References	S36

## 1. Experimental Procedures Chemicals

Silver nitrate ( $\text{AgNO}_3$ ) was purchased from Rankem Chemicals. Triphenylphosphine and sodium borohydride ( $\text{NaBH}_4$ , 98%) were bought from Aldrich. The *meta*-carborane 9-thiol (MCT) ligands were purchased from Katchem s.r.o. (Czech Republic). MCT ligand was re-crystallized from hot chloroform/hexane solvents. Milli-Q water was used for  $\text{Ag}_{18}$  synthesis and its purification. Deuterated chloroform ( $\text{CDCl}_3$ , 99.8 atom % D) was received from Sigma-Aldrich. HPLC-grade solvents such as methanol, ethanol, acetone, dichloromethane (DCM), chloroform, 1, 2-dichlorobenzene (DCB), dimethylsulfoxide (DMSO) and dimethylformamide (DMF) were purchased from Rankem chemicals. All the chemicals are commercially available and used as such without any purification.

### Synthesis of $[\text{Ag}_{18}(\text{TPP})_{10}\text{H}_{16}]$ nanocluster

The  $[\text{Ag}_{18}(\text{TPP})_{10}\text{H}_{16}]$  nanocluster was synthesized by following a reported procedure.<sup>1,2</sup> Briefly, 20 mg of  $\text{AgNO}_3$  was dissolved in 5 ml methanol and 7 ml of chloroform was added to it. After that, 70 mg of triphenylphosphine dissolved in 2 ml of chloroform was added to the above reaction mixture under vigorous stirring conditions. After 20 min, 6.5 mg sodium borohydride dissolved in 0.75 ml of mill-Q water was added. Upon addition of the reducing agents, the colorless solution becomes yellow. The reaction was continued for 3.5 h. in dark condition. During the progress of the reaction, the color of the solution changes to brownish black and finally dark green, which indicate the formation of the nanocluster. Mixed solvents were removed by evaporation under reduced pressure. The solid green material was washed repeatedly to remove the excess reagents. The  $\text{Ag}_{18}$  nanocluster was characterized using UV-vis absorption spectroscopy and mass spectrometric studies (shown in Figure S1). Purified nanocluster was extracted in methanol and used for  $\text{Ag}_{21}$  synthesis. The yield of the product was 35% in terms of silver.

### Synthesis of $[\text{Ag}_{21}(\text{MCT})_{12}(\text{TPP})_2]$ nanocluster

The  $\text{Ag}_{21}$  nanocluster was prepared using the LEIST reaction of  $\text{Ag}_{18}$  nanocluster with MCT ligands. In brief, 8 mg of MCT ligands are added to a solution having 10 mg of  $\text{Ag}_{18}$  nanocluster in 5 ml methanol. After 10 min of the addition of thiol, the solution became yellowish and which eventually converted to dark red. After 2 hours of reaction, a dark reddish solution forms as an end product. After overnight size focusing, centrifugation of the reaction mixture ends up a reddish precipitate, which was extracted in DCM after the multiple cleaning of methanol. As prepared  $\text{Ag}_{21}$  nanoclusters are insoluble in methanol but soluble in DCM, chloroform and DMF. Suitable quality single crystals are grown following the vapor diffusion of hexane into a concentrated cluster solution in DCM. The yield of the product is 65% in terms of  $\text{Ag}_{18}$  nanocluster. As formed  $\text{Ag}_{21}$  nanocluster with twelve MCT and two TPP ligands is the predominant product during this LEIST reaction. There are no other cluster products during this synthetic reaction.

### Effect of heating

The thermal stability of  $\text{Ag}_{21}$  crystals was measured in ambient conditions after preparing a thin film of 8-10 mg microcrystalline powder. After 4 h of heating, we have measured Raman spectra as such and UV-vis spectra were recorded upon dissolving it in DCM. Figures 6d and 6e represent the combined results after each heating.

### Effect of light-illumination

The effect of photo-illumination of  $\text{Ag}_{21}$  crystals was measured in the solid state under ambient conditions. A white light source (Xe arc lamp) with varying lamp power of 50-200 W was used for the illumination. Light was exposed to the sample vertically using an optical light guide. After 4 h of light exposure, we have

measured the Raman spectra as such and UV-vis absorption spectra were recorded upon dissolving the sample in DCM. Figures 6g and 6h show the combined results after each light exposure.

## 2. Instrumentation

### Spectroscopic characterization

UV-vis absorption spectra were measured using Perkin Elmer Lambda 365 UV-Vis spectrophotometer in the wavelength region of 200 to 1100 nm with a bandpass filter of 1 nm. 20 mM purified cluster (in 2.5 ml of respective solvents) was used for the measurements. Mass spectra of all the nanoclusters were measured using the Waters Synapt G2 Si HDMS instrument. This mass spectrometer consists of an electrospray ionization source, quadrupole ion guide/trap, ion mobility cell and TOF analyzer. Nitrogen gas was used as the nebulizer gas. The mass spectra were collected in positive ion-mode. Mass spectrometric measurements were done by using the following conditions: Flow rate: 20  $\mu$ L/min, capillary voltage: 2.5 kV, cone voltage: 20 V, source temperature: 80  $^{\circ}$ C, desolvation temp: 150  $^{\circ}$ C, desolvation gas flow: 400 L/h. All the fragmentation experiments were performed by varying the collision energy of the selected ions inside the ion mobility cell using the same instrument. Circular dichroism (CD) spectra were recorded using an Applied Photophysics instrument having Chirscan software. 20 mM cluster dissolved in 2.5 ml DCM was used for the measurement. Photoluminescence spectra were measured using Jobin Yvon Nanolog fluorescence spectrometer with a bandpass of 3 nm for both emission and excitation spectra. FT-IR spectra were recorded using JASCO-4100 spectrometer. 1 mg crystals were finely grinded with dry KBr to prepare a thin pallet for the measurement. Multinuclear NMR spectra were recorded using Bruker 500 MHz FT-NMR spectrometer. Deuterated chloroform ( $\text{CDCl}_3$ ) was used for the measurements. Spectra were processed using MestRe-Nova NMR software. Powder XRD of the  $\text{Ag}_{21}$  nanocluster was measured using a D8 Advance Bruker instrument, using  $\text{Cu K}\alpha$  as an X-ray source ( $h\nu = 8047.8$  eV). 150 mg microcrystalline solids were spotted on a clean glass slide for the measurement. A high speed wide angle LYNXEYE detector was used for collecting the data. X-ray photoelectron spectroscopy was measured using ESCA probe TPD equipped with polychromatic  $\text{Mg K}\alpha$  X-ray source ( $h\nu = 1253.6$  eV). Samples dissolved in DCM were spotted on a sample stub and measurements were conducted with a constant analyzer energy of 50 eV for the survey scans and 20 eV for the specific regions. The binding energies in the spectra were calibrated with respect to the C 1s peak at 284.8 eV. Raman spectra were recorded using a CRM-Alpha 300S, WI Tec GmbH confocal Raman microscope, equipped with 532 nm frequency doubled Nd-YAG laser.

### Microscopic characterization

Optical microscopic images of the crystals were collected in reflected light mode using Keyence VHX-950F digital microscope. Scanning electron microscopy (SEM) was performed using Verios G4 UC, Thermo Scientific field emission scanning electron microscope (FESEM). The images were collected in high vacuum at an operating voltage at 2 kV. Transmission electron microscopy (TEM) was measured using a JEOL-3010, 300 kV instrument. A Gatan 794 multiscan CCD camera was used for image collection. The accelerating voltage was kept low to reduce beam-induced damage.

### TGA, DTG and DSC measurements

TGA, DTG, and DSC measurements in the temperature range of 25 to 800  $^{\circ}$ C were measured using a NETZSCH STA 449 F3 Jupiter instrument equipped with Proteus-6.1.0 software. About 8.7 mg crystalline sample was loaded in an alumina crucible for the measurement. Nitrogen was used as the environment with a flow rate of 10  $^{\circ}$ C/min. Low temperature DSC measurement was performed using NETZSCH 204F1

Phoenix instrument equipped with Proteus 80 software. About 3.22 mg crystalline sample was loaded in an alumina crucible for the measurement in nitrogen gas (flow rate of 60.0 ml/min). DSC data were measured for a cooling cycle from 25 to -90 °C, followed by a heating cycle from -90 to 200 °C.

### **Femtosecond (fs) transient absorption spectroscopy**

In our transient absorption spectrometer, 120 fs pulses centered at 800 nm are generated by Spectra physics Mai-Tai oscillator. The pulsed profile of the laser sources used in our experiment is Gaussian pulse with full width at half maximum (FWHM) of ~ 30 meV. This pulse is sent to Spectra physics Spitfire amplifier to generate high energy (4mJ/pulse) with a repetition rate of 1 KHz. To generate 400 nm pump pulse, one part of the beam is incident on the second harmonic  $\beta$ -barium borate crystal and output is separated from the fundamental beam with the help of a dichroic beam splitter. The residual 800 nm pulses are delayed with respect to the pump by a computer-controlled motion controller and pass through a CaF<sub>2</sub> crystal to generate the white light continuum probe beam. Here to avoid any photodamage, the crystal is continuously rotated throughout the experiment. Now both the pump and probe pulses are spatially overlapped onto the sample and the changes of absorbance ( $\Delta A$ ) of probe beam due to the pump is calculated using the equation

$$\Delta A = \log [I_{ex}(s)/I_0(s)] - [I_{ex}(r)/I_0(r)]$$

Where  $r$  and  $s$  correspond to the reference and sample,  $I_{ex}$  and  $I_0$  are transmitted intensities of probe pulse after excitation and in the ground state, respectively. The intensity of transmitted pulses is measured with the help of MS 2004 (600 lines/mm diffraction grating blazed at 600 nm) spectrometer and Si linear photodiode arrays. The TA data is chirped corrected before analyzing to compensate for the group velocity dispersion. The magnitude of the chirp is measured by using the instantaneous coherent artefact response of the ethanol solution. The measurements are carried out inside the motorized sample holder where it is continuously rotated during the experiment.

### **Nanosecond (ns) flash photolysis**

The ns transient absorption is measured using flash photolysis. In these measurements, we excite the sample using the second harmonic of Nd-YAG laser pump having the pulse width of 5 ns (< 10 meV) centred at 532 nm of Spectra Physics Quanta-Ray INDI laser system. The change in absorbance is determined by the white light (500-800 nm), which is produced using Xenon-Arc lamp (150 W). In the set-up, obtained probe beam is aligned in the cross beam configuration to the pump laser beam. The ns flash photolysis measurement is performed in a quartz cuvette. The change in the intensity is measured by Laser flash photolysis spectrometer (LKS80Applied Photophysics) with the combination of an oscilloscope (Agilent Infiniium DSO9064A).

### **Single crystal XRD measurements**

Single-crystal X-ray diffraction data were recorded using Bruker D8 VENTURE instrument equipped with Mo K $\alpha$  radiation source of wavelength 0.71073 Å. A PHOTON 100 CMOS detector has been used to record the diffraction spots. A suitable crystal was mounted on a Kapton loop with the help of paratone oil. The programme APEX3-SAINT (Bruker, 2016) was used for integrating the frames. A multi-scan absorption correction was done using the programme SADABS (Bruker, 2016). The structure was solved by SHELXT-2014 (Sheldrick, 2014) and refined by full-matrix least squares techniques using SHELXL-2018 (Sheldrick, 2018) computer programme. Hydrogen atoms were fixed at calculated positions and refined as riding model

with C-H = 0.93 Å, B-H = 1.10 Å and Uiso(H) = 1.2 Ueq(C) or 1.2 Ueq(B). Mercury 2020.2.0 software has been used for the visualization of the structure.

### 3. Theoretical calculations

The structural, electronic and optical absorption spectra were calculated using density functional theory (DFT) and time-dependent density functional theory (TD-DFT) as implemented in the Grid-based Projector Augmented Wave (GPAW) software package.<sup>3,4</sup> The atomic coordinates were taken from the single crystal structure to initiate the structural optimization. The exchange function Perdew-Burke-Ernzerhof (PBE)<sup>5</sup> was used in the real grid space with the spacing of 0.2 Å to understand the optimized geometry. The valence electronic configuration of Ag (4d<sup>10</sup> 5s<sup>1</sup> 5p<sup>6</sup>), S (3s<sup>2</sup> 3p<sup>4</sup>), P (3s<sup>2</sup> 3p<sup>3</sup>), C (2s<sup>2</sup> 2p<sup>2</sup>), B (2s<sup>2</sup> 2p<sup>1</sup>) and H (1s<sup>1</sup>) were used for the PAW setup and scalar relativistic effects were included for the Ag atoms. The geometry optimization was carried out with the convergence condition without taking any symmetry constraints with a residual force less than 0.05 eV/Å. The absorption spectrum was calculated using linear response time-dependent density functional theory (LR-TDDFT). The origin of each absorption feature was calculated using the ground state and excited state optimized geometry. The total density of states (DOSs) was calculated for each transition and the involvement of individual atomic orbitals was also analyzed. Visualization of structure and individual molecular orbitals were done with visual molecular dynamics (VMD) software.



**Table S1.** Crystal data and structure refinement for Ag<sub>21</sub> nanocluster.

Identification code	Ag <sub>21</sub> nanocluster	
Empirical formula	C <sub>60</sub> H <sub>162</sub> Ag <sub>21</sub> B <sub>120</sub> P <sub>2</sub> S <sub>12</sub>	
Formula weight	4893.02	
Temperature	190(2) K	
Wavelength	0.71073 Å	
Crystal system	Cubic	
Space group	P a -3	
Unit cell dimensions	a = 26.7447(17) Å	α = 90°.
	b = 26.7447(17) Å	β = 90°.
	c = 26.7447(17) Å	γ = 90°.
Volume	19130(4) Å <sup>3</sup>	
Z	4	
Density (calculated)	1.699 Mg/m <sup>3</sup>	
Absorption coefficient	2.274 mm <sup>-1</sup>	
F(000)	9324	
Crystal size	0.500 x 0.400 x 0.350 mm <sup>3</sup>	
Theta range for data collection	2.850 to 25.994°.	
Index ranges	-32<=h<=32, -32<=k<=32, -32<=l<=32	
Reflections collected	130622	
Independent reflections	6253 [R(int) = 0.0360]	
Completeness to theta = 25.242°	99.7 %	
Absorption correction	Semi-empirical from equivalents	
Max. and min. transmission	0.7457 and 0.5804	
Refinement method	Full-matrix least-squares on F <sup>2</sup>	
Data / restraints / parameters	6253 / 0 / 324	
Goodness-of-fit on F <sup>2</sup>	1.172	
Final R indices [I>2σ(I)]	R1 = 0.0748, wR2 = 0.1444	
R indices (all data)	R1 = 0.0952, wR2 = 0.1599	
Extinction coefficient	n/a	
Largest diff. peak and hole	2.620 and -1.877 e.Å <sup>-3</sup>	

**Table S2.** Atomic coordinates ( $\times 10^4$ ) and equivalent isotropic displacement parameters ( $\text{\AA}^2 \times 10^3$ ) for Ag21-1\_sq. U(eq) is defined as one third of the trace of the orthogonalized  $U^{ij}$  tensor.

	x	y	z	U(eq)
Ag(1)	29(1)	4493(1)	6731(1)	43(1)
Ag(2)	-595(1)	4902(1)	5856(1)	39(1)
Ag(3)	0	5000	5000	24(1)
Ag(4)	529(1)	4995(1)	5899(1)	37(1)
Ag(5)	1332(1)	3668(1)	6332(1)	45(1)
C(1)	2001(6)	5642(8)	7272(7)	96(6)
C(2)	1153(6)	5616(7)	7865(5)	88(5)
C(3)	-923(5)	6236(5)	7055(5)	55(3)
C(4)	-1462(6)	5787(6)	7762(7)	87(5)
C(5)	2449(4)	3436(4)	7025(4)	37(2)
C(6)	2720(4)	3295(5)	7446(4)	53(3)
C(7)	3177(5)	3513(5)	7541(5)	58(3)
C(8)	3368(5)	3863(6)	7231(6)	73(4)
C(9)	3109(6)	4002(6)	6820(7)	83(5)
C(10)	2655(5)	3794(5)	6714(5)	62(3)
S(1)	-854(1)	4597(1)	6712(1)	39(1)
S(2)	916(1)	4519(1)	6607(1)	42(1)
P(1)	1850(1)	3150(1)	6850(1)	34(1)
B(1)	1217(4)	4949(4)	7054(4)	32(2)
B(2)	1574(5)	4726(7)	7564(6)	60(4)
B(3)	2005(6)	5151(8)	7683(6)	79(6)
B(4)	1481(5)	5537(5)	6873(5)	51(3)
B(5)	1874(5)	5040(7)	7058(5)	62(4)
B(6)	945(4)	5519(4)	7253(4)	41(3)
B(7)	992(5)	5009(5)	7683(4)	46(3)
B(8)	1522(7)	5126(8)	8045(5)	82(6)
B(9)	1788(8)	5702(10)	7880(7)	102(8)
B(10)	1432(6)	5936(6)	7373(5)	63(4)

B(11)	-936(4)	5194(4)	7050(4)	34(2)
B(12)	-505(5)	5417(5)	7518(5)	45(3)
B(13)	-499(5)	6090(5)	7484(6)	58(4)
B(14)	-1187(5)	5737(5)	6758(5)	54(3)
B(15)	-549(4)	5738(4)	6934(5)	40(3)
B(16)	-1545(5)	5422(6)	7219(6)	58(4)
B(17)	-1104(6)	5233(5)	7686(5)	53(3)
B(18)	-862(6)	5773(5)	7932(5)	56(3)
B(19)	-1093(7)	6298(6)	7668(6)	68(4)
B(20)	-1522(5)	6091(6)	7201(7)	63(4)

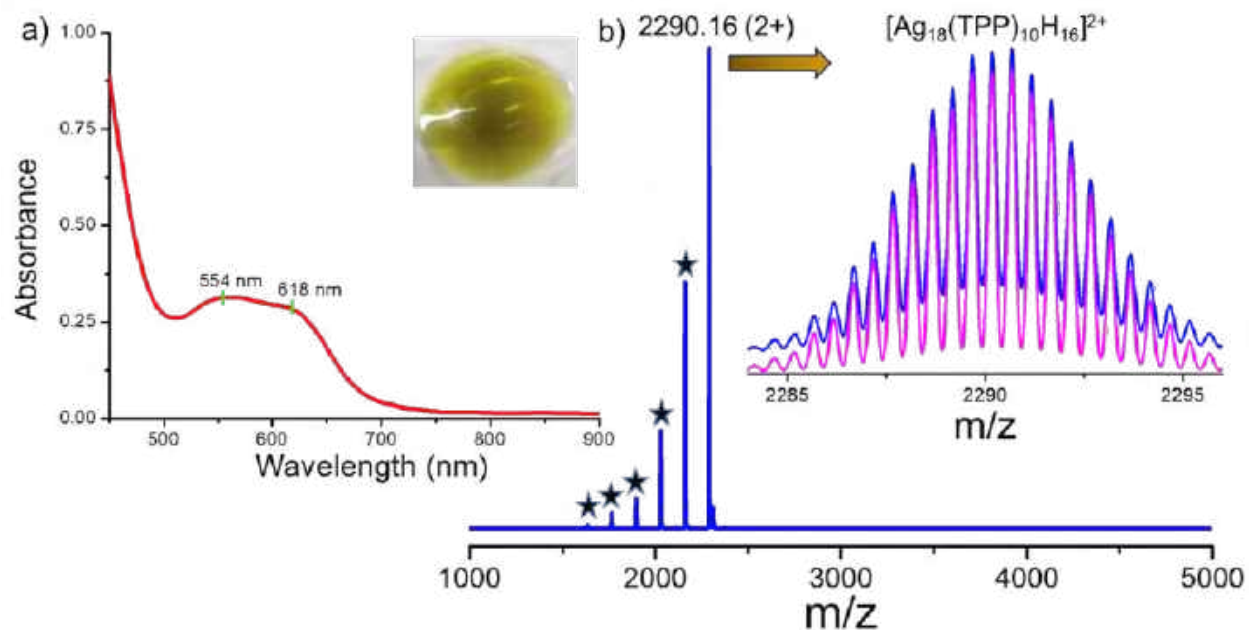


**Figure S1.** a) UV-vis absorption spectrum of Ag<sub>18</sub> nanocluster (left inset shows the photographic image of the nanocluster). b) The ESI-MS spectrum of Ag<sub>18</sub> nanocluster in positive ion mode. Each \* indicates sequential loss of TPP units from the parent nanocluster. The right inset shows the exact matching of the experimental spectrum (blue) with the theoretical spectrum (pink).

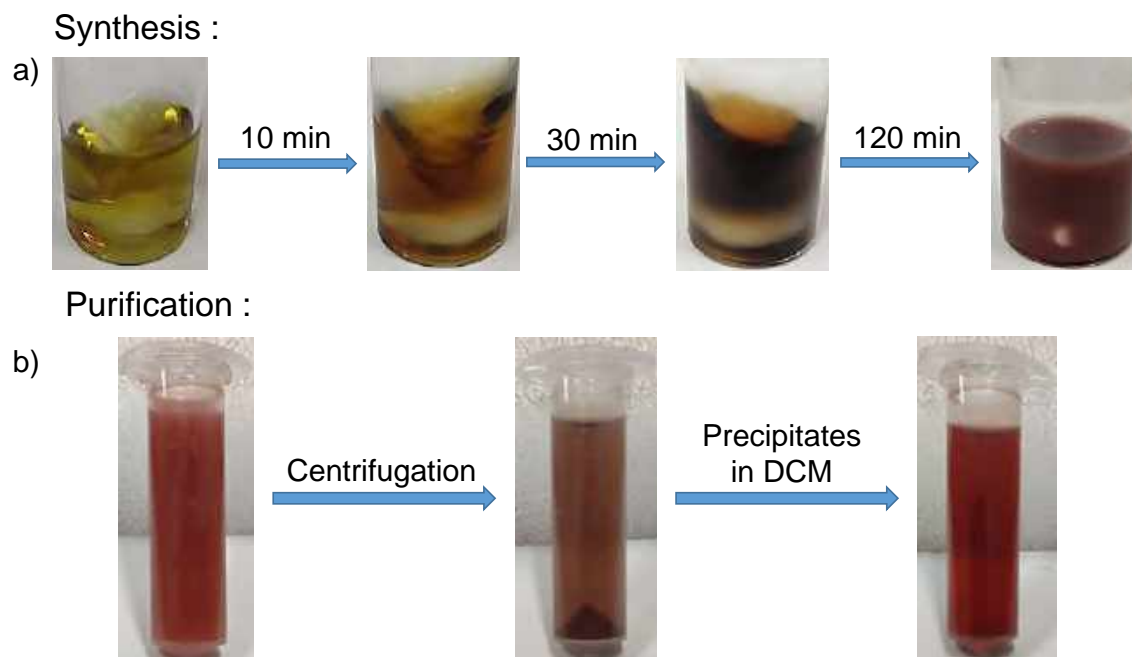


**Figure S2.** a) Photographic images show the progress of the LEIST reaction. b) Purification of the as synthesized nanoclusters through centrifugation.

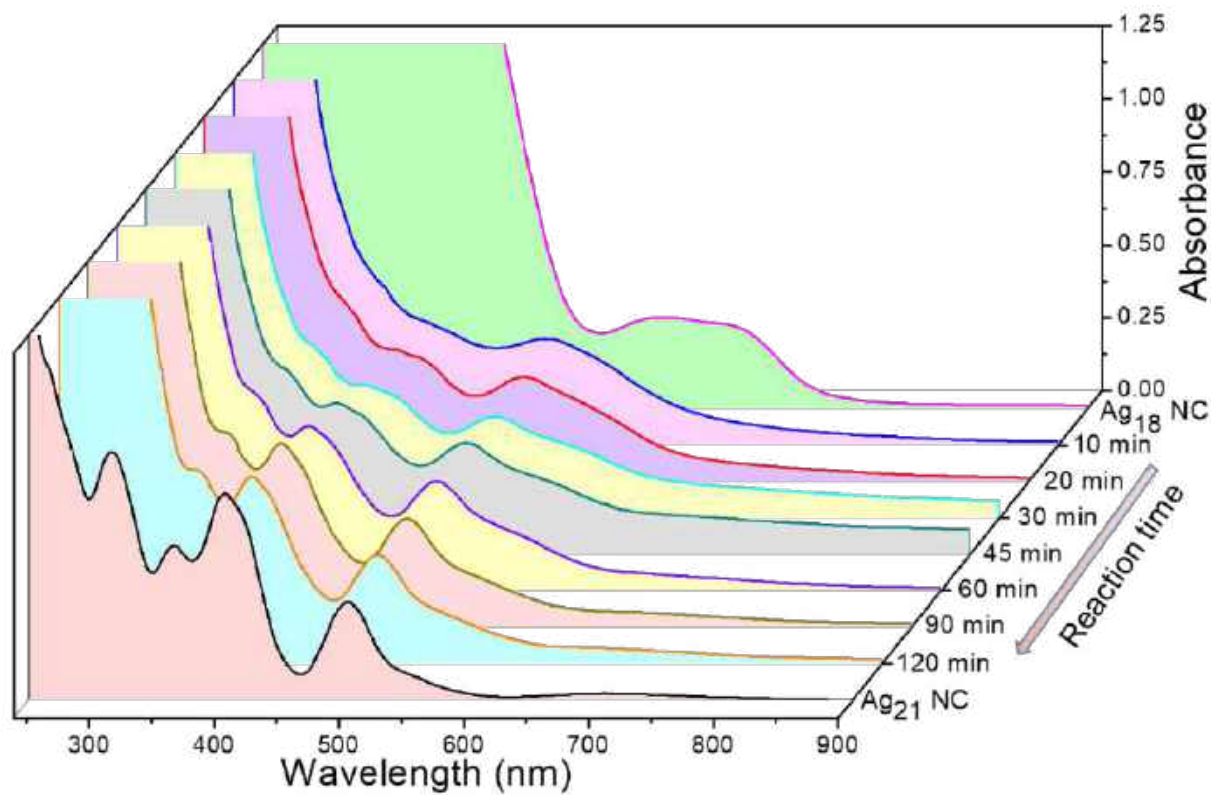


**Figure S3.** Time-dependent UV-vis absorption spectra show the formation of Ag<sub>21</sub> from Ag<sub>18</sub> nanocluster. All of these spectra were measured in methanol.

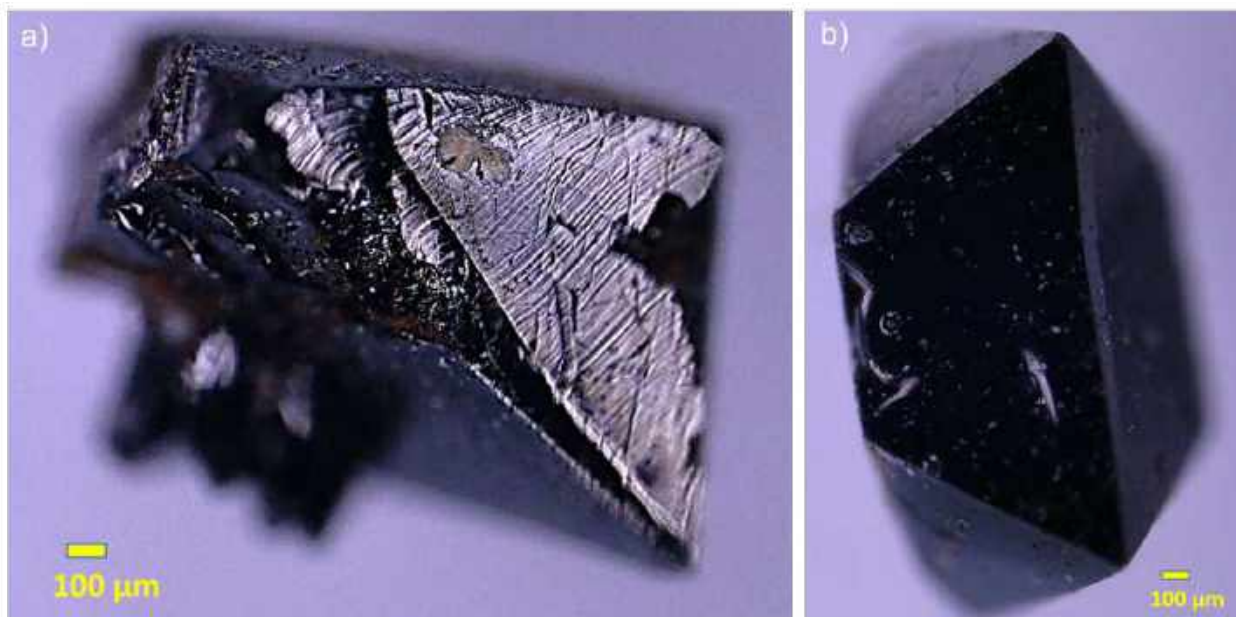


**Figure S4.** a, b ) Optical microscopic images of crystals having pyramidal facets.



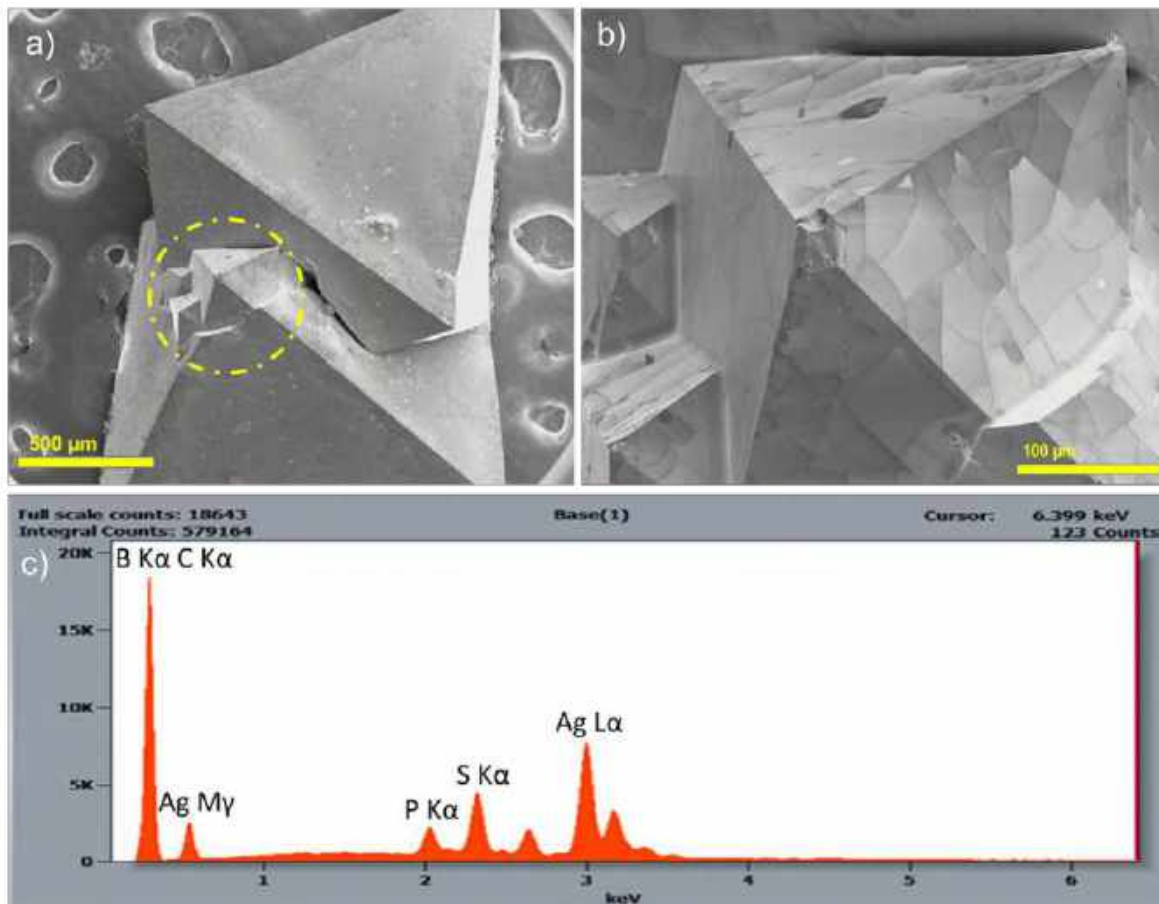


**Figure S5.** The FESEM microscopic image of a single crystal presenting different crystalline planes, a) lower magnification and b) higher magnification. c) The EDS spectrum indicates the presence of respective elements.

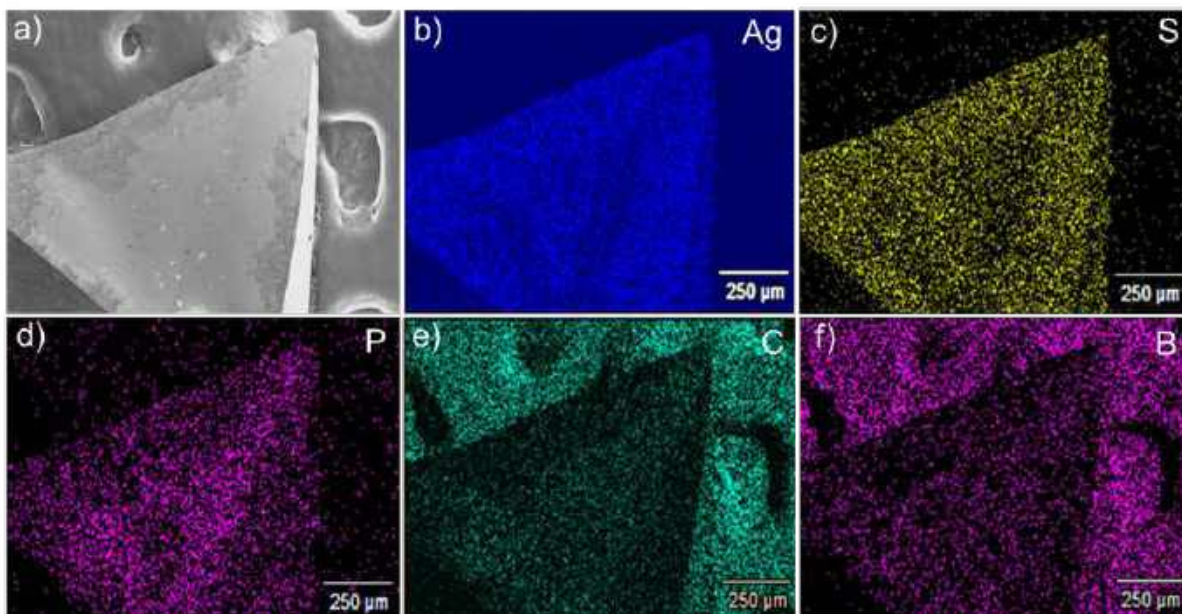


**Figure S6.** a) The FESEM image of a single crystal, b-f) the collected EDS elemental mapping of the same crystal, showing the respective elements of Ag, S, P, C and B, respectively.

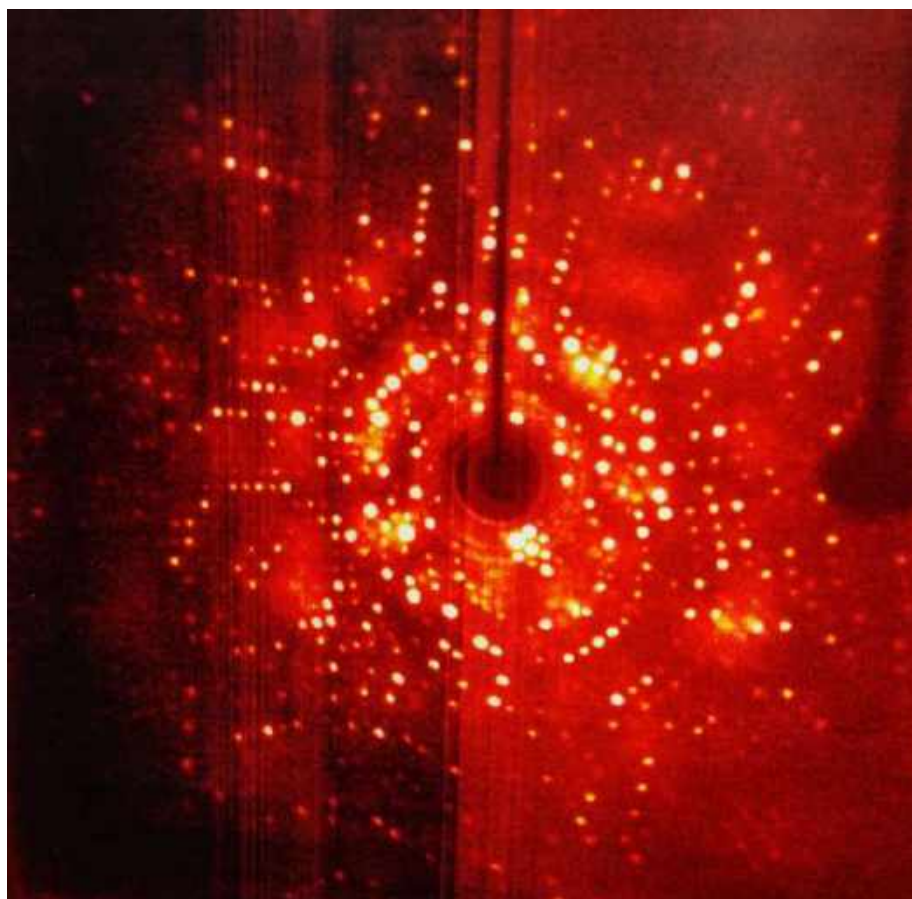


**Figure S7.** The collected frame of X-ray diffraction spots, indicating good crystallinity of these pyramidal crystals.

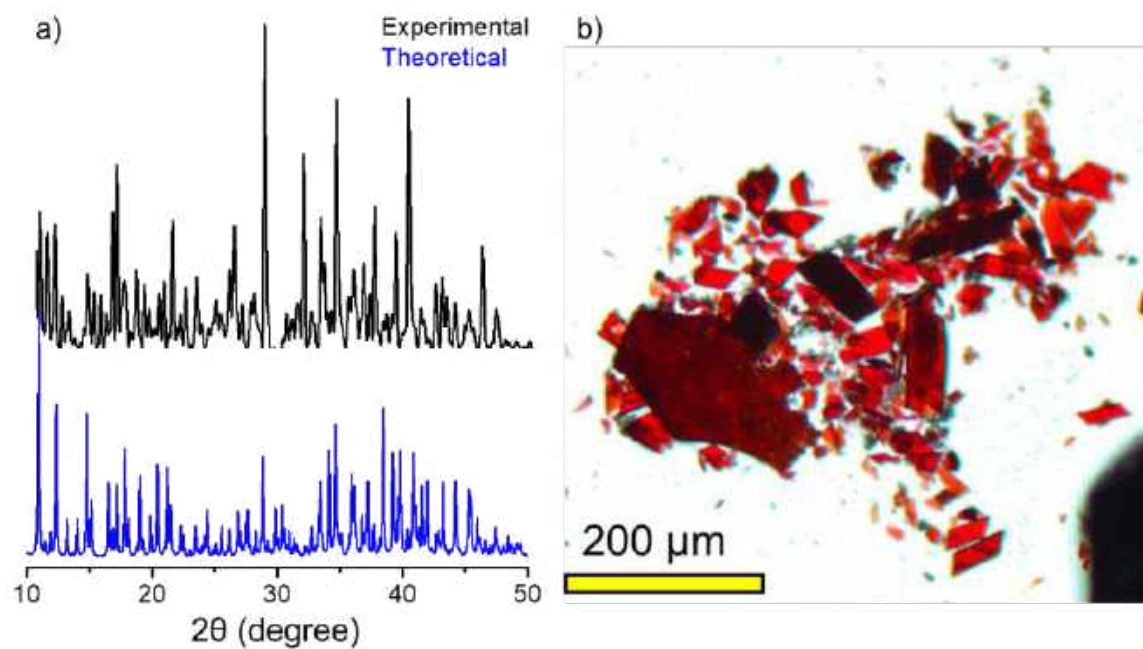


**Figure S8.** a) Experimental PXRD pattern of  $\text{Ag}_{21}$  microcrystals in comparison with the theoretical pattern. b) Microscopic image of respective microcrystals used for PXRD measurement.

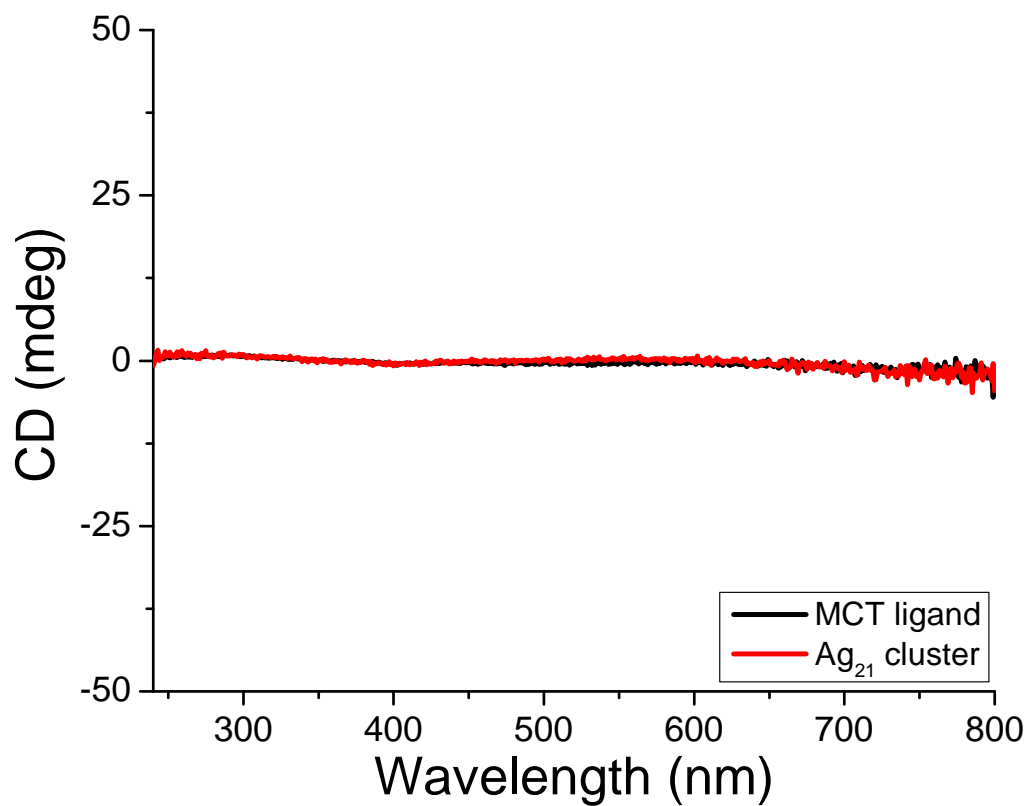


**Figure S9.** Circular dichroism (CD) spectra of Ag<sub>21</sub> cluster along with MCT ligand. Nearly zero CD spectral signature indicates the achiral nature of the cluster in DCM solution.

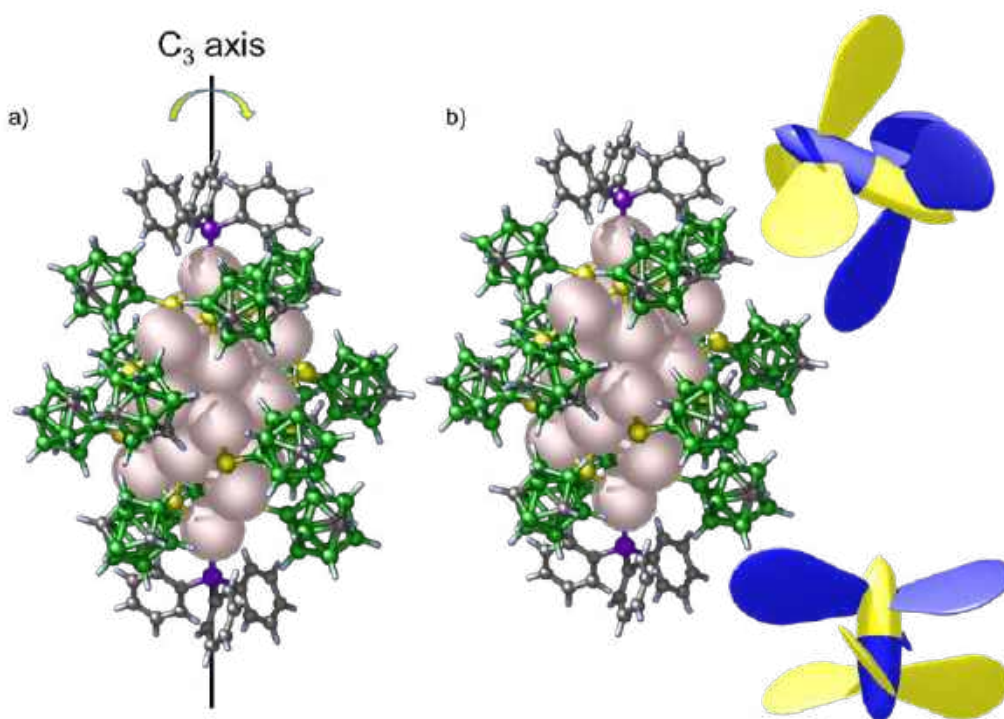


**Figure S10.** a) The C<sub>3</sub> axis present in the nanomolecule. b) Orientation of carboranes also viewed as an assembly of double rotors. Color code : light purple = silver, green = boron, violet = phosphorous, yellow = sulphur, black = carbon, white = hydrogen.



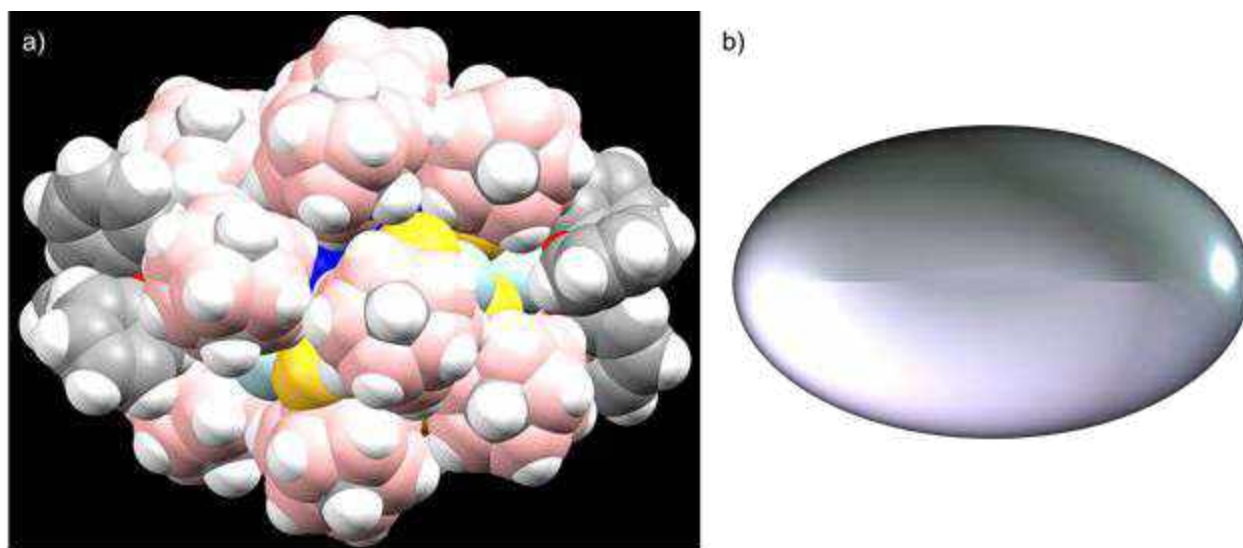


**Figure S11.** a) The space filling view of the Ag<sub>21</sub> nanomolecule has two TPP in its head and tail positions. b) A schematic representation of oval shape, which correlates with the structure.

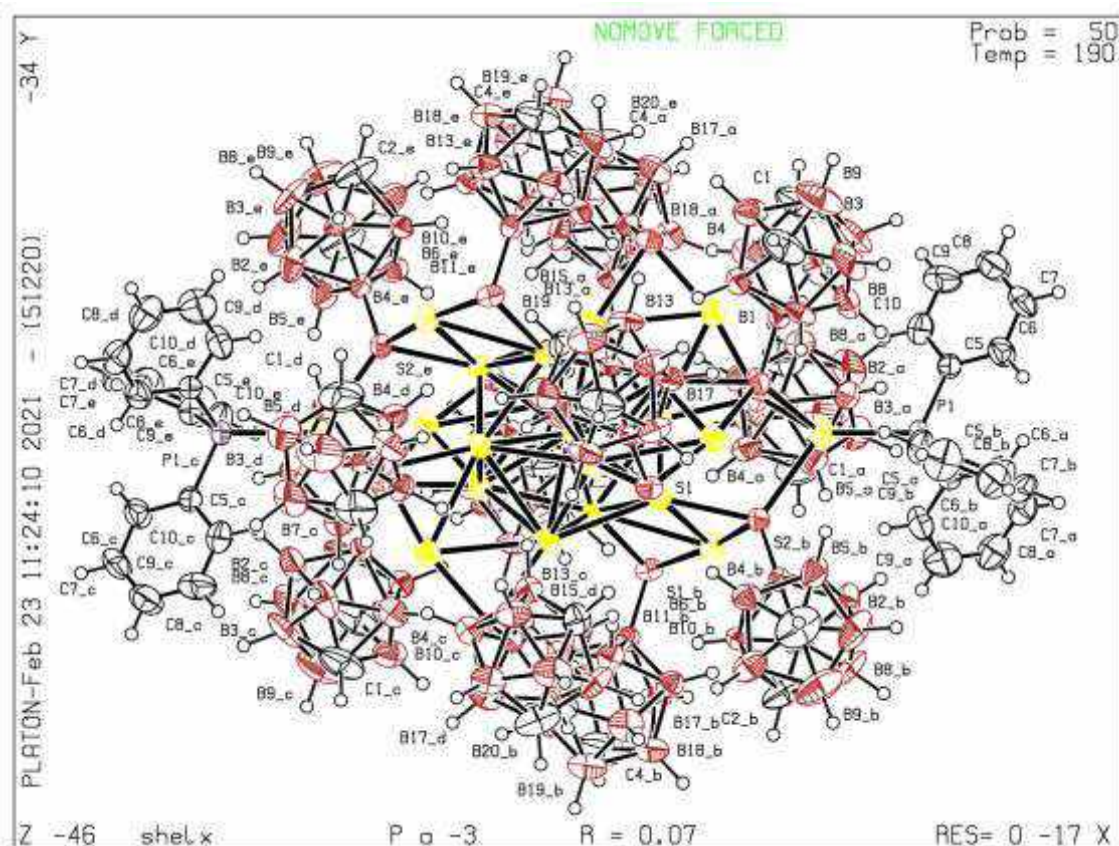


**Figure S12.** The ORTEP molecular structure of [Ag<sub>21</sub>(MCT)<sub>12</sub>(TPP)<sub>2</sub>] nanocluster.

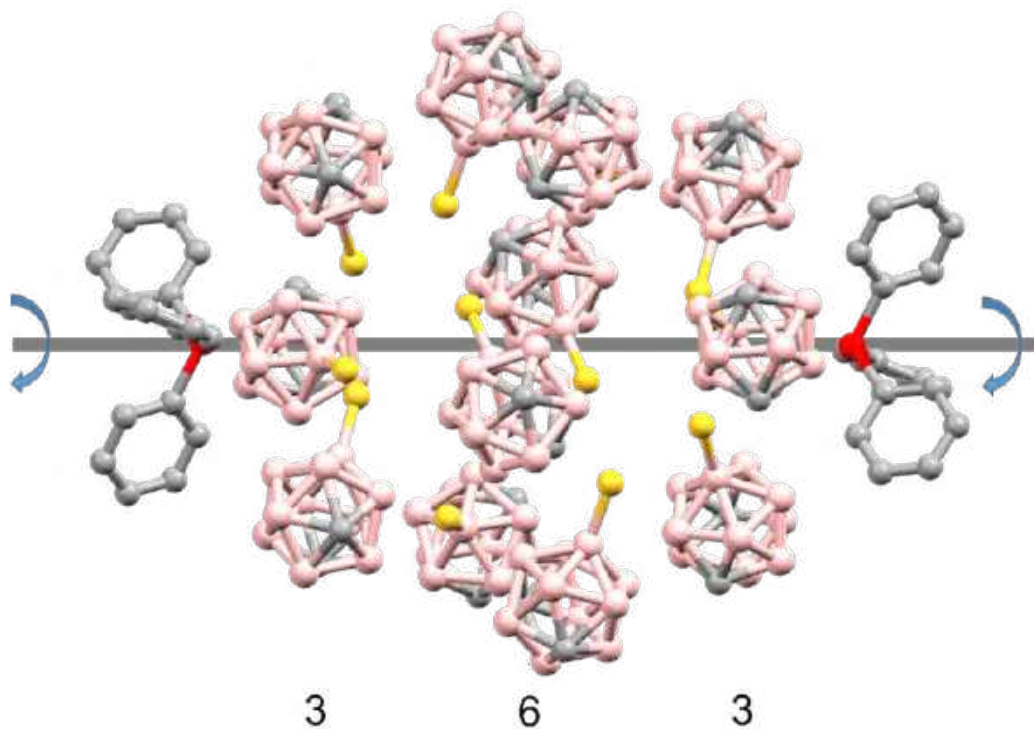


**Figure S13.** The arrangement of the twelve carborane ligands in 3: 6: 3 fashion along the P-P axis.

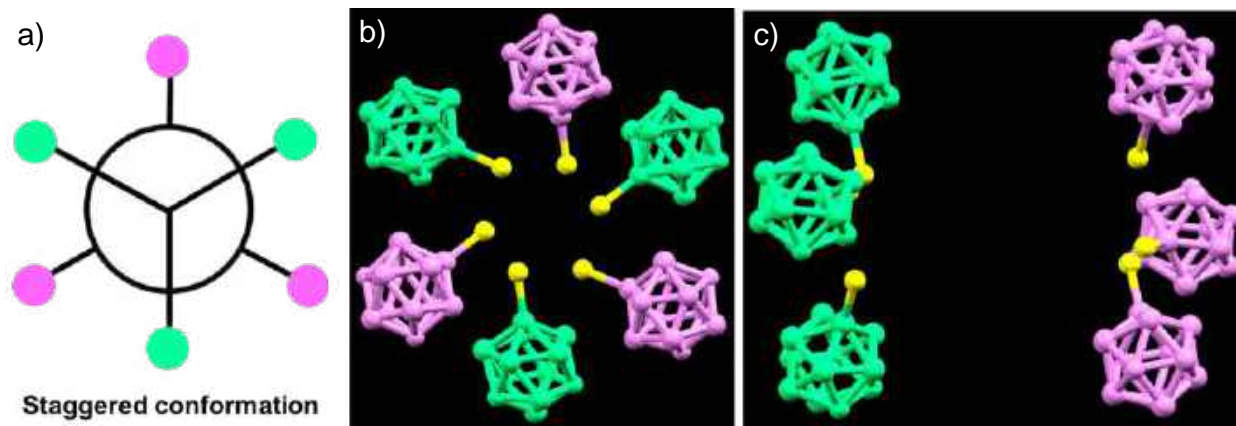


**Figure S14.** a) Schematic representation of the staggered conformation. b) Top view and c) side view of the respective carboranes. Atomic color code: green = top three carboranes and pink = bottom three carboranes.



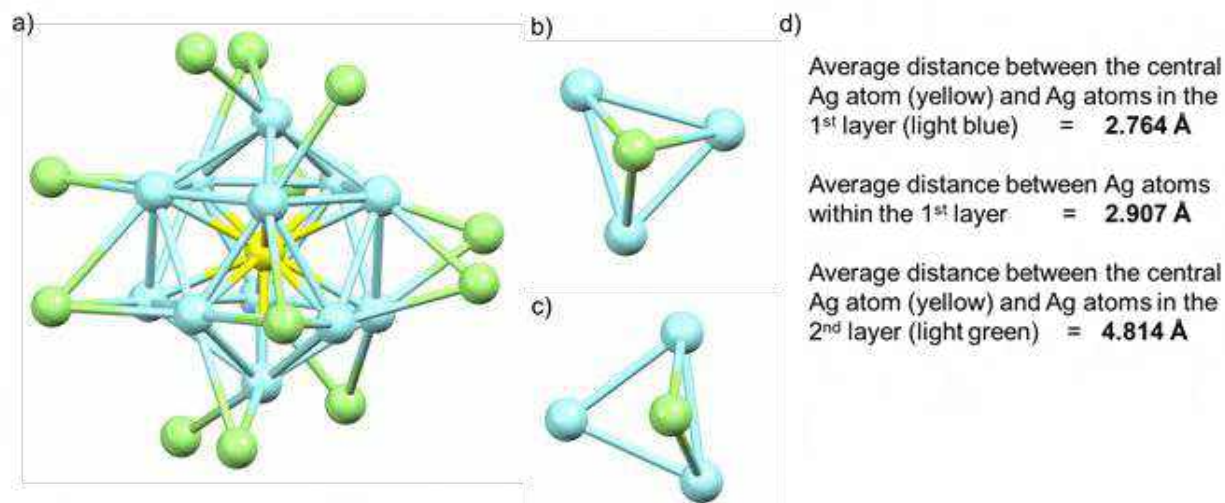


**Figure S15.** a) Atomic arrangements of the silver skeleton of Ag<sub>25</sub> nanocluster. b) Close to face-centred ( $\mu_3$ ) outer shell Ag atom configuration. c) Bridging off-centred ( $\mu_2$ ) outer shell Ag atom configuration. d) Different types of average intermetallic Ag-Ag bond distances. All atoms presented are silver here.

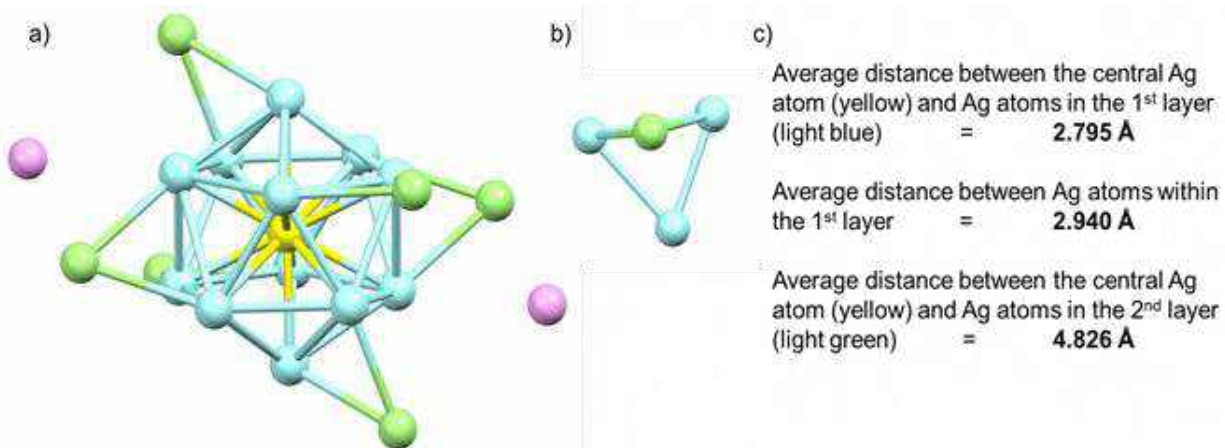


**Figure S16.** a) Atomic arrangements of the silver skeleton structure of our Ag<sub>21</sub> nanocluster. b) Bridging off-centred ( $\mu_2$ ) outer shell Ag atom configuration. c) Different types of average intermetallic Ag-Ag bond distances. All atoms presented are silver here.

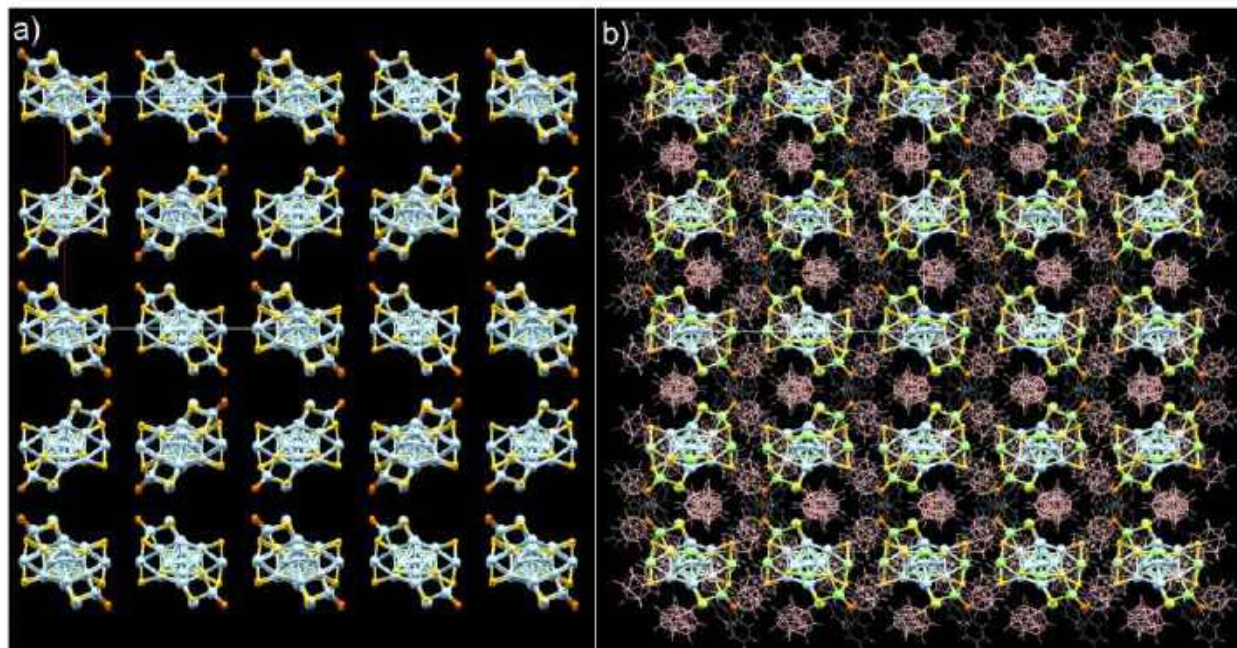


**Figure S17.** Extended view of intercluster packing along the axial direction of a) Ag<sub>21</sub>S<sub>12</sub>P<sub>2</sub> unit, and b) the full structure of Ag<sub>21</sub> nanocluster with both MCT and TPP ligands.

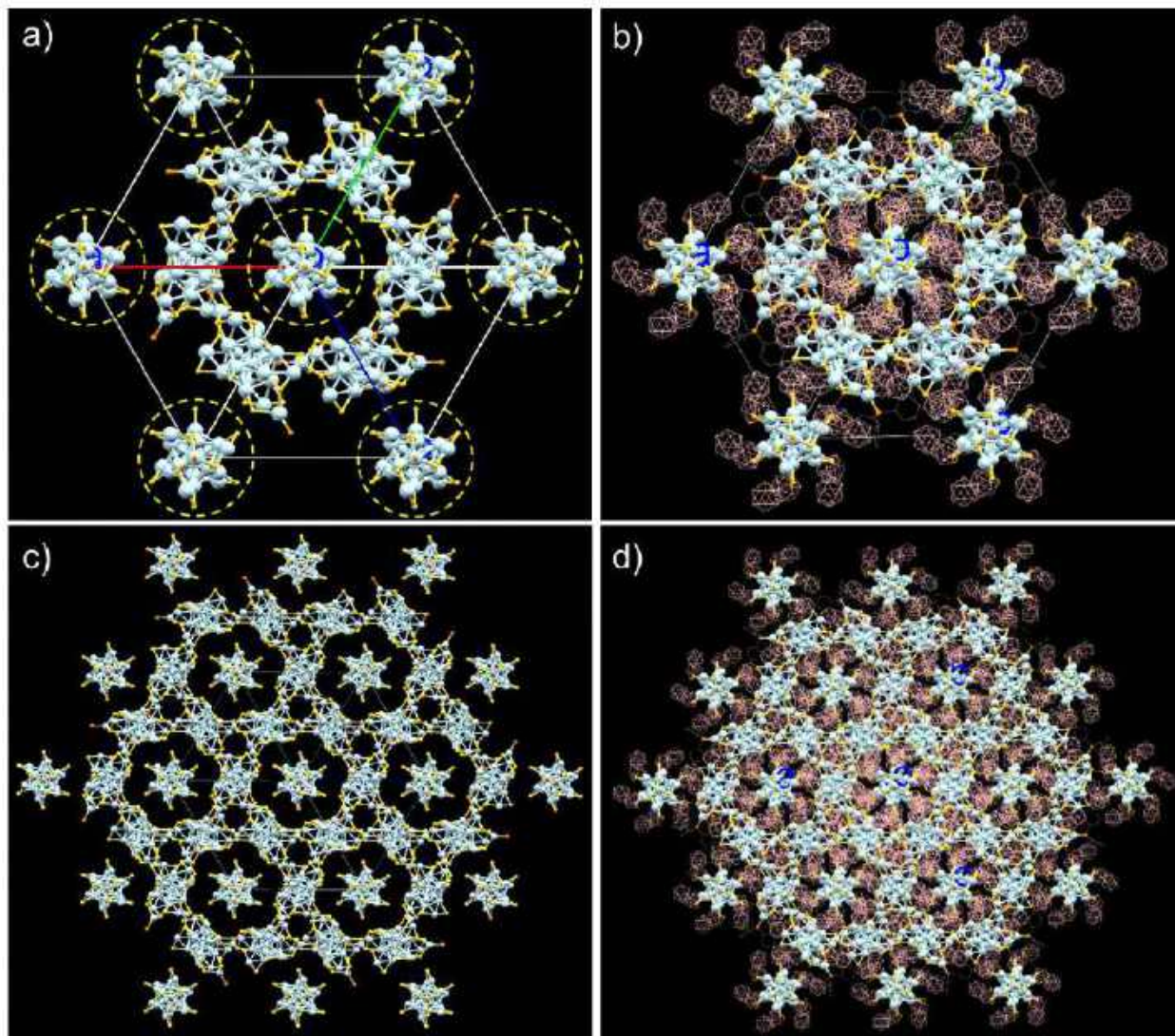


**Figure S18.** Intercluster packing along o-corner of the unit cell of a)  $\text{Ag}_{21}\text{S}_{12}\text{P}_2$  unit and b) full structure of  $\text{Ag}_{21}$  nanocluster. Encircled clusters have propeller orientation.  $2 \times 2 \times 2$  packing of c)  $\text{Ag}_{21}\text{S}_{12}\text{P}_2$  unit and d) full structure of  $\text{Ag}_{21}$  nanocluster. Hydrogen atoms are removed for clarity.



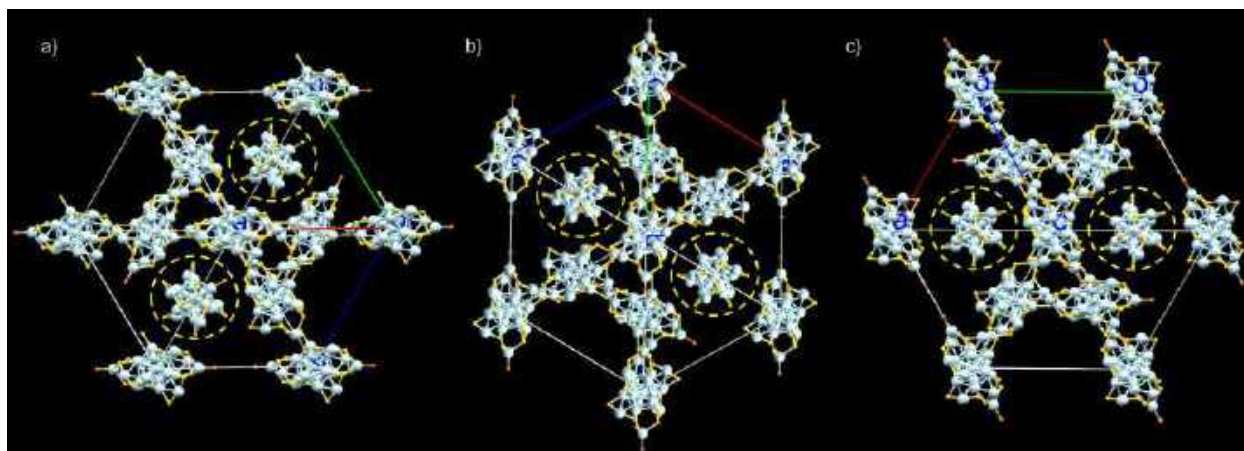


**Figure S19.** Intercluster packing of  $\text{Ag}_{21}\text{S}_{12}\text{P}_2$  unit along a) a, b) b and c) c-corners of the unit cell of  $\text{Ag}_{21}$  nanocluster. Encircled clusters have propeller orientation.

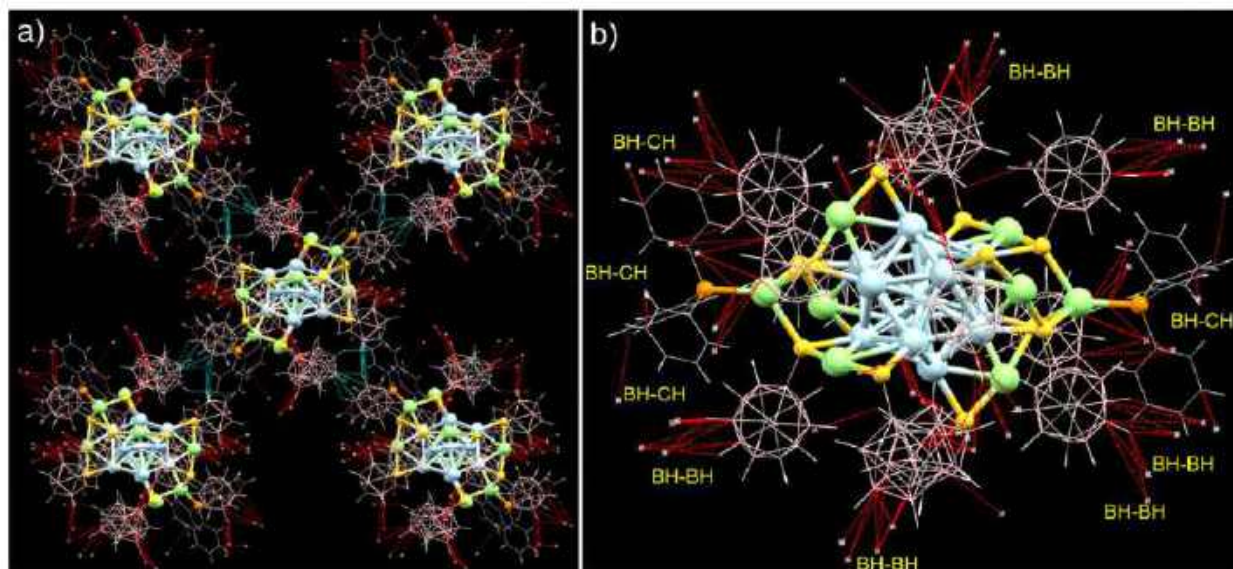


**Figure S20.** a, b) Intercluster packing of  $\text{Ag}_{21}$  shows the presence of several BH-BH and BH-CH interactions.

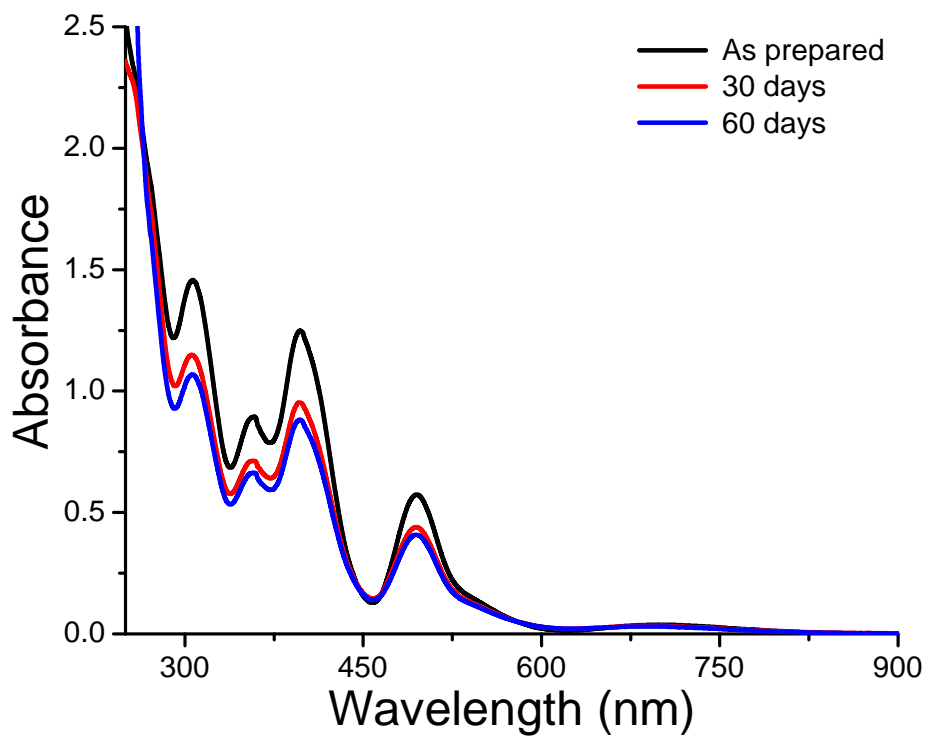


**Figure S21.** UV-vis absorption spectra of  $\text{Ag}_{21}$  nanocluster, indicating its stability up to 60 days.

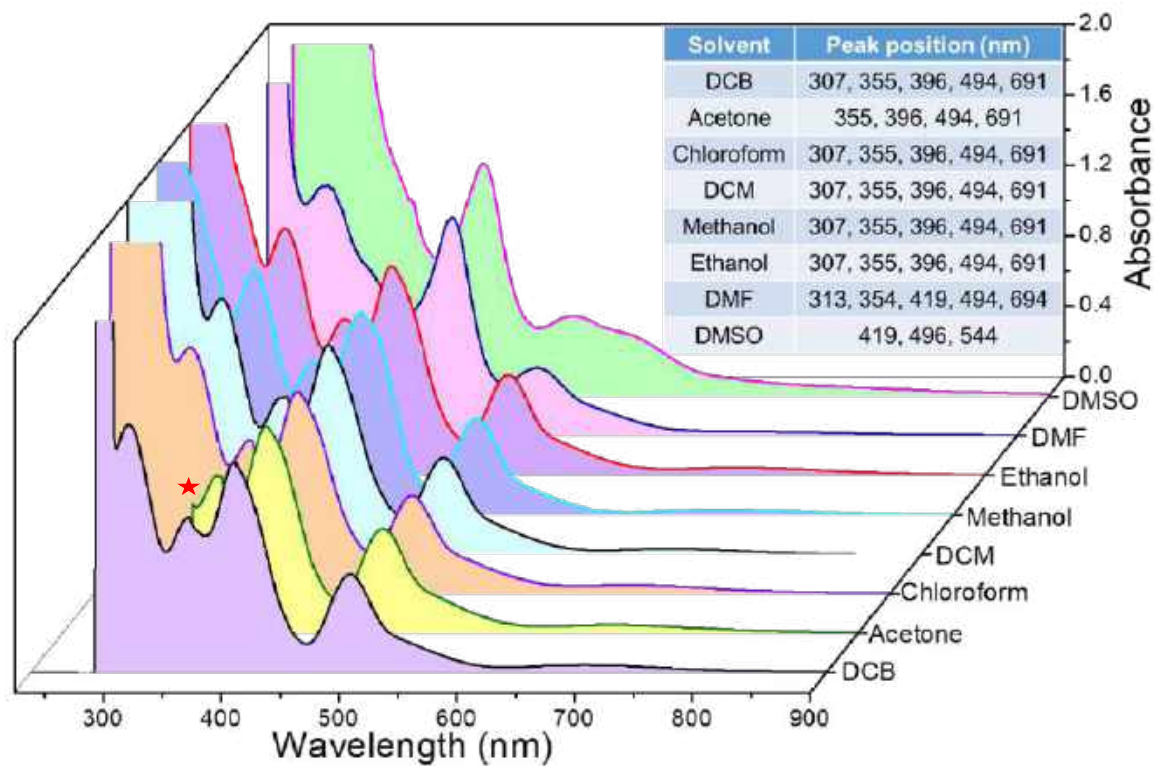


**Figure S22.** UV-vis absorption spectra of  $\text{Ag}_{21}$  nanocluster measured in different solvents. Identical peak pattern and position were observed in DCB, acetone, chloroform, DCM, methanol and ethanol solvents, whereas DMF and DMSO show difference in spectra due to solvatochromic effect. The inflection labeled \* indicates spectral cut-off in acetone.



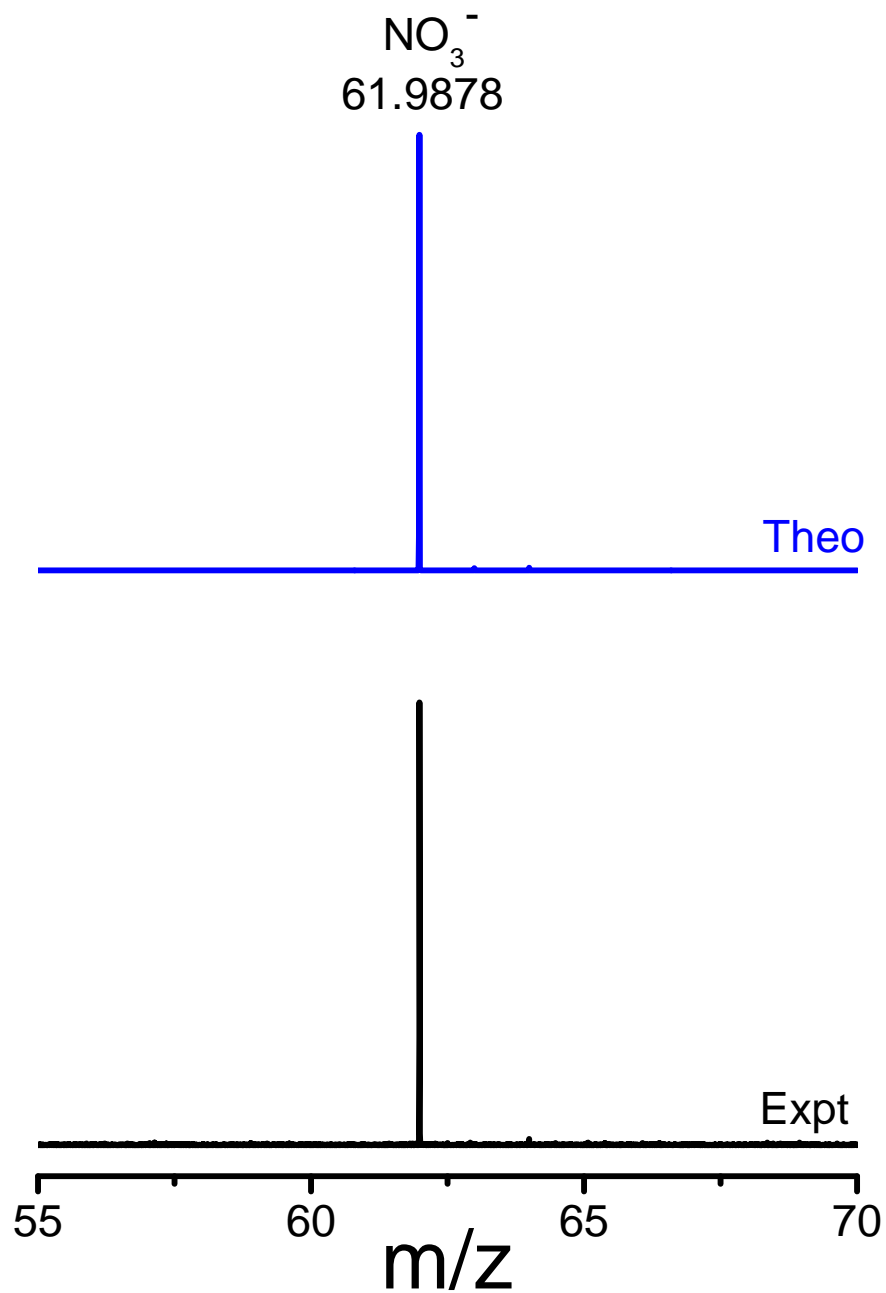


**Figure S23.** The experimental mass spectrum of  $\text{Ag}_{21}$  crystals in negative ion mode shows the presence of  $\text{NO}_3^-$  as a counter ion in the crystals.

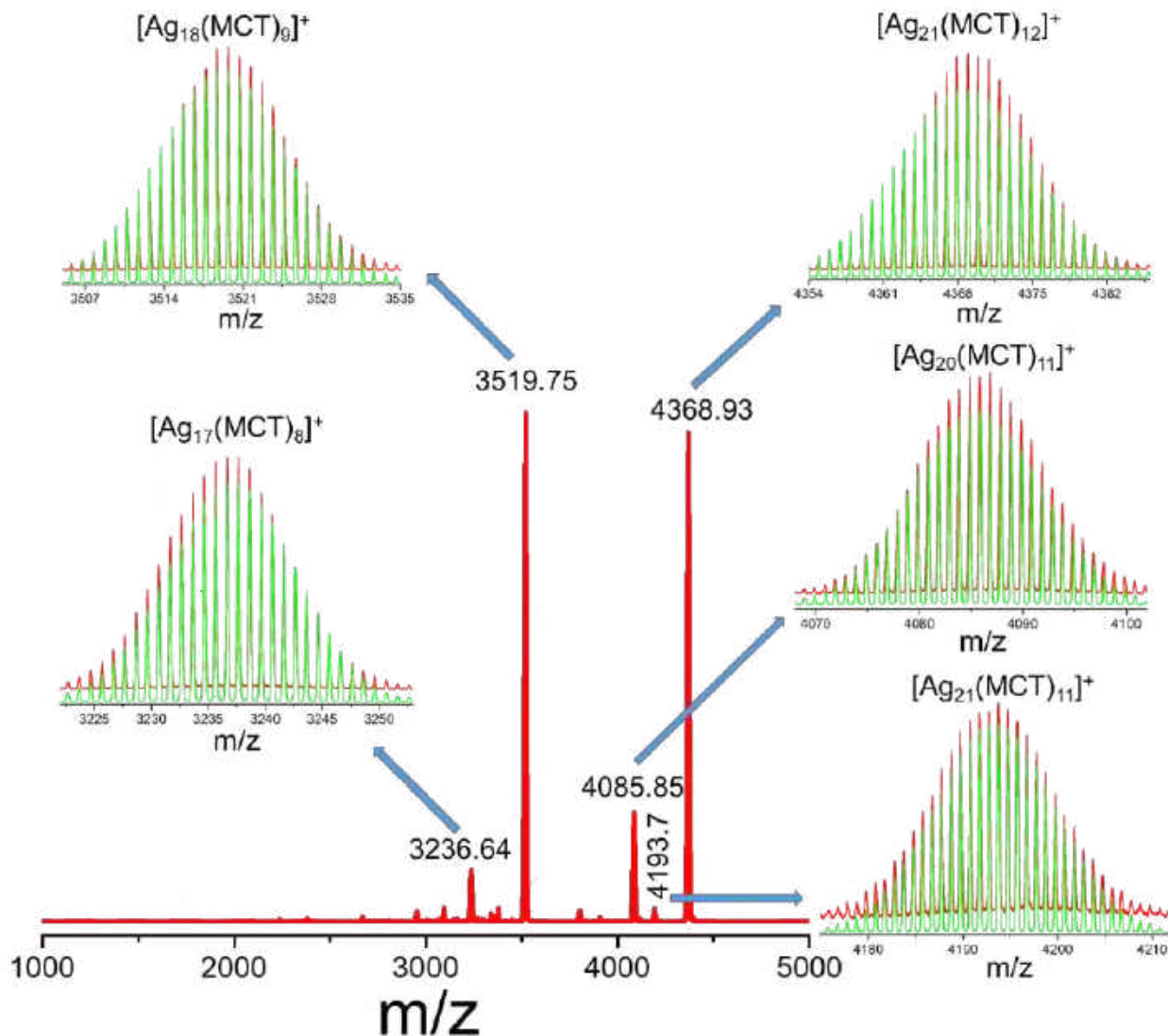


**Figure S24.** Expanded view of the MS/MS fragmentation spectrum at CE 75 in positive ion mode, indicating systematic loss of MCT and Ag units. Color codes: red = experimental spectrum; green = theoretical spectrum.

**Table S3.** Correlations between peak intensity and valence electron count of fragmented peaks formed at higher collision energy.

SI No	Clusters	Electron counting [Ne-L-q]	Remarks	Peak intensity
1	$[\text{Ag}_{21}(\text{MCT})_{12}(\text{TPP})_2]^+$	$[21-12-1] = 8$	Magic electrons	High
2	$[\text{Ag}_{21}(\text{MCT})_{12}(\text{TPP})]^+$	$[21-12-1] = 8$	Magic electrons	High
3	$[\text{Ag}_{21}(\text{MCT})_{12}]^+$	$[21-12-1] = 8$	Magic electrons	High
4	$[\text{Ag}_{21}(\text{MCT})_{11}]^+$	$[21-11-1] = 9$	Non-magic electrons	Low
5	$[\text{Ag}_{20}(\text{MCT})_{11}]^+$	$[20-11-1] = 8$	Magic electrons	High
6	$[\text{Ag}_{20}(\text{MCT})_{10}]^+$	$[20-10-1] = 9$	Non-magic electrons	Low
7	$[\text{Ag}_{19}(\text{MCT})_{10}]^+$	$[19-10-1] = 8$	Magic electrons	High
8	$[\text{Ag}_{19}(\text{MCT})_9]^+$	$[19-9-1] = 9$	Non-magic electrons	Low
9	$[\text{Ag}_{18}(\text{MCT})_9]^+$	$[18-9-1] = 8$	Magic electrons	High
10	$[\text{Ag}_{18}(\text{MCT})_8]^+$	$[18-8-1] = 9$	Non-magic electrons	Low
11	$[\text{Ag}_{17}(\text{MCT})_8]^+$	$[17-8-1] = 8$	Magic electrons	High
12	$[\text{Ag}_{17}(\text{MCT})_7]^+$	$[17-7-1] = 9$	Non-magic electrons	Low
13	$[\text{Ag}_{16}(\text{MCT})_7]^+$	$[16-7-1] = 8$	Magic electrons	High
14	$[\text{Ag}_{16}(\text{MCT})_6]^+$	$[16-6-1] = 9$	Non-magic electrons	Low
15	$[\text{Ag}_{15}(\text{MCT})_6]^+$	$[15-6-1] = 8$	Magic electrons	High

16	$[\text{Ag}_{15}(\text{MCT})_5]^+$	$[15-5-1] = 9$	Non-magic electrons	Low
17	$[\text{Ag}_{14}(\text{MCT})_5]^+$	$[14-5-1] = 8$	Magic electrons	High
18	$[\text{Ag}_{14}(\text{MCT})_4]^+$	$[14-4-1] = 9$	Non-magic electrons	Low
19	$[\text{Ag}_{13}(\text{MCT})_4]^+$	$[13-4-1] = 8$	Magic electrons	High

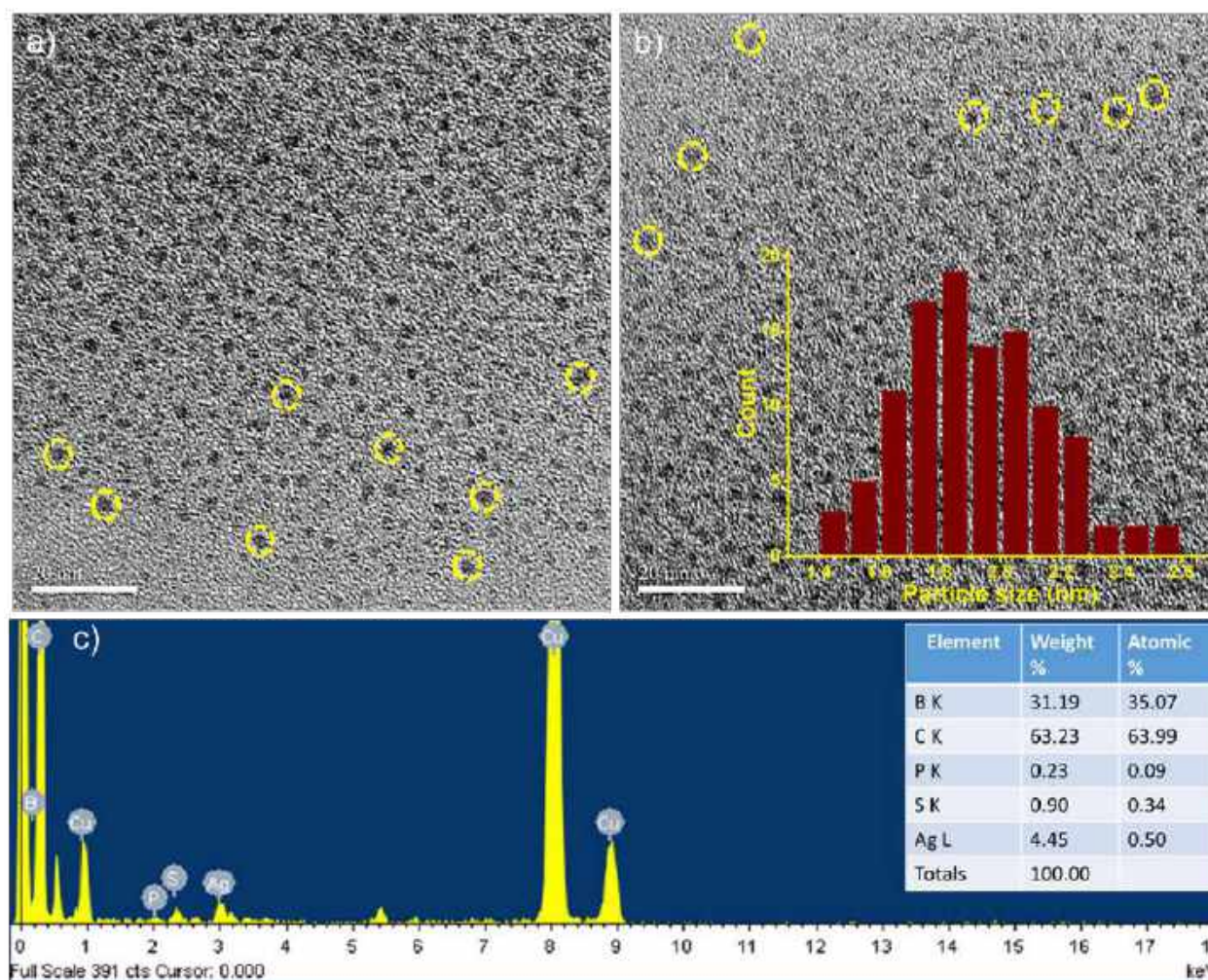


**Figure S25.** a, b) TEM images of the  $\text{Ag}_{21}$  nanocluster showed its particle nature. Inset shows the size distribution profile of 100 particles. Average particle dimension is  $1.91 \pm 0.2$  nm. c) The EDS spectrum of the nanocluster shows the existing elements (inset shows the atomic and elemental weight % of the existing elements).

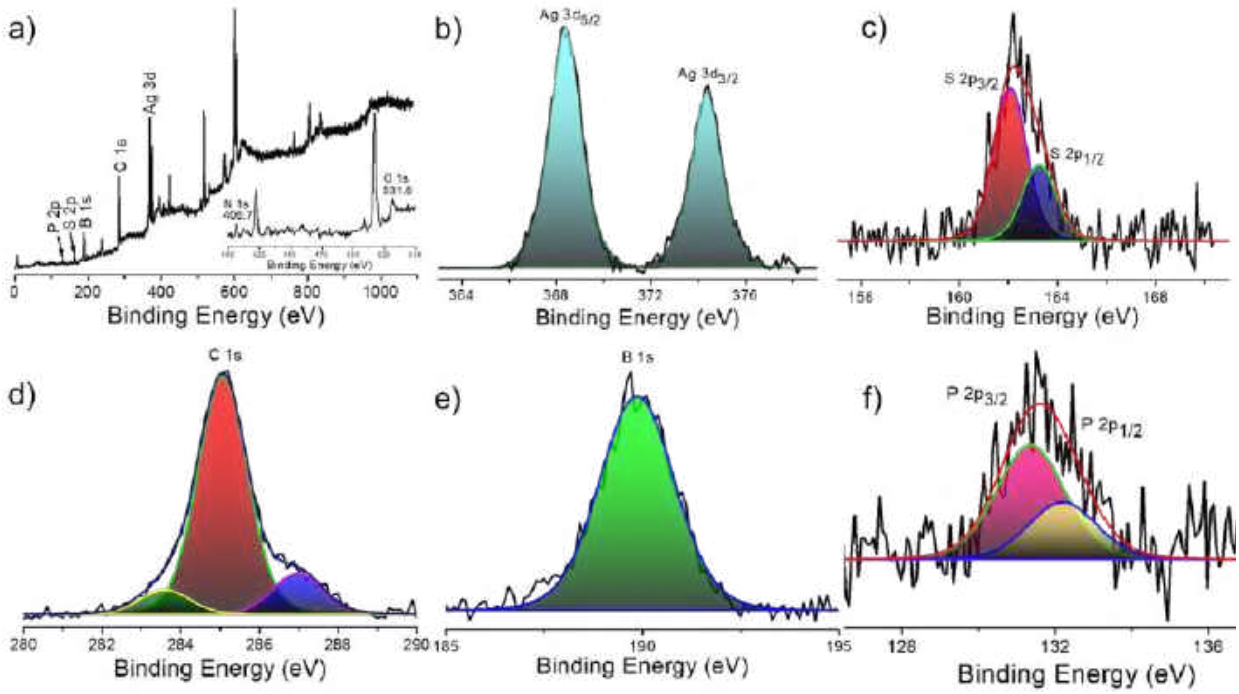


**Figure S26.** a) XPS survey spectrum of Ag<sub>21</sub> nanocluster showed the spectral signature of respective elements. Inset shows the N 1s and O 1s peaks at 406.7 and 531.6 eV, respectively due to nitrate counter ion. Spectral fitting of b) Ag 3d region, c) S 2p region, d) C 1s region, e) B 1s region and f) P 2p region.

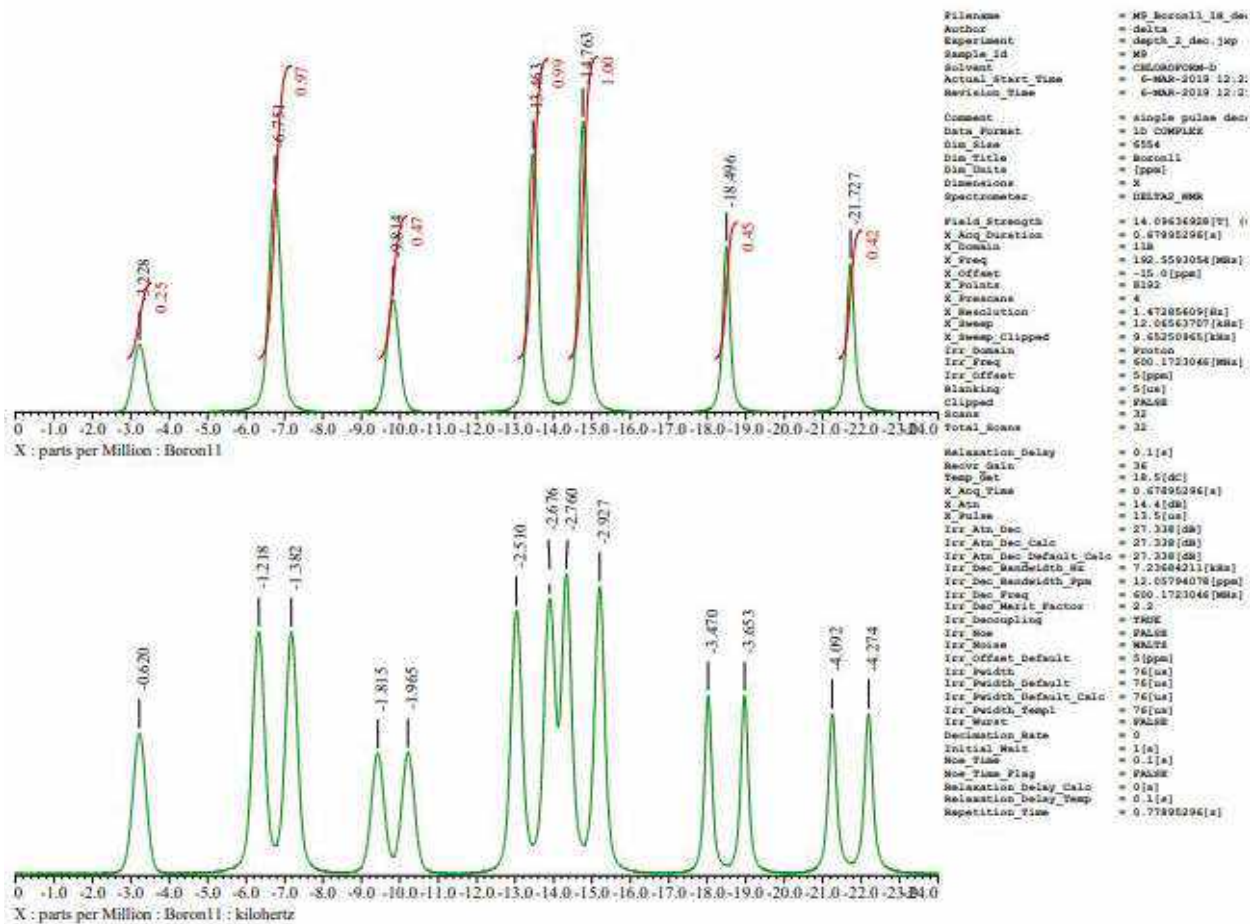


Figure S27.  $^{11}\text{B}$  NMR spectrum of MCT ligand in  $\text{CDCl}_3$  solvent.



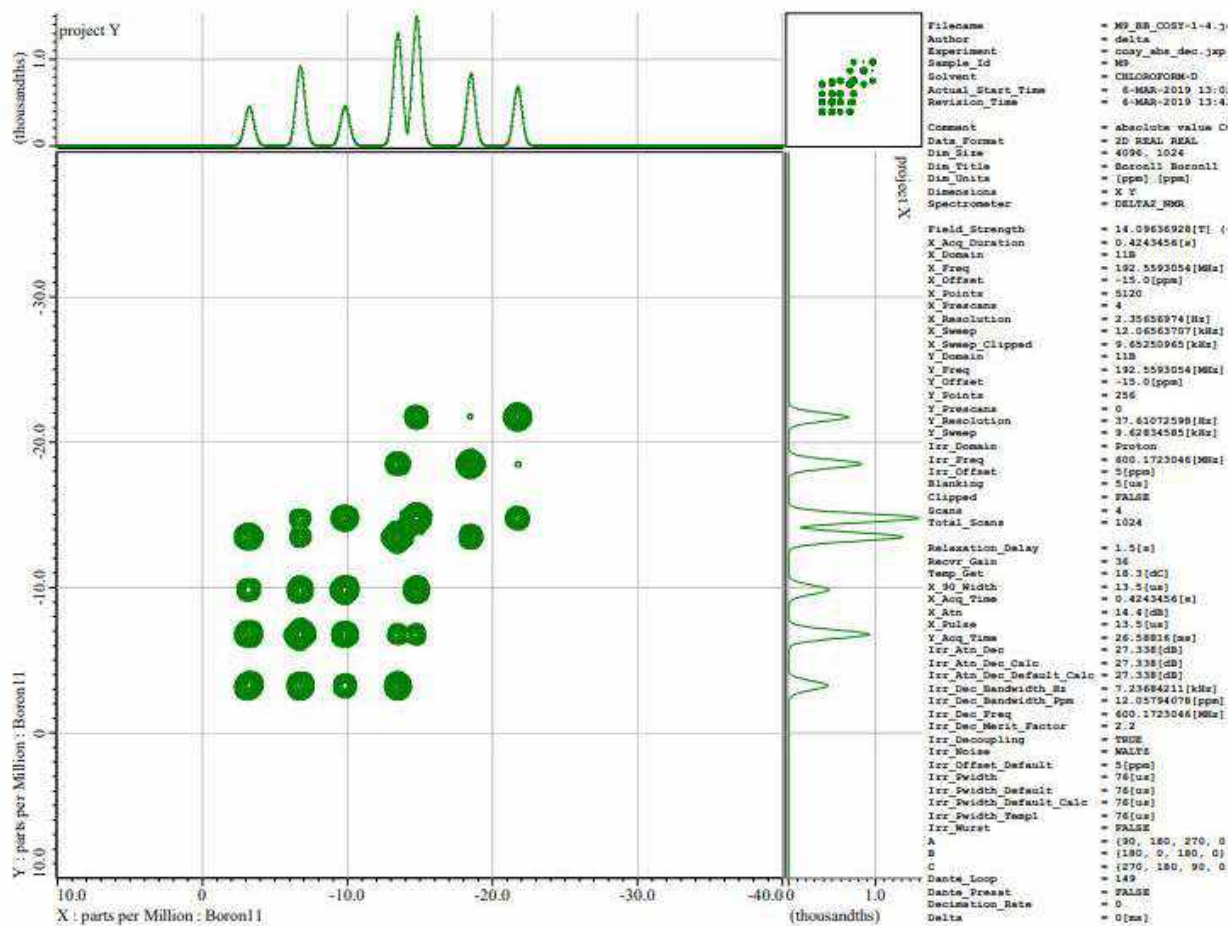


Figure S28.  $^{11}\text{B}$ - $^{11}\text{B}$  COSY NMR spectrum of MCT ligand in  $\text{CDCl}_3$  solvent.

Table S4.  $^{11}\text{B}$  NMR chemical shift data for the MCT ligand, measured in  $\text{CDCl}_3$  solvent.

MCT	
Assign.	$\delta(^{11}\text{B})$
1,7	-
2	-18.5
3,8	-14.8
4,12	-6.8
5,11	-13.5
6	-21.7
9	-3.2
10	-9.8

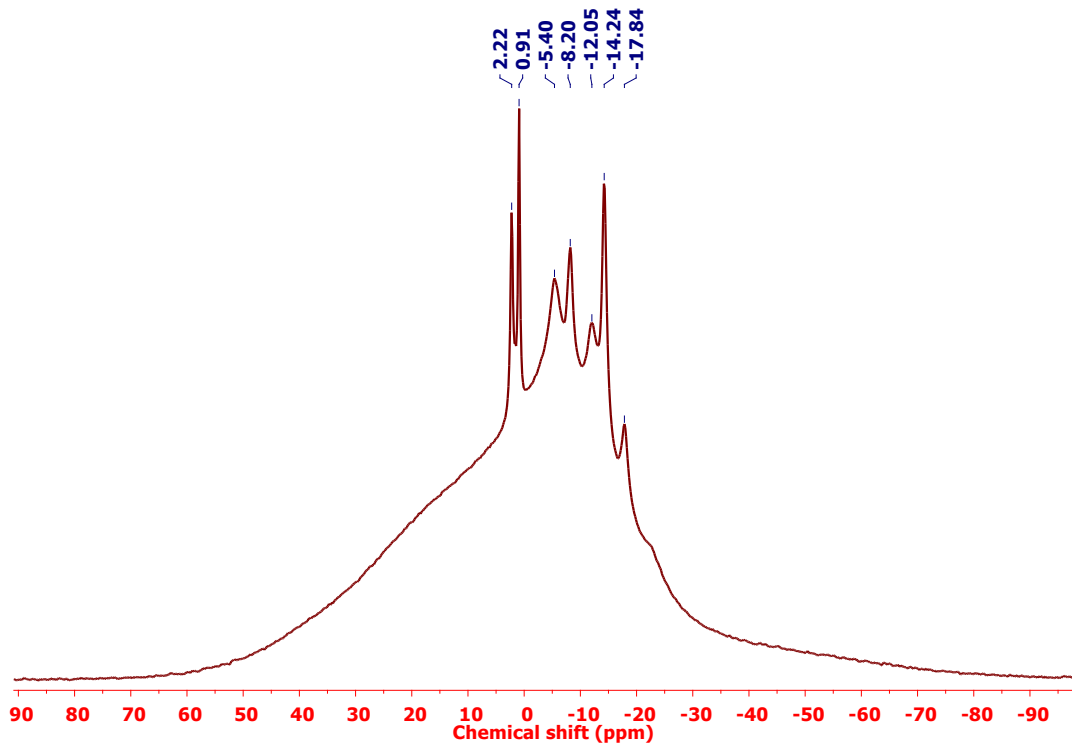


Figure S29.  $^{11}\text{B}$  NMR spectrum of  $\text{Ag}_{21}$  nanocluster in  $\text{CDCl}_3$  solvent.

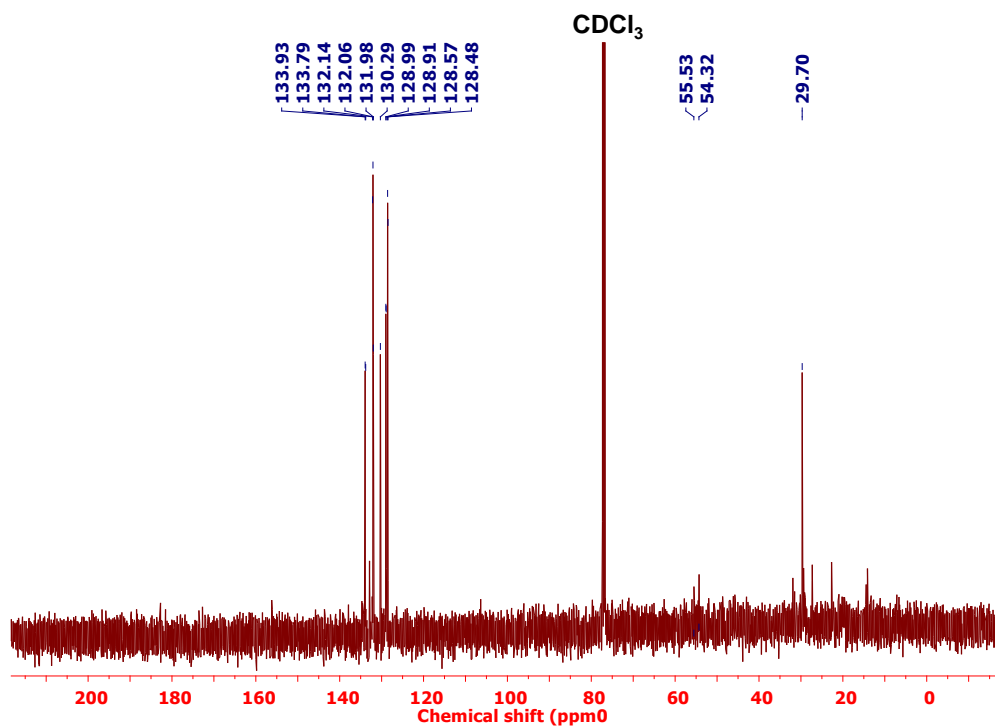


Figure S30. Proton-decoupled  $^{13}\text{C}$  NMR spectrum of  $\text{Ag}_{21}$  nanocluster in  $\text{CDCl}_3$  solvent.

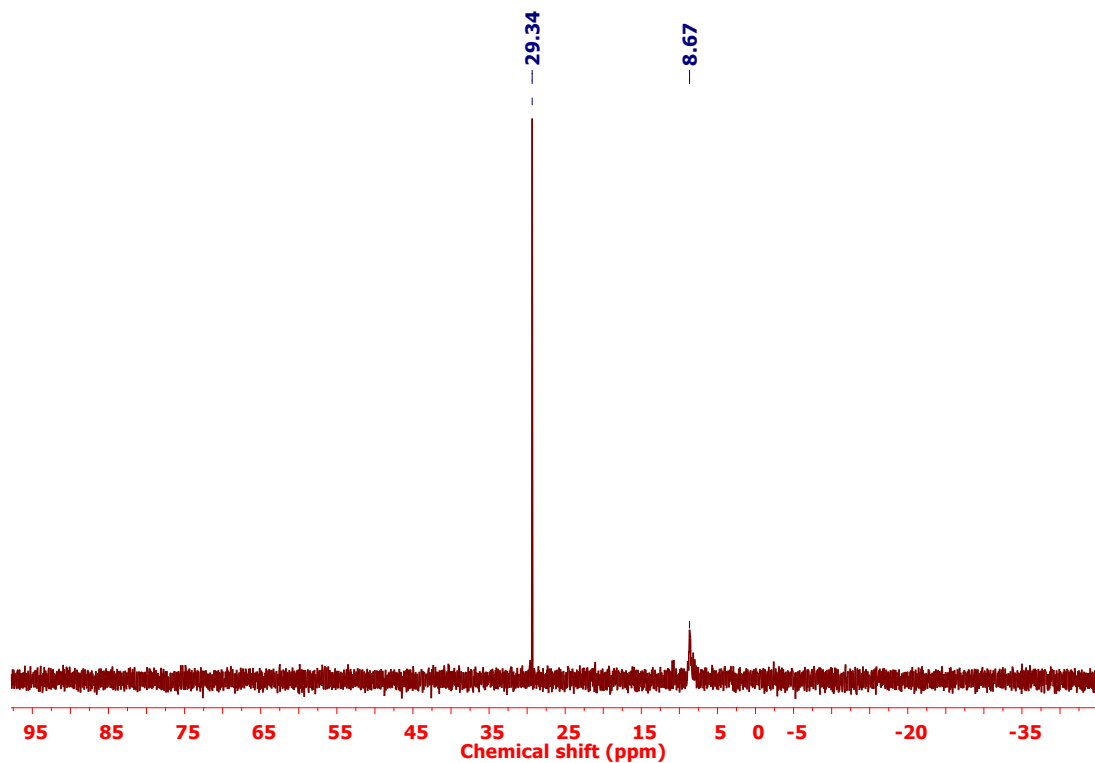


Figure S31.  $^{31}\text{P}$  NMR spectrum of  $\text{Ag}_{21}$  nanocluster in  $\text{CDCl}_3$  solvent.

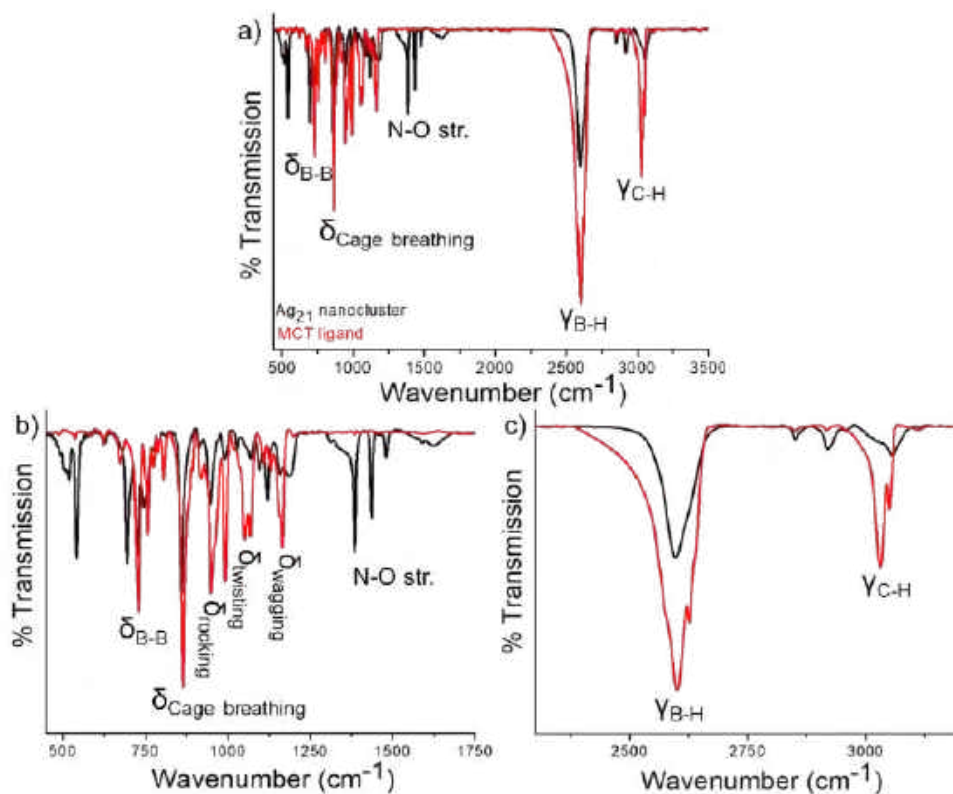
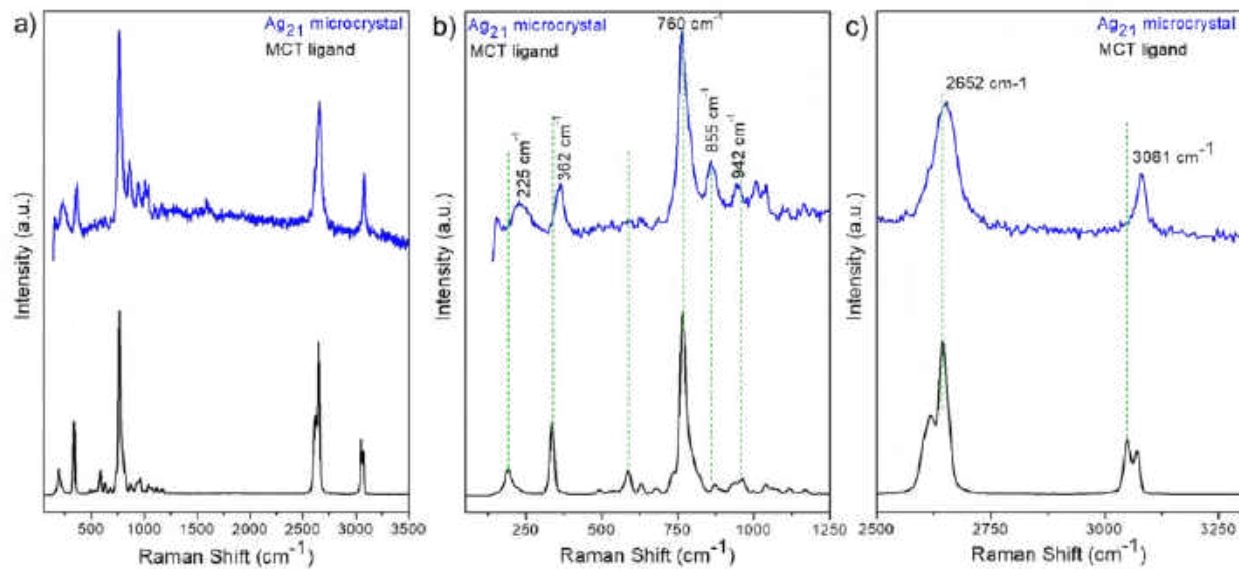


Figure S32. a) The full range FT-IR spectra of  $\text{Ag}_{21}$  in comparison with MCT ligands, b, c) expanded view of two different spectral regions, indicate the shifts of vibrational and rotational spectral features.



**Figure S33.** a) Full range comparative Raman spectra of  $\text{Ag}_{21}$  microcrystals along with MCT ligands, b, c) expanded view of two different spectral regions.

**Table S5.** Spectral assignments of vibrational Raman features of MCT ligand.

SI No	Peak position ( $\text{cm}^{-1}$ )	Spectral assignments
1.	3051, 3070	C-H stretching mode
2.	2618, 2645	B-H stretching mode + small contribution of S-H stretching mode
3.	1117, 1170	C-H bending mode
4.	1038, 1074	B-H bending mode
5.	871, 960	BBH bending mode
6.	762	Icosahedral breathing mode / pulsation of icosahedral cage
7.	586, 630, 678	BBB and BBC breathing mode
8.	191, 335, 491	B-B, B-S and B-C vibrational mode (decides cage regidity)

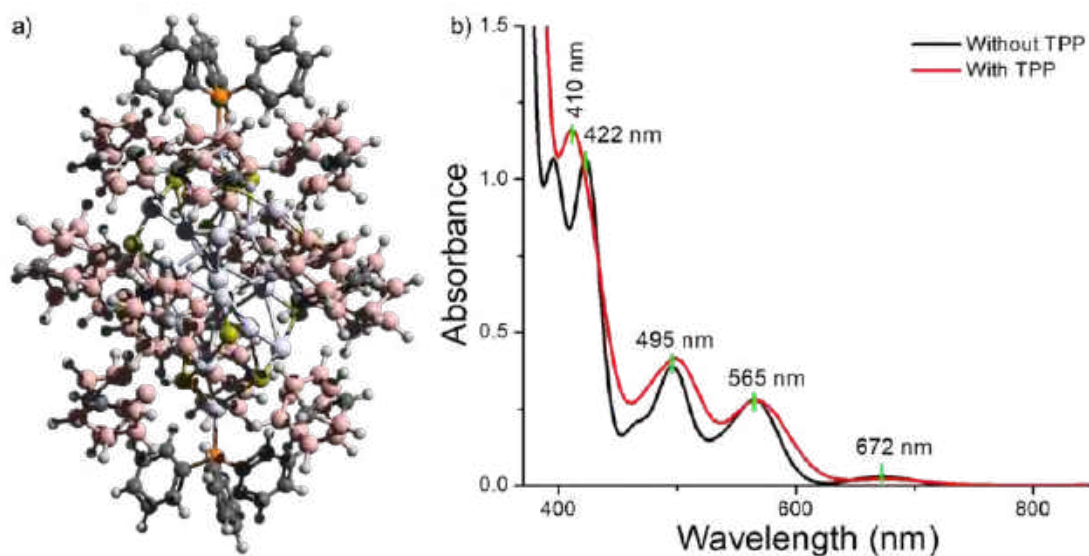


**Figure 34.** a) Theoretically optimized structure of  $\text{Ag}_{21}$  nanomolecule along with two TPP ligands. Color code: grey = silver, yellow = sulphur, pink = boron, black = carbon, orange = phosphorous, white = hydrogen. b) Theoretical absorption spectra showing nearly similar spectral feature for both the structures.

**Table S6.** Calculated oscillator strengths ( $f$ ) of transitions.

Sl. no	Respective transition (nm)	$f$ (Without TPP)	$f$ (With TPP)
1.	672	0.0291	0.0210
2.	565	0.280	0.270
3.	494	0.391	0.0414
4.	422	1.070	-
5.	410	-	1.0067

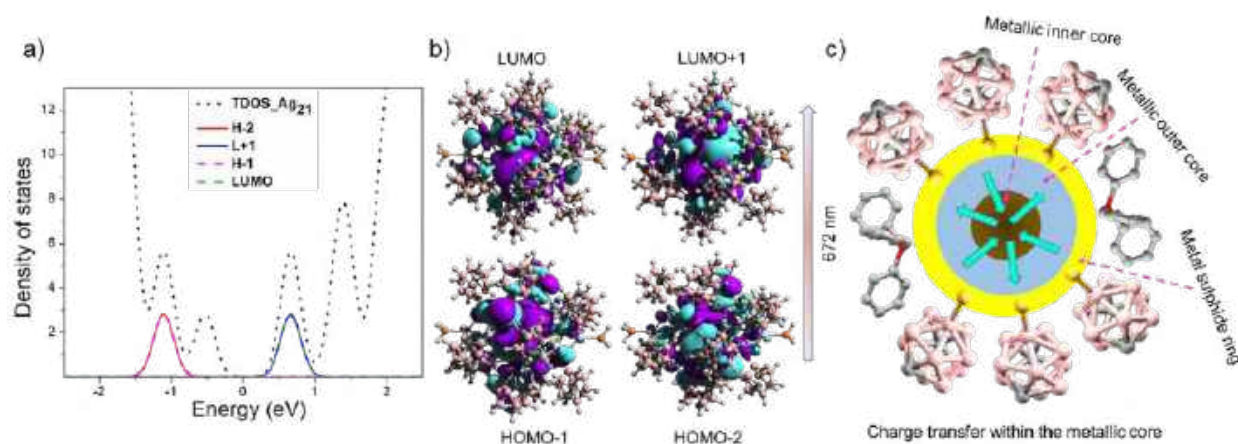


**Figure S35.** a) The DOS plots of molecular orbitals with the energy contribution for the transition at 672 nm. b) The electron density maps of molecular orbitals associated with the transition. c) Schematic representation shows associated charge transfer within the metallic core.



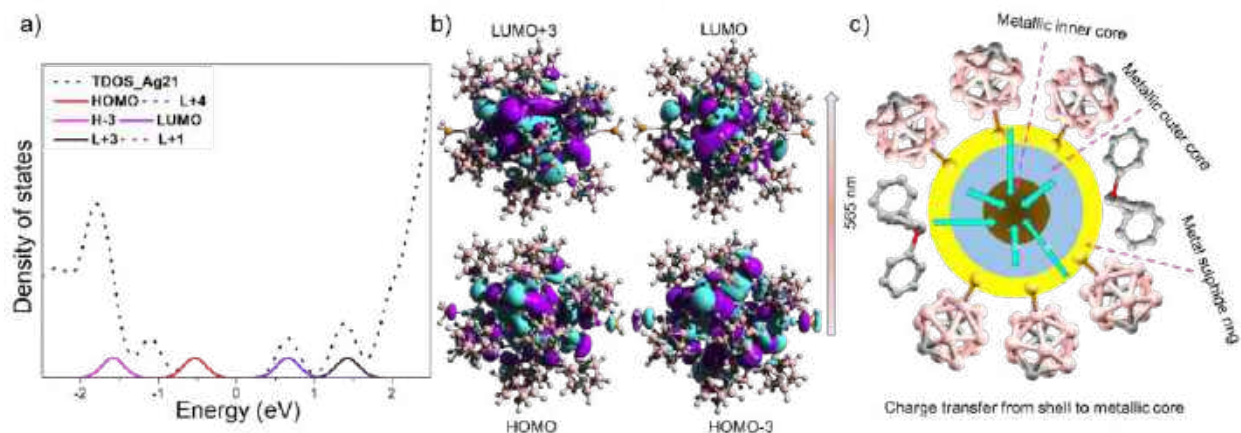


**Figure S36.** a) The DOS plots of molecular orbitals with the energy contribution for the transition at 565 nm. b) The electron density maps of molecular orbitals associated with the transition. c) Schematic representation shows associated charge transfer from the shell to the metallic core.

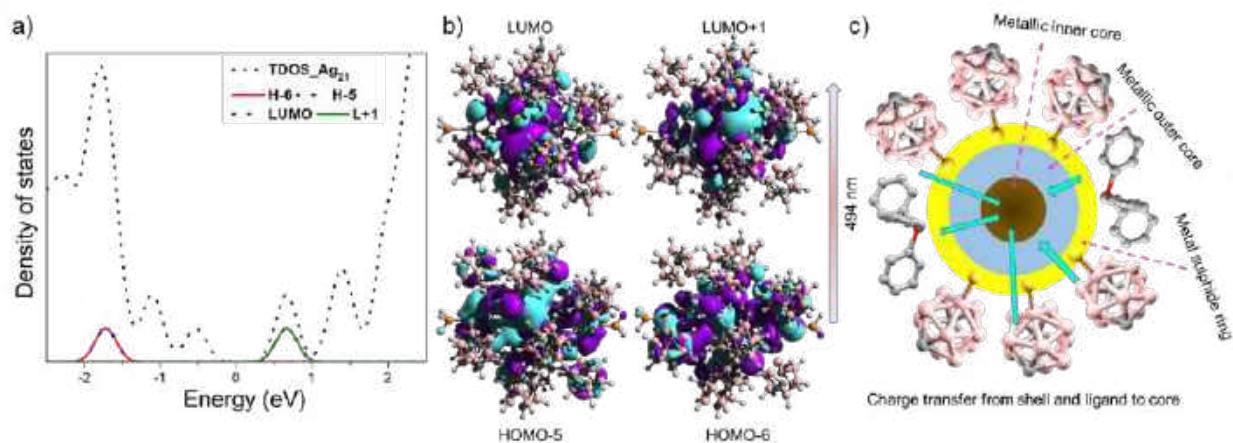


**Figure S37.** a) The DOS plots of molecular orbitals with the energy contribution for the transition at 494 nm. b) The electron density maps of molecular orbitals associated with the transition. c) Schematic representation shows associated charge transfer from the shell and ligand to the metallic core.

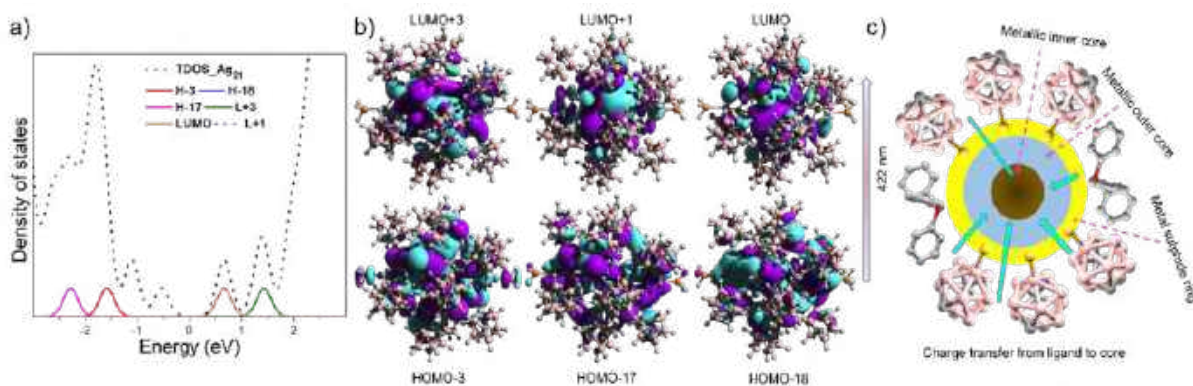


**Figure S38.** a) The DOS plots of molecular orbitals with the energy contribution for the transition at 422 nm. b) The electron density maps of molecular orbitals associated with the transition. c) Schematic representation shows associated charge transfer from the ligand to the metallic core.

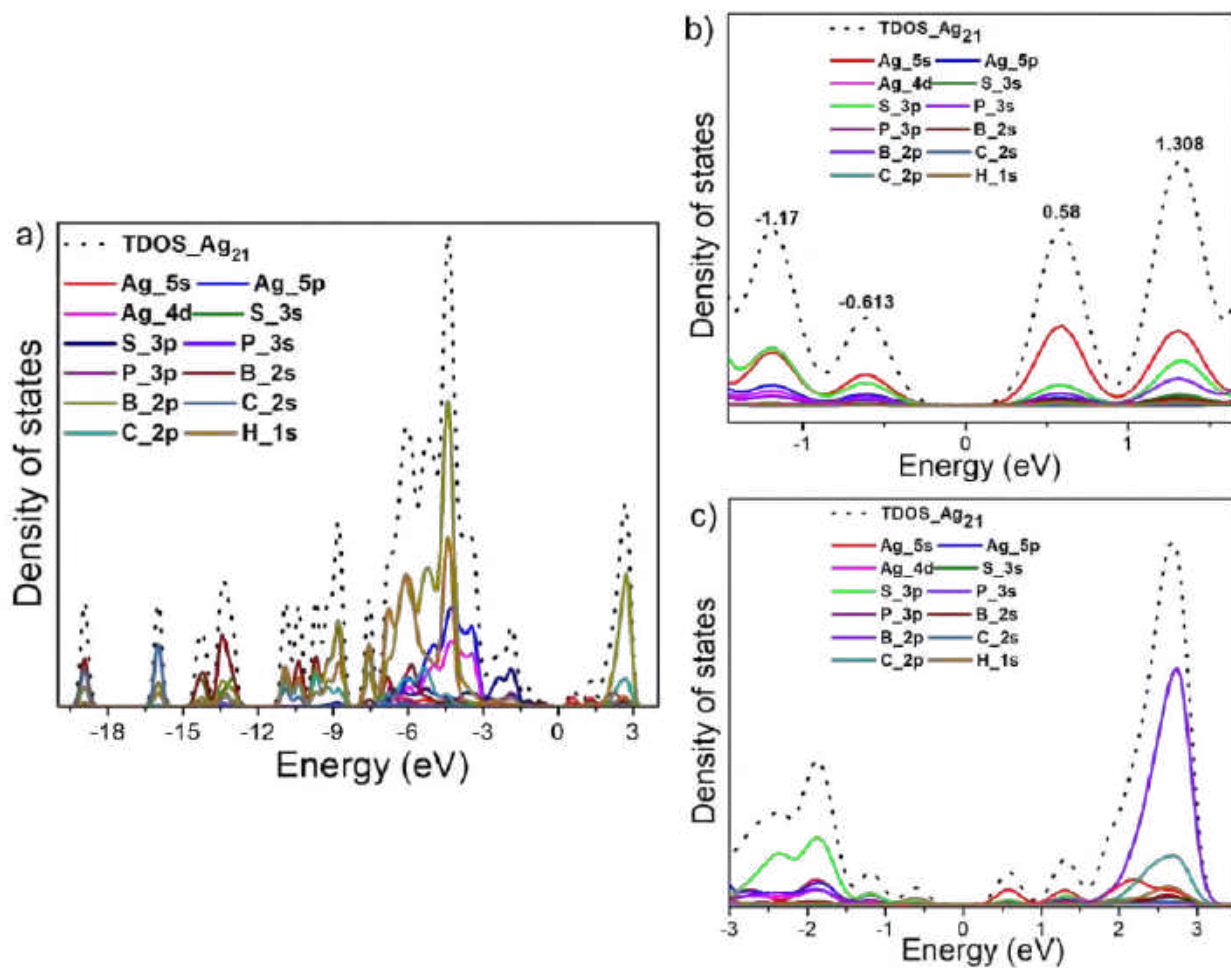


**Figure S39.** a) The full range density of states (DOS) in terms of atomic orbitals contribution. b, c) Enlarged view of the same spectrum for clarity.

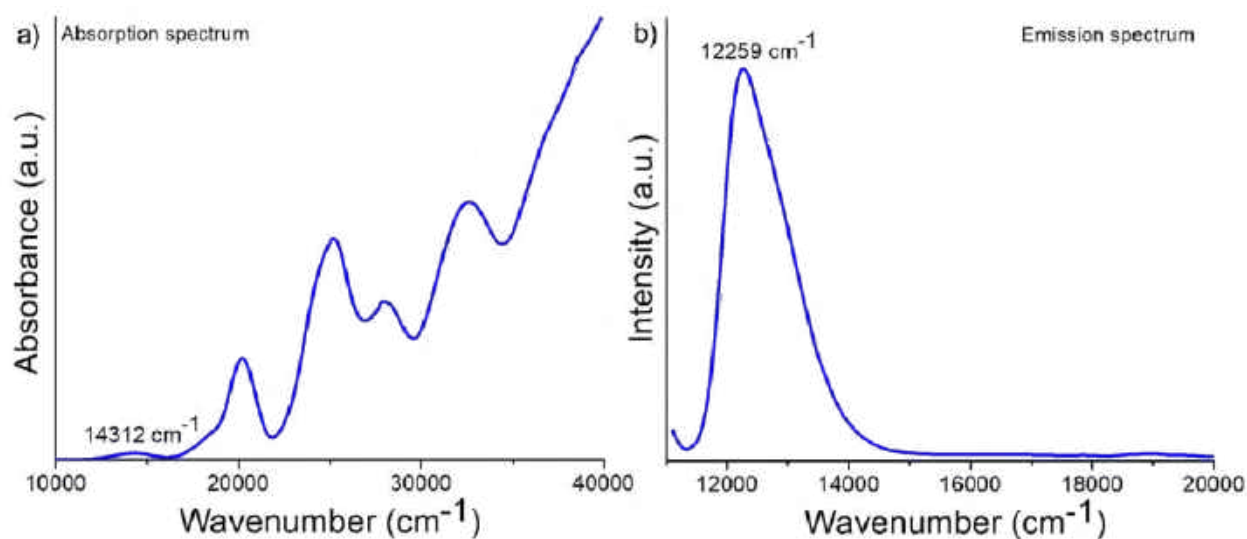


**Figure S40.** a) Absorption and b) emission spectra of  $\text{Ag}_{21}$  in energy scale. The apparent Stokes shift of  $2053 \text{ cm}^{-1}$  was calculated from the energy difference between the absorption edge and emission maximum.

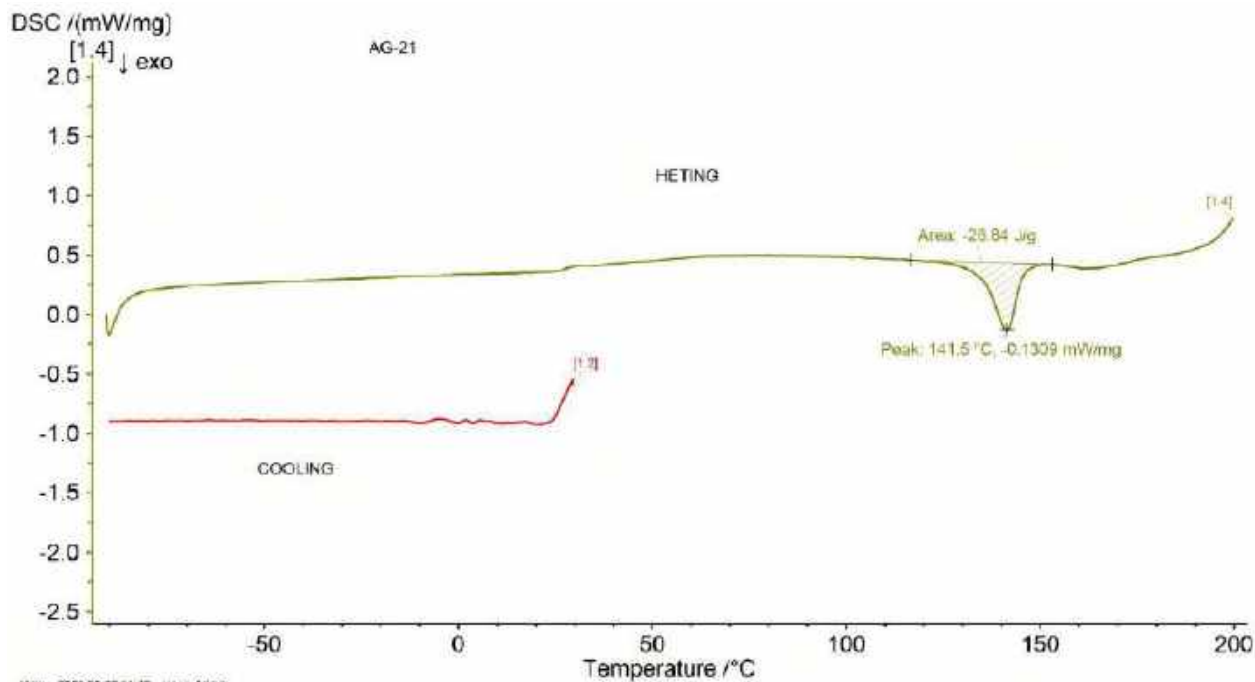


**Figure S41.** Differential scanning calorimetry (DSC) data of Ag<sub>21</sub> microcrystals. Data was collected in a cooling curve from room temperature (25 °C) to -90 °C followed by a heating curve from -90 to 200 °C. The first exothermic peak at 141.5 °C indicates a structural rearrangement of the cluster.

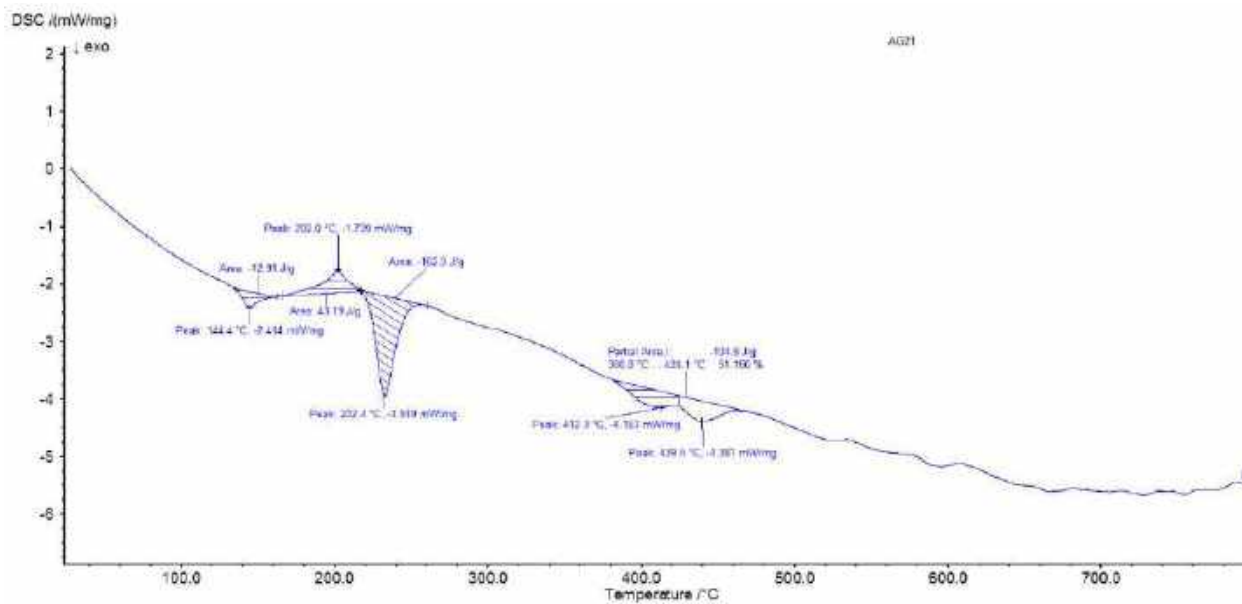


**Figure S42.** Differential scanning calorimetry (DSC) data of Ag<sub>21</sub> microcrystals for the heating curve from 25 to 800 °C.

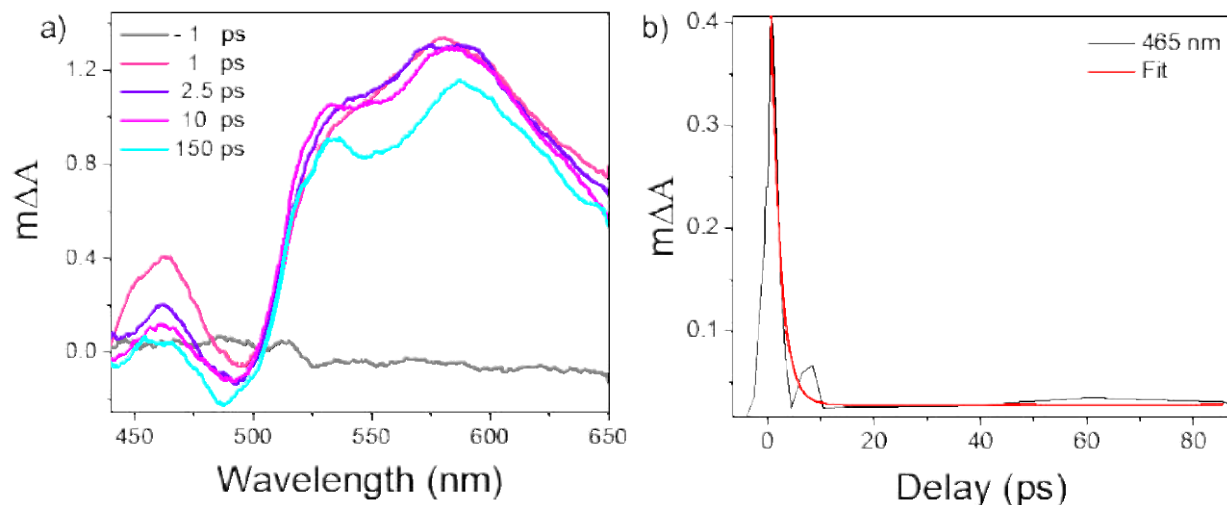


**Figure S43.** (a) Spectral slices of the TA at the selected time scales, showing fast decay profile of ESA at 465 nm. (b) Temporal evolution of 465 nm ESA features, where it decays in the early time scale.

## 4. References

- (1) Bootharaju, M. S.; Dey, R.; Gevers, L. E.; Hedhili, M. N.; Basset, J. M.; Bakr, O. M. A New Class of Atomically Precise, Hydride-Rich Silver Nanoclusters Co-Protected by Phosphines. *J. Am. Chem. Soc.* **2016**, *138*, 13770–13773.
- (2) Ghosh, A.; Bodiuzzaman, M.; Nag, A.; Jash, M.; Baksi, A.; Pradeep, T. Sequential Dihydrogen Desorption from Hydride-Protected Atomically Precise Silver Clusters and the Formation of Naked Clusters in the Gas Phase. *ACS Nano* **2017**, *11*, 11145–11151.
- (3) Enkovaara, J.; Rostgaard, C.; Mortensen, J. J.; Chen, J.; Dułak, M.; Ferrighi, L.; Gavnholt, J.; Glinsvad, C.; Haikola, V.; Hansen, H. A.; Kristoffersen, H. H.; Kuisma, M.; Larsen, A. H.; Lehtovaara, L.; Ljungberg, M.; Lopez-Acevedo, O.; Moses, P. G.; Ojanen, J.; Olsen, T.; Petzold, V.; Romero, N. A.; Stausholm-Møller, J.; Strange, M.; Tritsarlis, G. A.; Vanin, M.; Walter, M.; Hammer, B.; Häkkinen, H.; Madsen, G. K. H.; Nieminen, R. M.; Nørskov, J. K.; Puska, M.; Rantala, T. T.; Schiøtz, J.; Thygesen, K. S.; Jacobsen, K. W. Electronic Structure Calculations with GPAW: A Real-Space Implementation of the Projector Augmented-Wave Method. *J. Phys. Condens. Matter* **2010**, *22* (253202), 1–24.
- (4) Mortensen, J. J.; Hansen, L. B.; Jacobsen, K. W. Real-Space Grid Implementation of the Projector Augmented Wave Method. *Phys. Rev. B - Condens. Matter Mater. Phys.* **2005**, *71* (035109), 1–11.
- (5) Perdew, J. P.; Burke, K.; Ernzerhof, M. Generalized Gradient Approximation Made Simple. *Phys. Rev. Lett.* **1996**, *77* (18), 3865–3868.



# Accelerated Non-Enzymatic Fatty Acid Esterification during Microdroplet Collision: A Method for Enhanced Sustainability

Pallab Basuri, Jenifer Shantha Kumar, Subhashree Das, and Thalappil Pradeep\*

Cite This: *ACS Sustainable Chem. Eng.* 2022, 10, 8577–8587

Read Online

ACCESS |



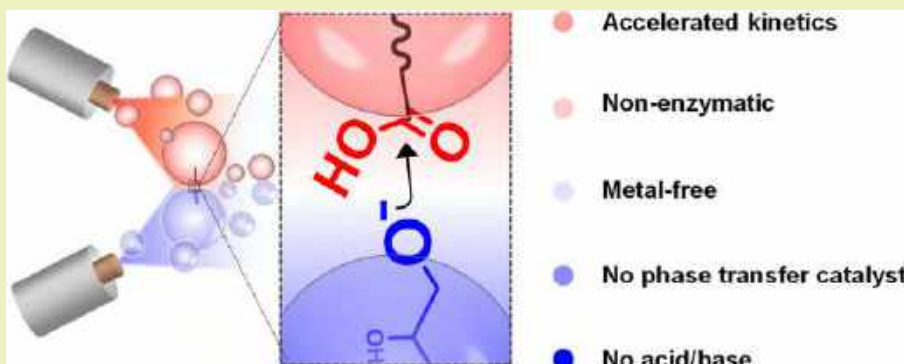
Metrics &amp; More



Article Recommendations



Supporting Information



**ABSTRACT:** Accelerated non-enzymatic and metal-free “reaction and extraction” of sugar esters at the interface of two immiscible liquid microdroplets is demonstrated. The bimolecular reaction occurs by collision of microdroplets originating from two home-built electro spray sonic ion sources, carrying sugar molecules in water and long-chain fatty acids in toluene, respectively. Our method shows that the rate of reaction is enhanced  $\sim 10^7$  times in comparison to the bulk, initiated by ultrasonic activation. Such a high rate of reaction in the microdroplets can be attributed to factors such as surface activity, concentration enhancement, partial solvation, and temperature-assisted dehydration of the species occurring in microdroplets. We provide evidence for an interfacial nucleophilic addition–elimination reaction mechanism. This method of synthesis is extended to 18 similar reactions. Microdroplet synthesis offers a sustainable method for biphasic reactions, eliminating the need for phase transfer reagents and activating agents such as acids/bases, metals, or enzymes.

**KEYWORDS:** microdroplets, reaction acceleration, mass spectrometry, sugar esters, fatty acids

## INTRODUCTION

Green chemistry is a long-term desire of chemists, and its associated 12 principles are well known.<sup>1,2</sup> Several unconventional energy sources such as ultrasound, mechanical forces, heat, and photons have been used in chemical synthesis to eliminate hazardous metal catalysts, strong acids, solvents, and reagents, contributing to green chemistry.<sup>3</sup> Nevertheless, advancements in developing greener preparative processes are always in high demand for a sustainable future.

Despite decade-long advancements in synthetic procedures for the esterification reaction, an ester C–O bond formation<sup>4</sup> has always been a challenge chemically.<sup>5</sup> One of the major limitations is that a reaction between a carboxylic acid and an alcohol is energetically unfavorable due to the low reactivity of the functional groups, and they are altered conventionally by using acid anhydrides<sup>6</sup> or acid chlorides<sup>7</sup> or by adding strong inorganic acids to activate the electrophilic C-center of the carboxylic acid.<sup>8,9</sup> Some of the classic examples are Fischer,<sup>10</sup> Steglich,<sup>11</sup> and Yamaguchi esterification reactions.<sup>12</sup> Several such reactions were also performed using transition-metal

catalysts.<sup>13</sup> Fatty acid esters of carbohydrates, called sugar esters (SEs), are commonly synthesized by the reaction of long-chain fatty acids and alcohol-functionalized sugar molecules by lipase enzymes (Scheme 1a).<sup>14,15</sup> An acyl-enzyme intermediate complex between the fatty acid and lipase is formed first, followed by the binding of alcohol onto this enzyme–substrate complex, leading to a lipase–ester complex, which finally releases the ester and the enzyme.<sup>16</sup> In general, enzyme extraction and purification is an intricate process that involves processes such as fermentation, vacuum filtration, separation, preconcentration, and drying, some of which are energy intensive. The ester products are biosurfactants and are metabolites found in several organisms. Biologically, such

Received: April 7, 2022

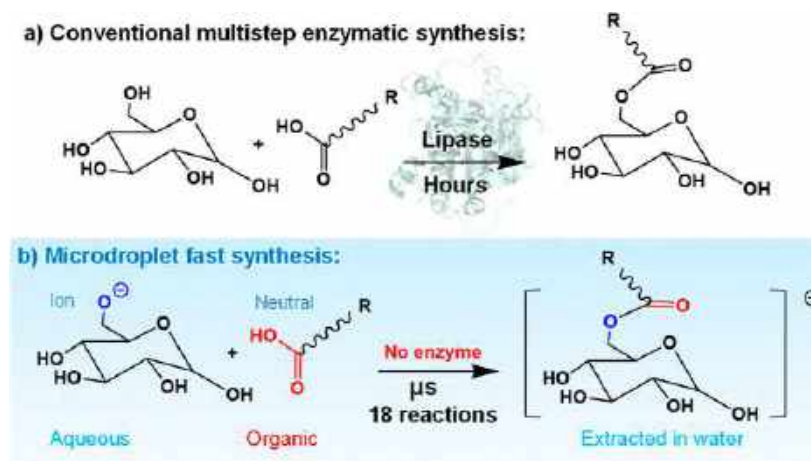
Revised: June 9, 2022

Published: June 23, 2022





Scheme 1. Sugar Esterification (a) Catalyzed by Lipase in Cell/Bulk Synthesis vs (b) Accelerated Microdroplet Synthesis



reactions are important because these compounds help in controlling cell adhesion, which affects the growth and localization of the organism.<sup>17</sup> These biosurfactants have a growing demand in comparison to synthetic surfactants due to their lower toxicity and biodegradability. SEs are used in several food, pharmaceutical, and cosmetic industries.<sup>15,17–19</sup> However, lipase-catalyzed esterification reactions are limited by the choice of the solvent system for making a homogeneous solution for lipids that are soluble in non-polar solvents and sugars soluble in water. To overcome the solution-phase heterogeneity, several ionic liquid-based synthetic protocols have been attempted in the past.<sup>20–22</sup> Use of a phase transfer catalyst is a general practice in such organic–aqueous mixed phase reactions.<sup>23</sup>

Since the development of electrospray ionization-mass spectrometry (ESI-MS) half a century ago, it has facilitated the advancement of molecular analysis. In ESI, solution-phase neutral molecules are converted to gas phase ions via charged microdroplets. Recently, these charged microdroplets have attracted the interest of many mass spectrometrists from the preparative point of view. This is because of the acceleration of rates of several organic reactions,<sup>24–31</sup> formation of reactive species,<sup>32–34</sup> and alternate reaction pathways<sup>35</sup> in such environments compared to similar chemistry in reaction vessels. In addition, microdroplet synthesis is a promising sustainable technique involving low solvent and energy consumption, catalyst-free chemical transformation, and with high atom economy.<sup>31</sup> Similarly, nanobubbles are becoming important in various aspects of environmental remediation.<sup>36</sup> These experiments are mainly performed in electrospray sonic ionization,<sup>29,35,37–39</sup> nanoelectrospray ionization,<sup>40,41</sup> paper spray ionization,<sup>42</sup> and individually levitated droplets.<sup>43</sup> Furthermore, the Zare group found that such reactions can also be performed in colliding microdroplets formed from two ESI sources kept at an angle such that the spray plumes intersect each other.<sup>26,44–47</sup> Many microdroplet reactions were scaled up to prepare gram-scale quantities of products. Methods such as multiplexed electrospray,<sup>39,45</sup> ultrasonic heated nebulized spray,<sup>46</sup> and solvent recycling electrospray<sup>48</sup> have been demonstrated in the literature for large-scale synthesis. A few hypotheses were made in the literature to understand such unique chemistry such as spatial distribution of solute molecules,<sup>49</sup> existence of a substantial pH gradient,<sup>50</sup> formation of reactive species,<sup>51</sup> restricted molecular rota-

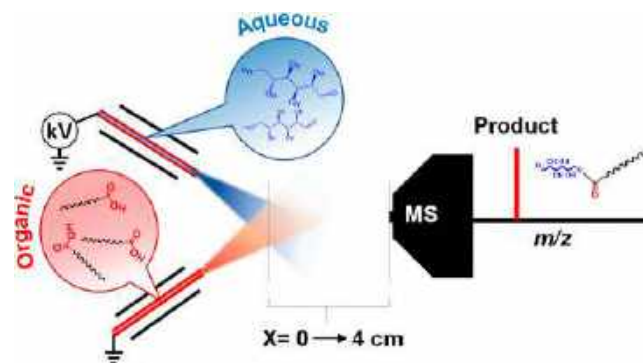
tions,<sup>52</sup> high interfacial electric field,<sup>53</sup> and partial solvation of molecules.<sup>31,54</sup> Recently, enzyme-catalyzed hydrolysis of lipids was monitored in microdroplet environments by the Badu-Tawiah group.<sup>55</sup> All the above studies encouraged us to perform C–O ester bond formation reactions in microdroplets.

In the present work, we have demonstrated a non-enzymatic, fast synthetic method leading to SEs using microdroplet chemistry under ambient conditions at an immiscible aqueous–organic interface, without adding any phase-transfer catalyst. Reaction and extraction were performed simultaneously. We used online MS monitoring to derive a mechanistic understanding of the reaction. Several control experiments were performed by varying parameters such as the spray distance, solvents, external surfactant, and so forth to realize the microdroplet reaction process. The scope of the microdroplet reaction was further tested by extending the synthesis to 18 different SEs.

## EXPERIMENTAL SECTION

**Microdroplet Collision Experiment.** The experimental setup for microdroplet collision is schematically presented in Scheme 2. The reactions were performed using two ESSI sources, which were held at

Scheme 2. Schematic of the Experimental Setup for Ester Bond Formation Reaction by the Collision of Aqueous and Organic Microdroplets Generated by Two ESSI Sources Coupled with a Mass Spectrometer<sup>a</sup>



<sup>a</sup>The distance from the collision point to the inlet of the mass spectrometer is given as X, in cm. While the aqueous spray tip is at high voltage, the organic spray tip is grounded.

an angle of 60° in front of the mass spectrometer. We used N<sub>2</sub> as a nebulization gas at 100 psi. To perform the reaction, we sprayed an aqueous solution of sugar (8 mM) at a flow rate of 5 μL/min at 2.5 kV spray potential of negative polarity through the first ESSI source. Using the second ESSI source, the organic solution of fatty acid (8 mM) was sprayed with N<sub>2</sub> gas at no applied potential. It should be noted that while we chose sugar to dissolve in water in all the experiments, the fatty acids were insoluble in water and we used toluene instead for their dissolution.

**MS Experiment.** Online MS measurements were performed using a Thermo Scientific LTQ XL mass spectrometer. We used an inlet temperature of 50 °C for most of the reactions otherwise mentioned in the respective places. Tube lens and capillary potentials were set to -35 and -110 V. The sheath gas flow rate was set to zero.

**MS Experiment of the Sonicated Bulk Reaction.** The aqueous phase was separated from toluene, it was diluted 1000 times with MeOH to quench the reaction, and ESI-MS was performed with a commercial ion source at 5 kV spray potential, 8 psi sheath gas flow rate, -35 V capillary potential, -110 V tube lens potential, and 275 °C inlet temperature for characterizing the intermediate and the product. We chose methanol for dilution to make a homogeneous system for electrospray as both water and toluene are miscible in methanol.

**Dark Field Imaging.** A CytoViva™ microscope was used for collecting the dark-field image of the droplets. The microscope was equipped with a high-resolution dark-field oil immersion condenser lens. We used a L1090-halogen lamp from International Light Technologies Inc. as a white light source for imaging the droplets. The image was captured using a Dage Excel M cooled CCD camera. The imaging experiment was performed by drop casting the liquid on clean glass slides (SCHOTT nexterion).

## RESULTS AND DISCUSSION

**Microdroplet Collision and Mass Spectrometry Analysis.** Scheme 1 compares the reaction between conventional synthesis and the microdroplet method. Scheme 2 shows the experimental setup for the reaction, where two ESSI sources were held at an angle of 60° in front of the mass spectrometer (detailed discussion on the setup is presented in the Experimental Section). Figure 1a,b shows the negative ion mass spectra of individual reagents collected by electrospraying (-2.5 kV spray voltage) one reagent at a time. Peaks at *m/z* 179 and 281 correspond to deprotonated glucose and oleic acid. The peaks were further confirmed using collision-induced dissociation experiments of the isolated ions (Figure S1). Interestingly, in Figure 1c two additional peaks at *m/z* 443 and 461 were observed along with the reagent peaks upon spraying both the reagents, as shown in Scheme 2. Note that we did not apply any potential to the oleic acid source, but still observed a peak corresponding to the deprotonated oleic acid (*m/z* 281) probably because of the charge transfer as discussed in detail in the next section. We collected a mass spectrum from the nebulized spray of oleic acid in toluene as well, where no such molecular ion peak at *m/z* 281 was observed (Figure S2). The two new peaks that appeared in Figure 1c were assigned to the product, glucose-oleate at *m/z* 443, and the intermediate peak of the esterification reaction at *m/z* 461. These assignments were further confirmed using the MS/MS spectra of the isolated peaks. The MS/MS spectrum of the product at *m/z* 443 shows neutral losses corresponding to CO<sub>2</sub>, CO, and water molecules to give a major peak at *m/z* 399 and two minor peaks at *m/z* 415 and 425 (Figure S3a). A few minor peaks in the mass range of *m/z* 390 to 330 and two intense peaks at *m/z* 315 and 297 were also observed, and their assignments are shown in Figure S3a. We also observed *m/z* 281, corresponding to deprotonated oleic acid, which was further

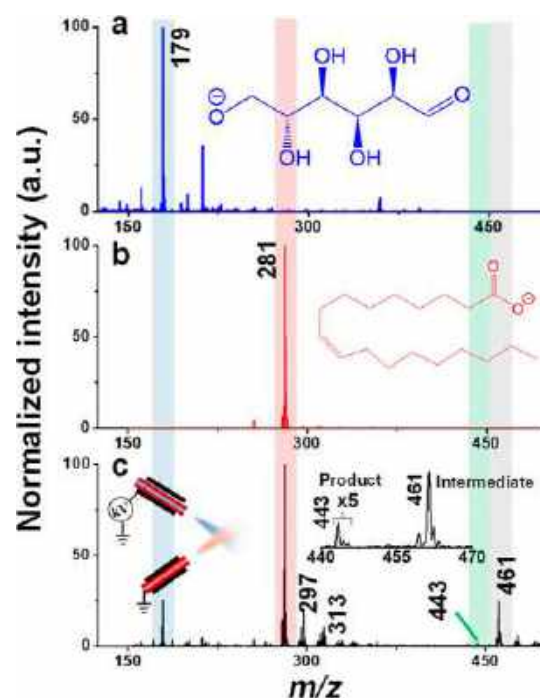


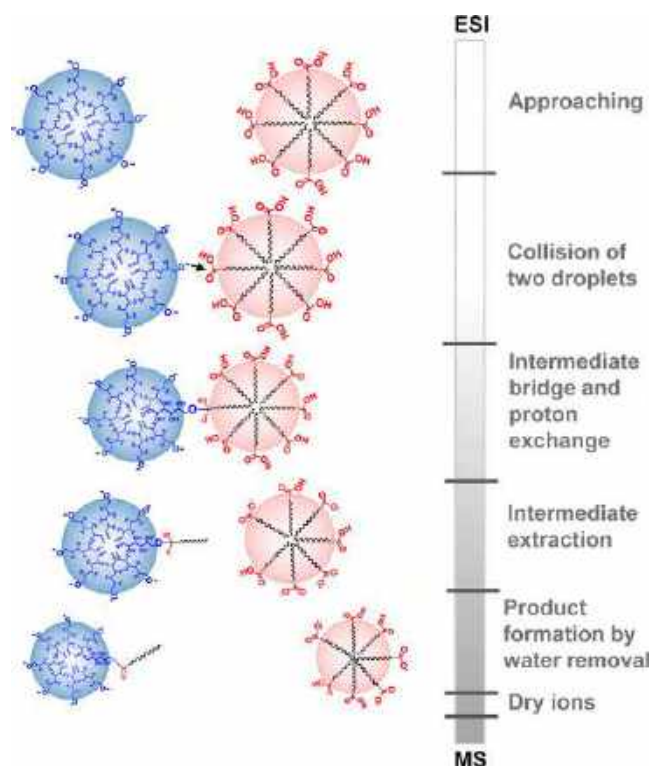
**Figure 1.** Microdroplet synthesis of glucose/oleic acid ester. (a,b) Negative ion ESSI mass spectra collected individually from 8 mM aqueous solution of glucose and 8 mM solution of oleic acid in toluene. The insets of (a,b) show the molecular structures of the reagents. (c) Mass spectrum collected by spraying both the reagents at a time. Insets of the spectrum represent the microdroplet collision and the zoomed-in spectrum of the selected mass range showing isotopic distributions of the product and the intermediate peaks. The peak at *m/z* 443 is multiplied five times. The ions at *m/z* 297 and 313 are oxides of oleic acid. Mass speaks are labeled.

confirmed by the MS/MS/MS spectrum of *m/z* 281, shown in Figure S3b. Similarly, the MS/MS spectrum (Figure S3c) of the intermediate at *m/z* 461 shows neutral loss of water molecules to give a base peak at *m/z* 443 (product peak) and three other peaks at *m/z* 399, 417, 425, and 433, corresponding to (H<sub>2</sub>O + CO<sub>2</sub>), CO<sub>2</sub>, and 2H<sub>2</sub>O and a CO loss from *m/z* 461. Noticeably, we did not observe poly-substituted products for the reaction, either due to low product ion concentration to undergo further reaction or a short time available for the reaction at the interface or inadequate energy of activation. We observed peaks at *m/z* 297 and 313, corresponding to mono- and dioxygen-added oleic acid, due to areal oxidation of oleic acid at the droplet surface. Such oxidation might occur due to the presence of airborne ozone.<sup>56</sup>

The conversion ratio (CR), that is, the ratio between the intensity of the product ion or the intermediate species and the sum of the intensities of the product, intermediate, and fatty acid (R) ions gives a rough idea about the yield of the reaction.<sup>57</sup> Note that we did not consider the intensities for the sugars in this equation. We observed that the intensities of sugar species were invariant with respect to different reaction conditions. This could be due to the fact that the resultant signal intensity of the sugar comprises both sugar from uncollided droplets and unreacted sugar from collided droplets. The calculated CRs of the reagent to intermediate and product are 20 and 1.2%, respectively. However, the absolute yield may vary due to a difference in the ionization efficiency of the species.

**Mechanistic Understanding of Simultaneous Microdroplet Reaction-Extraction of SEs.** Based on the above understanding and previous studies on microdroplet chemistry, we suggest that the sugar anion formed at the air/water interface of the aqueous microdroplet attains a specific orientation, by which the anionic alkoxide maximizes charge distribution (Scheme 3, blue droplets) and minimizes

**Scheme 3. Mechanistic Understanding of the Microdroplet Collision-Esterification Reaction<sup>a</sup>**

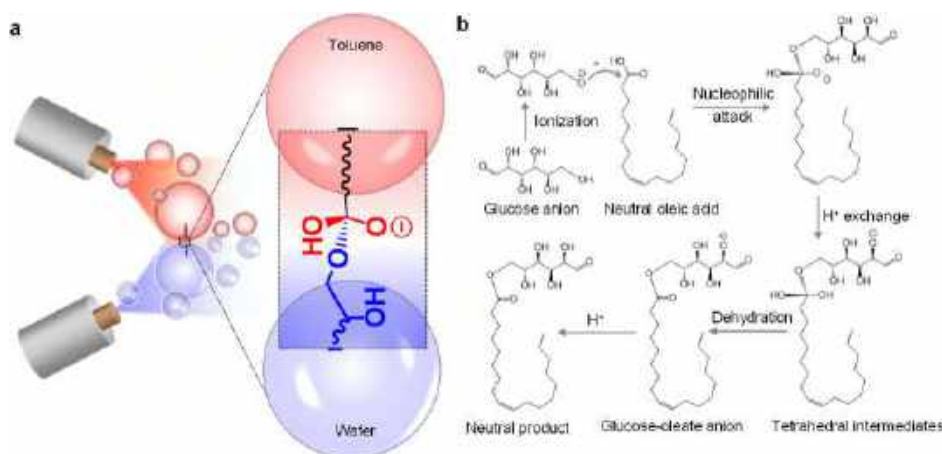


<sup>a</sup>The schematic demonstrates different steps involved in the collision, reaction, extraction, and product formation of the glucose/oleic acid esterification reaction on the surface of a microdroplet. The blue and the red color represent the aqueous and toluene droplets, respectively.

electrostatic repulsion. Such a charge distribution at the air/liquid interface has been reported previously.<sup>58</sup> This interfacial alkoxide anion acts as a strong nucleophile. On the other hand, the long-chain hydrophobic hydrocarbon part of the fatty acid, dissolved in organic microdroplets, will be at the core of the droplet due to the hydrophobic–hydrophobic interactions, whereas the hydrophilic carboxylic acid groups will occupy the interface to minimize the hydrophobic–hydrophilic repulsion energy (Scheme 3, red droplets). Strong interfacial concentration of molecules is one such reason for reaction acceleration in confined volumes.<sup>49</sup> Microdroplets undergo rapid desolvation, and the molecules at the interface are partially solvated, which help them overcome the activation barrier due to solvation. The recent experimental and computational results from Cooks et al. support such a limited solvation at the air/liquid interface of microdroplets.<sup>59,60</sup> Herein, we proposed a process involving interfacial molecular enrichment, specific molecular orientation, and partial solvation, for the C–O coupling reaction in microdroplets. These factors give more accessibility to the alkoxide nucleophile to attack the electrophilic C-center of the carboxylic acid on the interface, while two droplets are colliding with each other. However, such a nucleophilic addition in the bulk is limited by liquid–liquid phase separation, low nucleophilicity of the hydroxyl group, low electrophilicity of the carboxylic group, solvation of the reagents, and so forth, and consequently lipid esterification requires enzymatic activation. The microdroplet environment helps in overcoming such constraints to achieve chemical bond formation in the absence of an enzyme. Such a nucleophilic attack between the sugar and the fatty acid leads to the formation of a new C–O covalent bond (i.e., intermediate, *m/z* 461) at the aqueous organic interface between the two colliding droplets. In other words, the tetrahedral intermediate (Scheme 4a) forms due to the nucleophilic addition, creating a bridge between two flying droplets. Scheme 4b displays a schematic view of the overall reaction mechanism.

On the other hand, we propose a competitive reaction pathway to explain the ionization of oleic acid during microdroplet collision, schematically shown in Scheme S1. This represents a proton transfer from the carboxylic acid in the organic microdroplet to the alkoxide group of the sugar in

**Scheme 4. Understanding the Reaction Mechanism at the Interface of Two Droplets; (a) Schematic View of the Tetrahedral Intermediate Formed by the Nucleophilic Addition of the Alkoxide Group to the Carboxylic Group at the Interface of Two Droplets of Immiscible Liquids; (b) Reaction Mechanism of the Formation of Neutral Glucose-Oleate Ester**





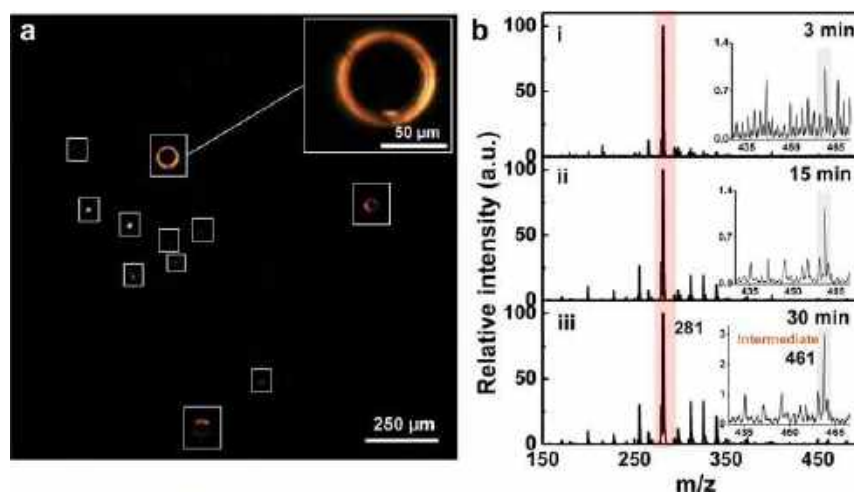


**Figure 2.** Esterification in bulk vs ultrasonicated toluene-in-water droplet. (a) Dark-field microscopy (DFM) of toluene microdroplets containing oleic acid in aqueous glucose solution. Moving droplets of different sizes were observed (white squares). One of the droplets is focused and a zoomed-in image of the same is shown in the inset. (b) Comparative mass spectra of the aqueous part of the reaction mixture after phase separation and dilution with methanol. Reaction was performed at 3, 15, and 30 min of ultrasonication. Insets show an expanded mass range, and the intermediate at  $m/z$  461 is marked.

the aqueous droplet, leaving the anion of the fatty acid detected in the mass spectrum ( $m/z$  281, Figure 1c). Due to such charge transfer across the water/toluene interface, both the droplets become negatively charged. Lee et al. found that the propulsion force by dry  $N_2$  during nebulization accelerate droplets to attain a high speed in air.<sup>44</sup> Therefore, electrostatic repulsion and momentum exchange during high speed collision between the two droplets in air will push them apart from each other and subsequently create a choice for the intermediate species to travel to either of the droplets.<sup>61</sup> It has previously been reported that microdroplet provides aqueous organic biphasic reactions that require no phase transfer catalyst.<sup>45,62</sup> However, whether the reaction occurs at the interface of the two droplets or they undergo a reaction followed by coalescence is not understood well. We proposed that during microdroplet collision, the intermediate species get extracted by the aqueous droplets preferentially. Such extraction of the analyte from one droplet to the other, termed as extractive electrospray ionization, was previously reported by Cooks et al.<sup>63</sup> This may be understood as the hydrogen bond strength between the hydroxyl unit of the sugar part of the intermediate and water is higher than the interaction energy between the long-chain hydrocarbon and toluene. This is also evident from the solvent dependency experiment and the infrared (IR) spectroscopy experiments (see below). Finally, subsequent loss of a water molecule from the intermediate leads to the formation of the product ester.

**Monitoring Bulk Reactions.** A bulk reaction was performed by mixing a toluene solution of oleic acid (8 mM) with glucose in water (8 mM) at a 1:1 (v/v) ratio. Due to the immiscibility of the two solvents, immediate phase separation occurred in the bulk. Upon examination of both the aqueous and organic phases using MS, we found that the reaction does not occur by mixing, in the bulk. However, we noticed the presence of oleic acid in the aqueous phase as evident from the mass spectrum (Figure S4a). Interestingly, the reaction does occur, but got stopped at the stage of intermediate formation ( $m/z$  461) during ultrasonication for 1 min (Figure S4b), but no product ( $m/z$  443) was observed. Sonication leads to water-in-oil and oil-in-water droplets,

which could drive the reaction. This was evident from the IR spectroscopy, DFM, and MS results. Figure S5 shows the ATR-IR spectrum of the aqueous phase of the reaction mixture, in which we observed peaks corresponding to CH stretch, asymmetric and symmetric stretches of  $CH_2$ , and C=O stretch at 3010, 2926, 2854, and 1707  $cm^{-1}$ , respectively. Two peaks at 693 and 725  $cm^{-1}$  were also observed due to the out of plane C–H bending of toluene. We suspected that oleic acid present in water and as a solvated species in toluene microdroplets made a heterogeneous system. To observe these toluene microdroplets, we performed DFM of the water sample. Figure 2a shows the DFM image of three individual droplets immersed in water. In the mass spectrum of the sonicated mixture (Figure S4b), we found a deprotonated peak of oleic acid at  $m/z$  281 along with a deprotonated peak of glucose at  $m/z$  179 and an intermediate peak at  $m/z$  461 with very low intensity.

Above findings led us to perform time-dependent reactions of oil-in-water microdroplets by sonicating the reaction mixture in an ultrasonicator (see the experimental section). Figure 2b(i–iii) shows the mass spectra of the aqueous phase after 3, 15, and 30 min of ultrasonication. We observed  $\sim 1\%$  of the intermediate peak intensity relative to oleic acid upon 3 min of sonication, which got intensified three times upon 30 min of sonication. We found no increase in relative signal intensity of the intermediate upon further sonication. The spectrum shows the intermediate at  $m/z$  461 and not the product at  $m/z$  443 as the reaction was performed in bulk water. Note that  $m/z$  443 is a result of elimination of water from  $m/z$  461. In the bulk reaction, removal of water needs a strong dehydrating agent and therefore its absence in ultrasonication is not surprising. This observation indicates that microdroplet promotes efficient dehydration from the reaction site. Comparing the intermediate ion yield of “15 min sonicated bulk reaction” with the microdroplet reaction, we calculated the apparent acceleration factor (AAF). A qualitative estimation of AAF can be made by taking a ratio between the time taken by the product to reach the same CR in both bulk and microdroplet conditions.<sup>64</sup> Note that the AAF was calculated by keeping X at 1 cm for microdroplet reaction.

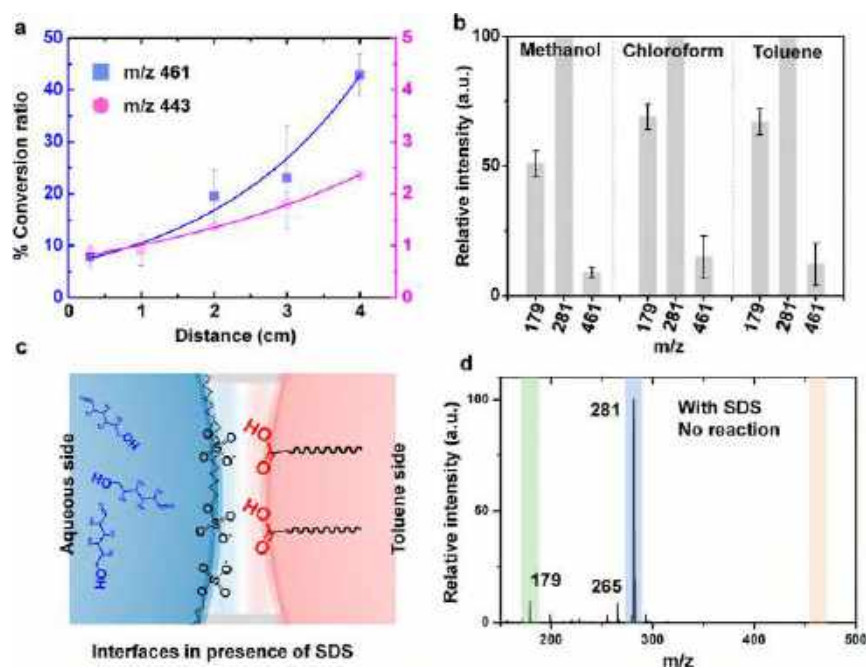


**Figure 3.** Factors that influence droplet reactions. (a) Distance vs CR plot. (b) Comparative CR of the intermediate at different solvent compositions. (c) Schematic illustration of the microdroplet interfaces at close proximity, showing surfactant-induced reaction barrier for nucleophilic addition. (d) Mass spectrum of the reaction mixture containing SDS (peak at  $m/z$  265) in the aqueous phase. Green, blue, and orange shades indicate the peak positions for deprotonated glucose, deprotonated acid, and intermediate species, respectively.

As there is no product peak observed in the sonication experiments, an exact AAF could not be calculated. However, a qualitative understanding can be made by comparing the intensities of the intermediate species at  $m/z$  461. We found that the glucose/oleic acid reaction shows very high AAF (approx  $10^7$ ). It should be noted that this value does not include factor such as the effects of ultrasonic cavitation for the bulk reaction.

**Distance Effect.** The distance from the point of crossing of two ESI plumes to the inlet of the mass spectrometer is considered as the effective microdroplet reaction zone.<sup>30</sup> Microdroplet reactions are known to be influenced by this distance,  $X$  (Scheme 2). In our experiment, a change in the distance shows a dramatic effect on the signal intensity for the intermediate species. However, the product peak intensity was varying slightly. Figure 3a shows the distance versus CR for both the intermediate and the product. The distance was varied from 0.3 to 4 cm. We observed that upon increasing the distance, the intensities of both the intermediate and the product peaks increase exponentially. A stack of mass spectra at different distances is shown in Figure S6, where a clear increase in the intensity of  $m/z$  461 is noticed. It suggests that droplets are not only colliding at the point-of-intersection, but collisions may occur during the entire length of flight, all the way toward the inlet of the mass spectrometer. We infer that this effect could be either due to increased collision frequency resulting from the increased number of droplets or due to the fact that smaller droplets have more concentration enhancement at their interfaces, which shifts the reaction toward the intermediate.

**Effect of Different Solvent Systems.** The interfacial reaction mechanism was further tested by varying solvent polarity. Experiments were conducted by dissolving oleic acid in three different solvent systems; methanol, toluene, and chloroform. Figure S7 shows the mass spectra of microdroplet

reactions between oleic acid in these three solvents and glucose in water. The reaction was performed by keeping  $X$  at 1 cm and 50 °C inlet temperature. One would expect better ionization for the polar intermediate in polar methanol than non-polar toluene and chloroform, which are non-friendly to electrospray.<sup>65</sup> However, we found that by changing the organic solvent from non-polar toluene to polar and protic methanol, the reactivity reduces. As a result, we observed low signal intensity of the intermediate in methanol than in toluene, as shown in Figure 3b. Methanol as an acyl receptor could also react with fatty acid to form methyl ester, which can be viewed as a competitive reaction to reduce the relative intensity of the intermediate ( $m/z$  461). However, we have not observed any methyl ester of the fatty acid, which may be used to neglect the possibility. We assessed that a reduction in chemical reactivity of oleic acid in methanol is due to better solvation of the acidic head group at the droplet interior, which eventually makes the  $sp^2$ -C center inaccessible to undergo nucleophilic addition. We also found that chloroform works similar to toluene due to its non-polar nature.

**Effect of the Surfactant.** The interfacial reaction mechanism was further investigated by manipulating the surface of the aqueous droplet. To do so, we added a surfactant to the glucose solution. The surfactant will occupy the droplet surface, which will prevent the alkoxide group to come to the air/water interface to make a nucleophilic attack. Figure 3c shows a schematic of this concept. We used 0.1 mM sodium dodecyl sulfate (SDS) along with 8 mM of glucose solution in water for the reaction. Figure 3d presents the mass spectrum of the oleic acid/glucose reaction with SDS. In the mass spectrum of SDS-added reaction mixture, we observed a significant loss of signal intensity for glucose at  $m/z$  179. We also observed peaks corresponding to SDS at  $m/z$  265 after sodium loss. However, peaks corresponding to the intermediate and the product were missing in the full mass



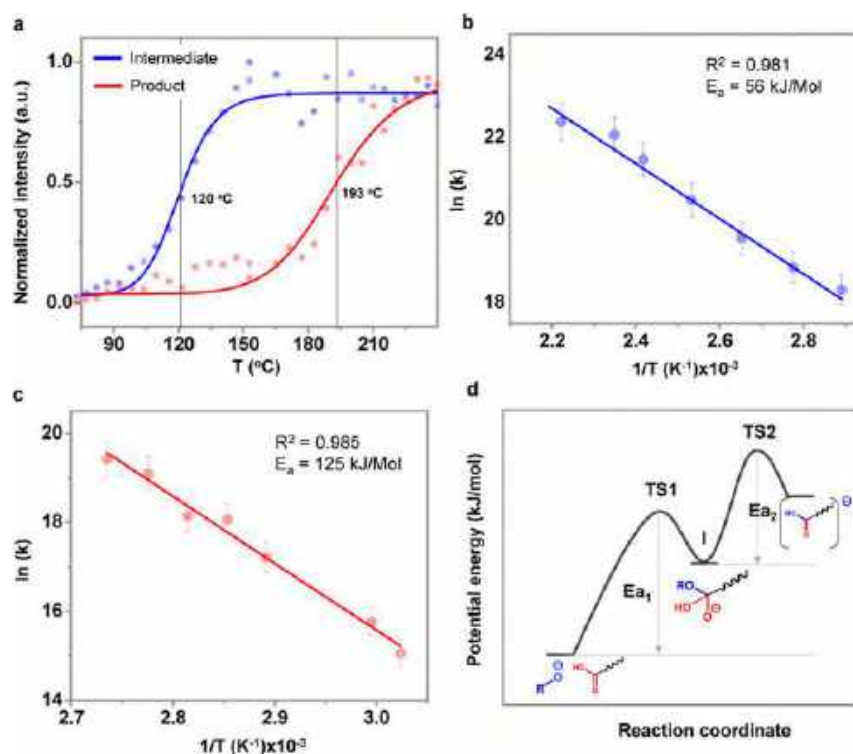


**Figure 4.** Effect of temperature in the interfacial microdroplet reactions. (a) Normalized intensity of the intermediate ( $m/z$  461) and the product ( $m/z$  443) vs temperature plot, showing sigmoidal growth of both the intermediate and the product intensity at 120 and 193 °C, respectively. Temperature dependency of the rate of formation of the intermediate (b) and the product (c) and their corresponding activation energies. (d) Schematic diagram of the energy profile of the reaction based on the temperature-dependent experiment.

spectrum. This suggests that the reaction does not occur upon droplet collision, which further supports our interfacial nucleophilic addition–elimination mechanism upon droplet collision.

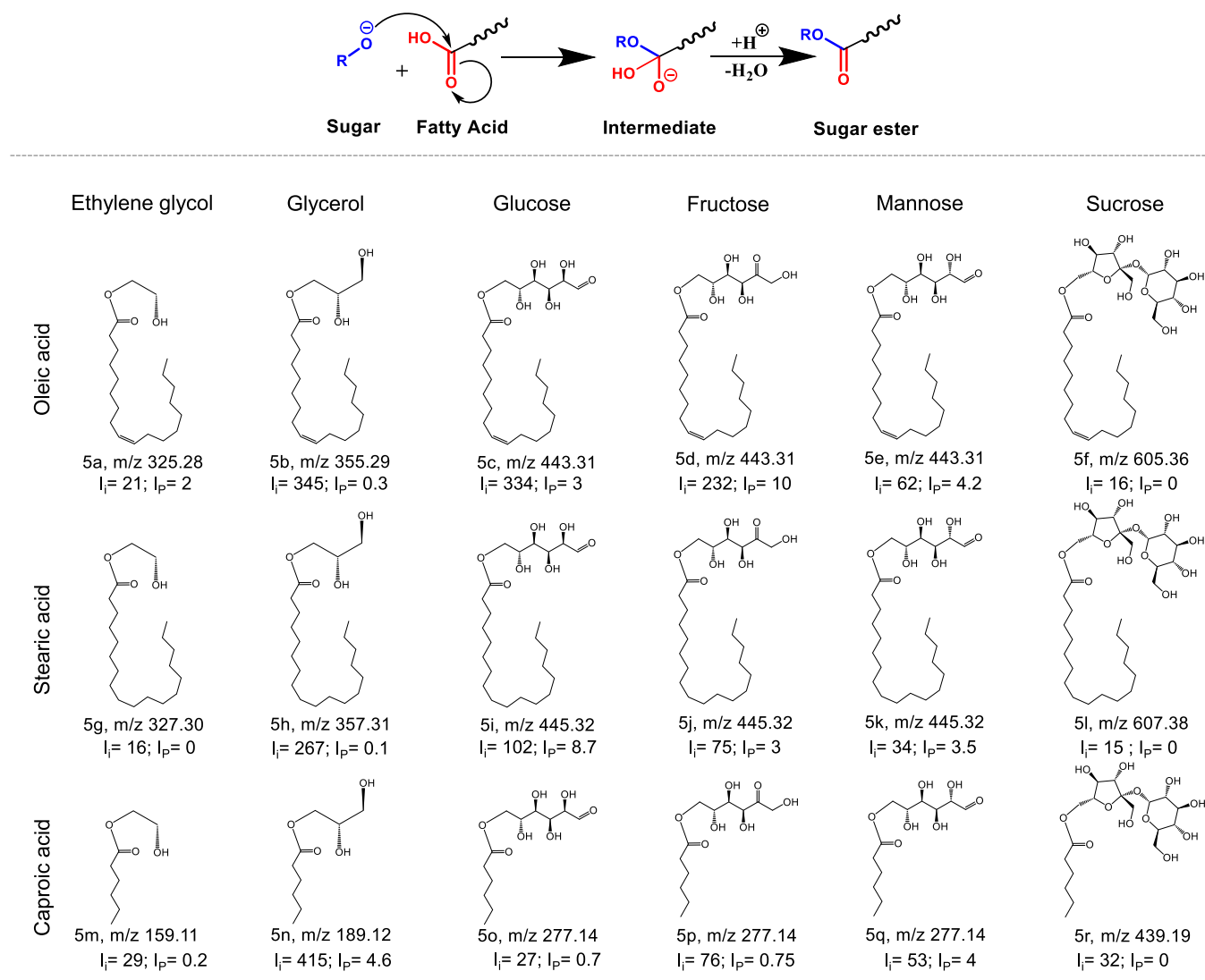
**Temperature Effect.** From our previous studies and existing literature, we understood that microdroplet reactions are significantly influenced by temperature.<sup>40,66</sup> Part of this is due to the increased rate of desolvation of the droplets,<sup>67</sup> dehydration from the reaction site,<sup>40</sup> and need of some activation energy.<sup>66</sup> To understand the effect of temperature on the rate of the reaction, an experiment was performed by varying the temperature of the inlet of the mass spectrometer from 50 to 400 °C during the reaction. Figure S8 shows a stack of the mass spectra collected with increasing inlet temperature alone while keeping all other parameters of the setup constant. We noticed a significant increment in signal intensity for both the intermediates and the product, with increasing temperature. Figure 4a,b displays relative intensity–temperature traces for the intermediate and the product. Note that we did not consider the change in the signal intensity of glucose as we used glucose in the electrospray ion source. Hence, it is expected that glucose intensity will increase with temperature due to enhanced droplet-to-gas phase ion transfer at elevated temperatures (Figure S9a). Hence, the signal intensity for glucose is not restricted to its interfacial concentration. The CR–temperature profile shows that the signal intensity of both the intermediate and the product follows a sigmoidal curve with increasing temperature. However, a noticeable difference in saturation temperature was observed for both of them. While the intermediate peak rises to the highest intensity at 152 °C, the product reached its saturation at 225 °C. We speculated that this additional 73 °C is required to eliminate a

water molecule from the intermediate and pull it from the reaction site at the air/water interface. However, one can expect that this process would be inefficient and be perturbed by the presence of water molecules coming from the droplet, according to Le Chatelier principle. As a result, we get a low product yield.

We observed loss of signal intensity for the intermediate peak after 245 °C. Partly, this is due to the intermediate to product conversion. However, some of the intermediates also undergo the newly formed C–O bond cleavage at higher temperature, which eventually regenerates the reagents. This can be seen in the temperature profile for the oleic acid peak (Figure S9b). The peak reduces significantly up to 150 °C and then starts increasing and saturates around 245 °C. This suggests that the reaction is reversible in microdroplets and such an equilibrium can be controlled by controlling the rate of desolvation. Considering the bulk reaction and the time associated with it, a plot of inverse temperature versus reaction rate gave us the corresponding activation energies for the formation of the intermediate and the product. Figure 4b,c shows the overall activation energies required for the conversion of reagents to the intermediate and subsequently to the product, which are 56 and 125 kJ/mol, respectively. The reaction is accelerated at the liquid–liquid interface of two immiscible microdroplets due to the generation of the active nucleophile, partial solvation, and specific orientation of these reactants, as shown in Scheme 3. The temperature of the inlet helps in overcoming such activation barriers. Based on the estimated activation energies, in Figure 4d, we present a schematic of the energy profile of the reaction.

**Scope of the Microdroplet Reaction of Sugar Esterification.** This systematic study of the microdroplet

**Scheme 5. General Reaction Scheme along with the Structures of the SEs Synthesized in This Work (a–r) and the Percentage Intensities of the Intermediate or Product Peaks Relative to Their Corresponding Fatty Acid Peaks**



reaction mechanism led us to extend the esterification reaction by changing both the sugar and the fatty acid. We chose 6 different sugars, 3 different acids, and all possible combinations to perform 18 reactions. Scheme 5 summarizes the results of all the reactions, where we report the relative intensities (i.e., the ratio between the intermediate or product and the corresponding fatty acids) of the product and the intermediates, considering 150 °C inlet temperature for microdroplet reactions. The product yield is always less in comparison to the intermediate yield, and that can be understood by the relative signal intensities (Figures S10–S26). Interestingly, we observed only monosubstituted products. Esterification at multiple sites of the sugar has not been observed primarily because of the low concentration of the product ester. In addition, we found that the reaction rate is high for glycerol. This could be due to the small size of the reactant, which helps it to overcome the steric effect for nucleophilic addition. Interestingly, glycerol/caproic acid combination gave the highest CR for the intermediate peak. However, the low reactivity of ethylene glycol could be due to its smallest size, which restricts it to attain a specific orientation at the surface in

favor of the reaction. On the other hand, sugars with similar functionality show similar reactivity.

**Qualitative Sustainability Assessment.** A qualitative assessment of sustainability was performed to determine the greenness of the method. Sugars and fatty acids are biomolecules, and their reactions do not lead to any toxic byproducts. In comparison to the conventional esterification synthesis, herein, no catalysts including strong acids/bases, metals, or enzymes were used. This biphasic microdroplet collision method allows zero use of the phase transfer catalyst as well. The microdroplet method involves a minimal solvent volume along with 100% solvent recovery as demonstrated in the literature. The process involves direct formation of a solid crude product from solution-phase reagents. In microdroplet synthesis, unreacted reagents can also be reused easily after separation and extraction as limited chemical species were used in the reaction. The method also shows low energy wastage because we used electrical energy directly as an input for the reaction to proceed, while conventional methods utilize electrical energy in the form of heat, ultrasound, microwave, or photons. This resulted in net dissipation of energy during each conversion. Therefore, the reaction presents the use of

microdroplets as a sustainable alternative to conventional chemical synthesis.

## CONCLUSIONS

In summary, we demonstrated a sustainable method of accelerating interfacial chemistry between analytes dissolved in two immiscible liquids, which is cumbersome in the conventional process due to the requirement of a phase transfer catalyst and agitation. In this work, bimolecular sugar–lipid esterification occurs efficiently with two-step nucleophilic addition and water elimination, which completely eliminates the need for conventional lipase enzymes, leading to improved sustainability. However, understanding the reaction mechanism in such a microdroplet environment through spectroscopy is a scope of further investigation. We utilized online MS to detect the species formed during the reaction. We have shown evidence for an interfacial microdroplet mechanism. Our understanding of reaction acceleration in microdroplets stands on a combination of four major mechanisms: (i) interfacial enrichment, (ii) partial solvation of molecules, (iii) specific orientations of the reagents at the interface, and (iv) dehydration at the reaction site. Concepts (i) and (ii) have been understood previously through theory and experiments. However, the current work provides strong evidence for (iii) and (iv). A specific molecular orientation was demonstrated by the surfactant and solvent effects. Dehydration at the reaction site was observed directly from the temperature effects. An analogy between ultrasonic and microdroplet experiments also indicates the same. Successful esterification reactions using a minimal amount of reagents is demonstrated. Moreover, these studies are also important in understanding interfacial chemistry that can occur in electrospray microdroplets. In fact, such enhanced chemical reactivity in aerosols can have profound implications in cellular, atmospheric, and prebiotic chemistries. Improved product yield and enhanced conversion efficiency are in the scope of our future work.

## ASSOCIATED CONTENT

### Supporting Information

The Supporting Information is available free of charge at <https://pubs.acs.org/doi/10.1021/acssuschemeng.2c02070>.

MS and MS/MS of the reagent, intermediate, and product; IR of the reaction mixture; and MS and MS/MS of several other reactions (PDF)

## AUTHOR INFORMATION

### Corresponding Author

**Thalappil Pradeep** – DST Unit of Nanoscience (DST UNS) and Thematic Unit of Excellence (TUE), Department of Chemistry, Indian Institute of Technology Madras, Chennai 600036, India; [orcid.org/0000-0003-3174-534X](https://orcid.org/0000-0003-3174-534X); Email: [pradeep@iitm.ac.in](mailto:pradeep@iitm.ac.in)

### Authors

**Pallab Basuri** – DST Unit of Nanoscience (DST UNS) and Thematic Unit of Excellence (TUE), Department of Chemistry, Indian Institute of Technology Madras, Chennai 600036, India

**Janifer Shantha Kumar** – DST Unit of Nanoscience (DST UNS) and Thematic Unit of Excellence (TUE), Department of Chemistry, Indian Institute of Technology Madras, Chennai 600036, India

**Subhashree Das** – DST Unit of Nanoscience (DST UNS) and Thematic Unit of Excellence (TUE), Department of Chemistry, Indian Institute of Technology Madras, Chennai 600036, India

Complete contact information is available at:

<https://pubs.acs.org/10.1021/acssuschemeng.2c02070>

### Author Contributions

P.B. and T.P. designed and performed the experiments. P.B., J.S.K., and S.D. helped in performing reactions and microscopy of droplets. P.B. wrote the initial draft of the paper with input from all the authors. The project was conceived under the supervision of T.P.

### Notes

The authors declare no competing financial interest.

## ACKNOWLEDGMENTS

P.B. and J.S.K. thank IIT Madras for a doctoral fellowship. T.P. acknowledges the support of DST. T.P. acknowledges funding for the Centre of Excellence on Molecular Materials and Functions under the Institution of Eminence scheme of IIT Madras.

## ABBREVIATIONS

ESI MS, electrospray ionization mass spectrometry; SE, sugar esters; CR, conversion ratio; AAF, apparent acceleration factor.

## REFERENCES

- (1) Anastas, P. T.; Warner, J. C. *Green Chemistry: Theory and Practice*; Oxford University Press: New York, 1998, p 30.
- (2) Varma, R. S. Greener and Sustainable Trends in Synthesis of Organics and Nanomaterials. *ACS Sustainable Chem. Eng.* **2016**, *4*, 5866–5878.
- (3) *Sustainable Organic Synthesis: Tools and Strategies*; Protti, S.; Palmieri, A., Eds.; The Royal Society of Chemistry: London, U.K., 2022.
- (4) Otera, J.; Nishikido, J. *Esterification: Methods, Reactions, and Applications*, 2nd ed.; John Wiley & Sons: New York, 2009.
- (5) Khan, Z.; Javed, F.; Shamair, Z.; Hafeez, A.; Fazal, T.; Aslam, A.; Zimmerman, W. B.; Rehman, F. Current Developments in Esterification Reaction: A Review on Process and Parameters. *J. Ind. Eng. Chem.* **2021**, *103*, 80–101.
- (6) Procopiou, P. A.; Baugh, S. P. D.; Flack, S. S.; Inglis, G. G. A. An Extremely Powerful Acylation Reaction of Alcohols with Acid Anhydrides Catalyzed by Trimethylsilyl Trifluoromethanesulfonate. *J. Org. Chem.* **1998**, *63*, 2342–2347.
- (7) Van Waes, F. E. A.; Drabowicz, J.; Cukalovic, A.; Stevens, C. V. Efficient and Catalyst-Free Condensation of Acid Chlorides and Alcohols Using Continuous Flow. *Green Chem.* **2012**, *14*, 2776–2779.
- (8) Greene, T. W.; Wuts, P. G. M. *Protective Groups in Organic Synthesis*; John Wiley & Sons: New York, 1999.
- (9) Manabe, K.; Sun, X.-M.; Kobayashi, S. Dehydration Reactions in Water. Surfactant-Type Brønsted Acid-Catalyzed Direct Esterification of Carboxylic Acids with Alcohols in an Emulsion System. *J. Am. Chem. Soc.* **2001**, *123*, 10101–10102.
- (10) Fischer, E.; Speier, A. Darstellung Der Ester. *Ber. Dtsch. Chem. Ges.* **1895**, *28*, 3252–3258.
- (11) Neises, B.; Steglich, W. Simple Method for the Esterification of Carboxylic Acids. *Angew. Chem., Int. Ed. Engl.* **1978**, *17*, 522–524.
- (12) Inanaga, J.; Hirata, K.; Saeki, H.; Katsuki, T.; Yamaguchi, M. A Rapid Esterification by Means of Mixed Anhydride and Its Application to Large-Ring Lactonization. *Bull. Chem. Soc. Jpn.* **1979**, *52*, 1989–1993.



- (13) Liu, B.; Hu, F.; Shi, B.-F. Recent Advances on Ester Synthesis via Transition-Metal Catalyzed C–H Functionalization. *ACS Catal.* **2015**, *5*, 1863–1881.
- (14) Khan, N. R.; Rathod, V. K. Enzyme Catalyzed Synthesis of Cosmetic Esters and Its Intensification: A Review. *Process Biochem.* **2015**, *50*, 1793–1806.
- (15) Neta, N. S.; Teixeira, J. A.; Rodrigues, L. R. Sugar Ester Surfactants: Enzymatic Synthesis and Applications in Food Industry. *Crit. Rev. Food Sci. Nutr.* **2015**, *55*, 595–610.
- (16) Stergiou, P.-Y.; Foukis, A.; Filippou, M.; Koukouritaki, M.; Parapouli, M.; Theodorou, L. G.; Hatziloukas, E.; Afendra, A.; Pandey, A.; Papamichael, E. M. Advances in Lipase-Catalyzed Esterification Reactions. *Biotechnol. Adv.* **2013**, *31*, 1846–1859.
- (17) Devulapalle, K. S.; Gómez de Segura, A.; Ferrer, M.; Alcalde, M.; Mooser, G.; Plou, F. J. Effect of Carbohydrate Fatty Acid Esters on *Streptococcus Sobrinus* and Glucosyltransferase Activity. *Carbohydr. Res.* **2004**, *339*, 1029–1034.
- (18) Szűts, A.; Szabó-Révész, P. Sucrose Esters as Natural Surfactants in Drug Delivery Systems—A Mini-Review. *Int. J. Pharm.* **2012**, *433*, 1–9.
- (19) Habulin, M.; Šabeder, S.; Knez, Ž. Enzymatic Synthesis of Sugar Fatty Acid Esters in Organic Solvent and in Supercritical Carbon Dioxide and Their Antimicrobial Activity. *J. Supercrit. Fluids* **2008**, *45*, 338–345.
- (20) Lee, S. H.; Dang, D. T.; Ha, S. H.; Chang, W.-J.; Koo, Y.-M. Lipase-Catalyzed Synthesis of Fatty Acid Sugar Ester Using Extremely Supersaturated Sugar Solution in Ionic Liquids. *Biotechnol. Bioeng.* **2008**, *99*, 1–8.
- (21) Ganske, F.; Bornscheuer, U. T. Optimization of Lipase-Catalyzed Glucose Fatty Acid Ester Synthesis in a Two-Phase System Containing Ionic Liquids and *t*-BuOH. *J. Mol. Catal. B: Enzym.* **2005**, *36*, 40–42.
- (22) Ganske, F.; Bornscheuer, U. T. Lipase-Catalyzed Glucose Fatty Acid Ester Synthesis in Ionic Liquids. *Org. Lett.* **2005**, *7*, 3097–3098.
- (23) Wang, H.; Lin, H.; Li, X.; Ren, R.; Pu, J.; Zhang, H.; Zheng, Y.; Zhao, J.; Ng, S.; Zhang, H. Application of Phase Transfer Catalysis in the Esterification of Organic Acids: The Primary Products from Ring Hydrocarbon Oxidation Processes. *Catalysts* **2019**, *9*, 851–864.
- (24) Badu-Tawiah, A. K.; Campbell, D. I.; Cooks, R. G. Accelerated C–N Bond Formation in Dropcast Thin Films on Ambient Surfaces. *J. Am. Soc. Mass Spectrom.* **2012**, *23*, 1461–1468.
- (25) Espy, R. D.; Wlekinski, M.; Yan, X.; Cooks, R. G. Beyond the Flask: Reactions on the Fly in Ambient Mass Spectrometry. *TrAC, Trends Anal. Chem.* **2014**, *57*, 135–146.
- (26) Lee, J. K.; Banerjee, S.; Nam, H. G.; Zare, R. N. Acceleration of Reaction in Charged Microdroplets. *Q. Rev. Biophys.* **2015**, *48*, 437–444.
- (27) Yan, X.; Bain, R. M.; Cooks, R. G. Organic Reactions in Microdroplets: Reaction Acceleration Revealed by Mass Spectrometry. *Angew. Chem., Int. Ed.* **2016**, *55*, 12960–12972.
- (28) Saidykhan, A.; Nazir, Y.; Martin, W. H.; Gallagher, R. T.; Bowen, R. D. Accelerated Generation of (Protonated) Imines and Quinoxalines by Formation of C=N Bonds in the Microdroplets of a Nebuliser. *Eur. J. Mass Spectrom.* **2017**, *24*, 3–11.
- (29) Bain, R. M.; Ayrton, S. T.; Cooks, R. G. Fischer Indole Synthesis in the Gas Phase, the Solution Phase, and at the Electrospray Droplet Interface. *J. Am. Soc. Mass Spectrom.* **2017**, *28*, 1359–1364.
- (30) Marsh, B. M.; Iyer, K.; Cooks, R. G. Reaction Acceleration in Electrospray Droplets: Size, Distance, and Surfactant Effects. *J. Am. Soc. Mass Spectrom.* **2019**, *30*, 2022–2030.
- (31) Wei, Z.; Li, Y.; Cooks, R. G.; Yan, X. Accelerated Reaction Kinetics in Microdroplets: Overview and Recent Developments. *Annu. Rev. Phys. Chem.* **2020**, *71*, 31–51.
- (32) Kumar, A.; Mondal, S.; Banerjee, S. Aqueous Microdroplets Capture Elusive Carbocations. *J. Am. Chem. Soc.* **2021**, *143*, 2459–2463.
- (33) Huang, K.-H.; Wei, Z.; Cooks, R. G. Accelerated Reactions of Amines with Carbon Dioxide Driven by Supercid at the Microdroplet Interface. *Chem. Sci.* **2021**, *12*, 2242–2250.
- (34) Feng, L.; Yin, X.; Tan, S.; Li, C.; Gong, X.; Fang, X.; Pan, Y. Ammonium Bicarbonate Significantly Accelerates the Microdroplet Reactions of Amines with Carbon Dioxide. *Anal. Chem.* **2021**, *93*, 15775–15784.
- (35) Gnanamani, E.; Yan, X.; Zare, R. N. Chemoselective N-Alkylation of Indoles in Aqueous Microdroplets. *Angew. Chem., Int. Ed. Engl.* **2020**, *59*, 3069–3072.
- (36) English, N. J. Sustainable Exploitation and Commercialization of Ultradense Nanobubbles: Reinventing Liquidity. *ACS Sustainable Chem. Eng.* **2022**, *10*, 3383–3386.
- (37) Banerjee, S.; Zare, R. N. Syntheses of Isoquinoline and Substituted Quinolines in Charged Microdroplets. *Angew. Chem., Int. Ed.* **2015**, *54*, 14795–14799.
- (38) Girod, M.; Moyano, E.; Campbell, D. I.; Cooks, R. G. Accelerated Bimolecular Reactions in Microdroplets Studied by Desorption Electrospray Ionization Mass Spectrometry. *Chem. Sci.* **2011**, *2*, 501–510.
- (39) Müller, T.; Badu-Tawiah, A.; Cooks, R. G. Accelerated Carbon–Carbon Bond-Forming Reactions in Preparative Electrospray. *Angew. Chem., Int. Ed.* **2012**, *51*, 11832–11835.
- (40) Basuri, P.; Gonzalez, L. E.; Morato, N. M.; Pradeep, T.; Cooks, R. G. Accelerated Microdroplet Synthesis of Benzimidazoles by Nucleophilic Addition to Protonated Carboxylic Acids. *Chem. Sci.* **2020**, *11*, 12686–12694.
- (41) Sahota, N.; AbuSalim, D. I.; Wang, M. L.; Brown, C. J.; Zhang, Z.; El-Baba, T. J.; Cook, S. P.; Clemmer, D. E. A Microdroplet-Accelerated Biginelli Reaction: Mechanisms and Separation of Isomers Using IMS-MS. *Chem. Sci.* **2019**, *10*, 4822–4827.
- (42) Sarih, N. M.; Romero-Perez, D.; Bastani, B.; Rauytanapanit, M.; Boisdon, C.; Praneenarat, T.; Tajuddin, H. A.; Abdullah, Z.; Badu-Tawiah, A. K.; Maher, S. Accelerated Nucleophilic Substitution Reactions of Dansyl Chloride with Aniline under Ambient Conditions via Dual-Tip Reactive Paper Spray. *Sci. Rep.* **2020**, *10*, 21504.
- (43) Bain, R. M.; Pulliam, C. J.; Thery, F.; Cooks, R. G. Accelerated Chemical Reactions and Organic Synthesis in Leidenfrost Droplets. *Angew. Chem., Int. Ed.* **2016**, *55*, 10478–10482.
- (44) Lee, J. K.; Kim, S.; Nam, H. G.; Zare, R. N. Microdroplet Fusion Mass Spectrometry for Fast Reaction Kinetics. *Proc. Natl. Acad. Sci. U.S.A.* **2015**, *112*, 3898–3903.
- (45) Yan, X.; Cheng, H.; Zare, R. N. Two-Phase Reactions in Microdroplets without the Use of Phase-Transfer Catalysts. *Angew. Chem., Int. Ed.* **2017**, *56*, 3562–3565.
- (46) Liu, C.; Li, J.; Chen, H.; Zare, R. N. Scale-up of Microdroplet Reactions by Heated Ultrasonic Nebulization. *Chem. Sci.* **2019**, *10*, 9367–9373.
- (47) Lee, J. K.; Nam, H. G.; Zare, R. N. Microdroplet Fusion Mass Spectrometry: Accelerated Kinetics of Acid-Induced Chlorophyll Demetallation. *Q. Rev. Biophys.* **2017**, *50*, 1–7.
- (48) Nie, H.; Wei, Z.; Qiu, L.; Chen, X.; Holden, D. T.; Cooks, R. G. High-Yield Gram-Scale Organic Synthesis Using Accelerated Microdroplet/Thin Film Reactions with Solvent Recycling. *Chem. Sci.* **2020**, *11*, 2356–2361.
- (49) Xiong, H.; Lee, J. K.; Zare, R. N.; Min, W. Strong Concentration Enhancement of Molecules at the Interface of Aqueous Microdroplets. *J. Phys. Chem. B* **2020**, *124*, 9938–9944.
- (50) Wei, H.; Vejerano, E. P.; Leng, W.; Huang, Q.; Willner, M. R.; Marr, L. C.; Vikesland, P. J. Aerosol Microdroplets Exhibit a Stable pH Gradient. *Proc. Natl. Acad. Sci. U.S.A.* **2018**, *115*, 7272–7277.
- (51) Gao, D.; Jin, F.; Lee, J. K.; Zare, R. N. Aqueous Microdroplets Containing Only Ketones or Aldehydes Undergo Dakin and Baeyer–Villiger Reactions. *Chem. Sci.* **2019**, *10*, 10974–10978.
- (52) Kang, J.; Lhee, S.; Lee, J. K.; Zare, R. N.; Nam, H. G. Restricted Intramolecular Rotation of Fluorescent Molecular Rotors at the Periphery of Aqueous Microdroplets in Oil. *Sci. Rep.* **2020**, *10*, 1–10.

(53) Xiong, H.; Lee, J. K.; Zare, R. N.; Min, W. Strong Electric Field Observed at the Interface of Aqueous Microdroplets. *J. Phys. Chem. Lett.* **2020**, *11*, 7423–7428.

(54) Mondal, S.; Acharya, S.; Biswas, R.; Bagchi, B.; Zare, R. N. Enhancement of Reaction Rate in Small-Sized Droplets: A Combined Analytical and Simulation Study. *J. Chem. Phys.* **2018**, *148*, 244704.

(55) Burris, B. J.; Badu-Tawiah, A. K. Enzyme-Catalyzed Hydrolysis of Lipids in Immiscible Microdroplets Studied by Contained-Electrospray Ionization. *Anal. Chem.* **2021**, *93*, 13001–13007.

(56) Gallo, A., Jr.; Muszkopf, N. H.; Liu, X.; Yang, Z.; Petry, J.; Zhang, P.; Thoroddsen, S.; Im, H.; Mishra, H. On the Formation of Hydrogen Peroxide in Water Microdroplets. *Chem. Sci.* **2022**, *13*, 2574–2583.

(57) Wei, Z.; Zhang, X.; Wang, J.; Zhang, S.; Zhang, X.; Cooks, R. G. High Yield Accelerated Reactions in Nonvolatile Microthin Films: Chemical Derivatization for Analysis of Single-Cell Intracellular Fluid. *Chem. Sci.* **2018**, *9*, 7779–7786.

(58) Kwan, V.; Malevanets, A.; Consta, S. Where Do the Ions Reside in a Highly Charged Droplet? *J. Phys. Chem. A* **2019**, *123*, 9298–9310.

(59) Narendra, N.; Chen, X.; Wang, J.; Charles, J.; Cooks, R. G.; Kubis, T. Quantum Mechanical Modeling of Reaction Rate Acceleration in Microdroplets. *J. Phys. Chem. A* **2020**, *124*, 4984–4989.

(60) Qiu, L.; Wei, Z.; Nie, H.; Cooks, R. G. Reaction Acceleration Promoted by Partial Solvation at the Gas/Solution Interface. *Chempluschem* **2021**, *86*, 1362–1365.

(61) Kropotova, S.; Strizhak, P. Collisions of Liquid Droplets in a Gaseous Medium under Conditions of Intense Phase Transformations: Review. *Energies* **2021**, *14*, 6150–6177.

(62) Zhu, X.; Zhang, W.; Lin, Q.; Ye, M.; Xue, L.; Liu, J.; Wang, Y.; Cheng, H. Direct Microdroplet Synthesis of Carboxylic Acids from Alcohols by Preparative Paper Spray Ionization without Phase Transfer Catalysts. *ACS Sustainable Chem. Eng.* **2019**, *7*, 6486–6491.

(63) Chen, H.; Venter, A.; Cooks, R. G. Extractive Electrospray Ionization for Direct Analysis of Undiluted Urine, Milk and Other Complex Mixtures without Sample Preparation. *Chem. Commun.* **2006**, *19*, 2042–2044.

(64) Fedick, P. W.; Iyer, K.; Wei, Z.; Avramova, L.; Capek, G. O.; Cooks, R. G. Screening of the Suzuki Cross-Coupling Reaction Using Desorption Electrospray Ionization in High-Throughput and in Leidenfrost Droplet Experiments. *J. Am. Soc. Mass Spectrom.* **2019**, *30*, 2144–2151.

(65) Jiang, P.; Lucy, C. A. Enhancement of Ionization Efficiency of Mass Spectrometric Analysis from Non-Electrospray Ionization Friendly Solvents with Conventional and Novel Ionization Techniques. *Anal. Chim. Acta* **2015**, *897*, 45–52.

(66) Banerjee, S.; Zare, R. N. Influence of Inlet Capillary Temperature on the Microdroplet Chemistry Studied by Mass Spectrometry. *J. Phys. Chem. A* **2019**, *123*, 7704–7709.

(67) Xia, Z.; Williams, E. R. Effect of Droplet Lifetime on Where Ions Are Formed in Electrospray Ionization. *Analyst* **2019**, *144*, 237–248.

## Recommended by ACS

### Mobility-Classified Mass Spectrometry Reveals a Complete Picture of the Electrospray Outcome

Christian Lübbert and Wolfgang Peukert

SEPTEMBER 25, 2020  
THE JOURNAL OF PHYSICAL CHEMISTRY A

READ 

### Enzyme-Catalyzed Hydrolysis of Lipids in Immiscible Microdroplets Studied by Contained-Electrospray Ionization

Benjamin J. Burris and Abraham K. Badu-Tawiah

SEPTEMBER 15, 2021  
ANALYTICAL CHEMISTRY

READ 

### Simple and Reproducible Derivatization with Benzoyl Chloride: Improvement of Sensitivity for Multiple Lipid Classes in RP-UHPLC/MS

Ondřej Peterka, Michal Holčápek, *et al.*

OCTOBER 08, 2021  
ANALYTICAL CHEMISTRY

READ 

### Synthesis of Starch-Based Plasmonic Core-Shell Microparticles for SERS Applications

Ke Luo, Young-Rok Kim, *et al.*

JULY 25, 2022  
ACS SUSTAINABLE CHEMISTRY & ENGINEERING

READ 

Get More Suggestions >



# Accelerated Non-Enzymatic Fatty Acid Esterification During Microdroplet Collision: A Method for Enhanced Sustainability

*Pallab Basuri<sup>†</sup>, Jenifer Shantha Kumar<sup>†</sup>, Subhashree Das<sup>†</sup>, and Thalappil Pradeep<sup>†\*</sup>*

<sup>†</sup> DST Unit of Nanoscience (DST UNS) and Thematic Unit of Excellence (TUE), Department of Chemistry, Indian Institute of Technology Madras, Chennai 600036, India.

\* Corresponding author

**Thalappil Pradeep** – DST Unit of Nanoscience (DST UNS) and Thematic Unit of Excellence (TUE), Department of Chemistry, Indian Institute of Technology Madras, Chennai-600 036, India;  
orcid.org/0000-0003-3174-534X;

Email: [pradeep@iitm.ac.in](mailto:pradeep@iitm.ac.in)

This supporting information contains:

- 28 pages (S1-S28)

- 26 figures (Figure S1-S26)

- 1 scheme (Scheme S1)

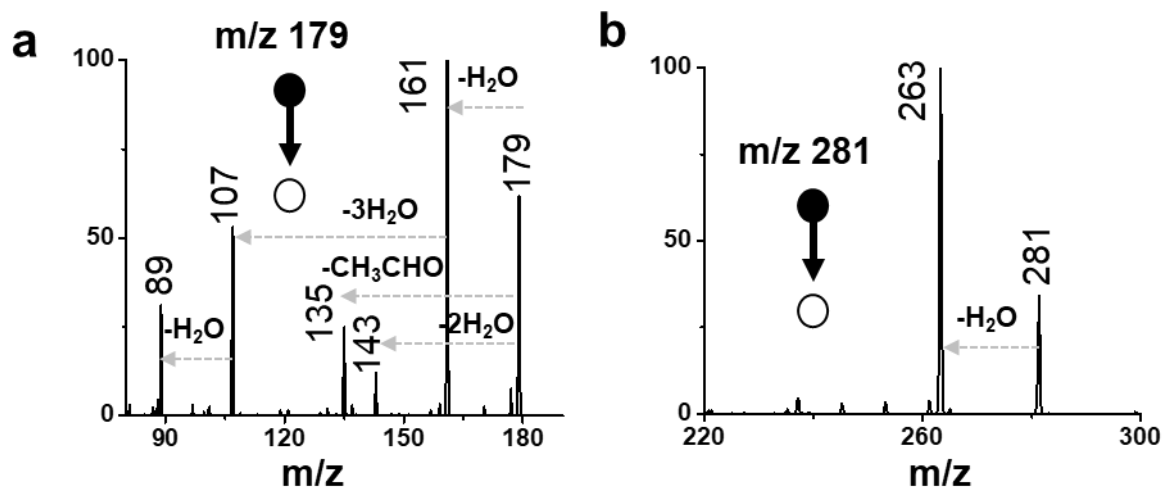


**Figure S1.** MS/MS spectrum of isolated peaks of a) glucose and b) oleic acid in negative ion mode.

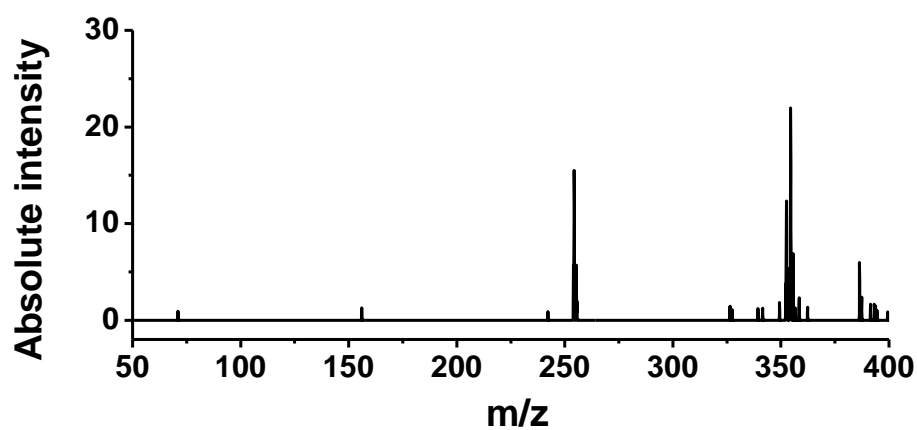


**Figure S2.** Mass spectrum collected from a nebulized spray of oleic acid in toluene. No potential was applied for the spray. The peaks observed here have absolute intensity lower than 30, while a typical spectrum shows intensity in the range of  $10^5$ - $10^6$ . The origin of such low intense peaks could be due to chemical or electronic noise from the instrument. We did not observe any peak corresponding to deprotonated oleic acid at m/z 281.

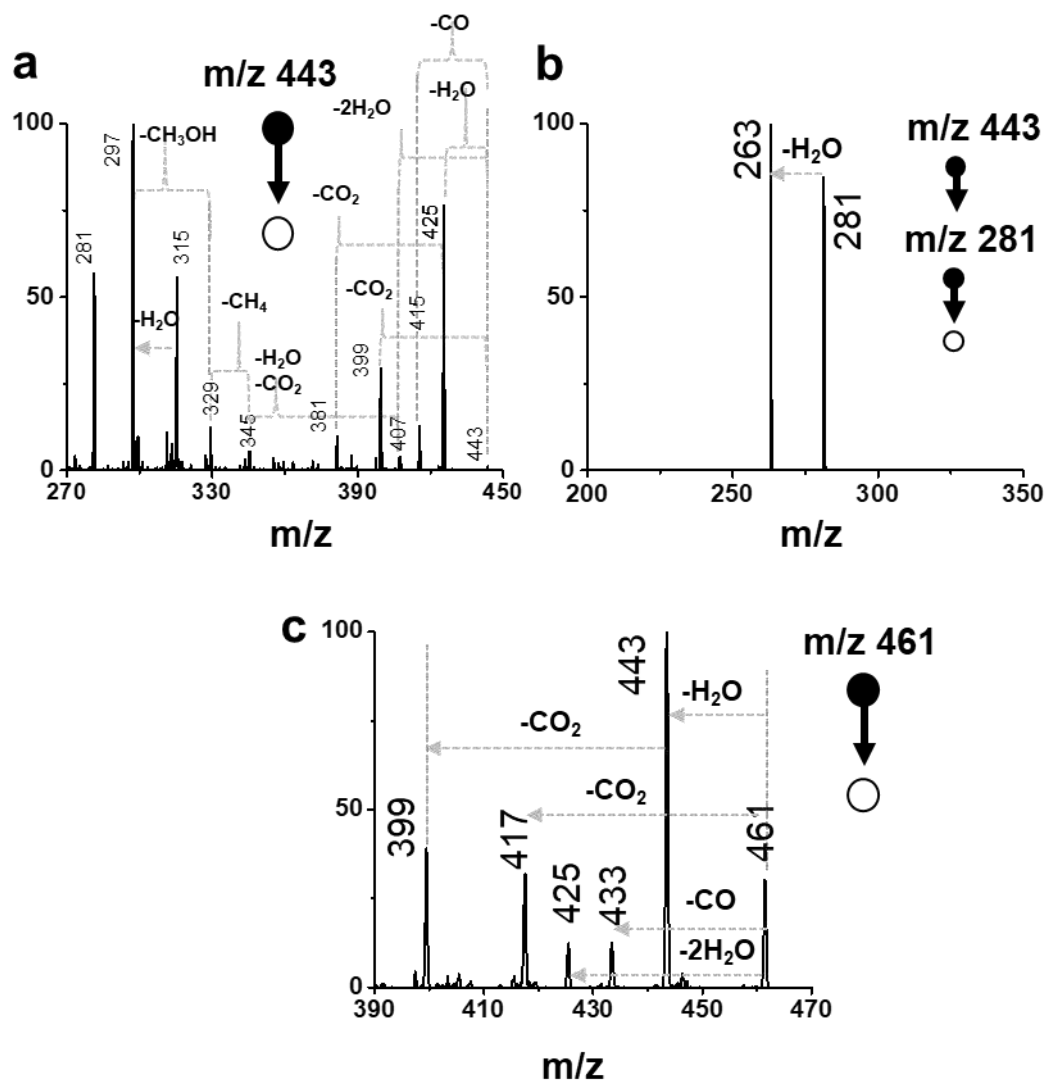
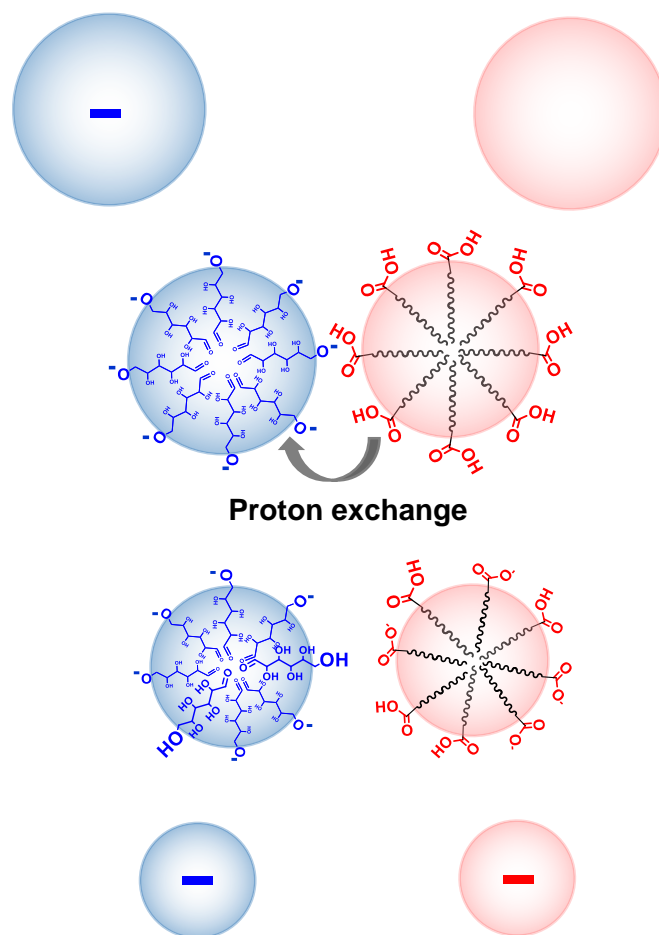
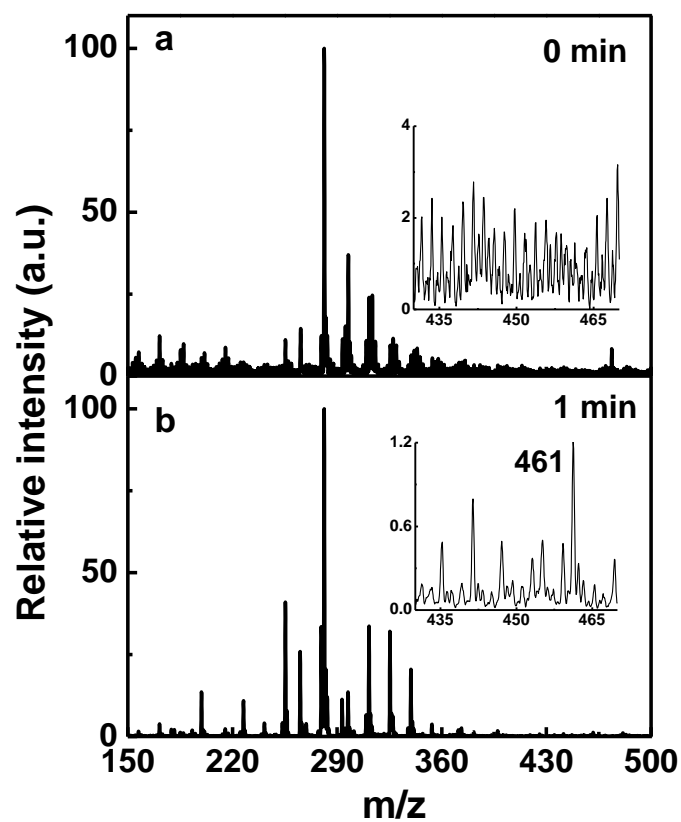


**Figure S3.** MS/MS and MS/MS/MS mass spectra of m/z (a), 443 (b), 281 and (c) 461 in negative ion mode. The noise in the spectra is due to low signal intensities during ion isolation.

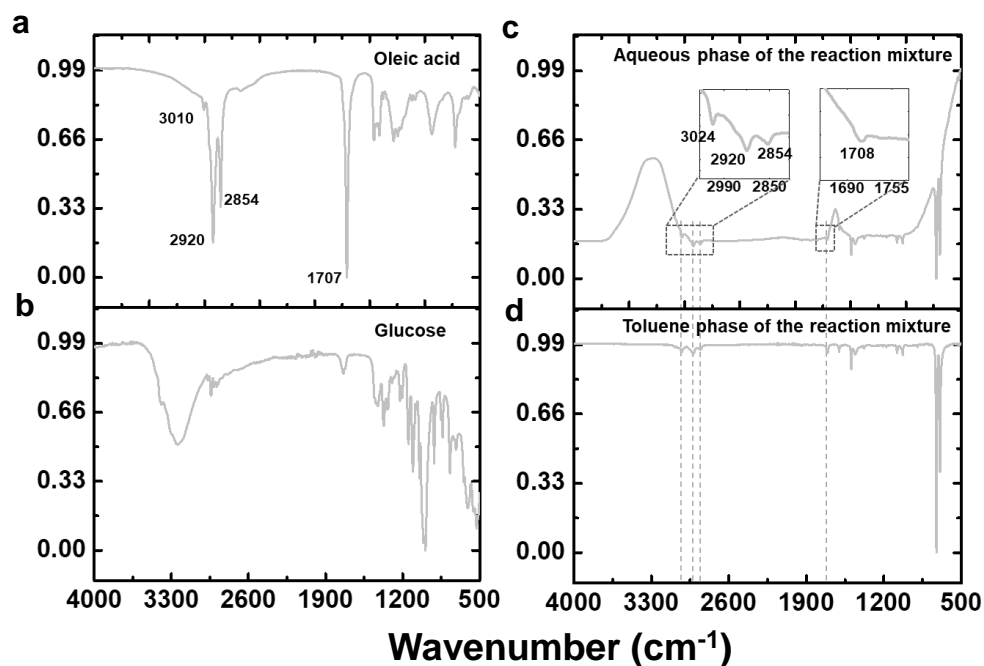




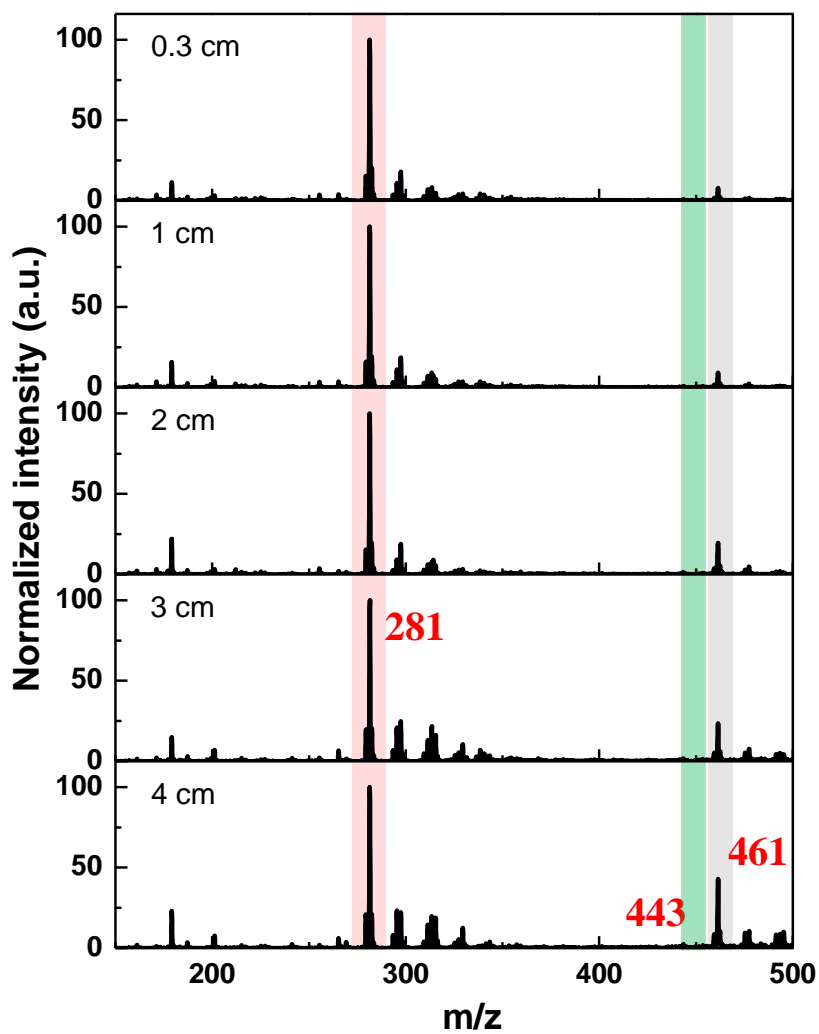
**Scheme S1.** Schematic illustration of microdroplet collision, showing proton exchange at the interface making both the droplets negatively charged.



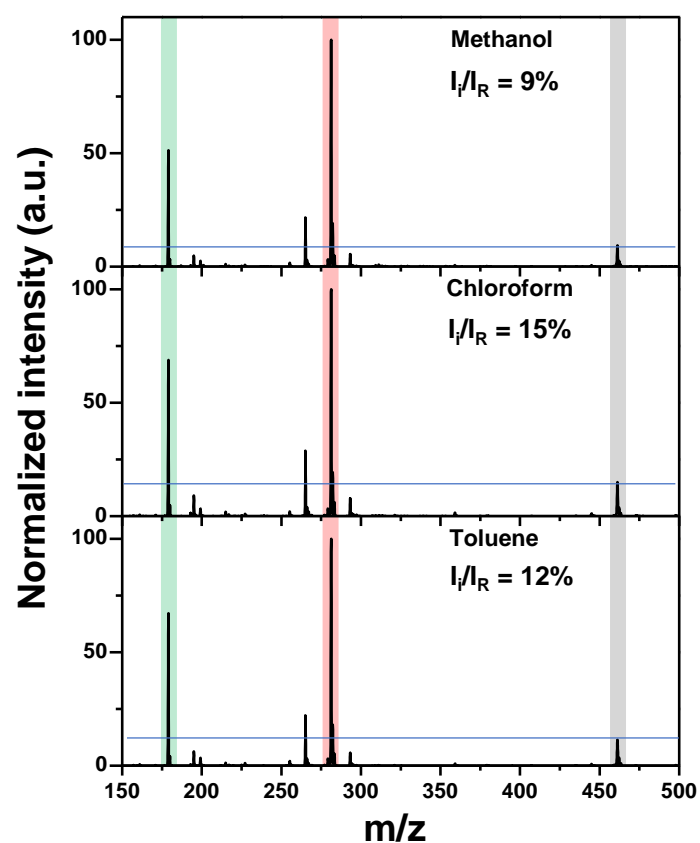
**Figure S4.** Mass spectra collected from the aqueous phase a) after bulk reaction and b) after 1 min of sonication. Insets of both Figures show the zoomed-in view of the selected mass range to display the peak intensity of m/z 461.



**Figure S5.** IR-spectra of a,b) standard oleic acid and glucose, and c,d) aqueous and toluene phase after extraction, showing the presence of oleic acid and toluene, respectively. Dotted lines in the aqueous and toluene phase indicate the characteristic peaks of oleic acid resulting from the CH stretch, asymmetric and symmetric stretches of CH<sub>2</sub>, and C=O stretch at 3010, 2926, 2854, and 1707 cm<sup>-1</sup>, respectively, suggesting the presence of oleic acid in aqueous solution.

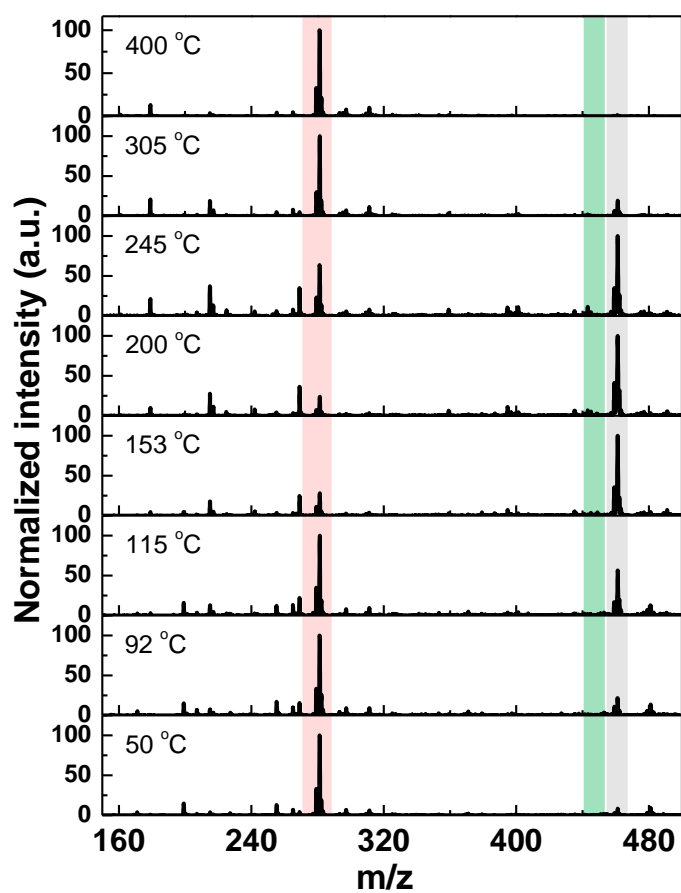


**Figure S6.** Distance dependence mass spectra of glucose/oleic acid reaction mixture. Red, green, and grey shades indicate the peak positions for deprotonated oleic acid, product, and intermediate, respectively.

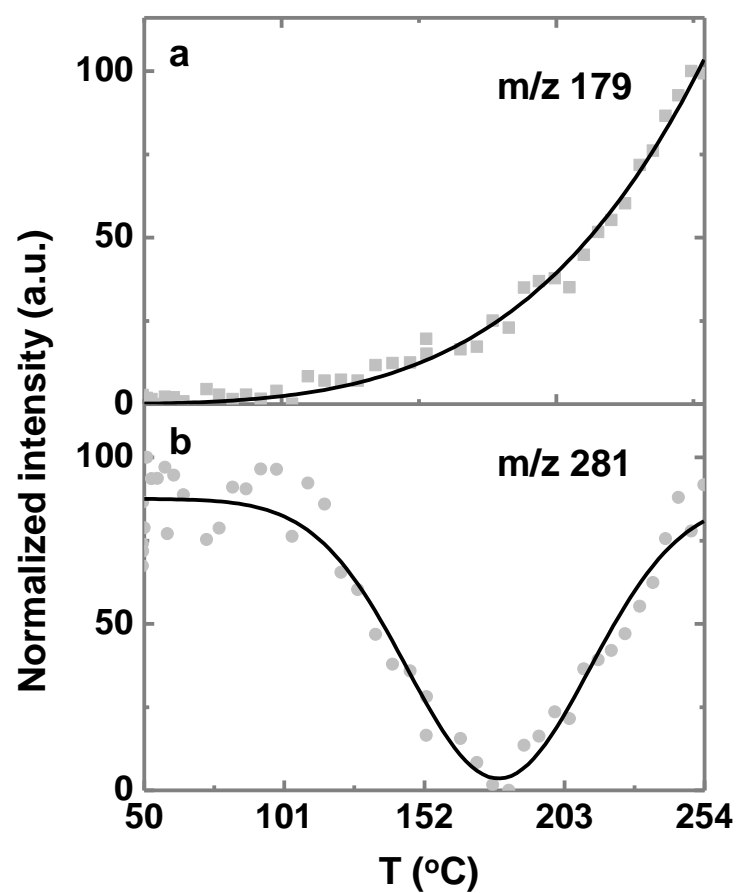


**Figure S7.** Mass spectra of reaction mixtures in methanol, chloroform, and toluene, showing better reaction yield in a nonpolar solvent system in comparison to a polar solvent. Red, green and grey shades indicate the peak positions for deprotonated oleic acid, glucose, and intermediate, respectively. Higher relative ratio of the peak intensity (indicated by blue horizontal lines) in chloroform and toluene than that of methanol shows better reaction in the nonpolar medium.

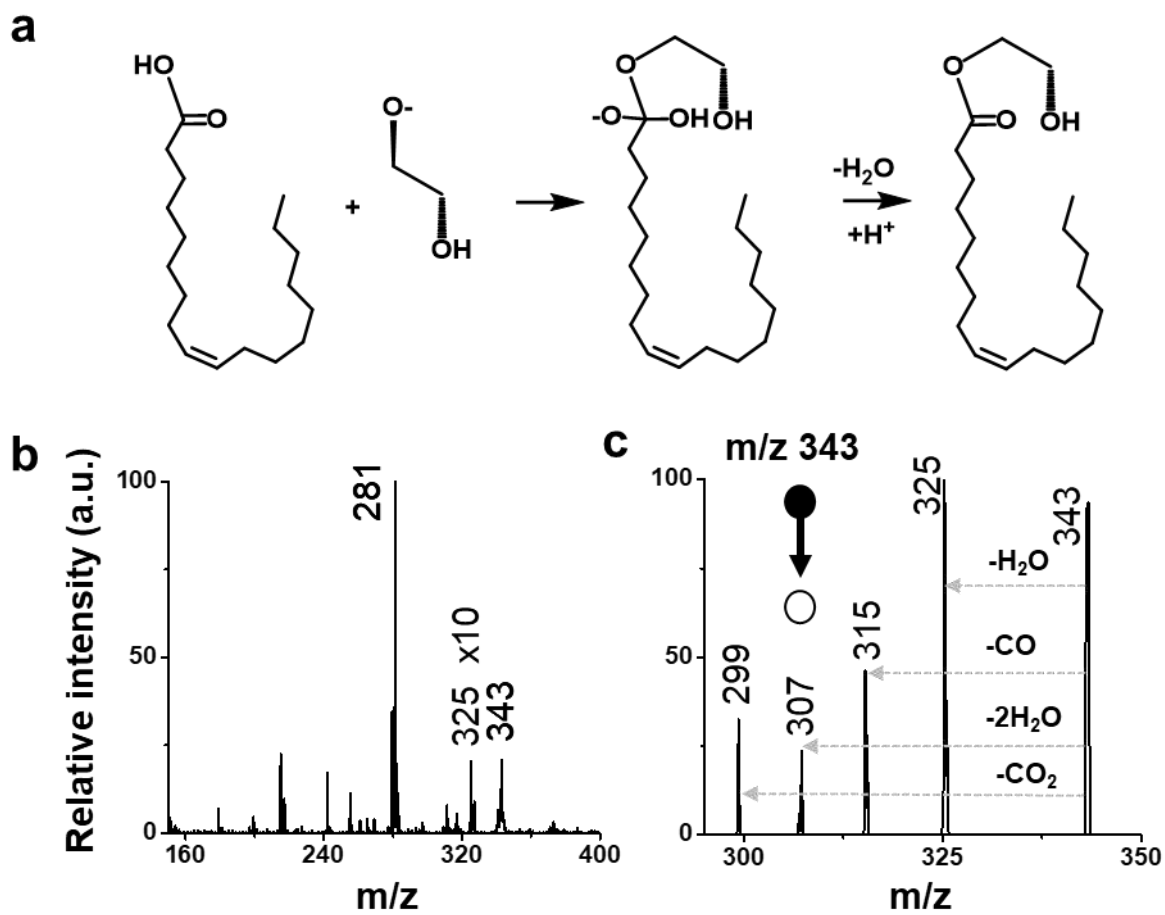




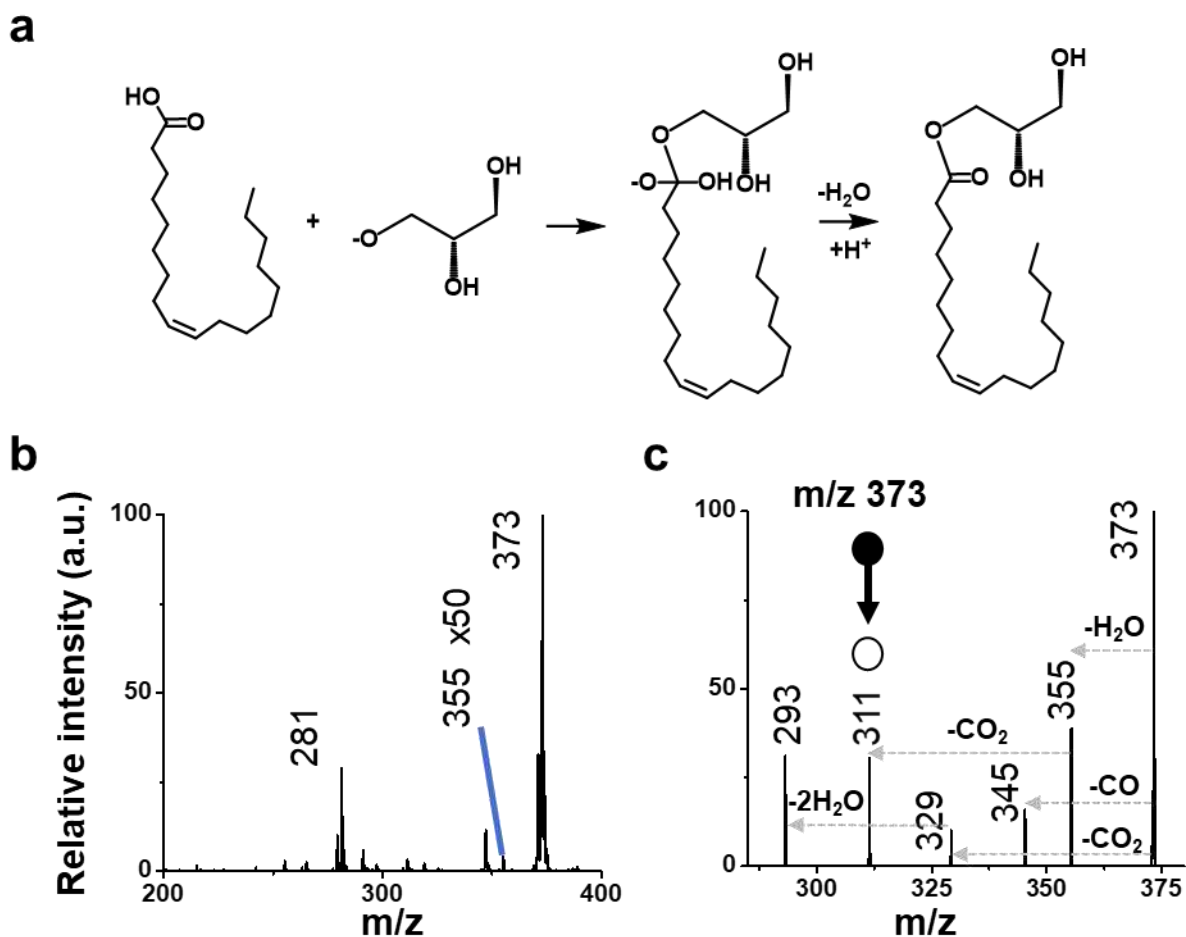
**Figure S8.** Temperature dependent mass spectra of glucose/oleic acid reactions. Red, green, and grey shades highlight the peak positions at  $m/z$  281, 443, and 461, respectively.



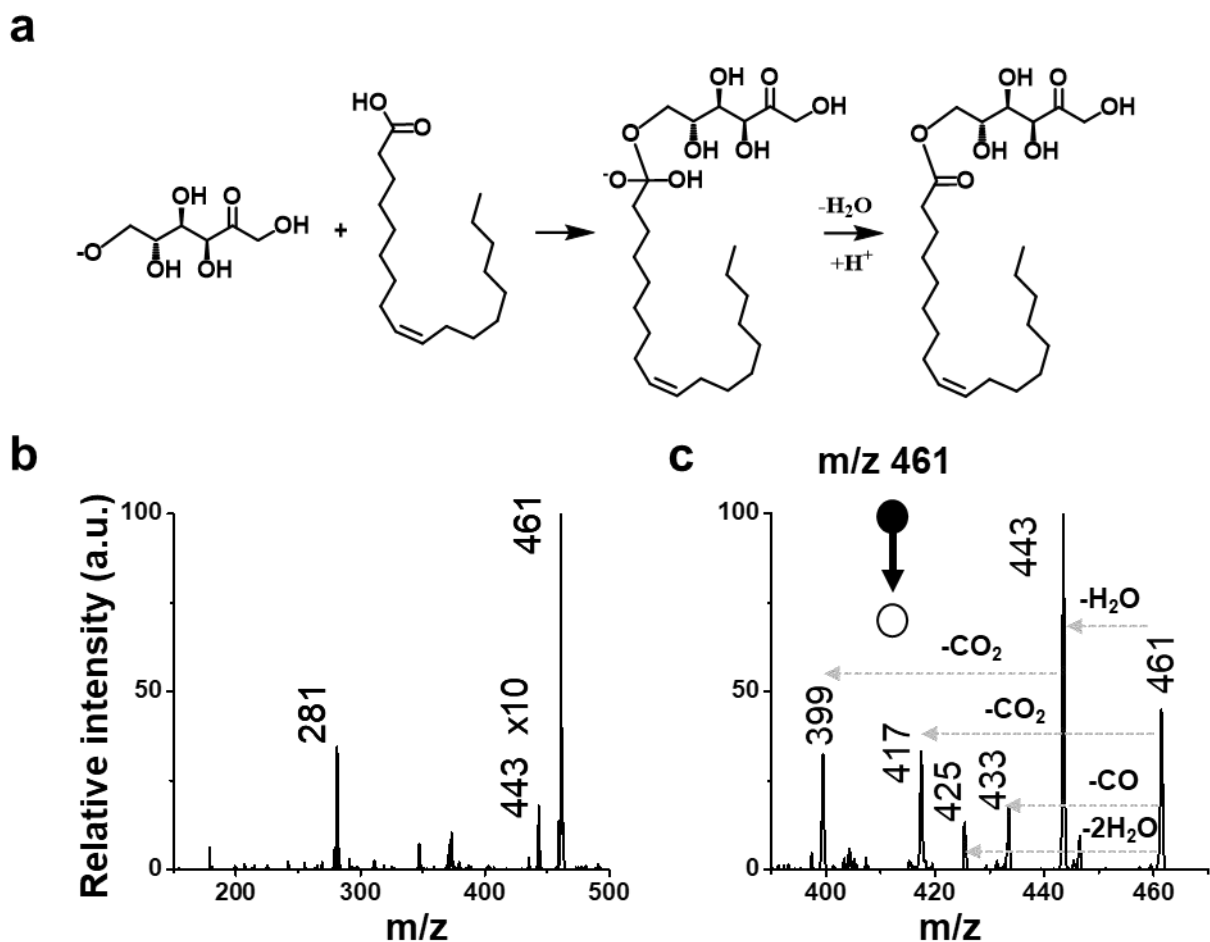
**Figure S9.** Ion intensity Vs temperature plot for a) glucose (m/z 179) and b) oleic acid (m/z 281).



**Figure S10.** Microdroplet synthesis of ethylene glycol/oleic acid ester. A) Reaction scheme showing the formation of the tetrahedral intermediate and neutral product after a water loss. B) Full range mass spectrum of the microdroplet reaction showing peaks for reagent, product, and intermediate species at  $m/z$  281, 325, and 343, respectively. Peak at  $m/z$  325 is multiplied 10 times. Note that the additional peaks in the spectrum are due to chemical or electrical noise. C) MS/MS spectrum of the intermediate peak.

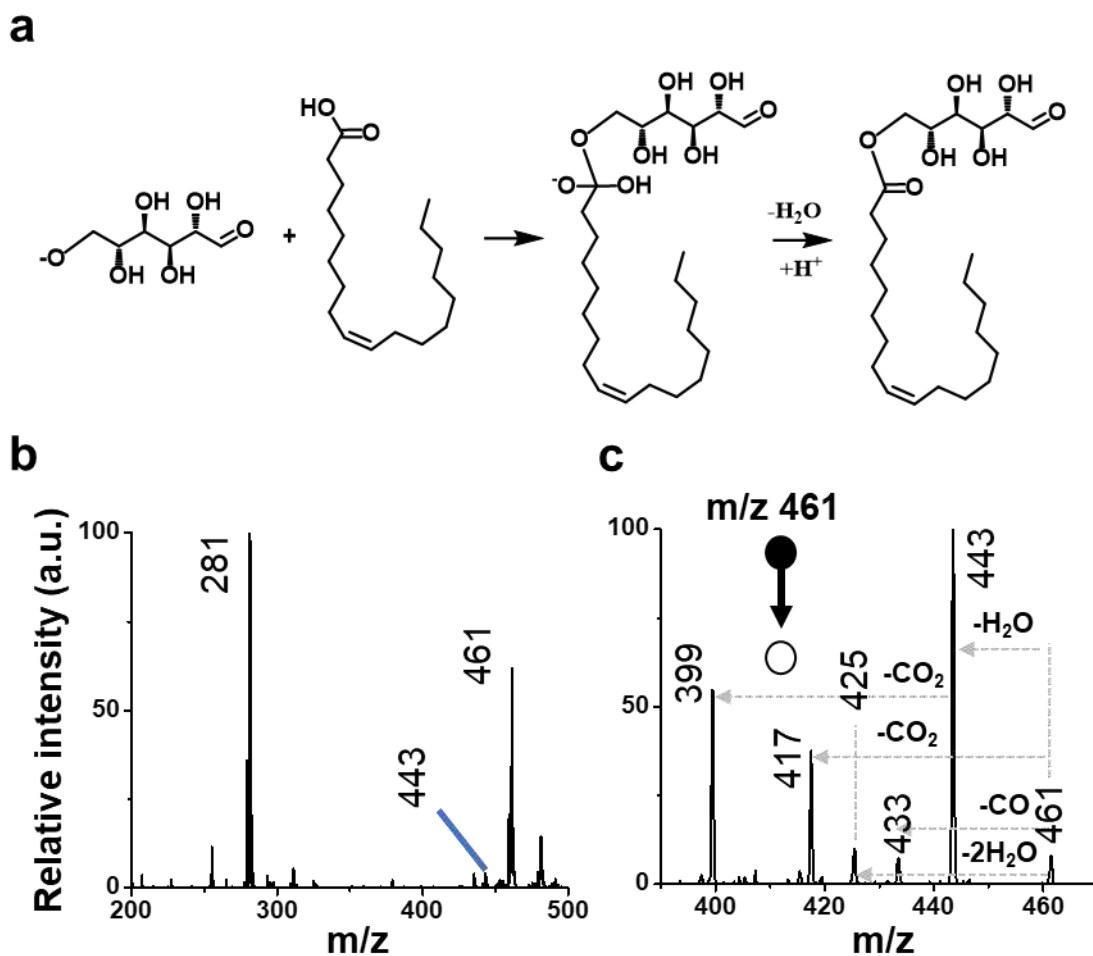


**Figure S11.** Microdroplet synthesis of glycerol/oleic acid ester. A) Reaction scheme showing the formation of the tetrahedral intermediate and neutral product after a water loss. B) Full range mass spectrum of the microdroplet reaction showing peaks for reagent, product and intermediate species at  $m/z$  281, 355 and 373, respectively. Peak at  $m/z$  335 is multiplied 50 times. Note that the additional peaks in the spectrum are due to chemical or electrical noise. C) MS/MS spectrum of the intermediate peak at  $m/z$  373.

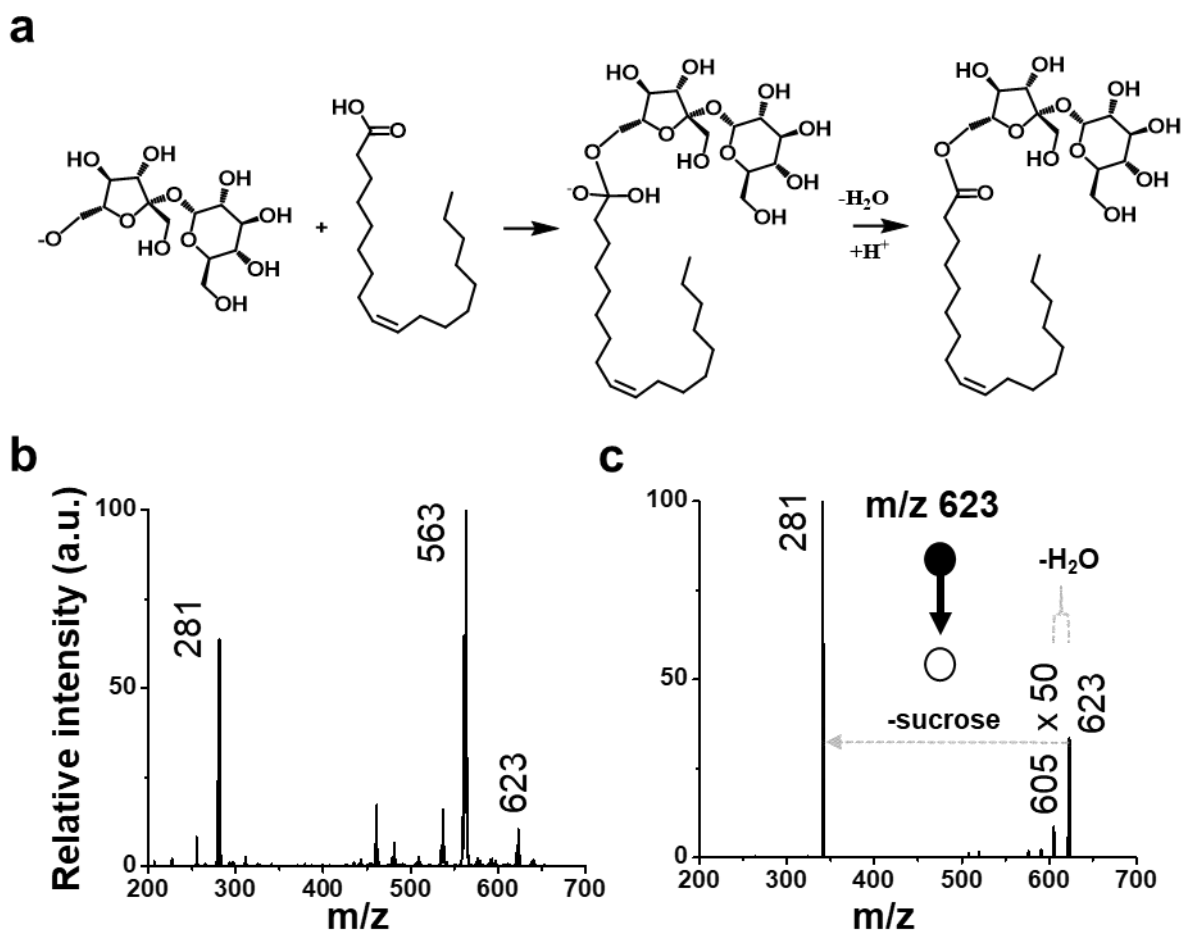


**Figure S12.** Microdroplet synthesis of fructose/oleic acid ester. A) Reaction scheme showing the formation of the tetrahedral intermediate and neutral product after a water loss. B) Full range mass spectrum of the microdroplet reaction showing deprotonated reagent, product, and intermediate peak at  $m/z$  281, 443, and 461, respectively. Peak at  $m/z$  443 is multiplied 10 times. Note that the other peaks in the spectrum are due to chemical or electrical noise. C) MS/MS spectrum of the intermediate peak at  $m/z$  461.

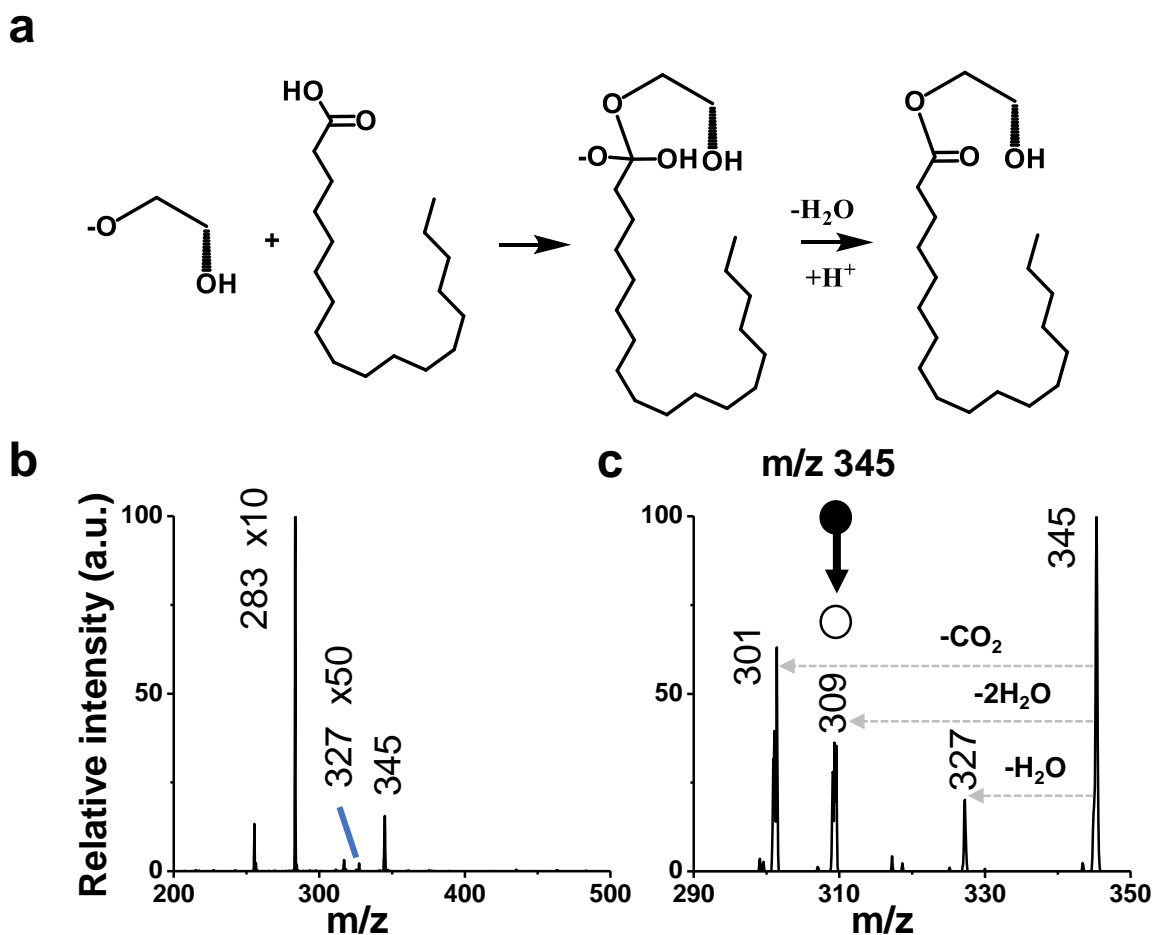




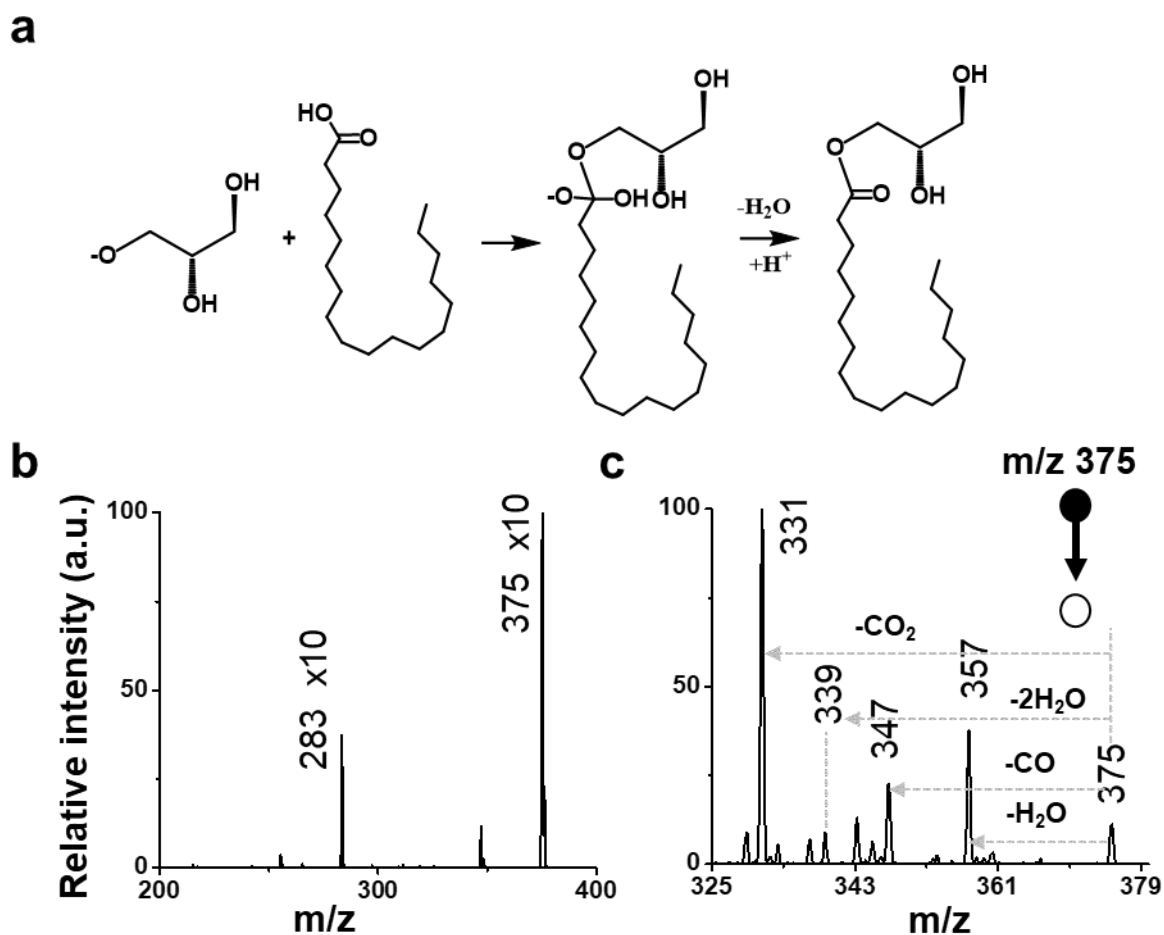
**Figure S13.** Microdroplet synthesis of mannose/oleic acid ester. A) Reaction scheme showing the formation of the tetrahedral intermediate and neutral product after a water loss. B) Full range mass spectrum of the microdroplet reaction showing deprotonated reagent, product, and intermediate peak at  $m/z$  281, 443, and 461, respectively. Note that the other peaks in the spectrum are due to chemical or electrical noise. C) MS/MS spectrum of the intermediate peak at  $m/z$  461.



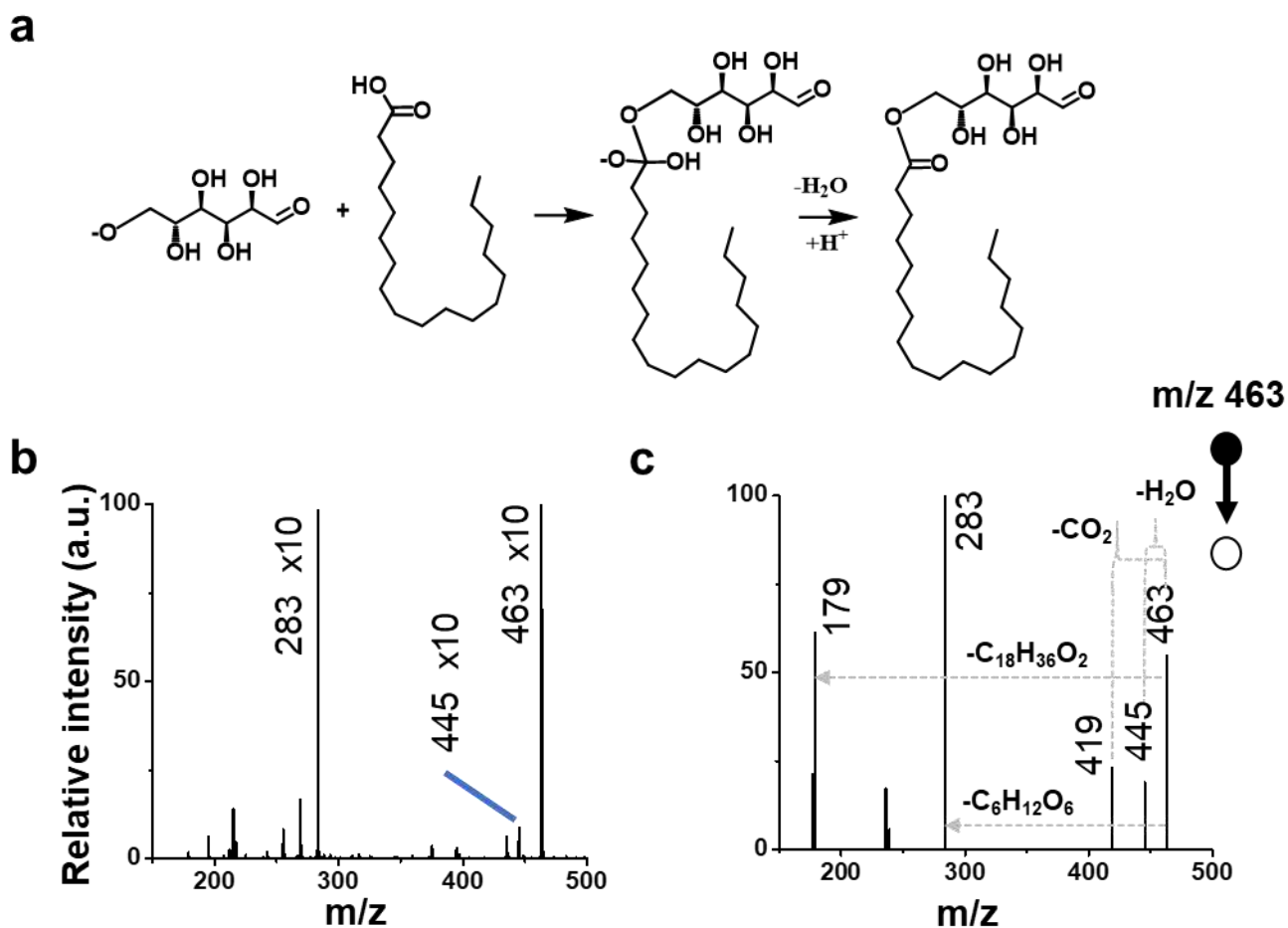
**Figure S14.** Microdroplet synthesis of glycerol/oleic acid ester. A) Reaction scheme showing the formation of the tetrahedral intermediate and neutral product after a water loss. B) Full range mass spectrum of the microdroplet reaction showing deprotonated reagent and intermediate peak at  $m/z$  281 and 623, respectively. The base peak at  $m/z$  563 corresponds to a dimer of oleic acid. Note that the other peaks in the spectrum are due to chemical or electrical noise. C) MS/MS spectrum of the intermediate peak at  $m/z$  623. Peak at  $m/z$  605 is multiplied 50 times.



**Figure S15.** Microdroplet synthesis of ethylene glycol/stearic acid ester. A) Reaction scheme showing the formation of the tetrahedral intermediate and neutral product after a water loss. B) Full range mass spectrum of the microdroplet reaction showing deprotonated reagent, product, and intermediate peak at  $m/z$  281, 327, and 345, respectively. Peaks at  $m/z$  283 and 327 are multiplied 10 and 50 times. Note that the other peaks in the spectrum are due to chemical or electrical noise. C) MS/MS spectrum of the intermediate at  $m/z$  345.

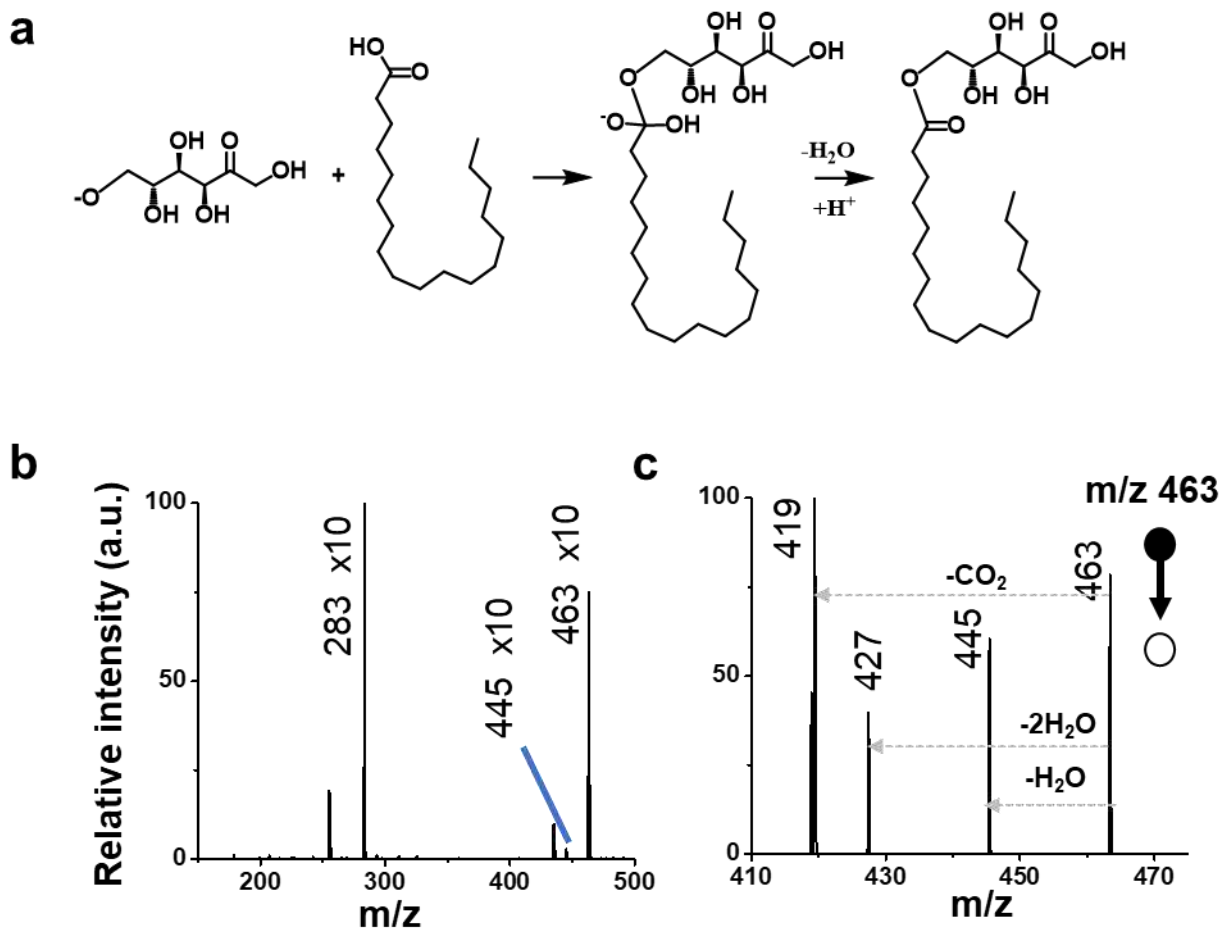


**Figure S16.** Microdroplet synthesis of glycerol/stearic acid ester. A) Reaction scheme showing the formation of the tetrahedral intermediate and neutral product after a water loss. B) Full range mass spectrum of the microdroplet reaction showing deprotonated reagent and intermediate peak at  $m/z$  281 and 375, respectively. Peaks are multiplied 10 times. Note that the other peaks in the spectrum are due to chemical or electrical noise. C) MS/MS spectrum of the intermediate at  $m/z$  375.

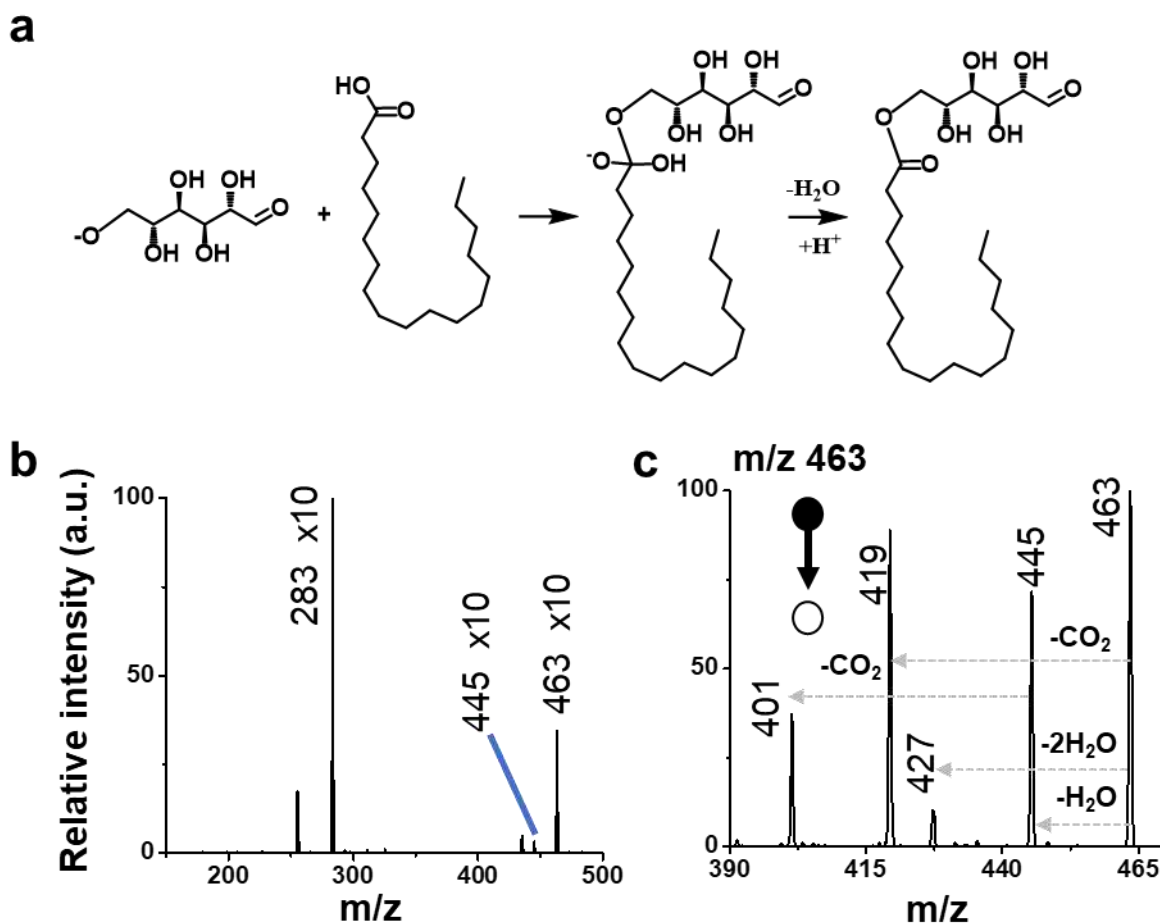


**Figure S17.** Microdroplet synthesis of glucose/stearic acid ester. A) Reaction scheme showing the formation of the tetrahedral intermediate and neutral product after a water loss. B) Full range mass spectrum of the microdroplet reaction showing deprotonated reagent, product, and intermediate peak at  $m/z$  281, 445, and 463, respectively. Peaks are multiplied 10 times. Note that the other peaks in the spectrum are due to chemical or electrical noise. C) MS/MS spectrum of the intermediate at  $m/z$  463.

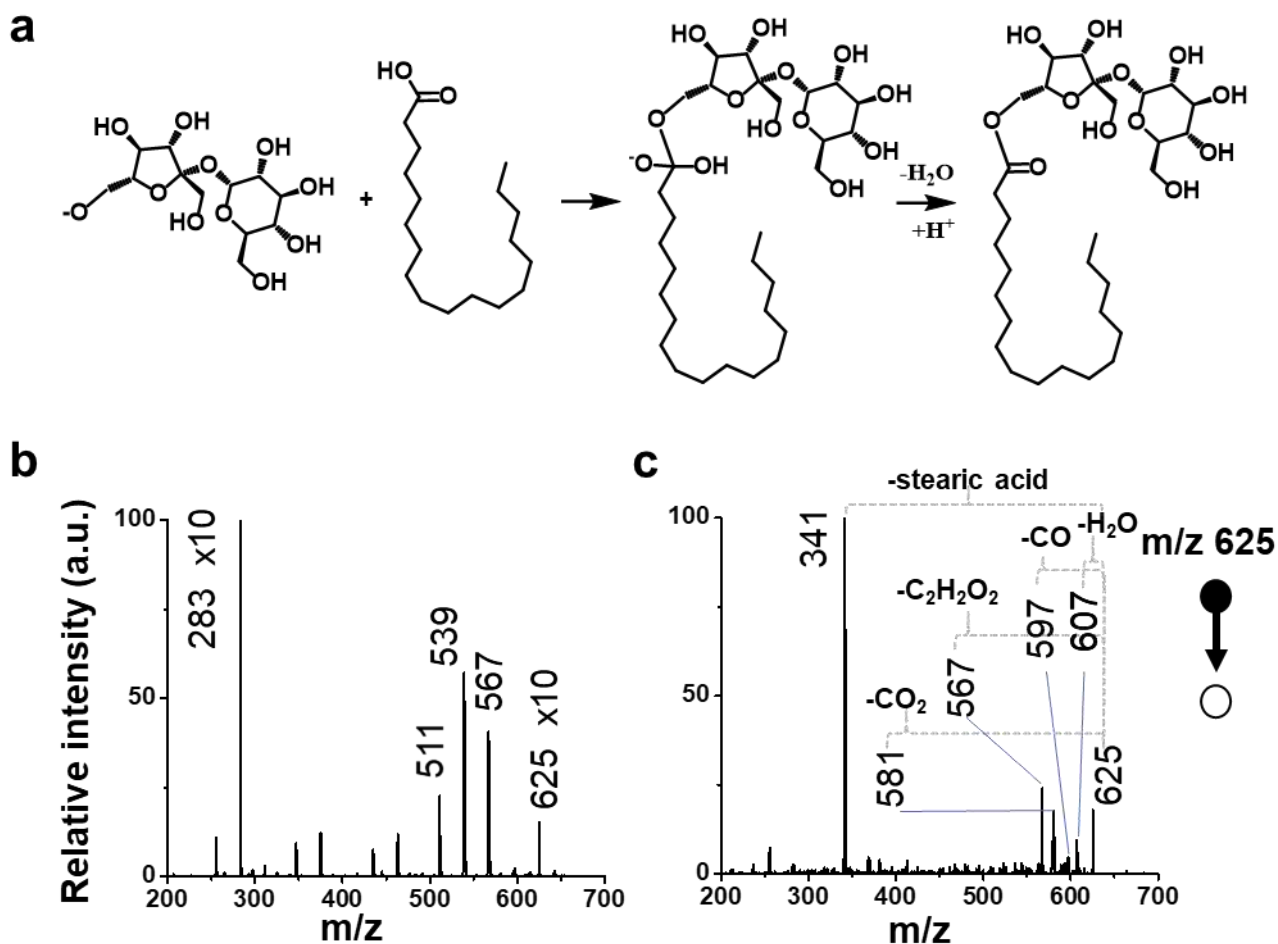




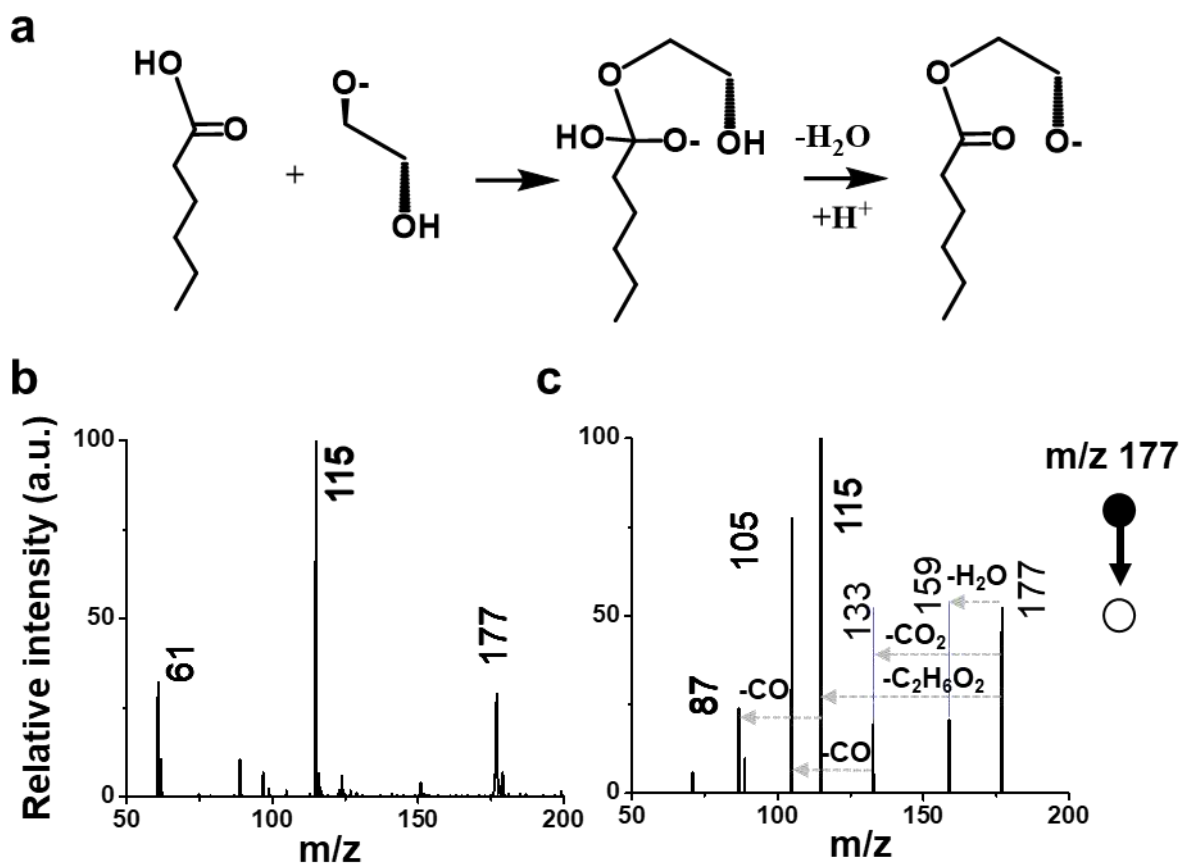
**Figure S18.** Microdroplet synthesis of fructose/stearic acid ester. A) Reaction scheme showing the formation of the tetrahedral intermediate and neutral product after a water loss. B) Full range mass spectrum of the microdroplet reaction showing deprotonated reagent, product, and intermediate peak at  $m/z$  281, 445, and 463, respectively. Peaks are multiplied 10 times. Note that the other peaks in the spectrum are due to chemical or electrical noise. C) MS/MS spectrum of the intermediate at  $m/z$  463.



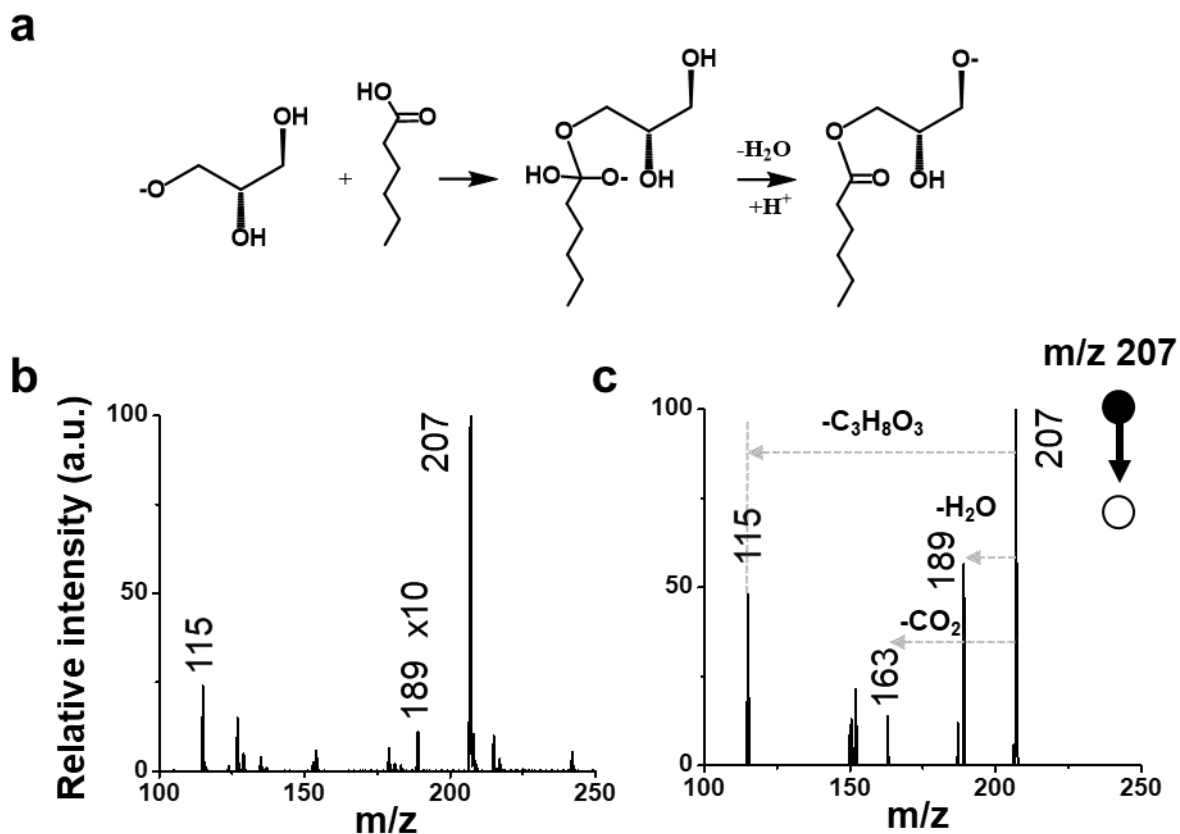
**Figure S19.** Microdroplet synthesis of mannose/stearic acid ester. A) Reaction scheme showing the formation of the tetrahedral intermediate and neutral product after a water loss. B) Full range mass spectrum of the microdroplet reaction showing deprotonated reagent, product, and intermediate peak at  $m/z$  281, 445, and 463, respectively. Peaks are multiplied 10 times. Note that the other peaks in the spectrum are due to chemical or electrical noise. C) MS/MS spectrum of the intermediate at  $m/z$  463.



**Figure S20.** Microdroplet synthesis of sucrose/stearic acid ester. A) Reaction scheme showing the formation of the tetrahedral intermediate and neutral product after a water loss. B) Full range mass spectrum of the microdroplet reaction showing deprotonated reagent, product, and intermediate peak at  $m/z$  281, 325, and 343, respectively. Peaks at  $m/z$  283 and 625 are multiplied 10 times. Note that the peak at  $m/z$  567 corresponds to the dimer of stearic acid. The other two peaks at  $m/z$  511 and 539 were either fragmented species or chemical contamination. Peaks with lower intensity in the spectrum are due to chemical or electrical noise. C) MS/MS spectrum of the intermediate at  $m/z$  625.

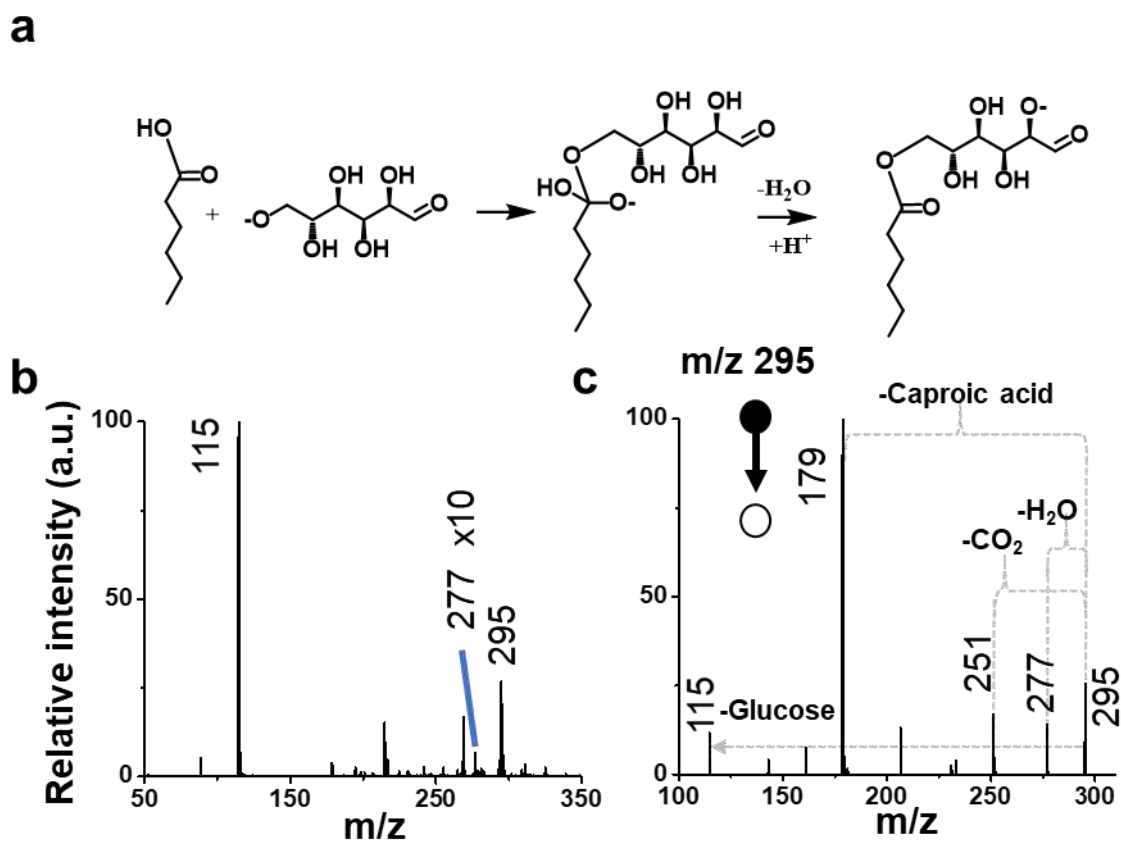


**Figure S21.** Microdroplet synthesis of ethylene glycol/caproic acid ester. A) Reaction scheme showing the formation of the tetrahedral intermediate and neutral product after a water loss. B) Full range mass spectrum of the microdroplet reaction showing deprotonated reagents and intermediate peak at  $m/z$  61, 115, and 117, respectively. Note that the other peaks in the spectrum are due to chemical or electrical noise. C) MS/MS spectrum of the intermediate at  $m/z$  117.

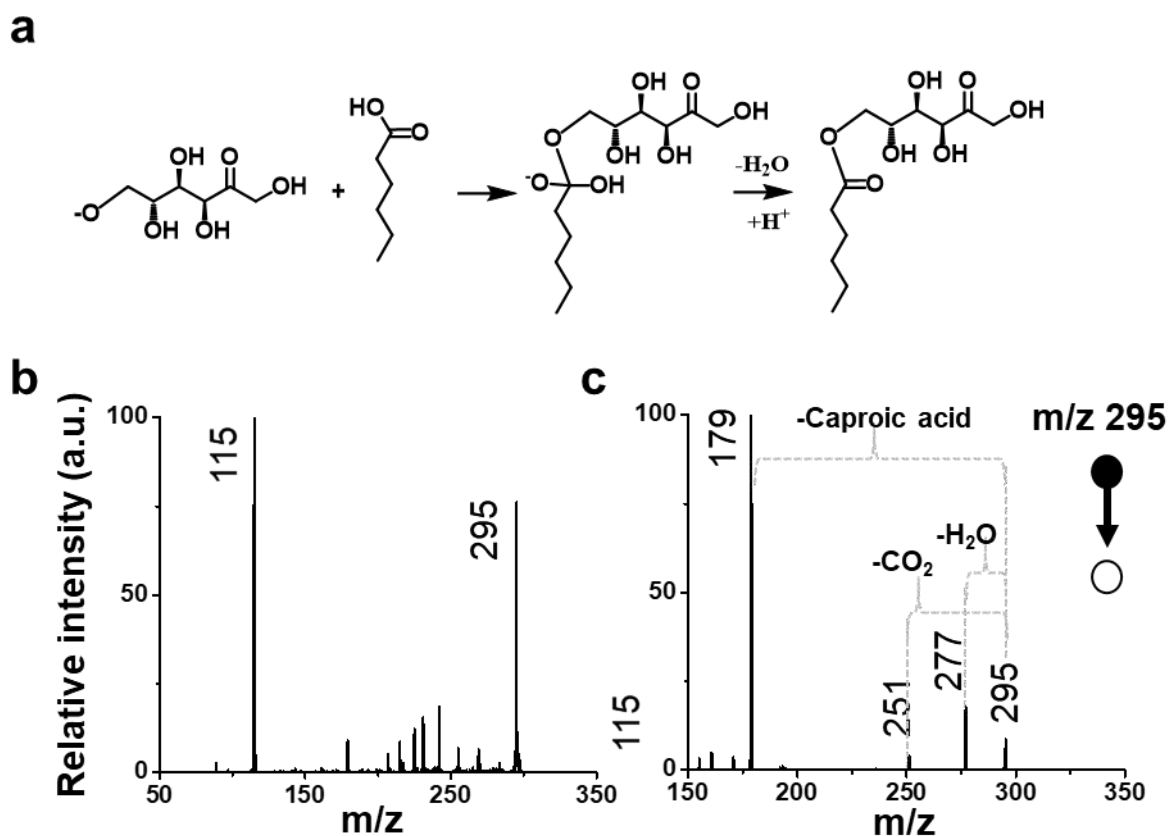


**Figure S22.** Microdroplet synthesis of glycerol/caproic acid ester. A) Reaction scheme showing the formation of tetrahedral intermediate and neutral product after water loss. B) Full range mass spectrum of the microdroplet reaction showing deprotonated reagent, product, and intermediate peak at  $m/z$  115, 189, and 207, respectively. Peak at  $m/z$  189 is multiplied 10 times. Note that the other peaks in the spectrum are due to chemical or electrical noise. C) MS/MS spectrum of the intermediate at  $m/z$  207.

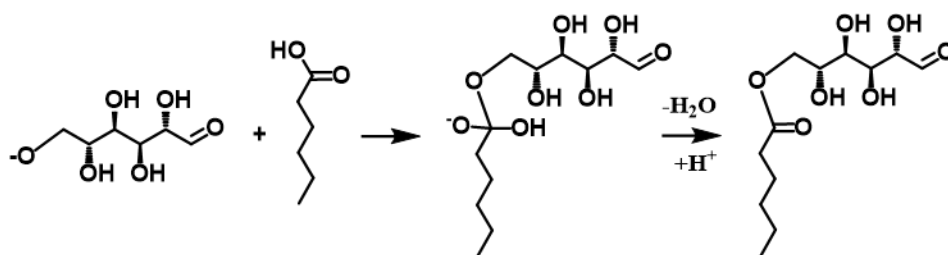
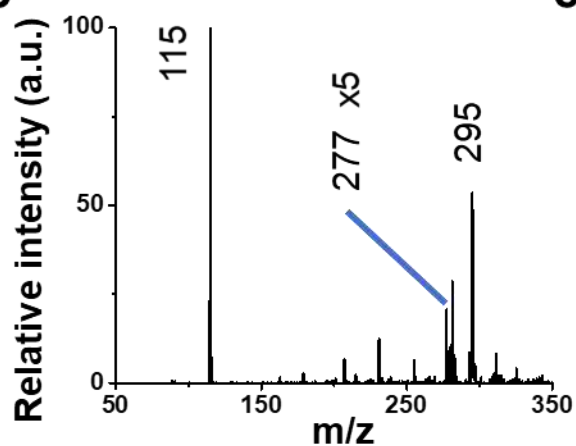
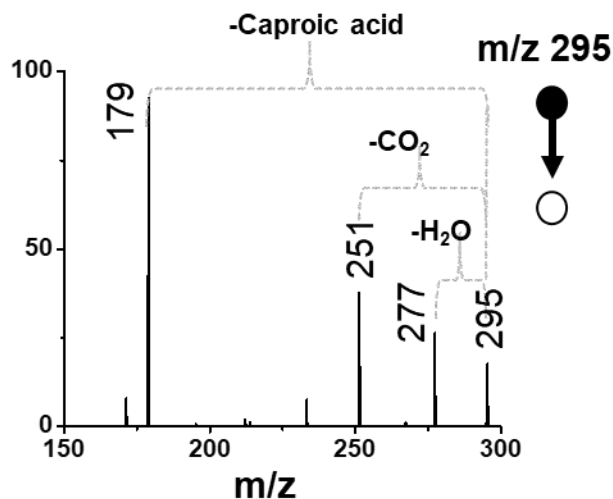




**Figure S23.** Microdroplet synthesis of glucose/caproic acid ester. A) Reaction scheme showing the formation of the tetrahedral intermediate and neutral product after a water loss. B) Full range mass spectrum of the microdroplet reaction showing deprotonated reagent, product, and intermediate peak at  $m/z$  115, 277, and 295, respectively. Peak at  $m/z$  277 is multiplied 10 times. Note that the other peaks in the spectrum are due to chemical or electrical noise. C) MS/MS spectrum of the intermediate at  $m/z$  295.



**Figure S24.** Microdroplet synthesis of fructose/caproic acid ester. A) Reaction scheme showing the formation of the tetrahedral intermediate and neutral product after a water loss. B) Full range mass spectrum of the microdroplet reaction showing deprotonated reagent and intermediate peak at  $m/z$  115 and 295, respectively. Note that the other peaks in the spectrum are due to chemical or electrical noise. C) MS/MS spectrum of the intermediate at  $m/z$  295.

**a****b****c**

**Figure S25.** Microdroplet synthesis of mannose/caproic acid ester. A) Reaction scheme showing the formation of the tetrahedral intermediate and neutral product after a water loss. B) Full range mass spectrum of the microdroplet reaction showing deprotonated reagent, product, and intermediate peak at  $m/z$  115, 277, and 295, respectively. Peak at  $m/z$  277 is multiplied 5 times. Note that the other peaks in the spectrum are due to chemical or electrical noise. C) MS/MS spectrum of the intermediate at  $m/z$  295.

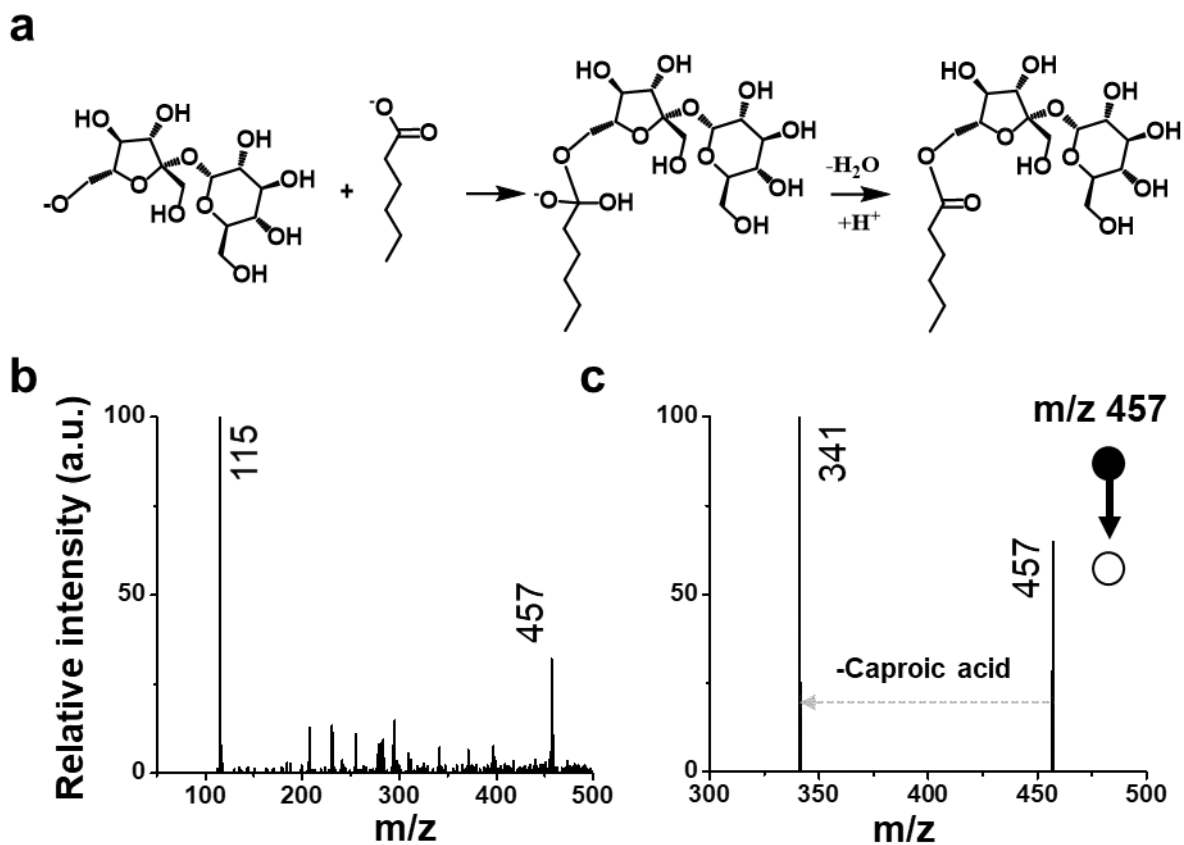


**Figure S26.** Microdroplet synthesis of sucrose/caproic acid ester. A) Reaction scheme showing the formation of the tetrahedral intermediate and neutral product after a water loss. B) Full range mass spectrum of the microdroplet reaction showing deprotonated reagent and intermediate peak at  $m/z$  115 and 457, respectively. Note that the other peaks in the spectrum are due to chemical or electrical noise. C) MS/MS spectrum of the intermediate at  $m/z$  457.

# Strong and Elastic Membranes via Hydrogen Bonding Directed Self-Assembly of Atomically Precise Nanoclusters

Anirban Som, Alessandra Griffo, Indranath Chakraborty, Hendrik Hähl, Biswajit Mondal, Amrita Chakraborty, Karin Jacobs, Päivi Laaksonen, Olli Ikkala,\* Thalappil Pradeep,\* and Nonappa\*

2D nanomaterials have provided an extraordinary palette of mechanical, electrical, optical, and catalytic properties. Ultrathin 2D nanomaterials are classically produced via exfoliation, delamination, deposition, or advanced synthesis methods using a handful of starting materials. Thus, there is a need to explore more generic avenues to expand the feasibility to the next generation 2D materials beyond atomic and molecular-level covalent networks. In this context, self-assembly of atomically precise noble nanoclusters can, in principle, suggest modular approaches for new generation 2D materials, provided that the ligand engineering allows symmetry breaking and directional internanoparticle interactions. Here the self-assembly of silver nanoclusters (NCs) capped with *p*-mercaptobenzoic acid ligands ( $\text{Na}_4\text{Ag}_{44}\text{-pMBA}_{30}$ ) into large-area freestanding membranes by trapping the NCs in a transient solvent layer at air–solvent interfaces is demonstrated. The patchy distribution of ligand bundles facilitates symmetry breaking and preferential intralayer hydrogen bondings resulting in strong and elastic membranes. The membranes with Young's modulus of  $14.5 \pm 0.2$  GPa can readily be transferred to different substrates. The assemblies allow detection of Raman active antibiotic molecules with high reproducibility without any need for substrate pretreatment.

properties.<sup>[1–12]</sup> They are classically prepared using exfoliation, exploiting promoted intralayer bonding over weak interlayer interactions of their 3D counterparts.<sup>[4]</sup> The exfoliation of graphene<sup>[1]</sup> has triggered searches for other covalently interconnected atomically thin 2D nanomaterials, such as transition metal dichalcogenides,<sup>[5]</sup> Mxenes,<sup>[6]</sup> boron nitrides,<sup>[7]</sup> and clays,<sup>[8]</sup> based on exfoliation and delamination,<sup>[9]</sup> molecular beam epitaxy,<sup>[10]</sup> and advanced synthesis.<sup>[11]</sup> In ultrathin 2D nanomaterials, the quantum confinement of electrons in two dimensions opens novel applications, e.g., in flexible optoelectronic devices.<sup>[4,12,13]</sup> Beyond atomic and molecular-level networks, a less studied approach deals with the self-assembly of metal nanoparticles (NPs) to form 2D monolayer membranes, i.e., of nanometric thickness. That this could be relevant, is suggested by the tunable optoelectronic and mechanical properties of self-assembled 2D materials of narrow

size dispersed plasmonic NPs.<sup>[14–17]</sup> However, metal NPs classically suffer from uncontrolled aggregation tendency, polydispersity, and lack of directional interactions.<sup>[18–21]</sup> Additionally, nonspecific bindings and slow diffusion of colloidal-level

## 1. Introduction

Atomically thin 2D nanomaterials have gained immense interest because of their remarkable mechanical and optoelectronic

A. Som, O. Ikkala, Nonappa  
Department of Applied Physics  
Aalto University  
Espoo FI-02150, Finland  
E-mail: olli.ikkala@aalto.fi

A. Griffo, P. Laaksonen, O. Ikkala  
Department of Bioproducts and Biosystems  
Aalto University  
Espoo FI-02150, Finland

A. Griffo, H. Hähl, K. Jacobs  
Department of Experimental Physics  
Saarland University  
66123 Saarbrücken, Germany

 The ORCID identification number(s) for the author(s) of this article can be found under <https://doi.org/10.1002/smll.202201707>.

© 2022 The Authors. Small published by Wiley-VCH GmbH. This is an open access article under the terms of the Creative Commons Attribution License, which permits use, distribution and reproduction in any medium, provided the original work is properly cited.

DOI: 10.1002/smll.202201707

A. Griffo, K. Jacobs  
Max Planck School Matter to Life  
Jahnstraße 29, 69120 Heidelberg, Germany

I. Chakraborty, B. Mondal, A. Chakraborty, T. Pradeep  
DST Unit of Nanoscience and Thematic Unit of Excellence  
Department of Chemistry  
Indian Institute of Technology Madras  
Chennai 600036, India  
E-mail: pradeep@iitm.ac.in

I. Chakraborty  
School of Nano Science and Technology  
Indian Institute of Technology  
Kharagpur 721302, India

Nonappa  
Faculty of Engineering and Natural Sciences  
Tampere University  
Tampere FI-33720, Finland  
E-mail: nonappa@tuni.fi



particles could result in a mixture of different structures rather than the desired homogeneous or precise end-product.<sup>[22,23]</sup> Nevertheless, 2D close-packed arrays of gold nanoparticles, binary superlattices, and nanoparticle–polymer composite arrays have been achieved using evaporation induced assembly, interfacial assembly, binary solvents, antisolvent approach, dip coating, and Langmuir–Blodgett film formation methods.<sup>[24–27]</sup> Still, achieving a combination of precision and reproducibility of self-assembled large-area NP superstructures remains a grand challenge.<sup>[28]</sup>

Recent studies in the literature suggest that the nanoparticle size dispersity, ligand structure, and density hinders the reproducibility, sensitivity, and mechanical properties of NP-based 2D assemblies. Mueggenburg et al. have shown that NP membranes composed of dodecane thiol ligand-capped gold NPs with an average diameter of 9.4 nm show highly scattered elastic modulus with a range of 3–39 GPa.<sup>[29]</sup> The large distribution of elastic modulus is attributed to the uncertainty and compositional differences in membranes made from different nanoparticle batches. The mechanical properties of such membranes strongly depends on the ligand interdigitation and NP packing efficiency. In such systems, the core–core interactions account for less than 10% of the observed overall strength.<sup>[30]</sup> Cheng et al. used a microhole drying method to prepare DNA-capped nanoparticle membranes with inter-nanoparticle distances tunable up to 20 nm and Young's moduli within a narrow range of  $6.49 \pm 1.57$  GPa. However, the observed average moduli values are much less than other NP membranes.<sup>[31]</sup> Gold nanoparticle-based 2D assemblies have been studied for nanoparticle–organic memory field-effect transistors.<sup>[32a]</sup> In such assemblies, the reproducibility of NP density depends on NP size and capping ligands, which in turn affect the device performances.<sup>[32a,b]</sup> Furthermore, the uniform size, density, and inter-nanoparticle distances in monolayers of plasmonic silver nanoparticles have been shown to significantly improve the surface enhanced Raman spectroscopy (SERS) sensitivity and reproducibility.<sup>[17,33–35]</sup> Therefore, there is a need to develop methods for the uniform and reproducible fabrication of precision nanoparticle assemblies.

Atomically precise, monolayer ligand-protected noble metal nanoclusters (NCs) offer tunable size, shape, composition, and oxidation states.<sup>[36]</sup> While a vast number of NCs have been synthesized over the last decade, understanding their structure, optoelectronic properties, catalysis, and biological properties remains the central theme.<sup>[36–38]</sup> NCs are excellent building blocks for well-defined assemblies, composites, and hybrid materials allowing large design flexibility and unique optoelectronic properties.<sup>[39]</sup> Therefore, the next logical step would be the creation of rationally designed assemblies of NCs to attain the desired properties. In their crystalline state, ligand–ligand interactions between the spatially arranged neighboring NCs dictate the packing geometry. Depending on the functionality, these ligands can interact through hydrogen bonding, electrostatic, dipolar,  $\pi$ -stacking, and van der Waals interactions.<sup>[39]</sup> The ability to manipulate such supramolecular forces in detail is the key toward controlling the geometry of the nanocluster assemblies.

Large area monolayer 2D assemblies of NCs with well-defined internal order require a restriction of the NC

crystallization in a particular direction, i.e., symmetry breaking. It has been shown using *para*-mercaptobenzoic acid (*p*MBA)-protected gold NCs ( $\text{Au}_{102}$ -*p*MBA<sub>44</sub>) that symmetry breaking can be achieved by exploiting the anisotropic or patchy hydrogen bonding (H-bonding) ligand distribution.<sup>[40,41]</sup> On the other hand, atomically precise silver NCs have been utilized to achieve hydrogen bonding mediated assembly of tellurium nanowires into 2D cross-bilayer structures,<sup>[42]</sup> and selective encapsulation of plasmonic gold nanorods.<sup>[43]</sup> Liquid–liquid interfaces have also been utilized to create NC 2D assemblies.<sup>[44]</sup> However, precise control over layer thickness and structure in nanoparticle membranes covering a large area and studies on their mechanical properties is still lacking.

Here we report the fabrication of large-area (extending over  $\text{cm}^2$ ) freestanding monolayer membranes of  $\text{Na}_4\text{Ag}_{44}$ -*p*MBA<sub>30</sub> NCs with long-range hexagonally close-packed internal structure. The membranes are prepared by processing at air–water interfaces hosting a transient solvent layer. Specifically, we utilize the selective in-plane growth of the cluster assemblies by facilitating the intralayer H-bonding between the carboxylic acid groups of *p*MBA ligands. The packing of the NCs was analyzed using high resolution transmission electron microscopy (HR-TEM). The ultrathin membranes were also directly deposited across micrometer sized holes. The atomic force microscopy (AFM)-based force spectroscopy showed non-hysteretic elastic deformation upon nanoindentation. The observed Young's modulus of  $14.5 \pm 0.2$  GPa, is significant for a noncovalently interconnected ultrathin membrane of colloidal units. The membranes allow detection of Raman active antibiotics dissolved in water using surface enhanced Raman spectroscopy with high reproducibility, unlike the classic nanoparticles with finite-size distributions and defected structures.

## 2. Results and Discussions

### 2.1. Microscale 2D Colloidal Crystals

We utilized atomically precise silver nanoclusters,  $\text{Na}_4\text{Ag}_{44}$ -*p*MBA<sub>30</sub> (Figure 1a) synthesized according to a reported literature procedure (see Figure S1, Supporting Information, for details).<sup>[45,46]</sup> Formation of  $\text{Na}_4\text{Ag}_{44}$ -*p*MBA<sub>30</sub> was confirmed through UV–vis spectroscopy and ESI mass spectrometry (Figure S2, Supporting Information). The solid state structure of  $\text{Na}_4\text{Ag}_{44}$ -*p*MBA<sub>30</sub> consists of a 32 atom Ag core (concentric icosahedral and dodecahedral Ag atom shells), which is protected by six  $\text{Ag}_2$ -*p*MBA<sub>5</sub> units in an octahedral geometry (Figure 1a).

This arrangement results in the formation of *p*MBA ligand bundles or patches, which break the spherical symmetry. The ligand bundles are classified into L2 (bundle of two) and L3 (bundle of three) *p*MBA groups (Figure 1b), which act as the inter-nanocluster interaction patches to drive the 3D network formation. Incidentally, all the six L2 bundles are located along an imaginary equatorial plane and drive the crystal growth in the lateral dimension (along *ab*-plane). The six L3 bundles are placed above (three) and below (three) the equatorial plane and form H-bonded bridges between the layers (along the *c*-axis). In this way, a single

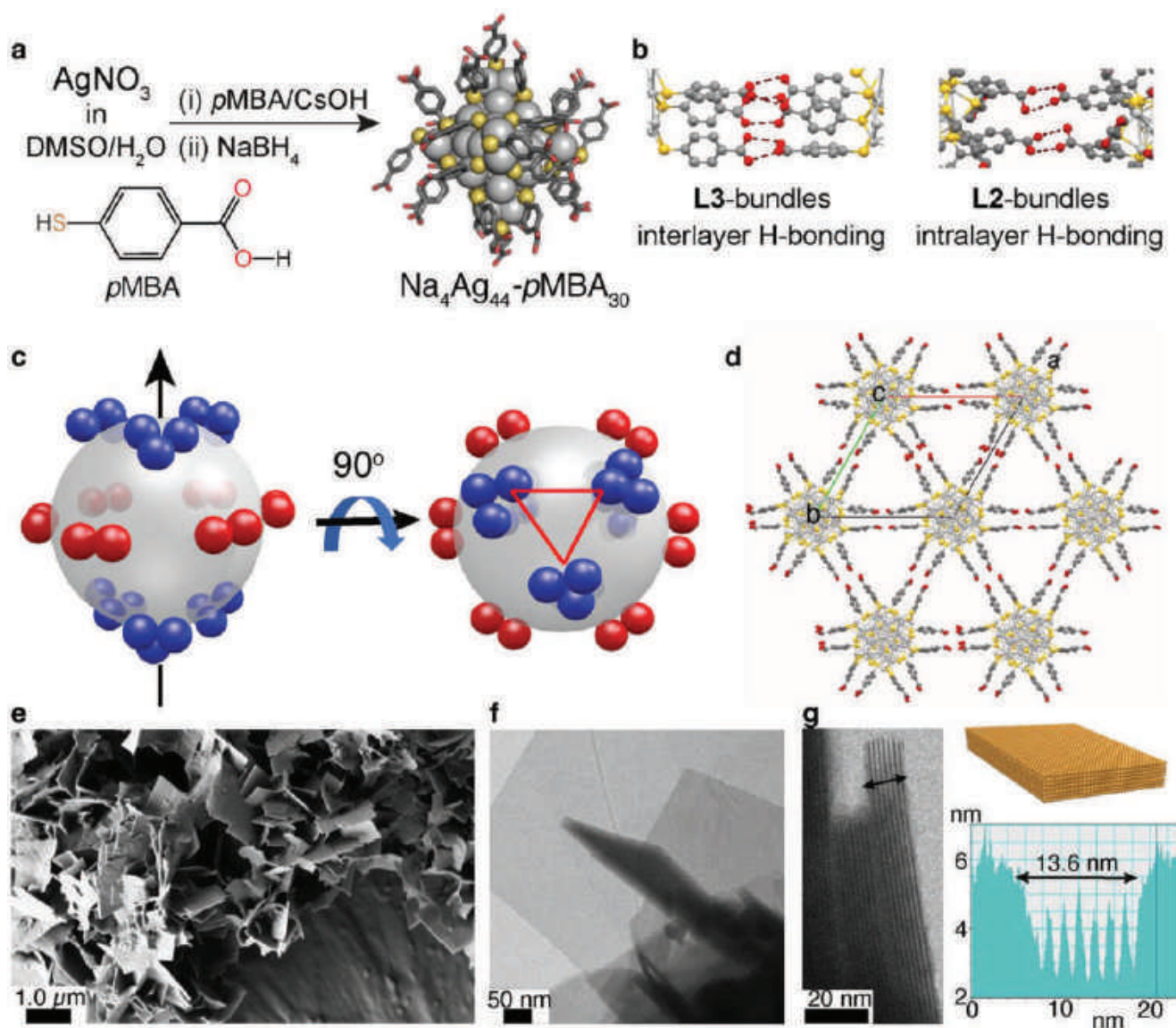


**Figure 1.** Synthesis, patchy ligand distribution, and 2D colloidal crystals. a) Synthesis scheme, and X-ray crystal structure of  $\text{Na}_4\text{Ag}_{44}\text{-pMBA}_{30}$  (CSD entry XIMHOS, hydrogen atoms are not shown for clarity).<sup>[46]</sup> b) Representative L2 and L3 ligand bundles of  $\text{Na}_4\text{Ag}_{44}\text{-pMBA}_{30}$ . c) Schematic representation showing the patchy distribution of L2 (red spheres) and L3 (blue spheres) bundles. The six L2 bundles are located around an imaginary equatorial plane. d) Intralayer packing of the clusters in the crystal structure directed by L2 bundles, showing the possibility of a 2D assembly (see Figure S2d, Supporting Information, for interlayer packing via L3 bundles). e) SEM image of 2D nanosheets of  $\text{Na}_4\text{Ag}_{44}\text{-pMBA}_{30}$  in methanol. f) TEM image of nanosheets. g) TEM image suggests that these nanosheets contain a few layers, as shown in the histogram.

$\text{Na}_4\text{Ag}_{44}\text{-pMBA}_{30}$  is involved in 24 H-bonds ( $6 \times \text{L2}$ ) with clusters from the same layer (Figure 1c). The L3 bundles contribute to 18 inter-nanocluster H-bonds each with clusters from layers above and below, respectively (Figure S2d, Supporting Information).

We envisaged that  $\text{Na}_4\text{Ag}_{44}\text{-pMBA}_{30}$  provides a feasible starting point to create 2D NC superstructures (Figure 1d), as it intrinsically allows a larger number of intralayer H-bonds between the NCs compared to the interlayer bonds. The creation of 2D assemblies of  $\text{Na}_4\text{Ag}_{44}\text{-pMBA}_{30}$  would thus require selectively restricting the formation of interlayer L3 H-bonds to drive the crystal growth along the lateral direction and to limit the growth in the perpendicular direction. Herein we expected that kinetically controlled self-assembly

could be feasible. To test our hypothesis, we first screened solvents to facilitate 2D colloidal crystal growth of  $\text{Na}_4\text{Ag}_{44}\text{-pMBA}_{30}$ , before aiming the monolayer membranes. Thus we found that, when a dispersion of  $\text{Na}_4\text{Ag}_{44}\text{-pMBA}_{30}$  in *N,N'*-dimethylformamide (DMF) was added to methanol (nonsolvent), an immediate precipitation was observed. The scanning electron microscopy (SEM) images of the dispersion revealed the presence of microscopic 2D colloidal crystals (Figure 1e). A closer examination of TEM images revealed that these sheets are, in fact, stacks with a few layer thicknesses (Figure 1f). For example, in Figure 1g the TEM image shows a stack of seven layers (Figure S3c–e, Supporting Information, for HR-TEM images). Therefore, this

strategy offered a certain degree of control on the 2D stacking of  $\text{Na}_4\text{Ag}_{44}\text{-pMBA}_{30}$ . However, precisely controlling the layer thickness and limiting it to a monolayer necessitated identifying more refined strategies.

## 2.2. Freestanding Monolayer Membrane

Self-assembly of molecules at interfaces (air–liquid or liquid–liquid) leading to monomolecular membranes has been investigated extensively for several decades.<sup>[47,48]</sup> Therein Langmuir–Blodgett (LB) processing allows thin membranes of a variety of nanomaterials at the air–water interface taken that they are sufficiently hydrophobic.<sup>[49]</sup> However, the  $\text{Na}_4\text{Ag}_{44}\text{-pMBA}_{30}$  NCs could not be assembled using the LB-processing, as they are dispersible in water. To achieve monolayer membranes, we carried out a systematic study using a series of solvents. When a dispersion of  $\text{Na}_4\text{Ag}_{44}\text{-pMBA}_{30}$  in DMF was added to ethanol, propanol, butanol, and acetone, they all resulted in mesoscale colloidal crystals similar to those in methanol (Figure S3f–i, Supporting Information). Interestingly, a stable dispersion of  $\text{Na}_4\text{Ag}_{44}\text{-pMBA}_{30}$  without immediate precipitation was obtained in 1-pentanol. Exploiting this property, we first dispersed the clusters in 1-pentanol, which was subsequently transferred in a dropwise manner on a water surface (Figure S1, Supporting Information). 1-Pentanol, due to its longer alkyl chain length, has low solubility in water ( $22 \text{ g L}^{-1}$ ) compared to lower alcohols.

In the literature 1-pentanol has been used as a cosurfactant for stable microemulsion preparation and interface synthesis of gold mesocrystals.<sup>[50]</sup> In our experiment, when a dispersion of  $\text{Na}_4\text{Ag}_{44}\text{-pMBA}_{30}$  in 1-pentanol was placed on the surface of the water, pentanol quickly spreads to form a membrane. The clusters trapped inside this pentanol layer assemble through the formation of H-bonds and float at the air–water interface (Figure 2a). The resulting freestanding  $\text{Na}_4\text{Ag}_{44}\text{-pMBA}_{30}$  membrane can be picked from the air–water interface and transferred onto suitable substrates as shown using a glass coverslip ( $d \approx 1.2 \text{ cm}$ ). An immediate transfer of the membrane on to the substrate is better for the stability and to avoid any degradation upon contact with water for longer time. Increased concentration of 1-pentanol in water may also be detrimental for membrane preparation. For example, in a control experiment when  $\text{Na}_4\text{Ag}_{44}\text{-pMBA}_{30}$  in 1-pentanol was added on the surface containing a mixture of 1-pentanol/water (2/75 v/v) resulted in droplets and no film formation was observed (Figure S1, Supporting Information).

The membranes were examined using TEM by transferring them onto TEM grids with lacey, holey, or ultrathin carbon support films. That the membrane extended over micrometer area can be seen in the large area TEM image (Figure 2b). The HR-TEM images, fast Fourier transform (FFT), and inverse fast Fourier transform (IFFT) analysis of the membrane deposited on TEM grid with ultrathin carbon support indicate the well-defined overall hexagonally close-packed (hcp) assembly as well as the membrane is of monolayer thickness (Figure 2c,d). Further analysis of the  $\text{Na}_4\text{Ag}_{44}\text{-pMBA}_{30}$  monolayer membrane revealed an average interparticle distance of 2.33 nm and periodicity of 2.01 nm (Figure 2e).

The UV–vis spectrum of the  $\text{Na}_4\text{Ag}_{44}\text{-pMBA}_{30}$  monolayer membranes showed the same characteristic peaks as observed for the individual solvent dispersed  $\text{Na}_4\text{Ag}_{44}\text{-pMBA}_{30}$  NCs. This suggests that the intrinsic properties of the NCs are retained in the monolayer membranes (Figure 2f,g). However, the absorption peaks turned broader in the monolayer membrane, indicating a possible electronic coupling between the NCs. In the Raman spectrum,  $\text{Na}_4\text{Ag}_{44}\text{-pMBA}_{30}$  monolayer membranes exhibit several peaks ranging from 300 to  $1800 \text{ cm}^{-1}$  of which two strong bands at 1077 and  $1584 \text{ cm}^{-1}$  are due to  $\nu_{12}$  and  $\nu_{8a}$  aromatic ring vibrations (of the pMBA ligands), respectively (Figure 2h; Figure S5a,b, Supporting Information). For comparison, the Raman spectrum of a drop-casted  $\text{Na}_4\text{Ag}_{44}\text{-pMBA}_{30}$  film on a coverslip was taken, which shows a similar spectral pattern. Still, the peaks are better resolved in the case of  $\text{Na}_4\text{Ag}_{44}\text{-pMBA}_{30}$  monolayer membranes. The most intense peak at  $1584 \text{ cm}^{-1}$  was utilized to construct the Raman spectral image (Figure S5c, Supporting Information), which resembles the optical image of the  $\text{Na}_4\text{Ag}_{44}\text{-pMBA}_{30}$  monolayer membrane (Figure S5d, Supporting Information). A few regions show higher intensity (Raman spectra in Figure 2h) because of multilayers at those locations due to the folding or crumpling of  $\text{Na}_4\text{Ag}_{44}\text{-pMBA}_{30}$  monolayer membranes while transferring onto the substrate.

## 2.3. Mechanical Properties of $\text{Na}_4\text{Ag}_{44}\text{-pMBA}_{30}$ Membranes

After a successful demonstration of the feasibility of freestanding  $\text{Na}_4\text{Ag}_{44}\text{-pMBA}_{30}$  monolayer membrane formation, we turned our attention to determine the mechanical properties of the nanometric membranes. The freshly prepared  $\text{Na}_4\text{Ag}_{44}\text{-pMBA}_{30}$  monolayer membrane was transferred onto Quantifoil gold grids with a holey carbon support film, having a hole diameter of  $0.6 \mu\text{m}$  (Figure 3a).

That the freestanding membrane stretched across the holes could be seen from the TEM images (Figure S6, Supporting Information). However, for high magnification imaging, the Quantifoil grids with holey carbon support were not suitable. Therefore, the grids were sputter-coated with platinum before transferring the membranes (see Figure S6c,d, Supporting Information, for TEM image of a pristine sputter-coated grid). The sputter-coated grid allowed for better imaging of  $\text{Na}_4\text{Ag}_{44}\text{-pMBA}_{30}$  monolayer membranes stretched across holey grids (Figure 3b–d; Figure S7, Supporting Information). It is important to note that NCs are inherently electron beam sensitive and, therefore, at higher magnification, beam damage and their aggregation into larger nanoparticles can be observed. The HR-TEM images and IFFT suggests that the monolayer membrane stretched across the hole still incorporated a hexagonal nanocluster assembly (Figure 3d).

AFM measurements showed that the  $\text{Na}_4\text{Ag}_{44}\text{-pMBA}_{30}$  monolayer membranes within the holes were smooth and flat (Figure 3e,f). Height profile images indicate that the monolayer membrane drape over the hole (Figure 3g; Figure S8, Supporting Information). Importantly, the height of various 2D membranes deposited on holey support films has been discussed in the literature.<sup>[51–55]</sup> We used the Quantitative Nanomechanical Measurement-mode of the AFM to obtain the



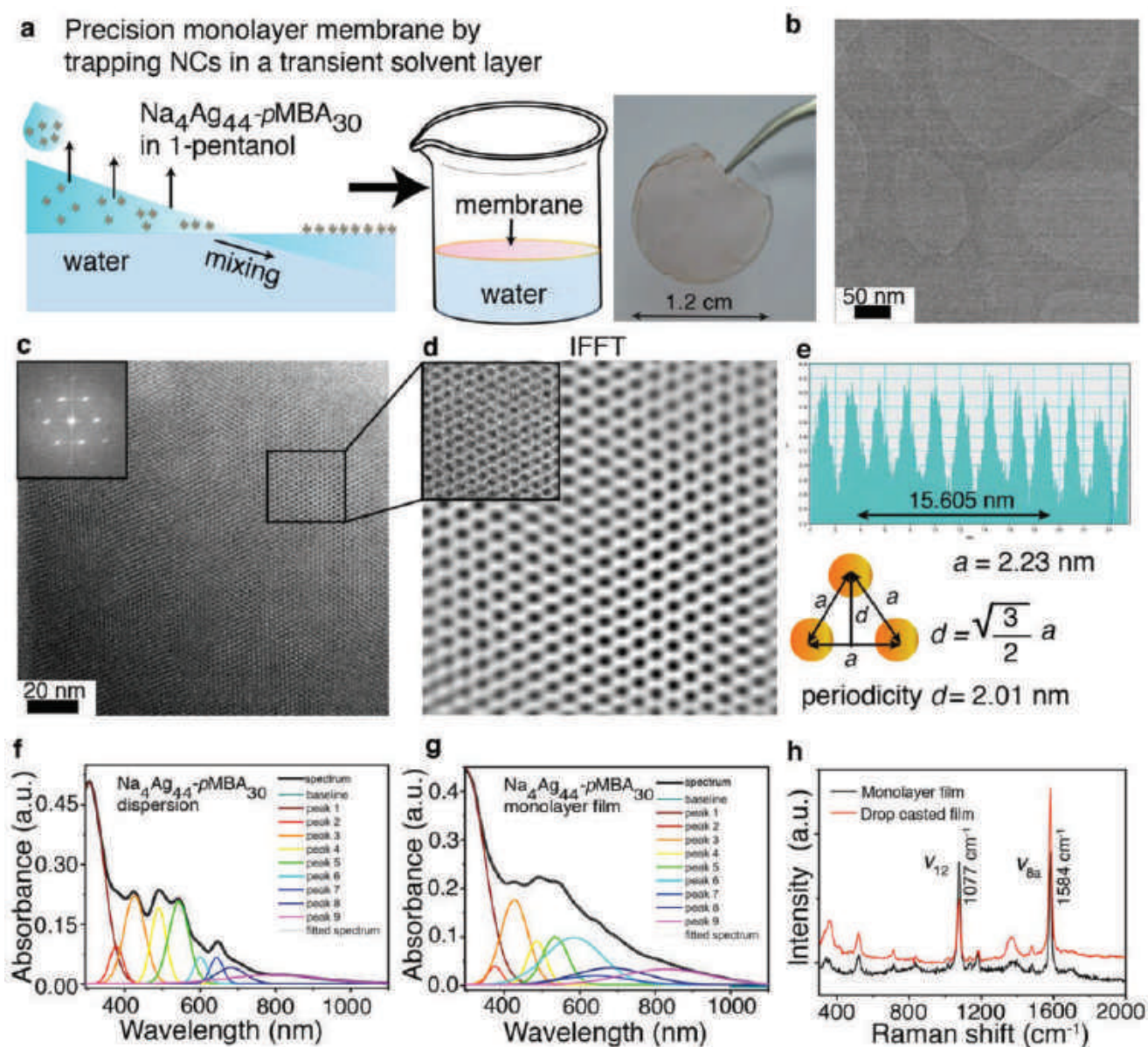


**Figure 2.** Freestanding  $\text{Na}_4\text{Ag}_{44}\text{-pMBA}_{30}$  membranes. a) Schematics showing the formation of the monolayer  $\text{Na}_4\text{Ag}_{44}\text{-pMBA}_{30}$  assembly in a liquid-assisted air–water interface method (left). Large area  $\text{Na}_4\text{Ag}_{44}\text{-pMBA}_{30}$  monolayer membrane transferred onto a microscope coverslip (right). b) TEM image of the monolayer assembly stretched over a lacey carbon support membrane. c) TEM image suggesting the hexagonal packing of  $\text{Na}_4\text{Ag}_{44}\text{-pMBA}_{30}$  NCs (inset shows the FFT). d) IFFT image from the marked area in image c. e) Profile showing the inter-nanoparticle distance and periodicity. f) UV–vis spectrum of  $\text{Na}_4\text{Ag}_{44}\text{-pMBA}_{30}$  in aq. dispersion along with peak fitting. g) UV–vis spectrum of  $\text{Na}_4\text{Ag}_{44}\text{-pMBA}_{30}$  monolayer membrane. h) Raman spectra of  $\text{Na}_4\text{Ag}_{44}\text{-pMBA}_{30}$  monolayer membrane (black) and that of drop-casted  $\text{Na}_4\text{Ag}_{44}\text{-pMBA}_{30}$  dispersion (red) showing the presence of the characteristic bands (see Figure S4, Supporting Information).

correct height of the membrane. In this mode, the contact point is evaluated and used as height information which is hence independent of the force applied by the probe. The obtained “real height” images show that the membrane (rather than recessed) is suspended on the rim of the holes whose height is  $\approx 20 \text{ nm}$  (see the image of the control grid in Figure S10, Supporting Information).

Next, AFM indentation experiments were carried out on freestanding monolayer membranes suspended on grids having a hole radius of  $0.6 \mu\text{m}$ . For the characterization of the

membrane elasticity, force curves were recorded at the center of the holes. A typical trace of the force–displacement curve is presented in Figure 4b. For each sample, several holes covered with the membrane were probed. We observed consistent force–displacement curves for multiple indents on a single spot without breaking the membrane. An increasing force starting from  $10 \text{ nN}$  was applied until the value of  $\approx 16\text{--}18 \text{ nN}$  was reached, which represents the maximum load that the suspended membrane can withstand before breaking (Figure S11, Supporting Information, for additional force–displacement

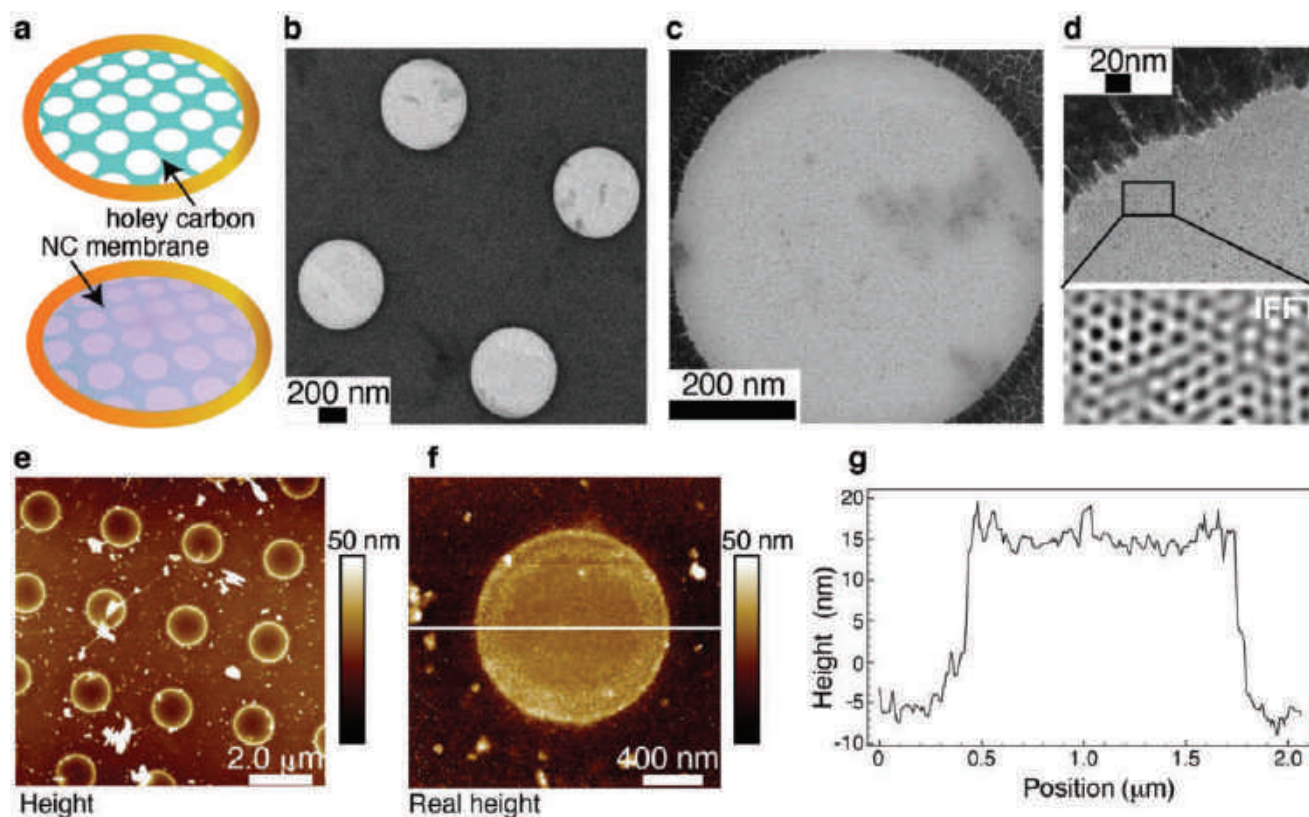


**Figure 3.** TEM and AFM imaging of  $\text{Na}_4\text{Ag}_{44}\text{-pMBA}_{30}$  membranes. a) Schematics showing the deposition of  $\text{Na}_4\text{Ag}_{44}\text{-pMBA}_{30}$  membrane on a gold grid with a holey carbon support membrane. b) TEM image showing cluster monolayers spanned across the holes (Figure S5, Supporting Information, for additional images). c) TEM image of one of the holes showing the cluster membrane being present across the hole. d) High-magnification TEM image and IFFT of the marked area showing hcp array of  $\text{Na}_4\text{Ag}_{44}\text{-pMBA}_{30}$  (note: NCs are sensitive to electron beam). e) Large area AFM height image of the cluster monolayer deposited on a TEM grid. f,g) AFM image of one of the holes, showing the cluster membrane spanned across the hole, and the corresponding height profile.

curves over different covered holes). Figure 4c,d shows the membrane before and after breakage upon a series of indents, respectively. As expected, the higher is the load applied, the deeper is the penetration depth (Figure 4e; Figures S11 and S12, Supporting Information, for additional AFM images and overlap of multiple  $F\delta$  curves, respectively). For small indentations,  $\delta$ , all curves are linear in force,  $F$ . However, when  $\delta$  considerably exceeds the membrane thickness,  $h$ , they turn nonlinear/cubic ( $F \approx \delta^3$ ). At large indentation, the obtained cubic term dominates, allowing to extract Young's modulus,  $E$ .<sup>[31,56]</sup> This is an essential point for the determination of  $E$  (see Equation (1)) since the apparent spring constant,  $k$ , for small  $\delta$ , depends on the prestretch of the membrane that is a priori unknown and cannot be used to determine  $E$  at small indentations. However, the prestretching of the monolayer membranes can be neglected for larger indentations, where the stretching energy dominates.

For homogeneous membranes, the effective  $E$  can be extracted using Equation (1), by analyzing the force curves within the framework of elasticity theory<sup>[57,58]</sup>

$$F = k\delta + \frac{\pi E h}{3R^2} \delta^3 \quad (1)$$

where  $h$  is the membrane thickness,  $R$  is the hole radius,  $\delta$  is the indentation depth, and  $k$  is the spring constant that depends on the prestrain of the membrane and used as a fitting parameter.

The model is applicable for  $\delta/h \gg 1$  and a point-like force. This is the case if the tip diameter is small compared to the hole radius, which is valid only for sharp styluses. The Scanasyt tip used in our measurements has a nominal radius of curvature of 2 nm (maximum nominal value at 12 nm). The tip radius was also estimated by tip qualification measurement and revealed a value of  $\approx 11$  nm, which closely matches the maximum nominal value and is much smaller than the hole radius. The  $E$  values extracted by the fit of the  $F(\delta)$  curves, fall in the range between 10 and 30 GPa as shown in the histograms of Figure 4g with Gaussian distribution centered at  $14.5 \pm 0.2$  GPa. The absence of hysteresis between the loading/unloading curves confirms the elastic nature of the  $\text{Na}_4\text{Ag}_{44}\text{-pMBA}_{30}$  monolayer membrane. At higher applied loads, however, when the membrane is close to the rupture, sometimes a slight hysteretic behavior is observed, indicating probably that the membrane is damaged or stretched irreversibly beyond a yield point, as also reflected by the low prestress values associated. The calculated average values for Young's modulus of  $\text{Na}_4\text{Ag}_{44}\text{-pMBA}_{30}$  membranes fall slightly above the range observed for deformations of



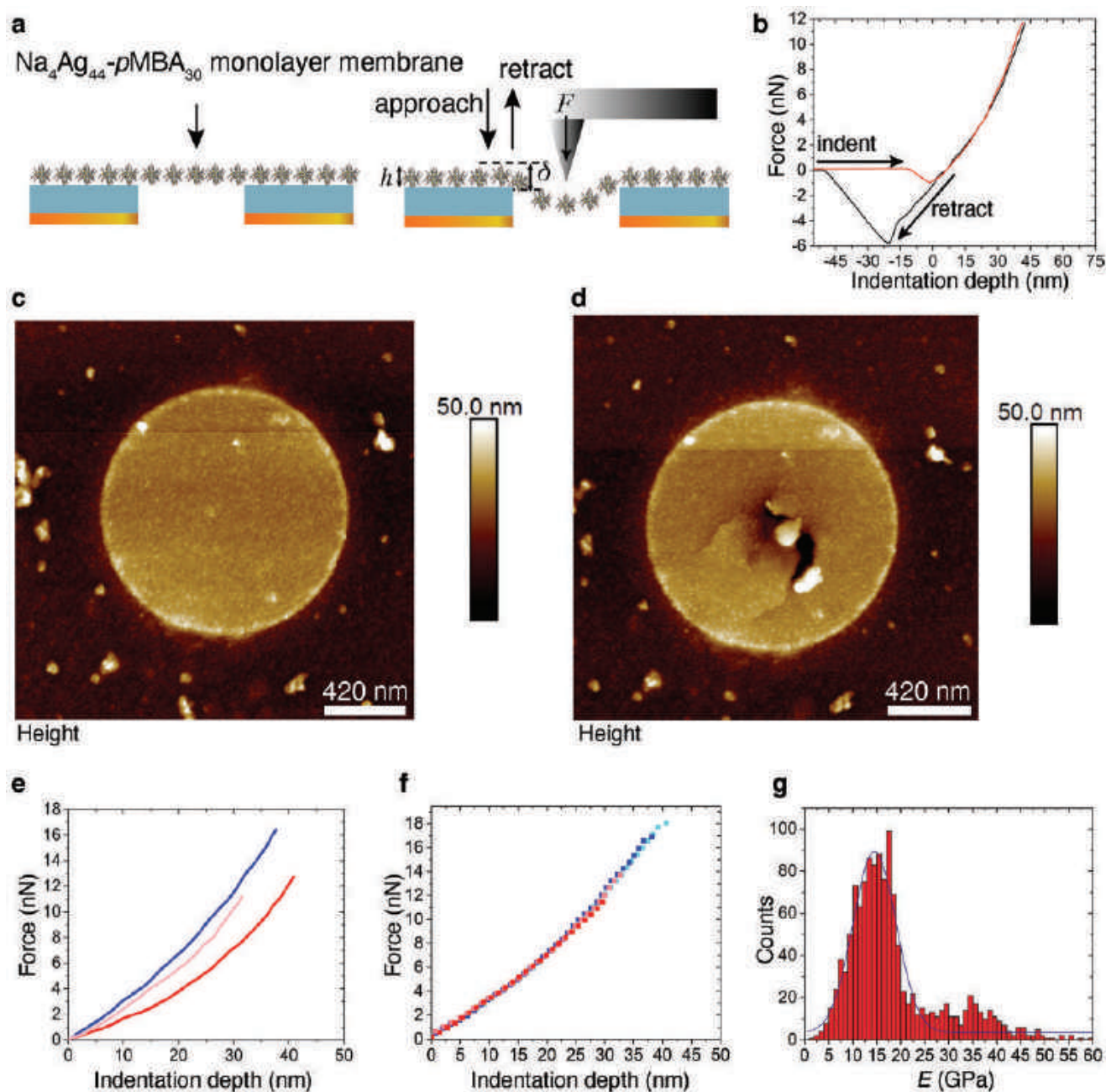


**Figure 4.** AFM measurements. a) A cartoon representation of the membrane deposited on top of the TEM grid and related AFM experimental setup. b) A typical force–displacement curve and the absence of hysteresis suggests the elastic nature of the membrane. c) AFM height image of the membrane before indentation. d) AFM image of the membrane after many indentation cycles at different close spots. e) Overlap of  $F(\delta)$  curves recorded on three different holes covered with membrane. f)  $F(\delta)$  curves recorded on the same spot of a hole covered with membrane by increasing force. g) Histogram reporting the  $E$  modulus value extracted by fitting the  $F(\delta)$  curves.

several larger nanoparticle-based membranes,<sup>[31,32,54,59]</sup> yet, the distribution of the obtained values is much narrower than the wide distribution range (3–39 GPa) of gold nanoparticle membranes reported earlier.<sup>[31]</sup>

The high modulus of  $\text{Na}_4\text{Ag}_{44}\text{-pMBA}_{30}$  membranes can be attributed to the well-defined H-bonded connectivity of nanoparticles and their structural integrity. In contrast to the narrow size dispersed alkanethiol-capped plasmonic nanoparticle

membranes,<sup>[29]</sup> the  $\text{Na}_4\text{Ag}_{44}\text{-pMBA}_{30}$  clusters are atomically precise with covalently bound short and rigid ligands. Therefore, the  $\text{Na}_4\text{Ag}_{44}\text{-pMBA}_{30}$  membranes are devoid of ligand entanglement, a common feature in polymer membranes. Importantly, the solid state structure of  $\text{Na}_4\text{Ag}_{44}\text{-pMBA}_{30}$  shows highly directional H-bonding distances between  $\text{O}\cdots\text{H}$  is 1.54 and 2.6 Å for the  $\text{O}\cdots\text{O}$ , and with the angle  $\angle\text{OHO}$  of  $177^\circ$ .<sup>[43,44]</sup>

## 2.4. Surfaced Enhanced Raman Spectroscopy

Noble metal nanoparticles deposited on functionalized surfaces have been studied in the literature as SERS substrate for detection and monitoring antibiotics.<sup>[60]</sup> Plasmonically coupled metallic nanostructures with ultrasmall ( $\approx 1$  nm or smaller) nanogaps can generate very strong and tunable electromagnetic fields that result in strong SERS signals from Raman dyes in the gap. However, even small changes ( $<1$  nm) in the structure of the coupled plasmonic nanogaps can significantly affect the localization of electrons and thereby, signal intensity in such plasmonically fabricated metamaterials.<sup>[61]</sup> High-yield synthetic strategies with nanometer-level structural control and reproducibility are greatly challenging owing to the inherent polydispersity in the size of nanoparticles. While the existing methods utilize highly sophisticated fabrication methods, we show that the  $\text{Na}_4\text{Ag}_{44}\text{-pMBA}_{30}$  membranes can overcome some of these challenges. Notably, the membrane can be readily transferred to the substrate and require no surface pretreatment to detect the target Raman-active molecules such as amphotericin B (Amp B, see Supporting Information for details). The Raman spectrum of standard Amp B shows the specific bands at  $1559\text{ cm}^{-1}$  corresponding to the C=C stretch due to the hydrophobic polyene domain and at  $1157\text{ cm}^{-1}$ , corresponding to the C—C stretching.<sup>[62,63]</sup> As shown in **Figure 5a**, when Amp B ( $250\text{ }\mu\text{g mL}^{-1}$ ) was drop-casted on  $\text{Na}_4\text{Ag}_{44}\text{-pMBA}_{30}$  film, the peak at  $1157\text{ cm}^{-1}$  emerged.

Besides, the peak at  $1429\text{ cm}^{-1}$  due to the stretching of  $-\text{COO}$  in  $\text{Na}_4\text{Ag}_{44}\text{-pMBA}_{30}$  film suffered a significant blue shift. These spectral features are highly reproducible, as shown using multiple membranes (**Figure S14b**, Supporting Information). Amp B has been detected before using AgNP as the plasmonic entity.<sup>[63]</sup> Here, we show that  $\text{Na}_4\text{Ag}_{44}\text{-pMBA}_{30}$  films can detect as low as  $2.5\text{ }\mu\text{g mL}^{-1}$  of Amp B. Whereas, at this concentration, the characteristic peak was not observed in the case of a similar film containing polydispersed AgNPs (**Figure S14d**, Supporting Information). Thus, as a proof of concept, it is shown that the precision film made of  $\text{Na}_4\text{Ag}_{44}\text{-pMBA}_{30}$  assemblies is more efficient SERS substrate as compared to traditionally used AgNPs.

## 3. Conclusions

Here we showed self-assembly of atomically precise  $\text{Na}_4\text{Ag}_{44}\text{-pMBA}_{30}$  NCs into freestanding elastic membranes with long-range hexagonal intralayer structure over  $\text{cm}^2$ -scale. This was accomplished by utilizing the hydrogen bonding dimerizations between the terminal *p*-mercaptobenzoic acid protecting ligands of the neighboring NCs. The patchy distribution of ligands around the metal core directed preferentially intralayer hexagonal assembly (in the *ab*-plane) and only to a lesser amount interplane hydrogen bonds (in the *c*-direction). Thereby the lateral growth perpendicular to the layers could be limited upon trapping the clusters in a transient solvent layer on the air–water interface facilitating a long-range intralayer structure within the monolayer. TEM imaging indicates an extended hexagonal 2D packing of the  $\text{Na}_4\text{Ag}_{44}\text{-pMBA}_{30}$  NCs in the membrane with a cluster-to-cluster distance of 2.33 nm. This agrees with the triclinic unit cell parameters *a* and *b* in the 3D  $\text{Na}_4\text{Ag}_{44}\text{-pMBA}_{30}$  X-ray single crystal structure. The membranes could easily be transferred onto various substrates for desired applications. This is an important asset as well-defined colloidal structures have often been achieved upon templating with a specific substrate. On the other hand, the shown freestanding membranes with long-range order are expected to be relevant in applications to combine the mechanical and optoelectronic properties. The membranes behave elastically without any observable hysteresis, and display high Young's modulus of  $14.5 \pm 0.2$  GPa (based on the Gaussian distribution center resulting from a set of experiments). Finally, the distinct constituent nanocluster spectral peaks remain observable in the membranes, even if slightly broadened, therefore indicating that the intrinsic properties of the individual NCs are retained in self-assembled membranes. These findings suggest that 2D colloidal materials where ligand capped NCs are bound together by H-bonds could raise unique elasticity and stiffness values, also suggesting to combine with optoelectronic properties of the nanoclusters for future single-electron transistors, metamaterials, and multifunctional devices.

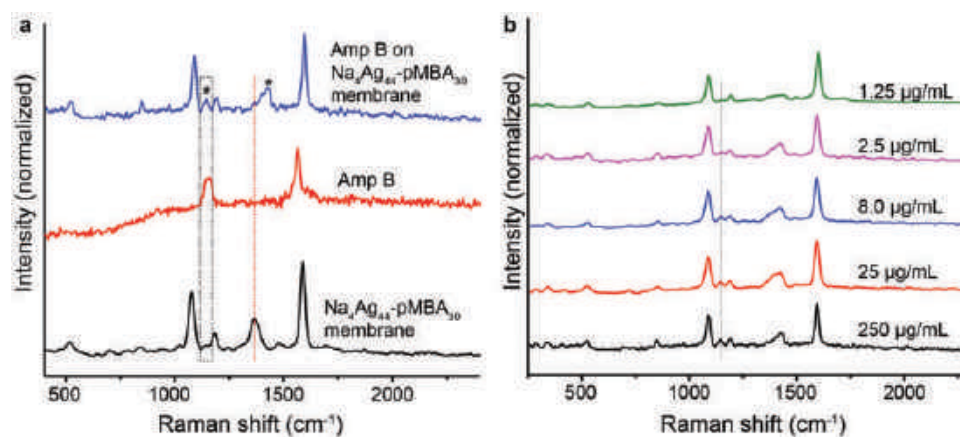


**Figure 5.** Surface enhanced Raman spectroscopy (SERS) measurements. a) Raman spectra of  $\text{Na}_4\text{Ag}_{44}\text{-pMBA}_{30}$  membrane, Amp B, and Amp B ( $250\text{ }\mu\text{g mL}^{-1}$ ) deposited over  $\text{Na}_4\text{Ag}_{44}\text{-pMBA}_{30}$  membrane. b) Variable concentration SERS spectra of Amp B deposited on  $\text{Na}_4\text{Ag}_{44}\text{-pMBA}_{30}$  membrane.

## Supporting Information

Supporting Information is available from the Wiley Online Library or from the author.

## Acknowledgements

The authors acknowledge the support by Academy of Finland Centre of Excellence in Molecular Engineering in Biosynthetic Hybrid Materials (HYBER, 2014-2019), ERC-Advanced Grant (DRIVEN), Photonics Research and Innovation (PREIN) Flagship, Department of Science and Technology, Government of India through Nano Mission, Centre of Excellence on Molecular Materials and Functions, IIT Madras, German Research Foundation (DFG, SFB 1027, Project B1) and Max Planck School Matter to Life supported by the German Federal Ministry of Education and Research (BMBF). This work made use of the Nanomicroscopy Center (Aalto-NMC) premises and the AFM facilities at Aalto University.

## Conflict of Interest

The authors declare no conflict of interest.

## Author Contributions

A.S., A.G., and I.C. contributed equally to this work. A.S., I.C., and N. conceived and carried out the synthesis and characterization. A.S. and N. carried out self-assembly, electron microscopy imaging, ESI mass spectrometry, and Raman spectroscopy measurements. A.G. conceived and carried out the AFM measurements and analyzed the data together with H.H., K.J., and P.L. T.P., O.I., and N. directed the experimental research. B.M. and A.C. performed the synthesis of NCs and membranes for SERS measurements. All authors contributed to preparation of the final manuscript.

## Data Availability Statement

The data that support the findings of this study are available from the corresponding author upon reasonable request.

## Keywords

2D membranes, colloids, nanoclusters, nanoparticle self-assembly, precision nanoparticles

Received: March 17, 2022

Revised: May 9, 2022

Published online:

- [1] K. S. Novoselov, A. K. Geim, S. V. Morozov, D. Jiang, Y. Zhang, S. V. Dubonos, I. V. Grigorieva, A. A. Firsov, *Science* **2004**, 306, 666.
- [2] X. Peng, L. Peng, C. Wu, Y. Xie, *Chem. Soc. Rev.* **2014**, 43, 3303.
- [3] L. Chen, J. Wen, P. Zhang, B. Yu, C. Chen, T. Ma, X. Lu, S. H. Kim, L. Qian, *Nat. Commun.* **2018**, 9, 1542.
- [4] D. Akinwande, N. Petrone, J. Hone, *Nat. Commun.* **2014**, 5, 5678.
- [5] M. Chhowalla, H. S. Shin, G. Eda, L.-J. Li, K. P. Loh, H. Zhang, *Nat. Chem.* **2013**, 5, 263.

- [6] M. Naguib, V. N. Mochalin, M. W. Barsoum, Y. Gogotsi, *Adv. Mater.* **2014**, 26, 992.
- [7] L. H. Li, Y. Chen, *Adv. Funct. Mater.* **2016**, 26, 2594.
- [8] S. Rosenfeldt, M. Stöter, M. Schlenk, T. Martin, R. Q. Albuquerque, S. Förster, J. Breu, *Langmuir* **2016**, 32, 10582.
- [9] J. N. Coleman, M. Lotya, A. O'Neill, S. D. Bergin, P. J. King, *Science* **2011**, 331, 568.
- [10] J. M. Wofford, S. Nakhaie, T. Krause, X. Liu, M. Ramsteiner, M. Hanke, H. Riechert, J. M. J. Lopes, *Sci. Rep.* **2017**, 7, 43644.
- [11] A. Narita, X.-Y. Wang, X. Feng, K. Müllen, *Chem. Soc. Rev.* **2015**, 44, 6616.
- [12] Q. H. Wang, K. Kalantar-Zadeh, A. Kis, J. N. Coleman, M. S. Strano, *Nat. Nanotechnol.* **2012**, 7, 699.
- [13] F. Xia, H. Wang, D. Xia, M. Dubey, A. Ramasubramanian, *Nat. Photonics* **2014**, 8, 899.
- [14] W. Cheng, N. Park, M. T. Walter, M. R. Hartman, D. Luo, *Nat. Nanotechnol.* **2008**, 3, 682.
- [15] T. Wen, S. A. Majetich, *ACS Nano* **2011**, 5, 8868.
- [16] C. Yu, X. Guo, M. Muzzio, C. T. Seto, S. Sun, *ChemPhysChem* **2019**, 20, 23.
- [17] W. J. Cho, Y. Kim, J. K. Kim, *ACS Nano* **2012**, 6, 249.
- [18] R. Sardar, A. M. Funston, P. Mulvaney, R. W. Murray, *Langmuir* **2009**, 25, 13840.
- [19] S. Zhang, G. Leem, L. Srisombat, T. R. Lee, *J. Am. Chem. Soc.* **2008**, 130, 113.
- [20] C. S. Weisbecker, M. V. Merritt, G. M. Whitesides, *Langmuir* **1996**, 12, 3763.
- [21] V. N. Manoharan, *Science* **2015**, 349, 1253751.
- [22] K. E. B. Doncom, L. D. Blackman, D. B. Wright, M. I. Gibson, R. O'Reilly, *Chem. Soc. Rev.* **2017**, 46, 4119.
- [23] T. J. Woehl, T. Prozorov, *J. Phys. Chem. C* **2015**, 119, 21261.
- [24] T. P. Bignioni, X.-M. Lin, T. T. Nguyen, E. I. Crowin, T. A. Witten, H. M. Jaeger, *Nat. Mater.* **2006**, 5, 265.
- [25] A. Desireddy, C. P. Joshi, M. Sestak, S. Little, S. Kumar, N. J. Podraza, S. Masillac, R. W. Collins, T. P. Bignioni, *Thin Solid Films* **2011**, 519, 6077.
- [26] A. Dong, J. Chen, P. M. Vora, J. M. Kikkawa, C. B. Murray, *Nature* **2010**, 266, 474.
- [27] J. Pang, S. Xiong, F. Jaeckel, Z. Sun, D. Dunphy, C. J. Brinker, *J. Am. Chem. Soc.* **2008**, 130, 3284.
- [28] C. Klinke, *Europhys. Lett.* **2017**, 119, 36002.
- [29] K. E. Mueggenburg, X.-X. Lin, R. H. Goldsmith, H. M. Jaeger, *Nat. Mater.* **2007**, 6, 656.
- [30] A. Raveendran, M.-V. Meli, *ACS Omega* **2017**, 2, 4411.
- [31] W. Cheng, M. J. Campolongo, J. J. Cha, S. J. Tan, C. C. Umbach, D. A. Muller, D. Luo, *Nat. Mater.* **2009**, 8, 519.
- [32] a) F. Alibert, S. Pleutin, D. Guérin, C. Novembre, S. Lenfant, K. Lmimouni, C. Gamrat, D. Vuillaume, *Adv. Funct. Mater.* **2010**, 22, 330; b) F. Alibert, S. Pleutin, O. Bichler, C. Gamrat, T. Serrano-Gotarrendona, B. Linares-Barranco, D. Vuillaume, *Adv. Funct. Mater.* **2012**, 8, 609.
- [33] J. Langer, D. J. de Aberasturi, J. Aizpurua, R. A. Alvarez-Puebla, B. Auguie, J. J. Baumberg, G. C. Bazan, S. E. J. Bell, A. Boisen, A. G. Brolo, J. Choo, D. Cialla-May, V. Deckert, L. Fabris, K. Faulds, F. J. G. de Abajo, R. Goodacre, D. Graham, A. J. Haes, C. L. Haynes, C. Huck, T. Itoh, M. Käll, J. Kneipp, N. A. Kotov, H. Kuang, E. C. L. Ru, H. K. Lee, J.-F. Li, X. Y. Ling, et al., *ACS Nano* **2020**, 14, 28.
- [34] P. Pal, A. Bonyar, M. Veres, L. Himics, L. Balazs, L. Juhasz, I. A. Csarnovics, *Sens. Actuators, A* **2020**, 314, 112225.
- [35] R. X. He, R. Liang, P. Peng, *J. Nanopart. Res.* **2017**, 19, 267.
- [36] a) I. Chakraborty, T. Pradeep, *Chem. Rev.* **2017**, 117, 8208; b) R. Jin, C. Zeng, M. Zhou, Y. Chen, *Chem. Rev.* **2016**, 116, 10346; c) H. Häkkinen, *Nat. Chem.* **2012**, 4, 443.

- [37] a) Y. Li, M. Zhou, R. Jin, *Adv. Mater.* **2021**, *33*, 2006591; b) B. Zhang, J. Chen, Y. Cao, O. J. H. Chai, J. Xie, *Small* **2021**, *17*, 2004381.
- [38] a) T. Kawawaki, A. Ebina, Y. Hosokawa, S. Ozaki, D. Suzuki, S. Hossain, Y. Negishi, *Small* **2021**, *17*, 2005328; b) F. Gao, Q. Yuan, P. Cai, L. Gao, L. Zhao, M. Liu, Y. Yao, Z. Chai, X. Gao, *Adv. Sci.* **2019**, *6*, 1801671; c) L. Gao, Y. Zhang, L. Zhao, W. Niu, Y. Tang, F. Gao, P. Cai, Q. Yuan, X. Wang, H. Jiang, X. Gao, *Sci. Adv.* **2020**, *6*, 1421.
- [39] a) S. Chandra, Nonappa, G. Beaune, A. Som, S. Zhou, J. Lahtinen, H. Jiang, J. V. I. Timonen, O. Ikkala, R. H. A. Ras, *Adv. Opt. Mater.* **2019**, *7*, 1900620; b) J. V. Rival, P. Mymoona, K. M. Lakshmi, Nonappa, T. Pradeep, E. Shibu, *Small* **2021**, *17*, 2005718; c) V. Hynninen, S. Chandra, S. Das, M. Amini, Y. Dai, S. Lepikko, P. Mohammadi, S. Hietala, R. H. A. Ras, Z. Sun, O. Ikkala, Nonappa, *Small* **2021**, *17*, 2005205; d) A. Chakraborty, H. Dave, B. Mondal, Nonappa, E. Khatun, T. Pradeep, *J. Phys. Chem. B* **2022**, *126*, 1842.
- [40] Nonappa, T. Lahtinen, J. S. Haataja, T.-R. Tero, H. Häkkinen, O. Ikkala, *Angew. Chem., Int. Ed.* **2016**, *55*, 16035.
- [41] Nonappa, O. Ikkala, *Adv. Funct. Mater.* **2018**, *28*, 1704328.
- [42] A. Som, I. Chakraborty, T. A. Maark, S. Bhat, T. Pradeep, *Adv. Mater.* **2016**, *28*, 2827.
- [43] A. Chakraborty, A. C. Fernandez, A. Som, B. Mondal, G. Natarajan, G. Paramasivam, T. Lahtinen, H. Häkkinen, Nonappa, T. Pradeep, *Angew. Chem., Int. Ed.* **2018**, *57*, 6522.
- [44] Z. Wu, C. Dong, Y. Li, H. Hao, H. Zhang, Z. Lu, B. Yang, *Angew. Chem., Int. Ed.* **2013**, *52*, 9952.
- [45] A. Desireddy, B. E. Conn, J. Guo, B. Yoon, R. N. Barnett, B. M. Monahan, K. Kirschbaum, W. P. Griffith, R. L. Whetten, U. Landman, T. P. Bigioni, *Nature* **2013**, *501*, 399.
- [46] B. Yoon, W. D. Luedtke, R. N. Barnett, J. Gao, A. Desireddy, B. E. Conn, T. P. Bigioni, U. Landman, *Nat. Mater.* **2014**, *13*, 807.
- [47] J. Zasadzinski, R. Viswanathan, L. Madsen, J. Garnæs, D. K. Schwartz, *Science* **1994**, *263*, 1726.
- [48] K. Ariga, Y. Yamauchi, T. Mori, J. P. Hill, *Adv. Mater.* **2013**, *25*, 6477.
- [49] a) D. H. McCullough, S. L. Regen, *Chem. Commun.* **2004**, 2787; b) K. Ariga, *Langmuir* **2020**, *36*, 7158.
- [50] a) G. Palazzo, L. Carbone, G. Colafermina, R. Angelico, A. Ceglie, M. Giustini, *Phys. Chem. Chem. Phys.* **2004**, *6*, 1423; b) H. You, Y. Ji, L. Wang, S. Yang, Z. Yang, J. Fang, X. Song, B. Ding, *J. Mater. Chem.* **2012**, *22*, 1998.
- [51] A. Lipatov, H. Lu, M. Alhabeb, B. Anasori, A. Gruverman, Y. Gogotsi, A. Sinitskii, *Sci. Adv.* **2018**, *4*, 0491.
- [52] R. Zhang, V. Koutsos, R. Cheung, *Appl. Phys. Lett.* **2016**, *108*, 042104.
- [53] A. Zandiatashbar, G.-H. Lee, S.-J. An, S. Lee, N. Mathew, M. Terrones, T. Hayashi, C. R. Picu, J. Hone, N. Koratkar, *Nat. Commun.* **2014**, *5*, 3186.
- [54] C. Lee, X. Wei, J. W. Kysar, J. Hone, *Science* **2008**, *321*, 385.
- [55] J. He, P. Kanjanaboos, N. L. Frazer, A. Weis, X.-M. Lin, H. M. Jaeger, *Small* **2010**, *6*, 1449.
- [56] M. Kocun, W. Mueller, M. Maskos, I. Mey, B. Geil, C. Steinemd, A. Janshoff, *Soft Matter* **2010**, *6*, 2508.
- [57] U. Komaragiri, M. R. Begley, J. G. Simmonds, *J. Appl. Mech.* **2005**, *72*, 203.
- [58] K. Tak, W. Shu, G. David, A. Dillard, *Thin Solid Films* **2003**, *425*, 150.
- [59] Y. Wang, H. Chan, B. Narayanan, S. P. McBride, S. K. R. Sankaranarayanan, S. X.-M. Lin, H. M. Jaeger, *ACS Nano* **2017**, *11*, 8026.
- [60] S. J. Clarke, R. E. Littleford, W. E. Smith, R. Goodacre, *Analyst* **2005**, *130*, 1019.
- [61] J.-M. Nam, J.-W. Oh, H. Lee, Y. D. Suh, *Acc. Chem. Res.* **2016**, *49*, 2746.
- [62] R. Miyaoka, M. Hosokawa, M. Ando, T. Mori, H. Hamaguchi, H. Takeyama, *Mar. Drugs* **2014**, *12*, 2827.
- [63] W. V. La Via, J. L. Lambert, M. J. Pelletier, J. M. Morookian, S. J. Sirk, D. Mickiene, T. J. Walsh, M. S. Borchert, *Med. Mycol.* **2006**, *44*, 169.



## Supporting Information

for *Small*, DOI: 10.1002/smll.202201707

Strong and Elastic Membranes via Hydrogen Bonding  
Directed Self-Assembly of Atomically Precise  
Nanoclusters

*Anirban Som, Alessandra Griffo, Indranath Chakraborty,  
Hendrik Hähl, Biswajit Mondal, Amrita Chakraborty,  
Karin Jacobs, Päivi Laaksonen, Olli Ikkala,\* Thalappil  
Pradeep,\* and Nonappa\**



## Supporting Information

**Strong and elastic membranes via hydrogen bonding directed self-assembly of atomically precise nanoclusters**

*Anirban Som, Alessandra Griffo, Indranath Chakraborty, Hendrik Hähl, Biswajit Mondal, Amrita Chakraborty, Karin Jacobs, Päivi Laaksonen, Olli Ikkala\*, Thalappil Pradeep\*, Nonappa\**

**Contents**

- General methods and materials
- Synthesis of Na<sub>4</sub>Ag<sub>44</sub>-pMBA<sub>30</sub> nanoclusters
- Self-assembly of Na<sub>4</sub>Ag<sub>44</sub>-pMBA<sub>30</sub> nanoclusters
- Preparation of Na<sub>4</sub>Ag<sub>44</sub>-pMBA<sub>30</sub> monolayer membranes
- Instrumentation and Imaging
- Figure S1. Synthesis of Na<sub>4</sub>Ag<sub>44</sub>-pMBA<sub>30</sub> nanoclusters and membrane formation.
- Figure S2. Absorption spectra and mass spectrometric characterization of Na<sub>4</sub>Ag<sub>44</sub>-pMBA<sub>30</sub>
- Figure S3. TEM images of 2D crystals obtained when Na<sub>4</sub>Ag<sub>44</sub>-pMBA<sub>30</sub> dispersion in DMF was dispersed in various solvents
- Figure S4. HR-TEM of Na<sub>4</sub>Ag<sub>44</sub>-pMBA<sub>30</sub> monolayer membranes
- Figure S5. Raman spectra, optical images, and FT-IR spectra of Na<sub>4</sub>Ag<sub>44</sub>-pMBA<sub>30</sub> monolayer membrane and the drop casted Ag<sub>44</sub> solution
- Figure S6. TEM micrographs of Na<sub>4</sub>Ag<sub>44</sub>-pMBA<sub>30</sub> monolayer membranes.
- Figure S7. TEM micrographs of Na<sub>4</sub>Ag<sub>44</sub>-pMBA<sub>30</sub> membranes deposited on holey grid after sputter coating with platinum
- Figure S8. Real height images of Na<sub>4</sub>Ag<sub>44</sub>-pMBA<sub>30</sub> monolayer membrane suspended on holey carbon grid
- Figure S9. Real height images of Na<sub>4</sub>Ag<sub>44</sub>-pMBA<sub>30</sub> membranes deposited on silicon wafers
- Figure S10. AFM image of the holey carbon support without the Na<sub>4</sub>Ag<sub>44</sub>-pMBA<sub>30</sub> monolayer membrane deposited
- Figure S11. AFM approaching curves upon indentation on a fixed spot.
- Figure S12. AFM height images before and after indentation of Na<sub>4</sub>Ag<sub>44</sub>-pMBA<sub>30</sub> monolayer membranes
- Figure S13. Overlap of multiple Force – indentation curves
- Figure S14. Surface enhanced Raman spectroscopy (SERS) measurements

## 1.0 Materials and methods

All chemicals were commercially available and were used without further purification. Silver nitrate ( $\text{AgNO}_3$ , 99%), *p*-mercaptobenzoic acid (*p*MBA, 97%) and sodium borohydride ( $\text{NaBH}_4$ , 99.99%) were purchased from Sigma-Aldrich. Also, dimethylformamide (DMF, AR grade), dimethylsulfoxide (DMSO, AR grade), toluene (AR grade), methanol (AR grade), citric acid and cesium hydroxide ( $\text{CsOH}$ ) were procured from Sigma-Aldrich. Milli-Q water was used throughout the experiment.

## 2.0 Synthesis of $\text{Na}_4\text{Ag}_{44}$ -*p*MBA<sub>30</sub> nanoclusters

$\text{Na}_4\text{Ag}_{44}$ -*p*MBA<sub>30</sub> clusters were synthesized using a reported procedure.<sup>27,28</sup> To a stirred solution of  $\text{AgNO}_3$  (28 mg) in a mixture of DMSO and water (4:7 volume ratios) under constant stirring, 173 mg of solid *p*MBA was added, and stirring was continued. Subsequently, a 50% aqueous solution of  $\text{CsOH}$  was added dropwise till the cloudy nature of thiolates became clear and a greenish yellow color appeared. To the reaction mixture, a solution of  $\text{NaBH}_4$  (283 mg in 9 mL water) was added dropwise. Upon adding the  $\text{NaBH}_4$ , the color of the reaction mixture changed to deep brown, and after 1 h it turned deep red, confirming cluster formation. This crude cluster was precipitated by adding DMF, and the mixture was centrifuged at 5000 rpm. After removing the centrifugate, the cluster was dispersed in citric acid containing DMF solution. The dispersion cluster was then reprecipitated by adding excess toluene and centrifuged at 5000 rpm. The acidification step was repeated one more time. After this, the precipitate was re-dissolved in DMF to get the purified cluster.

## 3.0 Self-assembly of $\text{Na}_4\text{Ag}_{44}$ -*p*MBA<sub>30</sub>

### 3.1 Microscale colloidal crystals

To precipitate microscale colloidal crystal sheets, 20  $\mu\text{L}$  of the as synthesized dispersion in  $\text{Na}_4\text{Ag}_{44}$ -*p*MBA<sub>30</sub> in DMF was added to 200  $\mu\text{L}$  of the solvent (methanol, ethanol, propanol, 1-butanol, pentanol, or acetone). The resulted precipitate was then used to prepare the SEM and TEM samples.

### 3.2. Preparation of $\text{Na}_4\text{Ag}_{44}$ -*p*MBA<sub>30</sub> monolayer membranes

To prepare large area monolayer membranes, the purified clusters were first precipitated by adding toluene to 2.0 mL of as synthesized  $\text{Na}_4\text{Ag}_{44}$ -*p*MBA<sub>30</sub> dispersion in DMF. The solvent was decanted and the precipitate was re-dispersed in 2.0 mL of 1-pentanol. The  $\text{Na}_4\text{Ag}_{44}$ -*p*MBA<sub>30</sub> dispersion in 1-pentanol was slowly dropped over the surface of milli-Q water in a

beaker using pipette until the entire water surface was covered. The  $\text{Na}_4\text{Ag}_{44}\text{-pMBA}_{30}$  thin membrane which was formed at the water-air interface was subjected to characterization. It is important to mention here that an immediate transfer is better for the stability of the membrane.

#### 4.0 Instrumentation

UV-visible absorption spectra were recorded using a Perkin-Elmer Lambda 25 spectrophotometer in the range 200-1100 nm. Raman spectra were recorded using a Witec Alpha300 S confocal Raman spectrometer with 633 nm (He-Ne) laser using a Zeiss 20x objective. Raman imaging was performed using a Nikon 100x objective using a piezoelectric scanner. Data were processed by Witec Project Plus software package. FT-IR spectral measurements were performed using a Nicolet 380 instrument equipped with an ATR cell. Transmission electron microscopy (TEM) and transmission electron microscopy (TEM) were performed at an accelerating voltage of 300 kV on JEOL 3200FSC. Image acquisition was done by a Gatan 794 multiscan CCD camera. Data were processed by Gatan Digital Micrograph software.  $\text{Na}_4\text{Ag}_{44}\text{-pMBA}_{30}$  monolayer membrane floating on water was transferred on 300 mesh carbon coated copper grid and holey carbon grids and dried before TEM analysis. The TEM images were processed using Gatan Digital micrograph software. For IFFT, an area of interest in the given image was selected and transformed using available in-built functions in Gatan Digital Micrograph.

#### 4.1 Sample Preparation for AFM

Quantifoil R1.2/1.3 (Electron Microscopy Sciences) grids were plasma cleaned for 10 s in a Solarus plasma cleaner (Gatan, Pleasantown, CA, USA).  $\text{Na}_4\text{Ag}_{44}\text{-pMBA}_{30}$  monolayer membrane was transferred and dried in air and was used for AFM measurements.

#### 4.2 AFM Imaging

Topographical images were recorded by AFM (Bruker Multimode 8) in Quantitative Nanomechanical mapping mode (QNM) in air. In this mode, the probe oscillates much below the resonance frequency of the cantilever recording fast force-distance curves on the sample resulting in high resolution force volume maps. Evaluating these maps, therefore, allows also for a precise determination of the true sample surface. The images were scanned using silicon (Scanasyst, tip radius 2 nm, Bruker) and silicon nitride (MLCT-F, tip radius 20 nm, Bruker) cantilevers, with respectively a resonance frequency of 70 kHz and 125 kHz and a force constant of  $0.4 \text{ N m}^{-1}$  and  $0.6 \text{ N m}^{-1}$ . The scanned image sizes were from 1.5 to  $10 \mu\text{m}^2$ .

### 4.3 AFM indentation

The AFM indentation experiments were performed with a Bruker Multimode 8.0 Instrument at room temperature using Scanasyst cantilevers (spring constant 0.4 N/m). For each cantilever, the spring constant was calibrated by thermal methods. The Scanasyst probe had soft triangular cantilevers and pyramidal tips (with pyramid angle of 35° and a maximum nominal curvature radius of 12 nm). The actual tip diameter was estimated by tip qualification with Nanoscope software and reported a value of 23.0 nm. The tip qualification measurement was performed with an unused tip. The tip qualification was not performed for every probe used since this procedure might lead to small tip damages. Yet, indentation measurements with probes with and without known tip diameter were compared and no significant difference in the determined  $E$  values was found. In the force curve measurements, the approaching and retracting velocity was kept at 500 nm/s, scan rate at 1.25 Hz and the ramp size at 250 nm. Tens of experiments were carried out on samples having been first checked by TEM analysis. The TEM analysis permitted to discard grids not having a uniform coverage or showing bilayers prior to the force indentation  $F(\delta)$  experiments. For each sample, after having recorded the image, AFM indentation measurements were performed at the center of the suspended membrane in two ways: keeping the indentation force constant or increasing it until the rupture of the membrane. The data were processed using a homemade MATLAB script for baseline and contact point correction and extraction of the elastic modulus by the fitting of the approaching curve. The relative humidity was maintained below 50% and the temperature was maintained between 22 -23 °C.

### 4.4 Raman Spectroscopy

For SERS studies, a WITec GmbH confocal Raman microscope was used. It was equipped with a frequency doubled Nd: YAG diode laser (532 nm) for Raman excitation of the sample. This instrument was equipped with an Olympus BX41 optical microscope (inverted microscope with a 100 × 1.4 NA air objective lens) and a thermoelectrically cooled charge-coupled detector (ANDOR CCD Detection System) with a 1024 × 1024-pixel format, operating at -80 °C. The initial signals were calibrated using the 520 cm<sup>-1</sup> vibrational mode of silicon. A total of 600 grooves/mm grating was used for collecting SERS spectra. Acquisition time was 0.5 s for all measurements.

### 4.5 Sample preparation for SERS studies

The AmpB was diluted to the desired concentration using milliQ water. The film of Ag<sub>44</sub> was collected on thoroughly cleaned regular glass coverslips. These were held vertically on kim

wipe tissue paper to soak all the excess solvents. Then a drop of 3  $\mu\text{L}$  AmpB was added on top of the film. It was left at room temperature in dark to get dried.

#### 4.6 Preparation of AgNP films

Synthesizing pMBA-functionalized AgNP and making a thin film out of that itself is a synthetic challenge. Therefore, we made Ag<sub>44</sub> film as usual and kept it overnight at 50 °C. TEM image confirmed that the AgNCs were converted to AgNP while maintaining the morphology of the film. This gave the closest comparable system to our AgNC film. Amp B of desired concentration was then dropcasted on it in as stated above.

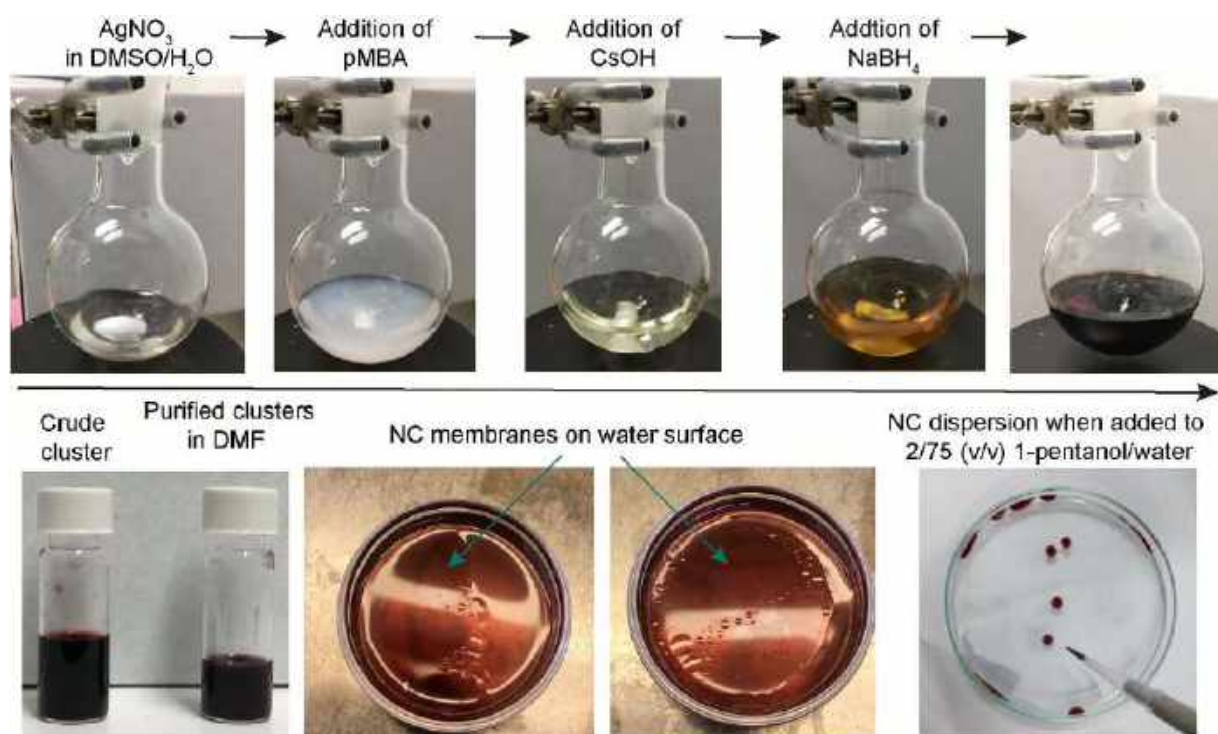


**Figure S1.** Synthesis of  $\text{Na}_4\text{Ag}_{44}\text{-pMBA}_{30}$  nanoclusters and membrane formation.



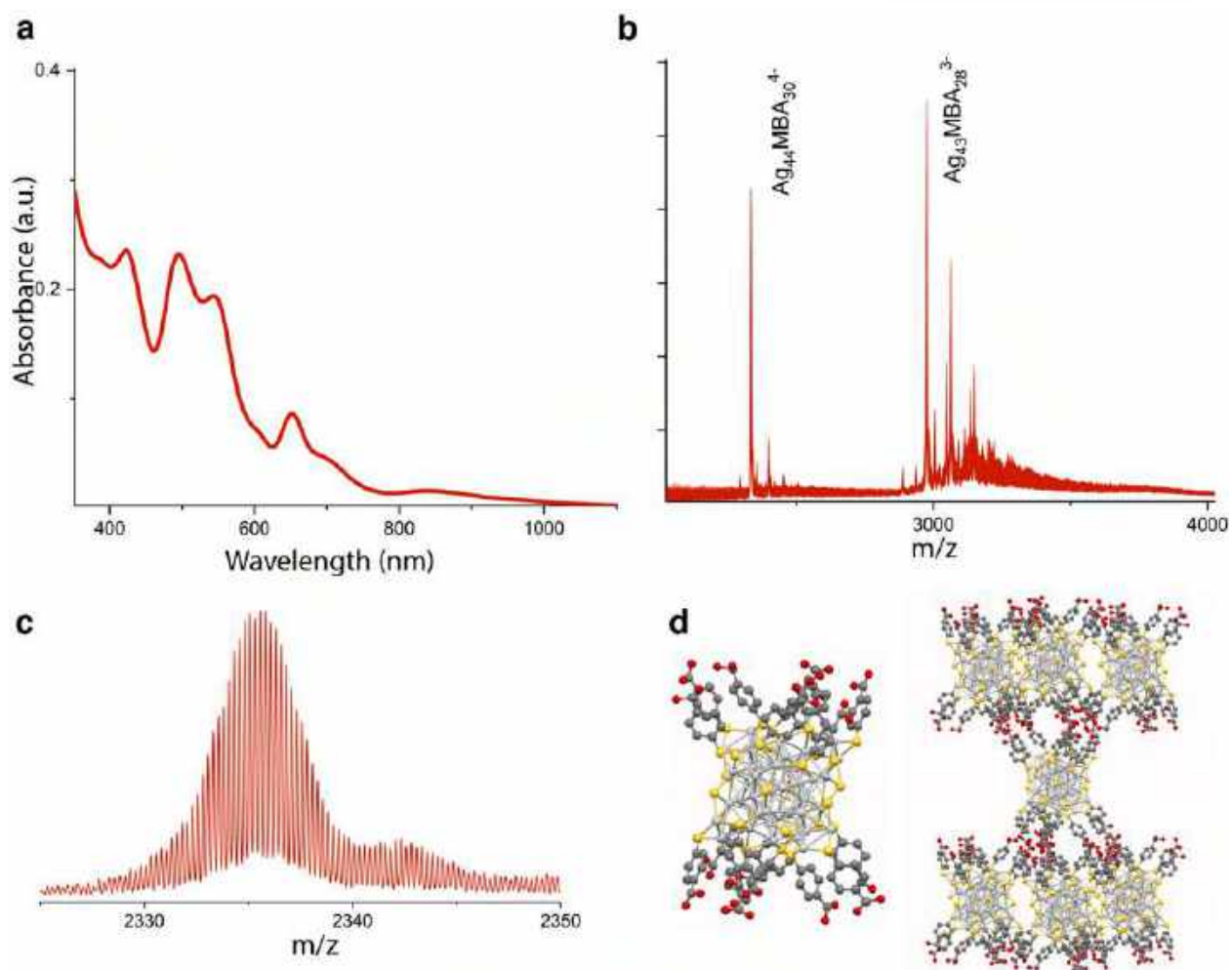


**Figure S2.** Absorption spectra and mass spectrometric characterization of  $\text{Na}_4\text{Ag}_{44}\text{-pMBA}_{30}$ . a) UV-Vis spectra of  $\text{Na}_4\text{Ag}_{44}\text{-pMBA}_{30}$  nanoclusters in solution. b and c) ESI-Mass spectra of  $\text{Na}_4\text{Ag}_{44}\text{-pMBA}_{30}$ . d) Shows the top view of **L3** *pMBA* ligand bundles and interlayer H-bonding (note: **L2** bundles are not shown for clarity).

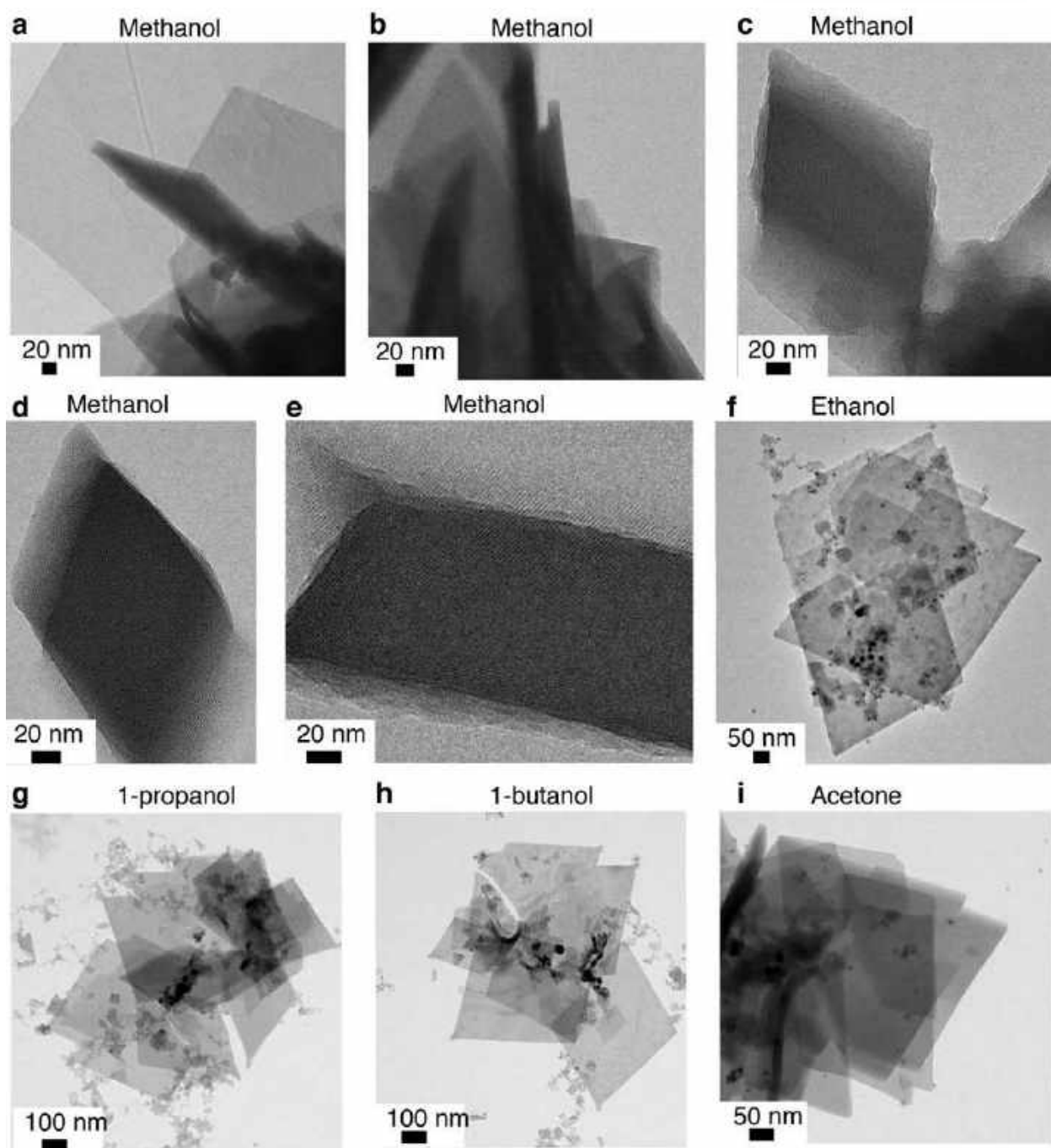


**Figure S3.** TEM images of 2D crystals obtained when  $\text{Na}_4\text{Ag}_{44}\text{-pMBA}_{30}$  dispersion in DMF was dispersed in various solvents. a and b) TEM images of 2D nanosheets obtained upon adding a solution of  $\text{Na}_4\text{Ag}_{44}\text{-pMBA}_{30}$  in DMF to methanol. c-e) HR-TEM of 2D nanosheets in methanol showing Moiré patterns due to overlapping layers. f) Ethanol. g) 1-Propanol. h) 1-Butanol and i) Acetone.

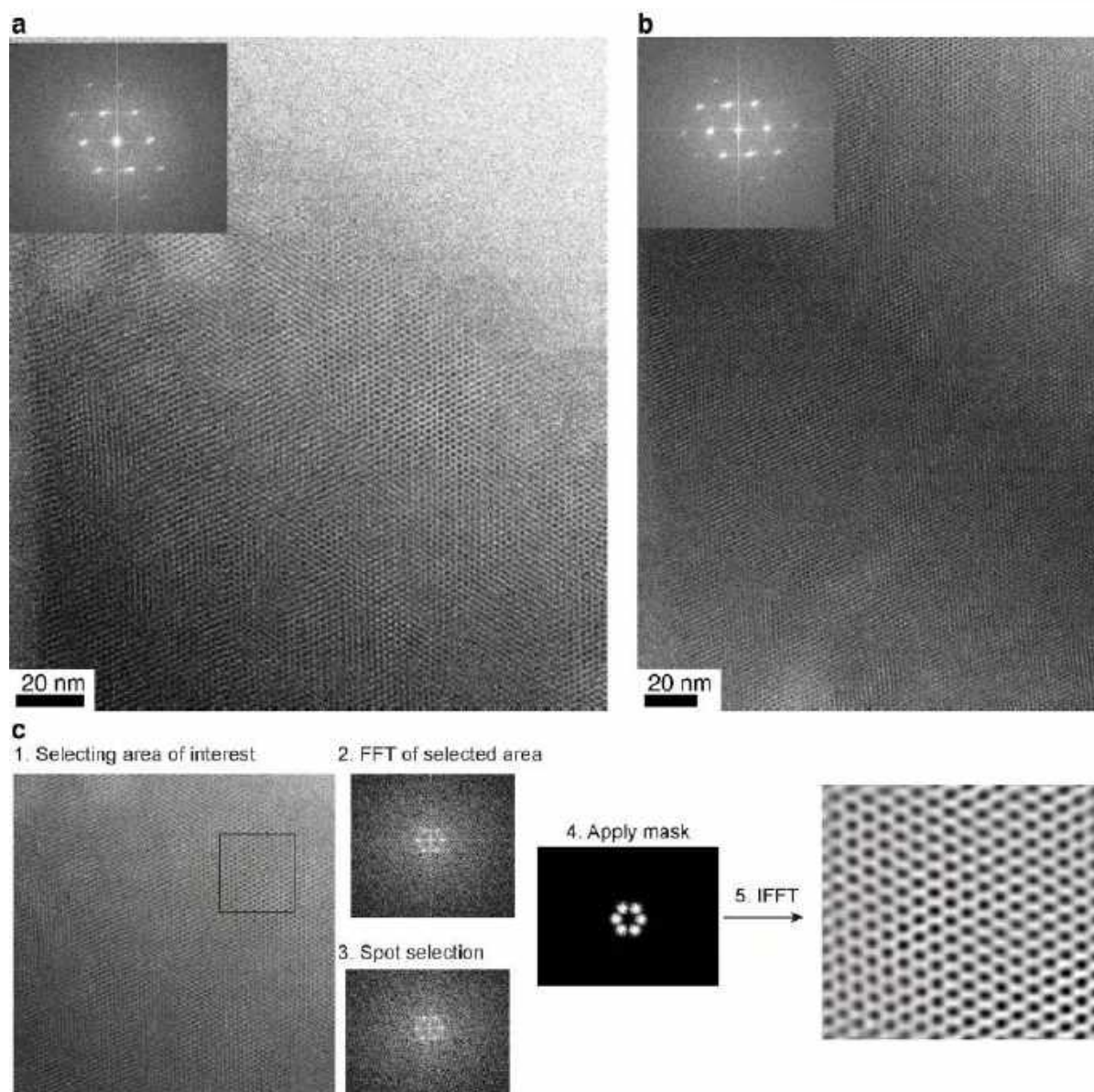


**Figure S4.** HR-TEM of  $\text{Na}_4\text{Ag}_{44}\text{-pMBA}_{30}$  monolayer membranes. a and b) HR-TEM of the selected area of monolayer membrane deposited on 300 mesh gold grid with ultrathin carbon support membrane. Insets showing the FFTs of the respective images indicating long range hexagonal array of  $\text{Na}_4\text{Ag}_{44}\text{-pMBA}_{30}$  monolayer membranes. c) The steps involved in IFFT.

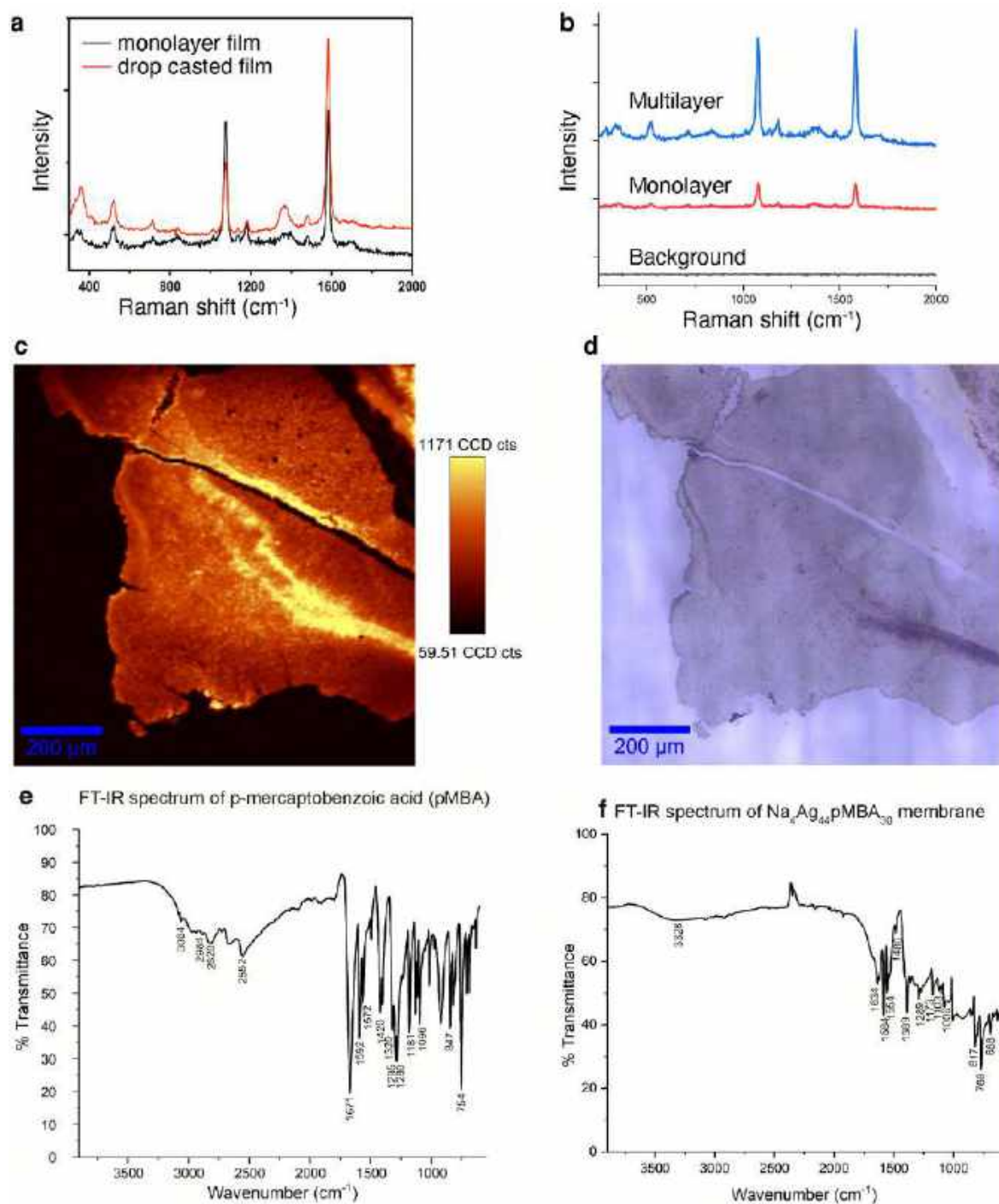


**Figure S5.** Raman spectra and optical images of  $\text{Na}_4\text{Ag}_{44}\text{-pMBA}_{30}$  monolayer membrane and the dropcasted  $\text{Na}_4\text{Ag}_{44}\text{-pMBA}_{30}$  dispersion. a) Raman spectra showing a comparison between  $\text{Ag}_{44}\text{ML}$  and the dropcasted  $\text{Ag}_{44}$  solution. b) Comparison of different spectral region reveal the presence of monolayer and overlapping layers with bright peaks in Raman imaging (c). d) Optical image of a portion of the membrane obtained using interfacial assembly. e) FT-IR spectra of *p*MBA. f) FT-IR spectra of  $\text{Na}_4\text{Ag}_{44}\text{-pMBA}_{30}$  membrane.



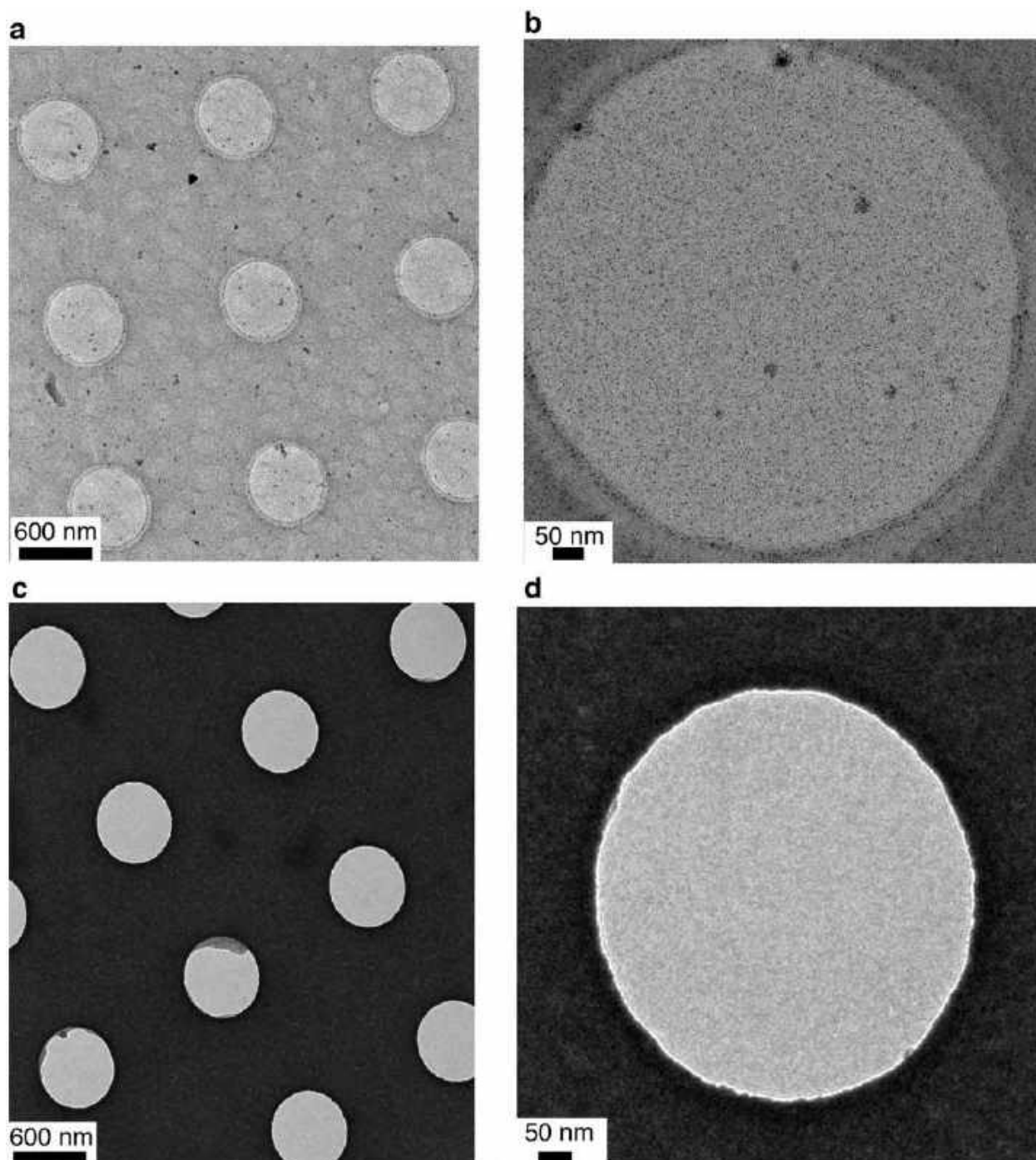


**Figure S6.** TEM micrographs of  $\text{Na}_4\text{Ag}_{44}\text{-pMBA}_{30}$  monolayer membranes. a) TEM image of  $\text{Na}_4\text{Ag}_{44}\text{-pMBA}_{30}$  monolayer membrane stretched over a holey carbon support membrane on a gold grid. b) TEM image of a  $\text{Na}_4\text{Ag}_{44}\text{-pMBA}_{30}$  monolayer membrane in a single hole. c) TEM image of holey grid after sputter coating with platinum showing the holes are empty as confirmed by high magnification image in d.



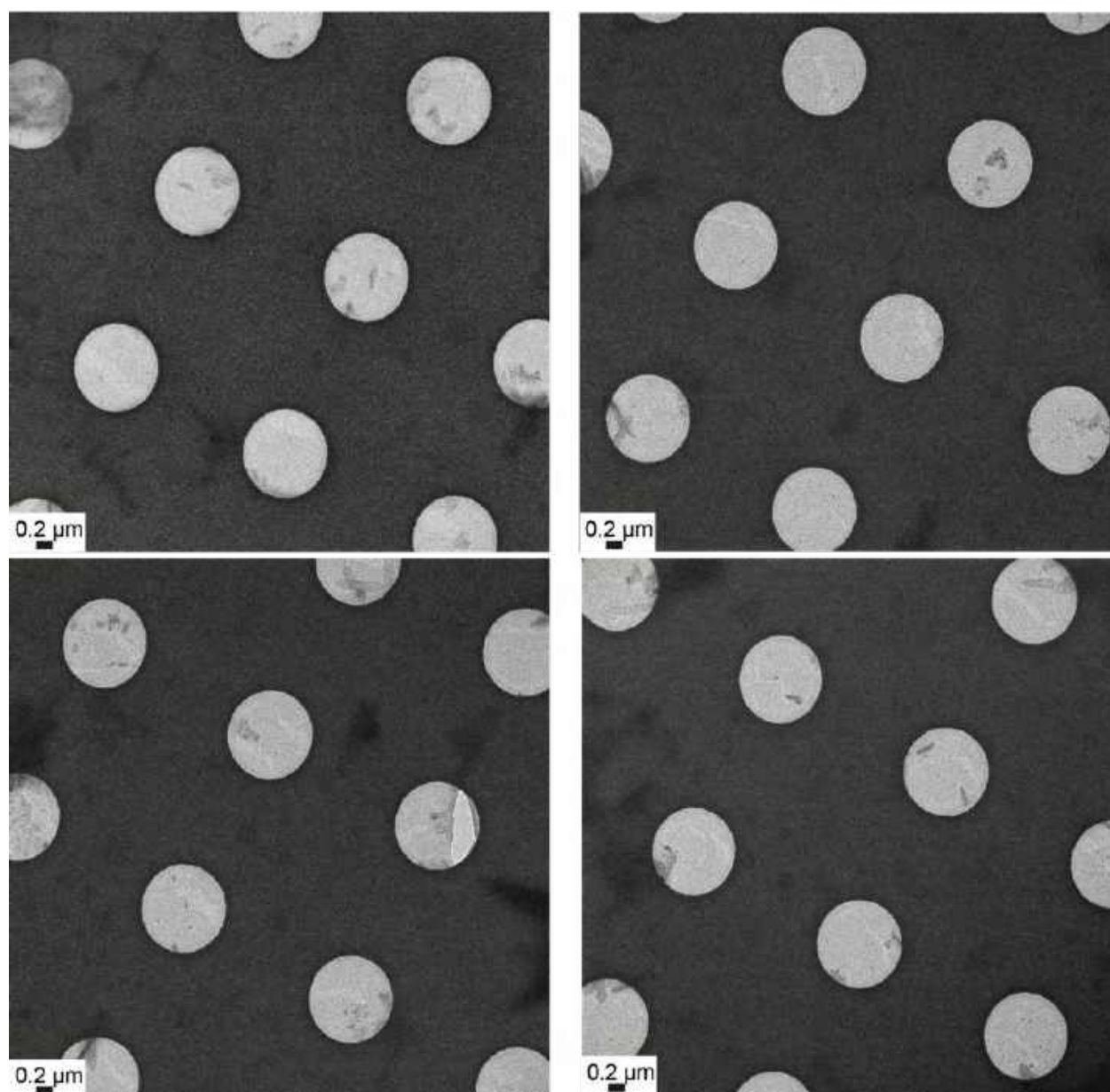


**Figure S7.** TEM micrographs of  $\text{Na}_4\text{Ag}_{44}\text{-pMBA}_{30}$  membranes deposited on holey grid after sputter coating with platinum.

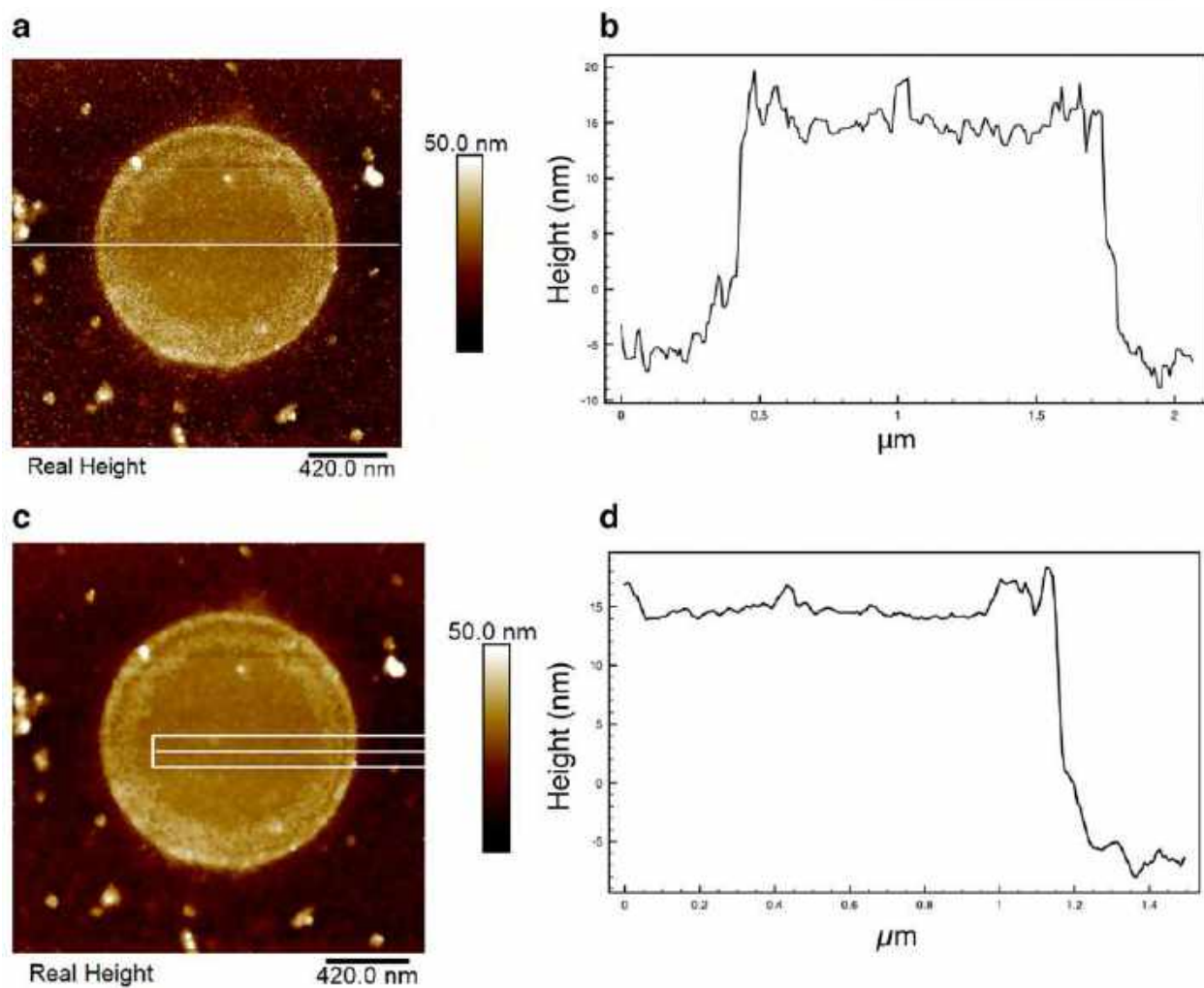


**Figure S8.** Real height images of  $\text{Na}_4\text{Ag}_{44}\text{-pMBA}_{30}$  membrane suspended on holey carbon grid. a and b) Scan sizes 2.1  $\mu\text{m}$ , c and d) Scan sizes 3.5  $\mu\text{m}$ .

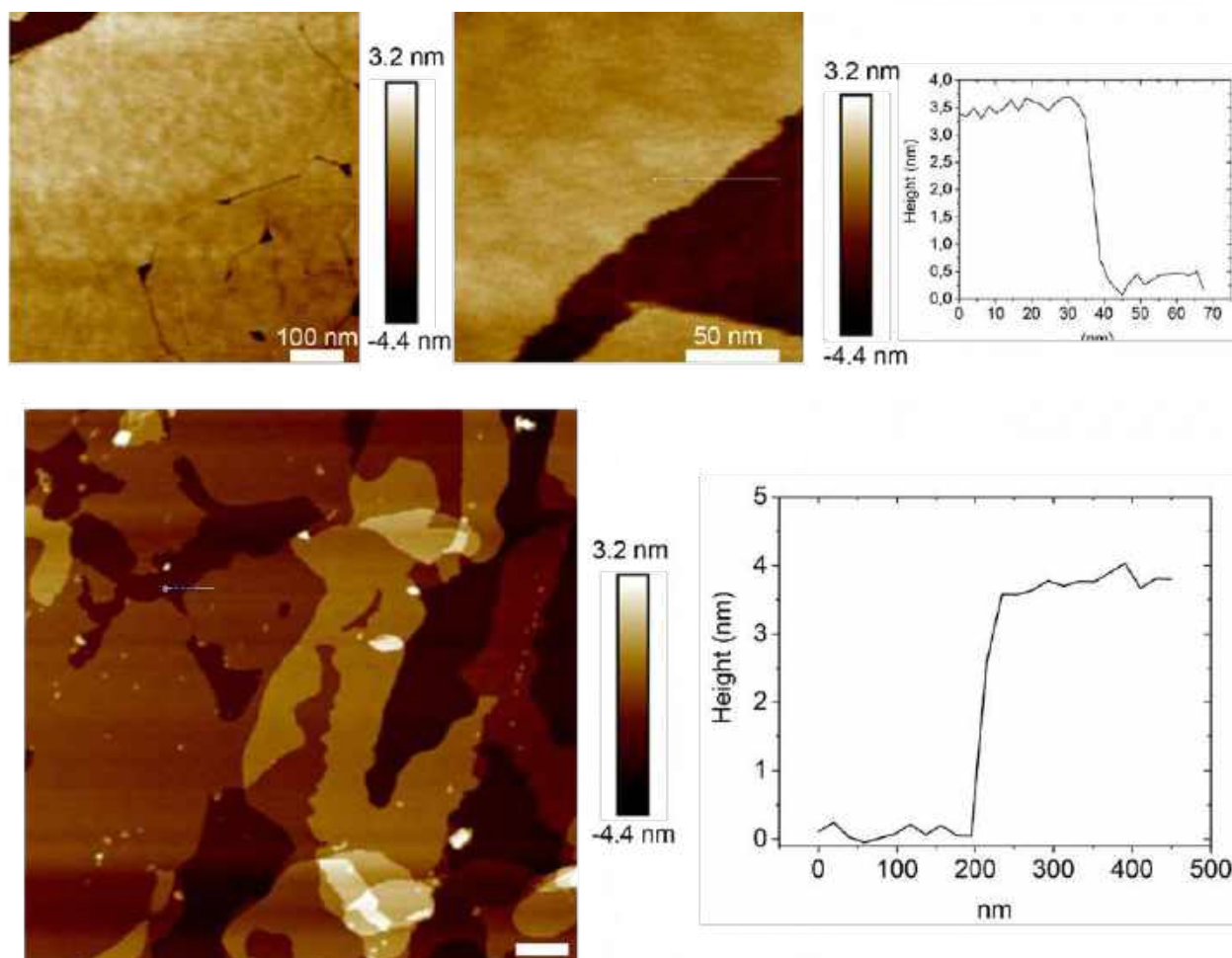


**Figure S9.** Real height images of  $\text{Na}_4\text{Ag}_{44}\text{-pMBA}_{30}$  membranes deposited on silicon wafers.

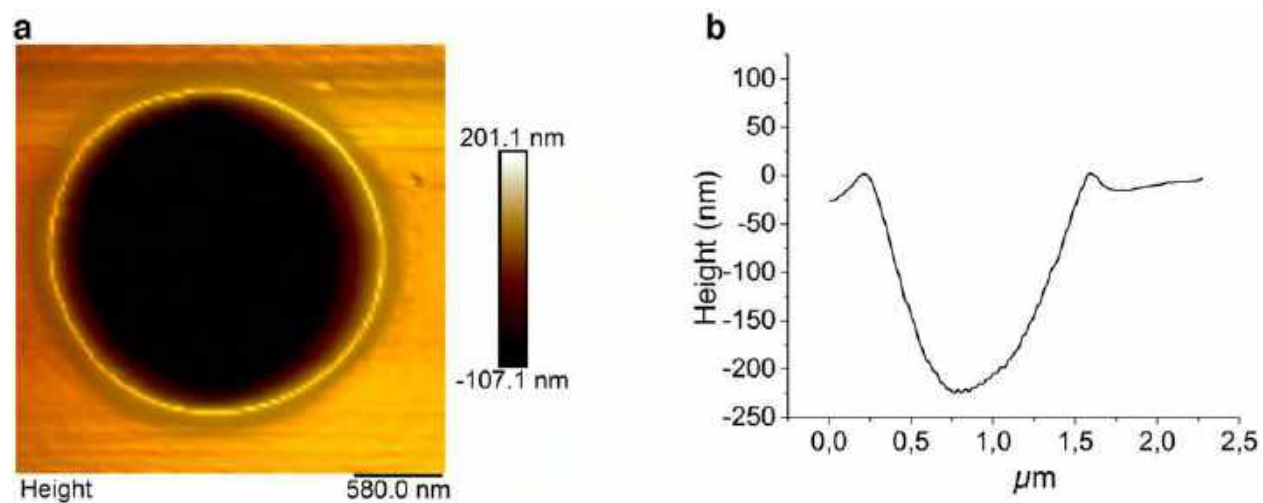


**Figure S10.** AFM image of the holey carbon support without the  $\text{Na}_4\text{Ag}_{44}\text{-pMBA}_{30}$  monolayer membrane deposited. a and b) 3D view of the AFM image and height profile, respectively, showing an estimated rim height is 20 nm.

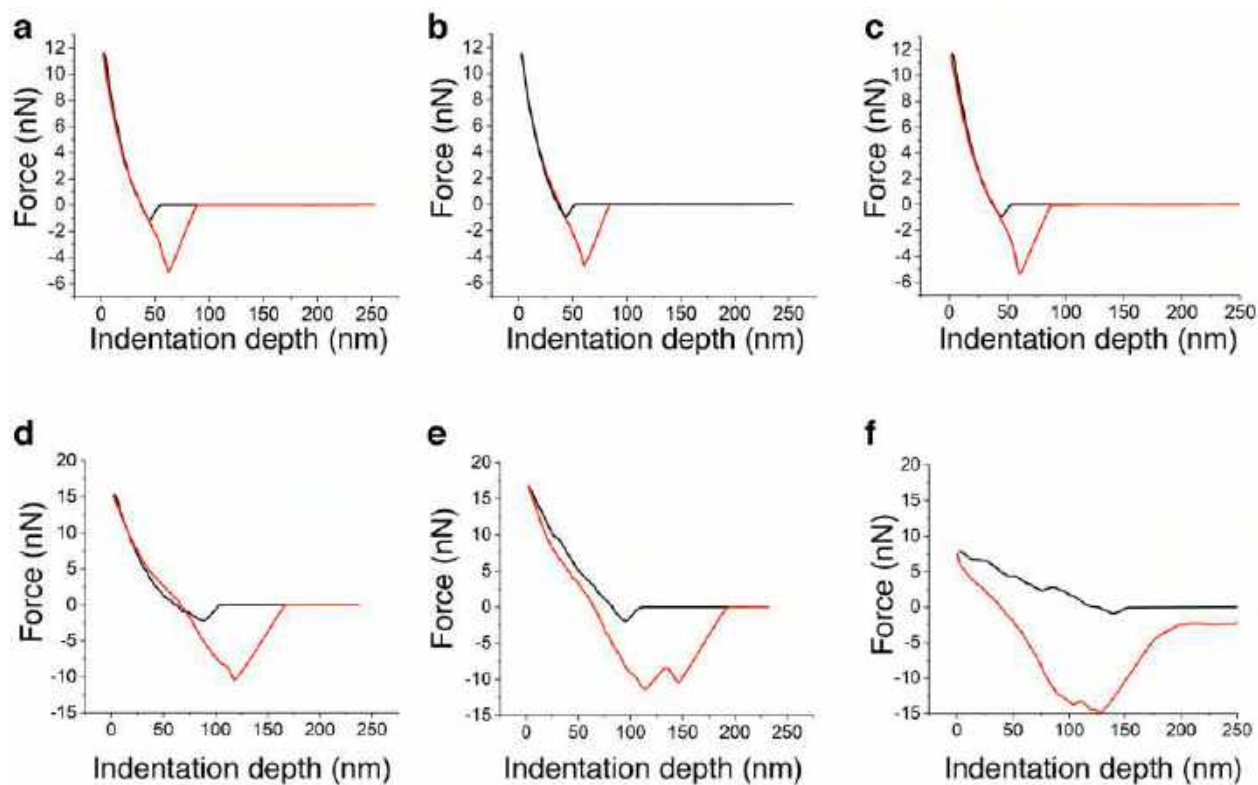


**Figure S11.** AFM approaching curves upon indentation on a fixed spot. a-d) Force is progressively increased until rupture of the membrane (e-f).

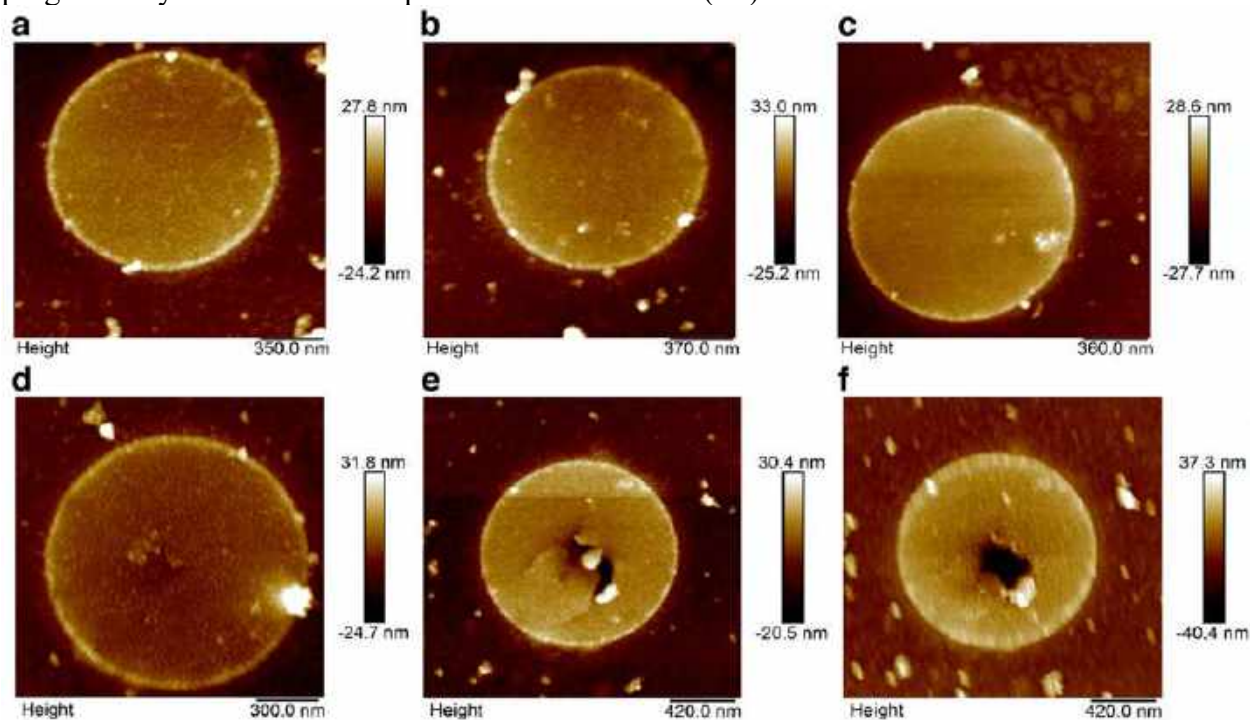


**Figure S12.** AFM height images before and after indentation of  $\text{Na}_4\text{Ag}_{44}\text{-pMBA}_{30}$  monolayer membranes. a-c) AFM height images recorded at different scan sizes for  $\text{Na}_4\text{Ag}_{44}\text{-pMBA}_{30}$  monolayer membrane suspended on the TEM grid with holey carbon substrate. d-e) AFM images after indentation upon one or more closely different spots.



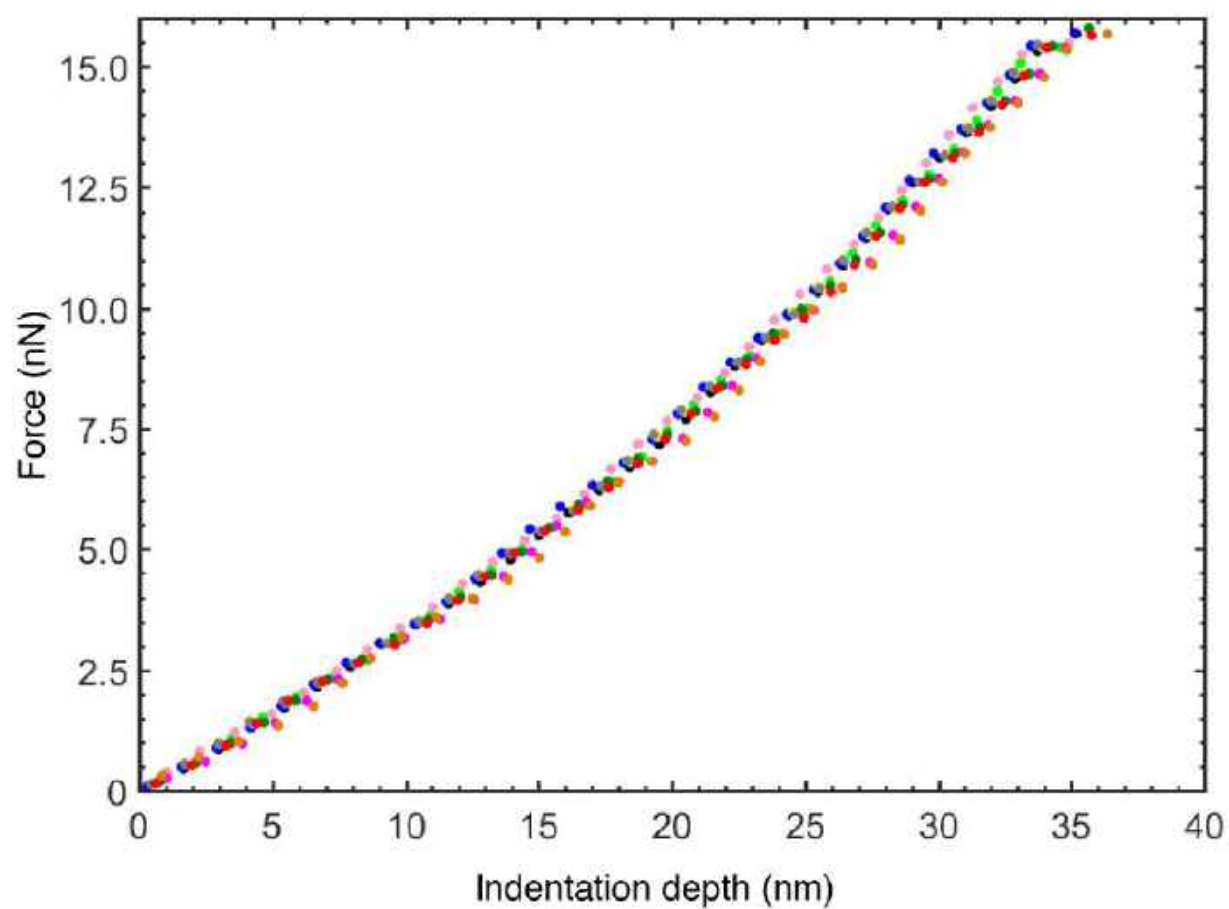


**Figure S13.** Overlap of multiple Force – indentation curves. Overlap of 11  $F(\delta)$  approaching curves indenting at the center of a  $\text{Na}_4\text{Ag}_{44}\text{-pMBA}_{30}$  monolayer membrane suspended on the TEM grid with holey carbon support.



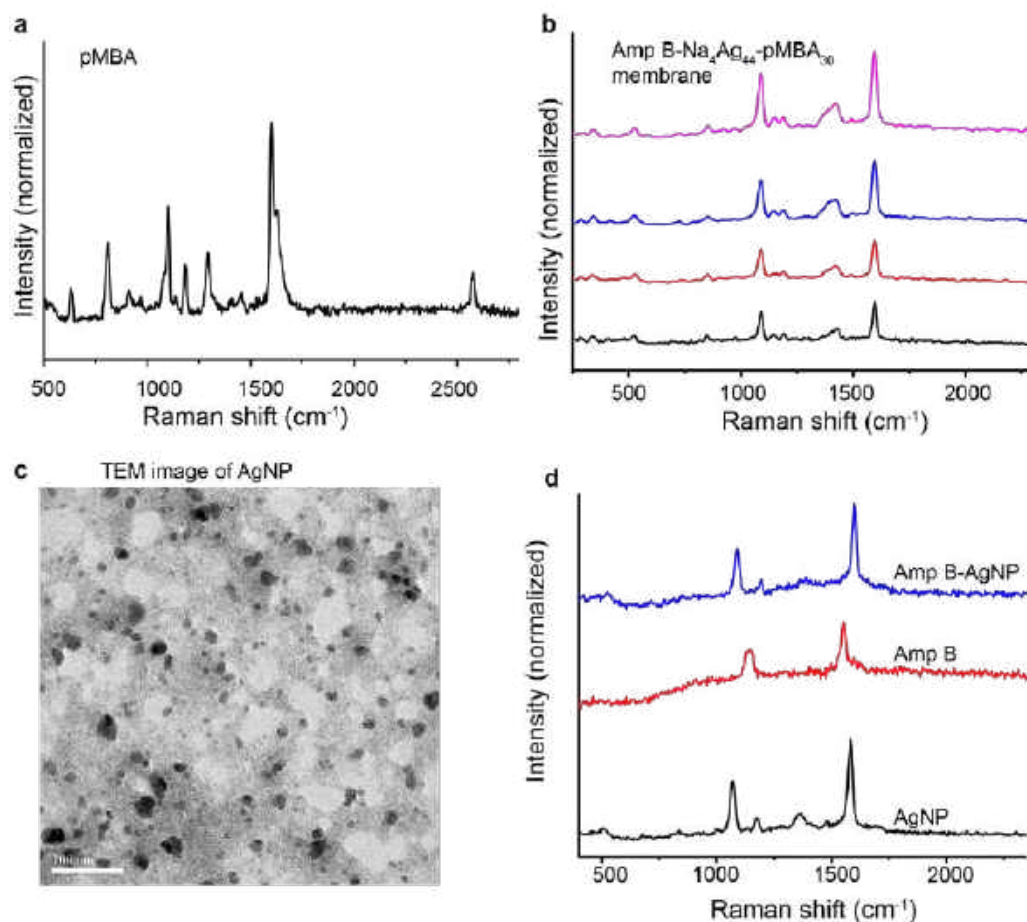


**Figure S14. SERS measurements.** a) Raman spectra of *p*MBA. b) The reproducibility of SERS spectra of Amp B deposited on multiple Na<sub>4</sub>Ag<sub>44</sub>-*p*MBA<sub>30</sub> membranes. c) TEM image of thermally treated Na<sub>4</sub>Ag<sub>44</sub>-*p*MBA<sub>30</sub> membrane resulted in larger AgNPs. d) Raman spectra of AgNP, Amp B and Amp B deposited over AgNP film showing no detectable changes in SERS spectra.

## Selective and Practical Graphene-Based Arsenite Sensor at 10 ppb

Sourav Kanti Jana,<sup>†</sup> Kamalesh Chaudhari,<sup>†</sup> Md Rabiul Islam, Ganapati Natarajan, Tripti Ahuja, Anirban Som, Ganesan Paramasivam, Addanki Raghavendra, Chennu Sudhakar, and Thalappil Pradeep\*Cite This: *ACS Appl. Nano Mater.* 2022, 5, 11876–11888

Read Online

ACCESS |



Metrics &amp; More

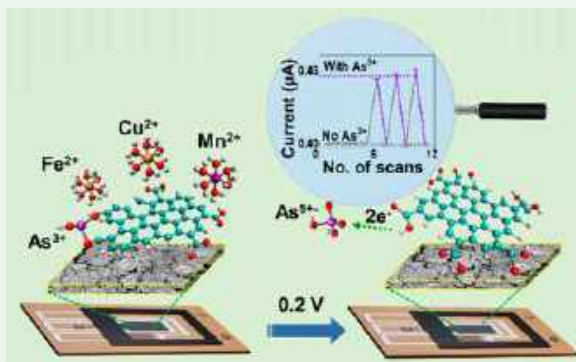


Article Recommendations



Supporting Information

**ABSTRACT:** Arsenic detection in field water samples at concentrations of relevance with affordable and simple equipment is of global interest. We report a biomimetic electrode using electrochemically reduced graphene oxide (ERGO) for highly selective and sensitive reagent-free arsenite ( $\text{As}^{3+}$ ) detection in field water samples, down to the ten parts per billion level, enabling measurement of drinking water quality affordably for millions of arsenic-affected people. This electronically and structurally optimized ERGO electrode shows selective detection of  $\text{As}^{3+}$  in both phosphate buffered saline (PBS, pH  $\sim 7$ ) and field water samples, even though more than 100 times larger conductivity and total dissolved solids (TDS), respectively, are present in them. Raman and FTIR spectroscopies were used to understand the mechanism of selectivity and sensitivity. The sensing mechanism involved two processes, namely, selective binding of  $\text{As}^{3+}$  with the  $-\text{COOH}$  groups of ERGO followed by its electro-oxidation by an applied potential. Density functional theory (DFT) and force-field calculations were used to obtain crucial insights into the site selectivity and mechanism of oxidation of  $\text{As}^{3+}$ . A two-electron transfer process from  $\text{As}^{3+}$  to ERGO followed by associative O ligand addition to  $\text{As}^{3+}$  by a ketone oxygen atom, and concomitant regeneration of  $-\text{COOH}$  group is presented. The ion selectivity depends both on structural and electronic factors. First, the compact pyramidal-shaped  $\text{As}^{3+}$  species may closely approach the edge  $-\text{COOH}$  functional group to a greater extent than the other ions enabling covalent binding of the As center with the ketone O atom. Furthermore, closer proximity of the lowest unoccupied molecular orbital (LUMO) acceptor level of the positively charged ERGO and the highest occupied molecular orbital (HOMO) donor level of the  $\text{As}^{3+}$  species suggests that a uniquely selective resonant charge-transfer effect occurs between the  $\text{As}^{3+}$  species and ERGO.



**KEYWORDS:** graphene, ERGO, biomimetic device, arsenic sensor, chronoamperometry, electron transfer, density functional theory, Raman spectroscopy

## INTRODUCTION

Availability of clean water (CW) globally necessitates continuous monitoring of water sources and service lines. Development of reliable, cost-effective, and compact sensors for water quality is thus an important need.<sup>1</sup> Biosensors offer high sensitivity and selectivity to specific contaminants with a quick response time and regenerability.<sup>2–4</sup> Enzymes have been used extensively as active constituents of biosensors for the detection of contaminants, especially in the biological context.<sup>5–7</sup> For example, glucose oxidase (GOx) is commonly used for rapid screening of the glucose concentration in human blood, for diabetes management.<sup>8</sup> Arsenic (As), a notorious natural poison, found in many water bodies and one of the world's deadliest environmental hazards, affecting over 300 million people globally, can be detected by an enzyme, arsenite oxidase (AiO). Long-term consumption of arsenic contaminated drinking-water and food can cause skin lesions and even cancer. It has also been associated with cardiovascular disease and diabetes. It impairs cognitive development. Specific additional health effects include hyperpigmentation, keratosis,

anemia, burning sensation of eyes, liver fibrosis, chronic lung disease, and neuropathy. Therefore, its quantitative and selective detection in drinking water with an affordable device like a glucometer is essential. Elemental As exists in two ionic forms, arsenite ( $\text{As}^{3+}$ ) and arsenate ( $\text{As}^{5+}$ ), in natural water and the former is more toxic.<sup>9–12</sup> AiO immobilized electrode was shown to be capable of detecting As selectively in water.<sup>9</sup>  $\text{As}^{3+}$  binds with the molybdenum (Mo) center of AiO thorough nucleophilic interaction and subsequently,  $\text{As}^{3+}$  is oxidized by the concurrent reduction of molybdenum of AiO ( $\text{Mo}^{6+}$  to  $\text{Mo}^{4+}$ ) during the catalytic cycle.<sup>9,13</sup> Despite its selectivity to  $\text{As}^{3+}$ , its complex extraction and purification procedure,

Received: July 1, 2022

Accepted: August 8, 2022

Published: August 17, 2022



stability at ambient temperatures, and more importantly, binding to a particular substrate inhibit the use of AiO for field applications as of now.<sup>14,15</sup>

Several chemical entities such as metal complexes, porphyrins, fullerene derivatives, gold nanoparticles, and rare earth nanoparticles that exhibit structural diversity (size, shape, and morphology), specific crystallographic orientation, and surface charge have been shown to mimic various natural enzymes.<sup>16–18</sup> Currently, As<sup>3+</sup> sensing using nanomaterials is exclusively based on anodic stripping voltammetry (ASV).<sup>19–23</sup> Efforts to synthesize different nanostructured materials, with an aim of developing a biomimetic electrode with activity similar to AiO but with superior physical and chemical stability has been reviewed.<sup>24</sup> The performance of most of these materials for selective As<sup>3+</sup> sensing in natural water samples, composed of numerous other species, typically at several orders of magnitude larger concentrations, is not satisfactory for field-deployment. Thus, the need to develop an electrode for selective As<sup>3+</sup> sensing is obvious.

Although reduced graphene oxide is a common material now-a-days, controlled modulation of functional groups and subsequent changes in its electronic properties are expanding areas of research for developing chemical/biological sensors, especially for toxic metal ions in water. Graphene oxide (GO) and reduced graphene oxide (rGO) have found applications in biomimetic chemistry because of the presence of various functional groups that can interact with a wide range of target molecules through different binding mechanisms.<sup>25,26</sup> Moreover, rGO was shown to possess greater affinity toward target molecules than even natural enzymes because of the higher synergetic effect due to its high surface area and electronic conductivity.<sup>27–29</sup> Electronic properties of rGO can be tuned by modifying the oxygen-containing functional groups. Such tunable electronic properties and surface charge of rGO facilitated its application as biosensors.<sup>30</sup> In view of that, we have fabricated an rGO-based arsenite sensor.

Here we report an electrode composed of a few layers of electrochemically reduced graphene oxide (ERGO) as an alternative to AiO for selective and sensitive As<sup>3+</sup> sensing, in natural waters. Tailoring the functional groups of the ERGO film in a controlled fashion is imperative to mimic the characteristics of AiO. We propose an approach to bind the arsenic species with the functional groups of ERGO and subsequent oxidation of the bound species at the surface upon application of a potential. Various electro-analytical and spectro-electrochemical measurements were employed to understand the biomimetic activity of the ERGO electrode. Spectroscopic studies confirmed that As<sup>3+</sup> binds with –COOH functional groups, which resulted in a change in the molecular orientation of ERGO. These bound species were oxidized at the surface of the electrode and released from the surface as As<sup>5+</sup> after application of a potential. These processes and the selectivity mechanism of the sensor toward different ions were modeled computationally.

## ■ MATERIALS AND METHODS

**Chemicals.** Flexible gold (Au) strips were purchased from Bio Nano Consulting (BNC), London, UK. Approximate thickness of Au was maintained as 10 nm over polyethylene terephthalate (PET) substrate. Sodium 2-mercaptoethanesulfonate (MESA, HSCH<sub>2</sub>CH<sub>2</sub>SO<sub>3</sub>Na) of 99.9% purity was purchased from Sigma-Aldrich and it was used for surface modification of Au strips. For the synthesis of GO using modified Hummer's method, we used several

chemicals. Graphite flakes (95% of carbon) were obtained from Active Carbon India Pvt. Ltd. Sulfuric acid (H<sub>2</sub>SO<sub>4</sub>, 95–98%), hydrochloric acid (HCl, 36%), ammonia (NH<sub>3</sub>, 30%), and hydrazine hydrate (N<sub>2</sub>H<sub>4</sub>·H<sub>2</sub>O), were obtained from Rankem Chemicals Pvt. Ltd., India. Hydrogen peroxide (H<sub>2</sub>O<sub>2</sub>, 98%) was purchased from Merck, India, and phosphorus pentoxide (P<sub>2</sub>O<sub>5</sub>, 95%) was from SD Fine Chemicals Pvt. Ltd., India. Sodium nitrate (NaNO<sub>3</sub>) was procured from Loba Chemie, India. Potassium peroxydisulfate (K<sub>2</sub>S<sub>2</sub>O<sub>8</sub>, 98%) and potassium permanganate (KMnO<sub>4</sub>, 98.5%) were bought from Sisco Research Laboratories Pvt. Ltd., India. Detailed synthesis process of GO is described in the [Supporting Information](#). The experimental procedure including detailed synthesis of ERGO electrodes, followed by their morphological and structural characterization and study of As<sup>3+</sup> sensing via several electroanalytical and in situ spectroelectrochemical techniques, is shown in [Figure S1](#).

**Electrode Fabrication.** The complete fabrication process of ERGO electrodes comprised the synthesis of GO by modified Hummer's method,<sup>31</sup> pretreatment of Au strips with sodium 2-mercaptoethanesulfonate (MESA), coating of GO on Au strip by the drop cast method, and finally electroreduction of the GO film. Each of these steps is described in detail in the [Supporting Information](#). We prepared three different ERGO electrodes by varying the electroreduction time (1, 3, and 6 h) of GO coating over flexible Au strips and the samples were named accordingly (ERGO1, ERGO3, and ERGO6, respectively).

**Instrumentation.** Surface morphology and elemental analysis of the electrodes were performed by FESEM–EDX (Thermo Scientific Verios G4 UC). Backscattered electrons and secondary electrons were used for imaging at an accelerating voltage of 10 kV under high vacuum condition.

Raman spectroscopy was performed on ERGO1 and ERGO6 using a confocal Raman instrument (Witec GmbH, Alpha-SNOM alpha300S) equipped with a 633 nm laser (power ~10 mW) as the excitation source. Raman spectra were collected for electrodes in air and in the presence of DI water. In-situ spectro-electrochemical measurements were carried out using electrodes in the presence of As<sup>3+</sup> mixed with DI water. Electrode strips were connected with an electrochemical workstation through a strip holder, which was mounted on a piezoelectric scan stage of the Raman spectrometer. Measurements were carried out with a 20× objective (Plan-Apochromat, Zeiss) for solid state measurements. Spectro-electrochemical measurements were carried out using a 60× water objective (Nikon Fluor). Spectro-electrochemical measurements were performed using an EMSTAT potentiostat, in presence and absence of a DC potential, with 100 μL of aqueous As<sup>3+</sup> solution on both the electrodes. The spectra were collected at the laser excitation wavelength with an acquisition time of 1 s. A long band-pass filter was placed in the path of the Raman signal, to cut off the Rayleigh scattering. The signal was then dispersed using a 600 grooves/mm grating, and finally, the dispersed light was collected with a Peltier-cooled charge coupled device.

IR spectra of ERGO electrodes were acquired by a PerkinElmer FT-IR spectrometer. All the electrodes were dried completely under vacuum condition before performing IR measurements.

X-ray photoelectron spectroscopy (XPS) measurements were carried out using an Omicron Nanotechnology ESCA probe TPD spectrometer. Polychromatic Al K $\alpha$  was used as the X-ray source ( $h\nu = 1486.6$  eV). All the ERGO samples were placed on a carbon tape attached on the sample stub. Constant analyzer with energy of 20 eV was used during measurements. Prior to measurements, binding energy was calibrated with respect to C 1s at 284.8 eV. All the XPS spectra of the samples were deconvoluted using CasaXPS software.

**Electroanalytical Measurements.** Change in electronic conductivity and interfacial transport property of ERGO samples were investigated by electrochemical impedance spectroscopy (EIS). Surface charge of ERGO electrodes was studied using Mott–Schottky (M-S) analysis and the interfacial (electrode/electrolyte) electron transport property was evaluated using the Nyquist plot. M-S analysis was performed by measuring impedance of each electrode by varying applied DC potential at a given frequency of the AC signal (in our



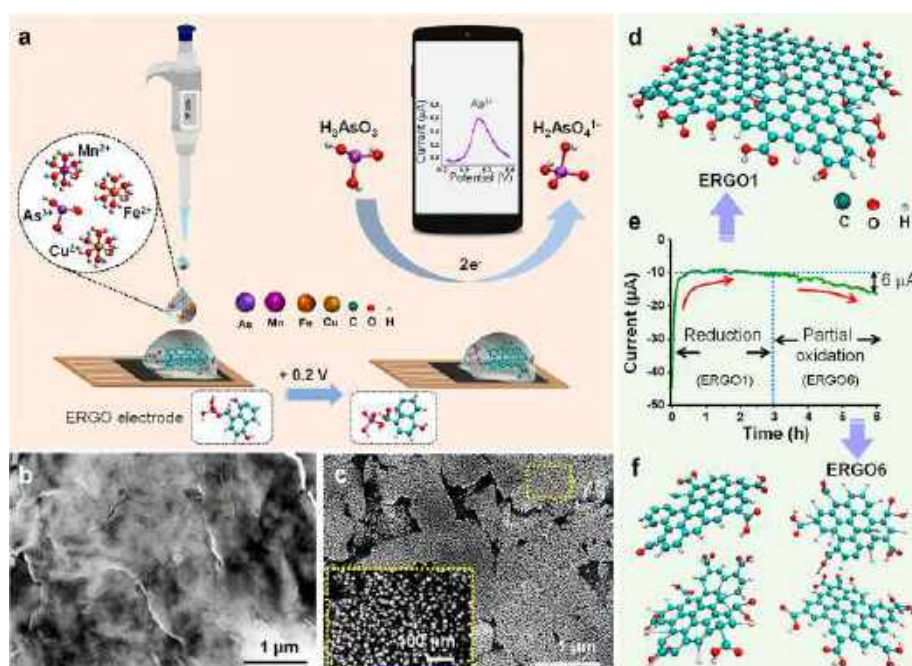


**Figure 1.** (a) Schematic representation of selective  $\text{As}^{3+}$  sensing by ERGO electrode. The geometric area of the working electrode is  $\sim 0.2 \text{ cm}^2$  ( $0.7 \text{ cm} \times 0.3 \text{ cm}$ ). FESEM images of (b) ERGO1, (c) ERGO6 electrode at the same magnification. Inset of Figure 1c shows a magnified FESEM image of the chosen area. Figure 1d, f represent changes in the molecular structure of ERGO during the electroreduction process. Figure 1e corresponds to the chronoamperometry (CA) curve of electroreduction during the preparation of ERGO strips. Here, current decreased from  $-45$  to  $-10 \mu\text{A}$  within 15 min and it remained constant up to 3 h, implying electroreduction of the oxygen-containing functional groups (C–O, C–OH). Afterward, it started to increase slowly from  $-10$  to  $-16 \mu\text{A}$ , which could be attributed to the breaking of a large sheet into small nanosheets and the edges of ERGO6 nanosheets being oxidized. Figure 1f represents the molecular structure of ERGO6, which suggests that the top surface of ERGO6 consists of several nanosheets, in agreement with the SEM image in c.

case, it was 1 kHz), while Nyquist plot was deduced by measuring impedance of the electrodes in the frequency range of 5 MHz to 100 Hz. Amplitude of the signal was maintained as 10 mV during measurements. Both measurements were performed in the presence of phosphate buffered saline (PBS). Electroanalytical measurements with ERGO electrodes were carried out via cyclic voltammetry (CV), linear sweep voltammetry (LSV), and chronoamperometry (CA) measurements in PBS and field water samples for  $\text{As}^{3+}$  sensing. The sensing mechanism was further analyzed by in situ electrochemical measurements with Raman and FTIR spectroscopy. Experimental details are presented in detail in the Supporting Information.

**DFT Calculations.** We modeled the analyte–sensor binding interaction, oxidation mechanism, and the selectivity of the sensor toward different analyte ions using density-functional theory (DFT) calculations and our methods are described in detail in the Supporting Information.

## RESULTS AND DISCUSSION

Biomimetic activity of ERGO electrode with exceptional sensitivity and selectivity toward  $\text{As}^{3+}$  is displayed schematically in Figure 1a.  $\text{As}^{3+}$  binds selectively with the acid functional group of ERGO and upon application of a low DC potential, it was oxidized and released as  $\text{As}^{5+}$  into the solution. In this process, a signal was detected and active sites were regenerated. Therefore, it is necessary to analyze the change in structural and electronic properties, brought about by tailoring the surface functional groups of the active ERGO electrode.

**Morphological and Structural Evolution of the ERGO Electrodes.** ERGO samples were prepared by electroreduction of GO coated Au strips at  $-1.1 \text{ V}$ . Electroreduction was performed for different time periods (1, 3, and 6 h) and corresponding electrodes were labeled as ERGO1, ERGO3,

and ERGO6, respectively. Surface morphology of these ERGO electrodes and structural changes upon electrochemical reduction can be seen from FESEM micrographs. Morphology of ERGO1 resembled that of a continuous wrinkled thin film (Figure 1b). On the other hand, ERGO6 (Figure 1c) was composed of many smaller sheets with varying sizes ( $\sim 1\text{--}2 \mu\text{m}$ ). Moreover, an expanded SEM image (inset of Figure 1c) showed that each ERGO6 sheet was an assembly of smaller particles of reduced graphene oxide, having particle sizes in the range of  $\sim 10\text{--}20 \text{ nm}$ . Additional SEM images and detailed EDS analysis of ERGO6 is presented in Figure S2. EDS spectrum (Figure S2d) taken from one of these small particles confirms the elemental composition (carbon C and oxygen O). Presence of fluorine (F) is associated with Nafion, used as a binder for electrode fabrication.

XPS analysis was performed to study the possible changes in elemental composition during the electroreduction process. We carried out this analysis on GO, ERGO1, and ERGO6. XPS spectra of C 1s and O 1s of all the electrodes are shown in Figure S3. The C 1s region of GO, ERGO1, and ERGO6 samples are shown in Figure S3a–c and O 1s spectra are shown in Figure S3d–f, respectively. Spectral features of deconvoluted C 1s and O 1s peaks are presented in Table S1, and are in agreement with the reported values.<sup>32–34</sup> Before electroreduction, population of oxygen containing functional groups of GO was higher than in ERGO samples. After the electroreduction process, a significant decrease in the population of oxygen-containing functional groups, especially of hydroxyl and epoxy groups, was observed from parent GO. Population of O–C=O functional groups was similar for both ERGO1 and ERGO3. Surprisingly, an increase in the

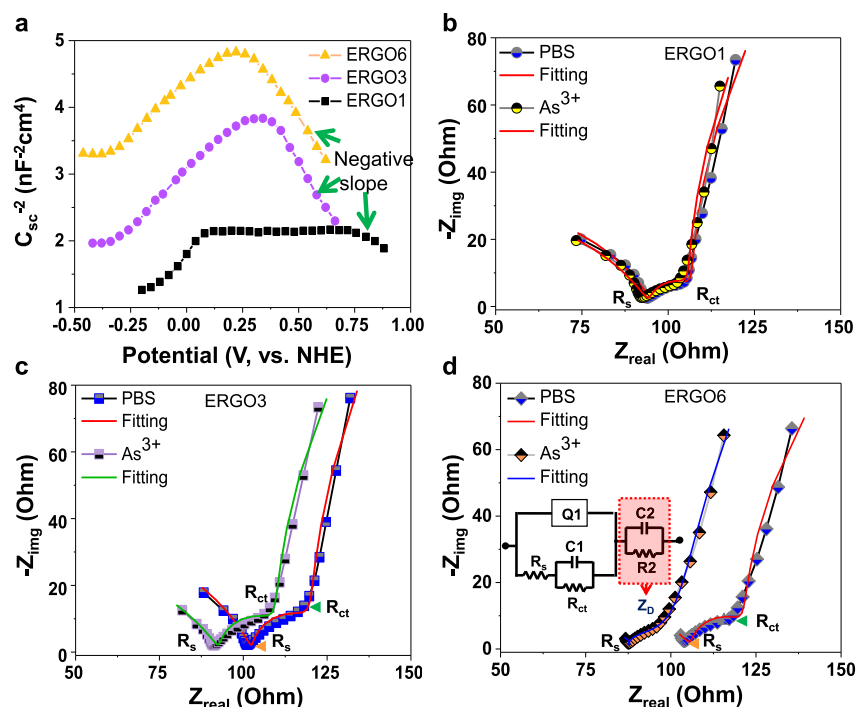


**Figure 2.** (a) Mott–Schottky analysis of ERGO samples to determine surface charge of the electrodes. Nyquist plots of different ERGO samples with and without  $\text{As}^{3+}$ , (b) ERGO1, (c) ERGO3, and (d) ERGO6. The equivalent electrical circuit, which was deduced after fitting the impedance spectra of all the electrodes, is shown in the inset of Figure 2d. The value of each fitting circuit elements is shown in Figure S4c.

population of C=O and C–O functional groups was observed for ERGO6, compared to ERGO1, as seen in Figure S3d–f. This was attributed to the reoxidation of ERGO during electrode preparation, as noticed from the CA profile (Figure 1e). The electroreduction current reached a constant value within 15 min and remained unchanged up to 3.5 h. Beyond this point, the current started increasing, indicating partial reoxidation and at 6 h, the current was maximum. This enhanced current signified that a continuous larger sheet structure got fragmented into tiny sheets, which remained assembled (Figure 1c). Figure 1d, f show schematic representations of the molecular structures of ERGO1 and ERGO6, respectively. Therefore, initial reduction and subsequent controlled oxidation in ERGO6 optimized the size and functional groups present on the surface, which further modulated the surface electronic conductivity, and interfacial transport property, thereby enabling sensitive and selective  $\text{As}^{3+}$  sensing.

**Change in Electronic Conductivity and Interfacial Charge Transport Property of ERGO.** The presence of different functional groups such as hydroxyl and carboxyl made GO negatively charged in solution. During electroreduction, some of these functional groups present at the surface of the electrode were reduced, which was expected to enhance the electron density at the edges of ERGO. Thus, electronic conductivity of the electrodes got enhanced.<sup>35</sup> Electronic properties including surface charge densities of each of the ERGO electrodes were investigated by Mott–Schottky (M-S) analysis performed at 1 kHz, in which reciprocal of the square of capacitance was plotted as a function of the potential applied to the electrodes.<sup>35</sup> M-S profiles of all three ERGO electrodes are shown in Figure 2a. Prominent inverse V shaped M-S profiles were observed for both ERGO3 and ERGO6 confirming simultaneous existence of both positive and

negative charges on the electrodes.<sup>36,37</sup> A higher negative slope observed for these two indicated greater accumulation of positive charges ( $\text{H}^+$  or  $\text{H}_3\text{O}^+$ ) at the edges, compared to ERGO1 in the aqueous medium, since the dielectric constant was similar for all the electrodes (Figure S4a). They formed Stern Layers at the surface of the respective electrodes, when the electrodes were dipped into an aqueous solution. ERGO6 was found to possess a higher charge density compared to the other two electrodes, with positive charge density being dominant over negative charge density (Figure S4b). This made ERGO6 highly protonated ( $\text{H}^+$  /  $\text{H}_3\text{O}^+$ ) and p-type (positively charged) in solution.

To understand the interfacial charge transfer property of individual ERGO electrode at the electrolyte interface, we measured total impedance of each electrode by varying the frequency of the AC signal at a constant DC potential of 0.1 V. Figure 2b–d represent the Nyquist plots of ERGO1, ERGO3, and ERGO6, respectively, before and after exposure to  $\text{As}^{3+}$ . Each experimentally obtained Nyquist spectrum was fitted with the impedance spectrum of an equivalent electronic circuit (inset of Figure 2d). In Nyquist plots, it is seen that each semicircle has two intercepts to the X-axis, first of which corresponds to the equivalent series resistance ( $R_s$ ) and the second one indicates the charge transfer resistance ( $R_{ct}$ ).  $R_s$  is associated with combined effect of solution conductivity and bulk electronic property of ERGO while  $R_{ct}$  is related to charge transfer kinetics at the ERGO/electrolyte interface. C1 corresponds to the space charge capacitance. Q1 represents an impedance which is the combination of interfacial resistances and capacitances of porous electrode material, and the combination of C2 and R2 constitutes an impedance representing the bulk diffusion of ions toward the interface of the electrode and into the porous network of the electrode. Before the addition of  $\text{As}^{3+}$  to the electrolyte, an increasing



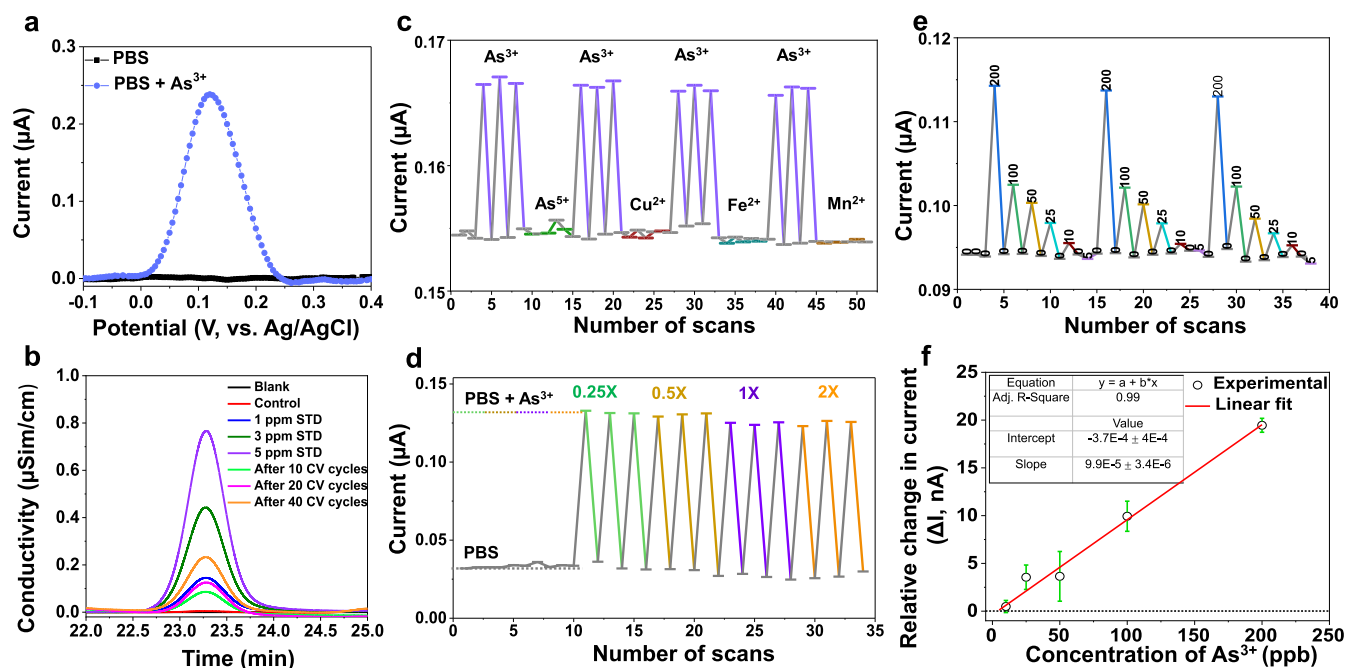


**Figure 3.** (a) LSV response of ERGO6 without and with 1 ppm  $\text{As}^{3+}$ , (b) Chronograms obtained from ion chromatography (IC) measurement with the solutions obtained after different number of CV cycles and same measurement with standard (STD)  $\text{As}^{3+}$  solutions of different concentrations. (c) Interference study performed with several heavy metal ions with ERGO6 electrode. Concentration of  $\text{As}^{3+}$  was fixed at 200 ppb, while 1 ppm was maintained for interfering ions. (d) Investigation of CA current response of 1 ppm  $\text{As}^{3+}$  spiked in PBS with different ionic conductivity. We prepared PBS solutions of different conductivity by changing their ionic concentrations and used them further as electrolytes during CA measurements. (e) CA measurement with different concentrations of  $\text{As}^{3+}$ . (f) Calibration curve showing linearity down to 10 ppb.

trend in  $R_s$  (90  $\Omega$  to 104  $\Omega$ ) with increasing electroreduction time of ERGO samples (ERGO1 to ERGO6) was observed. However, with an increase in electroreduction time,  $R_s$  of ERGO was expected to decrease as the conductivity of the electrode increased. This anomaly was presumably due to the accumulation of higher positive surface charge ( $\text{H}^+$ ) at the surface of ERGO (ERGO3 and ERGO6), which increased the space charge capacitance at the interface of electrodes, between the current collector and active electrode (Au/ERGO), as well as between the electrode and electrolyte (ERGO/PBS). These space charge capacitances tend to increase  $R_s$ . In presence of  $\text{As}^{3+}$ , value of  $R_s$  did not change. This is likely due to insufficient positive charge accumulation at the surface of ERGO1, which could not facilitate the electrostatic interaction between the  $\text{As}(\text{OH})_3$  moiety and the ERGO1 surface. However, the presence of higher positive surface charge on ERGO3 and ERGO6, enabled these electrodes to bind with  $\text{As}(\text{OH})_3$ . Adsorption of  $\text{As}^{3+}$  on ERGO3 and ERGO6 decreased the space charge capacitance, leading to a reduction in  $R_s$  for both. No significant change in  $R_{ct}$ , even after exposure of  $\text{As}^{3+}$ , was observed for ERGO1 and ERGO3, whereas a decrease (from 15  $\Omega$  to 7  $\Omega$ ) could be seen in the case of ERGO6. This decrease in  $R_{ct}$  implies that electron transfer happens at the ERGO6/electrolyte interface through faradaic reaction. Impedance spectroscopy results thus reveal that ERGO6 alone is sensitive to  $\text{As}^{3+}$ .

**Selectivity and Sensitivity of ERGO6 Electrode toward  $\text{As}^{3+}$ .** To be considered as a biomimetic electrode for  $\text{As}^{3+}$  sensing, an electrode has to exhibit high sensitivity and selectivity toward  $\text{As}^{3+}$ . Further, the ionic conductivity and total dissolved solids (TDS) of the electrolyte medium should not affect the  $\text{As}^{3+}$  response of the electrode, for it to be used in the field. To demonstrate the sensitive and selective

detection of  $\text{As}^{3+}$  with ERGO6 electrode, we employed electroanalytical measurements [cyclic voltammetry (CV), linear sweep voltammetry (LSV) and chronoamperometry (CA)].

**Sensitivity.** The sensitivity of the ERGO6 electrode toward  $\text{As}^{3+}$  was evaluated by LSV using 1 ppm of  $\text{As}^{3+}$ . Corresponding voltammogram showed a peak at 0.1 V (Figure 3a) due to the electro-oxidation of  $\text{As}^{3+}$  at the surface of ERGO6. CV was performed with all the ERGO electrodes using same concentration of  $\text{As}^{3+}$ , and only ERGO6 electrode responded to  $\text{As}^{3+}$  (Figure S5). In the CA profile (Figure S6a), the initial ten data points referred to the CA current measured with only PBS using ERGO6 electrode, while the next four cycles showed current response of 70 nA after the addition of 1 ppm of  $\text{As}^{3+}$ . Electrochemical oxidation of  $\text{As}^{3+}$  into  $\text{As}^{5+}$  at ERGO6 electrode was confirmed by ion chromatography (IC). A solution of  $\text{As}^{3+}$  was subjected to 50 CV cycles (Figure S6b) using ERGO6 electrode and the resulting solution was used for IC measurements. This electrochemically reacted  $\text{As}^{3+}$  solution and standard  $\text{As}^{5+}$  solution showed ionic conductivity at the same retention time (Figure 3b). Interaction of  $\text{As}^{3+}$  with ERGO6 through adsorption was determined by scan rate ( $\nu$ ) dependent CV with 200 ppb  $\text{As}^{3+}$  (Figure S7a). Linear oxidation peak current as a function of square root  $\nu$  (Figure S7c) indicated that the adsorption of  $\text{As}^{3+}$  took place onto the active sites of ERGO through a diffusion-controlled process. These surface adsorbed species were oxidized upon application of an external potential, with the response being linear with concentration of  $\text{As}^{3+}$  (Figure S7d).

To determine the limit of detection (LOD) of  $\text{As}^{3+}$  by ERGO6 electrode, we performed CA measurements at various  $\text{As}^{3+}$  concentrations (starting from 200 to 5 ppb) in PBS (Figure 3c). The experiment was repeated thrice using the

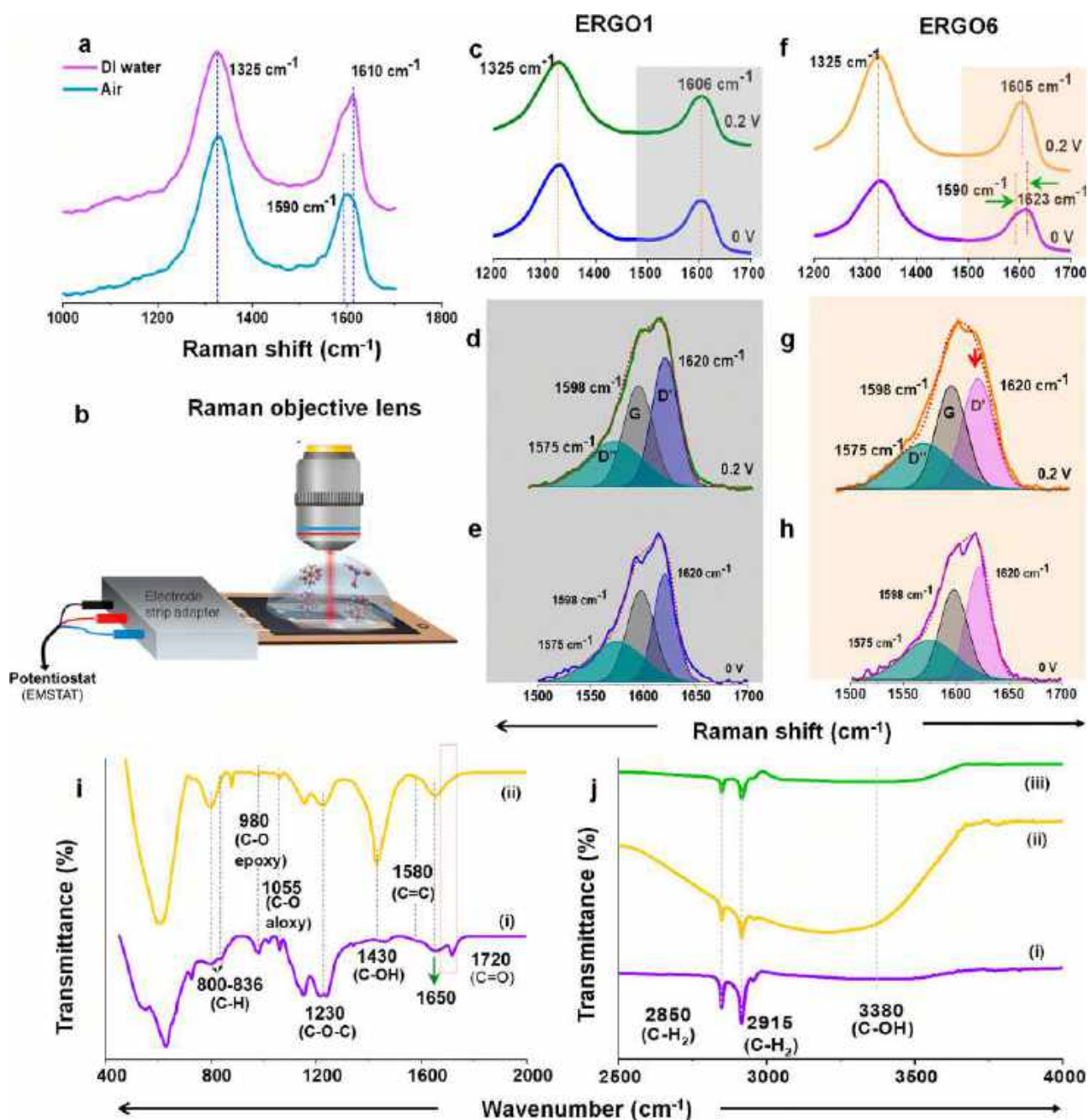


**Figure 4.** (a) Raman spectra of ERGO6 without (air) and with DI water. (b) Schematic depicts spectro-electrochemical (SPEC) measurement setup. During SPEC measurements, the Raman objective was focused at the surface of ERGO6 strips with and without As<sup>3+</sup>-containing DI water on it and a DC potential of 0.2 V was applied to the electrode. (c) Raman spectra of ERGO1 in the presence of As<sup>3+</sup> without and with the application of potential (+0.2 V). Gaussian peak fitting was performed on the G bands of Raman spectra of ERGO1 (d) with and (e) without the application of potential. (f) Raman spectra of ERGO6 in the presence of As<sup>3+</sup> without and with application of +0.2 V. Gaussian peak fitting was performed on the G bands of the Raman spectra of ERGO6 (g) with and (h) without the application of potential. Decrease in the intensity of D' is marked with a downward arrow. FTIR spectra of ERGO6 (i) without (purple trace) and with As<sup>3+</sup> (yellow trace), (j) FTIR spectra of the same strip without As<sup>3+</sup> (purple trace), with As<sup>3+</sup> (yellow trace), and after electrochemical oxidation (green trace) to show the changes in OH deformation peak at higher wavenumber.

same ERGO6 strip. We further calculated statistical average of three sets of measured current, for each concentration of As<sup>3+</sup>, and plotted them as a function of As<sup>3+</sup> concentration (Figure 3d). The limit of detection (LOD) was up to 10 ppb within a standard deviation of 5% and the experiment was highly reproducible for multiple strips. CV was performed to check As<sup>3+</sup> response of ERGO6 in field water samples (spiked with 1 ppm As<sup>3+</sup>) and the response was observed at a different

potential (+0.18 V). The corresponding voltammogram is shown in Figure S8a. Figure S8b represents a linear variation in response current with different As<sup>3+</sup> dosages spiked into the same field water and it was recognized that LOD of As<sup>3+</sup> in field water was close to 15 ppb.

**Selectivity.** The ability of ERGO6 to selectively detect As<sup>3+</sup> was evaluated by performing CA in the presence of four potentially interfering metal ions (As<sup>5+</sup>, Cu<sup>2+</sup>, Fe<sup>2+</sup>, and Mn<sup>2+</sup>),

as these are seen along with  $\text{As}^{3+}$  commonly in nature. The measurement was carried out at +0.1 V with 200 ppb of  $\text{As}^{3+}$  in PBS. Individual concentrations of these interfering ions were kept 5 times higher (1 ppm). Current response was observed only with  $\text{As}^{3+}$  (Figure 3e), confirming the high specificity of ERGO6 toward  $\text{As}^{3+}$ . Selective  $\text{As}^{3+}$  response exhibited by ERGO6 electrode was also tested by measuring CV in the presence of cations ( $\text{As}^{5+}$ ,  $\text{Fe}^{2+}$ ,  $\text{Cu}^{2+}$ ,  $\text{Mn}^{2+}$ ,  $\text{Ca}^{2+}$ ,  $\text{Na}^+$ ,  $\text{K}^+$ , and  $\text{Mg}^+$ ) and anions ( $\text{SO}_4^{2-}$ ,  $\text{NO}_3^-$ ,  $\text{Cl}^-$ , and  $\text{F}^-$ ) common in field conditions and the potential window was kept fixed between -0.4 to +0.4 V for all ions. No peak was observed in the voltammograms for either of these ions (Figure S9), establishing the electrochemical inertness of ERGO6 to the aforementioned ions within this potential window. However, the presence of  $\text{Cl}^-$  in water passivates the electrode surface, which caused the oxidation potential of  $\text{As}^{3+}$  to shift to a higher value (+0.18 V). Moreover, this  $\text{Cl}^-$  passivation reduced the response current of 1 ppm  $\text{As}^{3+}$  (from 70 to 60 nA) in field water.

**Ionic Conductivity.** Having established that ERGO6 is highly sensitive and selective to  $\text{As}^{3+}$ , we set out to explore the effect of ionic conductivity on the sensitivity. In the first set of experiments, PBS solutions of different conductivities prepared in Milli-Q water were used as electrolytes during CA measurements (Figure 3f). Three sets of CA scans were carried out for each of the PBS solutions spiked with 1 ppm of  $\text{As}^{3+}$ . It was observed that  $\text{As}^{3+}$  response was independent of ionic conductivity of the electrolyte solution (within 5% of standard deviation).

In the second set of experiments, we carried out CA measurements with field water samples having different conductivity and TDS (total dissolved solids) levels, keeping the real-world application of our electrode in mind. The amplitude of the ionic current response for all these field samples was similar (Figure S10). Arsenic response of ERGO6 strip was also tested in the field water samples by spiking these with 1 ppm  $\text{As}^{3+}$ . It was noticed that the current responses for 1 ppm  $\text{As}^{3+}$  in these different field samples were close to that in PBS. As the  $\text{As}^{3+}$  response of ERGO6 electrodes remain practically unaffected by TDS and the conductivity of the field samples, these are suitable for CA-based  $\text{As}^{3+}$  sensing.

**Spectroscopic understanding of the interaction of ERGO with  $\text{As}^{3+}$ .** *Raman measurements.* Electrochemical measurements indicated that specific interactions drive the selective binding of  $\text{As}^{3+}$  with the ERGO surface when it was exposed to  $\text{As}^{3+}$ -contaminated water in the presence of different ions. We used Raman spectroscopy to understand the  $\text{As}^{3+}$  interaction with in-plane ( $\text{sp}^2$ ) and out-of-plane ( $\text{sp}^3$ ) carbons of ERGO. Raman spectra of pristine a ERGO6 electrode (Figure 4a) in air (cyan trace) exhibited two characteristic features at 1325 (D band) and 1590  $\text{cm}^{-1}$  (G band). The origin of D and G bands is well established in the literature.<sup>38,39</sup> In brief, the D band originated from the structural imperfections due to the existence of large number of functional groups (hydroxyl and epoxides) on the basal plane of  $\text{sp}^2$  carbon, while the G band was due to first-order scattering of the  $\text{E}_{2g}$  vibrational mode of  $\text{sp}^2$ -bonded carbon atoms. The Raman intensity of the D band was slightly higher than that of the G band, resulting from the  $\text{sp}^3$ -hybridized bonds. In the presence of DI water (purple trace), the G band was shifted to a higher wavenumber (1610  $\text{cm}^{-1}$ ) due to the spectral overlap of G band of ERGO with the bending mode of H-OH (1635  $\text{cm}^{-1}$ ) of adsorbed water. To confirm this, we

performed Z-scan-dependent confocal Raman spectroscopy measurement in the presence of DI water from an ERGO6 electrode (Figure S11). At  $Z = 0$ , the Raman objective was focused on the surface of ERGO6, while at highest  $Z$  ( $Z = 400 \mu\text{m}$ ), the objective was focused at bulk DI water. When  $Z$  was increased, the signal became weak and the G band shifted to a higher wavenumber. At maximum  $Z$ , both D and G bands diminished and the bending mode of H-OH appeared at 1635  $\text{cm}^{-1}$ .

The G band of ERGO6 electrode (with and without DI water) was deconvoluted and fitted to be composed of three Gaussian peaks (Figure S12). Among these three fitted peaks, the first peak (D'') at 1572  $\text{cm}^{-1}$  corresponds to the amorphous phase of carbon.<sup>39</sup> The second peak (G), positioned at 1590  $\text{cm}^{-1}$ , is due to the in-plane vibration of  $\text{sp}^2$  carbon (C=C). The third peak (D', at 1620  $\text{cm}^{-1}$ ) is associated with structural defects or the presence of  $\text{sp}^2$  clusters/smaller sheets (as seen in the FESEM images) in the basal plane of ERGO.<sup>40,41</sup>

To probe  $\text{As}^{3+}$  binding to the electrode surface and its subsequent oxidation upon application of DC potential in situ, we designed a spectro-electrochemical (SPEC) measurement. Figure 4b represents a schematic illustration of the SPEC measurement setup. The objective lens of the Raman microscope was focused on the electrode to monitor the spectroscopic changes. Raman spectra were collected from ERGO1 and ERGO6 in the presence of  $\text{As}^{3+}$ -contaminated water for a comparative study, with and without an externally applied DC potential (oxidation potential of  $\text{As}^{3+}$ ). Application of potential did not show any spectral changes in the presence of DI water for either of these electrodes (Figure S13). Spectral changes were not observed even in the presence of  $\text{As}^{3+}$ -contaminated water for ERGO1, before and after application of potential (Figure 4c). The fitted peaks of the G band remained unchanged in their shape and intensity (Figure 4d, e). No change in current in the CA profile (red trace, Figure S14) during SPEC measurement was observed as well. These indicated that  $\text{As}^{3+}$  did not oxidize at the surface of ERGO1. On the other hand, changes in the G band could be clearly observed for ERGO6, after application of potential (Figure 4f). Analysis of deconvoluted peaks of G band showed a decrease in the intensity of D' (marked with a downward arrow) peak upon application of potential (Figure 4g, h). Some of the  $\text{sp}^2$  carbon atoms at the edges of nanosheets of ERGO6 gain partial  $\text{sp}^3$  character due to adsorption of  $\text{As}^{3+}$ . Upon application of potential, this bound  $\text{As}^{3+}$  was released into the solution as  $\text{As}^{5+}$  and the said C atoms gain their  $\text{sp}^2$  character back, resulting in a decrease in the intensity of D' peak. This was concurrent with an increase in CA current (green trace, Figure S14). ERGO6 electrode was washed with DI water and SPEC measurements were repeated with the same electrode to ensure the reproducibility.

This confirmed that active sites of the electrode surface were regenerated after electrochemical sensing measurements. Furthermore, ERGO6 electrode showed excellent stability (Figure S15), and the  $\text{As}^{3+}$  response did not deteriorate at high temperature (50 °C) and high humidity (80% RH) conditions.

We carried out further SPEC experiments to check for spectral changes at different potentials (from 0 to +0.5 V) and found that the intensity of the D' peak was reduced only at +0.2 V (Figure S16). Changes in the SPEC features of an ERGO6 electrode was also explored for a few interfering ions ( $\text{Cu}^{2+}$ ,  $\text{As}^{5+}$ ,  $\text{Fe}^{3+}$ ,  $\text{Mn}^{2+}$ ). Spectral changes were not observed



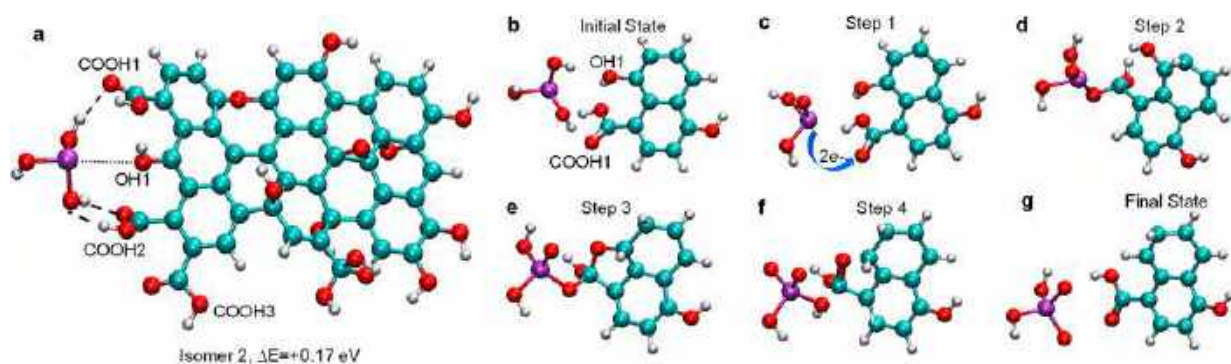


**Figure 5.** Suggested mechanism for oxidation of  $\text{As}(\text{OH})_3$  by interaction with the COOH1 and OH1 groups of ERGO. The initial configuration is shown as (a) the structure of isomer 2 and (b) a close-up view of isomer 2 at the active sites COOH1 and OH1. The steps of the mechanism are shown at the active sites in c–g, with the four steps being (c) approach of arsenite  $\text{As}(\text{OH})_3$ , its deprotonation (to the solvent) to form  $\text{H}_2\text{AsO}_3^{1-}$  and electron transfer to ERGO (step 1); (d) covalent binding (step 2) to the C(COOH1) site, which is converted from  $\text{sp}^2$  to an unsaturated  $\text{sp}^3$  bonding configuration; (e) regeneration intermediate formed by binding of O from an OH edge group to the C(COOH1) site (step 3); (f) detachment of  $\text{H}_2\text{AsO}_4^{1-}$  and reversion of  $\text{sp}^3$  to  $\text{sp}^2$  C(COOH1) as C–O is converted to C=O (step 4), with (g) replanarization and reorientation of the COOH group and the conversion of the edge COH group to CH in the final step. In the close-up views in b–g, only the atoms in the active region are shown based on a cutout cluster model of the initial configuration of isomer 2, and the viewing direction has been inverted for clarity. All structures have been optimized using the Universal Force Field. The color scheme followed for the atomic spheres is red for O, cyan for C, white for H, and purple for arsenic.<sup>51</sup>

for any of these individual interfering ions, while a response for  $\text{As}^{3+}$  could be detected even from a solution containing all (Figure S17).

**FTIR Measurements.** To identify the specific binding sites (arrangement of functional groups) of ERGO6 responsible for its exclusive attachment with  $\text{As}^{3+}$ , FTIR measurements with and without  $\text{As}^{3+}$  were carried out. Characteristic bands related to C–O (epoxy at  $950\text{ cm}^{-1}$ ), C–O (alkoxy at  $1055\text{ cm}^{-1}$ ), C–O–C (at  $1230\text{ cm}^{-1}$ ), and C–OH (at  $1430\text{ cm}^{-1}$ ) present along with carboxylic acid and carbonyl moieties on ERGO sheets (Figure 4i). The stretching vibration of C=O at  $1720\text{ cm}^{-1}$ , the C–O (epoxy) stretching vibration at  $980\text{ cm}^{-1}$ , and the C–O (alkoxy) stretching peak at  $1055\text{ cm}^{-1}$  were observed.<sup>42,43</sup> A shoulder peak was noticed at  $1580\text{ cm}^{-1}$ , associated with the asymmetric stretching of  $\text{sp}^2$  hybridized C=C.<sup>44</sup> The out-of-plane OH bending frequency occurred at  $\sim 600\text{ cm}^{-1}$ , while an O–H deformation peak was seen at  $\sim 1430\text{ cm}^{-1}$ . The vibrational features at  $2850$  and  $2915\text{ cm}^{-1}$  are due to the asymmetric and symmetric  $\text{CH}_2$  stretching of ERGO, respectively (Figure 4j).

Upon  $\text{As}^{3+}$  [ $\text{As}(\text{OH})_3$ ] binding, two prominent spectral changes were noticed. An increase in the intensity of O–H deformation peak and OH bending mode was observed. Second, the stretching frequency of C=O at  $1720\text{ cm}^{-1}$  diminished selectively (Figure 4i). Enhancement in the intensity of OH stretching frequency of ERGO6 at  $\sim 3380\text{ cm}^{-1}$  was also evident upon  $\text{As}^{3+}$  exposure and reverted back upon application of potential (Figure 4j). To ascertain that the  $\text{As}^{3+}$  ions were chemically bound onto the ERGO surface, we collected IR spectra from an ERGO6 electrode in steps: (i) pristine electrode, (ii) treatment with  $\text{As}^{3+}$  solution and drying, (iii) thorough washing with DI water and drying, and (iv) after electrochemical CA measurement at  $0.2\text{ V}$  (Figure S18a). Disappearance of the peak at  $1720\text{ cm}^{-1}$  upon exposure points to interaction of the  $\text{As}^{3+}$  species to the COOH group and conversion of C=O bond into a single bond. This was explored through DFT calculation (discussed later). Vigorous washing of the strip with DI water did not bring peak at  $1720\text{ cm}^{-1}$  back, confirming  $\text{As}^{3+}$  ions were chemically bound to the surface of ERGO. Electrochemical oxidation at  $+0.2\text{ V}$ , do,

however, brought the peak at  $1720\text{ cm}^{-1}$  back and the IR spectrum resembles that of pristine ERGO6. The electrode was regenerated at this step as oxidized species ( $\text{HASO}_4^{1-}$ ) was released into the solution. Disappearance of the C=O peak was not observed upon interaction of other interfering ions with the ERGO6 electrode (mixture of  $\text{As}^{5+}$ ,  $\text{Cu}^{2+}$ ,  $\text{Fe}^{2+}$ ,  $\text{Mn}^{2+}$ ). In the presence of  $\text{As}^{3+}$  along with the interfering ions, C=O peak disappeared while the signal corresponding to C–OH became prominent (Figure S18b). However, ERGO1 did not exhibit similar spectral changes upon exposure to  $\text{As}^{3+}$  (Figure S18c).

**Understanding of Molecular Interactions between  $\text{As}^{3+}$  and ERGO from DFT Calculations.** Binding of  $\text{As}^{3+}$  and other analyte species in the proximity of the ERGO electrode along with the oxidation mechanism of  $\text{As}^{3+}$  was investigated by density-functional theory (DFT) calculations. Details of our computational methodology can be found in Figures S21–S23. We first studied the binding of neutral  $\text{As}(\text{OH})_3$  species as this was indicated by the Pourbaix diagram to be the prevalent species, at  $\text{pH} \sim 7$ . Similar binding configurations for other arsenite species such the negative ion  $\text{H}_2\text{AsO}_3^-$  are expected, as their structures are very similar. In addition to isotropic noncovalent interactions such as van der Waals binding and Coulombic interactions, directional noncovalent interactions such as hydrogen bonding and weak  $\text{As}^+-\text{OH}^-$  interactions were primarily responsible for the binding and orientation of the arsenite molecule to the epoxide, COOH, and OH groups of ERGO. We obtained six lowest-energy isomers, isomers 1 to 6, for the arsenite-ERGO adduct from our DFT geometry optimizations, where binding occurs at different sites of ERGO and these geometries can be visualized in Figure S22. The details of the binding site, number and type of bonding interaction, and bonding distances, as well as their total and relative energies with respect to the lowest energy isomer 1, are provided in Table S4. We found that the most stable isomer 1 was at the surface position with  $\text{As}(\text{OH})_3$  making two hydrogen bonds, one to an epoxide group (EP1) O atom and the other to an O atom of a surface OH group (OH2), marked with dashed lines. A third, but weaker interaction occurs between the electropositive As

atom and an O atom of another surface OH group of ERGO (dotted line). The bond lengths of the hydrogen bonds were 1.91 Å with the hydroxyl group (OH2), 1.88 Å with the epoxide group (EP1), and that of the  $\text{As}^+-\text{OH}^-$  (OH4) interaction at 2.55 Å. In addition, the delocalized  $\pi$ -electron system of graphenic areas of the ERGO surface strongly interact through an electrostatic attraction with the partially positive As atom, increasing the binding strength at the surface position. Our lowest-energy isomer binding site at the surface agrees with the study of Reynosa-Martinez et al.,<sup>45</sup> in which the graphenic-surface site binding energy was found to be the lowest, followed by edge or surface hydroxyl and epoxide groups, although COOH groups were not considered in their models.

The next-lowest-energy isomer has  $\text{As}(\text{OH})_3$  near an OH group (OH1) sandwiched between two neighboring COOH groups, COOH1 and COOH2, in an edge position (Figure 5a and Figure S22b). The relative energy to the lowest isomer is 0.17 eV and binding occurs via three hydrogen bonds to the COOH1 and COOH2 groups (dashed lines) and an  $\text{As}^+-\text{OH}^-$  interaction with the OH1 (dotted line), with bond lengths shown in Table S4. Isomer 3, with relative energy of 0.21 eV, the  $\text{As}(\text{OH})_3$  is bonded by two hydrogen bonds to the COOH1 group. Isomers 4 and 5, possess higher relative-energy (0.4–0.5 eV) and involve only one hydrogen bond between  $\text{As}(\text{OH})_3$  and COOH1 group, and an edge lactone (COC1) group, respectively. Lastly, isomer 6 involves only a weak  $\text{As}^+-\text{OH}^-$  interaction with an edge hydroxyl (OH7) group, without any hydrogen bonding with higher relative energy of 0.65 eV compared to isomer 1. The stability of the ERGO- $\text{As}(\text{OH})_3$  isomers in the edge position was found to increase with the number of hydrogen bonding interactions with COOH (see Table S4) and weak  $\text{As}^+-\text{OH}^-$  interactions. From our starting configurations for isomers 1 to 6, after local minimization of the potential energy surface, we found only noncovalent binding modes of arsenite are accessible in our calculations. However, direct covalent binding of arsenic to oxygen has been observed experimentally in the interaction of arsenite [ $\text{As}(\text{OH})_3$ ] with the COOH and OH functional groups present in natural organic matter (NOM) by X-ray absorption fine structure spectroscopy. Presence of  $\text{As}-\text{O}-\text{C}$  bond, forming between arsenite and the oxygen atoms in the functional groups, was seen. This binding is thought to occur via a ligand-exchange reaction involving the displacement of one of the arsenite OH ligands into the aqueous solvent by the ketone or hydroxyl group O atom, hence, the As center remains triply coordinated with O atoms.<sup>46</sup> Since the COOH and OH functional groups of NOM are also found in ERGO, it is possible that covalent binding of arsenite to the COOH group of ERGO could also occur, as shown in the structure presented in Figure S21, which we also verified to be stable using DFT. The stability of  $\text{As}-\text{O}(\text{COOH})$  bonding and its identification in NOM, which has similar functional groups to ERGO, supports the possibility of As covalently binding to a ketone O atom during the oxidation mechanism.

Our experiments also show that the arsenite oxidation mechanism involves structural changes (IR spectrum) and preferably occurs at COOH sites with some binding to OH groups. Since the binding of  $\text{As}(\text{OH})_3$  preferentially occurs at ERGO surface sites, and the second site preference is at the edge sites with COOH moieties, the question arises as to why the less energetically favorable edge sites are preferred for oxidation. Surface epoxide and hydroxyl groups are associated

with higher energy barriers which would arise in the mechanism during the covalent binding of the epoxide or hydroxyl O atom to arsenite to form and its subsequent detachment to form arsenate. Higher energy barriers are associated with the detachment of oxygen atoms from ERGO surface-bonded OH and epoxide functional groups, as these are both strongly covalently bonded to the carbon atoms and are subject to stronger noncovalent interactions with the graphenic surface of ERGO. A further energy barrier that may exist during the release of  $\text{As}^{5+}$  species into the solution from the surface of ERGO is due to the stronger electrostatic and van der Waals interactions of  $\text{As}^{5+}$  species with the surface and any steric hindrance from the stacked sheets of ERGO. On the other hand, one would expect much lower energy barriers in mechanistic pathways involving the edge sites. Our proposed mechanism involves the oxidation of arsenite by the ketone oxygen which cleaves to form the arsenate species.

We may conceive the oxidation mechanism to be occurring in four stages: (1) approach of  $\text{As}^{3+}$  to edge functional groups of ERGO, (2) covalent binding interaction of As with a ketone O atom and formation of the four-coordinated As metastable intermediate, (3) regeneration of COOH by binding of a nearby hydroxyl O atom to a COOH carbon atom, and (4) detachment of  $\text{As}^{5+}$  from ERGO and release into the solution. A possible mechanistic pathway beginning from an edge site configuration of COOH1 and OH1 of isomer 2 is depicted in the active site region (Figure 5b–5g). The conversion of  $\text{As}^{3+}$  to  $\text{As}^{5+}$  involves the binding of an additional O atom to As which originates from the electron-rich nucleophilic ketone on the edges of graphene oxide. After a  $2e^-$  electron transfer from  $\text{As}^{3+}$  in the vicinity of a COOH group, as shown in Figure 5c, highly electropositive As atom would be strongly electrostatically attracted to the electrons of the lone-pair O 2p orbitals and electron-rich double bond of the ketone O atom. This would facilitate the reorientation of the  $\text{As}^{5+}$  intermediate and the formation of an  $\text{As}-\text{O}$  (ketone) covalent bond to form the four-coordinated As center as shown in step 2 in Figure 5d. In step 3, the carbon atom of the COOH group would be converted to  $\text{sp}^3$  and a neighboring hydroxyl oxygen would bind as a  $\text{C}(\text{COOH})-\text{O}-\text{C}(\text{OH})$  bridge, as seen in Figure 5e. In step 4, the  $\text{H}_2\text{AsO}_4$  structural unit would detach with the former ketone O atom, and would be released into the solution as  $\text{H}_2\text{AsO}_4^-$ , leaving the COOH group intact and with the loss of an O atom from an edge hydroxyl group from ERGO (Figure 5f, g). The mechanism described is consistent with the changes observed in the IR spectra at the COOH and OH functional groups and the overall reaction is a transfer of an O atom from ERGO to  $\text{As}^{3+}$  to form  $\text{As}^{5+}$ , and a transfer of  $2e^-$  from  $\text{As}^{3+}$  to ERGO. The same mechanism with the entire GO sheet is presented in Figure S28. In the case of the structure shown in Figure S23, where  $\text{As}(\text{OH})_3$  is initially covalently bonded to a COOH or OH group, a similar mechanism may also occur but it would begin at step 2 (Figure 5c).

The mechanism proposed depends on the proximity of the COOH and OH group, and several studies indicate that there is a tendency for clustering of functional groups, or oxygen atoms, in rGO or ERGO which supports the mechanism.<sup>47</sup> In the case that the COOH group is more isolated, a slightly more distant OH group may migrate by diffusive site-to-site hopping along either from the edges or surface of ERGO, by a thermal and potential-driven process,<sup>48,49</sup> to regenerate the COOH group in the final step of the mechanism.<sup>50</sup> In the absence of nearby COOH and OH groups, the regeneration of COOH



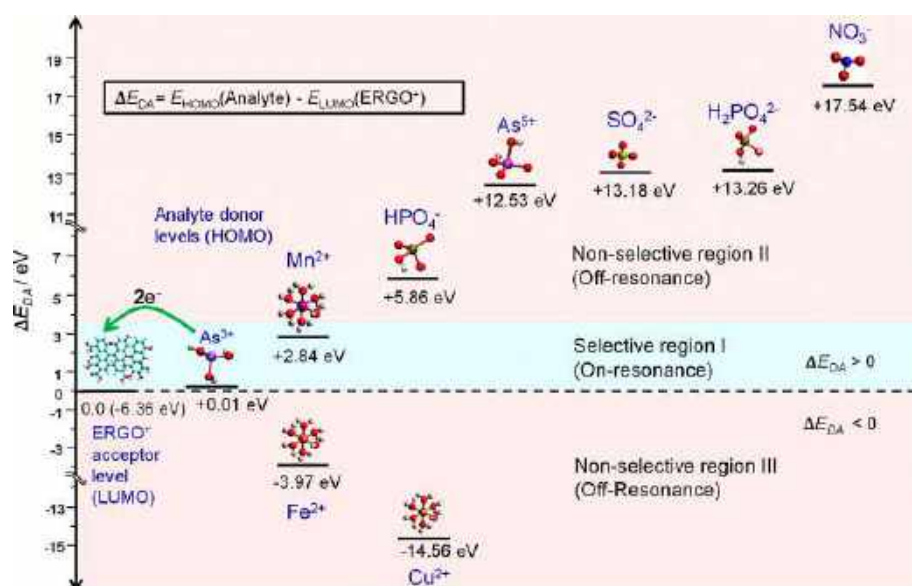


**Figure 6.** Donor–acceptor energy-level difference diagram for the ERGO LUMO acceptor level and the analyte ions' HOMO donor levels computed using DFT. The value of the donor–acceptor energy-level difference,  $\Delta E_{DA} = E_{\text{HOMO}}(\text{Analyte}) - E_{\text{LUMO}}(\text{ERGO}^+)$  is shown below the energy level for each ion. Lower positive values of  $\Delta E_{DA}$  indicate higher selectivity, hence, the unique sensitivity and selectivity toward  $\text{As}^{3+}$  with  $\Delta E_{DA} = 0.01$  eV. The donor analyte levels of As and Mn lie in the selectivity window of  $\Delta E_{DA}$  of 0 to 3 eV, in which resonant charge transport occurs from these analyte ions to ERGO, and is shown by the central blue-shaded region. The other analyte anions and cation donor levels lie in the nonselective region (red-shaded background) having larger and negative values of  $\Delta E_{DA}$ , respectively. The color scheme followed for the atomic spheres is red for O, cyan for C, white for H, purple for As, magenta for Mn, orange for Fe, gold for Cu, brown for P, yellow for S, and blue for N.

group may not be possible and the bound  $\text{As}^{3+}$  species may detach from the O atom of the COOH group and recover its original structural and electronic configuration in the solution in order to stabilize the COOH group.

The binding of other analyte species to ERGO, COOH groups of isomer 2 was tested and several analytes ( $\text{Fe}^{2+}$ ,  $\text{Cu}^{2+}$ ,  $\text{Mn}^{2+}$ ,  $\text{As}^{5+}$ ,  $\text{SO}_4^{2-}$ ,  $\text{HPO}_4^{2-}$ ,  $\text{H}_2\text{PO}_4^{2-}$ ,  $\text{NO}_3^-$ , etc.) were found to be able to bind as strongly as arsenite using hydrogen bonding (see optimized structures in Figures S24 to S27 and binding energies in Table S5). Hence, the ion selectivity cannot be explained based on differences in the binding energies of different analytes to ERGO. The compact  $\text{XY}_3$  pyramidal shape and three-coordinated As center of arsenite make it sterically more feasible, compared to the other ions, which have higher coordination numbers of four or more (apart from nitrate), to engage in inner-sphere bonding with O atoms of COOH groups. We probed the ion-selectivity mechanism occurring via electron transfer from analyte ions to ERGO, by conducting an energy-level analysis of ERGO and analyte ions based on DFT calculations of the frontier-orbital energies. The details of our method are given in section S22. According to electron-transfer theory, electron transfer occurs from the HOMO of the donor analyte molecule, when it is above the LUMO of the acceptor,  $\text{ERGO}^+$ . However, in biomolecules such as proteins and enzymes, such as the biomimicking arsenic oxidase (AiO) enzyme, electron transfer generally occurs over longer ranges, and may be attributed to a tunneling electron transfer process, which is equivalently known as “on-resonance” charge transfer.<sup>52</sup> Similar resonant charge-transfer processes are also found to occur in molecular junctions when the electrode and frontier orbitals are aligned.<sup>53</sup>

Similarly, in the initial steps of the mechanism, the ERGO electrode would be involved in noncovalent binding interactions with the analyte, and hence a similar tunneling

electron transport process may be expected to occur from the solvated analyte species, when they are within a range of  $\sim 0.5$  nm, or weakly bound to the ERGO electrode, which leads to the binding of the analyte in an intermediate step.

Subsequently, as already described in our suggested mechanism, inner-sphere structural changes involving the oxidation of the molecular analyte and the further reduction of the ERGO may occur.

In resonant charge transfer processes, the alignment and proximity of the donor and acceptor levels is the main criterion for charge transfer to occur by tunneling, and the degree of alignment is given by energy difference, between the donor level and the acceptor level,  $\Delta E_{DA} = E_{\text{HOMO}}(\text{Analyte}) - E_{\text{LUMO}}(\text{ERGO}^+)$ . For close energy levels, termed “on-resonance”, corresponding to smaller values of  $\Delta E_{DA}$ , resonant tunneling will lead to enhanced electron transport kinetics. The energy-level diagram of relative positions of donor levels of the analyte ions and acceptor level  $\text{ERGO}^+$  model is shown in Figure 6 and the values are tabulated in Table S7. The values of  $\Delta E_{DA}$  computed using DFT, show that the  $\text{As}^{3+}$  ( $\Delta E_{DA} = 0.01$  eV) and  $\text{Mn}^{2+}$  ( $\Delta E_{DA} = 2.84$  eV) ions are found to lie closer and just above the acceptor level of ERGO compared with all the other cations and ions. This suggests that ion-selectivity mechanism is mediated by the occurrence resonant charge-transport which leads to the electron transfer which initiates the oxidation mechanism, when donor and acceptor levels are close in energy with a small  $\Delta E_{DA}$ , or “on-resonance”. We may define an ion-selectivity window based on the observed correspondence between selectivity indicate by the calculations and experimental results, as the energy region,  $0 < \Delta E_{DA} < 3$  eV, indicated by the central blue shaded band in Figure 6 encloses the levels of  $\text{As}^{3+}$  and  $\text{Mn}^{2+}$ .<sup>54</sup> It is seen in Figure 6 that donor HOMO energy levels of all the other analyte ions, which are not found to be selective in experiment, also lie outside the selectivity window in the nonselective

region indicated by red shading in Figure 6, corresponding to  $\Delta E_{\text{DA}}$  either less than zero or above 3 eV. This nonselective region where HOMO levels of the analyte ions are further away in energy from the LUMO of ERGO<sup>+</sup> and are “off-resonance” so that resonant charge transport does not occur. Remarkably, out of all the analyte species considered, the HOMO donor level of arsenite, As(OH)<sub>3</sub>, is found to be the closest and slightly above ( $\Delta E_{\text{DA}} = +0.01$  eV) to the LUMO acceptor level of ERGO<sup>+</sup> for all the different types of ERGO<sup>+</sup> models (rectangular sheet model 1, model 2, and hexagonal flake model 3), which explains the unique selectivity and high sensitivity of the sensor toward As<sup>3+</sup>. The next closest donor level is Mn at  $\Delta E_{\text{DA}} = 2.84$  eV, which is also detectable but at different potential (0.35 V), which leads to “on-resonance” electron transfer for both As<sup>3+</sup> and Mn<sup>2+</sup> ions, at their respective electrode potentials. Furthermore, it is seen that the HOMO levels of the Fe<sup>2+</sup> and Cu<sup>2+</sup> lie further below the LUMO of ERGO6<sup>+</sup> with  $\Delta E_{\text{DA}} = -3.57$  eV and  $-14.6$  eV, respectively, and are off-resonance and also energetically unfavorable as  $\Delta E_{\text{DA}} < 0$ . Finally, for the anionic species, although their donor levels lie above the ERGO<sup>+</sup> acceptor level satisfying the energetic-favorability condition ( $\Delta E_{\text{DA}} > 0$ ), their HOMO donor levels are in the higher-energy range, i.e., “off-resonance” with  $\Delta E_{\text{DA}} > 5$  eV) and most lie above  $\Delta E_{\text{DA}}$  value of 12 eV, so resonant charge transfer does not occur. Furthermore, it is also found that when the neutral ERGO models are used, their LUMO levels are much higher at 3.71–3.51 eV and further away from the arsenite HOMO level (see Table S6), hence, the positive surface charge density of ERGO6 is also a necessary factor in the selectivity and electron transfer mechanism. Thus, the high selectivity and sensitivity to As<sup>3+</sup>, and also to Mn<sup>2+</sup> at a different potential, and also the nonselectivity to Fe<sup>2+</sup>, Cu<sup>2+</sup>, HPO<sub>4</sub><sup>-</sup>, As<sup>5+</sup>, H<sub>2</sub>PO<sub>4</sub><sup>2-</sup>, SO<sub>4</sub><sup>2-</sup>, and NO<sub>3</sub><sup>-</sup>, is attributed to a resonant charge transfer effect similar to that found in molecular junctions and bionanoelectronic systems.

## CONCLUSION

Electrochemically reduced graphene oxide (ERGO) with modified electronic properties and functionalities prepared through controlled electro-reduction of its functional groups exhibits highly sensitive and selective As<sup>3+</sup> sensing in water samples down to 10 ppb. The chronoamperometric response of ERGO with As<sup>3+</sup> was independent of the ionic conductivity of the electrolyte. The biomimicking activity of the electrode was manifested through several analytical and spectroscopy measurements. Spectroelectrochemical measurements confirmed that sensing mechanism of As<sup>3+</sup> involved two processes: selective adsorption of As<sup>3+</sup> by the acid functional groups of ERGO and the subsequent electro-oxidation of As<sup>3+</sup> ion on the surface of ERGO upon application of a potential. The compact pyramidal shape of As<sup>3+</sup> and the possibility of forming a four-coordinated As<sup>5+</sup> species make it a more suitable candidate among various analytes to undergo oxidation with concomitant structural changes at an ERGO COOH functional group. DFT calculations showed that noncovalent directional hydrogen bonding and weaker As<sup>3+</sup>–O<sup>-</sup> interactions are involved in the initial mechanistic steps of binding of As<sup>3+</sup> ions to ERGO, prior to electron transfer and binding to the ketone O atom of the COOH group. Subsequently, As<sup>5+</sup> species are formed, which are released into the solution with regeneration of the COOH group, by the addition of oxygen atoms from the neighboring OH functional groups. The origin of unique selectivity and

sensitivity of the sensor toward As<sup>3+</sup> was understood by an energy-level correlation analysis of the analyte species and models of ERGO. The computed energy-level diagram showed an almost perfect matching of the donor HOMO level of As<sup>3+</sup> and the LUMO acceptor level of the positively charged ERGO model, which is not the case for any of the other analyte ions considered. Based on this, a resonant charge-transfer mechanism is proposed to explain the selectivity, similar to that found in electronic transport in bionanoelectronic systems and molecular junctions. Thus, the surface of ERGO exhibits enzyme-like selective sensing mechanism for As<sup>3+</sup>, similar to the arsenite oxidase enzyme. Hence, this electrode can be a potential candidate for arsenic sensing with excellent selectivity and sensitivity.

## ASSOCIATED CONTENT

### Supporting Information

The Supporting Information is available free of charge at <https://pubs.acs.org/doi/10.1021/acsnm.2c02860>.

Details of characterizations including FESEM-EDX analysis, XPS, EIS fitting parameters, and calculation of dielectric constant, As<sup>3+</sup> concentration-dependent response of ERGO6 and selectivity study, As<sup>3+</sup> in field water, spectroelectrochemistry analysis with and without As<sup>3+</sup> for both ERGO1 and ERGO6, ion chromatography analysis, FTIR analysis of ERGO1 and ERGO6, coordinates of ERGO models and ERGO-analyte adduct structures, and the structures involved in the steps of the oxidation mechanism (PDF)

## AUTHOR INFORMATION

### Corresponding Author

Thalappil Pradeep – HSB 148, Unit of Nanoscience, Department of Chemistry, Indian Institute of Technology Madras, Chennai 600036, India; [orcid.org/0000-0003-3174-534X](https://orcid.org/0000-0003-3174-534X); Email: [pradeep@iitm.ac.in](mailto:pradeep@iitm.ac.in)

### Authors

Sourav Kanti Jana – HSB 148, Unit of Nanoscience, Department of Chemistry, Indian Institute of Technology Madras, Chennai 600036, India; [orcid.org/0000-0001-5772-7022](https://orcid.org/0000-0001-5772-7022)

Kamalesh Chaudhari – HSB 148, Unit of Nanoscience, Department of Chemistry, Indian Institute of Technology Madras, Chennai 600036, India; International Centre for Clean Water, Chennai, Tamil Nadu 600113, India

Md Rabiul Islam – HSB 148, Unit of Nanoscience, Department of Chemistry, Indian Institute of Technology Madras, Chennai 600036, India

Ganapati Natarajan – International Centre for Clean Water, Chennai, Tamil Nadu 600113, India

Tripti Ahuja – HSB 148, Unit of Nanoscience, Department of Chemistry, Indian Institute of Technology Madras, Chennai 600036, India

Anirban Som – HSB 148, Unit of Nanoscience, Department of Chemistry, Indian Institute of Technology Madras, Chennai 600036, India; [orcid.org/0000-0002-6646-679X](https://orcid.org/0000-0002-6646-679X)

Ganesan Paramasivam – HSB 148, Unit of Nanoscience, Department of Chemistry, Indian Institute of Technology Madras, Chennai 600036, India

Addanki Raghavendra – National Institute of Technology Calicut, Kattangal, Kerala 673601, India; International

Centre for Clean Water, Chennai, Tamil Nadu 600113, India

Chennu Sudhakar – HSB 148, Unit of Nanoscience, Department of Chemistry, Indian Institute of Technology Madras, Chennai 600036, India

Complete contact information is available at: <https://pubs.acs.org/10.1021/acsnm.2c02860>

### Author Contributions

<sup>†</sup>S.K.J. and K.C. contributed equally to this work. S.K.J. planned and designed the whole project. He fabricated the electrodes and performed characterization and optimization of those. K.C. helped during sensing measurements and analyzed the sensing data. R.I. prepared GO samples and helped to carry out IR measurements. G.N. designed and supervised the computational study and carried out the calculations. A.S. helped in editing the manuscript. P.G. performed all-electron DFT optimizations of the arsenite-ERGO adducts. A.R. created additional sheet and hexagonal flake models of ERGO, carried out force-field calculations of the oxidation mechanism, and contributed to the production of figures. T.A. and C.S. helped to carry out Raman and XPS measurements, respectively. T.P. supervised the whole project.

### Notes

The authors declare no competing financial interest.

### ACKNOWLEDGMENTS

All authors are thankful to E. Sundarraj for FESEM measurements. We acknowledge the use of computing resources at HPCE, IIT Madras. R.I. thanks CSIR, Government of India, for a research fellowship. G.P. thanks IIT Madras for an Institute Post-Doctoral Fellowship. The authors thank A. Chakraborty and A. R. Kini for help in making the figures. T.A. and S.C. thank IIT Madras for their fellowships. A.R. thanks the International Centre for Clean Water for an internship. T.P. thanks the Department of Science and Technology, Government of India, for research funding.

### ABBREVIATIONS

GO, graphene oxide; ERGO, electrochemically reduced graphene oxide; CV, cyclic voltammetry; CA, chronoamperometry; DFT, density functional theory

### REFERENCES

- (1) Nagar, A.; Pradeep, T. Clean Water through Nanotechnology: Needs, Gaps, and Fulfillment. *ACS Nano* **2020**, *14* (6), 6420–6435.
- (2) Sabir, F.; Zeeshan, M.; Laraib, U.; Barani, M.; Rahdar, A.; Cucchiari, M.; Pandey, S. DNA Based and Stimuli-Responsive Smart Nanocarrier for Diagnosis and Treatment of Cancer: Applications and Challenges. *Cancers* **2021**, *13* (14), 3396.
- (3) Barani, M.; Mukhtar, M.; Rahdar, A.; Sargazi, S.; Pandey, S.; Kang, M. Recent Advances in Nanotechnology-Based Diagnosis and Treatments of Human Osteosarcoma. *Biosensors* **2021**, *11* (2), 55.
- (4) Sargazi, S.; Mukhtar, M.; Rahdar, A.; Bilal, M.; Barani, M.; Diez-Pascual, A. M.; Behzadmehr, R.; Pandey, S. Opportunities and Challenges of Using High-Sensitivity Nanobiosensors to Detect Long Noncoding RNAs: A Preliminary Review. *Int. J. Biol. Macromol.* **2022**, *205*, 304–315.
- (5) Wei, H.; Wang, E. Nanomaterials with Enzyme-like Characteristics (Nanozymes): Next-Generation Artificial Enzymes. *Chem. Soc. Rev.* **2013**, *42* (14), 6060–6093.
- (6) Lee, J. H.; Jin, H.-E.; Desai, M. S.; Ren, S.; Kim, S.; Lee, S.-W. Biomimetic Sensor Design. *Nanoscale* **2015**, *7* (44), 18379–18391.

- (7) Breslow, R. Biomimetic Chemistry and Artificial Enzymes: Catalysis by Design. *Acc. Chem. Res.* **1995**, *28* (3), 146–153.
- (8) Heller, A.; Feldman, B. Electrochemical Glucose Sensors and Their Applications in Diabetes Management. *Chem. Rev.* **2008**, *108* (7), 2482–2505.
- (9) Male, K. B.; Hrapovic, S.; Santini, J. M.; Luong, J. H. T. Biosensor for Arsenite Using Arsenite Oxidase and Multiwalled Carbon Nanotube Modified Electrodes. *Anal. Chem.* **2007**, *79* (20), 7831–7837.
- (10) Podgorski, J.; Berg, M. Global Threat of Arsenic in Groundwater. *Science* **2020**, *368* (6493), 845–850.
- (11) Conrads, T.; Hemann, C.; George, G. N.; Pickering, I. J.; Prince, R. C.; Hille, R. The Active Site of Arsenite Oxidase from *Alcaligenes Faecalis*. *J. Am. Chem. Soc.* **2002**, *124* (38), 11276–11277.
- (12) Masscheleyn, P. H.; Delaune, R. D.; Patrick, W. H. Effect of Redox Potential and PH on Arsenic Speciation and Solubility in a Contaminated Soil. *Environ. Sci. Technol.* **1991**, *25* (8), 1414–1419.
- (13) Ellis, P. J.; Conrads, T.; Hille, R.; Kuhn, P. Crystal Structure of the 100 KDa Arsenite Oxidase from *Alcaligenes Faecalis* in Two Crystal Forms at 1.64 Å and 2.03 Å. *Structure* **2001**, *9* (2), 125–132.
- (14) Duval, S.; Santini, J. M.; Nitschke, W.; Hille, R.; Schoepp-Cothenet, B. The Small Subunit AroB of Arsenite Oxidase: LESSONS ON THE [2Fe-2S] RIESKE PROTEIN SUPERFAMILY. *J. Biol. Chem.* **2010**, *285* (27), 20442–20451.
- (15) Teoh, W. K.; Salleh, F. M.; Shahir, S. Characterization of *Thiomonas Delicata* Arsenite Oxidase Expressed in *Escherichia Coli*. *3 Biotech* **2017**, *7* (2), 97.
- (16) Karakoti, A.; Singh, S.; Dowding, J. M.; Seal, S.; Self, W. T. Redox-Active Radical Scavenging Nanomaterials. *Chem. Soc. Rev.* **2010**, *39* (11), 4422–4432.
- (17) Xie, J.; Zhang, X.; Wang, H.; Zheng, H.; Huang, Y.; Xie, J. Analytical and Environmental Applications of Nanoparticles as Enzyme Mimetics. *TrAC Trends Anal. Chem.* **2012**, *39*, 114–129.
- (18) Celardo, I.; Pedersen, J. Z.; Traversa, E.; Ghibelli, L. Pharmacological Potential of Cerium Oxide Nanoparticles. *Nanoscale* **2011**, *3* (4), 1411–1420.
- (19) Dai, X.; Nekrassova, O.; Hyde, M. E.; Compton, R. G. Anodic Stripping Voltammetry of Arsenic(III) Using Gold Nanoparticle-Modified Electrodes. *Anal. Chem.* **2004**, *76* (19), 5924–5929.
- (20) Luong, J. H. T.; Lam, E.; Male, K. B. Recent Advances in Electrochemical Detection of Arsenic in Drinking and Ground Waters. *Anal. Methods* **2014**, *6* (16), 6157–6169.
- (21) Gupte, T.; Jana, S. K.; Mohanty, J. S.; Srikrishnarka, P.; Mukherjee, S.; Ahuja, T.; Sudhakar, C.; Thomas, T.; Pradeep, T. Highly Sensitive As<sup>3+</sup> Detection Using Electrodeposited Nanostructured MnOx and Phase Evolution of the Active Material during Sensing. *ACS Appl. Mater. Interfaces* **2019**, *11* (31), 28154–28163.
- (22) Gao, C.; Yu, X.-Y.; Xiong, S.-Q.; Liu, J.-H.; Huang, X.-J. Electrochemical Detection of Arsenic(III) Completely Free from Noble Metal: Fe<sub>3</sub>O<sub>4</sub>Microspheres-Room Temperature Ionic Liquid Composite Showing Better Performance than Gold. *Anal. Chem.* **2013**, *85* (5), 2673–2680.
- (23) Subramanian, V.; Lee, S.; Jena, S.; Jana, S. K.; Ray, D.; Kim, S. J.; Thalappil, P. Enhancing the Sensitivity of Point-of-Use Electrochemical Microfluidic Sensors by Ion Concentration Polarisation-A Case Study on Arsenic. *Chem. Sens. Actuators B* **2020**, *304* (18), 127340.
- (24) Kempahanumakkagari, S.; Deep, A.; Kim, K.-H.; Kumar Kailasa, S.; Yoon, H.-O. Nanomaterial-Based Electrochemical Sensors for Arsenic - A Review. *Biosens. Bioelectron.* **2017**, *95*, 106–116.
- (25) Wei, X.-Q.; Hao, L.-Y.; Shao, X.-R.; Zhang, Q.; Jia, X.-Q.; Zhang, Z.-R.; Lin, Y.-F.; Peng, Q. Insight into the Interaction of Graphene Oxide with Serum Proteins and the Impact of the Degree of Reduction and Concentration. *ACS Appl. Mater. Interfaces* **2015**, *7* (24), 13367–13374.
- (26) Kumar, S.; Parekh, S. H. Linking Graphene-Based Material Physicochemical Properties with Molecular Adsorption, Structure and Cell Fate. *Commun. Chem.* **2020**, *3* (1), 1–11.



- (27) Liu, M.; Zhao, H.; Chen, S.; Yu, H.; Quan, X. Interface Engineering Catalytic Graphene for Smart Colorimetric Biosensing. *ACS Nano* **2012**, *6* (4), 3142–3151.
- (28) Song, Y.; Qu, K.; Zhao, C.; Ren, J.; Qu, X. Graphene Oxide: Intrinsic Peroxidase Catalytic Activity and Its Application to Glucose Detection. *Adv. Mater.* **2010**, *22* (19), 2206–2210.
- (29) Liu, M.; Zhao, H.; Chen, S.; Yu, H.; Quan, X. Stimuli-Responsive Peroxidase Mimicking at a Smart Graphene Interface. *Chem. Commun.* **2012**, 48 (56), 7055–7057.
- (30) Bolotsky, A.; Butler, D.; Dong, C.; Gerace, K.; Glavin, N. R.; Muratore, C.; Robinson, J. A.; Ebrahimi, A. Two-Dimensional Materials in Biosensing and Healthcare: From *In Vitro* Diagnostics to Optogenetics and Beyond. *ACS Nano* **2019**, *13* (9), 9781–9810.
- (31) Islam, M. R.; Gupta, S. S.; Jana, S. K.; Srikrishnarka, P.; Mondal, B.; Chennu, S.; Aluja, T.; Chakraborty, A.; Pradeep, T. A Covalently Integrated Reduced Graphene Oxide-Ion-Exchange Resin Electrode for Efficient Capacitive Deionization. *Adv. Mater. Interfaces* **2021**, *8* (5), 2001998.
- (32) Tu, N. D. K.; Choi, J.; Park, C. R.; Kim, H. Remarkable Conversion Between N- and p-Type Reduced Graphene Oxide on Varying the Thermal Annealing Temperature. *Chem. Mater.* **2015**, *27* (21), 7362–7369.
- (33) Tan, S.; Bélanger, D. Characterization and Transport Properties of Nafion/Polyaniline Composite Membranes. *J. Phys. Chem. B* **2005**, *109* (49), 23480–23490.
- (34) Zhao, X.; Hayner, C. M.; Kung, M. C.; Kung, H. H. Flexible Holey Graphene Paper Electrodes with Enhanced Rate Capability for Energy Storage Applications. *ACS Nano* **2011**, *5* (11), 8739–8749.
- (35) Jana, S. K.; Banerjee, S.; Bayan, S.; Inta, H. R.; Mahalingam, V. Rectification and Amplification of Ionic Current in Planar Graphene/Graphene-Oxide Junctions: An Electrochemical Diode and Transistor. *J. Phys. Chem. C* **2018**, *122* (21), 11378–11384.
- (36) Meng, F.; Li, J.; Cushing, S. K.; Zhi, M.; Wu, N. Solar Hydrogen Generation by Nanoscale p-n Junction of p-Type Molybdenum Disulfide/n-Type Nitrogen-Doped Reduced Graphene Oxide. *J. Am. Chem. Soc.* **2013**, *135* (28), 10286–10289.
- (37) Li, J.; Meng, F.; Suri, S.; Ding, W.; Huang, F.; Wu, N. Photoelectrochemical Performance Enhanced by a Nickel Oxide-Hematite p-n Junction Photoanode. *Chem. Commun.* **2012**, 48 (66), 8213–8215.
- (38) Ferrari, A. C.; Basko, D. M. Raman Spectroscopy as a Versatile Tool for Studying the Properties of Graphene. *Nat. Nanotechnol.* **2013**, *8* (4), 235–246.
- (39) Ferrari, A. C.; Meyer, J. C.; Scardaci, V.; Casiraghi, C.; Lazzeri, M.; Mauri, F.; Piscanec, S.; Jiang, D.; Novoselov, K. S.; Roth, S.; Geim, A. K. Raman Spectrum of Graphene and Graphene Layers. *Phys. Rev. Lett.* **2006**, *97* (18), 187401.
- (40) Lopez-Diaz, D.; Lopez Holgado, M.; Garcia-Fierro, J. L.; Velazquez, M. M. Evaluation of the Raman Spectrum with the Chemical Composition of Graphene Oxide. *J. Phys. Chem. C* **2017**, *121*, 20489–20497.
- (41) Eckmann, A.; Felten, A.; Mishchenko, A.; Britnell, L.; Krupke, R.; Novoselov, K. S.; Casiraghi, C. Probing the Nature of Defects in Graphene by Raman Spectroscopy. *Nano Lett.* **2012**, *12* (8), 3925–3930.
- (42) Zhang, J.; Yang, H.; Shen, G.; Cheng, P.; Zhang, J.; Guo, S. Reduction of Graphene Oxide Via L-Ascorbic Acid. *Chem. Commun.* **2010**, 46 (7), 1112–1114.
- (43) Acik, M.; Mattevi, C.; Gong, C.; Lee, G.; Cho, K.; Chhowalla, M.; Chabal, Y. J. The Role of Intercalated Water in Multilayered Graphene Oxide. *ACS Nano* **2010**, *4* (10), 5861–5868.
- (44) Acik, M.; Lee, G.; Mattevi, C.; Pirkle, A.; Wallace, R. M.; Chhowalla, M.; Cho, K.; Chabal, Y. The Role of Oxygen during Thermal Reduction of Graphene Oxide Studied by Infrared Absorption Spectroscopy. *J. Phys. Chem. C* **2011**, *115* (40), 19761–19781.
- (45) Reynosa-Martínez, A. C.; Tovar, G. N.; Gallegos, W. R.; Rodríguez-Meléndez, H.; Torres-Cadena, R.; Mondragón-Solórzano, G.; Barroso-Flores, J.; Alvarez-Lemus, M. A.; Montalvo, V. G.; López-Honorato, E. Effect of the Degree of Oxidation of Graphene Oxide on As(III) Adsorption. *J. Hazard. Mater.* **2020**, *384*, 121440.
- (46) Biswas, A.; Besold, J.; Sjöstedt, C.; Gustafsson, J. P.; Scheinost, A. C.; Planer-Friedrich, B. Complexation of Arsenite, Arsenate, and Monothioarsenate with Oxygen-Containing Functional Groups of Natural Organic Matter: An XAS Study. *Environ. Sci. Technol.* **2019**, *53* (18), 10723–10731.
- (47) Mouhat, F.; Coudert, F.-X.; Bocquet, M.-L. Structure and Chemistry of Graphene Oxide in Liquid Water from First Principles. *Nat. Commun.* **2020**, *11* (1), 1566.
- (48) Kumar, P. V.; Bardhan, N. M.; Chen, G.-Y.; Li, Z.; Belcher, A. M.; Grossman, J. C. New Insights into the Thermal Reduction of Graphene Oxide: Impact of Oxygen Clustering. *Carbon* **2016**, *100*, 90–98.
- (49) Boukhvalov, D. W. Modeling of Hydrogen and Hydroxyl Group Migration on Graphene. *Phys. Chem. Chem. Phys.* **2010**, *12* (47), 15367.
- (50) Novotny, Z.; Nguyen, M.-T.; Netzer, F. P.; Glezakou, V.-A.; Rousseau, R.; Dohnálek, Z. Formation of Supported Graphene Oxide: Evidence for Enolate Species. *J. Am. Chem. Soc.* **2018**, *140* (15), 5102–5109.
- (51) Rappe, A. K.; Casewit, C. J.; Colwell, K. S.; Goddard, W. A.; Skiff, W. M. UFF, a Full Periodic Table Force Field for Molecular Mechanics and Molecular Dynamics Simulations. *J. Am. Chem. Soc.* **1992**, *114* (25), 10024–10035.
- (52) Fereiro, J. A.; Yu, X.; Pecht, I.; Sheves, M.; Cuevas, J. C.; Cahen, D. Tunneling Explains Efficient Electron Transport via Protein Junctions. *Proc. Natl. Acad. Sci. U. S. A.* **2018**, *115* (20), E4577–E4583.
- (53) Shi, W.; Deng, T.; Wong, Z. M.; Wu, G.; Yang, S.-W. A Molecular Roadmap towards Organic Donor-Acceptor Complexes with High-Performance Thermoelectric Response. *Npj Comput. Mater.* **2021**, *7* (1), 1–8.
- (54) Warelou, T. P.; Pushie, M. J.; Cotelesage, J. J. H.; Santini, J. M.; George, G. N. The Active Site Structure and Catalytic Mechanism of Arsenite Oxidase. *Sci. Rep.* **2017**, *7* (1), 1757.

## Supporting information

# A Selective and Practical Graphene-based Arsenite Sensor at 10 ppb

*Sourav Kanti Jana<sup>‡</sup>, Kamalesh Chaudhari<sup>‡+</sup>, Md Rabiul Islam<sup>‡</sup>, Ganapati Natarajan<sup>+</sup>, Tripti Ahuja<sup>‡</sup>, Anirban Som, Ganesan Paramasivam<sup>‡</sup>, Addanki Raghavendra<sup>#+</sup>, Chennu Sudhakar<sup>‡</sup>, Thalappil Pradeep<sup>\*‡</sup>*

Address:

<sup>‡</sup> HSB 148, Unit of Nanoscience, Department of Chemistry, Indian Institute of Technology Madras, Chennai 600036, India.

<sup>+</sup>International Centre for Clean Water, 2nd Floor, B-Block, IIT Madras Research Park, Kanagam Road, Tharamani, Chennai, Tamil Nadu 600113, India.

<sup>#</sup>National Institute of Technology Calicut, Calicut Mukkam Road, Kattangal, Kerala, 673601, India.

\*Email: pradeep@iitm.ac.in

<sup>‡</sup> Contributed equally

### Table of contents

Sl. No.	Description	Page No.
S1	Experimental methods	3-6
S2	SEM and EDS measurements of ERGO1 and ERGO6 samples	7-8
S3	XPS analysis of GO and ERGO electrodes	9-10
S4	Results of impedance spectroscopy	11
S5	Calculation of dielectric constant of ERGO1 and ERGO6 samples from impedance spectroscopy results	12
S6	Charge carrier density of different rGO samples including our ERGO electrode	13
S7	CV of ERGO samples in presence of 1 ppm As <sup>3+</sup>	14
S8	Ion chromatography measurements and experimental results	15-16
S9	Scan rate and concentration dependent CV using ERGO6 electrode	17-18



S10	Concentration dependent chronoamperometry measurements in PBS and field sample	19
S11	Interference measurements with As <sup>3+</sup> in presence of different cations and anions	20-22
S12	Concentrations of cations and anions in synthetic field water	23
S13	Chronoamperometry measurements with different field samples	24-25
S14	Raman spectra of ERGO6 measured at different scan depths in water	26
S15	Gaussian fitting of G band of Raman spectra of ERGO6 with and without DI water	27
S16	In-situ SPEC measurements of ERGO1 and ERGO6 in DI water alone, in presence and absence of external potential	28
S17	Chronoamperometry profiles of ERGO1 and ERGO6 in presence and absence of 1000 ppm As <sup>3+</sup>	29
S18	Electrochemical stability of the electrodes	30
S19	Effect of potential on the G band of in-situ Raman spectra	31
S20	In-situ spectroelectrochemical study of ERGO6 in presence of different cations, including As <sup>3+</sup>	32
S21	FTIR spectra of ERGO6 and ERGO1 electrodes with and without As <sup>3+</sup> and after electrochemical oxidation	33
S22	Computational methodology	34-35
S23	Methodology of generation of ERGO models and binding of arsenite and analyte ions to ERGO	36-44
S24	Methodology of arsenite oxidation mechanism at COOH group of ERGO	45-47
S25	Methodology of ion-selectivity mechanism	48-50
S26	Atomic coordinates of the optimized structures	51-86
	References	87-88

## **S1. Experimental methods**

### **(i) Synthesis of GO**

GO was synthesized from graphite powder based on the modified Hummer's method (Step1 of Figure S1). Briefly, graphite powder (2 g) was oxidized in a hot solution (100°C) of concentrated H<sub>2</sub>SO<sub>4</sub> (25 mL), K<sub>2</sub>S<sub>2</sub>O<sub>8</sub> (4 g), and P<sub>2</sub>O<sub>5</sub> (4 g). The resulting dark blue mixture was allowed to cool to room temperature over a period of 6 h. The mixture was diluted to 200 mL with DI water and the solution was filtered. Finally, the filtrated product was dried overnight at 60°C in a hot air oven. As synthesized pre-oxidized graphite powder (2 g) was further added to 92 mL of cold H<sub>2</sub>SO<sub>4</sub> (0°C). KMnO<sub>4</sub> (12 g) was gradually added to the mixture under continuous stirring in ice-bath. After 15 min, NaNO<sub>3</sub> (2 g) was added to the mixture. The solution was further stirred for 2 h at 35 °C and distilled water (200 mL) was added dropwise during stirring. The reaction was stopped after simultaneous addition of a mixture of 300 mL distilled water and 10 mL of H<sub>2</sub>O<sub>2</sub> (30 %) to the solution. The final product was washed sequentially with different solvents; at first, with diluted HCl (1:10) and then with water, and at last, the product was suspended in distilled water. The brown dispersion was dialyzed extensively to remove residual metal ions and acids. Finally, the dispersion was exfoliated via ultrasonication (300 W) for 2 h and unexfoliated graphite oxide was removed by centrifugation (12000 rpm for 20 min using Centrifuge KUBOTA (Tokyo, Japan)).

### **(ii) ERGO fabrication on Au coated test strips**

At first, flexible and patterned Au strips, on which ERGO was fabricated, was pre-treated with 3 mM of sodium 2-mercaptoethanesulfonate (MESA, HSCH<sub>2</sub>CH<sub>2</sub>SO<sub>3</sub>Na). Au strips were dipped in MESA for 72 h to create self-assembled monolayer of thiols on the Au surface. The aim of thiol pre-treatment was to deposit a self-assembled monolayer (SAM) on the Au surface (Step 2 of Figure S1). Test strips were rinsed to remove excess thiols from the Au surface, and dried under N<sub>2</sub> gas. To check the electrochemical activity of thiol modified Au surface, we measured cyclic voltammetry (CV) of the test strips (with and without thiol treatment) with a

solution mixture of 1 mM potassium ferricyanide and 100 mM KCl. The resulting voltammogram is shown in Figure S1 (Step 3), where the potential difference of redox peak ( $\Delta E_p$ ) of thiol treated sample was 60-80 mV, which ensures a one electron transfer process at the interface between the SAM modified Au strip and the electrolyte. We observed  $\Delta E_p$  of about 300 mV for the untreated Au strip, and less than 100 mV after MESA treatment. Before starting ERGO fabrication process on the MESA treated Au substrate, we prepared 6.25  $\mu\text{g/ml}$  of GO suspension from 0.1 mg/ml of stock solution. A mixture with a volume ratio of 2:1 of diluted GO and 1% Nafion (Step 4), respectively was prepared. About 5  $\mu\text{L}$  of GO solution mixture was then dropcasted on the Au working electrode, followed by vacuum drying for 3 h (Step 5). Finally, electro-reduction of GO film was performed at -1.1 V with phosphate buffered saline (PBS) as the electrolyte for reduction. The electro-reduction was carried out for different time durations (1, 2, 3 and 6 h). For scaled-up preparation of electrode, we have developed a homemade set-up with PCB (printed circuit board) using multiple adapters that can produce multiple ERGO coated strips simultaneously, shown in Figure S1 (Step 6). Digital photographs of freshly prepared GO and ERGO coated Au strips are also shown in Figure S1(i). Scale bar corresponds to the actual dimension of electrodes (working, counter, and reference) which are patterned on the Au test strips. The geometrical surface area of the active working electrode (ERGO) was maintained as  $\sim 0.25 \text{ cm}^2$  for all the test strips. Morphology and chemical analysis of these electrodes were done by FESEM-EDX (Figure S1 (ii)) and XPS techniques (Figure 1 of the manuscript), respectively. We used these ERGO coated strips for further analytical measurements using cyclic voltammetry (CV), linear sweep voltammetry (LSV) and chronoamperometric (CA) techniques.

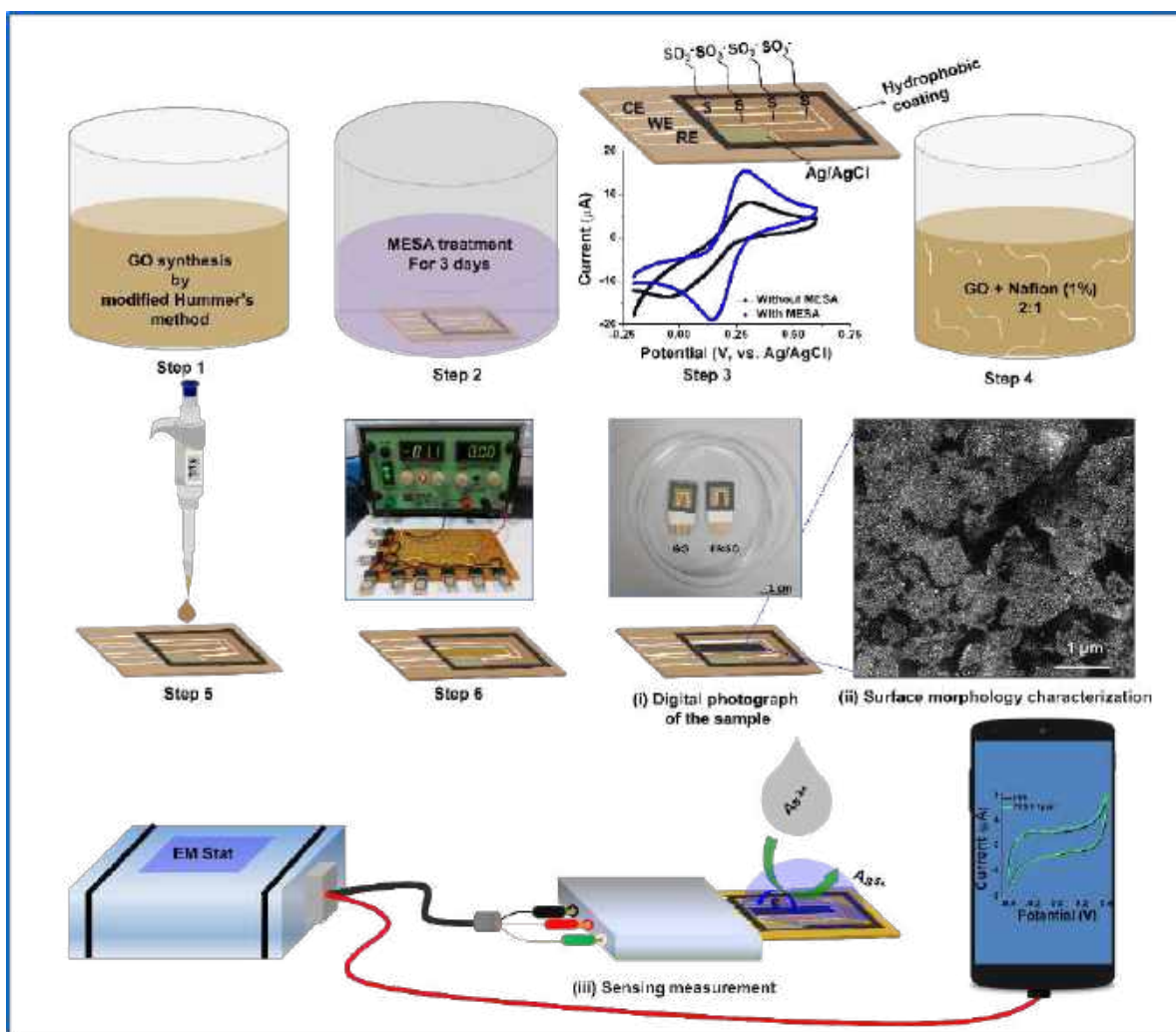


**Figure S1.** Schematic representation experimental steps involved in the fabrication of ERGO electrodes, steps involved in characterization using digital photography and microscopy, and finally, electro-analytical measurements for  $\text{As}^{3+}$  sensing. **Step 1:** Wet chemical synthesis of graphene oxide (GO) by modified Hummer's method, **Step 2:** Pre-treatment of Au strips with sodium-2 mercaptoethane sulphonate (MESA) for decoration of self-assembled monolayer, **Step 3:** Au strip decorated with monolayer of MESA (top image) and cyclic voltammogram (bottom Figure) of Au strip before and after MESA treatment, **Step 4:** Dilution of as synthesized GO solution and mixture with Nafion (1% by weight) in 2:1 (by volume) ratio. **Step 5:** Dropcasting of solution mixture (5  $\mu\text{L}$ ) on working electrode (WE) of Au strip, **Step 6:** Electro-reduction of GO coated strip (bottom image) at -1.1 V using home-built setup (top

image), **(i)** Digital photograph of the electrode strips before and after electro-reduction (top image). The electro-reduced sample was used for further characterization (bottom image), **(ii)** Scanning electron microscopy (SEM) image of the as-prepared ERGO6 sample, and **(iii)** Sensitivity of ERGO6 electrode to  $\text{As}^{3+}$  was measured through cyclic voltammetry (CV) using EMSTAT (Plamsense) and corresponding voltammogram is shown in the right side image.



## S2. SEM and EDS measurements of ERGO1 and ERGO6 samples

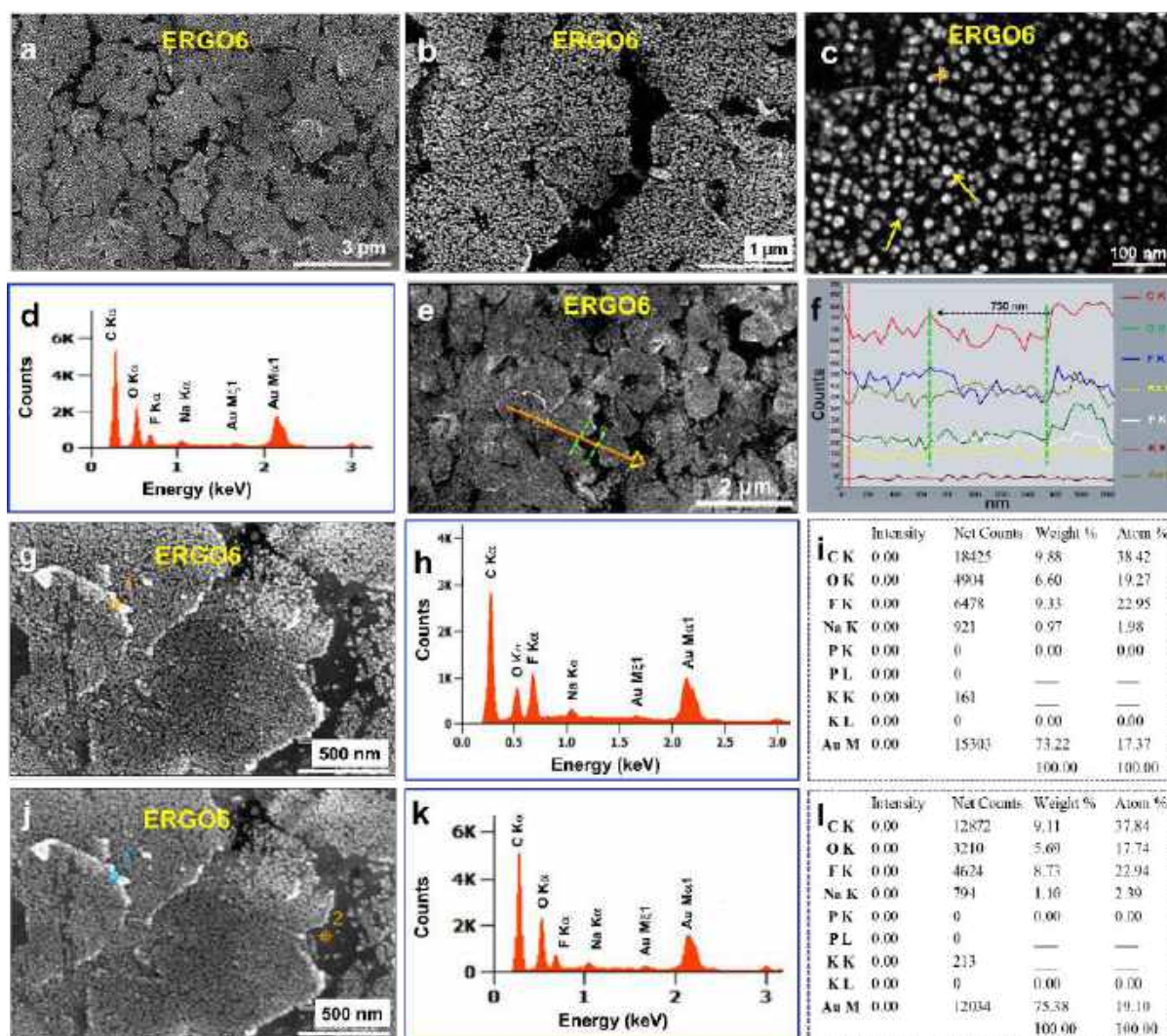


**Figure S2.** Morphological characterization and elemental analysis of as prepared ERGO electrodes. FESEM image of ERGO6 at different magnifications: (a) 3  $\mu\text{m}$ , (b) 1  $\mu\text{m}$  and (c) 100 nm. (d) EDS spectrum collected from a single nanosheets at the “+” marked point. (e) EDS line scan on the surface of ERGO6 in the direction of arrow. (f) Variation of possible elements of the electrode. Black portion on the electrode surface marked with dotted green lines indicates that there is a crack (width  $\sim 750$  nm) on the electrode surface. In this region, the overall film thickness is less compared to other regions. In the deep region, the intensity of both carbon (C) and fluorine (F) is reduced, however, intensities of other elements is the same. (g) Point EDS spectrum was taken at the region marked as ‘1’, (h) EDS spectrum at ‘1’, (i) atomic percentage

of all the elements from (h). (j) Point EDS spectrum was taken at the region marked as '2', (k) EDS spectrum at '2' and (l) atomic percentage of all the elements from (k).

FESEM images of ERGO6 at different magnifications are shown in Figure S2a-c. Figure S2d represents the EDS analysis of small nanosheets of ERGO6. The EDS spectrum was collected at the marked point (+) of Figure S2c. There are several microcracks present on the surface of ERGO6, and chemical composition of the film is uniform throughout the surface, as confirmed by elemental mapping through EDS line scan across the crack (Figure S2e-f). In the EDS line scan spectrum (Figure S2e), all major elements (C, O, and F) of ERGO6 were noted. However, a dip was observed in both carbon and fluorine (F) line profiles, which clearly indicated that cracks were formed within a few layers of ERGO6. Same EDX line profiles indicated that there might be a continuous ERGO film beneath the microcracks. Therefore, surface of ERGO6 was uneven as the edges of the smaller particles were exposed and the edges of the ERGO particles are marked with arrows as seen in an FESEM image (Figure S2c). Moreover, point EDX scan was performed on both nanoparticles-assembled sheet (marked on Figure S2g) and a microcracked portion of the sheet (marked on Figure S2j). The corresponding elemental analyses are shown in Figure S2h-i and Figure S2k-l, respectively. These results also confirm that both the electrodes are formed by stacking a few layers of thin ERGO sheets. However, the top layer of ERGO6 constitutes a large number of planar sheets, which are assembled from smaller nanosheets.

### S3. XPS analysis of GO and ERGO electrodes

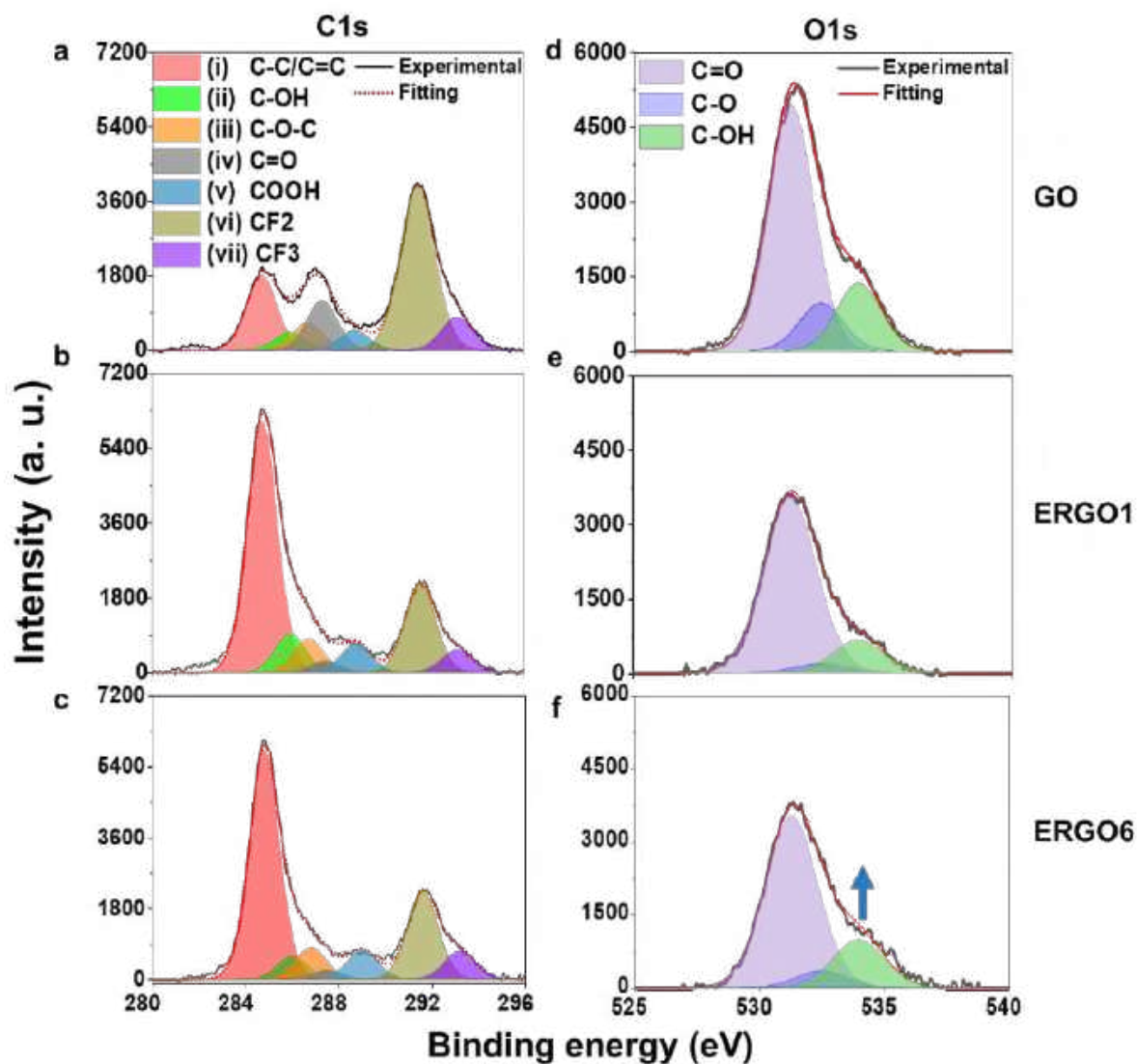


**Figure S3.** XPS C1s (a-c) and O1s spectra (d-f) for GO, ERGO1 and ERGO6, respectively.

The blue arrow in (f) indicates an increase of C-OH intensity, which could be attributed to the oxidation at the edges of small ERGO nanosheets.

**Table S1.** Binding energies of both C1s and O1s for GO/ERGO electrodes

<b>Binding energies of C1s (eV)</b>	<b>Binding energies of O1s (eV)</b>
284.7 (C-C/C=C)	531.2 (O-C=O)
286 (C-OH)	532.4 (C=O)
286.8 (C-O-C)	533.9 (C-O)
287.5 (C=O)	
289.1 (COOH)	
292.6 (CF2)	
293.2 (CF3)	

The deconvoluted C1s are assigned as (i), (ii), (iii), (iv), (iv), (v), (vi), and (vii) in Figure S3a and their corresponding binding energies at 284.7, 286.0, 286.8, 287.5, 289.1, 292.6, and 293.2 eV are due to several functional groups on the basal plane of GO and ERGO samples. Peak (i) is responsible for carbon to carbon bonds in both  $sp^2$  (C=C) and  $sp^3$  (C-C) configurations, while (ii) and (iii) are assigned to C-O bond of hydroxyl (C-OH) and epoxide (C-O-C) functional groups, respectively. The peaks (iv) and (v) can be attributed to C=O bond of ester groups and carboxylic acid groups. The two peaks ((vi) and (vii)) of the spectra correspond to di-, and tri-fluorocarbon (CF<sub>2</sub> and CF<sub>3</sub>) which are the main functional groups of Nafion binder used in electrode fabrication. Electrochemical reduction of GO minimizes the oxygen functional groups in the ERGO samples, resulting in the decrease of photo-emitted electron intensity associated with C-O bonds. Each O1s spectrum is decomposed into three peaks corresponding to O-C=O (~531.2 eV), C=O (532.4 eV), and C-O (533.9 eV) functional groups.

#### S4. Calculation of dielectric constant of ERGO1 and ERGO6 samples from impedance spectroscopy results

The dielectric constant of both ERGO1 and ERGO6 can be expressed as,<sup>1</sup>

$$\epsilon = \epsilon' - \epsilon''$$

Where,  $\epsilon' = \frac{Z'' \cdot l}{2\pi f \epsilon_0 A Z^2}$  and  $\epsilon'' = \frac{Z' \cdot l}{2\pi f \epsilon_0 A Z^2}$

The above equation can be simplified as,  $\epsilon = \frac{l}{2\pi \epsilon_0 A} \left[ \frac{Z'' - Z'}{Z^2 \cdot f} \right]$

Here,  $Z'$  and  $Z''$  are the real and imaginary parts of total impedance ( $Z$ ) of all the samples obtained from Nyquist plot,  $f$  is the frequency maintained during EIS measurements,  $\epsilon_0$  is permittivity of the free space,  $A$  is the area and  $l$  is the thickness of the samples. The term, which is outside the bracket, is constant and same for all the electrodes.



## S5. Some more results of impedance spectroscopy

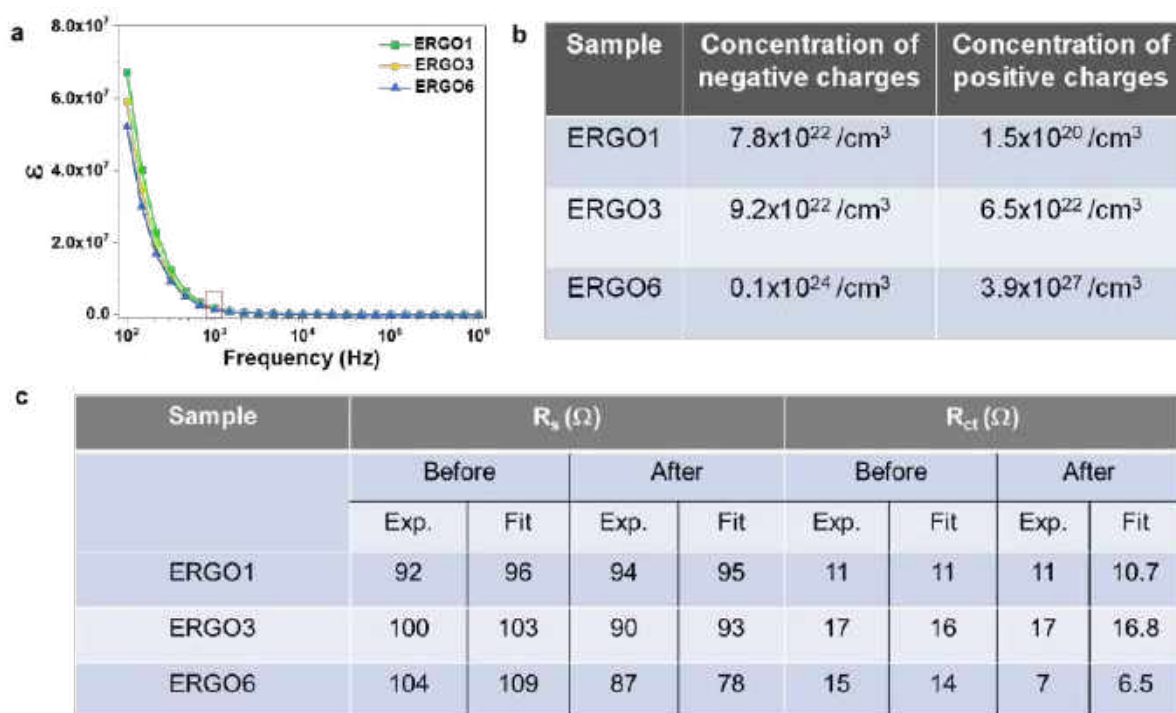


**Figure S4.** (a) Variation of dielectric constant of ERGO samples. Mott-Schottky measurements of all the samples were performed at a frequency of 1 kHz and the dielectric constant of all the electrodes at this frequency is the same as indicated in red shaded area. (b) Tabulated data of charge carrier concentration for all the ERGO electrodes. (c) Results obtained after fitting the impedance spectroscopy data and a tabulated data of interfacial resistances of each electrode before and after exposure to  $\text{As}^{3+}$ .

S6.

**Table S2.** Charge carrier density of different rGO samples including our ERGO electrode

<b>Sample</b>	<b>Charge carrier</b>	<b>Carrier concentration</b>	<b>Measurement method</b>	<b>Reference</b>
Thermally reduced graphene oxide (rGO) film	Electron	$2.21 \times 10^{20} / \text{cm}^3$	Hall measurement	2
Laser annealed rGO film	Electron	$4.7 \times 10^{21} / \text{cm}^3$	Hall measurement	3
Mechanically exfoliated graphene	Electron	$7.5 \times 10^{11} / \text{cm}^2$	Back gated field effect method	4
Graphene formed by chemical vapour depositon (CVD)	Electron	$0.3\text{-}1.9 \times 10^{12} / \text{cm}^2$	Back-gated field-effect method	5
CVD graphene	Electron	$0.4 \times 10^{12} / \text{cm}^2$	Electrolyte-gated field effect method	6
Electrochemical reduced graphene oxide (ERGO)	Positive and negative charge	$\sim 3.9 \times 10^{27} / \text{cm}^3$ (positive charge density) and $\sim 10^{23} / \text{cm}^3$ (negative charge density)	Electrochemical impedance spectroscopy: Mott-Schottky method	This work

**S7. CV of ERGO samples with 1 ppm of  $\text{As}^{3+}$**

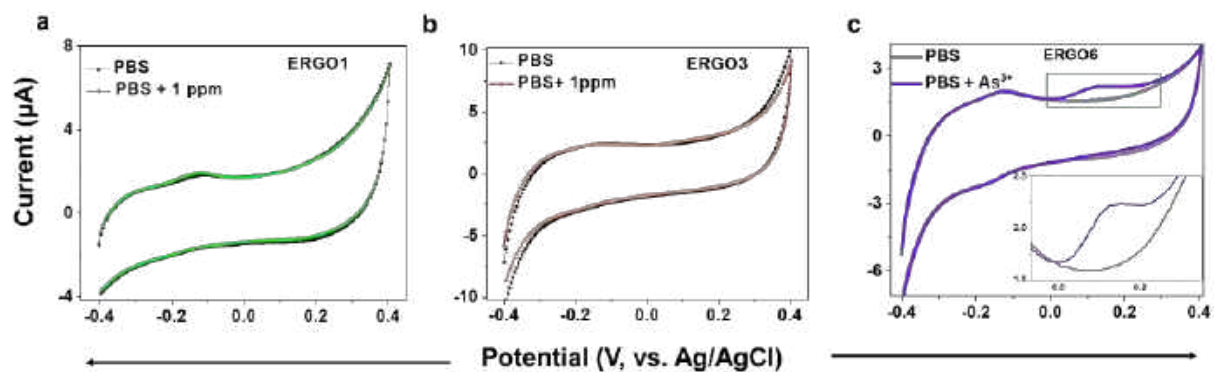


**Figure S5.** CV of (a) ERGO1, (b) ERGO3, and (c) ERGO6 using 1 ppm  $\text{As}^{3+}$  in PBS, inset figure shows the zoomed portion of the selected area of parent voltammogram.

## S8. Ion chromatography measurements and experimental results

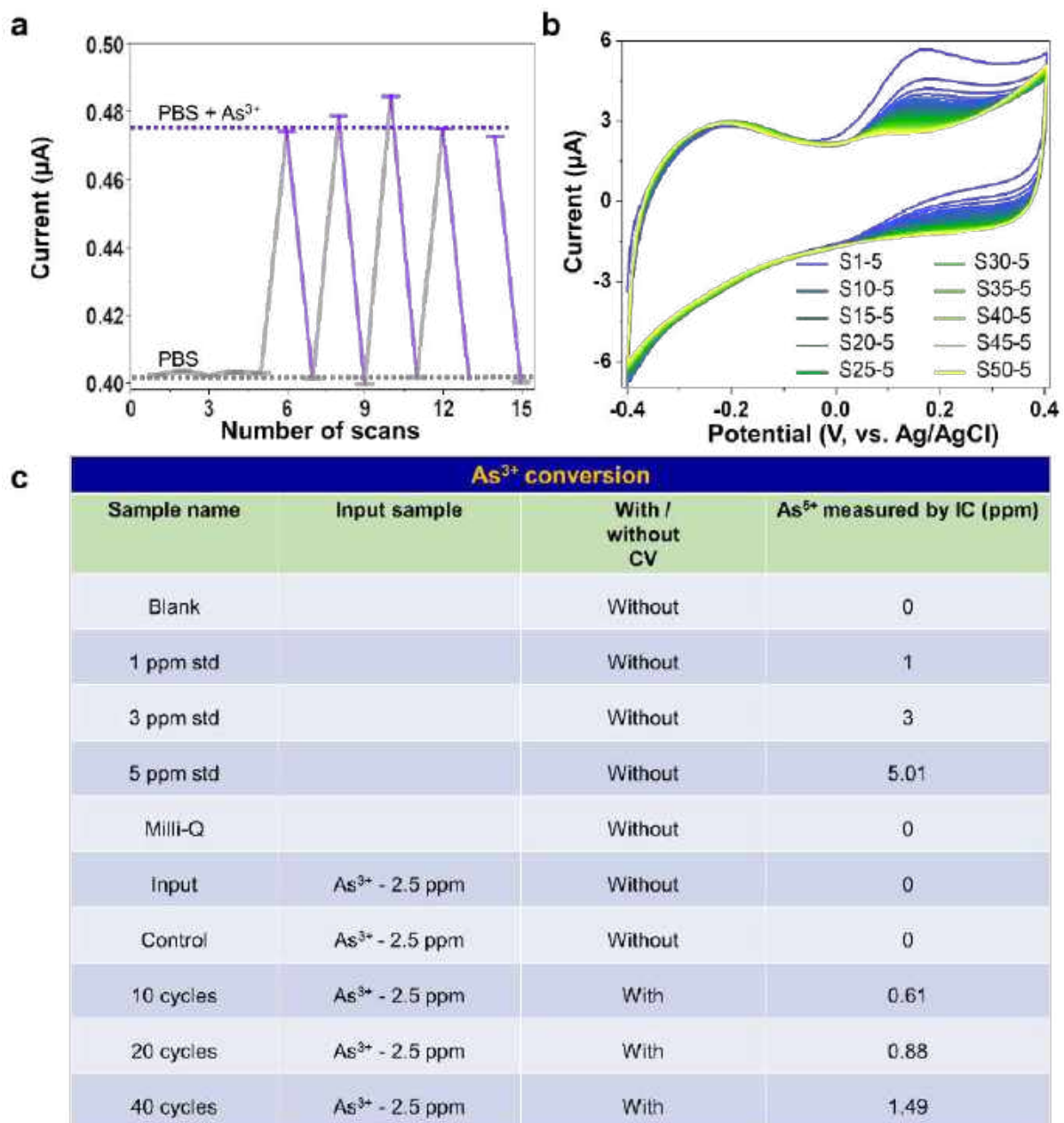


**Figure S6.** (a) Chronoamperometric (CA) response of ERGO6 with 1 ppm As<sup>3+</sup> in PBS (pH~7) with respect to the response current of PBS alone. CA was performed by keeping the potential fixed at +0.1 V and measurement was continued for 30 s in each scan. (b) Continuous CV scans for 50 cycles with 2.5 ppm of As<sup>3+</sup> in DI water, and (c) summary of the ion chromatography (IC) measurements after electrochemical conversion of As<sup>3+</sup>.

For IC measurement, we performed continuous CV scans for 50 cycles (voltammogram shown in Figure S6b) with 2.5 ppm of  $\text{As}^{3+}$  solution prepared in distilled water. Subsequently, we carried out IC measurement of the resulting solution and the chronogram is shown in Figure 3b in manuscript. In this Figure, we observed a peak at a retention time of  $\sim 23.25$  s and this was assigned by measuring the chronogram with standard (STD)  $\text{As}^{5+}$  solutions of different concentrations. 1, 3 and 5 ppm of  $\text{As}^{5+}$  solutions were purged into the IC column and chronograms were recorded. We observed three peaks with different intensities at the same retention time. Therefore, the peak observed at the retention time of  $\sim 23.25$  s corresponded to  $\text{As}^{5+}$  only. Furthermore, we investigated CV cycle number-dependent conversion of  $\text{As}^{3+}$  to  $\text{As}^{5+}$  and measured IC of the resulting solutions after a certain number of CV cycles. Here, we measured IC chronograms of the input solution (2.5 ppm of  $\text{As}^{3+}$ ) after 10, 20 and 40 CV cycles and the results are shown in Figure S6b. The conductivities of three standard  $\text{As}^{5+}$  solutions (1, 3 and 5 ppm) were also measured along with the blank (solution without  $\text{As}^{5+}$ ), control sample (2.5 ppm of  $\text{As}^{3+}$  solution) which was kept for overnight in air and three electrochemically oxidized solutions (after CV cycles). In the chronogram, it is seen that both blank and control sample do not show any peak at the retention time of  $\text{As}^{5+}$  (23.25 s), while three electrochemically oxidized samples showed three peaks of different conductivity at the same retention time. Figure S6c presents a summary of the IC data of the resulting solutions after electrochemical oxidation at ERGO6 electrode.



S9. Scan rate dependence of CV with  $\text{As}^{3+}$  and concentration dependence of CV using ERGO6 electrode

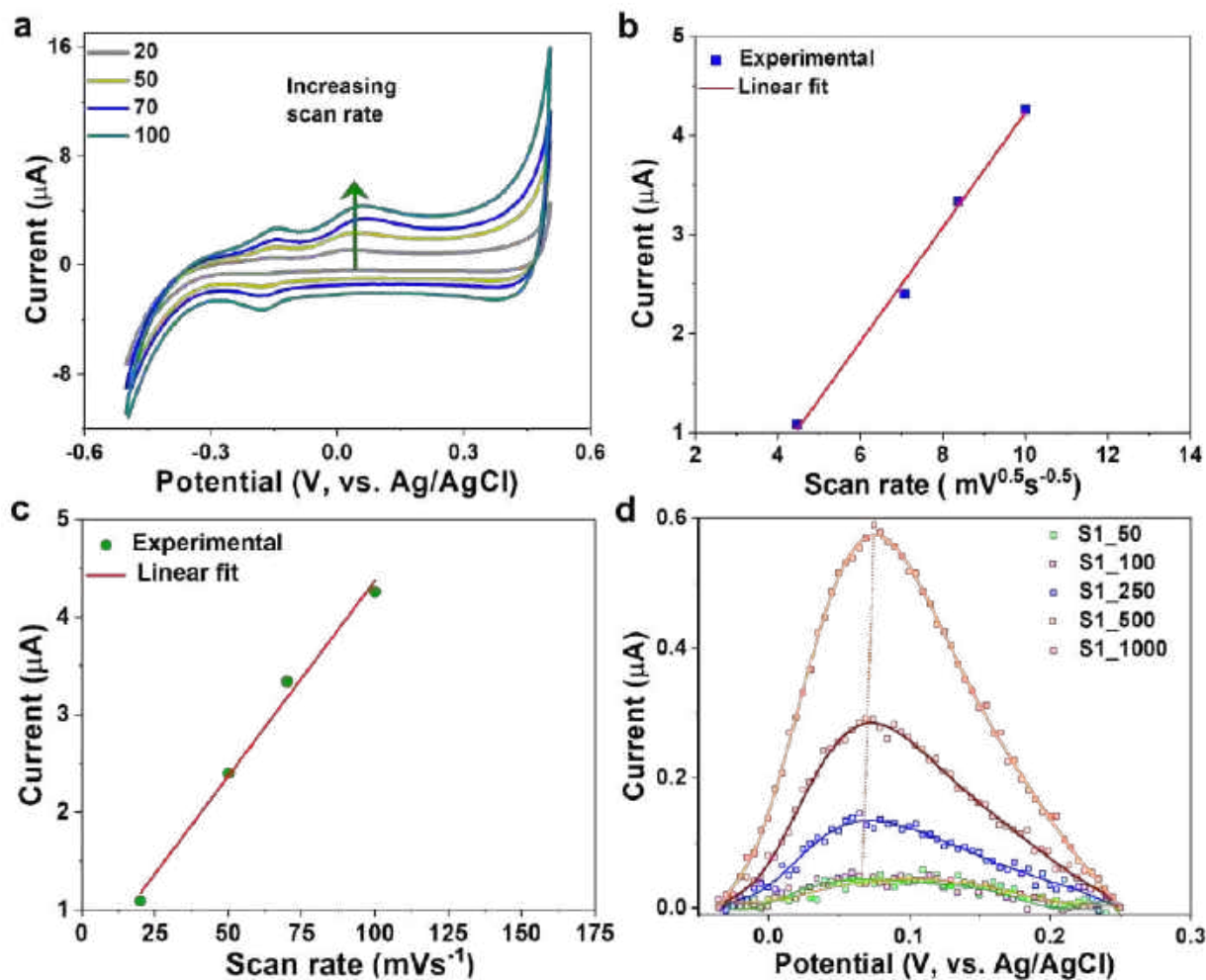


**Figure S7.** (a) Scan rate-dependent cyclic voltammogram of ERGO6 using 200 ppb of  $\text{As}^{3+}$  in PBS. Variation of peak current with (b) square root of the scan rate, (c) scan rate with corresponding linear fits and (d) linear sweep voltammogram of ERGO6 with different concentrations (50 -1000 ppb) of  $\text{As}^{3+}$  at a fixed scan rate of 50  $\text{mVs}^{-1}$ .

To understand the nature of  $\text{As}^{3+}$  interaction with the surface of ERGO6 and possible electron transfer at the ERGO6/electrolyte interface, we measured the CV at different scan rates (v) with an aqueous solution of 200 ppb of  $\text{As}^{3+}$  (Figure S7a). We plotted the peak current  $i_p$  (A)

as a linear function of both  $v^{1/2}$  (Randles-Sevcik equation) and  $v$ , as shown in Figure S7b and S7c, respectively. Figure S7b represents the adsorption and subsequent oxidation of  $\text{As}^{3+}$  is a diffusion controlled process, while Figure S7c illustrates the surface adsorbed species ( $\text{As}^{3+}$ ) on ERGO6.

Linear sweep voltammetry (LSV) measurements were performed with different concentrations of  $\text{As}^{3+}$ , the peak at  $\sim +0.1\text{V}$  in the voltammogram is the current response corresponding to  $\text{As}^{3+}$  oxidation. The voltammogram shown in Figure S7d corresponds to the increasing  $\text{As}^{3+}$  oxidation with gradual increase of  $\text{As}^{3+}$  concentration and the response is linear.

**S10. Concentration dependent chronoamperometry measurements in PBS and field water**

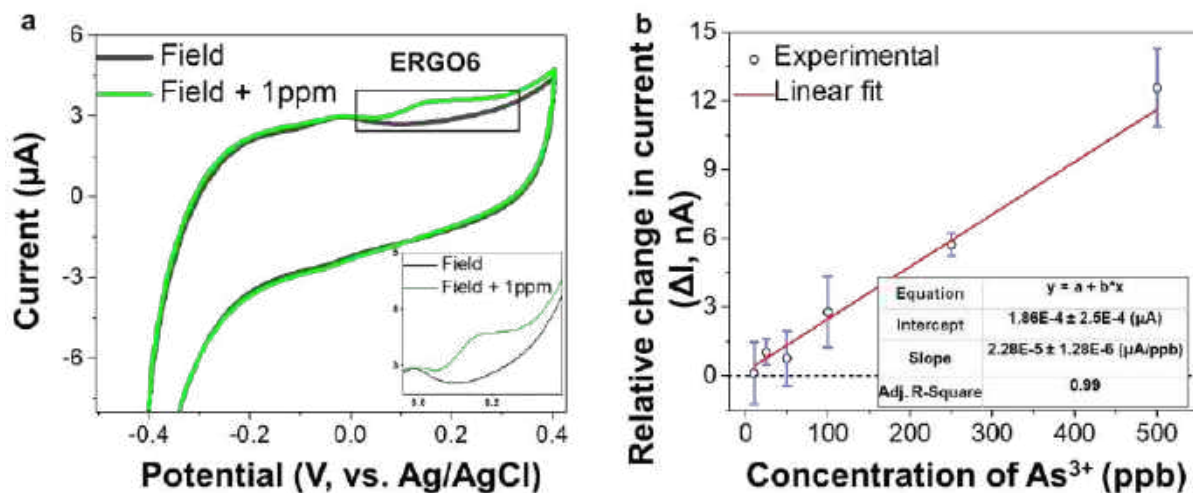


**Figure S8.** (a) CV performed with the same ERGO6 electrode with field sample (F1), inset figure shows the zoomed curve of the selected area of the parent voltammogram. (b) Measurement of the calibration curve to determine the LOD in field sample.

**S11. Interference measurements of bare ERGO6 and bare Au electrode with different cations and anions**

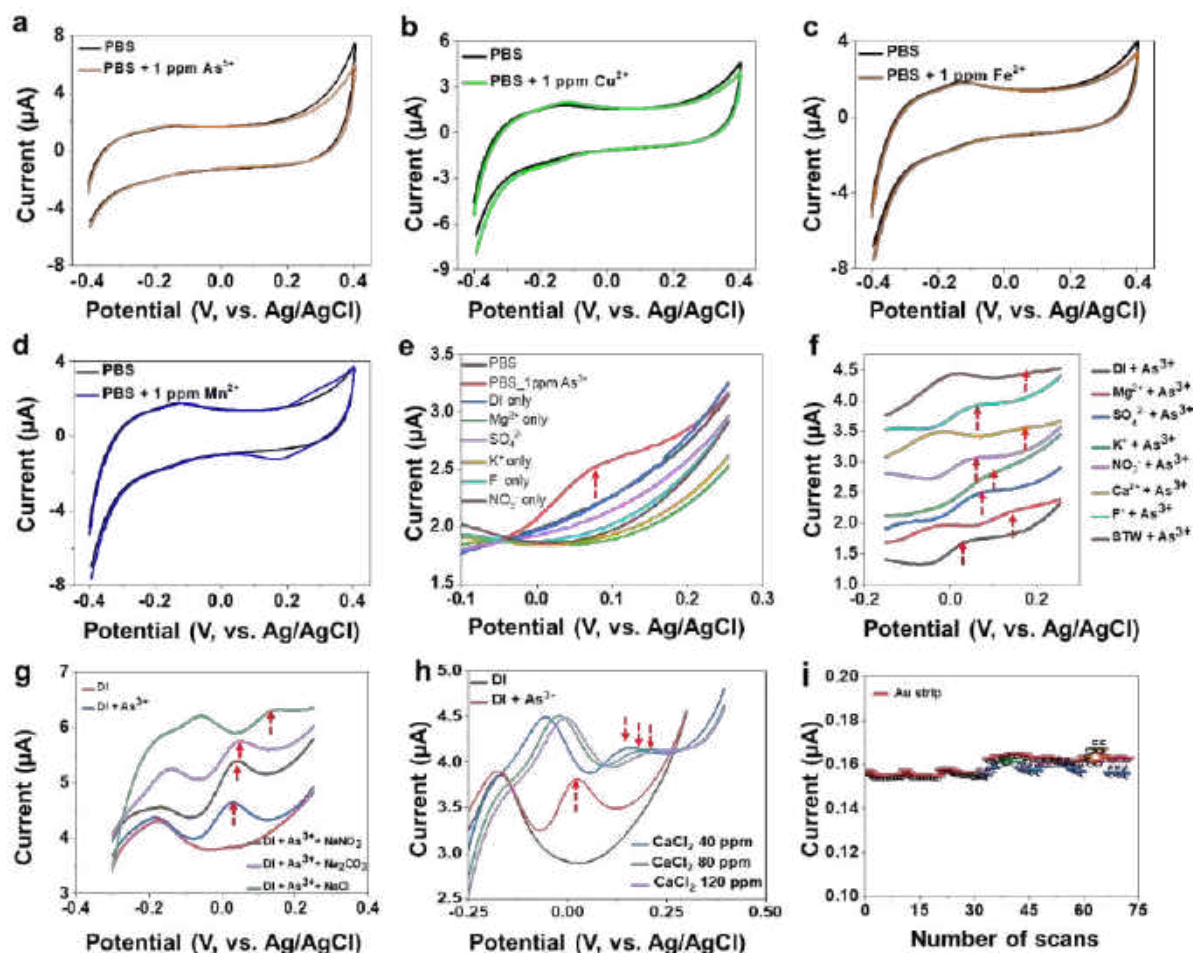


**Figure S9.** CVs of ERGO6 in presence of different heavy metal ions (a) As<sup>5+</sup>, (b) Cu<sup>2+</sup>, (c) Fe<sup>2+</sup>, and (d) Mn<sup>2+</sup>, respectively. CV of ERGO6 to study the (e) responsivity of several cations and anions separately without As<sup>3+</sup>, (f) effect of some other cations and anions on As<sup>3+</sup> response, (g) effect of different anions on the As<sup>3+</sup> response (in presence of Na<sup>+</sup>), (h) effect of Cl<sup>-</sup> concentration on the As<sup>3+</sup> response (in presence of Ca<sup>2+</sup>). Concentration of the cations was maintained similar to their concentration in simulated synthetic tap water. Concentration of As<sup>3+</sup> was maintained at 1 ppm in all the cases. Red dotted arrow line indicates the response of arsenic. For clarity, we have shown oxidation cycle of the each CV. (i) Chronoamperometry current of pristine Au strip in presence of Cu<sup>2+</sup>, Fe<sup>2+</sup>, and Mn<sup>2+</sup> along with As<sup>3+</sup>. Concentration of each ion was maintained at 1 ppm.

Figure S9a-d represent the CVs of ERGO6 in presence of four major heavy metal ions and the experiment was carried out in PBS. In the voltammograms, there was no peak observed in the potential window (-0.4 to +0.4 V) due to any of the ions. Oxidation (+0.3 V) and reduction peaks (+0.17 V) of  $\text{Mn}^{2+}$ , did not interfere with the chronomaperometric response of  $\text{As}^{3+}$ , as the peak positions were different compared to  $\text{As}^{3+}$  (~+0.1V)

We have further studied the electrochemical response (CV) with a few more cations ( $\text{Ca}^{2+}$ ,  $\text{K}^+$ , and  $\text{Mg}^{2+}$ ) and anions ( $\text{F}^-$ ,  $\text{SO}_4^{2-}$ ,  $\text{CO}_3^{3-}$ ,  $\text{Cl}^-$  and  $\text{NO}_3^-$ ) of relevance in order to prove the selective response. The results are shown in Figure S9e. ERGO6 responded to  $\text{As}^{3+}$  only and there was no response towards other ions. We used three common anions ( $\text{F}^-$ ,  $\text{SO}_4^{2-}$ , and  $\text{NO}_3^-$ ) and a common counter cation ( $\text{Na}^+$ ), while, for  $\text{Cl}^-$  anion, two counter cations ( $\text{Ca}^{2+}$  and  $\text{Mg}^{2+}$ ) were used. The concentrations of both cations and anions were chosen as per standard concentrations used for the preparation of synthetic tap water (STW) as mentioned in the supporting information of S. Mukherjee et al.<sup>7</sup> Concentrations of cations and anions used during the experiments are shown in Table S3

. The results are shown in Figure S9f and  $\text{As}^{3+}$  response was seen in all cases. The peak corresponding to  $\text{As}^{3+}$  oxidation shifted to a higher potential in presence of  $\text{Ca}^{2+}$  and  $\text{Mg}^{2+}$ . Also peak height decreased for the two ions. The presence of high concentrations (40 to 120 ppm) of  $\text{Cl}^-$  passivated the ERGO surface and formed an extra electrical double layer, so that charge transfer kinetics due  $\text{As}^{3+}$  oxidation was slower. This could lead to shifting of oxidation peaks to higher potential and diminishing of the corresponding peak height. To verify the hypothesis, we performed CV with different anions ( $\text{NO}_3^-$ ,  $\text{CO}_3^{3-}$ , and  $\text{Cl}^-$ ) in presence of 1 ppm of  $\text{As}^{3+}$  and the same counter cation ( $\text{Na}^+$ ) was chosen. The results are shown in Figure S9g in which  $\text{As}^{3+}$  response was detected for all the anions. In presence of  $\text{Cl}^-$ ,  $\text{As}^{3+}$  reduction peak shifted to higher potential with diminished peak height. For further confirmation, CV was performed with  $\text{As}^{3+}$  in presence of different  $\text{Cl}^-$  concentrations. On increasing of  $\text{Cl}^-$



concentration, the peak gradually shifted to higher potentials and the peak height diminished gradually with increasing  $\text{Cl}^-$  concentrations. The results are presented in Figure S9h. To verify that ERGO6 is exclusively responsible for  $\text{As}^{3+}$  sensing, we carried out a control experiment by measuring the CA current of bare Au strip with four metal ions ( $\text{As}^{5+}$ ,  $\text{Cu}^{2+}$ ,  $\text{Fe}^{2+}$ , and  $\text{Mn}^{2+}$ ) including  $\text{As}^{3+}$ . The result is shown in Figure S9i. The concentration of each ion was maintained at 1 ppm. It was seen that Au did not show any response toward these metal ions.

## S12. Concentrations of cations and anions in synthetic tap water

**Table S3.** Concentration of cations and anions used in the interference study of ERGO6 electrode

Cations / Anions	Concentration (ppm)
Na	63.6
Cl	87
Mg	14.34
SO <sub>4</sub>	32.41
F	0.57
Ca	28.72
CO <sub>3</sub>	43.22
NO <sub>3</sub>	1.84

### S13. Chronoamperometry measurements with various field samples

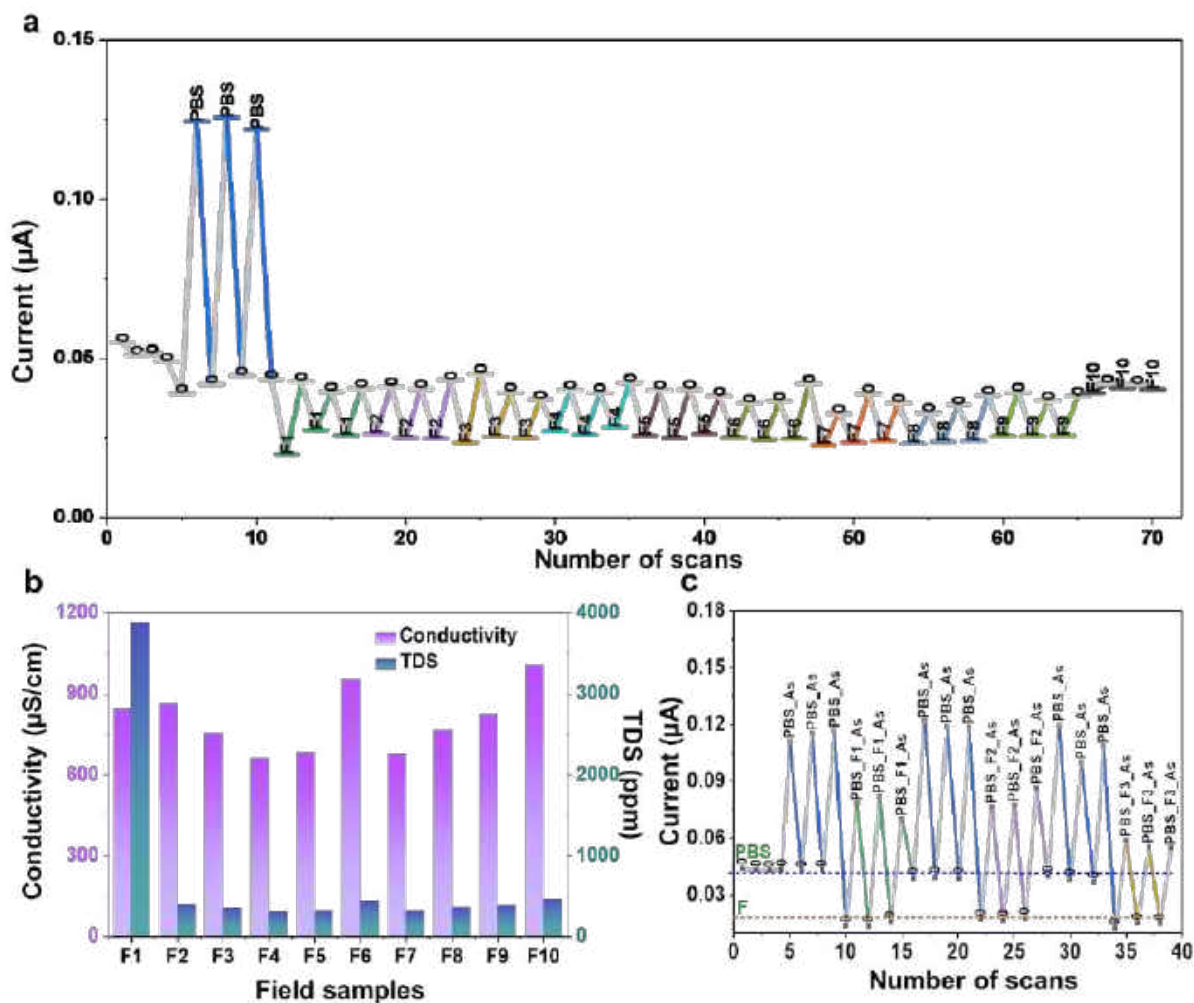


**Figure S10.** (a) Repetitive CA current response of ERGO6 with different field samples (marked as F1-F10) of different conductivity and TDS levels. CA response of various field samples (no arsenic was found). We tested with ten individual field samples. Each field sample was measured thrice. The first three samples in PBS had 1 ppm As<sup>3+</sup>. (b) Variation of conductivity and TDS of all field water samples. (c) CA current response of 1 ppm As<sup>3+</sup> spiked PBS and different field samples. Initial three cycles represents current response of As<sup>3+</sup> in PBS, while each three sets of the rest of the cycles represent current response of the electrode with a particular field sample having no As<sup>3+</sup>. This experiment was carried out with three different field samples (F1-F3). Here, F stands for field water sample using same strip.

Figure 10a presents CA responses of different field water samples. All the field water samples were collected from different locations of South 24 Parganas district of West Bengal, India. Before starting the CA measurements with field water samples, total As concentration of all the water samples was measured by ICPMS and no As (less than 1 ppb) was found in these water samples. The current responses of all the field water samples were measured with respect to the current response of blank PBS. Before starting the CA measurements with field water samples,  $\text{As}^{3+}$  response was tested with ERGO6 strip for three scans followed by the same measurements performed with different field samples. It was seen that ERGO6 showed lower current response in presence of field sample with respect to the current response of blank PBS. The amplitude of the current response of all the field samples was similar, although there were differences in conductivity and TDS. Variation of TDS and conductivity of all the field samples is shown in Figure S10b. Negative response by ERGO6 strips with field water samples was owing to the presence of  $\text{Cl}^-$  in the field samples, as we have seen already in Figure S9h. The concentration of  $\text{Cl}^-$  ions in the field samples was around 1- 2 ppm.  $\text{Cl}^-$  ions might passivate some of the active sites of ERGO6, thus decreasing overall ionic current of the electrode in field samples compared to PBS. In addition, arsenic response of ERGO6 strip was checked in both PBS and field samples with spiking of 1 ppm  $\text{As}^{3+}$ . The results are depicted in Figure S10c.  $\text{As}^{3+}$  response was observed in both cases; however, the amplitude of the current response of  $\text{As}^{3+}$  in field water sample (~ 60 nA) is lower than the response in PBS (~ 70 nA).

**S14: Raman spectra of ERGO6 measured at different scan depths in presence of water**

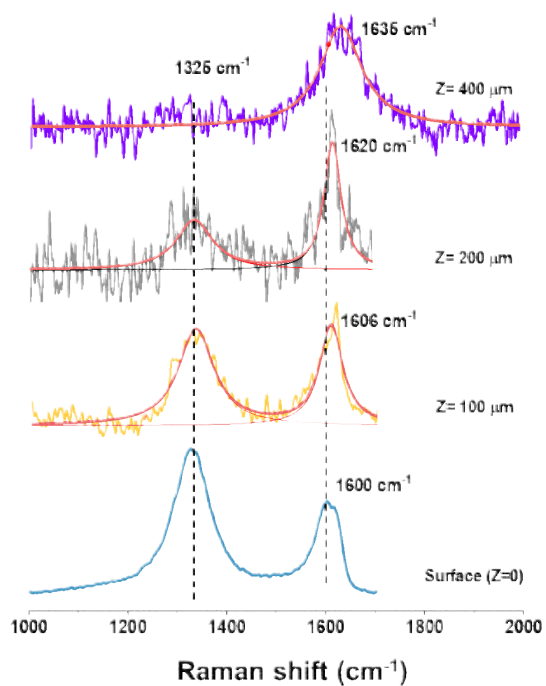


**Figure S11:** Raman spectra of the same electrode at different scan depths ( $Z$ ) with respect to the surface of the electrode and measurement was carried out in presence of water.



**S15. Gaussian fitting of G band of Raman spectra of ERGO6 without and with DI water**

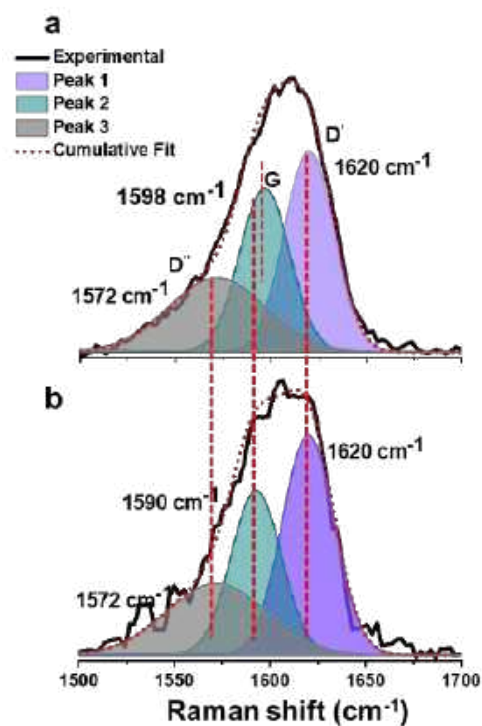


**Figure S12.** Fitting of G band of Raman spectra of ERGO6 electrode (a) with, and (b) without DI water.

**S16. In-situ SPEC measurements of ERGO1 and ERGO6 in presence of only DI water, without and with external potential**

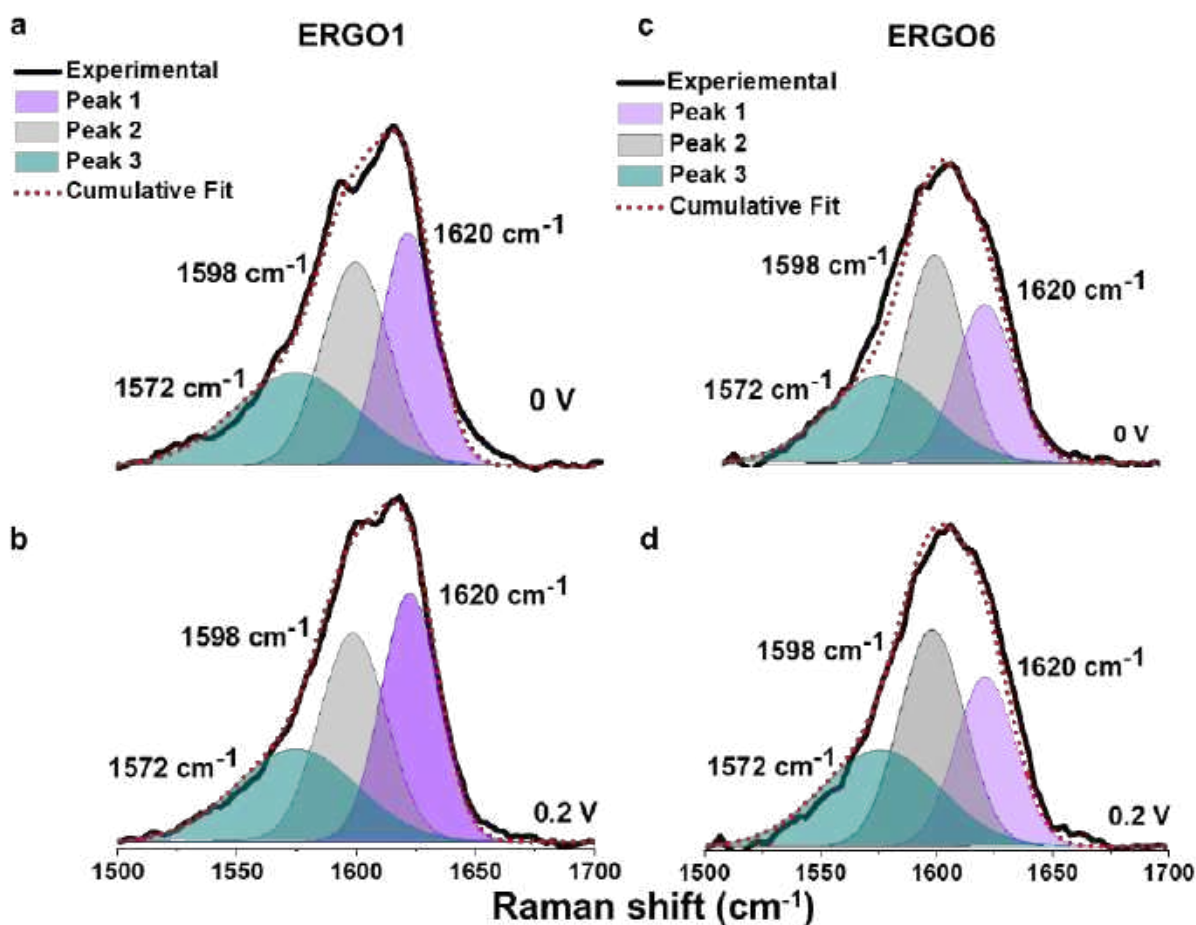


**Figure S13.** Gaussian fitting of G band of Raman spectra of ERGO1 electrode in presence of DI water acquired at (a) 0 V, and (b) 0.2 V. Gaussian fitting of G band of Raman spectra of ERGO6 electrode in presence of DI water acquired at (c) 0 V, and (d) 0.2 V.

**S17. Chronoamperometry profiles of ERGO1 and ERGO6 without and with As<sup>3+</sup> during in-situ spectroscopy measurements**

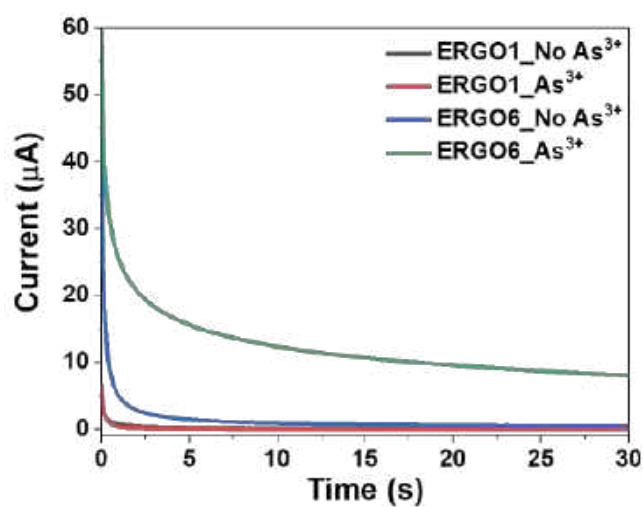


**Figure S14.** CA current of both ERGO1 and ERGO6 at 0.2 V in absence and presence of 1000 ppm of As<sup>3+</sup>.

### S18. Study of electrochemical stability of the electrodes

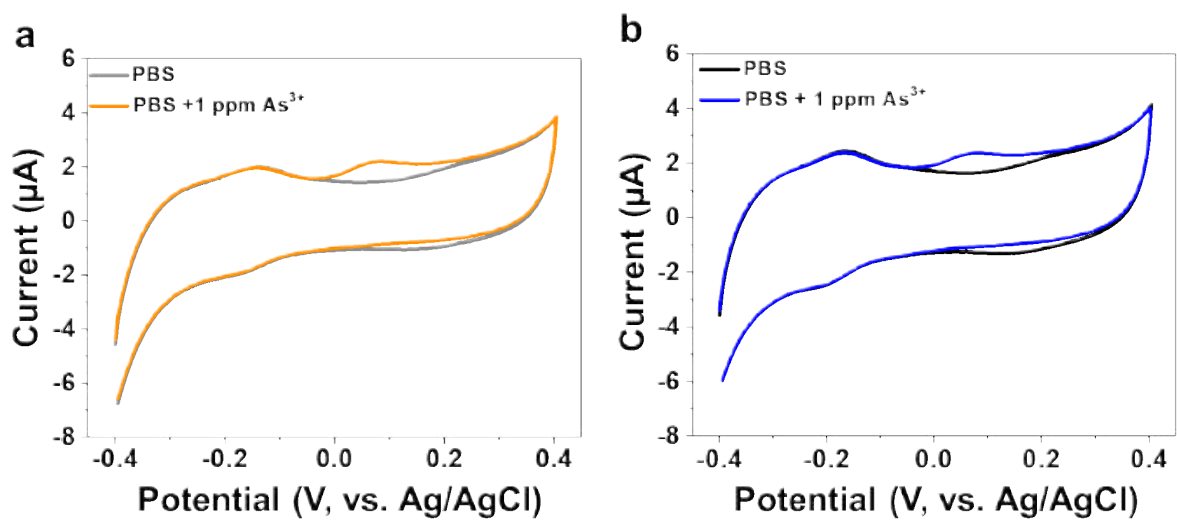


**Figure S15.** CV with 1 ppm  $\text{As}^{3+}$  using (a) as prepared ERGO6 and (b) the same strip after 2 months.

### S19. Effect of potential on the G band of in-situ Raman spectra

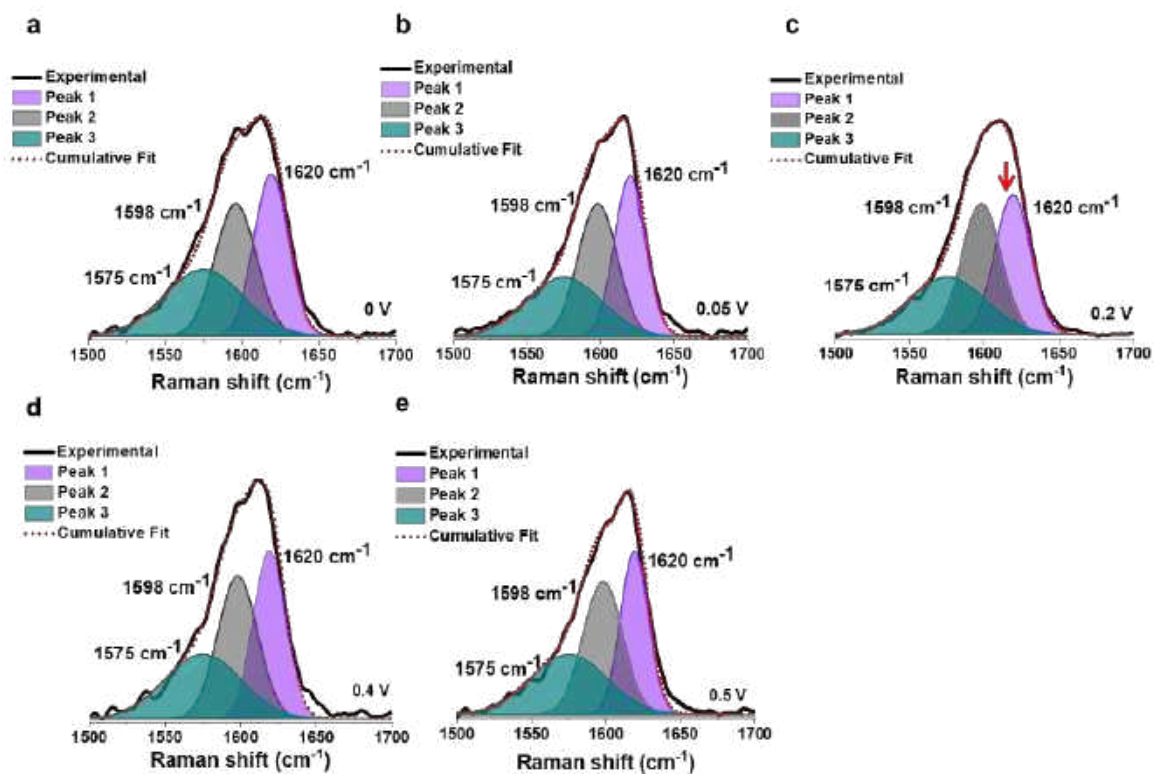


**Figure S16.** Gaussian fitting of G band of Raman spectra of ERGO6 in presence of  $As^{3+}$  acquired at different potentials: (a) 0 V, (b) 0.05 V, (c) 0.2 V, (d) 0.4 V, and (e) 0.5 V.



## S20. In-situ spectroelectrochemical study of ERGO6 in presence of different cations including $\text{As}^{3+}$

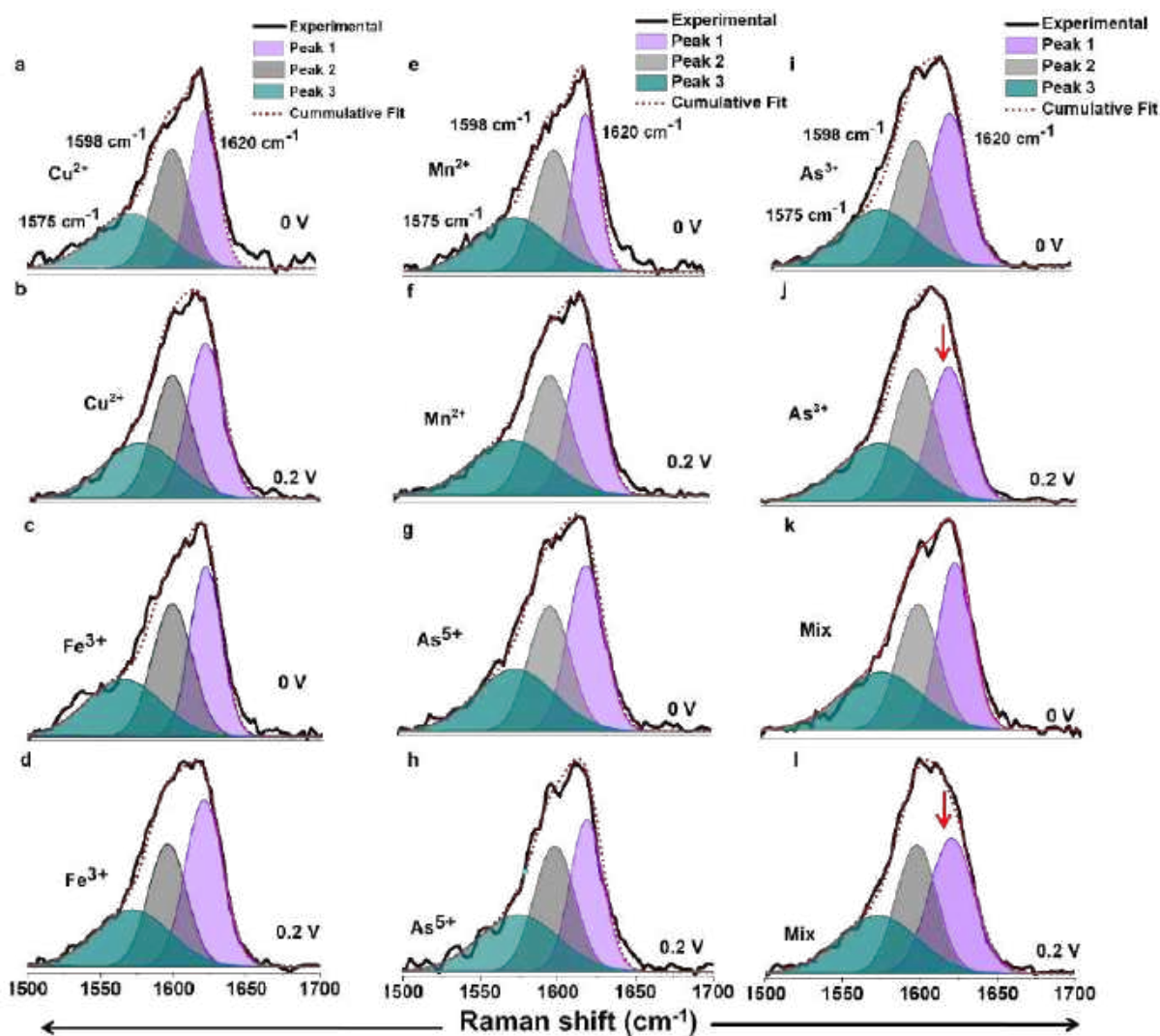


**Figure S17.** In-situ Raman spectra (G band) of ERGO6 electrodes in presence (a-b)  $\text{Cu}^{2+}$ , (c-d)  $\text{Fe}^{3+}$ , (e-f)  $\text{Mn}^{2+}$ , (g-h)  $\text{As}^{5+}$ , (i-j)  $\text{As}^{3+}$ , and (k-l) mixture of ions. Spectra were recorded for each ion at 0 V and 0.2 V. Concentration of each ionic species was maintained at 1000 ppm.

**S21. FTIR spectra of ERGO6 and ERGO1 electrodes with and without As<sup>3+</sup> and after electrochemical oxidation**

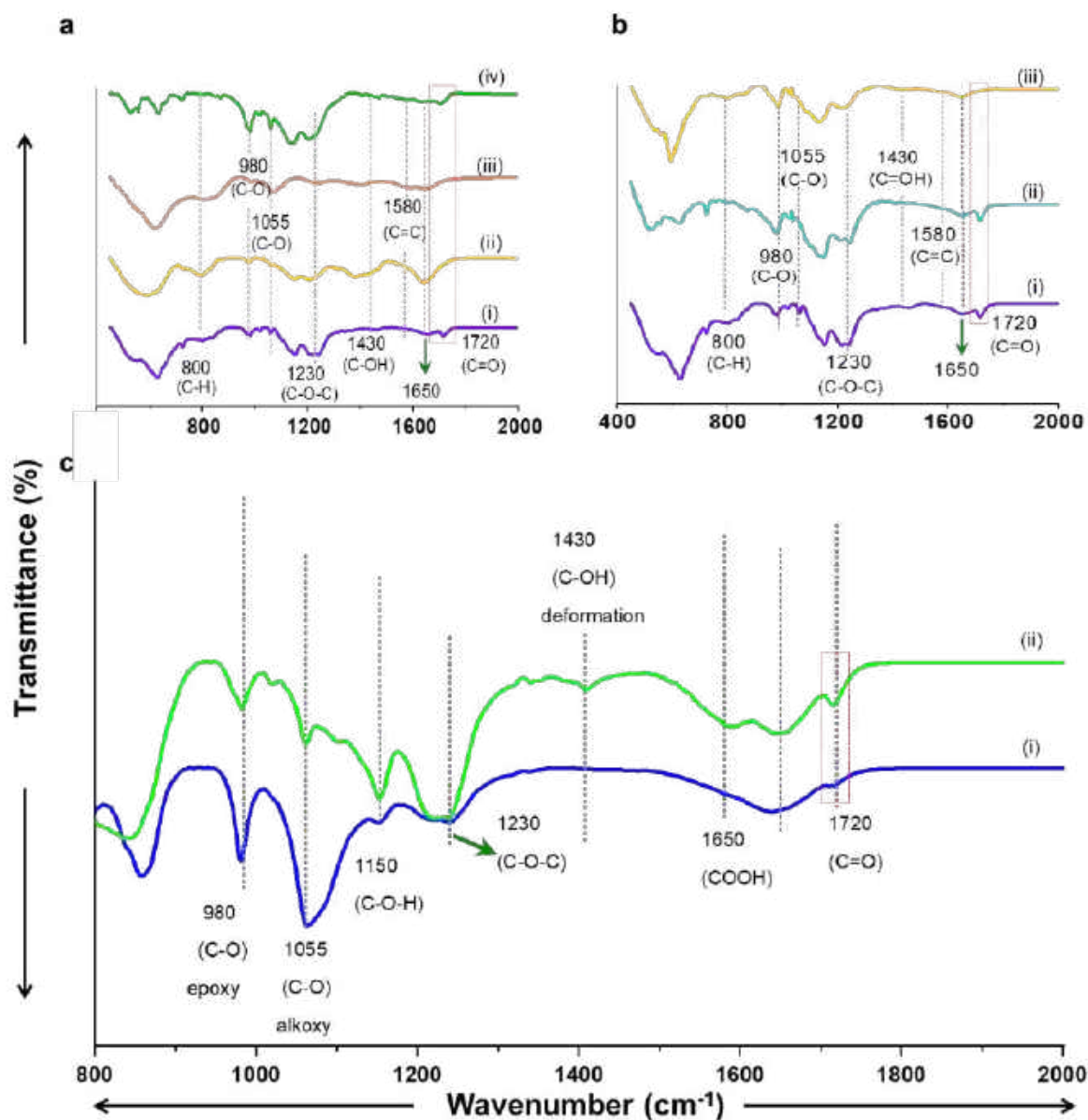


**Figure S18.** (a) FTIR spectra of the same strip without As<sup>3+</sup> (purple trace), with As<sup>3+</sup> (yellow trace), after washing with DI water (orange trace), and after electrochemical oxidation (green trace). (b) FTIR spectra of bare ERGO6 electrode (purple trace), same electrode with mixture of interfering ions (blue trace) and interfering ions along with As<sup>3+</sup> (yellow trace). (c) FTIR spectra of ERGO1 with (1000 ppm) and without As<sup>3+</sup>.

## S22. Computational Methodology

We used the Avogadro program package<sup>8</sup> for building up the structures of the analyte ions and the ERGO-analyte adducts, and for structure visualization and analysis, and for our UFF force field simulations. The Visual Molecular Dynamics (VMD) package was used to visualize and render the images of the structures.<sup>9</sup>

The geometry optimization of the As(OH)<sub>3</sub>-ERGO adduct isomers 1 to 6 shown below were performed using all-electron density-functional theory DFT at the B3LYP/6-31G\* level of theory in the neutral-charge state using the NWChem 7.0 package.<sup>10</sup> Among the six isomers, we have shown lowest energy isomer (isomer 2) in the manuscript (Figure 5a). For reasons of computational efficiency for all our other calculations, we used the grid-based projector augmented wave method as implemented in the GPAW software package.<sup>11</sup> We employed the linear combination of atomic orbitals (LCAO) mode of GPAW with a double-zeta plus polarization (DZP) basis set with GGA-PBE exchange-correlation functional<sup>12</sup> for all calculations. The valence electronic configuration of the GPAW setups were the default valence electronic configurations of those elements. A grid spacing of 0.2 Å was used, and the simulation box size was 32 Å for all calculations regardless of the model size for the purpose of being able to comparing Kohn-Sham eigenvalues between different molecular systems. During geometry optimizations, the stopping criterion for the maximum force on atoms was 0.04 eV/Å. To accelerate electronic structure convergence of ERGO and analyte molecules, we used a Fermi broadening of 0.02 eV for the electronic occupations. For the calculations involving Mn and Fe atoms in 3d<sup>5</sup> configuration, we used spin-polarized DFT and set the magnetic moment to be constrained to its initial value of  $\mu = \sqrt{n(n+2)} = 5.91\mu_B$ , where the number of unpaired electrons,  $n$ , is 5, which corresponds to total spin  $S=5/2$ , and spin multiplicity of 6.

In our simulations, we neglect all solvent effects, both implicit and explicit, except where we include aqua ligands as part of the solvated species of the  $\text{Fe}^{2+}$ ,  $\text{Cu}^{2+}$  and  $\text{Mn}^{2+}$  ions. Furthermore, our simulations are performed neglecting temperature, potential and electric field, and dynamical effects in our simulations. The positive surface-charge density of ERGO6 electrode at constant potential has been simulated approximately, by charging the model in DFT. For structural property, we used neutral model of ERGO as it is sufficient for bonding properties.

We describe our detailed simulation methodology in three stages, (1) Site-selectivity and binding of arsenite and other analytes to ERGO, (2) Oxidation mechanism of arsenite with ERGO (3) Ion-selectivity mechanism, in sections S22, S23, and S24, respectively, below. Additional results are also presented in the relevant section.

## S23. Methodology of generation of ERGO models and binding of arsenite and analyte ions to ERGO

We now describe the process of (a) generating structural models of ERGO, (b) optimizing As-(OH)<sub>3</sub>-ERGO adduct isomers and (c) Fe, Cu, Mn, and H<sub>2</sub>PO<sub>4</sub><sup>-</sup> adduct isomers and binding energy study, in the respective sections below.

### (a) ERGO models 1, 2 and 3

We first generated a rectangular-sheet model of ERGO (model 1) containing a total of 85 atoms of dimensions 7x10 Å (C<sub>46</sub>O<sub>19</sub>H<sub>22</sub>), with a realistic oxygen/carbon surface atom ratio<sup>13</sup> using the MakeGraphitics<sup>14</sup> package which generates reduced graphene oxide models of the Lerf-Klinowski<sup>15</sup> type. The model contained four different types of functional groups – epoxide, hydroxyl (OH) groups, and C-O-C lactone groups and carboxylate (COOH) groups. The dimensions of the model 1 were 7x10 Å. The size of the model was chosen to be as small as possible but with realistic number of functional groups to model the analyte ion-ERGO interactions. Model 1 was then geometry-optimized using all-electron density-functional theory DFT at the B3LYP/6-31G\* level of theory in the neutral-charge state using the NWChem 7.0 package<sup>10</sup>. The optimized geometry of model 1 is shown in Figure S19, below.

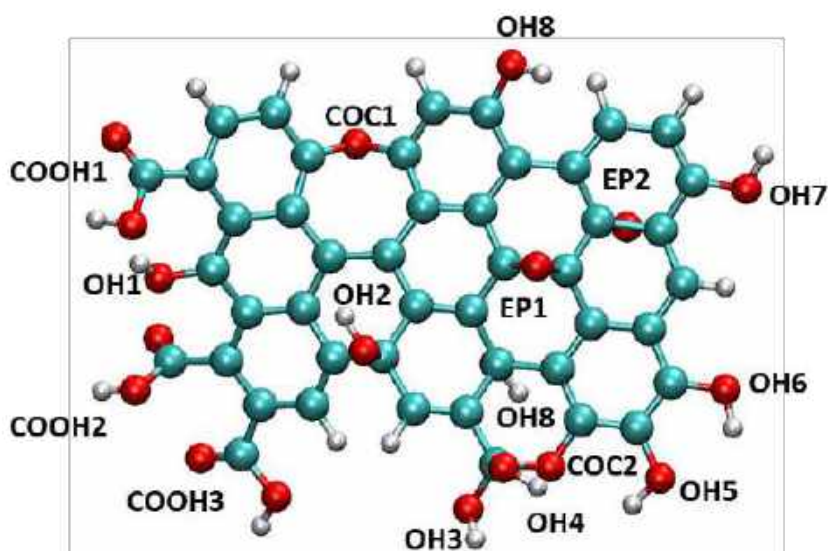




**Figure S19. Model 1** – DFT-optimized structure of ERGO rectangular sheet with 85 atoms ( $C_{46}H_{22}O_{17}$ ). The model has two pairs of epoxide and OH groups on the surface, and three COOH groups, and eight hydroxyl groups. The functional groups carboxylate (COOH), hydroxyl (OH), COC(lactone) and expoxide (EP) are labelled as indicated in brackets. Atom sphere colors are cyan for carbon, red for oxygen and white for hydrogen.

We created additional models of ERGO which were used in the ion-selectivity study, models 2 and 3, and their structures are shown in Figures S20 and S21, below. Model 2 was an ERGO sheet model with a lower ratio of edge functional groups and model 3 is a hexagonal flake model, and these were also optimized in the neutral and +1 charge states.

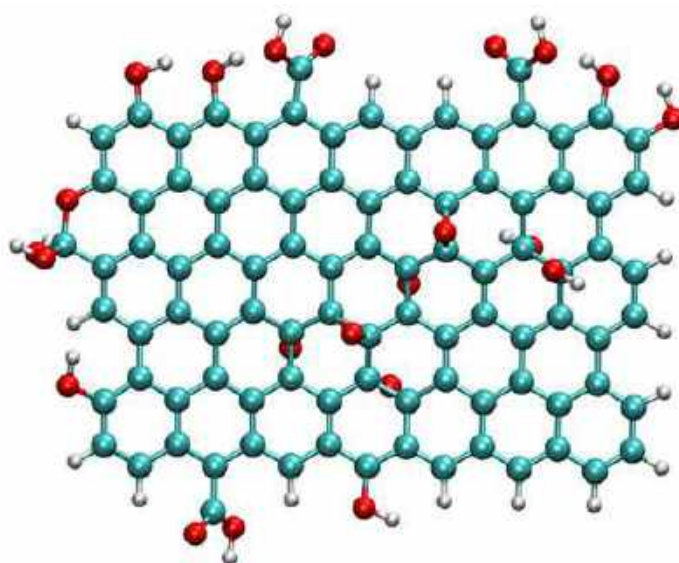


**Figure S20. Model 2-** DFT-optimized structure of a larger rectangular sheet with 144 atoms, ( $C_{91}O_{22}H_{31}$ ). The model has three epoxide/OH group pairs on the surface pair, and the size of the model is  $\sim 12 \times 18$  Å. Atom sphere colors are cyan for carbon, red for oxygen and white for hydrogen.

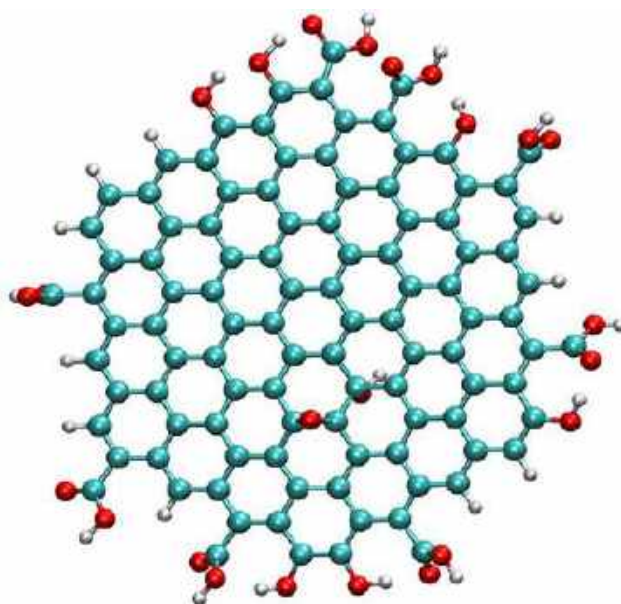


**Figure S21. Model 3** - DFT-optimized structure of a hexagonal flake model of ERGO ( $C_{101}O_{22}H_{30}$ ) with 153 atoms. The model has a single surface epoxide/OH group pair, and edges are decorated with 8 OH and 8 COOH groups. The size of the model is  $\sim 10$  Å. Atom sphere colors are cyan for carbon, red for oxygen and white for hydrogen.

**(b)  $As(OH)_3$ -ERGO adduct isomers 1 to 6**

We investigated the binding-site selectivity of the arsenite molecule  $As(OH)_3$  to the various functional groups on the surface and edges of ERGO sheet model 1. Geometry optimizations were carried out using NWCHEM with the  $As(OH)_3$  molecule initially placed near to different functional group environments on the surface and edge of model 1, and in different orientations, with the As facing towards and away from the functional group. We obtained a set of six lowest-energy isomers, named as isomers 1 to 6, the structure of isomer 2 is shown in Figure 5 and structures of remaining isomers are shown in Figure S22. The types and number of bonds, and their lengths, are shown in Table S4 below. The additional covalently bonded adduct isomer structure with an As-O bond shown in Figure S22 was optimized using GPAW using the same calculation methodology described below.

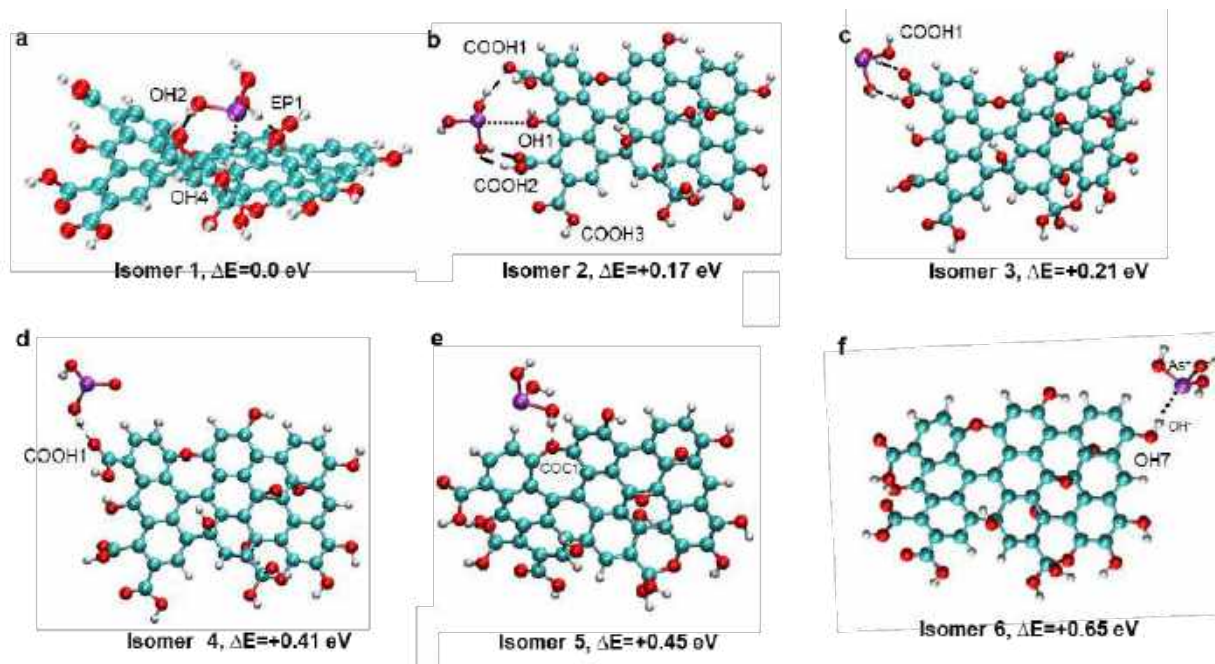


**Figure S22.**  $\text{As}(\text{OH})_3$  binding at different sites of ERGO model from DFT calculations. Isomers 1 to 6, showing binding possibilities of the  $\text{As}^{3+}$  species to the functional groups present on the surface and edges of the ERGO model. (a) Side view of the lowest-energy isomer 1 showing  $\text{As}(\text{OH})_3$  on the GO surface bound by two hydrogen bonds (HBs), indicated by dashed lines, between  $\text{As}(\text{OH})_3$  and ERGO epoxide (EP1) and hydroxyl group (OH2), and also a weak  $\text{As}^+-\text{O}^-$  interaction, indicated by dotted lines, with a surface hydroxyl group (OH4). (b) Isomer 3, binding to the COOH1 group by two HB's. (c) Isomer 4, binding to the COOH1 group via a single HB. (d) Isomer 5 involves binding via a single hydrogen bond to an edge C-O-C group. (e) Isomer 6, which is the highest-energy isomer has a weak  $\text{As}^+-\text{O}^-$  interaction with a hydroxyl group (OH7) and no HBs. The functional groups interacting with the  $\text{As}(\text{OH})_3$  are labelled according to Figure S23. The color scheme for the atomic spheres is purple for arsenic, cyan for carbon, red for oxygen, and white for hydrogen.

**Table S4.** Binding sites of As(OH)<sub>3</sub> on ERGO, the number of hydrogen bonds (HBs) and As<sup>+</sup>-(OH)<sup>-</sup> interactions, bonding distances, and relative energies of isomers 1 to 6. The functional groups are labelled as in Figure 7 in the manuscript.

Isomer	Binding Sites on ERGO	No of HBs/As <sup>+</sup> -(OH) <sup>-</sup> interactions	Bonding Distances/Å	Total Energy/a.u.	Relative Energy/eV
1	Surface OH2 and OH4 groups and epoxide group (EP1)	2/1	As---OH4: 2.55  HB(OH2): 1.91  HB(EP1): 1.88	-5657.099479	0.0
2	Edge COOH1 and COOH2 groups and OH1 group	3/1	HB(COOH1): 1.93  HB(COOH1): 1.89  HB(COOH2): 2.16  As---OH1: 3.26	-5657.093368	0.17
3	Edge COOH1 group	2/0	HB(COOH1): 1.71  HB(COOH1): 1.82	-5657.091603	0.21
4	Edge COOH1 group	1/0	HB(COOH1): 1.88	-5657.08450	0.41
5	Surface C-O-C group	1/0	HB(COC1): 1.94	-5657.08269	0.45
6	Edge OH7 group	0/1	As---OH7: 2.67	-5657.075732	0.65

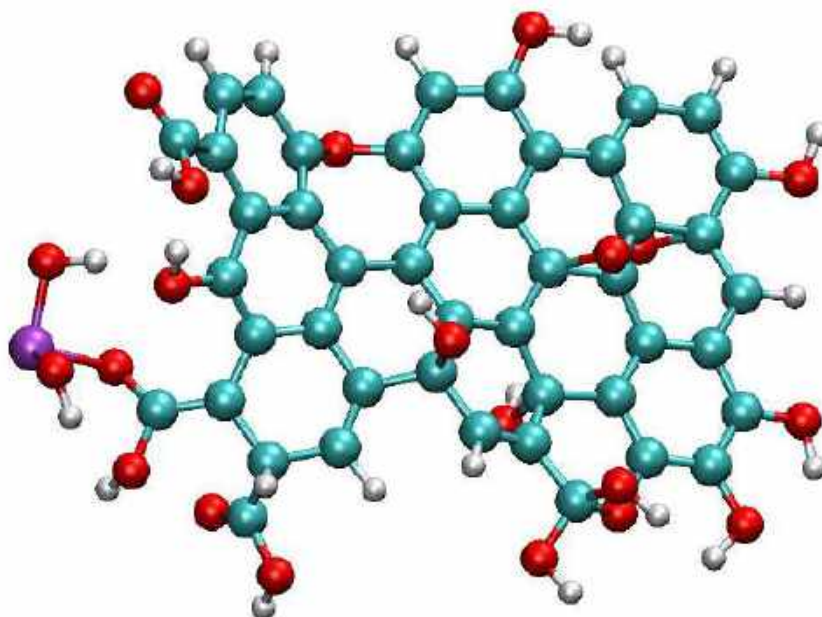


**Figure S23.** Covalent-bonded  $\text{As}^{3+}$ -ERGO adduct. The third hydrogen atom of  $\text{As}(\text{OH})_3$  been lost to the solvent and is not shown. The violet sphere represents the arsenic atom, red - oxygen, cyan - carbon, and white - hydrogen.

### (c) Analyte ion-ERGO adducts and binding energies

We further investigated the binding of several metal ions,  $[\text{M}(\text{H}_2\text{O})_6]^{2+}$ , where  $\text{M}=\text{Fe}$ ,  $\text{Mn}$ ,  $\text{Cu}$ , and also  $\text{H}_2\text{PO}_4^-$ , to ERGO by substituting the  $\text{As}(\text{OH})_3$  molecule in isomer 2 with these four ions and optimizing their structures using GPAW. The optimized structures of the four adducts are shown in Figures S24 to S27, below. To create these isomers, we selected the structure of isomer 2 as it was the lowest-energy isomer in which  $\text{As}(\text{OH})_3$  is bound to edge COOH groups, since our experiments indicated structural changes at the COOH group. We also optimized the structure of isomer 2 itself, using GPAW, so that its binding energy could be compared with the other analyte ions. We computed binding energies approximately without basis-set superposition error (BSSE) corrections as  $E(\text{Binding})=E(\text{Adduct})-E(\text{ERGO})-E(\text{Analyte})$ , and these are listed in Table S5, below.



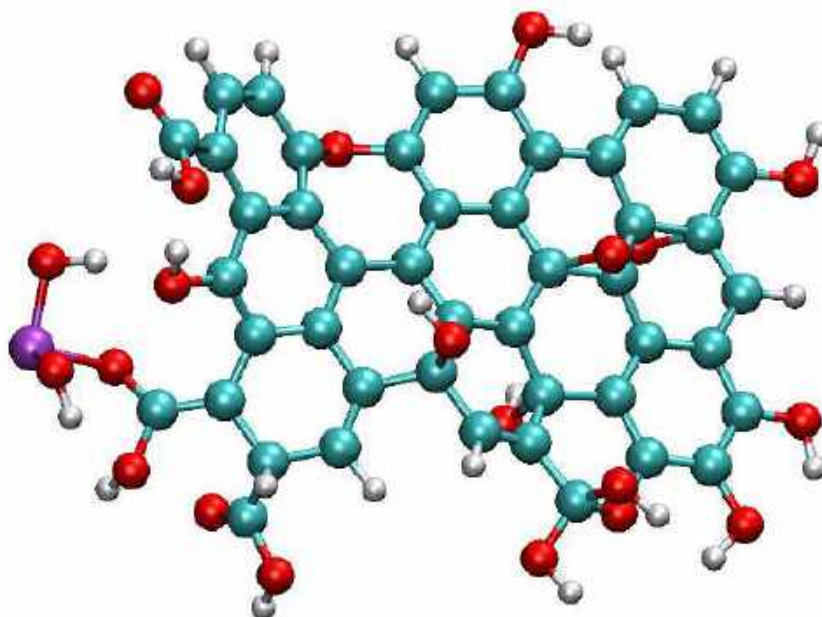


**Figure S24.** The optimized structure of  $\text{Mn}(\text{H}_2\text{O})_6\text{-ERGO}$ . The magenta sphere is the manganese atom, red -oxygen, cyan- carbon, and white- hydrogen.

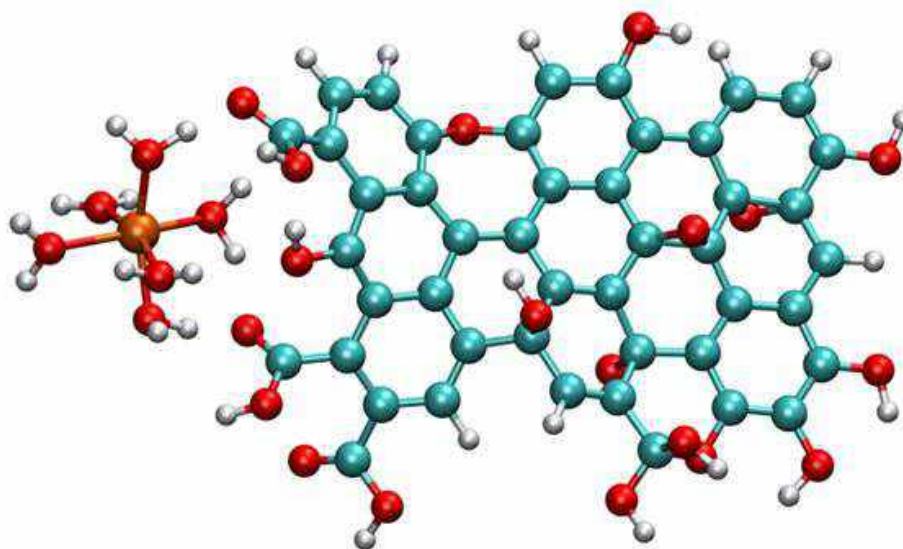


**Figure S25.** The optimized structure of  $\text{Fe}^{2+}\text{-ERGO}$ , rust-orange sphere is the iron atom; red – oxygen, cyan - carbon and white - hydrogen.

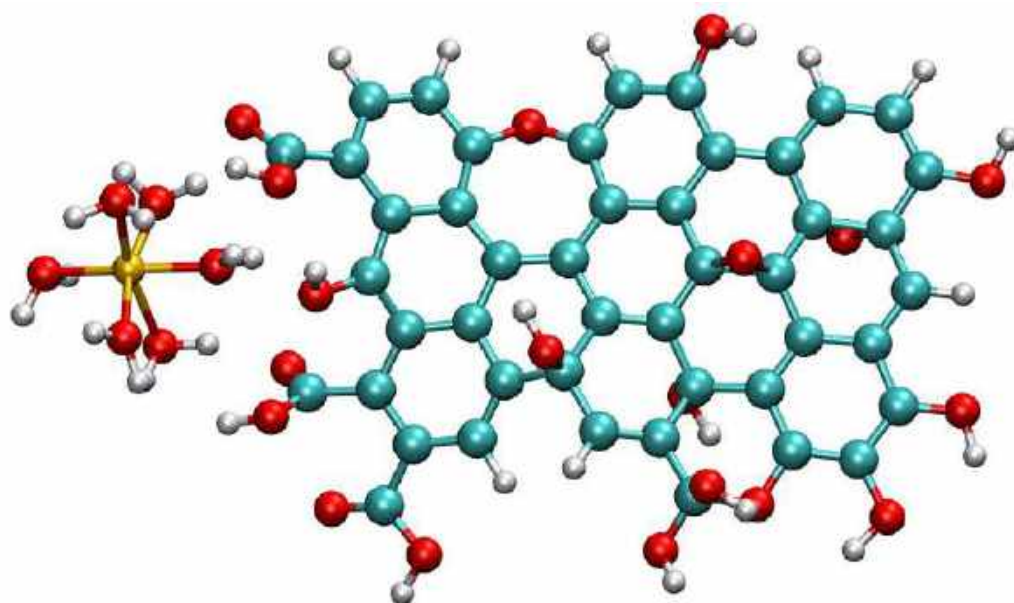


**Figure S26.** The optimized structure of Cu<sup>2+</sup>-ERGO, gold sphere is the copper atom; red – oxygen; cyan - carbon and white - hydrogen.

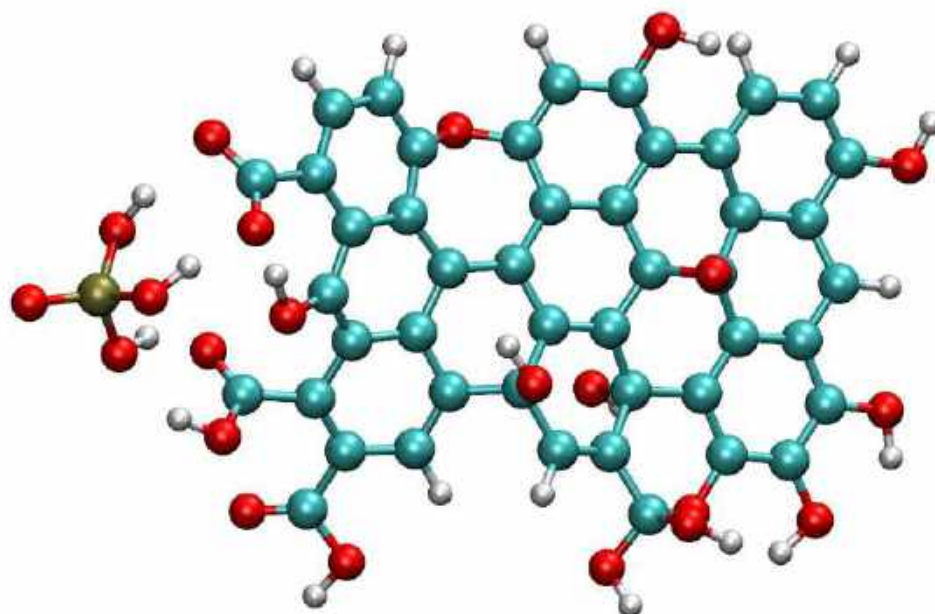


**Figure S27.** The optimized structure of H<sub>2</sub>PO<sub>4</sub>-ERGO adduct. In (c) a small structural change is observed as the H atom of the COOH group has moved its position. Brown spheres are phosphorus atoms; red - oxygen, cyan - carbon and white - hydrogen.

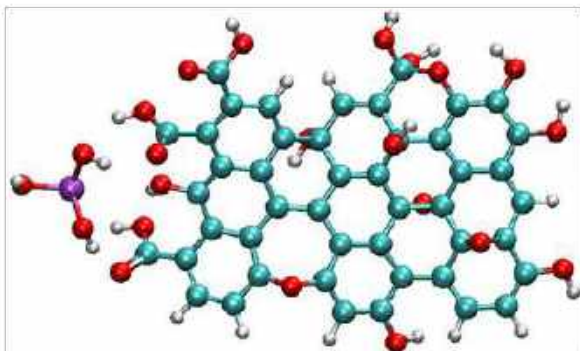
**Table S5.** The binding energies of selected analyte-ion-ERGO adducts are computed as the difference between the total adduct energy and the sum of the analyte and ERGO energies.

Analyte ion	Species	Analyte total energy/eV	Total adduct energy/eV	Total ERGO energy/eV	Binding energy/eV
Mn <sup>2+</sup>	[Mn(H <sub>2</sub> O) <sub>6</sub> ] <sup>2+</sup>	-72.110	-661.513	-582.859	-6.54
As <sup>3+</sup>	As(OH) <sub>3</sub>	-33.426	-617.064	-582.859	-0.78
Fe <sup>2+</sup>	[Fe(H <sub>2</sub> O) <sub>6</sub> ] <sup>2+</sup>	-32.927	-620.215	-582.859	-4.43
Cu <sup>2+</sup>	[Cu(H <sub>2</sub> O) <sub>6</sub> ] <sup>2+</sup>	-66.301	-655.560	-582.859	-6.39
Phosphate	HPO <sub>4</sub> <sup>-</sup>	-34.465	-625.719	-582.859	-8.39

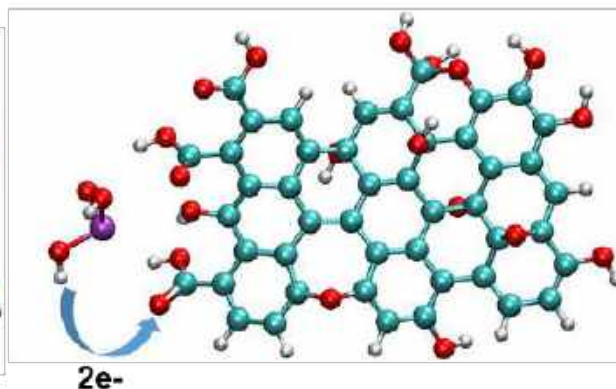
#### **S24. Methodology of arsenite oxidation mechanism at COOH group of ERGO**

We investigated the oxidation mechanism of arsenite with ERGO using universal force field<sup>16</sup> (UFF) simulations based on the starting structure of isomer 2, by reorienting the  $\text{As}(\text{OH})_3$  and then manually introducing an As-O bond at the ketone O atom followed by a force-field optimization. We then sequentially modified and optimized the geometry to generate a series of intermediate structures, starting from the approach and the covalent binding of  $\text{As}(\text{OH})_3$  (steps 1 and 2 in Figure S28(b) and (c)) to the regeneration of COOH (steps 3 and 4, in Figure S28(d) and (e)) and final detachment of  $\text{HAsO}_4^-$  with a regenerated COOH group and conversion of COH to CH (Figure S28 (f)). We also cut out a cluster of atoms from the structure of isomer 2 containing only the arsenite and the COOH1 and OH1 groups and their two neighbouring benzene rings, and performed a similar stepwise structure optimization for the intermediate structures, and these are shown in Figure 5 in the manuscript.

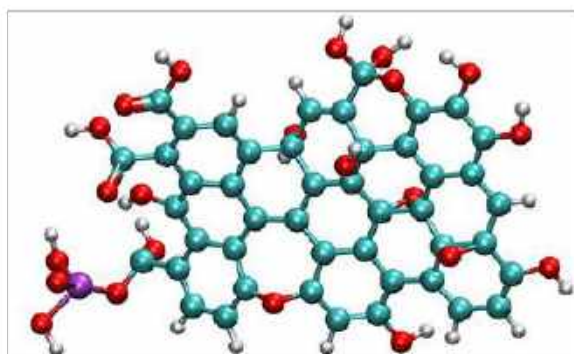
(a) Initial state:  $\text{As}(\text{OH})_3$  close to COOH group – label COOH and OH



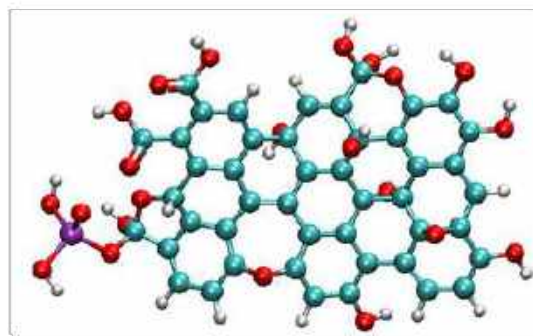
(b) Step 1: Approach of As towards ketone O



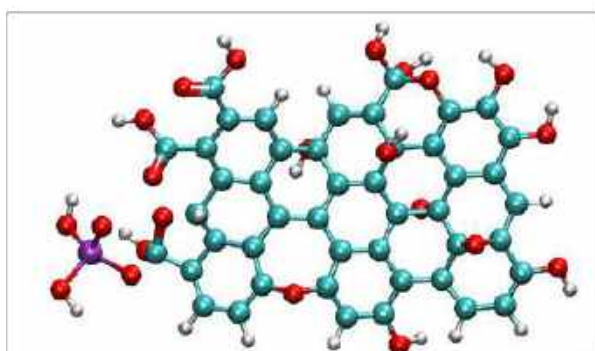
(c) Step 2: Covalent binding to ketone O  
 $\text{C}=\text{O}$  goes to  $\text{C}-\text{O}$  and  $\text{C}(\text{COOH})$  becomes  $\text{sp}^3$



(d) Step 3: OH group O forms bridge to COOH1 C atom  
 $\text{O}(\text{OH})$  to  $\text{O}(\text{COC})$  bridging to  $\text{sp}^3$  carbon of initial COOH



(e) Step 4: Detachment of  $\text{H}_2\text{AsO}_4^{2-}$  and regeneration of COOH



(f) Final state:  $\text{H}_2\text{AsO}_4^{2-}$  with regenerated COOH1 and OH1 converted to H

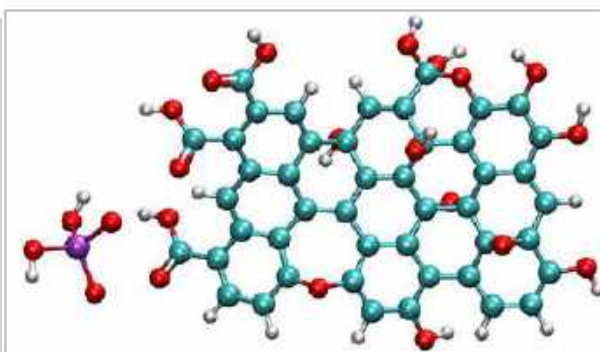


**Figure S28.** Mechanism of arsenite oxidation, showing the full ERGO sheet. The orientation of the ERGO sheet has been rotated  $180^\circ$  anticlockwise about a horizontal axis in the plane of the page, compared to that in of both Figure 5 and Figure S22 to show the COOH1 group active site clearly. (a) The initial state in the configuration of isomer 2, (b) Step 1, approach of  $\text{As}^{3+}$  and electron transfer to COOH1 group of ERGO. (c) Step 2, Covalent binding of As to ketone



O to form intermediate  $\text{As}^{5+}$  species, (d) Step 3, regeneration intermediate step where the oxygen atom of the hydroxyl group binds to the initial COOH1 carbon. (e) Step 4, detachment of  $\text{H}_2\text{AsO}_4^{1-}$ . (f) Final state of  $\text{As}^{5+}$  with COOH group restored with loss of OH oxygen atom from ERGO. Double bonds of  $\text{C}=\text{O}$  are explicitly shown here for clarity in this figure. Atomic colors are violet for arsenic, cyan for carbon, red for oxygen and white for hydrogen.

## S25. Methodology of ion-selectivity mechanism

To understand the ion-selectivity mechanism occurring via electron transfer from analyte species to ERGO, we conducted a frontier orbital energy-level analysis of ERGO model and analyte ions. The analyte species considered were,  $\text{As(OH)}_3$ ,  $\text{HAsO}_4$ ,  $[\text{Mn(H}_2\text{O)}_6]^{2+}$ ,  $[\text{Fe(H}_2\text{O)}_6]^{2+}$ ,  $[\text{Cu(H}_2\text{O)}_6]^{2+}$ ,  $\text{H}_2\text{PO}_4^-$ ,  $\text{HPO}_4^{2-}$ ,  $\text{SO}_4^{2-}$ , and  $\text{NO}_3^-$ . The values of the HOMO and LUMO levels for all the analyte ions and ERGO models 1, ERGO(6)<sup>+</sup> were after geometry optimization in GPAW. The ERGO sheet model 1 was optimized in the +1 charge state, and this model referred was to as ERGO(6)<sup>+</sup>. We computed the acceptor energy level (LUMO) of the neutral and positively charged charge states of ERGO models 1, 2 and 3, and the results are shown in Table S6 below. We also computed the donor level, which is the HOMO of each analyte species, and results are shown graphically in Figure 6 in the manuscript and tabulated below in Table S7.

**Table S6.** LUMO acceptor level and HOMO energies for the neutral and positively charged (denoted by affix "+" to the model number) ERGO models 1, 2 and 3 and their band gaps. The neutral model 3 has an unpaired spin, hence, the band gap,  $E_{\text{gap}}$ , is slightly larger than in the other models.

<b>ERGO model</b>	<b>Model type and oxygen-carbon ratio</b>	<b>Charge</b>	<b>LUMO/eV</b>	<b>HOMO/eV</b>	<b><math>E_{\text{gap}}</math>/eV</b>
Model 1 (ERGO)	rectangular sheet $N_{\text{Oxygen}}/N_{\text{Carbon}}=0.6$	0	-3.71	-3.89	0.18
Model 1 <sup>+</sup> (ERGO <sup>+</sup> or ERGO6)	rectangular sheet, ERGO <sup>+</sup> $N_{\text{Oxygen}}/N_{\text{Carbon}}=0.6$	+1	-6.36	-6.53	0.17
Model 2	rectangular sheet $N_{\text{Oxygen}}/N_{\text{Carbon}}=0.3$	0	-3.71	-3.99	0.28
Model 2 <sup>+</sup>	rectangular sheet $N_{\text{Oxygen}}/N_{\text{Carbon}}=0.3$	+1	-5.88	-5.99	0.11
Model 3	hexagonal flake $N_{\text{Oxygen}}/N_{\text{Carbon}}=0.3$	0	-3.51	-4.21	0.7*
Model 3 <sup>+</sup>	hexagonal flake $N_{\text{Oxygen}}/N_{\text{Carbon}}=0.3$	+1	-6.25	-6.43	0.18

**Table S7.** Analyte ion donor-level (HOMO) energies and donor-acceptor energy level differences,  $\Delta E_{DA} = E_{\text{HOMO}}(\text{Analyte}) - E_{\text{LUMO}}(\text{ERGO}(6)^+)$ , where the acceptor level energy is  $E_{\text{LUMO}}(\text{ERGO}(6)^+) = -6.36$  eV. ERGO<sup>+</sup> is the optimized geometry of model 1 (ERGO) in the positive charge state.

Analyte ion	Species	HOMO energy ( $E_{\text{HOMO}}$ ) /eV	$\Delta E_{DA}$ /eV
As <sup>3+</sup>	As(OH) <sub>3</sub>	-6.35	0.01
Mn <sup>2+</sup>	[Mn(H <sub>2</sub> O) <sub>6</sub> ] <sup>2+</sup>	-3.52	2.84
Fe <sup>2+</sup>	[Fe(H <sub>2</sub> O) <sub>6</sub> ] <sup>2+</sup>	-10.33	-3.97
Cu <sup>2+</sup>	[Cu(H <sub>2</sub> O) <sub>6</sub> ] <sup>2+</sup>	-14.56	-14.56
Phosphate	HPO <sub>4</sub> <sup>-</sup>	-0.5	5.86
As <sup>5+</sup>	HAsO <sub>4</sub> <sup>2-</sup>	6.17	12.53
Sulfate	SO <sub>4</sub> <sup>2-</sup>	6.83	13.18
Phosphate	H <sub>2</sub> (PO <sub>4</sub> ) <sup>2-</sup>	6.90	13.26
Nitrate	NO <sub>3</sub> <sup>-</sup>	11.54	17.54

## S26. Atomic coordinates of the optimized structures

All coordinates in XYZ file format in Angstroms and the optimization method is indicated.

### (a) Non-covalently bound As(OH)<sub>3</sub>-ERGO adduct isomers 1 to 6

All geometries were optimized using NWChem at B3LYP/6-31G\* level

#### Isomer 1:

92

C	-0.29887	-0.37517	0.97869
C	0.84738	-1.07854	0.79955
C	2.14422	-0.38256	0.76262
C	3.34529	-1.03843	0.26396
C	4.52101	-0.30829	0.11645
C	5.78598	-0.95585	-0.08089
C	6.95294	-0.21236	-0.17665
C	-0.34383	1.06202	0.93450
C	0.74036	1.86098	0.65247
C	2.05212	1.16979	0.68508
C	3.22303	1.83826	0.07991
C	4.51646	1.13065	0.15510
C	5.68672	1.86534	0.06823
C	6.90805	1.18686	-0.06530
C	-0.43780	4.10060	0.61844
C	0.74755	3.33839	0.52427
C	1.96453	4.07790	0.36241
C	3.18781	3.34417	0.01469
C	4.43902	4.07915	0.01201
C	5.73192	3.35311	0.32146
C	6.92081	3.97891	-0.37178
C	-0.37349	5.47067	0.86051
C	0.83813	6.12422	0.84356
C	2.03901	5.50347	0.43337
C	3.25524	6.25026	0.09728
C	4.42137	5.44882	-0.12305
C	5.64843	6.09915	-0.73335
C	6.87347	5.23669	-0.80546
C	-0.04385	9.30327	0.26971
C	1.02051	8.44604	0.43896
C	2.31727	8.68130	-0.09554
C	3.38699	7.71006	-0.03550
C	4.70959	8.28389	-0.09493
C	5.87535	7.46834	-0.15534
C	7.11590	7.98266	0.11824
C	0.12766	10.47048	-0.48082
C	1.38012	10.84690	-0.93094
C	2.53930	10.02842	-0.59834
C	3.85460	10.53738	-0.51502
C	4.92201	9.70026	-0.09698
C	6.21908	10.23165	0.21017
C	7.28721	9.36412	0.39154
O	0.93007	-2.42624	0.63203
H	3.32912	-2.10683	0.09272



O	5.82678	-2.30575	-0.14404
C	1.33579	12.05872	-1.78316
O	4.17432	11.82440	-0.75017
C	6.40280	11.71332	0.46677
H	-1.24139	-0.90771	1.08939
H	-1.30935	1.48989	1.16614
O	8.13165	-0.88976	-0.33632
O	8.10933	1.81679	-0.02382
O	-1.69986	3.58218	0.53662
H	-1.28280	6.01749	1.08111
C	8.22838	3.20924	-0.52973
H	7.72659	5.67240	-1.31618
H	-0.99397	9.05582	0.72884
H	-0.71643	11.11028	-0.71008
H	7.98826	7.34246	0.12889
C	8.61799	9.86856	0.83184
H	0.03437	-2.79301	0.55251
H	6.75894	-2.57387	-0.24550
O	0.42646	12.86024	-1.83558
O	2.41122	12.19611	-2.64250
H	2.22951	13.00394	-3.16021
H	3.64117	12.17558	-1.49266
O	6.02963	12.26052	1.47542
O	7.03768	12.33364	-0.54810
H	7.18072	13.25197	-0.24800
H	8.85131	-0.23264	-0.33723
H	7.94365	2.89344	-2.42881
H	-1.66711	2.77734	-0.00577
O	8.68493	3.12781	-1.83108
O	9.21063	3.78925	0.23225
H	10.06259	3.46877	-0.11492
O	8.85981	10.99383	1.21659
O	9.57937	8.90979	0.77794
H	10.39261	9.33979	1.09907
O	2.36495	0.50295	1.89913
O	2.96818	2.44664	-1.19513
O	0.82846	7.41592	1.32149
O	5.35653	6.30378	-2.16256
H	4.49210	6.74303	-2.23174
O	5.87847	3.55127	1.76347
H	6.65955	3.04589	2.05391
As	5.88367	3.14794	-3.91989
O	4.17313	3.50280	-3.51833
O	6.28088	4.81701	-4.43434
O	5.77187	2.45886	-5.56711
H	5.38770	3.13682	-6.15432
H	5.87229	5.41925	-3.77256
H	3.86910	2.96373	-2.76352

### Isomer 2:

92

C	0.42181	-0.78880	0.52151
C	1.67326	-1.30753	0.60469
C	2.84237	-0.41873	0.70213
C	4.18779	-0.90998	0.45707
C	5.25137	-0.01320	0.38024

C	6.61301	-0.46210	0.41230
C	7.65914	0.44231	0.31361
C	0.17100	0.61393	0.33201
C	1.15505	1.55870	0.15366
C	2.53292	1.09828	0.45258
C	3.67162	1.88888	-0.04975
C	5.02857	1.40116	0.23837
C	6.08348	2.29934	0.15375
C	7.39157	1.81449	0.19747
C	-0.33111	3.57930	-0.17970
C	0.95710	3.00958	-0.06811
C	2.05376	3.92844	-0.08335
C	3.40847	3.38603	-0.25143
C	4.52463	4.30708	-0.14472
C	5.88709	3.79334	0.27026
C	7.01167	4.55560	-0.38994
C	-0.51439	4.93848	0.05752
C	0.57091	5.76831	0.23459
C	1.89996	5.34964	-0.00406
C	3.02402	6.27427	-0.18022
C	4.31757	5.65794	-0.28405
C	5.48707	6.49162	-0.78378
C	6.82839	5.81173	-0.77942
C	-0.68487	8.88926	-0.18791
C	0.45417	8.13186	-0.00823
C	1.75541	8.55299	-0.39652
C	2.95253	7.74098	-0.27199
C	4.18453	8.49764	-0.20906
C	5.46226	7.86199	-0.16793
C	6.58694	8.54967	0.20821
C	-0.60162	10.15663	-0.77534
C	0.62792	10.67839	-1.12160
C	1.83569	9.93853	-0.82446
C	3.07105	10.59968	-0.71189
C	4.20242	9.92929	-0.20956
C	5.37344	10.64229	0.22429
C	6.53144	9.93947	0.49947
O	1.97658	-2.63439	0.58758
H	4.35419	-1.97651	0.38508
O	6.86068	-1.78580	0.55918
C	0.56704	12.01273	-1.76324
O	3.19949	11.92668	-0.99920
C	5.23819	12.12107	0.51335
H	-0.43636	-1.45809	0.53167
H	-0.87275	0.89514	0.36497
O	8.93946	-0.05446	0.35480
O	8.48289	2.65199	0.17784
O	-1.46667	2.86844	-0.44648
H	-1.51950	5.33486	0.14495
C	8.33863	3.86300	-0.62976
H	7.63139	6.36936	-1.24901
H	-1.62887	8.49219	0.16706
H	-1.49746	10.74356	-0.94728
H	7.53997	8.04228	0.28633
C	7.71462	10.63645	1.07329
H	1.16913	-3.14234	0.40605
H	7.82599	-1.90535	0.60772
O	-0.16729	12.92746	-1.43887

O	1.36562	12.13187	-2.87923
H	1.20382	13.03108	-3.22770
H	2.86943	12.08916	-1.90491
O	4.57238	12.50871	1.45824
O	5.83312	12.91015	-0.37822
H	5.53004	13.83466	-0.18694
H	9.54686	0.69774	0.45476
H	8.97201	2.68250	-2.02524
H	-1.22007	2.06958	-0.93950
O	8.40727	3.47326	-1.97362
O	9.38293	4.69012	-0.26600
H	10.15687	4.44216	-0.79875
O	7.71219	11.75839	1.53452
O	8.83477	9.86896	1.05058
H	9.53103	10.41131	1.46525
O	2.73738	0.58054	1.75737
O	3.51337	2.42077	-1.36403
O	0.28285	7.00927	0.75472
O	5.28809	6.66939	-2.22104
H	4.41716	7.08378	-2.34189
O	5.89867	4.10572	1.70258
H	6.67456	3.66277	2.09136
As	2.72239	15.14463	-0.78007
O	1.50043	14.69819	0.46497
O	4.14151	15.00383	0.34666
O	2.66056	16.93431	-0.73496
H	2.87140	17.22456	0.17164
H	3.97295	14.28940	1.00560
H	0.78616	14.20087	0.02304

### Isomer 3:

92

C	-0.03892	-0.14621	0.03346
C	1.08646	-0.73953	-0.45478
C	2.38718	-0.06532	-0.29890
C	3.59251	-0.53368	-1.00362
C	4.78108	0.18198	-0.89703
C	6.04844	-0.35725	-1.30104
C	7.22053	0.33908	-1.02894
C	-0.06672	1.22770	0.46262
C	1.00872	2.08252	0.36092
C	2.30790	1.40890	0.13780
C	3.49050	2.22887	-0.24903
C	4.78371	1.50269	-0.31944
C	5.95217	2.17287	-0.02441
C	7.17051	1.56159	-0.33860
C	-0.18376	4.28621	0.76629
C	1.00750	3.55249	0.53972
C	2.21257	4.31276	0.47817
C	3.46356	3.64407	0.08176
C	4.71669	4.34781	0.32697
C	5.94837	3.53960	0.65032
C	7.21749	4.25715	0.27725
C	-0.11860	5.61793	1.16649
C	1.08779	6.28678	1.16950
C	2.28233	5.72014	0.68478

C	3.51657	6.49406	0.45326
C	4.71651	5.71499	0.27926
C	5.99174	6.38749	-0.19096
C	7.23321	5.54434	-0.06431
C	0.12231	9.39709	0.64420
C	1.22660	8.59242	0.83185
C	2.50679	8.87690	0.29255
C	3.61722	7.94268	0.36080
C	4.92606	8.56431	0.31786
C	6.12190	7.78957	0.34852
C	7.32910	8.37507	0.64045
C	0.24747	10.56382	-0.11279
C	1.48346	10.99036	-0.57276
C	2.67807	10.22366	-0.22910
C	3.98062	10.77005	-0.17731
C	5.07920	9.98937	0.26573
C	6.34334	10.58544	0.59006
C	7.44209	9.77108	0.83593
O	1.13186	-1.94187	-1.08872
H	3.55630	-1.47624	-1.53464
O	6.08388	-1.56037	-1.93171
C	1.39076	12.17410	-1.46205
O	4.25486	12.06184	-0.44576
C	6.46259	12.07806	0.80423
H	-0.98180	-0.68999	0.02077
H	-1.01188	1.56378	0.87071
O	8.40711	-0.24824	-1.39017
O	8.38780	2.08360	0.03277
O	-1.44550	3.77382	0.63786
H	-1.02618	6.13275	1.46026
C	8.50200	3.47460	0.42853
H	8.16245	6.00165	-0.38113
H	-0.81624	9.11356	1.10760
H	-0.62353	11.16671	-0.34521
H	8.23166	7.78118	0.71696
C	8.74290	10.34107	1.28711
H	0.22554	-2.25951	-1.23117
H	7.01410	-1.78352	-2.09977
O	0.39003	12.88232	-1.53281
O	2.46010	12.37448	-2.26631
H	2.32524	13.16900	-2.87710
H	3.66868	12.39461	-1.16380
O	6.03594	12.64389	1.77913
O	7.12436	12.68475	-0.20341
H	7.21897	13.62056	0.06847
H	9.12194	0.38289	-1.20480
H	10.32407	4.00306	0.22201
H	-1.41632	3.04589	-0.00703
O	9.51329	4.04914	-0.31720
O	8.86003	3.40423	1.80197
H	9.12539	2.47823	1.96854
O	8.93738	11.47887	1.66566
O	9.74520	9.42208	1.26318
H	10.53440	9.88864	1.60194
O	2.63444	0.37485	1.06502
O	3.29867	3.12060	-1.35541
O	1.07381	7.55060	1.71687
O	5.87975	6.51411	-1.64290

H	5.10756	7.07949	-1.82645
O	5.89259	3.36001	2.09560
H	6.77555	3.06328	2.38898
As	0.67066	14.87605	-4.79550
O	0.47653	13.14214	-5.32954
O	2.30046	14.44490	-4.00897
O	-0.25210	14.97127	-3.29870
H	-0.07306	14.22692	-2.67414
H	2.85070	14.10163	-4.74095
H	-0.30446	13.04351	-5.89644

**Isomer 4:**

92

C	-0.25497	0.18117	0.49210
C	0.88416	-0.55035	0.59324
C	2.19241	0.11743	0.68649
C	3.43080	-0.60746	0.45987
C	4.63649	0.08655	0.37625
C	5.89811	-0.59436	0.41739
C	7.08737	0.10919	0.30500
C	-0.25202	1.60173	0.27272
C	0.88583	2.35226	0.08305
C	2.15703	1.66252	0.40728
C	3.42110	2.23144	-0.09264
C	4.66783	1.51569	0.21440
C	5.86525	2.21237	0.12099
C	7.06700	1.50575	0.17045
C	-0.21967	4.58433	-0.35185
C	0.94761	3.80865	-0.17719
C	2.18581	4.52630	-0.17611
C	3.42651	3.75155	-0.31374
C	4.68516	4.46161	-0.19883
C	5.93329	3.71761	0.22670
C	7.17798	4.26894	-0.42749
C	-0.17371	5.96316	-0.16991
C	1.02968	6.60242	0.03260
C	2.27805	5.95519	-0.12163
C	3.55567	6.66461	-0.24064
C	4.71990	5.82820	-0.32602
C	6.02969	6.45756	-0.77311
C	7.22459	5.54439	-0.79399
C	0.40614	9.87542	-0.60562
C	1.36993	8.95080	-0.26598
C	2.76373	9.14592	-0.48179
C	3.76481	8.12309	-0.27855
C	5.10740	8.63080	-0.09037
C	6.23658	7.76329	-0.05937
C	7.44853	8.18997	0.41609
C	0.77760	11.08365	-1.20069
C	2.11506	11.41779	-1.32732
C	3.13504	10.51194	-0.81525
C	4.41779	10.94912	-0.43174
C	5.37468	10.02956	0.06102
C	6.63578	10.46593	0.59225
C	7.63735	9.53480	0.82612
O	0.94598	-1.91014	0.59928



H	3.40620	-1.68738	0.40178
O	5.90876	-1.93927	0.58285
C	2.34329	12.65625	-2.08794
O	4.77951	12.25542	-0.44876
C	6.83766	11.90858	1.00465
H	-1.21837	-0.32502	0.50775
H	-1.22912	2.06564	0.28983
O	8.26009	-0.60566	0.35156
O	8.29016	2.13639	0.13437
O	-1.45007	4.06820	-0.64047
H	-1.09676	6.53079	-0.14798
C	8.35369	3.34713	-0.68240
H	8.11509	5.96028	-1.25289
H	-0.63351	9.64599	-0.40297
H	0.00756	11.75870	-1.55631
H	8.28424	7.50490	0.47814
C	8.92374	9.93676	1.46086
H	0.06207	-2.26874	0.41758
H	6.83802	-2.22593	0.63404
O	1.53946	13.55981	-2.27029
O	3.55988	12.72998	-2.72580
H	3.54288	13.57007	-3.22431
H	4.56682	12.63914	-1.32234
O	6.36558	12.38236	2.00901
O	7.61590	12.58761	0.13560
H	7.74974	13.46715	0.53714
H	8.99143	0.02878	0.43785
H	8.71918	2.05283	-2.07242
H	-1.32833	3.21485	-1.08718
O	8.32962	2.94309	-2.02450
O	9.53831	3.97247	-0.34570
H	10.23458	3.60769	-0.91680
O	9.15893	11.01086	1.97434
O	9.85080	8.94375	1.42880
H	10.63287	9.30492	1.88543
O	2.25657	1.13983	1.72198
O	3.37206	2.76824	-1.41293
O	0.92254	7.89810	0.48196
O	5.89904	6.75361	-2.19650
H	5.11504	7.31798	-2.30336
O	5.99082	4.03248	1.65813
H	6.65678	3.44474	2.05853
As	-2.04404	14.12244	-2.51335
O	-0.87087	14.68045	-1.26478
O	-3.38892	14.97620	-1.67617
O	-2.32471	12.42360	-1.92034
H	-2.59941	12.46659	-0.98612
H	-3.00263	15.36303	-0.86865
H	0.02313	14.34599	-1.48657

**Isomer 5:**

92

C	0.70027	-0.70103	1.10266
C	1.93033	-1.25851	0.95842
C	3.12506	-0.40661	0.84511
C	4.39046	-0.93763	0.36695
C	5.45156	-0.07215	0.10590
C	6.78415	-0.56158	-0.09902
C	7.82543	0.31247	-0.37415
C	0.46276	0.70866	0.95578
C	1.42748	1.62335	0.59753
C	2.82229	1.12021	0.65059
C	3.88032	1.87787	-0.04371
C	5.25199	1.34895	0.00735
C	6.30401	2.21671	-0.25830
C	7.58501	1.69333	-0.43956
C	-0.03689	3.69175	0.49736
C	1.23560	3.08061	0.39950
C	2.34055	3.96371	0.18775
C	3.63087	3.38077	-0.20467
C	4.77646	4.26912	-0.29187
C	6.17362	3.71434	-0.10660
C	7.19764	4.45243	-0.93873
C	-0.13530	5.06202	0.73597
C	0.99087	5.84714	0.71170
C	2.24414	5.38792	0.27470
C	3.34906	6.27585	-0.08503
C	4.58899	5.62482	-0.39498
C	5.68355	6.43615	-1.07155
C	6.98862	5.71990	-1.28910
C	-0.29570	8.87029	0.19756
C	0.87694	8.17477	0.34975
C	2.12399	8.58259	-0.18091
C	3.30448	7.74522	-0.17602
C	4.54927	8.47211	-0.27466
C	5.79427	7.79667	-0.43737
C	6.98203	8.44248	-0.21071
C	-0.28489	10.07027	-0.52670
C	0.90989	10.63164	-0.95046
C	2.16857	9.96394	-0.63561
C	3.41459	10.62653	-0.54552
C	4.59329	9.90214	-0.21715
C	5.83868	10.56601	0.05084
C	7.00845	9.82157	0.12281
O	2.18341	-2.59339	0.88744
H	4.50889	-2.00788	0.26601
O	7.01279	-1.89373	-0.00061
C	0.70494	11.84734	-1.77777
O	3.56314	11.95878	-0.68938
C	5.86807	12.04276	0.38796
H	-0.16184	-1.34361	1.26928
H	-0.54834	1.02190	1.17420
O	9.07839	-0.22244	-0.55484
O	8.68361	2.49782	-0.64238
O	-1.22441	3.01943	0.43788
H	-1.09849	5.49292	0.98388
C	8.44416	3.72369	-1.40237

H	7.71931	6.26029	-1.88084
H	-1.20446	8.48818	0.64827
H	-1.20965	10.59078	-0.74659
H	7.92060	7.90976	-0.28853
C	8.29811	10.46001	0.50665
H	1.34143	-3.07487	0.85426
H	7.96769	-2.04236	-0.11897
O	-0.32062	12.49347	-1.84570
O	1.77592	12.18259	-2.58182
H	1.48757	12.96807	-3.08389
H	2.98432	12.29196	-1.40402
O	5.49189	12.48395	1.44901
O	6.36802	12.79042	-0.61822
H	6.44861	13.69482	-0.25993
H	9.71643	0.51057	-0.55716
H	8.79734	2.54587	-2.89504
H	-1.09202	2.20478	-0.07185
O	8.27555	3.35257	-2.74257
O	9.55960	4.51537	-1.21095
H	10.22861	4.24608	-1.86153
O	8.43173	11.58054	0.94731
O	9.36125	9.63378	0.32954
H	10.13639	10.13997	0.63342
O	3.23588	0.59150	1.90075
O	3.51277	2.41333	-1.31491
O	0.83779	7.12074	1.22240
O	5.26247	6.63763	-2.45708
H	4.40131	7.08594	-2.43520
O	6.42584	4.01592	1.30593
H	7.22259	3.52308	1.57150
As	-0.12655	9.17742	4.48386
O	0.55629	7.53869	4.08006
O	0.33546	8.98328	6.22570
O	-1.88344	8.81184	4.64278
H	-1.99299	8.12530	5.33732
H	0.84675	8.15300	6.27285
H	0.64085	7.44656	3.10704

### Isomer 6:

92

C	0.50719	-0.54540	0.53673
C	1.73582	-1.12542	0.50808
C	2.95176	-0.29689	0.56393
C	4.25313	-0.83761	0.21097
C	5.35158	0.01340	0.09796
C	6.68982	-0.49525	0.01510
C	7.76832	0.36429	-0.12343
C	0.31761	0.87410	0.41625
C	1.33227	1.77878	0.19870
C	2.70056	1.24455	0.39119
C	3.84255	2.00267	-0.14982
C	5.18900	1.44099	0.02974
C	6.27841	2.29448	-0.09148
C	7.56080	1.75159	-0.16237
C	-0.07784	3.86645	-0.02161

C	1.18843	3.24271	0.02966
C	2.32158	4.11636	-0.00535
C	3.63804	3.52084	-0.27136
C	4.80083	4.38285	-0.19080
C	6.15983	3.78684	0.10956
C	7.27697	4.53502	-0.57914
C	-0.19549	5.22886	0.23781
C	0.92725	6.01029	0.39885
C	2.23403	5.54054	0.12929
C	3.39881	6.41681	-0.02449
C	4.65186	5.74750	-0.23180
C	5.83760	6.56933	-0.71155
C	7.13524	5.82456	-0.86287
C	-0.15164	9.18857	-0.04473
C	0.94399	8.39183	0.20240
C	2.28463	8.78387	-0.07475
C	3.41718	7.89116	0.01542
C	4.69125	8.55853	0.16343
C	5.92198	7.84634	0.07581
C	7.09582	8.39937	0.51425
C	0.02901	10.45922	-0.59882
C	1.29805	10.98171	-0.76599
C	2.45579	10.20263	-0.34944
C	3.69391	10.78378	0.00183
C	4.78567	9.96893	0.39108
C	6.00990	10.53402	0.88605
C	7.13464	9.73011	1.00542
O	1.97602	-2.46070	0.41002
H	4.36259	-1.90636	0.08596
O	6.88545	-1.83521	0.08923
C	1.28901	12.29050	-1.45900
O	3.89464	12.11839	0.04998
C	6.05068	11.96247	1.38547
H	-0.38438	-1.16656	0.58121
H	-0.70677	1.20198	0.53422
O	9.02429	-0.19067	-0.19707
O	8.68937	2.53929	-0.22955
O	-1.25020	3.20975	-0.26100
H	-1.17981	5.66727	0.35480
C	8.54162	3.79314	-0.96314
H	7.93243	6.38016	-1.34499
H	-1.13656	8.81345	0.20885
H	-0.82294	11.06232	-0.89139
H	8.01487	7.82816	0.48477
C	8.39254	10.25663	1.60382
H	1.14280	-2.93248	0.23010
H	7.84552	-1.99628	0.06594
O	0.33088	13.02462	-1.58046
O	2.47796	12.61844	-2.08633
H	2.30872	13.47411	-2.52552
H	3.50354	12.54202	-0.74185
O	5.57518	12.31004	2.43881
O	6.69222	12.78761	0.53154
H	6.73377	13.65093	0.98490
H	9.67110	0.52955	-0.10964
H	8.96354	2.63427	-2.45315
H	-1.05092	2.39116	-0.74349
O	8.48251	3.47042	-2.32705

O	9.65488	4.55090	-0.65511
H	10.35988	4.29894	-1.27458
O	8.51616	11.31360	2.18753
O	9.43874	9.40292	1.44800
H	10.19201	9.83403	1.89217
O	2.96131	0.66384	1.65874
O	3.63115	2.60204	-1.42680
O	0.68959	7.25913	0.92540
O	5.57652	6.93037	-2.10193
H	4.71758	7.38463	-2.12477
O	6.27351	4.02337	1.55297
H	7.02176	3.48963	1.87616
As	-1.12946	-4.29461	-0.21634
O	-1.75257	-5.24708	-1.62528
O	-1.80858	-5.46801	0.95178
O	-2.34400	-2.98598	-0.05192
H	-3.21075	-3.36105	0.18958
H	-2.16828	-6.21703	0.44223
H	-1.35151	-4.93484	-2.45359

### (b) Covalently bonded As(OH)<sub>3</sub>-ERGO model

Geometry was optimized using GPAW at GGA-LCAO basis level and atomic positions are in Angstroms.

91

C	12.1677668600	9.0251289400	17.6885076800
C	13.4053704300	8.4516831400	17.5057732800
C	14.6181720900	9.2928537800	17.4028667800
C	15.8915886100	8.7475741500	16.9321399400
C	16.9697034700	9.6179303000	16.6817014000
C	18.3093981300	9.1237747800	16.4810008700
C	19.3644328400	10.0028629000	16.2004435700
C	11.9461727900	10.4438310100	17.5767685600
C	12.9327092600	11.3571578800	17.2031791400
C	14.3260427100	10.8283557100	17.2256398000
C	15.3940655400	11.5856903100	16.5230990800
C	16.7729064100	11.0499569500	16.5725701500
C	17.8390473400	11.9214224800	16.3123835300
C	19.1351426300	11.3940772900	16.1317715900
C	11.4896357600	13.4473613200	17.1958160300
C	12.7636087000	12.8178706100	17.0499705000
C	13.8806801100	13.6964030800	16.8286807000
C	15.1576754000	13.1013069800	16.3959467400
C	16.3178191900	13.9790751300	16.2869490600
C	17.7209726500	13.4263117900	16.4326425700
C	18.7072803200	14.1360498000	15.5320096600
C	11.4173629200	14.8161597200	17.4937948000
C	12.5614780300	15.6066501900	17.4512582400
C	13.8046397600	15.1323401400	16.9401484400
C	14.9047383500	16.0104020200	16.5200405200
C	16.1258995700	15.3472927800	16.1477764400
C	17.1709294600	16.1234170100	15.3516769500
C	18.4523610300	15.3735536200	15.0765267900
C	11.2889060900	18.7130875500	17.0789533000
C	12.4625988800	17.9483406000	17.1324971900



C 13.6698357600 18.3208555900 16.4805460900  
C 14.8750223900 17.4853279300 16.4239107900  
C 16.1035184700 18.2010495300 16.2339357100  
C 17.3620507000 17.5140237900 15.9208814700  
C 18.5572181300 18.1572265200 15.8402429300  
C 11.2626066200 19.8737108800 16.2982261200  
C 12.4362344900 20.3554163800 15.6887561400  
C 13.6960477300 19.6649645500 15.9240891300  
C 14.9730872200 20.3140675500 15.8461055200  
C 16.1561768700 19.6408269100 16.2161939600  
C 17.4318964800 20.3386058200 16.4190017200  
C 18.7412365800 19.6255347000 16.1216404000  
O 13.6359547800 7.1042406900 17.3859506600  
H 16.0163109500 7.6546196700 16.8483356700  
O 18.5588037200 7.7821385600 16.5870308500  
C 12.1787627700 21.5115747400 14.7951607900  
O 15.0816603900 21.6428368100 15.4900076600  
C 17.5156667600 21.5749245200 17.0263850500  
H 11.2922469400 8.3665124600 17.8625970500  
H 10.9286176100 10.7766363900 17.8501212600  
O 20.6157641500 9.4384893400 16.0130335200  
O 20.2407877100 12.1971167400 15.9166591500  
O 10.2880075600 12.7881277700 17.1134193000  
H 10.4497914300 15.2667167400 17.7780985600  
C 19.9682840000 13.4016743000 15.0995662400  
H 19.1645179400 15.8596610000 14.3830514700  
H 10.4017995600 18.3584771800 17.6351238500  
H 10.3287465100 20.4458540200 16.1414529400  
H 19.4665925100 17.6021005600 15.5414200100  
C 19.7805251000 19.7288276900 17.2628634600  
H 12.7590249000 6.6524983800 17.3644108800  
H 19.5327253000 7.6735925000 16.4440099300  
O 11.1662389400 22.2100323700 14.7791981700  
O 13.1697212500 21.7267465200 13.8093589400  
H 12.8283598900 22.5181802700 13.3163133900  
H 14.4621225600 21.7948116800 14.7059199500  
O 16.5637208200 22.1331211900 17.7832772600  
O 18.7141934500 22.2850630100 16.9240759800  
H 21.2487228600 10.1951762600 15.9424466800  
H 20.4342863600 12.2448462500 13.6138661700  
H 10.4673779400 11.9237782000 16.6674316400  
O 19.7858072900 12.9769648500 13.7636899200  
O 21.0746131000 14.2360681000 15.2713306000  
H 21.8194431700 13.8231873200 14.7700181100  
O 19.5804533700 20.0220337200 18.4366844600  
O 21.0199911800 19.3936007600 16.7750031600  
H 21.6137924300 19.4113648600 17.5682545100  
O 14.7450414100 10.2839854400 18.4926202400  
O 15.0112527600 12.1501443300 15.2465777000  
O 12.4232598100 16.8729546300 18.0048822000  
O 16.6160886700 16.2833837800 13.9992672300  
H 15.8120809000 16.8471087600 14.1150386500  
O 18.1781063900 13.7782706900 17.7960783000  
H 17.6136155500 13.2377497000 18.4035666600  
As 16.0802972400 23.9969795300 17.5436022500  
O 14.3735845900 23.6419806700 17.1942134000  
O 16.6412965400 24.2032287100 15.8218255600  
H 17.6024087500 23.9501117800 15.8155410200

H 14.4478124600 22.8606232300 16.5539830400  
H 19.2645631700 20.0669711800 15.2314524200  
H 19.0113216100 22.4730159100 17.8509776900

**(c)Analyte-ERGO adducts for selected analyte ions**

All geometries were optimized using GPAW with a DZP basis set and a GGA-PBE functional.

**ERGO-[Mn(H<sub>2</sub>O)<sub>6</sub>]<sup>2+</sup>**

104

C	0.4082500000	-0.8237100000	0.5226400000
C	1.6500600000	-1.3054500000	0.6008700000
C	2.8002500000	-0.3857400000	0.6118100000
C	4.1906000000	-0.9411500000	0.4084900000
C	5.3157400000	0.0261200000	0.3237300000
C	6.6298100000	-0.4401400000	0.4030000000
C	7.6843400000	0.4651100000	0.3366800000
C	0.1425200000	0.6168900000	0.3737600000
C	1.1397900000	1.5305700000	0.1946300000
C	2.5384900000	1.0333700000	0.3545700000
C	3.6732400000	1.9085200000	0.0216300000
C	5.0652800000	1.4031800000	0.1792600000
C	6.1246800000	2.3021600000	0.1825200000
C	7.4273300000	1.8267700000	0.2310500000
C	-0.3386600000	3.5752700000	-0.0880700000
C	0.9369300000	3.0233200000	-0.0043200000
C	2.0606400000	3.9215400000	-0.0437400000
C	3.4271400000	3.3423600000	-0.1388300000
C	4.5774000000	4.2281400000	-0.3303400000
C	5.8996800000	3.7970600000	0.3159800000
C	7.0254900000	4.5554800000	-0.3419400000
C	-0.4955200000	4.8944100000	0.1330900000
C	0.5528700000	5.7753500000	0.2293400000
C	1.8896700000	5.3558700000	0.0047300000
C	3.0316900000	6.2488500000	-0.1426500000
C	4.3005000000	5.6810400000	-0.3007600000
C	5.4739600000	6.4917800000	-0.7892300000
C	6.8291800000	5.8045800000	-0.7916300000
C	-0.6687100000	8.9219100000	-0.1273000000
C	0.4381100000	8.1034600000	0.0181300000
C	1.7326900000	8.5227200000	-0.2829400000
C	2.9469100000	7.7097500000	-0.2323000000
C	4.1922400000	8.4428400000	-0.1796400000
C	5.4411100000	7.8251000000	-0.1663800000
C	6.6074800000	8.5260600000	0.2100500000
C	-0.5903700000	10.1298300000	-0.7284300000
C	0.6404100000	10.6294200000	-1.0963700000
C	1.8421300000	9.8695200000	-0.7297600000
C	3.1264300000	10.4155000000	-0.6966500000
C	4.1993000000	9.7983900000	-0.1479100000

C	5.3497500000	10.5326300000	0.2474700000
C	6.5438700000	9.8802400000	0.5111200000
O	1.8756800000	-2.6312300000	0.6255100000
H	4.3697100000	-2.0315300000	0.4362000000
O	6.8818900000	-1.7551900000	0.5504100000
C	0.5509300000	11.9213400000	-1.8169400000
O	3.4494100000	11.4751200000	-1.3434200000
C	5.2679400000	11.9606300000	0.4840300000
H	-0.4337100000	-1.4998300000	0.5221800000
H	-0.8920800000	0.8507800000	0.4017500000
O	8.9488200000	0.0206900000	0.3966900000
O	8.4435800000	2.7044800000	0.1729000000
O	-1.4363000000	2.8746100000	-0.4149000000
H	-1.5072500000	5.3031000000	0.1473400000
C	8.3527800000	3.8563300000	-0.5909100000
H	7.6508100000	6.3271000000	-1.2758800000
H	-1.6465200000	8.5308500000	0.1362500000
H	-1.5116200000	10.6753000000	-0.9346000000
H	7.5562000000	8.0276800000	0.2722000000
C	7.7468300000	10.5849400000	1.0416500000
H	1.1648600000	-3.2566300000	0.4473400000
H	7.7907300000	-2.0776700000	0.6197800000
O	-0.2713200000	12.7630800000	-1.4750400000
O	1.1631500000	12.0601100000	-3.0049600000
H	1.0993100000	12.8984500000	-3.4819900000
H	3.2690000000	11.4925100000	-2.2768700000
O	4.6988000000	12.3593700000	1.4933000000
O	5.9113500000	12.7940500000	-0.3668200000
H	5.9468200000	13.7495000000	-0.2818000000
H	9.6868500000	0.6390400000	0.4280600000
H	8.9758700000	2.7064500000	-2.0602100000
H	-1.3673300000	2.1352200000	-1.0371200000
O	8.4128500000	3.5235800000	-1.9656200000
O	9.4091300000	4.7087300000	-0.2464400000
H	10.1921400000	4.4397500000	-0.7923800000
O	7.6868900000	11.7274600000	1.4804400000
O	8.9095000000	9.9257400000	1.1087600000
H	9.6816700000	10.3617100000	1.4818900000
O	2.7231700000	0.5420800000	1.6718300000
O	3.4832800000	2.4631500000	-1.2498400000
O	0.0666900000	6.9430000000	0.3253200000
O	5.2710000000	6.6827600000	-2.1784100000
H	4.3885300000	7.0903100000	-2.3724600000
O	5.8814100000	4.1223800000	1.6872300000
H	6.6769700000	3.6965800000	2.1148800000
Mn	2.6327700000	15.3280100000	-0.8682000000
O	1.1821000000	14.9747500000	0.3934900000
O	3.8819400000	15.0734000000	0.5503800000
H	0.7841200000	14.0883200000	0.2174300000
H	0.4690500000	15.5448800000	0.0579500000
O	2.5012700000	17.1625200000	-0.3234300000
H	4.7415500000	15.4268400000	0.1972500000
O	4.1613600000	15.6160100000	-2.0967500000
O	2.6774200000	13.5999100000	-1.1293300000
H	3.2182700000	17.8222000000	-0.1982900000

H	2.6845200000	13.3889500000	-2.0714900000
H	2.4957400000	13.0557000000	-0.3016900000
H	2.3976200000	16.9094800000	0.6385800000
O	1.4684300000	15.4942900000	-2.4491000000
H	1.7425200000	16.3766100000	-2.7905100000
H	4.0474200000	14.1356000000	0.5120100000
H	5.1044500000	15.3767400000	-1.8951900000
H	4.0766200000	16.1545300000	-2.9179900000
H	1.9287000000	14.9699500000	-3.1758700000

**ERGO-[Fe(H<sub>2</sub>O)<sub>6</sub>]<sup>2+</sup>**

104

C	12.02339875	8.09792337	17.20049159
C	13.29301262	7.54865481	17.22459679
C	14.47643848	8.43519184	17.30743529
C	15.82636868	7.91266422	17.05156442
C	16.91898813	8.80272089	17.00252874
C	18.27387611	8.31988887	17.07612691
C	19.35348539	9.22209598	17.06698072
C	11.79726258	9.50753416	17.04803266
C	12.81135765	10.45055577	16.84268188
C	14.19052585	9.94736409	17.09823790
C	15.35058754	10.74777505	16.59975491
C	16.71527306	10.22893018	16.89226767
C	17.79339716	11.11535217	16.87608184
C	19.11343818	10.60716419	16.96734486
C	11.33683109	12.50007430	16.50962430
C	12.63685293	11.89912979	16.64073049
C	13.74816817	12.80691642	16.61062864
C	15.10461137	12.23510039	16.44790489
C	16.25341562	13.14509329	16.55038953
C	17.61986347	12.61392184	16.97479923
C	18.75937114	13.34769188	16.30410246
C	11.17512809	13.87668248	16.75653244
C	12.28680898	14.70257486	16.89416217
C	13.61576371	14.24048810	16.64737849
C	14.75865787	15.13507695	16.41913628
C	16.06450303	14.49555350	16.33682924
C	17.24586278	15.29136921	15.80200777
C	18.58406812	14.59459848	15.83803576
C	11.11064722	17.95861251	16.59126993
C	12.22985651	17.09544183	16.64316613
C	13.51212972	17.43533718	16.13012062
C	14.70793249	16.59015835	16.25800032
C	15.96103355	17.33328973	16.31092056
C	17.23486452	16.68351733	16.38089184
C	18.37090891	17.36860860	16.81225806
C	11.18924170	19.17199747	15.91910860
C	12.41300732	19.58094581	15.32516207
C	13.62579885	18.79210509	15.58543212
C	14.89499054	19.42194957	15.62453489
C	15.99618130	18.77282178	16.26502333
C	17.15041229	19.48186435	16.73877723
C	18.31200972	18.75358677	17.10165448
O	13.59004593	6.21980552	17.19123078

H	15.98355431	6.82062953	17.00886353
O	18.50426452	6.98446711	17.18248454
C	12.29920973	20.74438382	14.47059329
O	15.10615477	20.71055462	15.18721272
C	17.13297809	20.95230788	16.94604851
H	11.14302183	7.42797033	17.26048467
H	10.74105281	9.81929049	17.15174656
O	20.61332289	8.67752486	17.16436451
O	20.21652148	11.43094836	16.99979232
O	10.20326525	11.81298787	16.20336605
H	10.15855061	14.29947532	16.84815785
C	20.10282151	12.64033454	16.14398966
H	19.41651430	15.12757023	15.33947589
H	10.17067348	17.61409027	17.05893366
H	10.29401299	19.80575602	15.77439849
H	19.32067510	16.82603206	16.97916166
C	19.39385328	19.41384043	17.90123966
H	12.75421017	5.71001750	17.05693400
H	19.48669548	6.86514534	17.24869265
O	11.42282650	21.65694691	14.57150525
O	13.21470884	20.80555484	13.40974101
H	12.91757151	21.57694850	12.86021714
H	14.54051556	20.83958213	14.36814210
O	16.22644946	21.58785922	17.56582791
O	18.18726219	21.59444214	16.39417051
H	18.27885820	22.47095681	16.85035522
H	21.25312421	9.43021025	17.21810251
H	20.90438064	11.53304552	14.75584803
H	10.47373635	10.92528506	15.85730836
O	20.19556339	12.22208212	14.80075859
O	21.11955037	13.49577792	16.56238577
H	21.97184260	13.12980319	16.22138584
O	19.21079875	20.41030462	18.60711861
O	20.58883920	18.76284735	17.80295103
H	21.20230627	19.25131803	18.41177876
O	14.40728599	9.40684753	18.41865640
O	15.20310178	11.31320975	15.27115697
O	12.00222714	15.96988675	17.39640127
O	17.02843659	15.42546212	14.35820645
H	16.15537761	15.87531514	14.24712449
O	17.75335129	12.98769370	18.39592187
H	17.28943654	12.27992953	18.91141786
Fe	13.94499534	24.14928251	16.18713956
O	12.98164626	24.60317181	17.99728404
O	15.90166981	24.01464466	16.80864635
O	14.22165308	26.37001345	15.75791899
H	14.82659197	26.87546319	16.35400685
H	16.11945214	23.06163526	17.20019137
O	13.57490681	22.18688784	17.17768935
O	12.39905218	23.98612996	14.84256154
O	15.36606174	24.18818943	14.21302365
H	15.22652307	25.06879040	13.78558449
H	11.95165432	23.03976068	14.68035467
H	14.44998419	21.71267119	17.33838849
H	13.65011548	27.06088919	15.34280676
H	16.35927299	24.03471647	15.92607362
H	11.64688697	24.62280898	14.88564917
H	13.03121774	21.51266587	16.69099521



H	12.74578502	25.39037608	18.54004187
H	12.76554606	23.79486348	18.52567179
H	15.49026241	23.55913331	13.46288951

**ERGO-[Cu(H<sub>2</sub>O)<sub>6</sub>]<sup>2+</sup>**

104

C	12.11275922	7.90846026	17.19738051
C	13.38622239	7.35991921	17.24947737
C	14.56231667	8.26279961	17.32934468
C	15.93118231	7.79588193	17.09508591
C	17.00015785	8.69013984	17.02014958
C	18.38201544	8.23506183	17.08586773
C	19.45251646	9.15675141	17.02868818
C	11.86575785	9.30955829	17.03054209
C	12.88251527	10.25010342	16.83800597
C	14.25469579	9.79147183	17.14475454
C	15.39389074	10.60545105	16.62793446
C	16.76374726	10.11714378	16.91094489
C	17.81741728	11.02179252	16.84695863
C	19.16006579	10.53940569	16.90407883
C	11.36646801	12.21891643	16.55593347
C	12.69356404	11.68017832	16.66706059
C	13.78005693	12.61688531	16.68296749
C	15.13385249	12.08741795	16.47425160
C	16.26026944	13.01381194	16.56897472
C	17.62725939	12.51146988	16.95296120
C	18.75951552	13.27443239	16.31060161
C	11.18565458	13.56552336	16.80987922
C	13.62481760	14.03838494	16.70922792
C	14.74727013	14.94906744	16.49937342
C	16.06366112	14.34412047	16.36146649
C	17.22675464	15.17209946	15.86694772
C	18.56750221	14.52336965	15.88169194
C	11.01552040	17.66693982	16.55838757
C	12.14147473	16.84176095	16.67401791
C	13.47330221	17.22758235	16.38260664
C	14.67357418	16.38419523	16.46323578
C	15.92998606	17.10629266	16.57466560
C	17.21774581	16.50150614	16.54608898
C	18.36240671	17.19909499	16.89951244
C	11.12183540	18.91122889	15.95924775
C	12.38308968	19.37926513	15.55275324
C	13.56686127	18.60418489	15.90041002
C	14.86251395	19.14693488	15.93720457
C	15.95984674	18.52742291	16.59227359
C	17.14042614	19.27122351	16.92819678
C	18.32598396	18.58655644	17.19347162
O	13.70031955	6.03013328	17.30424409
H	16.10548623	6.70696930	17.10735180
O	18.56693262	6.90168714	17.22803858
C	12.23963212	20.66392315	14.84835400
O	15.25623559	20.27218724	15.26195973
C	17.03347679	20.74766664	17.20840022
H	11.24942902	7.21231550	17.22072430
H	10.79740369	9.61127606	17.08632650
O	20.72799955	8.63379984	17.08123870

O	20.25925023	11.36827629	16.90531293
O	10.19453045	11.57103943	16.26938114
H	10.18211790	14.02729786	16.83211639
C	20.09678229	12.61370864	16.05863437
H	19.38931900	15.07390676	15.39256219
H	10.04472281	17.21881981	16.83930600
H	10.19344904	19.46070833	15.72881322
H	19.33755314	16.69125162	16.95465683
C	19.49478734	19.33350718	17.76253870
H	12.87272790	5.51059870	17.13665576
H	19.53677157	6.70924739	17.29707641
O	11.46242274	21.56213801	15.19834388
O	13.02938229	20.74715355	13.65080445
H	12.73917042	21.60432635	13.23331103
H	14.92834200	20.18033440	14.33479920
O	16.34956457	21.19589136	18.13721280
O	17.64832804	21.47486243	16.20720764
H	17.66519834	22.42425647	16.50045078
H	21.36610525	9.39581185	17.11168728
H	20.71122929	11.43020675	14.63219811
H	10.41385192	10.82861679	15.65968526
O	20.12217830	12.21929731	14.70797409
O	21.14379512	13.43529276	16.43826747
H	21.91801527	13.15808299	15.89310091
O	19.41248699	20.48884691	18.18308227
O	20.62323878	18.55379603	17.75896374
H	21.34116847	19.11156567	18.16236177
O	14.47518396	9.23754258	18.44852384
O	15.22218631	11.15270516	15.28964930
O	11.74742777	15.65786753	17.21107423
O	17.01682843	15.40370789	14.41947969
H	16.11633898	15.80558374	14.33822015
O	17.59085503	12.83839377	18.40313211
H	18.39105653	12.41469979	18.79986783
Cu	14.30343536	24.24161398	15.83036746
O	12.73139541	23.67356486	17.24106117
O	15.76541989	23.81126952	17.41655155
H	12.45251156	22.78340196	16.89694099
H	12.11851028	24.27679128	16.75142994
O	14.15963131	26.08477722	16.46162068
H	16.52521987	24.17624875	16.91449551
O	15.95947569	24.33522342	14.50891116
O	14.43745214	22.35211844	15.58168284
H	14.99743818	26.60381491	16.46325950
H	14.37035024	21.92266554	14.69578527
H	14.21581934	21.64989989	16.23677756
H	14.10181927	25.66100084	17.36128937
O	13.09301963	24.24409937	14.05134222
H	13.41126605	25.16022728	13.86143092
H	15.81753602	22.80890454	17.30627469
H	16.89985552	24.11545278	14.69584877
H	15.92070503	24.90733454	13.71284289
H	13.63728620	23.66699731	13.46649446

**ERGO-[H<sub>2</sub>PO<sub>4</sub>]<sup>-</sup>**

C	12.07227457	8.28426574	17.09508163
C	13.34078182	7.75751656	17.18488471
C	14.52083390	8.64587348	17.29027844
C	15.87052504	8.13897491	17.05933154
C	16.94457748	9.04862645	16.97515744
C	18.31360717	8.60516744	17.01404176
C	19.36904792	9.51936095	16.91497296
C	11.82358990	9.69246727	16.90541148
C	12.83035142	10.64173690	16.72982231
C	14.21015809	10.16165023	17.04312226
C	15.36240185	10.95923303	16.53542053
C	16.72689417	10.46972293	16.82288503
C	17.79250448	11.38106134	16.72941849
C	19.11282806	10.90477107	16.78483175
C	11.33962393	12.67533752	16.37207317
C	12.63714055	12.09253572	16.51093945
C	13.74301554	13.01358121	16.50067559
C	15.10036011	12.45905911	16.32745932
C	16.22674689	13.38654437	16.41839679
C	17.59598674	12.87439460	16.82825321
C	18.72883619	13.63880923	16.17306162
C	11.15406329	14.04112727	16.64045455
C	12.25352618	14.87366830	16.83783525
C	13.59029744	14.44342341	16.58582259
C	14.71841156	15.36987021	16.40429725
C	16.02320129	14.74812083	16.27876248
C	17.19938278	15.58555751	15.78907290
C	18.54036143	14.90413563	15.76645117
C	10.99465639	17.98542738	16.35058775
C	12.14865753	17.23775869	16.59185132
C	13.45465082	17.67498880	16.22436175
C	14.65345378	16.83141566	16.33578845
C	15.90062464	17.56843135	16.42435467
C	17.19077326	16.93723415	16.45330322
C	18.32510859	17.64235277	16.82717770
C	11.08597394	19.27727749	15.80464062
C	12.33581259	19.83784177	15.52280570
C	13.53281631	19.05853614	15.75809974
C	14.84611373	19.67170068	15.73477326
C	15.93349488	18.99591153	16.39733665
C	17.08196214	19.73420493	16.82428347
C	18.26168564	19.03920999	17.12972124
O	13.62626774	6.40970148	17.17330278
H	16.04999843	7.05195588	17.05060862
O	18.58192599	7.26306942	17.17856619
C	12.27402993	21.29320996	15.07397358
O	15.14894073	20.79228154	15.14278500
C	16.87095763	21.22649092	16.99652846
H	11.20335502	7.59437876	17.11271270
H	10.76023342	9.99129494	16.95849564
O	20.66151128	9.01439346	16.97910298
O	20.22634855	11.75030383	16.78532739
O	10.21239694	11.96394872	16.02880326
H	10.13244780	14.45443393	16.72790285

C	20.07436248	12.96067578	15.96453018
H	19.36035610	15.47383623	15.28927098
H	10.02431499	17.55912704	16.66724874
H	10.18975094	19.90869609	15.65821005
H	19.30307162	17.12984142	16.88576234
C	19.43309443	19.74936873	17.70499888
H	12.78050858	5.94014837	16.97993437
H	19.56881459	7.19939166	17.21758595
O	11.38206289	22.04480179	15.52850000
O	13.17170764	21.69626744	14.18313164
H	13.82829858	23.18176340	14.24320131
H	14.22361000	21.19339037	14.57092742
O	15.99485250	21.63533877	17.78175035
O	17.59989968	22.00552486	16.18085965
H	17.14887278	22.91563342	16.20641211
H	21.25109499	9.80931880	16.98499996
H	20.65635852	11.71038896	14.60482256
H	10.53821102	11.09958483	15.67291012
O	20.19411493	12.58393313	14.59626418
O	21.11567019	13.81668306	16.34683172
H	21.87426019	13.56520148	15.76602295
O	19.41469010	20.86209067	18.23374748
O	20.59339890	19.00321185	17.60819334
H	21.26666608	19.58204391	18.04819017
O	14.38679649	9.64970900	18.38312687
O	15.19380211	11.48504306	15.19223045
O	11.96559806	16.11573899	17.38872568
O	16.97691591	15.82404232	14.35296661
H	16.14322006	16.35537636	14.30576243
O	17.63507429	13.21552993	18.27376168
H	18.09893625	12.45763280	18.70738771
P	14.39098669	24.61650760	15.82867466
O	13.20936299	23.83341027	16.64189653
O	15.73476335	23.99094327	16.57990378
O	14.41401816	26.11012613	15.86976525
H	15.51476563	23.16960942	17.14120644
H	12.49776948	23.41348252	16.06620794
O	14.37361756	24.03957198	14.31662571

1

### ERGO-As(OH)<sub>3</sub>

92

C	12.10320340	8.16042135	17.09583290
C	13.37253580	7.63933020	17.18735935
C	14.54366690	8.53624226	17.28387197
C	15.89372588	8.02976366	17.04663905
C	16.96906287	8.93200329	16.96585760
C	18.33361420	8.47691755	17.01969807
C	19.39578721	9.38416725	16.92459482
C	11.85416790	9.56752753	16.90276738
C	12.85549186	10.52041835	16.71450638
C	14.23533471	10.05099928	17.02123070
C	15.38535484	10.84386463	16.51261881
C	16.74777127	10.35153075	16.80721991
C	17.81357948	11.25363550	16.72461217
C	19.13517782	10.76661266	16.78954580

C	11.36473306	12.54819138	16.36191366
C	12.66410979	11.97113210	16.49970655
C	13.76765158	12.89423682	16.49650734
C	15.12738756	12.34579984	16.32458270
C	16.25592537	13.26839752	16.43267821
C	17.62706643	12.75015540	16.82878033
C	18.75213983	13.50694146	16.15106898
C	11.18080843	13.91689468	16.62299658
C	12.27775195	14.75187604	16.82613703
C	13.61611070	14.32444017	16.58376843
C	14.74613863	15.25052073	16.40377296
C	16.05188941	14.62921851	16.29486394
C	17.22229265	15.45903488	15.77543322
C	18.56736746	14.77615693	15.75326592
C	11.02123929	17.89553097	16.41498670
C	12.17329398	17.12197068	16.59562605
C	13.47684744	17.53938953	16.18744137
C	14.68094427	16.71432342	16.30487984
C	15.92698048	17.47153210	16.36781390
C	17.21151166	16.83329250	16.39752472
C	18.34901983	17.53140953	16.77342963
C	11.10353824	19.16191809	15.81329024
C	12.34754625	19.67803039	15.43334684
C	13.56132463	18.92425300	15.71718321
C	14.82201606	19.57958414	15.79994800
C	15.94948886	18.90993366	16.35968652
C	17.11851010	19.63702467	16.79143032
C	18.29165158	18.92709116	17.07233845
O	13.68828633	6.30381877	17.18187149
H	16.06277653	6.94050177	16.99478630
O	18.58228399	7.14379149	17.19138509
C	12.26903963	21.01830698	14.80003064
O	15.02543167	20.86485860	15.41154414
C	16.96189733	21.12299913	17.06935733
H	11.23789590	7.46811588	17.11523067
H	10.79053271	9.86125116	16.95753363
O	20.67621165	8.86623150	16.99757914
O	20.23756845	11.61036910	16.79067303
O	10.24164656	11.82841821	16.03231662
H	10.15794859	14.32425546	16.70991423
C	20.08664160	12.81183677	15.92706959
H	19.38615974	15.34080686	15.26824208
H	10.06124336	17.48399848	16.77421284
H	10.19769242	19.77315925	15.64233793
H	19.32228766	17.01525991	16.84969601
C	19.47709232	19.62520310	17.65231435
H	12.86407867	5.79654442	16.99068379
H	19.56673781	7.04887277	17.22370891
O	11.50701918	21.93819549	15.11661644
O	13.12497960	21.16989842	13.69069803
H	12.98315253	22.10984845	13.39654165
H	14.43452636	21.05801478	14.62377153
O	16.20094156	21.49515863	17.98280451
O	17.59639880	21.94162457	16.21470035
H	17.18801726	22.86442711	16.39434965
H	21.28410430	9.64624919	17.00052276
H	20.76812655	11.60597513	14.56818728
H	10.56156151	10.95967112	15.68265425



O	20.15319268	12.38090758	14.58210726
O	21.13920104	13.66098139	16.27602644
H	21.91734890	13.36539583	15.74386929
O	19.47787373	20.75658666	18.13835824
O	20.60372349	18.83112538	17.61105650
H	21.29958352	19.38688037	18.04571406
O	14.43126441	9.54855191	18.35938015
O	15.23071911	11.38702583	15.17963509
O	11.98881720	15.99663286	17.37887790
O	16.98244292	15.63640607	14.33519711
H	16.12496265	16.12524848	14.26488858
O	17.67590739	13.08822459	18.26879687
H	18.37001023	12.50128071	18.66062068
As	14.47950179	24.01365897	15.74715880
O	13.23828496	23.58384400	17.01127947
O	15.90515302	23.91801080	16.90814731
O	14.40292280	25.82331079	15.77276645
H	14.61066725	26.06890555	16.71120800
H	15.75339886	23.12356843	17.53164286
H	12.51038739	23.11244791	16.52328483

**(d) Force-field optimized geometries of oxidation mechanism steps for the cluster-cutout model of Figure 8 in the manuscript**

**Initial state**

30

C	-0.68487	8.88926	-0.18791
C	0.45417	8.13186	-0.00823
C	1.75541	8.55299	-0.39652
C	2.95253	7.74098	-0.27199
C	4.18453	8.49764	-0.20906
C	-0.60162	10.15663	-0.77534
C	0.62792	10.67839	-1.12160
C	1.83569	9.93853	-0.82446
C	3.07105	10.59968	-0.71189
C	4.20242	9.92929	-0.20956
C	0.56704	12.01273	-1.76324
O	3.19949	11.92668	-0.99920
H	-1.62887	8.49219	0.16706
H	-1.49746	10.74356	-0.94728
O	-0.16729	12.92746	-1.43887
O	1.36562	12.13187	-2.87923
H	1.20382	13.03108	-3.22770
H	2.86943	12.08916	-1.90491
O	0.28285	7.00927	0.75472
As	2.72239	15.14463	-0.78007
O	1.50043	14.69819	0.46497
O	4.14151	15.00383	0.34666
O	2.66056	16.93431	-0.73496
H	3.97295	14.28940	1.00560
H	0.78616	14.20087	0.02304
H	2.92701	6.71008	-0.23171
H	5.08067	7.98797	-0.16223
H	4.99109	10.18867	-0.88456

H	1.00930	6.44193	0.92317
H	2.88190	16.98777	0.08488

### Step 1

29

C	-0.68487	8.88926	-0.18791
C	0.45417	8.13186	-0.00823
C	1.75541	8.55299	-0.39652
C	2.95253	7.74098	-0.27199
C	4.18453	8.49764	-0.20906
C	-0.60162	10.15663	-0.77534
C	0.62792	10.67839	-1.12160
C	1.83569	9.93853	-0.82446
C	3.07105	10.59968	-0.71189
C	4.20242	9.92929	-0.20956
C	0.56704	12.01273	-1.76324
O	3.19949	11.92668	-0.99920
H	-1.62887	8.49219	0.16706
H	-1.49746	10.74356	-0.94728
O	-0.16729	12.92746	-1.43887
O	1.36562	12.13187	-2.87923
H	1.20382	13.03108	-3.22770
H	2.86943	12.08916	-1.90491
O	0.28285	7.00927	0.75472
As	2.52196	15.02689	-1.18335
O	1.66614	16.57922	-0.86637
O	3.65251	15.18856	0.23050
O	3.73186	15.51476	-2.41093
H	4.28639	16.22035	-2.02982
H	0.73181	16.46798	-1.12614
H	2.92701	6.71008	-0.23171
H	5.08067	7.98797	-0.16223
H	4.99109	10.18867	-0.88456
H	1.00930	6.44193	0.92317

### Step 2

29

C	-0.68487	8.88926	-0.18791
C	0.45417	8.13186	-0.00823
C	1.75541	8.55299	-0.39652
C	2.95253	7.74098	-0.27199
C	4.18453	8.49764	-0.20906
C	-0.60162	10.15663	-0.77534
C	0.62792	10.67839	-1.12160
C	1.83569	9.93853	-0.82446
C	3.07105	10.59968	-0.71189
C	4.20242	9.92929	-0.20956
C	0.55748	12.05492	-1.75667
O	3.29135	11.87573	-1.12709
H	-1.62887	8.49219	0.16706
H	-1.49746	10.74356	-0.94728
O	-0.44229	12.87916	-1.21452

O	0.37393	11.94397	-3.13544
H	1.15283	12.41177	-3.53048
H	2.77014	12.52508	-1.59426
O	0.28285	7.00927	0.75472
As	0.32922	13.90283	0.11049
O	-0.91229	15.15642	0.63808
O	1.12216	14.30226	1.72349
O	0.57670	14.95259	-1.38082
H	1.55027	15.13317	-1.39636
H	-1.72425	14.63112	0.85209
H	2.92701	6.71008	-0.23170
H	5.08067	7.98797	-0.16223
H	4.33822	10.24711	0.80309
H	1.00930	6.44193	0.92317

### Step 3

29

C	-0.68487	8.88926	-0.18791
C	0.45417	8.13186	-0.00823
C	1.75541	8.55299	-0.39652
C	2.95253	7.74098	-0.27199
C	4.18453	8.49764	-0.20906
C	-0.60162	10.15663	-0.77534
C	0.62792	10.67839	-1.12160
C	1.83569	9.93853	-0.82446
C	2.81221	10.70774	-0.44878
C	4.20242	9.92929	-0.20956
C	1.14071	12.03053	-1.45127
O	2.51936	11.92023	-1.04603
H	-1.62887	8.49219	0.16706
H	-1.49746	10.74356	-0.94728
O	0.34204	12.91014	-0.68748
O	1.01475	12.27844	-2.82376
H	1.55821	13.08534	-3.01329
O	0.28285	7.00927	0.75472
As	1.11844	14.51430	-0.22489
O	-0.25000	15.56230	0.41781
O	2.29237	14.29226	1.16465
O	1.86662	15.37397	-1.66516
H	2.84037	15.24353	-1.55252
H	-0.93537	14.91370	0.72426
H	2.55219	10.91848	0.59046
H	2.92701	6.71008	-0.23170
H	5.08067	7.98797	-0.16223
H	4.58185	10.24220	0.74072
H	1.00930	6.44193	0.92317

### Step 4

C	-0.6848700000	8.8892600000	-0.1879100000
C	0.4541700000	8.1318600000	-0.0082300000
C	1.7554100000	8.5529900000	-0.3965200000
C	2.9525300000	7.7409800000	-0.2719900000
C	4.1845300000	8.4976400000	-0.2090600000
C	-0.6016200000	10.1566300000	-0.7753400000
C	0.6279200000	10.6783900000	-1.1216000000
C	1.8356900000	9.9385300000	-0.8244600000
C	2.8122100000	10.7077400000	-0.4487800000
C	4.2024200000	9.9292900000	-0.2095600000
C	1.1407100000	12.0305300000	-1.4512700000
O	2.5193600000	11.9202300000	-1.0460300000
H	-1.6288700000	8.4921900000	0.1670600000
H	-1.4974600000	10.7435600000	-0.9472800000
O	0.3420400000	12.9101400000	-0.6874800000
O	1.0147500000	12.2784400000	-2.8237600000
H	1.5582100000	13.0853400000	-3.0132900000
O	0.2828500000	7.0092700000	0.7547200000
As	1.1184400000	14.5143000000	-0.2248900000
O	-0.2500000000	15.5623000000	0.4178100000
O	2.2923700000	14.2922600000	1.1646500000
O	1.8666200000	15.3739700000	-1.6651600000
H	-0.9353700000	14.9137000000	0.7242600000
H	2.5521900000	10.9184800000	0.5904600000
H	2.9270100000	6.7100800000	-0.2317000000
H	5.0806700000	7.9879700000	-0.1622300000
H	4.5818500000	10.2422000000	0.7407200000
H	-0.2745200000	13.0496000000	-1.4232200000
H	1.0093000000	6.4419300000	0.9231700000

### Final step

C	-0.68487	8.88926	-0.18791
C	0.45417	8.13186	-0.00823
C	1.75541	8.55299	-0.39652
C	2.95253	7.74098	-0.27199
C	4.18453	8.49764	-0.20906
C	-0.60162	10.15663	-0.77534
C	0.62792	10.67839	-1.12160
C	1.83569	9.93853	-0.82446
C	2.99235	10.60783	-0.70561
C	4.20242	9.92929	-0.20956
C	0.60763	12.03393	-1.79800
O	-0.43858	12.66283	-1.87978
H	-1.62887	8.49219	0.16706
H	-1.49746	10.74356	-0.94728
O	-0.83935	15.07075	0.05360
O	1.70148	12.54223	-2.40464
H	1.67942	13.39377	-2.86394
O	0.28285	7.00927	0.75472
As	0.81015	15.88288	0.07326

O	0.69242	17.52345	0.89593
O	1.99871	14.81031	0.97757
O	1.37932	16.09870	-1.66166
H	2.30382	15.74401	-1.66738
H	-0.17435	17.50225	1.37442
H	3.07215	11.66553	-0.87410
H	2.92701	6.71008	-0.23170
H	5.08067	7.98797	-0.16223
H	4.36445	10.25149	0.79783
H	1.00930	6.44193	0.92317

**(e) Force-field optimized geometries of oxidation mechanism steps for the full-sheet model**

**Initial state**

92

C	0.42181	-0.78880	0.52151
C	1.67326	-1.30753	0.60469
C	2.84237	-0.41873	0.70213
C	4.18779	-0.90998	0.45707
C	5.25137	-0.01320	0.38024
C	6.61301	-0.46210	0.41230
C	7.65914	0.44231	0.31361
C	0.17100	0.61393	0.33201
C	1.15505	1.55870	0.15366
C	2.53292	1.09828	0.45258
C	3.67162	1.88888	-0.04975
C	5.02857	1.40116	0.23837
C	6.08348	2.29934	0.15375
C	7.39157	1.81449	0.19747
C	-0.33111	3.57930	-0.17970
C	0.95710	3.00958	-0.06811
C	2.05376	3.92844	-0.08335
C	3.40847	3.38603	-0.25143
C	4.52463	4.30708	-0.14472
C	5.88709	3.79334	0.27026
C	7.01167	4.55560	-0.38994
C	-0.51439	4.93848	0.05752
C	0.57091	5.76831	0.23459
C	1.89996	5.34964	-0.00406
C	3.02402	6.27427	-0.18022
C	4.31757	5.65794	-0.28405
C	5.48707	6.49162	-0.78378
C	6.82839	5.81173	-0.77942
C	-0.68487	8.88926	-0.18791
C	0.45417	8.13186	-0.00823
C	1.75541	8.55299	-0.39652
C	2.95253	7.74098	-0.27199
C	4.18453	8.49764	-0.20906
C	5.46226	7.86199	-0.16793
C	6.58694	8.54967	0.20821
C	-0.60162	10.15663	-0.77534
C	0.62792	10.67839	-1.12160
C	1.83569	9.93853	-0.82446
C	3.07105	10.59968	-0.71189
C	4.20242	9.92929	-0.20956



C	5.37344	10.64229	0.22429
C	6.53144	9.93947	0.49947
O	1.97658	-2.63439	0.58758
H	4.35419	-1.97651	0.38508
O	6.86068	-1.78580	0.55918
C	0.56704	12.01273	-1.76324
O	3.19949	11.92668	-0.99920
C	5.23819	12.12107	0.51335
H	-0.43636	-1.45809	0.53167
H	-0.87275	0.89514	0.36497
O	8.93946	-0.05446	0.35480
O	8.48289	2.65199	0.17784
O	-1.46667	2.86844	-0.44648
H	-1.51950	5.33486	0.14495
C	8.33863	3.86300	-0.62976
H	7.63139	6.36936	-1.24901
H	-1.62887	8.49219	0.16706
H	-1.49746	10.74356	-0.94728
H	7.53997	8.04228	0.28633
C	7.71462	10.63645	1.07329
H	1.16913	-3.14234	0.40605
H	7.82599	-1.90535	0.60772
O	-0.16729	12.92746	-1.43887
O	1.36562	12.13187	-2.87923
H	1.20382	13.03108	-3.22770
H	2.86943	12.08916	-1.90491
O	4.57238	12.50871	1.45824
O	5.83312	12.91015	-0.37822
H	5.53004	13.83466	-0.18694
H	9.54686	0.69774	0.45476
H	8.97201	2.68250	-2.02524
H	-1.22007	2.06958	-0.93950
O	8.40727	3.47326	-1.97362
O	9.38293	4.69012	-0.26600
H	10.15687	4.44216	-0.79875
O	7.71219	11.75839	1.53452
O	8.83477	9.86896	1.05058
H	9.53103	10.41131	1.46525
O	2.73738	0.58054	1.75737
O	3.51337	2.42077	-1.36403
O	0.28285	7.00927	0.75472
O	5.28809	6.66939	-2.22104
H	4.41716	7.08378	-2.34189
O	5.89867	4.10572	1.70258
H	6.67456	3.66277	2.09136
As	2.72239	15.14463	-0.78007
O	1.50043	14.69819	0.46497
O	4.14151	15.00383	0.34666
O	2.66056	16.93431	-0.73496
H	2.87140	17.22456	0.17164
H	3.97295	14.28940	1.00560
H	0.78616	14.20087	0.02304

**Step 1**

C	0.42181	-0.78880	0.52151
C	1.67326	-1.30753	0.60469
C	2.84237	-0.41873	0.70213
C	4.18779	-0.90998	0.45707
C	5.25137	-0.01320	0.38024
C	6.61301	-0.46210	0.41230
C	7.65914	0.44231	0.31361
C	0.17100	0.61393	0.33201
C	1.15505	1.55870	0.15366
C	2.53292	1.09828	0.45258
C	3.67162	1.88888	-0.04975
C	5.02857	1.40116	0.23837
C	6.08348	2.29934	0.15375
C	7.39157	1.81449	0.19747
C	-0.33111	3.57930	-0.17970
C	0.95710	3.00958	-0.06811
C	2.05376	3.92844	-0.08335
C	3.40847	3.38603	-0.25143
C	4.52463	4.30708	-0.14472
C	5.88709	3.79334	0.27026
C	7.01167	4.55560	-0.38994
C	-0.51439	4.93848	0.05752
C	0.57091	5.76831	0.23459
C	1.89996	5.34964	-0.00406
C	3.02402	6.27427	-0.18022
C	4.31757	5.65794	-0.28405
C	5.48707	6.49162	-0.78378
C	6.82839	5.81173	-0.77942
C	-0.68487	8.88926	-0.18791
C	0.45417	8.13186	-0.00823
C	1.75541	8.55299	-0.39652
C	2.95253	7.74098	-0.27199
C	4.18453	8.49764	-0.20906
C	5.46226	7.86199	-0.16793
C	6.58694	8.54967	0.20821
C	-0.60162	10.15663	-0.77534
C	0.62792	10.67839	-1.12160
C	1.83569	9.93853	-0.82446
C	3.07105	10.59968	-0.71189
C	4.20242	9.92929	-0.20956
C	5.37344	10.64229	0.22429
C	6.53144	9.93947	0.49947
O	1.97658	-2.63439	0.58758
H	4.35419	-1.97651	0.38508
O	6.86068	-1.78580	0.55918
C	0.56704	12.01273	-1.76324
O	3.19949	11.92668	-0.99920
C	5.23819	12.12107	0.51335
H	-0.43636	-1.45809	0.53167
H	-0.87275	0.89514	0.36497
O	8.93946	-0.05446	0.35480
O	8.48289	2.65199	0.17784
O	-1.46667	2.86844	-0.44648
H	-1.51950	5.33486	0.14495
C	8.33863	3.86300	-0.62976
H	7.63139	6.36936	-1.24901

H	-1.62887	8.49219	0.16706
H	-1.49746	10.74356	-0.94728
H	7.53997	8.04228	0.28633
C	7.71462	10.63645	1.07329
H	1.16913	-3.14234	0.40605
H	7.82599	-1.90535	0.60772
O	-0.16729	12.92746	-1.43887
O	1.36562	12.13187	-2.87923
H	1.20382	13.03108	-3.22770
H	2.86943	12.08916	-1.90491
O	4.57238	12.50871	1.45824
O	5.83312	12.91015	-0.37822
H	5.53004	13.83466	-0.18694
H	9.54686	0.69774	0.45476
H	8.97201	2.68250	-2.02524
H	-1.22007	2.06958	-0.93950
O	8.40727	3.47326	-1.97362
O	9.38293	4.69012	-0.26600
H	10.15687	4.44216	-0.79875
O	7.71219	11.75839	1.53452
O	8.83477	9.86896	1.05058
H	9.53103	10.41131	1.46525
O	2.73738	0.58054	1.75737
O	3.51337	2.42077	-1.36403
O	0.28285	7.00927	0.75472
O	5.28809	6.66939	-2.22104
H	4.41716	7.08378	-2.34189
O	5.89867	4.10572	1.70258
H	6.67456	3.66277	2.09136
As	2.52196	15.02689	-1.18335
O	1.66614	16.57922	-0.86637
O	3.65251	15.18856	0.23050
O	3.73186	15.51476	-2.41093
H	3.19401	15.65117	0.97131
H	0.73181	16.46798	-1.12614

## Step 2

91

C	0.42181	-0.78880	0.52151
C	1.67326	-1.30753	0.60469
C	2.84237	-0.41873	0.70213
C	4.18779	-0.90998	0.45707
C	5.25137	-0.01320	0.38024
C	6.61301	-0.46210	0.41230
C	7.65914	0.44231	0.31361
C	0.17100	0.61393	0.33201
C	1.15505	1.55870	0.15366
C	2.53292	1.09828	0.45258
C	3.67162	1.88888	-0.04975
C	5.02857	1.40116	0.23837
C	6.08348	2.29934	0.15375
C	7.39157	1.81449	0.19747
C	-0.33111	3.57930	-0.17970
C	0.95710	3.00958	-0.06811

C	2.05376	3.92844	-0.08335
C	3.40847	3.38603	-0.25143
C	4.52463	4.30708	-0.14472
C	5.88709	3.79334	0.27026
C	7.01167	4.55560	-0.38994
C	-0.51439	4.93848	0.05752
C	0.57091	5.76831	0.23459
C	1.89996	5.34964	-0.00406
C	3.02402	6.27427	-0.18022
C	4.31757	5.65794	-0.28405
C	5.48707	6.49162	-0.78378
C	6.82839	5.81173	-0.77942
C	-0.68487	8.88926	-0.18791
C	0.45417	8.13186	-0.00823
C	1.75541	8.55299	-0.39652
C	2.95253	7.74098	-0.27199
C	4.18453	8.49764	-0.20906
C	5.46226	7.86199	-0.16793
C	6.58694	8.54967	0.20821
C	-0.60162	10.15663	-0.77534
C	0.62792	10.67839	-1.12160
C	1.83569	9.93853	-0.82446
C	3.07105	10.59968	-0.71189
C	4.20242	9.92929	-0.20956
C	5.37344	10.64229	0.22429
C	6.53144	9.93947	0.49947
O	1.97658	-2.63439	0.58758
H	4.35419	-1.97651	0.38508
O	6.86068	-1.78580	0.55918
C	0.55748	12.05492	-1.75667
O	3.29135	11.87573	-1.12709
C	5.26971	12.12412	0.51094
H	-0.43636	-1.45809	0.53167
H	-0.87275	0.89514	0.36497
O	8.93946	-0.05446	0.35480
O	8.48289	2.65199	0.17784
O	-1.46667	2.86844	-0.44648
H	-1.51950	5.33486	0.14495
C	8.33863	3.86300	-0.62976
H	7.63139	6.36936	-1.24901
H	-1.62887	8.49219	0.16706
H	-1.49746	10.74356	-0.94728
H	7.53997	8.04228	0.28633
C	7.71462	10.63645	1.07329
H	1.16913	-3.14234	0.40605
H	7.82599	-1.90535	0.60772
O	-0.44229	12.87916	-1.21452
O	0.37393	11.94397	-3.13544
H	1.15283	12.41177	-3.53048
H	2.77014	12.52508	-1.59426
O	4.28202	12.57057	1.08083
O	6.20858	12.98670	0.06257
H	6.13317	13.94022	0.21069
H	9.54686	0.69774	0.45476
H	8.97201	2.68250	-2.02524
H	-1.22007	2.06958	-0.93950
O	8.40727	3.47326	-1.97362
O	9.38293	4.69012	-0.26600

H	10.15687	4.44216	-0.79875
O	7.71219	11.75839	1.53452
O	8.83477	9.86896	1.05058
H	9.53103	10.41131	1.46525
O	2.73738	0.58054	1.75737
O	3.51337	2.42077	-1.36403
O	0.28285	7.00927	0.75472
O	5.28809	6.66939	-2.22104
H	4.41716	7.08378	-2.34189
O	5.89867	4.10572	1.70258
H	6.67456	3.66277	2.09136
As	0.32922	13.90283	0.11049
O	-0.91229	15.15642	0.63808
O	1.12216	14.30226	1.72349
O	0.57670	14.95259	-1.38082
H	1.55027	15.13317	-1.39636
H	-1.72425	14.63112	0.85209

### Step 3

91

C	0.42181	-0.78880	0.52151
C	1.67326	-1.30753	0.60469
C	2.84237	-0.41873	0.70213
C	4.18779	-0.90998	0.45707
C	5.25137	-0.01320	0.38024
C	6.61301	-0.46210	0.41230
C	7.65914	0.44231	0.31361
C	0.17100	0.61393	0.33201
C	1.15505	1.55870	0.15366
C	2.53292	1.09828	0.45258
C	3.67162	1.88888	-0.04975
C	5.02857	1.40116	0.23837
C	6.08348	2.29934	0.15375
C	7.39157	1.81449	0.19747
C	-0.33111	3.57930	-0.17970
C	0.95710	3.00958	-0.06811
C	2.05376	3.92844	-0.08335
C	3.40847	3.38603	-0.25143
C	4.52463	4.30708	-0.14472
C	5.88709	3.79334	0.27026
C	7.01167	4.55560	-0.38994
C	-0.51439	4.93848	0.05752
C	0.57091	5.76831	0.23459
C	1.89996	5.34964	-0.00406
C	3.02402	6.27427	-0.18022
C	4.31757	5.65794	-0.28405
C	5.48707	6.49162	-0.78378
C	6.82839	5.81173	-0.77942
C	-0.68487	8.88926	-0.18791
C	0.45417	8.13186	-0.00823
C	1.75541	8.55299	-0.39652
C	2.95253	7.74098	-0.27199
C	4.18453	8.49764	-0.20906
C	5.46226	7.86199	-0.16793

C	6.58694	8.54967	0.20821
C	-0.60162	10.15663	-0.77534
C	0.62792	10.67839	-1.12160
C	1.83569	9.93853	-0.82446
C	2.81221	10.70774	-0.44878
C	4.20242	9.92929	-0.20956
C	5.37344	10.64229	0.22429
C	6.53144	9.93947	0.49947
O	1.97658	-2.63439	0.58758
H	4.35419	-1.97651	0.38508
O	6.86068	-1.78580	0.55918
C	1.14071	12.03053	-1.45127
O	2.51936	11.92023	-1.04603
C	5.26971	12.12412	0.51094
H	-0.43636	-1.45809	0.53167
H	-0.87275	0.89514	0.36497
O	8.93946	-0.05446	0.35480
O	8.48289	2.65199	0.17784
O	-1.46667	2.86844	-0.44648
H	-1.51950	5.33486	0.14495
C	8.33863	3.86300	-0.62976
H	7.63139	6.36936	-1.24901
H	-1.62887	8.49219	0.16706
H	-1.49746	10.74356	-0.94728
H	7.53997	8.04228	0.28633
C	7.71462	10.63645	1.07329
H	1.16913	-3.14234	0.40605
H	7.82599	-1.90535	0.60772
O	0.34204	12.91014	-0.68748
O	1.01475	12.27844	-2.82376
H	1.55821	13.08534	-3.01329
O	4.28202	12.57057	1.08083
O	6.20858	12.98670	0.06257
H	6.13317	13.94022	0.21069
H	9.54686	0.69774	0.45476
H	8.97201	2.68250	-2.02524
H	-1.22007	2.06958	-0.93950
O	8.40727	3.47326	-1.97362
O	9.38293	4.69012	-0.26600
H	10.15687	4.44216	-0.79875
O	7.71219	11.75839	1.53452
O	8.83477	9.86896	1.05058
H	9.53103	10.41131	1.46525
O	2.73738	0.58054	1.75737
O	3.51337	2.42077	-1.36403
O	0.28285	7.00927	0.75472
O	5.28809	6.66939	-2.22104
H	4.41716	7.08378	-2.34189
O	5.89867	4.10572	1.70258
H	6.67456	3.66277	2.09136
As	1.11844	14.51430	-0.22489
O	-0.25000	15.56230	0.41781
O	2.29237	14.29226	1.16465
O	1.86662	15.37397	-1.66516
H	2.84037	15.24353	-1.55252
H	-0.93537	14.91370	0.72426
H	2.55219	10.91848	0.59046



## Step 4

91

C	0.42181	-0.78880	0.52151
C	1.67326	-1.30753	0.60469
C	2.84237	-0.41873	0.70213
C	4.18779	-0.90998	0.45707
C	5.25137	-0.01320	0.38024
C	6.61301	-0.46210	0.41230
C	7.65914	0.44231	0.31361
C	0.17100	0.61393	0.33201
C	1.15505	1.55870	0.15366
C	2.53292	1.09828	0.45258
C	3.67162	1.88888	-0.04975
C	5.02857	1.40116	0.23837
C	6.08348	2.29934	0.15375
C	7.39157	1.81449	0.19747
C	-0.33111	3.57930	-0.17970
C	0.95710	3.00958	-0.06811
C	2.05376	3.92844	-0.08335
C	3.40847	3.38603	-0.25143
C	4.52463	4.30708	-0.14472
C	5.88709	3.79334	0.27026
C	7.01167	4.55560	-0.38994
C	-0.51439	4.93848	0.05752
C	0.57091	5.76831	0.23459
C	1.89996	5.34964	-0.00406
C	3.02402	6.27427	-0.18022
C	4.31757	5.65794	-0.28405
C	5.48707	6.49162	-0.78378
C	6.82839	5.81173	-0.77942
C	-0.68487	8.88926	-0.18791
C	0.45417	8.13186	-0.00823
C	1.75541	8.55299	-0.39652
C	2.95253	7.74098	-0.27199
C	4.18453	8.49764	-0.20906
C	5.46226	7.86199	-0.16793
C	6.58694	8.54967	0.20821
C	-0.60162	10.15663	-0.77534
C	0.62792	10.67839	-1.12160
C	1.83569	9.93853	-0.82446
C	2.81221	10.70774	-0.44878
C	4.20242	9.92929	-0.20956
C	5.37344	10.64229	0.22429
C	6.53144	9.93947	0.49947
O	1.97658	-2.63439	0.58758
H	4.35419	-1.97651	0.38508
O	6.86068	-1.78580	0.55918
C	1.14071	12.03053	-1.45127
O	2.51936	11.92023	-1.04603
C	5.26971	12.12412	0.51094
H	-0.43636	-1.45809	0.53167
H	-0.87275	0.89514	0.36497
O	8.93946	-0.05446	0.35480
O	8.48289	2.65199	0.17784
O	-1.46667	2.86844	-0.44648
H	-1.51950	5.33486	0.14495

C	8.33863	3.86300	-0.62976
H	7.63139	6.36936	-1.24901
H	-1.62887	8.49219	0.16706
H	-1.49746	10.74356	-0.94728
H	7.53997	8.04228	0.28633
C	7.71462	10.63645	1.07329
H	1.16913	-3.14234	0.40605
H	7.82599	-1.90535	0.60772
O	0.34204	12.91014	-0.68748
O	1.01475	12.27844	-2.82376
H	1.55821	13.08534	-3.01329
O	4.28202	12.57057	1.08083
O	6.20858	12.98670	0.06257
H	6.13317	13.94022	0.21069
H	9.54686	0.69774	0.45476
H	8.97201	2.68250	-2.02524
H	-1.22007	2.06958	-0.93950
O	8.40727	3.47326	-1.97362
O	9.38293	4.69012	-0.26600
H	10.15687	4.44216	-0.79875
O	7.71219	11.75839	1.53452
O	8.83477	9.86896	1.05058
H	9.53103	10.41131	1.46525
O	2.73738	0.58054	1.75737
O	3.51337	2.42077	-1.36403
O	0.28285	7.00927	0.75472
O	5.28809	6.66939	-2.22104
H	4.41716	7.08378	-2.34189
O	5.89867	4.10572	1.70258
H	6.67456	3.66277	2.09136
As	1.11844	14.51430	-0.22489
O	-0.25000	15.56230	0.41781
O	2.29237	14.29226	1.16465
O	1.86662	15.37397	-1.66516
H	2.84037	15.24353	-1.55252
H	-0.93537	14.91370	0.72426
H	2.89937	10.74265	0.67654

## Final state

91

C	0.42181	-0.78880	0.52151
C	1.67326	-1.30753	0.60469
C	2.84237	-0.41873	0.70213
C	4.18779	-0.90998	0.45707
C	5.25137	-0.01320	0.38024
C	6.61301	-0.46210	0.41230
C	7.65914	0.44231	0.31361
C	0.17100	0.61393	0.33201
C	1.15505	1.55870	0.15366
C	2.53292	1.09828	0.45258
C	3.67162	1.88888	-0.04975

C	5.02857	1.40116	0.23837
C	6.08348	2.29934	0.15375
C	7.39157	1.81449	0.19747
C	-0.33111	3.57930	-0.17970
C	0.95710	3.00958	-0.06811
C	2.05376	3.92844	-0.08335
C	3.40847	3.38603	-0.25143
C	4.52463	4.30708	-0.14472
C	5.88709	3.79334	0.27026
C	7.01167	4.55560	-0.38994
C	-0.51439	4.93848	0.05752
C	0.57091	5.76831	0.23459
C	1.89996	5.34964	-0.00406
C	3.02402	6.27427	-0.18022
C	4.31757	5.65794	-0.28405
C	5.48707	6.49162	-0.78378
C	6.82839	5.81173	-0.77942
C	-0.68487	8.88926	-0.18791
C	0.45417	8.13186	-0.00823
C	1.75541	8.55299	-0.39652
C	2.95253	7.74098	-0.27199
C	4.18453	8.49764	-0.20906
C	5.46226	7.86199	-0.16793
C	6.58694	8.54967	0.20821
C	-0.60162	10.15663	-0.77534
C	0.62792	10.67839	-1.12160
C	1.83569	9.93853	-0.82446
C	2.99235	10.60783	-0.70561
C	4.20242	9.92929	-0.20956
C	5.37344	10.64229	0.22429
C	6.53144	9.93947	0.49947
O	1.97658	-2.63439	0.58758
H	4.35419	-1.97651	0.38508
O	6.86068	-1.78580	0.55918
C	0.60763	12.03393	-1.79800
O	-0.43858	12.66283	-1.87978
C	5.26971	12.12412	0.51094
H	-0.43636	-1.45809	0.53167
H	-0.87275	0.89514	0.36497
O	8.93946	-0.05446	0.35480
O	8.48289	2.65199	0.17784
O	-1.46667	2.86844	-0.44648
H	-1.51950	5.33486	0.14495
C	8.33863	3.86300	-0.62976
H	7.63139	6.36936	-1.24901
H	-1.62887	8.49219	0.16706
H	-1.49746	10.74356	-0.94728
H	7.53997	8.04228	0.28633
C	7.71462	10.63645	1.07329
H	1.16913	-3.14234	0.40605
H	7.82599	-1.90535	0.60772
O	-0.83935	15.07075	0.05360
O	1.70148	12.54223	-2.40464
H	1.67942	13.39377	-2.86394
O	4.28202	12.57057	1.08083
O	6.20858	12.98670	0.06257
H	6.13317	13.94022	0.21069
H	9.54686	0.69774	0.45476

H	8.97201	2.68250	-2.02524
H	-1.22007	2.06958	-0.93950
O	8.40727	3.47326	-1.97362
O	9.38293	4.69012	-0.26600
H	10.15687	4.44216	-0.79875
O	7.71219	11.75839	1.53452
O	8.83477	9.86896	1.05058
H	9.53103	10.41131	1.46525
O	2.73738	0.58054	1.75737
O	3.51337	2.42077	-1.36403
O	0.28285	7.00927	0.75472
O	5.28809	6.66939	-2.22104
H	4.41716	7.08378	-2.34189
O	5.89867	4.10572	1.70258
H	6.67456	3.66277	2.09136
As	0.81015	15.88288	0.07326
O	0.69242	17.52345	0.89593
O	1.99871	14.81031	0.97757
O	1.37932	16.09870	-1.66166
H	2.30382	15.74401	-1.66738
H	-0.17435	17.50225	1.37442
H	3.07215	11.66553	-0.87410

## References

- (1) Lanfredi, S.; Rodrigues, A. C. M. Impedance Spectroscopy Study of the Electrical Conductivity and Dielectric Constant of Polycrystalline LiNbO<sub>3</sub>. *J. Appl. Phys.* **1999**, *86* (4), 2215–2219. <https://doi.org/10.1063/1.371033>.
- (2) Wang, Y.; Chen, Y.; Lacey, S. D.; Xu, L.; Xie, H.; Li, T.; Danner, V. A.; Hu, L. Reduced Graphene Oxide Film with Record-High Conductivity and Mobility. *Mater. Today* **2018**, *21* (2), 186–192. <https://doi.org/10.1016/j.mattod.2017.10.008>.
- (3) Gupta, S.; Joshi, P.; Narayan, J. Electron Mobility Modulation in Graphene Oxide by Controlling Carbon Melt Lifetime. *Carbon* **2020**, *170*, 327–337. <https://doi.org/10.1016/j.carbon.2020.07.073>.
- (4) Yin, Y.; Cheng, Z.; Wang, L.; Jin, K.; Wang, W. Graphene, a Material for High Temperature Devices – Intrinsic Carrier Density, Carrier Drift Velocity and Lattice Energy. *Sci. Rep.* **2014**, *4* (1), 5758. <https://doi.org/10.1038/srep05758>.
- (5) Lee, J.-K.; Sung, H.; Jang, M. S.; Yoon, H.; Choi, M. Reliable Doping and Carrier Concentration Control in Graphene by Aerosol-Derived Metal Nanoparticles. *J. Mater. Chem. C* **2015**, *3* (32), 8294–8299. <https://doi.org/10.1039/C5TC01443C>.
- (6) Brown, M. A.; Crosser, M. S.; Leyden, M. R.; Qi, Y.; Minot, E. D. Measurement of High Carrier Mobility in Graphene in an Aqueous Electrolyte Environment. *Appl. Phys. Lett.* **2016**, *109* (9), 093104. <https://doi.org/10.1063/1.4962141>.
- (7) Mukherjee, S.; Ramireddy, H.; Baidya, A.; Amala, A. K.; Sudhakar, C.; Mondal, B.; Philip, L.; Pradeep, T. Nanocellulose-Reinforced Organo-Inorganic Nanocomposite for Synergistic and Affordable Defluoridation of Water and an Evaluation of Its Sustainability Metrics. *ACS Sustain. Chem. Eng.* **2020**, *8* (1), 139–147. <https://doi.org/10.1021/acssuschemeng.9b04822>.
- (8) Hanwell, M. D.; Curtis, D. E.; Lonie, D. C.; Vandermeersch, T.; Zurek, E.; Hutchison, G. R. Avogadro: An Advanced Semantic Chemical Editor, Visualization, and Analysis Platform. *J. Cheminformatics* **2012**, *4* (1), 17. <https://doi.org/10.1186/1758-2946-4-17>.
- (9) Humphrey, W.; Dalke, A.; Schulten, K. VMD: Visual Molecular Dynamics. *J. Mol. Graph.* **1996**, *14* (1), 33–38. [https://doi.org/10.1016/0263-7855\(96\)00018-5](https://doi.org/10.1016/0263-7855(96)00018-5).
- (10) Valiev, M.; Bylaska, E. J.; Govind, N.; Kowalski, K.; Straatsma, T. P.; Van Dam, H. J. J.; Wang, D.; Nieplocha, J.; Apra, E.; Windus, T. L.; de Jong, W. A. NWChem: A Comprehensive and Scalable Open-Source Solution for Large Scale Molecular

- Simulations. *Comput. Phys. Commun.* **2010**, *181* (9), 1477–1489. <https://doi.org/10.1016/j.cpc.2010.04.018>.
- (11) Enkovaara, J.; Rostgaard, C.; Mortensen, J. J.; Chen, J.; Du\lak, M.; Ferrighi, L.; Gavnholt, J.; Glinsvad, C.; Haikola, V.; Hansen, H. A.; Kristoffersen, H. H.; Kuisma, M.; Larsen, A. H.; Lehtovaara, L.; Ljungberg, M.; Lopez-Acevedo, O.; Moses, P. G.; Ojanen, J.; Olsen, T.; Petzold, V.; Romero, N. A.; Stausholm-Møller, J.; Strange, M.; Tritsarlis, G. A.; Vanin, M.; Walter, M.; Hammer, B.; Häkkinen, H.; Madsen, G. K. H.; Nieminen, R. M.; Nørskov, J. K.; Puska, M.; Rantala, T. T.; Schiøtz, J.; Thygesen, K. S.; Jacobsen, K. W. Electronic Structure Calculations with GPAW: A Real-Space Implementation of the Projector Augmented-Wave Method. *J. Phys. Condens. Matter* **2010**, *22* (25), 253202. <https://doi.org/10.1088/0953-8984/22/25/253202>.
- (12) Perdew, J. P.; Burke, K.; Ernzerhof, M. Generalized Gradient Approximation Made Simple. *Phys. Rev. Lett.* **1996**, *77* (18), 3865–3868. <https://doi.org/10.1103/PhysRevLett.77.3865>.
- (13) Mouhat, F.; Coudert, F.-X.; Bocquet, M.-L. Structure and Chemistry of Graphene Oxide in Liquid Water from First Principles. *Nat. Commun.* **2020**, *11* (1), 1566. <https://doi.org/10.1038/s41467-020-15381-y>.
- (14) Sinclair, R. C.; Coveney, P. V. Modeling Nanostructure in Graphene Oxide: Inhomogeneity and the Percolation Threshold. *J. Chem. Inf. Model.* **2019**, *59* (6), 2741–2745. <https://doi.org/10.1021/acs.jcim.9b00114>.
- (15) Lerf, A.; He, H.; Forster, M.; Klinowski, J. Structure of Graphite Oxide Revisited. *J. Phys. Chem. B* **1998**, *102* (23), 4477–4482. <https://doi.org/10.1021/jp9731821>.
- (16) Rappe, A. K.; Casewit, C. J.; Colwell, K. S.; Goddard, W. A.; Skiff, W. M. UFF, a Full Periodic Table Force Field for Molecular Mechanics and Molecular Dynamics Simulations. *J. Am. Chem. Soc.* **1992**, *114* (25), 10024–10035. <https://doi.org/10.1021/ja00051a040>.



# Toward Continuous Breath Monitoring on a Mobile Phone Using a Frugal Conducting Cloth-Based Smart Mask

Pillalamarri Srikrishnarka, Raaga Madhuri Dasi, Sourav Kanti Jana, Tripti Ahuja, Jenifer Shantha Kumar, Ankit Nagar, Amoghavarsha Ramachandra Kini, Boby George,\* and Thalappil Pradeep\*



Cite This: <https://doi.org/10.1021/acsomega.2c05017>



Read Online

ACCESS |



Metrics & More

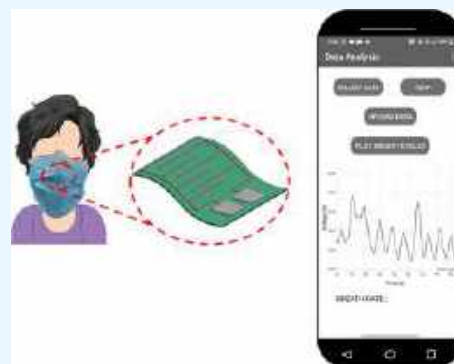


Article Recommendations



Supporting Information

**ABSTRACT:** A frugal humidity sensor that can detect changes in the humidity of exhaled breath of individuals has been fabricated. The sensor comprises a humidity-sensitive conducting polymer that is *in situ* formed on a cloth that acts as a substrate. Interdigitated silver electrodes were screen-printed on the modified cloth, and conducting threads connected the electrodes to the measurement circuit. The sensor's response to changing humidity was measured as a voltage drop across the sensor using a microcontroller. The sensor was capable of discerning between fast, normal, and slow breathing based on the response time. A response time of  $\sim 1.3$  s was observed for fast breathing. An Android-based mobile application was designed to collect sensor data *via* Bluetooth for analysis. A time series classification algorithm was implemented to analyze patterns in breathing. The sensor was later stitched onto a face mask, transforming it into a smart mask that can monitor changes in the breathing pattern at work, play, and sleep.



## INTRODUCTION

With ever growing concerns pertaining to the health and environmental impact caused by air pollution across the globe, a quick, affordable and noninvasive health monitoring device is the need of the hour. A recent investigation of the disease burden in 2017 revealed that  $\sim 544.9$  million people suffer from chronic respiratory diseases globally.<sup>1</sup> Monitoring humidity is crucial in many industries including those of food processing, semiconductor manufacturing, packaging, agriculture, and medicine.<sup>2–4</sup> Respiration is vital to sustaining human life, and the exhaled breath is a treasure trove that contains a vast variety of components such as water vapor, carbon dioxide, and volatile organic components, which can reveal vital information on health.<sup>5,6</sup> Apart from analyzing these components, measurement of the tidal volume and breath rate assists in determining the physiological state of the individual. A humidity sensor that is flexible, fast-responsive, affordable, and mobile phone-enabled can be deployed for continuous monitoring of breath rate and can eventually help determine the status of health.

In this regard, there have been advances toward fabricating humidity sensors that are capable of detecting humidity levels in exhaled breath. Typically, sensing is achieved by measuring with various transducing methods, including capacitance,<sup>7,8</sup> resistance,<sup>9,10</sup> absorbance,<sup>11–13</sup> surface acoustic waves,<sup>14–17</sup> and adsorption on quartz crystal microbalance,<sup>18–21</sup> and by devices such as a field effect transistor.<sup>22,23</sup> A variety of materials including conducting polymers, metal oxides, noble metal nanoparticles, carbon nanotubes, and graphene oxide

have been investigated for their humidity-sensing capabilities. A humidity sensor reported by Moger et al. showed a response time of  $\sim 10$  ms, which is one of the fastest responding supramolecular systems.<sup>20,24,25</sup> Yi et al. fabricated an optical fiber-based humidity sensor that utilized a microknott resonator incorporated into a Mach–Zehnder (MZ) interferometer and observed a response time of 84 ms. Although these sensors possess quick response times, their major drawbacks are high cost and complicated fabrication methods.<sup>10</sup> Textiles and paper-based substrates have paved the way for flexible/wearable electronics, especially sensors and nanogenerators. These are ideal as they are robust, nontoxic, high in availability, affordable, and have easy processability. Whitesides and colleagues first fabricated a paper-based flexible humidity sensor having digitally printed graphite electrodes on a piece of paper that was attached to a surgical mask.<sup>26</sup> Duan et al. further simplified the fabrication process of humidity sensors by utilizing a conducting polyester tape on a regular printing paper to detect changes in the exhaled breath.<sup>27</sup> Cellulose was chosen as an ideal substrate for humidity sensing as it offers ease in chemical modification, thus making it conducive for large-scale sensor fabrication.<sup>28–32</sup> A highly porous paper-

Received: August 6, 2022

Accepted: September 15, 2022

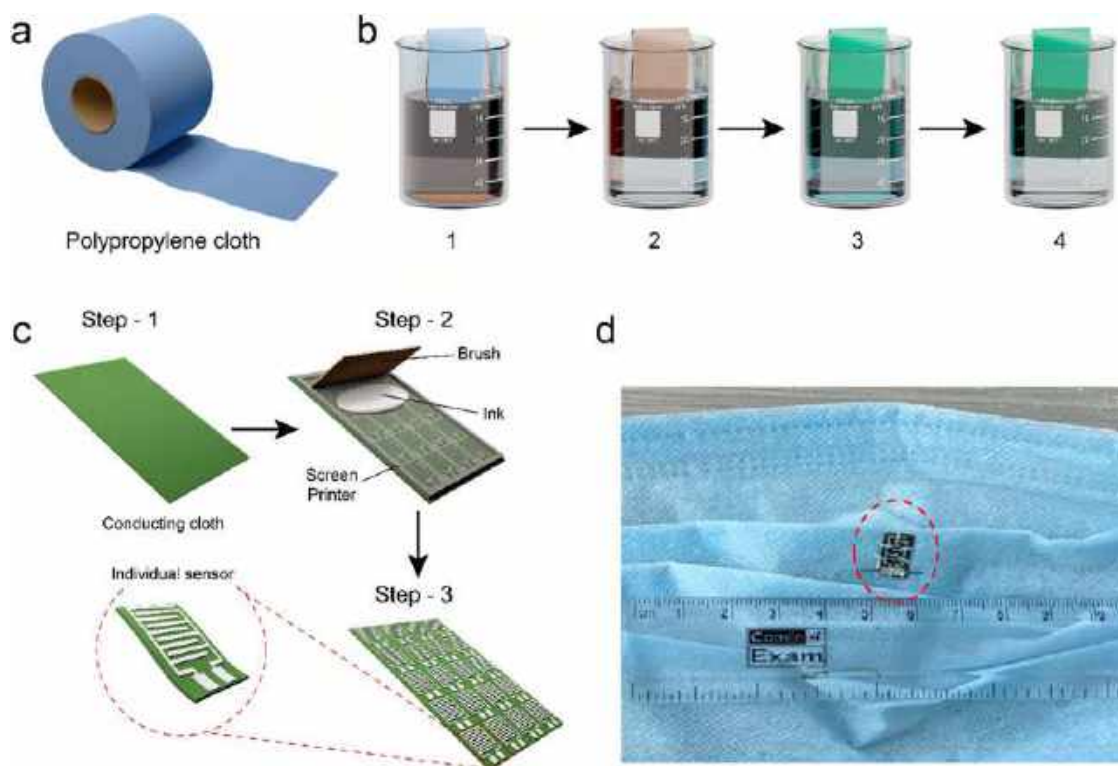


**Figure 1.** Schematic representation of the sensor fabrication process. (a) Roll of polypropylene (PP) mat. (b) SILAR procedure where a small piece of PP was immersed in beaker 1 containing aniline in HCl (aq). The mat was subsequently transferred to beaker 2 containing DI water. From this beaker, it was further immersed in beaker (3), which contained 12 g of APS in 1 M HCl (in water). Finally, the mat was rinsed in beaker (4) containing DI water, wherein its color changed from blue to green. (c) The dried conducting cloth was stretched on a frame for screen printing. The interdigitated electrode template was placed on top of the conducting cloth upon which silver paste was spread as shown in step 3. Finally, the sensor array cloth was dried, from which individual sensors were trimmed. A magnified view of a single sensor is shown in the dashed circle. (d) The sensor stitched on a common surgical mask. The sensor is marked with a circle.

based humidity sensor was fabricated by treating the copy paper with hydrochloric acid to remove calcium carbonate and washing to create porous structures.<sup>33</sup> After electrodes were screen-printed, the time periods for response and recovery were 0.8 and 0.78 s, respectively.<sup>33</sup> Recently, Chen and co-workers fabricated a flexible paper-based humidity sensor using origami, and conducting polyester electrodes were assembled onto the paper substrate that was folded along a predesigned pattern. They obtained a response and recovery time of 155 and 58 s, respectively, and their sensor was sensitive in a large humidity range.<sup>34</sup> A similar response and recovery time were observed from a carbon ink-coated filter paper-based humidity sensor.<sup>35</sup> Additionally, this sensor was self-powered and delivered an output voltage of 0.19 V and was highly flexible for  $\sim 1000$  bends.<sup>35</sup> However, due to the fragile nature of the paper, under continuous breathing, the paper could potentially become moist and subject to tare under stress. This could render the sensor difficult to use.

On the other hand, textiles are far more robust, flexible, and easy to process, thus making them ideal substrates for wearable electronics.<sup>36–38</sup> Wang et al. deposited graphene oxide (GO) on a bovine serum albumin (BSA)-coated nonwoven cloth by soaking the cloth in GO suspension and transforming it into a resistance-based humidity sensor. This sensor noted an average response of  $\sim 8.9$  s and a recovery of  $\sim 11.6$  s.<sup>39</sup> Recently, Allison et al. coated a commercially available cotton cloth with p-doped conjugated poly(3,4 ethylenedioxythiophene)/chloride *via* chemical vapor deposition. Integrating this modified cotton on a face mask enabled the user to freely move, and the

sensor was capable of differentiating different breathing patterns such as shallow and deep.<sup>40</sup> Wu and co-workers designed a flexible humidity sensor capable of respiration monitoring by creating interdigitated electrodes based on silver nanowires as the ink on a flexible leather cloth. Leather was chosen as it is biocompatible, low-cost, and convenient.<sup>41</sup> Recently, metal-organic frameworks (MOFs) have been investigated for their various sensing capabilities. In this aspect, Rauf et al. reported a smart textile containing a MOF film grown using the Langmuir–Blodgett (LB) technique resulting in a sensor capable of detecting water vapor in the presence of several volatile organic compounds.<sup>42</sup> Recently, Bokka et al. fabricated a water-soluble MoSSe quantum dots/poly(vinyl alcohol) (PVA) film as a humidity sensor that was capable of discerning different breathing patterns.<sup>43</sup> The breathing data were analyzed using a neural network algorithm for classifying them into different breathing patterns. Liu et al. recently fabricated a fabric-based humidity sensor using a hydrophobic-hydrophilic patterned polyester-spandex fabric as a substrate that was subsequently treated with polydopamine-acid carbon nanotubes (aCNTs) that were quick and sensitive to a large humidity range.<sup>44</sup> They observed a quick response and recovery time of 0.46 and 0.56 s, respectively.

Although there have been many humidity sensors with fast response time, ease of fabrication, and good sensitivity, they are not economical due to expensive raw materials, longer processing steps, or the requirement of complex electronic circuitry. From our previous work, we observed that conducting polymers such as polyaniline (PANi) can be *in*

*situ* polymerized on electrospun nanofibers of poly(vinylidene fluoride) (PVDF) by successive ionic layer adsorption and reaction (SILAR).<sup>45</sup> It is a versatile technique with upscaling capabilities due to its simplicity. We used SILAR for *in situ* polymerization of PANi on various substrates. This modified cloth was capable of sensing the changes in breath humidity over extended periods with a response time of  $\sim 0.31$  s. This was integrated into a face mask that transformed it into a smart mask. Conversion of the smart mask as a personal health monitoring and evaluation device integrated into a mobile phone is also presented.

## EXPERIMENTAL METHODS

**Materials.** Commercially available nonwoven polypropylene (PP) cloth and woven cotton, silk, and polyester cloth were procured locally. Aniline and ammonium persulfate (APS) were from RANKEM India. Hydrochloric acid was from Sigma Aldrich. Ethanol, lithium chloride (LiCl), magnesium chloride ( $\text{MgCl}_2$ ), potassium carbonate ( $\text{K}_2\text{CO}_3$ ), magnesium nitrate ( $\text{MgNO}_3$ ), sodium bromide (NaBr), sodium chloride (NaCl), and potassium chloride (KCl) were from Alfa Aesar. Millipore-produced deionized water ( $\sim 18$  M $\Omega$ ) was used throughout the experiment, and all of the chemicals were used as received without further purification unless mentioned otherwise.

**Methods. Fabrication of the Conducting PP Cloth.** From a roll of nonwoven PP fabric shown in Figure 1a, a small cloth of 12 cm  $\times$  12 cm dimension was cut and soaked in water for 12 h to ensure complete wetting; this is a vital step to ensure complete coverage of PANi. About 6 mL of aniline and 12 g of APS were added to two different beakers containing 80 mL of 1 M aqueous HCl solution. This wet cloth was later immersed in aniline solution for 5 min (Figure 1b1) and subsequently transferred to another beaker containing clean water to remove any unbound aniline molecules (Figure 1b2). Further, the cloth was soaked in a beaker containing APS for 10 min (Figure 1b3). The cloth was finally transferred into another beaker containing deionized (DI) water, as shown in Figure 1b4. This cycle was repeated 17 times for the growth of PANi on the mat (Figure 1). The cloth was later dried at 75 °C for 12 h for further use. Due to the growth of polyaniline on the cloth, the blue cloth was transformed to green. Interdigitated electrodes, with a gap of 0.6 mm, were screen-printed on the sensor *via* screen printing with commercial grade Ag paste. Upon drying of the ink, the cloth was cut into individual sensor elements for further analysis.

**Electrochemical Analysis of the Sensor.** The sensor element was taped to a glass slide for support, and electrical contacts were made with silver paste on the screen-printed silver pads. The other ends of the contact wires were connected to a Palmsense Emstat electrochemical workstation. An input bias potential of 3 V was provided to the sensor, and the chronoamperometric response in the presence of humidity was noted. All of the experiments were performed at  $45 \pm 5\%$  relative humidity (RH) and 25 °C, recorded using standard sensors. Exhaled air through the nose and mouth was directly pointed toward the sensors for sensing changes in humidity. A commercially available Eurolab plastic thermos-hygrometer was used to measure humidity.

A detailed description of the sensor unit is given in the Supporting Information. All of the components necessary for the measurement are presented in Table S3.

**Fabrication of a Prototype Smart Mask.** From the conducting mat with interdigitated electrodes printed on it, an individual sensor of size 6 mm  $\times$  12 mm was cut and stitched onto a surgical mask. The sensor was placed almost at the center of the mask, where the flux of the exhaled breath was maximum. The region was selected such that it is not interfered with by any creases and is directly exposed to exhaled breath. Stainless steel conducting threads were used to connect the sensor to a microcontroller. The conducting thread and sensor were coupled using silver paste (Electrolube Silver conducting paint) and kept for drying. The schematic of the controller is shown in Figure S6. A detailed cost analysis for different components used for the sensor is given in Table S3.

**Smart Mask Deployment.** A sample size of 23 volunteers was selected who were in the age range of 21–58, of which 14 were male and 9 were female. An average body mass index (BMI) of  $24.2 \pm 4.8$  for the interest group was noted. They were asked to exhale orally and through the nose to determine the breathing pattern and test the sensors' versatility in discerning different breathing patterns. Furthermore, the volunteers were asked to periodically cough for 5 s and breath for 10 s for a total period of 120 s so as to artificially introduce noise into the breathing pattern. Similarly, the subjects were asked to periodically withhold breathing for 10 s and breath for 10 s for a total of 120 s. These breathing data were used to train a deep neural network and several other classification algorithms for identifying the breathing frequency and to differentiate between normal and abnormal breathing.

**Characterization.** To investigate the size and morphology of bare and PANi-coated PP mat, they were characterized using a Thermo Scientific Verios U4 GHC field-emission scanning electron microscope (FESEM) with a retractable detector operating at 2 kV. The samples were sputter-coated with gold using a CRESSINGTON sputter-coater for 120 s. To understand the conformation of organic functional groups anchored on the fibers, infrared (IR) spectra were collected using a Perkin Elmer Spectrum One Fourier-transform infrared spectroscopy (FTIR) in the attenuated total reflection (ATR) mode. Raman spectral analysis was performed using a WiTec GmbH confocal Raman microscope ( $\alpha$ -300 s). A laser with a wavelength of 532 nm neodymium-doped yttrium aluminum garnet (Nd–YAG), with an excitation power of 0.2–0.5 mW, was maintained throughout the experiment. A 100 $\times$  objective lens was used for visualizing the fibers. Time-lapse Raman spectra were collected by placing the sensor under the objective, and oral breath was exhaled on the sensor. Spectra were collected for 50 s, with a time interval of 1 s. Impedance spectroscopy was performed on the sensor using a Biologic CH electrochemical workstation. The spectrum was collected using an alternating current (AC) signal of 20 mV with a direct current (DC) potential of 2 V. The frequency of the AC signal was varied between 7 MHz and 9 Hz, and the subsequent change in the impedance spectrum was noted. Contact angle measurements were performed using a Holmarc contact angle meter with a 3  $\mu\text{L}$  sessile water droplet. Then, 3  $\times$  3 cm<sup>2</sup> bare and PANi-treated PP mats were placed on a glass slide, which in turn were brought under the droplet for calculating the water contact angle.

## RESULTS AND DISCUSSION

For the fabrication of a flexible, wearable sensor, nonwoven PP cloth was chosen as the substrate. It possesses structural



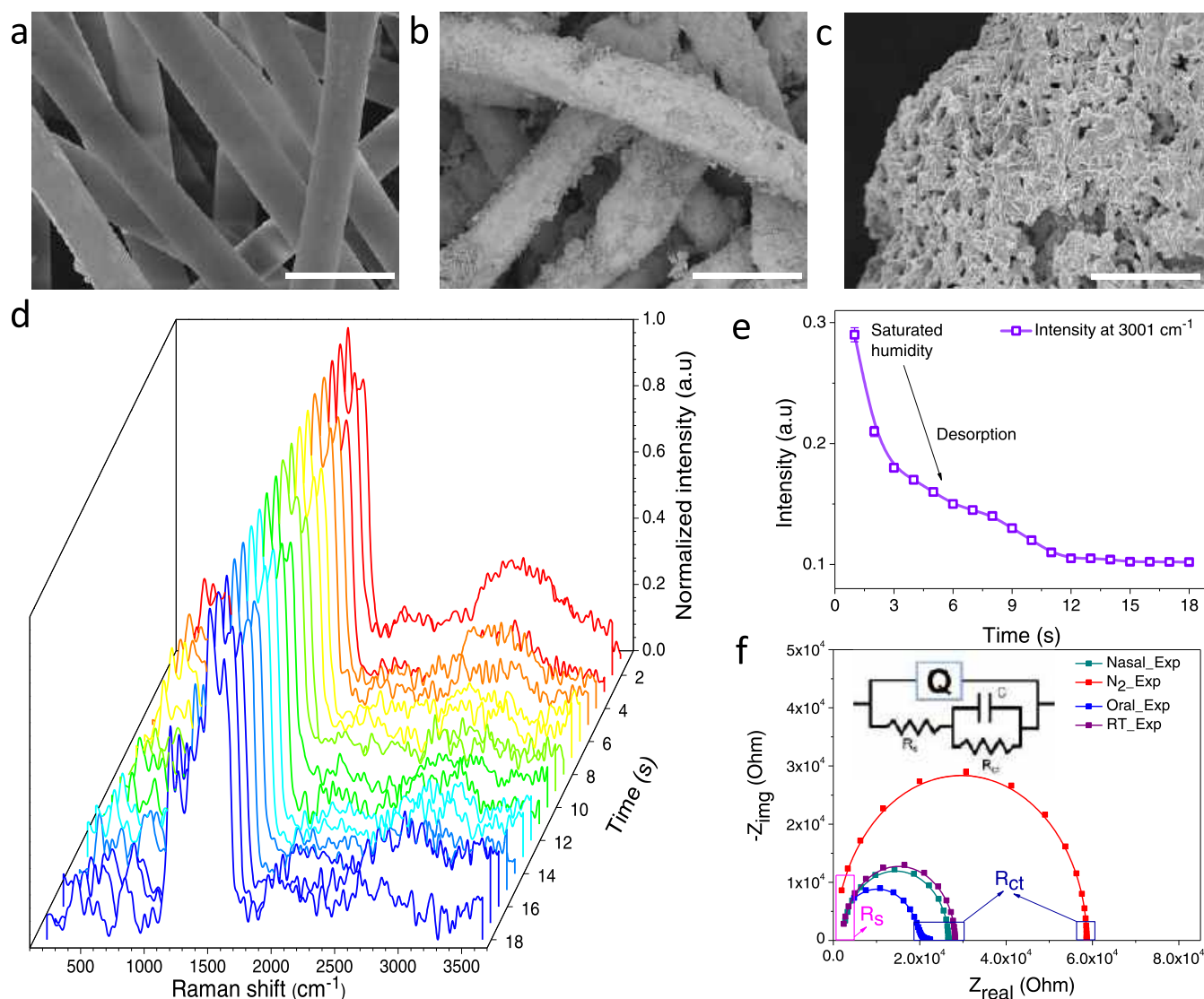


**Figure 2.** Scanning electron micrographs of (a) bare PP and (b, c) PANi-coated PP (scale bar is 50  $\mu\text{m}$  for (a, b) and 1  $\mu\text{m}$  for (c), respectively). (d) Time-dependent Raman spectra for understanding water desorption. (e) Variation in intensity for the peak at 3001  $\text{cm}^{-1}$ . (f) Nyquist plot to determine the  $R_s$  and  $R_{ct}$  of the sensor at room temperature and in dry air and nasal and oral breath exhalation. The circuit arrangement used for fitting the Nyquist plot is shown in the inset.

integrity against multiple bending cycles and offers high flexibility and the least resistance to the passage of air. A schematic representation of the fabrication process is depicted in Figure 1 (details are provided in the Materials and Methods Sections). Upon performing SILAR, the color of the mat changed from blue to green.

To visualize the morphological changes occurring during SILAR treatment, high-resolution scanning electron micrographs were collected for both bare and PANi-coated PP mats (Figure 2a–c). Fibers of the PP mat were randomly arranged, and their surfaces appeared smooth. The fibers were uniform in diameter ( $\sim 20 \mu\text{m}$ ), as observed in Figure 2a. Upon SILAR, aniline was polymerized on the PP fibers as evident from the deposits, making the surface of the fibers extremely rough as seen in Figure 2b. These structures are highly porous in nature (Figure 2c), which could assist in enhancing the sensitivity.

To confirm the presence of PANi on PP, FTIR and Raman spectroscopic analyses were performed, and the corresponding results are shown in Figure S1. FTIR spectra of untreated and PANi-coated PP are shown in Figure S1a. All of the

characteristic peaks were assigned and are listed in Table S2. Peaks at 1245, 1303, and 3203  $\text{cm}^{-1}$  for the PANi-coated PP mat were assigned to  $\gamma(\text{C}-\text{N})$ , aromatic  $\gamma(\text{C}-\text{N})$ , and  $\gamma(\text{N}-\text{H})$  stretching, respectively, thereby confirming the presence of PANi. A comparative study of the vibrational features of both bare and PANi-coated PP mats was performed using Raman spectroscopy (Figure S1b). The black trace represents bare PP, and the red trace represents a PANi-coated mat. A summary of these results is presented in Table S3.

To understand the adsorption–desorption dynamics of water molecules from the sensor, a time-dependent Raman spectral analysis on the cloth was performed. The conducting cloth was saturated with humidity by continuous exposure to exhaled breath, and time-lapse Raman spectra were collected for 18 s, at an interval of 1 s, as shown in Figure 2d. A broad peak at  $\sim 3001 \text{cm}^{-1}$  is attributed to the grouped frequencies of C–H and N–H, as observed in our previous work.<sup>45</sup> We believe that there could be a hydrogen bond between  $-(\text{NH})^+$  of PANi and  $\text{H}_2\text{O}$ , which assists in proton hopping. The peak intensity at 3001  $\text{cm}^{-1}$  reduced as the water molecule desorbed

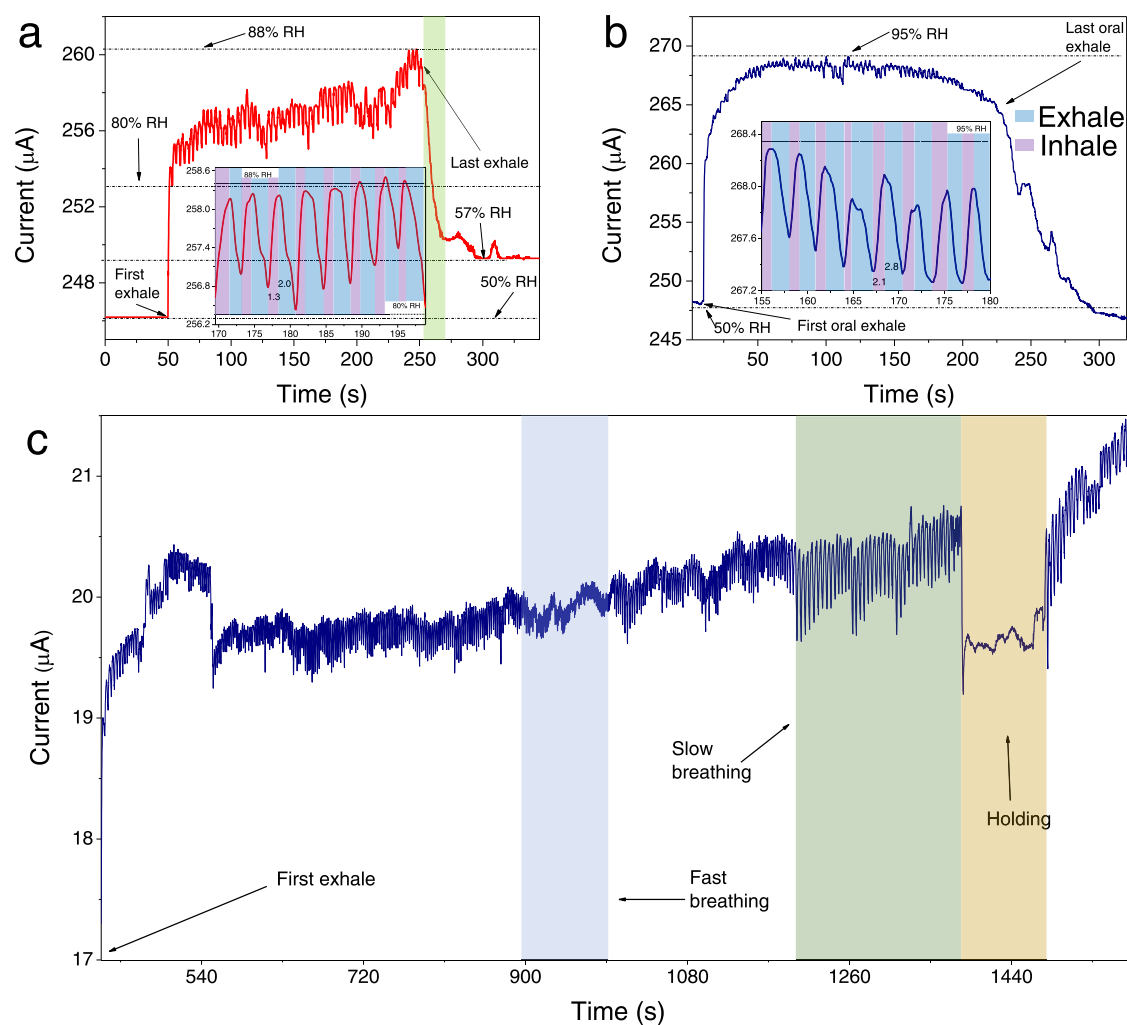


**Figure 3.** Chronoamperometric analysis for (a) nasal and (b) oral breath. Insets show magnified regions for understanding the response and recovery time. (c) Response of the sensor stitched on a surgical mask to nasal breathing over a longer period under various breathing styles (fast breathing, slow breathing, and holding). The data in (a, b) were measured using copper leads, while that in (c) were measured using the conducting thread.

from the surface of PANi. The intensity was plotted as a function of time (Figure 2e). The intensity dropped instantaneously within 1 s, reducing by  $\sim 27.7\%$ , and continued to drop as time progressed. The intensity stabilized after  $\sim 12$  s, indicating complete desorption of water molecules from the surface.

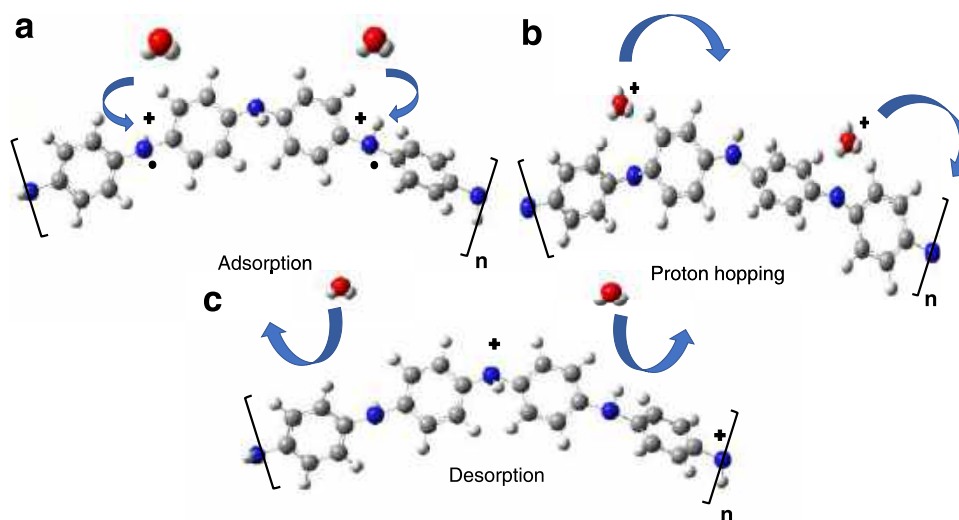
We further performed impedance spectroscopy to elucidate the mechanism of the sensing element under varying humidity. The Nyquist plots obtained in each case are shown in Figure 2f. Each Nyquist spectrum has two intercepts to the X axis, the first intercept corresponds to the surface resistance ( $R_s$ ) of the sensing material. The second intercept represents a change in the resistance ( $R_{ct}$ ), which is related to proton hopping caused by the adsorption/desorption of water molecules from the surface. In Nyquist spectra,  $R_s$  is not clearly seen, as it was not possible to measure the impedance beyond 7 MHz due to the limitation of the electrochemical analyzer.

The impedance of our sensor was measured by maintaining dry-air conditions by purging  $\text{N}_2$  over the sensor (Figure 2f). The corresponding  $R_{ct}$  decreased from 58 to 26  $\text{k}\Omega$ , which is a result of the adsorption of ambient water molecules on the surface of the mat. Upon nasal exhalation on the sensor, the resistance decreased to 24  $\text{k}\Omega$  and was further reduced to

$\sim 21.9 \text{ k}\Omega$  upon oral exhalation. This reduction in  $R_{ct}$  was attributed to the increased adsorption of water molecules in a high-humidity atmosphere, which results in increased proton hopping between the two contact pads. The capacitance of the sensor was  $0.87 \times 10^{-12} \text{ F}$  under the dry-air condition and increased to  $0.94 \times 10^{-12} \text{ F}$  under the room-temperature condition. Upon nasal exhalation, the capacitance increased to  $3.4 \times 10^{-12} \text{ F}$ , and in the presence of oral exhalation, it reached  $22 \times 10^{-12} \text{ F}$ . This increase in capacitances could be due to the formation of a capacitive double layer due to the spontaneous adsorption of moisture on the surface. The electronic circuit used to fit each Nyquist spectrum is shown in the inset in Figure 2f. The values have been tabulated and shown in Table S4.

An ideal sensor must possess a quick response and recovery time, which is possible if the sensor has an affinity toward water molecules and simultaneously undergoes fast desorption. To achieve these, the surface of the sensor should be amphiphilic in nature. To understand the wetting property of the sensor surface, the water contact angle before and after PANi coating was measured (Figure S2). The results suggested that the PP mat is hydrophobic in nature as the contact angle was  $143^\circ$  (Figure S2a). After growing PANi on the mat, the

**Scheme 1. Schematic Representation of the Sensing Mechanism.** (a) Adsorption of H<sub>2</sub>O on PANi, (b) Proton Transfer between the Partially Protonated PANi Backbone and H<sub>2</sub>O, and (c) Desorption of Water Molecules after Proton Transfer



contact angle reduced to 120°, which suggested that the mat lost its hydrophobic nature slightly, as seen in Figure S2b. We believe that due to this complex behavior, quick response and recovery are observed.

**Chronoamperometric Response of the Sensor.** To study the performance of the sensor under oral and nasal exhaled breath, the sensor was connected to a PalmSens electrochemical workstation, and a chronoamperometric study was performed with an applied external voltage of 3 V to the sensor. Subsequently, the current was measured under different breathing conditions, as shown in Figure 3. The sensor was initially allowed to stabilize at room temperature for 50 s, after which the first nasal exhalation was performed. As a result, the current rose from 246 to 256  $\mu\text{A}$  as shown in Figure 3a. It took  $\sim 13$  s for humidity to desorb completely from the surface of the sensor, as marked in the green box in Figure 3a. It is evident that the sensor is versatile in determining inhalation and exhalation (Figure 3a inset). We observed a response time of  $\sim 1.3 \pm 0.19$  s and a recovery time of  $\sim 2.07 \pm 0.32$  s. The sensor was further subjected to oral exhalation, and the resulting chronoamperometric analysis is shown in Figure 3b. Upon first oral exhalation, the current rose by 17  $\mu\text{A}$ . Oral inhalation and exhalation were continued further for 200 s. From the sensing results, it is evident that the time required for the desorption of water molecules from the surface of the sensor is  $\sim 65$  s. However, in the case of oral exhalation, the sensor was capable of distinguishing both with a response time of  $\sim 2.1 \pm 0.23$  s and a recovery time of  $\sim 2.8 \pm 0.31$  s (Figure 3b inset).

Further, to collect real-time data by conducting field trials using facemasks, the sensor was stitched to a mask. Since copper wires do not stitch well, they were replaced with conducting threads and silver paste. A chronoamperometric study was then performed to determine the sensor response (Figure 3c). The sensor was capable of discerning different breathing patterns. Upon the first exhalation, a rise of 3  $\mu\text{A}$  was recorded, and the peaks were present clearly even after continuous breathing. Initially, the volunteer was asked to breathe normally for a period of 420 s. The time period for a cycle of inhalation and exhalation was  $\sim 2.4 \pm 0.5$  s. For a period of  $\sim 2$  min (from 900 to 1020 s), the volunteer performed fast breathing. During this period, the inhalation–

exhalation cycles lasted for  $\sim 1.2$  s with a breath rate of  $\sim 82$  breaths/min. Subsequently, the volunteer was asked to execute deep inhalation and slow exhalation. In this regime, the time period for one breath cycle was  $\sim 4.4 \pm 0.3$  s. Finally, at the end of 1380 s, upon the last exhalation, the volunteer was asked to hold his/her breath for a period of  $\sim 60$  s, after which the breathing continued. We observed a slight increase in the overall current as time progressed. This could be attributed to the increased adsorption of moisture on the sensor during the breath-holding time.

The exhaled breath comprised several different compounds. An analysis of these compounds would relate to understanding the well-being of an individual. Acetone and ethanol are some of the commonly known components of exhaled breath in diabetics<sup>46</sup> and alcoholics,<sup>47</sup> respectively. Droplets containing different concentrations of an ethanol–water mixture were brought close to the sensor, and the response from the sensor was recorded (Figure S3a). As the concentration of ethanol increased, the drop in current also increased. A plot of concentration vs current shows the drop (Figure S3b). Similarly, the sensor's response in the presence of acetone–water mixture is shown in Figure S3c. A plot depicting a drop in current vs concentration of acetone is shown in Figure S3d. The drop was the highest for pure ethanol compared to acetone; however, at 5% concentration in water, there was a gain in current in the case of ethanol, unlike acetone. An increase in water content in the droplet results in a decrease in the current drop, which suggests that the sensing mechanism is based on Grotthuss proton hopping. In pure droplets of acetone and water, in the absence of H<sub>2</sub>O molecules, no H<sub>3</sub>O<sup>+</sup> species are observed, which is necessary for proton hopping. As the concentration of water in each of the droplets increases, the overall current drop also reduces. As soon as the droplet of acetone or ethanol is brought near the vicinity of the sensor, due to their high vapor pressure, the vapors of these volatile molecules disperse the adsorbed moisture on the sensor, and in the absence of protons on the surface of the sensor, a dip in the conductivity is observed with a drop in current. In the case of binary mixtures, due to the lower surface tension of ethanol/acetone within the droplet, these molecules tend to move toward the surface of the water droplet.<sup>48</sup> From the surface, the vapors of acetone/ethanol evaporate and they disperse the



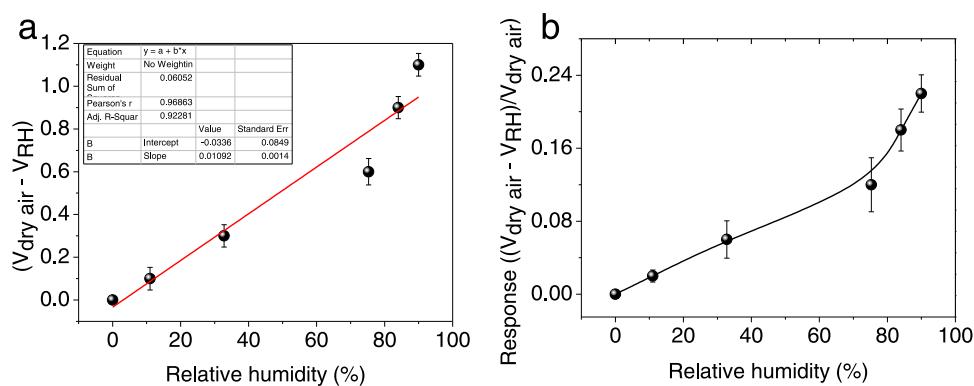


**Figure 4.** (a) Difference between the output voltage and the output voltage at different relative humidity conditions vs % relative humidity. (b) Sensor's response at different % RH values.



**Figure 5.** (a) Photograph of a volunteer wearing the mask. (b) Screen grabs of the Android application designed to monitor the breathing pattern. (c) Breathing patterns of a volunteer recorded using the mobile application depicting normal breathing.

adsorbed water molecules on the surface of the sensor. We suspect that as the concentrations of these volatile species decrease inside the droplet, the overall vapor pressure reduces, resulting in a decrease in the current drop. When a drop of the water–ethanol mixture (95% water, 5% ethanol) was brought close to the surface of the sensor, there was an increase in the current, which reduced as the droplet was retracted from the surface. We suspect that as the ethanol molecules evaporated from the droplet, a small number of water molecules might have evaporated along with them. With the increase of protons

on the surface of the sensor, the conductivity might have increased.

**Sensing Mechanism.** We believe that the Grotthuss proton hopping is the underlying mechanism of sensing.<sup>49</sup> Adsorption of H<sub>2</sub>O molecules on the surface of PANi is driven by the formation of intermolecular hydrogen bonds as shown in **Scheme 1a**. This acts as a “switch” throughout the surface, resulting in an increase in the conductivity with an increase in the ambient %RH levels. The Emeraldine salt form of PANi in a partially protonated state enables it to form a “switch” in the

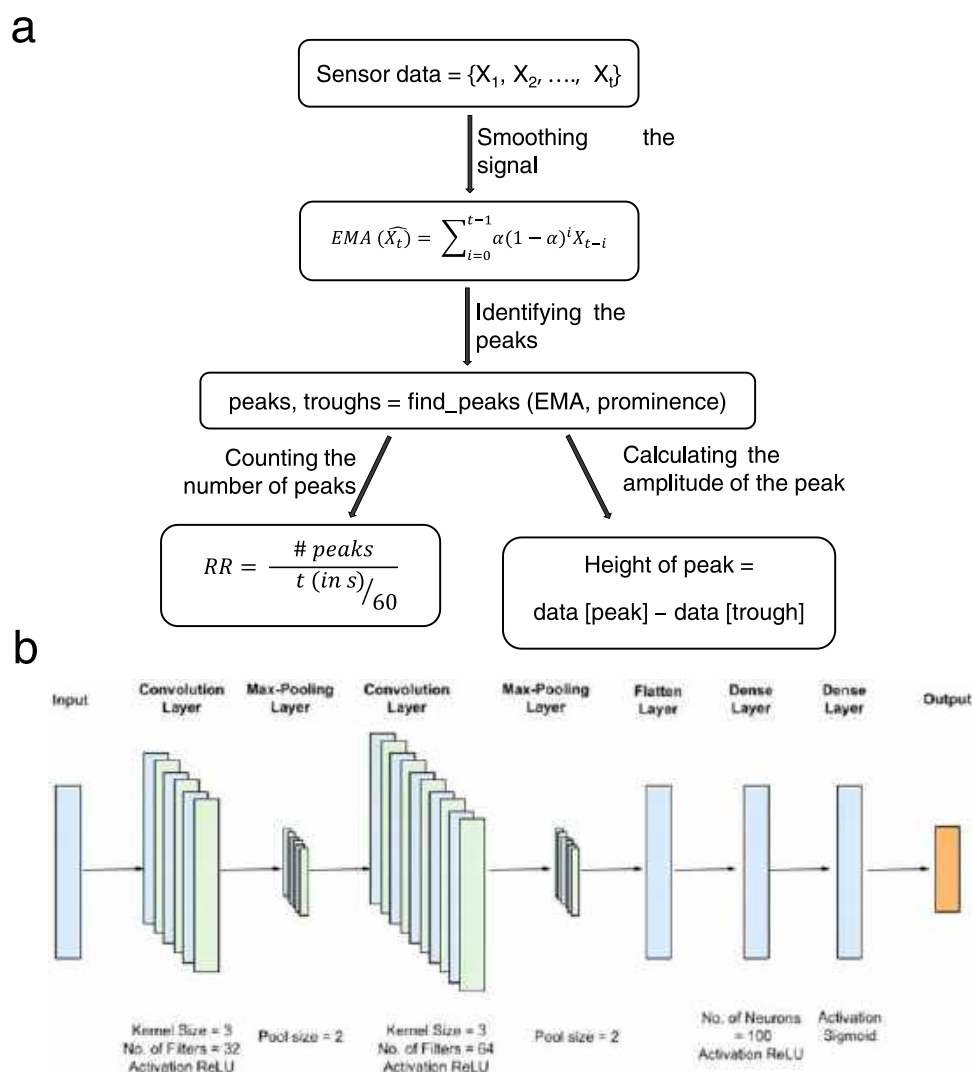


**Figure 6.** (a) Flow chart describing the process of obtaining the respiration rate (RR). (b) 1D convolutional neural network used for binary classification.

presence of the adsorbed water molecules. This results in the formation of  $\text{H}_3\text{O}^+$  intermediary species, which are then transferred to the neighboring nitrogen atom as shown in Scheme 1b. Finally, desorption of the  $\text{H}_2\text{O}$  species occurs due to the hydrophobic nature of the PP backbone (Scheme 1c).

**Antibacterial Activity.** Due to the close vicinity of the sensor to the mouth, there is a possibility of bacterial growth on the sensor. To understand the bacterial inhibition property of the sensor, untreated PP and PANi-coated PP were placed on agar plates inoculated with Gram-negative (*Escherichia coli*) and Gram-positive (*Bacillus subtilis*) bacteria. Fresh bacterial cultures of *E. coli* (MTCC 443), *E. coli* (MTCC 739), and *B. subtilis* were spread on nutrient agar plates along with  $\sim 1 \text{ cm} \times 1 \text{ cm}$  pieces of the mats placed on top. Digital photographs of the agar plate containing the sensors with the bacterial lawn are shown in Figure S4. After overnight incubation at  $37^\circ \text{C}$ , the bacterial lawn formed was observed to not interact with PP and PANi-coated PP along its boundaries. This was confirmed through a thin, observable zone of inhibition along PP, though it was not prominent in the latter.

**Calibration of the Sensor.** The sensor's response under different controlled humidity conditions was measured as shown in Figure S5. Supersaturated salt solutions were used to

control humidity inside a bottle. A plot of  $(V_{\text{dry air}} - V_{\text{RH}})$  vs % RH is shown in Figure 4a; the slope of this curve shows the sensitivity of the sensor. The calibration curve depicting the response of the sensor in different humidity conditions is shown in Figure 4b. Details pertaining to the amount of salt used are given in Table S1.

**Design and Assembly of a Real-Time Monitoring Sensor through a Mobile Application.** The sensor unit after calibration was stitched on a disposable surgical mask, and a conducting thread was used to connect the mask to the prototype board (Figure S6). The components needed for the circuitry along with the cost of each component are provided in Table S5. All of the procured components were commercially available, and their overall cost can be further reduced with scale. A volunteer was requested to wear the modified surgical mask and breathe on the sensor (Figure 5a). An Android mobile application was developed to record the readings and record the number of breath cycles. The screen grabs from the application are shown in Figure 5b. Upon opening the application, the user is directed to the home page that directly leads to the "Find devices tab," where the user selects the available device. Thereafter, the user profile details are recorded. The user can then start measuring the breath

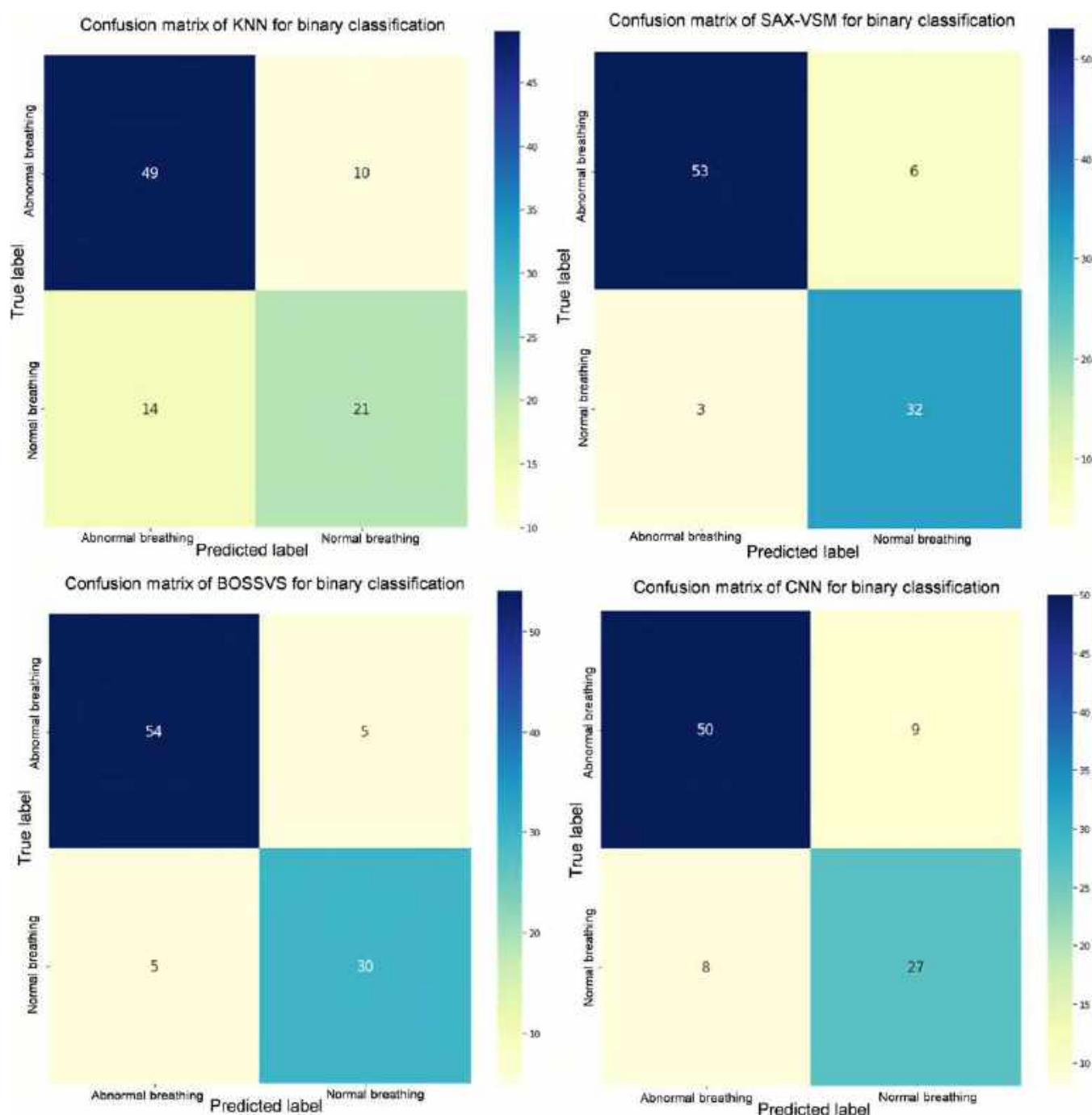


Figure 7. Comparing the performance of different classifiers on the collected data.

data. Once he/she is satisfied with the duration of breathing, the user can upload the data or directly plot the data, which gives the breath rate. The data obtained can be stored in their personal drive for future analysis. The responses obtained from the microcontroller in the presence of different breathing patterns are plotted in Figure S7.

Unlike in the case of the chronoamperometric study, wherein exhalation resulted in a rise in the current, the output voltage across the sensor decreased. We suspect this to be due to the increased capacitive nature of the sensor in the presence of humidity. Sensitivity is presented as the ratio of output voltage under dry air conditions to output voltage under exhalation. The time taken for one breath cycle was  $\sim 5.1$  s, as

the volunteer was asked to breathe normally. From Figure S7a,b, the breathing frequency of 13 and 6 breaths per min were observed for normal and slow breathing, respectively. As soon as the volunteer exhaled onto the sensor, an increase in the sensitivity was observed, which took  $\sim 2.89$  s to reach the maximum. Subsequently, as soon as the volunteer started to inhale, the sensitivity decreased (Figure S7a). When the volunteer exhaled slowly through the nose, there was a gradual increase in the sensitivity. The individual needed  $\sim 10.3$  s for one exhalation–inhalation cycle. This rise and fall in sensitivity is almost synchronous to the normal breathing rate of the individual. The breathing response of six different volunteers is shown in Figure S8. The sensor was able to differentiate

between slow, normal, and fast breathing, as the amplitude and time period of each peak was different for each breathing pattern. The fast-breathing pattern had a smaller amplitude compared to that of the normal or slow pattern. For some volunteers, the relative humidity of the nasal breath and oral exhalation was ~65 and ~80%, respectively.

Sleep apnea is a serious sleeping disorder in which, due to irregular breathing, sleep is often disturbed, leaving the patients tired. The sensor's capability to discern between breathing and breath holding was tested by asking a volunteer to breathe normally through the nose 5 times and hold the breath for 10 s. This cycle was repeated for a total duration of 120 s. The recorded response is shown in Figure S9. As soon as the volunteer began to hold his/her breath, a dip in the sensitivity was observed as humidity desorbed from the sensor. The response reversed as the volunteer followed up with a deep inhalation.

Furthermore, a volunteer was requested to wear the mask for an extended period while comfortably sitting and working on the laptop (Figure S10). While doing chores, no anomalies in the sensor's response were observed. An analysis of breath quality under stress for several volunteers falls under the scope of future work.

**Categorization of Breathing Patterns.** The flow from the collection of raw data to classification is shown in Figure 6a. Initial raw data were collected from Arduino Uno, from which exponentially weighted moving average (EMA), a smoothing technique, was applied to the time-ordered sequence of data. From the smoothed data, peaks and peak amplitude were calculated using the "find\_peaks" function of the SciPy library. As shown in Figure 6b, a one-dimensional (1D) convolutional neural network with two convolutional layers and two fully connected layers was used, since neural networks are capable of automatically extracting features from time series. There was a max pooling layer after every convolutional layer. The last layer performed the binary classification, and a sigmoid activation function was used. A binary cross-entropy loss function with the Adam optimizer was used. A batch size of 8 was selected, and the number of epochs was 50. These hyperparameters were chosen empirically.

The data collected from the smart mask were modeled as a time series since the humidity of exhaled breath varied with time. It was cleaned (filtered and smoothed) and split into segments of 1 min. A label was assigned to the segment based on the nature of breathing cycles in it. Segments with normal nasal and oral breathing were assigned the label "normal." Segments with deep nasal and oral breathing were assigned the label "slow." Segments with quick nasal and oral breathing were assigned the label "fast." A total of 373 segments were obtained from all of the volunteers with 139 for normal breathing, 136 for deep breathing, and 98 for quick breathing. These segments were then used to form the dataset for training the classification algorithms. The binary classification was implemented to classify the samples as normal and abnormal (fast and slow). The algorithm used logistic regression, 1D convolutional neural network (1D CNN), Bag-of-Symbolic Fourier Approximation (SFA) Symbols in Vector Space (BOSSVS), k-Nearest Neighbors (kNN), and Symbolic Aggregate approxImation in Vector Space Model (SAX-VSM) for classifying the breathing pattern. The performance metrics used were accuracy (Acc), true positive rate (TPR), and false positive rate (FPR), which are defined below.

Abnormal breathing was assigned as positive and normal breathing as negative for evaluating the accuracy of each model.

$$\text{Acc} = \frac{\text{TP} + \text{TN}}{\text{TP} + \text{TN} + \text{FP} + \text{FN}}$$

$$\text{TPR} = \frac{\text{TP}}{\text{TP} + \text{FN}}$$

$$\text{FPR} = \frac{\text{FP}}{\text{FP} + \text{TN}}$$

As concluded from Figure 7, an accuracy of 60.6% was observed for logistic regression, 81.91% for the 1D convolutional neural network, 89.36% for BOSSVS, and 74.46% for kNN, and the best accuracy of 90.42% was observed for SAX-VSM (Figure 7). These results have been tabulated in Table S6.

For studying the breathing pattern, smart masks were provided to 23 volunteers, and they were asked to exhale both orally and through the nasal passage. Some of their responses are shown in Figure S11. While wearing the masks, the volunteers were seated and were asked to breathe continuously for 120 s to calculate the time needed for slow breath, albeit oral or nasal. The time period was recorded to be 8.02 s, with outliers at 16.0 and 2.0 s. The longest time to take a complete breath, i.e., both inhalation and exhalation, was 16.0 s. On the other hand, the average time needed for a normal breath cycle was 3.2 s, the slowest being at 5.1 s and the fastest at 2.0 s for a complete breathing cycle. When the volunteers were asked to breathe faster, the average time was observed to be 1.8 s, and the slowest and fastest times were ~2.9 and 1.1 s, respectively. Thus, the sensor showed dynamic sensing capability by being able to distinguish between slow, fast, and normal breathing patterns. We believe that the sensor can be worn for extended periods of time and the breathing data can be collected for detailed analysis.

A comparison of different humidity sensors that have been employed for breath monitoring is given in Table S7. The absence of exotic materials such as graphene, carbon nanotubes, quantum dots, and MoS<sub>2</sub>, yet having almost a similar performance, makes our sensor compelling for everyday breath monitoring. SILAR is frugal and simplistic in fabrication and therefore can be fabricated by anyone with a basic understanding of the technique and can be further expanded to use other conducting polymers and applied on different fabric materials as well. We believe that due to its ease of fabrication and affordability, our sensor can be upscaled and deployed at a large scale for recording breathing patterns. The sensors were found to be extremely stable even after 1 year, although these sensors were fabricated in February 2020 and were tested during July–December 2021 due to multiple lockdowns. They were stable for long-term use. One of the volunteers wore the mask continuously for 120 min, and data were collected. Additionally, as the breathing data can be recorded on a mobile phone, the data can be shared with a specialist who could then analyze and provide appropriate suggestions on the medical condition. Furthermore, these data can be analyzed using a neural network algorithm for further improvement in the accuracy of the prediction.

A major challenge is device validation through clinical trials having larger datasets, which improves the accuracy of the models utilized. The electronic components used are the major



contributors to the price and the physical size of the device, which require optimization. Addressing these issues may help in providing everyone with a smart mask that is minimalistic, trendy, and affordable for everyday use.

## CONCLUSIONS

A frugal humidity sensor was fabricated by *in situ* polymerization of aniline on nonwoven PP cloth using SILAR. The fabrication process is scalable and affordable, thereby making it conducive for large-scale manufacturing. The sensor was later stitched on a disposable surgical mask, thereby transforming it into a smart mask for continuous monitoring of changes in the exhaled breath. The sensor was also capable of detecting various concentrations of acetone and ethanol, thus making it versatile. Bacterial growth studies indicated that even though the zone of inhibition was limited, the growth over the sensor cloth was not observed, thus rendering it safe for prolonged use. An Android phone application was designed to collect and analyze the user's breathing pattern and categorize it into fast, slow, and normal regimes. Our scalable, versatile, and affordable sensor along with analytics can help analyze the health of people. Such smart masks could be used for daily breath monitoring in hospitals and during workouts.

## ASSOCIATED CONTENT

### Supporting Information

The Supporting Information is available free of charge at <https://pubs.acs.org/doi/10.1021/acsomega.2c05017>.

Volatile organic compound testing protocol; sensor fabrication process; 1D convolutional neural network; (BOSSVS) algorithm; (SAX-VSM) algorithm; (kNN) classifier; FTIR and Raman spectra of bare PP and PANi-coated PP mats; contact angle measurements of bare PP and PANi-coated PP; table containing the parameters obtained from the Nyquist plot; calibration curve of the sensor under various values of humidity; response of the sensor in the presence of ethanol and acetone; antibacterial response of the sensor; fabrication of the sensor and the circuit diagram of the sensor assembly; breathing response of various volunteers; table containing the bill of materials; breathing response of a volunteer while performing various activities; performance of the various classification algorithms used; and the flow chart followed to calculate the breathing rate (PDF)

## AUTHOR INFORMATION

### Corresponding Authors

**Boby George** – Department of Electrical Engineering, Indian Institute of Technology, Chennai 600036, India;  
Email: [boby@iitm.ac.in](mailto:boby@iitm.ac.in)

**Thalappil Pradeep** – DST Unit of Nanoscience and Thematic Unit of Excellence, Department of Chemistry, Indian Institute of Technology, Chennai 600036, India; International Centre for Clean Water, IIT Madras Research Park, Chennai 600113, India; [orcid.org/0000-0003-3174-534X](https://orcid.org/0000-0003-3174-534X);  
Email: [pradeep@iitm.ac.in](mailto:pradeep@iitm.ac.in)

### Authors

**Pillalamarri Srikrishnarka** – DST Unit of Nanoscience and Thematic Unit of Excellence, Department of Chemistry, Indian Institute of Technology, Chennai 600036, India;

Department of Chemical Engineering, Indian Institute of Technology, Chennai 600036, India; [orcid.org/0000-0001-5187-6879](https://orcid.org/0000-0001-5187-6879)

**Raaga Madhuri Dasi** – Department of Electrical Engineering, Indian Institute of Technology, Chennai 600036, India;  
[orcid.org/0000-0002-1166-318X](https://orcid.org/0000-0002-1166-318X)

**Sourav Kanti Jana** – DST Unit of Nanoscience and Thematic Unit of Excellence, Department of Chemistry, Indian Institute of Technology, Chennai 600036, India; [orcid.org/0000-0001-5772-7022](https://orcid.org/0000-0001-5772-7022)

**Tripti Ahuja** – DST Unit of Nanoscience and Thematic Unit of Excellence, Department of Chemistry, Indian Institute of Technology, Chennai 600036, India

**Jenifer Shantha Kumar** – DST Unit of Nanoscience and Thematic Unit of Excellence, Department of Chemistry, Indian Institute of Technology, Chennai 600036, India

**Ankit Nagar** – DST Unit of Nanoscience and Thematic Unit of Excellence, Department of Chemistry, Indian Institute of Technology, Chennai 600036, India

**Amoghavarsha Ramachandra Kini** – DST Unit of Nanoscience and Thematic Unit of Excellence, Department of Chemistry, Indian Institute of Technology, Chennai 600036, India

Complete contact information is available at:

<https://pubs.acs.org/10.1021/acsomega.2c05017>

## Author Contributions

P.S. and R.M.D. contributed equally to this work. T.P. designed the problem, and P.S. optimized the sensor and characterized it. Electrochemical testing of the sensor was performed by S.K.J., R.M.D. designed the circuit and the Android application, which was evaluated by B.G.. T.A. performed the time-dependent Raman studies, and AK assisted with the figures. S.K.J. performed the antibacterial studies. All authors contributed to the writing of the manuscript.

## Notes

The authors declare no competing financial interest.

Code will be provided upon request from the authors.

## ACKNOWLEDGMENTS

The authors thank the Department of Science and Technology, Government of India, for supporting our research on nanomaterials. P.S., S.K.J., T.A., A.N., and S.K.J. thank IIT Madras for their research fellowship. AK thanks the Council of Science and Industrial Research (CSIR), Government of India, for a research fellowship. The authors acknowledge Professor Pijush Ghosh, Department of Applied Mechanics, IIT Madras, for helping them with contact angle measurements. They also thank all volunteers for their participation in this study, Dr. Premkumar for his assistance in presenting the sensing mechanism, and Dr. Joseph G. Manion of CG Figures for providing blender files needed for making the beakers.

## REFERENCES

- (1) Soriano, J. B.; Kendrick, P. J.; Paulson, K. R.; Gupta, V.; Abrams, E. M.; Adedoyin, R. A.; Adhikari, T. B.; Advani, S. M.; Agrawal, A.; Ahmadian, E.; Alahdab, F.; Aljunid, S. M.; Altirkawi, K. A.; Alvis-Guzman, N.; Anber, N. H.; Andrei, C. L.; Anjomshoa, M.; Ansari, F.; Antó, J. M.; Arabloo, J.; Athari, S. M.; Athari, S. S.; Awoke, N.; Badawi, A.; Banoub, J. A. M.; Bennett, D. A.; Bensenor, I. M.; Berfield, K. S. S.; Bernstein, R. S.; Bhattacharyya, K.; Bijani, A.; Brauer, M.; Bukhman, G.; Butt, Z. A.; Cámara, L. A.; Car, J.; Carrero, J. J.; Carvalho, F.; Castañeda-Orjuela, C. A.; Choi, J.-Y. J.

- Christopher, D. J.; Cohen, A. J.; Dandonna, L.; Dandonna, R.; Dang, A. K.; Daryani, A.; Courten, de Demeke, F. M.; Demoz, G. T.; Neve, J.-W. D.; Desai, R.; Dharmaratne, S. D.; Diaz, D.; Douiri, A.; Driscoll, T. R.; Duken, E. E.; Eftekhari, A.; Elkout, H.; Endries, A. Y.; Fadhil, I.; Faro, A.; Farzadfar, F.; Fernandes, E.; Filip, I.; Fischer, F.; Foroutan, M.; Garcia-Gordillo, M. A.; Gebre, A. K.; Gebremedhin, K. B.; Gebremeskel, G. G.; Gezae, K. E.; Ghoshal, A. G.; Gill, P. S.; Gillum, R. F.; Goudarzi, H.; Guo, Y.; Gupta, R.; Hailu, G. B.; Hasanzadeh, A.; Hassen, H. Y.; Hay, S. I.; Hoang, C. L.; Hole, M. K.; Horita, N.; Hosgood, H. D.; Hostiu, M.; Househ, M.; Ilesanmi, O. S.; Ilic, M. D.; Irvani, S. S. N.; Islam, S. M. S.; Jakovljevic, M.; Jamal, A. A.; Jha, R. P.; Jonas, J. B.; Kabir, Z.; Kasaeian, A.; Kasahun, G. G.; Kassa, G. M.; Kefale, A. T.; Kengne, A. P.; Khader, Y. S.; Khafaie, M. A.; Khan, E. A.; Khan, J.; Khubchandani, J.; Kim, Y.-E.; Kim, Y. J.; Kisa, S.; Kisa, A.; Knibbs, L. D.; Komaki, H.; Koul, P. A.; Koyanagi, A.; Kumar, G. A.; Lan, Q.; Lasrado, S.; Lauriola, P.; Vecchia, C. L.; Le, T. T.; Leigh, J.; Levi, M.; Li, S.; Lopez, A. D.; Lotufo, P. A.; Madotto, F.; Mahotra, N. B.; Majdan, M.; Majeed, A.; Malekzadeh, R.; Mamun, A. A.; Manafi, N.; Manafi, F.; Mantovani, L. G.; Meharie, B. G.; Meles, H. G.; Meles, G. G.; Menezes, R. G.; Mestrovic, T.; Miller, T. R.; Mini, G. K.; Mirakhimov, E. M.; Moazen, B.; Mohammad, K. A.; Mohammed, S.; Mohebi, F.; Mokdad, A. H.; Molokhia, M.; Monasta, L.; Moradi, M.; Moradi, G.; Morawska, L.; Mousavi, S. M.; Musa, K. I.; Mustafa, G.; Naderi, M.; Naghavi, M.; Naik, G.; Nair, S.; Nangia, V.; Nansseu, J. R.; Nazari, J.; Ndwandwe, D. E.; Negoi, R. I.; Nguyen, T. H.; Nguyen, C. T.; Nguyen, H. L. T.; Nixon, M. R.; Ofori-Asenso, R.; Ogbo, F. A.; Olagunju, A. T.; Olagunju, T. O.; Oren, E.; Ortiz, J. R.; Owolabi, M. O.; A, M. P.; Pakhale, S.; Pana, A.; Panda-Jonas, S.; Park, E.-K.; Pham, H. Q.; Postma, M. J.; Pourjafar, H.; Poustchi, H.; Radfar, A.; Rafiei, A.; Rahman, F.; Rahman, M. H. U.; Rahman, M. A.; Rawaf, S.; Rawaf, D. L.; Rawal, L.; R, C. R., Jr; Reitsma, M. B.; Roeber, L.; Ronfani, L.; Roro, E. M.; Roshandel, G.; Rudd, K. E.; Sabde, Y. D.; Sabour, S.; Saddik, B.; Safari, S.; Saleem, K.; Samy, A. M.; Santric-Milicevic, M. M.; Jose, B. P. S.; Sartorius, B.; Satpathy, M.; Savic, M.; Sawhney, M.; Sepanlou, S. G.; Shaikh, M. A.; Sheikh, A.; Shigematsu, M.; Shirkoohi, R.; Si, S.; Siabani, S.; Singh, V.; Singh, J. A.; Soljak, M.; Somayaji, R.; Soofi, M.; Soyiri, I. N.; Tefera, Y. M.; Temsah, M.-H.; Tesfay, B. E.; Thakur, J. S.; Toma, A. T.; Tortajada-Girbés, M.; Tran, K. B.; Tran, B. X.; Car, L. T.; Ullah, I.; Vacante, M.; Valdez, P. R.; Boven, J. F. M. van.; Vasankari, T. J.; Veisani, Y.; Violante, F. S.; Wagner, G. R.; Westerman, R.; Wolfe, C. D. A.; Wondafraash, D. Z.; Wondmieneh, A. B.; Yonemoto, N.; Yoon, S.-J.; Zaidi, Z.; Zamani, M.; Zar, H. J.; Zhang, Y.; Vos, T. Prevalence and Attributable Health Burden of Chronic Respiratory Diseases, 1990–2017: A Systematic Analysis for the Global Burden of Disease Study 2017. *Lancet Respir. Med.* **2020**, *8*, 585–596.
- (2) Wyrwa, J.; Barska, A. Innovations in the Food Packaging Market: Active Packaging. *Eur. Food Res. Technol.* **2017**, *243*, 1681–1692.
- (3) Benabdellah, N.; Bourhaleb, M.; Nasri, M.; Benazzi, N.; Dahbi, S. In *Design of Temperature and Humidity Sensors for an Electronic Nose Used in Rotten Food*, International Conference on Electrical and Information Technologies (ICEIT), 2016.
- (4) Brown, M. E.; de Beurs, K. M.; Marshall, M. Global Phenological Response to Climate Change in Crop Areas Using Satellite Remote Sensing of Vegetation, Humidity and Temperature over 26years. *Remote Sens. Environ.* **2012**, *126*, 174–183.
- (5) Popov, T. A. Human Exhaled Breath Analysis. *Ann. Allergy, Asthma, Immunol.* **2011**, *106*, 451–456.
- (6) Das, S.; Pal, M. Review—Non-Invasive Monitoring of Human Health by Exhaled Breath Analysis: A Comprehensive Review. *J. Electrochem. Soc.* **2020**, *167*, No. 037562.
- (7) Kim, Y.; Jung, B.; Lee, H.; Kim, H.; Lee, K.; Park, H. Capacitive Humidity Sensor Design Based on Anodic Aluminum Oxide. *Sens. Actuators, B* **2009**, *141*, 441–446.
- (8) Zampetti, E.; Pantalei, S.; Pecora, A.; Valletta, A.; Maiolo, L.; Minotti, A.; Macagnano, A.; Fortunato, G.; Bearzotti, A. Design and Optimization of an Ultra Thin Flexible Capacitive Humidity Sensor. *Sens. Actuators, B* **2009**, *143*, 302–307.
- (9) Hijikagawa, M.; Miyoshi, S.; Sugihara, T.; Jinda, A. A Thin-Film Resistance Humidity Sensor. *Sens. Actuators* **1983**, *4*, 307–315.
- (10) Yi, Y.; Jiang, Y.; Zhao, H.; Brambilla, G.; Fan, Y.; Wang, P. High-Performance Ultrafast Humidity Sensor Based on Microknot Resonator-Assisted Mach–Zehnder for Monitoring Human Breath. *ACS Sens.* **2020**, *5*, 3404–3410.
- (11) Zhao, Z.; Duan, Y. A Low Cost Fiber-Optic Humidity Sensor Based on Silica Sol–Gel Film. *Sens. Actuators, B* **2011**, *160*, 1340–1345.
- (12) Ando, M.; Kobayashi, T.; Haruta, M. Humidity-Sensitive Optical Absorption of Co<sub>3</sub>O<sub>4</sub> Film. *Sens. Actuators, B* **1996**, *32*, 157–160.
- (13) Hashim, A.; Hadi, A. Synthesis and Characterization of (MgO–Y<sub>2</sub>O<sub>3</sub>–CuO) Nanocomposites for Novel Humidity Sensor Application. *Sens. Lett.* **2017**, *15*, 858–861.
- (14) Wu, J.; Yin, C.; Zhou, J.; Li, H.; Liu, Y.; Shen, Y.; Garner, S.; Fu, Y.; Duan, H. Ultrathin Glass-Based Flexible, Transparent, and Ultrasensitive Surface Acoustic Wave Humidity Sensor with ZnO Nanowires and Graphene Quantum Dots. *ACS Appl. Mater. Interfaces* **2020**, *12*, 39817–39825.
- (15) Sheng, L.; Dajing, C.; Yuquan, C. A Surface Acoustic Wave Humidity Sensor with High Sensitivity Based on Electrospun MWCNT/Nafion Nanofiber Films. *Nanotechnology* **2011**, *22*, No. 265504.
- (16) Caliendo, C.; Verona, E.; D’Amico, A.; Furlani, A.; Iucci, G.; Russo, M. V. Surface Acoustic Wave Humidity Sensor. *Sens. Actuators, B* **1993**, *16*, 288–292.
- (17) Penza, M.; Anisimkin, V. I. Surface Acoustic Wave Humidity Sensor Using Polyvinyl-Alcohol Film. *Sens. Actuators, A* **1999**, *76*, 162–166.
- (18) Chen, Q.; Feng, N.; Huang, X.; Yao, Y.; Jin, Y.; Pan, W.; Liu, D. Humidity-Sensing Properties of a BiOCl-Coated Quartz Crystal Microbalance. *ACS Omega* **2020**, *5*, 18818–18825.
- (19) Qi, P.; Xu, Z.; Zhang, T.; Fei, T.; Wang, R. Chitosan Wrapped Multiwalled Carbon Nanotubes as Quartz Crystal Microbalance Sensing Material for Humidity Detection. *J. Colloid Interface Sci.* **2020**, *560*, 284–292.
- (20) Tang, L.; Chen, W.; Chen, B.; Lv, R.; Zheng, X.; Rong, C.; Lu, B.; Huang, B. Sensitive and Renewable Quartz Crystal Microbalance Humidity Sensor Based on Nitrocellulose Nanocrystals. *Sens. Actuators, B* **2021**, *327*, No. 128944.
- (21) Pascal-Delannoy, F.; Sorli, B.; Boyer, A. Quartz Crystal Microbalance (QCM) Used as Humidity Sensor. *Sens. Actuators Phys.* **2000**, *84*, 285–291.
- (22) Wu, S.; Wang, G.; Xue, Z.; Ge, F.; Zhang, G.; Lu, H.; Qiu, L. Organic Field-Effect Transistors with Macroporous Semiconductor Films as High-Performance Humidity Sensors. *ACS Appl. Mater. Interfaces* **2017**, *9*, 14974–14982.
- (23) Song, S.-H.; Yang, H.-H.; Han, C.-H.; Ko, S.-D.; Lee, S.-H.; Yoon, J.-B. Metal-Oxide-Semiconductor Field Effect Transistor Humidity Sensor Using Surface Conductance. *Appl. Phys. Lett.* **2012**, *100*, No. 101603.
- (24) Mogera, U.; Sagade, A. A.; George, S. J.; Kulkarni, G. U. Ultrafast Response Humidity Sensor Using Supramolecular Nanofibre and Its Application in Monitoring Breath Humidity and Flow. *Sci. Rep.* **2014**, *4*, No. 4103.
- (25) Lin, Q.; Li, Y.; Yang, M. Highly Sensitive and Ultrafast Response Surface Acoustic Wave Humidity Sensor Based on Electrospun Polyaniline/Poly(Vinyl Butyral) Nanofibers. *Anal. Chim. Acta* **2012**, *748*, 73–80.
- (26) Güder, F.; Anila, A.; Redson, J.; Mosadegh, B.; Glavan, A.; Martin, T. J.; Whitesides, G. M. Paper-Based Electrical Respiration Sensor. *Angew. Chem., Int. Ed.* **2016**, *55*, 5727–5732.
- (27) Duan, Z.; Jiang, Y.; Yan, M.; Wang, S.; Yuan, Z.; Zhao, Q.; Sun, P.; Xie, G.; Du, X.; Tai, H. Facile, Flexible, Cost-Saving, and Environment-Friendly Paper-Based Humidity Sensor for Multifunctional Applications. *ACS Appl. Mater. Interfaces* **2019**, *11*, 21840–21849.



- (28) Guan, X.; Hou, Z.; Wu, K.; Zhao, H.; Liu, S.; Fei, T.; Zhang, T. Flexible Humidity Sensor Based on Modified Cellulose Paper. *Sens. Actuators, B* **2021**, *339*, No. 129879.
- (29) Zhu, P.; Ou, H.; Kuang, Y.; Hao, L.; Diao, J.; Chen, G. Cellulose Nanofiber/Carbon Nanotube Dual Network-Enabled Humidity Sensor with High Sensitivity and Durability. *ACS Appl. Mater. Interfaces* **2020**, *12*, 33229–33238.
- (30) Wang, Y.; Zhang, L.; Zhou, J.; Lu, A. Flexible and Transparent Cellulose-Based Ionic Film as a Humidity Sensor. *ACS Appl. Mater. Interfaces* **2020**, *12*, 7631–7638.
- (31) Zhao, H.; Zhang, T.; Qi, R.; Dai, J.; Liu, S.; Fei, T. Drawn on Paper: A Reproducible Humidity Sensitive Device by Handwriting. *ACS Appl. Mater. Interfaces* **2017**, *9*, 28002–28009.
- (32) Zhu, P.; Kuang, Y.; Wei, Y.; Li, F.; Ou, H.; Jiang, F.; Chen, G. Electrostatic Self-Assembly Enabled Flexible Paper-Based Humidity Sensor with High Sensitivity and Superior Durability. *Chem. Eng. J.* **2021**, *404*, No. 127105.
- (33) Zhang, X.; He, D.; Yang, Q.; Atashbar, M. Z. Rapid, Highly Sensitive, and Highly Repeatable Printed Porous Paper Humidity Sensor. *Chem. Eng. J.* **2022**, *433*, No. 133751.
- (34) Chen, X.; Li, Y.; Wang, X.; Yu, H. Origami Paper-Based Stretchable Humidity Sensor for Textile-Attachable Wearable Electronics. *ACS Appl. Mater. Interfaces* **2022**, *14*, 36227–36237.
- (35) Li, X.; Guo, Y.; Meng, J.; Li, X.; Li, M.; Gao, D. Self-Powered Carbon Ink/Filter Paper Flexible Humidity Sensor Based on Moisture-Induced Voltage Generation. *Langmuir* **2022**, *38*, 8232–8240.
- (36) Ismar, E.; Kurşun Bahadır, S.; Kalaoglu, F.; Koncar, V. Futuristic Clothes: Electronic Textiles and Wearable Technologies. *Global Challenges* **2020**, *4*, No. 1900092.
- (37) Ma, C.; Yuan, Q.; Du, H.; Ma, M.-G.; Si, C.; Wan, P. Multiresponsive MXene (Ti<sub>3</sub>C<sub>2</sub>Tx)-Decorated Textiles for Wearable Thermal Management and Human Motion Monitoring. *ACS Appl. Mater. Interfaces* **2020**, *12*, 34226–34234.
- (38) Wu, J.; Wang, Z.; Liu, W.; Wang, L.; Xu, F. Bioinspired Superelastic Electroconductive Fiber for Wearable Electronics. *ACS Appl. Mater. Interfaces* **2019**, *11*, 44735–44741.
- (39) Wang, Y.; Zhang, L.; Zhang, Z.; Sun, P.; Chen, H. High-Sensitivity Wearable and Flexible Humidity Sensor Based on Graphene Oxide/Non-Woven Fabric for Respiration Monitoring. *Langmuir* **2020**, *36*, 9443–9448.
- (40) Allison, L. K.; Rostamina, S.; Kiaghadi, A.; Ganesan, D.; Andrew, T. L. Enabling Longitudinal Respiration Monitoring Using Vapor-Coated Conducting Textiles. *ACS Omega* **2021**, *6*, 31869–31875.
- (41) Xie, R.; Du, Q.; Zou, B.; Chen, Y.; Zhang, K.; Liu, Y.; Liang, J.; Zheng, B.; Li, S.; Zhang, W.; Wu, J.; Huo, F. Wearable Leather-Based Electronics for Respiration Monitoring. *ACS Appl. Bio Mater.* **2019**, *2*, 1427–1431.
- (42) Rauf, S.; Vijjapu, M. T.; Andrés, M. A.; Gascón, I.; Roubeau, O.; Eddaoudi, M.; Salama, K. N. Highly Selective Metal–Organic Framework Textile Humidity Sensor. *ACS Appl. Mater. Interfaces* **2020**, *12*, 29999–30006.
- (43) Bokka, N.; Karhade, J.; Sahatiya, P. Deep Learning Enabled Classification of Real-Time Respiration Signals Acquired by MoS<sub>2</sub> Quantum Dot-Based Flexible Sensors. *J. Mater. Chem. B* **2021**, *9*, 6870–6880.
- (44) Liu, L.; Ni, Y.; Mao, J.; Li, S.; Ng, K. H.; Chen, Z.; Huang, J.; Cai, W.; Lai, Y. Flexible and Highly Conductive Textiles Induced by Click Chemistry for Sensitive Motion and Humidity Monitoring. *ACS Appl. Mater. Interfaces* **2022**, *14*, 37878–37886.
- (45) Iyengar, S. A.; Srikrishnarka, P.; Jana, S. K.; Islam, M. R.; Ahuja, T.; Mohanty, J. S.; Pradeep, T. Surface-Treated Nanofibers as High Current Yielding Breath Humidity Sensors for Wearable Electronics. *ACS Appl. Electron. Mater.* **2019**, *1*, 951–960.
- (46) Tanda, N.; Hinokio, Y.; Washio, J.; Takahashi, N.; Koseki, T. Breath Acetone in Type 1 and Type 2 Diabetes Mellitus. In *Interface Oral Health Science 2011*; Sasaki, K.; Suzuki, O.; Takahashi, N., Eds.; Springer Japan: Tokyo, 2012; pp 212–214.
- (47) Wu, L.; McIntosh, M.; Zhang, X.; Ju, H. Amperometric Sensor for Ethanol Based on One-Step Electropolymerization of Thionine-Carbon Nanofiber Nanocomposite Containing Alcohol Oxidase. *Talanta* **2007**, *74*, 387–392.
- (48) Liu, C.; Bonaccorso, E.; Butt, H.-J. Evaporation of Sessile Water/Ethanol Drops in a Controlled Environment. *Phys. Chem. Chem. Phys.* **2008**, *10*, 7150–7157.
- (49) Farahani, H.; Wagiran, R.; Hamidon, M. Humidity Sensors Principle, Mechanism, and Fabrication Technologies: A Comprehensive Review. *Sensors* **2014**, *14*, 7881–7939.

# Supporting Information for

## Toward Continuous Breath Monitoring on a Mobile Phone Using a Frugal Conducting Cloth-Based Smart Mask

*Pillalamarri Srikrishnarka,<sup>†,‡</sup> Raaga Madhuri Dasi,<sup>‡</sup> Sourav Kanti Jana,<sup>†</sup> Tripti Ahuja,<sup>†</sup> Jenifer  
Shantha Kumar,<sup>†</sup> Ankit Nagar,<sup>†</sup> Amoghavarsha Ramachandra Kini,<sup>†</sup> Bobby George<sup>\*‡</sup> and  
Thalappil Pradeep<sup>\*†</sup>*

<sup>†</sup> DST Unit of Nanoscience and Thematic Unit of Excellence, Department of Chemistry, Indian  
Institute of Technology Madras, India 600036.

<sup>‡</sup> Department of Chemical Engineering, Indian Institute of Technology Madras, India 600036.

<sup>‡</sup> Department of Electrical Engineering, Indian Institute of Technology Madras, India 600036.

\*E-mail: [boby@iitm.ac.in](mailto:boby@iitm.ac.in), [pradeep@iitm.ac.in](mailto:pradeep@iitm.ac.in)

PS and DRM have contributed equally

### **SUPPORTING INFORMATION CONTENT**

Total number of pages: 27

Total number of figures: 11

Total number of tables: 7

## TABLE OF CONTENTS

Figure No.	Description	Page No.
Note S1	Volatile organic compound (VOC) testing	S3
Note S2	Sensor calibration protocol	S3
Table S1	Quantities of salt needed to create controlled humidity	S3
Note S3	Classification of sensor data	S3
Figure S1	FTIR and Raman spectra of the bare and PANi coated PP mat	S6
Table S2	FTIR peak assignment for PP and PANI coated PP mat	S7
Table S3	Raman peak assignment for PP and PANi-coated PP mat	S8
Figure S2	Water contact angle measurement	S9
Table S4	Parameters from the Nyquist plot	S10
Figure S3	Response of the sensor in the presence of ethanol and acetone	S11
Figure S4	Antibacterial response of the sensor	S12
Figure S5	Schematic for humidity sensor calibration set-up	S13
Figure S6	Photograph of the circuit and the circuit diagram	S14
Table S5	Bill of material	S15
Figure S7	(a)Slow and (b) normal breathing response of an individual recorded on the mobile phone	S16
Figure S8	Breathing response of various volunteers	S17
Figure S9	Breathing response of a volunteer while cycling between breathing and holding breath	S18
Figure S10	Breathing response of a volunteer while working	S19
Figure S11	(a) Bar chart depicting the number of male and female volunteers in the study. (b) BMI distribution of all the volunteers. (c and d)	S20

	Time required for completing a total breathing cycle orally and through the nose, respectively	
Table S6	Comparing the accuracy of different classifiers used	S21
Table S7	Comparison of different humidity sensors	S21
	References	S22

### **Note S1. Volatile organic compound (VOC) testing**

To study the sensor's selectivity to VOCs, 5  $\mu$ L of ethanol-water mixtures of varying compositions were brought at  $\sim$  1 mm distance to the sensor and the response of the sensor was noted. Similar experiment was repeated with the acetone-water mixture.

### **Note S2. Calibration of the sensor**

Sensor's response was calibrated under controlled humidity using supersaturated salt solutions in a bottle as shown in Figure S5a. Details pertaining to the quantity of salt and the corresponding humidity achieved is given below in Table S1.

**Table S1.** Details regarding the quantity of salt needed to create controlled humidity.

Salt name	Quantity (g)	Volume of water (mL)	Relative humidity (%RH)
LiCl	29.3	10	11
MgCl <sub>2</sub>	100	10	32.8
NaCl	41.1	10	75.3
KCl	31.2	10	84.3

### **Note S3. Classification of sensor data**

Binary classification was implemented on the uniformly segmented dataset to classify the samples into the following categories – normal and abnormal (deep breathing and fast breathing).

The dataset was randomly split into training and test data, and four kinds of classification algorithms were applied to investigate their feasibility in detecting breathing patterns. These algorithms were chosen as they have been commonly used in machine learning in the medical field and for classifying time series.

Logistic regression was firstly used to see if treating the time series as a tabular data affected the accuracy of the classifier. Each time series was iteratively split into segments with window sizes ranging from 26 data points to 522 data points. In each iteration, features such as mean, standard deviation, maximum value, minimum value and median were extracted for every segment and a 10-fold cross validation was implemented to identify critical features. The segment size with the best cross-validation score was used to fit the classifier model.

Time series-specific classification algorithms such as Bag-of-SFA Symbols in Vector Space (BOSSVS), k-Nearest Neighbours (kNN) and Symbolic Aggregate approxXimation in Vector Space Model (SAX-VSM) were also implemented with the help of the Python packages *pyts* and *pyt*. For the kNN classifier, DTW was selected as the distance metric.

Bag-of-SFA Symbols in Vector Space (BOSSVS) algorithm transform the time series and its labels into a document-term matrix format using tf-idf statistics. The time series was split into sliding windows with a window size of 48 and Symbolic Fourier Approximation (SFA) was applied to each sliding window. This transformed the time series into an unordered set of SFA words. A histogram was constructed to store the frequencies of the SFA words. For each class, a tf-idf vector was computed by using these histograms. For a new time series, the label with the highest cosine similarity between its tf vector and the tf-idf vectors of each class was chosen as the predicted class.

Symbolic Aggregate approxiMation in Vector Space Model (SAX-VSM) algorithm also transforms the time series and its labels to a document-term matrix using the tf-idf statistics. First, the real-valued time series was transformed into a bag of words using Symbolic Aggregate approximation (SAX) algorithm. This algorithm reduced the time series to a Piecewise Aggregate Approximation (PAA) representation by dividing the dataset into equal-sized segments and computing the mean of the points within each segment. A window size of 36 was chosen for the segments. Then, the classes were transformed into a Vector Space Model (VSM) using term frequencies (tf) and inverse document frequencies (idf). The bag of SAX words was then transformed into a class-characteristic weight vectors using the tf-idf weighting, and these vectors were classified using the Cosine similarity. The algorithm automatically discovers and ranks time series patterns by their similarity to the label. For classifying an unlabeled time series, SAX-VSM computes cosine similarity values between the term frequency vector of the new time series and the tf-idf weight vectors representing the training classes. It is then assigned to the class whose vector yields the maximal cosine similarity value.



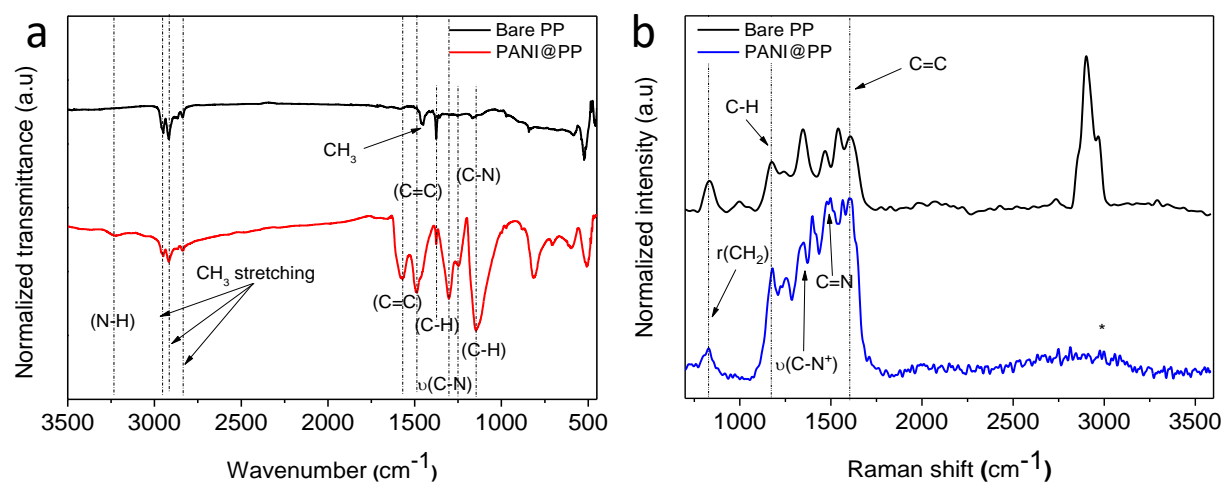


**Figure S1.** (a) FT-IR and (b) Raman spectrum of untreated PP and PANI@PP cloth. Prominent peaks are labeled.

**Table S2.** FTIR peak assignment for PP and PANI coated PP mat.

Wavenumber (cm <sup>-1</sup> )	PP mat	PANi@PP mat	Assignment
808	No	Yes	C-C stretching
840	Yes	No	C-H rocking <sup>1</sup>
1142	No	Yes	$\delta$ (C-H) stretching <sup>2</sup>
1161	Yes	No	(C-H) wagging <sup>3</sup>
1245	No	Yes	$\delta$ (C-N) stretching <sup>4</sup>
1303	No	Yes	$\gamma$ (C-N) aromatic stretching
1379	Yes	Yes	CH <sub>3</sub> stretching
1456	Yes	No	CH <sub>3</sub> symmetric bending
1493	No	Yes	Benzoid stretching <sup>5</sup>
1570	No	Yes	Quinonoid ring stretching <sup>5</sup>
2836	Yes	Yes	CH <sub>2</sub> asymmetric stretching
2866	Yes	Yes	CH <sub>3</sub> stretching
2949	Yes	Yes	CH <sub>3</sub> asymmetric stretching
3230	No	Yes	$\gamma$ (C-N) stretching <sup>3</sup>

**Table S3.** Raman peak assignment for PP and PANi-coated PP mat.

Raman shift (cm <sup>-1</sup> )	PP	PANi@PP	Assignment
829	Yes	Yes	r(CH <sub>3</sub> )
1167	Yes	Yes	C-C stretching
1345	Yes	Yes	Graphitic disorder
1350	No	Yes	$\gamma$ (C-N <sup>+</sup> ) stretching
1457	Yes	Yes	$\delta$ (C-H) stretching
1489	No	Yes	$\gamma$ (C=N) stretching
1500	No	Yes	$\delta$ (N-H) stretching <sup>6</sup>
1567	No	Yes	N-H bending
1606	Yes	Yes	C=C stretching
2818	Yes	No	$\gamma$ (CH <sub>3</sub> ) symmetric stretching <sup>7</sup>
2966	Yes	No	$\gamma$ (CH <sub>3</sub> ) asymmetric stretching <sup>7</sup>

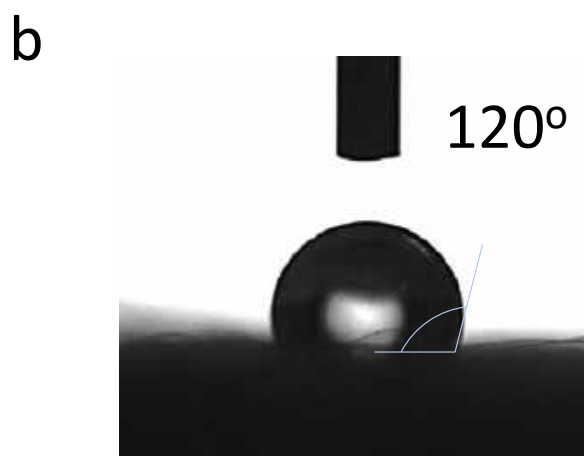
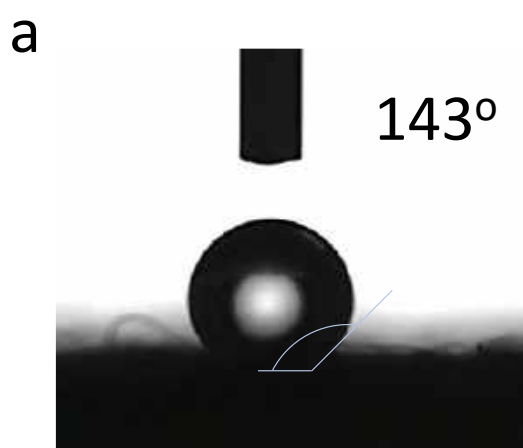


**Figure S2.** Contact angle measurements performed on (a) untreated PP mat, and (b) PANI@PP mat.

**Table S4.** Parameters obtained from the Nyquist plot.

Parameter	N <sub>2</sub>	Room temperature	Nasal exhalation	Oral exhalation
R <sub>s</sub> (kΩ)	2.4	2.2	1	0.63
R <sub>ct</sub> (kΩ)	58	26	24	21.9
C (F)	0.87 x 10 <sup>-12</sup>	0.94 x 10 <sup>-12</sup>	3.4 x 10 <sup>-12</sup>	11.6 x 10 <sup>-12</sup>

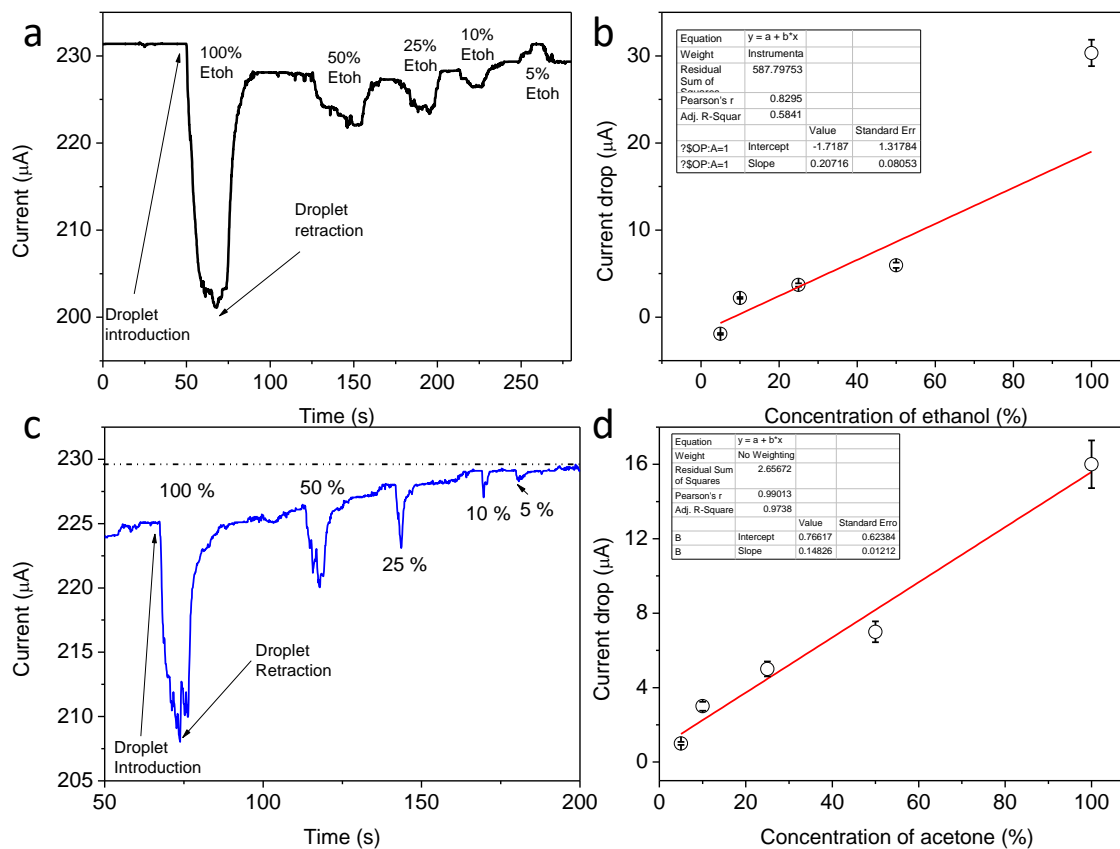


**Figure S3.** (a, c) Chronoamperometric response of the sensor in presence of a droplet of ethanol-water and acetone-water mixture at different concentrations. (b and d) Plot of ethanol-water and acetone-water concentrations, with respect to the current difference.



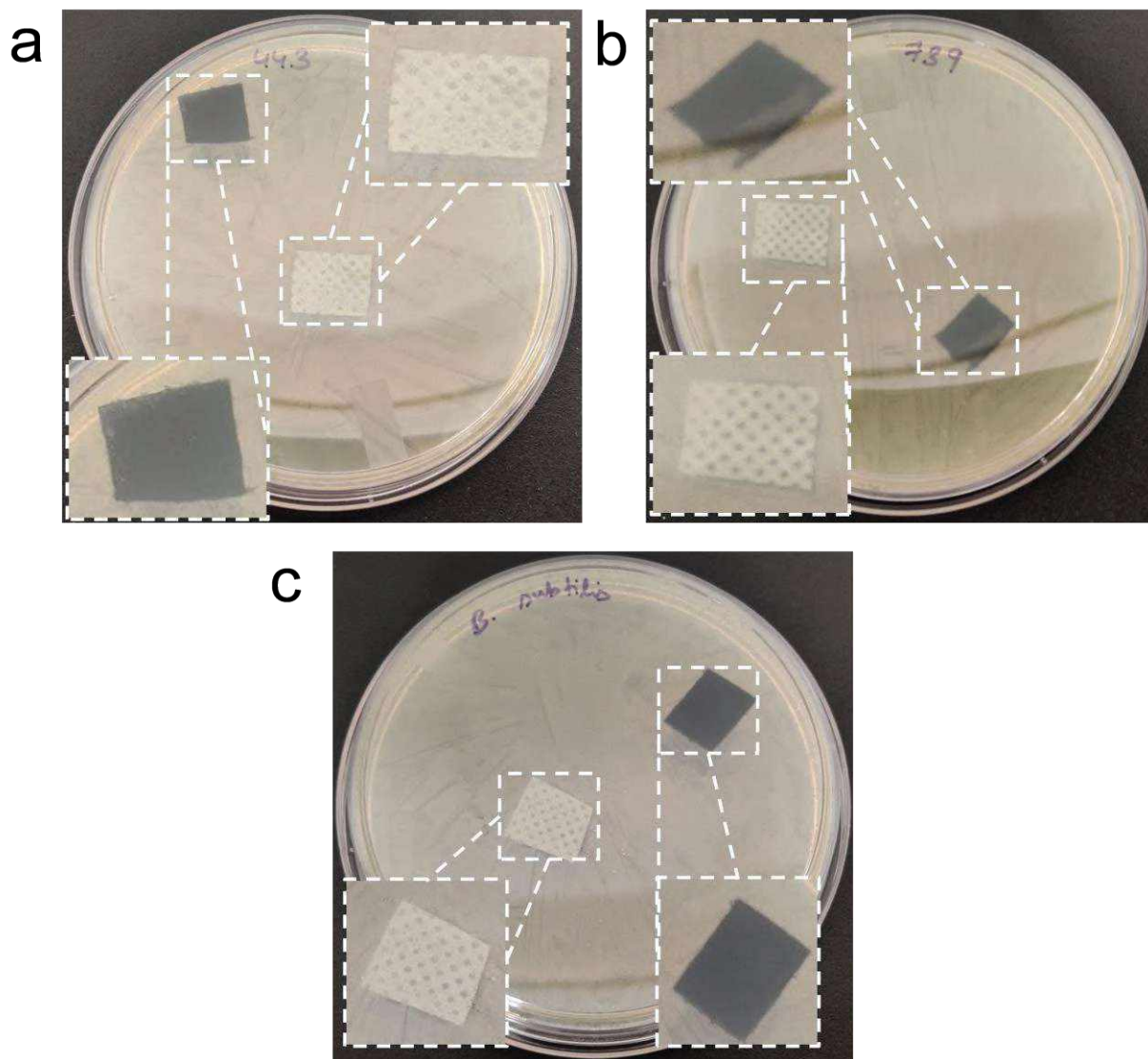


**Figure S4.** Testing of the antibacterial property the mats using (a) *E. coli* 443, (b) *E. coli* 739 and (c) *B. subtilis*. Here, PP and PANi@PP mats are presented in blue and green color, respectively. Magnified regions of the mats are present in the inset.

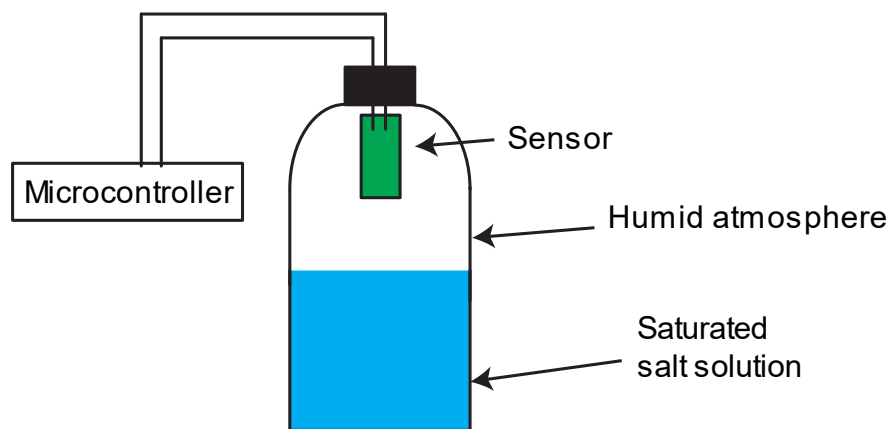


**Figure S5.** Schematic of the sensor calibration set-up. The microcontroller in the rectangular box represents the entire circuit system along with the microcontroller used for measuring the output voltage.

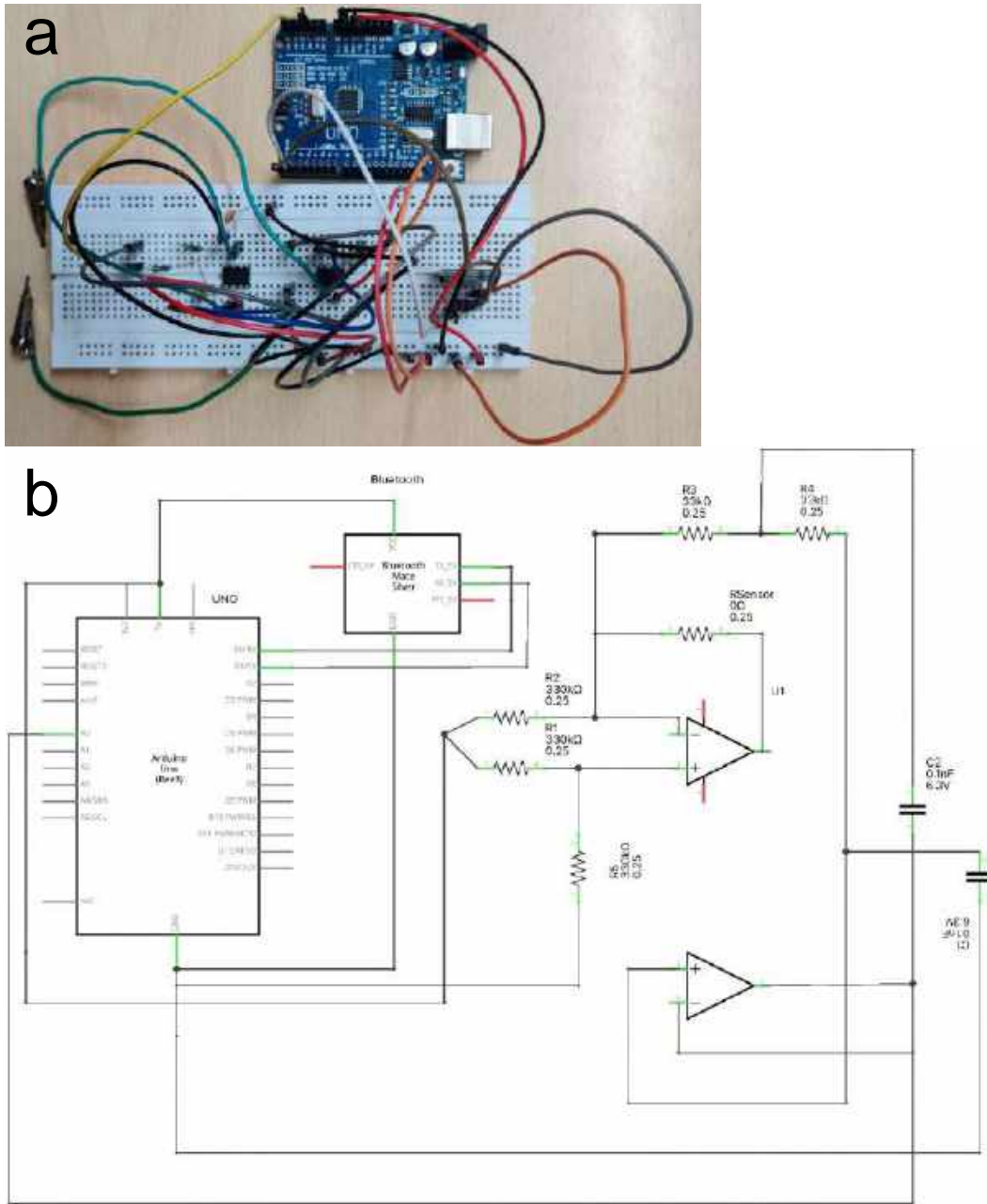


**Figure S6.** (a) Photograph of circuit used for measuring the humidity in the exhaled breath. (b) Schematic of the electrical circuit needed for making the entire sensing prototype.

**Table S5.** Bill of materials.

S.No	Component name	Cost (\$)	Quantity	Overall cost (\$)
1	Arduino Nano	7.54	1	7.54
2	HC-05 Bluetooth module	6.20	1	6.20
3	Male-male jumper cable	0.04	30	1.31
4	Breadboard	2	1	2
5	Resistors: 1. 330 k $\Omega$ 2. 33 k $\Omega$	0.0078	500	3.93
6	Capacitors: 1. 0.1 $\mu$ F	0.012	555	6.23
7	Conducting thread	8.22	5 m	8.22
8	Silver conductive paint	19.95	1	19.95
9	LM741 Op amp IC	0.24	10	2.48
10	Surgical mask	0.003	100	3.93
	Total for 1 smart mask	18.15	1	18.15

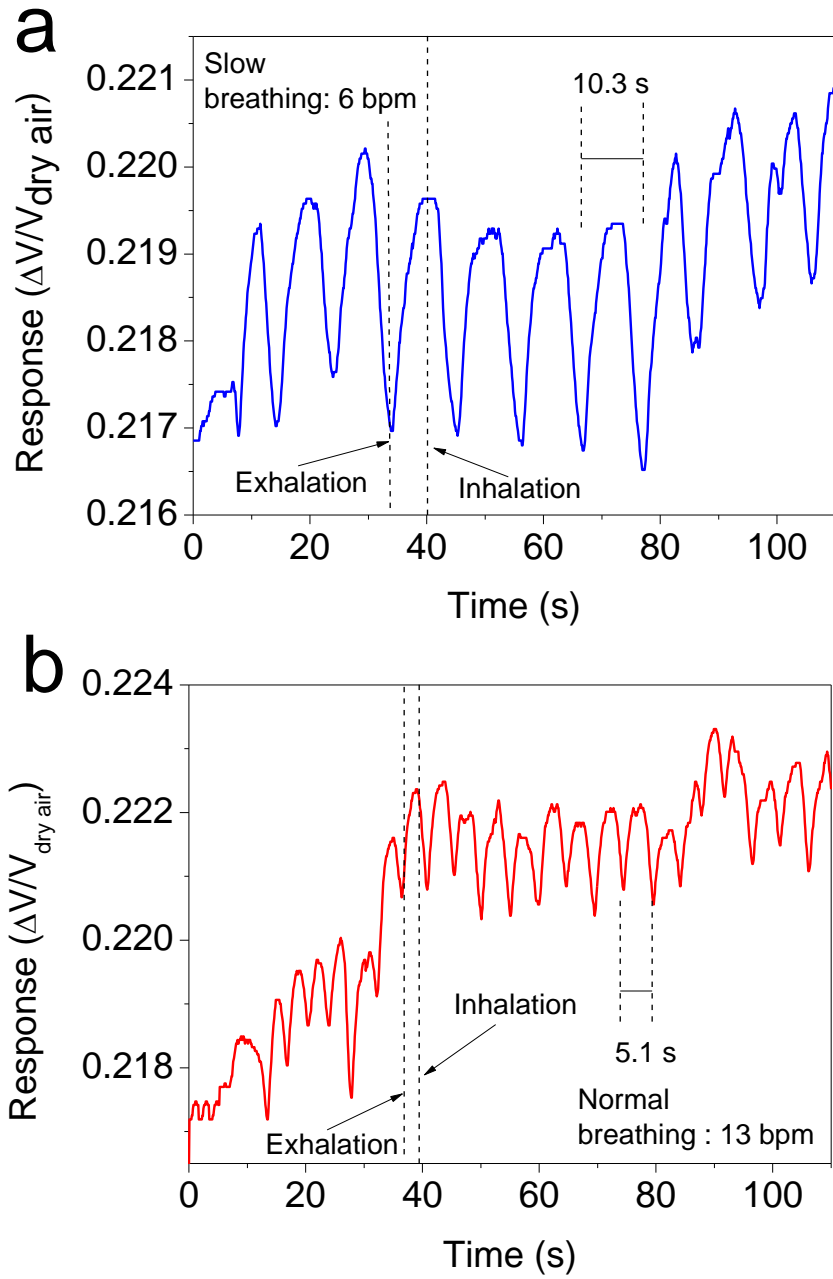


**Figure S7.** (a) Slow and (b) normal breathing response of an individual recorded on the mobile phone.

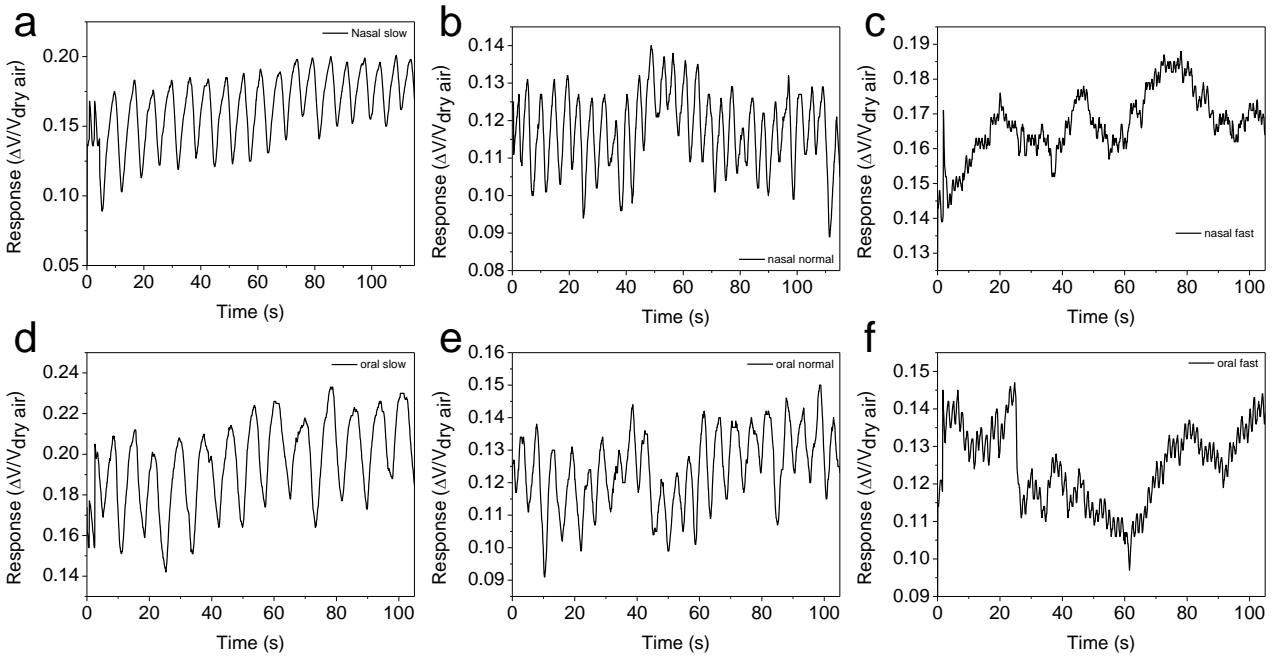


**Figure S8.** Breathing response from 6 different volunteers. For nasal breath: (a) slow, (b) normal and (c) fast. For oral breath: (d) slow, (e) normal and (f) fast.



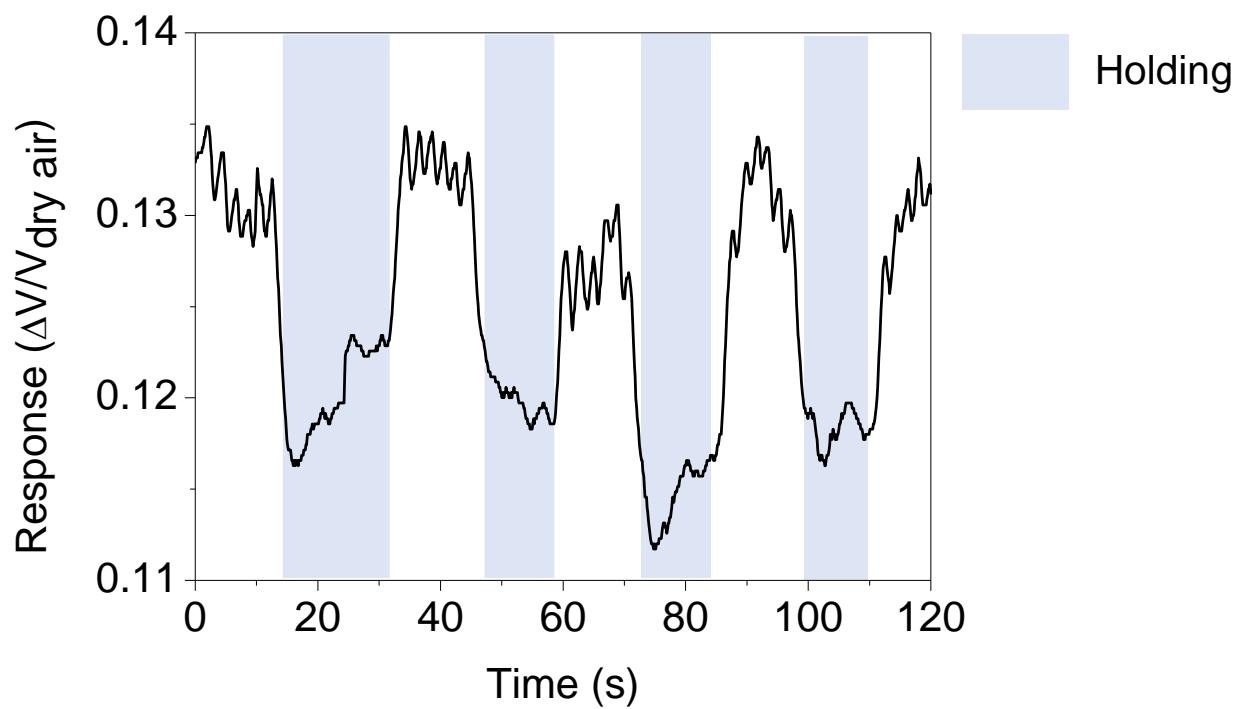


**Figure S9.** Sensor response for a volunteer performing a breath cycle comprising breathing and holding of breath.

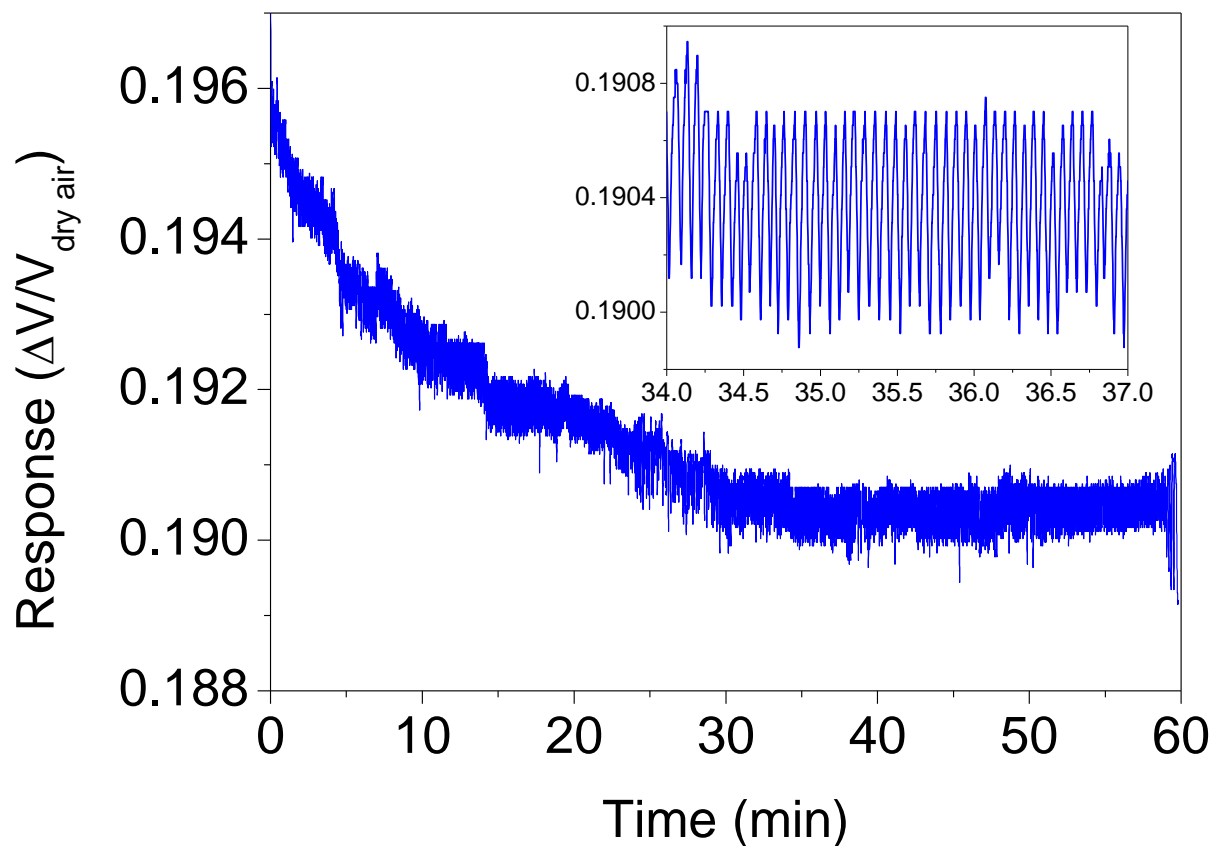


**Figure S10.** Breathing response of a volunteer while working. Working duration corresponds to the volunteer sitting in a comfortable position while working on his laptop. Inset shows the magnified region between 34-37 min.

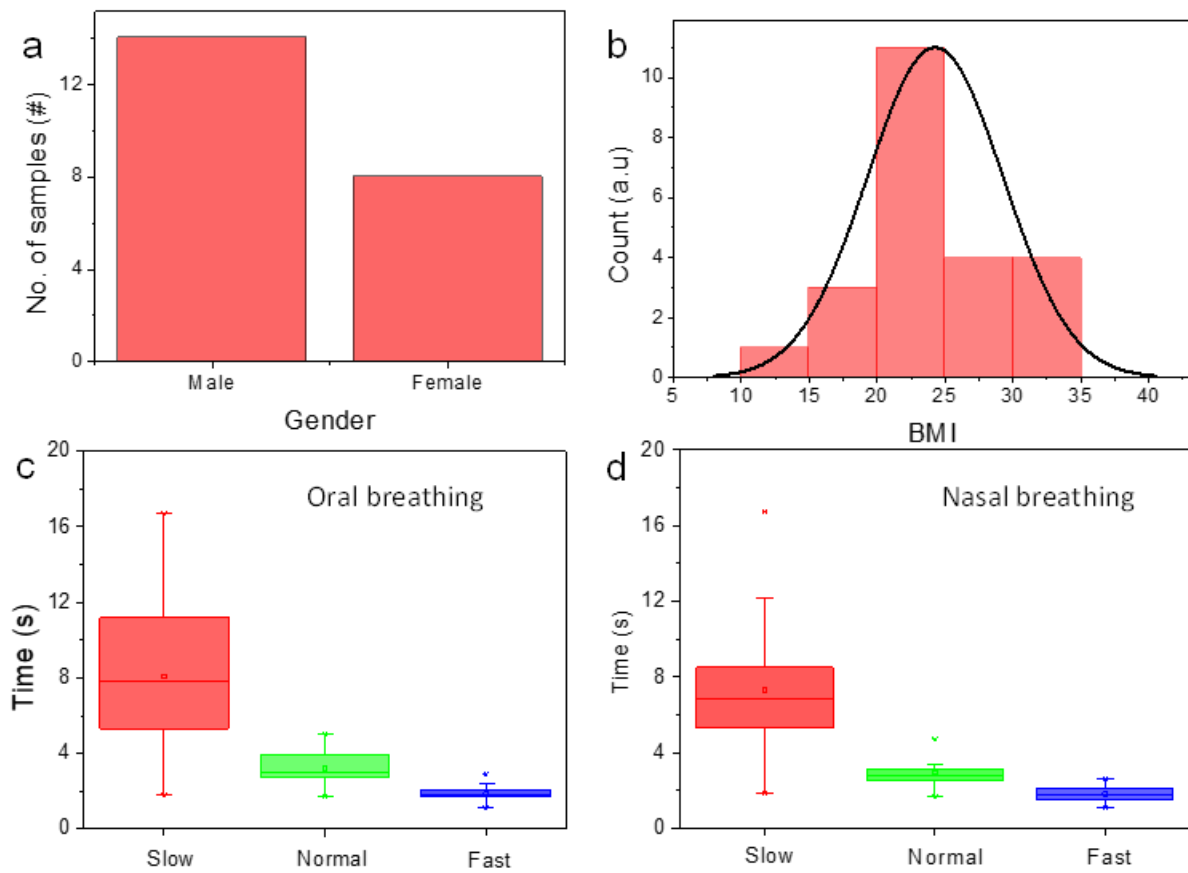


**Figure S11.** (a) Bar chart depicting the number of male and female volunteers in the study. (b) BMI distribution of all the volunteers. (c and d) Time required for completing a total breathing cycle orally and through the nose, respectively.

**Table S6.** Comparing the performance of different classifiers on the collected data.

<b>Algorithm</b>	<b>Accuracy (%)</b>	<b>True positive rate (TPR) (%)</b>	<b>False Positive rate (FPR) (%)</b>
SAX-VSM	90.42	94.64	15.79
BOSSVS	89.36	91.52	14.28
kNN	74.46	77.78	32.26
1D CNN	81.91	86.2	25
Logistic Regression	60.6	0	0

**Table S7.** Comparison of the properties of different humidity sensors.

<b>Sensing material</b>	<b>Response time (s)</b>	<b>Recovery Time (s)</b>	<b>Breath differentiation</b>	<b>Mobile phone integration</b>	<b>Breathing pattern classification</b>	<b>Ref</b>
<i>MoSSe/PVA</i>	~ 0.18	1.14	Yes	Yes	Yes	8
<i>g-C<sub>3</sub>N<sub>4</sub>/TiO<sub>2</sub>/Ti<sub>3</sub>C<sub>2</sub>T<sub>x</sub></i>	-	-	Yes	No	No	9
<i>Graphene-paper</i>	218	230	Yes	No	No	10
<i>Si nano crystals</i>	0.04	0.04	Yes	No	No	11
<i>Supramolecular ionic</i>	0.037	0.037	Yes	No	No	12

<i>material (SIM)</i>						
<i>Graphene oxide-modified PDA</i>	0.02	0.017	Yes	Yes	No	13
<i>Natural polymer sphere QCM</i>	-	-	Yes	Yes	No	14
<i>ACNT@PU fibers</i>	-	-	Yes	No	No	15
<i>Fabric@GO@BSA</i>	8.9	11.6	Yes	No	No	16
<i>1T/2H-MoS<sub>2</sub> nanoparticles</i>	76	382	Yes	No	No	17
<i>Laser induced graphene</i>	63	8	Yes	No	No	18
<i>GO/Li-doped GO /B-doped GO</i>	23	4	No	No	No	19
<i>PANi@PP</i>	1.2	2.8	Yes	Yes	Yes	This work

## References

- (1) Fang, J.; Zhang, L.; Sutton, D.; Wang, X.; Lin, T. Needleless Melt-Electrospinning of Polypropylene Nanofibres. *J. Nanomater.* **2012**, *2012*, e382639. <https://doi.org/10.1155/2012/382639>.

- (2) *Infrared and Raman Characteristic Group Frequencies: Tables and Charts, 3rd Edition* / Wiley. Wiley.com. <https://www.wiley.com/en-us/Infrared+and+Raman+Characteristic+Group+Frequencies%3A+Tables+and+Charts%2C+3rd+Edition-p-9780470093078> (accessed 2022-05-19).
- (3) Kang, E. T.; Neoh, K. G.; Tan, K. L. Polyaniline: A Polymer with Many Interesting Intrinsic Redox States. *Prog. Polym. Sci.* **1998**, *23* (2), 277–324. [https://doi.org/10.1016/S0079-6700\(97\)00030-0](https://doi.org/10.1016/S0079-6700(97)00030-0).
- (4) Trchová, M.; Stejskal, J. Polyaniline: The Infrared Spectroscopy of Conducting Polymer Nanotubes (IUPAC Technical Report). *Pure Appl. Chem.* **2011**, *83* (10), 1803–1817. <https://doi.org/10.1351/PAC-REP-10-02-01>.
- (5) *Vibrational Analysis of Polyaniline: A Model Compound Approach* | *The Journal of Physical Chemistry B*. <https://pubs.acs.org/doi/10.1021/jp972652o> (accessed 2021-08-18).
- (6) Trchová, M.; Morávková, Z.; Bláha, M.; Stejskal, J. Raman Spectroscopy of Polyaniline and Oligoaniline Thin Films. *Electrochimica Acta* **2014**, *122*, 28–38. <https://doi.org/10.1016/j.electacta.2013.10.133>.
- (7) Andreassen, E. Infrared and Raman Spectroscopy of Polypropylene. In *Polypropylene: An A-Z reference*; Karger-Kocsis, J., Ed.; Polymer Science and Technology Series; Springer Netherlands: Dordrecht, 1999; pp 320–328. [https://doi.org/10.1007/978-94-011-4421-6\\_46](https://doi.org/10.1007/978-94-011-4421-6_46).
- (8) Bokka, N.; Karhade, J.; Sahatiya, P. Deep Learning Enabled Classification of Real-Time Respiration Signals Acquired by MoSSe Quantum Dot-Based Flexible Sensors. *J. Mater. Chem. B* **2021**, *9* (34), 6870–6880. <https://doi.org/10.1039/D1TB01237A>.
- (9) Guo, X.; Kuang, D.; Zhu, Z.; Ding, Y.; Ge, L.; Wu, Z.; Du, B.; Liang, C.; Meng, G.; He, Y. Humidity Sensing by Graphitic Carbon Nitride Nanosheet/TiO<sub>2</sub> Nanoparticle/Ti<sub>3</sub>C<sub>2</sub>Tx



- Nanosheet Composites for Monitoring Respiration and Evaluating the Waxing of Fruits. *ACS Appl. Nano Mater.* **2021**, *4* (10), 11159–11167.  
<https://doi.org/10.1021/acsanm.1c02625>.
- (10) Liu, H.; Zheng, H.; Xiang, H.; Wang, W.; Wu, H.; Li, Z.; Zhuang, J.; Zhou, H. Paper-Based Wearable Sensors for Humidity and VOC Detection. *ACS Sustain. Chem. Eng.* **2021**, *9* (50), 16937–16945. <https://doi.org/10.1021/acssuschemeng.1c05156>.
- (11) Kano, S.; Kim, K.; Fujii, M. Fast-Response and Flexible Nanocrystal-Based Humidity Sensor for Monitoring Human Respiration and Water Evaporation on Skin. *ACS Sens.* **2017**, *2* (6), 828–833. <https://doi.org/10.1021/acssensors.7b00199>.
- (12) Yan, H.; Zhang, L.; Yu, P.; Mao, L. Sensitive and Fast Humidity Sensor Based on A Redox Conducting Supramolecular Ionic Material for Respiration Monitoring. *Anal. Chem.* **2017**, *89* (1), 996–1001. <https://doi.org/10.1021/acs.analchem.6b04350>.
- (13) He, J.; Xiao, P.; Shi, J.; Liang, Y.; Lu, W.; Chen, Y.; Wang, W.; Théato, P.; Kuo, S.-W.; Chen, T. High Performance Humidity Fluctuation Sensor for Wearable Devices via a Bioinspired Atomic-Precise Tunable Graphene-Polymer Heterogeneous Sensing Junction. *Chem. Mater.* **2018**, *30* (13), 4343–4354. <https://doi.org/10.1021/acs.chemmater.8b01587>.
- (14) Yang, J.; Feng, L.; Chen, Y.; Feng, L.; Lu, J.; Du, L.; Guo, J.; Cheng, Z.; Shi, Z.; Zhao, L. High-Sensitivity and Environmentally Friendly Humidity Sensors Deposited with Recyclable Green Microspheres for Wireless Monitoring. *ACS Appl. Mater. Interfaces* **2022**. <https://doi.org/10.1021/acami.2c00489>.
- (15) Huang, X.; Li, B.; Wang, L.; Lai, X.; Xue, H.; Gao, J. Superhydrophilic, Underwater Superoleophobic, and Highly Stretchable Humidity and Chemical Vapor Sensors for


- Human Breath Detection. *ACS Appl. Mater. Interfaces* **2019**, *11* (27), 24533–24543.  
<https://doi.org/10.1021/acsami.9b04304>.
- (16) Wang, Y.; Zhang, L.; Zhang, Z.; Sun, P.; Chen, H. High-Sensitivity Wearable and Flexible Humidity Sensor Based on Graphene Oxide/Non-Woven Fabric for Respiration Monitoring. *Langmuir* **2020**, *36* (32), 9443–9448.  
<https://doi.org/10.1021/acs.langmuir.0c01315>.
- (17) Taufik, A.; Asakura, Y.; Hasegawa, T.; Kato, H.; Kakihana, M.; Hirata, S.; Inada, M.; Yin, S. Surface Engineering of 1T/2H-MoS<sub>2</sub> Nanoparticles by O<sub>2</sub> Plasma Irradiation as a Potential Humidity Sensor for Breathing and Skin Monitoring Applications. *ACS Appl. Nano Mater.* **2020**, *3* (8), 7835–7846. <https://doi.org/10.1021/acsanm.0c01352>.
- (18) Zou, S.; Tao, L.-Q.; Wang, G.; Zhu, C.; Peng, Z.; Sun, H.; Li, Y.; Wei, Y.; Ren, T.-L. Humidity-Based Human–Machine Interaction System for Healthcare Applications. *ACS Appl. Mater. Interfaces* **2022**, *14* (10), 12606–12616.  
<https://doi.org/10.1021/acsami.1c23725>.
- (19) Rathi, K.; Pal, K. Impact of Doping on GO: Fast Response–Recovery Humidity Sensor. *ACS Omega* **2017**, *2* (3), 842–851. <https://doi.org/10.1021/acsomega.6b00399>.



# Aggregation of molecules is controlled in microdroplets†

 Cite this: *Chem. Commun.*, 2022, 58, 12657

 Received 19th August 2022,  
 Accepted 29th September 2022

 Pallab Basuri,‡<sup>a</sup> Jenifer Shantha Kumar,‡<sup>a</sup> Keerthana Unni,<sup>a</sup> Sujan Manna<sup>a</sup> and Thalappil Pradeep <sup>\*ab</sup>

DOI: 10.1039/d2cc04587g

rsc.li/chemcomm

**Molecular de-aggregation was observed at the air/water interface of aqueous microdroplets. We probed this phenomenon using dyes such as Rhodamine 6G (R6G), Rhodamine B, acridine orange, and fluorescein, which show aggregation-induced shift in fluorescence. The fluorescence micrographs of microdroplets derived from the aqueous solutions of these dyes show that they are monomeric at the air/water interface, but highly aggregated at the core. We propose that rapid evaporation of the solvent influences the de-aggregation of molecules at the air–water interface of the microdroplets.**

The behaviour of molecules in a confined volume is distinctly different compared to those present in bulk liquids.<sup>1</sup> This is evident from several microdroplet studies where molecules show accelerated reaction kinetics,<sup>2,3</sup> restricted rotation,<sup>4</sup> spatial localization,<sup>5</sup> spontaneous oxidation–reduction,<sup>6–11</sup> and partial solvation.<sup>12,13</sup> These contribute to interfacial electric fields<sup>14</sup> and extraordinary pH changes<sup>15,16</sup> in microdroplets. Such microdroplets are generated usually using electrospray and pneumatic spray and less commonly by effects such as Leidenfrost, acoustic levitation and trapping on hydrophobic surfaces. Nevertheless, most of these phenomena occur at the gas–liquid interface of the droplets. These properties were understood mainly by mass spectrometry or by in-droplet molecular spectroscopy. Very few studies involved imaging of microdroplets to probe such extraordinary properties of molecules. For example, the Cooks group used a super-resolution Nikon Ti-E microscope for 3D structured illumination microscopy (SIM) to image Rhodamine B containing microdroplets created by nano-electrospray ionization (nESI).<sup>17</sup> The authors found that the acceleration of reactions in microdroplets is strongly associated with processes at their

gas–liquid interfaces. The Zare group used microscopy to image deposited droplets on a glass surface created by nebulized ESI and observed the same phenomenon.<sup>18</sup> Very recently, they reported spatial localization of charged molecules in water-in-oil microdroplets using fluorescence microscopy.<sup>5</sup> Our recent investigation using nanoparticles showed anisotropic particle distribution in microdroplets along with the observation of microvacuoles at the interior of the droplets.<sup>19</sup> However, this subject is still lacking critical information on the properties of molecules present in small volumes.

Dye molecules such as R6G, Rhodamine B, acridine orange, *etc.* show emission spectral shift induced by molecular aggregation, which is used as a measure of local concentrations.<sup>20</sup> The R6G emission peak maximum shows a redshift and a reduction in fluorescence quantum yield due to polymerization at higher concentrations.<sup>21,22</sup> The dimerization of cationic R6G could occur in two ways, such as head-to-head and head-to-tail denoted as H and J aggregates, respectively.<sup>23,24</sup> It should be noted that the extent of aggregation and the corresponding molecular structure can also be controlled by parameters such as temperature,<sup>25</sup> light,<sup>26</sup> addition of ionic or macromolecular species,<sup>27</sup> and solvent polarity.<sup>28</sup>

Herein, we used a combined approach involving (i) aggregation-induced emission (AIE), (ii) emission spectral shift (ESS), and (iii) fluorescence quenching of dye molecules to have an in-depth understanding of molecular behaviour in microdroplets. Fluorescence microscopy was utilized to image microdroplets. A few factors such as the droplet traveling distance, nebulization gas pressure, potential, and pH of the solution have been varied, and their effects have been documented.

We observed that solid R6G, a dark red powder, shows no luminescence owing to its highly aggregated state. A photograph of R6G powder taken on a Petri dish under visible light is shown in Fig. 1a. But 100  $\mu\text{M}$  R6G solution exhibits red colour in visible light and is bright yellow in UV light (Fig. 1b). However, when 0.1  $\mu\text{L}$  of the same 100  $\mu\text{M}$  solution was dropcast on a glass slide and allowed to dry, we observed bright red emission (Fig. 1c). This shows that the dropcast thin-film induces aggregation in comparison to the solution state

<sup>a</sup> DST Unit of Nanoscience (DST UNS), Thematic Unit of Excellence (TUE), Department of Chemistry, Indian Institute of Technology Madras, Chennai 600036, India. E-mail: pradeep@iitm.ac.in

<sup>b</sup> International Centre for Clean Water, Chennai, Tamil Nadu 600113, India

† Electronic supplementary information (ESI) available: Experimental details, other images of droplets, and potential and pH dependent experiments. See DOI: <https://doi.org/10.1039/d2cc04587g>

‡ These authors contributed equally.

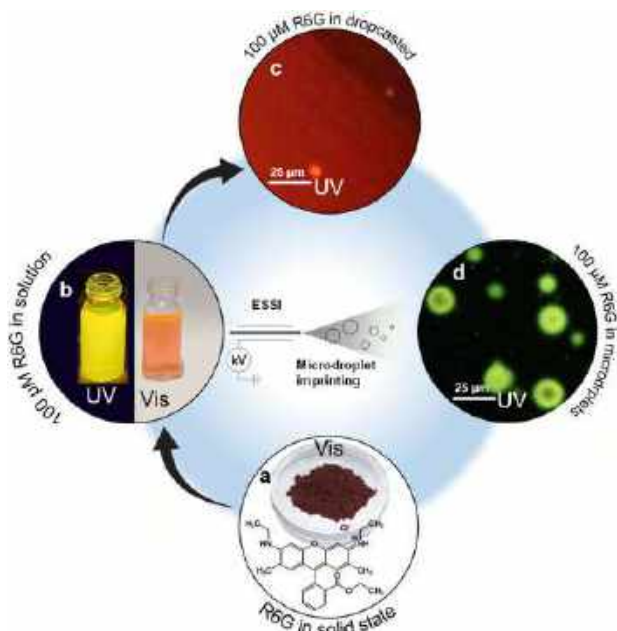


**Fig. 1** Different states of R6G under visible and UV light. (a) R6G in the powder form is dark red under visible light and shows no luminescence under UV light. The inset shows the molecular structure of R6G. (b) An aqueous R6G solution of 100  $\mu\text{M}$  concentration. (c) 0.1  $\mu\text{L}$  dropcast of the same solution on a clean glass slide for fluorescence microscopy. (d) Fluorescence microscopy image of imprinted microdroplets generated from a 100  $\mu\text{M}$  solution using an ESSI source, as shown schematically in the inset, at the centre of the image. The scale bar is 25  $\mu\text{m}$ . UV illumination was applied using a DAPI (4',6'-diamidino-2-phenylindole) filter for (c) and (d).

(Fig. S3, ESI<sup>†</sup>). Note that, in bulk solution, the solvation helps to restrict molecular aggregation, and as a result we observed yellow luminescence. However, molecules form aggregates in the film to reduce the overall energy, which eventually redshifts the emission. Surprisingly, when the same solution was electro-sprayed and the droplets were imprinted on a glass slide (see experimental details, Fig. S1 in the ESI<sup>†</sup>), we observed green luminescence (Fig. 1d). The experimental details and a schematic representation of droplet imaging by fluorescence microscopy are presented in the ESI<sup>†</sup> (Fig. S1 and S2, ESI<sup>†</sup>). This suggests that molecules are likely to de-aggregate and become monomeric in microdroplets. Such a drastic difference between the solution phase, dropcast solid thin film, and imprinted microdroplets encouraged us to investigate the effect further and its dependence on the other parameters of droplet generation. The detailed mechanism of de-aggregation at the interface is not clear at present. We suggest that the fast evaporation of the solvent at the dynamic interface and the relatively slow movement of large non-volatile dye molecules result in de-aggregation. To verify this, we generated microdroplets with a solvent of different volatility. Fig. S4 (ESI<sup>†</sup>) shows the fluorescence images of water and methanol microdroplets containing R6G, imprinted on glass slides. We observed that the dye molecules in methanol droplets (Fig. S4a, ESI<sup>†</sup>) are completely monomeric in nature, whereas the water microdroplets (Fig. S4b, ESI<sup>†</sup>) show the monomeric form predominantly at the interface and are aggregated at the interior.

The tip-to-inlet distance plays an important role in determining the chemistry of the molecules in microdroplets.<sup>17</sup> We observed that the degree of de-aggregation increased with increasing distance. Fig. 2a displays a schematic diagram of the variable distance droplet deposition setup. The fluorescence images of droplets at 0.3, 1.5, and 3 cm distances are shown in Fig. 2b–d. Interestingly, the droplets sprayed from a distance of 0.3 cm show predominantly red luminescence at the interior and green luminescence towards the periphery. Notably, the red colour at the interior of the droplet is dull in comparison to the dropcast sample shown in Fig. 1c. We suggest that the droplet core exhibited a higher order of aggregation than that of the dropcast sample. Also, microdroplets induce fluorescence quenching at the core. The droplets, allowed to travel a 1.5 cm distance, showed red and green colours at the core and green emission towards the periphery. Further increase of the travel distance to 3 cm led to higher de-aggregation of the dye leading to green emission throughout the droplet (Fig. 2d). The spray distance is known to affect the size of the droplets. These observations suggest that the core of the droplets at shorter distances exhibits bulk-like properties, resulting in AIE in the red region. The longer the droplet travels, the more the de-aggregated dye molecules form which appeared green. This shows that the droplets at a 1.5 cm spray distance may be at an intermediate state, showing a mixed composition of aggregated and de-aggregated dye molecules. Previous reports on droplet imaging show that the imprinting of droplets on a solid surface retains the spatial distribution of molecules in the droplets and reliably reflects the nature of droplets in the electro-spray.<sup>29,30</sup>

Similar to the distance effect, it was observed that the nebulization gas pressure also affected the aggregation/de-aggregation dynamics of R6G molecules significantly.

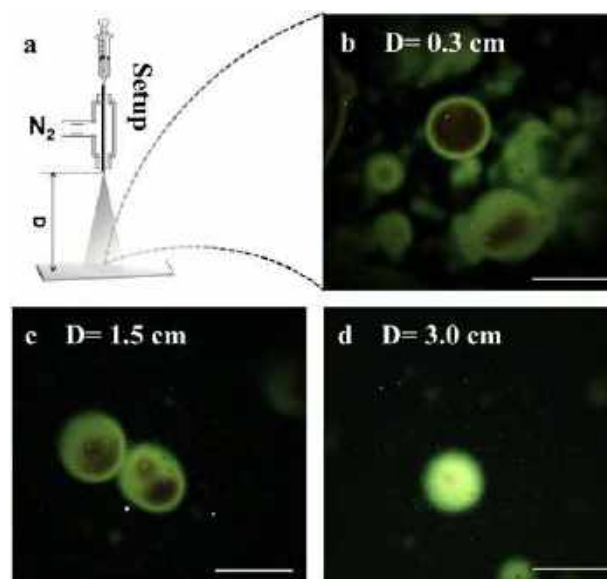


**Fig. 2** Effect of the tip-to-deposition surface distance on the distribution of the polymeric R6G solution (100  $\mu\text{M}$ ). (a) Schematic diagram of the droplet deposition setup. Fluorescence microscopy images of droplets at a distance of (b) 0.3 cm, (c) 1.5 cm and (d) 3 cm. The scale bar is 100  $\mu\text{m}$ .

At a sufficiently low nebulization gas pressure of 5 psi, the droplets were larger and red-emitting towards the centre and green-emitting towards the periphery (Fig. S5a, ESI<sup>†</sup>). Similar to the distance effect, we found fluorescence quenching at the core of the droplets. While increasing the gas pressure, the droplet size varied drastically, showing a decrease in the droplet size due to solvent evaporation. An increase in gas pressure from 5 to 20 psi led to a blueshift in the emission and showed green colour (Fig. S5b, ESI<sup>†</sup>). Only at the highest pressure applied (30 psi), the droplets were fully green (Fig. S5c, ESI<sup>†</sup>). These observations indicate that the spray parameters of microdroplets significantly influence the aggregation dynamics of the molecules in the droplet.

We have collected hyperspectral fluorescence images of the droplet to understand the extent of aggregation in an individual droplet (Fig. S6a and b, ESI<sup>†</sup>). The fluorescence spectra collected at and near the surface of the microdroplet reveal that R6G is predominantly monomeric (Fig. S6c and d; Fig. S6b, Locations 1 and 2, ESI<sup>†</sup>). However, at the interior, majorly R6G is in the polymeric form (Fig. S6e; Fig. S6b, Location 3, ESI<sup>†</sup>). Interestingly, the gas-liquid interface of the microbubble shows completely monomeric form of the dye (Fig. S6f; Fig. S6b, Location 4, ESI<sup>†</sup>). We have reported the formation of microbubbles in microdroplets.<sup>19</sup> Herein, the droplet also contains a microbubble, as indicated in Fig. S6a (ESI<sup>†</sup>). The inner portion of the droplet periphery shows both green and red emissions (Fig. S6d, ESI<sup>†</sup>). The fluorescence spectrum at the interface of the microbubble shows the presence of only monomeric R6G (Fig. S6f, ESI<sup>†</sup>). We observed that, as the microbubbles form *in situ* during the flight of microdroplets, the gas-liquid interface could be more dynamic, resulting in such de-aggregation behaviour of the dye molecule.

Fig. 3 correlates the aggregation/de-aggregation properties of R6G at different concentrations between the bulk solution phase, dropcast solid thin film, and imprinted microdroplets. Fig. 3a and b show the bulk phase R6G luminescence under visible and ultraviolet light for five different concentrations: 1 mM, 100  $\mu$ M, 10  $\mu$ M, 1  $\mu$ M, and 100 nM, respectively (Fig. 3(i-v)). Fig. 3c and d show the fluorescence microscopy emission of the dropcast R6G and sprayed sample from a distance of 1.5 cm for five different concentrations. Herein, 1 mM concentration of R6G, the bulk phase as well as the dropcast sample show a red emission. But, in the microdroplets, the emission from the interface is green and that from the core is red. As mentioned earlier, the dull red colour at the core can be attributed to the high-level aggregated nature of R6G and the monomeric nature of R6G at the interface of the microdroplet. Similarly, at 100  $\mu$ M concentration, the bulk phase and dropcast sample show red emission, whereas microdroplets show green emission at the interface and in the core. As the concentration decreases from 1 mM to 100  $\mu$ M, the core of the microdroplets shifts from red emission to green because at lower concentrations the microdroplet core can be even more de-aggregated. Therefore, the molecules present in these microdroplets are already monomeric. At 10  $\mu$ M, bulk droplets themselves show green emission in ultraviolet light. In contrast, the dropcast sample from the

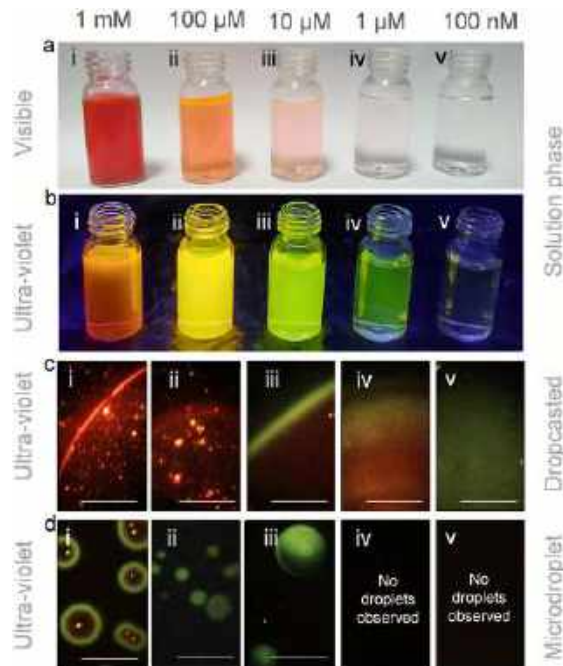


Fig. 3 Concentration effect on aggregation induced emission spectral shift depicted by five different concentrations (1 mM, 100  $\mu$ M, 10  $\mu$ M, 1  $\mu$ M and 100 nM). Bulk phase R6G luminescence under (a) visible light and (b) UV light. (c) Fluorescence images of dropcast R6G and (d) R6G at different concentrations sprayed from a distance of 1.5 cm. The scale bar is 125  $\mu$ m.

same solution shows both green and red emissions, which signifies the aggregated and monomeric nature of the droplet. The microdroplet of the same shows green emission, irrespective of the core and interface. As the concentration decreases from 10  $\mu$ M to 1  $\mu$ M and 100 nM, the emission intensity falls as the concentration of R6G is significantly less. Green emission is much more prominent in the dropcast sample of 100 nM concentration. Microdroplets at 1  $\mu$ M show complete green colour. Because of extensive dilution, microdroplets corresponding to 100 nM were invisible under a fluorescence microscope. From the above observations, we can conclude that microdroplets regulate aggregation/de-aggregation induced emission shift. At higher concentrations, R6G particles tend to aggregate in the dropcast sample and inside the core of the microdroplet. However, the extent of aggregation is more in the core than in the dropcast sample. Strikingly, even at higher concentrations, particles show monomeric nature at the air-water interface of the microdroplet. For the same concentration, the extent of polymerization of R6G is different in different cases. The microdroplet induces de-aggregation and the dropcast induces aggregation compared to the bulk solution.

We found that the applied potential dramatically affects the aggregation/de-aggregation kinetics of the molecules in microdroplets. The DFM images of droplets containing 100  $\mu$ M R6G, sprayed at 0 and 4 kV applied potential with a 1.5 cm tip-to-substrate distance, are shown in Fig. S7a and b (ESI<sup>†</sup>). We observed that droplets at 0 kV show a green interface with a red interior. Droplets at 4 kV were green in colour. It should also be noted that the application of potential causes droplet splitting,



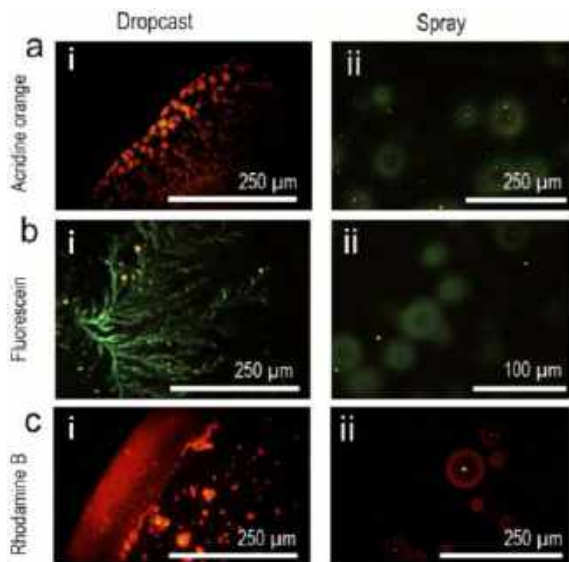


Fig. 4 Fluorescence microscopy images of dropcast vs. microdroplets of a few other dye solutions such as (a) acridine orange, (b) fluorescein, and (c) Rhodamine B at 500  $\mu\text{M}$ .

which reduces the size of the droplets and may show a phenomenon similar to the distance effect. Moreover, the smaller the size of the droplets, the higher the surface to volume ratio, due to which de-aggregation is enhanced, resulting in completely green fluorescence (Fig. S5 and S7, ESI<sup>†</sup>).

The experiments were further extended to other dyes such as acridine orange, fluorescein, and Rhodamine B. The dyes were taken at 500  $\mu\text{M}$  concentrations in water. The fluorescence images of the dropcast thin-film vs microdroplets were compared as shown in Fig. 4. A similar phenomenon of de-aggregation was observed for acridine orange. The dropcast image (Fig. 4a(i)) shows bright orange, while the droplet shows a green periphery and dull red interior (Fig. 4a(ii)). The aggregation of fluorescein and Rhodamine B molecules at the core of the microdroplets is evident from fluorescence quenching (Fig. 4b(ii) and c(iii)) which is different from the dropcast sample (Fig. 4b(i) and c(i)). Such aggregation induced quenching of these dye molecules is reported in the earlier literature.<sup>31,32</sup>

In conclusion, we observed that microdroplets assist molecular de-aggregation. Fluorescence microscopy imaging shows that R6G and a few other dye molecules are monomeric in microdroplets than in the solution phase or dropcast solid films. This phenomenon of de-aggregation occurred first at the interface of the droplet, whereas the interior of the droplet still shows aggregation. While the droplets move in the air, the extent of de-aggregation increases until all the molecules become monomeric. We believe that such de-aggregation dynamics at the air/liquid interface helps in overcoming intermolecular interactions and clustering, favouring the chemical reactivity in microdroplets. Such molecular behaviour in droplets could be utilized in understanding prebiotic, cellular and cloud chemistry.

P. B. and T. P. designed and performed the experiments. P. B., J. S. K., K. U. and S. M. conducted the experiments. P. B. wrote the initial draft of the paper with input from all the authors.

## Conflicts of interest

The authors declare no competing financial interest.

## References

- 1 J. Rebek, *Acc. Chem. Res.*, 2009, **42**, 1660–1668.
- 2 Z. Wei, Y. Li, R. G. Cooks and X. Yan, *Annu. Rev. Phys. Chem.*, 2020, **71**, 31–51.
- 3 X. Yan, R. M. Bain and R. G. Cooks, *Angew. Chem., Int. Ed.*, 2016, **55**, 12960–12972.
- 4 J. Kang, S. Lhee, J. K. Lee, R. N. Zare and H. G. Nam, *Sci. Rep.*, 2020, **10**, 1–10.
- 5 S. Lhee, J. K. Lee, J. Kang, S. Kato, S. Kim, R. N. Zare and H. G. Nam, *Sci. Adv.*, 2020, **6**, eaba0181.
- 6 A. Gallo Jr., N. H. Musskopf, X. Liu, Z. Yang, J. Petry, P. Zhang, S. Thoroddsen, H. Im and H. Mishra, *Chem. Sci.*, 2022, **13**, 2574–2583.
- 7 A. Gallo Jr., N. H. Musskopf, X. Liu, Z. Yang, J. Petry, P. Zhang, S. Thoroddsen, H. Im, H. Mishra, C. Zhu, J. S. Francisco, J. K. Lee, H. S. Han, S. Chaikasetin, D. P. Marron, R. M. Waymouth, F. B. Prinz, R. N. Zare, K. L. Walker, H. S. Han, J. Kang, F. B. Prinz, R. M. Waymouth, H. G. Nam and R. N. Zare, *Proc. Natl. Acad. Sci. U. S. A.*, 2019, **116**, 19222–19224.
- 8 D. Gao, F. Jin, J. K. Lee and R. N. Zare, *Chem. Sci.*, 2019, **10**, 10974–10978.
- 9 J. K. Lee, H. S. Han, S. Chaikasetin, D. P. Marron, R. M. Waymouth, F. B. Prinz and R. N. Zare, *Proc. Natl. Acad. Sci. U. S. A.*, 2020, **117**, 30934–30941.
- 10 J. K. Lee, K. L. Walker, H. S. Han, J. Kang, F. B. Prinz, R. M. Waymouth, H. G. Nam and R. N. Zare, *Proc. Natl. Acad. Sci. U. S. A.*, 2019, **116**, 19294–19298.
- 11 C. Zhu and J. S. Francisco, *Proc. Natl. Acad. Sci. U. S. A.*, 2019, **116**, 19222–19224.
- 12 L. Qiu, Z. Wei, H. Nie and R. G. Cooks, *ChemPlusChem*, 2021, **86**, 2192–6506.
- 13 N. Narendra, X. Chen, J. Wang, J. Charles, R. G. Cooks and T. Kubis, *J. Phys. Chem. A*, 2020, **124**, 4984–4989.
- 14 H. Xiong, J. K. Lee, R. N. Zare and W. Min, *J. Phys. Chem. Lett.*, 2020, **11**, 7423–7428.
- 15 H. Wei, E. P. Vejerano, W. Leng, Q. Huang, M. R. Willner, L. C. Marr and P. J. Vikesland, *Proc. Natl. Acad. Sci. U. S. A.*, 2018, **115**, 7272–7277.
- 16 P. Basuri, L. E. Gonzalez, N. M. Morato, T. Pradeep and R. G. Cooks, *Chem. Sci.*, 2020, **11**, 12686–12694.
- 17 B. M. Marsh, K. Iyer and R. G. Cooks, *J. Am. Soc. Mass Spectrom.*, 2019, **30**, 2022–2030.
- 18 K. Luo, J. Li, Y. Cao, C. Liu, J. Ge, H. Chen and R. N. Zare, *Chem. Sci.*, 2020, **11**, 2558–2565.
- 19 P. Basuri, A. Chakraborty, T. Ahuja, B. Mondal, J. Shantha Kumar and T. Pradeep, *Chem. Sci.*, 2022, DOI: [10.1039/D2SC04589C](https://doi.org/10.1039/D2SC04589C).
- 20 Z. Arsov, I. Urbančić and J. Štrancar, *Spectrochim. Acta, Part A*, 2018, **190**, 486–493.
- 21 F. L. Arbeloa, P. R. Ojeda and I. L. Arbeloa, *J. Chem. Soc., Faraday Trans. 2*, 1988, **84**, 1903–1912.
- 22 R. Vogel, M. Harvey, G. Edwards, P. Meredith, N. Heckenberg, M. Trau and H. Rubinsztein-Dunlop, *Macromolecules*, 2002, **35**, 2063–2070.
- 23 J. P. Cassidy, J. A. Tan and K. L. Wustholz, *J. Phys. Chem. C*, 2017, **121**, 15610–15618.
- 24 V. Martínez Martínez, F. López Arbeloa, J. Bañuelos Prieto and I. López Arbeloa, *J. Phys. Chem. B*, 2005, **109**, 7443–7450.
- 25 O. A. Yeshchenko, I. S. Bondarchuk, V. V. Kozachenko and M. Y. Losytsky, *J. Lumin.*, 2015, **158**, 294–300.
- 26 M. Shirakawa, T. Kobayashi and E. Tokunaga, *Appl. Sci.*, 2020, **10**, 3563.
- 27 O. Valdes-Aguilera and D. C. Neckers, *Acc. Chem. Res.*, 1989, **22**, 171–177.
- 28 P. Bojarski, A. Matczuk, C. Bojarski, A. Kowski, B. Kukliński, G. Zurkowska and H. Diehl, *Chem. Phys.*, 1996, **210**, 485–499.
- 29 Y. Bai, P. Luan, Y. Bai, R. N. Zare and J. Ge, *Chem. Sci.*, 2022, **13**, 8341–8348.
- 30 J. K. Lee, D. Samanta, H. G. Nam and R. N. Zare, *J. Am. Chem. Soc.*, 2019, **141**, 10585–10589.
- 31 F. L. Arbeloa, P. R. Ojeda and I. L. Arbeloa, *J. Lumin.*, 1989, **44**, 105–112.
- 32 S. De and R. Kundu, *J. Photochem. Photobiol., A*, 2011, **223**, 71–81.



This journal is © The Royal Society of Chemistry 2022

## Aggregation of Molecules is Controlled in Microdroplets

Pallab Basuri<sup>†</sup>, Jenifer Shantha Kumar<sup>†</sup>, Keerthana Unni, Sujan Manna, and Thalappil Pradeep\*

*DST Unit of Nanoscience (DST UNS), Thematic Unit of Excellence (TUE), Department of Chemistry, Indian Institute of Technology Madras, Chennai 600036, India.*

E-mail: [pradeep@iitm.ac.in](mailto:pradeep@iitm.ac.in)

### Table of Contents

Serial no.	Details	Page no.
Experimental details	Microdroplet imprinting experiment	2
	Microdroplet imaging experiment.	3
Fig. S1	Schematic of droplet generation and imprinting	2
Fig. S2	Schematic of dark field microscopy	3
Fig. S3	Fluorescence spectra collected from dropcast and bulk solution	4
Fig. S4	Fluorescence microscopy images of microdroplets in water and methanol	5
Fig. S5	Effect of nebulization gas pressure	6
Fig. S6	Local Fluorescence spectra and mapping	7
Fig. S7	Effect of potential	8

## 1 Experimental section:

**1.1 Microdroplet imprinting experiment.** The droplet generation and deposition setup are already discussed in our recent work.<sup>1</sup> Briefly, a custom-built setup was used for droplet generation and imprinting. The electro-spray sonic ionization (ESSI) set up with a transfer tube, as seen in the schematic in Fig. S1, was clamped together and mounted on an XYZ translational stage so that the emitter tube of the ESSI source could go inside the transfer tube. The dye-containing solution was kept in a syringe and purged through a fused silica capillary with a 150  $\mu\text{m}$  internal diameter using a syringe pump. We used  $\text{N}_2$  for nebulization with a gas pressure of 20 psi for most of the experiments otherwise mentioned. The droplets were imprinted on clean glass slides (SCHOTT nexterion®). All the droplet imprinting and fluorescence imaging experiments were conducted in a dark environment to prevent the photobleaching of the dye.

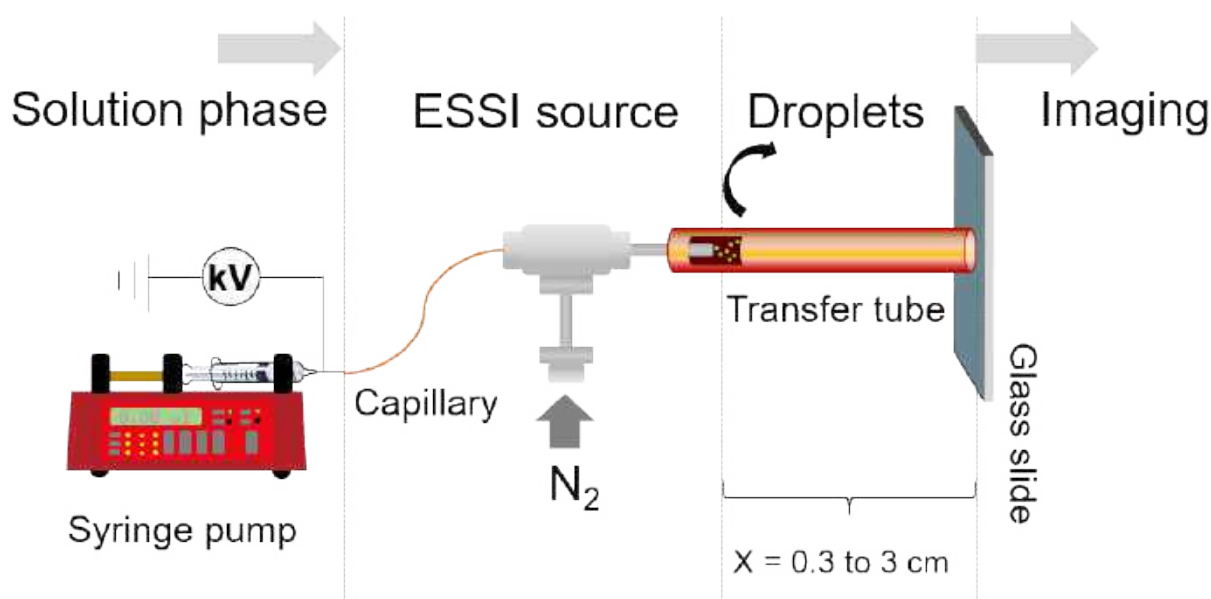


**Fig. S1** Schematic of microdroplet generation and deposition experiment. It has been segmented into four parts; Solution phase, ESSI source, droplet flight path, and deposition for imaging. A high voltage DC power supply was connected to the syringe for the potential to apply optionally.

**1.2 Microdroplet imaging experiment.** The imprinted droplets were immediately transferred to the micromechanical stage of the dark field microscope (CytoViva™) for fluorescence imaging. The microscope has a high-resolution dark-field oil immersion condenser lens and a 100x oil immersion objective (UPLFLN, Olympus). We used a white light source for illuminating the dye with an L1090-halogen lamp from International Light Technologies Inc. Fluorescence imaging of microdroplets was also done on the CytoViva™ microscope with a triple bandpass filter for the green emission. A Dage Excel M cooled CCD (Charge coupled Device) camera was used for capturing the images. Clean glass slides (SCHOTT nexterion®) were used for all the imaging experiments.

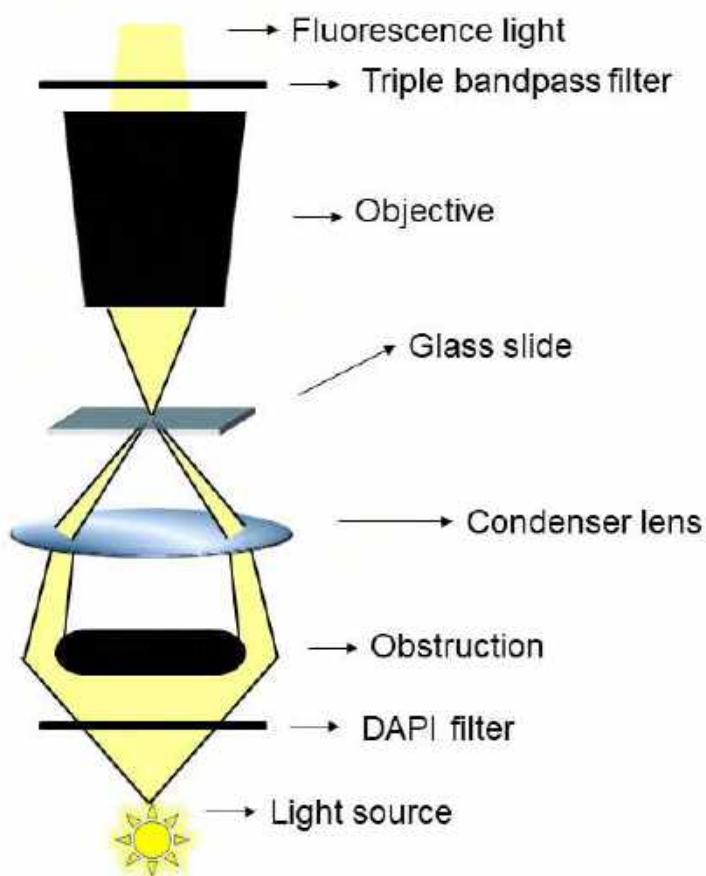


**Fig. S2** Schematic view of Fluorescence microscopy. (DAPI - 4',6-diamidino-2-phenylindole).

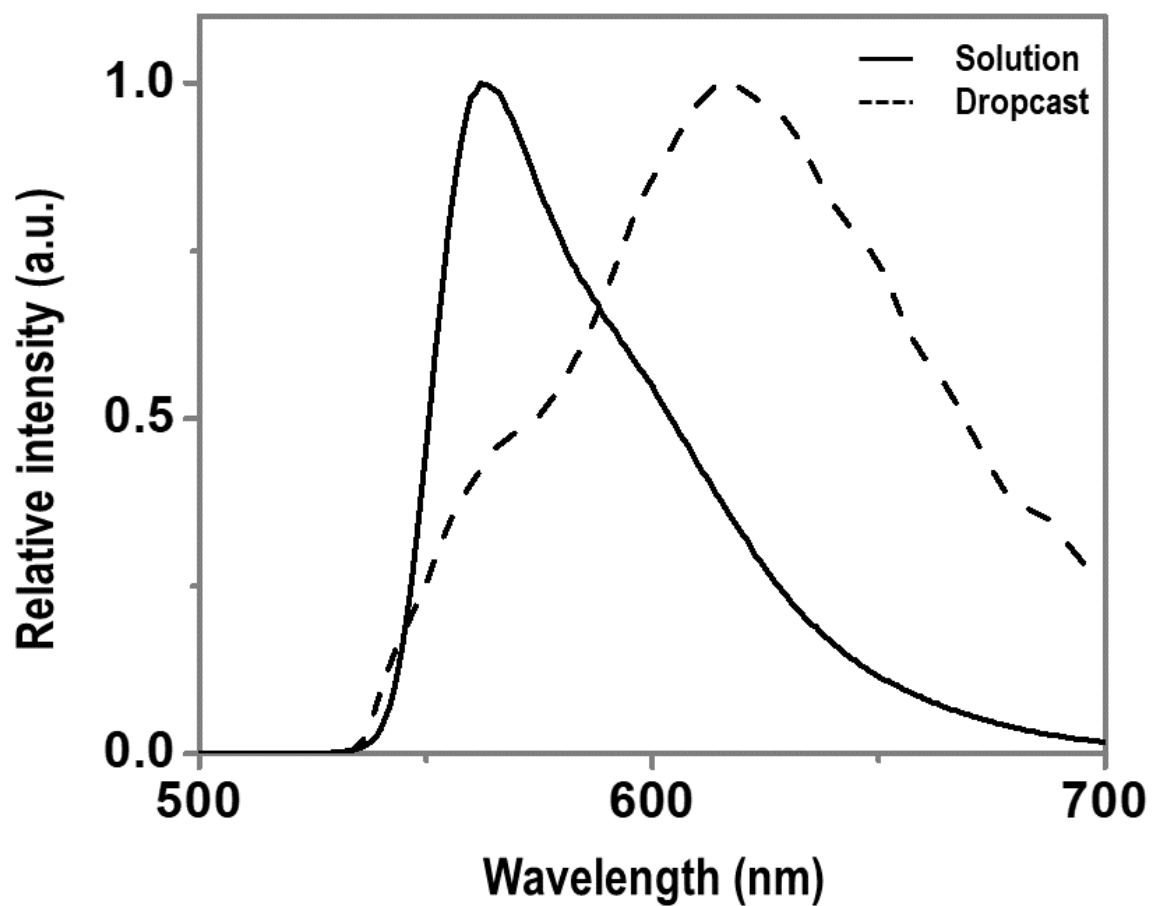


**Fig. S3** Fluorescence spectra collected from the dropcast film and bulk solution of R6G.

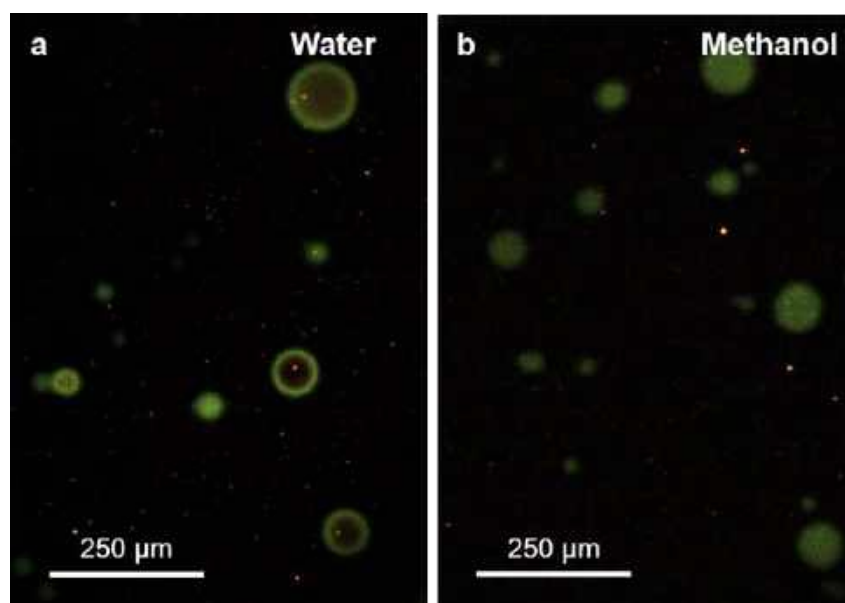


**Fig. S4** Fluorescence microscopy images of microdroplets containing 100  $\mu\text{M}$  R6G in a) water and b) methanol.

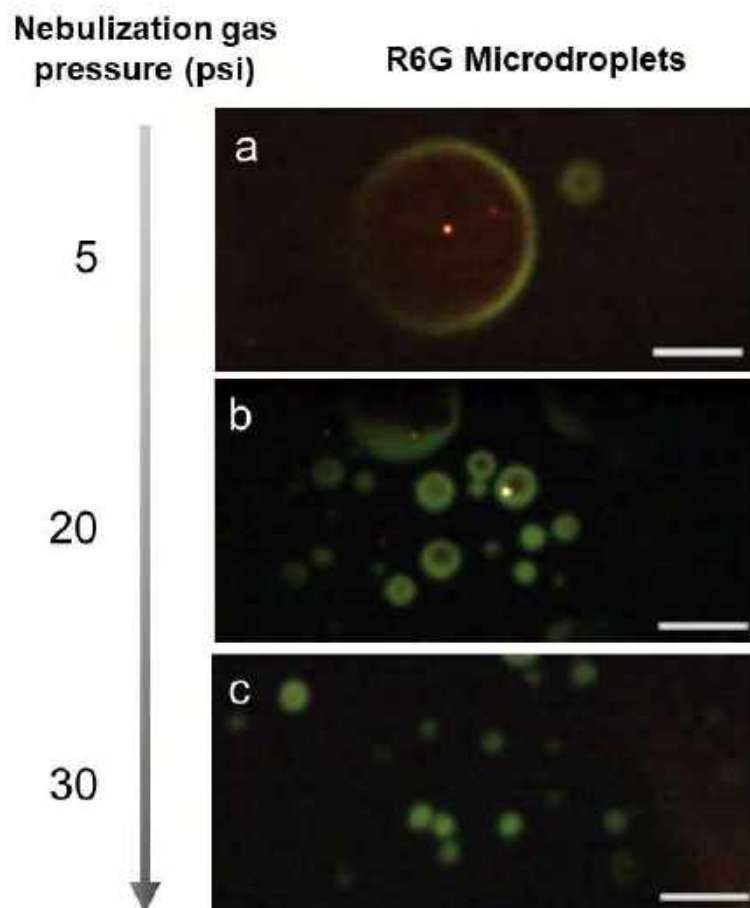


**Fig. S5** Pressure dependency of the fluorescence emission of the microdroplets. The scale bar is 250  $\mu\text{m}$ .



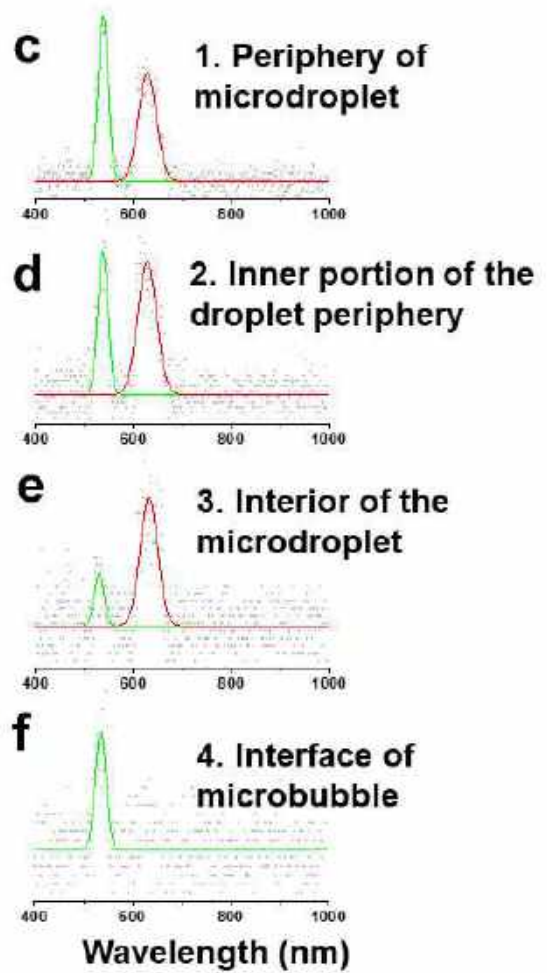
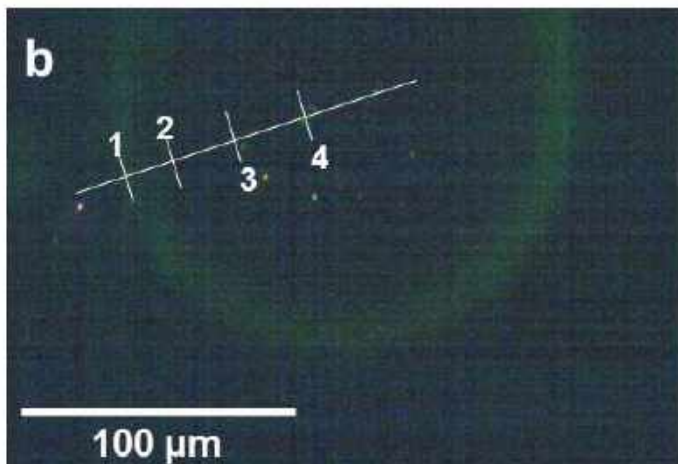
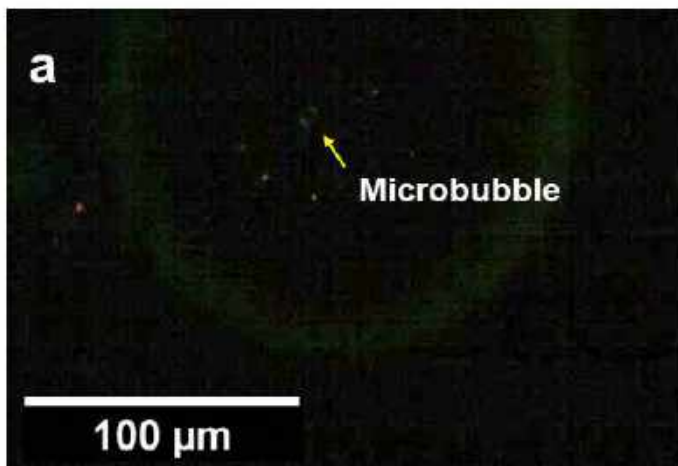


**Fig. S6** Scattering spectrum of the microdroplet at the different regions from the droplet. a) and b) Fluorescence microscopy image of a droplet using two different filters. c-f) Fluorescence spectra of R6G at different locations of the droplet as indicated in b.

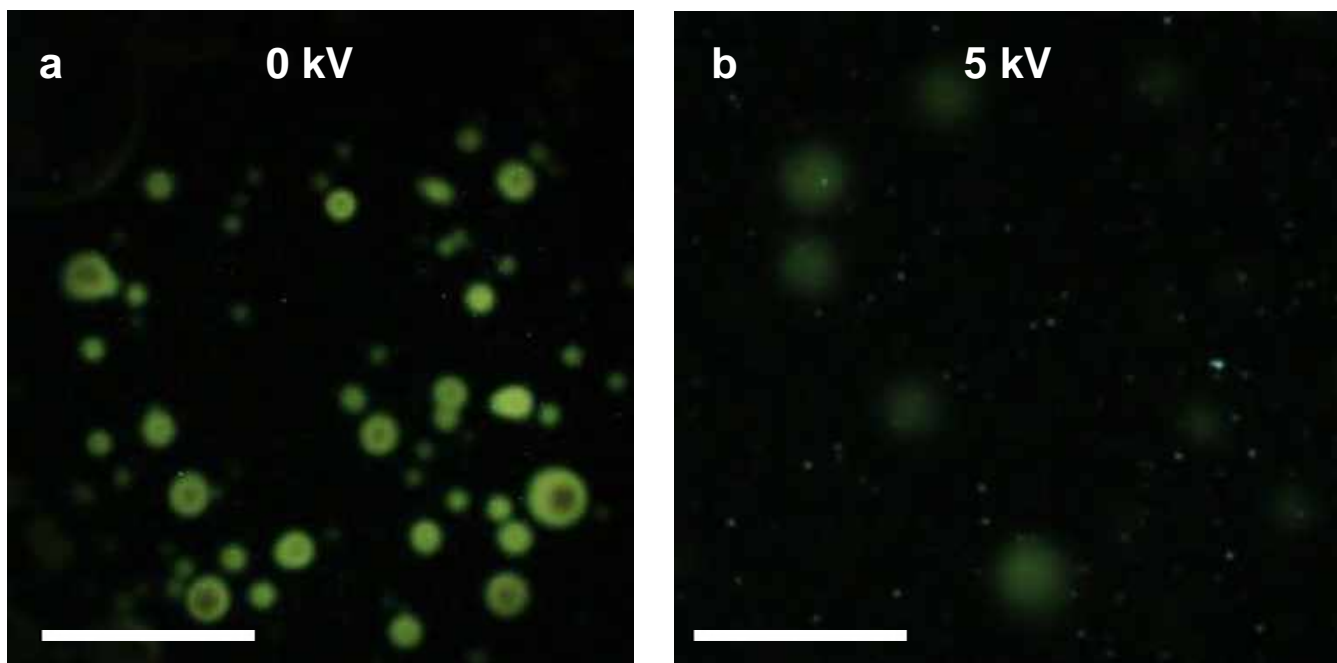


**Fig. S7** The potential effect on microdroplets sprayed with R6G at 100  $\mu\text{M}$  (at a spray distance of 1.5 cm). Scale bar is 250  $\mu\text{m}$ .

**References:**

1. P. Basuri, A. Chakraborty, T. Ahuja, B. Mondal, J. Shantha Kumar and T. Pradeep, (*Submitted*), 2022.

# Formation of Ethane Clathrate Hydrate in Ultrahigh Vacuum by Thermal Annealing

Bijesh K. Malla, Gaurav Vishwakarma, Soham Chowdhury, Premkumar Selvarajan, and Thalappil Pradeep\*



Cite This: *J. Phys. Chem. C* 2022, 126, 17983–17989



Read Online

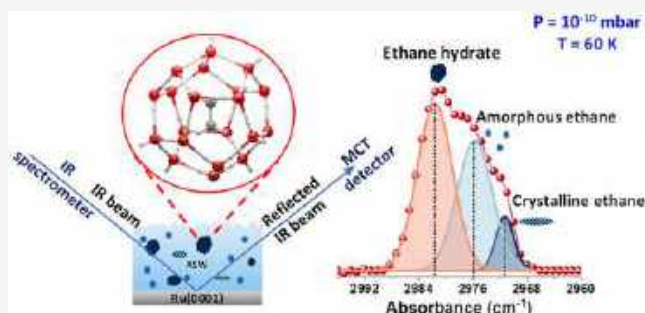
ACCESS |

Metrics & More

Article Recommendations

Supporting Information

**ABSTRACT:** The existence of many molecules in the form of clathrate hydrates (CHs) in ultrahigh vacuum (UHV) and cryogenic conditions has not been explored adequately. In the present study, a detailed investigation by reflection absorption infrared spectroscopy confirmed that the three phases of ethane, i.e., amorphous, crystalline, and CH, coexist in a vapor-deposited ethane–water mixture at 60 K in UHV. Experiments were conducted with vapor-deposited ice films at 10 K, which were annealed to 60 K for tens of hours, and the IR spectral evolution was monitored systematically. Upon maintaining the system at 60 K, three phases of ethane were seen to coexist, but a gradual increase in the hydrate phase was noticed. The evolution of ethane CH from the amorphous ethane–water ice mixture was observed for the very first time in UHV under cryogenic conditions. The formation of the CH was further confirmed by temperature-programmed desorption (TPD) mass spectrometry. Quantum chemical calculation suggested the formation of 5<sup>12</sup>6<sup>2</sup> cage of structure I CH in the ice matrix. The formation of ethane CH in a thin ice film at such a low temperature under UHV suggests its existence in the cometary environment.



## INTRODUCTION

Clathrate hydrates (CHs), cages of water molecules formed by hydrogen bonding, are known since 1810.<sup>1</sup> These crystalline inclusion compounds are commonly known to have three types of structures: structure I (sI, cubic  $Pm\bar{3}n$ ), structure II (sII, cubic  $Fd\bar{3}m$ ), and structure H (sH, hexagonal  $P6/mmm$ ).<sup>2</sup> CHs are considered as potential sources of energy and are likely to play an essential role in some of the planet's significant environmental challenges,<sup>3</sup> such as energy storage and transportation,<sup>4</sup> CO<sub>2</sub> sequestration,<sup>5</sup> and water desalination.<sup>6</sup> These molecular solids are found on the ocean floor and in the permafrost region of the earth. It is also believed to be present in the solar system, like the martian surface,<sup>7,8</sup> titan surface,<sup>9</sup> and icy moons.<sup>10</sup> The capability of forming these structures depends mainly upon the pressure and temperature conditions.<sup>11</sup> Macroscopic deposits of hydrates generally occur at higher pressures,<sup>12</sup> typically greater than 25 atm for methane.<sup>13,14</sup> CHs are also known to exist in vacuum, even under cryogenic conditions.<sup>15–17</sup> In our previous study,<sup>18</sup> we have shown the existence of sI methane hydrate at 30 K and 10<sup>–10</sup> mbar. Upon annealing the methane–water ice mixture deposited at 10 to 30 K for an extended period, methane CH was formed. Such pressure and temperature conditions resemble the interstellar medium (ISM).

While X-ray diffraction, differential scanning calorimetry, and Raman spectroscopy were typically used to examine CHs

in bulk,<sup>19,20</sup> their existence in UHV is typically studied by infrared spectroscopy, temperature-programmed desorption mass spectrometry, and reflection high-energy electron diffraction<sup>21</sup> performed on a thin film.<sup>22–24</sup> Recently, Bauer et al. showed the detection of methane and carbon dioxide CH in a high vacuum by in situ synchrotron X-ray diffraction.<sup>17</sup> Cryo-electron microscopy has been used to examine the different crystalline states of water but has not been used yet for CH studies.<sup>25</sup>

Hydrates formed at the cryogenic temperature in UHV have several consequences. Dissociation of these hydrates could lead to the formation of crystalline ice. In UHV, CHs of acetone and formaldehyde were converted to cubic and hexagonal ices upon dissociation of the hydrate cages.<sup>21,26</sup> Also, it has been observed that ice XVI can be created by subjecting neon hydrate to pumping in a vacuum.<sup>27</sup> Physical properties such as density and refractive index of such ice forms may have important relevance for planetary objects. Similar could be the implication of chemistry of molecules confined in cages in the

**Received:** September 1, 2022

**Revised:** October 3, 2022

**Published:** October 14, 2022



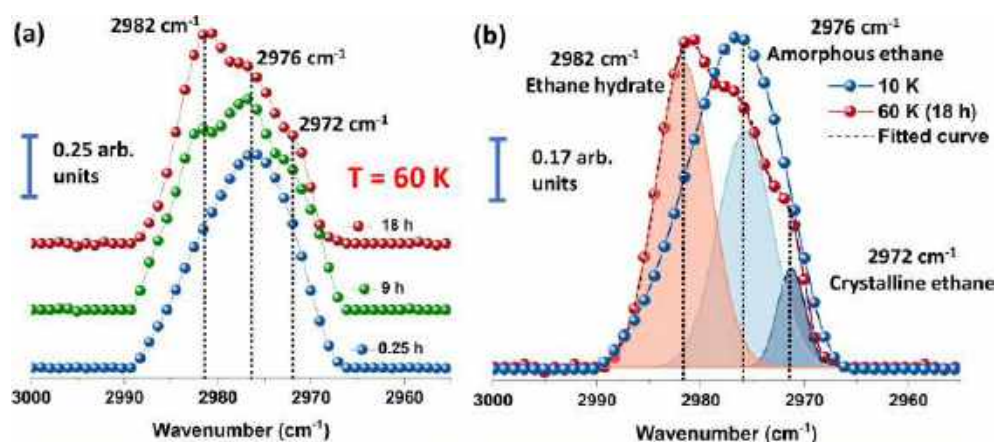


**Figure 1.** CH formation of ethane was studied by RAIR spectroscopy. (a) Normalized time-dependent RAIR spectra of 300 ML ethane/H<sub>2</sub>O (1:1) ice mixture at 60 K in C–H antisymmetric stretching region. (b) A comparison of the normalized RAIR spectra of 300 ML ethane/H<sub>2</sub>O (1:1) mixed ice at 10 and 60 K (after 18 h). The spectrum labeled as 60 K (18 h) was deconvoluted to three components, shown in orange (2982 cm<sup>-1</sup>), light blue (2976 cm<sup>-1</sup>), and dark blue (2972 cm<sup>-1</sup>) shades. For these experiments, ethane and water vapor were codeposited on Ru(0001) at 10 K then the resulting ice mixture was annealed to 60 K at a ramping rate of 2 K min<sup>-1</sup>.

astrochemical environment.<sup>28</sup> The existence of methane hydrate could be likely in such an environment. In the ISM environment, more than two hundred and 70 molecules, including water, have been detected in various temperature and pressure regions, suggesting the existence of hydrates in various astrophysical environments.<sup>29</sup> Chemical processes in these hydrates may lead to relevant cometary and prebiotic science.<sup>30,31</sup> Expanding the exploration of CH to other molecules may be rewarding from this background.

Mixed hydrates of ethane and oxirane (commonly referred to as ethylene oxide) are known to exist in a high vacuum (10<sup>-7</sup> mbar) at 90 K,<sup>32</sup> however, to the best of our knowledge, pure ethane CH in UHV has not been reported yet. In the previous work of Richardson et al.,<sup>32</sup> ethane-oxirane mixed hydrates nucleated over oxirane hydrate upon subsequent deposition of the ethane-oxirane-water mixture at 120 K in high vacuum (10<sup>-7</sup> mbar). The presence of oxirane in the ice mixture helped to induce the nucleation of ethane-oxirane mixed hydrate. Several attempts were unsuccessful to prepare pure ethane hydrate in high vacuum. So, no high vacuum method was developed for the direct formation of ethane CH from ethane–water ice mixture. In this work, we present the formation of pure ethane CH from vapor-deposited ethane–water ice mixtures. This study is carried out at a lower pressure of 10<sup>-10</sup> mbar and at a lower temperature of 60 K than all the previous related studies. Our results of ethane hydrate from binary mixtures of ethane and water may have direct relevance to the cometary environment, where ethane and water are present approximately in the ratio of 100:0.4.<sup>33,34</sup>

## EXPERIMENTAL SECTION

All the experiments were carried out in an ultrahigh vacuum instrument (with a base pressure of ~10<sup>-10</sup> mbar), discussed in detail elsewhere.<sup>35</sup> The instrument is made of stainless steel, and it has three UHV chambers (namely ionization, octupole, and scattering chamber) equipped with low energy ion scattering (LEIS), temperature-programmed desorption (TPD) mass spectrometry, Cs<sup>+</sup> ion-based secondary ion mass spectrometry (SIMS), and reflection absorption infrared spectroscopy (RAIRS). The base pressure of the vacuum chambers is maintained by six turbomolecular pumps, further backed by several oil-free diaphragm pumps. The vacuum of

the chambers is monitored by a Bayard-Alpert gauge, controlled by a MaxiGauge vacuum gauge controller (Pfeiffer, Model TPG 256 A).

We used a highly polished Ru(0001) single crystal as a substrate to create thin ice films. The substrate is mounted on a copper holder, and it is attached to the tip of the helium cryostat (Cold Edge technology), which can maintain a temperature as low as 8 K. The substrate can be heated up to 1000 K by a resistive heater (25 Ω), controlled by a temperature controller (lakeshore 336). A K-type thermocouple sensor is used to measure the substrate temperature with an accuracy of 0.5 K. Repeated heating to 400 K before each vapor deposition experiment ensured surface cleanliness, adequate for the present experiments. It is worth noting that the surface has no effect in this study due to the multilayer deposition.

Millipore water (H<sub>2</sub>O of 18.2 MΩ resistivity) was taken in a vacuum-sealed test tube (with a glass-to-metal seal) and was further purified by several freeze–pump–thaw cycles. Ethane (Akkaran gas and energy, 99.9%) was directly connected to the sample line through a needle valve. Ethane and water were connected to the UHV chamber through two different sample inlet lines. The deposition of two samples was controlled through all metal leak valves, and monolayer coverage was calculated assuming that 1.33 × 10<sup>-6</sup> mbar s = 1 ML, which was estimated to contain ~1.1 × 10<sup>15</sup> molecules cm<sup>-2</sup>.<sup>36</sup> For 300 ML of 1:1 mixed ethane and water deposition, the chamber was backfilled at a total pressure of 5 × 10<sup>-7</sup> mbar where ethane pressure was 2.5 × 10<sup>-7</sup> mbar, and water pressure was 2.5 × 10<sup>-7</sup> mbar. During vapor deposition, mass spectra were recorded simultaneously to check the purity and the ratio of the deposited molecules.

The formation of ethane CH was examined by RAIR spectroscopy and TPD mass spectrometry. RAIR spectra were collected in the 4000–550 cm<sup>-1</sup> range with a spectral resolution of 2 cm<sup>-1</sup> using a Bruker Vertex 70 FT-IR spectrometer with a liquid-nitrogen-cooled mercury cadmium telluride (MCT) detector. The IR beam path outside the UHV chamber was purged with dry nitrogen gas. TPD-MS experiments were performed by a quadrupole mass spectrometer supplied by Extrel.



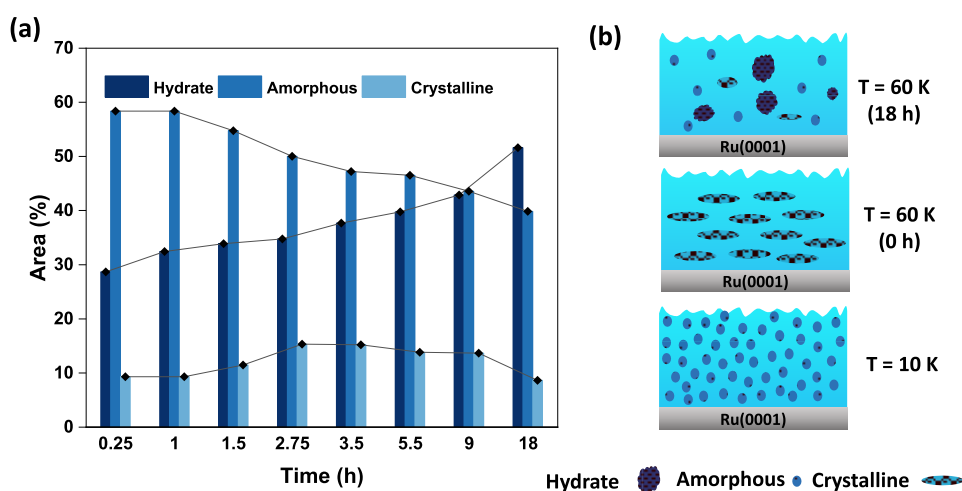


**Figure 2.** (a) Time-dependent growth of ethane CH. The dark blue, the blue, and the light blue bar represent ethane in hydrate, amorphous, and crystalline phases, respectively. (b) Schematic illustration of the formation of ethane hydrate, where amorphous ethane converts to crystalline ethane followed by the formation of ethane hydrate in side ice matrix.

## COMPUTATIONAL DETAILS

Density functional theory (DFT) calculations were carried out to understand the effect of ethane upon inclusion in different-sized CH cages. The Gaussian 16 software was employed to perform the DFT calculations. Structural optimization and vibrational energy studies of  $S^{12}$ ,  $S^{12}6^2$ , and  $S^{12}6^4$  CH cages and ethane included  $S^{12}$ ,  $S^{12}6^2$ , and  $S^{12}6^4$  CH cages were performed at B3LYP/6-311++G(d,p) level of theory. The molecular structures of  $S^{12}$ ,  $S^{12}6^2$ , and  $S^{12}6^4$  CH cages reported by Ningru Sun et al.<sup>37</sup> were considered for the calculations. The CH cages were optimized structurally, and their vibrational modes were calculated. The optimized molecular structure of ethane was inserted into the center of the optimized CH cages, and the whole system was further optimized. The vibrational modes of the ethane inserted in CH cages were calculated. The absence of imaginary vibrational modes in the ethane inserted CH cages revealed that the optimized structures corresponded to global minima.

## RESULTS AND DISCUSSION

The formation of ethane CH was studied by preparing a thin film of 300 ML ethane/H<sub>2</sub>O (1:1) ice mixture on Ru(0001) at 10 K. The vapor-deposited pure ethane exists in the amorphous phase at 10 K, which converts to a crystalline phase upon heating to 30 K before desorbing from the substrate at 60 K (results are shown in Figure S1a (RAIR spectra), S1b (TPD-MS data)).<sup>38–40</sup> However, in ethane–water ice, ethane stays as amorphous at 10 K (full-scale RAIR spectrum showed in Figure S2) and converts to crystalline phase at 50 K. Upon further annealing to 60 K, ethane molecules desorb while leaving a fraction of ethane trapped in the ASW matrix. These trapped molecules undergo a phase evolution in the course of time.

Figure 1a shows the normalized time-dependent RAIR spectra of the ice mixture at 60 K for 0.25, 9, and 18 h in the C–H antisymmetric region of ethane, while the parent IR spectra are shown in Figure S3. The spectrum at 0.25 h (Figure 1a, blue trace) shows three distinct peaks at 2972, 2976, and 2982  $\text{cm}^{-1}$  corresponding to the crystalline, amorphous, and CH phases, respectively. After 9 h (green trace), a slight increase in the relative intensity of the peak at 2982  $\text{cm}^{-1}$  can

be seen, which further increased after 18 h (red trace) along with a relative decrease in the peak intensity at 2976  $\text{cm}^{-1}$ . The assignment of the CH peak at 2982  $\text{cm}^{-1}$  is based on the previous IR studies.<sup>32,41</sup> Also, it is well-known that the vibrational frequency of a molecule entrapped in a CH cage should fall between the vibrational frequencies of the solid and gaseous phases, and the guest molecule within the CH cage behaves as a free molecule.<sup>42</sup> The observed CH peak at 2982  $\text{cm}^{-1}$  is close to the vibrational frequency of the gas phase ethane (at 2985  $\text{cm}^{-1}$ ) in the C–H antisymmetric region,<sup>43</sup> indicating the entrapment of ethane in the CH cage. The RAIR spectral peak at 2976  $\text{cm}^{-1}$  for the amorphous phase and the peak at 2972  $\text{cm}^{-1}$  for the crystalline phase of ethane in ethane–water ice mixture at 60 K are based on a comparison with the data of amorphous<sup>44</sup> and crystalline<sup>38,44</sup> ethane ices (Figure S1a).

To present a clear view of the phase separation of ethane inside the ice matrix at 60 K, we have done an isothermal time-dependent RAIR study of pure ethane at 53 K (Figure S4). The intensity of the IR peak in the C–H antisymmetric region gradually decreases with the desorption of ethane from the substrate. We have not observed any peak other than the peak at 2974  $\text{cm}^{-1}$  in pure ethane, which is attributed to the crystalline phase. Therefore, the peaks at 2976 and 2982  $\text{cm}^{-1}$  in Figure 1b are two entirely new peaks that arise due to the formation of amorphous and CH phases inside the ice matrix. The spectrum obtained at 60 K after 18 h of annealing was deconvoluted (shown in Figure 1b) to evaluate the ratio of the three coexisting phases. Taking the area under each deconvoluted peak, the ratios of three phases, CH, amorphous and crystalline forms of ethane in the ice matrix, were estimated to be 52:40:8 by molar ratio. Although the concentration of the CH form appears to be large, it was estimated to be  $\sim 2.5\%$  of the total ethane deposited.

In UHV and at cryogenic temperatures, CH formation depends on the mobility and hydrogen bonding of the host and guest molecules. Keeping the ethane–water ice mixture near the desorption temperature of ethane (60 K) is crucial for CH formation of ethane. At this temperature, higher ethane mobility leads to the formation of a clathrate-like structure in the ice matrix. We have also monitored the O–H stretching and dangling O–H region during the formation of CH. In the

O–H stretching region (Figure S5a), no significant changes were noticed, but in the dangling O–H region, the peak at  $3667\text{ cm}^{-1}$  disappeared upon the formation of CH (Figure S5b), which suggested the collapse of micropores in ASW.<sup>45,46</sup> To see the temperature dependency of CH formation, we annealed the ethane/H<sub>2</sub>O (1:1) ice mixture at 55 K for 18 h. We did not observe any peak arising at  $2982\text{ cm}^{-1}$  (Figure S6). Hence, we concluded that CH formation of ethane in UHV at cryogenic temperatures depends significantly on the temperature and annealing time. Figure 2a shows the time-dependent growth of ethane CH relative to the amorphous and crystalline phases. Although the overall intensity of the time-dependent RAIR spectra in the C–H antisymmetric region decreases with time, the hydrate peak intensity decreases slower relative to the amorphous peak intensity. Each RAIR spectrum in the C–H antisymmetric region at a particular time was deconvoluted into three peaks (for CH, amorphous, and crystalline phase) to estimate the area under each peak. The ratios of ethane in three phases were derived, converted into percentages, and plotted in Figure 2a. A relative increase in the fraction of the CH phase and a relative decrease in the amorphous phase was noticed, whereas the change in the fraction of the crystalline phase was roughly the same (considering the error involved in fitting). A relative increase in the fraction of the CH phase could be due to the conversion of amorphous ethane into the CH phase. The physical transformation of ethane from the amorphous to CH phase through the crystalline phase is illustrated in Figure 2b.

The formation of ethane CH in UHV was further confirmed using TPD-MS studies. Two sets of TPD-MS experiments were performed, and the results are shown in Figure 3. In the first experiment, we deposited 300 ML of ethane/H<sub>2</sub>O (1:1) ice mixture at 10 K and heated it to 200 K with a ramping rate of  $30\text{ K min}^{-1}$ . The desorption of ethane was monitored by  $m/z = 28$  ( $\text{C}_2\text{H}_4^+$ ). TPD-MS spectra were plotted as  $\text{C}_2\text{H}_4^+$  ion intensity versus substrate temperature (blue trace). Two peaks were observed at 60 and 140 K. The peak at 60 K is attributed

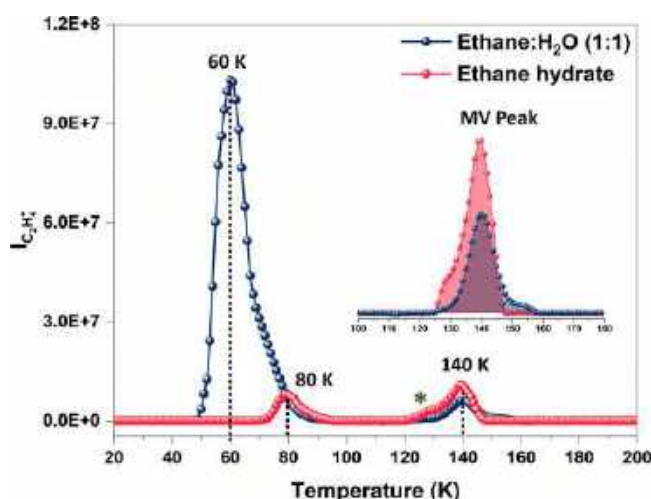


**Figure 3.** TPD mass spectra of 300 ML of codeposited ethane/H<sub>2</sub>O (1:1) ice mixture (ramping rate =  $30\text{ K min}^{-1}$ ). Here, the intensity of  $\text{C}_2\text{H}_4^+$  ( $m/z = 28$ ) versus substrate temperature is plotted. The desorption profile of ethane after CH formation is shown with a red trace while before CH formation is shown with a blue trace. MV peak is shown in the inset. The peak labeled (\*), is attributed to predissociation of ethane CH.

to the bulk desorption of ethane from ASW; the long tail of this peak is due to the molecules that are trapped in ASW pores which slowly desorbed until reaching 90 K. The peak at 140 K is attributed to the so-called molecular volcano (MV) peak.<sup>47,48</sup> The MV peak occurs due to the abrupt gas release from ASW during the process of ASW crystallization. In the second experiment, we created amorphous ethane/H<sub>2</sub>O (1:1) ice mixture at 10 K, and after annealing the sample at 60 K for 18 h (to create ethane CH), the sample was cooled to 10 K. Now, the sample was further heated to 200 at  $30\text{ K min}^{-1}$ , and the TPD spectrum was recorded (red trace). Here, also, two peaks were observed at 80 and 140 K. The peak at 80 K is attributed to the desorption of trapped ethane (amorphous or crystalline) from the ASW matrix. The peak shift from 60 to 80 K for ethane desorption may be due to the formation of CH as well as the compactness of the ice sample (a result of prolonged annealing). In this case, the MV peak (at 140 K, red trace) shows a higher peak intensity with respect to the previous MV peak (blue trace). An increase in the intensity of MV peak for the latter case is due to the release of the trapped ethane from the ASW pores as well as due to dissociation of the CH cage. Here, it is worth noting that, in both experiments, the number of molecules of ethane and water deposited on the Ru(0001) was approximately the same. The peak marked by an asterisk around 125 K is the desorption of ethane due to the predissociation of CH cages.<sup>18</sup>

The vibrational shift in the infrared/Raman spectra upon enclathration of guest molecules inside the water cage plays a major role in understanding the types of CH structure formed.<sup>49</sup> Quantum chemical calculations have been used to understand the spectral properties of molecules in specific cages.<sup>50</sup>

Particularly, DFT calculations are widely used to find the vibrational shifts in Raman and IR frequencies of methane sl CH structure.<sup>51</sup> Such studies performed at B3LYP (level of theory) are known to reproduce spectral behavior accurately.<sup>18,49,50</sup> In this study, we examined different cages and the effect of entrapment of ethane in them at B3LYP/6-311++G(d,p) level of theory. We calculated the harmonic vibrational frequencies of pure ethane, empty water cages ( $5^{12}$ ,  $5^{12}6^2$ , and  $5^{12}6^4$ ), and ethane entrapped in three different CH cages. Figure 4 shows the optimized structures of ethane entrapped in different CH cages ( $5^{12}$ ,  $5^{12}6^2$ , and  $5^{12}6^4$ ). Full-scale IR spectra of ethane and ethane trapped in three cages are shown in Figure S7. The frequency shifts in the C–H antisymmetric region for free ethane and ethane engaged in  $5^{12}$ ,  $5^{12}6^2$ , and  $5^{12}6^4$  cages are presented in Table 1. Here, positive frequency shifts were found in all three CH cages due to the dispersion interaction between the entrapped ethane and water molecules of the cage.<sup>51</sup> A higher blue shift was found for the small cage compared to the large cages due to larger confinement, leading to the higher interaction between ethane and water. Figure 5 compares the experimental and theoretical shifts in the C–H antisymmetric stretching region. The peak shift between the deconvoluted hydrate peak and condensed ethane–water ice mixture peak at 10 K is shown in Figure 5a, whereas the peak shift between pure ethane and ethane engaged inside  $5^{12}6^2$  cage is shown in Figure 5b. The experimental shift ( $6\text{ cm}^{-1}$ ) closely matches the theoretical shift ( $7\text{ cm}^{-1}$ ) for the  $5^{12}6^2$  cage. From the above results, it was concluded that ethane forms sl CH in UHV at cryogenic temperatures.<sup>32,52</sup>



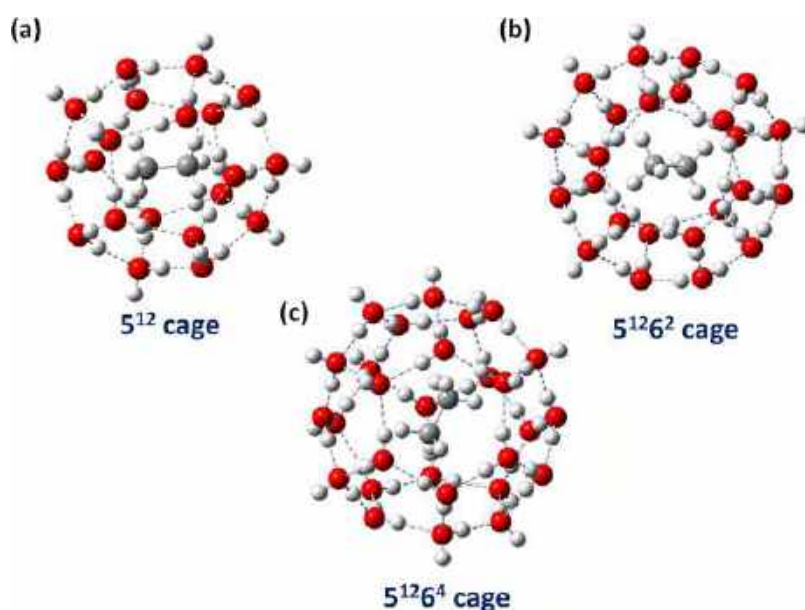


**Figure 4.** DFT-optimized structures of ethane trapped within different CH cages, such as (a)  $5^{12}$  cage, (b)  $5^{12}6^2$  cage, and (c)  $5^{12}6^4$  cage. Here, water cage and the guest molecule ethane are shown. Color code used: gray, C atom; red, O atom; white, H atom.

**Table 1. Comparison of the Computational and Experimental Vibrational Shifts of Ethane CH Compared to Free Ethane in the C–H Antisymmetric Region**

ethane clathrate hydrate	$5^{12}$ cage	$5^{12}6^2$ cage	$5^{12}6^4$ cage
Vibrational Shift (computational)	$41\text{ cm}^{-1}$	$7\text{ cm}^{-1}$	$2\text{ cm}^{-1}$
Vibrational Shift (Experimental)		$6\text{ cm}^{-1}$	

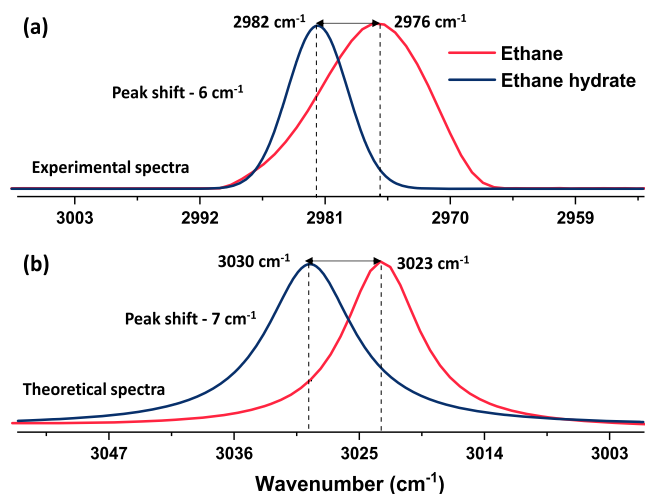


**Figure 5.** Comparison of experimental and theoretical IR vibrational shift in the C–H antisymmetric region of ethane due to the formation of ethane hydrate. (a) Comparison between the RAIR spectra of ethane in the ASW matrix at 10 K (red trace) and the ethane hydrate (blue trace). The hydrate peak is a deconvoluted peak from the parent RAIR spectrum collected after 18 h at 60 K in the hydrate experiment. (b) Comparison between the IR spectra of pure ethane (red trace) and ethane trapped in  $5^{12}6^2$  CH cage (blue trace).

## CONCLUSION

In this study, we reported the formation of ethane CH from ethane–water ice mixture at 60 K in UHV for the first time. Upon the formation of ethane CH, a  $6\text{ cm}^{-1}$  blue shift was observed in the IR spectrum, which closely matches the

theoretical shift ( $7\text{ cm}^{-1}$ ) calculated from a DFT study. Along with CH, two other ethane phases (amorphous and crystalline) also coexist in the ice mixture for a longer period at 60 K. All three phases are metastable at this temperature; therefore, upon waiting for 18 h, ethane molecules slowly desorbed from the ASW matrix. We have also discussed the evolution of three phases with respect to time and showed an approximate percentage of the distinct phases at a particular time. After waiting at 60 K for 18 h, it was seen that only 2.5% of ethane molecules stayed in the CH phase from the total deposited ethane molecules. Higher mobility of the ethane molecules near its desorption temperature leads to the formation of CH at cryogenic temperatures. RAIRS and TPD-MS were used to prove the formation of CH. Quantum chemical calculations were carried out to study the spectral behavior of ethane inside different water cages, which suggests the formation of sl CH ( $5^{12}6^2$  cage) within the ice matrix. Our study gives direct evidence for the possibility of finding ethane CH in cometary environments.

## ASSOCIATED CONTENT

### Supporting Information

The Supporting Information is available free of charge at <https://pubs.acs.org/doi/10.1021/acs.jpcc.2c06264>.

Temperature and time-dependent RAIR spectra of pure ethane and ethane–water ice mixture, TPD-MS spectra of pure ethane and ethane–water ice mixture, theoretical IR spectra of ethane CH (PDF)

## AUTHOR INFORMATION

### Corresponding Author

Thalappil Pradeep – DST Unit of Nanoscience (DST UNS) and Thematic Unit of Excellence (TUE), Department of Chemistry, Indian Institute of Technology Madras, Chennai 600036, India; International Centre for Clean Water, IIT Madras Research Park, Chennai 6000113, India; [orcid.org/0000-0003-3174-534X](https://orcid.org/0000-0003-3174-534X); Email: [pradeep@iitm.ac.in](mailto:pradeep@iitm.ac.in)

## Authors

**Bijesh K. Malla** – DST Unit of Nanoscience (DST UNS) and Thematic Unit of Excellence (TUE), Department of Chemistry, Indian Institute of Technology Madras, Chennai 600036, India

**Gaurav Vishwakarma** – DST Unit of Nanoscience (DST UNS) and Thematic Unit of Excellence (TUE), Department of Chemistry, Indian Institute of Technology Madras, Chennai 600036, India

**Soham Chowdhury** – DST Unit of Nanoscience (DST UNS) and Thematic Unit of Excellence (TUE), Department of Chemistry, Indian Institute of Technology Madras, Chennai 600036, India

**Premkumar Selvarajan** – DST Unit of Nanoscience (DST UNS) and Thematic Unit of Excellence (TUE), Department of Chemistry, Indian Institute of Technology Madras, Chennai 600036, India

Complete contact information is available at:

<https://pubs.acs.org/10.1021/acs.jpcc.2c06264>

## Author Contributions

B.K.M and G.V designed the experiments, B.K.M., G.V., and S.C performed the experiments and analyzed the results. P.S. performed the theoretical calculations. T.P. proposed the project and supervised the progress. The manuscript was written with the contributions of all authors.

## Notes

The authors declare no competing financial interest.

## ACKNOWLEDGMENTS

We acknowledge the Science and Engineering Research Board (SERB), Department of Science and Technology (DST), and Government of India for support. T.P. acknowledges funding from the Centre of Excellence on Molecular Materials and Functions under the Institution of Eminence scheme of IIT Madras. B.K.M. thanks the Council of Scientific and Industrial Research (CSIR) for his research fellowship. G.V. and S.C. thanks IITM for their research fellowships.

## REFERENCES

- (1) Davy, H., VIII On a Combination of Oxymuriatic Gas and Oxygene Gas. *Philos. Trans. R. Soc. London* **1811**, 101, 155–162.
- (2) Chong, Z. R.; Yang, S. H. B.; Babu, P.; Linga, P.; Li, X. Sen. Review of Natural Gas Hydrates as an Energy Resource: Prospects and Challenges. *Appl. Energy* **2016**, 162, 1633–1652.
- (3) Sloan, E. D. Fundamental Principles and Applications of Natural Gas Hydrates. *Nature*; Nature Publishing Group, 2003; pp 353–359.
- (4) Yin, Z.; Zheng, J.; Kim, H.; Seo, Y.; Linga, P. Hydrates for Cold Energy Storage and Transport: A Review. *Adv. Appl. Energy* **2021**, 2, 100022.
- (5) Zheng, J.; Chong, Z. R.; Qureshi, M. F.; Linga, P. Carbon Dioxide Sequestration via Gas Hydrates: A Potential Pathway toward Decarbonization. *Energy Fuels* **2020**, 34 (9), 10529–10546.
- (6) Bhattacharjee, G.; Goh, M. N.; Arumuganainar, S. E. K.; Zhang, Y.; Linga, P. Ultra-Rapid Uptake and the Highly Stable Storage of Methane as Combustible Ice. *Energy Environ. Sci.* **2020**, 13 (12), 4946–4961.
- (7) Thomas, C.; Mousis, O.; Picaud, S.; Ballenegger, V. Variability of the Methane Trapping in Martian Subsurface Clathrate Hydrates. *Planet. Space Sci.* **2009**, 57 (1), 42–47.
- (8) Chastain, B. K.; Chevrier, V. Methane Clathrate Hydrates as a Potential Source for Martian Atmospheric Methane. *Planet. Space Sci.* **2007**, 55 (10), 1246–1256.
- (9) Tobie, G.; Lunine, J. I.; Sotin, C. Episodic Outgassing as the Origin of Atmospheric Methane on Titan. *Nature* **2006**, 440 (7080), 61–64.
- (10) Mousis, O.; Lunine, J. I.; Picaud, S.; Cordier, D. Volatile Inventories in Clathrate Hydrates Formed in the Primordial Nebula. *Faraday Discuss.* **2010**, 147 (0), 509–525.
- (11) Cui, J.; Sun, Z.; Wang, X.; Yu, B.; Leng, S.; Chen, G.; Sun, C. Fundamental Mechanisms and Phenomena of Clathrate Hydrate Nucleation. *Chin. J. Chem. Eng.* **2019**, 27 (9), 2014–2025.
- (12) Englezos, P. *REVIEWS Clathrate Hydrates* **1993**.
- (13) Truong-Lam, H. S.; Seo, S.; Kim, S.; Seo, Y.; Lee, J. D. In Situ Raman Study of the Formation and Dissociation Kinetics of Methane and Methane/Propane Hydrates. *Energy Fuels* **2020**, 34 (5), 6288–6297.
- (14) Nagashima, H. D.; Ohmura, R. Phase Equilibrium Condition Measurements in Methane Clathrate Hydrate Forming System from 197.3 to 238.7 K. *J. Chem. Thermodyn* **2016**, 102, 252–256.
- (15) Fleyfel, F.; Devlin, J. P. FT-IR Spectra of 90 K Films of Simple, Mixed, and Double Clathrate Hydrates of Trimethylene Oxide, Methyl Chloride, Carbon Dioxide, Tetrahydrofuran, and Ethylene Oxide Containing Decoupled D2O. *J. Phys. Chem.* **1988**, 92, 631–635.
- (16) Blake, D.; Allamandola, L.; Sandford, S.; Hudgins, D.; Freund, F. Clathrate Hydrate Formation in Amorphous Cometary Ice Analogs in Vacuo. *Science (80-)* **1991**, 254 (5031), 548–551.
- (17) Bauer, R. P. C.; Ravichandran, A.; Tse, J. S.; Appathurai, N.; King, G.; Moreno, B.; Desgreniers, S.; Sammynaiken, R. In Situ X-Ray Diffraction Study on Hydrate Formation at Low Temperature in a High Vacuum. *J. Phys. Chem. C* **2021**, 125 (48), 26892–26900.
- (18) Ghosh, J.; Methikkalam, R. R. J.; Bhuin, R. G.; Ragupathy, G.; Choudhary, N.; Kumar, R.; Pradeep, T. Clathrate Hydrates in Interstellar Environment. *Proc. Natl. Acad. Sci. U. S. A* **2019**, 116 (5), 1526–1531.
- (19) Murshed, M. M.; Schmidt, B. C.; Kuhs, W. F. Kinetics of Methane-Ethane Gas Replacement in Clathrate-Hydrates Studied by Time-Resolved Neutron Diffraction and Raman Spectroscopy. *J. Phys. Chem. A* **2010**, 114 (1), 247–255.
- (20) Thakre, N.; Jana, A. K. Physical and Molecular Insights to Clathrate Hydrate Thermodynamics. *Renew. Sustain. Energy Rev.* **2021**, 135, 110150.
- (21) Ghosh, J.; Bhuin, R. G.; Vishwakarma, G.; Pradeep, T. Formation of Cubic Ice via Clathrate Hydrate, Prepared in Ultrahigh Vacuum under Cryogenic Conditions. *J. Phys. Chem. Lett.* **2020**, 11 (1), 26–32.
- (22) Ghosh, J.; Bhuin, R. G.; Ragupathy, G.; Pradeep, T. Spontaneous Formation of Tetrahydrofuran Hydrate in Ultrahigh Vacuum. *J. Phys. Chem. C* **2019**, 123 (26), 16300–16307.
- (23) Cwiklik, L.; Devlin, J. P. Hindering of Rotational Motion of Guest Molecules in the Type I Clathrate Hydrate. *Chem. Phys. Lett.* **2010**, 494 (4–6), 206–212.
- (24) Fleyfel, F.; Devlin, J. P. FT-IR Spectra of 90 K Films of Simple, Mixed, and Double Clathrate Hydrates of Trimethylene Oxide, Methyl Chloride, Carbon Dioxide, Tetrahydrofuran, and Ethylene Oxide Containing Decoupled D2O. *J. Phys. Chem.* **1988**, 92 (3), 631–635.
- (25) Egelman, E. H. Cryo-EM: Ice Is Nice, but Good Ice Can Be Hard to Find. *Biophys. J.* **2020**, 118 (6), 1238.
- (26) Ghosh, J.; Vishwakarma, G.; Das, S.; Pradeep, T. Facile Crystallization of Ice Ih via Formaldehyde Hydrate in Ultrahigh Vacuum under Cryogenic Conditions. *J. Phys. Chem. C* **2021**, 125 (8), 4532–4539.
- (27) Falenty, A.; Hansen, T. C.; Kuhs, W. F. Formation and Properties of Ice XVI Obtained by Emptying a Type SII Clathrate Hydrate. *Nature* **2014**, 516 (7530), 231–233.
- (28) Horowitz, Y.; Asscher, M. Electron-Induced Chemistry of Methyl Chloride Caged within Amorphous Solid Water. *J. Chem. Phys.* **2013**, 139 (15), 154707.
- (29) Van Dishoeck, E. F.; Herbst, E.; Neufeld, D. A. Interstellar Water Chemistry: From Laboratory to Observations. *Chemical Reviews* **2013**, 113, 9043–9085.

- (30) Öberg, K. I. Photochemistry and Astrochemistry: Photochemical Pathways to Interstellar Complex Organic Molecules. *Chem. Rev.* **2016**, *116* (17), 9631–9663.
- (31) Singh, S. K.; Zhu, C.; La Jeunesse, J.; Fortenberry, R. C.; Kaiser, R. I. Experimental Identification of Aminomethanol (NH<sub>2</sub>CH<sub>2</sub>OH)—the Key Intermediate in the Strecker Synthesis. *Nat. Commun.* **2022**, *13* (1), 1–7.
- (32) Richardson, H. H.; Wooldridge, P. J.; Devlin, J. P. FT-IR Spectra of Vacuum Deposited Clathrate Hydrates of Oxirane H<sub>2</sub>S, THF, and Ethane. *J. Chem. Phys.* **1985**, *83* (9), 4387.
- (33) Mumma, M. J.; DiSanti, M. A.; Dello Russo, N.; Fomenkova, M.; Magee-Sauer, K.; Kaminski, C. D.; Xie, D. X. Detection of Abundant Ethane and Methane, along with Carbon Monoxide and Water, in Comet C/1996 B2 Hyakutake: Evidence for Interstellar Origin. *Science* (80-) **1996**, *272* (5266), 1310–1314.
- (34) Dello Russo, N.; Mumma, M. J.; DiSanti, M. A.; Magee-Sauer, K. Production of Ethane and Water in Comet C/1996 B2 Hyakutake. *J. Geophys. Res. Planets* **2002**, *107* (E11), 5-1–5-11.
- (35) Bag, S.; Bhuin, R. G.; Methikkalam, R. R. J.; Pradeep, T.; Kephart, L.; Walker, J.; Kuchta, K.; Martin, D.; Wei, J. Development of Ultralow Energy (1–10 eV) Ion Scattering Spectrometry Coupled with Reflection Absorption Infrared Spectroscopy and Temperature Programmed Desorption for the Investigation of Molecular Solids. *Rev. Sci. Instrum.* **2014**, *85* (1), 014103.
- (36) Kim, Y.; Moon, E.; Shin, S.; Kang, H. Acidic Water Monolayer on Ruthenium(0001). *Angew. Chem.* **2012**, *124* (51), 12978–12981.
- (37) Sun, N.; Li, Z.; Qiu, N.; Yu, X.; Zhang, X.; Li, Y.; Yang, L.; Luo, K.; Huang, Q.; Du, S. Ab Initio Studies on the Clathrate Hydrates of Some Nitrogen- and Sulfur-Containing Gases. *J. Phys. Chem. A* **2017**, *121* (13), 2620–2626.
- (38) Tejada, S. B.; Eggers, D. F. Infrared Spectra of Ordered Crystalline Ethane and Ethane-D<sub>6</sub>. *Spectrochim. Acta Part A Mol. Spectrosc.* **1976**, *32* (9), 1557–1562.
- (39) Chesters, M. A.; Gardner, P.; McCash, E. M. The Reflection-Absorption Infrared Spectra of n-Alkanes Adsorbed on Pt(111). *Surf. Sci.* **1989**, *209* (1–2), 89–99.
- (40) Hudson, R. L.; Gerakines, P. A.; Moore, M. H. Infrared Spectra and Optical Constants of Astronomical Ices: II. Ethane and Ethylene. *Icarus* **2014**, *243*, 148–157.
- (41) Dartois, E.; Langlet, F. Ethane Clathrate Hydrate Infrared Signatures for Solar System Remote Sensing. *Icarus* **2021**, *357*, 114255.
- (42) Buch, V.; Devlin, J. P.; Monreal, I. A.; Jagoda-Cwiklik, B.; Uras-Aytemiz, N.; Cwiklik, L. Clathrate Hydrates with Hydrogen-Bonding Guests. *Phys. Chem. Chem. Phys.* **2009**, *11* (44), 10245–10265.
- (43) Hepp, M.; Herman, M. Weak Combination Bands in the 3-Mm Region of Ethane. *J. Mol. Spectrosc.* **1999**, *197* (1), 56–63.
- (44) Hudson, R. L.; Moore, M. H.; Raines, L. L. Ethane Ices in the Outer Solar System: Spectroscopy and Chemistry. *Icarus* **2009**, *203* (2), 677–680.
- (45) Maté, B.; Satorre, M.; Escribano, R. On the Spectral Features of Dangling Bonds in CH<sub>4</sub>/H<sub>2</sub>O Amorphous Ice Mixtures. *Phys. Chem. Chem. Phys.* **2021**, *23* (15), 9532–9538.
- (46) Li, H.; Karina, A.; Ladd-Parada, M.; Späh, A.; Perakis, F.; Benmore, C.; Amann-Winkel, K. Long-Range Structures of Amorphous Solid Water. *J. Phys. Chem. B* **2021**, *125* (48), 13320–13328.
- (47) Collings, M. P.; Anderson, M. A.; Chen, R.; Dever, J. W.; Viti, S.; Williams, D. A.; McCoustra, M. R. S. A Laboratory Survey of the Thermal Desorption of Astrophysically Relevant Molecules. *Mon. Not. R. Astron. Soc.* **2004**, *353*, 1133–1140, DOI: 10.1111/j.1365-2966.2004.08272.x.
- (48) May, R. A.; Smith, R. S.; Kay, B. D. The Release of Trapped Gases from Amorphous Solid Water Films. I. “Top-down” Crystallization-Induced Crack Propagation Probed Using the Molecular Volcano. *J. Chem. Phys.* **2013**, *138* (10), 104501.
- (49) Ghosh, J.; Bhuin, R. G.; Ragupathy, G.; Pradeep, T. Spontaneous Formation of Tetrahydrofuran Hydrate in Ultrahigh Vacuum. *J. Phys. Chem. C* **2019**, *123* (26), 16300–16307.
- (50) Li, M.; Li, K.; Yang, L.; Su, Y.; Zhao, J.; Song, Y. Evidence of Guest-Guest Interaction in Clathrates Based on in Situ Raman Spectroscopy and Density Functional Theory. *J. Phys. Chem. Lett.* **2022**, *13* (1), 400–405.
- (51) Ramya, K. R.; Pavan Kumar, G. V.; Venkatnathan, A. Raman Spectra of Vibrational and Librational Modes in Methane Clathrate Hydrates Using Density Functional Theory. *J. Chem. Phys.* **2012**, *136* (17), 174305.
- (52) Hoshikawa, A. Structural Changes Due to the Ordered Guest Molecules in Deuterated Ethane Hydrate. *Chem. Phys. Lett.* **2022**, *800*, 139679.

## Recommended by ACS

### Phase Behavior of Clathrate Hydrates in the Ternary H<sub>2</sub>O–NH<sub>3</sub>–Cyclopentane System

Claire Petuya, Ashley G. Davies, *et al.*

MARCH 23, 2020  
ACS EARTH AND SPACE CHEMISTRY

READ 

### CH/CH<sub>2</sub> Group Clusters Doping Methane Hydrate Cages

Lihua Wan, Shuanshi Fan, *et al.*

OCTOBER 20, 2022  
THE JOURNAL OF PHYSICAL CHEMISTRY LETTERS

READ 

### Hydrate Stability in the H<sub>2</sub>S–H<sub>2</sub>O system—Visual Observations and Measurements in a High-Pressure Optical Cell and Thermodynamic Models

Jiyue Sun, Lei Jiang, *et al.*

JUNE 30, 2020  
JOURNAL OF CHEMICAL & ENGINEERING DATA

READ 

### Structural Transition of the Methane–Ethane Mixture Hydrate in a Hydrate/Water/Hydrocarbon Three-Phase Coexistence System: Effect of Gas Concentration

Jiangtao Pang, Satoshi Takeya, *et al.*

NOVEMBER 03, 2020  
ACS SUSTAINABLE CHEMISTRY & ENGINEERING

READ 

Get More Suggestions >

# Formation of Ethane Clathrate Hydrate in Ultrahigh Vacuum by Thermal Annealing

*Bijesh K. Malla<sup>†</sup>, Gaurav Vishwakarma<sup>†</sup>, Soham Chowdhury<sup>†</sup>, Premkumar Selvarajan<sup>†</sup>, and Thalappil Pradeep<sup>†\*</sup>*

DST Unit of Nanoscience (DST UNS) and Thematic Unit of Excellence (TUE), Department of Chemistry, Indian Institute of Technology Madras, Chennai 600036, India

## **AUTHOR INFORMATION**

### **Corresponding Author**

\*E-mail: [pradeep@iitm.ac.in](mailto:pradeep@iitm.ac.in)

### **Table of contents**

Name	Description	Page number
Figure S1	Temperature-dependent RAIR spectra and TPD mass spectrum of pure ethane ice.	S3
Figure S2	Full-scale RAIR spectrum of ethane:H <sub>2</sub> O (1:1) ice mixture at 10 K.	S4

Figure S3	Temperature and time-dependent RAIR spectra of ethane:H <sub>2</sub> O (1:1) ice mixture at 60 K.	S5
Figure S4	Time-dependent RAIR spectra of pure ethane ice at 53 K.	S6
Figure S5	Time-dependent RAIR spectra of ethane:H <sub>2</sub> O (1:1) ice mixture at 60 K.	S7
Figure S6	Time-dependent RAIR spectra of ethane:H <sub>2</sub> O (1:1) ice mixture at 55 K.	S8
Figure S7	Full-scale theoretical IR spectra of ethane and ethane hydrate.	S9

### Supporting information 1:

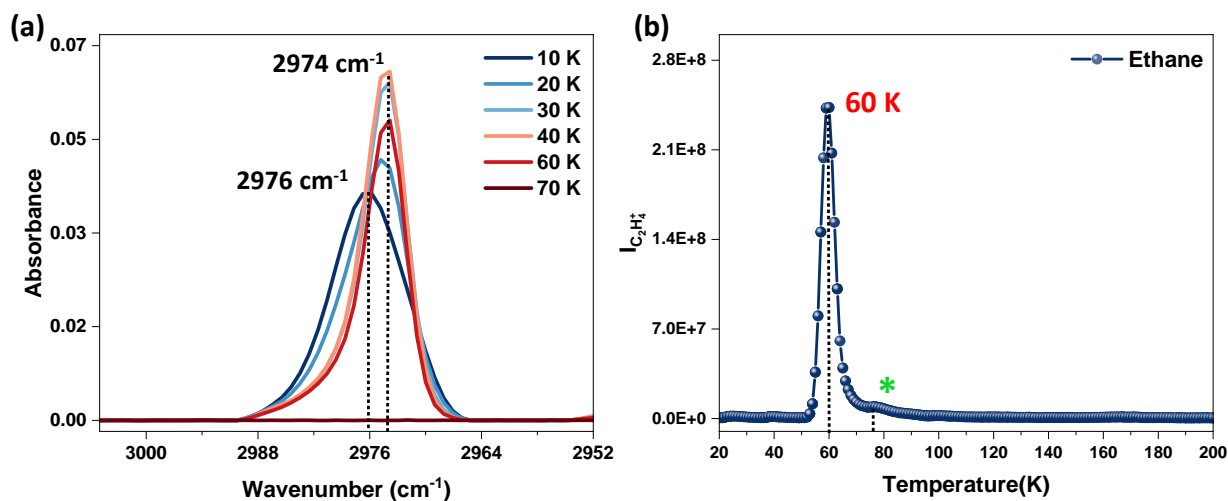


**Figure S1.** (a) Temperature-dependent RAIR spectra of 150 ML of pure ethane in C-H antisymmetric stretching region. Pure ethane was vapor-deposited on the Ru(0001) at 10 K and annealed with a ramping rate of 2 K min<sup>-1</sup>. (b) TPD-MS spectrum of 150 ML of pure ethane. The intensity of C<sub>2</sub>H<sub>4</sub><sup>+</sup> (m/z = 28) versus temperature of the Ru(0001) substrate is plotted. The peak at 60 K is attributed to multilayer desorption, and the peak marked by (\*) is attributed to monolayer desorption. The pure ethane was vapor-deposited on Ru(0001) at 10 K and further annealed to 200 K with a ramping rate of 30 K min<sup>-1</sup>.



Supporting information 2:

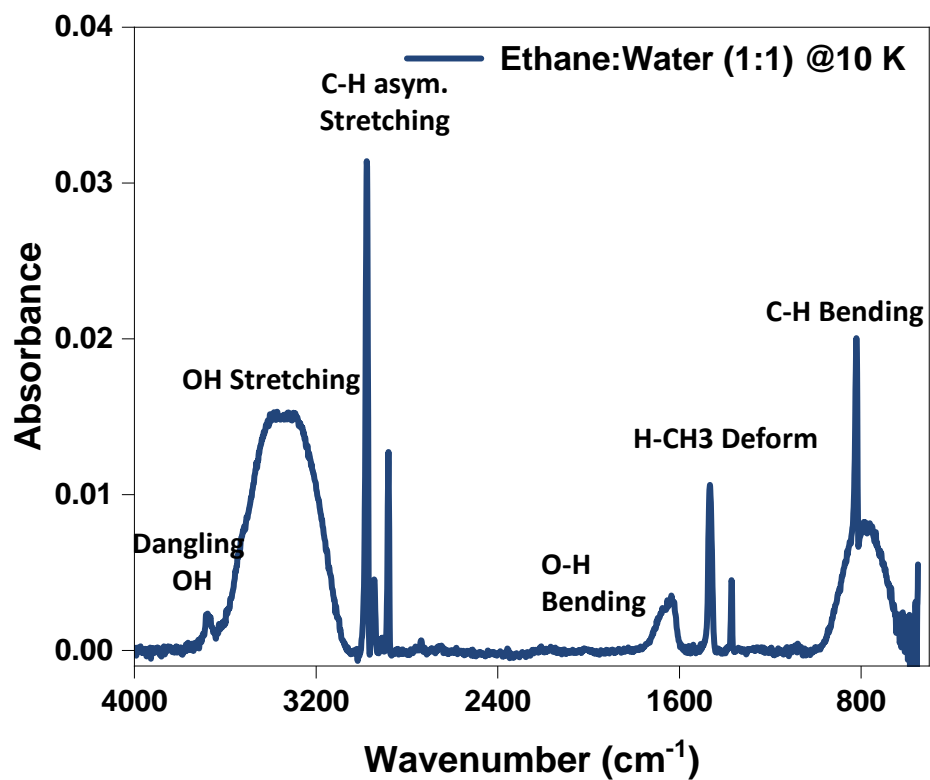


**Figure S2.** Full-scale RAIR spectrum of 300 ML of ethane:H<sub>2</sub>O (1:1) ice mixture at 10 K. Ethane and water vapor were co-deposited on Ru(0001) at 10 K.

### Supporting information 3:

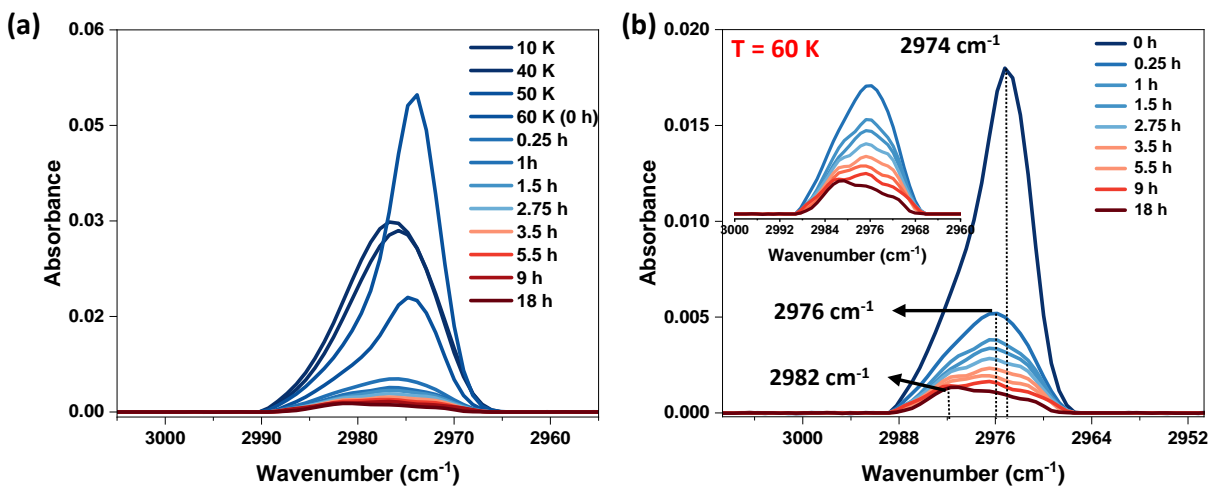


**Figure S3.** (a) Temperature and time-dependent RAIR spectra of 300 ML of ethane:H<sub>2</sub>O (1:1) ice mixture in the C-H antisymmetric region. (b) Time-dependent RAIR spectra of 300 ML of ethane:H<sub>2</sub>O (1:1) ice mixture at 60 K, in the left corner, the zoomed spectra from 0.25 h to 18 h are presented. Ethane and water vapor were co-deposited on the Ru(0001) at 10 K and annealed to 60 K at a ramping rate of 2 K min<sup>-1</sup>.

Supporting information 4:

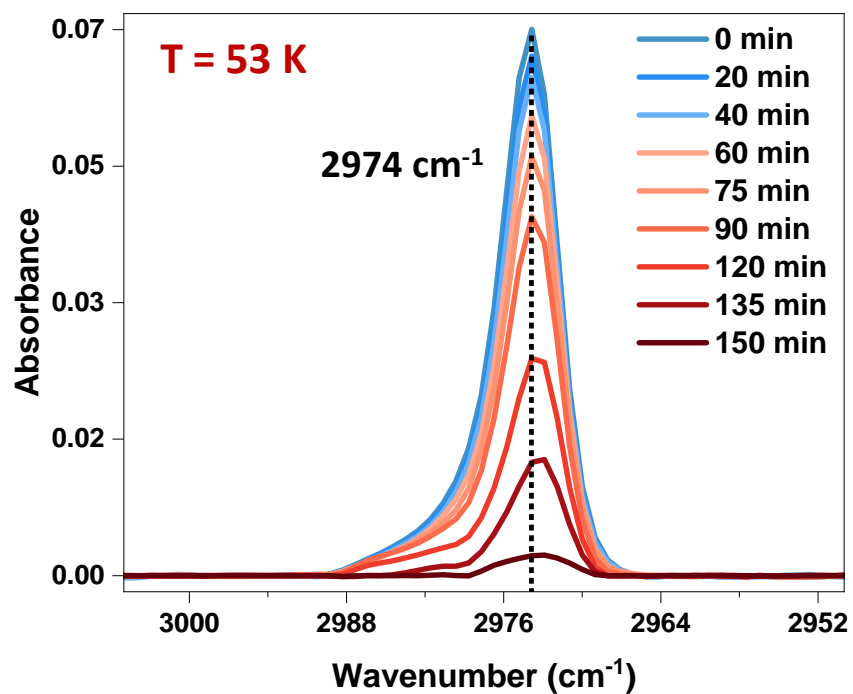


**Figure S4.** Time-dependent RAIR spectra of 150 ML of pure ethane film at 53 K in the C-H antisymmetric stretching region. Ethane vapor was deposited on Ru(0001) at 10 K and annealed to 53 K at a ramping rate of 2 K min<sup>-1</sup>.

### Supporting information 5:

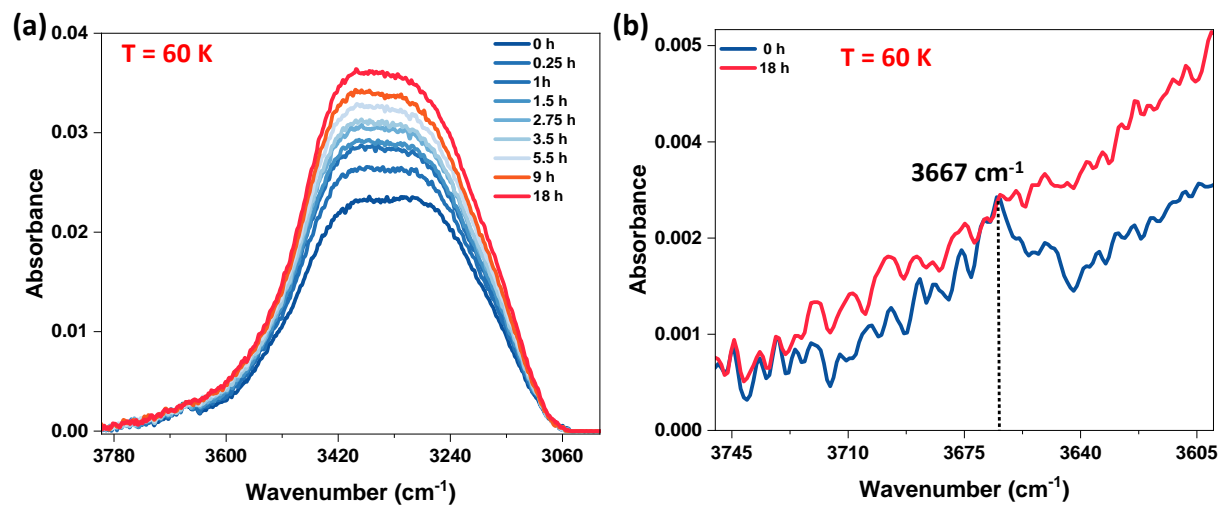


**Figure S5.** Time-dependent RAIR spectra of 300 ML of ethane:H<sub>2</sub>O (1:1) ice mixture in the, (a) O-H stretching region of H<sub>2</sub>O, and (b) Dangling O-H stretching region of H<sub>2</sub>O. Ethane and water vapor were co-deposited on Ru(0001) at 10 K and annealed to 60 K at a ramping rate of 2 K min<sup>-1</sup>.

Supporting Figure 6:

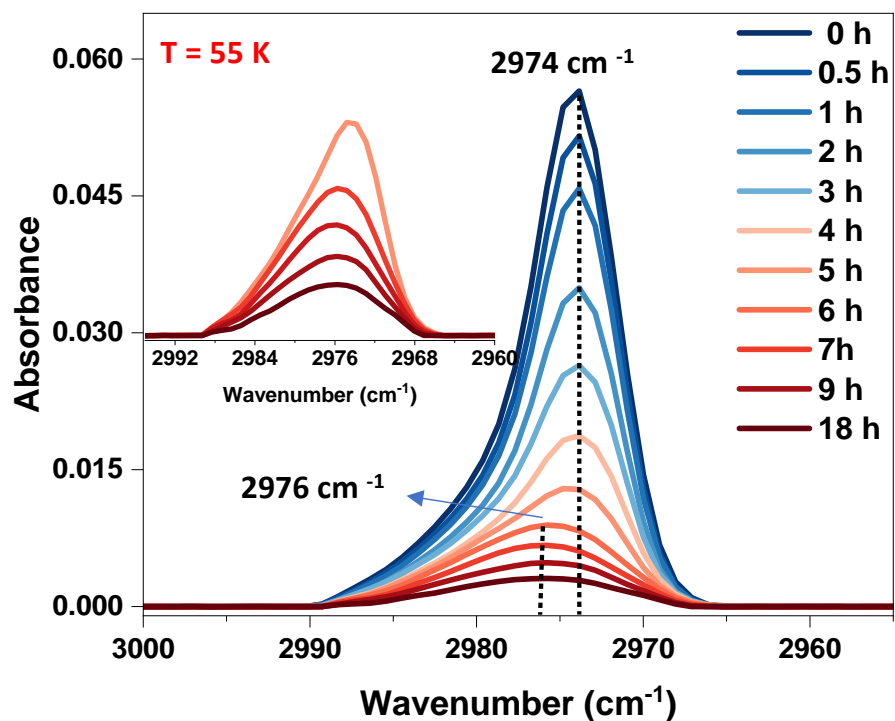


**Figure S6.** Time-dependent RAIR spectra of 300 ML of ethane:H<sub>2</sub>O (1:1) ice mixture at 55 K in the C-H antisymmetric region. The zoomed spectra from 5 h to 18 h are also shown in the left corner of the figure. The ethane-water mixture co-deposited on Ru(0001) at 10 K and annealed to 55 K at a ramping rate of 2 K min<sup>-1</sup>.

Supporting Figure 7:

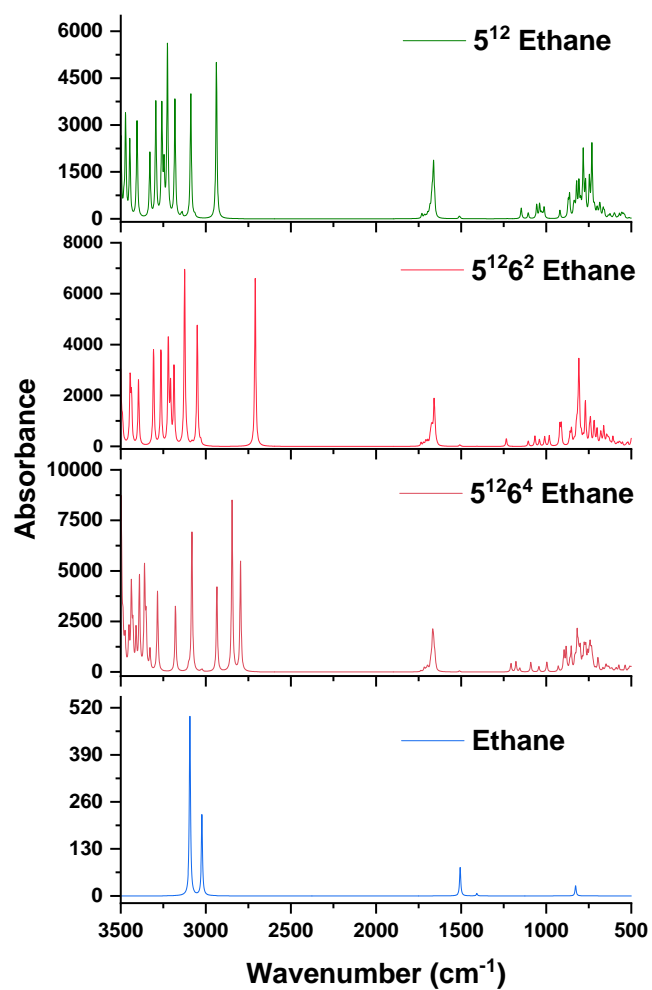



**Figure S7.** Full-scale computed IR spectra of ethane and ethane entrapped in  $5^{12}6^4$ ,  $5^{12}6^2$ , and  $5^{12}$  cages. All the data for IR spectra were calculated from the DFT study.



Cite this: *Chem. Sci.*, 2022, 13, 13321

All publication charges for this article have been paid for by the Royal Society of Chemistry

## Spatial reorganization of analytes in charged aqueous microdroplets†

Pallab Basuri,<sup>a</sup> Amrita Chakraborty,<sup>a</sup> Tripti Ahuja,<sup>a</sup> Biswajit Mondal,<sup>a</sup> Jenifer Shantha Kumar<sup>a</sup> and Thalappil Pradeep \*<sup>ab</sup>

Imprinted charged aqueous droplets of micrometer dimensions containing spherical gold and silver nanoparticles, gold nanorods, proteins and simple molecules were visualized using dark-field and transmission electron microscopies. With such studies, we hoped to understand the unusual chemistry exhibited by microdroplets. These droplets with sizes in the range of 1–100  $\mu\text{m}$  were formed using a home-built electrospray source with nitrogen as the nebulization gas. Several remarkable features such as mass/size-selective segregation and spatial localization of solutes in nanometer-thin regions of microdroplets were visualized, along with the formation of micro–nano vacuoles. Electrospray parameters such as distance between the spray tip and surface, voltage and nebulization gas pressure influenced particle distribution within the droplets. We relate these features to unusual phenomena such as the enhancement of rates of chemical reactions in microdroplets.

Received 16th August 2022  
Accepted 11th October 2022

DOI: 10.1039/d2sc04589c

rsc.li/chemical-science

## Introduction

Microdroplets formed by methods such as levitation of liquids, nebulization of bulk liquids, electrospray, microfluidics, and pressurized liquid jets, exhibit unusual behavior in comparison to their bulk counterparts.<sup>1–7</sup> For example, numerous organic reactions *e.g.*, Michael addition,<sup>8</sup> Schiff-base formation,<sup>8,9</sup> Claisen–Schmidt reaction,<sup>10</sup> Suzuki coupling,<sup>11</sup> benzimidazole synthesis,<sup>12</sup> Hantzsch reaction,<sup>13</sup> Biginelli reaction,<sup>14</sup> *etc.*, were found to occur with an acceleration factor of the order of  $10^1$ – $10^8$ .<sup>15</sup> These reactions were studied in droplets produced using electrospray sonic ionization (ESSI),<sup>16</sup> nanoelectrospray ionization (nESI),<sup>17</sup> desorption electrospray ionization (DESI),<sup>8</sup> or Leidenfrost effect<sup>1</sup> *via* on-line or off-line mass spectrometric methods. A few interfacial properties of these droplets worth noting are strong enrichment of reagent molecules,<sup>18,19</sup> existence of a stable pH gradient,<sup>20</sup> partial desolvation of the molecules,<sup>15,21</sup> presence of high electric field,<sup>22</sup> and restricted molecular rotations.<sup>23</sup>

Water at a heterogeneous interface shows distinct properties in terms of its molecular organization and hydrogen bond strength compared to bulk water.<sup>24–26</sup> Such molecular properties were mainly understood using spectroscopy at the interface.

However, it is likely that performing microscopy and spectroscopy at the surface of electrosprayed microdroplets during their time of flight is tricky. As a result, most of the studies were performed using static droplets created by methods such as liquids confined in a small volume, levitated droplets, droplets in a liquid trap such as oil-in-water systems, hanging droplets, *etc.* Goy *et al.* demonstrated that rapidly evaporating aqueous microdroplets reach a supercooled condition of  $-42$  °C.<sup>27</sup> Quite a few other properties of aqueous microdroplets were also realized by performing reactions using preparative electrospray ionization mass spectrometry utilizing water as a solvent. For example, aqueous microdroplets accelerate several enzymatic reactions,<sup>28–30</sup> induce spontaneous reduction of molecules,<sup>31</sup> lead to micromolar quantity of hydrogen peroxide,<sup>32–34</sup> favor energetically unfavorable reactions,<sup>35,36</sup> *etc.* Besides acceleration, they were also utilized in synthesizing nanomaterials under ambient conditions. Several nanomaterials such as gold nanoparticles,<sup>37</sup> metallic silver nanobrushes,<sup>38</sup> metallic palladium nanosheets,<sup>39</sup> nonstoichiometric copper sulfides,<sup>40</sup> *etc.*, were synthesized using ambient electrospray droplet deposition. Polydisperse metallic nanoparticles are shown to anneal to monodisperse ones in microdroplets.<sup>41</sup> Most of the microdroplet chemistry known today is concerning transformations of small molecules and the products were studied using in-droplet molecular spectroscopy. However, how do molecules and particles distribute within a microdroplet, is still not understood clearly.

In the past few years, microdroplets were considered as a model for membraneless protocell to understand elementary processes such as chemical transformations, replication, cell splitting, compartmentalization, *etc.*<sup>42–45</sup> However, this was

<sup>a</sup>DST Unit of Nanoscience, Department of Chemistry, Indian Institute of Technology, Madras, Chennai 600036, India. E-mail: pradeep@iitm.ac.in

<sup>b</sup>International Centre for Clean Water, Chennai, Tamil Nadu 600113, India

† Electronic supplementary information (ESI) available: DFM images of microdroplets containing silver and gold nanoparticles, TEM images of microdroplets, DFM images of dropcasted sample, characterization of AuNPs and GNRs, fluorescent images of microdroplets containing protein and dye. See DOI: <https://doi.org/10.1039/d2sc04589c>



originally proposed by Oparin over 100 years ago through which he suggested a compartmentalization model based on liquid–liquid phase separation, enrichment, and localization of electrolytes in aqueous droplets, called coacervates.<sup>46</sup> Interestingly, Moreau *et al.* observed that droplets formed by electrostatic complexation of poly(diallyl dimethylammonium chloride) and adenosine triphosphate (ATP) at pH 8 undergo vacuolization upon addition of a neutral molecule, tetramethylene glycol.<sup>47</sup> Liang *et al.* showed that poly-L-lysine (PLL) and single-stranded oligonucleotide filled microdroplets undergo circulation and vacuolization simultaneously in the presence of low electric field, such as  $10^3$  V m<sup>-1</sup>.<sup>48</sup> Recently, Perez-Mercader *et al.* performed radical polymerization reactions in microdroplets and observed high structural complexity in them. Authors compared such microdroplets crowded with macromolecules with living systems to understand how molecular complexity leads to microscopic outputs.<sup>49</sup> Nevertheless, such dynamic behavior within droplets was not observed in electrosprayed microdroplets.

Herein, we present a method of visualizing the evolution of interfacial particle enrichment within charged aqueous microdroplets in detail through optical and electron microscopy. A home-built electrospray ion source was used to create these microdroplets containing silver and gold nanoparticles (Au and AgNPs), gold nanorods (GNRs), a fluorescent-molecule tagged protein, and a fluorescent dye, both separately as well as in the form of binary mixtures. Imprints of these droplets on different surfaces were imaged using dark-field and transmission electron microscopies (TEM). The distribution of particles within the droplets were investigated at various electrospray parameters. Exceptional features such as spatial localization, following concentration gradient by mass and size-selective sorting of particles has been observed. We also observed formation of vacuoles in electrospray microdroplets displaying unprecedented analyte distribution.

## Results and discussion

### Understanding aqueous microdroplets containing silver and gold nanoparticles

Colloidal aqueous Ag and Au NPs prepared by the Turkevich method (synthetic protocol is presented in Experimental section) were electrosprayed using a home-built electrospray source. During spray, a 0.145 mm thick pre-cleaned glass slide (Schott) was quickly (~1 s) exposed to the spray plume to take imprints of the generated microdroplets on the glass surface. These imprinted droplets were transferred to the sample stage of a dark-field microscope for imaging.<sup>50</sup> Fig. 1A schematically presents the droplet imprinting setup and Fig. 1B shows a schematic of the confocal microscopy set-up for dark field imaging. In dark-field microscopy (DFM), the sample surface was scanned to obtain a series of images. Microdroplets with varying shapes and sizes were seen.

Droplet impact-induced pattern formation on solid surfaces is known.<sup>51,52</sup> And this is likely in electrospray deposition as well. However, upon careful inspection of ~200 droplets per cm<sup>2</sup> per s, we understood that AgNPs arrange commonly in two

ways. In the first, they were distributed evenly in the droplet, while in the second, there was more localization at the periphery. Fig. 1C shows a DFM image of a selected area of the glass slide where these two types of droplets are seen. Droplets marked with green squares, called NP1, had an even distribution of particles throughout. Whereas droplets marked with red squares, called NP2, show strong enrichment of AgNPs towards the periphery. In latter droplets, the core of the droplet either has no or reduced particle density. A few other images are also shown in Fig. S1† wherein several such droplets of both types were observed. We found an approximate distribution of NP1 and NP2 droplets in the ratio of 3 : 7. The observation of NP1 contradicts one of the common hypotheses and a recent observation that reagents are predominantly enriched at the air–liquid interface in electrosprayed microdroplets.<sup>18,19</sup> Rather, we ascertained that concentration gradient of reagents is highly influenced by the flight time of the droplet. This apparent difference made us explore imprint imaging further. A similar phenomenon was observed with droplets of AuNPs as well, shown in Fig. S2.†

Electrospray is known to affect particles in the droplet.<sup>41</sup> To understand any possible change in the particle shape and size, we performed TEM measurements. A detailed description of the sample preparation for TEM is in the Experimental section. Note that imprinting an individual droplet with perfect shape and size on a TEM grid is difficult and requires several attempts. Configuration of the TEM sample preparation set-up is schematically presented in Fig. S3A.† Fig. S3B† shows a TEM image of an individual droplet of approximately 10–15 μm in diameter. Strikingly, even after several attempts, we could not observe droplets of NP1 type in TEM (details are presented below). Rather we found that in all the droplets in TEM grids, AuNPs re-organized themselves towards the periphery which leads to a distribution similar to NP2. We also noticed that, while particles at the periphery are separated, some of them appear to be aggregated near the core. Collectively, the droplet appears as NP1. The size of these AuNP aggregates reduces from the center to the periphery of the droplet. Upon further magnification of this image, we observed no changes in the particle shape and size compared to the particles before (Fig. S3C†) and after (Fig. S3D†) spray. These particles are plasmonic with diameters over 20 nm and are stable in electrospray than the monolayer protected nanoparticles.<sup>41</sup> We note that the imprinted droplets on the TEM grid are 10 times smaller than the droplets in DFM experiments. This encouraged us to re-think that the phenomenon of particle enrichment may occur particularly in droplets below 10 μm.

The above results demonstrate that charged aqueous microdroplets generated from a single electrospray source acquire different size,<sup>53</sup> shape, and particle distribution. Such a different distribution can be a result of the anisotropic distribution of electric fields and forces acting on the nanoparticles within a droplet. A particle in a charged droplet experiences a centripetal force due to the rotations of the droplet, the electrostatic force resulting from the charge, and buoyancy of the liquid, and these influence the localization of the particle. We also note that upon droplet impact on the glass



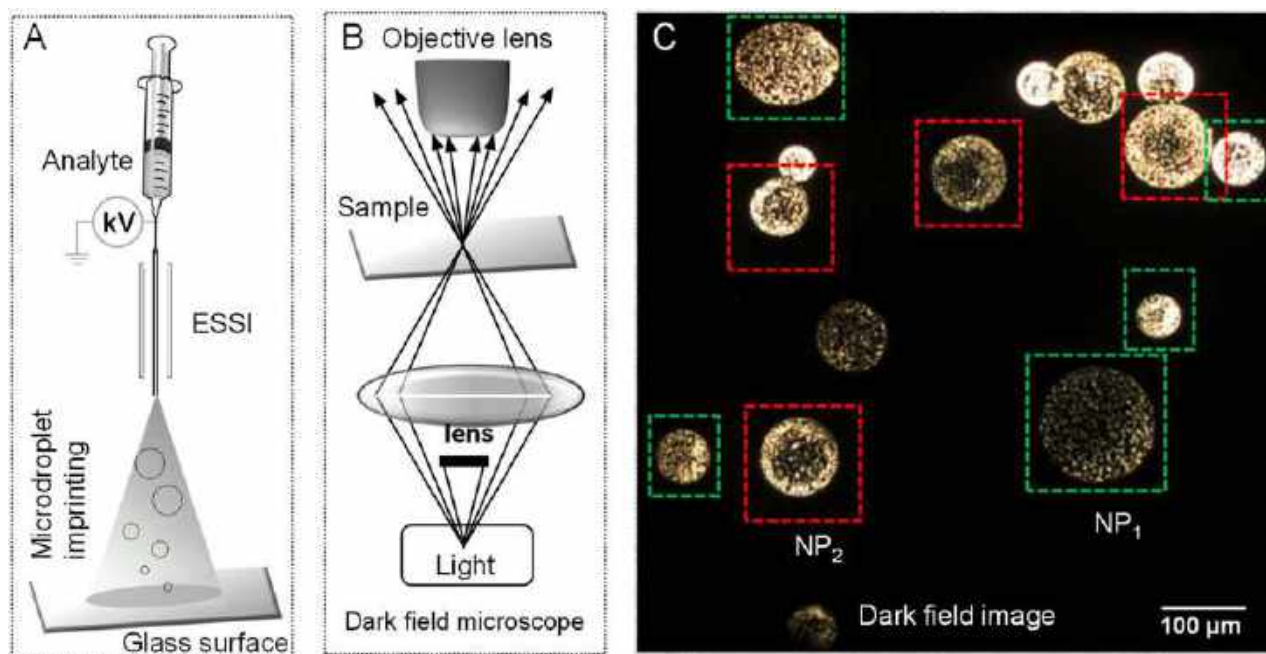


Fig. 1 Deposition and microscopy of microdroplets. (A) Schematic representation of our home-built droplet deposition setup, (B) experimental setup for dark-field microscopy of the deposited microdroplets, and (C) a representative dark-field image showing several microdroplets. Droplets are categorized into two types based on the particle size distribution; green box (NP1) and red box (NP2). Microdroplets were imprinted over a period of  $\sim 1$  s.

surface, drying may lead to an anisotropic distribution of the solute, termed as the coffee ring effect, which could have a role in the observed particle distribution.<sup>54</sup> The assembly of particles in an evaporating droplet was also understood theoretically.<sup>55</sup> A control experiment, to be discussed later, shows that droplet imprints on a glass surface, formed by simple drop casting resulted in coffee rings, but droplets imprinted by electrospray deposition, show different particle distributions. However, quantitative estimation of the forces to predict the observed particle distributions in charged microdroplets is difficult. It is noted that droplets of both types of distribution (NP1 and NP2)

were seen irrespective of the size and shape of the droplet in electrospray. Besides the distribution of the nanoparticles in the droplets, DFM helps in understanding a few events of droplets occurring in their time of flight. We found a few droplets with elongated and deformed shapes. In Fig. 2A–C, we show DFM images of droplets containing AgNPs which were elongated. Such elongation of droplets in a high electric field is expected.<sup>56</sup> Droplet elongation and splitting are the result of a heterogeneous electric field acting across the droplet. This is one of the reasons that a droplet gets split and become small in size in flight. Apart from an elongation, a few deformed droplets

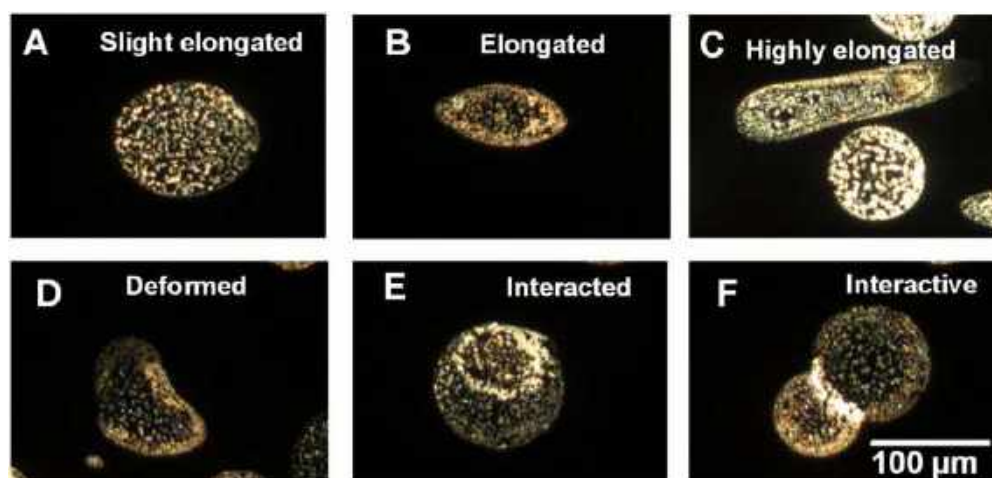


Fig. 2 Dark field images of microdroplets with different sizes and shapes demonstrating elongation (A–C), deformation (D), and interaction (E and F) of microdroplets. A few such droplets can also be found in Fig. 1 and S1† as well.





were also observed and one of them is presented in Fig. 2D. In Fig. 2E and F droplets appear to be interacting, although this may be a result of sequential deposition. Moreover, these results are consistent with the previous reports that concentration enhancement at the air–liquid interface of electro spray is indeed a part of droplet dynamics along with the change in size and shape during flight.<sup>18</sup>

### DFM studies of droplets with mixed particles

Based on the above understanding and to gain better insights, we performed a similar experiment with GNRs to understand the effect of mass and dimensions of nanoparticles in particle distributions. GNRs were prepared in water following a seedless synthesis procedure reported by Samal *et al.*<sup>57</sup> The particles were characterized before the experiments using UV-vis spectroscopy and TEM. Fig. S4† shows a spectrum with characteristic peaks at 525 and 836 nm in the UV-vis spectrum, along with a TEM image of GNRs. We noticed that a few spherical gold nanoparticles were remaining in the GNR suspension. We sprayed the dispersion to take imprints of droplets on a glass surface to perform DFM analysis. A representative DFM image of a few droplets is shown in Fig. 3A where we observed droplets with different sizes and particle distributions. A few other images are presented in Fig. S5.† Upon carefully reviewing all the droplets, we categorized them into four different types, called Mix1, Mix2, Mix3, and Mix4. These 4 types are also marked with different color codes in Fig. 3A. Fig. 3B–E display representative droplets of each one of

these types where the difference in particle distributions can be clearly visualized. In Mix1, marked with a green square, particles were distributed randomly without any localization or separation. In the second kind, namely Mix2, marked with a cyan square, we observed that particles tend to move towards the periphery of the droplet. These particles were further separated and localized in the third kind of droplet; Mix3, marked with a white square. Particles were finally concentrated at the periphery forming a sharp boundary which is presented as Mix4 and it is marked with a red square in Fig. 3A. By observing  $\sim 112$  droplets per  $\text{cm}^2$  per s we estimated that the percentage ratio between Mix1 : 2 : 3 : 4 follows 31 : 15 : 27 : 27. Such relocalization of particles is schematically presented in Fig. 3F. This set of data were compared with the typical coffee ring effect seen with macroscopic drops. For this, we drop cast 10  $\mu\text{L}$  of as-synthesized GNR suspension on a glass surface and performed DFM after air drying. A concentration enhancement of the particles at the boundary of the drop cast sample, forming a coffee ring was observed all the time (Fig. S6†). We also observed that some particles were distributed arbitrarily and nowhere close to the distributions of Mix1–Mix4 seen in Fig. 3.

### TEM investigations of microdroplets containing mixed nanoparticles

Droplets formed by electro spray of GNR were also imprinted carefully on a copper grid, to be characterized using TEM. As

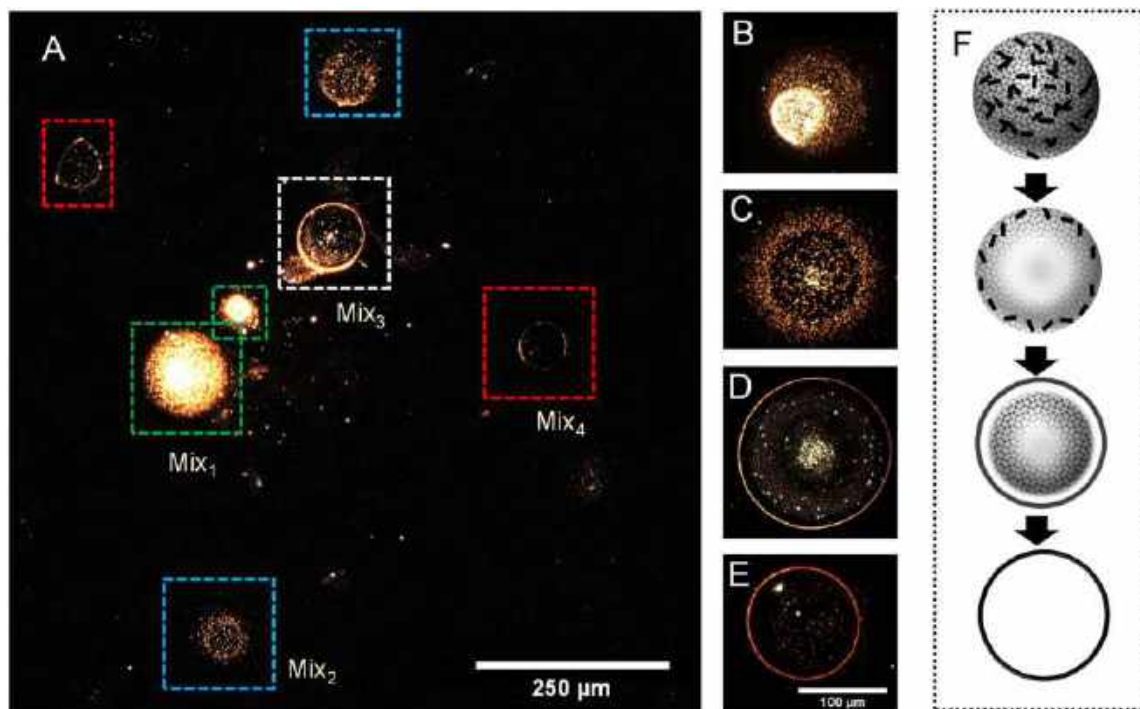


**Fig. 3** Dark-field microscopy of microdroplets of aqueous solution of GNRs. These GNRs also contained a small fraction of spherical AuNPs. (A) A representative DFM image showing microdroplets of 4 different particle distributions as shown in the zoomed-in view in (B–E). Different types of droplets such as Mix1–Mix4 were marked with green, cyan, white, and red squares. (F) Mechanism of particle re-localization. The mechanism proposes particle movement (from Mix1) towards the periphery of the droplet (Mix4) via the formation of Mix2 and Mix3 kind of distribution, as intermediate states.



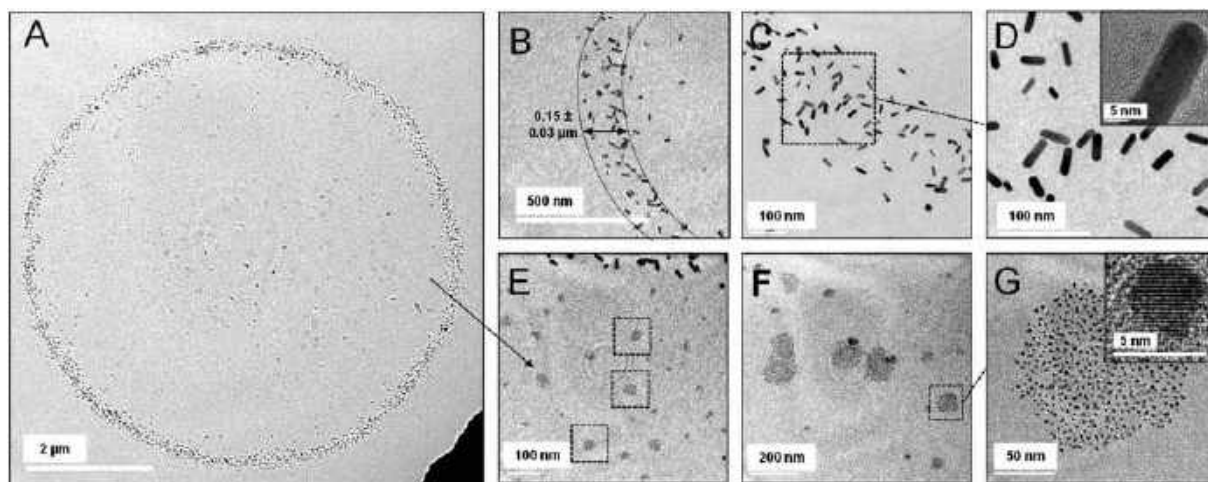


Fig. 4 TEM understanding of microdroplets formed by colloidal aqueous dispersion of as-synthesized GNR. These synthesized GNR solution contain tiny fraction of AuNPs as byproducts. (A) TEM image of an individual droplet (Mix3) showing nanoparticles forming a sharp rim at the periphery. (B–D) Zoomed-in image of outer rim, showing GNRs moved to the air–water interface of the droplet. The approximate width of the rim was measured to be  $0.15 \pm 0.03 \mu\text{m}$ . Inset of (D) showing a single GNR at higher magnification. (E–G) The zoomed-in image showing clusters of AuNPs present at the interior of the droplet. A few of such AuNP-clusters are indicated with black squares. (G) One of such clusters of AuNPs at different magnifications. Inset of (G) showing a single AuNP at higher magnification.

expected, we could not observe Mix1 and Mix2 type of particles in the smaller droplets (below  $\sim 10 \mu\text{m}$ ) imprinted on the TEM grid. However, in TEM, we found that the droplets of Mix3 show unexpected particle separation (Fig. 4). Fig. 4A displays a TEM image of a representative droplet of Mix3. Herein, we found that the droplet consists of a rim made of accumulated GNRs (Fig. 4B–D) and a few large AuNPs. Thickness of the rim is of the order of  $\sim 150 \text{ nm}$ , as shown in Fig. 4B.

Afterward, we have taken images at higher magnifications, at the interior of the droplet. These images are presented in Fig. 4E–G wherein we can observe that the interior of the droplet is fully decorated with smaller AuNPs having no or negligible trace of GNRs. Interestingly, we found that larger aggregates of AuNP are present at the center of the droplet while smaller aggregates are found more at the periphery. Such arrangements of the AuNPs were forming concentric ring-type structures in DFM as observed in Fig. 3D. The size of these AuNPs is in the range of 5–10 nm. These AuNPs were the inseparable particles during cleaning and they were formed as a by-product in the synthesis of GNRs. Therefore, the TEM studies suggest that droplets containing mixed particles undergo chromatographic separation within the droplet and localize at the air–water interface. It should be noted that the coffee ring effect is also known to separate particles based on their size. Generally, in the coffee ring effect, smaller particles concentrate at the rim, and larger particles concentrate at the core.<sup>54</sup> Several attempts have been made previously to suppress the coffee ring effect either by modifying the solution or the surface.<sup>58–60</sup> However, in clear contrast to these previous studies, imprinted droplets in our work show four different distributions as shown above. In an electrosprayed droplet, enhanced concentrations of large nanorods were found to be at the rim whereas smaller AuNPs were distributed towards the core.

To support this further, CTAB-protected GNR and CTAC-protected AuNPs were mixed in a 1:1 (v/v) ratio and were sprayed. Synthesis and characterization of the as-synthesized CTAC-protected AuNPs are presented in the Experimental section and Fig. S7,† respectively. The resultant droplets were imprinted on a glass slide for DFM. As expected, we observed similar results. Herein, both the GNR and CTAC-protected AuNPs moved towards the periphery to form the outer rim and small aggregates of AuNPs rearranged at the interior. A few representative DFM and TEM images containing various types of droplets are displayed in Fig. S8A–D.† Based on the above understanding, we proposed that in-droplet particle rearrangement during time-of-flight of the droplet results in such patterned imprints on the surface. These particles finally get localized at the air–water interface making a micron-level thick rim.

Such a concentration enhancement at a thin air–liquid interface of the droplet could significantly increase both the number of collisions between reagents and the probability of reaction. Due to the increased surface area in microdroplets than in the bulk, the rate of these reactions can be accelerated. This is one of the reasons for enhanced chemical reactivity as demonstrated previously by unusual accelerated reactions.<sup>18</sup>

In Fig. 3F, we schematically present the mechanism of such particle localization. We assessed that particles which were initially distributed randomly get enriched at the air–water interface of the droplet over time, during flight. Therefore, the distribution of Mix2 and Mix3 are expected to be two intermediate stages of such relocalisation of particles, resulting in concentration gradient. Such a timescale is likely to depend upon the centrifugal force acting on the particle, surface tension, viscosity, and buoyancy of the liquid droplet. Effect of these physical properties in particle reorganization was



observed previously in several situations such as liquid flow,<sup>61,62</sup> liquid/liquid interfaces,<sup>63</sup> cloud droplet,<sup>64</sup> *etc.*

### Effect of electrospray parameters

To understand the effect of electrospray parameters on the properties of the droplet, aspects such as potential applied on the source, nebulization gas pressure, and tip to collector distance were varied. It is certain that the droplet size will reduce with increasing gas pressure,<sup>65</sup> potential,<sup>66</sup> distance,<sup>67</sup> surface tension and vapor pressure of the solvent, amount of excess charge, *etc.*<sup>68</sup> In Fig. S9,† we have chosen a few representative droplets from a set where we observed such an effect. Change in the distance affects the distribution of the nanoparticles within the droplet. Upon increasing the distance, the droplet size decreases and particles get time to relocate. Spatial relocalization of particles within the droplet resulted in an increase in the percentage of Mix3, as shown in Fig. S10A.† While the number density of Mix4 increases up to 2.5 cm, it falls rapidly on further increase in the distance. This could be explained by droplet desolvation resulting in no droplet imprinting at higher distances. We have seen a similar effect with decreasing gas pressure. This is because, with decreasing gas pressure, the droplet velocity also decreases with a slow rate of desolvation, which in turn allows the particle to rearrange and get localized at the air–water interface of the droplet (Fig. S10B†). The fraction of Mix1 increasing and Mix4 decreasing with nebulization pressure suggests that charge and distance are the dominant factors in particle redistribution. Fig. S10C† suggests that the applied potential follows a similar trend as the distance in particle distribution within the droplet.

### Observation of vacuoles and implication to droplet reactions

While studying particle arrangements in a droplet, surprisingly, we found micron-scale bubbles inside several such droplets. Upon further magnification of DFM images, we clearly observed that bubbles of various sizes exist mostly at the core of the droplets. Fig. 5A shows a representative droplet in which several such micrometer-scale vacuoles were observed. These microvacuoles are marked with red squares. We noticed that such vacuolization has only occurred in the case of Mix3 and Mix4 and is absent in droplets of Mix1 and Mix2. This hints at the fact that the formation of such vacuoles needs some incubation time and driving force. It should also be noted that such vacuoles were not observed in the drop cast bulk dispersion (Fig. S6B†). While droplets are moving, during their time-of-flight, tiny bubbles were formed, which coalesce with each other to become big vacuoles. As a result, we observed that droplets of Mix3 contain smaller bubbles whereas, Mix4 droplets contain bigger bubbles (Fig. S11†). It should be noted that these droplets were imprinted on the same slide, in an independent experiment. It is likely that the bubbles formed in droplets are due to liquid–gas separation of the dissolved gases present in the droplet. We also noticed that particles were accumulated at the air–liquid interface of the vacuoles (Fig. 5) forming a bright rim in the DFM images. Unusual reaction rates in microdroplets have always been looked at from the

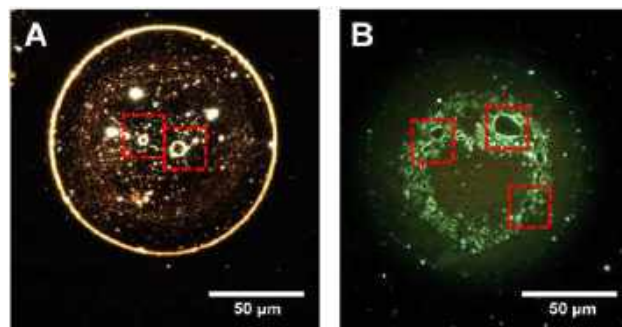


Fig. 5 Vacuolization in microdroplets. (A) DFM images of microdroplets containing as-synthesized GNR in water of Mix3. The red square showed an area with the formation of vacuoles inside of droplets. (B) DFM fluorescence image of R6G containing aqueous microdroplets with different shapes and sizes of vacuoles observed.

perspective of enhanced concentration of the reactants at the outermost interface of the droplet; however, air–liquid interfaces of these bubbles, at the interior of the droplets have not been considered before. These additional interfaces will certainly have an important role in accelerating the chemistry in microdroplets.

### Particle compartmentalization and understanding of protocell formation

The nanodroplet relocalization and formation of microvacuoles motivated us to understand in-droplet particle dynamics from the perspective of the protocell model. Origin of life has been looked at from many perspectives to understand the spontaneous assembly of microscale compartments. Proteins are well known as the building blocks of cell membranes and many proteinosomes have been investigated to understand the genesis of cell membrane-bound compartments in the cells.<sup>69</sup> In the previous literature, the self-organization of small peptides in vesicles has been proposed as the precursor step to the formation of a protocell.<sup>70,71</sup> To investigate the effect of proteins in microdroplets, we have used fluorescein isothiocyanate labeled bovine serum albumin (FITC-BSA) to visualize the droplets imprinted on glass slides through DFM. Fig. S12† shows fluorescence images of several spherical and elongated droplets containing FITC-BSA. To our surprise, vacuoles were observed within the droplets, comparable to membrane-less microcompartments in biological cells.<sup>72</sup> One or more vacuoles were observed inside a single droplet. To neglect the effect of surfactants used for the synthesis of nanorods or large protein molecules on vacuolization, we sprayed aqueous rhodamine 6G (R6G) solution. We observed the formation of vacuoles in such droplets as well (Fig. 5B). We observed suppression of vacuolization in a degassed liquid (Fig. S13†) which further supports our hypothesis of liquid–gas phase separation within microdroplets leading to vacuole formation. Several studies are being carried out to develop a model construct of membrane-less organelles in protocells to understand the mechanism of their functions inside the cell.<sup>73</sup> We suggest that the formation of vacuoles in microdroplets





carrying proteins and nanoparticles is comparable to such organelles. Droplets of this kind may be used to conduct further research on these processes.

## Experimental

### Synthesis of citrate-protected AuNPs and AgNPs in water

The colloidal aqueous suspension of citrate-capped AuNPs was synthesized using the Turkevich method, by the reduction of tetrachloroauric acid trihydrate ( $\text{HAuCl}_4 \cdot 3\text{H}_2\text{O}$ ) using trisodium citrate.<sup>74</sup> An aqueous solution of 5 mM  $\text{HAuCl}_4 \cdot 3\text{H}_2\text{O}$  of 10 mL was taken in a conical flask. It was then diluted with 180 mL of distilled water followed by heating until the solution started boiling. About 10 mL of 0.5% trisodium citrate was added to it and heated until the entire solution becomes wine red. In a similar way, AgNPs were made, taking  $\text{AgNO}_3$  as a precursor. The dispersions were then cooled and used directly for droplet imprinting.

### Synthesis of CTAB (cetyltrimethylammonium bromide)-protected GNRs in water

Gold nanorods were synthesized using a previously reported method with a few modifications.<sup>57</sup> Sequential addition of 2.5 mL of 10 mM  $\text{HAuCl}_4 \cdot 3\text{H}_2\text{O}$ , 325  $\mu\text{L}$  of 10 mM  $\text{AgNO}_3$ , and 350  $\mu\text{L}$  of 100 mM ascorbic acid to a 50 mL solution of 100 mM CTAB was performed with mild stirring at 28 °C in a synthesizer. After 5 min of incubation, a 500  $\mu\text{L}$  ice-cold aqueous solution of freshly prepared  $\text{NaBH}_4$  was added in one shot. The reaction mixture was kept overnight before washing the GNRs with water to get rid of the excess CTAB. The GNR dispersion was then centrifuged at 7000 rpm for 20 min to get rid of the larger particles and then centrifuged again in a stepwise fashion at 12 000 and 14 000 rpm in a similar way. The final precipitate was dispersed in deionized water and again centrifuged twice (each time for 15 min) at 12 500 rpm. The dispersion was vortexed to stop aggregation before use.

### Synthesis of spherical AuNPs

A seed mediated synthetic protocol, initially reported by Xia's group, was followed to synthesize gold nanospheres.<sup>75</sup>

For the synthesis of initial CTAB-capped seeds, 9.75 mL 100 mM CTAB solution was thoroughly mixed with 250  $\mu\text{L}$  of 10 mM  $\text{HAuCl}_4$  solution in a 20 mL glass bottle. 10 mM  $\text{NaBH}_4$  solution was prepared in ice cold water and 600  $\mu\text{L}$  of it was quickly added to the reaction mixture. After initial stirring for 2 min, the solution was kept undisturbed for 3 h at 28 °C.

For the synthesis of CTAC (cetyltrimethylammonium chloride)-capped AuNPs, 2 mL of 200 mM CTAC solution was taken in a glass bottle. Subsequently, 1.5 mL of 100 mM ascorbic acid and 50  $\mu\text{L}$  of the just prepared CTAB-capped seed solution were added to the vial under continuous stirring at 300 rpm. Finally, 2 mL of 0.5 mM  $\text{HAuCl}_4$  solution was injected with one shot, and the stirring was continued for 15 min at 28 °C. The solution was then centrifuged at 14 000 rpm for 30 min, and the pellet was dispersed in DI water. The centrifugation was performed one more time and the particles were finally

dispersed in 20 mM CTAC solution. To eliminate the effect of surface charge and surface ligand group on the droplet formation, we synthesized spherical AuNPs protected by CTAC, as it closely resembles CTAB that was used to prepare GNRs.

### Imprinting droplets on glass slides and TEM grids

Droplets were generated using a home-built electrospray ion source. Droplets were passed through an SS-tube of 0.63 cm internal diameter and 2.5 cm of length. To do the imprinting, we exposed the imprinting surface in front of the SS-tube. This process was done as quickly as possible to avoid excessive droplet deposition on the surface. In this way, only a specific area of the surface would be exposed to the spray which will help in performing DFM. The tip to surface distance was varied. For the TEM study, a copper grid, supported on an extra clean glass slide was held in front of the SS-tube with a tweezer. The glass support was used to prevent the copper grid from bending under high gas pressure.

### Dark-field optical microscopy of imprinted droplets

The dark-field imaging was done using a CytoViva™ microscope. The microscope was equipped with a high-resolution dark-field oil immersion condenser lens and a 100 $\times$  oil immersion objective (UPLFLN, Olympus). An L1090-halogen lamp from International Light Technologies Inc. was used as a white light source for imaging the nanoparticles. Fluorescence imaging of microdroplets was also done on the CytoViva™ microscope with a triple bandpass filter for the green emission. A Dage Excel M cooled CCD camera was used for capturing the images. Clean glass slides (SCHOTT Nexterion®) were used for all the imaging experiments.

## Conclusions

In this work, we presented in-droplet reorganization of nanoparticles and molecules contained within microdroplets, during flight. This was studied by imaging imprints of microdroplets by dark field optical microscopy and transmission electron microscopy. We propose a sequential change in the nanoparticle distribution by re-localization of particles as microdroplets move from the source to the target. In the process, nanoparticles with different sizes, morphology, and mass undergo spatial separation forming a density gradient of particle distribution. We observed an enhanced particle density at the periphery of droplets forming a sharp and  $\sim 150$  nm-thick boundary in the imprint. Such particle distribution alters the chemistry in the droplet. Additionally, we found the formation of nano-microvacuoles in microdroplets. Such vacuolization was also realized using protein-filled droplets and water droplets containing a dye molecule, enriched at the gas/liquid interface. These further suggest microdroplets to be a model system for the membraneless microcompartmentalization in protocells. Science demonstrated here has implications for the unusual reactivity of microdroplets in causing chemical and biological transformations.



## Author contributions

P. B. and T. P. designed and performed the experiments. T. A., A. C., B. M., and J. S. K. helped in performing microscopy of imprinted droplets. P. B. wrote the initial draft of the paper and it was finalised with input from all the authors. The project was conceived under the supervision of T. P.

## Conflicts of interest

There are no conflicts to declare.

## Acknowledgements

P. B., B. M., T. A. and J. S. K. thank IIT Madras for their research fellowships. A. C. thanks CSIR for her fellowship.

## References

- R. M. Bain, C. J. Pulliam, F. They and R. G. Cooks, *Angew. Chem., Int. Ed.*, 2016, **55**, 10478–10482.
- K. Aoki and K. Hasegawa, *AIP Adv.*, 2020, **10**, 55115.
- C. Liu, J. Li, H. Chen and R. N. Zare, *Chem. Sci.*, 2019, **10**, 9367–9373.
- M. Yamashita and J. B. Fenn, *J. Phys. Chem.*, 1984, **88**, 4451–4459.
- A. B. Theberge, F. Courtois, Y. Schaerli, M. Fischlechner, C. Abell, F. Hollfelder and W. T. S. Huck, *Angew. Chem., Int. Ed.*, 2010, **49**, 5846–5868.
- L. Kong, T. Lan, J. Chen, K. Wang and H. Sun, *Processes*, 2020, **8**, 676.
- P. Ben-Tzvi and W. Rone, *Microsyst. Technol.*, 2010, **16**, 333–356.
- M. Girod, E. Moyano, D. I. Campbell and R. G. Cooks, *Chem. Sci.*, 2011, **2**, 501–510.
- R. M. Bain, C. J. Pulliam, S. T. Ayrton, K. Bain and R. G. Cooks, *Rapid Commun. Mass Spectrom.*, 2016, **30**, 1875–1878.
- T. Müller, A. Badu-Tawiah and R. G. Cooks, *Angew. Chem., Int. Ed.*, 2012, **51**, 11832–11835.
- P. W. Fedick, K. Iyer, Z. Wei, L. Avramova, G. O. Capek and R. G. Cooks, *J. Am. Soc. Mass Spectrom.*, 2019, **30**, 2144–2151.
- P. Basuri, L. E. Gonzalez, N. M. Morato, T. Pradeep and R. G. Cooks, *Chem. Sci.*, 2020, **11**, 12686–12694.
- R. M. Bain, C. J. Pulliam and R. G. Cooks, *Chem. Sci.*, 2015, **6**, 397–401.
- N. Sahota, D. I. AbuSalim, M. L. Wang, C. J. Brown, Z. Zhang, T. J. El-Baba, S. P. Cook and D. E. Clemmer, *Chem. Sci.*, 2019, **10**, 4822–4827.
- Z. Wei, Y. Li, R. G. Cooks and X. Yan, *Annu. Rev. Phys. Chem.*, 2020, **71**, 31–51.
- S. Banerjee and R. N. Zare, *Angew. Chem., Int. Ed.*, 2015, **54**, 14795–14799.
- R. M. Bain, S. T. Ayrton and R. G. Cooks, *J. Am. Soc. Mass Spectrom.*, 2017, **28**, 1359–1364.
- H. Xiong, J. K. Lee, R. N. Zare and W. Min, *J. Phys. Chem. B*, 2020, **124**, 9938–9944.
- S. Lhee, J. K. Lee, J. Kang, S. Kato, S. Kim, R. N. Zare and H. G. Nam, *Sci. Adv.*, 2020, **6**, eaba0181.
- H. Wei, E. P. Vejerano, W. Leng, Q. Huang, M. R. Willner, L. C. Marr and P. J. Vikesland, *Proc. Natl. Acad. Sci. U. S. A.*, 2018, **115**, 7272–7277.
- S. Mondal, S. Acharya, R. Biswas, B. Bagchi and R. N. Zare, *J. Chem. Phys.*, 2018, **148**, 244704.
- H. Xiong, J. K. Lee, R. N. Zare and W. Min, *J. Phys. Chem. Lett.*, 2020, **11**, 7423–7428.
- J. Kang, S. Lhee, J. K. Lee, R. N. Zare and H. G. Nam, *Sci. Rep.*, 2020, **10**, 1–10.
- K. Tomobe, E. Yamamoto, D. Kojić, Y. Sato, M. Yasui and K. Yasuoka, *Sci. Adv.*, 2017, **3**, e1701400.
- J. Grdadolnik, F. Merzel and F. Avbelj, *Proc. Natl. Acad. Sci. U. S. A.*, 2017, **114**, 322–327.
- P. Ball, *Chem. Rev.*, 2008, **108**, 74–108.
- C. Goy, M. A. C. Potenza, S. Dederá, M. Tomut, E. Guillerme, A. Kalinin, K.-O. Voss, A. Schottelius, N. Petridis, A. Prosvetov, G. Tejada, J. M. Fernández, C. Trautmann, F. Caupin, U. Glasmacher and R. E. Grisenti, *Phys. Rev. Lett.*, 2018, **120**, 15501.
- K. J. Vannoy, I. Lee, K. Sode and J. E. Dick, *Proc. Natl. Acad. Sci. U. S. A.*, 2021, **118**, e2025726118.
- X. Zhong, H. Chen and R. N. Zare, *Nat. Commun.*, 2020, **11**, 1049.
- B. J. Burris and A. K. Badu-Tawiah, *Anal. Chem.*, 2021, **93**, 13001–13007.
- J. K. Lee, D. Samanta, H. G. Nam and R. N. Zare, *J. Am. Chem. Soc.*, 2019, **141**, 10585–10589.
- J. K. Lee, K. L. Walker, H. S. Han, J. Kang, F. B. Prinz, R. M. Waymouth, H. G. Nam and R. N. Zare, *Proc. Natl. Acad. Sci. U. S. A.*, 2019, **116**, 19294–19298.
- J. K. Lee, H. S. Han, S. Chaikasetsin, D. P. Marron, R. M. Waymouth, F. B. Prinz and R. N. Zare, *Proc. Natl. Acad. Sci. U. S. A.*, 2020, **117**, 30934–30941.
- C. Zhu and J. S. Francisco, *Proc. Natl. Acad. Sci. U. S. A.*, 2019, **116**, 19222–19224.
- I. Nam, H. G. Nam and R. N. Zare, *Proc. Natl. Acad. Sci. U. S. A.*, 2018, **115**, 36–40.
- I. Nam, J. K. Lee, H. G. Nam and R. N. Zare, *Proc. Natl. Acad. Sci. U. S. A.*, 2017, **114**, 12396–12400.
- J. K. Lee, D. Samanta, H. G. Nam and R. N. Zare, *Nat. Commun.*, 2018, **9**, 1562.
- D. Sarkar, M. K. Mahitha, A. Som, A. Li, M. Wlekinski, R. G. Cooks and T. Pradeep, *Adv. Mater.*, 2016, **28**, 2223–2228.
- D. Sarkar, R. Singh, A. Som, C. K. Manju, M. A. Ganayee, R. Adhikari and T. Pradeep, *J. Phys. Chem. C*, 2018, **122**, 17777–17783.
- A. Jana, S. K. Jana, D. Sarkar, T. Ahuja, P. Basuri, B. Mondal, S. Bose, J. Ghosh and T. Pradeep, *J. Mater. Chem. A*, 2019, **7**, 6387–6394.
- A. R. Chowdhuri, B. K. Spoorthi, B. Mondal, P. Bose, S. Bose and T. Pradeep, *Chem. Sci.*, 2021, **12**, 6370–6377.
- J. Li, X. Liu, L. K. E. A. Abdelmohsen, D. S. Williams and X. Huang, *Small*, 2019, **15**, 1902893.
- M. Li, X. Huang and S. Mann, *Small*, 2014, **10**, 3291–3298.



- 44 T.-Y. D. Tang, M. Antognozzi, J. A. Vicary, A. W. Perriman and S. Mann, *Soft Matter*, 2013, **9**, 7647–7656.
- 45 H. Sakuta, F. Fujita, T. Hamada, M. Hayashi, K. Takiguchi, K. Tsumoto and K. Yoshikawa, *ChemBioChem*, 2020, **21**, 3323–3328.
- 46 A. I. Oparin and A. Syngé, *The origin of life on the earth*, Academic Press, New York, 3rd edn, 1957.
- 47 N. G. Moreau, N. Martin, P. Gobbo, T.-Y. D. Tang and S. Mann, *Chem. Commun.*, 2020, **56**, 12717–12720.
- 48 Y. Yin, H. Chang, H. Jing, Z. Zhang, D. Yan, S. Mann and D. Liang, *Soft Matter*, 2018, **14**, 6514–6520.
- 49 G. Cheng, C. Lin and J. Perez-Mercader, *Small*, 2021, **17**, 2101162.
- 50 J. Kimling, M. Maier, B. Okenve, V. Kotaidis, H. Ballot and A. Plech, *J. Phys. Chem. B*, 2006, **110**, 15700–15707.
- 51 C. W. Visser, P. E. Frommhold, S. Wildeman, R. Mettin, D. Lohse and C. Sun, *Soft Matter*, 2015, **11**, 1708–1722.
- 52 C. Jossierand and S. T. Thoroddsen, *Annu. Rev. Fluid. Mech.*, 2016, **48**, 365–391.
- 53 A. Hollerbach, D. Logsdon, K. Iyer, A. Li, J. A. Schaber and R. G. Cooks, *Analyst*, 2018, **143**, 232–240.
- 54 T.-S. Wong, T.-H. Chen, X. Shen and C.-M. Ho, *Anal. Chem.*, 2011, **83**, 1871–1873.
- 55 P. Lebedev-Stepanov and K. Vlasov, *Colloids Surf., A*, 2013, **432**, 132–138.
- 56 S. Crotti, R. Seraglia and P. Traldi, *Eur. J. Mass Spectrom.*, 2011, **17**, 85–99.
- 57 A. K. Samal, T. S. Sreeprasad and T. Pradeep, *J. Nanoparticle Res.*, 2010, **12**, 1777–1786.
- 58 S. F. Shimobayashi, M. Tsudome and T. Kurimura, *Sci. Rep.*, 2018, **8**, 17769.
- 59 S. Das, A. Dey, G. Reddy and D. D. Sarma, *J. Phys. Chem. Lett.*, 2017, **8**, 4704–4709.
- 60 Y. Li, C. Diddens, T. Segers, H. Wijshoff, M. Versluis and D. Lohse, *Proc. Natl. Acad. Sci. U. S. A.*, 2020, **117**, 16756–16763.
- 61 F. Picano, G. Sardina and C. M. Casciola, *Phys. Fluids*, 2009, **21**, 93305.
- 62 Y. Gao, P. Magaud, L. Baldas and Y. Wang, *Micromachines*, 2021, **12**, 198.
- 63 J. K. Kim, P. A. Rühls, P. Fischer and J. S. Hong, *Rheol. Acta*, 2013, **52**, 327–335.
- 64 B. R. Bzdek, J. P. Reid, J. Malila and N. L. Prisle, *Proc. Natl. Acad. Sci. U. S. A.*, 2020, **117**, 8335–8343.
- 65 R. Wang, P. Allmendinger, L. Zhu, A. J. Gröhn, K. Wegner, V. Frankevich and R. Zenobi, *J. Am. Soc. Mass Spectrom.*, 2011, **22**, 1234–1241.
- 66 Y. Gan, Z. Jiang, H. Li, Y. Luo, X. Chen, Y. Shi, Y. Yan and Y. Yan, *Sci. Rep.*, 2019, **9**, 18791.
- 67 A. Wortmann, A. Kistler-Momotova, R. Zenobi, M. C. Heine, O. Wilhelm and S. E. Pratsinis, *J. Am. Soc. Mass Spectrom.*, 2007, **18**, 385–393.
- 68 P. Kebarle and U. H. Verkerk, *Mass Spectrom. Rev.*, 2009, **28**, 898–917.
- 69 X. Huang, M. Li, D. C. Green, D. S. Williams, A. J. Patil and S. Mann, *Nat. Commun.*, 2013, **4**, 2239.
- 70 M. Abbas, W. P. Lipiński, J. Wang and E. Spruijt, *Chem. Soc. Rev.*, 2021, **50**, 3690–3705.
- 71 M. Fishkis, *Orig. Life Evol. Biosph.*, 2007, **37**, 537–553.
- 72 S.-P. Wei, Z.-G. Qian, C.-F. Hu, F. Pan, M.-T. Chen, S. Y. Lee and X.-X. Xia, *Nat. Chem. Biol.*, 2020, **16**, 1143–1148.
- 73 C. Donau, F. Späth, M. Sosson, B. A. K. Kriebisch, F. Schnitter, M. Tena-Solsona, H.-S. Kang, E. Salibi, M. Sattler, H. Mutschler and J. Boekhoven, *Nat. Commun.*, 2020, **11**, 5167.
- 74 J. Kimling, M. Maier, B. Okenve and V. Kotaidis, *J. Phys. Chem. B*, 2006, **110**, 15700–15707.
- 75 Y. Zheng, X. Zhong, Z. Li and Y. Xia, *Part. Part. Syst. Charact.*, 2014, **31**, 266–273.



## Supplementary information:

# Spatial Reorganization of Analytes in Charged Aqueous Microdroplets

Pallab Basuri, Amrita Chakraborty, Tripti Ahuja, Biswajit Mondal, Jenifer Shantha Kumar, and Thalappil Pradeep\*

1 DST Unit of Nanoscience (DST UNS) and Thematic Unit of Excellence (TUE), Department of Chemistry, Indian Institute of Technology Madras, Chennai 600 036, India

Correspondence to: [pradeep@iitm.ac.in](mailto:pradeep@iitm.ac.in)

Serial no.	Details	Page no.
Fig. S1	DFM images of microdroplets containing AgNPs in water	2
Fig. S2	DFM images of microdroplets containing AuNPs in water	3
Fig. S3	TEM images of imprinted microdroplets containing AuNPs in water	4
Fig. S4	Characterization of as-synthesized GNRs	5
Fig. S5	DFM images of the imprinted droplets containing as-synthesized GNRs	6
Fig. S6	DFM of the drop casted sample of 10 $\mu$ L of bulk solution on a glass surface	7
Fig. S7	Characterization of as-synthesized CTAC-protected AuNPs	8
Fig. S8	DFM images of microdroplet containing 1:1 mixture of GNRs and CTAC-protected AuNPs in water	9
Fig. S9	Effect of ESI parameters on the droplet size	10
Fig. S10	Statistical analysis of droplet type distribution at various ESI parameters	11
Fig. S11	Vacuolization in aqueous microdroplets	12
Fig. S12	Microvacuoles in protein-filled microdroplets	13
Fig. S13	Microdroplets of degassed liquid	14

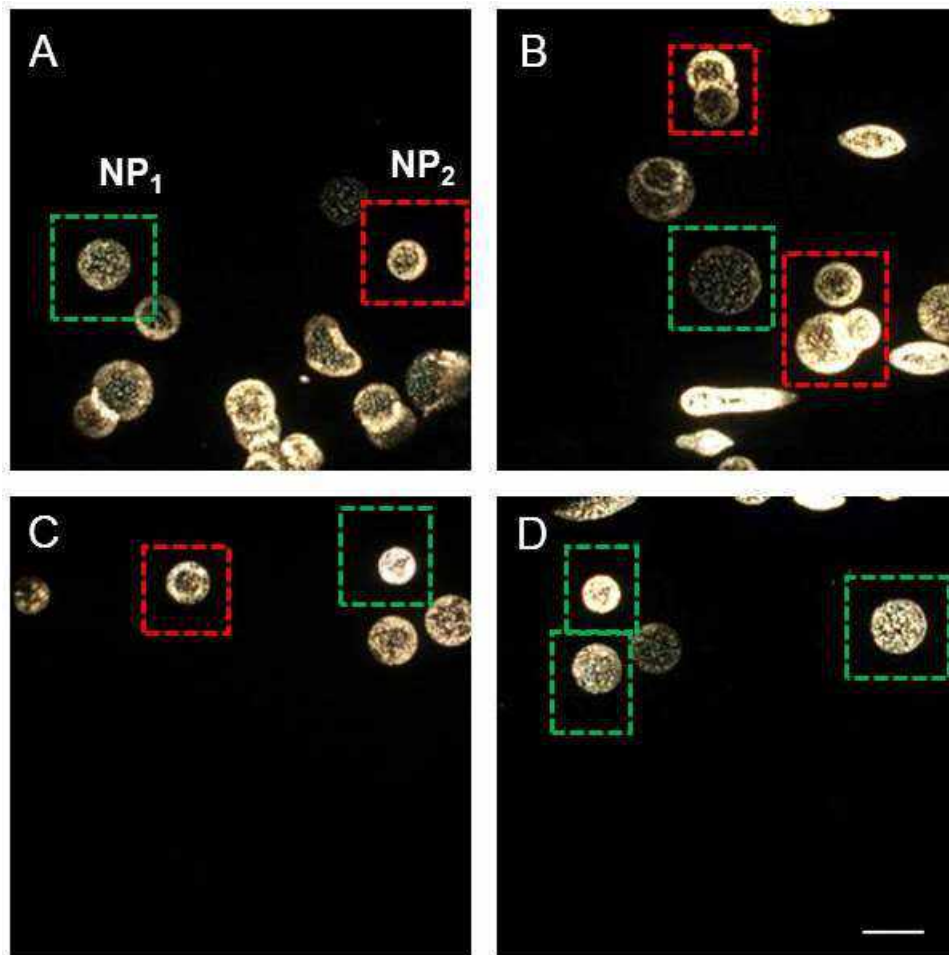


**Fig. S1** DFM images of microdroplets containing AgNPs in water, from different regions of the slide. Both NP1 and NP2 can be observed in all four images and are indicated by green (NP1) and red (NP2) squares. A-D) Images taken from different locations of the sample. The scale bar shown here is 100  $\mu\text{m}$ .

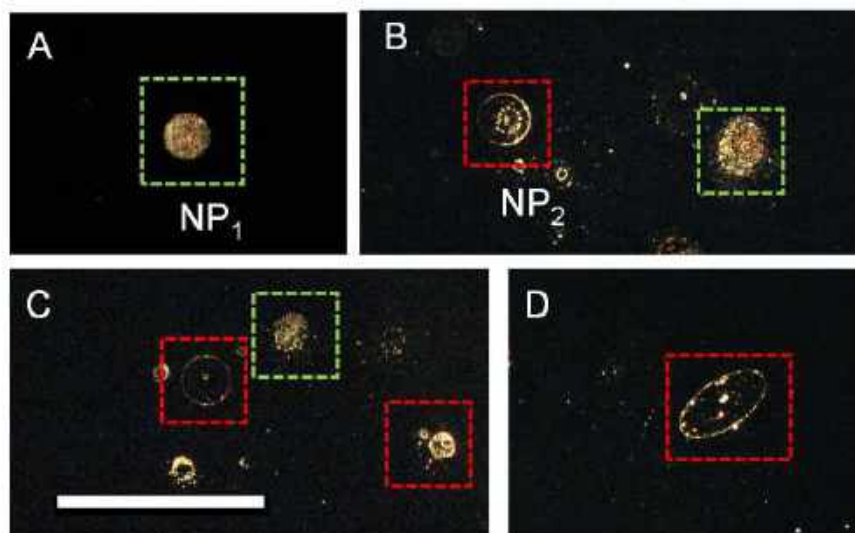


**Fig. S2** DFM images of microdroplets containing AuNPs in water. Both Type NP1 and NP2 can be observed in all four images and are indicated by green (NP1) and red (NP2) squares. A-D) Images taken from different locations of the sample. The scale bar shown here is 250  $\mu\text{m}$ .



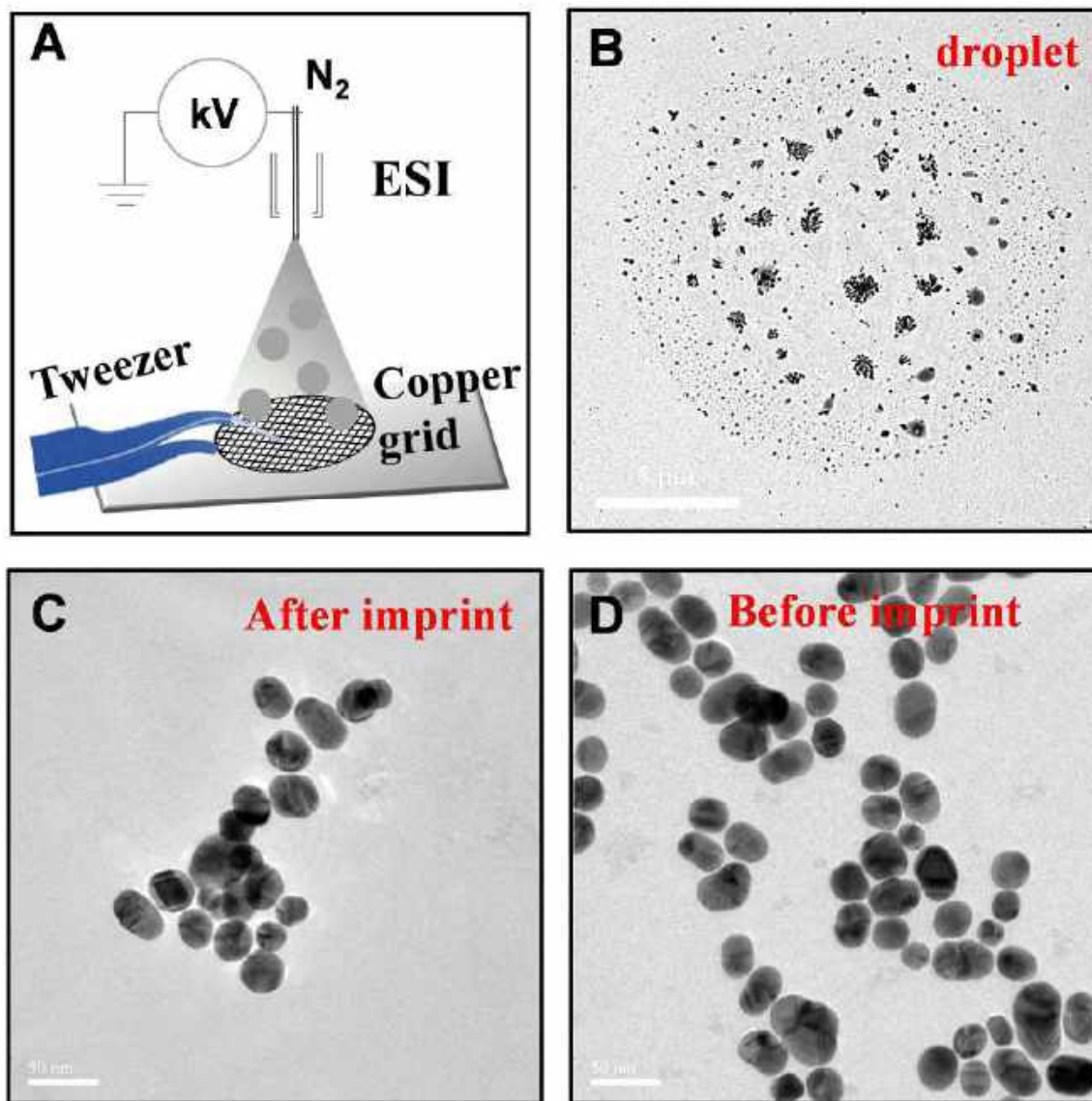


**Fig. S3** Transmission electron microscopy of imprinted droplets containing aqueous colloidal AuNPs. (A) Schematic view of the experimental setting of droplet imprinting in a TEM grid. (B) TEM image of a droplet (NP2). Clustering of AuNPs was also observed at the interior of the droplet. The scale bar shown here is 5  $\mu\text{m}$ . (C-D) TEM images of AuNPs before and after spray at higher magnifications. The scale bar shown here is 50 nm. Approximately 10  $\mu\text{L}$  of AuNPs dispersion were drop casted and dried on a TEM copper grid before the imprint experiments.

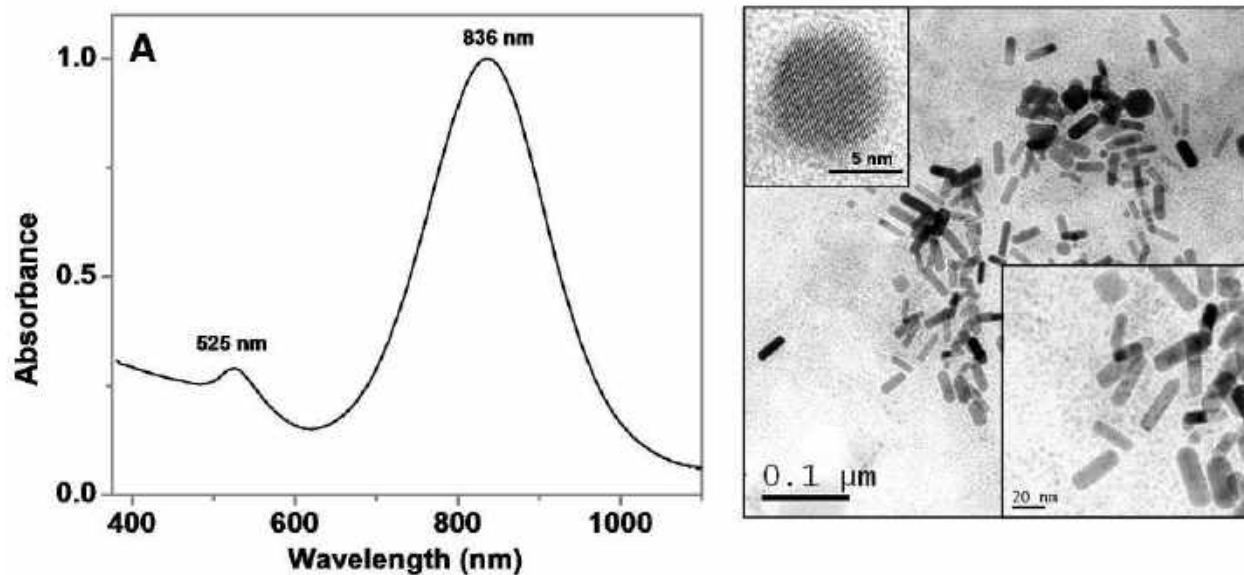


**Fig. S4** Characterization of as-synthesized gold nanorods. (A) UV Vis spectroscopy of GNRs showing two characteristic peaks at 525 and 836 nm. (B) TEM characterization of gold nanorods. The TEM image shows the impurity of AuNPs of different sizes and shapes.

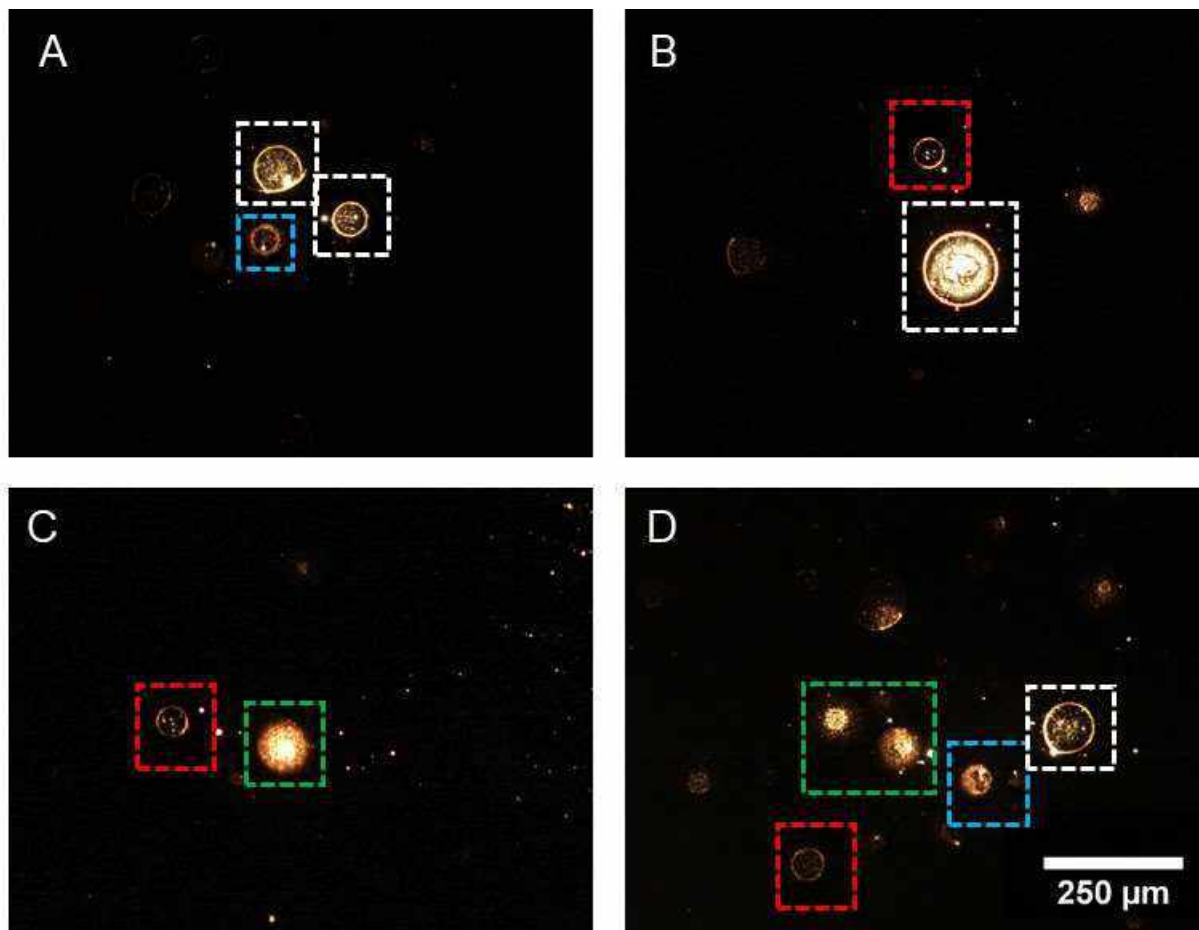


**Fig. S5** DFM images of the imprinted droplets containing as-synthesized GNR. These droplets were produced with electrospray parameters of 1.5 kV applied potential and 20 psi nebulization gas pressure. The droplets were imprinted at a 2.5 cm distance from the tip. A-D) Images from different location of sample. Different types of droplets such as Mix1-Mix4 were marked with green, cyan, white, and red squares.

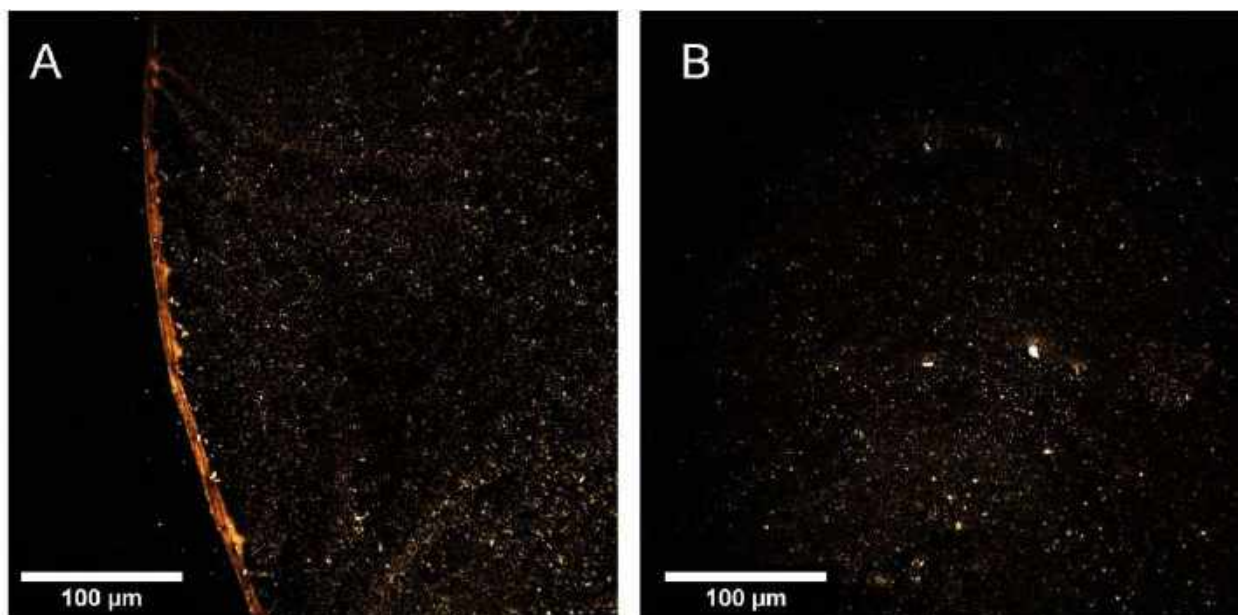


**Fig. S6** DFM of the drop casted sample of 10  $\mu\text{L}$  of bulk solution on a glass surface. A coffee ring was observed with higher concentration of particles at the periphery of the dried drop (A). However, no unique particle distribution and vacuoles were observed at the interior (B).

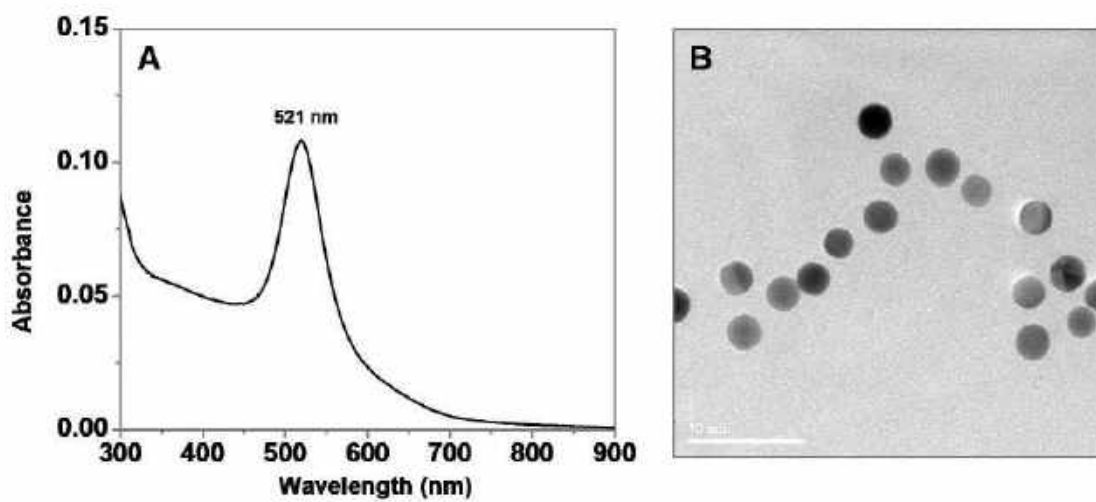


**Fig. S7** Characterization of as-synthesized CTAC-protected AuNPs. (A) UV Vis spectroscopy of AuNPs showing a characteristic peak at 521 nm. (B) TEM characterization of AuNPs.

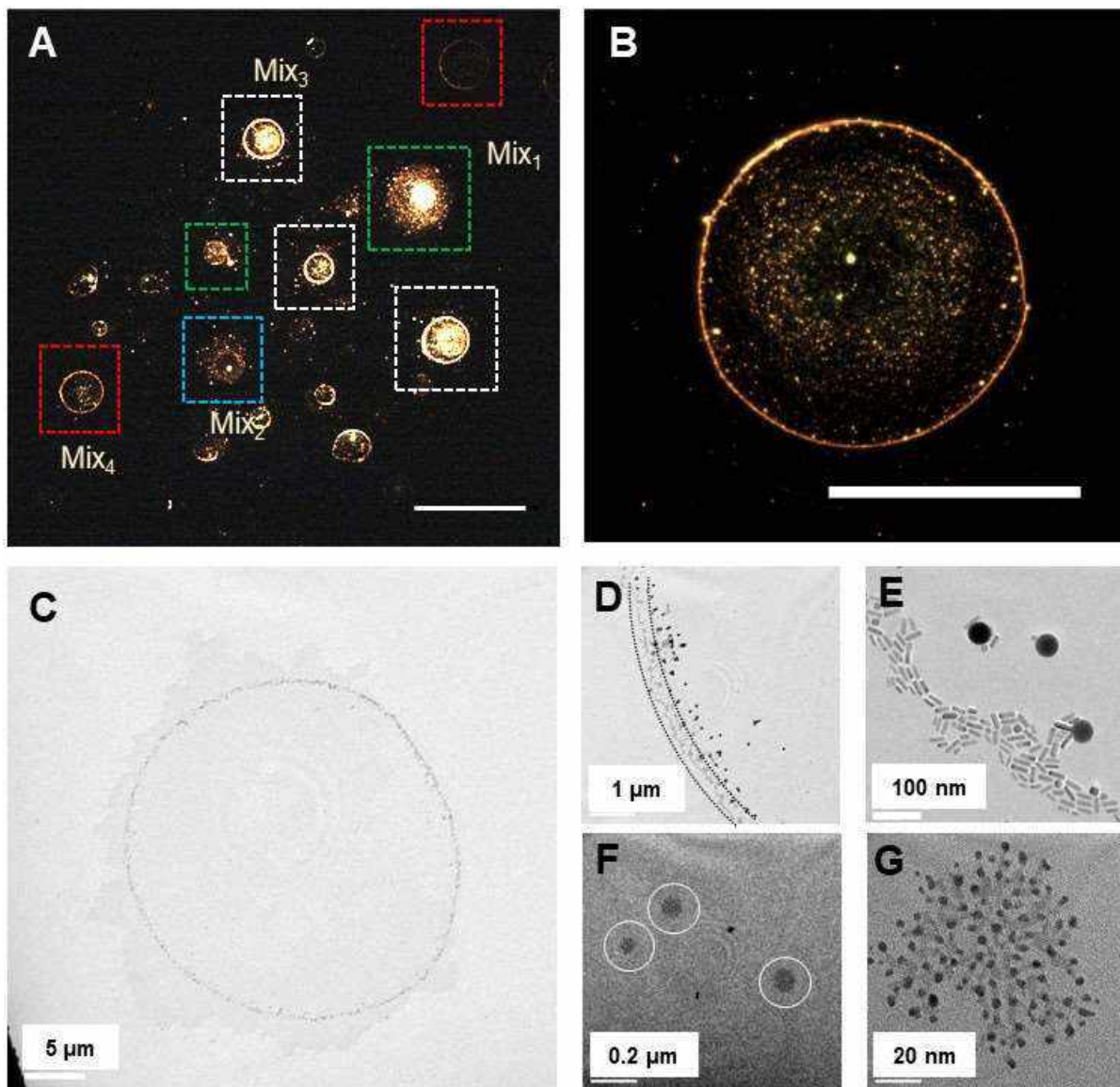


**Fig. S8** DFM and TEM images of microdroplets containing a 1:1 mixture of GNR and CTAC-protected AuNPs in water. (A) Different types (Mix1-Mix4) of droplets. Distributions of similar types are marked with the same colored squares. The scale bar shown here is 250  $\mu\text{m}$ . (B) Zoomed-in image of a droplet of Mix3. The scale bar shown here is 100  $\mu\text{m}$ . (C) TEM image of a droplet showing enrichment of GNRs and MBA protected-AuNPs at the periphery (D and E) along with clusters of nanoparticles at the interior (F and G).



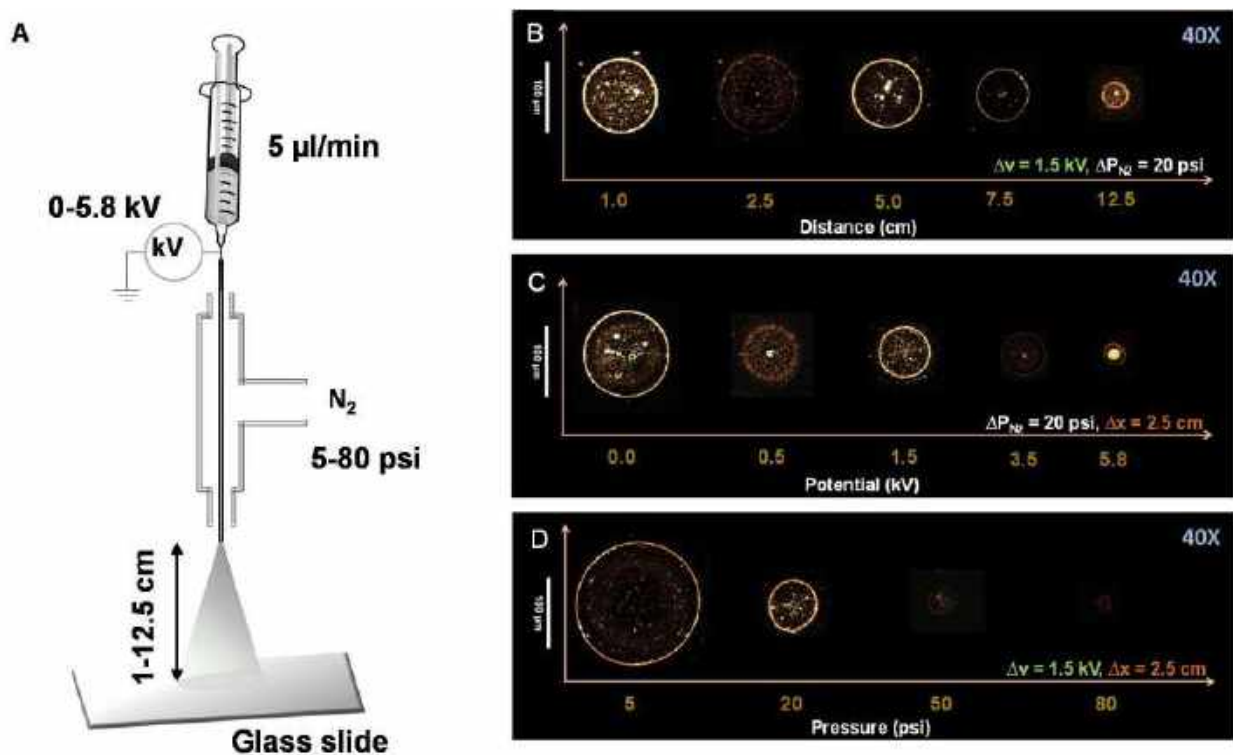


**Fig. S9** Effect of ESI parameters on the droplet size. (A) Schematic representation of the experimental settings. Three parameters such as tip-to-surface distance, spray potential, and nebulization gas pressure were varied. One parameter was varied at a time, keeping all others fixed. DFM images of droplets with varying tip-to-surface distance (B), potential (C), and nebulization gas pressure (D). We showed one representative droplet per parameter investigated. The scale bar is 100  $\mu\text{m}$ .

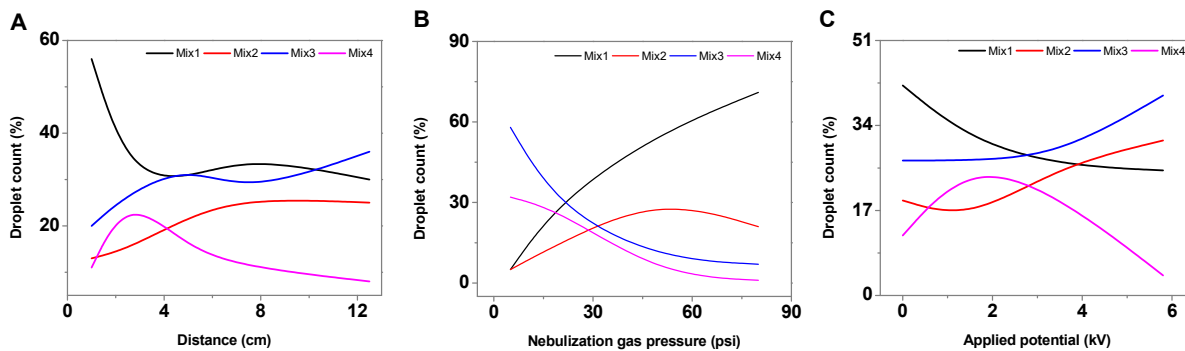


**Fig. S10** Statistical analysis of droplet type distribution at various ESI parameters such as A) distance, B) nebulization gas pressure, and C) applied potential. Particle redistribution occurs with increasing distance and applied potential and with decreasing gas pressure. This hints at the fact that applied potential and tip-to-deposition distance are the two major factors behind particle relocation within the droplet.

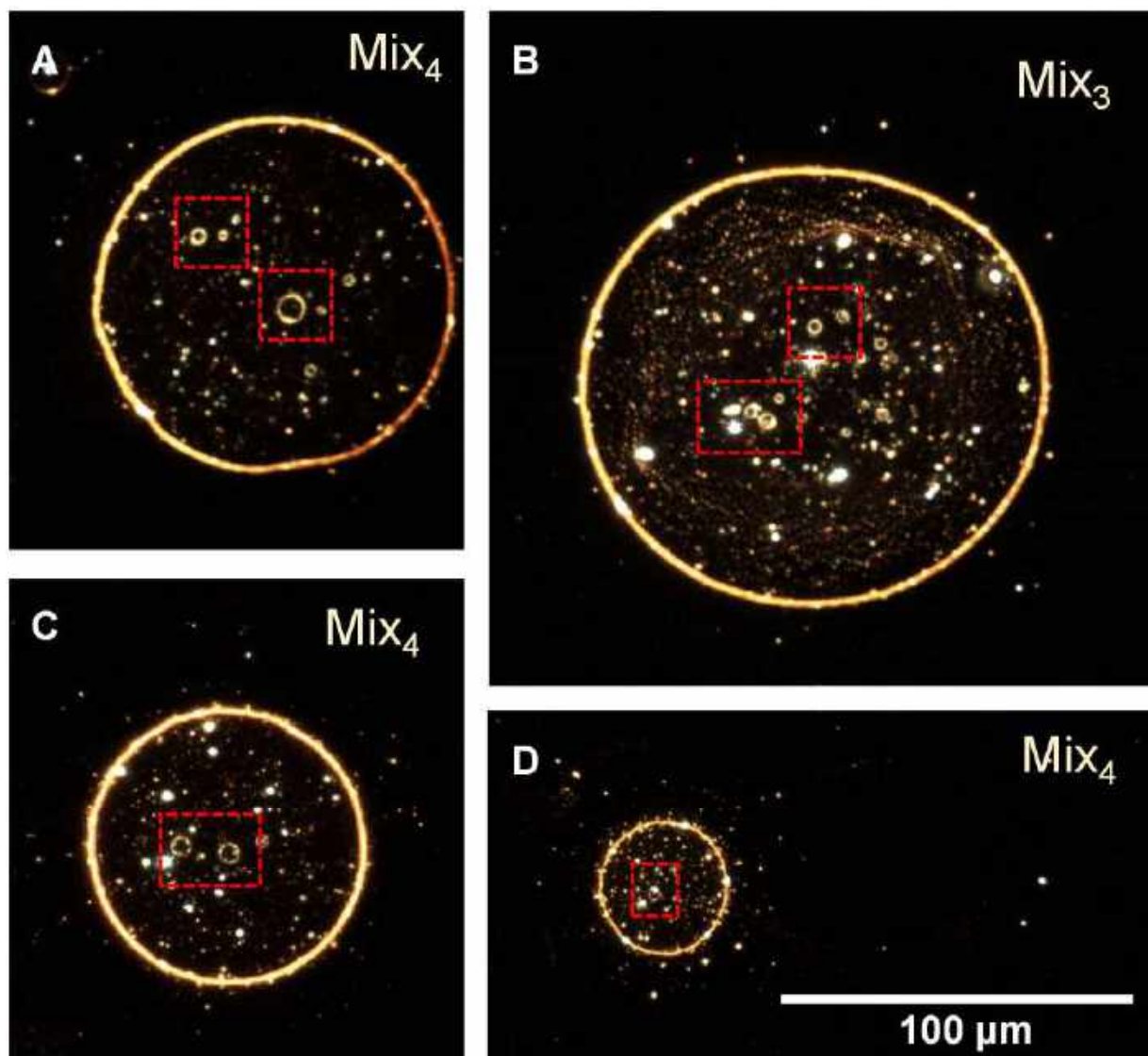


**Fig. S11** Vacuolization in aqueous microdroplets. Microvacuoles in the DFM images of the droplets of as-synthesized GNR are indicated with red squares. Single or multiple vacuoles with varying shapes and sizes were observed.

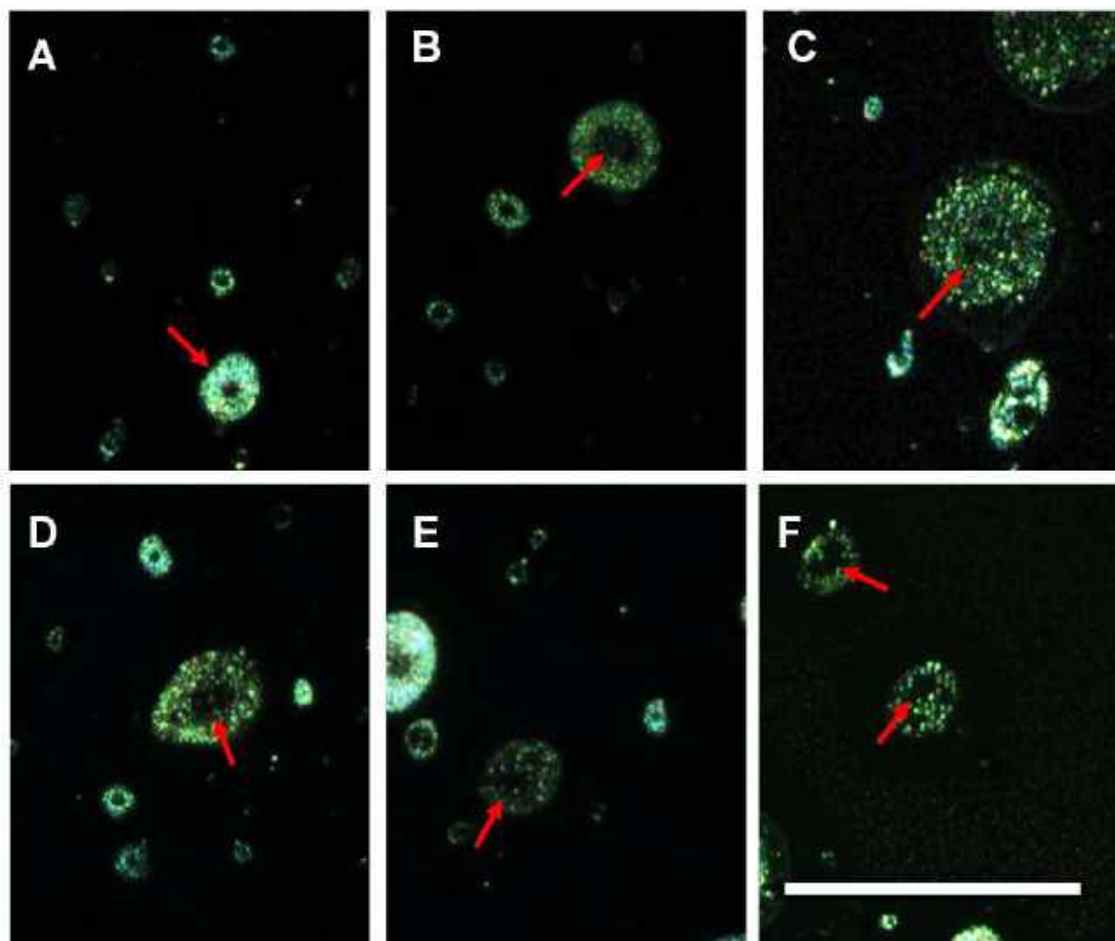


**Fig. S12** Microvacuoles observed in protein-filled microdroplets. Droplets having vacuoles are indicated by red arrows. Fluorescein isothiocyanate (FITC)-labeled bovine serum albumin (BSA) was used as an analyte. Several droplets were found to have distorted shapes as observed previously in case of nanoparticles containing droplets. The scale bar is 250  $\mu\text{m}$ .

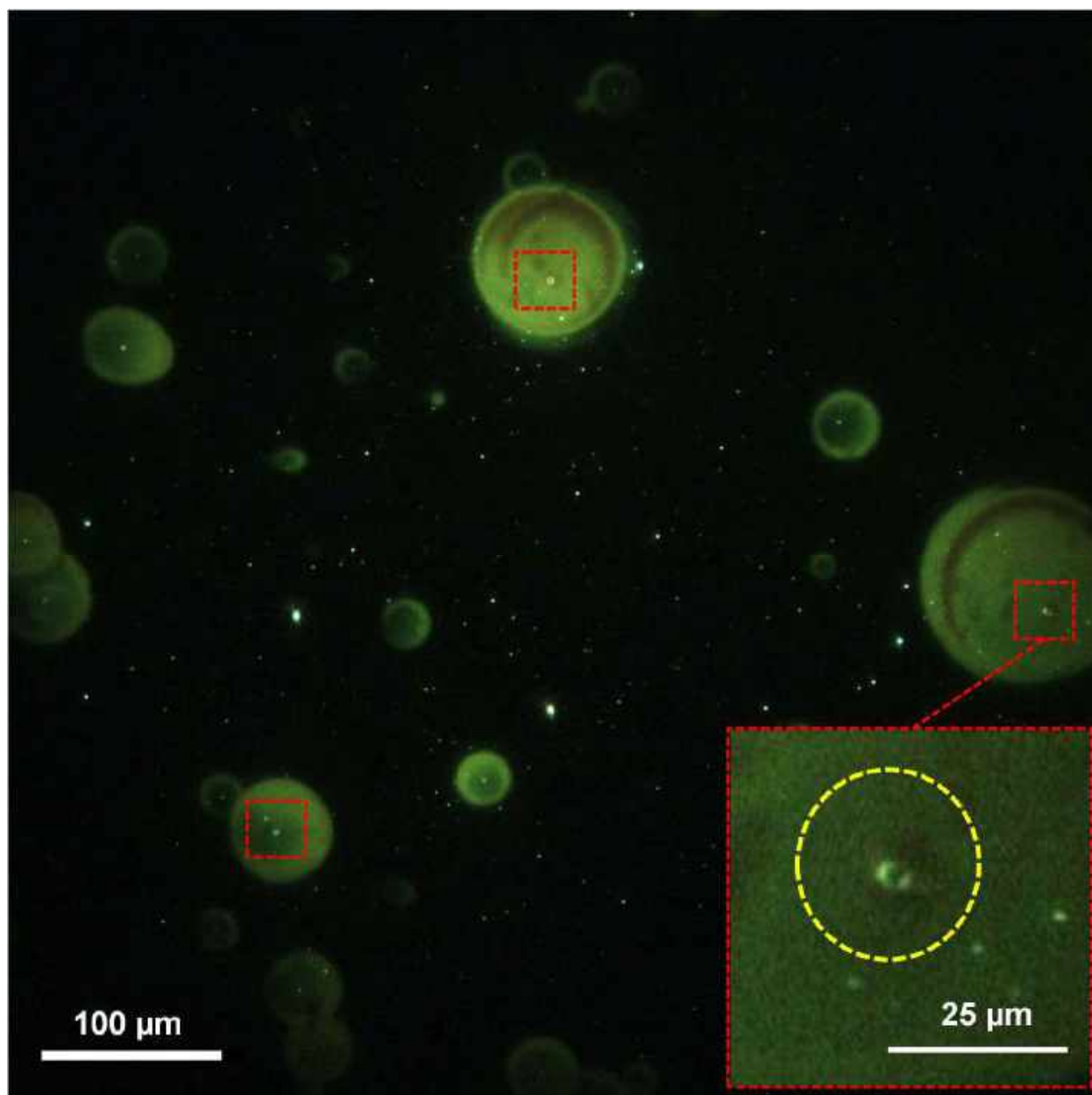


**Fig. S13** Fluorescence image of microdroplets containing R6G after degassing of the solution. The degassing was performed by freezing the solution at  $-80\text{ }^{\circ}\text{C}$  followed by melting it at room temperature under vacuum. The image contains several droplets but only very few are found to have bubbles that are marked with red squares. The scale bar is  $100\text{ }\mu\text{m}$ .



Cite this: *Phys. Chem. Chem. Phys.*, 2022, 24, 26200

# Rapid crystallization of amorphous solid water by porosity induction†

Gaurav Vishwakarma,<sup>a</sup> Bijesh K. Malla,<sup>a</sup> Rabin Rajan J. Methikkalam<sup>b</sup> and Thalappil Pradeep<sup>†</sup>  <sup>\*ac</sup>

Rapid crystallization of amorphous solid water (ASW) is often associated with crystallization that initiates at random nucleation sites in the bulk and expands in all directions. In this work, by preparing sandwich films of acetonitrile (ACN) and ASW in the form of ACN@ASW and ASW@ACN in an ultrahigh vacuum (UHV), we demonstrate a new method for rapid crystallization of ASW *via* ACN diffusion–desorption induced porosity in the ASW matrix even in the window of 128–134 K, well below the normal crystallization temperature of 155 K. By placing an HDO (5% D<sub>2</sub>O in H<sub>2</sub>O) probe layer in ASW, we found that when ACN diffuses and desorbs through ASW, it induces ASW crystallization where the crystal grows both from the top and from the bottom simultaneously into the bulk. Crystallization kinetics and activation energy ( $E_a$ ) for the formation of crystalline ice (CI) were evaluated using the Avrami equation and were compared with the previous reports. The evaluated  $E_a$  was  $\sim 53$  kJ mol<sup>-1</sup>, close to the  $E_a$  of crystal growth (47–56 kJ mol<sup>-1</sup>) and it suggested the absence of a nucleation process and supported rapid crystallization. Such occurrence of CI due to diffusion of ACN suggests a possible mechanism for the former's existence in many astrophysical environments.

Received 10th June 2022,  
Accepted 11th October 2022

DOI: 10.1039/d2cp02640f

rsc.li/pccp

## Introduction

A metastable form of solid water, ASW can be created by deposition of water vapour on a cold substrate below 130 K. The properties of ASW are of great importance for several reasons, including its use as a model for supercooled liquid water and in the context of astrophysical and planetary science.<sup>1–4</sup> Upon annealing, ASW gets converted to a metastable cubic CI at temperatures above 130 K, and a stable hexagonal CI at temperatures above 155 K in ultrahigh vacuum (UHV).<sup>5</sup> CI can also be formed by several other methods such as dissociation of clathrate hydrates,<sup>6–10</sup> sublimation/desorption of volatile molecules from the ice matrix,<sup>11,12</sup> and addition of neutral/acidic impurities into ASW.<sup>13–18</sup> The kinetics and mechanisms of ASW to CI transition have been investigated in several studies using various methods including temperature-programmed

desorption, electron diffraction and infrared spectroscopy.<sup>3,4,13,19–26</sup> Most of these studies suggested that ASW crystallization initiates at random nucleation sites in the bulk and expands in all directions, although, a few reported that nucleation may commence at the ASW–vacuum interface.<sup>27,28</sup> However, Yuan *et al.*<sup>22</sup> by placing an HDO (5% D<sub>2</sub>O in H<sub>2</sub>O) layer at specific positions in an ASW film (1000 ML) confirmed that ASW crystallization in vacuum proceeds by a “top-down” crystallization mechanism and suggested that the higher mobility of surface molecules compared to those in bulk is the reason for preferential nucleation at ASW–vacuum.

Water being ubiquitous, even in space, the diffusion of volatile molecules existing in space and consequently deposited on ASW at cryogenic temperatures can affect the chemistry of interstellar grains. Fundamental processes on dust grains are adsorption, desorption, diffusion, and reaction, which depend significantly on the morphology of ASW.<sup>5,29</sup> While ASW is the predominant form of water in the interstellar medium, crystalline ice (CI) has also been detected within many astrophysical environments.<sup>30–32</sup> However, there is a lack of mechanistic information on the formation of CI in such conditions. Along with water, more than 240 molecules have been detected in the interstellar and circumstellar medium.<sup>33</sup> Hence, the interactions of volatile molecules on top and within water-rich ices are of fundamental importance in understanding many interstellar processes.<sup>34</sup>

Diffusion of reacting atoms and molecules<sup>35</sup> is essential for the chemical evolution of interstellar ices and has been studied

<sup>a</sup> DST Unit of Nanoscience (DST UNS) and Thematic Unit of Excellence (TUE), Department of Chemistry, Indian Institute of Technology Madras, Chennai 600036, India

<sup>b</sup> Department of Chemistry, Mar Ivanios College, Thiruvananthapuram, Kerala 695015, India

<sup>c</sup> International Centre for Clean Water, IIT Madras Research Park, Chennai 600113, India. E-mail: pradeep@iitm.ac.in

† Electronic supplementary information (ESI) available: Experimental section, isothermal time-dependent RAIRS spectra and TPD-MS spectra of pure ACN, ACN@ASW and ASW@ACN films, crystallization parameters of ASW at different temperatures. See DOI: <https://doi.org/10.1039/d2cp02640f>



previously<sup>36,37</sup> (and references therein). The main focus of diffusion studies (of volatile species) was to elucidate the diffusion-desorption kinetics of volatile molecules and how it is affected by the ASW structure. A distinct mechanism for the release of trapped gases (Ar, Kr, Xe, CH<sub>4</sub>, N<sub>2</sub>, O<sub>2</sub>, or CO) from underneath the ASW films has been demonstrated in their low (1 monolayer) and high coverage (5 monolayers) regimes.<sup>38,39</sup> For low coverages of volatile species, the release mechanism is controlled by crystallization-induced cracks formed in the ASW overlayer. On the other hand, for the high coverage regime, two desorption pathways were suggested; the first occurs between 100–150 K and is due to pressure-induced structural failure of the ASW overlayer. The second pathway occurs at a low temperature below 100 K and is attributed to the diffusion through pores formed during ASW deposition. However, there is a lack of clarity on the effect of diffusion of volatile molecules on the structure of ASW. Here, we have investigated the effect of diffusion of ACN on the structure of ASW.

The ACN–water system has been studied from different perspectives such as adsorption/desorption of ACN on the top of ASW/crystalline ice surfaces, interactions with water and thermal processing of ACN and water ice.<sup>12,40–45</sup> However, to the best of our knowledge, multilayer ACN diffusion in ASW in ultrahigh vacuum conditions has not been explored yet. ACN has been detected in molecular clouds Sgr B and Sgr A<sup>46</sup> and comet Kohoutek<sup>47</sup> and is an important precursor of nitrogen-containing complex organic molecules including amino acids and nucleobases. Hence, the study of the diffusion of ACN in ASW will be of importance for planetary science, astrochemistry, and physical chemistry.

In the current work, we have studied the diffusion of ACN molecules in ASW from the top as well as beneath the ASW films and the consequence of this process on the structure of ASW in a narrow temperature window of 128–134 K, where systematic changes occur. While diffusion and desorption of ACN were monitored by temperature-programmed desorption mass spectrometry (TPD-MS), and Cs<sup>+</sup> ion based secondary ion mass spectrometry (SIMS), change in the ASW structure and the associated kinetics were investigated by reflection absorption infrared spectroscopy (RAIRS). We observed that when ACN diffuses in ASW from the top as well as underneath the ASW film, the process induces crystallization of the latter even at low temperatures well below the normal crystallization temperature of 155 K.

## Experimental section

### Experimental setup

All the experiments were carried out using the setup described elsewhere.<sup>48</sup> Briefly, the setup consists of a stainless steel UHV chamber, with a base pressure of  $\sim 5 \times 10^{-10}$  mbar at room temperature. The vacuum chamber is equipped with reflection absorption infrared spectroscopy (RAIRS), temperature-programmed desorption (TPD) mass spectrometry, secondary ion mass spectrometry (SIMS), and low energy ion scattering

(LEIS) mass spectrometry of mass-selected ions. The set-up has been used extensively to study molecular solids.<sup>6,7,12,49,50</sup> UHV was maintained by using several turbomolecular pumps backed by oil-free diaphragm pumps (Pfeiffer Vacuum). Pressure was monitored by a Bayard-Alpert gauge (Pfeiffer Vacuum), controlled by a MaxiGauge controller (Pfeiffer, Model TPG 256 A). A highly polished Ru(0001) single crystal was used as the substrate and was maintained at low temperature using a closed-cycle helium cryostat (ColdEdge Technologies). The substrate (1.5 cm diameter and 1 mm thick) was mounted on a copper holder and connected to the cold tip of the He cryostat. With the help of different thermal sensors (K-type thermocouple and a platinum sensor) and a resistive heater (25  $\Omega$ ), the substrate temperature could be varied in the range of 8–1000 K with a temperature accuracy/uncertainty of 0.5 K. Temperature (ramping) was controlled and monitored with a temperature controller (Lakeshore, Model 336).

### Sample preparation

Before preparing each sample, the Ru(0001) substrate was heated to 400 K multiple times to ensure the cleanness of the surface. Thin films of ices were created by vapour deposition at 10 K. Before vapour deposition, ACN (Merck, 99.9%), and Millipore water (H<sub>2</sub>O of 18.2 M $\Omega$  resistivity) were taken in a vacuum-sealed test tube and further purified by several freeze-pump-thaw cycles. During the introduction of ACN and H<sub>2</sub>O vapour to the UHV chamber, purity was further confirmed by the presence of their distinctive molecular ion peaks using a residual gas analyzer that was sensitive to a partial pressure of  $\sim 10^{-10}$  mbar. Two sample lines were connected to the UHV chamber through a high-precision all-metal leak valve and directed to the middle of the substrate. Out of two sample lines, one was used exclusively for ACN and the other was used exclusively for water vapour deposition. The molecular deposition was controlled through the leak valves and coverage was expressed in monolayers (ML) assuming  $1.33 \times 10^{-6}$  mbar s = 1 ML, which was estimated to have  $\sim 1.1 \times 10^{15}$  molecules cm<sup>-2</sup>, as suggested in several reports.<sup>50–52</sup>

### Experimental procedure

Diffusion of ACN in ASW was studied by creating layered ice thin films of ACN and H<sub>2</sub>O by varying the position of the ACN layer. In one set of experiments, ACN films were deposited on Ru(0001) followed by ASW films (ACN film underneath ASW film, hereafter referred to as ACN@ASW) and in the second set of experiments, ASW films were deposited on Ru(0001) followed by ACN films (ACN film on top of ASW film, hereafter referred to as ASW@ACN). These ice films were prepared sequentially at 10 K by backfilling the vacuum chamber with ACN/H<sub>2</sub>O vapours at a total pressure of  $\sim 5 \times 10^{-7}$  mbar, starting from a base vacuum of  $\sim 5 \times 10^{-10}$  mbar. Here, exposures were measured as the product of the dosing time and the chamber pressure of exposure.<sup>45,51,52</sup> For 50 ML of ACN film, the inlet pressure was kept at  $\sim 5 \times 10^{-7}$  mbar for 1 min 40 s and for 150 ML of ASW film, the inlet pressure was  $\sim 5 \times 10^{-7}$  mbar for 5 min. For other thicknesses of ACN and ASW films, the time of vapour

exposure to the vacuum chamber was varied accordingly. During sequential deposition, after the deposition of the first gas, we have waited sufficient time to get back the base pressure before the deposition of the second gas. Further, the as-deposited ice films were heated to the set temperatures at a rate of  $2 \text{ K min}^{-1}$ . Once a particular temperature was reached, the ice samples were investigated by RAIRS, TPD, and SIMS (additional experimental details are given in the ESI†).

## Results and discussion

### Diffusion of ACN in ASW

The diffusion of ACN in ASW was examined mainly by TPD-MS and SIMS experiments. Pure ACN desorbs at  $\sim 139 \text{ K}$  as shown in Fig. S1a (ESI†) (RAIRS data) and S1b (TPD-MS data). Fig. 1a shows the TPD-MS spectrum of 200 ML of ACN@ASW (with

50 ML of ACN deposited first followed by 150 ML ASW over it) film with a heating rate of  $10 \text{ K min}^{-1}$ . The peak at  $142 \text{ K}$  is attributed to the bulk desorption of ACN through ASW. This abrupt desorption is due to a pressure-induced structural change in the ASW overlayer.<sup>39</sup> The marked region 1 (in the  $120\text{--}130 \text{ K}$  range), shows an initial (small) desorption of ACN which is attributed to the diffusion of ACN through pores formed during ASW deposition.<sup>39</sup> During ACN diffusion through ASW, a fraction of ACN will trap in ASW which may desorb along with  $\text{H}_2\text{O}$  above  $150 \text{ K}$ . The marked region 3 (in the range  $150\text{--}160 \text{ K}$ ) shows trapped ACN desorption. So, Fig. 1a shows that the diffusion and desorption of ACN from underneath ASW will start below  $120 \text{ K}$ , and accelerates above  $130 \text{ K}$  giving a desorption maximum at  $142 \text{ K}$ . Similarly, Fig. 1b shows the TPD-MS spectrum of 200 ML of ASW@ACN (with 150 ML of ASW and 50 ML of ACN over it) film with a heating rate of  $10 \text{ K min}^{-1}$ . The peak at  $139 \text{ K}$  is due to the bulk desorption of

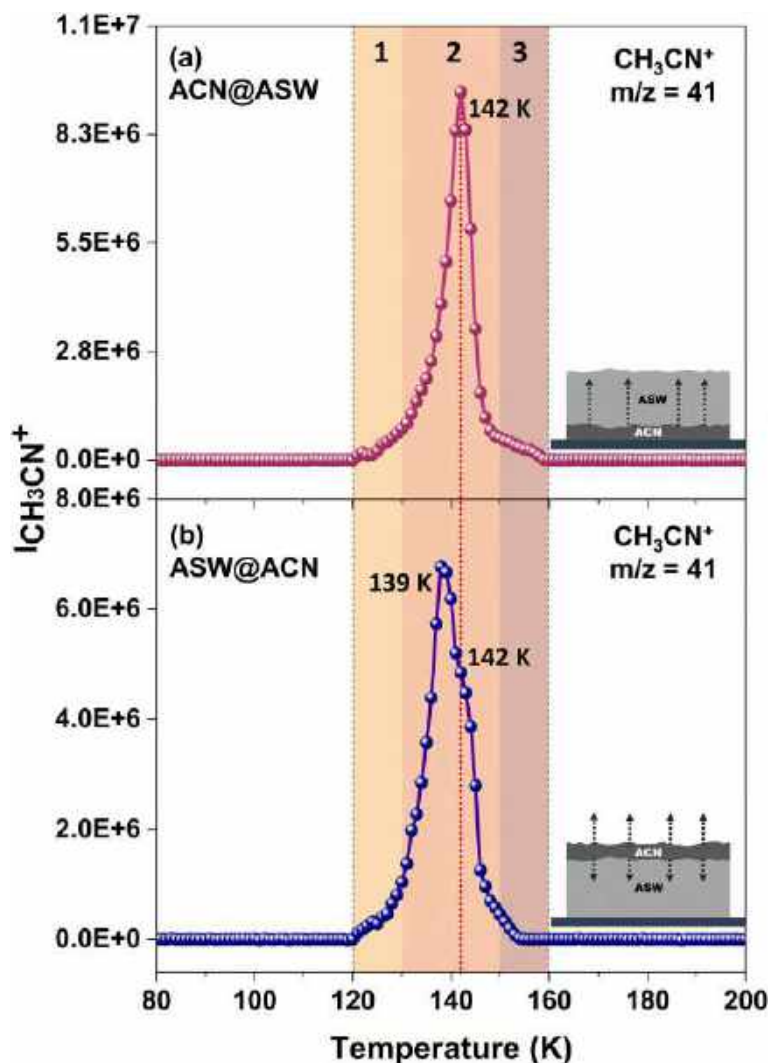


**Fig. 1** Desorption of 50 ML of ACN from 150 ML of ASW during  $10 \text{ K min}^{-1}$  TPD experiments. The marked region 1 indicates initial ACN desorption at  $120\text{--}130 \text{ K}$ , the region 2 shows bulk ACN desorption at  $130\text{--}150 \text{ K}$  and the region 3 shows trapped ACN desorption at  $150\text{--}160 \text{ K}$ . (a) TPD-MS spectra of 200 ML of ACN(50 ML)@ASW(150 ML). (b) TPD-MS spectra of 200 ML of ASW(150 ML)@ACN(50 ML). The inset pictures in (a) and (b) show the composition of sequentially deposited ACN and ASW films on Ru(0001) at  $10 \text{ K}$  and the dotted arrows show the diffusion and desorption path of ACN.

ACN from ASW surface and is similar to the desorption of pure ACN from the Ru(0001) substrate, as shown in Fig. S1b (ESI†). The shoulder at 142 K, in Fig. 1b, is assigned to the desorption of a fraction of ACN that diffused into ASW and returned to the surface as temperature was raised. This assignment is reasonable as this shoulder coincides with the peak at 142 K in Fig. 1a which is due to the desorption of ACN that diffuses through ASW. This was further confirmed in a separate experiment where instead of the ASW layer we have taken a crystalline H<sub>2</sub>O layer. TPD-MS data in Fig. S2a (ESI†) shows the desorption of 50 ML of ACN from the surface of 150 ML of crystalline H<sub>2</sub>O. The absence of a shoulder at 142 K in Fig. S2a (ESI†) suggests that ACN could not diffuse into crystalline H<sub>2</sub>O but desorbed at 140 K, similar to pure ACN desorption from the Ru(0001) substrate. These observations confirm that the shoulder at 142 K in Fig. 1b is due to a fraction of ACN that diffuses into ASW. In summary, when ACN was underneath ASW, it diffuses through ASW with a single desorption feature at 142 K, whereas when ACN was deposited on top of ASW, it desorbed with two desorption features where one coincides with pure ACN desorption at 139 K and the second coincides with the peak at 142 K, as in Fig. 1a. As the intensities of the peaks at 139 and 142 K are at a ~7:3 ratio we conclude that about ~30% of the ACN deposited diffuses into ASW and desorbs subsequently (Fig. S2b, ESI†).

To get a clearer picture of ACN diffusion in ASW, we have done SIMS experiments (see the experimental details in ESI†) on ACN@ASW, and ASW@ACN films. Here we have used the Cs<sup>+</sup> scattering technique, which is versatile to probe the top-most layer of solid surfaces.<sup>53–55</sup> We note that Cs<sup>+</sup> scattering at low energies is sensitive only to the first few layers of the surface. In the mass spectra shown in the Fig. 2, the peaks at *m/z* 151, 169 and 174 correspond to the adduct of Cs<sup>+</sup> (*m/z* 133) with H<sub>2</sub>O (Cs(H<sub>2</sub>O)<sup>+</sup>, Cs(H<sub>2</sub>O)<sub>2</sub><sup>+</sup>) and ACN (Cs(CH<sub>3</sub>CN)<sup>+</sup>), respectively. Fig. 2a shows a series of mass spectra for 200 ML of ACN@ASW (with 50 ML of ACN and 150 ML of ASW) film in the window of 10–150 K. Inset in each panel shows an expanded view in the *m/z* 170–178 window to see the evolution of Cs(CH<sub>3</sub>CN)<sup>+</sup> peak. At 10–100 K, we could observe only H<sub>2</sub>O (*m/z* 151) at the sample surface; although, at 110 K, we noted a small peak at *m/z* 174 along with a peak at *m/z* 151. This peak at *m/z* 174 suggests that a small fraction of ACN has diffused through ASW and reached the surface. The intensity of the peak at *m/z* 174 increased subsequently with temperature (up to 140 K), owing to the diffusion of a larger fraction of ACN to the surface. At 150 K, *m/z* 174 disappeared and only water peaks (*m/z* 151, and 169) were present. Fig. 2b shows a series of mass spectra for 200 ML of ASW@ACN (with 150 ML of ASW and 50 ML of ACN) film. At 10–90 K, only ACN (*m/z* 174) was observed, but at 100 K, we observed a small peak at *m/z* 151 along with another at *m/z* 174. This suggests the commencement of diffusion of ACN in ASW as well as H<sub>2</sub>O diffusion from the bottom, to the topmost surface. With an increase in substrate temperature from 100–140 K, the intensity of the peak at *m/z* 151 has increased and that of the peak at *m/z* 174 has roughly maintained the same intensity. At 140 K, the peak

at *m/z* 174 confirms ACN diffusion in ASW. If ACN could not have diffused into ASW, we would have seen a decrease in the peak intensity at 140 K. We understand that when ACN does not diffuse into CI, it desorbed at 140 K as shown in TPD-MS results (Fig. S2a, ESI†). At 150 K, the peak at *m/z* 174 has vanished (Fig. 2b) and, a new peak at 169 (Cs(H<sub>2</sub>O)<sub>2</sub><sup>+</sup>) along with a peak at *m/z* 151 was observed. In summary, the results of SIMS experiments in Fig. 2, along with the TPD-MS data suggest that when the ACN film was underneath ASW, it diffused through the pores of ASW and reached the surface even at 110 K, whereas, when ACN film was on top of ASW, a fraction of ACN deposited diffused into ASW and remained in the sample even at 140 K.

In the next sections, we will discuss the impact of ACN diffusion on ASW structure with the help of RAIRS experiments.

### Effect of ACN diffusion on ASW structure

In our previous report<sup>12</sup> on ACN–ASW system, we examined the composition-dependent phase separation of ACN and H<sub>2</sub>O, and associated structural changes in the ASW matrix. We observed that co-deposited ACN and H<sub>2</sub>O films (in 1:1, 1:5 and 5:1 ratios), when isothermally annealed at 125–135 K resulted in crystalline ice after ACN desorption. In interstellar and cometary ices, the molecular components are embedded in or frozen on top of the water ice, depending on the cosmochemical history of the ice. Therefore, studying the behaviour of water-ice in the sandwich (ACN@H<sub>2</sub>O) and mixed (ACN:H<sub>2</sub>O)<sup>12</sup> films upon ACN release is of greater significance. Therefore, in this paper, we monitored the diffusion of multilayer ACN into the bulk of ASW in the sandwich (ACN@ASW and ASW@ACN) films, and studied the consequence of this process on the ASW matrix systematically. For this, we deposited ACN and ASW sequentially at 10 K and heated the sample at a rate of 2 K min<sup>-1</sup> to the desired temperatures and IR spectral evolution was monitored subsequently. These experiments were done by varying ACN thickness (50–150 ML) in ACN@ASW and ASW@ACN films while keeping ASW thickness constant at 150 ML. During annealing from 10–133 K, a small fraction of ACN could have already diffused and desorbed through ASW (TPD-MS data, Fig. 1). At 133 K, the remaining ACN diffused and desorbed from the ACN@ASW and ASW@ACN films within 30 and 60 min, respectively (the spectral change in the C≡N stretching region with time can be seen in Fig. S3a and b, ESI†). We suppose that the ASW films after diffusion followed by desorption of ACN are highly porous. The porosity could range from microporosity to cracks of macroscopic dimensions. It is not possible to examine the pore size distribution of ASW by IR spectroscopy alone.<sup>37</sup> However, the O–H stretching band shows a major change after the diffusion and desorption of ACN from ASW (Fig. S4a–d and S5a–d, for ACN@ASW and ASW@ACN films, respectively, ESI†). For example, for 200 ML of ACN@ASW (50 ML ACN and 150 ML of ASW) film, in Fig. 3a; the first, broad spectrum (orange curve) at 0 min corresponds to the entirely amorphous nature of the sample, whereas, the last spectrum (blue curve) obtained after 130 min is attributed to the complete crystallization of ASW.<sup>13,27</sup> The obtained peak

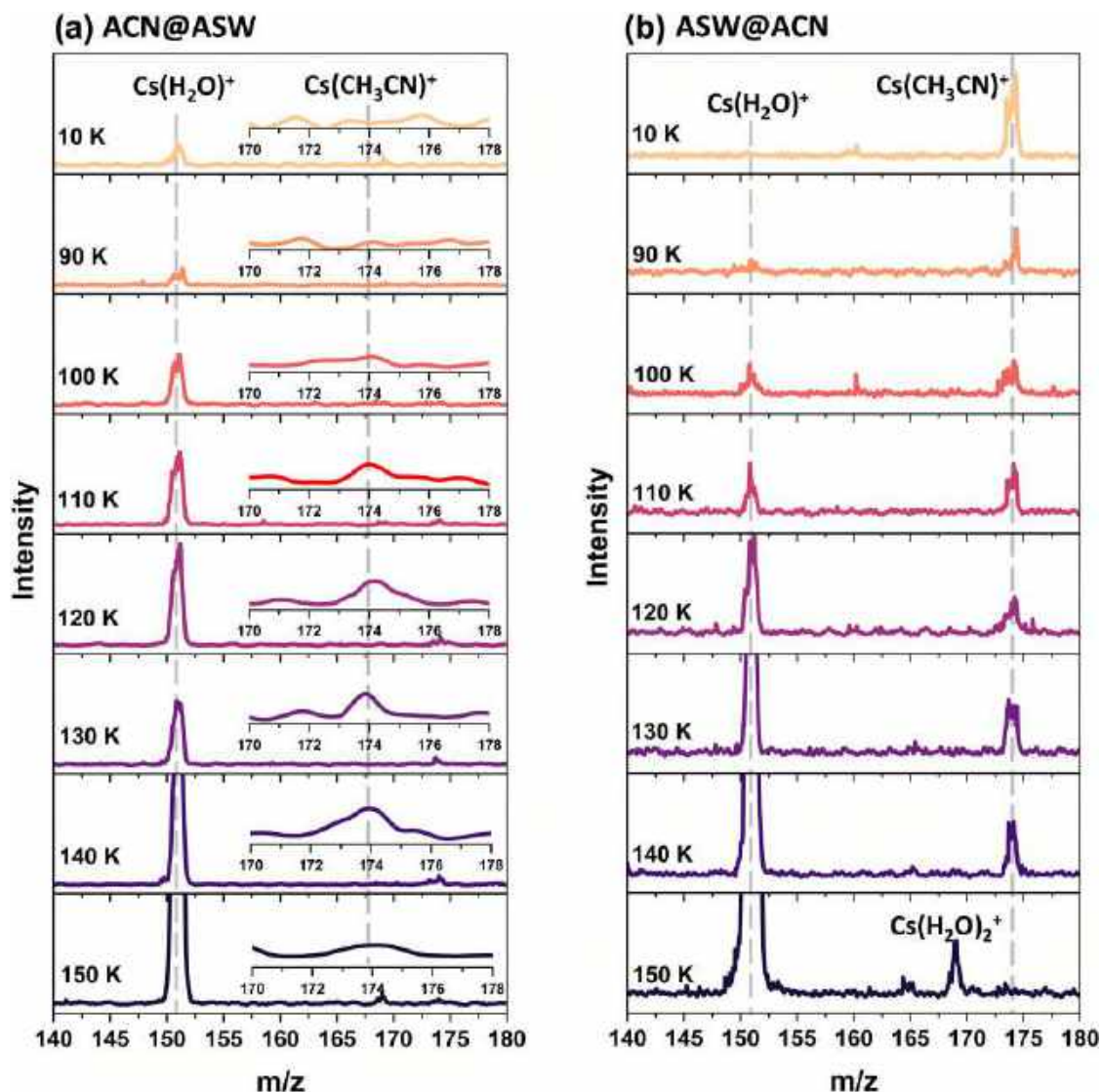


Fig. 2  $\text{Cs}^+$  scattering mass spectra of sequentially deposited ice layers of ACN and ASW. Deposited ices were collided with 120 eV  $\text{Cs}^+$  ions at 10–150 K. The mass spectra contain peaks corresponding to adducts of  $\text{Cs}^+$  ions with ACN and  $\text{H}_2\text{O}$ . The ions observed in mass spectra are  $\text{Cs}^+$  ( $m/z$  133) (not shown here),  $\text{Cs}(\text{H}_2\text{O})^+$  ( $m/z$  151),  $\text{Cs}(\text{H}_2\text{O})_2^+$  ( $m/z$  169),  $\text{Cs}(\text{CH}_3\text{CN})^+$  ( $m/z$  174). (a) Mass spectra of ACN(50 ML)@ASW(150 ML) in the  $m/z$  range of 140–180 at 10–150 K, where inset plots in each panel are expanded spectra in the  $m/z$  range of 170–178 to see the evolution of  $\text{Cs}(\text{CH}_3\text{CN})^+$ . (b) Mass spectra of ASW(150 ML)@ACN(50 ML), in the  $m/z$  range of 140–180 at 10–150 K where evolution of adducts of  $\text{Cs}^+$  ions with ACN and  $\text{H}_2\text{O}$  were monitored.

shape and bands correspond to the hexagonal ice (ice  $I_h$ ) (Fig. S6a, ESI<sup>†</sup>).<sup>7,12</sup> We will refer it as CI. In our previous reports,<sup>6,7,12</sup> we have seen that 150 ML of ASW cannot undergo crystallization at 120–135 K in similar experimental conditions (result of isothermal annealing of ASW at 133 K for several hours is shown in Fig. S6b, ESI<sup>†</sup>). This suggests that ACN diffusion in ASW has induced ASW crystallization.

Fig. 3b shows the combined crystallization fraction (CF) versus time curves for ACN@ASW (solid lines with square) and ASW@ACN (dashed line with circle) films obtained from the RAIRS measurement at 133 K from a vertical cut at  $3260\text{ cm}^{-1}$  in the O–H stretching band shown in Fig. S4a–d and S5a–d (ESI<sup>†</sup>). The ACN film with different thicknesses is shown in different colours (for example, 50 ML of ACN is shown

in orange and 150 ML in blue). Fig. 3b shows that the crystallization kinetics is faster and independent of ACN film thickness when ACN diffuses and desorbs from underneath ASW (solid lines with square) compared to the case when ACN diffuses and desorbs from the top of ASW (dashed line with circle) where crystallization kinetics is slower and increases with increase in ACN film thickness from 50–150 ML. If we compare the crystallization half-time (the time at which the CF = 0.5) the former took  $\sim 2080$  s whereas the latter took  $\sim 5260$  s for 50 ML of ACN with 150 ML of ASW. In the former case, the crystallization kinetics is roughly independent of ACN thickness (50–150 ML). We suggest that after the initial diffusion and desorption of a fraction of ACN through ASW, the latter possesses sufficient pores and cracks to release the



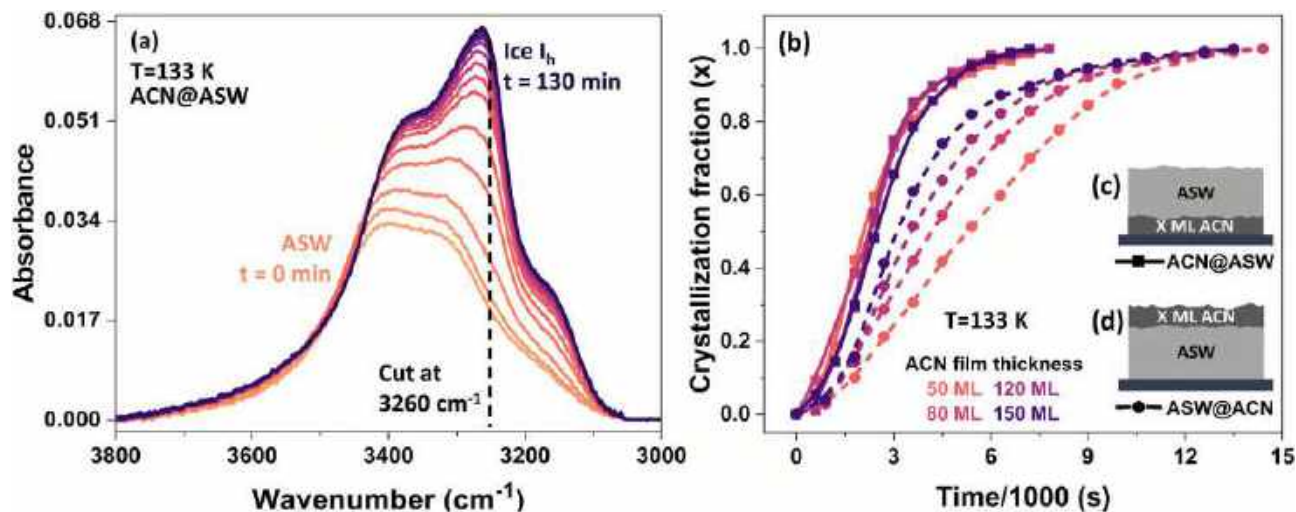


Fig. 3 (a) Time-dependent RAIRS spectra of 200 ML of ACN@ASW film at 133 K in the O–H stretching region. The film was sequentially deposited on Ru(0001) at 10 K and heated at a rate of  $2 \text{ K min}^{-1}$  to 133 K. The yellow curve (at 0 min) is the spectrum from complete amorphous film and blue curve (at 130 min) is the spectrum for a complete crystalline film. The vertical cut at  $3260 \text{ cm}^{-1}$  was utilized to determine the CF. (b) Combined CF versus time curves for ACN@ASW (solid lines with square) and ASW@ACN (dashed line with circle) films with varying ACN film thickness (50–150 ML) while keeping ASW film thickness constant at 150 ML. CF was obtained from isothermal RAIRS measurements at 133 K. The CF was calculated from a vertical cut at  $3260 \text{ cm}^{-1}$  in the O–H stretching band for the time-dependent RAIRS spectra shown in Fig. S4a–d (ESI<sup>†</sup>) (for ACN@ASW) and Fig. S5a–d (ESI<sup>†</sup>) (for ASW@ACN). (c and d) Composition of sequentially deposited ACN and ASW films on Ru(0001) at 10 K.

remaining ACN through it without much perturbation. To prove this, additionally, we examined the critical thickness of ACN layers required to induce ASW crystallization, for which we have placed 10, 20, and 30 ML of ACN layers below 150 ML of ASW and found that 30 ML of ACN is sufficient to induce ASW crystallization at 133 K (Fig. S7, ESI<sup>†</sup>). This is why the kinetics of ASW crystallization is almost similar for films containing 50–150 ML of ACN. While, in the latter case, crystallization increases with an increase in ACN film thickness. We propose that, as the ACN film thickness increases, the extent of diffusion of ACN in ASW also increases. This suggests that the more the diffusion of ACN in ASW, the higher will be the porosity, in turn, the faster will be the kinetics of crystallization. Thus, the results of Fig. 3 suggest that the diffusion of ACN in ASW is crucial for the commencement of ASW crystallization.

However, the differences in ASW crystallization kinetics for ACN@ASW and ASW@ACN films were thought to be due to a different crystallization mechanism that is involved in the process and this was investigated by placing HDO (5%  $\text{D}_2\text{O}$  in  $\text{H}_2\text{O}$ ) probe layers in ASW. This methodology for investigating the crystallization mechanism was used before.<sup>13,22</sup>

In separate experiments, we have embedded 50 ML of HDO probe layer in the ACN@ASW and ASW@ACN films at specific positions as shown in the inset pictures in Fig. 4a and b, and evaluated the CF at 133 K by monitoring the evolution in the O–D stretching band of HDO (Fig. S8 and S9, ESI<sup>†</sup>) as a function of time of crystallization. Fig. 4 shows the change in the CF of the HDO layer embedded at different locations; near the ACN layer (yellow curve), 50 ML away from ACN layer (brown curve) and 100 ML away from the ACN layer (blue curve) in the sample. These 50 and 100 ML spacer layers were made of ASW. Fig. 4a

shows that the HDO layer close and distant to the ACN layer crystallized first and almost at the same speed while the HDO layer embedded in the middle of the ASW crystallized later. This implies that diffusion of ACN from underneath ASW induced crystal growth both from the top and bottom simultaneously and the crystallization propagated from both directions into the bulk of ASW. Such an effect of diffusion of volatile gases on the ASW structure appears to be seen for the first time. The reason for such a mechanism is (1) at the ACN–ASW interface the required mobility for  $\text{H}_2\text{O}$  rearrangement to CI is obtained from the release of 50 ML of ACN through the ASW. This pressure-induced structural change in ASW due to ACN release will be maximum at the ACN–ASW interface compared to the bulk, (2) at the ASW–vacuum interface during annealing of the sample, ACN will diffuse through ASW and reach the surface before desorbing. The ASW films after diffusion followed by desorption of ACN are expected to be highly porous. The increased porosity consequently means more surface area and the formation of pre-crystallization nuclei<sup>56,57</sup> is more facile on the surface than in the bulk.

In contrast, in Fig. 4b the CF of the HDO embedded ASW@ACN films shows that the HDO layer closer to the ACN layer crystallized first followed by the middle and distant layers. This implies that the crystal growth has started at the ACN–ASW interface and propagated through the interior of ASW. If we see closely, the HDO layer which was placed in the middle, crystallized roughly along with the HDO layer near the ACN layer. This is because a small fraction of ACN diffused tens of ML into the ASW during isothermal annealing (confirmed with TPD and SIMS data, above). Diffusion and desorption of these ACN molecules will create more porosity in ASW as discussed above and subsequently will increase the speed of crystallization.

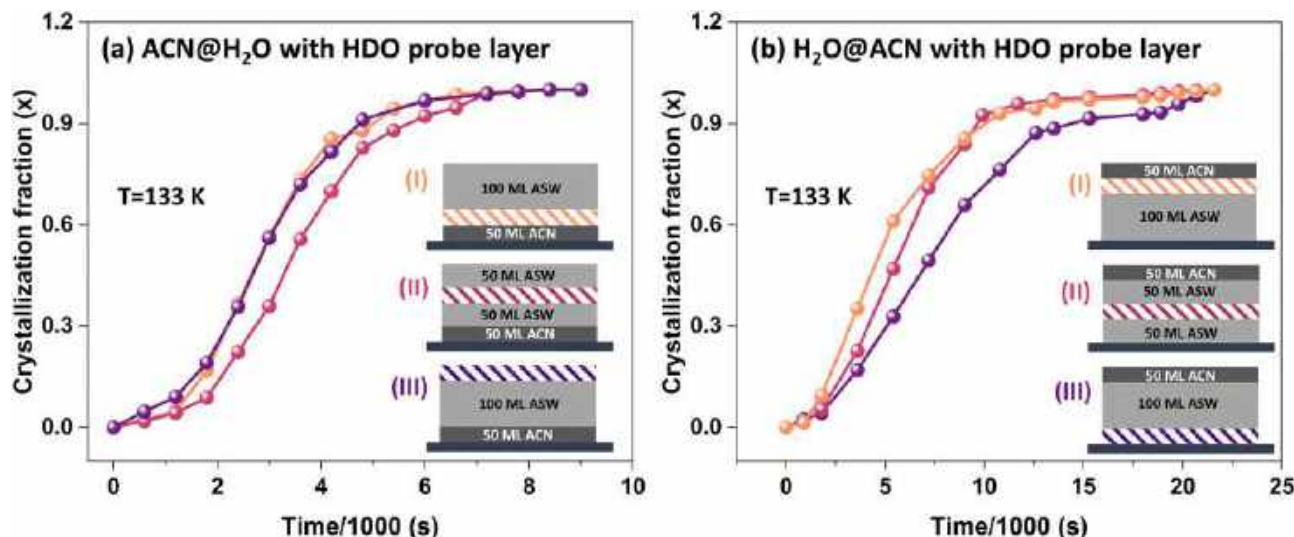


Fig. 4 The CF versus time curves for (a) ACN@H<sub>2</sub>O, and (b) H<sub>2</sub>O@ACN films with HDO (5% D<sub>2</sub>O in H<sub>2</sub>O) layer, obtained from isothermal RAIRS measurements at 133 K where a 50 ML of HDO layer was embedded at various positions in the ASW. The HDO layer is indicated by colored pattern in the inset pictures; HDO layer near ACN (0 ML away), 50 ML away, and 100 ML away from ACN layer are shown by (I) orange, (II) brown and (III) blue patterns, respectively. ASW layer is indicated by light grey. The colors of the obtained curves are shown by the corresponding colors. The CF was calculated from a vertical cut at 2424 cm<sup>-1</sup> in the O–D stretching band for the time-dependent RAIRS spectra shown in Fig. S8a–c and S9a–c (ESI<sup>†</sup>). ACN layer thickness was 50 ML.

When the ACN layer was on top of the ASW layer, it is clear that the crystallization had started at the surface and propagated into the interior and had slower kinetics as shown in Fig. 4b. But, when ACN was placed underneath ASW (Fig. 4a), we propose that the onset of crystallization was happening from top and bottom simultaneously and this was the reason for faster crystallization kinetics. To confirm whether crystallization had started at surfaces (or interfaces) or in the bulk, we have conducted thickness dependent experiments with ASW. As demonstrated in the previous reports<sup>13,58,59</sup> if nucleation occurs in bulk ASW, crystallization takes place faster in thicker ASW film than in thinner film whereas if crystallization initiates at the surface of the ASW film, it takes longer for a thicker film than in a thinner film. Fig. S10 (ESI<sup>†</sup>) shows the CF versus time curves for the ACN@ASW films with varying ASW film thickness (50–200 ML), obtained from isothermal RAIRS measurements at 133 K, keeping the ACN film thickness constant at 50 ML (Fig. S11, ESI<sup>†</sup>). We found that ASW with 50–100 ML thickness crystallizes faster than those with 150, 200 ML. Following the above arguments, these results suggest that crystallization has started at the surface and not in the bulk.

Thus, the results of Fig. 4 answer the question of the large difference in the ASW crystallization kinetics for ACN@ASW and ASW@ACN films, as shown in Fig. 3b. Faster kinetics in the former case is attributed to the crystal growth from the top and bottom simultaneously unlike in the latter case, where crystal growth propagates only from the top and required more time.

It should be noted that ASW overlayers grown over underlayer amorphous ACN, crystalline ACN films, and Ru(0001) substrate will have different porosities.<sup>39</sup> To examine this effect, 150 ML of ASW was grown over 50 ML of amorphous ACN,

50 ML of crystalline ACN, and bare Ru(0001) substrate. The resulting ices were annealed at 133 K isothermally, and the RAIRS spectra collected are presented in Fig. S12a, c and S6b (ESI<sup>†</sup>). Fig. S6b (ESI<sup>†</sup>) shows ASW grown over Ru(0001) substrate, which does not undergo crystallization at 133 K even after 6 h. Fig. S13 (ESI<sup>†</sup>) shows the crystallization fraction versus time curve, obtained from the RAIRS spectra presented in Fig. S12 (ESI<sup>†</sup>). The results suggest that the ASW grown over amorphous ACN crystallizes faster than when it was prepared over crystalline ACN. Following the above observation, we suggest that the ASW grown over amorphous ACN might have more porosity than when it was grown over Ru(0001) substrate or crystalline ACN film. The porosity might further increase due to the ACN burst above 130 K (Fig. 1a), where ASW undergoes pressure-induced structural failure.<sup>39,60</sup>

### Crystallization kinetics

Crystallization kinetics and related kinetic parameters of ASW crystallization were evaluated using time-dependent RAIRS spectra<sup>6,7,12,13,24</sup> under isothermal conditions at the corresponding temperatures, 128–134 K for the ACN@ASW film. As prepared ACN@ASW (with 50 ML of ACN and 150 ML of ASW) films at 10 K were annealed to the set temperatures and RAIRS spectra were recorded as a function of time. Fig. S14a–d (ESI<sup>†</sup>) shows the O–H stretching region for ACN@ASW films and were utilized to evaluate the crystallization kinetics. All the spectra shown in Fig. S14 (ESI<sup>†</sup>) have an isosbestic point, which indicates that the absorbance is due to the contributions of two states, amorphous and crystalline. In Fig. 5a, the first spectrum ( $t = 0$  min, orange trace) is due to the completely amorphous film and the final spectrum ( $t = 200$  min, blue trace) is from the completely crystalline film. The intermediate spectra represent



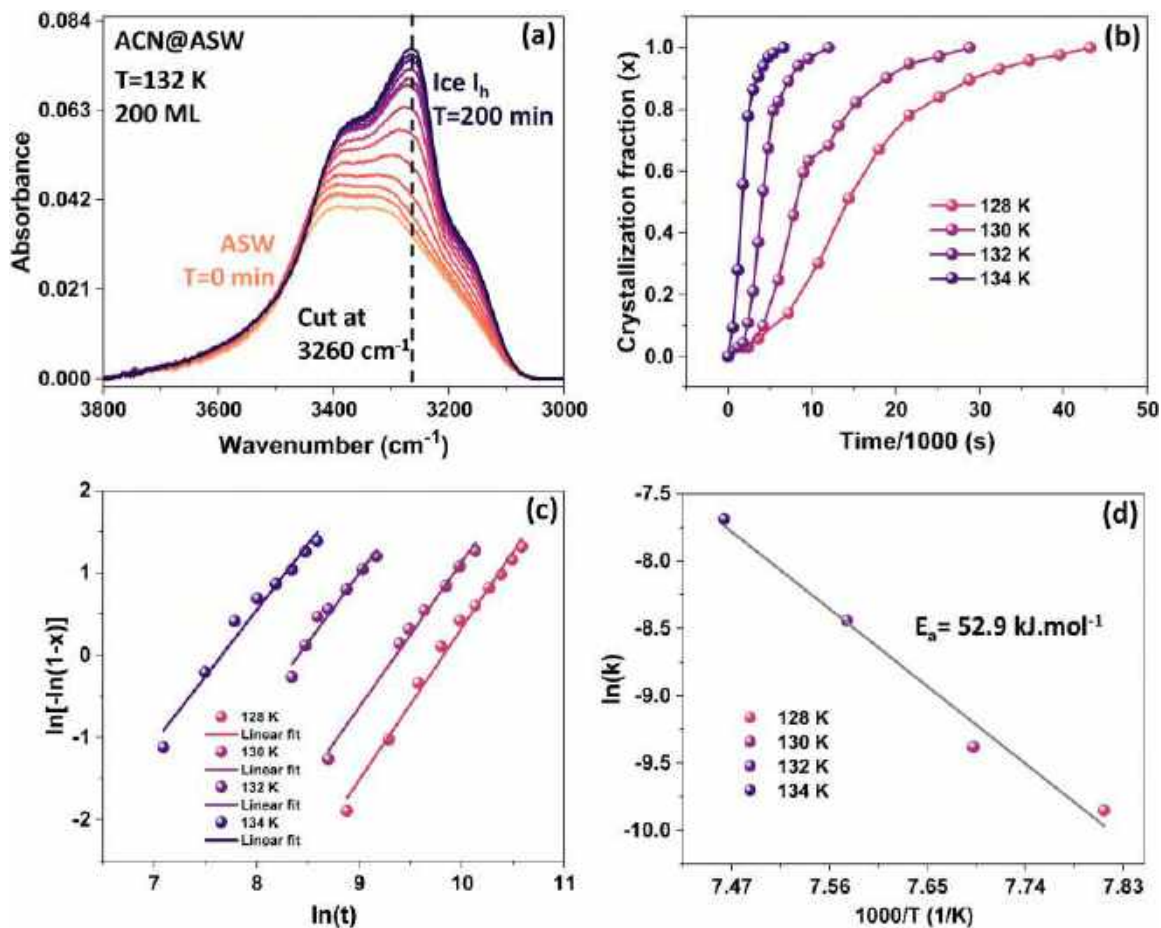


Fig. 5 (a) Time-dependent RAIRS spectra of 200 ML of ACN@ASW film at 132 K in the O–H stretching region. The film was sequentially deposited on Ru(0001) at 10 K and heated at a rate of 2 K min<sup>-1</sup> to 132 K. (b) CF versus time curves for 200 ML of ACN@ASW film obtained from isothermal RAIR measurements at 128, 130, 132 and 134 K. The fraction crystallized versus time was calculated from a vertical cut at 3260 cm<sup>-1</sup> in the O–H stretching band for a set of time-dependent RAIRS spectra shown in Fig. S14a–d (ESI<sup>†</sup>). (c) A plot of the linearized form of the Avrami equation for ASW crystallization. Plots of ln[-ln(1-x)] versus ln(t) at different temperatures of 128, 130, 132, and 134 K were evaluated using the O–H stretching bands. The obtained data points were fitted using the Avrami equation. (d) Arrhenius plot of ln k versus (1/T), achieved from the analysis of the slope and intercept of the linearly fitted lines of plot (c) for different temperatures. The activation energy ( $E_a$ ) of ice crystallization was calculated from the slope of the linearly fitted straight line of plot (d).

the progress of crystallization and are a combination of amorphous and crystalline spectra. The fraction crystallized with time can be calculated at a fixed wavenumber (3260 cm<sup>-1</sup>) by subtracting the spectrum obtained at 0 min from the spectrum obtained at time  $t$ , for each temperature. Fig. 5b shows the CF versus time curves for ACN@ASW films at 128–134 K, obtained from the isothermal RAIRS spectra, shown in Fig. S14 (ESI<sup>†</sup>). The CF( $x$ ) was calculated by eqn (1),

$$x(t) = \frac{\Delta A(1)}{\Delta A(2)} \quad (1)$$

where  $\Delta A(1)$  is the difference in the absorbance at a particular time  $t$  and that at time zero of an ACN@ASW film, and  $\Delta A(2)$  is the difference in absorbance of a completely crystallized film (when there is no further spectral change with time) and that of a completely amorphous film (at  $t = 0$ ) at the given temperature.

It is evident from the change of the shape of curves in Fig. 5b that the speed of crystallization increases with increasing

temperature. The nucleation and growth mechanism of ASW can be evaluated by fitting the CF to the Avrami equation.<sup>61,62</sup> The Avrami equation is given by,

$$x(t) = 1 - \exp(-k \cdot t^n) \quad (2)$$

where  $t$  is time,  $k$  is the crystallization rate constant, and  $n$  is the time exponent which predicts the crystallization mechanism. For all the temperatures,  $n$  can have an integer value between 1–4 where  $n = 4$  suggests three-dimensional growth with random nucleation in the bulk. However, when nucleation occurs at the surface of a film and crystal growth is perpendicular to the surface,  $n$  becomes close to 1.<sup>13,24,63</sup> eqn (2) can be rearranged in a linear form.

$$\ln(-\ln[1 - x(t)]) = n \ln(t) + n \ln k \quad (3)$$

Fig. 5c shows a plot between  $\ln(-\ln[1 - x(t)])$  and  $\ln(t)$  for different temperatures and the plots were evaluated by using eqn (3). The value of  $n$  and  $k$  for different temperatures were

obtained from the linearly fitted lines, listed in Table S1 (ESI<sup>†</sup>). The obtained value of  $k$  in the current study (for ACN@ASW) is closer to our previous study (obtained from the co-deposited ACN and H<sub>2</sub>O films)<sup>12</sup> and is larger than the previously reported values,<sup>7,24</sup> estimated in similar experimental conditions.

The estimated value of  $n$  from curve fitting was between 1.84 and 1.60. It reflects that the crystallization kinetics is diffusion-controlled with particles growing into a predominantly spherical geometry as the theory of phase transformation by nucleation and growth would suggest.<sup>25,64,65</sup> However, a lower value of  $n$  suggests a low dimensional growth and the direction of crystal growth is limited, namely perpendicular to the surface. It again proves that ASW crystallization in ACN@ASW film has started at the surface rather than in the bulk. This implies that the diffusion of ACN through ASW increases the mobility of H<sub>2</sub>O molecules more at the interfaces (ASW–vacuum interface and ASW–ACN interface) compared to the bulk. It should be noted that the value of  $n$  cannot distinguish whether the crystallization is happening top-down or bottom-up. Fig. 5d shows an Arrhenius plot of  $\ln k$  versus ( $1/T$ ), derived from the analysis of the slope and intercept of the linearly fitted lines of the plot (c) for different temperatures. The activation energy ( $E_a$ ) of ASW crystallization was estimated to be  $\sim 53.0$  kJ mol<sup>-1</sup> from the slope of the linearly fitted line in Fig. 5d. However, the activation energy for crystallization of pure ASW films was previously reported<sup>13,24,63,66</sup> between 60–77 kJ mol<sup>-1</sup>. Several researchers<sup>57,67</sup> by decoupling the nucleation and growth kinetics of phase change suggested the energy barrier of the growth step to be 47–56 kJ mol<sup>-1</sup>. Thus, the obtained  $E_a$  value in our results, 53.0 kJ mol<sup>-1</sup> explains the dramatic acceleration of crystallization kinetics, where only the growth step was required for crystallization to occur. The lower activation energy in this report is attributed to the diffusion-induced crystallization of ASW. ACN being a larger molecule, its diffusion through the ASW can enhance the mobility of water molecules to overcome the crystallization barrier even at low temperatures, than its usual crystallization temperature.

## Conclusions

We have studied the effect of diffusion of multilayer ACN on the structure of ASW and provided an associated mechanism for ASW crystallization. We observed that when the ACN layer is placed below ASW, it induces crystallization faster, compared to the case when ACN was placed at the top of ASW. The faster kinetics occurs because crystallization happens from the top and bottom of the ASW film simultaneously and propagates into the bulk. This suggests that the diffusion of ACN through ASW increases the mobility of H<sub>2</sub>O molecules, more at the interfaces compared to the bulk. The crystallization kinetics and activation energy of ASW crystallization was estimated. Minimum ACN thickness to induce crystallization was found to be 30 ML for 150 ML of ASW. It is known that CI is found in many astrophysical environments and diffusion of molecules is

a key process in the chemistry of interstellar ices. These findings will open a path for the study of molecular diffusion and its effects on ASW structure for several organic molecules of interstellar relevance.

## Author contributions

T. P. proposed the project and supervised the progress. G. V. designed the experiments. G. V. and B. K. M. have performed the experiment. G. V., B. K. M., and R. R. J. M. have analysed the results. The manuscript was written with the contributions of all authors.

## Conflicts of interest

The authors declare no competing financial interests.

## Acknowledgements

We acknowledge the Science and Engineering Research Board (SERB), Department of Science and Technology (DST), Government of India for research funding. T. P. acknowledges funding from the Centre of Excellence on Molecular Materials and Functions under the Institution of Eminence scheme of IIT Madras. We thank Dr Bhalamurugan Sivaraman for his valuable comments and discussions. We also thank Soham Chowdhury for his contributions to this work. G. V. thanks IITM for his research fellowship. B. K. M. thanks the Council of Scientific & Industrial Research (CSIR) for his research fellowship.

## References

- 1 C. A. Angell, Amorphous Water, *Annu. Rev. Phys. Chem.*, 2004, **55**, 559–583.
- 2 C. A. Angell, Insights into phases of liquid water from study of its unusual glass-forming properties, *Science*, 2008, **319**, 582–587.
- 3 P. Jenniskens and D. F. Blake, Structural Transitions in Amorphous Water Ice and Astrophysical Implications, *Science*, 1994, **265**, 753–756.
- 4 R. S. Smith, N. G. Petrik, G. A. Kimmel and B. D. Kay, Thermal and nonthermal physiochemical processes in nanoscale films of amorphous solid water, *Acc. Chem. Res.*, 2012, **45**, 33–42.
- 5 N. Watanabe and A. Kouchi, Ice surface reactions: A key to chemical evolution in space, *Prog. Surf. Sci.*, 2008, **83**, 439–489.
- 6 J. Ghosh, R. G. Bhui, G. Vishwakarma and T. Pradeep, Formation of Cubic Ice via Clathrate Hydrate, Prepared in Ultrahigh Vacuum under Cryogenic Conditions, *J. Phys. Chem. Lett.*, 2020, **11**, 26–32.
- 7 J. Ghosh, G. Vishwakarma, S. Das and T. Pradeep, Facile Crystallization of Ice I<sub>h</sub> via Formaldehyde Hydrate in

- Ultrahigh Vacuum under Cryogenic Conditions, *J. Phys. Chem. C*, 2021, **125**, 4532–4539.
- 8 A. Falenty, T. C. Hansen and W. F. Kuhs, Cubic Ice Formation and Annealing during CO<sub>2</sub> Clathrate Hydrate Decomposition at Low Temperatures, *Phys. Chem. Ice*, 2010, 411.
  - 9 A. Falenty and W. F. Kuhs, ‘Self-Preservation’ of CO<sub>2</sub> Gas Hydrates-Surface Microstructure and Ice Perfection, *J. Phys. Chem. B*, 2009, **113**, 15975–15988.
  - 10 W. F. Kuhs, G. Genov, D. K. Staykova and T. Hansen, Ice perfection and onset of anomalous preservation of gas hydrates, *Phys. Chem. Chem. Phys.*, 2004, **6**, 4917–4920.
  - 11 T. Hama, S. Ishizuka, T. Yamazaki, Y. Kimura, A. Kouchi, N. Watanabe, T. Sugimoto and V. Pirronello, Fast crystalline ice formation at extremely low temperature through water/neon matrix sublimation, *Phys. Chem. Chem. Phys.*, 2017, **19**, 17677.
  - 12 G. Vishwakarma, J. Ghosh and T. Pradeep, Desorption-induced evolution of cubic and hexagonal ices in an ultrahigh vacuum and cryogenic temperatures, *Phys. Chem. Chem. Phys.*, 2021, **23**, 24052–24060.
  - 13 D. H. Lee and H. Kang, Acid-Promoted Crystallization of Amorphous Solid Water, *J. Phys. Chem. C*, 2018, **122**, 24164–24170.
  - 14 S. M. McClure, E. T. Barlow, M. C. Akin, P. L. Tanaka, D. J. Safarik, T. M. Truskett and C. B. Mullins, Effect of dilute nitric acid on crystallization and fracture of amorphous solid water films, *J. Phys. Chem. C*, 2007, **111**, 10438–10447.
  - 15 R. Souda, Effects of methanol on crystallization of water in the deeply supercooled region, *Phys. Rev. B: Condens. Matter Mater. Phys.*, 2007, **75**, 184116.
  - 16 R. Souda, Crystallization of thin water films on graphite: Effects of *n*-hexane, formaldehyde, acetone, and methanol additives, *Appl. Surf. Sci.*, 2015, **357**, 1809–1815.
  - 17 R. A. May, R. S. Smith and B. D. Kay, Probing the interaction of amorphous solid water on a hydrophobic surface: Dewetting and crystallization kinetics of ASW on carbon tetrachloride, *Phys. Chem. Chem. Phys.*, 2011, **13**, 19848–19855.
  - 18 R. Souda, Probing surface properties and glass - Liquid transition of amorphous solid water: Temperature-programmed TOF-SIMS and TPD studies of adsorption/desorption of hexane, *J. Phys. Chem. B*, 2005, **109**, 21879–21883.
  - 19 R. Souda and T. Aizawa, Crystallization kinetics of water on graphite, *Phys. Chem. Chem. Phys.*, 2018, **20**, 21856–21863.
  - 20 R. A. May, R. S. Smith and B. D. Kay, Probing the interaction of amorphous solid water on a hydrophobic surface: Dewetting and crystallization kinetics of ASW on carbon tetrachloride, *Phys. Chem. Chem. Phys.*, 2011, **13**, 19848–19855.
  - 21 P. Jenniskens and D. F. Blake, Crystallization of Amorphous Water Ice in the Solar System, *Astrophys. J.*, 1996, **473**, 1104–1113.
  - 22 C. Yuan, R. S. Smith and B. D. Kay, Surface and bulk crystallization of amorphous solid water films: Confirmation of “top-down” crystallization, *Surf. Sci.*, 2016, **652**, 350–354.
  - 23 P. Löfgren, P. Ahlström, J. Lausma, B. Kasemo and D. Chakarov, Crystallization kinetics of thin amorphous water films on surfaces, *Langmuir*, 2003, **19**, 265–274.
  - 24 R. S. Smith, J. Matthiesen, J. Knox and B. D. Kay, Crystallization kinetics and excess free energy of H<sub>2</sub>O and D<sub>2</sub>O nanoscale films of amorphous solid water, *J. Phys. Chem. A*, 2011, **115**, 5908–5917.
  - 25 W. Hage, A. Hallbrucker, E. Mayer and G. P. Johari, Crystallization kinetics of water below 150 K, *J. Chem. Phys.*, 1994, **100**, 2743–2747.
  - 26 T. Kondo, H. S. Kato, M. Bonn and M. Kawai, Deposition and crystallization studies of thin amorphous solid water films on Ru(0001) and on CO-precovered Ru(0001), *J. Chem. Phys.*, 2007, **127**, 094703.
  - 27 E. H. G. Backus, M. L. Grecea, A. W. Kleyn and M. Bonn, Surface crystallization of amorphous solid water, *Phys. Rev. Lett.*, 2004, **92**, 236101.
  - 28 E. H. G. Backus and M. Bonn, Theory of bulk, surface and interface phase transition kinetics in thin films, *J. Chem. Phys.*, 2004, **121**, 1038.
  - 29 T. Hama and N. Watanabe, *Chem. Rev.*, 2013, **113**, 8783–8839.
  - 30 D. C. Jewitt and J. Luu, Crystalline water ice on the Kuiper belt object (50000) Quaoar, *Nature*, 2004, **432**(7018), 731–733.
  - 31 F. Merlin, A. Guilbert, C. Dumas, M. A. Barucci, C. De Bergh and P. Vernazza, Properties of the icy surface of the TNO 136108 (2003 EL), *Astron. Astrophys.*, 2007, **466**, 1185–1188.
  - 32 A. Omont, S. H. Moseley, T. Forveille, W. J. Glaccum, P. M. Harvey, L. Likkell, R. F. Loewenstein, C. M. Lisse, A. Omont, S. H. Moseley, T. Forveille, W. J. Glaccum, P. M. Harvey, L. Likkell, R. F. Loewenstein and C. M. Lisse, Observations of 40–70 Micron Bands of Ice in IRAS 09371 + 1212 and Other Stars, *Astrophys. J., Lett.*, 1990, **355**, L27.
  - 33 B. A. McGuire, 2021 Census of Interstellar, Circumstellar, Extragalactic, Protoplanetary Disk, and Exoplanetary Molecules, *Astrophys. J., Suppl. Ser.*, 2022, **259**, 30.
  - 34 D. J. Burke and W. A. Brown, Ice in space: surface science investigations of the thermal desorption of model interstellar ices on dust grain analogue surfaces, *Phys. Chem. Chem. Phys.*, 2010, **12**, 5947–5969.
  - 35 W. Tielens and A. G. G. M. Hagen, Model calculations of the molecular composition of interstellar grain mantles, *Astron. Astrophys.*, 1982, **114**, 245–260.
  - 36 B. Maté, S. Cazaux, M. Á. Satorre, G. Molpeceres, J. Ortigoso, C. Millán and C. Santonja, Diffusion of CH<sub>4</sub> in amorphous solid water, *Astron. Astrophys.*, 2020, **643**, 163.
  - 37 F. Mispelaer, P. Theulé, H. Aouididi, J. Noble, F. Duvernay, G. Danger, P. Roubin, O. Morata, T. Hasegawa and T. Chiavassa, Diffusion measurements of CO, H<sub>2</sub>CO, and NH<sub>3</sub> in amorphous water ice, *Astron. Astrophys.*, 2013, **555**, 13.
  - 38 R. A. May, R. S. Smith and B. D. Kay, The release of trapped gases from amorphous solid water films. I. ‘top-down’ crystallization-induced crack propagation probed using the molecular volcano, *J. Chem. Phys.*, 2013, **138**(10), 104501.
  - 39 R. Alan May, R. Scott Smith and B. D. Kay, The release of trapped gases from amorphous solid water films. II. ‘Bottom-up’ induced desorption pathways, *J. Chem. Phys.*, 2013, **138**, 104502.

- 40 R. Gopi, N. Ramanathan and K. Sundararajan, Acetonitrile-water hydrogen-bonded interaction: Matrix-isolation infrared and ab initio computation, *J. Mol. Struct.*, 2015, **1094**, 118–129.
- 41 V. K. S. Bahr, Interaction of acetonitrile with thin films of solid water, *J. Chem. Phys.*, 2009, **130**, 214509.
- 42 R. Souda, Hydration–Dehydration of Acetonitrile and Methanol in Amorphous Solid Water, *J. Phys. Chem. C*, 2016, **120**, 934–943.
- 43 R. G. Bhuin, R. R. J. Methikkalam, B. Sivaraman and T. Pradeep, Interaction of Acetonitrile with Water–Ice: An Infrared Spectroscopic Study, *J. Phys. Chem. C*, 2015, **119**, 11524–11532.
- 44 J. E. Schaff and J. T. Roberts, Interaction of Acetonitrile with the Surfaces of Amorphous and Crystalline Ice, *Langmuir*, 1999, **15**, 7232–7237.
- 45 J. E. Schaff and J. T. Roberts, Toward an understanding of the surface chemical properties of ice: Differences between the amorphous and crystalline surfaces, *J. Phys. Chem.*, 1996, **100**, 14151–14160.
- 46 P. M. Solomon, K. B. Jefferts, A. A. Penzias and R. W. Wilson, Detection of Millimeter Emission Lines from Interstellar Methyl Cyanide, *Astrophys. J.*, 1971, **168**, L107.
- 47 B. L. Ulich and E. K. Conklin, Detection of methyl cyanide in Comet Kohoutek, *Nature*, 1974, **248**, 121.
- 48 S. Bag, R. G. Bhuin, R. R. J. Methikkalam, T. Pradeep, L. Kephart, J. Walker, K. Kuchta, D. Martin and J. Wei, Development of ultralow energy (1–10 eV) ion scattering spectrometry coupled with reflection absorption infrared spectroscopy and temperature programmed desorption for the investigation of molecular solids, *Rev. Sci. Instrum.*, 2014, **85**, 1–7.
- 49 R. R. J. Methikkalam, R. G. Bhuin, J. Ghosh, B. Sivaraman and T. Pradeep, Interaction of Acetonitrile with Alcohols at Cryogenic Temperatures, *J. Phys. Chem. C*, 2017, **121**, 2822–2835.
- 50 J. Ghosh, R. R. J. Methikkalam, R. G. Bhuin, G. Ragupathy, N. Choudhary, R. Kumar and T. Pradeep, Clathrate hydrates in interstellar environment, *Proc. Natl. Acad. Sci. U. S. A.*, 2019, **116**, 1526–1531.
- 51 H. Kang, T. H. Shin, S. C. Park, I. K. Kim and S. J. Han, Acidity of hydrogen chloride on ice, *J. Am. Chem. Soc.*, 2000, **122**, 9842–9843.
- 52 Y. Kim, E. Moon, S. Shin and H. Kang, Acidic Water Monolayer on Ruthenium(0001), *Angew. Chem.*, 2012, **124**, 12978–12981.
- 53 H. Kang, Chemistry of Ice Surfaces. Elementary Reaction Steps on Ice Studied by Reactive Ion Scattering, *Acc. Chem. Res.*, 2005, **38**, 893–900.
- 54 Y. Kim, E. S. Moon, S. Shin and H. Kang, Acidic water monolayer on ruthenium(0001), *Angew. Chem., Int. Ed.*, 2012, **51**, 12806–12809.
- 55 J. Cyriac, T. Pradeep, H. Kang, R. Souda and R. G. Cooks, Low-Energy Ionic Collisions at Molecular Solids, *Chem. Rev.*, 2012, **112**, 5356–5411.
- 56 D. J. Safarik and C. B. Mullins, A new methodology and model for characterization of nucleation and growth kinetics in solids, *J. Chem. Phys.*, 2003, **119**, 12510.
- 57 D. J. Safarik and C. B. Mullins, The nucleation rate of crystalline ice in amorphous solid water, *J. Chem. Phys.*, 2004, **121**, 6003–6010.
- 58 D. J. Safarik, R. J. Meyer and C. B. Mullins, Thickness dependent crystallization kinetics of sub-micron amorphous solid water films, *J. Chem. Phys.*, 2003, **118**, 4660.
- 59 D. J. Safarik and C. B. Mullins, Surface phase transformation kinetics: A geometrical model for thin films of nonvolatile and volatile solids, *J. Chem. Phys.*, 2002, **117**, 8110–8123.
- 60 A. Bar-Nun, J. Dror, E. Kochavi and D. Laufer, Amorphous water ice and its ability to trap gases, *Phys. Rev. B: Condens. Matter Mater. Phys.*, 1987, **35**, 2427–2435.
- 61 M. Avrami, Kinetics of phase change. I: General theory, *J. Chem. Phys.*, 1939, **7**, 1103–1112.
- 62 M. Avrami, Kinetics of phase change. II Transformation-time relations for random distribution of nuclei, *J. Chem. Phys.*, 1940, **8**, 212–224.
- 63 T. Kondo, H. S. Kato, M. Bonn and M. Kawai, Deposition and crystallization studies of thin amorphous solid water films on Ru(0001) and on CO-precovered Ru(0001), *J. Chem. Phys.*, 2007, **127**, 094703.
- 64 C. N. R. Rao and K. J. Rao, *Phase transitions in solids: an approach to the study of the chemistry and physics of solids*, McGraw-Hill, New York, 1978.
- 65 R. H. Doremus, *Rates of phase transformations*, Academic Press, New York, 1985.
- 66 C. Yuan, R. S. Smith and B. D. Kay, Communication: Distinguishing between bulk and interface-enhanced crystallization in nanoscale films of amorphous solid water, *J. Chem. Phys.*, 2017, **146**, 031102.
- 67 Z. Dohnálek, G. A. Kimmel, R. L. Ciolli, K. P. Stevenson, R. S. Smith and B. D. Kay, The effect of the underlying substrate on the crystallization kinetics of dense amorphous solid water films, *J. Chem. Phys.*, 2000, **112**, 5932–5941.

## Supplementary information

### Rapid Crystallization of Amorphous Solid Water by Porosity Induction

Gaurav Vishwakarma<sup>a</sup>, Bijesh K. Malla<sup>a</sup>, Rabin Rajan J. Methikkalam<sup>b</sup> and Thalappil Pradeep<sup>a\*</sup>

<sup>a</sup>DST Unit of Nanoscience (DST UNS) and Thematic Unit of Excellence (TUE), Department of Chemistry, Indian Institute of Technology Madras, Chennai 600036, India

<sup>b</sup>Department of Chemistry, Mar Ivanios College, Thiruvananthapuram, Kerala 695015, India.

#### Corresponding author

\*Email: [pradeep@iitm.ac.in](mailto:pradeep@iitm.ac.in)

This PDF file includes:

Experimental section (page S2)

Fig. S1 to S14 (page S3-S16)

Table S1 (page S17)

## Experimental section

### RAIRS Setup

The ice films were investigated using a Bruker Vertex 70 FT-IR spectrometer connected to the vacuum chamber through a ZnSe viewport. IR beam was focused on the sample through a gold-plated mirror at an incident angle of  $80 \pm 7^\circ$ . The reflected beam from the sample was refocused to an external liquid nitrogen cooled MCT (mercury cadmium telluride) detector. The IR beam path outside the vacuum chamber was purged with dry nitrogen to avoid absorption by atmospheric gases, mainly water vapor and carbon dioxide. RAIRS spectra were collected in the range of  $4000\text{--}550\text{ cm}^{-1}$  and averaged to 512 scans with a spectral resolution of  $2\text{ cm}^{-1}$ .

### TPD setup

TPD is a well-known technique in surface science and have been used for analysis of molecular solids. The TPD module was purchased from Extrel CMS and was attached to the chamber on a 6-inch flange through a Z-axis manipulator. The module consisted of an electron impact source, a mass analyser and a detector. The mass analyser was a quadrupole with 1 to 500 mass range and 1 amu resolution. For TPD of ACN in different compositions, as deposited ices were heated at a rate of  $10\text{ K}\cdot\text{min}^{-1}$  and suitable masses of the desorbed species ( $m/z = 41$  for  $\text{CH}_3\text{CN}^+$ ,  $m/z = 18$  for  $\text{H}_2\text{O}^+$ ) were selected by the mass spectrometer analyzer, and the intensity of the desorbed species was plotted as a function of substrate temperature.

### SIMS setup

$\text{Cs}^+$  ( $m/z$  133) is a well-known projectile for SIMS and  $\text{Cs}^+$  scattering is a good technique to characterize molecular solids. We have carried out ion collision experiments using  $\text{Cs}^+$  of 120 eV kinetic energy produced from a low-energy alkali ion gun (Kimball Physics Inc.). The scattered ions consist of  $\text{Cs}^+$  and the products arising from two other processes, such as reactive ion scattering (RIS) and low energy sputtering. RIS is a peculiar property of the alkali ions (here  $\text{Cs}^+$ ). The low energy collision of  $\text{Cs}^+$  converts the neutral adsorbate species (X) to gas phase ions ( $\text{CsX}^+$ ) by association reaction. The resulting scattered ions were analysed using a quadruple mass analyser. We have used the RIS signal intensities, corresponding to  $\text{Cs}(\text{CH}_3\text{CN})^+$  ( $m/z$  174),  $\text{Cs}(\text{H}_2\text{O})^+$  ( $m/z$  151), and  $\text{Cs}(\text{H}_2\text{O})_2^+$  ( $m/z$  169), to identify and understand the molecules appearing on the surfaces upon heating. Here, the signal intensities are directly proportional to the surface population of the molecule on the ice surfaces. The sample preparation for SIMS is the same as described in Experimental section (Main article). As prepared samples were heated at a  $5\text{ K min}^{-1}$  to the set temperatures for SIMS experiments



### Supplementary information 1:

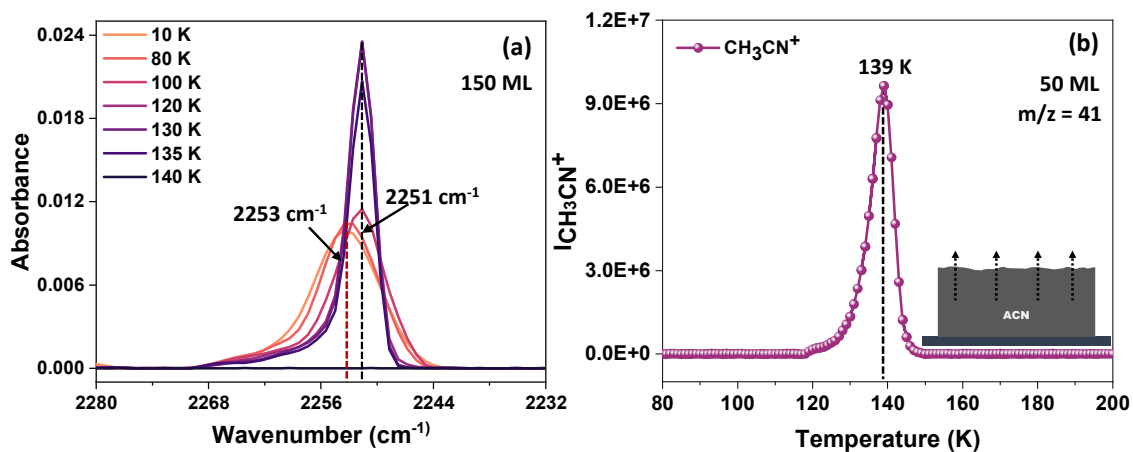


Fig. S1 (a) Temperature-dependent RAIRS spectra of 150 ML of pure ACN in the C≡N stretching region. ACN was deposited at 10 K and heated at a rate of 2 K  $\text{min}^{-1}$  to the desorption temperature of ACN. ACN was found in two phases - amorphous phase (broad peak at  $\sim 2253 \text{ cm}^{-1}$ ) in the window of 10-100 K, and crystalline phase (sharp peak at  $2251 \text{ cm}^{-1}$ ) above 100 K. ACN desorbed from the substrate at  $\sim 140 \text{ K}$ . (b) Desorption of 50 ML of ACN during  $10 \text{ K min}^{-1}$  TPD-MS experiment. Here, the intensity versus temperature of  $\text{CH}_3\text{CN}^+$  ( $m/z = 41$ ) desorption is plotted.

## Supplementary information 2:

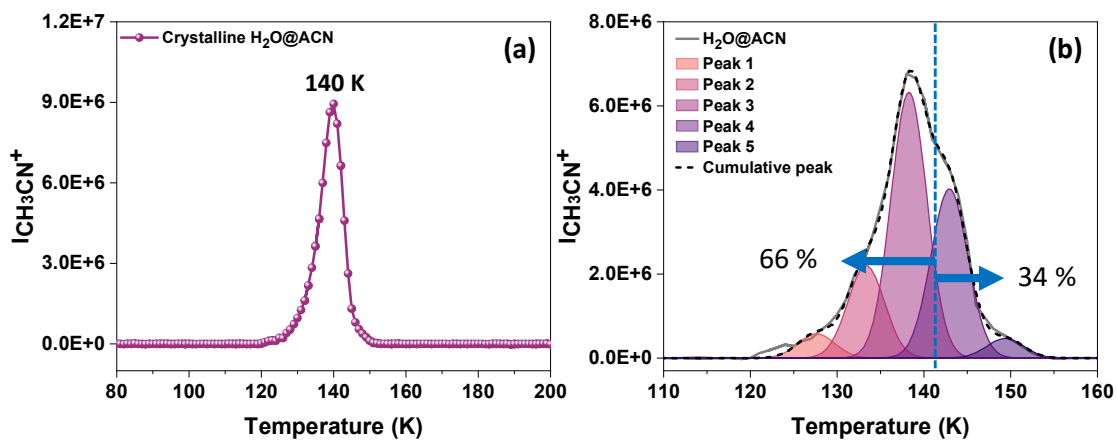
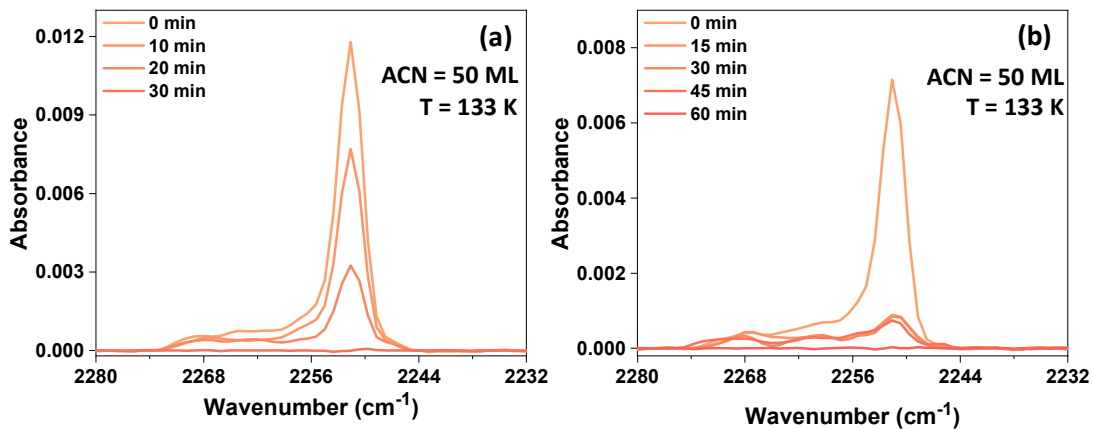


Fig. S2 (a) Desorption of 50 ML of ACN from 150 ML of crystalline H<sub>2</sub>O ice during 10 K min<sup>-1</sup> TPD-MS experiment. Here, the intensity versus temperature of CH<sub>3</sub>CN<sup>+</sup> (m/z = 41) desorption is plotted. 150 ML of crystalline H<sub>2</sub>O ice was prepared by deposition of H<sub>2</sub>O vapor on Ru(0001) at 10 K and heated to 150 K. The crystalline ice was then cooled down to 10 K and 50 ML of ACN was deposited on top of it. (b) Deconvoluted peaks of Fig. 1b (main article). It shows that about ~30% of the deposited ACN desorbs from ASW.

### Supplementary information 3:



**Fig. S3** Time-dependent RAIRS spectra of (a) ACN@ASW and (b) ASW@ACN films at 133 K in the C≡N stretching region. Ice films were prepared by vapor deposition on Ru(0001) at 10 K and heated to 133 K at a rate of 2 K min<sup>-1</sup>. The composition of films were (a) ACN(50 ML)@ASW(150 ML) and (b) ASW(150 ML)@ACN(50 ML). The peak intensity for ASW@ACN film is smaller than that of ACN@ASW film, because, when ACN was on top of ASW, a larger fraction of ACN will desorb in former case upon heating ice sample to 133 K. Also, the time required for complete ACN diffusion-desorption is nearly double in case of ASW@ACN film. The increased desorption time of ACN at 133 K is because, when ACN was on top of ASW, a fraction of ACN will diffuse into the ASW (through pores formed during ASW deposition) and will return to the surface and subsequently desorb which required an additional time.

#### Supplementary information 4:

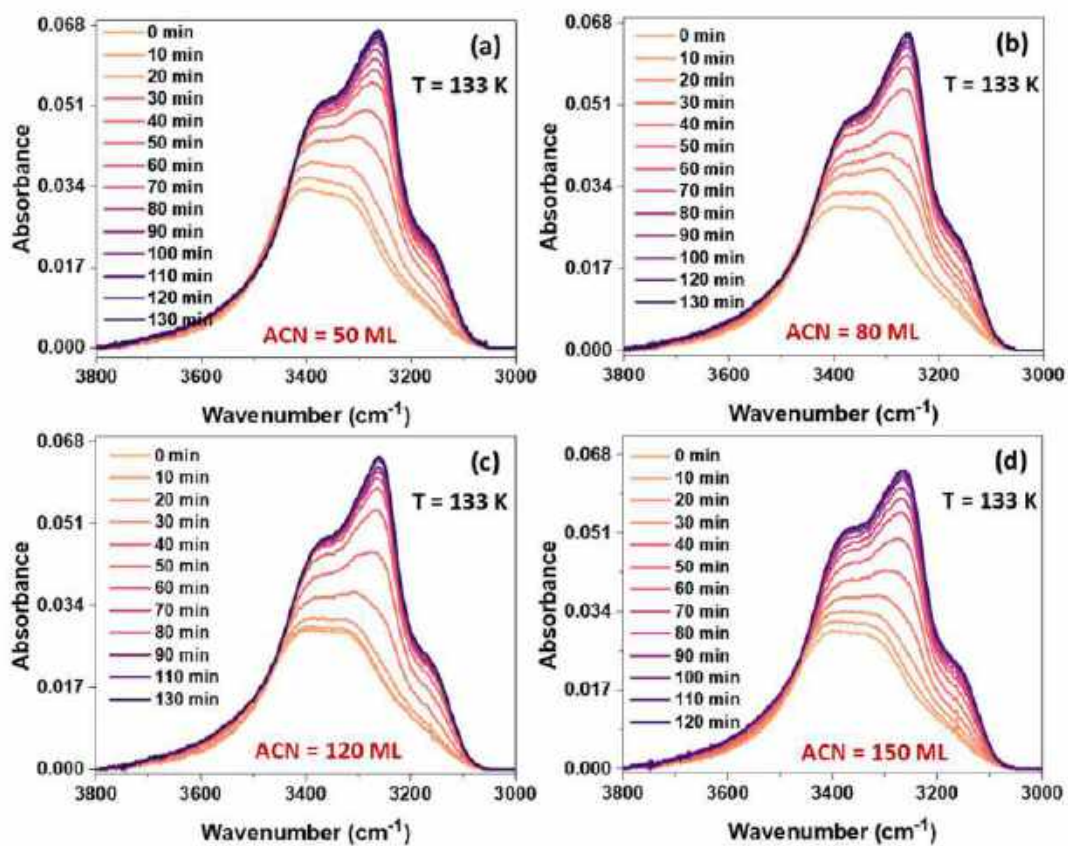


Fig. S4 Time-dependent RAIRS spectra of ACN@ASW films at 133 K in the O-H stretching region. ACN film thickness was varied from 50-150 ML while keeping ASW film thickness constant at 150 ML. Ice films were prepared by vapor deposition on Ru(0001) at 10 K and heated to 133 K at a rate of 2 K  $\text{min}^{-1}$ . The compositions of films were (a) ACN(50 ML)@ASW(150 ML), (b) ACN(80 ML)@ASW(150 ML), (c) ACN(120 ML)@ASW(150 ML) and (d) ACN(150 ML)@ASW(150 ML). The data show gradual crystallization of ASW after ACN desorption.

Supplementary information 5:

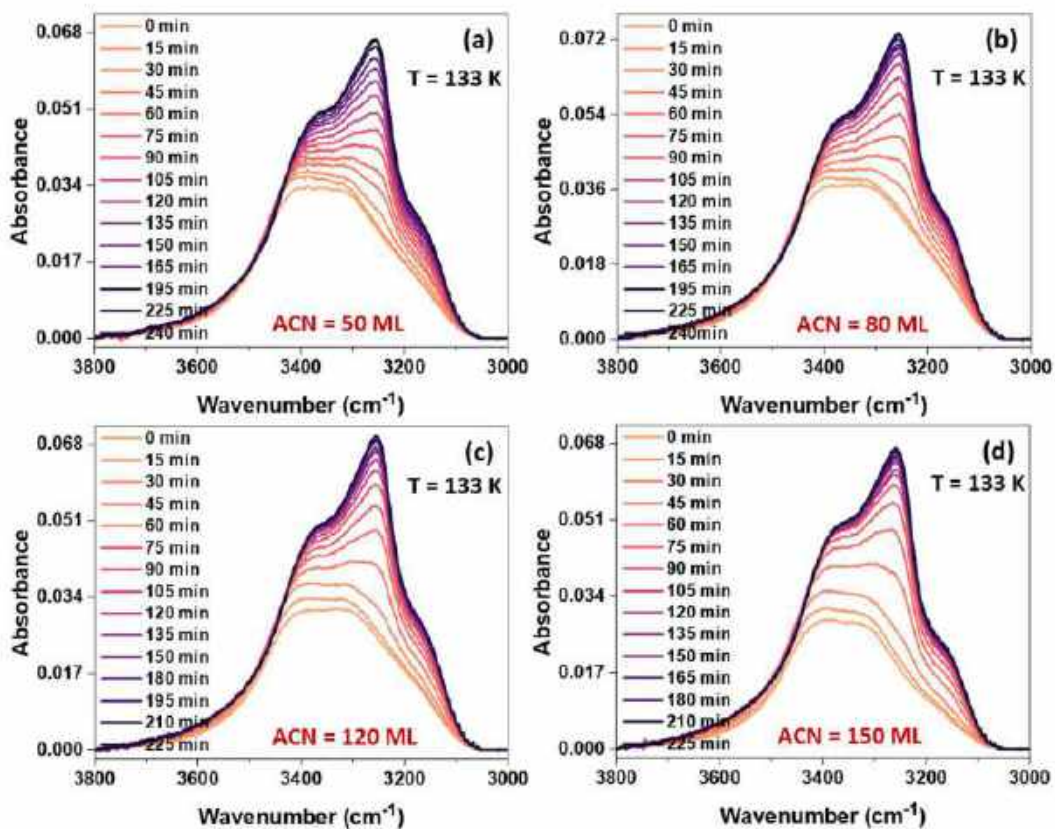
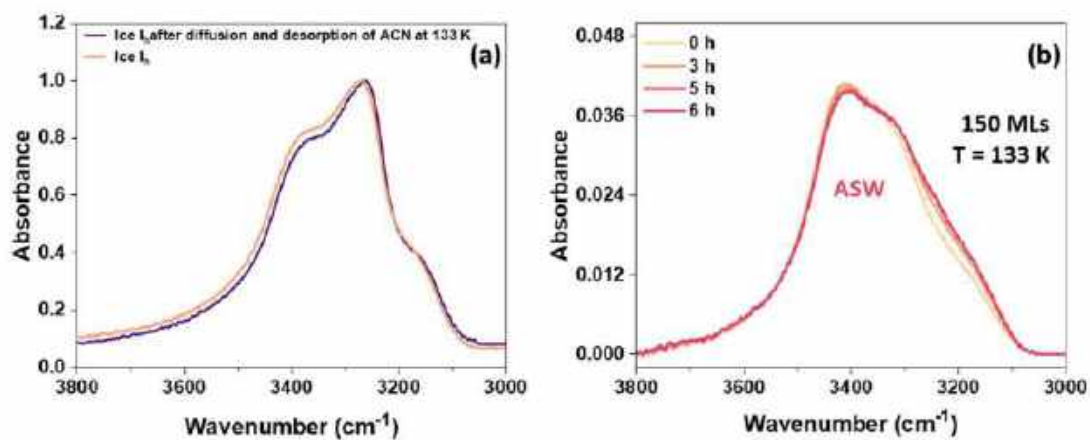


Fig. S5 Time-dependent RAIRS spectra of ASW@ACN films at 133 K in the O-H stretching region. ACN film thickness was varied from 50-150 ML while keeping the ASW film thickness constant at 150 ML. Ice films were prepared by vapor deposition on Ru(0001) at 10 K and heated to 133 K at a rate of 2 K min<sup>-1</sup>. The compositions of films were (a) ASW(150 ML)@ACN(50 ML), (b) ASW(150 ML)@ACN(80 ML), (c) ASW(150 ML)@ACN(120 ML) and (d) ASW(150 ML)@ACN(150 ML). The data show gradual crystallization of ASW after ACN diffusion and desorption.

## Supplementary information 6:



**Fig. S6** (a) Normalized RAIR spectra of Ice I<sub>h</sub> obtained after diffusion and desorption of ACN from ACN@H<sub>2</sub>O film at 133 K (blue trace) and Ice I<sub>h</sub> obtained after heating the vapor-deposited solid H<sub>2</sub>O at 155 K (orange trace). Samples were prepared at 10 K and heated at a rate of 2 K.min<sup>-1</sup> to the mentioned temperatures. Both the spectrum were almost identical and confirms the formation of Ice I<sub>h</sub> after diffusion and desorption of ACN from ACN@H<sub>2</sub>O film (b) Time-dependent RAIR spectra of 150 MLs of H<sub>2</sub>O film deposited on Ru(0001) at 10 K and annealed at a rate of 2 K.min<sup>-1</sup> to 133 K, in the O-H stretching region. At 133 K, ASW was kept for several hours but remains amorphous, which confirms pure H<sub>2</sub>O could not crystallize at such low temperatures without external deriving force. This also suggests the absence of any role for Ru(0001) in ASW crystallization.



## Supplementary information 7:

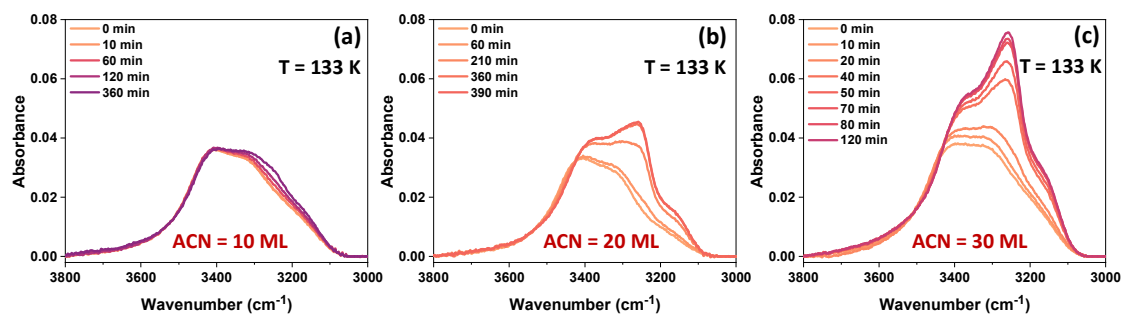


Fig. S7 Time-dependent RAIRS spectra of ACN@ASW films at 133 K in the O–H stretching region. ACN film thicknesses were varied from 10–30 ML and ASW film thicknesses were kept constant at 150 ML. Ice films were prepared by vapor deposition on Ru(0001) at 10 K and heated to 133 K at a rate of 2 K min<sup>-1</sup>. The composition of films were (a) ACN(10 ML)@ASW(150 ML), (b) ACN(20 ML)@ASW(150 ML) and (c) ACN(30 ML)@ASW(150 ML).

Supplementary information 8:

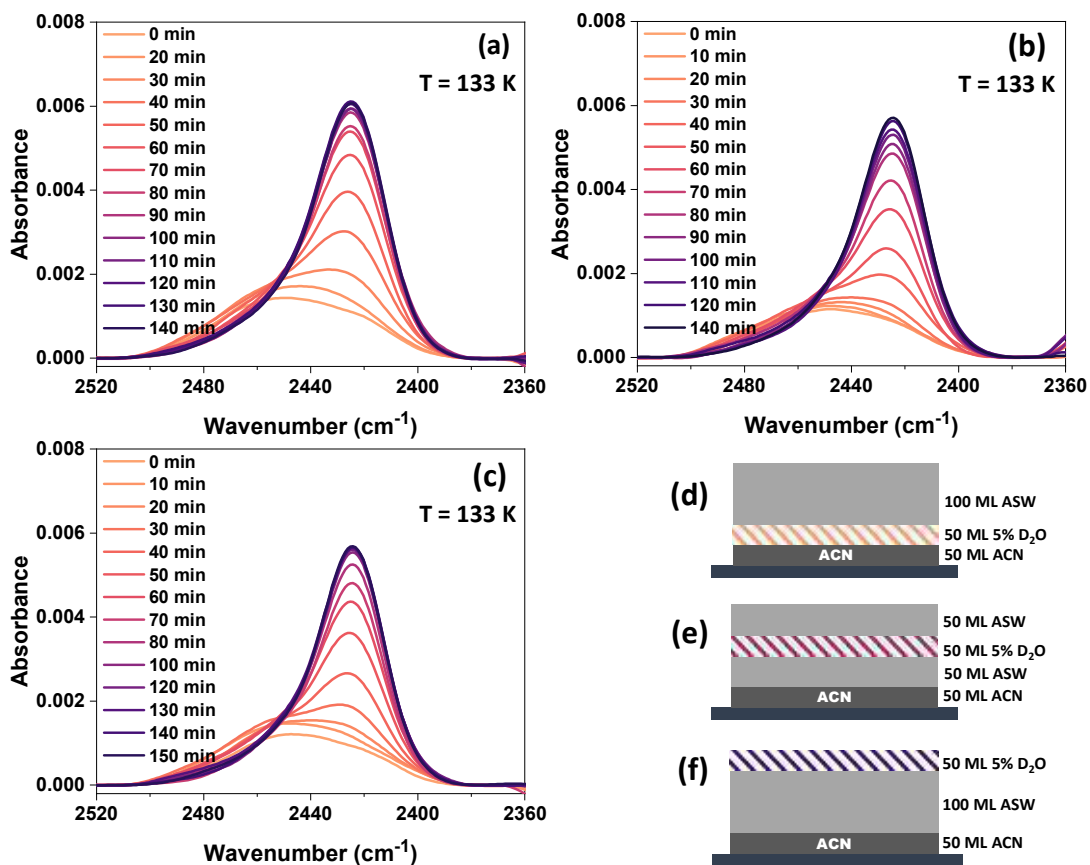


Fig. S8 Time-dependent RAIRS spectra of ACN@ASW film with HDO layer, at 133 K in the O–D stretching region. The ice films were prepared by placing a 50 ML HDO (5% D<sub>2</sub>O in H<sub>2</sub>O) layer in ASW, (a) near ACN film, (b) 50 ML away from ACN layer and (c) 100 ML away from ACN layer. The film was sequentially deposited on Ru(0001) at 10 K and heated at a rate of 2 K min<sup>-1</sup> to 133 K. Panels (d), (e), and (f) show the compositions of sequentially deposited ACN, ASW and HDO layers for which RAIRS spectra are given in (a), (b), and (c), respectively.

Supplementary information 9:

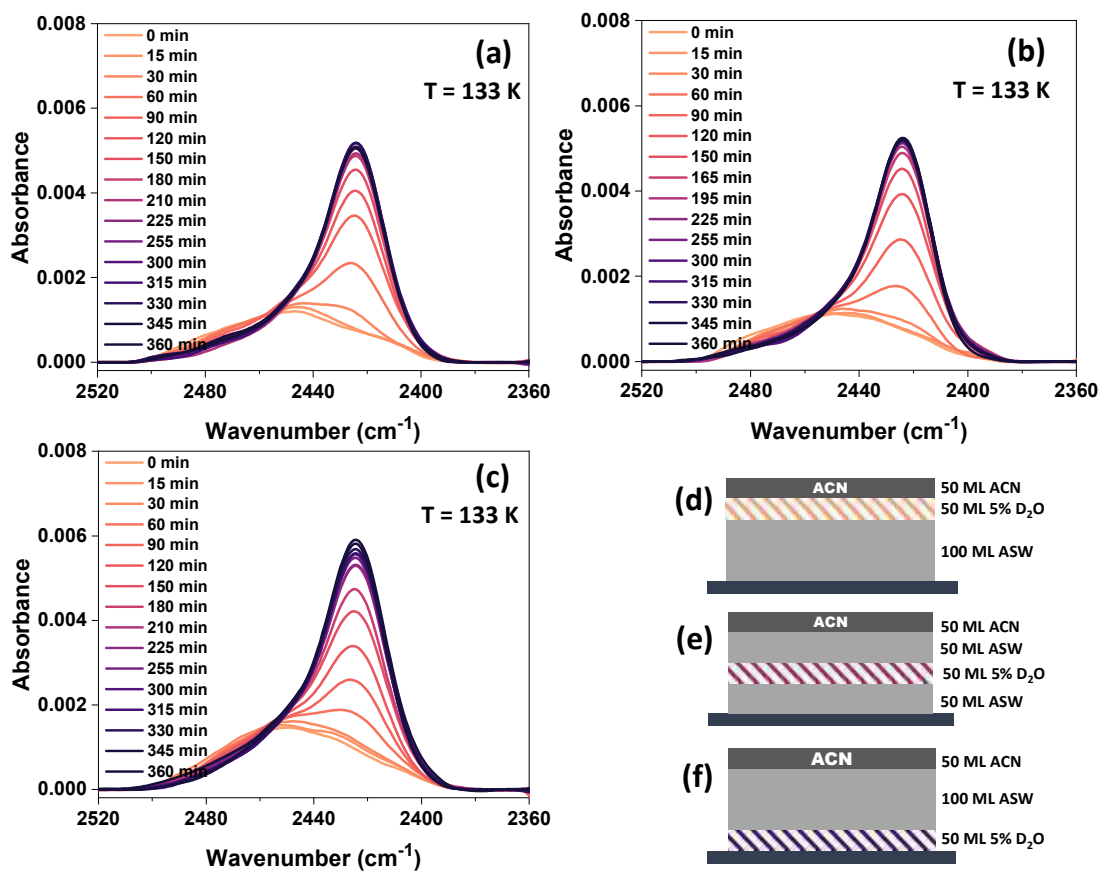


Fig. S9 Time-dependent RAIRS spectra of ASW@ACN film with HDO layer, at 133 K in the O–D stretching region. The ice films were prepared by placing a 50 ML HDO (5% D<sub>2</sub>O in H<sub>2</sub>O) layer in ASW, (a) near ACN film, (b) 50 ML away from ACN layer and (c) 100 ML away from ACN layer. The film was sequentially deposited on Ru(0001) at 10 K and heated at a rate of 2 K min<sup>-1</sup> to 133 K. Panels (d), (e), and (f) show the compositions of sequentially deposited ACN, ASW and HDO layers for which RAIRS spectra are given in (a), (b), and (c), respectively.

Supplementary information 10:

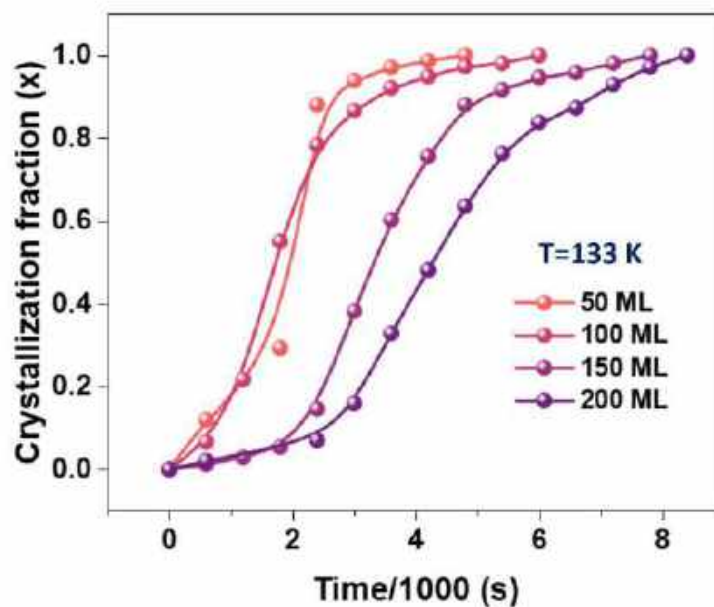


Fig. S10 The CF versus time curves for ACN@ASW films with varying ASW film thickness (50-200 ML), and keeping ACN layer thickness constant at 50 ML, obtained from isothermal RAIRS measurements at 133 K. The CF was calculated from a vertical cut at  $3260\text{ cm}^{-1}$  in the O-H stretching band of the time-dependent RAIRS spectra, shown in Fig. S10a, b, c and S5a.

## Supplementary information 11:

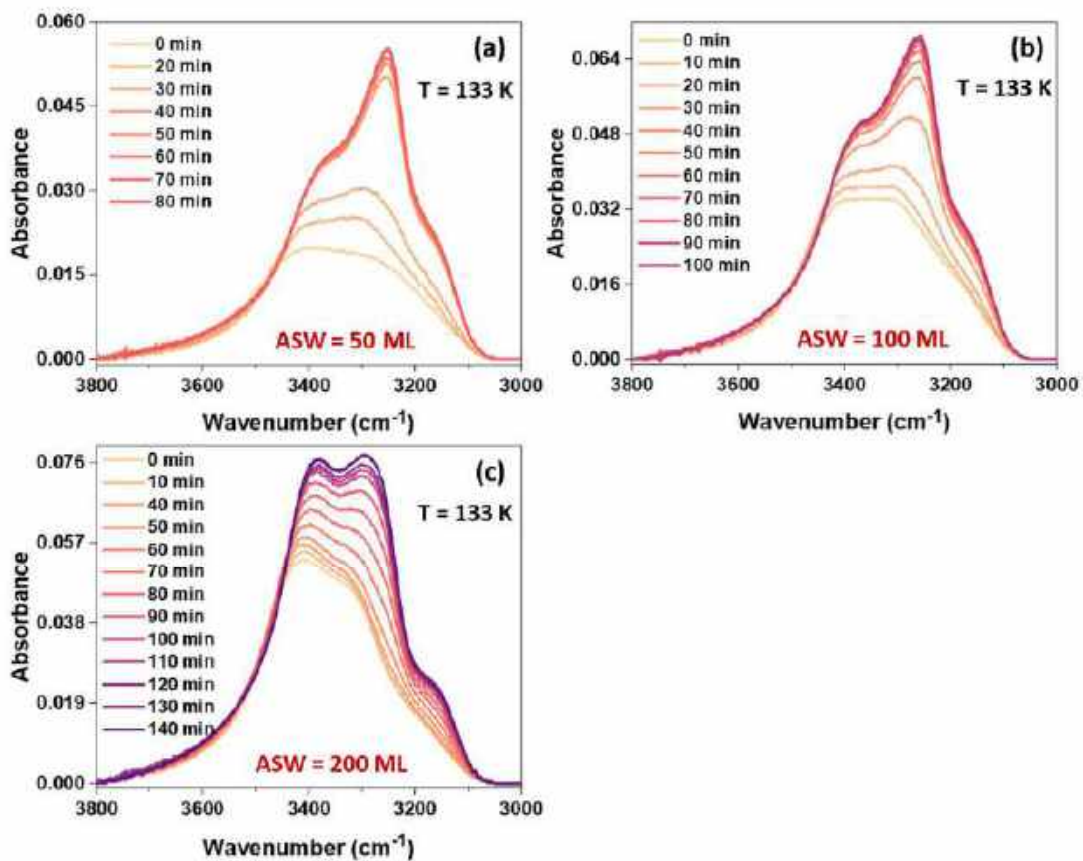


Fig. S11 Time-dependent RAIRS spectra of ACN@ASW films at 133 K in the O-H stretching region. ACN film thickness was kept constant, 50 ML and ASW film thickness was varied from 50-200 ML. Ice films were prepared by vapor deposition on Ru(0001) at 10 K and heated to 133 K at a rate of 2 K min<sup>-1</sup>. The composition of films are (a) ACN(50 ML)@ASW(50 ML), (b) ACN(50 ML)@ASW(100 ML), and (c) ACN(50 ML)@ASW(200 ML). The data shows that the time required for the crystallization increases with increase in ASW thickness.

Supplementary information 12:

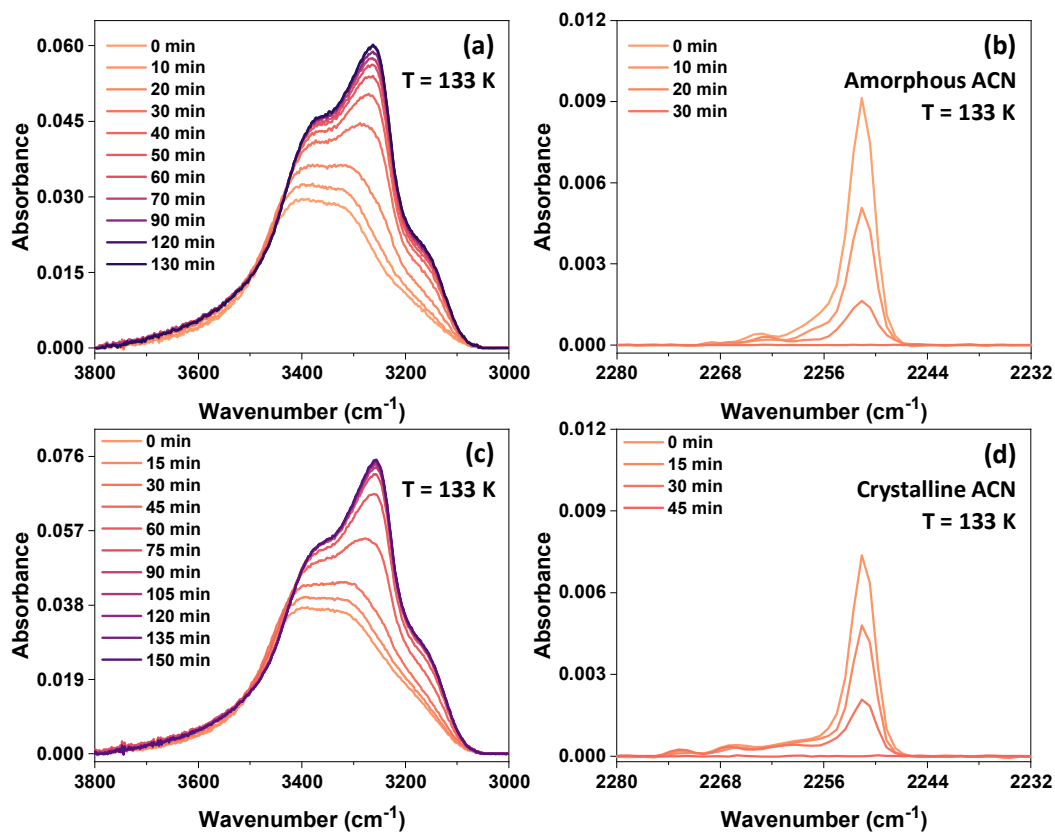


Fig. S12 (a) and (b) Time-dependent RARS spectra of ACN(50 ML)@ASW(150 ML) films at 133 K in the O-H and C≡N stretching region, respectively. Ice films were prepared by vapor deposition on Ru(0001) at 10 K and heated to 133 K at a rate of 2 K min<sup>-1</sup>. (c) and (d) Time-dependent RARS spectra of ACN(50 ML)@ASW(150 ML) films at 133 K in the O-H and C≡N stretching region, respectively. Here, first, 50 ML of ACN was deposited at 10 K and heated to 110 K, above crystallization temperature of ACN to prepare a crystalline ACN film, after that ACN film was cooled down to 10 K. Finally, H<sub>2</sub>O vapor was deposited on top of crystalline ACN film at 10 K. As prepared ice film was heated to 133 K at a rate of 2 K min<sup>-1</sup>.



Supplementary information 13:

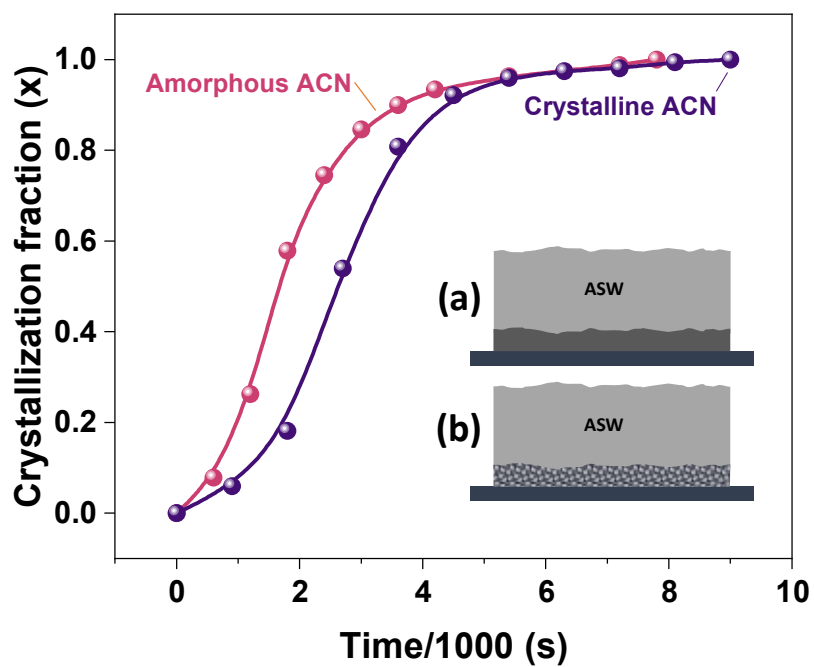


Fig. S13 CF versus time curves for ACN(50 ML)@ASW(150 ML) films with amorphous ACN film (brown curve) and crystalline ACN film (blue curve), obtained from isothermal RAIRS measurements at 133 K. The CF was calculated from a vertical cut at  $3260\text{ cm}^{-1}$  in the O-H stretching band of the time-dependent RAIRS spectra shown in Fig. S11a, c.

### Supplementary information 14:

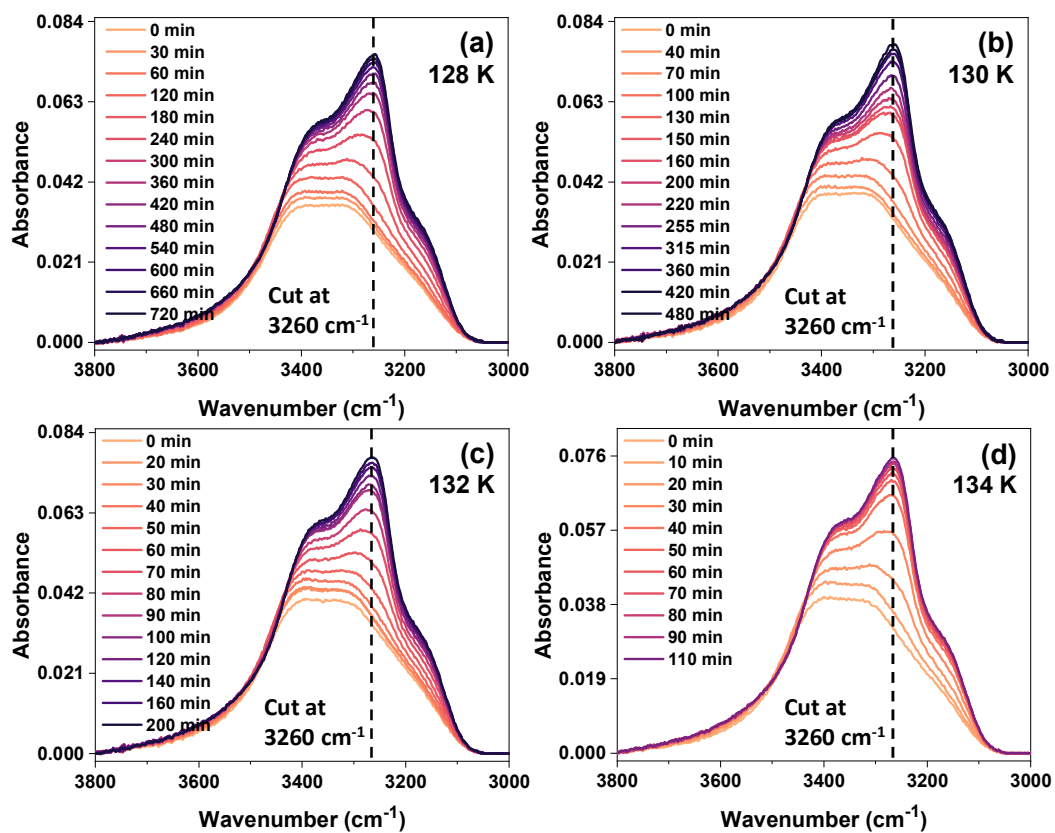


Fig. S14 Time-dependent RAIRS spectra of ACN@ASW films at (a) 128 K, (b) 130 K, (c) 132 K, and (d) 134 K in the O-H stretching region. ACN and ASW film thickness was kept constant, ACN(50 ML)@ASW(150 ML). Ice films were prepared by vapor deposition on Ru(0001) at 10 K and heated to set temperatures at a rate of  $2 \text{ K min}^{-1}$ . Vertical cut at  $3260 \text{ cm}^{-1}$  in O-H stretching band was used for the crystallization fraction evolution.

**Table S1.** The parameters of AWS crystallization at different temperatures.

	Temperature (K)	<i>n</i>	Rate constant; <i>k</i> (s <sup>-1</sup> )
O-H stretching	128	1.84	5.25×10 <sup>-05</sup>
	130	1.76	8.43×10 <sup>-05</sup>
	132	1.67	2.15×10 <sup>-04</sup>
	134	1.60	4.58×10 <sup>-04</sup>

# Ion-Exchanging Graphenic Nanochannels for Macroscopic Osmotic Energy Harvesting

Ankit Nagar, Md Rabiul Islam, Kartheek Joshua, Tanvi Gupte, Sourav Kanti Jana, Sujan Manna, Tiju Thomas,\* and Thalappil Pradeep\*



Cite This: <https://doi.org/10.1021/acssuschemeng.2c04138>



Read Online

ACCESS |



Metrics & More



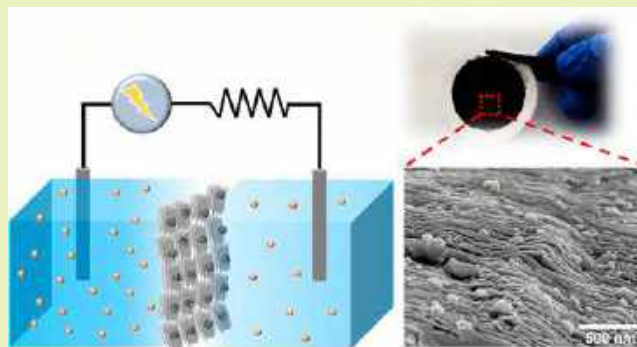
Article Recommendations



Supporting Information

**ABSTRACT:** The Gibbs free energy difference between seawater and river water can be tapped by selective ion transport across charged nanochannels, referred to as reverse electro dialysis (RED). However, existing single pore and micro/nanofluidic RED systems have shown poor prospects for scalability and practical implementation. Herein, we present a macroscopic RED system, utilizing a cation-selective membrane or an anion-selective membrane. The membranes comprise reduced graphene oxide (rGO) nanosheets decorated uniformly with TiO<sub>2</sub> nanoparticles. The nanosheets are covalently functionalized with polystyrene (PS) and subsequently linked to sulfonate or quaternary amine functional groups to obtain cation and anion selectivity, respectively. The membranes show excellent ion transport properties along with high power densities demonstrated under artificial salinity gradients. The cation-exchange membrane (CEM) delivered a power density of 448.7 mW m<sup>-2</sup> under a 500-fold concentration gradient, while the anion-exchange membrane (AEM) produced a substantial power output of 177.8 mW m<sup>-2</sup> under a similar gradient. The efficiencies ranged from 10.6% to 42.3% for CEM and from 9.7% to 46.1% in the case of AEM. Testing under varying pH conditions revealed higher power output under acidic conditions and substantial power output across the entire pH range, rendering them practically viable for sustainable energy harvesting in acidic and alkaline wastewaters.

**KEYWORDS:** reduced graphene oxide, electrochemistry, ion transport, osmotic energy harvesting, pH sensitivity



## INTRODUCTION

Escalating energy demands and the rapid depletion of fossil fuels have necessitated the development of sustainable and renewable sources of clean energy. The osmotic energy derived from the mixing of seawater and river water is one such source that holds the potential to provide ~2 trillion watts of energy globally.<sup>1</sup> Currently, reverse electro dialysis (RED) is among the most promising approaches for sustainable energy harvesting. In particular, membranes comprising nanofluidic channels showing cation or anion selectivity have recently attracted attention as promising osmotic energy collectors.<sup>2–7</sup> One-dimensional (1D) nanofluidic systems (single boron nitride nanotube, single-layer molybdenum disulfide nanopore, etc.) have shown promising performances as nanofluidic RED (NF-RED) devices for osmotic energy conversion.<sup>8,9</sup> However, their scalability and implementation are limited by low power output due to low pore density and complex and expensive fabrication procedures. It is noteworthy that the power density extrapolated from the performance of a single pore nanotube deviates significantly from the experimental performance of an actual NF-RED system comprising arrays of such nanotubes because the measured power density is not linearly propor-

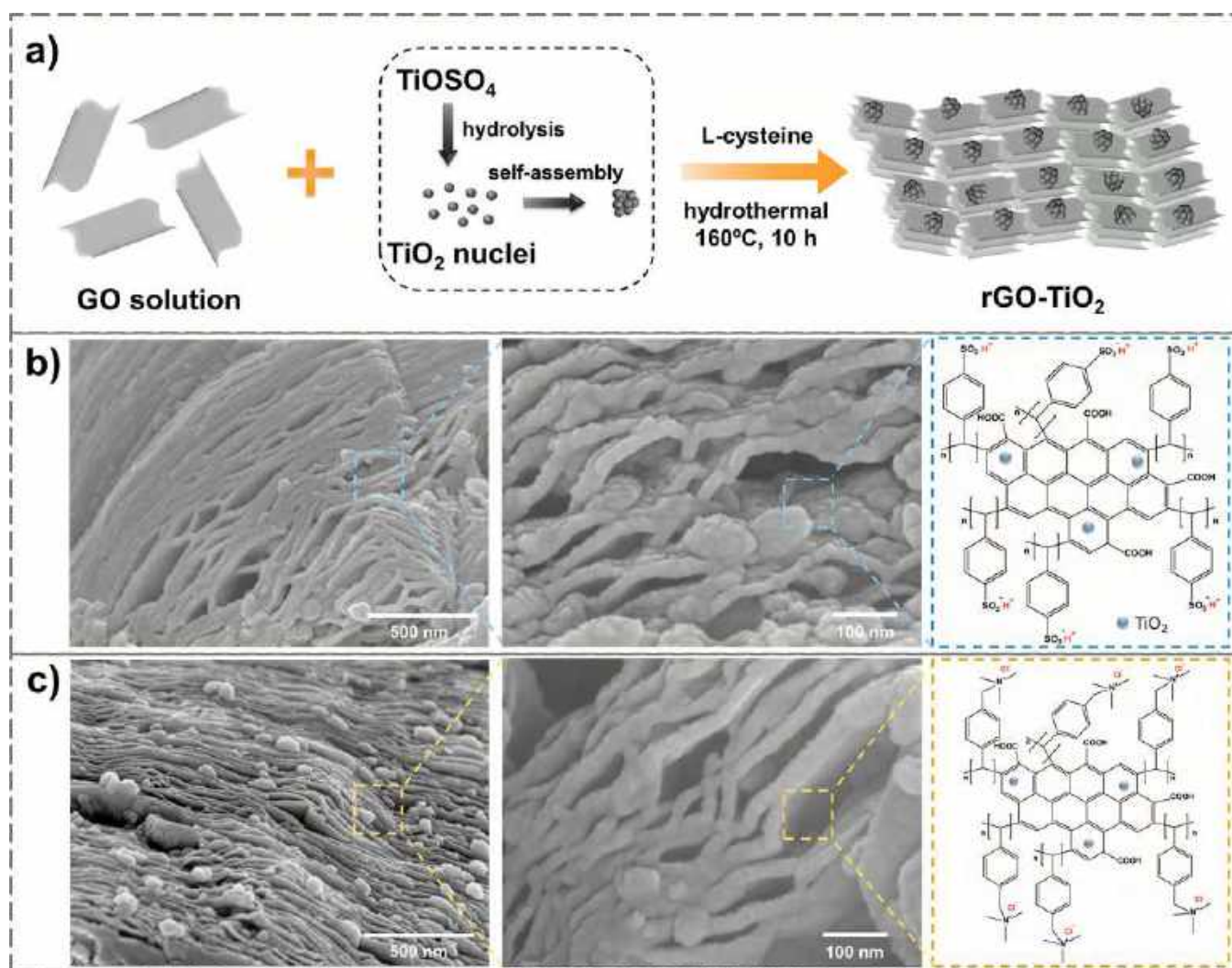
tional to the number of pores due to two primary reasons: (i) neighboring pores significantly influence the polarization and hydrodynamic flow in a pore, and (ii) an increase in number of pores results in increased interference of co-ions to hamper selective transport of counterions in the nanochannels.<sup>10–12</sup> The small membrane area is compensated for by putting a stack of membranes together, which adds to the overall infrastructural cost at a large scale. Therefore, it is desirable to have a large area membrane with high power output and efficiency.

The recent emergence of membranes based on two-dimensional (2D) materials (MXenes,<sup>13,14</sup> graphene,<sup>15</sup> polymeric carbon nitride,<sup>16</sup> kaolinite,<sup>17</sup> titanium carbide,<sup>18</sup> etc.) have opened avenues for scalable macroscopic energy harvesting.<sup>19</sup> The 2D configuration significantly reduces the ion

Received: July 11, 2022

Revised: October 31, 2022

Scheme 1. (a) Schematic for Hydrothermal Reaction for Formation of rGO-TiO<sub>2</sub> Nanocomposite. (b, c) FESEM Micrographs of Cation- and Anion-Exchange Resins, Respectively, Along with Their Simplified Molecular Structures



transport resistance and offers high packing density of nanosheets without compromising the surface-determined properties in the confined spaces. An assembly of nanosheets can create uniform and continuous 2D nanochannels with interlamellar spacing close to the Debye screening length. Surface charges on these nanosheets govern the ion transport behavior across the membrane. Most intriguingly, functionalization of nanosheets can be efficiently performed in the bulk solution prior to their self-assembly, thereby bypassing the challenge of uniform functionalization of the nanochannel arrays. Such a strategy of preassembly functionalization followed by a simple bottom-up assembly process is promising for large-scale and cost-effective production of 2D material systems. The simplicity in fabrication and scalability of 2D membranes enhance their practical significance for efficient osmotic energy harvesting. The subject matter of osmotic energy harvesting has been reviewed recently, and the reader may consult the cited papers for other efforts in the area.<sup>20,21</sup>

Herein, we demonstrate a macroscopic 2D membrane-based RED system wherein the membrane comprises reduced graphene oxide (rGO) nanosheets decorated with TiO<sub>2</sub> nanoparticles.

Graphene oxide (GO) is one of the principal derivatives of graphene, inheriting its properties such as superior mechanical and chemical robustness, atomic thickness, and oxygen-containing functionalities like carboxyl, epoxy, and hydroxyl, thereby offering possibilities of further functionalization and application.<sup>22–28</sup> Moreover, GO membranes can be easily prepared at large scale using methods like vacuum filtration, coating, templating, layer-by-layer assembly, etc.<sup>29</sup> The high surface charge density and low ion transport resistance of graphene-based nanochannels also render them promising for RED-based energy conversion. Therefore, it is essential to explore 2D carbon materials in depth for large-scale clean energy applications.

TiO<sub>2</sub> is a renowned photocatalyst known for its nontoxicity, cost effectiveness, and long-term chemical stability.<sup>30,31</sup> The presence of TiO<sub>2</sub> nanoparticles on the surfaces of graphene sheets increases the overall surface area, thus providing abundant nanochannels for ion transport. Also, they improve the dispersibility of graphene sheets in water, which is essential for membrane formation using vacuum filtration.

Despite having good ionic conductivities and mechanical stabilities, ion-exchange membranes with noncovalent surface modifications face several drawbacks. The functional group



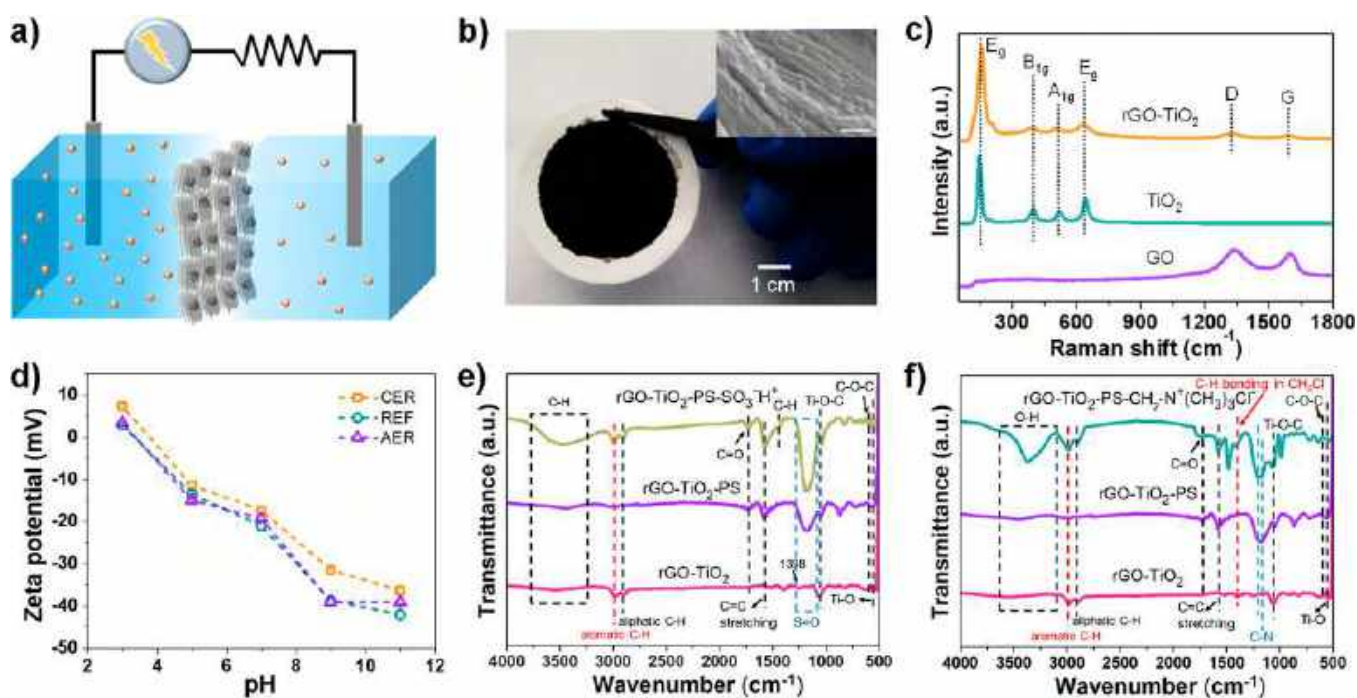


**Figure 1.** (a) Schematic of two-compartment setup for testing osmotic energy conversion under a salinity gradient. (b) Optical image of rGO-TiO<sub>2</sub> membrane. Inset shows the FESEM image of the membrane. Scale bar: 200 nm. (c) Raman spectra of GO, TiO<sub>2</sub>, and rGO-TiO<sub>2</sub>. (d) Zeta potentials of REF, CER, and AER with respect to pH. (e) FTIR spectra of rGO-TiO<sub>2</sub>, rGO-TiO<sub>2</sub>-PS, and rGO-TiO<sub>2</sub>-PS-SO<sub>3</sub>H. (f) FTIR spectra of rGO-TiO<sub>2</sub>, rGO-TiO<sub>2</sub>-PS, and rGO-TiO<sub>2</sub>-PS-CH<sub>2</sub>-N(CH<sub>2</sub>)<sub>3</sub>Cl.

withholds the risk of getting detached from the scaffold of the membrane due to weak electrostatic interaction.<sup>32</sup> Our group has previously proven that in situ polymerization of styrene on rGO nanosheets gives materials with exceptional electroadsorption properties.<sup>33</sup> Therefore, in order to create robust ion-exchange membranes, the rGO-TiO<sub>2</sub> nanosheets (REF) were covalently linked to polystyrene (PS) prior to functionalization with the charged groups. The resulting rGO-TiO<sub>2</sub>-PS composite was then covalently linked to sulfonate and quaternary amine groups, resulting in cation- and anion-exchange resins (CER and AER), respectively. Upon testing the energy conversion performances of the membranes under a 500-fold salinity gradient, the cation-exchange membrane (CEM) and anion-exchange membrane (AEM) revealed maximum output power densities (PD<sub>max</sub>) of 448.7 and 177.8 mW m<sup>-2</sup>, respectively. Upon further optimization of the pH conditions, maximum PD<sub>max</sub> was recorded as 309.87 mW m<sup>-2</sup> at pH 5 for CEM and 283.50 mW m<sup>-2</sup> at pH 3 for AEM, under a 100-fold concentration gradient. Moreover, the ion-selective membranes showed excellent electrochemical stability during cycling and exhibited pH-sensitive ion transport. Our results demonstrate excellent potential of graphene-based covalently linked ion-exchange membranes for macroscopic RED applications to overcome the low power outputs and scalability limitations of existing ion-exchange-based RED systems.

## RESULTS AND DISCUSSION

The rGO-TiO<sub>2</sub> nanosheets were prepared by a one-pot hydrothermal reaction between GO and titanium oxysulfate (TiOSO<sub>4</sub>) in the presence of L-cysteine, which acted as a reducing and a cross-linking agent (details in [Materials and Methods](#)). It is known that these composite materials form by the adsorption of positively charged titanyl ions (TiO<sup>2+</sup>) onto

the surfaces of the negatively charged GO sheets.<sup>34,35</sup> During the hydrothermal reaction, hydrolyses of TiO<sup>2+</sup> ions result in the formation of TiO<sub>2</sub> nuclei which grow to form surface-anchored nanoparticles, while GO reduces to rGO. The  $\pi$ - $\pi$  interaction between the rGO sheets and the coexistence of electrostatic interaction and hydrogen bonding among L-cysteine and rGO contribute toward the formation of an integrated lamellar structure. Lower concentrations of the Ti precursor do not result in any aggregation of TiO<sub>2</sub> nanoparticles; however, at larger concentrations, TiO<sub>2</sub> particles self-assemble into nanoaggregates.<sup>36</sup> The field emission scanning electron microscopy (FESEM) micrographs of CER and AER demonstrated arrays of nanosheets uniformly intercalated with nanoparticles ([Scheme 1](#)).

Further, the resins were self-assembled using vacuum filtration on a grade 42 Whatman paper support, and the resulting ion-exchange membranes were tested for ion transport and energy conversion ([Figure 1a, b](#); [Figure S1](#)). The test membranes were individually placed at the junction of a two-compartment electrochemical cell to evaluate their energy conversion performance ([Figure 1a](#)). Two Ag/AgCl electrodes were placed in either cell and connected to an external load resistance and a pico-ammeter. The morphology of the membrane reveals the presence of lamellar structures with uniformly anchored TiO<sub>2</sub> nanoparticles ([Scheme 1](#), [Figure 1b](#) inset, and [Figure S2](#)).

The Raman spectra of GO, TiO<sub>2</sub>, and rGO-TiO<sub>2</sub> nanocomposites are shown in [Figure 1c](#). The Raman spectrum of GO depicted its characteristic D- and G-band at 1353 and 1602 cm<sup>-1</sup>, respectively. The D-band was attributed to sp<sup>3</sup> defect-induced disorders on graphene sheets, and the G-band was ascribed to in-plane vibrations of sp<sup>2</sup> hybridized carbons and scattering of E<sub>2g</sub> phonons. It is evident from the spectra that conversion of GO to rGO results in downshifting of the



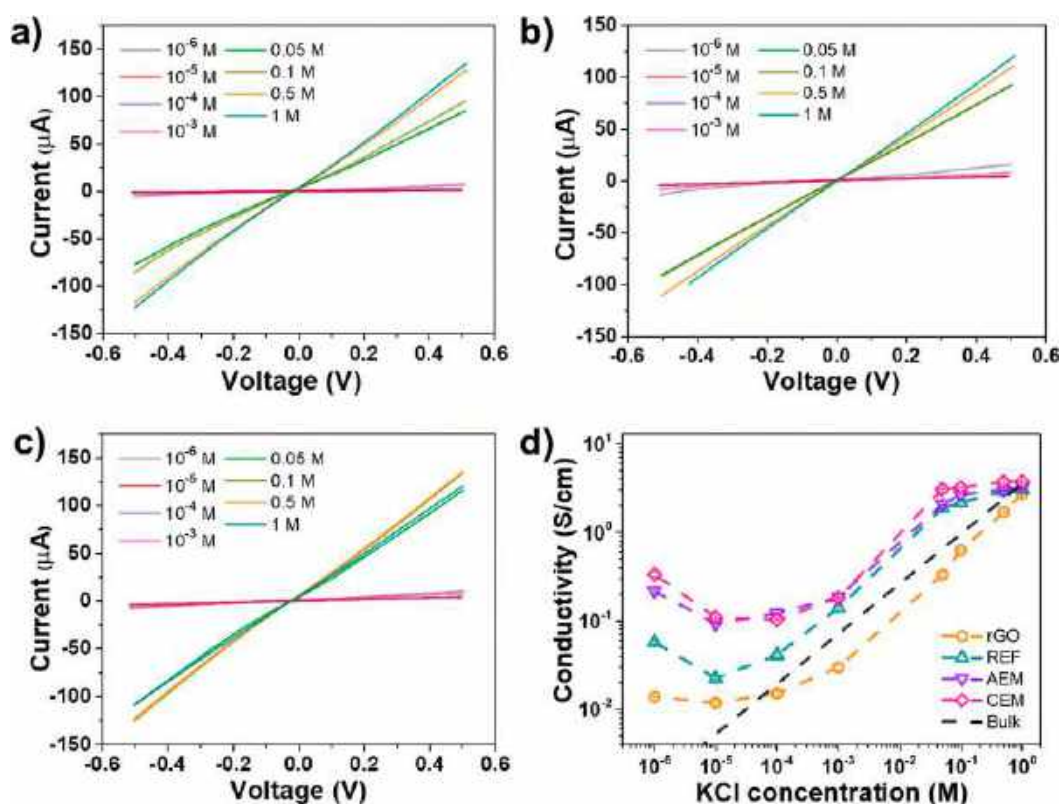


**Figure 2.** I–V characteristics of the membranes: (a) REF, (b) CEM, and (c) AEM. (d) Ionic conductivities of the membranes over a range of KCl concentrations ( $10^{-6}$  to 1 M), which deviates significantly from the bulk conductivity (dashed line) of the electrolyte. All measurements were performed at 300 K.

D-band peak from 1339 to 1327  $\text{cm}^{-1}$  and G-band peak from 1602 to 1593  $\text{cm}^{-1}$ . This confirmed successful hydrothermal reduction of GO to rGO.<sup>37</sup> The shift of the D-band could possibly be due to multiple foldings in the rGO-TiO<sub>2</sub> nanosheets, formed during the hydrothermal reduction (Figure S3). Broad peaks in the case of the rGO-TiO<sub>2</sub> nanocomposite were a result of stacking of multiple layers of rGO sheets due to the presence of a fewer number of oxide functional groups after reduction of the exfoliated GO, thereby causing structural disorder. In addition, the  $E_g$ ,  $B_{1g}$ ,  $A_{1g}$ , and  $E_g$  modes implied the existence of the anatase phase in the nanocomposite, also consistent with XRD results (Figure S4).

Surface charges of the resins were confirmed by zeta potential measurements (Figure 1d). Zeta potentials of REF, CER, and AER became increasingly negative as pH was varied from 3 to 11. The negative zeta potential was attributed to the oxygen-containing functional groups such as  $-\text{COOH}$  and  $-\text{OH}$ .<sup>38,39</sup> The variation in zeta potential with pH confirmed the strong dependence of surface charges on pH. Since sulfonate and quaternary amine are strong acid and strong base resins, respectively, they always undergo complete dissociation in an aqueous medium irrespective of pH and have an role in the pH-dependent zeta potential variation.

Figure 1e and f represents Fourier transform infrared (FT-IR) spectra for sulfonate and quaternary ammonium-functionalized rGO-TiO<sub>2</sub> nanocomposites alongside rGO-TiO<sub>2</sub> and rGO-TiO<sub>2</sub>-PS, prior to resin functionalization. The vibrational features confirmed the covalent linkage between rGO and polystyrene (PS), along with the covalently linked positively and negatively charged functionalities. The FT-IR spectrum of CER (Figure 1e) showed a broad peak in the range of 3421–

3561  $\text{cm}^{-1}$ , corresponding to O–H stretching. This feature could be attributed to the adsorbed humidity from the surroundings or the presence of NaOH used during the styrene polymerization process. Peaks at 2979 and 2899  $\text{cm}^{-1}$  were assigned to the asymmetric and symmetric stretching frequencies of aliphatic C–H, respectively. Also, the peaks at 2988, 1579, and 1438  $\text{cm}^{-1}$  were assigned to aromatic C–H stretching, C=C stretching, and C–H bending, respectively. Another peak at  $\sim 1719$   $\text{cm}^{-1}$  is due to C=O stretching of the carboxyl group. All the aforementioned peaks were also observed in cases of rGO-TiO<sub>2</sub>-PS and rGO-TiO<sub>2</sub>. The CER spectrum had a peak at 1180  $\text{cm}^{-1}$  which confirmed the presence of the S=O bond of the sulfonate group. The presence of Ti–O–C bonds in all spectra was confirmed by the peak at 1054  $\text{cm}^{-1}$ . In addition, the peak at 1438  $\text{cm}^{-1}$  confirmed C–H vibrations due to chloromethylation. The FTIR spectrum of AER (Figure 1f) showed peaks at 2982 and 2899  $\text{cm}^{-1}$  for aromatic and aliphatic C–H, respectively. The peak at 1573  $\text{cm}^{-1}$  depicted C=C stretching. Post amination, peaks at 1197 and 1161  $\text{cm}^{-1}$  were C–N stretching frequencies of the quaternary amine group. The broad features in 600–800  $\text{cm}^{-1}$  and the sharp feature in 1036–1060  $\text{cm}^{-1}$  across all spectra were ascribed to the presence of Ti–O–Ti and Ti–O–C stretching vibrations.<sup>40</sup>

The surface areas and pore sizes of the rGO-TiO<sub>2</sub> particles are critical in determining the membrane's ion transport and energy conversion properties. We performed Brunauer–Emmett–Teller (BET) surface area measurements on three rGO-TiO<sub>2</sub> composites with varying TiO<sub>2</sub> loadings from (0%–99% w/w). We found that an increase in TiO<sub>2</sub> loading leads to an increase in the specific surface area (Table S1). A larger

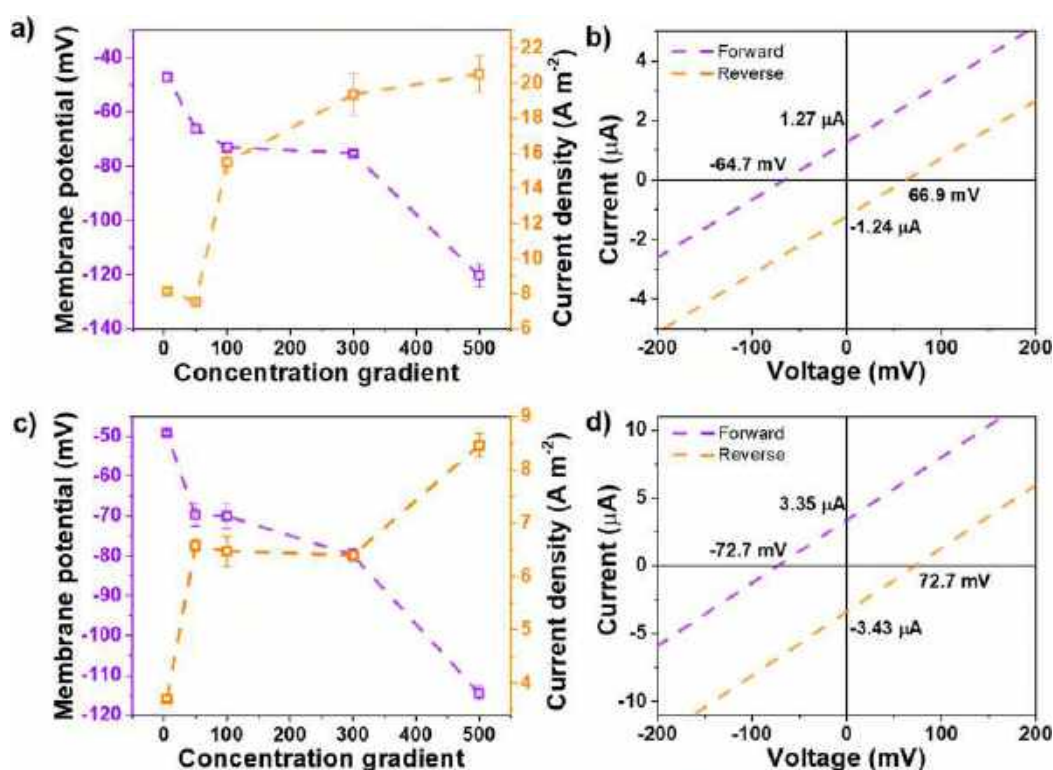


**Figure 3.** Membrane potential ( $V_{oc}$ ) and current density ( $J_{sc}$ ) represented as a function of concentration gradient for (a) CEM and (c) AEM. The bidirectional ion-transport behaviors of CEM and AEM are evident at a concentration gradient of 50 (0.01 M/0.5 M) from the I–V curves shown in (b) and (d), respectively.

surface area indicates the presence of abundant nanochannels.<sup>41</sup> Therefore, TiO<sub>2</sub> loading was kept at 99% (w/w) in the rGO-TiO<sub>2</sub> nanocomposite. All composites were found to be mesoporous in nature with pore sizes in the range of 2–10 nm (Figures S5, S6). The role of TiO<sub>2</sub> is also apparent from the improved dispersibility of the rGO-TiO<sub>2</sub> sheets in an aqueous medium, in comparison to rGO (Figures S7, S8).

The rGO-TiO<sub>2</sub> particles were vacuum filtered through a grade 42 Whatman paper support to create a membrane which was subsequently fixed at the junction of the two-compartment electrochemical cell (Figure 1a). A neutral probe molecule, ovalbumin, was chosen to permeate across the membrane to check for the presence of any macroscopic defects. However, the molecule failed to permeate, indicating that the prepared membrane was defect free (Figure S9).

**Transmembrane Ion Transport.** To investigate the ion transport characteristics, the membranes were individually placed at the junction of a homemade two-compartment electrochemical cell (see Materials and Methods). KCl was selected as the test electrolyte due to identical electrophoretic mobilities of K<sup>+</sup> and Cl<sup>-</sup> ions. The current–voltage (I–V) characteristics for the membranes were recorded under a series of KCl concentrations varying from 10<sup>-6</sup> to 1 M. Figure 2a–c shows I–V curves for REF, CEM, and AEM, respectively. All curves show linear ohmic behavior. The conductance vs concentration curves for the three membranes exhibit two distinct behaviors across the entire concentration range (Figure 2d). In the high concentration range (>10<sup>-3</sup> M), conductance follows the bulk rule and exhibits linear behavior. In the low concentration regime (<10<sup>-3</sup> M), the curves gradually deviate from the bulk electrolyte's linear curve. At lower concentrations, the Debye length significantly increases, and therefore,

surface charges dominantly govern ion transport across the nanochannels, thereby causing a deviation from linearity.<sup>42–46</sup> Moreover, the rGO-TiO<sub>2</sub> membrane has substantially better ionic conductivity compared to the rGO membrane across the entire concentration range, suggesting that the presence of TiO<sub>2</sub> nanoparticles enhances the overall ion transport. It is also evident from the conductivity curves that the conductances of CEMs and AEMs are nearly the same across the entire concentration range and about an order of magnitude higher than the conductance of REF in the low concentration range (Figure 2d). This implies that the introduction of ion-selective functional groups on the rGO-TiO<sub>2</sub> nanosheets significantly enhances their ionic conductivity and permselectivity.

It is also observed that for all the membranes, REF, AEM, and CEM, conductivities do not change significantly beyond 0.1 M KCl concentration. This is likely due to osmotic deswelling of the membrane at higher salt concentration, which reduces the available volume for ion transport within the membrane.<sup>47</sup>

**Concentration Gradient-Driven Transport.** Further, the ion transport properties of CEM and AEM were utilized for extracting artificial salinity gradient energy by placing a test membrane at the junction of two compartments containing the NaCl electrolyte of different concentrations.<sup>48,49</sup> The concentration in one compartment was kept fixed at 0.01 M, and the concentration in the other compartment was varied from 0.05 to 5 M. The cation- or anion-selective nature of the membranes allows selective permeation of counterions (Figure S10), thereby converting the chemical potential gradient into a finite ion diffusion current.<sup>50–52</sup> The energy conversion performance was characterized by the I–V curves. The short-circuit current ( $I_{sc}$ ) and open-circuit voltage ( $V_{oc}$ ) were

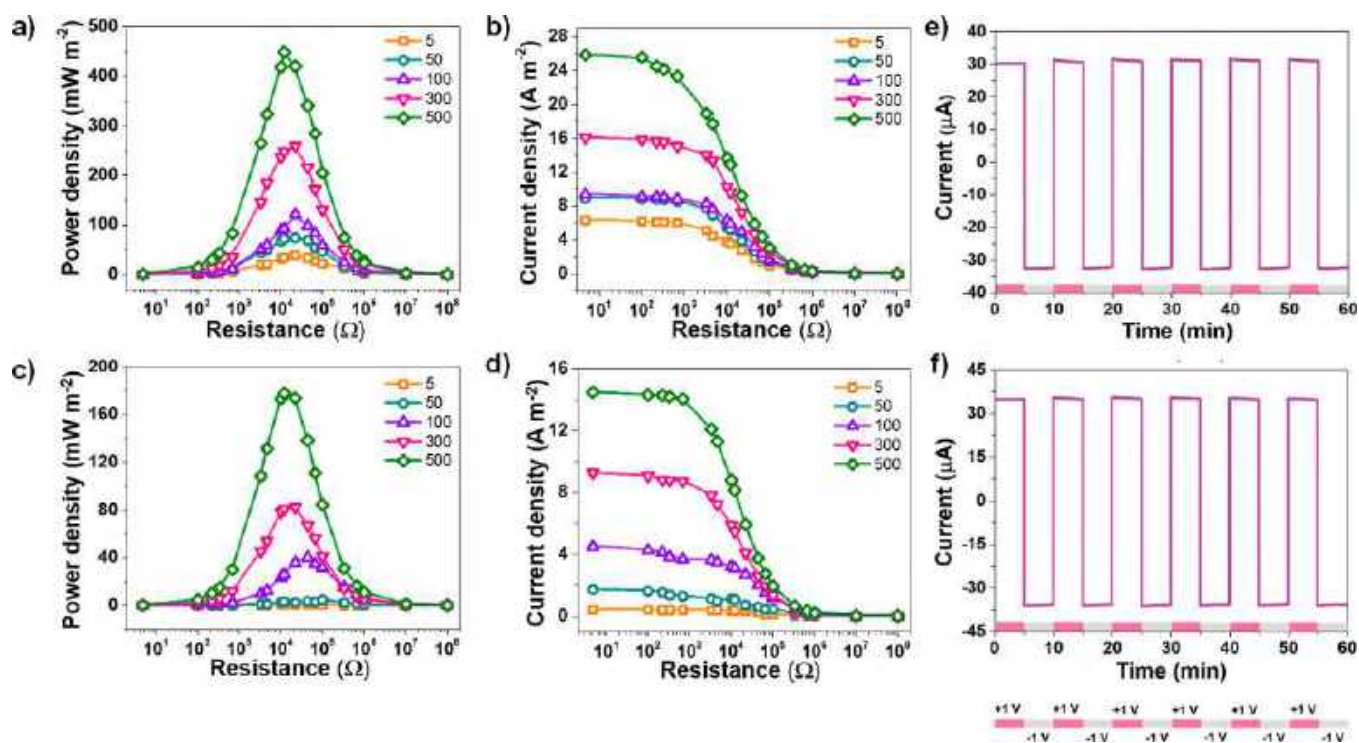


**Figure 4.** Energy harvesting performance. (a, c) Power densities of CEM and AEM, respectively, as a function of externally applied load resistance. Power output reaches a maximum at a certain moderate load. (b, d) Corresponding current densities of CEM and AEM, respectively. (e) Cyclic stabilities of the membranes were studied using a current–time curve. External biases of +1 V and –1 V were alternately applied, each for a 5 min period. Curve in (e) for CEM and (f) for AEM.

derived from the intercepts of the I–V curves measured at varied concentration gradients, ranging from 5 to 500. In the case of CEM, the membrane potential ranged from –47.4 mV under a 5-fold gradient up to –120.5 mV under a 500-fold gradient (Figure 3a). Similarly, the current density increased from 8.12 to 20.50 A m<sup>-2</sup> when the gradient was varied from 5-fold to 500-fold, respectively (Figure 3c). On the contrary, the membrane potential for AEM was measured to be –49.2 mV under a 5-fold gradient and a maximum of –114.5 mV under a 500-fold gradient. The current density ranged from 3.71 to 8.46 A m<sup>-2</sup> at a 500-fold gradient. Consistent increases in both  $V_{oc}$  and  $J_{sc}$  were observed with increases in concentration gradients for both CEM and AEM (Tables S2, S3). Figure 3b and d shows that on reversing the concentration gradient  $V_{oc}$  and  $I_{sc}$  do not change significantly, confirming that there is no preferred direction for ion transport.

Further, ion selectivities of the membranes were evaluated by the ion transference number  $t_n$  using the following equation:  $t_n = 0.5 (1 + V_{os}/V_{redox})$ ;  $t_+$  for CEM and  $t_-$  for AEM. The transference number equals 1 for a perfectly ion selective system and 0.5 for a nonselective system. In the equation above,  $V_{os}$  is the osmotic potential, and  $V_{redox}$  is the potential drop at the electrode–solution interface. The osmotic potential can be calculated by subtracting the contribution of redox potential from the open circuit potential, i.e.,  $V_{os} = V_{oc} - V_{redox}$  (Figure S11). The transference number for CEM,  $t_+$ , varies from 0.73 to 0.96, indicating a high charge selectivity (Table S2). AEM shows similar selectivity as  $t_-$  varies from 0.72 to 0.98 (Table S3). The energy efficiency for CEM ranges from 10.6% at 100-fold and 300-fold gradients and up to 42.3% at a 5-fold gradient. For AEM, the efficiency ranges from 9.6% at a 100-fold gradient and up to 46.1% at 5-

fold gradient. Therefore, both CEM and AEM promise high-cation selectivities and excellent energy efficiencies in a macroscopic RED system.

**Osmotic Energy Harvesting.** A two-compartment setup was used to investigate the energy harvesting behaviors of the CEM and AEM membranes. Artificial salinity gradients were created using the NaCl electrolyte. The membranes were tested under five concentration gradients ranging from 5 to 500. The concentration on one side was kept fixed at 0.01 M and varied on the other side from 0.05 to 5 M. Each measurement was performed using fresh solutions.

Irrespective of the membrane type (CEM or AEM), it was observed that current densities decreased systematically with an increase in the load resistance (Figure 4b, d). Output power density was calculated using the equation  $P_L = (I^2 \times R_L)/A$ , where  $P_L$  is the areal power density,  $I$  the measured current in the external circuit,  $R_L$  the externally applied load, and  $A$  the actual membrane area available for ion transport. For a fixed concentration gradient, the diffusion current decreases with an increase in the external load. This was true for both CEM and AEM under all gradients (Figure 4b, d). Moreover, the diffusion current increases with an increase in the concentration gradient. The aforementioned equation for power density implies that power output will be maximum upon application of a certain moderate load. The CEM showed  $PD_{max}$  values of nearly 448.6, 259.4, 121.5, 74.2, and 38.2 mW m<sup>-2</sup>, and AEM delivered  $PD_{max}$  of 177.8, 82.1, 39.9, 3.4, and 0.7 mW m<sup>-2</sup>, under artificial salinity gradients of 500, 300, 100, 50, and 5, respectively (Figure 4a, c). Due to higher power densities obtained in the case of CEM, we decided to further investigate its ion transport for different electrolytes containing chloride ions, keeping a constant concentration



gradient of 50 (0.01 M/0.5 M) to assess the membrane performance under varied practical working conditions. The obtained  $PD_{\max}$  values for LiCl, NaCl, and KCl electrolytes were 460.38, 223.2, and 120.3  $mW m^{-2}$ , respectively (Figure S12). Therefore, the ion current follows the following order: LiCl > NaCl > KCl. On the contrary, hydrated diameters of the aforementioned ions follow the opposite trend:  $Li^+$  (7.6 Å) >  $Na^+$  (7.2 Å) >  $K^+$  (6.6 Å). Therefore, the governing factor for ion transport must be the binding affinity of the sulfonate group to test ions, which follows as  $K^+$  >  $Na^+$  >  $Li^+$ . A higher binding affinity and smaller size allows easier condensation of cation–sulfonate pairs, thereby preventing dissociation for fast ion transport.<sup>53</sup>

Cyclic stabilities of the membranes were studied by applying an external bias of +1/−1 V alternately and subsequently recording the current–time characteristics for both the membranes (Figure 4e, f). The duration for each cycle was 5 min. A total of 12 cycles was performed for a duration of 60 min. The positive and negative currents at the applied biases remain nearly constant across the entire duration indicating remarkably stable ion transports for both CEM and AEM. Further, the output power density was observed to remain stable in the case of CEM for a period of 15 days under a 500-fold gradient (Figure S13).

In Figure 5 and Table S4, we compare the energy harvesting performance of CEM alongside the three kinds of membrane-

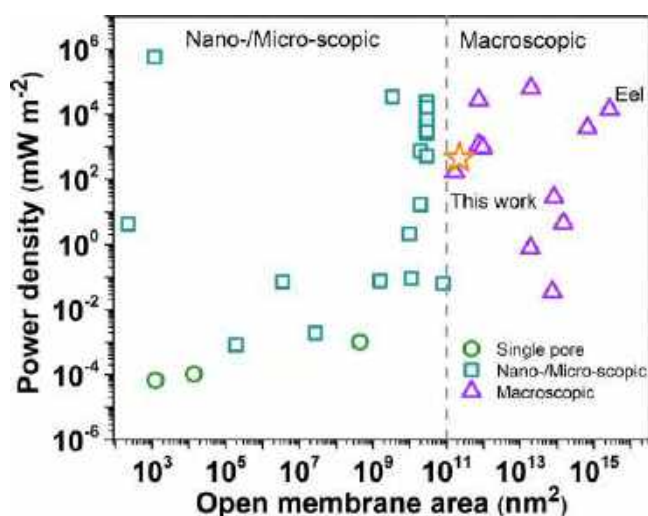


**Figure 5.** Osmotic energy conversion performance of state-of-the-art RED devices alongside this work (cation-exchange membrane). Power densities were calculated by normalizing the obtained power with the total active membrane area used for ion transport. The threshold for distinguishing the nano/microscopic systems from the macroscopic systems is  $10^{11} nm^2$  (or  $0.1 mm^2$ ).

based single-stage RED systems: single pore, nano/microscopic, and other macroscopic devices. For the sake of simplicity, we only show CEM, since it offers slightly better performance and efficiency compared to AEM at a 500-fold gradient. The three types of devices are distinguished based on the active membrane area utilized for ion transport. The majority of the data obtained for comparison in Figure 5 was at a 1000-fold concentration gradient, while CEM's performance used for comparison was at a 500-fold gradient (Table S3). As evident from the figure, electric eels outperform all artificial RED systems in the context of large-area power conversion.

Several 2D/3D macroscopic systems such as MXene-GO composite,<sup>54</sup> MXene-bacterial cellulose composite,<sup>55</sup> metal–organic frameworks,<sup>56</sup> covalent–organic frameworks,<sup>56</sup> etc., have higher power densities in comparison to this work, as shown in Figure 5. However, such reports lack discussion on ion transference number or energy efficiency at the highest recorded power density. Also, some of the systems highlight power densities corresponding to stacks of several membranes, while power density in this work was generated from a single membrane in a two-compartment electrochemical cell.

While a few single pore systems generate higher power densities in comparison to a live eel, they require sophisticated methods to enhance the number of pores to achieve substantial power for practical use. On the contrary, graphene-based nanochannels presented in this work do not require precise nanofabrication. The membrane areas of CEM and AEM used in this study are  $\sim 0.22 mm^2$ , which are apt for practical purposes, in comparison to the sub- $\mu m^2$  active area of other reported membranes. Moreover, small testing areas do not precisely project the performance of a large-scale RED system as power density does not vary linearly with the membrane area. An extension of this work for further optimization of membrane thicknesses and their degree of functionalization could help approach the performance of a live electric eel.

**Ion Transport Model.** To understand the molecular interactions and confirm that permselectivities of the membranes play roles behind excellent ion transport, we performed molecular dynamic (MD) simulations on the CEM. Details of the method used are provided in Materials and Methods. As a simplified model, graphene sheets of  $5 nm^2$  areas were generated and functionalized with epoxy, hydroxyl, and carboxyl groups (Figure S14a). The sheets were further functionalized with  $-SO_3H$  to create a simplified mimic of the experimentally synthesized material (Figure S14b). After functionalization, sheets were replicated with a 1.5 nm interlayer separation. A total of four replica layers were created, resulting in three nanochannels.

To understand the interaction of  $Na^+$  and  $Cl^-$  ions with the  $-SO_3H$  and oxygen-containing groups of rGO, we focused on a single nanochannel between two functionalized rGO sheets. Three NaCl electrolyte concentrations of 0.5, 1.0, and 1.5 M were chosen to permeate across the nanochannel with the application of an external pressure. To understand interactions between the ions and the functional groups, the proximities of  $Na^+$  and  $Cl^-$  ions were monitored during the simulation to scan for the presence of any sulfur and oxygen atoms in their vicinity. Figure 6a depicts an example of the 1.0 M system with its initial and final states. Figure S15 shows such representations at all concentrations. The interactions were analyzed by calculating the radial distribution function (RDF),  $g(r)$ . For the 0.5 M concentration, the flat RDF profile in case of  $Cl^-$ -S indicated the absence of any  $Cl^-$ -S interaction (Figure 6b). We conclude that  $Cl^-$  ions do not interact with sulfonate groups at this condition. Similarly, the  $Cl^-$ -S interaction begins at 8.0 and 7.0 Å for 1.0 and 1.5 M concentrations, respectively. This suggests negligible interactions between sulfonate groups and chloride ions during electrolyte permeation. On the other hand,  $Cl^-$  ions significantly interact with the oxygen atoms on the rGO sheet, indicated by shorter interaction distances (Figure 6c). At 0.5 M,  $Cl^-$ -O interaction starts at 3.0 Å, and a highly stable confirmation and interaction is observed at 4 Å, suggested by the peak. Similarly, a  $Cl^-$ -O interaction is observed at 3 and 3.5 Å for 1.0 and 1.5 M, respectively. These

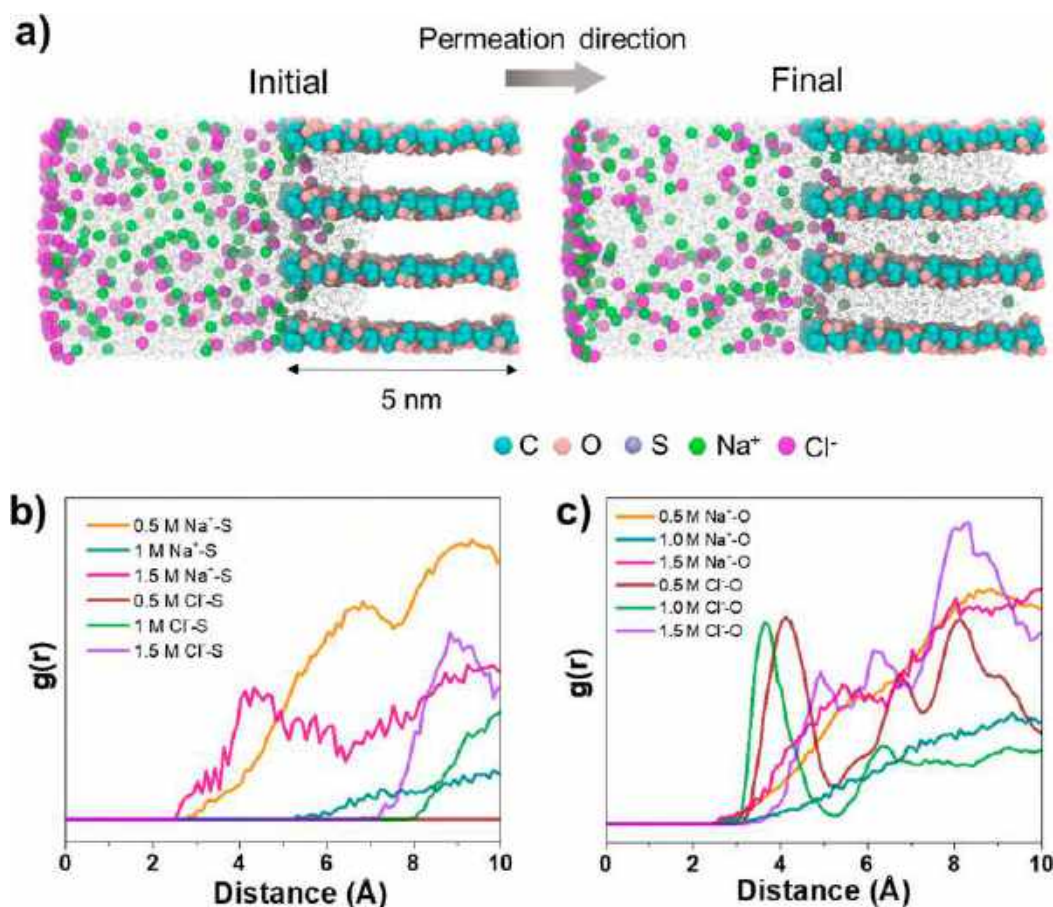


**Figure 6.** (a) Representations of initial and final conformations of the ion-permeation simulation performed at 1.0 M concentration. The glassy-colored water molecules are also shown. (b, c) Atom density profiles,  $g(r)$ , of NaCl electrolyte diffusing through a sulfonate-functionalized graphene oxide nanochannel at 300 K for 0.5, 1.0, and 1.5 M, electrolyte concentrations.

collectively suggest that Cl<sup>-</sup> ions preferentially interact with oxygen-containing groups and are rejected by the sulfonate groups.

At a 0.5 M concentration, Na<sup>+</sup>-S and Na<sup>+</sup>-O interactions begin at 2.8 and 2.5 Å, respectively (Figure 6c). Also, stable Na<sup>+</sup>-S interactions are observed at 6.8 Å, as indicated by the peak in the RDF curve, which imply that sulfur atoms cause Na<sup>+</sup> ions to stabilize within the channel. In the case of a 1.0 M concentration, the Na<sup>+</sup>-O interaction begins at 2.5 Å, while Na<sup>+</sup>-S at 5.2 Å. At a 1.5 M concentration, the Na<sup>+</sup>-O interaction begins at 2.5 Å, and most stable conformations are found at 5.5 Å. The radial distribution interaction values are provided in Table S5. Negligible Cl<sup>-</sup>-S interactions across all concentrations, and stable interactions between Cl<sup>-</sup>-O, Na<sup>+</sup>-O, and Na<sup>+</sup>-S, as suggested by the local maxima in RDF curves, verify the permselective behaviors of the sulfonated nanochannels.

#### pH Sensitive Ion Transport and Energy Conversion.

From the results of zeta potential with respect to pH (Figure 1d), it was observed that the surface charge densities of the functionalized nanosheets increase consistently with an increase in pH from 3 to 11. Since nanoscale ion transport is highly dependent on the surface charge densities of the nanochannels, transport is expected to be highly pH sensitive. To confirm this, we carried out the energy harvesting experiments with varying pH under a 100-fold artificial salinity gradient. Electrolytes in both the compartments were maintained at the same pH. PD<sub>max</sub> values for both CEM and

AEM were observed to be higher in an acidic environment. CEM and AEM recorded highest PD<sub>max</sub> values of 309.87 and 283.50 mW m<sup>-2</sup> at pH of 5 and 3, respectively (Figure 7a, c). Higher ion currents in acidic conditions imply excellent proton transport abilities of CEM and AEM (Figure 7b, d). It is known that strong-acid cation-exchange resin and strong-base anion-exchange resin always undergo complete dissociation independent of pH. Therefore, sulfonate- and quaternary amine-functionalities cannot show pH responsivity. On the contrary, weak-acid resins containing carboxylic acid groups have high affinity for H<sup>+</sup> ions. Therefore, they are prone to protonation in acidic conditions, thereby losing their ionic state. On the contrary, carboxylic acid groups remain ionized in alkaline conditions. Therefore, the graphene nanosheets are inherently pH sensitive. In basic conditions, the ionized carboxylic acid groups on nanosheets restrict the movement of anions within the nanochannel, thereby resulting in lower ion current in alkaline pH. In acidic conditions, the protonated carboxylic acid groups offer lower resistance to the movement of protons across the channels, thereby producing higher ion current in acidic pH.

**Aspects of Sustainability.** It is known that RED is a sustainable methodology for harvesting blue energy. Upon further optimization of membrane thickness and active area, and by putting together a stack of membranes, it is possible that osmotic energy harvesting through this method becomes practically viable.



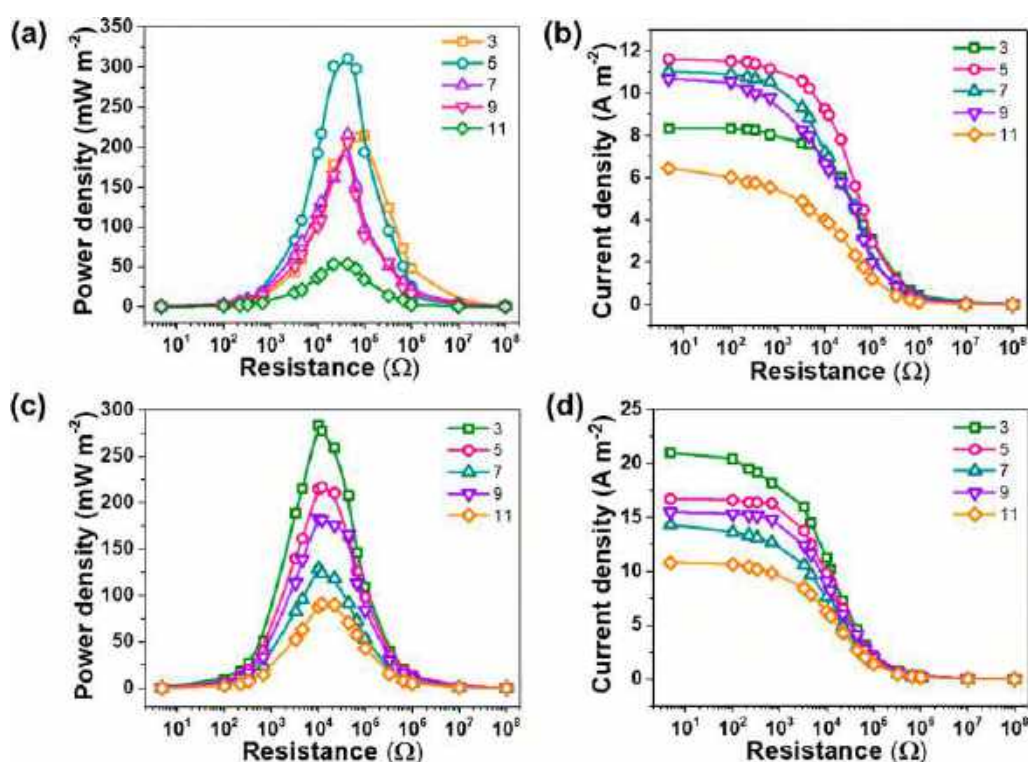


**Figure 7.** pH-sensitive ion transport. Power densities of CEM and AEM (a, c) and their respective current densities (b, d) measured under varying pH conditions (3–11).

## CONCLUSION

In conclusion, we fabricated an array of wrinkled rGO-TiO<sub>2</sub> nanosheets that were covalently linked to sulfonate or quaternary amine functional groups to create cation- and anion-exchange resins. The membranes prepared from these resins show ion selectivity confirmed from their ionic conductivity curves. The highest ever macroscopic osmotic energy conversion performance was obtained when the membranes were tested under artificial salinity gradients. At a concentration gradient of 500, the cation-exchange membrane (CEM) produces a power density as high as 448.7 mW m<sup>-2</sup>, while the anion-exchange membrane could deliver a maximum power density of 177.9 mW m<sup>-2</sup>. The robust functionalization of nanochannels assured through covalently linked ion-selective groups also delivered an improved power density for CEM in the case of a LiCl electrolyte. The membranes were also found susceptible to pH changes, showing excellent proton transport abilities. The tunable nanochannel sizes and surface charge densities, pH responsiveness, and functional robustness render the materials promising for sustainable energy harvesting.

## MATERIALS AND METHODS

**Chemicals.** Flakes of natural graphite were purchased from Active Carbon India Pvt. Ltd. Sulfuric acid (H<sub>2</sub>SO<sub>4</sub>, 95%–98%) and hydrochloric acid (HCl, 36%) were obtained from Rankem Chemicals Pvt. Ltd. The styrene monomer (C<sub>8</sub>H<sub>8</sub>) was procured from Avra Synthesis Pvt. Ltd. Nitric acid (HNO<sub>3</sub>, 65%–68%) and potassium chloride (KCl, 99%) were obtained from Merck, India. Lithium chloride anhydrous (LiCl, 99%) was obtained from Sisco Research Laboratories Pvt. Ltd.

**Characterization.** FE-SEM images were captured using a Thermo Scientific Verios G4 UC SEM. IR spectra of rGO-TiO<sub>2</sub> and related functionalized composites were measured by a PerkinElmer FT-IR

spectrometer. Samples were freeze-dried using an Eyla freeze-dryer (Model No: FDU-1200). Powder XRD data were measured using a Bruker D8 Advance X-ray diffractometer with Cu K $\alpha$  as the source of irradiation ( $h\nu = 8047.8$  eV).

**Resin Preparation and Membrane Fabrication.** The rGO-TiO<sub>2</sub> powdered material was prepared by carrying out a hydrothermal reaction between the TiOSO<sub>4</sub> solution (1.0 g) and GO suspension (1 mL) in the presence of L-cysteine. The mixture of these precursors was kept in an autoclave for 12 h at 160 °C. Post reaction, the product was thoroughly washed in a 1:1 water–methanol mixture.

Before polystyrene functionalization, the prepared rGO-TiO<sub>2</sub> powder (100 mg), styrene monomer (15 mg), and divinylbenzene (1.5 mg) were mixed in deionized (di) water (25 mL). The polymerization process was performed in atmosphere by purging N<sub>2</sub> gas. Under constant stirring, K<sub>2</sub>S<sub>2</sub>O<sub>8</sub> (320 mg) was added to the mixture. Stirring was carried out for another 30 min at room temperature. The temperature of the mixture was then increased to 70 °C and maintained for 1 h. After 1 h, the temperature was increased to 90 °C and maintained under stirring for the next 12 h. After completion, the product was washed two to three times with di water and kept in a hot air oven at 90 °C for drying. For sulfonation, the prepared rGO-TiO<sub>2</sub>-PS powder was suspended in H<sub>2</sub>SO<sub>4</sub> (4 M) for 24 h at 100 °C under constant stirring. The product was later washed in a 1:1 water–methanol mixture.

For AER, anion-exchange rGO-TiO<sub>2</sub>-PS was functionalized with chloromethyl groups by the Friedel–Craft alkylation reaction. Next, the resulting composite (1 g) was added to a mixture of chloromethyl methyl ether (3 mL) and di water (10 mL). After stirring at room temperature (RT) for 2 h, ZnCl<sub>2</sub> (380 mg) was added and stirring was continued for another 12 h at ~35 °C. The chloromethylated product was rinsed in acetone and dried at 65 °C overnight. It was then allowed to swell in 1,2-dichloromethane for 2 h. Further, trimethylamine hydrochloride (1 g) was added to the mixture and kept for stirring at RT for 6 h. The final chloro-aminated resin (rGO-TiO<sub>2</sub>-PS-CH<sub>2</sub>-N<sup>+</sup>(CH<sub>3</sub>)<sub>3</sub>Cl<sup>-</sup>) was dried in an oven at 65 °C. Membranes (CEM and AEM) were prepared by vacuum filtration



of the obtained corresponding powdered materials through grade 42 Whatman filter paper.

**Electrical Measurements.** Ionic conductivity measurements were performed using a CH Instruments electrochemical analyzer (CH 600A). The test membrane was mounted at the junction of a two-compartment cell, each a 40 mL volume. The conductivity and energy conversion experiments were performed by placing an Ag/AgCl electrode in either compartment. For the energy conversion experiments, the electrodes were connected to a picoammeter (Keithley 6485). For the pH-dependent studies, the pH values of the electrolytes were adjusted using stock solutions. Here, 0.01 M stock solutions of NaOH and HCl were used for obtaining alkaline or acidic conditions, respectively. Fresh electrolytes were used for all measurements.

**MD Simulations.** Graphene sheets of 5 nm<sup>2</sup> areas were generated using the GOPY package.<sup>57</sup> The sheets were further functionalized with -SO<sub>3</sub>H to create cation-exchange nanochannels. MD simulation-related parameters and charges of the carboxyl, epoxy, and hydroxyl groups were adopted from a computational study where authors had conducted extensive studies on the biomolecular interactions with GO, rGO, and graphene sheets.<sup>58</sup> Parameters for -SO<sub>3</sub>H were obtained from GAFF through the antechamber program of Ambertools21.<sup>59–61</sup> MD simulations were performed with GROMACS version 2021.2. Force field parameters for GO were taken from a previous study and implemented in AMBER99.<sup>58</sup> The TIP3P water model was used to construct the water box. All carbon atoms constituting the GO sheets were positionally restrained (1000 kJ mol<sup>-1</sup> nm<sup>-2</sup>) throughout the simulation for all the systems to maintain an intersheet separation of 1.5 nm. The LINCS algorithm was used to constrain H-bonds, and periodic boundary conditions were applied in all three directions. For long-range electrostatic interactions, particle mesh Ewald (PME) was used. The Coulomb and van der Waals (VdW) cutoff values were set at 1.4 nm. Systems were energy minimized, followed by the equilibration of all the systems for 1 ns. Later, a production run of 5 ns was performed in all three systems along with the 1 ns-short production simulation. The trajectories were analyzed using GROMACS and Python scripts in MDAnalysis suite of programs and visual molecular dynamics (VMD).<sup>62,63</sup>

For the nonequilibrium molecular dynamic (NEMD) simulation, the SO<sub>3</sub>H-rGO filters were placed between the feed side on the left and permeate side on the right, with dimensions of 5 nm × 5 nm × 15 nm in X, Y, and Z directions, respectively. The permeate side consisted of an empty box. For the 0.5 M system, the feed side was filled with 2543 water molecules and 75 Na<sup>+</sup> and 75 Cl<sup>-</sup> ions. Similarly, the 1.0 M system contained 2493 water molecules and 151 Na<sup>+</sup> and 151 Cl<sup>-</sup> ions. The 1.5 M system consisted of 2443 water molecules and 226 Na<sup>+</sup> and 226 Cl<sup>-</sup> ions. A graphene sheet was placed at each end of the simulation box to act as pistons to exert pressure.

## ■ ASSOCIATED CONTENT

### SI Supporting Information

The Supporting Information is available free of charge at <https://pubs.acs.org/doi/10.1021/acssuschemeng.2c04138>.

Ion selectivities of membranes, pore size measurements, powder XRD, SEM-EDS, and tabular performance comparison with previously reported membrane systems (PDF)

## ■ AUTHOR INFORMATION

### Corresponding Authors

**Tiju Thomas** – Department of Metallurgical and Materials Engineering, Indian Institute of Technology Madras, Chennai 600036, India; Email: [tijuthomas@iitm.ac.in](mailto:tijuthomas@iitm.ac.in)

**Thalappil Pradeep** – International Centre for Clean Water, Chennai 600113, India; DST Unit of Nanoscience, Thematic

Unit of Excellence, Department of Chemistry, Indian Institute of Technology Madras, Chennai 600036, India;

orcid.org/0000-0003-3174-534X; Email: [pradeep@iitm.ac.in](mailto:pradeep@iitm.ac.in)

## Authors

**Ankit Nagar** – DST Unit of Nanoscience, Thematic Unit of Excellence, Department of Chemistry and Department of Metallurgical and Materials Engineering, Indian Institute of Technology Madras, Chennai 600036, India

**Md Rabiul Islam** – DST Unit of Nanoscience, Thematic Unit of Excellence, Department of Chemistry, Indian Institute of Technology Madras, Chennai 600036, India

**Karthek Joshua** – DST Unit of Nanoscience, Thematic Unit of Excellence, Department of Chemistry, Indian Institute of Technology Madras, Chennai 600036, India

**Tanvi Gupte** – DST Unit of Nanoscience, Thematic Unit of Excellence, Department of Chemistry, Indian Institute of Technology Madras, Chennai 600036, India; orcid.org/0000-0002-0518-8482

**Sourav Kanti Jana** – DST Unit of Nanoscience, Thematic Unit of Excellence, Department of Chemistry, Indian Institute of Technology Madras, Chennai 600036, India; orcid.org/0000-0001-5772-7022

**Sujan Manna** – DST Unit of Nanoscience, Thematic Unit of Excellence, Department of Chemistry, Indian Institute of Technology Madras, Chennai 600036, India

Complete contact information is available at:

<https://pubs.acs.org/10.1021/acssuschemeng.2c04138>

## Notes

The authors declare no competing financial interest.

## ■ ACKNOWLEDGMENTS

The authors thank the Department of Science and Technology (DST), Government of India, for supporting their research program. A.N., T.G., and S.M. thank IIT Madras for their doctoral student fellowships. M.R.I. thanks the Council of Scientific & Industrial Research (CSIR) for his fellowship.

## ■ REFERENCES

- (1) Logan, B. E.; Elimelech, M. Membrane-Based Processes for Sustainable Power Generation Using Water. *Nature* **2012**, *488* (7411), 313–319.
- (2) Post, J. W.; Veerman, J.; Hamelers, H. V. M.; Euverink, G. J. W.; Metz, S. J.; Nymeijer, K.; Buisman, C. J. N. Salinity-Gradient Power: Evaluation of Pressure-Retarded Osmosis and Reverse Electrodialysis. *J. Membr. Sci.* **2007**, *288* (1–2), 218–230.
- (3) Porada, S.; Van Egmond, W. J.; Post, J. W.; Saakes, M.; Hamelers, H. V. M. Tailoring Ion Exchange Membranes to Enable Low Osmotic Water Transport and Energy Efficient Electrodialysis. *J. Membr. Sci.* **2018**, *552*, 22–30.
- (4) Hong, J. G.; Gao, H.; Gan, L.; Tong, X.; Xiao, C.; Liu, S.; Zhang, B.; Chen, Y. Nanocomposite and Nanostructured Ion-Exchange Membrane in Salinity Gradient Power Generation Using Reverse Electrodialysis. In *Advanced Nanomaterials for Membrane Synthesis and Its Applications*; Elsevier, 2019; pp 295–316.
- (5) Cusick, R. D.; Kim, Y.; Logan, B. E. Energy Capture from Thermolytic Solutions in Microbial Reverse-Electrodialysis Cells. *Science* (80-). **2012**, *335* (6075), 1474–1477.
- (6) Zhu, X.; Hao, J.; Bao, B.; Zhou, Y.; Zhang, H.; Pang, J.; Jiang, Z.; Jiang, L. Unique Ion Rectification in Hypersaline Environment: A High-Performance and Sustainable Power Generator System. *Sci. Adv.* **2018**, *4* (10), eaau1665.

- (7) Mei, Y.; Liu, L.; Lu, Y.-C.; Tang, C. Y. Reverse Electrodialysis Chemical Cell for Energy Harvesting from Controlled Acid–Base Neutralization. *Environ. Sci. Technol.* **2019**, *53* (8), 4640–4647.
- (8) Siria, A.; Poncharal, P.; Bianco, A.-L.; Fulcrand, R.; Blase, X.; Purcell, S. T.; Bocquet, L. Giant Osmotic Energy Conversion Measured in a Single Transmembrane Boron Nitride Nanotube. *Nature* **2013**, *494* (7438), 455–458.
- (9) Feng, J.; Graf, M.; Liu, K.; Ovchinnikov, D.; Dumcenco, D.; Heiranian, M.; Nandigana, V.; Aluru, N. R.; Kis, A.; Radenovic, A. Single-Layer MoS<sub>2</sub> Nanopores as Nanopower Generators. *Nature* **2016**, *536* (7615), 197–200.
- (10) Macha, M.; Marion, S.; Nandigana, V. V. R.; Radenovic, A. 2D Materials as an Emerging Platform for Nanopore-Based Power Generation. *Nat. Rev. Mater.* **2019**, *4* (9), 588–605.
- (11) Gadaleta, A.; Sempere, C.; Gravelle, S.; Siria, A.; Fulcrand, R.; Ybert, C.; Bocquet, L. Sub-Additive Ionic Transport across Arrays of Solid-State Nanopores. *Phys. Fluids* **2014**, *26* (1), 012005.
- (12) Siria, A.; Bocquet, M.-L.; Bocquet, L. New Avenues for the Large-Scale Harvesting of Blue Energy. *Nat. Rev. Chem.* **2017**, *1* (11), 1–10.
- (13) Ding, L.; Xiao, D.; Lu, Z.; Deng, J.; Wei, Y.; Caro, J.; Wang, H. Oppositely Charged Ti<sub>3</sub>C<sub>2</sub>T<sub>x</sub> MXene Membranes with 2D Nanofluidic Channels for Osmotic Energy Harvesting. *Angew. Chem.* **2020**, *132* (22), 8798–8804.
- (14) Lin, X.; Liu, P.; Xin, W.; Teng, Y.; Chen, J.; Wu, Y.; Zhao, Y.; Kong, X.; Jiang, L.; Wen, L. Heterogeneous MXene/PS-b-P2VP Nanofluidic Membranes with Controllable Ion Transport for Osmotic Energy Conversion. *Adv. Funct. Mater.* **2021**, *31* (45), 2105013.
- (15) Esfandiari, A.; Radha, B.; Wang, F. C.; Yang, Q.; Hu, S.; Garaj, S.; Nair, R. R.; Geim, A. K.; Gopinadhan, K. Size Effect in Ion Transport through Angstrom-Scale Slits. *Science* (80-). **2017**, *358* (6362), 511–513.
- (16) Xiao, K.; Giusto, P.; Wen, L.; Jiang, L.; Antonietti, M. Nanofluidic Ion Transport and Energy Conversion through Ultrathin Free-Standing Polymeric Carbon Nitride Membranes. *Angew. Chemie Int. Ed.* **2018**, *57* (32), 10123–10126.
- (17) Cheng, H.; Zhou, Y.; Feng, Y.; Geng, W.; Liu, Q.; Guo, W.; Jiang, L. Electrokinetic Energy Conversion in Self-Assembled 2D Nanofluidic Channels with Janus Nanobuilding Blocks. *Adv. Mater.* **2017**, *29* (23), 1700177.
- (18) Liu, P.; Sun, Y.; Zhu, C.; Niu, B.; Huang, X.; Kong, X.-Y.; Jiang, L.; Wen, L. Neutralization Reaction Assisted Chemical-Potential-Driven Ion Transport through Layered Titanium Carbides Membrane for Energy Harvesting. *Nano Lett.* **2020**, *20* (5), 3593–3601.
- (19) Xin, W.; Jiang, L.; Wen, L. Two-Dimensional Nanofluidic Membranes toward Harvesting Salinity Gradient Power. *Acc. Chem. Res.* **2021**, *54* (22), 4154–4165.
- (20) Zhang, Z.; Wen, L.; Jiang, L. Nanofluidics for Osmotic Energy Conversion. *Nat. Rev. Mater.* **2021**, *6* (7), 622–639.
- (21) Laucirica, G.; Toimil-Molares, M. E.; Trautmann, C.; Marmisollé, W.; Azzaroni, O. Nanofluidic Osmotic Power Generators—Advanced Nanoporous Membranes and Nanochannels for Blue Energy Harvesting. *Chem. Sci.* **2021**, *12*, 12874.
- (22) Yu, W.; Sisi, L.; Haiyan, Y.; Jie, L. Progress in the Functional Modification of Graphene/Graphene Oxide: A Review. *RSC Adv.* **2020**, *10* (26), 15328–15345.
- (23) Zhou, K.-G.; Vasu, K. S.; Cherian, C. T.; Neek-Amal, M.; Zhang, J. C.; Ghorbanfekr-Kalashami, H.; Huang, K.; Marshall, O. P.; Kravets, V. G.; Abraham, J.; Su, Y.; Grigorenko, A. N.; Pratt, A.; Geim, A. K.; Peeters, F. M.; Novoselov, K. S.; Nair, R. R. Electrically Controlled Water Permeation through Graphene Oxide Membranes. *Nature* **2018**, *559* (7713), 236–240.
- (24) Xue, S.; Ji, C.; Kowal, M. D.; Molas, J. C.; Lin, C.-W.; McVerry, B. T.; Turner, C. L.; Mak, W. H.; Anderson, M.; Muni, M.; Hoek, E. M. V.; Xu, Z.-L.; Kaner, R. B. Nanostructured Graphene Oxide Composite Membranes with Ultrapermeability and Mechanical Robustness. *Nano Lett.* **2020**, *20* (4), 2209–2218.
- (25) Abraham, J.; Vasu, K. S.; Williams, C. D.; Gopinadhan, K.; Su, Y.; Cherian, C. T.; Dix, J.; Prestat, E.; Haigh, S. J.; Grigorieva, I. V.; Carbone, P.; Geim, A. K.; Nair, R. R. Tunable Sieving of Ions Using Graphene Oxide Membranes. *Nat. Nanotechnol.* **2017**, *12* (6), 546.
- (26) Huang, X.; Marsh, K. L.; McVerry, B. T.; Hoek, E. M. V.; Kaner, R. B. Low-Fouling Antibacterial Reverse Osmosis Membranes via Surface Grafting of Graphene Oxide. *ACS Appl. Mater. Interfaces* **2016**, *8* (23), 14334–14338.
- (27) Sanad, M. F.; Chava, V. S. N.; Shalan, A. E.; Enriquez, L. G.; Zheng, T.; Pilla, S.; Sreenivasan, S. T. Engineering of Electron Affinity and Interfacial Charge Transfer of Graphene for Self-Powered Nonenzymatic Biosensor Applications. *ACS Appl. Mater. Interfaces* **2021**, *13* (34), 40731–40741.
- (28) Deng, S.; Gao, E.; Wang, Y.; Sen, S.; Sreenivasan, S. T.; Behura, S.; Král, P.; Xu, Z.; Berry, V. Confined, Oriented, and Electrically Anisotropic Graphene Wrinkles on Bacteria. *ACS Nano* **2016**, *10* (9), 8403–8412.
- (29) Alkhouzaam, A.; Qiblawey, H. Functional GO-Based Membranes for Water Treatment and Desalination: Fabrication Methods, Performance and Advantages. A Review. *Chemosphere* **2021**, *274*, 129853.
- (30) Liu, S.; Yu, J.; Jaroniec, M. Anatase TiO<sub>2</sub> with Dominant High-Energy {001} Facets: Synthesis, Properties, and Applications. *Chem. Mater.* **2011**, *23* (18), 4085–4093.
- (31) Pelaez, M.; Nolan, N. T.; Pillai, S. C.; Seery, M. K.; Falaras, P.; Kontos, A. G.; Dunlop, P. S. M.; Hamilton, J. W. J.; Byrne, J. A.; O’Shea, K.; Entezari, M. H.; Dionysiou, D. D. A Review on the Visible Light Active Titanium Dioxide Photocatalysts for Environmental Applications. *Appl. Catal. B Environ.* **2012**, *125*, 331–349.
- (32) Wang, M.; Jia, Y.; Yao, T.; Wang, K. The Endowment of Monovalent Selectivity to Cation Exchange Membrane by Photo-Induced Covalent Immobilization and Self-Crosslinking of Chitosan. *J. Membr. Sci.* **2013**, *442*, 39–47.
- (33) Islam, M. R.; Gupta, S. S.; Jana, S. K.; Srikrishnarka, P.; Mondal, B.; Chennu, S.; Ahuja, T.; Chakraborty, A.; Pradeep, T. A Covalently Integrated Reduced Graphene Oxide–Ion-Exchange Resin Electrode for Efficient Capacitive Deionization. *Adv. Mater. Interfaces* **2021**, *8* (5), 2001998.
- (34) Luzan, S. M.; Talyzin, A. V. Hydration of Graphite Oxide in Electrolyte and Non-Electrolyte Solutions. *J. Phys. Chem. C* **2011**, *115* (50), 24611–24614.
- (35) Chen, S.; Zhu, J.; Wu, X.; Han, Q.; Wang, X. Graphene Oxide–MnO<sub>2</sub> Nanocomposites for Supercapacitors. *ACS Nano* **2010**, *4* (5), 2822–2830.
- (36) Liu, W.; Cai, J.; Ding, Z.; Li, Z. TiO<sub>2</sub>/RGO Composite Aerogels with Controllable and Continuously Tunable Surface Wettability for Varied Aqueous Photocatalysis. *Appl. Catal. B Environ.* **2015**, *174*, 421–426.
- (37) Sher Shah, M. S. A.; Park, A. R.; Zhang, K.; Park, J. H.; Yoo, P. J. Green Synthesis of Biphasic TiO<sub>2</sub>–Reduced Graphene Oxide Nanocomposites with Highly Enhanced Photocatalytic Activity. *ACS Appl. Mater. Interfaces* **2012**, *4* (8), 3893–3901.
- (38) Li, Y.; Zhu, H.; Shen, F.; Wan, J.; Lacey, S.; Fang, Z.; Dai, H.; Hu, L. Nanocellulose as Green Dispersant for Two-Dimensional Energy Materials. *Nano energy* **2015**, *13*, 346–354.
- (39) Cote, L. J.; Kim, F.; Huang, J. Langmuir–Blodgett Assembly of Graphite Oxide Single Layers. *J. Am. Chem. Soc.* **2009**, *131* (3), 1043–1049.
- (40) Hafeez, H. Y.; Lakhera, S. K.; Narayanan, N.; Harish, S.; Hayakawa, Y.; Lee, B.-K.; Neppolian, B. Environmentally Sustainable Synthesis of a CoFe<sub>2</sub>O<sub>4</sub>–TiO<sub>2</sub>/RGO Ternary Photocatalyst: A Highly Efficient and Stable Photocatalyst for High Production of Hydrogen (Solar Fuel). *ACS omega* **2019**, *4* (1), 880–891.
- (41) Zhou, S.; Xie, L.; Zhang, L.; Wen, L.; Tang, J.; Zeng, J.; Liu, T.; Peng, D.; Yan, M.; Qiu, B.; Liang, Q.; Liang, K.; Jiang, L.; Kong, B. Interfacial Super-Assembly of Ordered Mesoporous Silica–Alumina Heterostructure Membranes with Ph-Sensitive Properties for Osmotic Energy Harvesting. *ACS Appl. Mater. Interfaces* **2021**, *13* (7), 8782–8793.
- (42) Daiguji, H. Ion Transport in Nanofluidic Channels. *Chem. Soc. Rev.* **2010**, *39* (3), 901–911.

- (43) Laucirica, G.; Albesa, A. G.; Toimil-Molares, M. E.; Trautmann, C.; Marmisollé, W. A.; Azzaroni, O. Shape Matters: Enhanced Osmotic Energy Harvesting in Bullet-Shaped Nanochannels. *Nano Energy* **2020**, *71*, 104612.
- (44) Yan, F.; Yao, L.; Chen, K.; Yang, Q.; Su, B. An Ultrathin and Highly Porous Silica Nanochannel Membrane: Toward Highly Efficient Salinity Energy Conversion. *J. Mater. Chem. A* **2019**, *7* (5), 2385–2391.
- (45) Lu, J.; Zhang, H.; Hou, J.; Li, X.; Hu, X.; Hu, Y.; Easton, C. D.; Li, Q.; Sun, C.; Thornton, A. W.; Hill, M. R.; Zhang, X.; Jiang, G.; Liu, J. Z.; Hill, A. J.; Freeman, B. D.; Jiang, L.; Wang, H. Efficient Metal Ion Sieving in Rectifying Subnanochannels Enabled by Metal–Organic Frameworks. *Nat. Mater.* **2020**, *19* (7), 767–774.
- (46) Zhu, C.; Liu, P.; Niu, B.; Liu, Y.; Xin, W.; Chen, W.; Kong, X.-Y.; Zhang, Z.; Jiang, L.; Wen, L. Metallic Two-Dimensional MoS<sub>2</sub> Composites as High-Performance Osmotic Energy Conversion Membranes. *J. Am. Chem. Soc.* **2021**, *143* (4), 1932–1940.
- (47) Kamcev, J.; Sujanani, R.; Jang, E.-S.; Yan, N.; Moe, N.; Paul, D. R.; Freeman, B. D. Salt Concentration Dependence of Ionic Conductivity in Ion Exchange Membranes. *J. Membr. Sci.* **2018**, *547*, 123–133.
- (48) Xiao, K.; Jiang, L.; Antonietti, M. Ion Transport in Nanofluidic Devices for Energy Harvesting. *Joule* **2019**, *3* (10), 2364–2380.
- (49) Pakulski, D.; Czepa, W.; Buffa, S. D.; Ciesielski, A.; Samori, P. Atom-Thick Membranes for Water Purification and Blue Energy Harvesting. *Adv. Funct. Mater.* **2020**, *30* (2), 1902394.
- (50) Chen, C.; Liu, D.; He, L.; Qin, S.; Wang, J.; Razal, J. M.; Kotov, N. A.; Lei, W. Bio-Inspired Nanocomposite Membranes for Osmotic Energy Harvesting. *Joule* **2020**, *4* (1), 247–261.
- (51) Xin, W.; Xiao, H.; Kong, X.-Y.; Chen, J.; Yang, L.; Niu, B.; Qian, Y.; Teng, Y.; Jiang, L.; Wen, L. Biomimetic Nacre-like Silk-Crosslinked Membranes for Osmotic Energy Harvesting. *ACS Nano* **2020**, *14* (8), 9701–9710.
- (52) Pendse, A.; Cetindag, S.; Rehak, P.; Behura, S.; Gao, H.; Nguyen, N. H. L.; Wang, T.; Berry, V.; Kral, P.; Shan, J.; Kim, S. Highly Efficient Osmotic Energy Harvesting in Charged Boron-Nitride-Nanopore Membranes. *Adv. Funct. Mater.* **2021**, *31* (15), 2009586.
- (53) Guo, Y.; Ying, Y.; Mao, Y.; Peng, X.; Chen, B. Polystyrene Sulfonate Threaded through a Metal–Organic Framework Membrane for Fast and Selective Lithium-ion Separation. *Angew. Chem.* **2016**, *128* (48), 15344–15348.
- (54) Wang, F.; Wang, Z.; Wang, S.; Meng, X.; Jin, Y.; Yang, N.; Sunarso, J.; Liu, S. Mechanically Intensified and Stabilized MXene Membranes via the Combination of Graphene Oxide for Highly Efficient Osmotic Power Production. *J. Membr. Sci.* **2022**, *647*, 120280.
- (55) Xu, Y.; Zhang, K.; Chen, S.; Zhang, X.; Chen, Y.; Li, D.; Xu, F. Two-Dimensional Lamellar MXene/Three-Dimensional Network Bacterial Nanocellulose Nanofiber Composite Janus Membranes as Nanofluidic Osmotic Power Generators. *Electrochim. Acta* **2022**, *412*, 140162.
- (56) Liu, Y.-C.; Yeh, L.-H.; Zheng, M.-J.; Wu, K. C.-W. Highly Selective and High-Performance Osmotic Power Generators in Subnanochannel Membranes Enabled by Metal–Organic Frameworks. *Sci. Adv.* **2021**, *7* (10), eabe9924.
- (57) Muraru, S.; Burns, J. S.; Ionita, M. GOPY: A Tool for Building 2D Graphene-Based Computational Models. *SoftwareX* **2020**, *12*, 100586.
- (58) Baweja, L.; Balamurugan, K.; Subramanian, V.; Dhawan, A. Hydration Patterns of Graphene-Based Nanomaterials (GBNMs) Play a Major Role in the Stability of a Helical Protein: A Molecular Dynamics Simulation Study. *Langmuir* **2013**, *29* (46), 14230–14238.
- (59) Wang, J.; Wolf, R. M.; Caldwell, J. W.; Kollman, P. A.; Case, D. A. Development and Testing of a General Amber Force Field. *J. Comput. Chem.* **2004**, *25* (9), 1157–1174.
- (60) Bayly, C. I.; Cieplak, P.; Cornell, W.; Kollman, P. A. A Well-Behaved Electrostatic Potential Based Method Using Charge Restraints for Deriving Atomic Charges: The RESP Model. *J. Phys. Chem.* **1993**, *97* (40), 10269–10280.
- (61) Jakalian, A.; Bush, B. L.; Jack, D. B.; Bayly, C. I. Fast, Efficient Generation of High-quality Atomic Charges. AM1-BCC Model: I. Method. *J. Comput. Chem.* **2000**, *21* (2), 132–146.
- (62) Abraham, M. J.; Murtola, T.; Schulz, R.; Páll, S.; Smith, J. C.; Hess, B.; Lindahl, E. GROMACS: High Performance Molecular Simulations through Multi-Level Parallelism from Laptops to Supercomputers. *SoftwareX* **2015**, *1*, 19–25.
- (63) Humphrey, W.; Dalke, A.; Schulten, K. VMD: Visual Molecular Dynamics. *J. Mol. Graph.* **1996**, *14* (1), 33–38.

# Supporting Information

## Ion-Exchanging Graphenic Nanochannels for Macroscopic Osmotic Energy Harvesting

Ankit Nagar<sup>†,‡</sup>, Md Rabiul Islam<sup>†</sup>, Kartheek Joshua<sup>†</sup>, Tanvi Gupte<sup>†</sup>, Sourav Kanti Jana<sup>†</sup>,  
Sujan Manna<sup>†</sup>, Tiju Thomas<sup>\*,‡</sup> and Thalappil Pradeep<sup>\*,§,†</sup>

<sup>†</sup>DST Unit of Nanoscience, Thematic Unit of Excellence, Department of Chemistry, Indian  
Institute of Technology Madras, Chennai 600036, India.

<sup>‡</sup>Department of Metallurgical and Materials Engineering, Indian Institute of Technology  
Madras, Chennai 600036, India.

<sup>§</sup>International Centre for Clean Water, 2<sup>nd</sup> Floor, B-Block, IIT Madras Research Park,  
Kanagam Road, Taramani, Chennai 600113, India

Note	Figure/Table	Details	Page No.
1	Figure S1	Photograph of a contorted membrane	S2
	Figure S2	Microscopy images of the rGO-TiO <sub>2</sub> membrane	S2
	Figure S3	HRTEM micrographs of rGO and rGO-TiO <sub>2</sub>	S3
	Figure S4	Powder XRD of all prepared materials	S4
2	Table S1	Specific surface areas of the materials	S5
	Figure S5	Pore size distribution curves	S5
	Figure S6	Pore characterization of rGO-TiO <sub>2</sub> (TiO <sub>2</sub> 99% w/w)	S5
	Figure S7	Zeta potential vs pH	S6
	Figure S8	Photographs of the dispersions	S6
3	Figure S9	Molecule-exclusion test	S8
4	Figure S10	SEM-EDX of REF, AER and CER	S9
5	Figure S11	Circuit diagram to measure osmotic power	S10
	Table S2	Osmotic current and potential for CEM	S10
	Table S3	Osmotic current and potential for AEM	S10

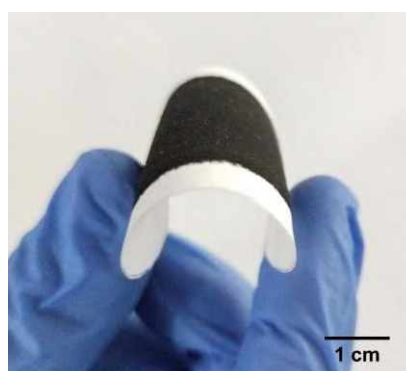


	Figure S12	Power output for different electrolytes for CEM	S11
	Figure S13	Power output of CEM for 15 days	S11
6	Table S4	Literature survey of existing RED devices	S11
7	Figure S14	Simulated system for ion transport	S16
	Figure S15	Simulation conformations at different concentrations	S17
	Table S5	Interaction distances at different concentrations	S18

12

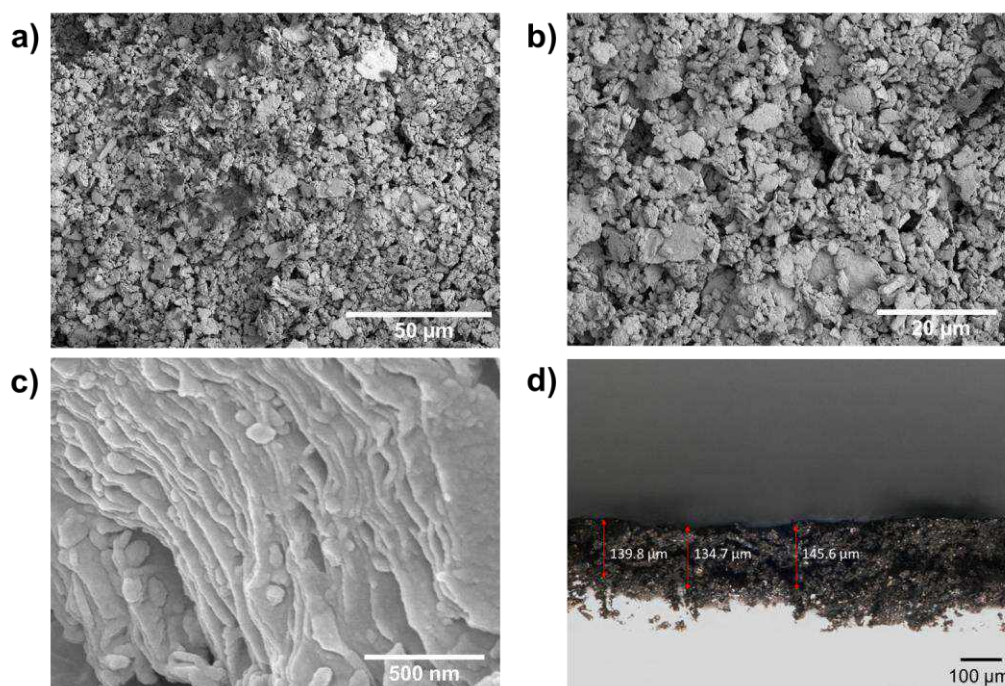
13 **Note 1. Characterization of the resins and corresponding membranes**

14



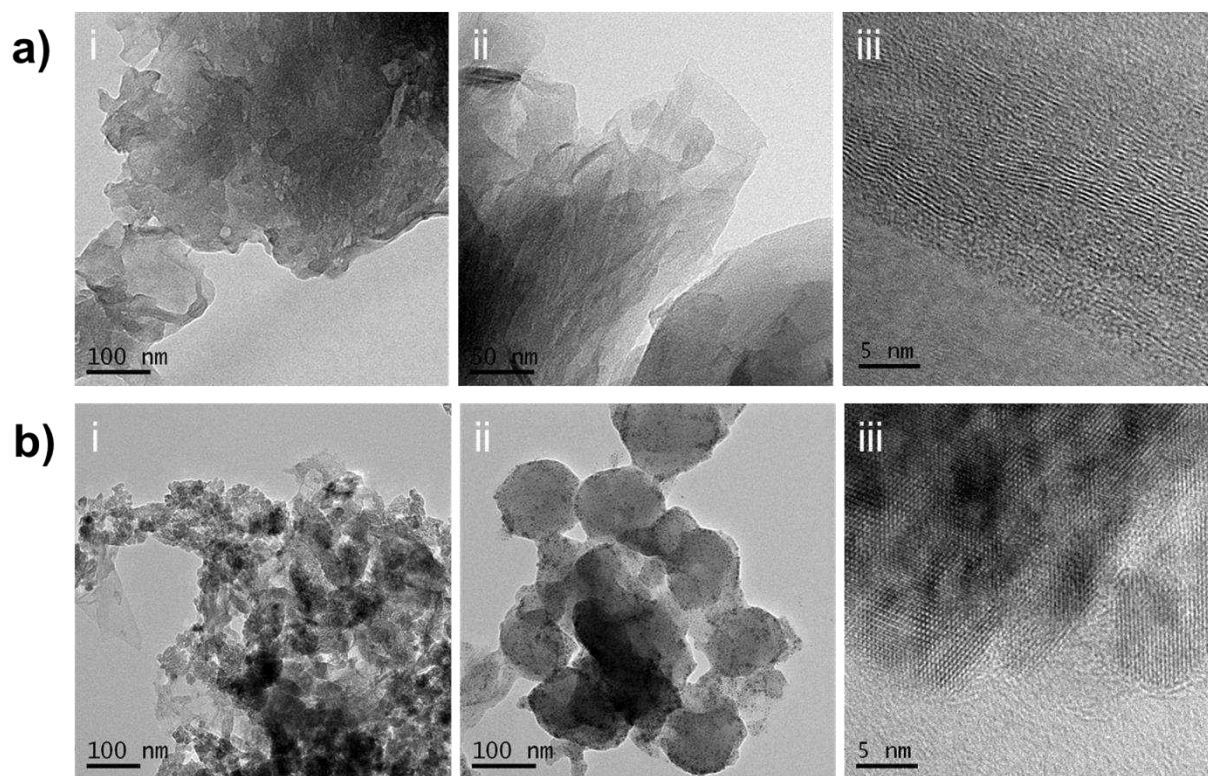
15

16 **Figure S1.** The optical image showing flexibility of a vacuum-filtered membrane contorted  
 17 manually without any observable damage.



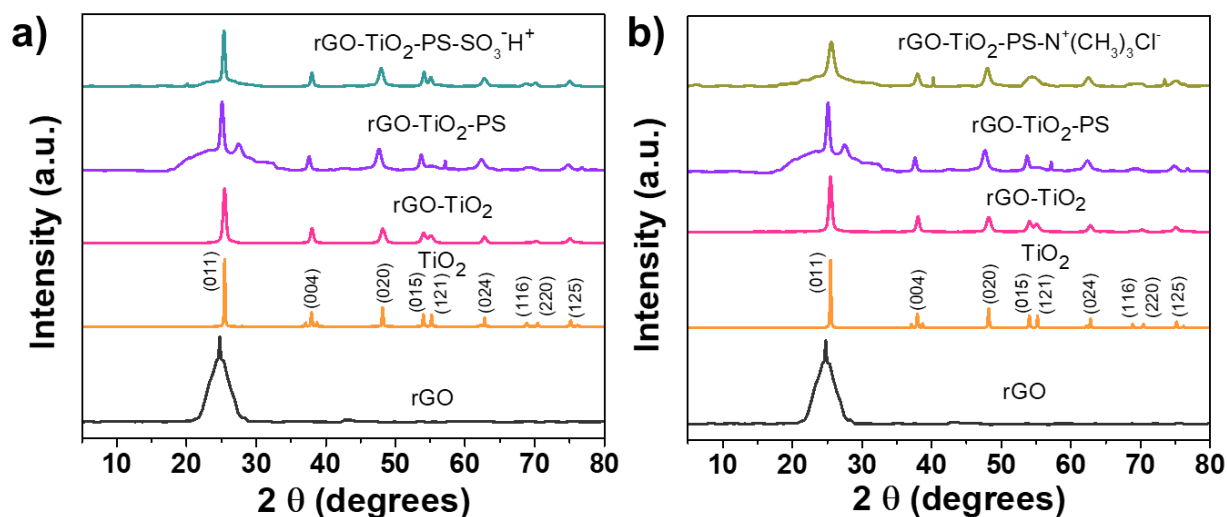
18

19 **Figure S2.** a,b) Top-view FESEM images of the reference rGO-TiO<sub>2</sub> membrane. c) Surface  
20 morphology of a particle. It shows presence of arrays of wiggly rGO nanosheets covered and  
21 intercalated uniformly with TiO<sub>2</sub> nanoparticles. d) Optical image of the cross-section of the  
22 membrane depicting film thickness. The white region below the film is the filter paper. Due to  
23 vacuum filtration, particles have penetrated the depth of the filter paper. Therefore, measured  
24 film thicknesses are tentative. The mean membrane thickness is  $140.0 \pm 4.5 \mu\text{m}$ .



25  
26 **Figure S3.** HRTEM micrographs of a) rGO, and b) rGO-TiO<sub>2</sub>. The folding and overlapping  
27 of rGO sheets are apparent from a-i and b-i.





28

29 **Figure S4.** Powder XRD patterns for rGO, TiO<sub>2</sub>, rGO-TiO<sub>2</sub> alongside a) rGO-TiO<sub>2</sub>-PS-SO<sub>3</sub>H  
 30 (CER) and b) rGO-TiO<sub>2</sub>-PS-N<sup>+</sup>(CH<sub>3</sub>)<sub>3</sub>Cl<sup>-</sup> (AER). Pure rGO shows a broad peak at 24.8°. Characteristic peaks of TiO<sub>2</sub> shown in a) and b) confirm the presence of anatase phase. The  
 31 rGO-TiO<sub>2</sub>-PS, CER and AER composites show signature peaks of anatase TiO<sub>2</sub>, as well as  
 32 peak broadening around 24.8° corresponding to rGO.  
 33

#### 34 **Note 2. Role of TiO<sub>2</sub> in the nanocomposite**

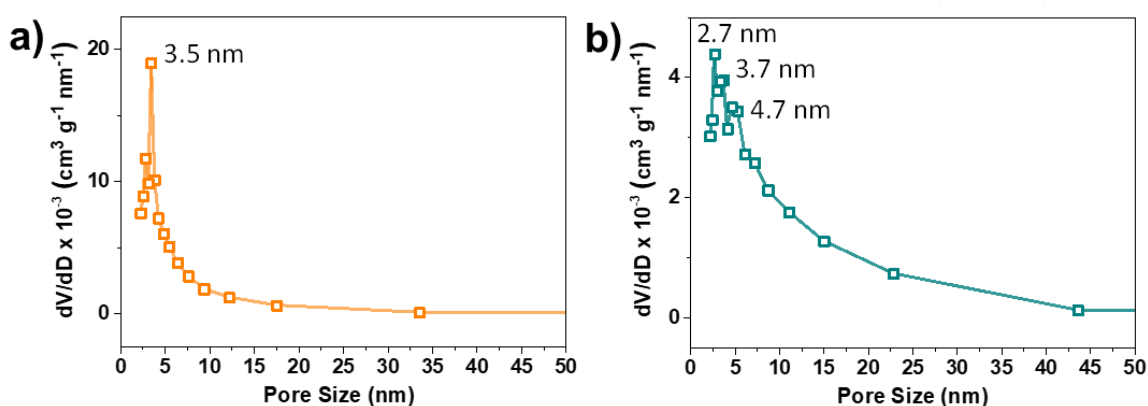
35 We performed surface area measurements using the Brunauer–Emmett–Teller (BET) method  
 36 on three rGO-TiO<sub>2</sub> composites with varying TiO<sub>2</sub> loading in the range of 0-99 % w/w. It was  
 37 observed that an increase in the TiO<sub>2</sub> loading leads to an increase in the specific surface area  
 38 (Table S1). For a 50 % (w/w) TiOSO<sub>4</sub> precursor, the resulting composite, referred to as rGO-  
 39 TiO<sub>2</sub> (50% w/w), has nearly double the surface area, compared to rGO. And for a 99% TiOSO<sub>4</sub>  
 40 precursor, the obtained composite has three-fold higher surface area compared to rGO. Larger  
 41 surface area indicates presence of abundant nanochannels. Therefore, TiO<sub>2</sub> loading was kept at  
 42 99% (w/w) in the rGO-TiO<sub>2</sub> nanocomposite. All composites were found to be mesoporous in  
 43 nature with pore size in the range 2-10 nm (Figure S4, S5). The pore distribution curves  
 44 obtained from the desorption profile reveal highest mesoporous character in the rGO-TiO<sub>2</sub>

45 (TiO<sub>2</sub> 99% w/w), compared to the other two materials, with majority of the pores having a size  
 46 of 9.9 nm.

47 **Table S1.** Specific surface areas of rGO and rGO-TiO<sub>2</sub> composites from BET measurements.

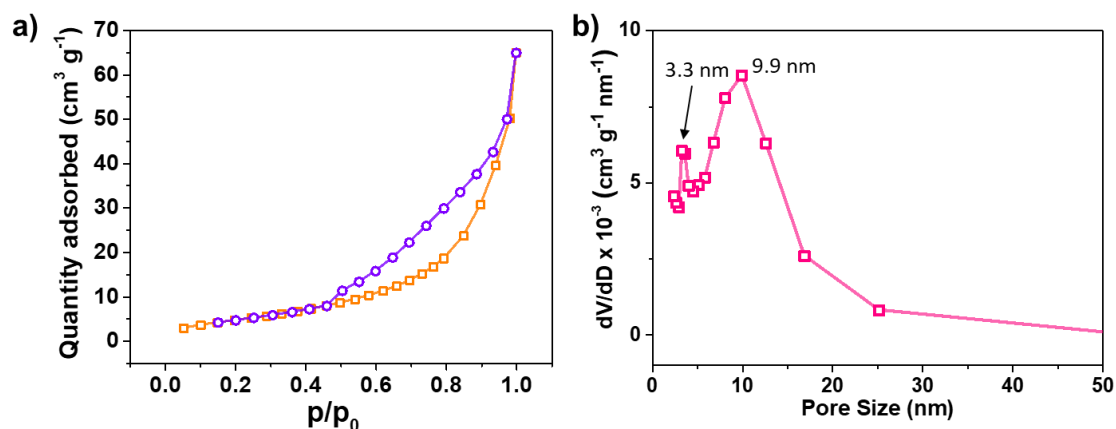
Material	BET surface area (m <sup>2</sup> /g)
rGO	6.546
rGO-TiO <sub>2</sub> (50% w/w)	12.618
rGO-TiO <sub>2</sub> (99% w/w)	21.262

48



49

50 **Figure S5.** Pore size distributions of a) rGO, and b) rGO-TiO<sub>2</sub> (TiO<sub>2</sub> 50% w/w).

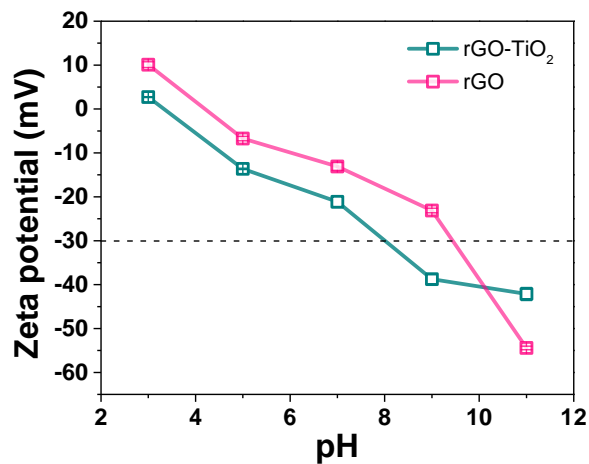


51

52 **Figure S6.** rGO-TiO<sub>2</sub> (TiO<sub>2</sub> 99% w/w): a) The nitrogen adsorption-desorption isotherm loop,  
 53 and b) pore size distribution.

54 It is well-known that for a suspension to be stable, it should have a zeta potential value of either  
 55 +30 mV or higher, or -30 mV or lower. From Figure R5, it is apparent that rGO-TiO<sub>2</sub> has a  
 56 more negative surface charge relative to rGO across the entire pH range. Also, rGO-TiO<sub>2</sub>

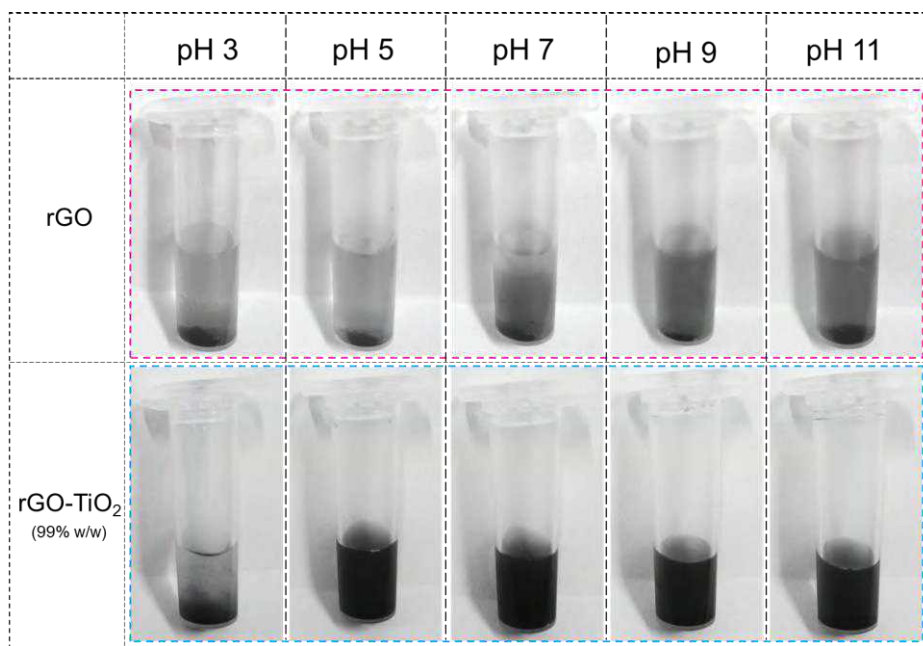
57 suspension is stable over a wider range of pH, i.e., 8.0-11.0, in comparison to the rGO  
58 suspension, which was stable in the range of 9.4-11.0 (Figure S5).



59

60 **Figure S7.** Zeta potential as a functional of pH in the range 3-11 for rGO and rGO-TiO<sub>2</sub>

61 suspensions in deionized water.



62

63 **Figure S8.** Optical images of rGO and rGO-TiO<sub>2</sub> suspensions in deionized water in the pH

64 range 3-11.

65

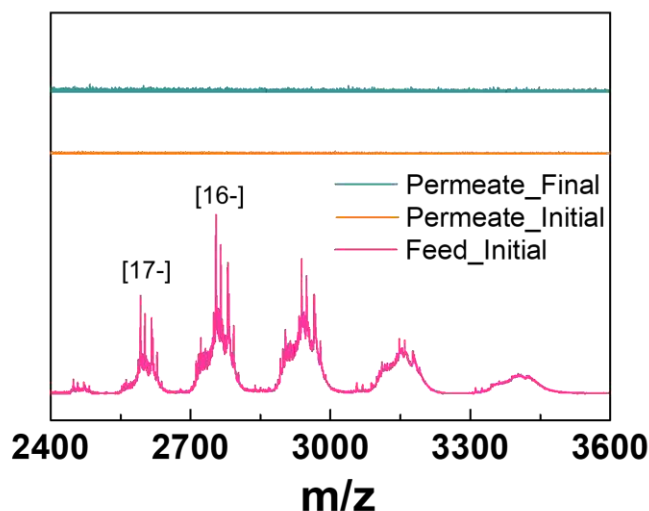
66

### 67 **Note 3. Molecule-exclusion test for membrane defect characterization**

68 In order to confirm the defect-free nature of the membrane, we chose to check the permeation  
69 of a neutral molecule, ovalbumin, across the membrane. Ovalbumin was procured from Merck  
70 & Co. (A5503- 10 G). The chosen protein molecule is neutral at its isoelectric point (~5).  
71 Ovalbumin molecule is slightly ellipsoid-shaped with dimensions of 7 nm × 4.5 nm × 5 nm,  
72 resulting in an effective spherical diameter of 5 nm.<sup>[1]</sup> Also, at the isoelectric point, there is  
73 negligible electrostatic interaction between the graphene sheets and ovalbumin. Possibility of  
74 hydrogen bond formation is also minimal at this point.<sup>[2]</sup> Therefore, the molecule will not  
75 undergo adsorption prominently on the graphene sheets during the experiment.

76 The rGO-TiO<sub>2</sub> particles were assembled by vacuum filtration through a Whatman paper to  
77 form a membrane. The resulting membrane was put at the junction of the two-compartment  
78 setup (Figure 1a in the manuscript). One of the compartments (feed side) was filled with a 5  
79 mg/ml concentration of Ovalbumin. The other compartment (permeate side) was filled with  
80 deionized water. The system was left for 24 h in order to allow concentration gradient-induced  
81 diffusion of the probe molecule through the membrane. Samples from feed and permeate sides  
82 were collected at t= 0 (initial) and t= 24 h (final). The samples were analysed for the presence  
83 of ovalbumin using ion mobility mass spectrometry. In order to ionize the protein molecule for  
84 mass spectrometry, 2 ml of the protein solution was mixed with a 50 µl solution of formic acid  
85 solution. The formic acid solution was made by mixing 80 µl formic acid in 1 ml of milli-Q  
86 water. To obtain a well-resolved mass spectrum, following instrumental parameters were  
87 applied: capillary voltage, 2.75 kV; cone voltage, 50 V; source offset, 50 V; source  
88 temperature, 100 °C; dissolution temperature, 150 °C; desolvation gas flow, 400 L/h. Mass of  
89 the as-available protein was measured to be 44.2 kDa. The obtained mass spectra for initial  
90 feed solutions, and initial and final permeate solutions are shown in the combined plot in Figure  
91 S6. While ovalbumin was found in 16 and 17 charge states in the negative-ion mode for the

92 feed solution, there was no signature of the molecule in the permeate solutions, thereby  
93 confirming that the protein molecule did not permeate across the membrane. This shows that  
94 the membrane does not contain any macroscopic defects.

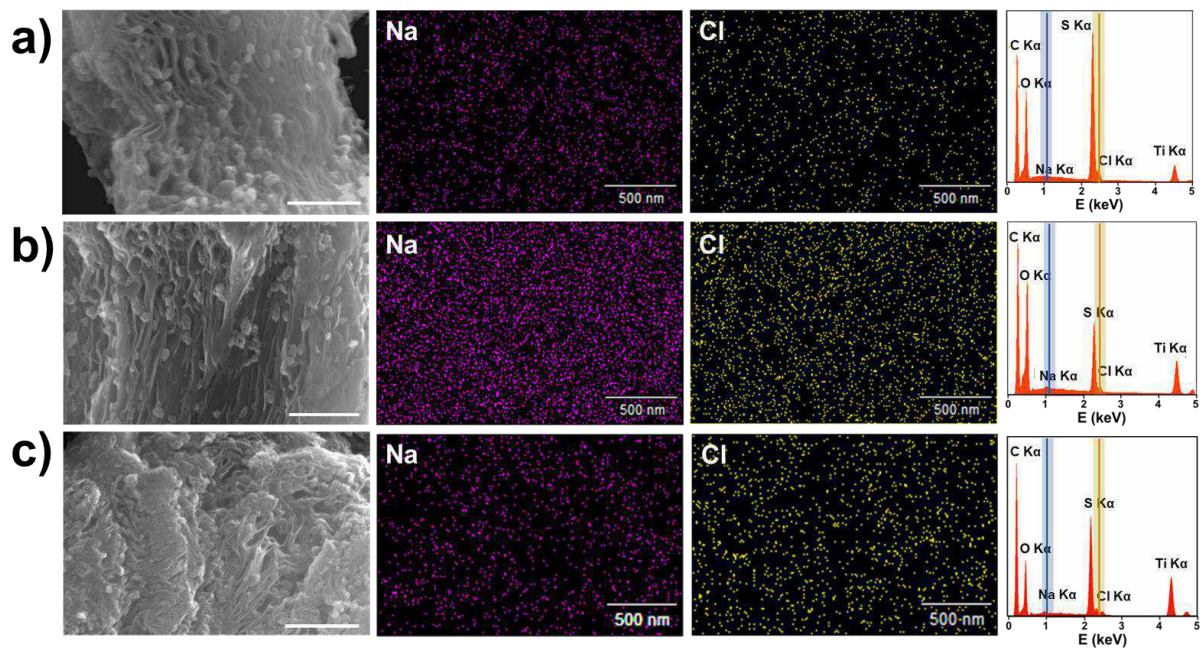


95

96 **Figure S9.** Mass spectra of the initial feed solution, plotted along with the initial and final  
97 permeate solutions.

#### 98 **Note 4. Ion selectivity of the resins**

99 The covalently linked sulfonate and quaternary amine groups impart ion selectivity to the  
100 cation- and anion- exchange resins, respectively. The resins and rGO-TiO<sub>2</sub> were soaked in 0.01  
101 M NaCl solution for 24 h and Energy-dispersive X-Ray spectroscopy (EDX) was performed  
102 thereafter. There was insignificant amount of Na<sup>+</sup> and Cl<sup>-</sup> in the rGO-TiO<sub>2</sub> membrane since  
103 their peak intensities are negligible. However, based on the intensities of the signature peaks  
104 of sodium (1.04 keV) and chloride ions (2.62 keV) in cases of CER and AER, it is evident that  
105 amount of sodium ions is much higher in the CER, and that of Cl<sup>-</sup> is much higher in AER, with  
106 respect to their respective counter ions. This verifies the cation- and anion- selectivity of CER  
107 and AER.



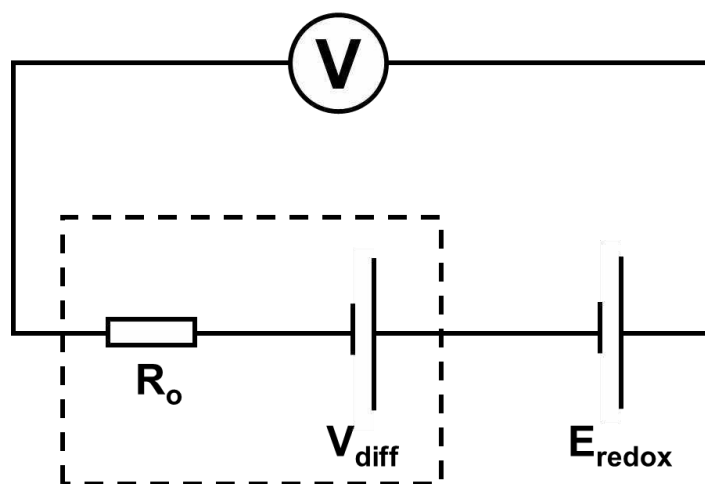
108

109 **Figure S10.** SEM image, elemental mapping and EDX spectrum of a) rGO-TiO<sub>2</sub>, b) cation-  
 110 exchange resin, and c) anion-exchange resin after soaking in 0.01 M NaCl solution.

111 **Note 5. Osmotic potential and current**

112 The salinity gradient energy conversion is studied by performing I-V characterisation. The  
 113 sweep voltage was varied from -0.4 V to 0.4 V at a rate of 50 mV s<sup>-1</sup>. The experimental setup  
 114 can be visualised in terms of an equivalent circuit showed in Figure S6. V<sub>oc</sub>, V<sub>redox</sub> and V<sub>os</sub>  
 115 represent the measured open circuit potential, redox potential from the unequal potential drop  
 116 at the electrode-solution interface, and the diffusion (or osmotic) potential due to ion selectivity  
 117 of the test membrane, respectively.





118

119 **Figure S11.** Equivalent circuit diagram of the membrane-based power source. The measured

120  $V_{oc}$  has two components,  $E_{redox}$  and  $V_{diff}$ .

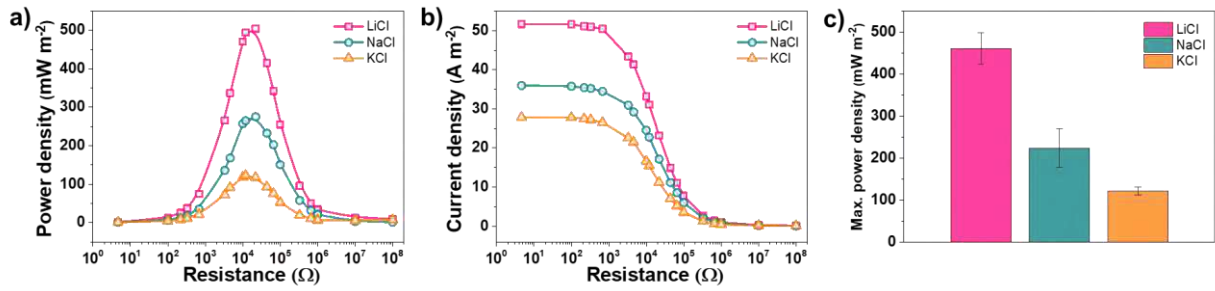
121 **Table S2.** List of  $V_{oc}$ ,  $V_{redox}$  and  $V_{os}$  with respect to salinity gradient for the CEM.

	5	50	100	300	500
$V_{oc}$ (mV)	47.35	66.28	73.21	75.35	120.45
$V_{redox}$ (mV)	12.17	19.84	23.89	15.90	7.90
$V_{os}$ (mV)	35.18	46.44	49.32	59.45	112.55
$t_+$	0.96	0.76	0.73	0.73	0.90
$\eta$ (%)	42.3	13.5	10.6	10.6	32

122

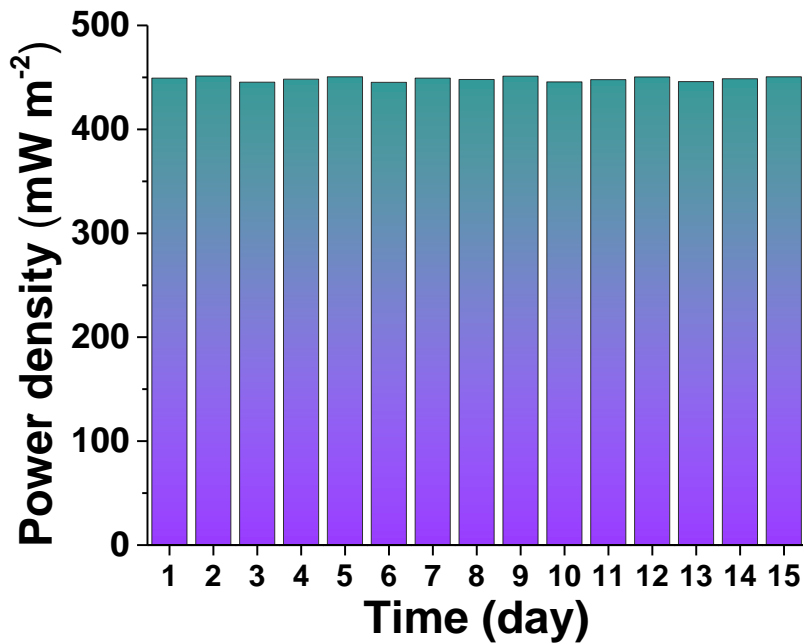
123 **Table S3.** List of  $V_{oc}$ ,  $V_{redox}$  and  $V_{os}$  with respect to salinity gradient for the AEM.

Concentration gradient (M/M)	5	50	100	300	500
$V_{oc}$ (mV)	49.22	69.75	70.08	79.88	114.54
$V_{redox}$ (mV)	12.17	19.84	23.89	15.90	7.90
$V_{os}$ (mV)	37.05	49.91	46.19	63.98	106.64
$t_+$	0.98	0.77	0.72	0.75	0.88
$\eta$ (%)	46.1	14.6	9.7	12.5	28.9



124

125 **Figure S12.** Osmotic energy performance of the CEM under a 100-fold salinity gradient (0.01  
 126 M/ 1 M). a) Power density, b) Current density, and c) Max. power density.



127

128 **Figure S13.** Power output of the CEM for a period of 15 days. The salinity gradient was 500-  
 129 fold (0.01 M/ 5 M NaCl). The electrolyte solutions in both the compartments were replenished  
 130 after every measurement.

131 **Note 6. Literature survey of existing RED devices**

132 **Table S4.** A literature survey of single-pore, macroscopic, and nano-/ micro- scopic RED  
 133 devices.

134

Material system	Electrolyte, concentration gradient (high/low)	Membrane area (nm <sup>2</sup> )	Power (pW)	Power density (mW m <sup>-2</sup> )	Maximum efficiency (%)	Scalability
<b>Single pore system</b>						
Silica nanochannel <sup>[3]</sup>	KCl, 1000 mM/1 mM	$1.40 \times 10^4$	9.87	$9.87 \times 10^{-5}$	46.08	Medium
Functionalized single pore polyamide membrane <sup>[4]</sup>	KCl, 1000 mM/1 mM	$1.26 \times 10^3$	45.12	$6.39 \times 10^{-5}$	29.34	Medium
Single MoS <sub>2</sub> pore <sup>[5]</sup>	KCl, 1000 mM/ 1 mM	78.5	78.5		17.6	Low
Single BNNT pore <sup>[6]</sup>	KCl, 1000 mM/ 1 mM	$5.03 \times 10^3$	20.1		8.36	Low
Single-ion-selective polyimide nanopore <sup>[7]</sup>	KCl, 1000 mM/ 1 mM	$3.13 \times 10^6$	26		4	Medium
Chitosan/poly(acrylic acid) functionalized conical nanopore <sup>[8]</sup>	NaCl, 1000 mM/ 1 mM	$4.56 \times 10^8$	35.5	$9.61 \times 10^{-4}$	3.48	High
Single conical mesopore <sup>[9]</sup>	KCl, 500 mM/ 1 mM	$1.29 \times 10^5$	87.3		4	Medium
<b>Nano- / microscopic system</b>						
Porous block copolymer - PET asymmetric heterogeneous membrane <sup>[10]</sup>	KCl, 1000 mM/ 1 mM	$3.61 \times 10^6$	1.26	$6.87 \times 10^{-2}$	30.57	Low
Single layer nanoporous membrane comprising core-rim polycyclic aromatic hydrocarbons <sup>[11]</sup>	KCl, 1000 mM/ 1 mM	$1.20 \times 10^3$	450	$5.73 \times 10^5$	6.85	Medium
Nanoporous graphene on PET <sup>[12]</sup>	NaCl, 1000 mM/ 1 mM	$2.27 \times 10^2$	$6.13 \times 10^{-3}$	4.09	39	Low
Vertically oriented GO membrane <sup>[13]</sup>	KCl, 1000 mM/ 1 mM	$3.54 \times 10^9$	$1.19 \times 10^5$	$3.36 \times 10^4$	34.16	High
Packed silica nanoparticles <sup>[14]</sup>	KCl, 100 mM/ 0.1 mM	$1.60 \times 10^9$	$1.17 \times 10^3$	$7.3 \times 10^{-2}$	42.32	Medium
Hydrogel functionalized nanoporous PET membrane <sup>[15]</sup>	NaCl, 1000 mM/ 1 mM	$1.94 \times 10^5$	21.88	$7.82 \times 10^{-4}$	3.92	High

Freestanding silica nanochannel membrane <sup>[16]</sup>	KCl, 1000 mM/ 1 mM	$2.83 \times 10^7$	434	$1.8 \times 10^{-3}$	15.68	Medium
10 silica nanochannels <sup>[17]</sup>	KCl, 1000 mM/ 1 mM	$4.00 \times 10^5$	3.08		31	Medium
BN nanosheets/ aramid nanofibers nanocomposite membrane <sup>[18]</sup>	NaCl, 1000 mM/ 1 mM	$3.00 \times 10^{10}$	$7.00 \times 10^5$	$2.33 \times 10^4$	7.22	High
MXene/ Kevlar nanofiber composite membrane <sup>[19]</sup>	KCl, 100 mM/ 0.1 mM	$3.00 \times 10^{10}$	$1.34 \times 10^5$	$4.46 \times 10^3$	8.82	High
Polymer/MOF hybrid nanochannel membrane <sup>[20]</sup>	NaCl, 500 mM/ 10 mM	$3.00 \times 10^{10}$	$8.62 \times 10^4$	$2.87 \times 10^3$	23.16	High
Polyelectrolyte hydrogel/ porous aramid nanofiber composite membrane <sup>[21]</sup>	NaCl, 500 mM/ 10 mM	$3.00 \times 10^{10}$	$1.17 \times 10^5$	$3.90 \times 10^3$	19.2	High
2-hydroxyethyl methacrylate phosphate (HEMAP) hydrogel membrane <sup>[22]</sup>	KCl, 500 mM/ 1 mM	$3.00 \times 10^{10}$	$5.8 \times 10^5$	$1.96 \times 10^4$	5.85	High
Graphene oxide nanosheets/ cellulose nanofibers composite membrane <sup>[23]</sup>	KCl, 500 mM/ 10 mM	$3.00 \times 10^{10}$	$1.76 \times 10^5$	$5.85 \times 10^3$	32	High
Graphene oxide nanosheets/ silk nanofibers composite membrane <sup>[24]</sup>	KCl, 5000 mM/ 10 mM	$3.00 \times 10^{10}$	$4.86 \times 10^5$	$1.62 \times 10^4$	16.4	High
Ionic diode membrane <sup>[25]</sup>	NaCl, 1 mM/ 0.001 mM	$3.00 \times 10^{10}$	$1.04 \times 10^4$	3.46	12.6	High
Block co-polymer-poly(styrenesulfonate) Janus Membrane <sup>[26]</sup>	KCl, 10 mM/ 0.01 mM	$1.00 \times 10^{10}$	$2.04 \times 10^1$	2.04	8.9	High
Mxene <sup>[1]</sup>	KCl, 1000 mM/ 1 mM	$1.63 \times 10^{10}$	$3.4 \times 10^5$	$2.09 \times 10^4$	40.6	High
Nanoporous polycarbonate track-etch membranes <sup>[27]</sup>	KCl, 1000 mM/ 1 mM	$8.32 \times 10^{10}$	$4.83 \times 10^3$	$6.15 \times 10^{-2}$	5.31	High
PDMS microfluidic channels covered in carboxylate polystyrene nanoparticles <sup>[28]</sup>	KCl, 100 mM/ 0.1 mM	$2.00 \times 10^{10}$	$3.27 \times 10^2$	16.4	10.4	Medium

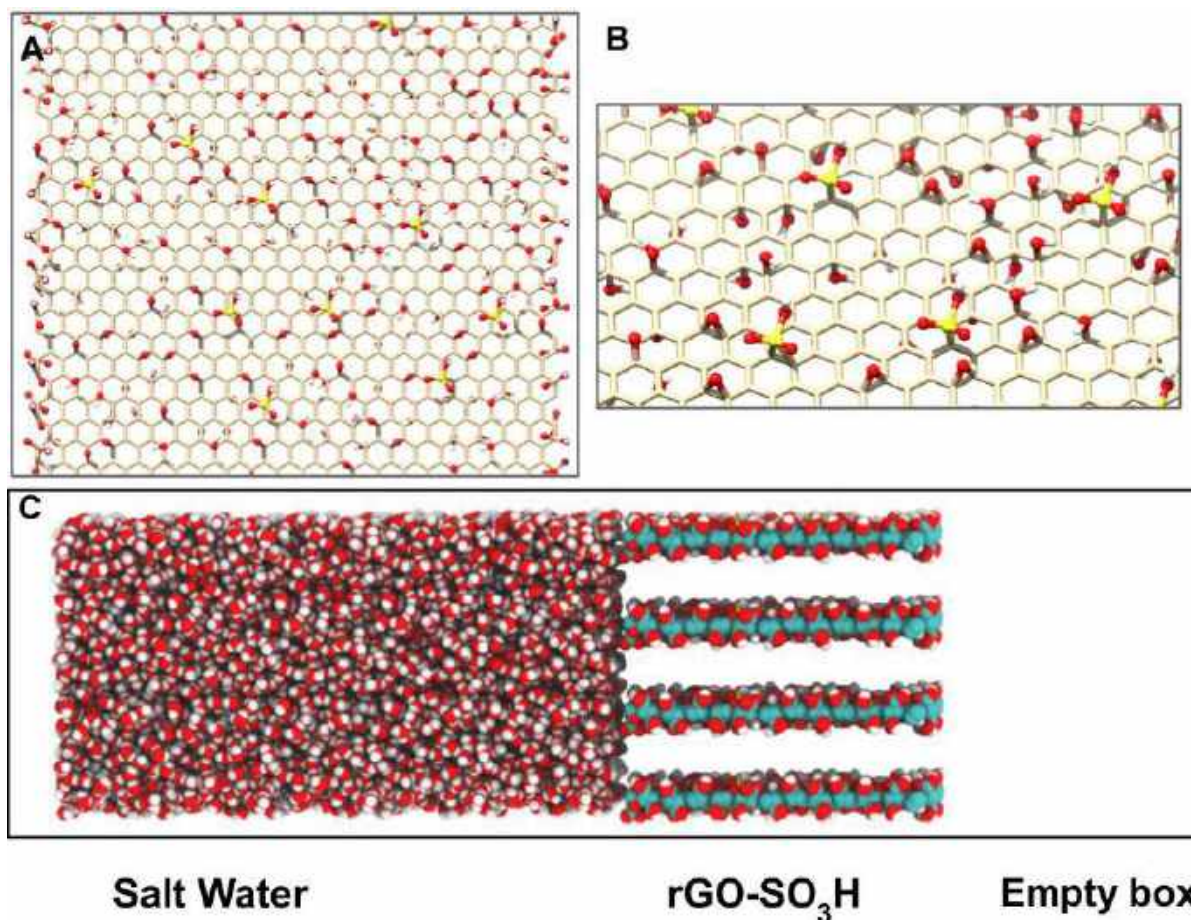
Polyether sulfone/sulfonated polyether sulfone <sup>[29]</sup>	NaCl, 500 mM/1 mM	$3.00 \times 10^{10}$	$7.44 \times 10^4$	$2.48 \times 10^3$	6.48	High
Cation selective Nafion microchannels <sup>[30]</sup>	KCl, 2000 mM/1 mM	$1.15 \times 10^{10}$	$8.68 \times 10^3$	$8.68 \times 10^{-2}$	36	Medium
2,2,6,6-tetramethylpiperidine-1-oxyl (TEMPO)-oxidized bacterial cellulose (TOBC) nanofibers/ Graphene oxide fibers <sup>[31]</sup>	NaCl, 500 mM/1 mM	$2.00 \times 10^{10}$	$1.46 \times 10^4$	$7.30 \times 10^2$	25	High
Silk nanofibril-AAO hybrid membrane <sup>[32]</sup>	KCl, 1 mM/0.001 mM	$3.00 \times 10^{10}$	$8.58 \times 10^4$	$2.86 \times 10^3$	11.8	High
Cellulose nanofibers <sup>[33]</sup>	NaCl, 5000 mM/10 mM	$3.00 \times 10^{10}$	$3.61 \times 10^5$	$12.04 \times 10^3$	-	High
Poly(ionic liquid) <sup>[34]</sup>	NaCl, 5000 mM, 10 mM	$3.00 \times 10^{10}$	$6.00 \times 10^4$	$15.46 \times 10^3$	-	Medium
GO-intercalated Black Phosphorous <sup>[35]</sup>	NaCl, 500 mM/10 mM	$3.00 \times 10^{10}$	$1.50 \times 10^4$	$0.5 \times 10^3$	14.0	Medium
MoS <sub>2</sub> -Cellulose nanofibers <sup>[36]</sup>	NaCl, 5000 mM/10 mM	$3.00 \times 10^{10}$	$4.68 \times 10^5$	$15.6 \times 10^3$	32.0	Medium
Covalent Organic Framework- Aramid Nanofibers <sup>[37]</sup>	NaCl, 500 mM/10 mM	$3.00 \times 10^{10}$	$2.04 \times 10^5$	$6.8 \times 10^3$	20.5	High
<b>Macroscopic system</b>						
Anion-selective polyelectrolytic AAO nanoporous membrane <sup>[38]</sup>	NaCl, 510 mM/17 mM	$1.57 \times 10^{14}$	$1.36 \times 10^6$	4.35	30.89	High
BN nanopore <sup>[39]</sup>	KCl, 1000 mM, 1 mM	$1.75 \times 10^{11}$	$9.75 \times 10^6$	165.85	11.38	High
Electric-eel-inspired hydrogel <sup>[40]</sup>	NaCl, 2500 mM/15 mM	$8.66 \times 10^{13}$	$2.3 \times 10^6$	27	44.14	High
Functionalized Montmorillonite lamellae <sup>[41]</sup>	KCl, 100 mM/0.1 mM	$7.85 \times 10^{11}$	$1.18 \times 10^5$	150	32.20	High
Ion selective Nafion (NR211) membrane <sup>[42]</sup>	KCl, 30mM/0.1 mM	$2.00 \times 10^{13}$	$1.50 \times 10^4$	0.75	7.2	High

Live eels <sup>[40]</sup>	NaCl, 500 mM/ 15 mM	$2.80 \times 10^{15}$	$2.3 \times 10^{10}$	$1.36 \times 10^4$	50	High
Platinum coated nanoporous anodic Alumina membrane <sup>[43]</sup>	KCl, 1000 mM/1 mM	$7.85 \times 10^{13}$	$2.62 \times 10^3$	$3.34 \times 10^{-2}$	0.98	High
Self-Assembled kaolin-based Janus 2D nanochannels <sup>[44]</sup>	KCl, 500 mM/1 mM	$2.00 \times 10^{11}$	$1.8 \times 10^5$	$0.90 \times 10^2$	44.2	High
Silica-coated alumina nanoporous membrane <sup>[45]</sup>	NaCl, 100 mM/10 mM	$3.05 \times 10^{13}$	$5.39 \times 10^5$	0.31	15.68	Medium
MXene <sup>[46]</sup>	NaCl, 5 mM/0.01 mM	$7.80 \times 10^{11}$		$1.1 \times 10^3$	27.1	High
MXene/GO composite membrane <sup>[47]</sup>	NaCl, 500 mM/10 mM	$7.10 \times 10^{14}$	$26.27 \times 10^8$	$3.7 \times 10^3$	-	High
UiO-66-NH <sub>2</sub> MOF @ANM <sup>[48]</sup>	KBr, 1000 mM/10 mM	$7.85 \times 10^{11}$	$2.08 \times 10^7$	$26.5 \times 10^3$	43.7	Medium
Lignin microrods-based nanofluidic membrane <sup>[49]</sup>	NaCl, 5000 mM/10 mM	$5.00 \times 10^{11}$	$5.95 \times 10^6$	$1.19 \times 10^3$	-	
MXene/ Bacterial nanocellulose <sup>[50]</sup>	NaCl, 10000 mM/10 mM	$1.00 \times 10^{12}$	$0.91 \times 10^6$	$0.91 \times 10^3$	2.0	High
Covalent Organic Framework- Aramid Nanofibers <sup>[37]</sup>	Artificial <i>Salt-Dome</i> solution/ river water, 500-fold	$2.07 \times 10^{13}$	$1.30 \times 10^9$	$62.9 \times 10^3$	-	High
<b>Our work (CEM)</b>	<b>NaCl, 5000 mM/10 mM</b>	<b><math>2.24 \times 10^{11}</math></b>	<b><math>1.00 \times 10^5</math></b>	<b>448.67</b>	<b>32.0</b>	<b>High</b>
<b>Our work (AEM)</b>	<b>NaCl, 5000 mM/10 mM</b>	<b><math>2.24 \times 10^{11}</math></b>	<b><math>3.98 \times 10^4</math></b>	<b>177.84</b>	<b>28.9</b>	<b>High</b>

135

136





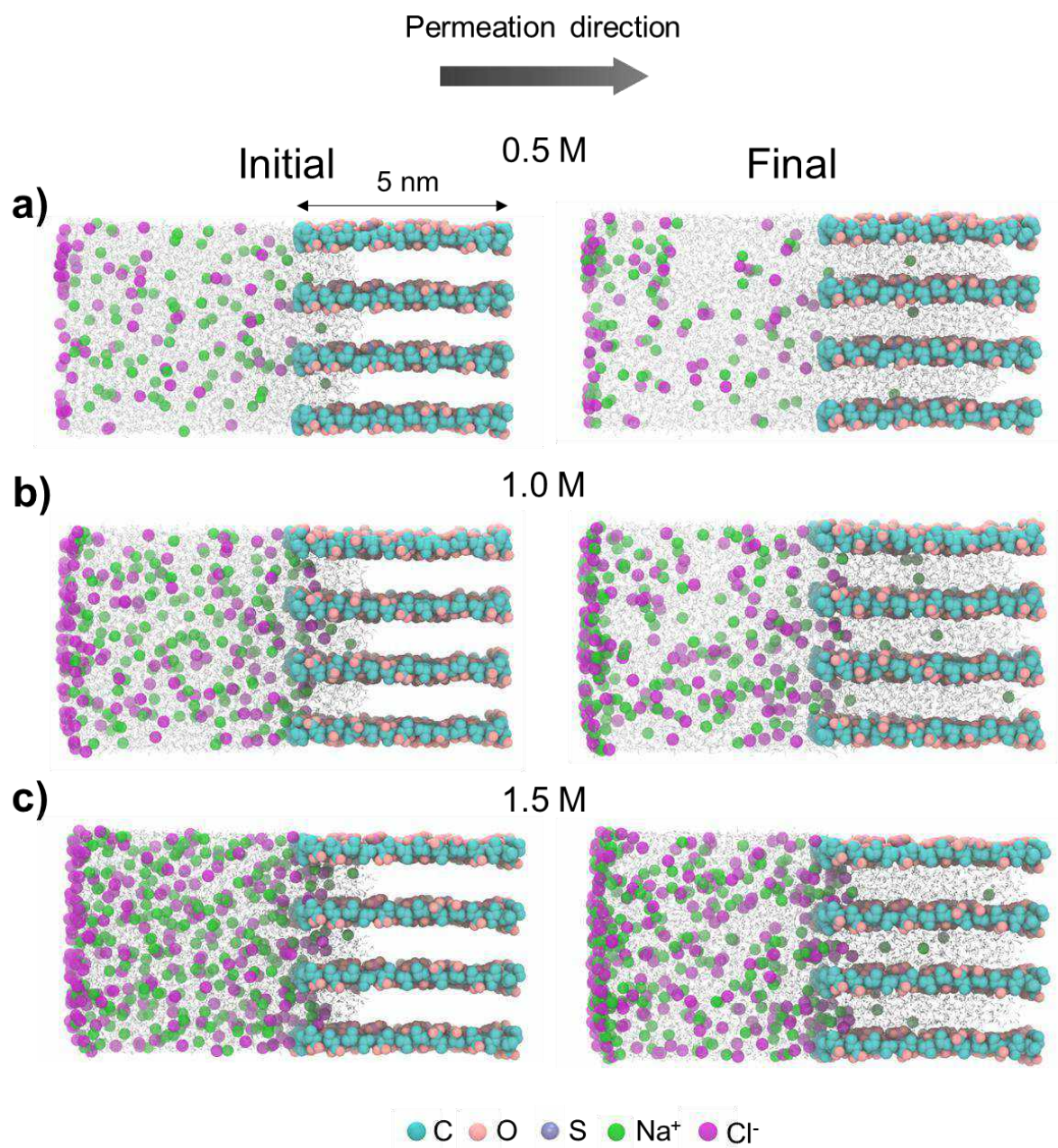
138

139 **Figure S14.** Simulated system for understanding ion transport. a) Reduced graphene oxide  
140 sheet functionalized with -SO<sub>3</sub>H. b) Ball-and-stick representation of a single functionalized  
141 graphene sheet (S: yellow, O: red). c) The simulation box. Channel length is 5 nm.

142

143

144



145

146 **Figure S15.** Simulation boxes showing water,  $\text{Na}^+$ , and  $\text{Cl}^-$  ions permeating across graphenic

147 nanochannels. Images on the left and right show initial and final conformations at a) 0.5 M, b)

148 1.0 M, and c) 1.5 M electrolyte concentration.

149

150

151 **Table S5.** The values of initial interaction distances of Na-O, Na-S, Cl-O, and Cl-S at three  
 152 different concentrations

Distance (Å)	0.5 M	1.0 M	1.5 M
Na <sup>+</sup> -O	3.0	2.5	2.5
Na <sup>+</sup> -S	4.0	5.2	2.5
Cl <sup>-</sup> -O	3.0	3.0	3.5
Cl <sup>-</sup> -S	No interaction	8.0	7.0

153

#### 154 **References**

- 155 [1] S. Hong, F. Ming, Y. Shi, R. Li, I. S. Kim, C. Y. Tang, H. N. Alshareef, P. Wang, *ACS*  
 156 *Nano* **2019**, *13*, 8917.
- 157 [2] L. Chen, D. Zheng, Y. Zhang, Y. Wang, Z. Xu, *J. Sep. Sci.* **2017**, *40*, 1765.
- 158 [3] Y. Zhang, Z. Huang, Y. He, X. Miao, *Nanotechnology* **2019**, *30*, 295402.
- 159 [4] L. Cao, W. Guo, W. Ma, L. Wang, F. Xia, S. Wang, Y. Wang, L. Jiang, D. Zhu,  
 160 *Energy Environ. Sci.* **2011**, *4*, 2259.
- 161 [5] J. Feng, M. Graf, K. Liu, D. Ovchinnikov, D. Dumcenco, M. Heiranian, V. Nandigana,  
 162 N. R. Aluru, A. Kis, A. Radenovic, *Nature* **2016**, *536*, 197.
- 163 [6] A. Siria, P. Poncharal, A.-L. Biance, R. Fulcrand, X. Blase, S. T. Purcell, L. Bocquet,  
 164 *Nature* **2013**, *494*, 455.
- 165 [7] W. Guo, L. Cao, J. Xia, F. Nie, W. Ma, J. Xue, Y. Song, D. Zhu, Y. Wang, L. Jiang,  
 166 *Adv. Funct. Mater.* **2010**, *20*, 1339.
- 167 [8] S. Balme, T. Ma, E. Balanzat, J.-M. Janot, *J. Memb. Sci.* **2017**, *544*, 18.
- 168 [9] M. Gao, P. Tsai, Y. Su, P. Peng, L. Yeh, *Small* **2020**, *16*, 2006013.
- 169 [10] Z. Zhang, X.-Y. Kong, K. Xiao, Q. Liu, G. Xie, P. Li, J. Ma, Y. Tian, L. Wen, L.  
 170 Jiang, *J. Am. Chem. Soc.* **2015**, *137*, 14765.
- 171 [11] X. Liu, M. He, D. Calvani, H. Qi, K. B. Gupta, H. J. M. de Groot, G. J. Sevink, F.  
 172 Buda, U. Kaiser, G. F. Schneider, *Nat. Nanotechnol.* **2020**, *15*, 307.
- 173 [12] Y. Fu, X. Guo, Y. Wang, X. Wang, J. Xue, *Nano Energy* **2019**, *57*, 783.
- 174 [13] Z. Zhang, W. Shen, L. Lin, M. Wang, N. Li, Z. Zheng, F. Liu, L. Cao, *Adv. Sci.* **2020**,  
 175 *7*, 2000286.
- 176 [14] W. Ouyang, W. Wang, H. Zhang, W. Wu, Z. Li, *Nanotechnology* **2013**, *24*, 345401.

- 177 [15] T. Ma, E. Balanzat, J.-M. Janot, S. Balme, *ACS Appl. Mater. Interfaces* **2019**, *11*,  
178 12578.
- 179 [16] F. Yan, L. Yao, K. Chen, Q. Yang, B. Su, *J. Mater. Chem. A* **2019**, *7*, 2385.
- 180 [17] D.-K. Kim, C. Duan, Y.-F. Chen, A. Majumdar, *Microfluid. Nanofluidics* **2010**, *9*,  
181 1215.
- 182 [18] C. Chen, D. Liu, L. He, S. Qin, J. Wang, J. M. Razal, N. A. Kotov, W. Lei, *Joule* **2020**,  
183 *4*, 247.
- 184 [19] Z. Zhang, S. Yang, P. Zhang, J. Zhang, G. Chen, X. Feng, *Nat. Commun.* **2019**, *10*, 1.
- 185 [20] R. Li, J. Jiang, Q. Liu, Z. Xie, J. Zhai, *Nano Energy* **2018**, *53*, 643.
- 186 [21] Z. Zhang, L. He, C. Zhu, Y. Qian, L. Wen, L. Jiang, *Nat. Commun.* **2020**, *11*, 1.
- 187 [22] W. Chen, Q. Wang, J. Chen, Q. Zhang, X. Zhao, Y. Qian, C. Zhu, L. Yang, Y. Zhao,  
188 X.-Y. Kong, B. Lu, L. Jiang, L. Wen, *Nano Lett.* **2020**, *20*, 5705.
- 189 [23] Y. Wu, W. Xin, X.-Y. Kong, J. Chen, Y. Qian, Y. Sun, X. Zhao, W. Chen, L. Jiang, L.  
190 Wen, *Mater. Horizons* **2020**, *7*, 2702.
- 191 [24] W. Xin, H. Xiao, X.-Y. Kong, J. Chen, L. Yang, B. Niu, Y. Qian, Y. Teng, L. Jiang, L.  
192 Wen, *ACS Nano* **2020**, *14*, 9701.
- 193 [25] J. Gao, W. Guo, D. Feng, H. Wang, D. Zhao, L. Jiang, *J. Am. Chem. Soc.* **2014**, *136*,  
194 12265.
- 195 [26] Z. Zhang, X. Sui, P. Li, G. Xie, X.-Y. Kong, K. Xiao, L. Gao, L. Wen, L. Jiang, *J. Am.*  
196 *Chem. Soc.* **2017**, *139*, 8905.
- 197 [27] K. Kwon, S. J. Lee, L. Li, C. Han, D. Kim, *Int. J. Energy Res.* **2014**, *38*, 530.
- 198 [28] E. Choi, K. Kwon, D. Kim, J. Park, *Lab Chip* **2015**, *15*, 168.
- 199 [29] X. Huang, Z. Zhang, X.-Y. Kong, Y. Sun, C. Zhu, P. Liu, J. Pang, L. Jiang, L. Wen,  
200 *Nano Energy* **2019**, *59*, 354.
- 201 [30] T.-C. Tsai, C.-W. Liu, R.-J. Yang, *Power Generation by Reverse Electrodialysis in a*  
202 *Microfluidic Device with a Nafion Ion-Selective Membrane*, Vol. 7, **2016**.
- 203 [31] N. Sheng, S. Chen, M. Zhang, Z. Wu, Q. Liang, P. Ji, H. Wang, *ACS Appl. Mater.*  
204 *Interfaces* **2021**, *13*, 22416.
- 205 [32] W. Xin, Z. Zhang, X. Huang, Y. Hu, T. Zhou, C. Zhu, X.-Y. Kong, L. Jiang, L. Wen,  
206 *Nat. Commun.* **2019**, *10*, 3876.
- 207 [33] Q. Luo, P. Liu, L. Fu, Y. Hu, L. Yang, W. Wu, X.-Y. Kong, L. Jiang, L. Wen, *ACS*  
208 *Appl. Mater. Interfaces* **2022**, *14*, 13223.
- 209 [34] Y. Hu, Y. Teng, Y. Sun, P. Liu, L. Fu, L. Yang, X.-Y. Kong, Q. Zhao, L. Jiang, L.  
210 Wen, *Nano Energy* **2022**, *97*, 107170.
- 211 [35] Z. Zhang, P. Zhang, S. Yang, T. Zhang, M. Löffler, H. Shi, M. R. Lohe, X. Feng,  
212 *Proc. Natl. Acad. Sci.* **2020**, *117*, 13959.
- 213 [36] C. Zhu, P. Liu, B. Niu, Y. Liu, W. Xin, W. Chen, X.-Y. Kong, Z. Zhang, L. Jiang, L.  
214 Wen, *J. Am. Chem. Soc.* **2021**, *143*, 1932.

- 215 [37] Z. Man, J. Safaei, Z. Zhang, Y. Wang, D. Zhou, P. Li, X. Zhang, L. Jiang, G. Wang, *J.*  
216 *Am. Chem. Soc.* **2021**, *143*, 16206.
- 217 [38] S. H. Kwak, S.-R. Kwon, S. Baek, S.-M. Lim, Y.-C. Joo, T. D. Chung, *Sci. Rep.* **2016**,  
218 *6*, 1.
- 219 [39] A. Pendse, S. Cetindag, P. Rehak, S. Behura, H. Gao, N. H. L. Nguyen, T. Wang, V.  
220 Berry, P. Král, J. Shan, *Adv. Funct. Mater.* **2021**, *31*, 2009586.
- 221 [40] T. B. H. Schroeder, A. Guha, A. Lamoureux, G. VanRenterghem, D. Sept, M. Shtein,  
222 J. Yang, M. Mayer, *Nature* **2017**, *552*, 214.
- 223 [41] C. Wu, T. Xiao, J. Tang, Q. Zhang, Z. Liu, J. Liu, H. Wang, *Nano Energy* **2020**, *76*,  
224 105113.
- 225 [42] H.-K. Chang, E. Choi, J. Park, *Lab Chip* **2016**, *16*, 700.
- 226 [43] Y. Wang, H. Wang, C. Q. Wan, *Energy* **2018**, *160*, 863.
- 227 [44] H. Cheng, Y. Zhou, Y. Feng, W. Geng, Q. Liu, W. Guo, L. Jiang, *Adv. Mater.* **2017**,  
228 *29*, 1700177.
- 229 [45] J. Kim, S. J. Kim, D.-K. Kim, *Energy* **2013**, *51*, 413.
- 230 [46] P. Liu, Y. Sun, C. Zhu, B. Niu, X. Huang, X.-Y. Kong, L. Jiang, L. Wen, *Nano Lett.*  
231 **2020**, *20*, 3593.
- 232 [47] F. Wang, Z. Wang, S. Wang, X. Meng, Y. Jin, N. Yang, J. Sunarso, S. Liu, *J. Memb.*  
233 *Sci.* **2022**, *647*, 120280.
- 234 [48] Y.-C. Liu, L.-H. Yeh, M.-J. Zheng, K. C.-W. Wu, *Sci. Adv.* **2021**, *7*, eabe9924.
- 235 [49] P. Cheng, S. Chen, X. Li, Y. Xu, F. Xu, A. J. Ragauskas, *Energy Convers. Manag.*  
236 **2022**, *255*, 115321.
- 237 [50] Y. Xu, K. Zhang, S. Chen, X. Zhang, Y. Chen, D. Li, F. Xu, *Electrochim. Acta* **2022**,  
238 *412*, 140162.
- 239
- 240



# Human Skin-Cell-Based Sensor for Environmental Arsenic Detection and for Creating Social Awareness

Tanvi Gupte, Suryalakshmi Pandurangan, Md Rabiul Islam, Pillalamarri Srikrishnarka, Ankit Nagar, Niraikulam Ayyadurai, Tiju Thomas, and Thalappil Pradeep\*



Cite This: *ACS Sustainable Chem. Eng.* 2022, 10, 17124–17133



Read Online

ACCESS |

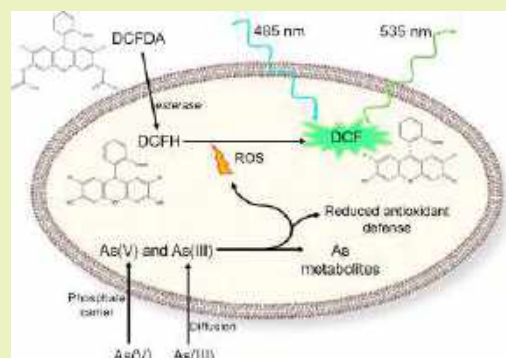
Metrics & More

Article Recommendations

Supporting Information

**ABSTRACT:** Arsenic (As) toxicity is a significant threat to global public health. Moreover, the lacks of social awareness and understanding of the impact of As in affected communities are also of concern. Therefore, subppm level detection of As in environmental waters and associated public awareness are crucial for remediation programs. We developed a sustainable As sensing methodology by merging the fundamental concepts of As cytotoxicity with an alternative approach for selectivity. A cellular platform was prepared on an electrospun scaffold using As-sensitive keratinocyte cells. Arsenic-induced reactive oxygen species (ROS) were quantified using a fluorimetric probe, 2',7'-dichlorofluorescein diacetate, commonly used to detect oxidative stress within cells. Experiments were conducted with a mixture of arsenite and arsenate, the predominant forms of As present in natural conditions, in a 1:1 ratio. We also quantified unknown As concentrations in real water samples. The selectivity to As was achieved by exposing the contaminated water composed of several ions to an As adsorbing material, namely, confined metastable 2-line ferrihydrite (CM2LF). An adsorption–desorption protocol enabled As extraction in field conditions. The ROS resulting from cells' responses to the As extract were used as the signature of As concentration. The sensor could precisely quantify even 5 ppb of As in tap water, and the theoretical limit of detection (LOD) was 2.7 ppb. A sustainable device using the cellular platform is proposed for As detection in field conditions that can also be used for social awareness, demonstrating the impact of As on human biology in affected regions.

**KEYWORDS:** sensor, cellular platform, reactive oxygen species, fluorescence detection, keratinocytes



## INTRODUCTION

Affordable clean water for all is a goal of sustainable development, and new technologies are essential in addressing diverse challenges in providing this basic need.<sup>1</sup> Arsenic (As) is a major water pollutant affecting over 94 to 220 million people, according to a recent study on global groundwater arsenic prediction.<sup>2</sup> It is naturally present in minerals<sup>3</sup> (e.g., realgar, arsenopyrite, and orpiment)<sup>4</sup> and ores from where it percolates into the water due to processes such as weathering and erosion. It is also released into the environment through volcanic activities.<sup>5</sup> Anthropogenic sources of As are mining, industrial waste disposal, pharmaceutical industries, agricultural pesticides, combustion of fossil fuels, and ore production and processing.<sup>5</sup> Chronic exposure to As has carcinogenic potential<sup>6</sup> and can cause various other pathophysiological damages. One of the most common and earliest manifestations of As toxicity is the appearance of skin lesions.<sup>7</sup> As-induced skin lesions are characterized by hyperpigmentation and hyperkeratosis on the palms and soles. Patients with such precancerous lesions are at higher risk for the development of cancer. Skin cancers linked to As exposure are Bowen's disease, invasive squamous cell carcinoma, and basal cell carcinoma.<sup>8</sup>

The two biologically relevant oxidation states of arsenic which are predominantly toxic are trivalent arsenite, As(III), and pentavalent arsenate, As(V). Exposure in humans occurs through inhalation, ingestion of contaminated food and water, and absorption through the skin. As(III) exists in the trihydroxylated uncharged form, As(OH)<sub>3</sub>, at physiological pH and is transported via aquaglyceroporin membrane proteins and hexose transporters. As(V) has a negative charge at physiological pH and enters the cells through phosphate transport systems (due to structural similarity with phosphate), where it is reduced to arsenite.<sup>9</sup> The As is metabolized to methylated species, and in the process, reactive oxygen species (ROS), including peroxy, superoxide, and hydroxyl radicals, are generated.<sup>10</sup> Production of ROS mediates carcinogenesis mechanisms such as oxidative stress, hindered cellular

**Received:** August 1, 2022

**Revised:** November 24, 2022

**Published:** December 12, 2022





respiration, DNA hypomethylation, altered growth factors, and abnormal gene expression.<sup>5,10,11</sup> Arsenic also disrupts the endogenous cellular antioxidants that are primarily proteins with cysteine as the functional site. Arsenic has a high binding affinity to the sulfhydryl groups of enzymes and proteins. When the cellular antioxidant defense is unsuccessful in maintaining safe levels of ROS, the excess ROS triggers oxidative stress.<sup>12</sup> The deleterious effects include lipid peroxidation, protein oxidation, damage to nucleic acids, collapse of mitochondrial membrane potential,<sup>13</sup> and neuronal death.<sup>14</sup> This oxidative stress activates a cascade that eventually results in cell apoptosis, autophagy, or necrosis.<sup>12</sup>

Oxidative stress is one of the quickest responses of the cells to As. Hence, it could be used to develop an ideal As sensor. As skin lesions are one of the early signs of As toxicity, the HaCaT cell line (immortal keratinocyte cell line from adult human skin) was chosen in the present work with an aim to evaluate ROS generation due to As. The keratinocytes were cultured on an optimized electrospun polycaprolactone (PCL) scaffold. PCL is a biocompatible and biodegradable polymer known to support a wide variety of cell lines.<sup>15</sup> Porosity of a scaffold determines the ease of nutrition diffusion and cell migration.<sup>16</sup> Electrospinning is one of the most commonly used techniques for preparing nanofibers for tissue engineering applications.<sup>17</sup> Therefore, this versatile technique was used to generate porous PCL fibers with uniform diameters to develop the keratinocyte–cellular platform.

Biosensors have applications in diverse areas including clinical diagnostics, environmental analysis, food analysis, and drug discovery.<sup>18</sup> The majority of cellular biosensors or whole cell biosensors are genetically modified organisms such as *Bacillus subtilis* and *E. coli*. Their use in environmental biosensing is generally focused on imaging or determining the toxicity of the contaminant rather than detecting and quantifying it.<sup>19</sup> Table S1 shows various reported cell-based and cell-free biosensors along with the comparison of the analytical performance of our sensor with them. Very limited research has happened in the area of using mammalian cells for the precise sensing and quantification of heavy metals. Researchers have reported a genetically encoded fluorescence-based nanosensor containing As-binding protein (ArsR) for assessing cellular As(III) levels.<sup>11</sup> The sequence was expressed in human embryonic kidney (HEK)-293T cells, and the flux of As(III) in the cellular environment was studied through its conjugation with fluorophores. However, a eukaryotic cell-based sensor for quantifying the toxic metal ion in real water samples has not been achieved yet. In environmental water samples, several ions coexist with As. Therefore, sustainably sensing and quantifying As in the presence of high concentrations of interfering ions is challenging.

We have explored an alternative approach to utilize the cells' responses to arsenic as a sensing methodology. For evaluating the As-induced stresses in keratinocytes as a measure of its concentration, it is crucial to selectively expose As in the water to cells. The success of confined metastable 2-line ferrihydrite (CM2LF) in adsorbing both As(III) and As(V) in field conditions<sup>20,21</sup> made us explore the possibility of selective As adsorption followed by its release to obtain As affordably in real water samples. The keratinocyte–cellular platform was treated with the As extract. The As concentration-dependent ROS production was detected using 2',7'-dichlorofluorescein diacetate (DCFDA) dye, and the response was quantified.

Studies were conducted to evaluate the performance of the cellular platform (CP) sensor using tap water. The maximum permissible level for As in drinking water, as recommended by the World Health Organization (WHO) and US Environmental Protection Agency (EPA), is 10 ppb (0.134  $\mu\text{M}$ ).<sup>22,23</sup> The sensor was able to quantify even 5 ppb (0.068  $\mu\text{M}$ ) of As in tap water, and the theoretical limit of detection (LOD) of the sensor was 0.036  $\mu\text{M}$  (2.7 ppb). The developed cellular platform (CP) could detect and quantify environmentally relevant concentrations of As in natural water samples.

Apart from being a sensitive, sustainable, and robust sensor, it also has the potential to serve a social cause. Despite severe health implications of As, an overall lack of social awareness among the As-affected population is observed. The WHO has recognized the necessity of education and community involvement for ensuring successful interventions and to prevent further As exposure.<sup>24</sup> Since human keratinocytes are the primary component of the CP sensor, it will help in effectively creating awareness about the risks of chronic As exposure. A prototype using the CP sensor is proposed to address this need.

## EXPERIMENTAL SECTION

**Materials and Instrumentation.** Please refer to the [Supporting Information](#).

**Preparation of Electrospun Nanofibers.** PCL nanofibers were electrospun after optimizing the polymer concentration at 30% (w/v) PCL and solvent system as dimethylformamide (DMF):dichloromethane (DCM) at a 30:70 volume ratio. It was stirred overnight at 45 °C to get a clear and viscous polymeric solution. Nanofibers were electrospun using the ESPIN-NANO electrospinning machine at room temperature. The humidity and temperature of the room during electrospinning were 50% and 25 °C, respectively. The solution was loaded into a 2 mL syringe with a blunt-ended 21-gauge needle. The electrospinning parameters were kept constant at a flow rate of 1 mL/h, a working distance of 12 cm, and a potential of 10 kV for 3, 5, and 8 min (named P3, P5, and P8, respectively). The nanofibers were collected on a circular microscopic cover glass substrate (diameter 12 mm) placed on a grounded static collector. They were stored in a covered Petri dish at room temperature until further use.

**Development of Cellular Platform Using Keratinocytes.** Individual nanofibrous scaffolds electrospun on a circular microscopic cover glass were placed into the tissue culture plate (tcp) wells and sterilized with UV radiation for about 1 h. They were washed with PBS thrice and incubated with Dulbecco's modified Eagle medium (DMEM) overnight to make the scaffold surface more efficient for cell attachment. The skin cell platform was obtained by culturing keratinocytes on the scaffolds. The cells were transferred from the culture flask, seeded at a cell density of  $\sim 10^5$  cells/mL, and allowed to adhere and proliferate on the scaffold. The progressive stages of cell adhesion and proliferation were observed with an inverted light microscope.

**Arsenic-Induced Reactive Oxygen Species Generation.** ROS generation was determined using the DCFDA assay. The working solution of 5  $\mu\text{M}$  DCFDA was prepared by diluting the stock solution with complete DMEM growth medium without phenol red. The cells cultured on P5 were exposed to different concentrations of arsenite (0, 0.5, 1, 3, 5, 7, and 10  $\mu\text{M}$ ) after 24 h of cell seeding. To determine the optimal time to observe ROS generation in HaCaT cells, they were stained with DCFDA at 2, 16, and 24 h.

To observe the effect of As mixtures on ROS generation, the cellular platform was exposed to 0, 0.2, 0.5, 1, 3, 5, and 7  $\mu\text{M}$  of a 1:1 mixture. The cells treated with 1%  $\text{H}_2\text{O}_2$  for 6 h were taken as the positive control. A similar control study with cells grown on tcp was also performed.

For staining, the cells were incubated with diluted DCFDA dye at 37 °C for 45 min in the dark. The ROS generation was quantified by

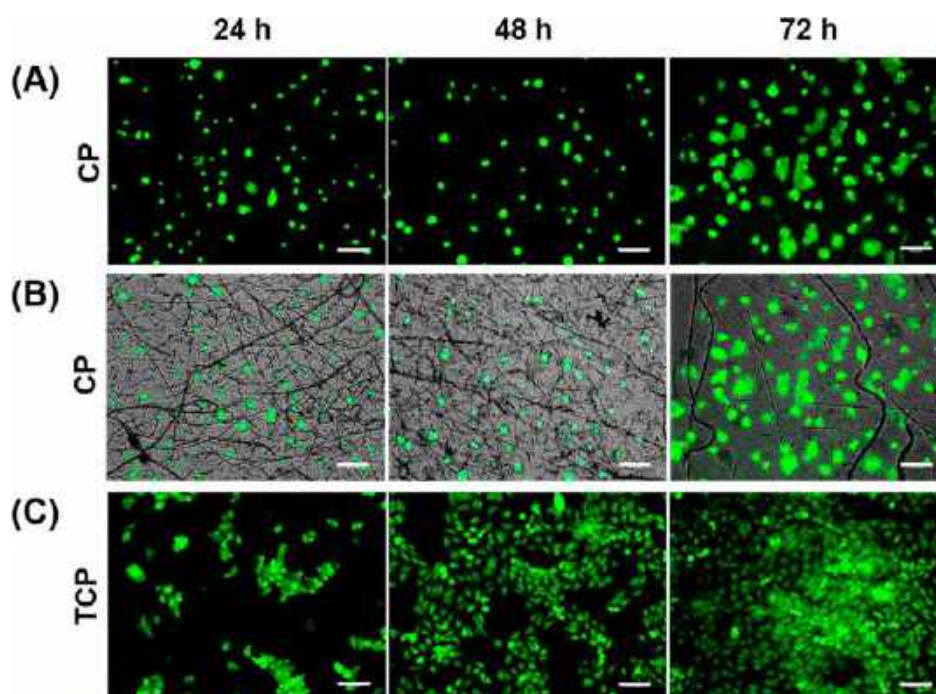


**Figure 1.** Representative micrographs of live HaCaT cells stained by FDA and imaged at 24, 48, and 72 h. (A) Fluorescence micrographs and (B) overlay of optical and fluorescence images of the cellular platform (CP). (C) Fluorescence micrographs of HaCaT cells cultured on tcp. The scale bar is 100  $\mu\text{m}$ .

measuring the fluorescence intensity using a microplate reader at excitation/emission of 485/535 nm. ROS generation in cells was imaged using a fluorescence microscope with a FITC filter (Ex 460–500 nm, Em 512–542 nm). The estimation of the ROS-associated fluorescent signal was expressed as a fold change relative to the control ( $I/I_0$ , where  $I$  is the fluorescence intensity of As-treated cells, and  $I_0$  is the fluorescence intensity of the control group (0  $\mu\text{M}$  of As)). A calibration chart was developed based on the relative fold change in fluorescence intensity ( $I/I_0$ ) measured for the As mixture at 24 h post As exposure. All the experiments were performed in triplicate.

Details of nanofibrous scaffold characterization, cell culture, morphological characterization of the cultured cells, cell viability on the nanofibrous scaffold by a 3-(4,5-dimethylthiazol-2-yl)-2,5-diphenyltetrazolium bromide (MTT) assay, fluorescence imaging, arsenic-induced ROS generation, analysis of real water samples using CM2LF, and calculation of limit of detection (LOD) are reported in the [Supporting Information](#).

## RESULTS AND DISCUSSION

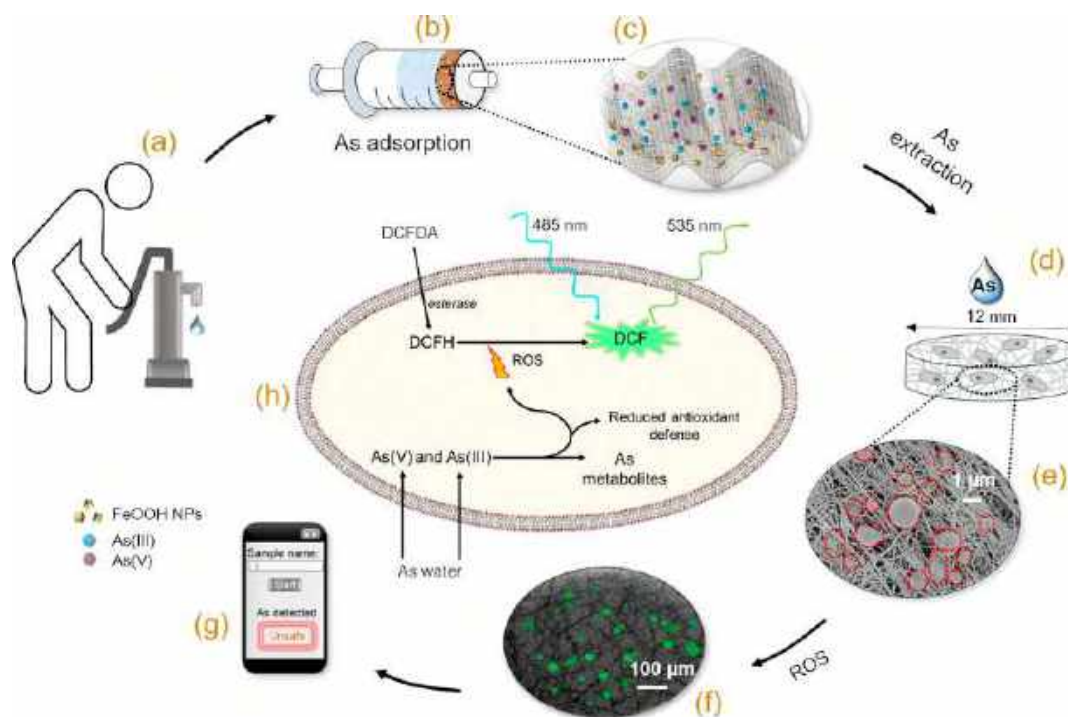
**Characterization of Nanofibrous Scaffolds.** The electrospun scaffold's morphology and diameter depend on parameters such as polymer concentration, solvent ratio, viscosity, applied voltage, flow rate, tip-collector distance, and needle diameter, as well as environmental factors such as humidity and temperature.<sup>25</sup> These processing variables were optimized to obtain uniform, bead-free electrospun fibers on microscopic cover glass, used as the substrate. The electrospinning time can affect the nanofibrous mat's density, porosity, and thickness. Hence, the polymer solution was electrospun for different time periods and characterized. The 3, 5, and 8 min spun fibers were termed P3, P5, and P8 scaffolds, respectively, which are relevant for the experiments. The fibers were observed by optical microscope and were found to be randomly arranged, forming an interconnected porous network of multiple layers in the case of all three scaffolds (Figure S1). The density of fibers increased with an increase in electro-

spinning time. Figure S2 shows the lateral view of the scaffolds used for quantifying the total thickness of electrospun fibers (including the cover glass substrate). The lens was tilted at 90°, and images were taken at 100X. The thickness was found to be  $142.3 \pm 3.6$ ,  $155.8 \pm 2.2$ , and  $177.5 \pm 5.5$   $\mu\text{m}$  for P3, P5, and P8 scaffolds, respectively. The average thickness of the cover glass substrate was  $130.4 \pm 3.9$   $\mu\text{m}$ . It can be concluded that the thickness of the nanofibrous mat increased by  $\sim 5$   $\mu\text{m}$  for each minute of electrospinning. Thus, the thicknesses of the layers were regulated by electrospinning the nanofibers for different intervals of time. The FESEM micrograph of the P5 scaffold is shown in Figure S3A. The fibers formed a three-dimensional network. The average fiber diameter for the P5 scaffold was  $115.4 \pm 42.4$  nm using ImageJ software (Figure S3B).

**Morphological Characterization of Cultured Cells by FESEM.** The HaCaT cells cultured on the optimized P5 scaffold and the blank microscopic cover glass were imaged by FESEM. Figure S4A shows the FESEM micrograph of cells embedded in the porous, three-dimensional network of the nanofibrous P5 scaffold. The cells uniformly infiltrated throughout the multilayers of the entire platform. Figure S4C and D illustrates the high magnification images of an individual cell adhering to the polymeric nanofibers. The spatial arrangements and orientations of nanofibers caused cells to be packed between the interfiber spaces, attaching at multiple points proving their biocompatibility. The cell sizes varied between 1 and 3.5  $\mu\text{m}$  depending on the space available in the pores of the scaffold. The cells cultured on the control cover glass (Figure S4B) showed spherical morphologies and enlarged sizes ranging from 10 to 20  $\mu\text{m}$ . The difference in cell sizes on the two substrates indicates an initial delay in proliferation in the case of the P5 scaffold. These results demonstrate the differential behaviors of live cells in the



**Scheme 1. Schematic Representation of Process Flow.** (a) Collection of As-Contaminated Real Water Sample. (b) Adsorption of As from Water by CM2LF Packed in a Syringe. (c) Structure of CM2LF with Embedded FeOOH Nanoparticles (NPs). As(III) (Blue Dots) and As(V) (Purple Dots) Are Shown Adsorbed On it. (d) Treatment of Cellular Platform (CP) with As Extract. (e) FESEM Micrograph of Keratinocytes Embedded in P5. Cells Are Outlined in Red. (f) As Concentration-Dependent Fluorescence Observed in CP Due to ROS Generation. DCFDA Dye Was Used to Stain ROS, which Were Subsequently Quantified. (g) Alert on Smartphone Regarding Safety of Water. (h) Cellular Interactions with As and Detection Mechanism with DCFDA Dye



porous 3D nanofibrous environment compared to the cell culture on flat 2D surfaces.

**HaCaT Cell Viability on Nanofibrous Scaffold by MTT Assay.** Cell viability on the nanofibrous scaffolds was quantified by the MTT assay. HaCaT cells cultured on tissue culture plates (tcp) without the scaffold were used as a control. The cell viabilities on the P3, P5, and P8 scaffolds relative to tcp control were verified at 24 h, as shown in Figure S5A. The relative cell viabilities at 24 h were 64%, 75%, and 46% for P3, P5, and P8, respectively. The initial delay in proliferation was observed in the case of all the scaffolds compared to tcp. Cells adhered and proliferated well on both P3 and P5 scaffolds. Better cell viability for P5 could be attributed to the optimal pore size generated by interfiber space for the adhesion of live HaCaT cells. In the case of P8, detachment of fibers from the glass substrate was observed within 24 h. This affected the cell adhesion and proliferation on P8. Moreover, the thickness and density of the nanofibrous layer of P8 reduced cell infiltration leading to decreased cell viability. Hence, the electrospinning time was optimized at 5 min based on the MTT assay results. The P5 scaffolds were used for further experiments. HaCaT cells cultured on P5 are referred to as the cellular platform (CP) in this paper. A control experiment was also performed to determine the cytotoxicities of different concentrations of arsenite (0–7  $\mu\text{M}$ ) on HaCaT cells cultured on tcp. The 0  $\mu\text{M}$  wells were composed of cells cultured on tcp without a scaffold and subjected to an equal volume of Milli-Q water instead of arsenite. As shown in Figure S5B, there was no apparent change in relative cell viability percentage at lower concentrations of arsenite (<1  $\mu\text{M}$ ), and no significant difference in

cell proliferation was observed compared to the control in 24 h. The cell viabilities decreased to 85%, 67%, and 66% for 3, 5, and 7  $\mu\text{M}$  arsenite. Figures S5(a–g) are the optical images of cell proliferation on tcp after 24 h treatment of arsenite (0–7  $\mu\text{M}$ ). The decline in cell viability at higher concentrations of arsenite can be clearly observed in the images. This indicates that the critical arsenite concentration that can cause a significant inhibitory effect on cell viability in 24 h is approximately  $\geq 1 \mu\text{M}$ . However, the lower concentrations have the potential to induce instabilities and cellular stress.

**Fluorescence Imaging. Assessing Cell Adhesion on P5.** To assess cell–scaffold interactions, CP was observed using FDA dye at different time points. Positive FDA results are considered a sign of viable cells. Figure 1 shows the representative images of live HaCaT cells cultured on CP and tcp stained by FDA at 24, 48, and 72 h. The viable cell densities increased with time for both the substrates; however, for CP, it was less than the control tcp. At 72 h, the viable cells on tcp occupied about  $60 \pm 10.80\%$  of the wells, representing the subconfluent state. While in the case of CP, the cells covered about  $14 \pm 1.40\%$  of the area. This indicated that cells proliferated and spread better on the plate surface than on the PCL nanofibrous scaffold. Thus, these images confirmed the initial delay in cell proliferation on P5, observed in MTT results. The surface properties of the substrates determine cell growth considerably. Cells prefer hydrophilic surfaces for adhesion and migration. PCL is a known hydrophobic polymer.<sup>16</sup> Cells were able to grow on the hydrophobic P5 as the porous nanofibrous structure mimicked the extracellular matrix (ECM). Figure S6 shows the quantitative representa-

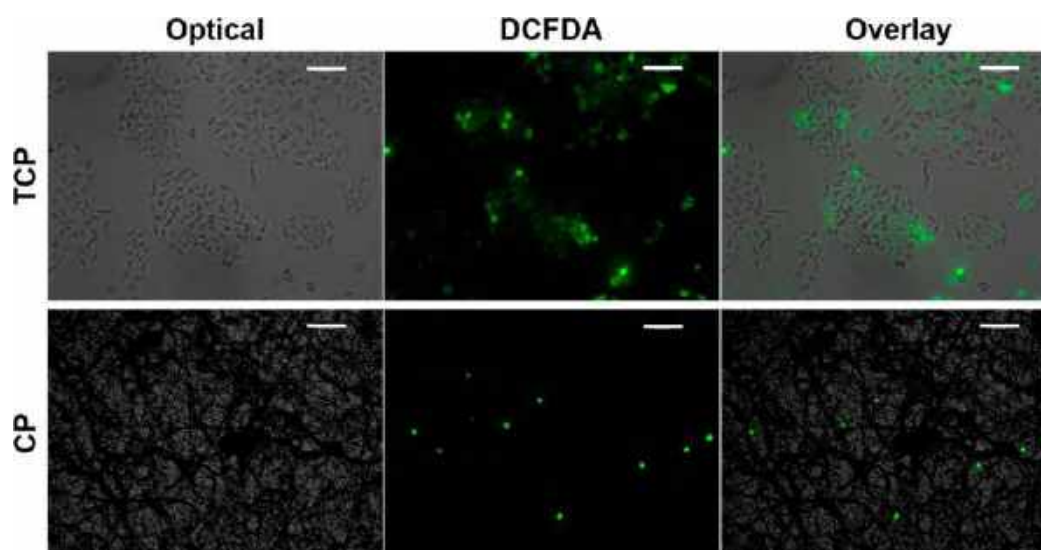


**Figure 2.** Representative fluorescence micrographs of intracellular ROS generation in CP compared to cells cultured on tcp, stained with DCFDA. Cells were treated with 5  $\mu\text{M}$  of the As mixture, and images were taken after 24 h. The scale bar is 100  $\mu\text{m}$ .

tion of percent coverage by live cells obtained from triplicate FDA fluorescence images at each time point. The percentage calculations were based on area measurement of live cells using ImageJ software. These data prove that the porous structures of PS scaffolds were able to provide growth environments and surface compatibilities to cells but at a slower growth rate. The cell density increased rapidly and significantly (>2 times) by 72 h. Hence, it can be concluded that the cell attachment and spreading on the PS scaffolds were time dependent, and the cell viability was maintained.

**Effect of Low Concentrations of Arsenite on Cell Viability.** The potential long-term cytotoxic cellular interactions with low arsenite concentrations were evaluated by a live/dead cell assay. This is a fluorometric assay to assess cell membrane integrity using a combination of inclusion and exclusion dyes, FDA and PI, respectively. PI produces red fluorescence in nonviable cells.<sup>26</sup> Whereas FDA stains the viable cells with green fluorescence. Thus, the FDA/PI staining helps estimate cell viability by differentiating between live and dead cells. The assay was performed after 24, 48, and 72 h incubation of HaCaT cells with arsenite at different concentrations ranging from 0.5 to 1  $\mu\text{M}$ . The representative fluorescence micrographs of FDA/PI-stained cells at different time intervals post arsenite exposure are shown in Figure S7. Cell viability was calculated using eq 1 (refer to Supporting Information) and was found to be inversely proportional to As concentration and exposure time. Table S2 shows the corresponding values of percentage mean cell viability and is graphically represented in Figure S8. The control group comprising untreated cells had a cell viability of ~99% throughout the experimental time period. For 0.5  $\mu\text{M}$  As(III), the cell viability stayed above 90% for the initial 48 h and decreased drastically to 3.6% at 72 h, with several cells showing red fluorescence (PI positive), indicative of damaged cell membranes. The 1  $\mu\text{M}$  As(III)-treated cells had 82% cell viability at 24 h, which decreased to 4.7% at 48 h with very few viable cells. Concentrations of 0.75 and 1  $\mu\text{M}$  had 100% PI-positive cells at 72 h, indicating no viable cells. It can be concluded that arsenite displayed concentration and time-dependent cytotoxicity. Lower doses of arsenite showed cytotoxic effects when the keratinocytes were exposed to sufficiently long periods. This experiment was conducted to

support the MTT assay results and determine the long-term cytotoxic impact of low doses of arsenic on skin cells.

**Arsenic-Induced Reactive Oxygen Species Generation.** The effects of As exposure vary with treatment time and concentration. The DCFDA dye is a fluorimetric probe commonly used to detect oxidative stress. It is a cell-permeable colorless dye that is deacetylated by cellular esterases to nonfluorescent dichlorodihydrofluorescein (DCFH), as shown in Scheme 1. The DCFH is cell impermeable, which gets oxidized by ROS into green fluorescent 2',7'-dichlorofluorescein (DCF) which can be quantified. The dye measures multiple cellular ROS such as superoxide ( $\text{O}_2^{\bullet-}$ ), hydroperoxy radical ( $\text{HO}_2^{\bullet}$ ), singlet oxygen ( $^1\text{O}_2$ ), peroxy radical ( $\text{RO}_2^{\bullet}$ ), and nitric oxide ( $^{\bullet}\text{NO}$ ).

The As-induced ROS generation and accumulation in CP was evaluated by comparing the fold change in fluorescence intensities of treated cells with that of untreated cells. To determine the optimal time for recording the ROS generation in the HaCaT cells, they were treated with As(III) concentrations ranging from 0 to 10  $\mu\text{M}$  for 2, 16, and 24 h. The 0  $\mu\text{M}$  sample served as the untreated control group, and its mean fluorescence intensity was termed  $I_0$ . Fold changes in intensities relative to the control were plotted for each concentration of As(III). Figure S9 illustrates that the fold change in fluorescence due to ROS was directly proportional to the concentration of As(III) and the exposure time. Moreover, As(III)-induced generation of ROS was observed in cells cultured on both the substrates (PS and tcp). The highest concentration (10  $\mu\text{M}$ )-treated CP showed a 2-fold increase in intensity, while the tcp culture showed only a 1.45-fold increase for the same concentration. The absolute fold change values for individual concentrations were found to be higher in the case of CP for all the concentrations. High amounts of ROS were formed in CP at 2 and 16 h postexposure too, with 1.5- and 1.7-fold increases in intensity, respectively, for 10  $\mu\text{M}$  treatment. The rapid increase in fluorescence indicates oxidative stress as the toxicity mechanism of As. A longer incubation time causes a chronic increase in ROS production. This causes damage to DNA, proteins, and lipids, impaired cellular metabolism, and eventually cell death.<sup>13</sup> Moreover, oxidative stress also

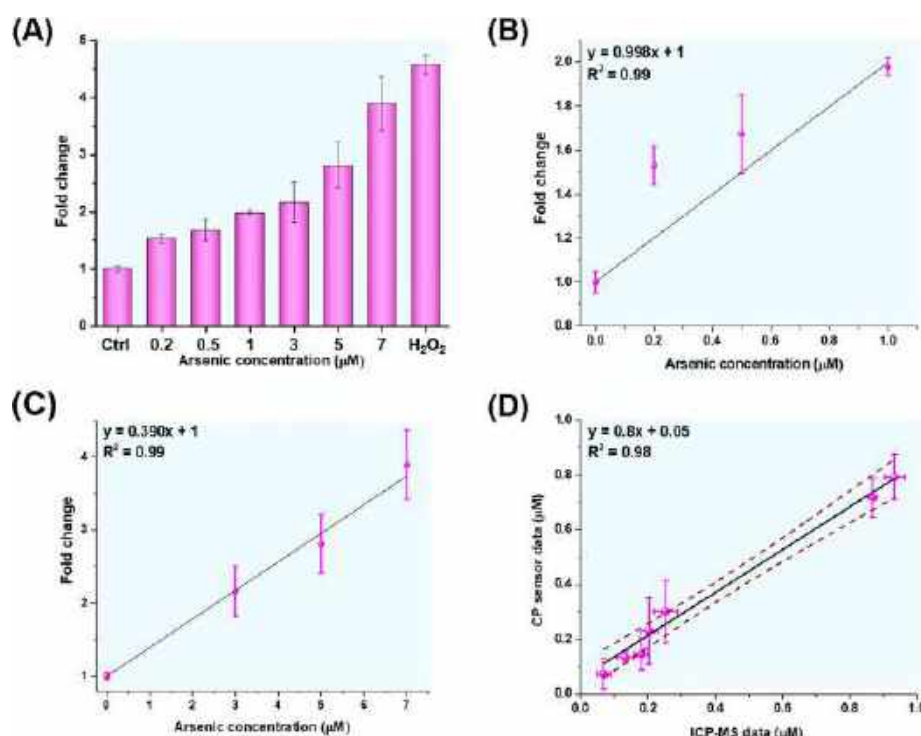


**Figure 3.** Arsenic concentration-dependent cellular ROS generation determined by DCFDA assay on CP. A 1:1 mixture of As(III) and As(V) was used. All the results represent the mean  $\pm$  SD of three independent experiments. (A) Spectrophotometric fluorescence intensity at 24 h measured in terms of fold change with respect to control. 1%  $\text{H}_2\text{O}_2$  for 6 h was used as a positive control. (B, C) Standard curves for quantitation of low and high micromolar concentrations of arsenic, respectively, at 24 h after arsenic exposure. (D) Correlation between the CP sensor and ICP-MS data in determining the concentration of As in real water samples. Each point represents a single water sample tested by both techniques. The dashed lines are 95% confidence bands.

contributes to reducing the cells' natural antioxidant defenses. Hence, for better quantification, a 24 h time point was chosen for studying As-induced ROS generation in further experiments.

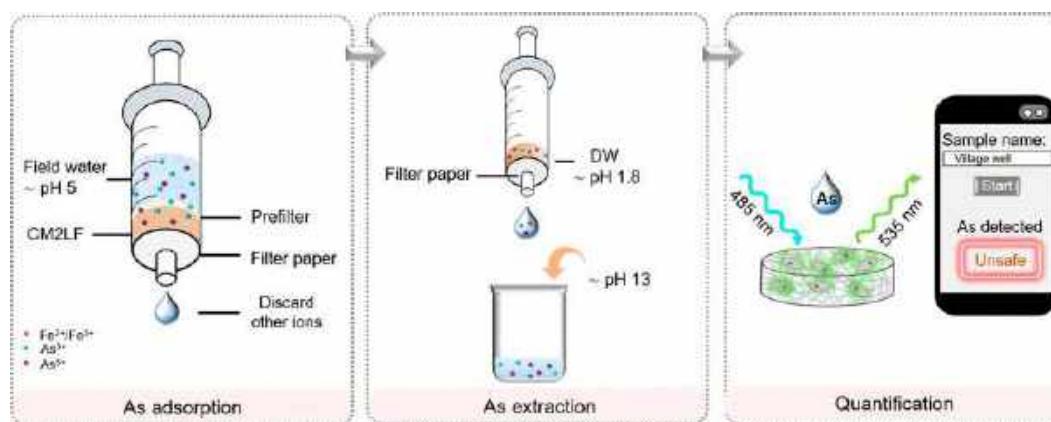
In natural waters, arsenic exists as a mixture of both arsenite (As(III)) and arsenate (As(V)) species. Hence, the DCFDA assay was also performed on CP exposed to different concentrations of a 1:1 mixture of As(III) and As(V). The visualization of ROS in HaCaT cells treated with As is possible with DCFDA staining. Figure 2 shows the representative images for intracellular ROS generation in HaCaT cells pre-treated with 5  $\mu\text{M}$  of the As mixture for 24 h. These panels show the typical fields of the optical, fluorescence, and overlay images for As-treated cells. Correlating these images with the MTT assay results, 5  $\mu\text{M}$  As concentration can potentially decrease the cell viability below 70%. Therefore, only the viable cells with a buildup of intracellular ROS showed strong green DCFDA-positive fluorescence. The fluorescence intensities of CP exposed to different concentrations of the As mixture were quantified and evaluated as indicators of the ROS generated. The fold changes in intensities at 24 h relative to the control (0  $\mu\text{M}$ ) are illustrated in Figure 3A. As expected, the concentration-dependent increase in ROS production was also observed for the As mixture. The 0.2  $\mu\text{M}$  As mixture produced a 1.5-fold increase while 7  $\mu\text{M}$  triggered a 4-fold increase in relative fluorescence intensity. Figure S10A illustrates the results of a similar experiment conducted on the tcp control. The concentration dependency in fold intensity was observed for tcp too. As observed previously in the case of arsenite treatment, the fold increase in intensity was significantly higher for CP compared to the tcp control for the

As mixture too. Figure S10B simplifies this comparative observation. For the highest concentration of 7  $\mu\text{M}$ , the control tcp presented a 1.3-fold increase which was lower than the fold change for the lowest As concentration treatment (0.2  $\mu\text{M}$ ) on CP. This is illustrated by black dashed lines on the plot. Therefore, it can be concluded that the CP was several times better than the control as a fluorescence As sensor.

To understand the concentration dependence better, a scatter chart was generated based on relative fold changes in fluorescence at 24 h post-exposure plotted against various concentrations of the As mixture (Figure S11). The chart was based on triplicate experiments at each concentration. Two distinct linear regimes were observed for As concentrations below and above 1  $\mu\text{M}$ , denoted by straight dashed lines. The CP responded to low concentrations of As with a sharp 2-fold increase in intensity, indicating rapid ROS generation and accumulation. A gradual linear increase up to 4-fold was observed for the high concentration range from 3 to 7  $\mu\text{M}$ . As noted in the cytotoxicity analysis, the 3–7  $\mu\text{M}$  concentrations start affecting the cell viability. Hence, a proportionate gradual rise in concentration-dependent ROS was manifested due to the shortage of a 20%–40% viable cell population. Accordingly, two standard curves of fold change versus As concentration ( $\mu\text{M}$ ) were designed based on the observed linearity. Figure 3B and C represents the linear fitted calibration curves for low and high micromolar concentrations. Linear regression analysis for the two concentration ranges yielded the following equations: for low As concentrations ( $\leq 1$   $\mu\text{M}$ ),  $y = 0.998x + 1$ ; and for higher As concentrations,  $y = 0.390x + 1$  (where  $y$  is the fold change in intensity, and  $x$  is the As concentration in  $\mu\text{M}$ ). In both cases, linearity was obtained



Scheme 2. Sustainable Prototype Cellular Arsenic Sensor as a Social Awareness Tool



with a correlation of 0.99. The regression equations of the fitted lines were used for quantifying unknown As concentrations in water. The theoretical limit of detection (LOD) was  $0.036 \mu\text{M}$  (2.7 ppb) which is well below the WHO permissible limit for As in drinking water. The LOD was estimated using eq 2 in the Supporting Information.

**Analysis of Real Water Sample Using CM2LF.** An alternate approach was employed to evaluate practical applications of the optimized CP sensor in real water analysis. Laboratory tap water spiked with As was used for this experiment. In such environmental water samples, several ions may coexist with As in significant concentrations. Therefore, to quantify As-induced oxidative stress specifically, it is important to selectively expose As present in the water to the CP. To achieve this, As-adsorbing media, CM2LF, was used. The As extract obtained from the adsorption–desorption protocol was used to treat the CP (for details of the protocol, refer to the [Experimental Section](#)). The selectivity of CM2LF was demonstrated by comparative measurements of concentrations of ions in real water samples and in the extract. The concentrations of magnesium, calcium, potassium, iron, and arsenic were recorded using ICP MS. [Figure S12](#) shows the values of concentrations of these ions in the extract expressed as recovery (%) determined from the extraction experiments using 5 mg of CM2LF. In the adsorption step, out of all the ions present in the water sample, only As gets adsorbed onto CM2LF, while large concentrations of other ions are discarded. The recovery (%) of arsenic is several times more than that compared to other ions in the extract.

The effects of different competitive anions (phosphate and carbonate) at ppm concentrations were also studied. The CP sensor performance was evaluated for seven different As extract solutions. Depending on the extraction conditions, one of these was As in alkaline water (no competitive anion), and the remaining six had As in alkaline water with different concentrations of phosphate or carbonate as follows: 500 ppm phosphate, 1000 ppm phosphate, 1000 ppm phosphate (high As concentration), 1000 ppm carbonate, 1500 ppm carbonate (high As concentration), and 1500 ppm carbonate ([Table S3](#)). The CP was treated with  $50 \mu\text{L}$  of As extracts in the presence of cell growth medium. The cells were stained with DCFDA post 24 h exposure to As extracts, and the ROS generated was quantified. All the experiments were performed in triplicate. The fold change value thus obtained was substituted in the regression equation, and the corresponding As concentration was calculated. To verify the results obtained

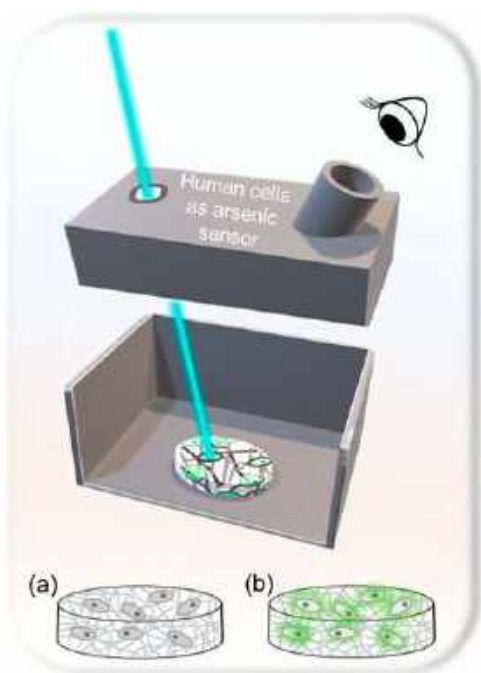
by the CP sensor, the As concentrations in all the extracts were measured independently, on a different aliquot of the same sample, by ICP-MS. [Figure S12](#) shows the comparative plot of As concentrations detected in the real water samples by the CP sensor and the predicted concentration (ICP-MS measurement). The results are reported in [Table S3](#). These outcomes validated the sensor's capability of analyzing As-containing tap water. The correlation between the CP sensor results and the ICP-MS analyses of the real water samples was evaluated by a least-squares linear regression curve-fitting algorithm ([Figure 3D](#)). Here, we plot the results of both the sensing methods on the axes of a regression graph. Statistical data analysis with a confidence level of 95% was performed. Each point on the graph represents a single water sample tested by both techniques. The analysis generated a line with the regression equation  $y = (0.8 \pm 0.04)x + (0.05 \pm 0.02)$  and the correlation coefficient  $R^2 = 0.98$ . Ideally, if the results obtained by the CP sensor are the same as ICP-MS values, the graph will be a straight line of regression with a slope of 1, an intercept of zero, and  $R = +1$ .<sup>27</sup> The dashed lines in [Figure 3D](#) indicate 95% confidence bands, implying that the accuracy was acceptable but could be improved further. In practice, small deviations are inevitable, and the results of our CP sensor are reliable. Moreover, the sensor also performed well in the presence of substantially high amounts of phosphates and carbonates ([Table S3](#)). Thus, the sensor was able to detect and quantify environmentally relevant concentrations of As.

**Sustainable Prototype Cellular Arsenic Sensor.** The results confirmed that the developed CP sensor could be helpful in environmental As detection. Moreover, as the CP is composed of keratinocytes, a human skin cell line, the observed effects of As can be directly linked to health effects seen in arsenicosis patients. [Scheme 2](#) illustrates the use of the optimized protocol to develop a prototype device that can be used for creating social awareness regarding the toxicity and adverse health effects of As. A kit containing a syringe packed with the iron removal prefilter and As adsorbing media (CM2LF), pH adjustment solutions,  $0.2 \mu\text{m}$  filter, and dye may be provided. As seen in the first panel of [Scheme 2](#), the adsorption of As from a test water sample onto the CM2LF, followed by decreasing the pH, can occur in the same syringe. Subsequently, the solution may be made alkaline (second panel). This As extract can then be exposed to the CP sensor after a  $0.2 \mu\text{m}$  syringe filtration. Post incubation, it may be stained with the DCFDA dye. Subsequently, a commercially available 485 nm light-emitting diode (LED) can be used as a



light source for the excitation of the reacted dye molecule, and a photodiode can detect the response. A microcontroller can capture this data and transmit it to a smartphone, where valuable information about the safety of the water may be displayed. While using the CP sensor device as a social awareness tool, the output on the screen could be as simple as “Safe” or “Unsafe” depending on the concentration of As found in tested water. Moreover, to demonstrate the effects of As on human skin cells to the affected communities, a setup as shown in Scheme 3 is proposed. It will be comprised of an opaque

**Scheme 3. Setup to Facilitate Visual Display of As Damage: (a) Healthy Cells and (b) Cells after Exposure to As-Containing Water above Threshold Concentration<sup>a</sup>**



<sup>a</sup>The case is shown open to present a perspective view of the cell matrix.

case with an arrangement to support the CP, a slit to allow access to excitation light, and an eyepiece to view the fluorescent cells before and after exposure to As-containing water samples. An emission filter will be fitted at the viewer end to block the unwanted excitation light. The lid of the box can be opened to place the As extract-treated CP. The visual display of As damage will help educate the typical person belonging to nonscientific communities. This may be placed typically in a school or a village health center in the affected region, which could store CP.

**Aspects of Sustainability.** The research describes a human cell-based fluorescence sensor for environmental As detection. The method is sustainable, without any toxic byproducts. The maintenance costs are minimal as expensive instruments are not required. Moreover, as the sensor output is visual, it has an immense potential to educate affected communities, especially the rural population. We believe that this research presents an appropriate, cost-effective, and sustainable solution to evaluate and display the environmental impact of As toxicity.

## CONCLUSION

This study established a unique, sensitive, quantitative, and environment-friendly cellular platform-based As sensor. We have demonstrated a sustainable sensing methodology by combining the fundamental concepts of As cytotoxicity with an alternative approach for selectivity. An optimized cellular platform was developed that comprised keratinocytes cultured on an electrospun scaffold. Arsenic-induced ROS production was quantified, and concentration-dependent calibration curves were generated. The approach of selectively extracting As from field water using CM2LF enabled precise quantification of unknown As concentration. The CP sensor's performance was tested with a mixture of arsenite and arsenate in a 1:1 ratio which is found in natural conditions. The sensor could detect and precisely quantify environmentally relevant concentrations of As, including as low as 5 ppb (0.068  $\mu\text{M}$ ) of As in tap water. The theoretical LOD was 0.036  $\mu\text{M}$  (2.7 ppb), well below the guideline value for As in drinking water (10 ppb or 0.134  $\mu\text{M}$ ) as per WHO and US EPA specifications. The outcomes proved the performance of the developed CP sensor as a robust and sensitive As sensing technique. Moreover, according to WHO, educating and preventing further As exposure in affected communities is essential. To address this, a prototype device is proposed for As detection in field conditions that can also be used for creating social awareness in the affected communities. The device will demonstrate the As-induced damage to human skin cells. The results are visual; hence, interpretation is simple for people of all age groups. Thus, it will serve the dual purpose of evaluating the water quality and alerting the communities to the chronic toxic effects of As.

## ASSOCIATED CONTENT

### Supporting Information

The Supporting Information is available free of charge at <https://pubs.acs.org/doi/10.1021/acssuschemeng.2c04586>.

Experimental section; optical images of electrospun P3, P5, and P8 scaffolds; average thickness of electrospun nanofibers; quantification of nanofiber diameter; cell viability analysis by MTT assay; quantitative assessment of cell adhesion on P5; HaCaT cells on tcp stained with FDA/PI; graphical representation of cell viability (%) of HaCaT cells; cell viability (%) values of HaCaT cells treated with low arsenite concentrations; arsenic concentration and time-dependent cellular ROS generation determined by DCFDA assay; effect of As mixture on intracellular ROS generation; As concentration-dependent fold change regimes; comparative plot of As concentration detected by CP in real water conditions; arsenic concentrations detected in seven different real water samples by the CP sensor compared to ICP-MS measurements; normalized DCFDA fluorescence intensity response of CP to increasing concentrations of As (calculation of LOD) (PDF)

## AUTHOR INFORMATION

### Corresponding Author

Thalappil Pradeep – DST Unit of Nanoscience (DST UNS) and Thematic Unit of Excellence, Department of Chemistry, Indian Institute of Technology Madras, Chennai 600036, India; International Centre for Clean Water, Taramani, Chennai 600113, India; [orcid.org/0000-0003-3174-534X](https://orcid.org/0000-0003-3174-534X); Email: [pradeep@iitm.ac.in](mailto:pradeep@iitm.ac.in)

## Authors

**Tanvi Gupte** – DST Unit of Nanoscience (DST UNS) and Thematic Unit of Excellence, Department of Chemistry, Indian Institute of Technology Madras, Chennai 600036, India; Department of Metallurgical and Materials Engineering, Indian Institute of Technology Madras, Chennai 600036, India; [orcid.org/0000-0002-0518-8482](https://orcid.org/0000-0002-0518-8482)

**Suryalakshmi Pandurangan** – Division of Biochemistry and Biotechnology, Council of Scientific and Industrial Research, Central Leather Research Institute, Chennai 600036, India

**Md Rabiul Islam** – DST Unit of Nanoscience (DST UNS) and Thematic Unit of Excellence, Department of Chemistry, Indian Institute of Technology Madras, Chennai 600036, India; International Centre for Clean Water, Taramani, Chennai 600113, India

**Pillalamarri Srikrishnarka** – DST Unit of Nanoscience (DST UNS) and Thematic Unit of Excellence, Department of Chemistry, Indian Institute of Technology Madras, Chennai 600036, India; [orcid.org/0000-0001-5187-6879](https://orcid.org/0000-0001-5187-6879)

**Ankit Nagar** – DST Unit of Nanoscience (DST UNS) and Thematic Unit of Excellence, Department of Chemistry, Indian Institute of Technology Madras, Chennai 600036, India; Department of Metallurgical and Materials Engineering, Indian Institute of Technology Madras, Chennai 600036, India

**Niraikulam Ayyadurai** – Division of Biochemistry and Biotechnology, Council of Scientific and Industrial Research, Central Leather Research Institute, Chennai 600036, India; [orcid.org/0000-0002-7333-6344](https://orcid.org/0000-0002-7333-6344)

**Tiju Thomas** – Department of Metallurgical and Materials Engineering, Indian Institute of Technology Madras, Chennai 600036, India

Complete contact information is available at:  
<https://pubs.acs.org/10.1021/acssuschemeng.2c04586>

## Author Contributions

All authors have given approval to the final version of the manuscript.

## Notes

The authors declare no competing financial interest.

## ACKNOWLEDGMENTS

The authors thank the Department of Science and Technology, Government of India, for supporting our research program. T.G., P.S., and A.N. thank IIT Madras for their fellowships. S.P. thanks DST for an INSPIRE fellowship. R.I. thanks the CSIR for his research fellowship. We thank Hydromaterials Pvt. Ltd., Chennai, for providing the arsenic-adsorbing media.

## REFERENCES

- (1) Nagar, A.; Pradeep, T. Clean Water through Nanotechnology: Needs, Gaps, and Fulfillment. *ACS Nano* **2020**, *14* (6), 6420–6435.
- (2) Podgorski, J.; Berg, M. Global Threat of Arsenic in Groundwater. *Science* **2020**, *368* (6493), 845–850.
- (3) Naga Jyothi, M. S. V.; Gayathri, S.; Pushparaj Gandhi, T.; Maliyekkal, S. M. Dissolved Arsenic in Groundwater Bodies: A Short Review of Remediation Technologies. *Energy, Environ. Sustain.* **2021**, *75*–111.
- (4) Zinke, L. Groundwater Arsenic. *Nat. Rev. Earth Environ.* **2020**, *1* (11), 558–558.
- (5) Mukherjee, S.; Gupte, T.; Jenifer, S. K.; Thomas, T.; Pradeep, T. Arsenic in Water: Speciation, Sources, Distribution, and Toxicology.

In *Encyclopedia of Water: Science, Technology, and Society*; John Wiley & Sons, Inc., 2019; pp 1–17. DOI: [10.1002/9781119300762.wsts0053](https://doi.org/10.1002/9781119300762.wsts0053).

(6) Vrijenhoek, E. M.; Waypa, J. J. Arsenic Removal from Drinking Water by a “Loose” Nanofiltration Membrane. *Desalination* **2000**, *130* (3), 265–277.

(7) Yu, S.; Liao, W. T.; Lee, C. H.; Chai, C. Y.; Yu, C. L.; Yu, H. S. Immunological Dysfunction in Chronic Arsenic Exposure: From Subclinical Condition to Skin Cancer. *J. Dermatol.* **2018**, *45* (11), 1271–1277.

(8) Mayer, J. E.; Goldman, R. H. Arsenic and Skin Cancer in the USA: The Current Evidence Regarding Arsenic-Contaminated Drinking Water. *Int. J. Dermatol.* **2016**, *55*, e585–e591.

(9) Maciaszczyk-Dziubinska, E.; Wawrzycka, D.; Wysocki, R. Arsenic and Antimony Transporters in Eukaryotes. *Int. J. Mol. Sci.* **2012**, *13* (3), 3527–3548.

(10) Yu, H.-S.; Liao, W.-T.; Chai, C.-Y. Arsenic Carcinogenesis in the Skin. *J. Biomed. Sci.* **2006**, *13*, 657–666.

(11) Soleja, N.; Manzoor, O.; Khan, P.; Mohsin, M. Engineering Genetically Encoded FRET-Based Nanosensors for Real Time Display of Arsenic (As<sup>3+</sup>) Dynamics in Living Cells. *Sci. Reports* **2019**, *9* (1), 1–14.

(12) Redza-Dutordoir, M.; Averill-Bates, D. A. Activation of Apoptosis Signalling Pathways by Reactive Oxygen Species. *Biochim. Biophys. Acta - Mol. Cell Res.* **2016**, *1863* (12), 2977–2992.

(13) Ayoubi, M.; Naserzadeh, P.; Hashemi, M. T.; Reza Rostami, M.; Tamjid, E.; Tavakoli, M. M.; Simchi, A. Biochemical Mechanisms of Dose-Dependent Cytotoxicity and ROS-Mediated Apoptosis Induced by Lead Sulfide/Graphene Oxide Quantum Dots for Potential Bioimaging Applications. *Sci. Rep.* **2017**, *7* (1), 1–10.

(14) Ahlawat, J.; Neupane, R.; Deemer, E.; Sreenivasan, S. T.; Narayan, M. Chitosan-Ellagic Acid Nanohybrid for Mitigating Rotenone-Induced Oxidative Stress. *ACS Appl. Mater. Interfaces* **2020**, *12* (16), 18964–18977.

(15) Pham, Q. P.; Sharma, U.; Mikos, A. G. Electrospun Poly ( $\epsilon$ -Caprolactone) Microfiber and Multilayer Nanofiber/Microfiber Scaffolds: Characterization of Scaffolds and Measurement of Cellular Infiltration. *Biomacromolecules* **2006**, *7* (10), 2796–2805.

(16) Siddiqui, N.; Asawa, S.; Birru, B.; Baadhe, R.; Rao, S. PCL-Based Composite Scaffold Matrices for Tissue Engineering Applications. *Mol. Biotechnol.* **2018**, *60* (7), 506–532.

(17) Sundaramurthi, D.; Krishnan, U. M.; Sethuraman, S. Electrospun Nanofibers as Scaffolds for Skin Tissue Engineering. *Polym. Rev.* **2014**, *54* (2), 348–376.

(18) Cooper, J. M.; Cass, A. E. G., Eds.; *Biosensors: A Practical Approach*, 2nd ed.; Oxford University Press: Oxford, UK, 2004.

(19) Saltepe, B.; Kehribar, E. Ş.; Su Yirmibeşoğlu, S. S.; Şafak Şeker, U. Ö. Cellular Biosensors with Engineered Genetic Circuits. *ACS Sensors* **2018**, *3* (1), 13–26.

(20) Kumar, A. A.; Som, A.; Longo, P.; Sudhakar, C.; Bhui, R. G.; Gupta, S. S.; Anshup; Sankar, M. U.; Chaudhary, A.; Kumar, R.; Pradeep, T. Confined Metastable 2-Line Ferrihydrite for Affordable Point-of-Use Arsenic-Free Drinking Water. *Adv. Mater.* **2017**, *29*, 1604260.

(21) Sudhakar, C.; Anil Kumar, A.; Bhui, R. G.; Sen Gupta, S.; Natarajan, G.; Pradeep, T. Species-Specific Uptake of Arsenic on Confined Metastable 2-Line Ferrihydrite: A Combined Raman-X-Ray Photoelectron Spectroscopy Investigation of the Adsorption Mechanism. *ACS Sustain. Chem. Eng.* **2018**, *6* (8), 9990–10000.

(22) *WHO Guidelines for Drinking-Water Quality*, 4th ed.; WHO Press: Geneva, Switzerland, 2011; pp 315–318.

(23) *USEPA Technical Factsheet: Final Rule for Arsenic in Drinking Water*; United States Environmental Protection Agency, 2001; pp 1–6.

(24) Smith, A. H.; Steinmaus, C. M. Arsenic in Drinking Water. *Br. Med. J.* **2011**, *342*, d2248.

(25) Haider, A.; Haider, S.; Kang, I. K. A Comprehensive Review Summarizing the Effect of Electrospinning Parameters and Potential

Applications of Nanofibers in Biomedical and Biotechnology. *Arab. J. Chem.* **2018**, *11* (8), 1165–1188.

(26) Khanam, N.; Mikoryak, C.; Draper, R. K.; Balkus, K. J. Electrospun Linear Polyethyleneimine Scaffolds for Cell Growth. *Acta Biomater.* **2007**, *3* (6), 1050–1059.

(27) Miller, J. N. Basic Statistical Methods for Analytical Chemistry. Part 2. Calibration and Regression Methods. A Review. *Analyst* **1991**, *116* (1), 3–14.

## Recommended by ACS

### DNA Antiadhesive Layer for Reusable Plasmonic Sensors: Nanostructure Pitch Effect

Remigiusz K. Trojanowicz, Lucia Petti, *et al.*

AUGUST 30, 2022  
ACS OMEGA

READ 

### Aptasensors Based on Graphene Field-Effect Transistors for Arsenite Detection

Jingwei Li, Zhaoli Gao, *et al.*

SEPTEMBER 06, 2022  
ACS APPLIED NANO MATERIALS

READ 

### Particle-Bound Hg(II) is Available for Microbial Uptake as Revealed by a Whole-Cell Biosensor

Yuping Xiang, Guibin Jiang, *et al.*

MAY 03, 2022  
ENVIRONMENTAL SCIENCE & TECHNOLOGY

READ 

### Reagent-Free Hydrogen Peroxide Sensing Using Carbon Nanotube Chemiresistors with Electropolymerized Crystal Violet

Vinay Patel, Ponnambalam Ravi Selvaganapathy, *et al.*

FEBRUARY 28, 2022  
ACS APPLIED NANO MATERIALS

READ 

Get More Suggestions >

## Supporting Information

### Human Skin-Cell-Based Sensor for Environmental Arsenic Detection and for Creating Social Awareness

*Tanvi Gupte<sup>a,b</sup>, Suryalakshmi Pandurangan<sup>c</sup>, Md Rabiul Islam<sup>a</sup>, Srikrishnarka Pillalamarri<sup>a</sup>,  
Ankit Nagar<sup>a,b</sup>, Niraikulam Ayyadurai<sup>c</sup>, Tiju Thomas<sup>b</sup>, Thalappil Pradeep<sup>ad\*</sup>*

<sup>a</sup>DST Unit of Nanoscience (DST UNS) and Thematic Unit of Excellence, Department of Chemistry, Indian Institute of Technology Madras

<sup>b</sup>Department of Metallurgical and Materials Engineering, Indian Institute of Technology Madras

<sup>c</sup>Division of Biochemistry and Biotechnology, Council of Scientific and Industrial Research - Central Leather Research Institute

<sup>d</sup>International Centre for Clean Water, 2nd Floor, B-Block, IIT Madras Research Park, Kanagam Road, Taramani, Chennai 600113, India.

\* Corresponding author: pradeep@iitm.ac.in (Prof. T. Pradeep)

Number of pages: 25

Number of figures: 14

Number of tables: 3

## TABLE OF CONTENTS

<b>Figure/ Table No.</b>	<b>Title</b>	<b>Page No.</b>
	<b>Experimental section</b>	S3
<b>Table S1</b>	Comparative characteristics of cell-based and cell-free arsenic biosensors	S8
	<b>Results and Discussion</b>	S9
<b>Figure S1</b>	Optical images of electrospun P3, P5, and P8 scaffolds	S9
<b>Figure S2</b>	Average thickness of electrospun nanofibers	S10
<b>Figure S3</b>	Quantification of nanofiber diameter	S11
<b>Figure S4</b>	FESEM micrographs of HaCaT cells	S12
<b>Figure S5</b>	Cell viability analysis by MTT assay	S13
<b>Figure S6</b>	Quantitative assessment of cell adhesion on P5	S14
<b>Figure S7</b>	HaCaT cells on tcp stained with FDA/PI	S15
<b>Figure S8</b>	Graphical representation of cell viability (%) of HaCaT cells	S16
<b>Table S2</b>	Cell viability (%) values of HaCaT cells treated with low arsenite concentrations	S17
<b>Figure S9</b>	Arsenic concentration and time-dependent cellular ROS generation determined by DCFDA assay	S18
<b>Figure S10</b>	Effect of As mixture on intracellular ROS generation	S19
<b>Figure S11</b>	As-concentration-dependent fold change regimes	S20
<b>Figure S12</b>	The concentration of various ions in the extract expressed as recovery (%) compared to As	S21
<b>Figure S13</b>	A comparative plot of As concentration detected by the CP in real water conditions	S22
<b>Table S3</b>	Arsenic concentrations detected in seven different real water samples by the CP sensor compared to the ICP-MS measurements	S23
<b>Figure S14</b>	DCFDA fluorescence intensity response of CP to low and high concentrations of As (Calculation of LOD)	S24
<b>Reference(s)</b>		S25

## **EXPERIMENTAL SECTION**

### **Materials**

Polycaprolactone (PCL (70-90 kDa)) was obtained from Sigma-Aldrich, USA. Dimethylformamide (DMF) and dichloromethane (DCM) were purchased from Avantor. Sodium arsenite ( $\text{NaAsO}_2$ ) and sodium arsenate ( $\text{Na}_3\text{AsO}_4$ ) were purchased from S D Fine Chem Ltd. and Finar Ltd., respectively. Stock solutions of As were prepared in Milli-Q water and filtered through a 0.2  $\mu\text{m}$  syringe filter. HaCaT cells were purchased from AddexBio Technologies, USA. Dulbecco's Modified Eagle Medium (DMEM), Fetal bovine serum (FBS), and the antibiotic antimycotic solution were purchased from Sigma Aldrich. Fluorescein diacetate (FDA) and propidium iodide (PI) were purchased from Sigma, USA. A stock solution of FDA was prepared by dissolving 5 mg/mL in DMSO. Three milligrams of PI were dissolved in 1 mL of phosphate buffered saline (PBS) to get its stock solution. Both the stocks were stored at  $-20\text{ }^\circ\text{C}$ . The fluorescent dye 2',7'-dichlorofluorescein diacetate (DCFDA) was purchased from Sigma Aldrich. 500  $\mu\text{M}$  stock solution of DCFDA was prepared in ethanol and stored at  $-20\text{ }^\circ\text{C}$ . As adsorbing media - CM2LF was gifted by Hydromaterials Pvt. Ltd., Chennai, an incubated company of IIT Madras. Sodium carbonate ( $\text{Na}_2\text{CO}_3$ ) and sodium phosphate monobasic dihydrate ( $\text{NaH}_2\text{PO}_4 \cdot 2\text{H}_2\text{O}$ ) were purchased from RFCL Limited (Rankem), India.

### **Instruments**

ESPIN-NANO electrospinning machine was used to prepare nanofibers. The morphology and thickness of the nanofibrous mat were observed by Keyence digital microscope (VH-Z100R). The FESEM analysis was carried out using Verios G4 UC, FEI. Inductively coupled plasma-mass spectrometry (ICP-MS) analysis was performed using NexION 300X (PerkinElmer). Leica fluorescence microscope with fluorescein isothiocyanate (FITC) or Rhodamine filter and Biotek fluorescence microplate reader was used for fluorescence imaging and quantifying fluorescence intensity.



### **Characterization of the nanofibrous scaffold**

The morphology, alignment, and thickness of electrospun fibers on the cover glass substrate were observed by optical microscopy. The average thickness was calculated based on these images. The electrospun P5 scaffold was sputter-coated with gold for 4 min and visualized using a field emission scanning electronic microscope (FESEM). The average fiber diameter was determined by analysing 50 random fibers observed in the FESEM images using Image-J software (National Institutes of Health).

### **Cell culture**

HaCaT cells (keratinocyte cell line from adult human skin) were cultured in T-25 flasks with 5 ml cell culture medium containing DMEM high glucose supplemented with 10% fetal bovine serum (FBS) and 1x antibiotic antimycotic solution at 37°C in a humidified atmosphere with 5% CO<sub>2</sub>. For As treatment experiments, required concentrations of As were prepared by serially diluting the stocks with Milli-Q water followed by filter sterilization. The As(III) and As(V) were taken in a 1:1 molar concentration ratio for the As mixture. Triplicate tissue culture plate (tcp) wells were prepared for each concentration, including the As untreated control wells.

### **Morphological characterization of the cultured cells**

The morphology of HaCaT cells cultured on the optimized P5 scaffold and the blank cover glass was observed by FESEM. Both the substrates were placed into wells of tcp, and the cells were cultured at a cell density of  $5 \times 10^4$  cells/ml for 24 h. They were then fixed with 4% paraformaldehyde and dehydrated with gradient concentrations of ethanol (30%, 50%, 70%, 90%, and 100%). Further, the samples were kept in a desiccator for three days to ensure complete dehydration. They were gold-sputtered and imaged by FESEM.

### **Cell viability on the nanofibrous scaffold by MTT assay**

The 3-(4,5-dimethylthiazol-2-yl)-2,5-diphenyltetrazolium bromide (MTT) assay was used to quantify viable cells. HaCaT cells were seeded at a cell density of  $5 \times 10^4$  cells/ml on the nanofibrous scaffold(s) and incubated in a CO<sub>2</sub> incubator. After the incubation period, the culture media was replaced with fresh media containing MTT solution (0.5 mg/mL) and incubated for 3 h at 37 °C. The tcp were wrapped with aluminum foil to avoid exposure to light. DMSO was used to dissolve the purple-coloured formazan formed by the live cells after 3 h. DMSO was set as the blank, and the absorbance was measured at 570 nm using a microplate spectrophotometer. The

viability of the control group (cells cultured on wells of tcp without a scaffold) was considered 100 %. The assay gives results in terms of percentage of relative cell viability. Experiments were performed in triplicate.

The electrospinning time was optimized based on the MTT assay. The cell viability on the P3, P5, and P8 scaffolds was evaluated at 24 h. The MTT assay was also performed on the tcp as a control experiment to assess the cytotoxic effects of As(III) concentration on HaCaT cells cultured on wells of tcp. The cells were exposed to different arsenite concentrations (0, 0.5, 1, 3, 5, and 7  $\mu\text{M}$ ) and incubated in a  $\text{CO}_2$  incubator. The negative controls (0  $\mu\text{M}$  wells) were cells cultured under the same condition, subjected to an equal volume of Milli-Q instead of As. The MTT assay was performed 24 h post-exposure for all the As(III) concentrations.

### **Fluorescence imaging**

*Assessing cell adhesion on P5:* Fluorescein diacetate (FDA) staining was performed to assess live HaCaT cells on P5 and tcp qualitatively. Cells were cultured on both the substrates for 24 h before staining with FDA. For quantitative analysis, three fluorescence images (taken at the same magnification) were obtained from both substrates. The percentage area covered by live cells at each time point was calculated using ImageJ software.

*Effect of low concentrations of arsenite on cell viability:* A live/dead assay was performed to observe the effect of lower concentrations of arsenite on HaCaT cells using fluorescein diacetate and propidium iodide (FDA/PI). This experiment was conducted to support the MTT assay results and determine the long-term cytotoxic effects of low doses of arsenite. Cells were cultured on the wells of tcp for 24 h before arsenic treatment. As(III) treated (0.5, 0.75, and 1  $\mu\text{M}$ ) and untreated cells (control) were incubated at 37  $^\circ\text{C}$  and 5%  $\text{CO}_2$  for 24, 48, and 72 h. The cells were classified as either viable or non-viable and counted using ImageJ software. Three different fluorescence images were evaluated to calculate the cell viability which was expressed as a percentage using the following equation.

$$\text{Cell viability (\%)} = \frac{\text{Number of living cells}}{\text{Total number of cells}} \times 100 \quad [1]$$

In both of these experiments, the working solutions of FDA and PI were prepared freshly. For FDA/PI staining, 10  $\mu\text{L}$  from FDA and 1  $\mu\text{L}$  from PI stock solution were added to 1 mL of pre-warmed cell culture medium without phenol red. Cells were incubated with the freshly prepared

solution for 5 min in a dark environment. The staining solution was discarded, and cells were washed with PBS. Finally, fresh PBS was added and observed under a fluorescence microscope using a FITC filter (Ex 460-500 nm, Em 512-542 nm) for FDA and Rhodamine filter (Ex 541-551 nm, Em 565-605 nm) for PI.

### **Analysis of real water samples using CM2LF**

A protocol was optimized to selectively expose As in the real water samples to the cellular platform. To achieve this, As adsorbing media, CM2LF was used. To demonstrate the selectivity of CM2LF, ICP-MS measurement of ions before and after extraction was performed. The concentrations of magnesium, calcium, potassium, iron, and arsenic in real water sample (tap water) and after performing the extraction protocol were recorded. The recovery (%) was calculated using equation 2.

$$\text{Recovery (\%)} = \frac{\text{Concentration in extract (ppb)}}{\text{Concentration in water sample (ppb)}} \times 100 \quad [2]$$

The first step of the extraction protocol included the removal of Fe(II) and Fe(III) ions from the laboratory tap water (pH ~7.8) using a prefilter containing iron removal media. The filtered water (100 ml) was spiked with 1 ppm As (1:1 mixture of As(III) and As(V)). It was made slightly acidic (pH 5) with 1 M HCl. To this, 5 mg of CM2LF was added for adsorption of As and allowed to stir at 350 rpm for 1 h. After completion of adsorption, the sample was centrifuged, and the supernatant was discarded. The residue (As adsorbed on CM2LF) was collected and treated with 20 ml of acidified Milli-Q (~ pH 2) for 2 h. During this step, ferric chloride (FeCl<sub>3</sub>) formed by acidification (HCl) and As ions get desorbed. The pH of the solution was then increased to 13 using 1 M NaOH. This alkaline solution was divided into five aliquots of 4 ml each. One was kept as such and termed alkaline water. Following competitive anions were added to the remaining four aliquots: 500 ppm phosphate, 1000 ppm phosphate, 1000 ppm carbonate, and 1500 ppm carbonate. The alkaline pH caused precipitation of ferric hydroxide (Fe(OH)<sub>3</sub>). The As solution thus obtained is filter-sterilized after 1 h using a 0.2 μm filter. The time periods for acid/base treatment were optimized based on time-dependent desorption experiments (data not shown).

Competitive anions were added to prevent the re-adsorption of As by Fe(OH)<sub>3</sub> precipitates. The effect of different competitive anions at ppm concentrations was studied for maximum possible As extraction. The cellular platform was treated with this As extract. Fluorescence response for As-

induced ROS generation was obtained using the DCFDA dye. Control for the fluorescence analysis comprised of tap water sample (non-spiked) subjected to the same adsorption/desorption protocol. Fold change in fluorescence intensity relative to control was quantified. The As concentrations were determined using the calibration curve's regression equation.

**Table S1.** Comparative characteristics of cell-based and cell-free arsenic biosensors

<b>Biosensor specifications</b>	<b>As species detected</b>	<b>LOD (<math>\mu\text{M}</math>)</b>	<b>Detection time (min)</b>	<b>Reference</b>
Aptamer– hemin– $\text{H}_2\text{O}_2$ system-based colorimetric biosensor	As(III)	0.08	15	1
DNA-based electrochemical biosensor with $[\text{Co}(\text{phen})_3]^{3+}$ as DNA marker	As(III)	1000	10	2
Surface plasmon resonance and cyclic voltammetry-based double stranded calf thymus deoxyribonucleic acid (dsCT-DNA) biosensor	As(III)	0.05	17.5	3
Cytochrome C-based electrochemical biosensor	As(III)	4.3	0.5	4
<i>E. coli</i> arsRp::luc-based biosensor	As(III)	0.05	120	5
pH based biosensor using <i>E. coli</i> JN109–pSB1A2–BBa_J15501 harboring arsR–lacZ and xyIE gene construct	As(V)	3750	1440	6
Human skin cell based cellular platform	As(III) and As(V)	0.036	1440	This work

## RESULTS AND DISCUSSION

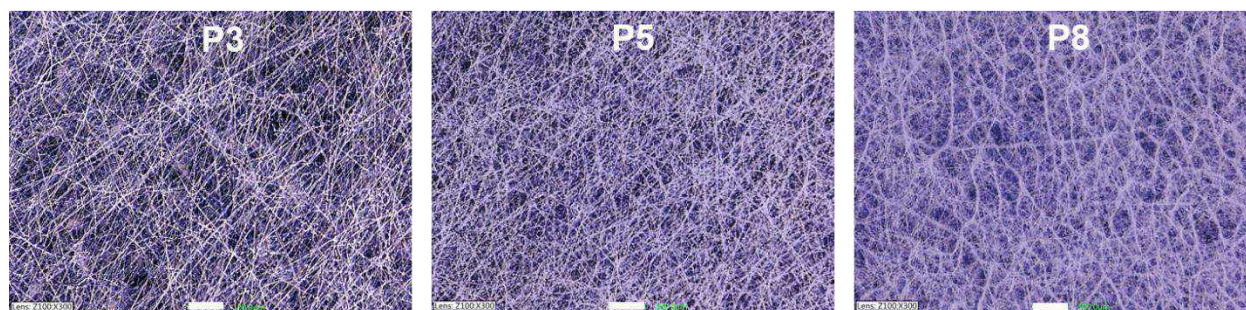


**Figure S1.** Optical images of electrospun polymer on a cover glass substrate taken at 300X. The spin times were varied for 3, 5, and 8 mins to obtain P3, P5, and P8 scaffolds. The scale bar is 100  $\mu\text{m}$ .



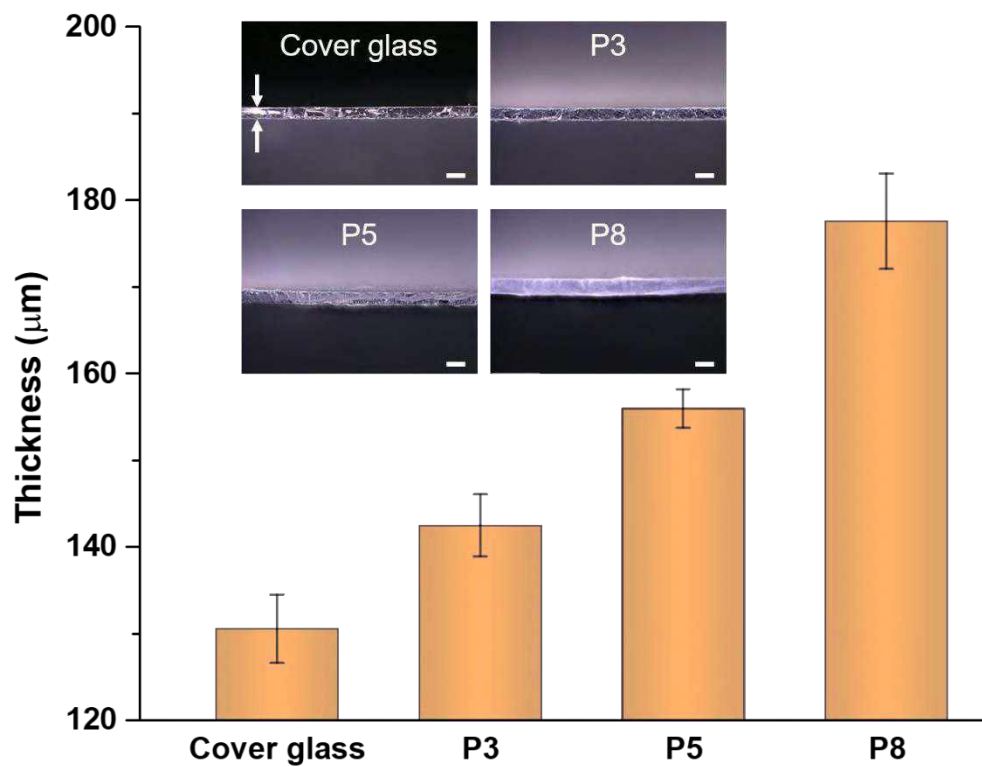


**Figure S2.** The average total thickness of electrospun nanofibers on the cover glass substrate. Inset images show the lateral view of the scaffolds taken at 100X. The scale bar is 200 μm.

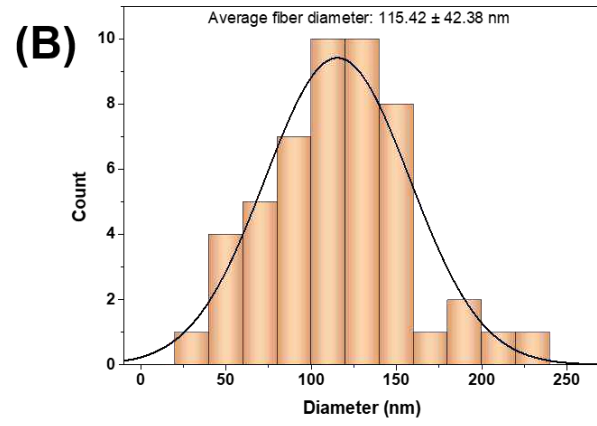
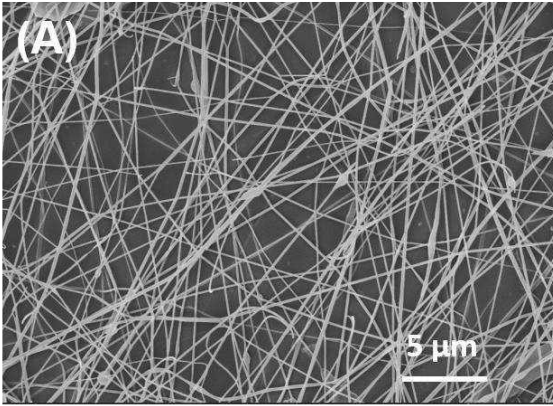


**Figure S3.** Quantification of nanofiber diameter. (A) FESEM micrograph of electrospun P5 scaffold. (B) Histogram of average fiber diameter determined from the FESEM image.

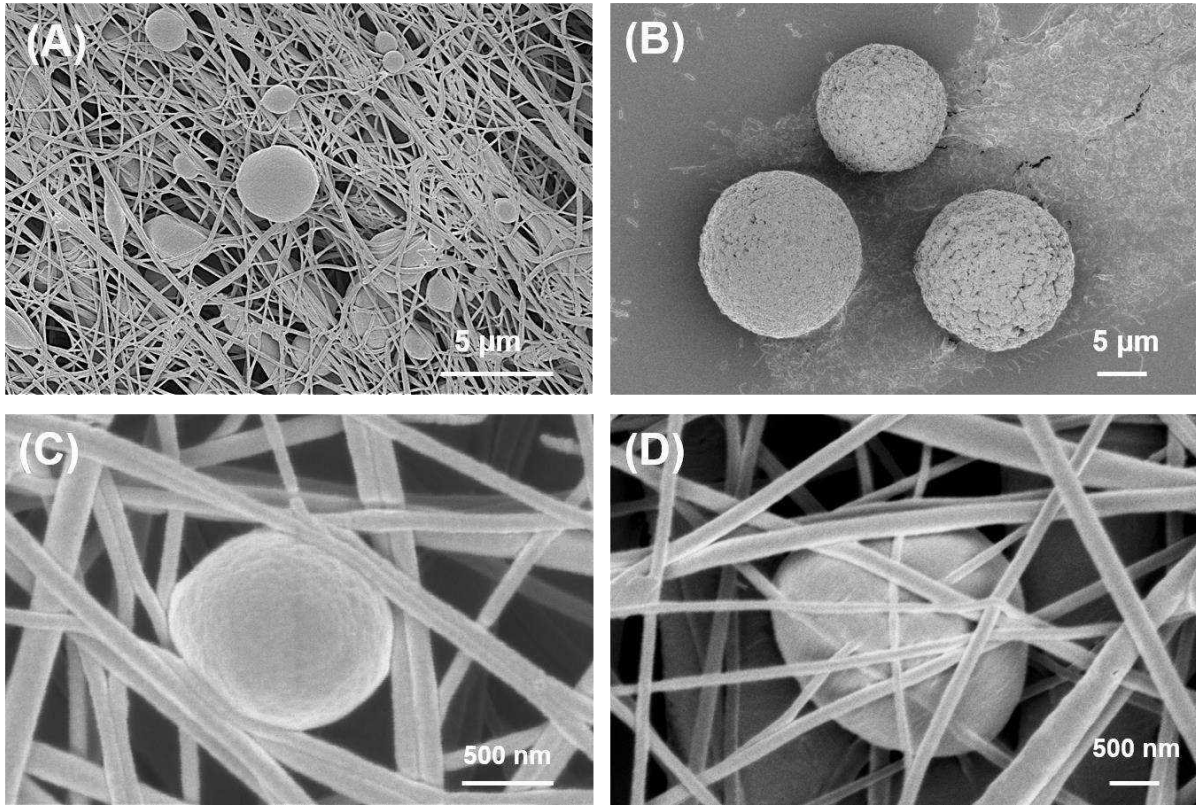


**Figure S4.** FESEM micrographs of HaCaT cell(s) cultured on (A) P5 scaffold and (B) microscopic cover glass. (C) and (D) are the high magnification images of an individual HaCaT cell embedded in the porous network of nanofibrous P5 scaffold.

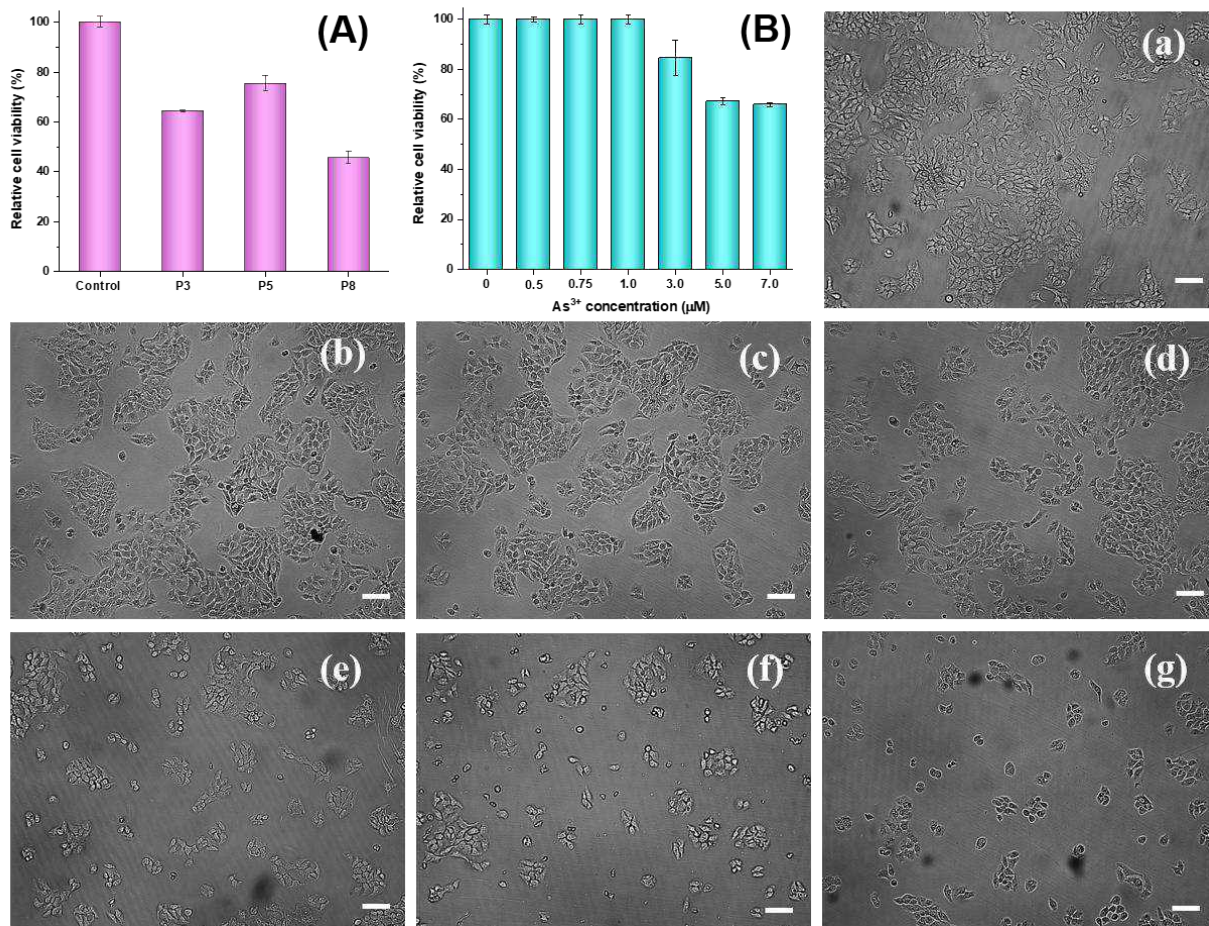


**Figure S5.** Cell viability analysis by MTT assay. (A) Electrospinning time optimization based on cell viability for P3, P5, and P8 scaffolds relative to tcp control at 24 h. (B) Concentration-dependent cytotoxic effects of  $As(III)$  on cells cultured on tcp at 24 h post-exposure. (a-g) Optical images of cell proliferation on tcp after 24 h  $As(III)$  exposure (a) 0 (control), (b) 0.5, (c) 0.75, (d) 1, (e) 3, (f) 5, and (g) 7  $\mu M$ . Scale bar is 50  $\mu m$ .

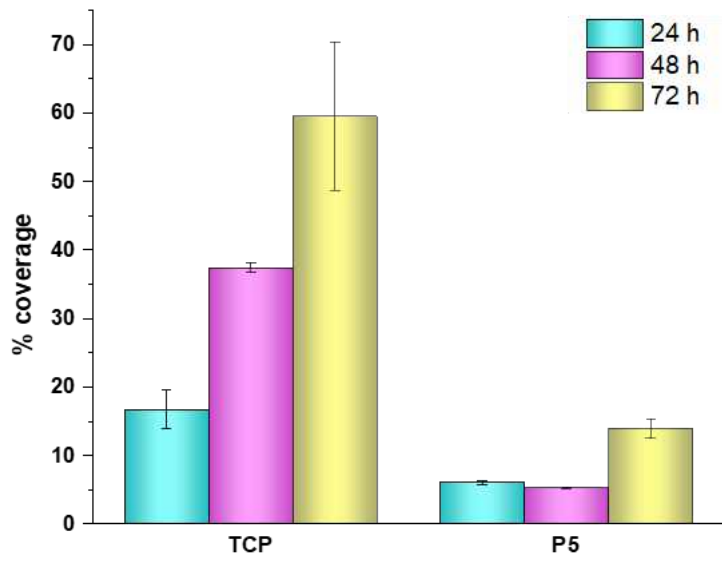


**Figure S6.** Quantitative assessment of cell adhesion on P5 from FDA fluorescence images. The percent coverage of live cells was calculated by area measurement using ImageJ software.

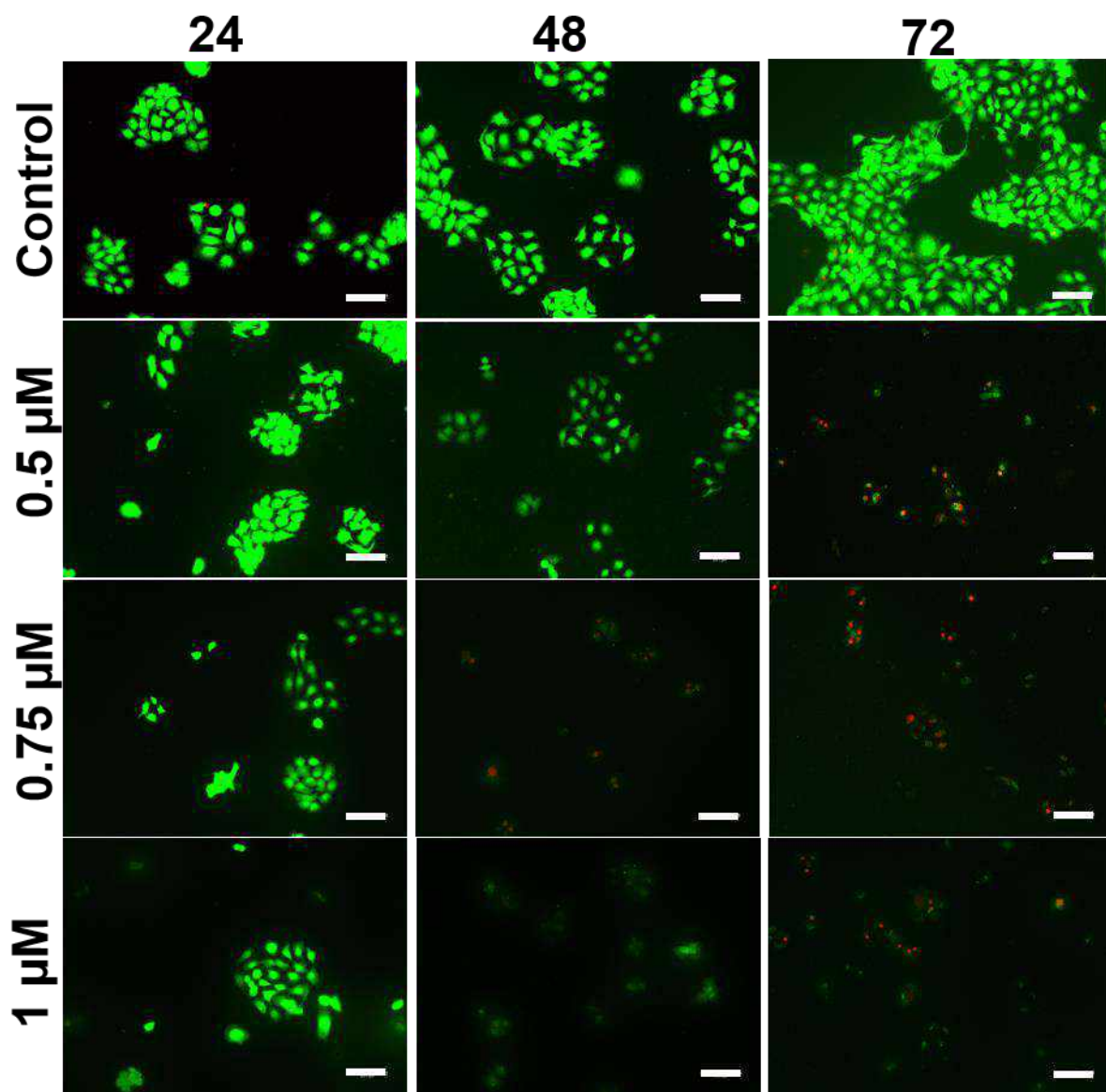


**Figure S7.** Fluorescence micrographs of HaCaT cells on tcp stained vital/dead with FDA/PI. The images are a composite of FDA (green) and PI (red) signals. Live cells were treated with different concentrations of As(III), and images were taken at 24, 48, and 72 h after exposure. The control group was comprised of untreated cells cultured on tcp and stained by FDA/PI. The scale bar is 100 μm.



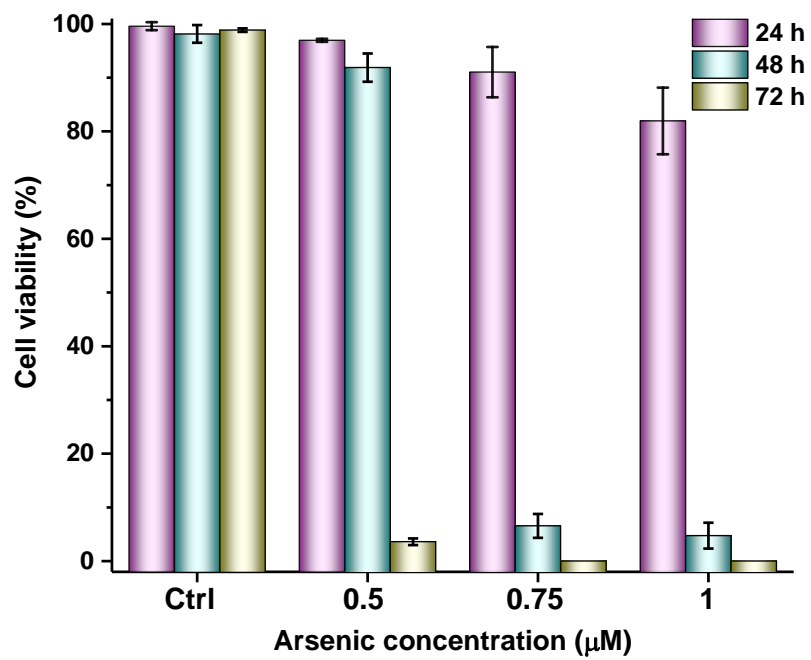


**Figure S8.** Graphical representation of the mean cell viability (%) of HaCaT cells treated with low arsenite concentrations at 24, 48, and 72 h.

**Table S2.** Mean cell viability (%) of HaCaT cells treated with low arsenite concentrations at various experimental times.

Arsenite concentration ( $\mu\text{M}$ )	Mean cell viability (%)		
	24 h	48 h	72 h
0	99.57 $\pm$ 0.74	98.14 $\pm$ 1.65	98.8 $\pm$ 0.33
0.5	96.94 $\pm$ 0.27	91.87 $\pm$ 2.63	3.60 $\pm$ 0.62
0.75	91.04 $\pm$ 4.68	6.55 $\pm$ 2.22	0
1	81.94 $\pm$ 6.20	4.73 $\pm$ 2.40	0

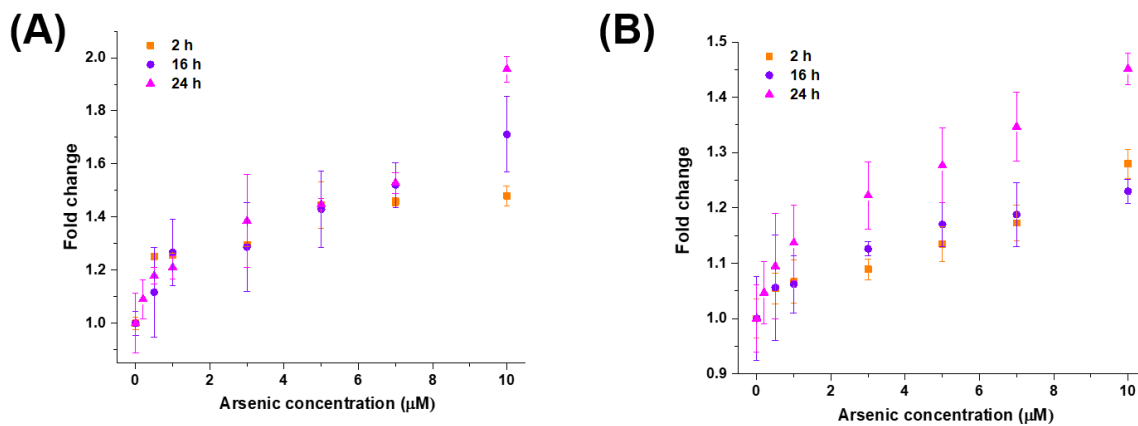


**Figure S9.** Arsenic concentration and time-dependent cellular ROS generation determined by DCFDA assay. (A) and (B) spectrophotometric fluorescence intensity measured in terms of fold change with respect to control for P5 and TCP, respectively. This indicates the gradual enhancement of ROS in cells treated with 0 to 10  $\mu\text{M}$  of As(III) at 2, 16, and 24 h.

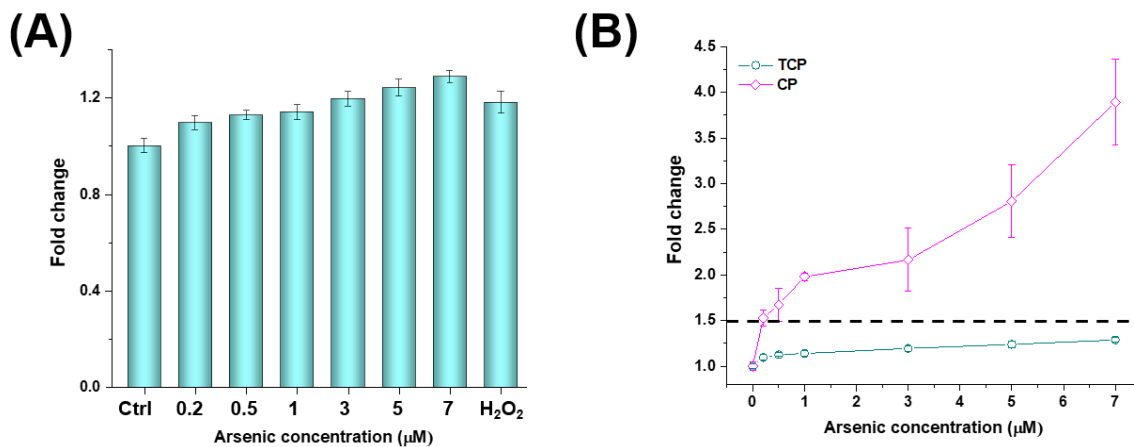


**Figure S10.** Effect of arsenic mixture concentration on intracellular ROS generation at 24 h determined by DCFDA assay. (A) fold change in fluorescence intensity measured for cells cultured on tcp treated with the 1:1 mixture of As(III) and As(V).  $\text{H}_2\text{O}_2$  was used as a positive control. (B) A comparative plot of fold change in fluorescence for As mixture treated CP and tcp. The dashed lines at 1.5 folds highlight the performance of CP as a sensor compared to the control tcp.

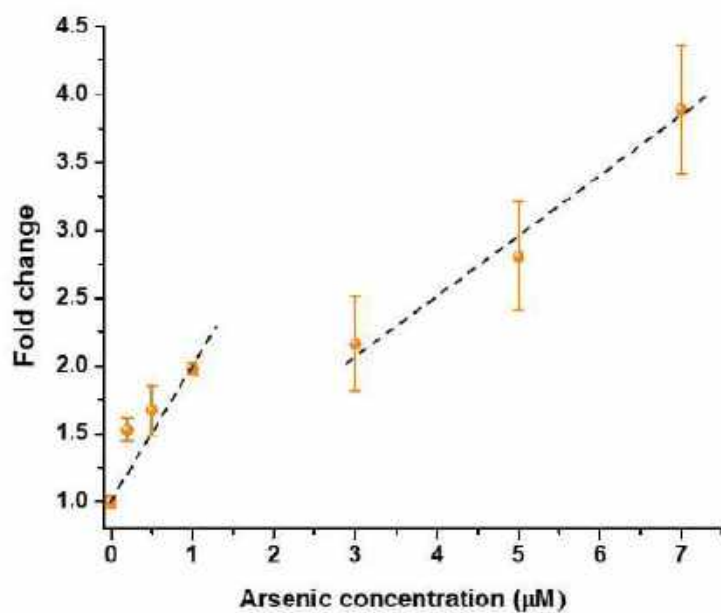


**Figure S11.** Fold change regime after 24 h exposure of CP to various As concentrations (1:1 mixture) determined by DCFDA assay. Straight dashed lines denote the distinct low-concentration and high-concentration regimes.

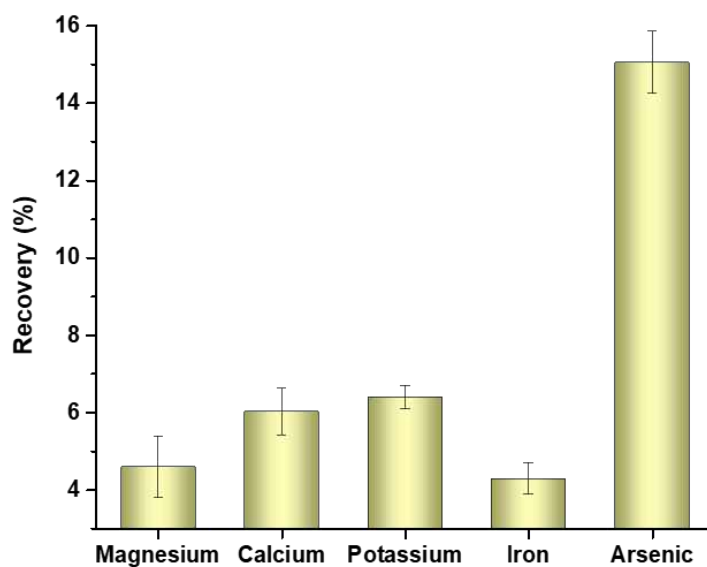


**Figure S12.** The concentration of various ions in the extract expressed as recovery (%) compared to As determined from the extraction experiments using 5 mg CM2LF.



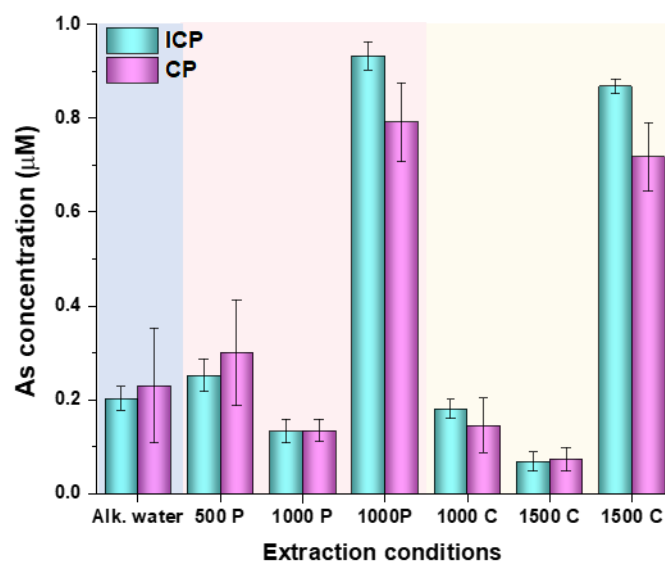


**Figure S13.** A comparative plot of As concentration detected by the cellular platform (CP) sensor and the expected concentration (determined by ICP analysis). The cell-based sensor was exposed to As-containing tap water extracted in different conditions. (Alk. Water represents alkaline water; 500 P and 1000 P represent 500 and 1000 ppm phosphate, respectively; 1000 C and 1500 C represent 1000 and 1500 ppm carbonate, respectively)

**Table S3.** Arsenic concentrations detected in seven different real water samples by the CP sensor compared to the ICP-MS measurements.

Extract	Arsenic concentration ( $\mu\text{M}$ )	
	CP sensor	ICP-MS
Alk water	$0.23 \pm 0.12$	$0.20 \pm 0.03$
500 P	$0.30 \pm 0.11$	$0.25 \pm 0.04$
1000 P	$0.13 \pm 0.02$	$0.13 \pm 0.03$
1000 P (high As)	$0.79 \pm 0.08$	$0.93 \pm 0.03$
1000 C	$0.14 \pm 0.06$	$0.18 \pm 0.02$
1500 C	$0.07 \pm 0.05$	$0.07 \pm 0.02$
1500 C (high As)	$0.72 \pm 0.07$	$0.87 \pm 0.02$

## Calculation of LOD

The theoretical limit of detection (LOD) was estimated using the following equation.<sup>7</sup>

$$\text{Limit of detection} = 3\sigma/m \quad [3]$$

Where  $\sigma$  is the standard deviation of blank measurement and  $m$  is the slope obtained from the fluorescence intensity versus As concentration graph (Figure S14 A and B).

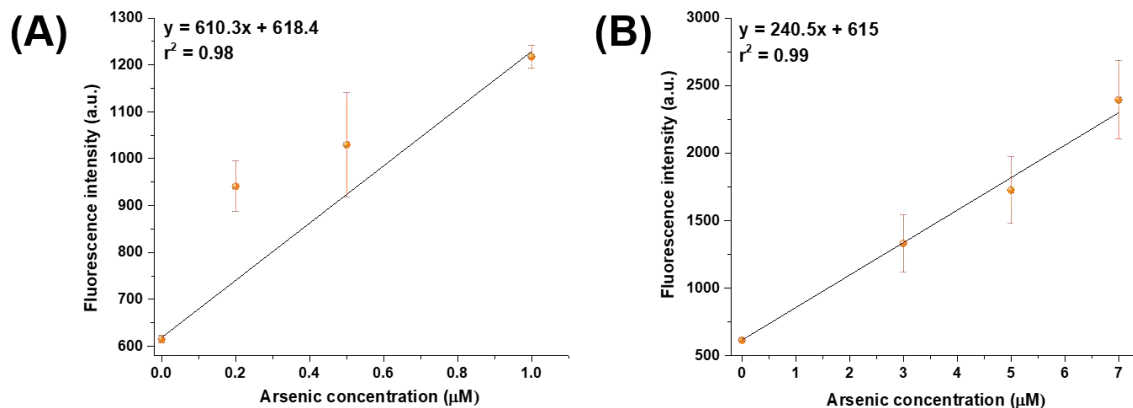


**Figure S14.** DCFDA fluorescence intensity response of CP to (A) low concentration and (B) high concentration regimes of As (1:1 mixture).

Therefore,

For low concentration regime ( $\leq 1 \mu\text{M}$ ),

$$\begin{aligned} LOD &= \frac{3 \times 7.5}{610.3} \\ &= 0.036 \mu\text{M} \\ &= 2.7 \text{ ppb} \end{aligned}$$

For high concentration regime,

$$\begin{aligned} LOD &= \frac{3 \times 7.5}{240.5} \\ &= 0.093 \mu\text{M} \\ &= 6.97 \text{ ppb} \end{aligned}$$

## References

- (1) Wu, Y.; Wang, F.; Zhan, S.; Liu, L.; Luo, Y.; Zhou, P. Regulation of Hemin Peroxidase Catalytic Activity by Arsenic-Binding Aptamers for the Colorimetric Detection of Arsenic(III). *RSC Adv.* **2013**, *3* (48), 25614–25619. <https://doi.org/10.1039/C3RA44346A>.
- (2) Ferancová, A.; Adamovski, M.; Gründler, P.; Zima, J.; Barek, J.; Mattusch, J.; Wennrich, R.; Labuda, J. Interaction of Tin(II) and Arsenic(III) with DNA at the Nanostructure Film Modified Electrodes. *Bioelectrochemistry* **2007**, *71* (1), 33–37. <https://doi.org/10.1016/J.BIOELECTCHEM.2006.07.013>.
- (3) Solanki, P. R.; Prabhakar, N.; Pandey, M. K.; Malhotra, B. D. Surface Plasmon Resonance-Based DNA Biosensor for Arsenic Trioxide Detection. *Int. J. Environ. Anal. Chem.* **2009**, *89* (1), 49–57. <https://doi.org/10.1080/03067310802398872>.
- (4) Fuku, X.; Iftikar, F.; Hess, E.; Iwuoha, E.; Baker, P. Cytochrome c Biosensor for Determination of Trace Levels of Cyanide and Arsenic Compounds. *Anal. Chim. Acta* **2012**, *730*, 49–59. <https://doi.org/10.1016/J.ACA.2012.02.025>.
- (5) Hou, Q. H.; Ma, A. Z.; Lv, D.; Bai, Z. H.; Zhuang, X. L.; Zhuang, G. Q. The Impacts of Different Long-Term Fertilization Regimes on the Bioavailability of Arsenic in Soil: Integrating Chemical Approach with Escherichia Coli ArsRp::Luc-Based Biosensor. *Appl. Microbiol. Biotechnol.* **2014**, *98* (13), 6137–6146. <https://doi.org/10.1007/S00253-014-5656-0/FIGURES/7>.
- (6) De Mora, K.; Joshi, N.; Balint, B. L.; Ward, F. B.; Elfick, A.; French, C. E. A PH-Based Biosensor for Detection of Arsenic in Drinking Water. *Anal. Bioanal. Chem.* **2011**, *400* (4), 1031–1039. <https://doi.org/10.1007/S00216-011-4815-8/FIGURES/10>
- (7) Miller JN. Basic statistical methods for analytical chemistry. Part 2. calibration and regression methods. A review. *Analyst.* 1991;116(1):3-14. <https://doi:10.1039/AN9911600003>.

# Phosphine-Protected Atomically Precise Silver–Gold Alloy Nanoclusters and Their Luminescent Superstructures

Madhuri Jash, Arijit Jana, Ajay K. Poonia, Esma Khatun, Papri Chakraborty, Ankit Nagar, Tripti Ahuja, K. V. Adarsh,\* and Thalappil Pradeep\*



Cite This: <https://doi.org/10.1021/acs.chemmater.2c03222>



Read Online

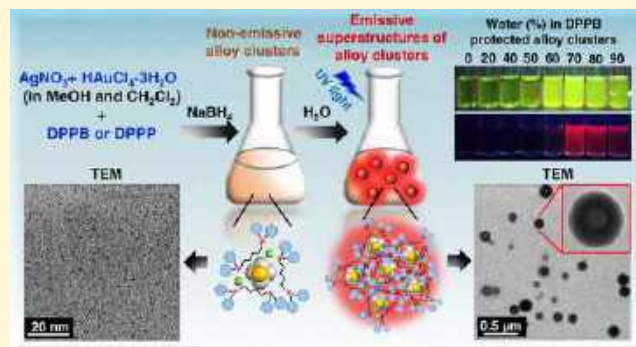
ACCESS |

Metrics & More

Article Recommendations

Supporting Information

**ABSTRACT:** Superstructures made by assemblies of metal nanoclusters (NCs) have gained interest due to their atomic precision and exciting photophysical properties. Although there are some reports of cluster-assembled materials of NCs protected with thiols, the preparation of stable thiol-free analogs is largely unexplored due to the poor stability of such structures. Herein, we report the synthesis of phosphine-protected alloy NCs of silver with varying gold doping and superstructures of such systems. We show that alloying of phosphine-protected silver clusters with gold results in comparatively more stable clusters than weakly ligated hydride- and phosphine-coprotected silver clusters. Two new Ag–Au alloy cluster series,  $[\text{Ag}_{11-x}\text{Au}_x(\text{DPPB})_5\text{Cl}_5\text{O}_2]^{2+}$ , where  $x = 1-10$  ( $\text{Ag}_{11-x}\text{Au}_x$  in short), and  $[\text{Ag}_{15-x}\text{Au}_x(\text{DPPP})_6\text{Cl}_5]^{2+}$ , where  $x = 1-6$  ( $\text{Ag}_{15-x}\text{Au}_x$  in short), have been synthesized using two different phosphines, 1,4-bis(diphenylphosphino)butane (DPPB) and 1,3-bis(diphenylphosphino)propane (DPPP), respectively. These alloy clusters possess aggregation-induced emission (AIE) property, which was unexplored till now for phosphine-protected silver clusters. A visibly nonluminescent methanol solution of these clusters showed strong red luminescence in the presence of water due to the formation of cluster-assembled spherical hollow superstructures without any template. A solvophobic effect along with  $\pi\cdots\pi$  and C–H $\cdots\pi$  interactions in the ligand shell make the alloy NCs assemble compactly within the hollow spheres. The assembly makes them highly emitting due to the restriction of intramolecular motion. The emissive states of the alloy clusters show a many-fold increase in lifetime in the presence of water. Femtosecond transient absorption studies revealed the lifetime of the excited-state charge carriers in their monomeric and aggregated states. Apart from enriching the limited family of phosphine-protected silver alloy NCs, this work also provides a new strategy to build a controlled assembly of NCs with tailored luminescence. These materials could be new phosphors for applications in composites, sensors, thin films, and photonic materials.



## INTRODUCTION

Metal nanoclusters (NCs) are molecular entities composed of a few to tens of metal atoms in their core. As their sizes decrease to the Fermi wavelength of electrons in the specific metal, discrete electronic states appear in them.<sup>1–3</sup> As a result, these ultrasmall NCs become sensitive to particle size, even to the extent of a single atom.<sup>4</sup> Metal NCs with atomic precision have been synthesized successfully by various research groups in the last two decades. They exhibit several unique properties, such as quantized charging,<sup>5</sup> magnetism,<sup>6</sup> luminescence,<sup>7</sup> chirality,<sup>8</sup> and so on, compared to their bulk counterparts. Among them, luminescence is the most remarkable property of such NCs due to applications in chemical sensing,<sup>9</sup> optoelectronics,<sup>10</sup> biosensing and bioimaging,<sup>11</sup> etc. Thus, the synthesis of highly luminescent NCs with good photostability, large Stokes shift, tunable emissive property, low toxicity, and biocompatibility is extremely important. However, poor stability and weak luminescence of NCs are limiting

factors for their practical applications. To overcome these issues, several synthetic strategies have been followed, and alloying of metal clusters is one of them.<sup>12,13</sup> Compositional tuning of NCs by doping with other metals offers a way to improve their luminescence property along with stability, and therefore, the topic has attracted intense research interest.<sup>14–16</sup>

The photophysical properties of luminescent NCs have been investigated mainly in solution, and there are several reports on this.<sup>17–19</sup> Their solid-state luminescence has also gained significant interest in the fields of light-emitting diodes (LEDs)<sup>20–22</sup> and sensors.<sup>23–25</sup> Aggregation-induced emission

Received: October 25, 2022

Revised: December 14, 2022

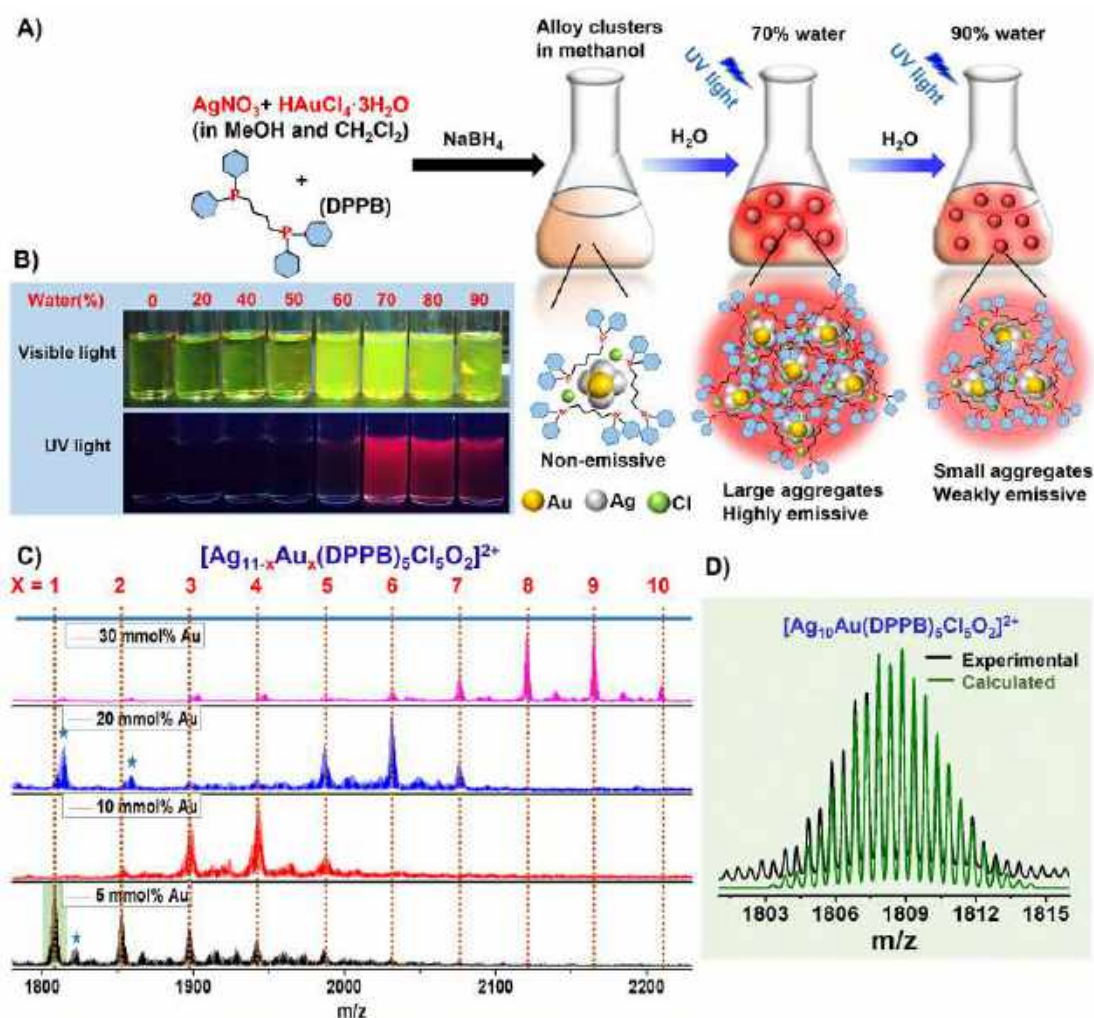


**Figure 1.** (A) Schematic illustration of the synthesis of the  $\text{Ag}_{11-x}\text{Au}_x$  clusters and the formation of luminescent spheres due to solvent-induced aggregation. (B) Corresponding photographs of the samples with different water fractions under visible light and UV light. (C) Positive-mode electrospray ionization mass spectrometry (ESI MS) of  $[\text{Ag}_{11-x}\text{Au}_x(\text{DPPB})_5\text{Cl}_5\text{O}_2]^{2+}$  ( $x = 1-10$ ), synthesized by varying the doped Au from 5 to 30 mmol %. The peaks labeled \* refer to fragmented species. (D) Comparison of the experimental and calculated isotopic distributions of the cluster  $[\text{Ag}_{11-x}\text{Au}_x(\text{DPPB})_5\text{Cl}_5\text{O}_2]^{2+}$ , when  $x = 1$ .

(AIE) has been a promising strategy for luminescence enhancement in the solid and solution states to fabricate novel photoluminescent materials.<sup>26-31</sup> AIE was discovered by Tang's group in 2001, and it mainly occurs due to the restriction of intramolecular motion, thus reducing the nonradiative relaxation pathways.<sup>32</sup> For metal NCs, in their aggregated state, due to the metallophilic interaction and/or suppressed molecular motion of ligands, radiative relaxation pathways are greatly enhanced, which result in luminescence enhancement with high quantum yield, large Stokes shift, higher emissive lifetime, and high chemical stability. Because of the AIE phenomenon, the construction of hierarchical self-assembly of NCs has been explored to achieve higher brightness compared to their elementary components. This self-assembly is an effective strategy to regulate the spatial distribution of NCs to form regular superstructures so that their luminescence property can be tuned. This approach involves the right balance of intercluster interactions, which are mainly attractive forces between the surface ligands or motifs of different NCs.<sup>33-36</sup>

As the properties<sup>2,3</sup> and reactivities<sup>37</sup> of metal NCs can be changed dramatically by changing the capping ligands, the nature of surface ligands also plays an important role in manipulating the attractive forces (metallophilic, electrostatic, dipole-dipole, hydrogen bonding, and hydrophobic interactions) to drive the formation of NC-assembled superstructures.<sup>33-36</sup> However, it has also been demonstrated that metal doping can reconstruct the metal-ligand motif and thus facilitate the radiative relaxation pathway of the excited electrons.<sup>38,39</sup> Furthermore, the emission energy of the cluster-assembled structures depends on the interatomic distance as well as the compactness of the superstructures.<sup>40</sup> The process of self-assembly can also be induced by external stimuli like metal ions, solvents, light, temperature, polymers, pH, etc.<sup>34</sup> These cluster-assembled superstructures provide innovative approaches in the field of LEDs, sensing, bioimaging, and theranostics.<sup>34</sup> They also have advantages over discrete NCs in terms of their sensitivity, photostability, and cellular retention. Therefore, creating self-assembly of different classes of metal NCs is necessary to better understand their structural details, associated luminescence enhancement,



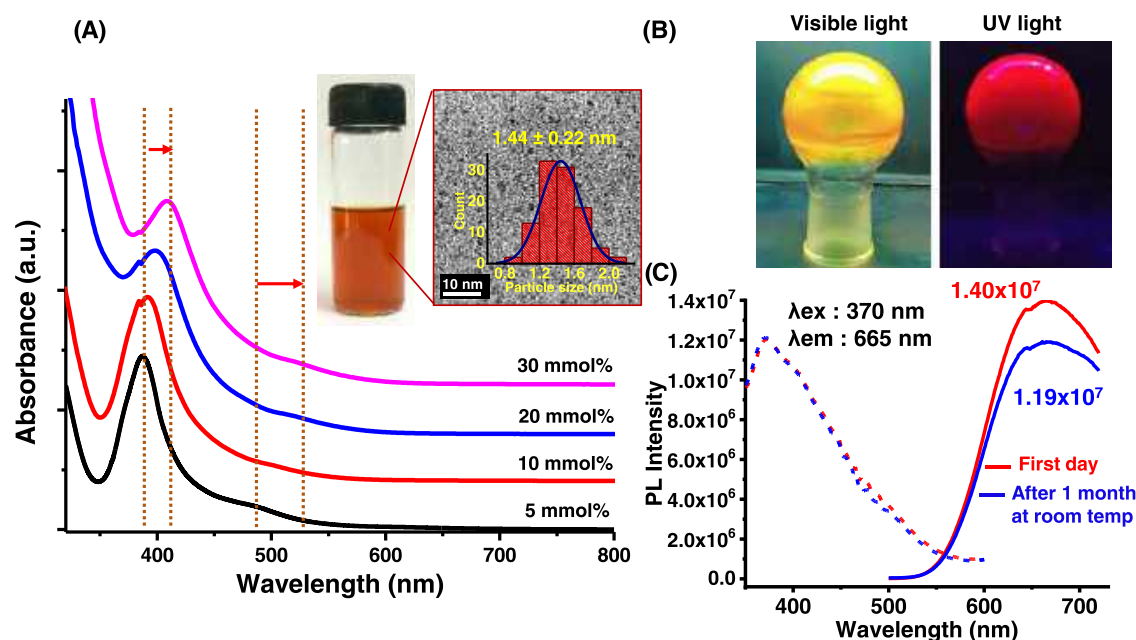


**Figure 2.** (A) UV–vis absorption spectra of the  $\text{Ag}_{11-x}\text{Au}_x$  clusters by varying the amount of doped gold from 5 to 30 mmol %. The shift in peak position is marked. The change in absorbance at 386 nm is due to a lamp change. Inset: photograph of cluster 1 in methanol (under visible light) with TEM micrograph and particle size distribution. (B) Photographs of the solid-state cluster 1 (vacuum dried) under visible light and UV light. (C) Excitation (dotted line) and emission spectra (solid line) of 1 in the solid state show room-temperature stability of the cluster.

and potential applications. However, there is limited diversity of ligands in making these self-assembled luminescent superstructures of metal clusters, and as of now, the most preferred choice for such structures is thiolate-protected NCs. Therefore, besides the fundamental interest in using different kinds of ligands in cluster-assembled materials, there is also interest in controlling the size, structure, density, and AIE properties of their assembled structures.

Herein, we have synthesized two new series of Ag–Au alloy NCs to explore the diversity and photophysical properties of phosphine-protected clusters in the absence of any thiolate ligand. During the synthesis, the concentration of incoming Au precursor was varied with two different phosphines, and the compositions of these two alloy cluster series were assigned as  $[\text{Ag}_{11-x}\text{Au}_x(\text{DPPB})_5\text{Cl}_5\text{O}_2]^{2+}$ , where  $x = 1–10$ , and  $[\text{Ag}_{15-x}\text{Au}_x(\text{DPPP})_6\text{Cl}_5]^{2+}$ , where  $x = 1–6$ , from their high-resolution electrospray ionization mass spectrometry (HRESI MS) data. These clusters are referred to as  $\text{Ag}_{11-x}\text{Au}_x$  and  $\text{Ag}_{15-x}\text{Au}_x$  respectively, in discussion. The most important finding here is the emergence of the AIE property of these phosphine-protected alloy clusters. We note that there are two reports of the AIE of phosphine-protected gold clusters but without any confined superstructures.<sup>41,42</sup> In this study, the silver-rich alloy clusters form luminescent hollow superstructures in their aggregated state, confirmed by dynamic light scattering (DLS), transmission electron microscopy (TEM), field emission scanning electron microscopy (FESEM), and hyperspectral imaging (HSI). Aggregates exhibit characteristic signatures in photoluminescence (PL) spectroscopy. The PL lifetimes of these cluster aggregates have also been determined using time-correlated single-photon counting (TCSPC) measurements. To further understand the excited-state relaxation dynamics of these alloy clusters, we have performed femtosecond transient absorption (fs-TA) spectroscopy for different forms (monomeric and aggregated) of the clusters. Thus, this work offers a strategy to build

spherical luminescent superstructures from atomically precise phosphine-protected alloy NCs along with an understanding of their structures and photophysical properties.

## RESULTS AND DISCUSSION

**Synthesis of Phosphine-Protected Alloy Clusters and their AIE Property.** We have synthesized phosphine- and chlorine-coprotected Ag–Au alloy NCs using a single-step coreduction method. So far, there is only one report of phosphine- and chlorine-protected heteroatom (Pt)-doped silver cluster using a single-step reaction.<sup>43</sup> Here, both the alloy NC series,  $\text{Ag}_{11-x}\text{Au}_x$  and  $\text{Ag}_{15-x}\text{Au}_x$  were synthesized by coreducing the mixture of silver and gold precursors in the presence of diphosphine ligands in  $\text{CH}_3\text{OH}$  and  $\text{CH}_2\text{Cl}_2$  as cosolvents. A detailed synthetic procedure is given in the [Experimental Section](#). During the synthesis of  $\text{Ag}_{11-x}\text{Au}_x$  after 8 h of reaction in the dark, the monomeric mixed alloy clusters were formed, and they were nonluminescent under UV light. An important finding of these phosphine-protected alloy NCs was that they generated strong luminescence in the solid state and in the presence of a poor solvent, namely, water, due to aggregation. In the absence of the gold precursor, the same reaction resulted in a hydride- and phosphine-protected  $[\text{Ag}_{27}\text{H}_{22}(\text{DPPB})_7]^{3+}$  cluster, which was nonluminescent both in the solution and in the aggregated state (in the aqueous phase). This comparatively less stable hydride and 1,4-bis(diphenylphosphino)butane (DPPB)-coprotected silver cluster was already reported by our group.<sup>44</sup> In this work, the luminescence intensity of the aggregated Ag–Au alloy clusters can be altered by changing the fraction of water ( $f_w = \text{vol } \% \text{ of water}$ ) in the methanol/water mixture due to the formation of differently sized aggregates. A schematic of the same is presented in [Figure 1A](#) for the  $\text{Ag}_{11-x}\text{Au}_x$  clusters. The corresponding photographs of the samples under visible and UV light are shown in [Figure 1B](#).

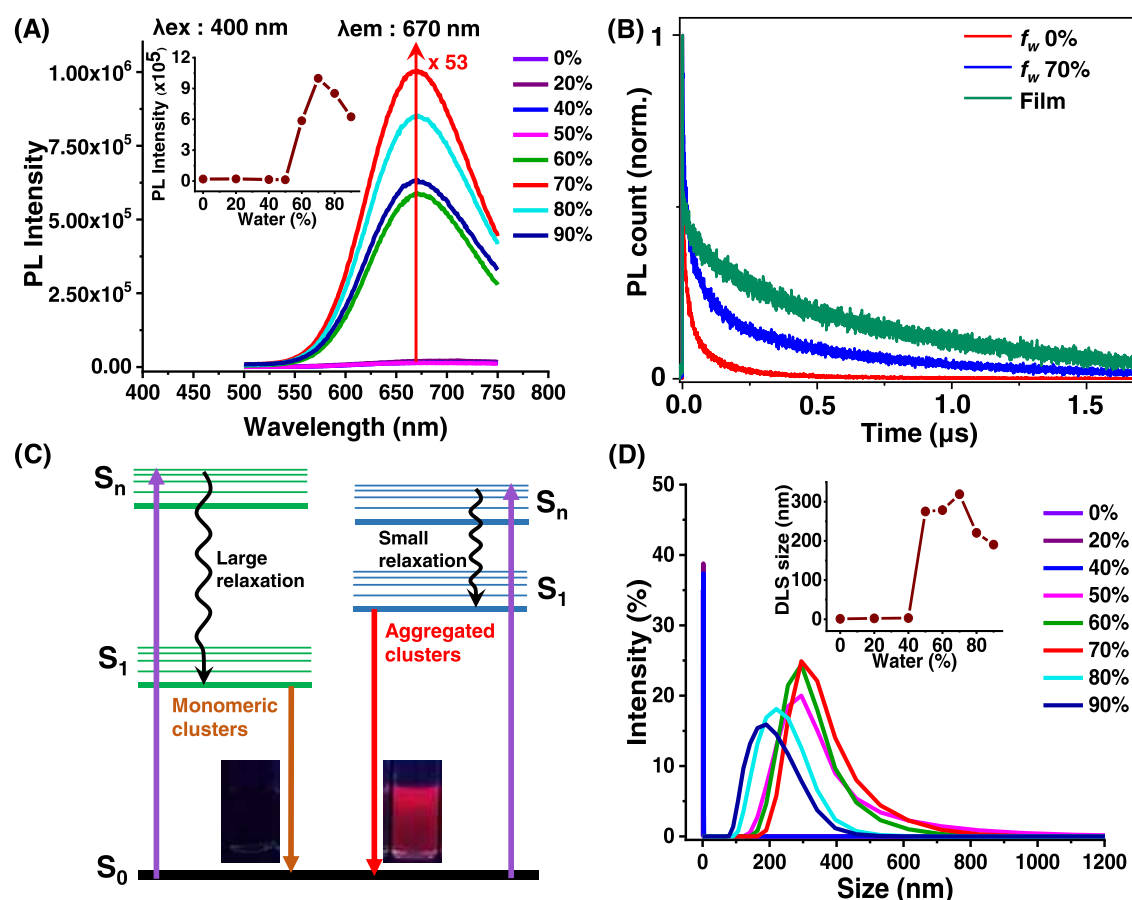


**Figure 3.** (A) PL emission spectra of **1** in methanol/water mixtures with different fractions of water. Inset: variation of luminescence intensity of the aggregates at different water fractions. (B) PL decay curves measured by TCSPC for  $f_w$  0%, 70%, and film of cluster **1**. (C) Schematic diagram showing the PL decay pathways of cluster **1** at different states. (D) DLS data of **1** in methanol/water mixtures with different fractions of water. Inset: variation of DLS size of the aggregates at different water fractions.

**Characterization of the  $\text{Ag}_{11-x}\text{Au}_x$  Clusters.** For characterization of the  $\text{Ag}_{11-x}\text{Au}_x$  clusters, the concentration of incoming Au precursor was varied from 5 to 30 mmol % to know the maximum doping position of Au in the alloy cluster core. Figure 1C represents the positive-mode HRESI MS data, where 5 mmol % Au doping exhibited a group of peaks in +2 charge state. Each of the peaks of this group was separated by  $m/z$  44.5, with a total mass difference of  $\Delta m = 44.5 \times 2 = 89$  ( $z = 2$ ). This mass difference signified a sequential replacement of Ag atoms in the parent cluster with Au atoms. Here, among the five peaks, the first sharp peak appeared at  $m/z$  1808.0, and the last peak appeared at a mass difference of  $\Delta m = 357$  ( $\Delta m/z = 178.5$ ,  $z = 2$ ), which indicates that 4 Ag atoms were replaced with Au atoms. The cluster composition was assigned as  $[\text{Ag}_{11-x}\text{Au}_x(\text{DPPB})_5\text{Cl}_5\text{O}_2]^{2+}$ , where  $x = 1-5$  for 5 mmol % Au. The origin of oxygen can be from the solvent or from the atmosphere. The mass spectrometric composition of the alloy clusters was further confirmed by the exact matching of the experimental spectrum with the calculated isotopic patterns of each of the species. Figure 1D represents the comparison between the experimental and calculated spectra of  $[\text{Ag}_{11-x}\text{Au}_x(\text{DPPB})_5\text{Cl}_5\text{O}_2]^{2+}$  when  $x = 1$ . By increasing the amount of doped Au from 5 to 30 mmol %, we were able to incorporate a maximum of 10 Au atoms in the alloy clusters, and the total composition was assigned as  $[\text{Ag}_{11-x}\text{Au}_x(\text{DPPB})_5\text{Cl}_5\text{O}_2]^{2+}$ , where  $x = 1-10$ .

Optical characterization of the  $\text{Ag}_{11-x}\text{Au}_x$  clusters was carried out by UV-vis and PL spectroscopy. The UV-vis spectra of 5–30 mmol % of Au doping are shown in Figure 2A. With increasing Au incorporation in the alloy cluster, the main absorption peak was red-shifted from 387 to 409 nm, and the shoulder peak was red-shifted from 485 to 520 nm, which is attributed to a reduction in the highest occupied molecular orbital–lowest unoccupied molecular orbital (HOMO–LUMO) gap.<sup>45,46</sup> During this Au incorporation, both the absorption peaks were broadened, while the shape of all of the spectra remained the same, indicating successful Au doping in the Ag NCs and similar geometrical structures for all of the alloy clusters. These nonluminescent alloy NCs were orange in color in methanol, and for 5 mmol % Au doping, the average size of the particles was found to be  $1.4 \pm 0.2$  nm in the TEM images (inset of Figure 2A). All of the  $\text{Ag}_{11-x}\text{Au}_x$  clusters with 5–30 mmol % Au doping showed AIE; for ease of measurement, alloy clusters with 5 mmol % gold doping were selected for further characterization and labeled as **1**. The methanol solution of **1** was nonemissive to the naked eye and very weakly emissive in the PL spectrum with a large Stokes shift, as shown in Figure S1. Interestingly, when the methanol solution was vacuum dried to get the cluster in the solid state, it showed strong red luminescence under UV light, as shown in Figure 2B. Excitation and emission spectra of **1** in the solid state have been recorded by drop-casting a methanol solution on a glass slide and making a film. The excitation wavelength

was 370 nm, and the emission wavelength was 665 nm, as shown in Figure 2C. This large Stokes shift (>250 nm) can minimize reabsorption losses during their application as solid-state emitters. To further investigate the stability of this solid-state alloy NCs, PL spectra of the same sample (film on a glass slide) were recorded after storing it in the dark and at room temperature for 1 month. After 1 month also, it emitted strong red luminescence at 665 nm, where the PL intensity was decreased from  $1.40 \times 10^7$  to  $1.19 \times 10^7$  (15%). UV-vis spectra of this sample were also recorded before and after 1 month, as shown in Figure S2.

For characterization of **1**,  $^{31}\text{P}$  nuclear magnetic resonance (NMR) spectroscopy was performed, and the data were compared with that of the ligand DPPB (Figure S3). The appearance of two new broad peaks at  $-1.21$  and  $-3.27$  ppm confirmed the formation of a bond between phosphine and the alloy metal core. More than one new peak also indicated the different ligand environments in **1**, and the disappearance of the peak at  $-16.15$  ppm confirmed the absence of any free phosphine ligand in the NCs. X-ray photoelectron spectroscopy (XPS) measurements were carried out to know the chemical state of Au and Ag in the alloy NCs. In Figure S4A, the XPS survey spectrum confirms the presence of elements C, O, P, Cl, Ag, and Au. The specific regions of Ag, Au, P, and Cl are deconvoluted in Figure S4B–E, respectively. The Ag  $3d_{5/2}$  peak appeared at 367.8 eV (i.e., oxidation side), which is slightly lower than the metallic Ag(0) value (368.0 eV), suggesting that the metal is between Ag(0) and Ag(I). The Au  $4f_{7/2}$  peak appeared at 85.4 eV, which is higher than the metallic Au(0) value (84.0 eV) and suggested that doped Au was present as Au(I).<sup>47</sup> The position of the Au  $4f_{7/2}$  peak indicates that the doping position of Au in the alloy cluster is not at the center; instead, it is at the outer shell of the cluster core, attached to the ligands. Transmission electron microscopy energy-dispersive X-ray spectroscopy (TEM EDS) analysis also confirmed the presence of Ag, Au, P, and Cl in **1** (Figure S5).

**Solvent-Induced Aggregation of the  $\text{Ag}_{11-x}\text{Au}_x$  Clusters.** For the solvent-induced aggregation, we have already observed that by adding different vol % of water to the methanol solution of the cluster, different luminescence intensities appear. To check their luminescence property, PL spectra were collected (for samples with different  $f_w$ ) upon excitation at 400 nm with a cluster concentration of 1 mg/mL (Figure 3A). The emission peak was blue-shifted from 695 to 670 nm when  $f_w$  was varied from 0 to 90%. During the addition of water, strong emission of the sample did not appear until  $f_w$  reached 60%, and an emission maximum appeared at 670 nm. The PL intensity reached its maximum value when  $f_w$  was 70% with 53-fold luminescence enhancement. This enhancement might be due to the  $\pi\cdots\pi$  and  $\text{C}-\text{H}\cdots\pi$  interactions of the phosphine ligands induced by the solvophobic effect, which restrict the intramolecular motion of the bulky phosphine ligands in the aggregated state.<sup>48,49</sup> Afterward, the luminescence intensity was gradually reduced from  $f_w$  70 to 90%, and the emission peak position appeared constant at 670 nm.<sup>50</sup> The inset of Figure 3A shows the variation of PL intensity at 670 nm with changing fractions of water. The UV-vis spectra for these solutions showed a small red shift for both the main peak and the shoulder peak after the formation of aggregates. Though there was a visible decrease in molar absorptivity due to the formation of aggregates, no change was observed in the absorption peak pattern (Figure

S6).<sup>51</sup> Notably, apart from the PL enhancement, aggregation of NCs also causes the manipulation of PL lifetime. To monitor it, we have measured the PL lifetime using TCSPC spectroscopy (instrumental details are given in the Supporting Information (SI)). The acquired PL decay curves of **1** in monomeric (in methanol or  $f_w$  0%), water-aggregated ( $f_w$  70%), and solid (film) states are shown in Figure 3B. It clearly shows the significant increase in the lifetime for aggregates in water and solid states of cluster **1** in comparison to the monomeric form. To determine the corresponding lifetime, TCSPC curves were fitted with the exponential function

$$y = y_0 + \sum_i^n A_i e^{-(t/\tau_i)}$$

and the average decay constants were calculated using

$$\tau_{\text{avg}} = \frac{\sum_i^n A_i \tau_i}{\sum A_i}$$

The average lifetime values of monomeric, water aggregates, and solid states were 26.8, 131.8, and 311.4 ns, respectively (see Table S1 for details).

To verify the nature of the excited state, the PL intensity of water aggregates of **1** was checked after oxygen exposure. The PL spectra were almost identical before and after oxygen-saturated conditions (Figure S7), which implies that this photophysical phenomenon is fluorescence in nature.<sup>52</sup> Here, the monomeric cluster **1** in methanol ( $f_w$  0%) exhibits emission maximum at 695 nm, whereas the water-aggregated ( $f_w$  70%) and solid-state film show almost the same blue-shifted peak position at 670 and 665 nm, respectively. Therefore, cluster **1** in methanol relaxes from a low-lying singlet state to  $S_0$  with 695 nm emission, and the nonradiative relaxation pathways become more dominant than the radiative pathways. At a higher water fraction ( $f_w$  70%) and in the solid state, there was the suppression of free rotation and vibration of the ligands in the cluster aggregates, which reduced the nonradiative relaxation pathways, and radiative decay occurred from a high-lying singlet state to  $S_0$  with an emission at 670 nm.<sup>53</sup> A schematic diagram of the PL decay pathway of cluster **1** at different states is shown in Figure 3C.

**Characterization of the Aggregated Structures of  $\text{Ag}_{11-x}\text{Au}_x$  Clusters.** To examine the sizes of these aggregates in the solvent mixtures, DLS experiments were performed, and the data are shown in Figure 3D. The DLS data indicated that for up to  $f_w$  40%, the particle sizes were in the range of 1–4 nm, which is in the size range of ligand-protected NCs in solution without any aggregation. For  $f_w$  50%, the aggregates started to form, and an average hydrodynamic diameter of ca. 280 nm was seen. Upon further increasing  $f_w$  to 60 and 70%, the average hydrodynamic diameters of the aggregates increased to ca. 290 and 315 nm, respectively, along with an increase in the PL intensity. The aggregates gradually decreased in size from  $f_w$  70 to 90% and gave a reduced diameter of ca. 180 nm, along with a reduced PL intensity. Hence, the difference in the luminescence intensity can be attributed to the different aggregation diameters of the clusters formed at different polarities of solvents.<sup>50</sup> The inset of Figure 3D shows the variation of DLS size of the particles with changing fractions of water.

To know more about the packing of clusters in these nanoscale aggregates, TEM images were collected for the solutions of different  $f_w$  values along with their average particle



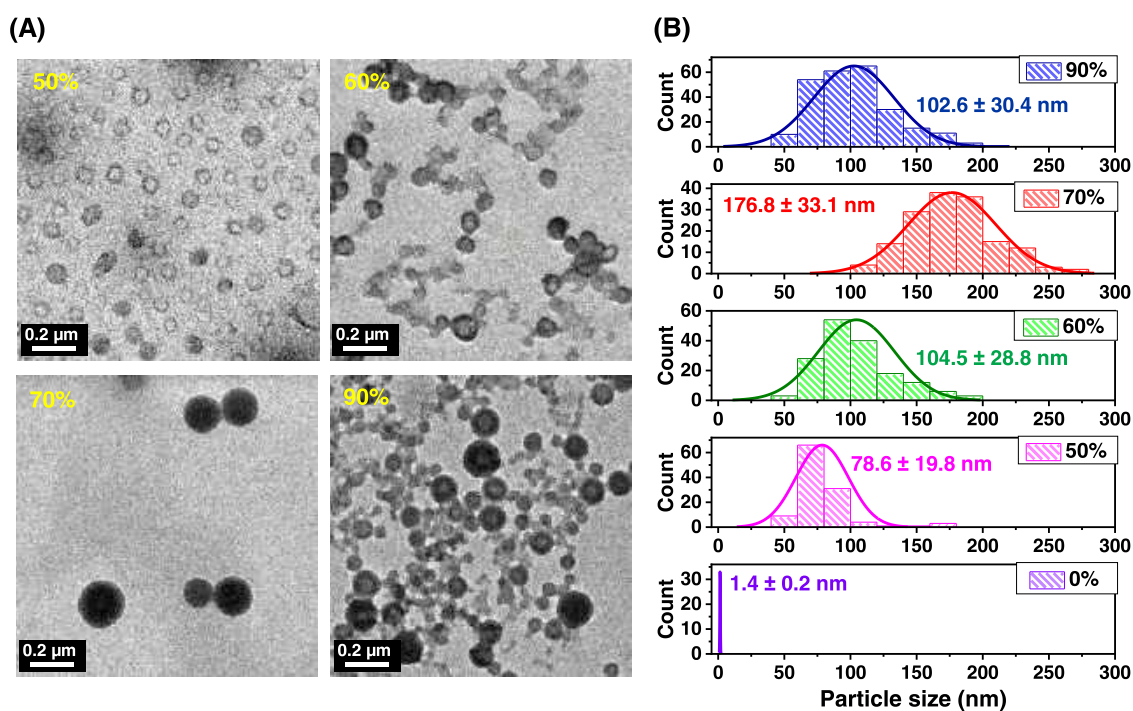


**Figure 4.** (A) TEM images of **1** during the formation of solvent-induced aggregates in the presence of 50, 60, 70, and 90% water. (B) Evolution of particle size distribution by increasing the water fraction in a methanol/water mixture.

sizes (Figure 4A,B). The spherical aggregates started to be observed when  $f_w$  reached 50%, and the clusters were loosely assembled in spheres of  $78.6 \pm 19.8$  nm diameter. At  $f_w$  60%, the average size of the aggregates increased to  $104.5 \pm 28.8$  nm, and at  $f_w$  70%, the average size became  $176.8 \pm 33.1$  nm. As observed from TEM images, upon increasing  $f_w$  from 50 to 70%, the sizes of aggregates become larger, denser, and solely spherical. For  $f_w$  90%, the average size of the spheres decreased to  $102.6 \pm 30.4$  nm and became less dense compared to the structures formed at  $f_w$  70%. Here, the larger and denser the aggregates, the higher the amount of restricted intra- and intermolecular motions and the brighter the luminescence would be. Thus, it was concluded that the ratio of methanol/water in the solution plays an important role in modulating the size of the aggregates, which leads to variation in their PL intensity.

At  $f_w$  70%, the sample exhibited the highest luminescence intensity due to the formation of bigger and denser spherical aggregates, and these structures were closely monitored with a transmission electron microscope and a field emission scanning electron microscope. In Figure 5A, we can see the formation of discrete spheres under TEM, which has been discussed before. Figure 5B represents a higher magnified view of a single sphere, whereas the inset of Figure 5A clearly shows that these spheres are actually made up of the assembly of small NCs. These spheres are hollow in nature, forming vesicle-like structures. They have visible peripheral and interior domains, and the former can be made by the assembly of NCs with varying packing densities. The inner layer of the periphery was denser compared to the outer layer, which sealed the hollow interior space. More TEM images of hollow spheres with different magnifications are shown in Figure S8A. However, the thickness of the peripheral bilayer can vary from one sphere to another, and they can be connected with each other through the outer layer of their periphery (Figure S8B). Figure

5C represents the TEM EDS of the aggregates, which shows the presence of all elements Ag, Au, P, and Cl along with their wt % and atom %. The morphology and size of these aggregates were also analyzed by FESEM after sputter coating the samples with Au–Pd. Figure 5D represents a large area view, whereas Figure 5E presents a magnified view of a single sphere. As SEM focuses on the surface, it shows only the spherical shape of the aggregates and does not show the interior hollow morphology as in TEM. The distribution of elements on a single sphere was examined using line scan profiles of the FESEM (Figure 5F). All of the elements (Ag, Au, P, Cl) were detected in the line scan, and the atomic ratio matches well with the atomic ratio of the alloy cluster except Au, which arises due to Au–Pd sputtering. During a line scan through the center of the sphere, the signals for all of the elements enhanced significantly across the sphere, as expected. The stability of these superstructures was checked after 1 week, and they were stable in the solution and solid states, as shown in Figure S9. The spatial distribution of these spheres was investigated by dark-field microscopy (Figure 5G), along with fluorescence microscopy (Figure 5H). A broadband white light was used as the source for hyperspectral imaging, where the light scattered by a single sphere was light green in color. Figure 5I presents the measured average scattering spectrum centered at 502 nm. The fluorescence micrograph showed that each sphere is red luminescent.

**Mechanism of the Formation of Superstructures.** The mechanism of the formation of such hollow spherical superstructures can be attributed to the presence of hydrophilic (Cl) and hydrophobic (diphosphine) ligands in the ligand shell of the alloy clusters. According to the directionality of these two types of ligands, there can be breaking of the spherical symmetry of the ligands, and thus, clusters can have some amphiphilic character.<sup>54,55</sup> The  $\pi \cdots \pi$  and C–H $\cdots$  $\pi$  interactions among the diphosphine ligands of alloy clusters

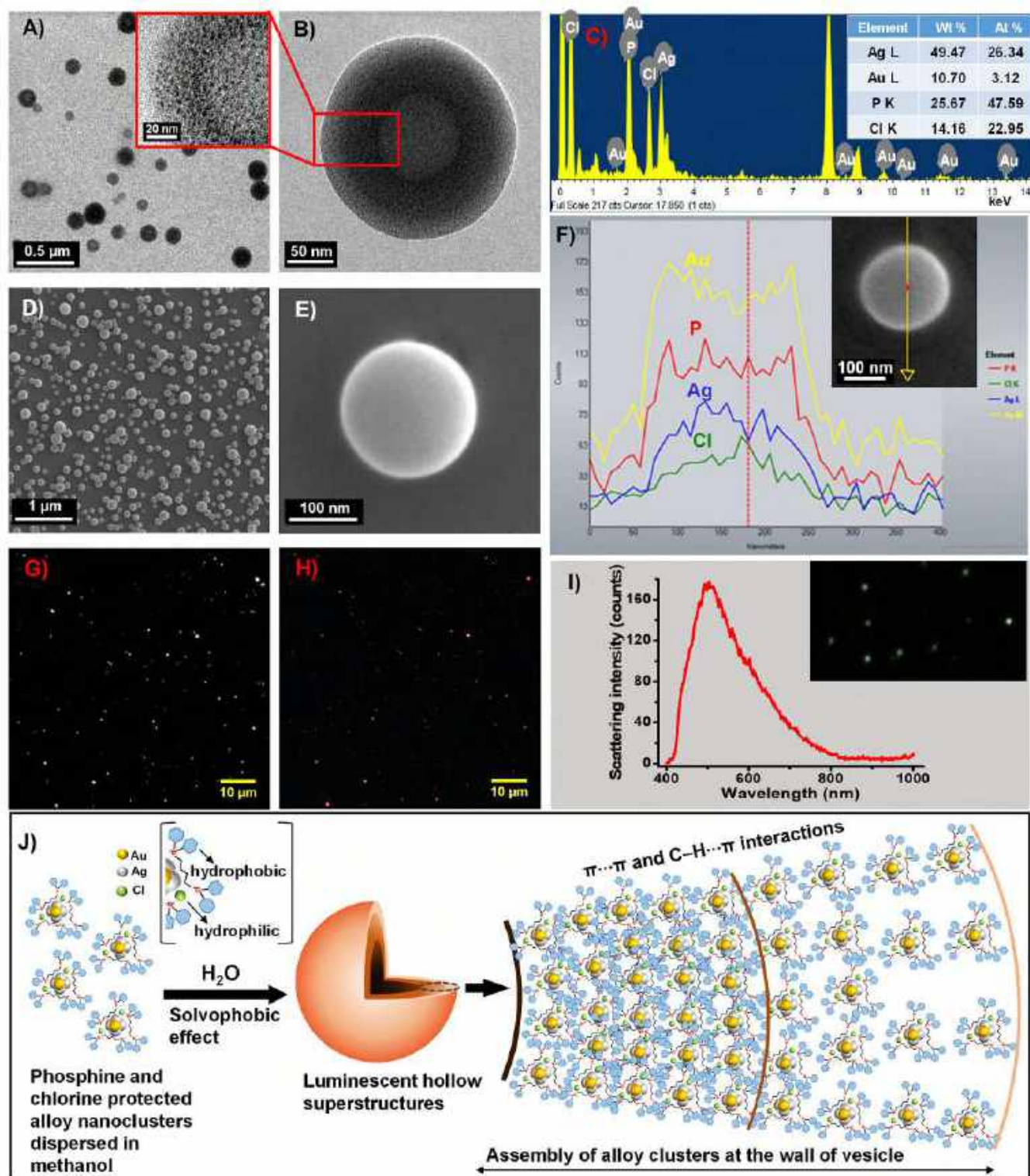


**Figure 5.** Microscopic characterization of the aggregates of **1** formed at  $f_w$  70%. (A, B) TEM images of the spheres with different magnifications. (C) TEM EDS spectrum and elemental composition of the aggregates. (D, E) FESEM images with different magnifications. (F) SEM EDS line scan is measured along a single sphere indicated by the arrow. (G) Dark-field and (H) fluorescence micrograph of the cluster aggregates, immobilized on an ultraclean glass slide. (I) Average scattering spectrum of the aggregates. (J) Schematic illustration of the possible assembly of clusters within the superstructures.

may contribute to the stabilization and growth of the cluster assembly.<sup>56</sup> Therefore, to achieve minimum surface energy, the assembly of amphiphilic NCs might tend to attain a spherical shape and make hollow vesicle structures.<sup>57,58</sup> Such an

assembly of clusters can be tuned by changing the solvent polarity. Based on the TEM result of superstructures, the NCs are located in the wall region of hollow vesicles. By increasing the water content, the wall becomes thicker, presumably to



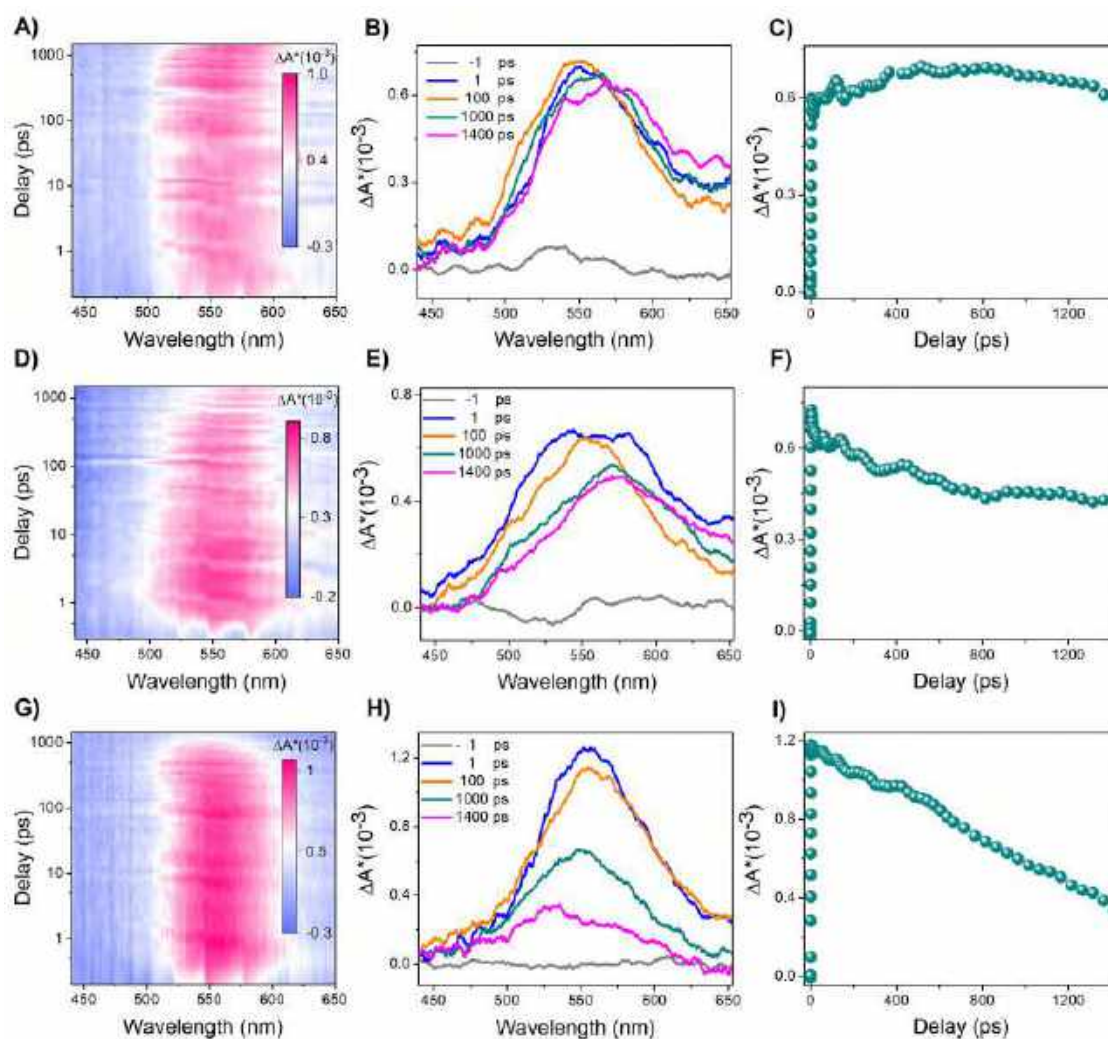


**Figure 6.** fs-TA pump–probe spectra of **1**. (A) Contour plot, (B) TA spectral profile as a function of time delay, and (C) transient kinetic trace at a selected wavelength of 552 nm for **1** in methanol. The same measurements have also been done for the aggregates formed at  $f_w$  70% (D–F) and in the solid state (G–I).

reduce the contact between NCs and highly polar solvent water, which has been seen for  $f_w$  50–70% in Figure 4A. For  $f_w$  90%, due to very high solvent polarity, the aggregate formation of **1** can be very fast, which can decrease the effective size of the spheres.<sup>51</sup> A schematic illustration of the possible assembly of clusters within the superstructures is presented in Figure S1J.

**TA Spectroscopy of the Monomeric and Aggregated Forms of  $\text{Ag}_{11-x}\text{Au}_x$  Clusters.** We have performed fs-TA spectroscopy to further understand the excited-state electronic transition of **1** in methanol and in aggregated states (with water and thin film). Our setup consists of pumping the carriers from HOMO to LUMO using an intense pump beam and then investigating the carrier's excited state and relaxation dynamics using a probe pulse. In the experiments, samples were first excited using a 120 fs pulse with a pump fluence of  $127 \mu\text{J}/\text{cm}^2$  centered at 400 nm. Then, a broadband pulse (440–655 nm), delayed with respect to the pump pulse, was used to probe the time evolution of carriers in the excited states. The instrumental setup and measurement details are given in the SI. Figure 6A–C summarizes the TA data of **1** in methanol. The contour plot of TA is in Figure 6A, and spectral profiles at selected time delays are plotted in Figure 6B, where the observed prominent feature is a band of photoinduced

absorption (PIA). Interestingly, no ground-state photobleaching (GSPB) (due to the Pauli blocking of electronic state by pump excited carriers) was observed corresponding to the UV–vis peak in the regime of 500 nm, which manifests the dominance of excited-state transitions in **1**, similar to the behavior observed in the protein-protected Ag–Au alloy clusters.<sup>59</sup> For a better insight into PIA, the time evolution of TA is shown in Figure 6C. It reveals the long lifetime of carriers in the excited state, which does not decay in the time window of our instrument.<sup>19</sup> Moreover, from the contour plot and spectral slices, it is also clear that the decay of excited states is accompanied by red-shifting of PIA with respect to the initial time scale, which indicates that PIA in different wavelength regimes consists of multiple components and arises from different states. Figure 6D–F shows the TA data of **1** in the water-aggregated state ( $f_w$  70%). Unlike the monomeric form upon photoexcitation, the aggregated cluster showed a broad PIA. Although the TA features are the same, the spectrum consists of relatively fast decay profiles (Figure 6F) and a more pronounced red shift of PIA. Similar spectral features with contrasting temporal behavior of both samples suggest the presence of the same type of electronic transition in the monomeric and aggregated forms but with different



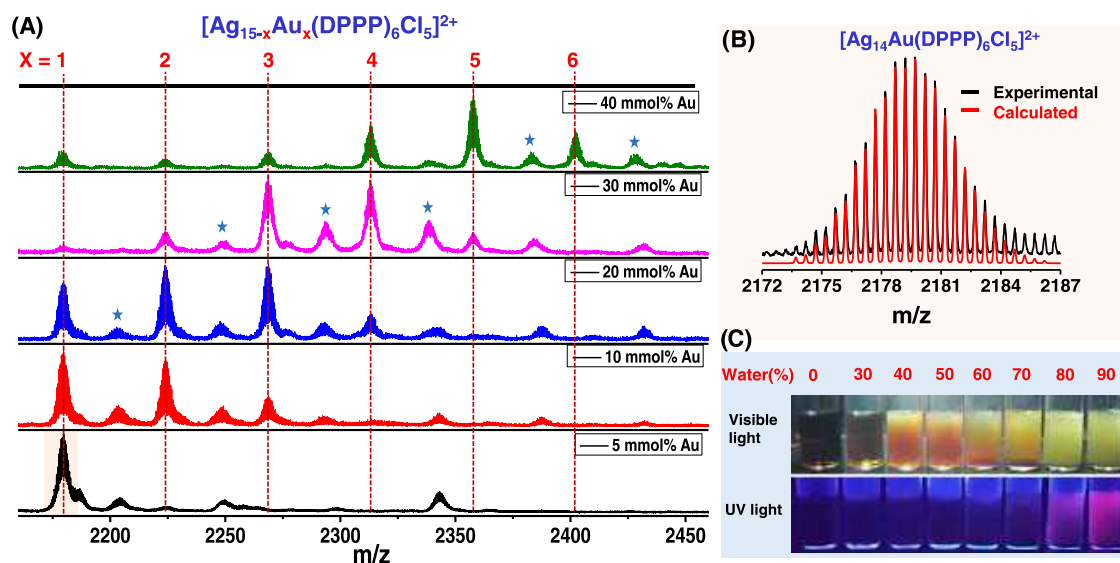


**Figure 7.** (A) Positive-mode ESI MS of  $[\text{Ag}_{15-x}\text{Au}_x(\text{DPPP})_6\text{Cl}_5]^{2+}$ , where  $x = 1-6$ , synthesized by varying the doped Au from 5 to 40 mmol %. The peaks labeled \* refer to solvent (water and methanol) added peaks of the clusters. (B) Comparison of the experimental and calculated isotopic distributions of the cluster  $[\text{Ag}_{15-x}\text{Au}_x(\text{DPPP})_6\text{Cl}_5]^{2+}$ , when  $x = 1$ . (C) Photographs of the samples in different fractions of water under visible light and UV light, showing the solvent-induced aggregation property of the cluster.

rates of transitions. This is further supported by the same type of UV-vis spectra in their monomeric and water-aggregated states as shown in Figure S6. In addition, the TA data of cluster 1 in the solid state (thin film) are shown in Figure 6G–I. It also has similar TA features but a relatively very short lifetime of PIA in contrast to monomeric and water-aggregated forms. In fact, instead of the red shift of PIA, a blue shift takes place at a delayed time. Here, it is interesting to see that in all forms of cluster 1, the excited-state carriers mainly exhibit the PIA, and the lifetime of PIA decreases in water and even more in the solid state compared to its monomeric form.

**Characterization of the  $\text{Ag}_{15-x}\text{Au}_x$  Clusters.** As we know, the size of the NCs is very much dependent on the ligand structure. Therefore, we have tried to synthesize the Ag–Au alloy NCs with different phosphines. We saw that among all of the phosphines studied (triphenylphosphine; bis(diphenylphosphino)methane; 1,2-bis(diphenylphosphino)ethane; 1,3-bis(diphenylphosphino)propane (DPPP); 1,4-bis(diphenylphosphino)butane (DPPB); 1,5-bis(diphenylphosphino)pentane, and 1,6-bis(diphenylphosphino)hexane), only DPPB and DPPP formed Ag–Au alloy clusters. Detailed synthetic procedure of  $\text{Ag}_{15-x}\text{Au}_x$  protected with DPPP is given in the Experimental Section. During the synthesis of  $\text{Ag}_{15-x}\text{Au}_x$ , the concentration of incoming Au precursor was varied from 5 to 40 mmol %. Figure 7A represents the positive-mode HRESI MS data of  $\text{Ag}_{15-x}\text{Au}_x$ , where 5 mmol % Au doping shows the presence of a single major peak. For 10 mmol % Au doping, there were a group of peaks separated by  $m/z$  44.5, and a total mass difference of  $\Delta m = 44.5 \times 2 = 89$  ( $z = 2$ ) appeared, corresponding to the mass difference between Au and Ag atoms. By increasing the doped Au concentration from 5 to 40 mmol %, a maximum of six Au atoms was possible to be incorporated, and the total composition was assigned as  $[\text{Ag}_{15-x}\text{Au}_x(\text{DPPP})_6\text{Cl}_5]^{2+}$ , where  $x = 1-6$ . The composition was also confirmed by the exact matching between the isotopic distributions of the experimental and calculated spectra as shown in Figure 7B. For this alloy cluster also, their methanol

solution was nonluminescent, and in the presence of water, it generated red luminescence. Corresponding photographs of the samples under visible and UV light are shown in Figure 7C, which show an increment in emission intensity from  $f_w$  0 to 90%.

The UV-vis spectra of  $\text{Ag}_{15-x}\text{Au}_x$  clusters are shown in Figure S10A. By increasing the fraction of Au, the peak positions were blue-shifted except for the peak at 495 nm. The blue shift was attributed to the increase in the HOMO–LUMO gap due to the modulation of their electronic structure during doping.<sup>16,19</sup> During alloying with different mmol % of Au,  $\text{Ag}_{11-x}\text{Au}_x$  showed a red shift, while  $\text{Ag}_{15-x}\text{Au}_x$  showed a blue shift in the absorption spectra, which is attributed to the unique nature of the electronic perturbation upon incorporating Au at different positions. The alloy NCs  $\text{Ag}_{15-x}\text{Au}_x$  were deep brown in color (inset of Figure S10A), and the solution was nonemissive to the naked eye and very weakly emissive in the PL spectrum (Figure S11). For ease of measurement, the alloy clusters with 5 mmol % gold doping labeled as 2 were selected for further characterization. Similar to 1, here also, we observed solid-state red luminescence after vacuum drying. Photographs of the solid-state cluster under visible and UV light are shown in Figure S10B. The PL spectrum showed an excitation peak at 395 nm and an emission peak at 660 nm, with a large Stokes shift. After 1 month, the PL intensity decreased from  $6.16 \times 10^6$  to  $5.07 \times 10^6$  (17%) (Figure S10C). UV-vis spectra of the same sample were also recorded before and after 1 month, which is shown in Figure S12.

In Figure S13,  $^{31}\text{P}$  NMR data of 2 were compared with that of the ligand DPPP, and it confirmed the formation of a bond between phosphine and the alloy metal core. In Figure S14A, the XPS survey spectrum confirms the presence of C, O, P, Cl, Ag, and Au. The specific regions of Ag, Au, P, and Cl were deconvoluted in Figure S14B–E, respectively. For this alloy cluster also, the Ag  $3d_{5/2}$  peak appeared slightly lower than that of Ag(0), and the Au  $4f_{7/2}$  peak appeared higher than that of Au(0). TEM EDS analysis also confirmed the presence of Ag, Au, P, and Cl in 2 (Figure S15).

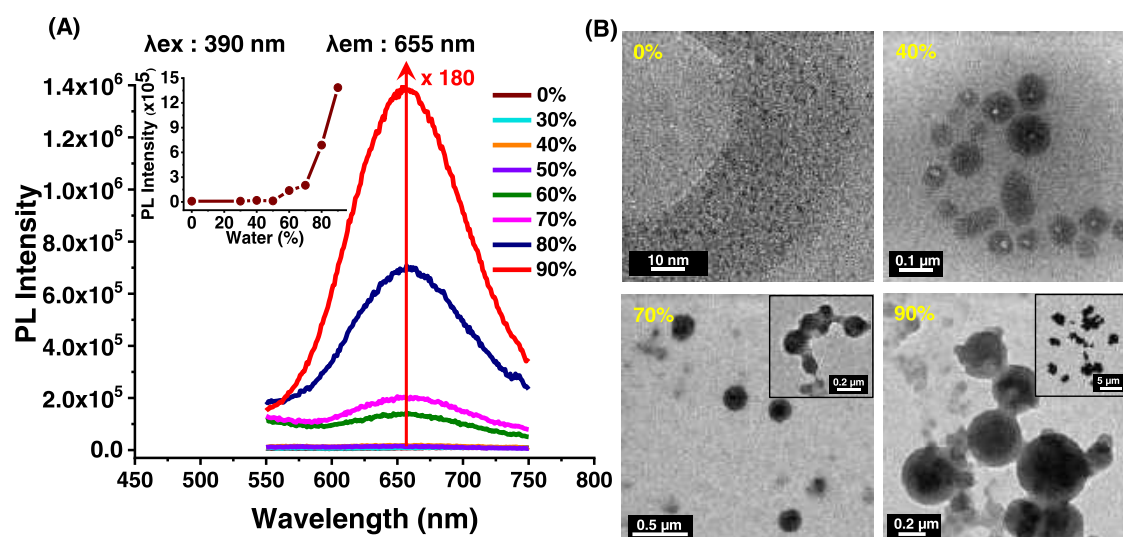


**Figure 8.** (A) PL emission spectra of **2** in methanol/water mixtures with different fractions of water. Inset: variation of luminescence intensity of the aggregates at different water fractions. (B) TEM images of **2** during the formation of solvent-induced aggregates in the presence of 0, 40, 70, and 90% water.

**Solvent-Induced Aggregation of the  $\text{Ag}_{15-x}\text{Au}_x$  Clusters.** Similar to **1**, sample **2** too exhibited aggregation-induced emission in the solid state and in the presence of a methanol/water mixture. The emission peak was blue-shifted from 710 to 655 nm when  $f_w$  was varied from 0 to 90%. At  $f_w$  60%, the emission peak centered at 655 nm started to appear, and it reached its maximum intensity at  $f_w$  90% (Figure 8A) with 180-fold luminescence enhancement.<sup>60</sup> The inset of Figure 8A shows the variation of the PL intensity at 655 nm with changing fractions of water. For these samples, the peak positions in the UV–vis spectra (Figure S16) showed a small red shift during aggregate formation. With the initial increase of  $f_w$  values, there was a hyperchromic shift of the spectrum due to the formation of aggregates and background scattering. Further increment of  $f_w$  values causes much bigger particles to form with a hypochromic shift and broadening of the spectrum.<sup>26</sup> Here also, no change was observed in the absorption peak pattern. The aggregation process of both clusters **1** and **2** was reversible. Further, PL lifetime measurements were also carried out on cluster **2** and in the aggregated form. Results for the three different forms are plotted in Figure S17. Average lifetimes of 53.9 and 153.9 ns were obtained for the monomeric and water-aggregated states, respectively. For the solid state, the PL decay is dominated ( $\approx 99\%$ ) by a fast decaying component, having a short lifetime compared to the IRF ( $\approx 400$  ps). The rest consists of two slow-decaying components having lifetimes of  $\approx 50$  and 500 ns. The lifetimes observed are given in Table S2. The PL spectra of water-aggregated states of **2** were almost identical before and after oxygen exposure (Figure S18), which implies that this is a fluorescence phenomenon. The blue shift in PL emission from monomeric to the aggregated state also suggests that similar to **1**, here also, radiative decay at  $f_w$  0% occurs from the low-lying singlet state to  $S_0$ , and for  $f_w$  70% and film, it occurs from the high-lying singlet state to  $S_0$ . The PL decay pathway is similar to that in Figure 3C.

**Characterization of the Aggregated Structures of  $\text{Ag}_{15-x}\text{Au}_x$  Clusters.** In Figure S19, the DLS data indicated that at  $f_w$  30%, the average hydrodynamic diameter of the particle was ca. 60 nm, while for  $f_w$  40–60%, they were 300–

400 nm, and for  $f_w$  70–90%, the sizes became microscopic. TEM images were also investigated for different  $f_w$ , as shown in Figure 8B. For  $f_w$  0%, there was the existence of only monomeric alloy NCs, and no aggregates were formed. The initial stage of formation of aggregates was noticed when  $f_w$  reached 40%, and the clusters were very loosely assembled in these 50–120 nm structures. At  $f_w$  70%, the average size of the aggregated spheres was increased to 100–200 nm, and at some places, these spheres were connected (shown in the inset). For  $f_w$  90%, the average sizes became 300 and 400 nm, and many of them were interconnected and precipitated by forming micrometer-sized aggregates (shown in the inset). This result is in accordance with the trend observed in the DLS data and PL spectra, where the larger and denser aggregates exhibited a higher luminescence intensity due to the large physical constraints of the ligands.

For an  $f_w$  value of 70%, the structures were closely studied with TEM and FESEM. Figure S20A represents some discrete spheres of aggregates under the transmission electron microscope. The high-magnification image in Figure S20B shows that these spheres are made by the assembly of small NCs, and they are hollow in nature. In contrast to **1**, here, the thickness of the peripheral domain was much higher compared to the interior domain, which can be due to the different ratios of hydrophilic and hydrophobic ligands present in these two NCs.<sup>54</sup> Figure S20C represents the TEM EDS of the aggregates. Figure S20D,E represents differently magnified FESEM images of a single sphere. The distribution of elements on a single sphere was examined by scanning the line profile in FESEM (Figure S20F), and all of the elements were successfully detected by it. The spatial distribution of these spheres was investigated by dark-field microscopy (Figure S20G) along with fluorescence microscopy (Figure S20H). As these particles have a tendency to connect with each other, the very bright spots observed in Figure S20G,H are likely to be due to the aggregation of multiple spheres. Figure S20I represents the measured average scattering spectrum centered at 510 nm.

**TA Spectroscopy of the Monomeric and Aggregated Forms of  $\text{Ag}_{15-x}\text{Au}_x$  Clusters.** To understand the nature of

electronic transitions of **2**, TA spectroscopy has been performed, and Figure S21A–C shows a summary of the TA data at a pump fluence of 127  $\mu\text{J}/\text{cm}^2$  in methanol. The TA spectral profiles plotted for selected time delays in Figure S21B reveal that the excited state features are dominated by the PIA. However, here, a weak GSPB signal is present, corresponding to the phase-space filling of the absorption peak in the region of 500 nm in the UV–vis spectrum. Possibly, in contrast to **1**, GSPB in **2** arises due to a sharper and more prominent absorption peak at 500 nm. Further, the time evolution of PIA in Figure S21C reveals a fast decay profile and indicates a short lifetime of excited-state carriers in the **2**. Figure S21D–F presents the TA data of **2** after adding water ( $f_w$  70%). It exhibits only PIA bands in the aggregated clusters, and no GSPB signal was observed. The time evolution of PIA in Figure S21F shows that the decay profile consists of an additional fast component at the early time compared to **2** in methanol and nearly the same time profile for the delayed time. The results of **2** in the solid state (thin film) are plotted in Figure S21G–I. It also shows nearly identical spectral and temporal features. From the obtained fs-TA results, it can be seen that compared to **1**, cluster **2** did not show much difference in the spectral and time evolution features in PIA among their monomeric, water-aggregated, and solid states. Possibly, the different behavior of clusters **1** and **2** is due to the different electronic structures corresponding to their different core compositions and ligands, which is also reflected in their different aggregation behavior at different water fractions.

**Stability of the  $\text{Ag}_{11-x}\text{Au}_x$  and  $\text{Ag}_{15-x}\text{Au}_x$  Clusters.** To check the stability of **1** and **2**, they were vacuum dried and stored at 4 °C. For the UV–vis characterization, the samples were dissolved in methanol, and the spectra were collected. The clusters exhibited the same absorption features, which reveals their higher stability, as shown in Figure S22.

## CONCLUSIONS

In conclusion, we have reported the synthesis of two new series of phosphine- and chlorine-protected Ag–Au alloy NCs [ $\text{Ag}_{11-x}\text{Au}_x(\text{DPPB})_5\text{Cl}_5\text{O}_2$ ] $^{2+}$ , where  $x = 1-10$ , and [ $\text{Ag}_{15-x}\text{Au}_x(\text{DPPP})_6\text{Cl}_5$ ] $^{2+}$ , where  $x = 1-6$ . The use of two different phosphines resulted in the formation of two different cluster cores, which are more stable compared to the reported hydride- and phosphine-coprotected silver clusters. Interestingly, these nonluminescent phosphine-protected Ag–Au alloy clusters show solid-state and solvent-induced red luminescence due to AIE. For solvent-induced aggregation, different PL intensities were observed at varying solvent polarity, which is due to the formation of differently dense superstructures. Such spherical discrete hollow superstructures are formed by the assembly of alloy NCs, revealed by different microscopic studies performed on them. The more the density or compactness of the aggregated superstructures, the more the rigidification on the cluster surfaces results in enhanced emission. The mechanism of rigidification-induced emission was attributed to the modification in the excited-state relaxation pathways in the aggregated state of clusters. The degree of assembly of clusters to differently dense superstructures depends on the cluster core, ligand composition, and polarity of the solvents. Along with the extent of aggregation, the different behavior of these two alloy clusters is also reflected in their fs-TA spectroscopy results. As these cluster-assembled superstructures exhibit strong red luminescence with large Stokes shift and higher stability, they have great

potential in numerous applications like photonic materials, bioimaging or bio-labeling, sensors, etc. These hollow superstructures also can be used to encapsulate other functional molecules or nanoparticles. Thus, this work provides a new path for creating luminescent functional materials with atomically precise NCs as the building blocks.

## EXPERIMENTAL SECTION

**Chemicals.** Silver nitrate ( $\text{AgNO}_3$ ) was purchased from Rankem India. Tetrachloroauric acid trihydrate ( $\text{HAuCl}_4 \cdot 3\text{H}_2\text{O}$ ) was prepared in our laboratory starting from elemental gold. 1,3-bis-(diphenylphosphino)propane (DPPP) and 1,4-bis-(diphenylphosphino)butane (DPPB) were purchased from Spectrochem. Sodium borohydride ( $\text{NaBH}_4$ , 98%) was purchased from Sigma-Aldrich. All solvents, such as dichloromethane (DCM) and methanol (MeOH), were purchased from Rankem and were of high-performance liquid chromatography (HPLC) grade. Deuterated solvent  $\text{CDCl}_3$  (99.8 atom % D) was purchased from Sigma-Aldrich for NMR measurements. All of the chemicals were used without further purification. Millipore water, obtained from Milli-Q (Millipore apparatus), was used for the experiments.

**Synthesis of  $[\text{Ag}_{11-x}\text{Au}_x(\text{DPPB})_5\text{Cl}_5\text{O}_2]^{2+}$ ,  $x = 1-10$ .** Synthesis of DPPB-protected alloy metal clusters has been done, followed by the coreduction method, where mmol % of incoming metal precursor is varied.  $\text{AgNO}_3$  and  $\text{HAuCl}_4 \cdot 3\text{H}_2\text{O}$  of different mmol % were dissolved in 5 mL of MeOH by keeping the total metal ion concentration at 0.118 mmol (Table 1).

**Table 1. Different mmol % of Ag and Au Precursors for  $[\text{Ag}_{11-x}\text{Au}_x(\text{DPPB})_5\text{Cl}_5\text{O}_2]^{2+}$  ( $x = 1-10$ ) Synthesis**

mmol	5% Au	10% Au	20% Au	30% Au
$\text{AgNO}_3$	0.112	0.106	0.094	0.082
$\text{HAuCl}_4 \cdot 3\text{H}_2\text{O}$	0.006	0.0118	0.0236	0.0354

To the mixture of Ag and Au precursors, 75 mg of DPPB, dissolved in 9 mL of DCM, was added with constant stirring. After 20 min of stirring, 35 mg of  $\text{NaBH}_4$  in 1 mL of ice-cold water was added. The addition of  $\text{NaBH}_4$  immediately changed the color of the reaction mixture from almost colorless to brown. After 8 h of vigorous stirring under dark conditions, the color of the solution turned orange, and it was kept aside at 4 °C for 1 day. Then, the crude product was obtained by rotary evaporation, and the cluster was extracted with 10 mL of MeOH. During extraction, the solution was centrifuged two times at 8000 rpm for 5 min to remove excess DPPB as a precipitate. After that, the methanol solution was vacuum dried, and the cluster was cleaned one more time with DCM. Finally, the dried alloy cluster was dissolved in methanol and used for further characterization.

**Synthesis of  $[\text{Ag}_{15-x}\text{Au}_x(\text{DPPP})_6\text{Cl}_5]^{2+}$ ,  $x = 1-6$ .** For the synthesis of the [ $\text{Ag}_{15-x}\text{Au}_x(\text{DPPP})_6\text{Cl}_5$ ] $^{2+}$  cluster, the above-mentioned procedure was followed only by exchanging DPPB with DPPP and keeping all other chemicals the same. Here, mmol % of  $\text{HAuCl}_4 \cdot 3\text{H}_2\text{O}$  was varied from 0 to 40% by keeping the total metal ion concentration at 0.118 mmol (Table 2).

After 8 h of continuous stirring in the dark, the reaction mixture became dark brown in color, and it was kept aside at 4 °C for 1 day. For cleaning this cluster, the above-mentioned procedure was followed. Finally, the dried alloy cluster was dissolved in methanol and used for further characterization.

**Table 2. Different mmol % of Ag and Au Precursors for  $[\text{Ag}_{15-x}\text{Au}_x(\text{DPPP})_6\text{Cl}_5]^{2+}$  ( $x = 1-6$ ) Synthesis**

mmol	5% Au	10% Au	20% Au	30% Au	40% Au
$\text{AgNO}_3$	0.112	0.106	0.094	0.082	0.071
$\text{HAuCl}_4 \cdot 3\text{H}_2\text{O}$	0.006	0.0118	0.0236	0.0354	0.0472



## ■ ASSOCIATED CONTENT

### SI Supporting Information

The Supporting Information is available free of charge at <https://pubs.acs.org/doi/10.1021/acs.chemmater.2c03222>.

These data correspond to the instrumentation and characterization of the clusters and aggregates by UV–vis, ESI MS, NMR, XPS, DLS, HSI, FESEM, TEM, TCSPC, and fs-TA spectroscopy (PDF)

## ■ AUTHOR INFORMATION

### Corresponding Authors

**K. V. Adarsh** – Department of Physics, Indian Institute of Science Education and Research Bhopal, Bhopal 462066, India; [orcid.org/0000-0002-6337-6545](https://orcid.org/0000-0002-6337-6545); Email: [adarsh@iiserb.ac.in](mailto:adarsh@iiserb.ac.in)

**Thalappil Pradeep** – DST Unit of Nanoscience (DST UNS) and Thematic Unit of Excellence (TUE), Department of Chemistry, Indian Institute of Technology Madras, Chennai 600036, India; International Centre for Clean Water, IIT Madras Research Park, Chennai 600113, India; [orcid.org/0000-0003-3174-534X](https://orcid.org/0000-0003-3174-534X); Email: [pradeep@iitm.ac.in](mailto:pradeep@iitm.ac.in)

### Authors

**Madhuri Jash** – DST Unit of Nanoscience (DST UNS) and Thematic Unit of Excellence (TUE), Department of Chemistry, Indian Institute of Technology Madras, Chennai 600036, India

**Arijit Jana** – DST Unit of Nanoscience (DST UNS) and Thematic Unit of Excellence (TUE), Department of Chemistry, Indian Institute of Technology Madras, Chennai 600036, India

**Ajay K. Poonia** – Department of Physics, Indian Institute of Science Education and Research Bhopal, Bhopal 462066, India; [orcid.org/0000-0002-5551-7299](https://orcid.org/0000-0002-5551-7299)

**Esma Khatun** – DST Unit of Nanoscience (DST UNS) and Thematic Unit of Excellence (TUE), Department of Chemistry, Indian Institute of Technology Madras, Chennai 600036, India

**Papri Chakraborty** – DST Unit of Nanoscience (DST UNS) and Thematic Unit of Excellence (TUE), Department of Chemistry, Indian Institute of Technology Madras, Chennai 600036, India; [orcid.org/0000-0002-1353-7734](https://orcid.org/0000-0002-1353-7734)

**Ankit Nagar** – DST Unit of Nanoscience (DST UNS) and Thematic Unit of Excellence (TUE), Department of Chemistry, Indian Institute of Technology Madras, Chennai 600036, India

**Tripti Ahuja** – DST Unit of Nanoscience (DST UNS) and Thematic Unit of Excellence (TUE), Department of Chemistry, Indian Institute of Technology Madras, Chennai 600036, India

Complete contact information is available at: <https://pubs.acs.org/doi/10.1021/acs.chemmater.2c03222>

### Notes

The authors declare no competing financial interest.

## ■ ACKNOWLEDGMENTS

The authors thank the Department of Science and Technology, Government of India for constantly supporting our research program. M.J. thanks UGC for her senior research fellowship. A.J., E.K., A.N., and T.A. thank IIT Madras for their

research fellowships. P.C. thanks IIT Madras for an Institute Postdoctoral Fellowship. K.V.A. and A.K.P. gratefully acknowledge the Science and Engineering Research Board for the grant CRG/2019/002808.

## ■ REFERENCES

- (1) Wilcoxon, J. P.; Abrams, B. L. Synthesis, Structure and Properties of Metal Nanoclusters. *Chem. Soc. Rev.* **2006**, *35*, 1162–1194.
- (2) Jin, R.; Zeng, C.; Zhou, M.; Chen, Y. Atomically Precise Colloidal Metal Nanoclusters and Nanoparticles: Fundamentals and Opportunities. *Chem. Rev.* **2016**, *116*, 10346–10413.
- (3) Chakraborty, I.; Pradeep, T. Atomically Precise Clusters of Noble Metals: Emerging Link between Atoms and Nanoparticles. *Chem. Rev.* **2017**, *117*, 8208–8271.
- (4) Niihori, Y.; Eguro, M.; Kato, A.; Sharma, S.; Kumar, B.; Kurashige, W.; Nobusada, K.; Negishi, Y. Improvements in the Ligand-Exchange Reactivity of Phenylethanethiolate-Protected Au<sub>25</sub> Nanocluster by Ag or Cu Incorporation. *J. Phys. Chem. C* **2016**, *120*, 14301–14309.
- (5) Chen, S.; Higaki, T.; Ma, H.; Zhu, M.; Jin, R.; Wang, G. Inhomogeneous Quantized Single-Electron Charging and Electrochemical–Optical Insights on Transition-Sized Atomically Precise Gold Nanoclusters. *ACS Nano* **2020**, *14*, 16781–16790.
- (6) Li, Y.; Biswas, S.; Luo, T.-Y.; Juarez-Mosqueda, R.; Taylor, M. G.; Mpourmpakis, G.; Rosi, N. L.; Hendrich, M. P.; Jin, R. Doping Effect on the Magnetism of Thiolate-Capped 25-Atom Alloy Nanoclusters. *Chem. Mater.* **2020**, *32*, 9238–9244.
- (7) Song, Y.; Li, Y.; Zhou, M.; Liu, X.; Li, H.; Wang, H.; Shen, Y.; Zhu, M.; Jin, R. Ultrabright Au@Cu<sub>14</sub> Nanoclusters: 71.3% Phosphorescence Quantum Yield in Non-degassed Solution at Room Temperature. *Sci. Adv.* **2021**, *7*, No. eabd2091.
- (8) Zeng, C.; Li, T.; Das, A.; Rosi, N. L.; Jin, R. Chiral Structure of Thiolate-Protected 28-Gold-Atom Nanocluster Determined by X-ray Crystallography. *J. Am. Chem. Soc.* **2013**, *135*, 10011–10013.
- (9) Yuan, X.; Luo, Z.; Yu, Y.; Yao, Q.; Xie, J. Luminescent Noble Metal Nanoclusters as an Emerging Optical Probe for Sensor Development. *Chem.—Asian J.* **2013**, *8*, 858–871.
- (10) Liu, Y.; Yao, D.; Zhang, H. Self-Assembly Driven Aggregation-Induced Emission of Copper Nanoclusters: A Novel Technology for Lighting. *ACS Appl. Mater. Interfaces* **2018**, *10*, 12071–12080.
- (11) Xiao, Y.; Wu, Z.; Yao, Q.; Xie, J. Luminescent Metal Nanoclusters: Biosensing Strategies and Bioimaging Applications. *Aggregate* **2021**, *2*, 114–132.
- (12) Khatun, E.; Pradeep, T. New Routes for Multicomponent Atomically Precise Metal Nanoclusters. *ACS Omega* **2021**, *6*, 1–16.
- (13) Kang, X.; Zhu, M. Tailoring the Photoluminescence of Atomically Precise Nanoclusters. *Chem. Soc. Rev.* **2019**, *48*, 2422–2457.
- (14) van der Linden, M.; van Bunningen, A. J.; Amidani, L.; Bransen, M.; Elnaggar, H.; Glatzel, P.; Meijerink, A.; de Groot, F. M. F. Single Au Atom Doping of Silver Nanoclusters. *ACS Nano* **2018**, *12*, 12751–12760.
- (15) Ganguly, M.; Jana, J.; Pal, A.; Pal, T. Synergism of Gold and Silver Invites Enhanced Fluorescence for Practical Applications. *RSC Adv.* **2016**, *6*, 17683–17703.
- (16) Bootharaju, M. S.; Joshi, C. P.; Parida, M. R.; Mohammed, O. F.; Bakr, O. M. Templated Atom-Precise Galvanic Synthesis and Structure Elucidation of a [Ag<sub>24</sub>Au(SR)<sub>18</sub>]<sup>−</sup> Nanocluster. *Angew. Chem., Int. Ed.* **2016**, *55*, 922–926.
- (17) Yu, Y.; Luo, Z.; Chevri er, D. M.; Leong, D. T.; Zhang, P.; Jiang, D.-E.; Xie, J. Identification of a Highly Luminescent Au<sub>22</sub>(SG)<sub>18</sub> Nanocluster. *J. Am. Chem. Soc.* **2014**, *136*, 1246–1249.
- (18) Wang, S.; Meng, X.; Das, A.; Li, T.; Song, Y.; Cao, T.; Zhu, X.; Zhu, M.; Jin, R. A 200-fold Quantum Yield Boost in the Photoluminescence of Silver-Doped Ag<sub>x</sub>Au<sub>25−x</sub> Nanoclusters: The 13 th Silver Atom Matters. *Angew. Chem., Int. Ed.* **2014**, *53*, 2376–2380.

- (19) Soldan, G.; Aljuhani, M. A.; Bootharaju, M. S.; Abdul-Halim, L. G.; Parida, M. R.; Emwas, A.-H.; Mohammed, O. F.; Bakr, O. M. Gold Doping of Silver Nanoclusters: A 26-Fold Enhancement in the Luminescence Quantum Yield. *Angew. Chem., Int. Ed.* **2016**, *55*, 5749–5753.
- (20) Niesen, B.; Rand, B. P. Thin Film Metal Nanocluster Light-Emitting Devices. *Adv. Mater.* **2014**, *26*, 1446–1449.
- (21) Koh, T. W.; Hiszpanski, A. M.; Sezen, M.; Naim, A.; Galfsky, T.; Trivedi, A.; Loo, Y. L.; Menon, V.; Rand, B. P. Metal Nanocluster Light-emitting Devices with Suppressed Parasitic Emission and Improved Efficiency: Exploring the Impact of Photophysical Properties. *Nanoscale* **2015**, *7*, 9140–9146.
- (22) Wang, Z.; Chen, B.; Zhu, M.; Kershaw, S. V.; Zhi, C.; Zhong, H.; Rogach, A. L. Stretchable and Thermally Stable Dual Emission Composite Films of On-Purpose Aggregated Copper Nanoclusters in Carboxylated Polyurethane for Remote White Light-Emitting Devices. *ACS Appl. Mater. Interfaces* **2016**, *8*, 33993–33998.
- (23) Huang, R.-W.; Wei, Y.-S.; Dong, X.-Y.; Wu, X.-H.; Du, C.-X.; Zang, S.-Q.; Mak, T. C. W. Hypersensitive Dual-function Luminescence Switching of a Silver-chalcogenolate Cluster-based Metal–organic Framework. *Nat. Chem.* **2017**, *9*, 689–697.
- (24) Wang, Y.-M.; Zhang, J.-W.; Wang, Q.-Y.; Li, H.-Y.; Dong, X.-Y.; Wang, S.; Zang, S.-Q. Fabrication of Silver Chalcogenolate Cluster Hybrid Membranes with Enhanced Structural Stability and Luminescence Efficiency. *Chem. Commun.* **2019**, *55*, 14677–14680.
- (25) Zhao, M.; Qian, Z.; Zhong, M.; Chen, Z.; Ao, H.; Feng, H. Fabrication of Stable and Luminescent Copper Nanocluster-Based AIE Particles and Their Application in  $\beta$ -Galactosidase Activity Assay. *ACS Appl. Mater. Interfaces* **2017**, *9*, 32887–32895.
- (26) Luo, Z.; Yuan, X.; Yu, Y.; Zhang, Q.; Leong, D. T.; Lee, J. Y.; Xie, J. From Aggregation-Induced Emission of Au(I)–Thiolate Complexes to Ultrabright Au(0)@Au(I)–Thiolate Core–Shell Nanoclusters. *J. Am. Chem. Soc.* **2012**, *134*, 16662–16670.
- (27) Goswami, N.; Yao, Q.; Luo, Z.; Li, J.; Chen, T.; Xie, J. Luminescent Metal Nanoclusters with Aggregation-Induced Emission. *J. Phys. Chem. Lett.* **2016**, *7*, 962–975.
- (28) Chang, H.; Karan, N. S.; Shin, K.; Bootharaju, M. S.; Nah, S.; Chae, S. I.; Baek, W.; Lee, S.; Kim, J.; Son, Y. J.; Kang, T.; Ko, G.; Kwon, S.-H.; Hyeon, T. Highly Fluorescent Gold Cluster Assembly. *J. Am. Chem. Soc.* **2021**, *143*, 326–334.
- (29) Li, Q.; Zhou, M.; So, W. Y.; Huang, J.; Li, M.; Kauffman, D. R.; Cotlet, M.; Higaki, T.; Peteanu, L. A.; Shao, Z.; Jin, R. A Monocuboctahedral Series of Gold Nanoclusters: Photoluminescence Origin, Large Enhancement, Wide Tunability, and Structure–Property Correlation. *J. Am. Chem. Soc.* **2019**, *141*, 5314–5325.
- (30) Wang, Z.; Xiong, Y.; Kershaw, S. V.; Chen, B.; Yang, X.; Goswami, N.; Lai, W.-F.; Xie, J.; Rogach, A. L. In Situ Fabrication of Flexible, Thermally Stable, Large-Area, Strongly Luminescent Copper Nanocluster/Polymer Composite Films. *Chem. Mater.* **2017**, *29*, 10206–10211.
- (31) Xie, Z.; Sun, P.; Wang, Z.; Li, H.; Yu, L.; Sun, D.; Chen, M.; Bi, Y.; Xin, X.; Hao, J. Metal–Organic Gels from Silver Nanoclusters with Aggregation-Induced Emission and Fluorescence-to-Phosphorescence Switching. *Angew. Chem., Int. Ed.* **2020**, *59*, 9922–9927.
- (32) Luo, J.; Xie, Z.; Lam, J. W. Y.; Cheng, L.; Chen, H.; Qiu, C.; Kwok, H. S.; Zhan, X.; Liu, Y.; Zhu, D.; Tang, B. Z. Aggregation-induced Emission of 1-methyl-1,2,3,4,5-pentaphenylsilole. *Chem. Commun.* **2001**, 1740–1741.
- (33) Kolay, S.; Bain, D.; Maity, S.; Devi, A.; Patra, A.; Antoine, R. Self-Assembled Metal Nanoclusters: Driving Forces and Structural Correlation with Optical Properties. *Nanomaterials* **2022**, *12*, No. 544.
- (34) Rival, J. V.; Mymoon, P.; Lakshmi, K. M.; Nonappa; Pradeep, T.; Shibu, E. S. Self-Assembly of Precision Noble Metal Nanoclusters: Hierarchical Structural Complexity, Colloidal Superstructures, and Applications. *Small* **2021**, *17*, No. 2005718.
- (35) Bera, D.; Goswami, N. Driving Forces and Routes for Aggregation-Induced Emission-Based Highly Luminescent Metal Nanocluster Assembly. *J. Phys. Chem. Lett.* **2021**, *12*, 9033–9046.
- (36) Wu, Z.; Yao, Q.; Zang, S.; Xie, J. Directed Self-Assembly of Ultrasmall Metal Nanoclusters. *ACS Mater. Lett.* **2019**, *1*, 237–248.
- (37) Krishnadas, K. R.; Natarajan, G.; Bakshi, A.; Ghosh, A.; Khatun, E.; Pradeep, T. Metal–Ligand Interface in the Chemical Reactions of Ligand-Protected Noble Metal Clusters. *Langmuir* **2019**, *35*, 11243–11254.
- (38) Wu, Z.; Du, Y.; Liu, J.; Yao, Q.; Chen, T.; Cao, Y.; Zhang, H.; Xie, J. Auophilic Interactions in the Self-Assembly of Gold Nanoclusters into Nanoribbons with Enhanced Luminescence. *Angew. Chem., Int. Ed.* **2019**, *58*, 8139–8144.
- (39) Chakraborty, S.; Bain, D.; Maity, S.; Kolay, S.; Patra, A. Controlling Aggregation-Induced Emission in Bimetallic Gold–Copper Nanoclusters via Surface Motif Engineering. *J. Phys. Chem. C* **2022**, *126*, 2896–2904.
- (40) Wu, Z.; Liu, J.; Gao, Y.; Liu, H.; Li, T.; Zou, H.; Wang, Z.; Zhang, K.; Wang, Y.; Zhang, H.; Yang, B. Assembly-Induced Enhancement of Cu Nanoclusters Luminescence with Mechanochromic Property. *J. Am. Chem. Soc.* **2015**, *137*, 12906–12913.
- (41) Sugiuchi, M.; Maeba, J.; Okubo, N.; Iwamura, M.; Nozaki, K.; Konishi, K. Aggregation-Induced Fluorescence-to-Phosphorescence Switching of Molecular Gold Clusters. *J. Am. Chem. Soc.* **2017**, *139*, 17731–17734.
- (42) Sugiuchi, M.; Zhang, M.; Hakoishi, Y.; Shichibu, Y.; Horimoto, N. N.; Yamauchi, Y.; Ishida, Y.; Konishi, K. Aggregation-Mode-Dependent Optical Properties of Cationic Gold Clusters: Formation of Ordered Assemblies in Solution and Unique Optical Responses. *J. Phys. Chem. C* **2020**, *124*, 16209–16215.
- (43) Bootharaju, M. S.; Kozlov, S. M.; Cao, Z.; Harb, M.; Maity, N.; Shkurenko, A.; Parida, M. R.; Hedhili, M. N.; Eddooudi, M.; Mohammed, O. F.; Bakr, O. M.; Cavallo, L.; Basset, J.-M. Doping-Induced Anisotropic Self-Assembly of Silver Icosahedra in  $[\text{Pt}_2\text{Ag}_{23}\text{Cl}_7(\text{PPh}_3)_{10}]$  Nanoclusters. *J. Am. Chem. Soc.* **2017**, *139*, 1053–1056.
- (44) Jash, M.; Khatun, E.; Chakraborty, P.; Sudhakar, C.; Pradeep, T.  $[\text{Ag}_{15}\text{H}_{13}(\text{DPPH})_5]^{2+}$  and  $[\text{Ag}_{27}\text{H}_{22}(\text{DPPB})_7]^{3+}$ : Two New Hydride and Phosphine Co-Protected Clusters and Their Fragmentation Leading to Naked Clusters,  $\text{Ag}_{13}^+$  and  $\text{Ag}_{25}^+$ . *J. Phys. Chem. C* **2020**, *124*, 20569–20577.
- (45) Mishra, D.; Lobodin, V.; Zhang, C.; Aldeek, F.; Lochner, E.; Mattoussi, H. Gold-doped Silver Nanoclusters with Enhanced Photophysical Properties. *Phys. Chem. Chem. Phys.* **2018**, *20*, 12992–13007.
- (46) Negishi, Y.; Iwai, T.; Ide, M. Continuous Modulation of Electronic Structure of Stable Thiolate-protected  $\text{Au}_{25}$  Cluster by Ag Doping. *Chem. Commun.* **2010**, *46*, 4713–4715.
- (47) Negishi, Y.; Nobusada, K.; Tsukuda, T. Glutathione-Protected Gold Clusters Revisited: Bridging the Gap between Gold(I)–Thiolate Complexes and Thiolate-Protected Gold Nanocrystals. *J. Am. Chem. Soc.* **2005**, *127*, 5261–5270.
- (48) Ihm, H.; Ahn, J.-S.; Lah, M. S.; Ko, Y. H.; Paek, K. Oligobisvelcralex: Self-Assembled Linear Oligomer by Solvophobic  $\pi$ – $\pi$  Stacking Interaction of Bisvelcralex Based on Resorcin[4]arene. *Org. Lett.* **2004**, *6*, 3893–3896.
- (49) Kang, X.; Wang, S.; Zhu, M. Observation of a New Type of Aggregation-induced Emission in Nanoclusters. *Chem. Sci.* **2018**, *9*, 3062–3068.
- (50) Sun, P.-P.; Han, B.-L.; Li, H.-G.; Zhang, C.-K.; Xin, X.; Dou, J.-M.; Gao, Z.-Y.; Sun, D. Real-Time Fluorescent Monitoring of Kinetically Controlled Supramolecular Self-Assembly of Atom-Precise  $\text{Cu}_8$  Nanocluster. *Angew. Chem., Int. Ed.* **2022**, *61*, No. e202200180.
- (51) Das, P.; Kumar, A.; Chowdhury, A.; Mukherjee, P. S. Aggregation-Induced Emission and White Luminescence from a Combination of  $\pi$ -Conjugated Donor–Acceptor Organic Luminescence. *ACS Omega* **2018**, *3*, 13757–13771.
- (52) Zhu, C.; Xin, J.; Li, J.; Li, H.; Kang, X.; Pei, Y.; Zhu, M. Fluorescence or Phosphorescence? The Metallic Composition of the Nanocluster Kernel Does Matter. *Angew. Chem., Int. Ed.* **2022**, *61*, No. e202205947.

(53) Deng, H.-H.; Shi, X.-Q.; Wang, F.-F.; Peng, H.-P.; Liu, A.-L.; Xia, X.-H.; Chen, W. Fabrication of Water-Soluble, Green-Emitting Gold Nanoclusters with a 65% Photoluminescence Quantum Yield via Host–Guest Recognition. *Chem. Mater.* **2017**, *29*, 1362–1369.

(54) Park, J.-e.; Seo, M.; Jang, E.; Kim, H.; Kim, J. S.; Park, S.-J. Vesicle-like Assemblies of Ligand-stabilized Nanoparticles with Controllable Membrane Composition and Properties. *Nanoscale* **2019**, *11*, 1837–1846.

(55) Nonappa; Lahtinen, T.; Haataja, J. S.; Tero, T.-R.; Häkkinen, H.; Ikkala, O. Template-Free Supracolloidal Self-Assembly of Atomically Precise Gold Nanoclusters: From 2D Colloidal Crystals to Spherical Capsids. *Angew. Chem., Int. Ed.* **2016**, *55*, 16035–16038.

(56) Hou, Y.; Wang, Y.; Xu, T.; Wang, Z.; Tian, W.; Sun, D.; Yu, X.; Xing, P.; Shen, J.; Xin, X.; Hao, J. Synergistic Multiple Bonds Induced Dynamic Self-Assembly of Silver Nanoclusters into Lamellar Frameworks with Tailored Luminescence. *Chem. Mater.* **2022**, *34*, 8013–8021.

(57) Jülicher, F.; Lipowsky, R. Domain-induced Budding of Vesicles. *Phys. Rev. Lett.* **1993**, *70*, 2964–2967.

(58) Zhou, Y.; Zeng, H. C. Simultaneous Synthesis and Assembly of Noble Metal Nanoclusters with Variable Micellar Templates. *J. Am. Chem. Soc.* **2014**, *136*, 13805–13817.

(59) Bhunia, S.; Kumar, S.; Purkayastha, P. Dependence of Ultrafast Dynamics in Gold–silver Alloy Nanoclusters on the Proportion of the Metal Content. *SN Appl. Sci.* **2019**, *1*, No. 449.

(60) Jin, S.; Liu, W.; Hu, D.; Zou, X.; Kang, X.; Du, W.; Chen, S.; Wei, S.; Wang, S.; Zhu, M. Aggregation-Induced Emission (AIE) in Ag–Au Bimetallic Nanocluster. *Chem.—Eur. J.* **2018**, *24*, 3712–3715.



## Supporting Information

# Phosphine-Protected Atomically Precise Silver-Gold Alloy Nanoclusters and Their Luminescent Superstructures

Madhuri Jash,<sup>†</sup> Arijit Jana,<sup>†</sup> Ajay K. Poonia,<sup>‡</sup> Esma Khatun,<sup>†</sup> Papri Chakraborty,<sup>†</sup> Ankit Nagar,<sup>†</sup> Tripti Ahuja,<sup>†</sup> K. V. Adarsh<sup>\*‡</sup> and Thalappil Pradeep<sup>\*†§</sup>

<sup>†</sup>DST Unit of Nanoscience (DST UNS) and Thematic Unit of Excellence (TUE), Department of Chemistry, Indian Institute of Technology Madras, Chennai 600036, India

<sup>‡</sup>Department of Physics, Indian Institute of Science Education and Research Bhopal, Bhopal 462066, India

<sup>§</sup>International Centre for Clean Water, IIT Madras Research Park, Chennai 600113, India

\*E-mail: pradeep@iitm.ac.in, adarsh@iiserb.ac.in

## Table of Contents

Name	Description	Page No.
	Instrumentation	3-5
Figure S1	PL spectra of <b>1</b> in methanol	6
Figure S2	Stability of <b>1</b> in solid state	7
Figure S3	<sup>31</sup> P NMR spectra of DPPB and <b>1</b>	8
Figure S4	XPS spectra of <b>1</b>	9
Figure S5	TEM EDS of <b>1</b>	10
Figure S6	UV-vis spectra of <b>1</b> in the aggregated state	11
Figure S7	PL spectra of aggregates of <b>1</b> after oxygen exposure	13
Figure S8	TEM images of the hollow spheres	14
Figure S9	Stability of superstructures	15
Figure S10	Optical properties of <b>2</b>	16
Figure S11	PL spectra of <b>2</b> in methanol	17
Figure S12	Stability of <b>2</b> in the solid state	18
Figure S13	<sup>31</sup> P NMR spectra of DPPP and <b>2</b>	19
Figure S14	XPS spectra of <b>2</b>	20

Figure S15	TEM EDS of <b>2</b>	21
Figure S16	UV-vis spectra of <b>2</b> in the aggregated state	22
Figure S17	Lifetime measurements of <b>2</b> and its aggregates	23
Figure S18	PL spectra of aggregates of <b>2</b> after oxygen exposure	24
Figure S19	DLS measurements of aggregates of <b>2</b>	25
Figure S20	Microscopic characterization of aggregates of <b>2</b>	26
Figure S21	TA pump-probe spectra of <b>2</b> in different states	27
Figure S22	Stability of Ag-Au alloy clusters at 4 °C	28

## **Instrumentation**

### **UV-vis absorption spectroscopy**

Perkin Elmer Lambda 25 UV-vis spectrometer was used to record the UV-vis spectra of nanoclusters. Absorption spectra were typically measured in the range of 200-1100 nm with a bandpass filter of 1 nm.

### **Photoluminescence (PL) spectroscopy**

Photoluminescence measurement was carried out in a HORIBA, Jobin Yvon NanoLog fluorescence spectrometer with a bandpass of 3 nm for both emission and excitation spectra.

### **Dynamic light scattering (DLS)**

DLS measurement was done using a Malvern Zetasizer ZSP instrument equipped with a 633 nm (He-Ne) laser.

### **Electrospray Ionization Mass Spectrometry (ESI MS)**

The electrospray ionization mass spectra were measured in Waters Synapt G2Si High Definition Mass Spectrometer. This mass spectrometer consists of an electrospray source, quadrupole ion guide/trap, ion mobility cell, and TOF analyzer. Nitrogen gas was used as the nebulizer gas, and all the mass spectra were collected in positive ion mode. Mass spectrometric measurements were done by using the following conditions:

Flow rate: 30  $\mu$ L/min, Capillary voltage: 3 kV, Cone voltage: 20 V, Source offset: 20 V, Source temperature: 100  $^{\circ}$ C, Desolvation temp: 150  $^{\circ}$ C, Desolvation gas flow: 400 L/h, Trap gas flow: 5 L/h.

### **Nuclear magnetic resonance (NMR) spectroscopy**

Nuclear magnetic resonance spectroscopy measurements were carried out at room temperature by using a Bruker 500 MHz NMR spectrometer. Pure ligands (DPPB and DPPP) and the alloy nanoclusters were dissolved in  $\text{CDCl}_3$  to collect  $^{31}\text{P}$  NMR spectra.

### **X-ray photoelectron spectroscopy (XPS)**

X-ray photoelectron spectroscopy (XPS) of alloy nanoclusters was performed by using an ESCA Probe TPD spectrometer of Omicron Nanotechnology. Monochromatic  $\text{Al K}\alpha$  (1486.69 eV) X-ray source was used. Samples were drop-casted on a sample stub, and measurements were carried out with constant analyzer energy of 50 eV for the survey scans and 20 eV for the specific regions. The binding energies in the spectra were calibrated with respect to the C 1s peak at 284.8 eV.

### **Field emission scanning electron microscopy (FESEM)**

Scanning electron microscopy and energy dispersive X-ray spectroscopy analysis were performed with a Verios G4 UC, FEI instrument. Samples were prepared by drop-casting the

materials on a substrate (TEM grid was used for the good quality of pictures with good contrast) and drying them at room temperature. The sample was sputter coated with Au/Pd mixture to produce better-quality images without charging.

### **Transmission electron microscopy (TEM) and energy dispersive X-ray spectroscopy (EDS)**

Transmission electron microscopy was performed using a JEOL 3010, 300 kV instrument at an accelerating voltage of 200 kV. The accelerating voltage was kept low to reduce beam-induced damage. Samples were prepared by drop casting the solution on a carbon-coated copper grid and dried under ambient conditions. EDS spectra were acquired using the attached Oxford Semistem system.

### **Hyperspectral microscopy (HSI)**

Dark-field imaging of the cluster was performed using an Olympus BX-51 microscope and 100 W quartz halogen light source on a hyperspectral microscope, CytoViva Inc. A broadband white light was used for the optical imaging via a dark field condenser. A 100x oil immersion objective was used for collecting the scattered/emitted light from the nanocluster spheres. To prepare the sample, 2  $\mu$ l of aggregates solution was drop-casted on a 1 mm thick ultrasonically cleaned glass slide and covered with a coverslip. Then it was sealed with nail polish on the sides to avoid drying of samples. In the overall procedure, care was taken such that only one side of the slide was exposed to chemicals. Imaging was done by a true-color charge-coupled device (CCD). A mercury lamp and appropriate filters (excitation and emission) were used for fluorescence images. Hyperspectral image analysis software was used for spectral analysis.

### **TCSPC measurements**

To study the time-resolved PL lifetime of clusters and their aggregated states, we employed the HORIBA DeltaFlex time-correlated single photon count (TCSPC) spectrometer. The measurements were performed using the HORIBA DeltaDiode 405 nm laser. The obtained emission was collected using the HORIBA PPD-850 detector. The instrument response of the present setup is shown below.

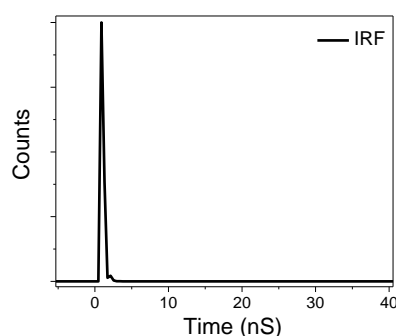
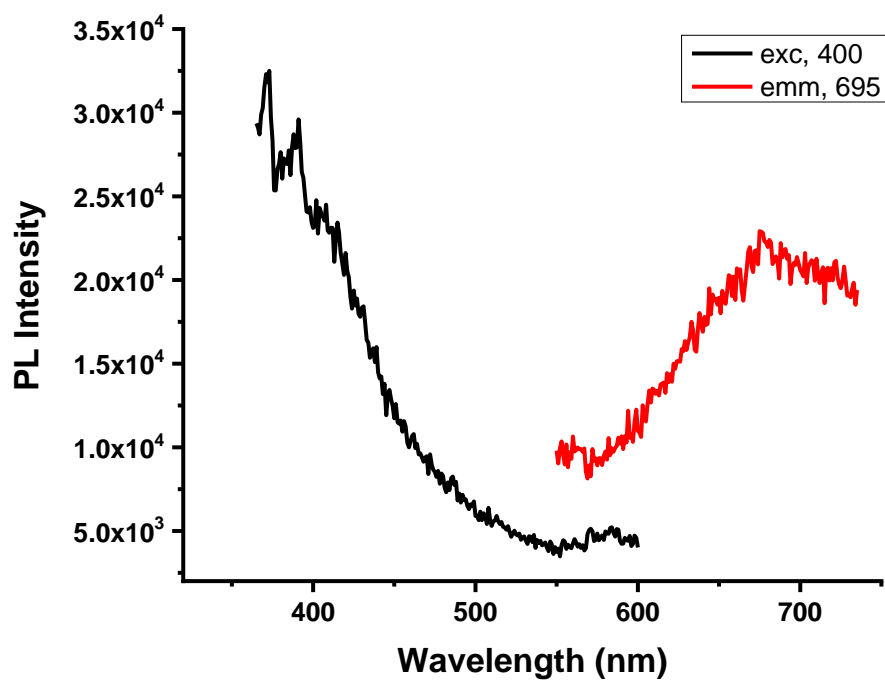


Figure. IRF of the TCSPC spectrometer.

### **Femtosecond pump-probe measurements**

In our study, the excited state dynamics of samples are analyzed using ultrafast transient absorption spectroscopy. The setup consists of Spectra-Physics MaiTai oscillator, Spitfire Ti:sapphire optical amplifier to generate the 120 fs pulses centered at 800 nm. The output beams are passed through a second harmonic  $\beta$ -barium borate crystal to generate the 400 nm pulses, which are used to excite the samples (pump beam). The second harmonic pulses are separated from the fundamental beam with the help of a dichroic beam splitter. Then both 400 and residual 800 nm are sent to CDP ExciPro pump-probe spectrometer. Here the pump beam passes through a chopper, and a rotating neutral density filter controls the averaging and intensity of pulses. The 800 nm pulses are sent to a computer-controlled motion controller and a rotating CaF<sub>2</sub> crystal to produce time delayed white light continuum probe beam. Both pump and probe beam spatially overlapped on the sample, and then a change in absorbance of the probe beam was detected with the help of MS 2004 (600 lines/mm diffraction grating blazed at 600 nm) spectrometer and Si linear photodiode arrays. Then obtained data is chirp corrected to compensate for the group velocity dispersion.

**PL spectra of 1 in methanol:**



**Figure S1.** Excitation (black trace) and emission spectra (red trace) of **1** in methanol with large Stokes shift. The emission spectrum represents the very weakly emissive nature of the cluster, which is not visible to the naked eye.



**Stability of 1 in the solid state:**

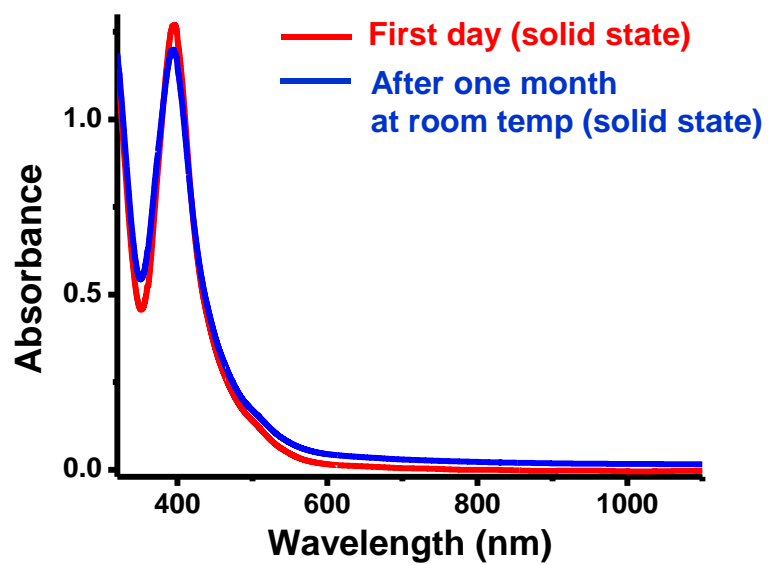
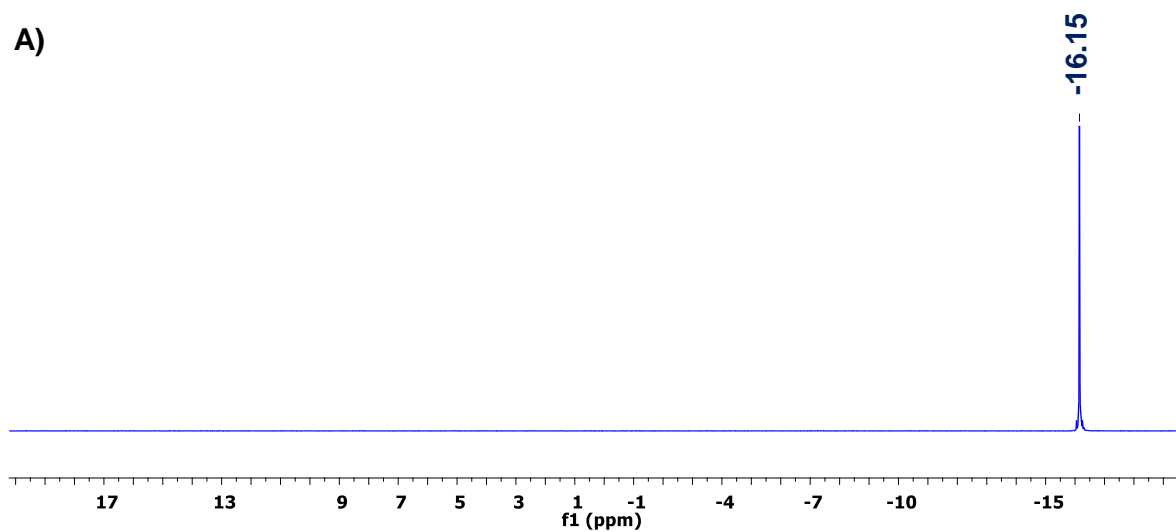


**Figure S2.** UV-vis spectrum of **1** in the solid state (red traces). The spectrum was also recorded after one month (blue trace) by storing the cluster film at room temperature and in the dark.

### $^{31}\text{P}$ NMR spectra of DPPB and **1**:

A)



B)

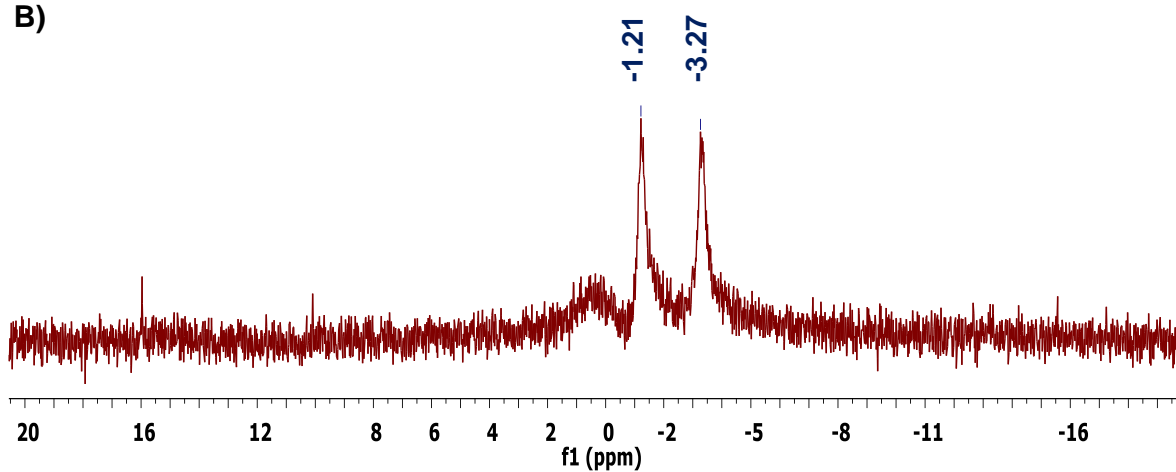


**Figure S3.**  $^{31}\text{P}$  NMR spectra of (A) DPPB and (B) cluster **1**. The  $^{31}\text{P}$  signal at -16.15 ppm for DPPB ligand disappears in **1** cluster due to the binding of ligands with the metal core, confirmed by the appearance of two new broad peaks at -3.27 and -1.21 ppm in the nanocluster.

## XPS spectra of 1:

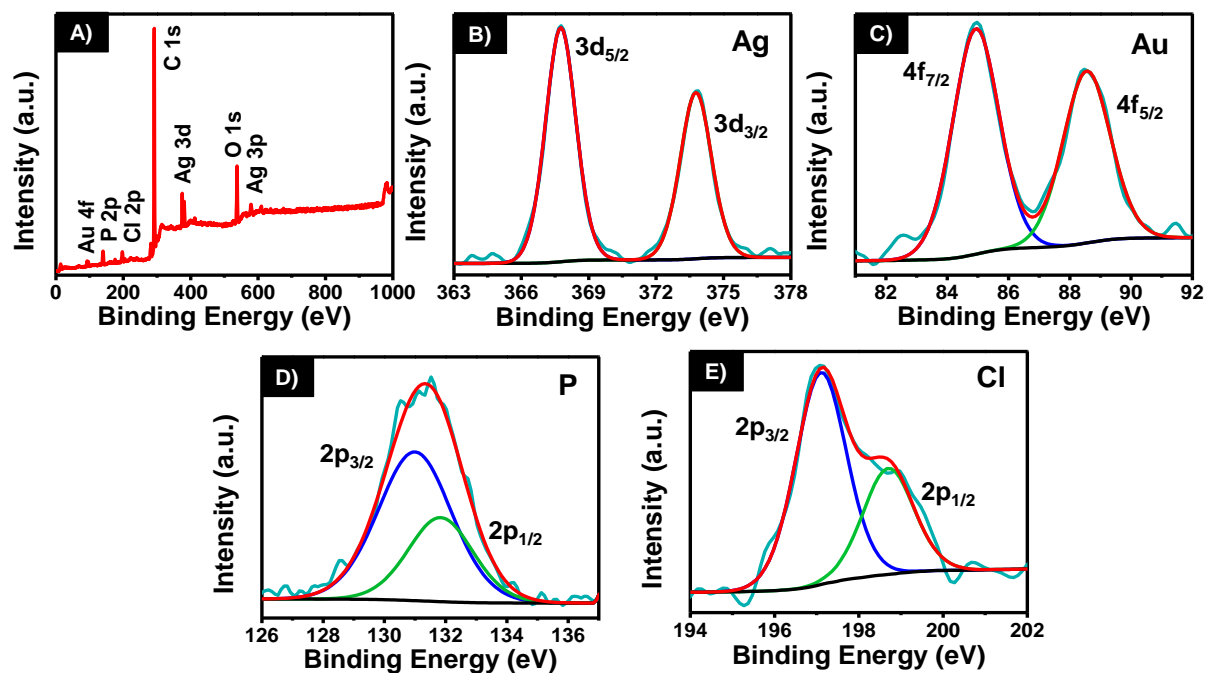


**Figure S4.** (A) XPS survey spectrum of **1** shows all the expected elements. (B) The Ag 3d region. Ag  $3d_{5/2}$  appeared at 367.8 eV. (C) The Au 4f region. Au  $4f_{7/2}$  appeared at 85.4 eV. (D) The P 2p region. P  $2p_{3/2}$  appears at 131.8 eV. (E) The Cl 2p region. Cl  $2p_{3/2}$  appears at 197.9 eV. P and Cl positions confirm their binding with the nanocluster.

### TEM EDS of 1:

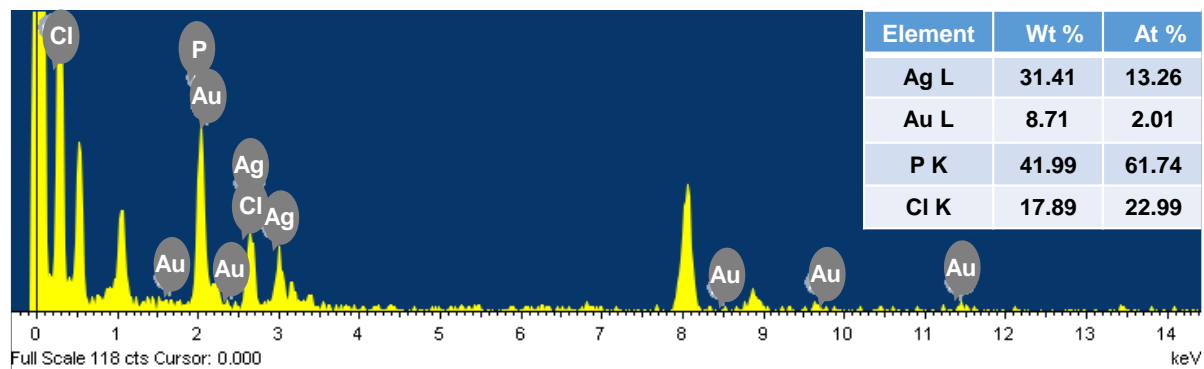


**Figure S5.** TEM EDS of 1 with quantification of the respective elements.

**UV-vis spectra of 1 in the aggregated state:**

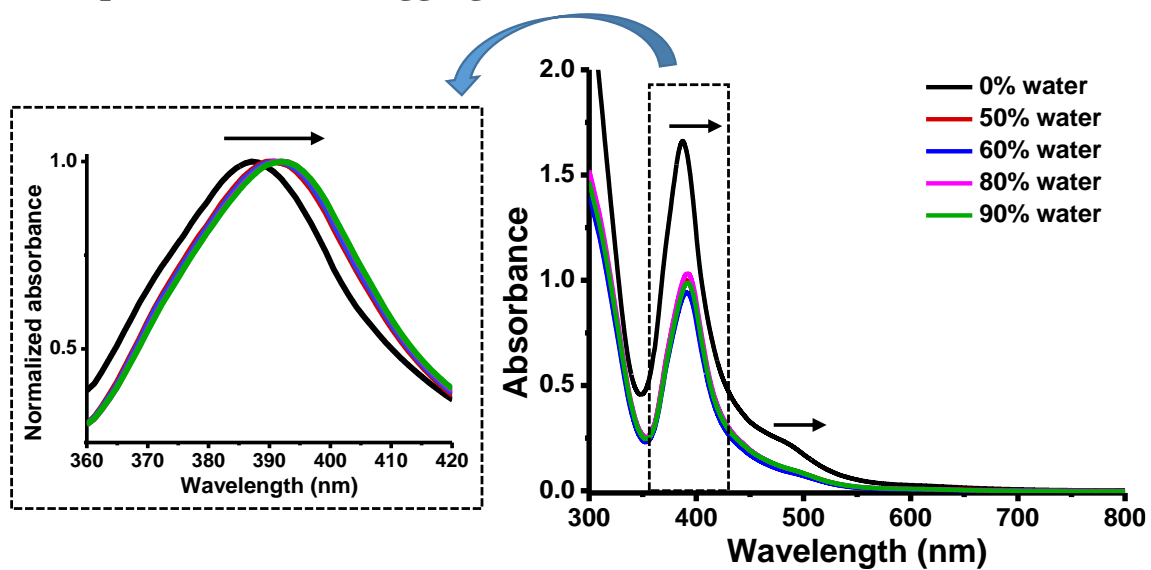


**Figure S6.** UV-vis spectra of **1** in methanol/water mixtures with different fractions of water. Here the cluster concentration was 1 mg/mL.

**Table S1.** Average lifetime of **1** in different states

<b>Sample</b>	<b><math>\tau_1</math> (ns) (<math>A_1</math>)</b>	<b><math>\tau_2</math> (ns)(<math>A_2</math>)</b>	<b><math>\tau_3</math> (ns)(<math>A_3</math>)</b>	<b><math>\tau_{avg}</math>(ns)</b>
$f_w$ 0%	1.56±0.02 (51)	19.36±0.22 (34)	130.31±1.08 (15)	26.8
$f_w$ 70%	5.82±0.12 (47)	60.35±1.02 (32)	498.70±6.78 (22)	131.8
Film	0.56±0.03 (52)	86.8±3.67 (13)	856.75±19.54 (35)	311.4



**PL spectra of aggregates of 1 after oxygen exposure:**

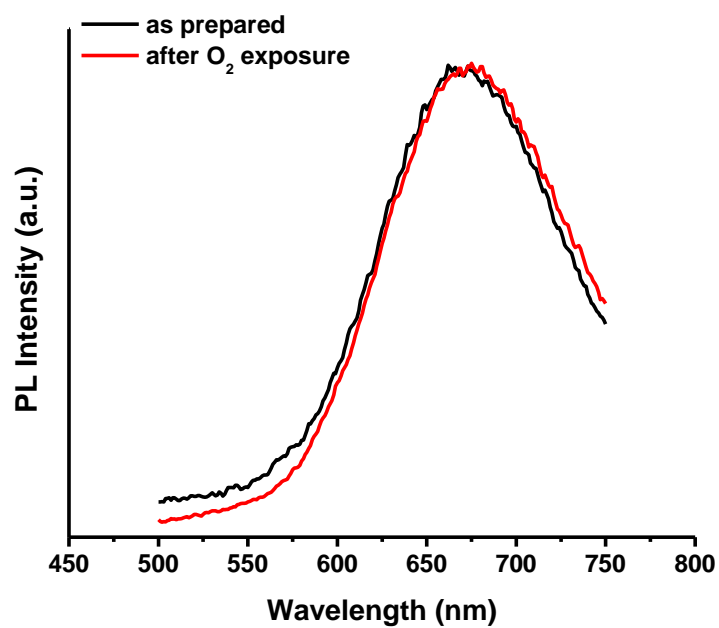
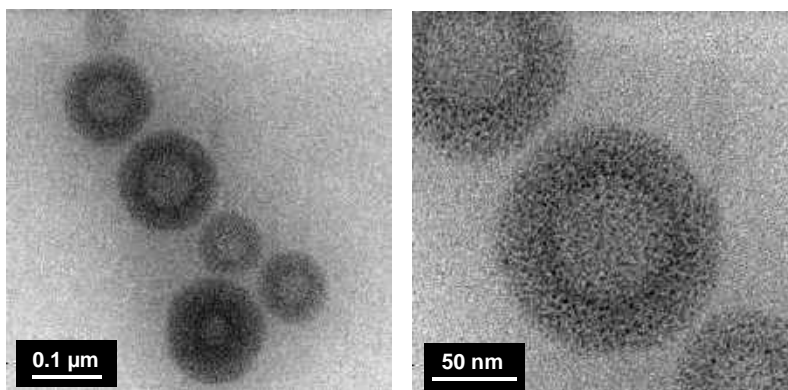


**Figure S7.** PL spectra of cluster **1** in methanol/water mixtures before (black) and after (red) exposure to O<sub>2</sub>, which does not show any luminescence change.

**TEM images of the hollow spheres:**

A)



B)

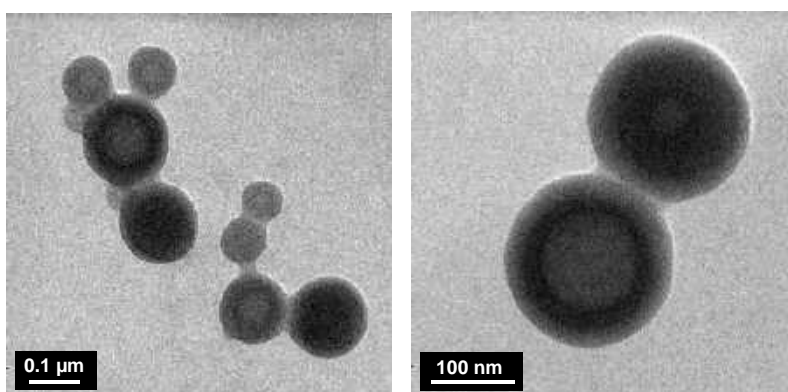
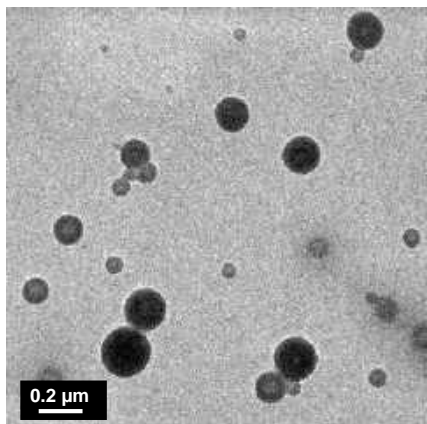


**Figure S8.** (A) TEM images of the hollow spheres with different magnifications. (B) TEM images presenting the assembly of more than one superstructure.

**Stability of superstructures:**

**A)**



**B)**

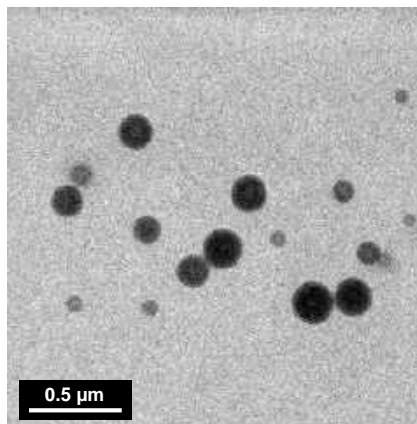


**Figure S9.** TEM images were collected after one week of the formation of aggregates of **1** for  $f_w$  70%. (A) The liquid sample was drop-casted after one week, and (B) the drop-casted sample was kept for one week to check its stability.

## Optical properties of 2:

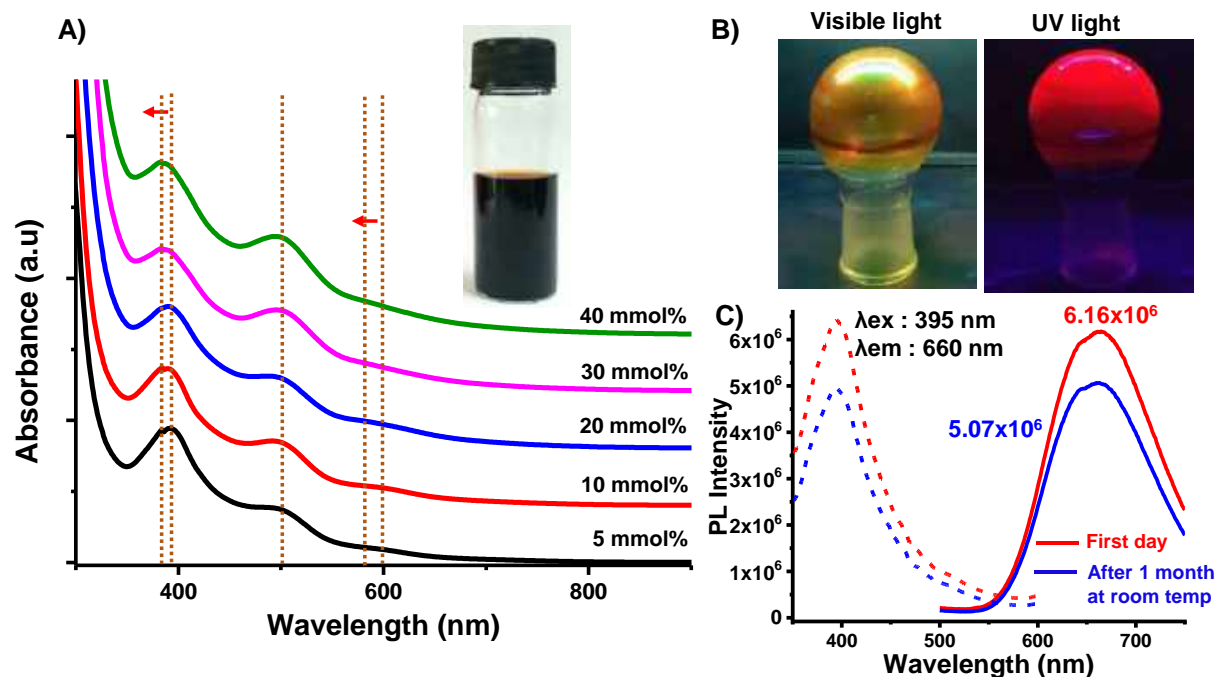


**Figure S10.** (A) UV-vis absorption spectra of  $\text{Ag}_{15-x}\text{Au}_x$  by varying the amount of doped gold from 5 mmol % to 40 mmol %. Inset: Photograph of the cluster in methanol under visible light. (B) Photograph of the solid-state cluster **2** (vacuum dried) under visible and UV light, respectively. (C) Excitation (dotted line) and emission spectra (solid line) of **2** in the solid state were collected on the first day and after storing the sample at room temperature for a month.

**PL spectra of 2 in methanol:**

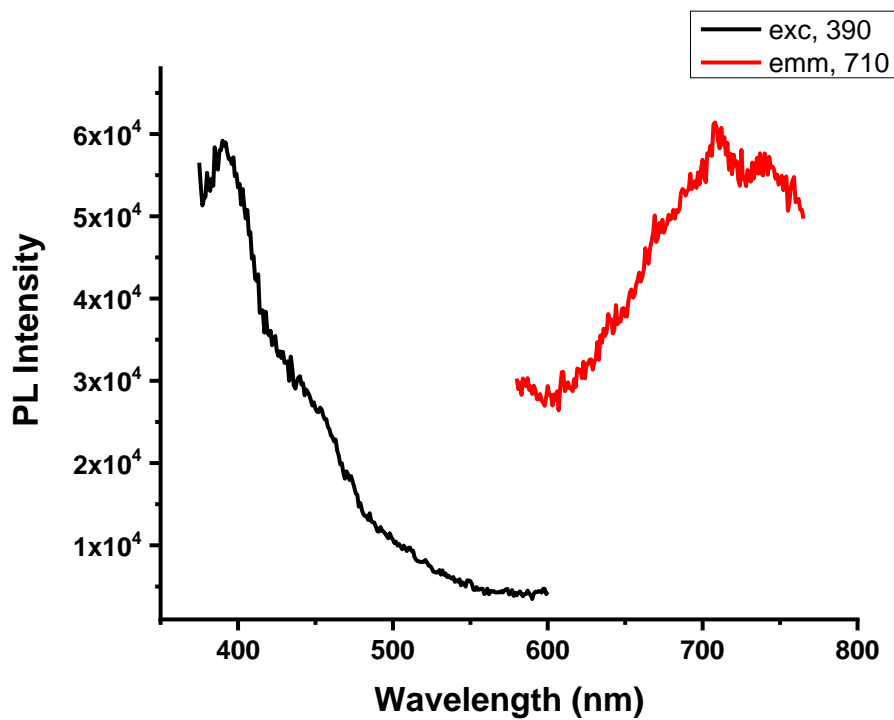


**Figure S11.** Excitation (black trace) and emission spectra (red trace) of **2** in methanol with large Stokes shift. The emission spectrum represents the weakly emissive nature of the cluster, which is not visible to the naked eye.

**Stability of 2 in the solid state:**

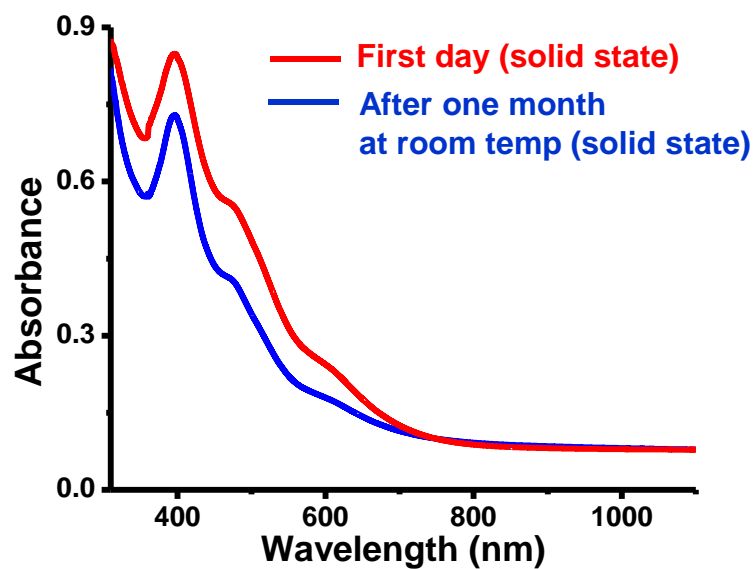


**Figure S12.** UV-vis spectrum of **2** in the solid state (red traces). The spectrum was also recorded after one month (blue trace) by storing the cluster film at room temperature and in the dark.



### $^{31}\text{P}$ NMR spectra of DPPP and **2**:

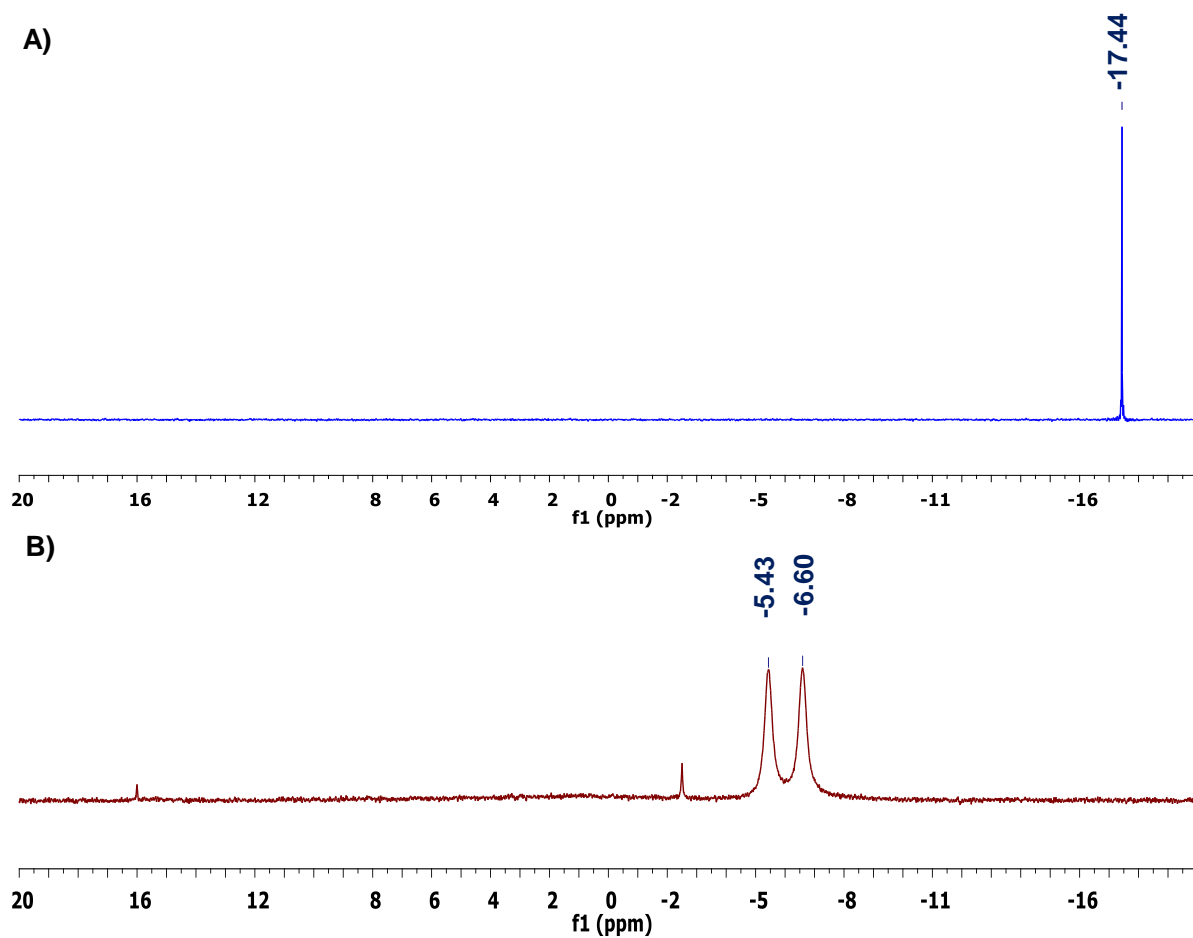


**Figure S13.**  $^{31}\text{P}$  NMR spectra of (A) DPPP and (B) cluster **2**. The  $^{31}\text{P}$  signal at -17.44 ppm for DPPP ligand disappears in **2** due to the binding of ligands with the metal core, which is also confirmed by the appearance of two new broad peaks at -6.60 and -5.43 ppm in the nanoclusters.

## XPS spectra of 2:

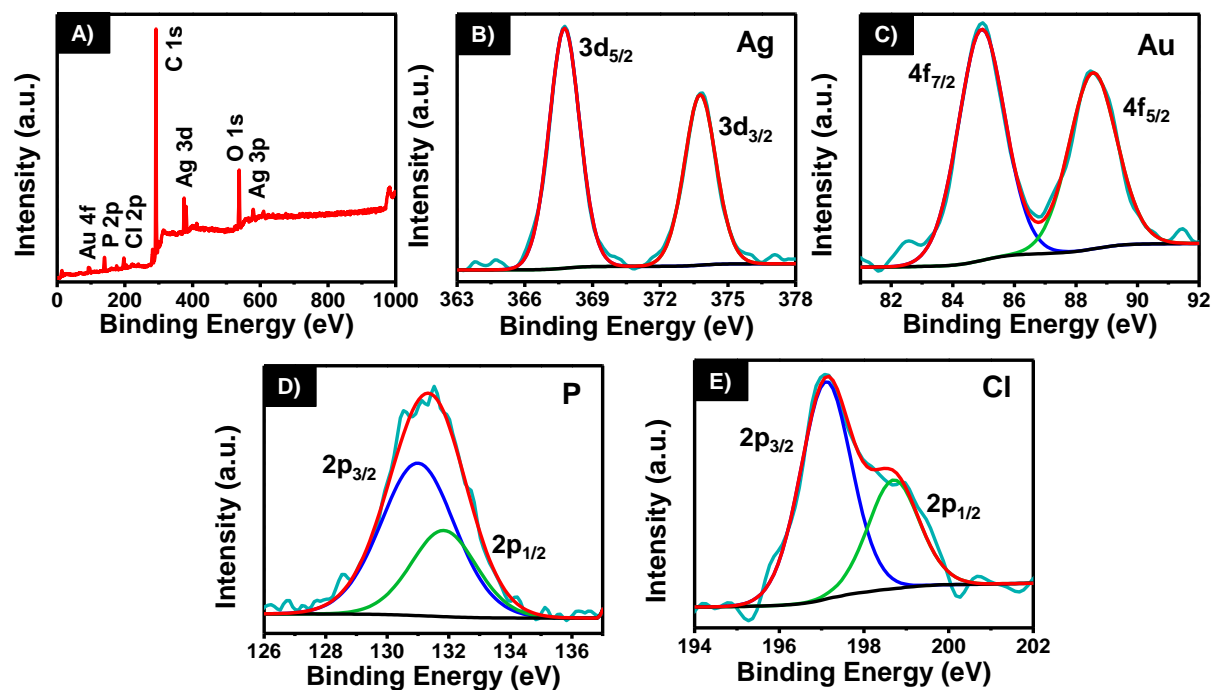


**Figure S14.** (A) XPS survey spectrum of **2** shows all the expected elements. (B) The Ag 3d region. Ag 3d<sub>5/2</sub> appeared at 367.7 eV. (C) The Au 4f region. Au 4f<sub>7/2</sub> appeared at 84.9 eV. (D) The P 2p region. P 2p<sub>3/2</sub> appears at 130.9 eV. (E) The Cl 2p region. Cl 2p<sub>3/2</sub> appears at 197.1 eV. The binding energies of P and Cl confirm their binding with the nanocluster.

## TEM EDS of 2:

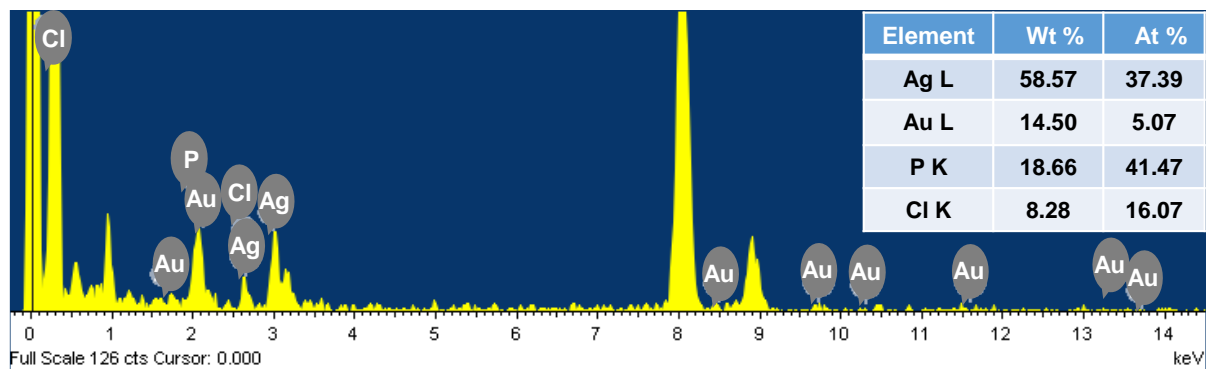


**Figure S15.** TEM EDS of **2** with quantification of the respective elements.

### UV-vis spectra of **2** in the aggregated state:

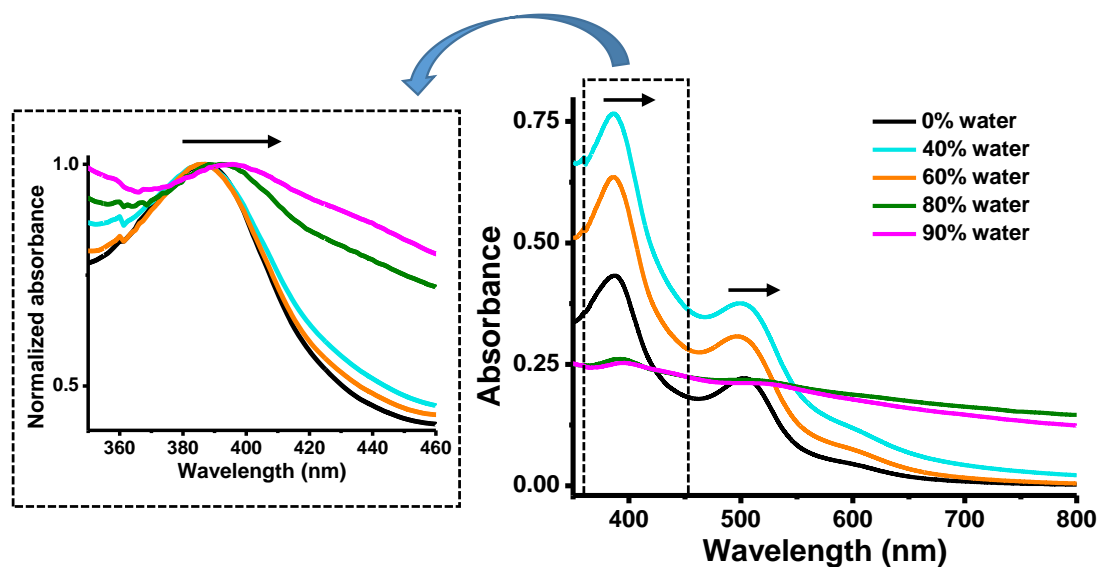


**Figure S16.** UV-vis spectra of **2** in methanol/water mixtures with different fractions of water. For  $f_w$  80% and 90%, the baseline of the UV-vis spectra went high due to the formation of bigger size particles. For all cases, the cluster concentration was 1 mg/mL.

**Lifetime measurements of 2 and its aggregates:**

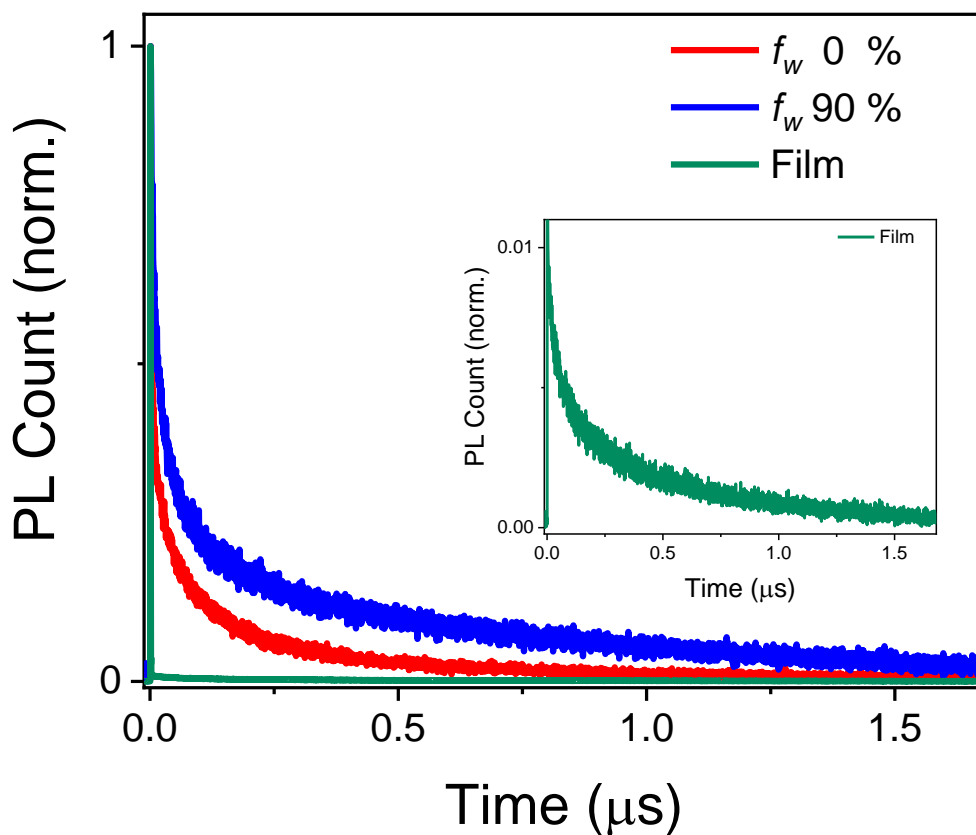


**Figure S17.** PL decay curves measured by TCSPC for  $f_w$  0%, 90%, and film of cluster 2.

**Table S2.** Average lifetime of 2 in different states

Sample	$\tau_1$ (ns) ( $A_1$ )	$\tau_2$ (ns) ( $A_2$ )	$\tau_3$ (ns) ( $A_3$ )	$\tau_{avg}$ (ns)
0%	$1.77 \pm 0.03$ (55)	$35.39 \pm 0.49$ (28)	$252.99 \pm 2.50$ (17)	53.9
70%	$6.57 \pm 0.18$ (44)	$51.50 \pm 1.06$ (34)	$607.20 \pm 10.46$ (22)	153.9

**PL spectra of aggregates of 2 after oxygen exposure:**

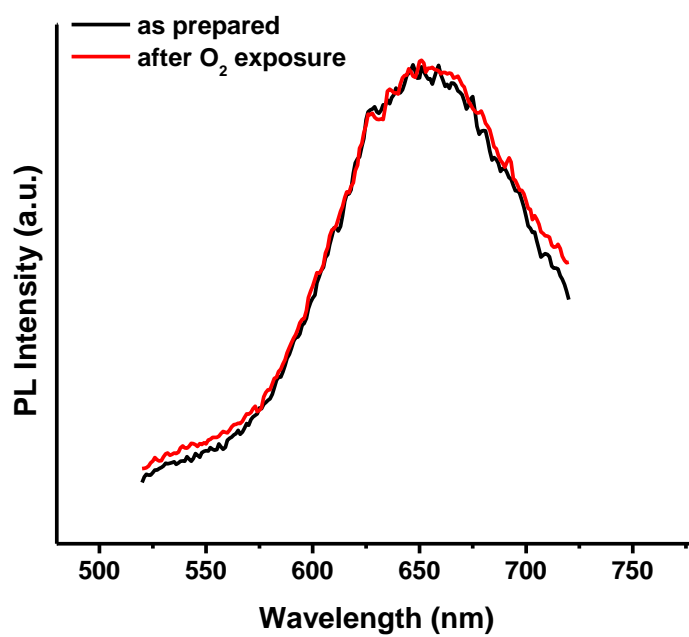


**Figure S18.** PL spectra of cluster 2 in methanol/water mixtures before (black) and after (red) exposure to O<sub>2</sub>, which does not show any luminescence change.



### DLS measurements of aggregates of 2:

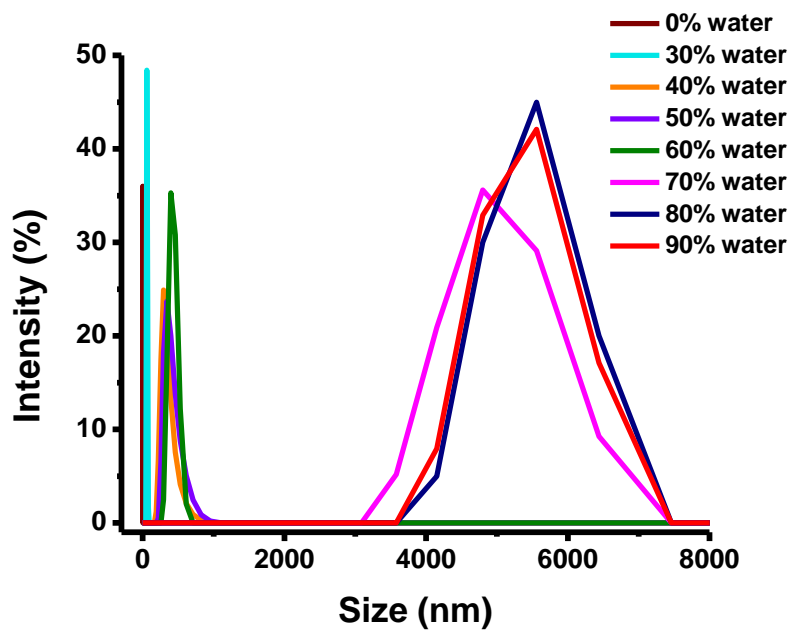


**Figure S19.** DLS spectra of 2 in methanol/water mixtures with different fractions of water. For all cases, the cluster concentration was 1 mg/mL.

## Microscopic characterization of aggregates of **2**:

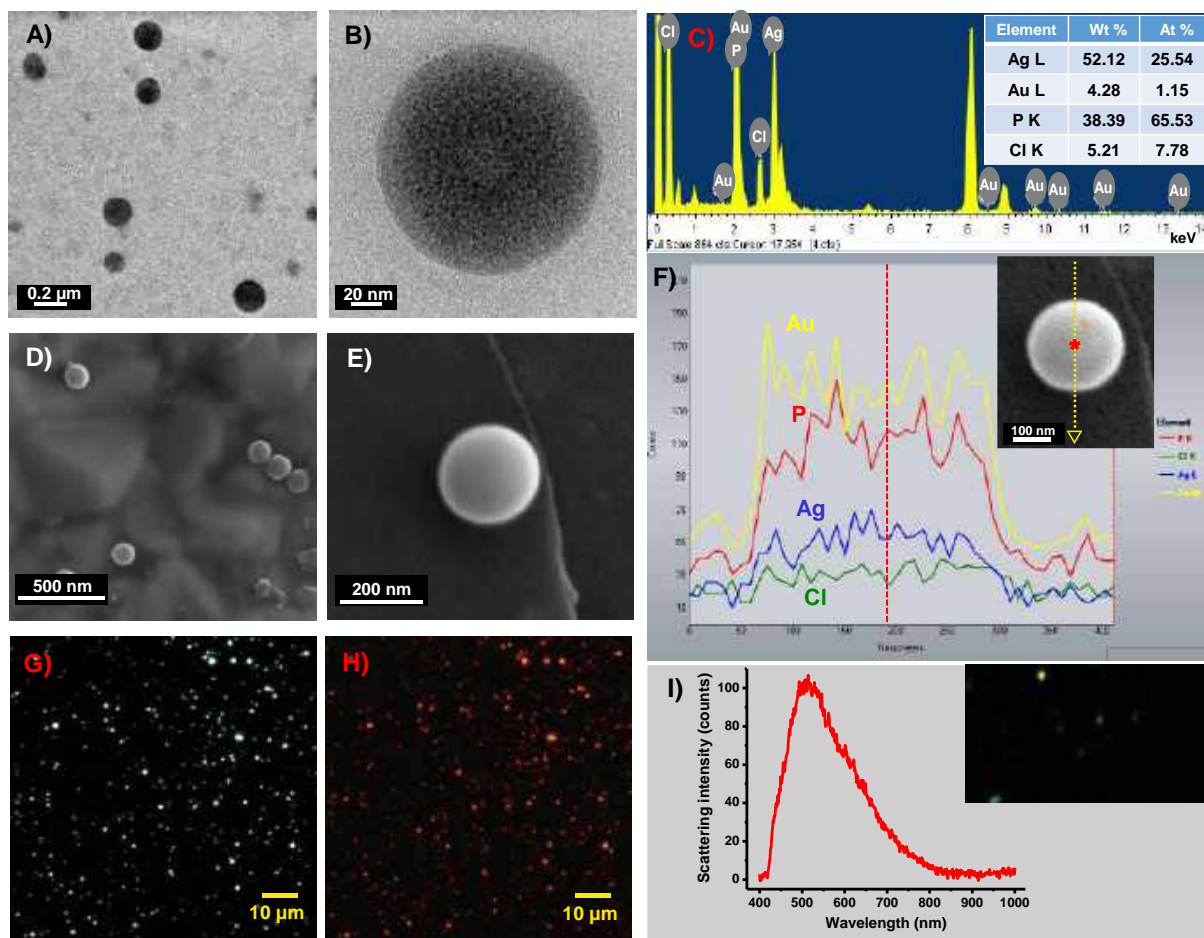


**Figure S20.** Microscopic characterization of the aggregates of **2** formed in  $f_w$  70%. (A) and (B) are the TEM images of the spheres with different magnifications. (C) TEM EDS and elemental composition of the aggregates. (D) and (E) are the FESEM images with different magnifications. (F) SEM EDS line scans were measured along a single sphere indicated by the arrow. (G) Dark field image and (H) fluorescence image of the cluster aggregates immobilized on an ultra-clean glass slide. (I) Average scattering spectrum of the aggregates.

**TA pump-probe spectra of 2 in different states:**

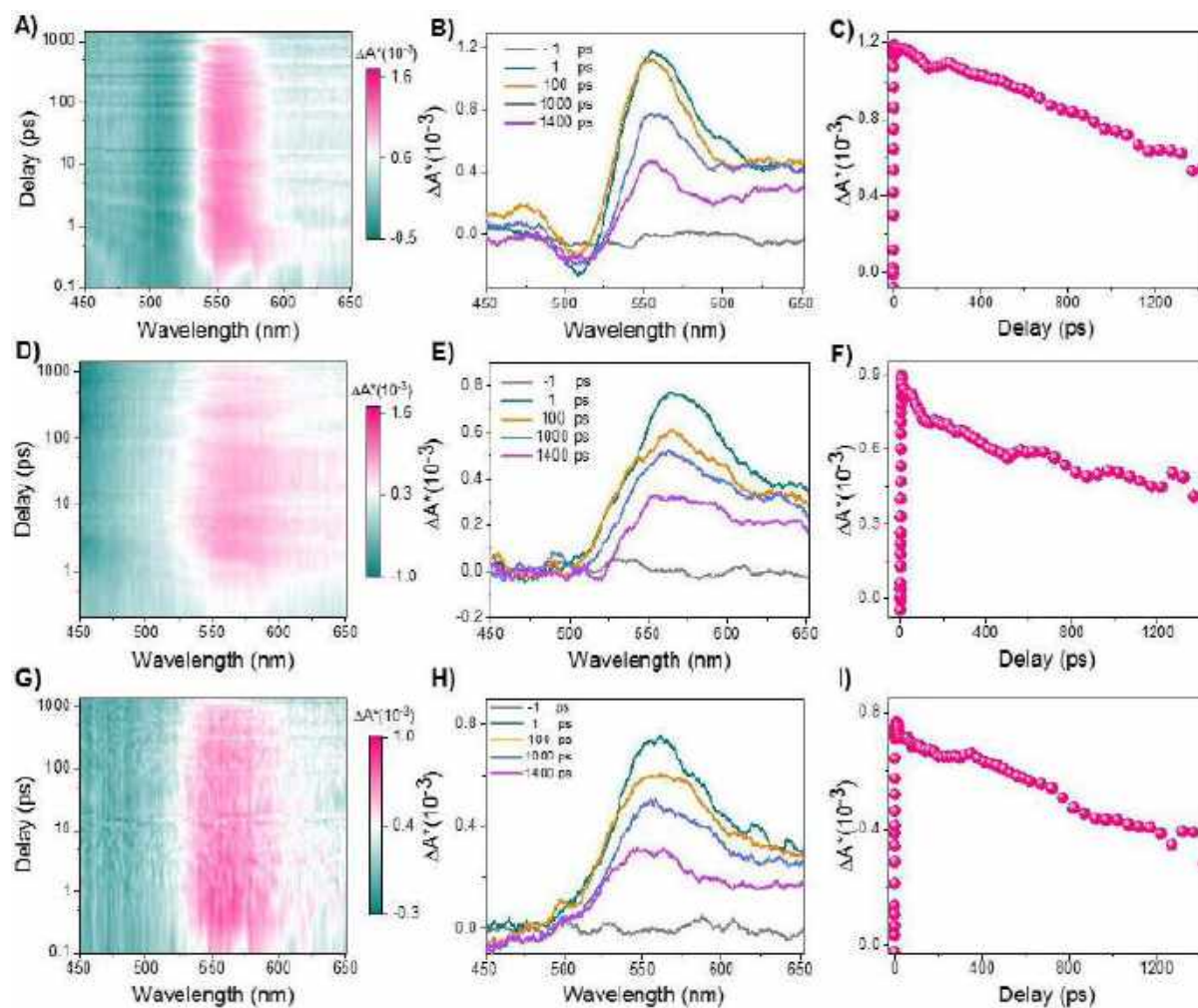


**Figure S21.** The fs-TA pump-probe spectra of 2. (A) Contour plot, (B) TA spectral profile as a function of time delay, and (C) transient kinetic traces at selected wavelength 555 nm peak measured for 2 in methanol. The same measurements have also been done for the aggregates formed in  $f_w$  70% (D-F) and in the solid state (G-I).

### Stability of Ag-Au alloy clusters at 4 °C:

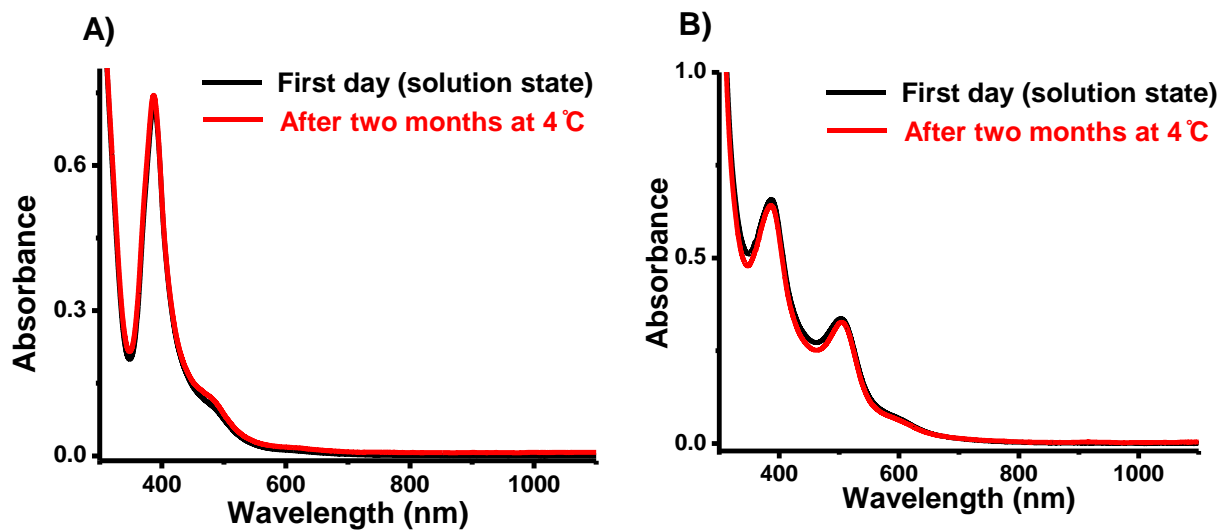


**Figure S22.** UV-vis spectra of (A) **1** and (B) **2** (black traces) in methanol. For both cases, the spectra were again recorded after two months (red trace) by dissolving the solid clusters stored at 4 °C.

## ARTICLE

## Carborane-thiol protected copper nanoclusters: Stimuli-responsive materials with tunable phosphorescence

Arijit Jana,<sup>a</sup> Madhuri Jash,<sup>a</sup> Wakeel Ahmed Dar,<sup>a</sup> Jayoti Roy,<sup>a</sup> Papri Chakraborty,<sup>b</sup> Ganesan Paramasivam,<sup>a</sup> Sergei Lebedkin,<sup>b</sup> Kaplan Kirakci,<sup>c</sup> Sujan Manna,<sup>a</sup> Sudhadevi Antharjanam,<sup>a</sup> Jan Machacek,<sup>c</sup> Monika Kucerakova,<sup>d</sup> Sundargopal Ghosh,<sup>a</sup> Kamil Lang,<sup>c</sup> Manfred M. Kappes,<sup>\*b</sup> Tomas Base\*<sup>c</sup> and Thalappil Pradeep\*<sup>a</sup>

Received 00th January 20xx,  
Accepted 00th January 20xx

DOI: 10.1039/x0xx00000x

Atomically precise nanomaterials with tunable solid-state luminescence attract global interest. In this work, we present a new class of thermally stable isostructural tetranuclear copper nanoclusters (NCs), shortly Cu<sub>4</sub>@oCBT, Cu<sub>4</sub>@mCBT and Cu<sub>4</sub>@ICBT, protected by nearly isomeric carborane thiols: *ortho*-carborane-9-thiol, *meta*-carborane-9-thiol and *ortho*-carborane 12-iodo 9-thiol, respectively. They have a square planar Cu<sub>4</sub> core and a butterfly-shaped Cu<sub>4</sub>S<sub>4</sub> staple, which is appended with four respective carboranes. For Cu<sub>4</sub>@ICBT, strain generated by the bulky iodine substituents on the carboranes makes the Cu<sub>4</sub>S<sub>4</sub> staple flatter in comparison to other clusters. High-resolution electrospray ionization mass spectrometry (HR ESI-MS) and collision energy-dependent fragmentation, along with other spectroscopic and microscopic studies confirm their molecular structure. Although none of these clusters show any visible luminescence in solution, bright μs-long phosphorescence is observed in their crystalline forms. The Cu<sub>4</sub>@oCBT and Cu<sub>4</sub>@mCBT NCs are green emitting with quantum yields (Φ) of 81 and 59 %, respectively, whereas Cu<sub>4</sub>@ICBT is orange emitting with a Φ of 18 %. Density functional theory (DFT) calculations reveal the nature of their respective electronic transitions. The green luminescence of Cu<sub>4</sub>@oCBT and Cu<sub>4</sub>@mCBT clusters get shifted to yellow after mechanical grinding, but it is regenerated after exposure to solvent vapour, whereas the orange emission of Cu<sub>4</sub>@ICBT is not affected by mechanical grinding. Structurally flatten Cu<sub>4</sub>@ICBT didn't show mechano-responsive luminescence in contrast to other clusters, having bent Cu<sub>4</sub>S<sub>4</sub> structures. Cu<sub>4</sub>@oCBT and Cu<sub>4</sub>@mCBT are thermally stable up to 400 °C. The Cu<sub>4</sub>@oCBT retained green emission even upon heating to 200 °C under ambient conditions, while Cu<sub>4</sub>@mCBT changed from green to yellow in the same window. This is the first report on structurally flexible carborane thiol appended Cu<sub>4</sub> NCs having stimuli-responsive tunable solid-state phosphorescence.

## Introduction

Atomically precise metal nanoclusters (NCs) are emerging nanomaterials with atom-specific tunable photoluminescence properties.<sup>1-3</sup> Closely spaced molecule-like electronic energy levels associated with interfacial charge transfer from metallic core to ligand shell or vice versa are responsible for their photoluminescence properties.<sup>4,5</sup> Atomic arrangements of the metallic core and the surrounding ligands define emission characteristics of NCs from the visible to the NIR region.<sup>6-8</sup> Noble metal nanoclusters (NMNCs) of specific nuclearity composed of gold,<sup>9</sup> silver<sup>10</sup> and their alloys,<sup>11</sup> exhibit luminescence in the red region with relatively low quantum yields with emission lifetimes ranging from picosecond to

nanosecond time scale. Expensive precursors, complex synthetic methods, poor stability of NMNCs and their weak luminescence limiting their practical applications have prompted the exploration of more stable clusters.<sup>12</sup> Thus, compared to gold and silver, synthesis of copper NCs from cheaper precursors with greater stability presents a promising alternative.<sup>13,14</sup> Copper NCs with nuclearity <15 could find use in different applications including light-emitting diodes (LED),<sup>15-17</sup> electroluminescence,<sup>18</sup> circularly polarized luminescence<sup>19</sup> and X-ray radioluminescence,<sup>20</sup> principally due to their stronger emission.

Phosphorescence, originating from the charge relaxation of the triplet excited state is of great interest in fundamental research as well as applications.<sup>21,22</sup> Generally, different organic luminophores such as carbonyl and thioether functionalized molecules,<sup>23-25</sup> fluorene,<sup>26</sup> borates,<sup>27</sup> etc., were reported with bright phosphorescence characteristics. Facile functionalization of organic luminophores using functional groups and counter ions promote their tunable emission due to efficient intersystem crossing.<sup>28,29</sup> On the other hand, metal centred phosphorescence especially from copper NCs is weak due to the absence of d-d transitions of Cu atoms with d<sup>10</sup> configuration.<sup>30,31</sup> Ligand to metal charge transfer (LMCT) or metal to ligand charge transfer (MLCT) is the primary reason behind their phosphorescence. Copper clusters with bi,<sup>32</sup> tri,<sup>33</sup> tetra,<sup>34</sup> and hexanuclearity<sup>35</sup> and higher orders<sup>36,37</sup> were reported with LMCT and MLCT characteristics due to facile charge transport between metal

<sup>a</sup> DST Unit of Nanoscience (DST UNS) and Thematic Unit of Excellence (TUE), Department of Chemistry, Indian Institute of Technology, Madras, Chennai – 600036, India.

<sup>b</sup> Institute of Physical Chemistry, Karlsruhe Institute of Technology (KIT), 76131, Karlsruhe, Germany. Institute of Nanotechnology, Karlsruhe Institute of Technology (KIT), 76344, Eggenstein Leopoldshafen, Germany.

<sup>c</sup> Department of Synthesis, Institute of Inorganic Chemistry, The Czech Academy of Science, 25068 Rez, Czech Republic.

<sup>d</sup> Institute of Physics, Academy of Sciences of the Czech Republic, Na Slovance 4 1999/2, 182 21, Prague 8, Czech Republic.

Electronic Supplementary Information (ESI) available: [details of any supplementary information available should be included here]. See DOI: 10.1039/x0xx00000x





atoms and ligands. Surrounding chemical environment also controls the emission characteristics of luminescent materials.<sup>38,39</sup> Intermolecular aggregation through favourable interactions such as CH $\cdots$ n, n $\cdots$ n and hydrogen bonding contributing to enhanced emission, is referred to as aggregation-induced emission (AIE) or aggregation-induced emission enhancement (AIEE).<sup>40</sup> Restriction of molecular motion in the aggregated state and opening of the radiative relaxation pathways result in emission enhancement. Different strategies of supramolecular assembly, such as host-guest complexation,<sup>41</sup> embedding within a rigid polymer matrix,<sup>42</sup> co-crystallization,<sup>43</sup> etc. have also been involved in improving the emission quantum yield of different luminescent materials. Other external stimuli, especially temperature and pressure, can also tune emission properties.<sup>44,45</sup>

For copper NCs, surface ligands protect the fragile metallic core and co-determine their photophysical properties. Thiols,<sup>46</sup> phosphines,<sup>47</sup> carbenes<sup>48</sup> and amino acids<sup>49</sup> are functional groups that have been reported as capping ligands of copper clusters with luminescence characteristics. Variation due to ligand isomerism was observed in copper clusters too.<sup>50</sup> Carborane (dicarba-*closo*-dodecaboranes of the general formula C<sub>2</sub>B<sub>10</sub>H<sub>12</sub>), a twelve-vertex nearly icosahedral molecule composed of ten boron and two carbon atoms, is a new family of materials with interesting properties.<sup>51</sup> Due to their rigid three-dimensional architectures with delocalized electrons over the molecular framework of CH and BH vertices, they strongly shield the unstable metal cores.<sup>52</sup> Carboranes have the potential for synthesizing coordination complexes,<sup>53</sup> luminescent supramolecular materials,<sup>54</sup> biologically active materials<sup>55</sup> and hypergolic materials<sup>56</sup> due to their rigid and robust three-dimensional architectures, chemical and thermal stability and unique electronic structure. From this perspective, carborane-thiol protected isostructural tetranuclear copper clusters are a new class of functional materials with tunable emission properties.

In this work, we synthesized three carborane-thiol (*ortho*-carborane-9-thiol, *meta*-carborane-9-thiol and *ortho*-carborane 12-iodo 9-thiol labelled as Cu<sub>4</sub>@oCBT, Cu<sub>4</sub>@mCBT and Cu<sub>4</sub>@ICBT, respectively) protected Cu<sub>4</sub> clusters with high yields and phase purity at room temperature using ligand exchange induced structural transformation (LEIST) reaction. Various structural, spectroscopic, thermal analysis studies were conducted to reveal novel phenomena. Cumulatively, this work presents an unexplored class of stimuli-responsive tunable phosphorescent materials.

## Results and Discussion

### Synthesis and crystallization

The copper clusters were synthesized by a LEIST reaction, starting from [Cu<sub>18</sub>(DPPE)<sub>6</sub>H<sub>16</sub>]<sup>2+</sup> (DPPE = 1,2-bis(diphenylphosphino) ethane).<sup>57</sup> Details of the syntheses are presented in the experimental section. Similar type of synthetic approach was also used for gold, silver and alloy nanoclusters.<sup>58-60</sup> Cu<sub>4</sub>@oCBT and Cu<sub>4</sub>@ICBT were obtained as microcrystalline solids with green and orange emission, respectively. The Cu<sub>4</sub>@mCBT did not precipitate, but formed green-emitting crystals. Fig. S1 shows the photographic images of the synthetic steps. Compared to high-temperature synthetic methods,<sup>61</sup> this method gives clusters with high yields under ambient conditions. Single crystals suitable for X-ray diffraction were grown in mixed

solvents after 6-8 days of crystallization at room temperature. Cu<sub>4</sub>@oCBT formed colourless hexagonal crystals in a mixture of acetone and dichloromethane (DCM) (3:1, volume ratio). The Cu<sub>4</sub>@mCBT and Cu<sub>4</sub>@ICBT NC formed brick-like and rhombus-shaped crystals, respectively, in DCM: acetone: methanol (3:1:1) mixtures. Fig. 1a-c show images of the individual crystals inspected with an optical microscope. Morphology of each crystal and basic elemental analysis were further confirmed using SEM imaging and EDS elemental analysis (shown in Fig. S2, S3 and S4 for Cu<sub>4</sub>@oCBT, Cu<sub>4</sub>@mCBT and Cu<sub>4</sub>@ICBT, respectively). EDS elemental maps of Cu<sub>4</sub>@oCBT and Cu<sub>4</sub>@mCBT showed the presence of Cu, S, C and B in the crystals, whereas Cu, S, I, C and B were detected in the Cu<sub>4</sub>@ICBT crystal.

### Single crystal structural details

Molecular structures of the clusters were resolved using single-crystal X-ray diffraction (SC-XRD) analysis. Cu<sub>4</sub>@oCBT crystallized in a trigonal crystal system with the space group of P3<sub>1</sub>21. The cell volume of the cluster was 3333 Å<sup>3</sup> (Table 1). Fig. 1d shows the atomic structure of the cluster consisting of a nearly square planar Cu<sub>4</sub> core protected by four *ortho*-carborane thiol ligands. The structural anatomy (shown in Fig. S5) reveals that four 'V-shaped' Cu-S-Cu motifs surround the Cu<sub>4</sub> core. The Cu-Cu bond distance ranges from 2.684 to 2.728 Å, which is shorter than the Cu-Cu van der Waals distance of 2.8 Å, indicating metallic bonding. The opposite Cu-S-Cu bond angles are 76.58° and 78.13°, respectively. The orientation of Cu<sub>4</sub>S<sub>4</sub> motifs resembles a butterfly with the opposite S-S distance of 5.54 Å (Fig. 1g). Four *ortho*-carborane ligands are connected to the Cu<sub>4</sub> core through the V-shaped Cu-S-Cu staples with an average Cu-S bond length of 2.16 Å. The anti-orientation of the carborane cages in the opposite corners of the Cu<sub>4</sub>S<sub>4</sub> unit makes the cluster flexible (shown in Fig. S6). Structurally similar Cu<sub>4</sub>@mCBT crystallized in a monoclinic crystal system with the space group of P2<sub>1</sub>/c and the cell volume of 4400 Å<sup>3</sup> (Table 1). The molecular structure of this cluster is nearly identical to Cu<sub>4</sub>@oCBT (shown in Fig. 1e), having a square planar Cu<sub>4</sub> core protected by four *meta*-carborane thiol ligands in a twisted orientation.

The Cu<sub>4</sub>@ICBT crystallized in a tetragonal crystal system with the space group of P4<sub>3</sub>2<sub>1</sub>2 and a cell volume of 6438 Å<sup>3</sup> (Table 1). In this structure, four carborane ligands are connected to the Cu<sub>4</sub> core through not only the S atoms but also three iodine atoms (Fig. 1f). The longer Cu-I distances of 3.11-3.31 Å, compared to B-I distances of 2.15-2.25 Å indicate weak coordination type of Cu-I interaction. Removal of one iodine atom from the carborane cage is probably due to steric restrictions within the structural framework. As a natural consequence of these competitive interactions, the Cu-Cu bonds in Cu<sub>4</sub>@ICBT become weak, exhibiting distances ranging from 2.80 to 2.85 Å. Similarly, the opposite S $\cdots$ S distance increases to 5.94 Å in comparison to 5.54 Å for Cu<sub>4</sub>@oCBT and 5.49 Å for Cu<sub>4</sub>@mCBT (Fig. 1g-i). Iodine substitution on carborane cage in the position adjacent to the SH group makes the Cu<sub>4</sub>S<sub>4</sub> "butterfly" flatter than in other clusters. The higher cell volume of Cu<sub>4</sub>@ICBT, along with other structural parameters, suggests structural expansion due to iodine-induced steric congestion. The ORTEP structures of these clusters are presented in Fig. S7, S8 and S9, respectively. The effects of these structural changes on the photophysical properties of this cluster system are discussed later.





## ARTICLE

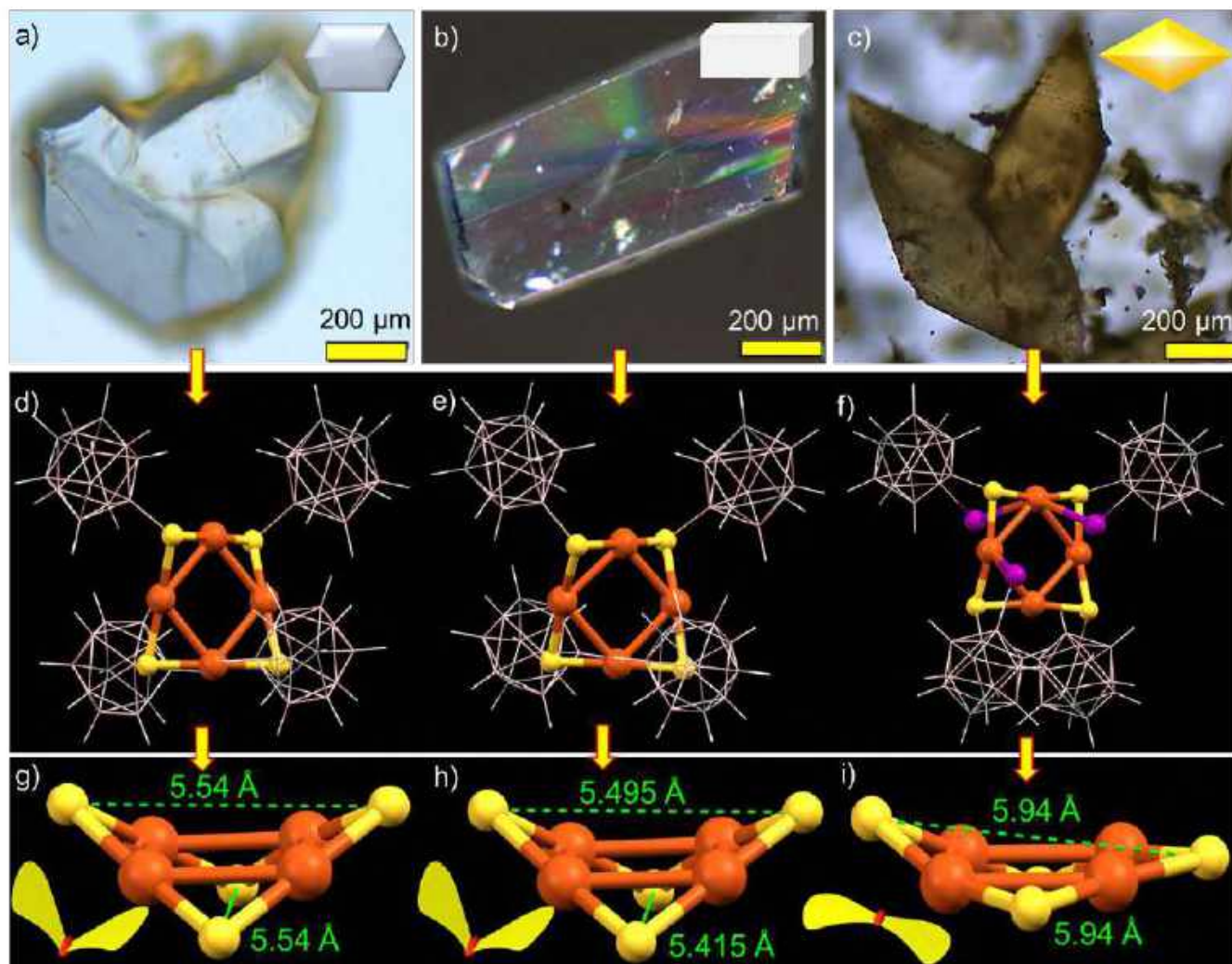


**Fig. 1** Optical microscopic images of the crystal of a) Cu<sub>4</sub>@oCBT, b) Cu<sub>4</sub>@mCBT and c) Cu<sub>4</sub>@ICBT (insets show schematic representations of the morphology). Single crystal structure of d) Cu<sub>4</sub>@oCBT, e) Cu<sub>4</sub>@mCBT and f) Cu<sub>4</sub>@ICBT having a nearly square planar Cu<sub>4</sub> core and a butterfly type Cu<sub>4</sub>S<sub>4</sub> staple, protected by four carboranes in a twisted fashion. g-i) The comparative structural analogy of the Cu<sub>4</sub>S<sub>4</sub> staple reveals that flattening Cu<sub>4</sub>S<sub>4</sub> staple for Cu<sub>4</sub>@ICBT NC in comparison to other clusters due to three iodine insertions in the structure. Inset shows the wing flapping of the respective butterfly. Color code: orange = copper, yellow = sulfur, pink = boron, violet = iodine, gray = carbon and white = hydrogen.

The unit cell and molecular packing of Cu<sub>4</sub>@oCBT (shown in Fig. S10) reveal six clusters packed on the opposite faces of the cuboid. The longest distance between the two centroids of Cu<sub>4</sub>S<sub>4</sub> unit is 29.440 Å along the c axis, whereas the distance between the other two pairs of the oppositely packed centroids is 11.434 Å. The extended molecular packing (shown in Fig. 2a, b) reveals ABC...ABC kind of layered packing. Three types of short-contact van der Waals interactions, CH...S, BH...B(H) and CH...B(B) are responsible for the packing of Cu<sub>4</sub>@oCBT. Careful analysis further reveals four BH...B(H), eight S...HC and four CH...B(B) interactions per cluster, promoting their crystallization. The Cu<sub>4</sub>@mCBT is packed in horizontally stacked

layers, where four clusters are packed inside the unit cell in an AB...AB packing mode (Fig. S11 and 2c, d). The Cu<sub>4</sub>@ICBT is packed in a type of AB...BA packing mode, where five clusters are packed inside the unit cell in undulated fashion (Fig. S12, 2e, f). The extended packing represents horizontally stacked wave-like layers of the clusters. In the case of Cu<sub>4</sub>@mCBT, one CH...HB, two B...S, four BH...S, two CH...S and nine BH...B(H) short contact interactions were observed. For the Cu<sub>4</sub>@ICBT, there are eight S...C(H), four BH...HB and three CH...HB interactions leading to intermolecular packing.



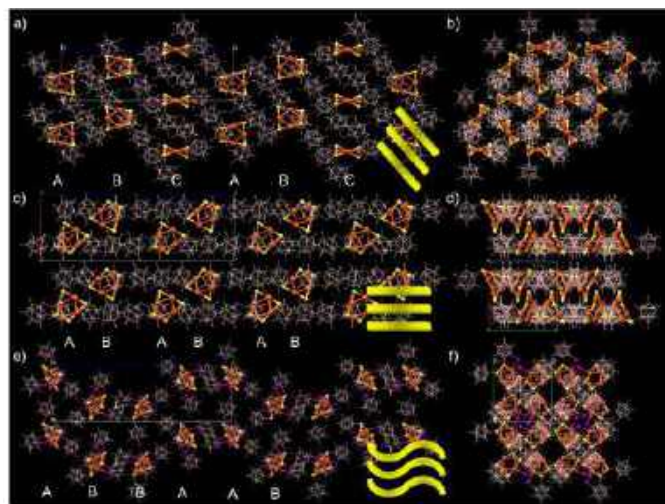


**Fig. 2** Supramolecular organization of  $\text{Cu}_4@o\text{CBT}$  (a, b),  $\text{Cu}_4@m\text{CBT}$  (c, d) and  $\text{Cu}_4@i\text{CBT}$  (e, f) clusters. a), c), e) Represent the packing view along b crystallographic axis and b), d), f) represent along c crystallographic axis. The rectangles correspond to unit cell. Color code: orange = copper, yellow = sulfur, pink = boron, violet = iodine, gray = carbon and white = hydrogen.

**Table 1.** Comparative unit cell parameters of the respective NCs.

Clusters	$\text{Cu}_4@o\text{CBT}$	$\text{Cu}_4@m\text{CBT}$	$\text{Cu}_4@i\text{CBT}$
Crystal system	Trigonal	Monoclinic	Tetragonal
Volume ( $\text{\AA}^3$ )	3333.4	4400.1	6438.0
Space group	$P3_121$	$P21/c$	$P4_32_12$
Density ( $\text{mg/m}^3$ )	1.428	1.442	1.375
Z	3	4	4

### Additional characterization

All three copper clusters were further characterized using high-resolution mass spectrometry (HRMS). Details of instrumentation and preparation of the samples are provided in the Supplementary information. We didn't observe any characteristic peaks from the as-prepared samples in either positive or negative ion modes, which suggests neutral charge for the clusters. In presence of formic acid,  $\text{Cu}_4@o\text{CBT}$  and  $\text{Cu}_4@i\text{CBT}$  ionized with characteristic peaks at  $m/z = 956.7$  (Fig. 3a) and 1334.06 (Fig. 3c), respectively. Proton addition promoted the ionization of these clusters. The molecular composition of  $\text{Cu}_4@i\text{CBT}$  with only three iodine atoms as determined in X-ray diffraction analysis was also confirmed by HRMS. In presence of caesium acetate,  $\text{Cu}_4@m\text{CBT}$  shows a peak at  $m/z = 1088.26$  (Fig. 3b), which is the  $\text{Cs}^+$  attached peak of the cluster. The experimental isotopic distribution of all the clusters matched well with the calculated ones (shown in the insets of Fig. 3a-c for  $\text{Cu}_4@o\text{CBT}$ ,  $\text{Cu}_4@m\text{CBT}$  and  $\text{Cu}_4@i\text{CBT}$ , respectively).

Collision-energy (CE) dependent fragmentation revealed additional insight into their structural details. The molecular ion peak at  $m/z = 956.7$  for  $\text{Cu}_4@o\text{CBT}$  was selected for fragmentation (Fig. 3d). At CE 50 (in instrumental unit), two new peaks observed at  $m/z$  781.20 and 674.26 were assigned to  $[\text{Cu}_4\text{S}_3(\text{C}_2\text{B}_{10}\text{H}_{11})_3]\text{H}^+$  and  $[\text{Cu}_4\text{S}_3(\text{C}_2\text{B}_{10}\text{H}_{11})_2(\text{B}_2\text{CH}_2)]\text{H}^+$ , respectively. Further increasing the collision energy up to CE 70 yielded fragments at  $m/z$  565.32 and 390.13, which were assigned as  $[\text{Cu}_4\text{S}_3(\text{C}_2\text{B}_{10}\text{H}_{11})(\text{B}_2\text{CH}_2)_2]\text{H}^+$  and  $[\text{Cu}_4(\text{SB}_2\text{CH}_2)]\text{H}^+$ , respectively. Fig. S13 shows both experimental and calculated isotopic distributions of the respective fragments. Fragmentation involves the initial loss of a carborane thiol and subsequent fragmentation of the cage structure of carborane of selected  $\text{Cu}_4@o\text{CBT}$  ions, which illustrates high stability of the tetranuclear copper core of the system, schematically illustrated in Fig. 3e. The fragmentation of the carborane cage structure was also observed for the  $\text{O}_9$  ligand (shown in Fig. S57b). Collision energy-dependent fragmentation of the  $\text{Cu}_4@i\text{CBT}$  (shown in Fig. 3f) shows four fragments at  $m/z$  1099.39, 925.36, 864.73 and 690.70. These peaks are assigned to  $[\text{Cu}_3\text{S}_3\text{I}_3(\text{C}_2\text{B}_{10}\text{H}_{10})_3]5\text{H}^+$ ,  $[\text{Cu}_3\text{S}_2\text{I}_3(\text{C}_2\text{B}_{10}\text{H}_{10})_2]5\text{H}^+$ ,  $[\text{Cu}_2\text{S}_2\text{I}_3(\text{C}_2\text{B}_{10}\text{H}_{10})_2]8\text{H}^+$  and  $[\text{Cu}_2\text{S}_3(\text{C}_2\text{B}_{10}\text{H}_{10})]8\text{H}^+$ , respectively. The theoretical isotopic distribution of these fragments matched well with the experimental spectra (shown in Fig. S14). The scission of Cu-Cu bonds in  $\text{Cu}_4@i\text{CBT}$  (shown in Fig. 3g) compared to  $\text{Cu}_4@o\text{CBT}$  indicates weaker bonding manifested by longer Cu-Cu bonds (2.80-2.85  $\text{\AA}$ ) in  $\text{Cu}_4@i\text{CBT}$ , compared to the shorter Cu-Cu bonds (2.68-2.73  $\text{\AA}$ ) in  $\text{Cu}_4@o\text{CBT}$ .

The size of the particles was analysed using TEM studies, shown in Fig. S15, S16 and S17 for  $\text{Cu}_4@o\text{CBT}$ ,  $\text{Cu}_4@m\text{CBT}$  and  $\text{Cu}_4@i\text{CBT}$ , respectively. We did not observe any cluster particles after 2 min beam exposure, apparently due to the presence of a fewer number of metal atoms, whereas 15 min beam exposure created larger particles (with a particle dimension of 4-5 nm) due to beam-induced aggregation. The lattice spacing of 2.6 nm indicates (1 0 2) plane of copper sulfide. The EDS elemental analysis of  $\text{Cu}_4@o\text{CBT}$  and  $\text{Cu}_4@m\text{CBT}$  (in SEM) shows a nearly 1: 1 atomic ratio of Cu: S. The atomic ratio of Cu: S: I of 6.75: 4.34: 4.15 for  $\text{Cu}_4@i\text{CBT}$  also indicates the presence of iodine in the cluster. We observed 10-15  $\mu\text{m}$  rhombohedral crystalline particles for  $\text{Cu}_4@i\text{CBT}$  due to their fast crystallization (shown in Fig. S18). The binding of the carborane ligands was confirmed using  $^{11}\text{B}\{^1\text{H}\}$  and  $^{13}\text{C}\{^1\text{H}\}$  NMR studies. The comparative  $^{11}\text{B}\{^1\text{H}\}$  NMR data of each cluster and respective carborane ligand are shown in Fig. S19, S21 and S23 and peak positions and other details are summarized in Table S9, S10 and S11, respectively.

The  $^{11}\text{B}$  NMR spectrum of  $\text{Cu}_4@o\text{CBT}$  at room temperature shows six peaks at  $\delta$  6.54, -1.36, -7.56, -12.63, -14.56 and -15.35 ppm in comparison to the peaks of  $\text{O}_9$  ligand at  $\delta$  5.01, -1.34, -7.58, -13.26, -14.52, -15.35 ppm. The appearance of  $^{11}\text{B}$  NMR peaks in the nearly same position indicates that the boron spectral region of the  $\text{O}_9$  ligand is less influenced by binding with the metal core. The chemical shift of the boron connected to sulphur is shifted to  $\delta$  6.54 ppm compared to 5.01 ppm for the  $\text{O}_9$  ligand. The  $^{13}\text{C}$  chemical shifts of  $\text{O}_9$  at  $\delta$  53.41 and 47.01 ppm were shifted to 54.95 and 46.44 ppm in  $\text{Cu}_4@o\text{CBT}$  (Fig. S20). The peak splitting increases from 6.4 ppm to 8.51 ppm for  $\text{Cu}_4@o\text{CBT}$  due to enhanced C-C coupling.  $\text{Cu}_4@m\text{CBT}$  and  $\text{Cu}_4@i\text{CBT}$  have characteristic  $^{11}\text{B}$  spectra similar to  $\text{M}_9$  and  $\text{I}_9$  ligands, respectively (Fig. S21, S23).





## ARTICLE

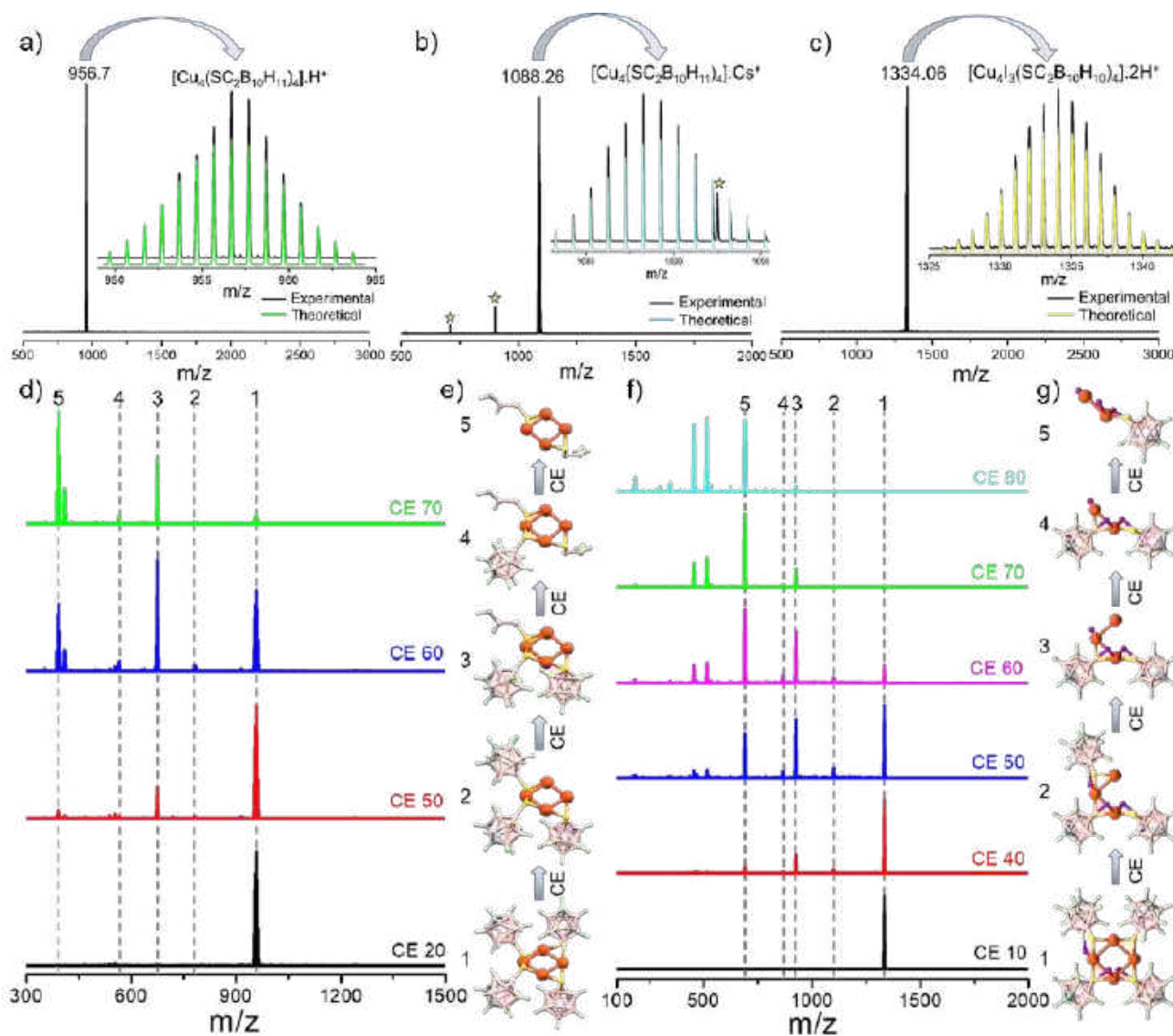


**Fig. 3** Positive ion-mode ESI-mass spectra of a)  $\text{Cu}_4@o\text{CBT}$ , b)  $\text{Cu}_4@m\text{CBT}$  and c)  $\text{Cu}_4@i\text{CBT}$ . Formic acid and cesium acetate were used for the measurements as ionization enhancers. Insets show matching of the experimental and theoretical spectra, respectively. Peaks labeled \* are due to  $\text{Cs}^+$  ion impurity. d) Collision energy dependent fragmentation of the molecular ion peak at  $m/z$  956.35 of  $\text{Cu}_4@o\text{CBT}$  shows the losses of different carborane thiol fragments without opening the  $\text{Cu}_4$  core. e) Schematic representation shows the respective fragmentations. f) Collision energy dependent fragmentation of molecular ion peak at  $m/z$  1334.06 of  $\text{Cu}_4@i\text{CBT}$  shows the losses of carborane thiol fragments along with the opening of  $\text{Cu}_4$  core. g) Schematic representation shows the losses of different fragments of  $\text{Cu}_4@i\text{CBT}$ . Color code: orange = copper, yellow = sulfur, pink = boron, violet = iodine, gray = carbon and green = hydrogen.

The  $^{13}\text{C}$  NMR spectra showed a single peak at  $\delta$  54.51 ppm due to  $\text{C}_1$  and  $\text{C}_7$  carbons of  $\text{M}_9$  ligand, which got split to  $\delta$  56.37 and 49.99 ppm for  $\text{Cu}_4@m\text{CBT}$  and the peaks at  $\delta$  45.97 and 44.41 ppm of  $\text{I}_9$  ligands were shifted to  $\delta$  51.50 and 46.91 ppm, respectively for  $\text{Cu}_4@i\text{CBT}$  (Fig. S22 and S24). Literature reports on the magnitude of dipole

moment and alteration in orientation of carboranes upon binding with the metal surface indicate changes in their electronic properties upon binding with metal atoms.<sup>62-64</sup>



## ARTICLE

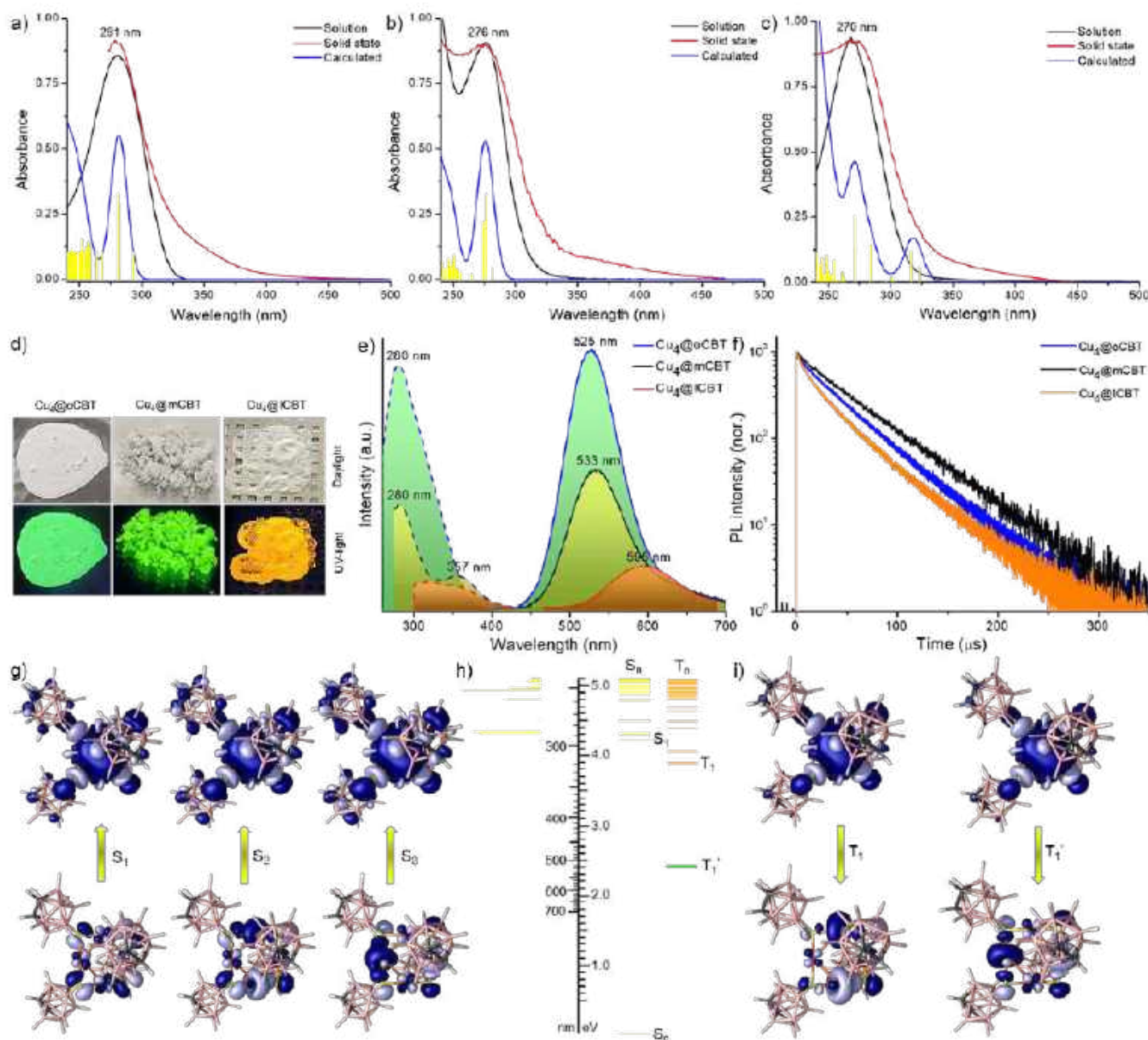


**Fig. 4** UV-vis absorption spectra of a) Cu<sub>4</sub>@oCBT, b) Cu<sub>4</sub>@mCBT and c) Cu<sub>4</sub>@iCBT in solid state and respective solutions. The calculated absorption spectrum of each cluster, also shown here, correlates well with the experimental spectrum. Yellow lines indicate relative oscillator strengths. The absorbance values refer only to the experimental spectra. d) Photographs of the clusters under daylight and UV-light. Green luminescence was observed from Cu<sub>4</sub>@oCBT and Cu<sub>4</sub>@mCBT, whereas Cu<sub>4</sub>@iCBT is orange emitting. e) Photoluminescence excitation and emission spectra of the clusters in their solid state. f) Emission decay profiles of the clusters at room temperature (25 °C). g) Electron density maps of natural transition orbitals (NTOs) responsible for the absorption feature of Cu<sub>4</sub>@oCBT. h) Schematic diagram of calculated excited states of Cu<sub>4</sub>@oCBT. i) NTOs responsible for triplet emission.

Infrared (IR) and Raman spectroscopy were performed to understand the vibrational spectral signatures of these clusters. IR spectra of Cu<sub>4</sub>@oCBT, Cu<sub>4</sub>@mCBT and Cu<sub>4</sub>@iCBT are shown in Fig. S25, S26 and S27, along with those of the respective ligands. The

appearance of BH and CH stretching peaks at 2600 and 3050 cm<sup>-1</sup> and other bending vibrational modes independently confirm the presence of carborane thiols in the cluster sample. The stretching vibrational spectral regions (especially BH and CH) become broad



upon binding to the copper core. The cage breathing vibrational modes at 860-878  $\text{cm}^{-1}$  confirm ligand binding. Theoretical calculations shown in Fig. S28 and S29 for  $\text{Cu}_4@o\text{CBT}$  and  $\text{Cu}_4@i\text{CBT}$ , respectively also support the experimental spectra. Raman spectra shown in Fig. S30, S31 and S32 also confirm the broadening of CH and BH spectral regions of the respective clusters. XPS spectra shown in Fig. S33, S34 and S35 of  $\text{Cu}_4@o\text{CBT}$ ,  $\text{Cu}_4@m\text{CBT}$  and  $\text{Cu}_4@i\text{CBT}$  manifest the characteristic Cu, S, C and B signatures. Peak fitting of Cu 2p region with  $2p_{3/2}$  and  $2p_{1/2}$  peaks at 930 and 950 eV of  $\text{Cu}_4@o\text{CBT}$  and the absence of satellite peaks indicate metal-like zero oxidation state for Cu. Similar spectra of Cu for  $\text{Cu}_4@m\text{CBT}$  and  $\text{Cu}_4@i\text{CBT}$  also suggest zero oxidation state. The  $3p_{3/2}$ ,  $3d_{5/2}$ , 4p and 4d peaks at 874, 619, 122, and 50 eV of iodine, respectively, were observed for  $\text{Cu}_4@i\text{CBT}$ .

### Photophysical properties

We have studied absorption and emission characteristics of these clusters in detail. UV-vis absorption spectra of the clusters as measured in their respective solutions ( $\text{Cu}_4@o\text{CBT}$  and  $\text{Cu}_4@m\text{CBT}$  in acetonitrile and  $\text{Cu}_4@i\text{CBT}$  in 5:1 DCM and acetone mixture) as well as in the crystalline state are presented in Fig. 4a-c. In solution, these clusters show a sharp absorption band in the window of 260-282 nm, whereas this absorption appears broadened in the crystalline state, with the onset  $\sim$ 400 nm. Generally, these clusters are non-emitting in solution, whereas bright emission (green for  $\text{Cu}_4@o\text{CBT}$  and  $\text{Cu}_4@m\text{CBT}$  and orange for  $\text{Cu}_4@i\text{CBT}$ ) were observed in crystalline state under UV light (shown in the inset of Fig. S36). Photographs of respective crystals are shown in Fig. 4d. PL measurements showed emission peaks at 525, 533 and 595 nm for  $\text{Cu}_4@o\text{CBT}$ ,  $\text{Cu}_4@m\text{CBT}$  and  $\text{Cu}_4@i\text{CBT}$  in the crystalline state (Fig. 4e). Such type of strong emission peaks are absent in their respective solutions (Fig. S36). These emission bands are associated with a broad excitation band in the window of 250-400 nm, which resembles their absorption band (Fig. 4e). These crystallization induced emission (CIE) features are reminiscent of cubane type  $[\text{Cu}_4\text{X}_4\text{L}_4]$  complexes which also showed poor luminescence properties in solution when compared to the solid and aggregated states.<sup>65,66</sup> We have further checked the aggregation-induced emission (AIE) behaviour of  $\text{Cu}_4@o\text{CBT}$  and  $\text{Cu}_4@m\text{CBT}$  clusters (shown in Fig. S37). Both of these clusters are non-emissive in acetonitrile. However, bright green luminescence was observed upon increasing the water content. PL spectral measurements show that aggregates started forming at a water fraction ( $f_w$ ) of 30 and 20 % for  $\text{Cu}_4@o\text{CBT}$  and  $\text{Cu}_4@m\text{CBT}$ , respectively, and the emission intensifies gradually up to  $f_w$  80 %.

To get additional insights into the CIE/AIE property, we have studied the structural variation from crystalline state to isolated solution state using density functional theory (DFT) calculations, which show structural relaxation of  $\text{Cu}_4@o\text{CBT}$  and  $\text{Cu}_4@m\text{CBT}$  in solution compared to their crystalline state (shown in Fig. S38). The Cu-S bond length decreases from 2.65 to 2.27 Å for  $\text{Cu}_4@o\text{CBT}$  and 2.60 to 2.28 Å for  $\text{Cu}_4@m\text{CBT}$ , upon changing from crystals to the clusters in solution. Increase in the Cu-S-Cu bond angle from 74.65° to 78.45° for  $\text{Cu}_4@o\text{CBT}$  and 73.65° to 78.08° for  $\text{Cu}_4@m\text{CBT}$  also suggests such relaxation. Intercluster interaction in the solid state is also responsible for the CIE/AIE behaviour. Non-covalent intermolecular interactions have significant effect on their electronic structure. The  $\text{Cu}_4@o\text{CBT}$  is packed in a trigonal crystal lattice through C-H...B(B) (3.04-3.06 Å), B-H...B-H (2.37-3.06 Å) and C-H...S (2.74-2.80 Å) van der Waals interactions (Fig. S39). Similar intermolecular interactions were also present for  $\text{Cu}_4@m\text{CBT}$  and  $\text{Cu}_4@i\text{CBT}$  (shown in Fig. S40 and S41, respectively). Disappearance of emission can be attributed

to the structural relaxation of the clusters in solution as well as quenching of the excited state by solvent molecules.

The emission lifetimes of 43, 42 and 35  $\mu\text{s}$  for  $\text{Cu}_4@o\text{CBT}$ ,  $\text{Cu}_4@m\text{CBT}$  and  $\text{Cu}_4@i\text{CBT}$  indicate phosphorescence nature originating from a triplet excited state (Fig. 4f). Respective fittings of each decay traces are shown in Fig. S42. To verify the nature of the excited state, we have measured PL intensity upon interaction with oxygen. Quenching the emission intensity of all these clusters upon oxygen exposure and subsequent PL recovery upon nitrogen exposure, verified prominent interaction of oxygen with the triplet excited state (Fig. S43). Similar experiments were performed to detect triplet state for metal nanoclusters.<sup>67,68</sup> The quantum yields of 81 %, 59 % and 18 % correlate with the emission intensity of the clusters. Detailed photophysical parameters are summarised in Table 2.

The excited states of these clusters were studied using Density Functional Theory (DFT) and Time-dependent DFT (TD-DFT) calculations. The calculated absorption features and their respective oscillator strength in solution match well with the experimental spectrum (shown in Fig. 4a-c). Natural transition orbitals (NTOs) of these singlet excitations (Fig. 4g, S44, and S45 for  $\text{Cu}_4@o\text{CBT}$ ,  $\text{Cu}_4@m\text{CBT}$ , and  $\text{Cu}_4@i\text{CBT}$ , respectively) show that the hole orbitals (*i.e.*  $S_0$ ) are located on  $\text{Cu}_4\text{S}_4$  core region, whereas excited electron orbitals (*i.e.*,  $S_1$ ,  $S_2$  and  $S_3$ ) with comparable energy are delocalized all over the copper carborane cluster framework. So, the absorption bands are due to the charge transfer from metal core to ligand shell (MCLS). The low energy absorption transition extends to the 'surface' of the clusters and it might depend on the intermolecular packing in the crystalline state. In the experimental spectra, such low energy transitions within *ca.* 300-400 nm are observed as a weak absorption tail. Their relative intensities are apparently overestimated by the calculations.

Next, we have calculated excited triplet states ( $T_n$ ). The calculated energies (shown in Table S12, S13) of the first triplet state ( $T_1$ ) are too high to correspond to the wavelength of the phosphorescence observed in the solid state. However, phosphorescence proceeds from relaxed triplet ( $T_1'$ ), and geometry optimization of  $T_1$  changes its energy drastically. The copper cores of the clusters undergo extensive rearrangement upon excited state relaxation (Fig. S46). While the  $T_1'$  energy of  $\text{Cu}_4@o\text{CBT}$  gets close to that of the observed solid state phosphorescence, the value calculated for  $\text{Cu}_4@i\text{CBT}$  decreases even more, perhaps due to inefficient calculation of the spin orbit coupling for the iodinated compound. The low energies of the relaxed excited states may explain why phosphorescence is not observed in solution.

NTOs of  $T_1$  and  $T_1'$  provide another insight into their properties (Fig. 4i and S47). In all these clusters, the hole orbitals are located along the  $\text{Cu}_4\text{S}_4$  rim, while the excited electron orbitals are mainly concentrated within the  $\text{Cu}_4$  core. In  $\text{Cu}_4@o\text{CBT}$  (Fig. 4i) and  $\text{Cu}_4@m\text{CBT}$  (Fig. S47a), the hole and electron orbitals are almost perfectly symmetric, unaffected by the different orientations of the carborane ligands and the  $T_1$  excitations proceeds concentrically from the rim of the cluster to its core. On the other hand, even though the iodine atoms of  $\text{Cu}_4@i\text{CBT}$  (Fig. S47b) participate in the NTOs to a limited extent, the hole orbital is shifted towards the pair of axially oriented carborane cages, where one copper atom is in close contact with two iodine atoms, while the electron orbital leans towards the equatorially attached ligand pair and the lone copper atom with no contact with iodine atoms. This shift creates a dipole between the excited electron and the hole that in solution interacts with the polarisable continuum of the solvent. This is why the  $T_1$





energies of Cu<sub>4</sub>@oCBT and Cu<sub>4</sub>@mCBT do not change in solution but that of Cu<sub>4</sub>@ICBT increases (Table S12 and S13).

View Article Online  
DOI: 10.1039/D2SC06578A

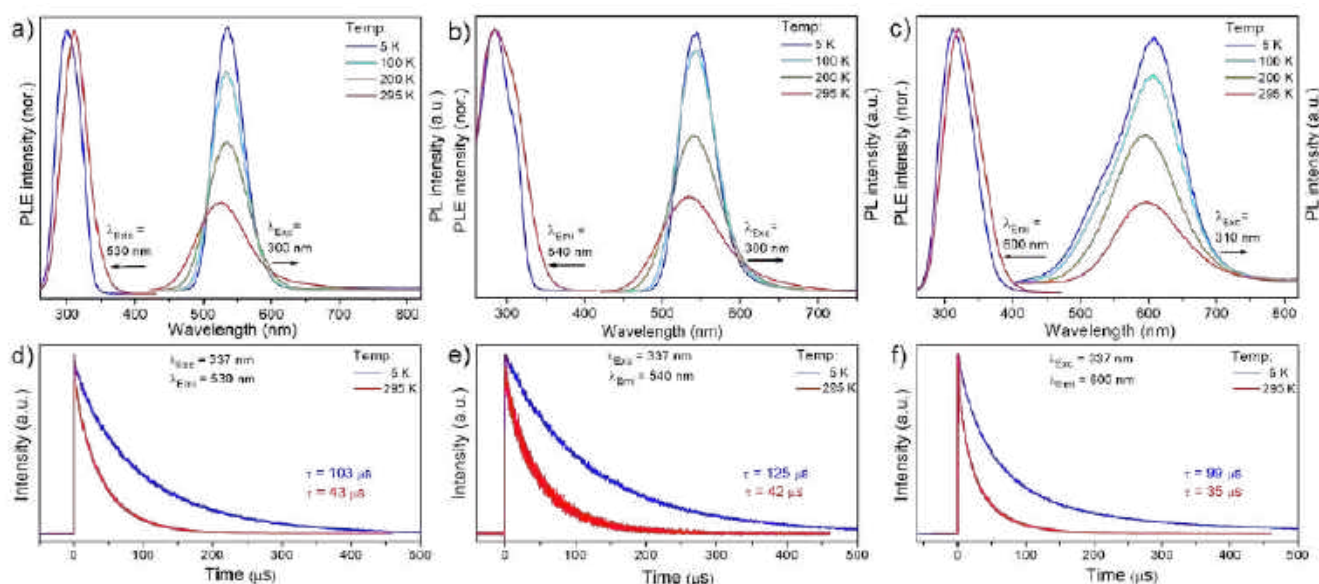


**Fig. 5** Low temperature (from 298 K to 5 K) photoluminescence excitation and emission spectra of a) Cu<sub>4</sub>@oCBT, b) Cu<sub>4</sub>@mCBT and c) Cu<sub>4</sub>@ICBT, respectively in solid (polycrystalline) phase. Comparative emission decay traces of d) Cu<sub>4</sub>@oCBT, e) Cu<sub>4</sub>@mCBT and f) Cu<sub>4</sub>@ICBT at 5 and 295 K, excited with a ns-pulsed laser at 337 nm. The PL decays of Cu<sub>4</sub>@oCBT and Cu<sub>4</sub>@mCBT follow exponential kinetics with the indicated lifetimes; those of Cu<sub>4</sub>@ICBT deviate from monoexponential curves; the indicated lifetimes are average values derived from biexponential fits.

In addition, we have performed low-temperature photophysical measurements. As shown in Fig. 5a, the emission maximum at 525 nm of the Cu<sub>4</sub>@oCBT was gradually shifted to 535 nm upon reducing the temperature from 295 to 5 K. Similar type of emission features were also observed for Cu<sub>4</sub>@mCBT, where emission centered at 533 nm was shifted to 543 nm with 1.5-fold emission enhancement (Fig. 5b). The 595 nm peak got shifted to 606 nm for Cu<sub>4</sub>@ICBT upon cooling the sample from 295 to 5 K (Fig. 5c). From the intensity variation, we have estimated that the quantum yields at 5 K approach ~100 % for Cu<sub>4</sub>@oCBT and Cu<sub>4</sub>@mCBT but ~50 % for Cu<sub>4</sub>@ICBT. Phosphorescence lifetimes of all these clusters moderately increase upon cooling down the sample to 5 K. For Cu<sub>4</sub>@oCBT, lifetime becomes 103 μs at 5 K compared to 43 μs at room temperature (Fig. 5d). For Cu<sub>4</sub>@mCBT and Cu<sub>4</sub>@ICBT, 42 and 35 μs lifetime at room temperature increases to 125 and 99 μs, respectively (Fig. 5e and 5f). Respective fittings of the lifetime profiles are shown in Fig. S48. The change in the emissive lifetime for all three clusters at low temperature showed their emission to be phosphorescence rather than thermally activated delayed fluorescence (TADF). Efficient spin-orbit coupling between copper and carborane-thiol promotes phosphorescence.

**Table 2.** Photophysical parameters of Cu<sub>4</sub> clusters in air atmosphere.

Clusters	$\lambda_{\max}$ (nm)	$\tau_{\text{air}}$ (μs)	$\Phi_{\text{air}}$
Cu <sub>4</sub> @oCBT	525 (295 K)	43 (295 K) <sup>a</sup>	81 % (295 K)
	535 (5 K)	103 (5 K) <sup>a</sup>	100 % (5 K)
Cu <sub>4</sub> @mCBT	533 (295 K)	42 (295 K) <sup>a</sup>	59 % (295 K)
	543 (5 K)	125 (5 K) <sup>a</sup>	98 % (5 K)
Cu <sub>4</sub> @ICBT	595 (295 K)	35 (295 K) <sup>b</sup>	18 % (295 K)

	606 (5 K)	99 (5 K) <sup>b</sup>	50 % (5 K)
--	-----------	-----------------------	------------

Note: <sup>a</sup>monoexponential decay profile, <sup>b</sup>average lifetime obtained from biexponential fit.

### Mechanoresponsive luminescence

Mechanoresponsive-luminescence has been observed in these materials similar to previously reported phosphine protected copper complexes.<sup>69-71</sup> We observed this by mechanical grinding. Cu<sub>4</sub>@oCBT and Cu<sub>4</sub>@mCBT clusters exhibit significant changes in their luminescence behavior upon mechanical grinding. The iodinated analogue, Cu<sub>4</sub>@ICBT is resistant to mechanical activity. Grinding the crystalline samples of Cu<sub>4</sub>@oCBT and Cu<sub>4</sub>@mCBT using a mortar and pestle leads to changes in emission from green to yellow, without change in their appearance to the naked eye (Fig. 6a and 6b). We have observed that 20-25 min grinding of Cu<sub>4</sub>@oCBT is required to complete the transition from green to yellow, whereas only 8-10 min grinding is required for Cu<sub>4</sub>@mCBT. Cu<sub>4</sub>@ICBT didn't show any visible luminescence change after 20 min of grinding (Fig. 6c). PL spectral measurements showed that the emission maxima at 525 and 533 nm of the as-prepared Cu<sub>4</sub>@oCBT and Cu<sub>4</sub>@mCBT clusters shifted to 566 and 594 nm, respectively, upon grinding (Fig. 6d and 6e). We have also observed an increase in full width at half maximum (fwhm) of the ground sample from 100 to 131 nm for Cu<sub>4</sub>@oCBT and from 97 to 120 nm for Cu<sub>4</sub>@mCBT. The broader emission is likely due to the higher structural heterogeneity by grinding. The emission maximum at 595 nm of Cu<sub>4</sub>@ICBT remains the same, *i.e.*, unaffected by grinding (Fig. 6f). We have also observed regeneration of luminescence from ground samples back to the initial state by exposure to DCM vapours. The yellow emission from the ground samples changed to green after 30 min of vapour exposure.

Powder X-ray diffraction studies were performed to understand the phase transitions during the grinding and vapour exposure process.





For all of these samples, the characteristic diffraction peaks matched well with the simulated PXRD pattern, which indicated crystalline purity (Fig. 6g, 6h, 6i and Tables S14, S15, S16). The broad diffraction features of the ground samples suggest crystalline to amorphous transition. The appearance of sharp diffraction peaks from the vapour exposed samples indicates an amorphous to crystalline phase transition, which is accompanied by regained green emission. The reversible mechanoluminescence of  $\text{Cu}_4@o\text{CBT}$  and  $\text{Cu}_4@m\text{CBT}$  make them suitable for pressure-sensing applications. Raman studies (Fig. S49 and S50 for  $\text{Cu}_4@o\text{CBT}$  and  $\text{Cu}_4@m\text{CBT}$ , respectively) were performed to understand structural details at the molecular level. The ground  $\text{Cu}_4@o\text{CBT}$  and  $\text{Cu}_4@m\text{CBT}$  samples show broad spectral signatures with a slight shift of BB, BC, BBB and BBC vibrational

features. We have observed a reversible shift of the icosahedral cage breathing vibrational mode from  $764$  to  $757$   $\text{cm}^{-1}$  upon grinding, which returned to  $763$   $\text{cm}^{-1}$  upon solvent exposure. Spectral shifts of  $26$  and  $18$   $\text{cm}^{-1}$  for BH stretching modes were also observed for  $\text{Cu}_4@o\text{CBT}$  and  $\text{Cu}_4@m\text{CBT}$ , respectively. These studies clearly confirm changes of structural microenvironments during respective operations, which was also observed for copper complexes, studied through solid state NMR studies.<sup>72,73</sup> The nearly planar structure of  $\text{Cu}_4@i\text{CBT}$  with longer Cu-Cu bond distances than the other clusters makes it so relaxed that it is unresponsive to mechanical grinding. Therefore, the variation of the changes in emission of  $\text{Cu}_4@o\text{CBT}$  and  $\text{Cu}_4@m\text{CBT}$  can be attributed to their structural relaxation upon grinding and subsequent rigidification upon solvent exposure.

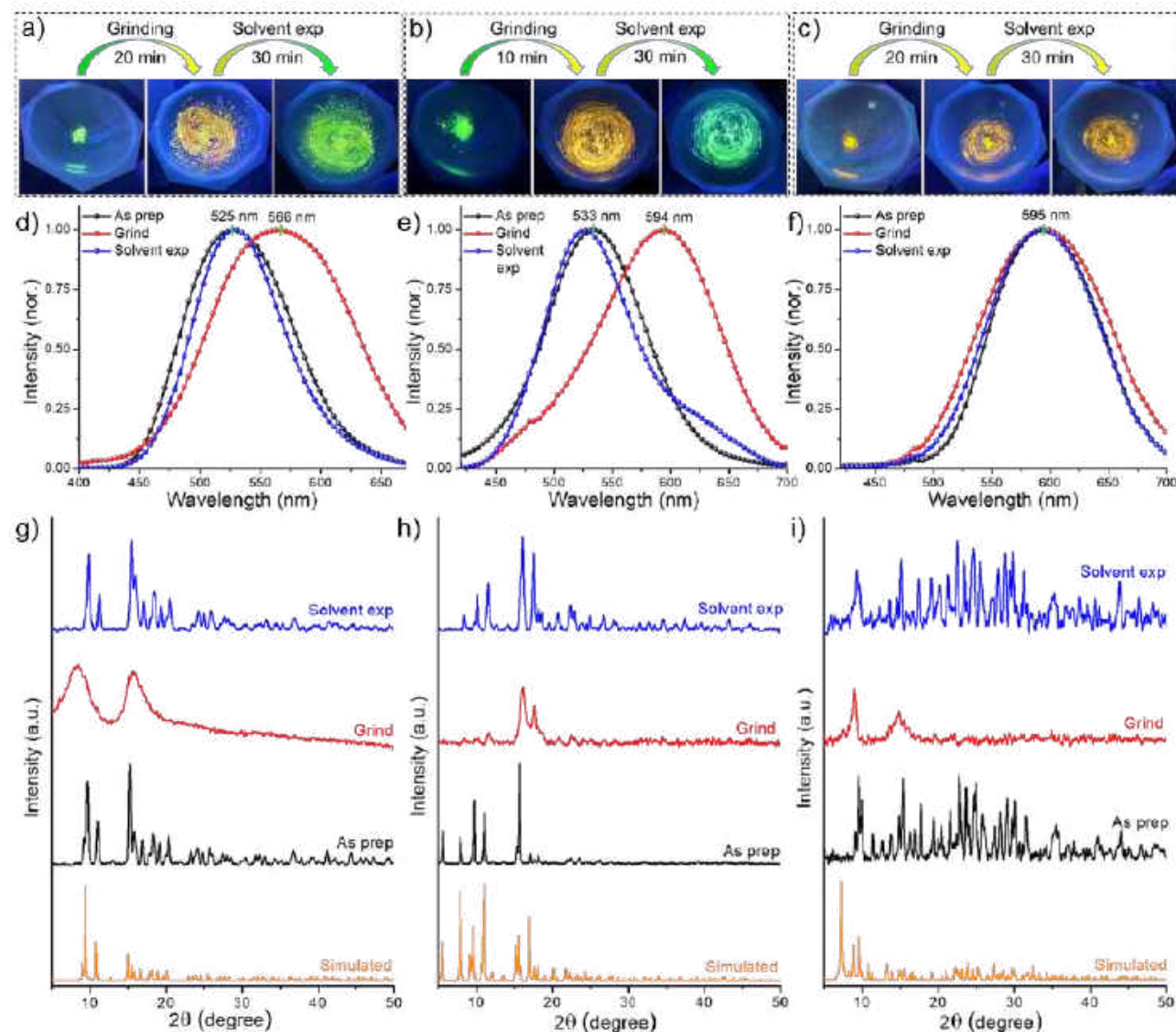


**Fig. 6** Photographic images of a)  $\text{Cu}_4@o\text{CBT}$  and b)  $\text{Cu}_4@m\text{CBT}$  clusters show visible luminescence changes from green to yellow upon mechanical grinding. Luminescence was regenerated upon exposure of vapours of DCM. c)  $\text{Cu}_4@i\text{CBT}$  shows unaltered mechanoresponsive behaviour. Photoluminescence spectra of the grinding-solvent exposure cycle of d)  $\text{Cu}_4@o\text{CBT}$ , e)  $\text{Cu}_4@m\text{CBT}$  and f)  $\text{Cu}_4@i\text{CBT}$ . PXRD spectra of g)  $\text{Cu}_4@o\text{CBT}$ , h)  $\text{Cu}_4@m\text{CBT}$  and i)  $\text{Cu}_4@i\text{CBT}$  reveal a reduction of crystallinity upon grinding and regenerating the crystallinity upon solvent exposure.



## ARTICLE

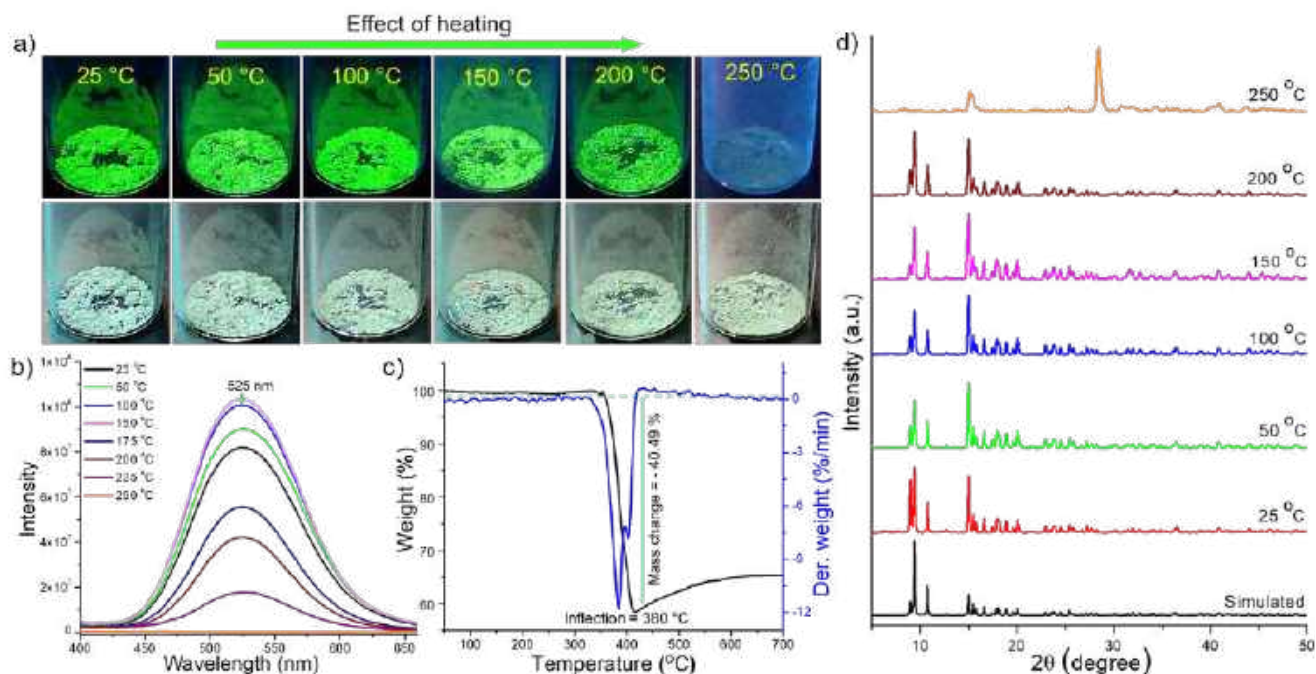


**Fig. 7** Thermo-stable luminescence of Cu<sub>4</sub>@oCBT crystals. a) Photographs show retained green emission up to 200 °C, without changes in visible color. b) Emission spectra measured after heating at different temperatures show that the emission peak position remains the same up to 200 °C. c) TG and DTG measured in nitrogen, shows thermal stability of the crystals up to 380 °C. d) PXRD patterns showed identical diffraction peaks up to 200 °C, which indicate superior structural stability. Simulated spectrum is built with the single crystal data. All the data correspond to samples at room temperature, exposed to the temperature mentioned for 4 h.

### Thermo-responsive luminescence

In addition to mechanoresponsive behaviour, we have investigated thermal dependence of luminescence as well. These experiments were carried out using ~150 mg microcrystals at ambient condition. Fig. 7a shows a series of photographs of Cu<sub>4</sub>@oCBT, exhibiting green emission from crystals after heating to 200 °C. No significant changes in the physical texture and color of the crystals were observed during thermal treatment. PL measurements (shown in Fig. 7b) show 1.1–1.3 fold emission enhancement up to 150 °C. Further heating, above 150 °C, slightly reduced the emission intensity. A 1.5, 2.0 and 4.5-fold reduction in emission was observed at 175, 200, 225 °C heating, respectively. Further heating of the sample above 250 °C, quenches the emission completely due to decomposition of the structure.

TG and DTG shown in Fig. 7c further confirms the stability of the Cu<sub>4</sub>@oCBT cluster. There is no mass loss up to 350 °C. Heating above 380 °C leads to the loss of 40 % of its mass due to degradation of two carborane-thiol ligands along with a sulfur atom. Differential scanning calorimetry (DSC) (Fig. S51) also confirms its superior thermal stability. Full range PXRD spectra of samples heated to different temperatures (Fig. 7d) show preservation of the diffraction pattern up to 200 °C. Upon heating the sample to 250 °C leads to quenching of luminescence, in addition to irreversible structural changes. Spectral analysis reveals no significant enhancement of the spectral sharpness at low angle (below 25°) diffraction peaks, which

indicates that there is no major phase transformation upon heating. The higher angle diffraction peaks, such as 2θ at 36.51°, 40.82°, 43.97° and 45.36° become sharper upon heating the sample to 150 °C (Fig. S52). This can be rationalized by better crystallinity of the sample along with slight emission enhancement upon initial heating. However, the PXRD diffraction pattern of 250 °C heated sample shows the complete loss of crystallinity, which is also manifested by the complete quenching of the luminescence. All together, these studies confirm that the rigid Cu<sub>4</sub>@oCBT crystals show high luminescence stability over a relatively broad temperature range.

On the other hand, nearly isostructural Cu<sub>4</sub>@mCBT shows interesting thermal dependence of luminescence in its crystalline state. Fig. 8a shows photographic images of the sample during heating. Crystalline samples heated up to 100 °C show bright green luminescence followed by a turn to yellow emission (at about 150 °C) which was observed up to 200 °C. Consistent with Cu<sub>4</sub>@oCBT, further heating to 250 °C leads to structural degradation (formation of black powder) and disappearance of the luminescence. PL measurements showed a 1.1–1.2 fold emission enhancement up to 100 °C (Fig. 8b). At 125 °C, there is 1.1-fold reduction in emission. The 533 nm peak position remains the same up to 125 °C, matching with the visible green emission. We have observed double emission peaks at 510 and 612 nm from the sample heated to 150 °C. Similar peaks were also observed with samples heated to 200 °C. The appearance of a double





emission band at 150 °C is probably due to the thermal expansion of the crystalline lattice and associated changes in the electronic excited state.

View Article Online  
DOI: 10.1039/D2SC06578A

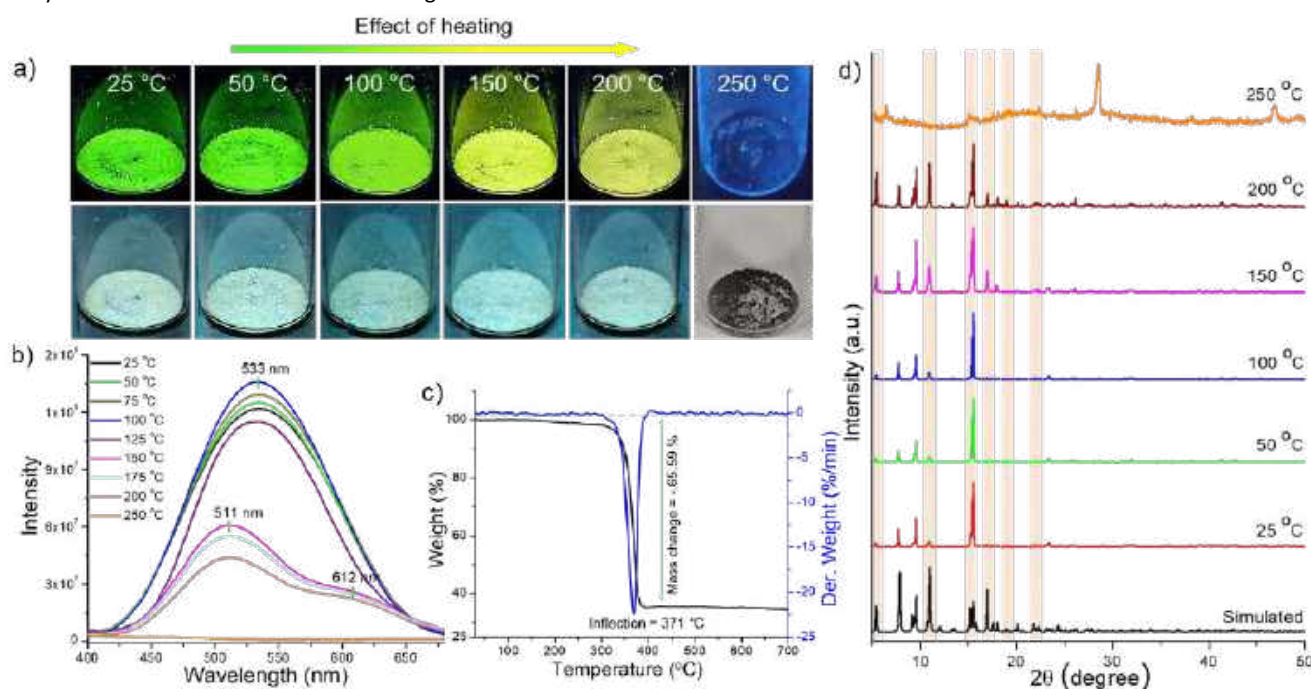


**Fig. 8** Temperature-dependent tunable luminescence of  $\text{Cu}_4@m\text{CBT}$  crystals; a) photographs show green emitting crystals become yellow emitting after heating at 150 °C. Similar yellowish emission was observed up to 200 °C. b) Photoluminescence spectra show nearly similar emission maximum (533 nm) up to 125 °C heating, whereas heating at 150 °C leads to new peaks at 511 and 612 nm. c) TG and DTG analyses show thermal stability of the crystals up to 371 °C. d) PXRD patterns show the appearance of new diffraction peaks after 150 °C heating, indicating structural transformation upon heating. Simulated spectrum was built with the single crystal data. All the data in Fig. a, b and d were measured at room temperature after heating the sample to the required temperature for 4 h.

TG and DTG showed thermal stability up to 371 °C (Fig. 8c). The 65.59 % mass loss indicates desorption of  $[\text{CuS}(\text{C}_2\text{B}_{10}\text{H}_{11}\text{S})_3]$  beyond 371 °C. We have not observed any phase transition in TG/DTG analysis. In contrast, the DSC result shows an exothermic peak in the window of 250–300 °C (Fig. S53). PXRD measurements of the heated samples showed the appearance of new diffraction peaks after heating the sample at 150 °C (Fig. 8d). Magnified spectra shown in Fig. S54 reveals the appearance of new diffraction peaks at  $2\theta$  of 9.197°, 9.395°, 16.986°, 18.059°, 18.962°, due to (012), (10-2), (121), (10-6), (21-3) lattice planes. Reduction of the peak intensity was also observed at higher angles. So the appearance of new lattice planes, along with the reduction of some others, is due to structural change inside the crystal lattice. The flexible nature makes emission properties of  $\text{Cu}_4@m\text{CBT}$  tunable.

Thermogravimetric analysis shows lower thermal stability of the  $\text{Cu}_4@i\text{CBT}$  compared to the other two clusters. At 130.5 °C, there is a mass loss of 13.68 % (Fig. S55) corresponding to one carboranethiolate ligand. DSC data show an endothermic peak at 129.3 °C (Fig. S56). We haven't observed any temperature dependence of luminescence for  $\text{Cu}_4@i\text{CBT}$ .

## Conclusions

This work presents a class of isostructural tetranuclear copper NCs protected by carborane thiol ligands. Single crystal XRD depicts all of these clusters have a square planar  $\text{Cu}_4$  core and a butterfly-shaped  $\text{Cu}_4\text{S}_4$  staple, surrounded by respective carboranes. Three iodine insertions in the  $\text{Cu}_4@i\text{CBT}$  makes the  $\text{Cu}_4\text{S}_4$  staple more flattened than other nanoclusters. High-resolution mass spectrometric studies and other spectroscopic and microscopic studies further confirm the

molecular composition of these clusters and associated structural details. All of these clusters emit negligibly in solution, whereas bright visible emission was observed in solid state due to intermolecular aggregation manifested by their CIE and AIE characteristics. Tuning the emission from green to yellow was observed due to structural flattening of  $\text{Cu}_4@i\text{CBT}$  in the crystalline state. Emission lifetimes of microsecond range indicate phosphorescence, originating from triplet states which was verified by oxygen quenching experiments. DFT calculation verified radiative relaxation from the relaxed triplet state. We observed mechanoresponsive luminescence switching of  $\text{Cu}_4@o\text{CBT}$  and  $\text{Cu}_4@m\text{CBT}$  upon mechanical grinding and subsequent solvent exposure.  $\text{Cu}_4@i\text{CBT}$  is silent to mechanical treatment. Among these clusters,  $\text{Cu}_4@m\text{CBT}$  shows thermoresponsive luminescence. Systematic investigations using different spectroscopic and microscopic studies proved that structural modification due to aggregation and external stimuli manifests in the change of their phosphorescence properties. This work thus presents a new class of coinage metal NCs with bright and thermally stable phosphorescence, which in addition can be efficiently tuned via manipulating the excited states.

## Experimental section

### Chemicals

*Ortho*-carborane 9-thiol ( $\text{O}_9$ ), *meta*-carborane 9-thiol ( $\text{M}_9$ ) and *ortho*-carborane 12-iodo 9-thiol ( $\text{I}_9$ ) were synthesized according to the literature.<sup>74,75</sup> The purity of each ligand was confirmed by their characteristic mass spectrometric analyses, presented in Fig. S57, S58 and S59, respectively. While the  $\text{O}_9$  and  $\text{M}_9$  X-ray single-crystal



structures were reported previously, the molecular structure of  $I_9$  ligand is provided together with the respective discussion of its supramolecular structure in the Supporting Information (Fig. S60-S62). Copper iodide (CuI) and sodium borohydride ( $\text{NaBH}_4$ , 98%) were purchased from Aldrich chemicals. 1,2-bis-(diphenylphosphino)ethane (DPPE) was purchased from Rankem chemicals. Solvent grade dichloromethane (DCM), chloroform ( $\text{CHCl}_3$ ), n-hexane, acetone, acetonitrile and methanol (99.5%) were purchased from Rankem and Finar India, respectively. Deuterated solvents such as  $\text{CDCl}_3$  and  $d_6$ -acetone were purchased from Sigma Aldrich. All of the chemicals were commercially available and used as received. Crystallization was achieved in HPLC-grade solvents.

#### Synthesis of $[\text{Cu}_{18}(\text{DPPE})_6\text{H}_{16}]^{2+}$

The  $[\text{Cu}_{18}(\text{DPPE})_6\text{H}_{16}]^{2+}$  (shortly,  $\text{Cu}_{18}$ ) cluster was prepared according to the literature.<sup>57</sup> In brief, 95 mg (0.49 mM) CuI was mixed with 120 mg (0.03 mM) DPPE under Argon and dissolved in 15 ml of acetonitrile. After 30 min, the as formed white complexes were reduced by directly adding 180-185 mg of  $\text{NaBH}_4$  powder. After another hour of stirring (750 rpm) at room temperature, an orange colored precipitate was formed which indicated the formation of the cluster. After another 6 hours, the mixture was centrifuged to yield an orange solid which was washed three times using 5 ml of acetonitrile and methanol to remove any starting reagents. Finally, dark orange colored  $\text{Cu}_{18}$  was extracted using DCM for the LEIST reaction. UV-vis and ESI-MS spectra (Fig. S63) were measured to confirm the  $\text{Cu}_{18}$  cluster. The yield was calculated to be 75 % relative to the respective copper precursor.

#### Synthesis of $\text{Cu}_4@o\text{CBT}$

The purified  $\text{Cu}_{18}$  nanocluster (~50 mg) in 15 ml DCM was reacted with 40 mg of  $\text{O}_9$  at room temperature. After 2 h of reaction, as formed yellowish solution yields white color precipitates. Bright green emission from these precipitates was observed under 365 nm UV lamp. After completing the reaction (5 h), microcrystalline white precipitates were washed several times using methanol and DCM to remove any excess of unreacted ligands. The purified microcrystalline cluster was used for further studies (Yield = 85 %).

#### Synthesis of $\text{Cu}_4@m\text{CBT}$ and $\text{Cu}_4@i\text{CBT}$

The  $\text{Cu}_4@m\text{CBT}$  and  $\text{Cu}_4@i\text{CBT}$  were synthesized following similar LEIST reaction as reported above. Instead of using  $\text{O}_9$ , we have used  $\text{M}_9$  and  $\text{I}_9$  as protecting ligands for synthesizing these clusters. As formed  $\text{Cu}_4@m\text{CBT}$  is soluble in DCM from which it was crystallized, whereas  $\text{Cu}_4@i\text{CBT}$  formed a yellow colored microcrystalline insoluble solid (Yield: 75% of  $\text{Cu}_4@m\text{CBT}$  and 80% of  $\text{Cu}_4@i\text{CBT}$ ).

#### Oxygen sensitivity

Nature of the excited state was verified by oxygen sensitivity experiments. A thin layer of the microcrystalline sample was casted on a glass slide, which was exposed to oxygen (exposure time 12 h). PL measurements were performed after oxygen exposure. Nitrogen was subsequently exposed to confirm oxygen sensitivity. Prior to the gas exposure, each sample was put in a vacuum for 1 h.

#### AIE property

The aggregation behaviours of  $\text{Cu}_4@o\text{CBT}$  and  $\text{Cu}_4@m\text{CBT}$  were studied upon dissolving them in acetonitrile. A varying fraction of

water was added to it by keeping the cluster concentration the same (1 mg/ml). Non-emitting acetonitrile solution of these clusters becomes green emitting upon increasing the fraction of water.

#### Grinding and solvent exposure experiments

95-100 mg of freshly prepared microcrystalline powder was ground mechanically using a clean mortar and pestle. Solvent exposure was accomplished by placing the mortar inside a closed chamber with DCM vapour.

#### Thermal heating experiments

A freshly prepared 150-160 mg crystalline powder was placed in a closed glass vial and heated at ambient conditions for 4 h. Just after heating at a specific condition, luminescence and PXRD studies were performed.

#### Author Contributions

A.J. performed the synthesis, crystallization and most of the experimental studies. M.J. and W.A.D. assisted A.J., especially in the synthesis. A.J., J.R. and P.C. performed mass spectrometric studies. A.J. and S.M. conducted Raman studies. G.P. and J.M. performed computational studies. J.M. and T.B. synthesized and purified the carborane thiols ligand used for this work. K.K. and K.L. performed room temperature lifetime and quantum yield measurements. Low temperature photophysical studies were performed by S.L. in the laboratory of M.M.K. Single crystal XRD structure solution performed by S.A. and M.K. S.G.G. was involved in the discussion of experimental data. The first draft of the manuscript was written by A.J. and all the authors have given approval to the final version of the manuscript. T.P. and T.B. supervised the project and finalized the manuscript.

#### Conflicts of interest

There are no conflicts to declare.

#### Acknowledgements

The authors would like to thank Sophisticated Analytical Instrumental Facility, Indian Institute of Technology Madras (SAIF-IITM) for single crystal XRD, solid state UV-vis absorption spectroscopy and thermogravimetric measurements. We acknowledge the CzechNanoLab Research Infrastructure supported by MEYS (CR LM2018110) for crystallographic analysis. For theoretical calculations, computational resources were supplied by the project "e-Infrastruktura CZ" (e-INFRA CZ LM2018140) supported by the Ministry of Education, Youth and Sports of the Czech Republic. A.J. acknowledge financial support from IIT Madras, and M.J. thanks UGC, Govt. of India for their research fellowships. T.P. acknowledges funding from the Centre of Excellence on Molecular Materials and Functions under the Institution of Eminence scheme of IIT Madras. This work is a result of a joint India-Czech project aimed at exploring the potential of atomically precise nanomaterials produced by combining metal and boron clusters, initiated by T.P. and T.B.

#### Funding Sources



Authors acknowledge the support of Department of Science and Technology (DST), Govt. of India and the Ministry of Education, Youth and Sports (MEYS) of Czech Republic for their financial support to the bilateral research projects, DST/INT/Czech/P-16/2020 and LTAIN19152, respectively.

## References

- R. Jin, C. Zeng, M. Zhou and Y. Chen, *Chem. Rev.*, 2016, **116**, 10346–10413.
- X. Kang and M. Zhu, *Chem. Soc. Rev.*, 2019, **48**, 2422–2457.
- I. Chakraborty and T. Pradeep, *Chem. Rev.*, 2017, **117**, 8208–8271.
- A. Jana, P. Chakraborty, W. A. Dar, S. Chandra, E. Khatun, M. P. Kannan, R. H. A. Ras and T. Pradeep, *Chem. Commun.*, 2020, 56, 12550–12553.
- P. Jena and Q. Sun, *Chem. Rev.*, 2018, **118**, 5755–5870.
- A. Jana, M. Jash, A. K. Poonia, G. Paramasivam, M. R. Islam, P. Chakraborty, S. Antharjanam, J. Machacek, S. Ghosh, K. N. V. D. Adarsh, T. Base and T. Pradeep, *ACS Nano*, 2021, **15**, 15781–15793.
- M. Xie, C. Han, Q. Liang, J. Zhang, G. Xie and H. Xu, *Sci. Adv.*, 2019, **5**, 1–9.
- L. L. M. Zhang, G. Zhou, G. Zhou, H. K. Lee, N. Zhao, O. V. Prezhdo and T. C. W. Mak, *Chem. Sci.*, 2019, **10**, 10122–10128.
- Y. Yu, Z. Luo, D. M. Chevrier, D. T. Leong, P. Zhang, D. E. Jiang and J. Xie, *J. Am. Chem. Soc.*, 2014, **136**, 1246–1249.
- L. G. AbdulHalim, M. S. Bootharaju, Q. Tang, S. Del Gobbo, R. G. AbdulHalim, M. Eddaoudi, D. E. Jiang and O. M. Bakr, *J. Am. Chem. Soc.*, 2015, **137**, 11970–11975.
- T. Chen, S. Yang, J. Chai, Y. Song, J. Fan, B. Rao, H. Sheng, H. Yu and M. Zhu, *Sci. Adv.*, 2017, **3**, 1–8.
- a) L. Chen, A. Black, W. J. Parak, C. Klinke and I. Chakraborty, *Aggregate*, 2022, **3**, 1–18. b) A. Jana, P. M. Unnikrishnan, A. K. Poonia, J. Roy, M. Jash, G. Paramasivam, J. Machacek, K. N. V. D. Adarsh, T. Base and T. Pradeep, *Inorg. Chem.*, 2022, **61**, 8593–8603.
- P. C. Ford, E. Cariati and J. Bourassa, *Chem. Rev.*, 1999, **99**, 3625–3647.
- X. Liu and D. Astruc, *Coord. Chem. Rev.*, 2018, **359**, 112–126.
- G. Smolentsev, C. J. Milne, A. Guda, K. Haldrup, J. Szlachetko, N. Azzaroli, C. Cirelli, G. Knopp, R. Bohinc, S. Menzi, G. Pamfilidis, D. Gashi, M. Beck, A. Mozzanica, D. James, C. Bacellar, G. F. Mancini, A. Tereshchenko, V. Shapovalov, W. M. Kwiatek, J. Czaplá-Masztafiak, A. Cannizzo, M. Gazzetto, M. Sander, M. Levantino, V. Kabanova, E. Rychagova, S. Ketkov, M. Olaru, J. Beckmann and M. Vogt, *Nat. Commun.*, 2020, **11**, 1–9.
- G. N. Liu, R. D. Xu, J. S. Guo, J. L. Miao, M. J. Zhang and C. Li, *J. Mater. Chem. C*, 2021, **9**, 8589–8595.
- L. Ai, W. Jiang, Z. Liu, J. Liu, Y. Gao, H. Zou, Z. Wu, Z. Wang, Y. Liu, H. Zhang and B. Yang, *Nanoscale*, 2017, **9**, 12618–12627.
- M. Olaru, E. Rychagova, S. Ketkov, Y. Shynkarenko, S. Yakunin, M. V. Kovalenko, A. Yablonskiy, B. Andreev, F. Kleemiss, J. Beckmann and M. Vogt, *J. Am. Chem. Soc.*, 2020, **142**, 373–381.
- J. J. Wang, H. T. Zhou, J. N. Yang, L. Z. Feng, J. S. Yao, K. H. Song, M. M. Zhou, S. Jin, G. Zhang and H. Bin Yao, *J. Am. Chem. Soc.*, 2021, **143**, 10860–10864.
- K. Kirakci, K. Fejfarová, J. Martinčík, M. Nikl and K. Lang, *Inorg. Chem.*, 2017, **56**, 4609–4614.
- V. W. W. Yam, V. K. M. Au and S. Y. L. Leung, *Chem. Rev.*, 2015, **115**, 7589–7728.
- K. Y. Zhang, Q. Yu, H. Wei, S. Liu, Q. Zhao and W. Huang, *Chem. Rev.*, 2018, **118**, 1770–1839.
- Kenry, C. Chen and B. Liu, *Nat. Commun.*, 2019, **10**, 1–15.
- O. Bolton, D. Lee, J. Jung and J. Kim, *Chem. Mater.*, 2014, **26**, 6644–6649.
- C. Chen, Z. Chi, K. C. Chong, A. S. Batsanov, Z. Yang, Z. Mao, Z. Yang and B. Liu, *Nat. Mater.*, 2021, **20**, 175–180.
- J. Wang, C. Wang, Y. Gong, Q. Liao, M. Han, T. Jiang, Q. Dang, Y. Li, Q. Li and Z. Li, *Angew. Chemie - Int. Ed.*, 2018, **57**, 16821–16826.
- Y. Shoji, Y. Iwabata, Q. Wang, D. Nemoto, A. Sakamoto, N. Tanaka, J. Seino, H. Nakai and T. Fukushima, *J. Am. Chem. Soc.*, 2017, **139**, 2728–2733.
- T. J. Penfold, E. Gindensperger, C. Daniel and C. M. Marian, *Chem. Rev.*, 2018, **118**, 6975–7025.
- Z. He, W. Zhao, J. W. Y. Lam, Q. Peng, H. Ma, G. Liang, Z. Shuai and B. Z. Tang, *Nat. Commun.*, 2017, **8**, 1–7.
- D. G. Cuttill, S. M. Kuang, P. E. Fanwick, D. R. McMillin and R. A. Walton, *J. Am. Chem. Soc.*, 2002, **124**, 6–7.
- T. Lu, J. Y. Wang, D. Tu, Z. N. Chen, X. T. Chen and Z. L. Xue, *Inorg. Chem.*, 2018, **57**, 13618–13630.
- A. Schinabeck, M. J. Leidl and H. Yersin, *J. Phys. Chem. Lett.*, 2018, **9**, 2848–2856.
- H. V. R. Dias, H. V. K. Diyabalanage, M. A. Rawashdeh-Omary, M. A. Franzman and M. A. Omary, *J. Am. Chem. Soc.*, 2003, **125**, 12072–12073.
- I. Roppolo, E. Celasco, A. Fargues, A. Garcia, A. Revaux, G. Dantelle, F. Maroun, T. Gacoin, J. P. Boilot, M. Sangermano and S. Perruchas, *J. Mater. Chem.*, 2011, **21**, 19106–19113.
- P. Ai, M. Mauro, L. De Cola, A. A. Danopoulos and P. Braunstein, *Angew. Chemie - Int. Ed.*, 2016, **55**, 3338–3341.
- A. Baghdasaryan and T. Bürgi, *Nanoscale*, 2021, **13**, 6283–6340.
- Y. Lu and W. Chen, *Chem. Soc. Rev.*, 2012, **41**, 3594–3623.
- J. Wang, X. Gu, H. Ma, Q. Peng, X. Huang, X. Zheng, S. H. P. Sung, G. Shan, J. W. Y. Lam, Z. Shuai and B. Z. Tang, *Nat. Commun.*, 2018, **9**, 1–9.
- Y. Ai, Y. Li, M. H. Y. Chan, G. Xiao, B. Zou and V. W. W. Yam, *J. Am. Chem. Soc.*, 2021, **143**, 10659–10667.
- J. Mei, N. L. C. Leung, R. T. K. Kwok, J. W. Y. Lam and B. Z. Tang, *Chem. Rev.*, 2015, **115**, 11718–11940.
- Z. Y. Zhang and Y. Liu, *Chem. Sci.*, 2019, **10**, 7773–7778.
- S. Cai, H. Ma, H. Shi, H. Wang, X. Wang, L. Xiao, W. Ye, K. Huang, X. Cao, N. Gan, C. Ma, M. Gu, L. Song, H. Xu, Y. Tao, C. Zhang, W. Yao, Z. An and W. Huang, *Nat. Commun.*, 2019, **10**, 1–8.
- L. Sun, W. Zhu, F. Yang, B. Li, X. Ren, X. Zhang and W. Hu, *Phys. Chem. Chem. Phys.*, 2018, **20**, 6009–6023.
- Z. Wu, J. Liu, Y. Gao, H. Liu, T. Li, H. Zou, Z. Wang, K. Zhang, Y. Wang, H. Zhang and B. Yang, *J. Am. Chem. Soc.*, 2015, **137**, 12906–12913.
- S. Perruchas, X. F. L. Goff, S. Maron, I. Maurin, F. Guillen, A. Garcia, T. Gacoin and J. P. Boilot, *J. Am. Chem. Soc.*, 2010, **132**, 10967–10969.
- W. Wei, Y. Lu, W. Chen and S. Chen, *J. Am. Chem. Soc.*, 2011, **133**, 2060–2063.
- S. Perruchas, C. Tard, X. F. Le Goff, A. Fargues, A. Garcia, S. Kahlal, J. Y. Saillard, T. Gacoin and J. P. Boilot, *Inorg. Chem.*, 2011, **50**, 10682–10692.
- S. Shi, M. C. Jung, C. Coburn, A. Tadde, D. M. R. Sylvinson, P. I. Djurovich, S. R. Forrest and M. E. Thompson, *J. Am. Chem. Soc.*, 2019, **141**, 3576–3588.
- K. Basu, S. Paul, R. Jana, A. Datta and A. Banerjee, *ACS Sustain. Chem. Eng.*, 2019, **7**, 1998–2007.
- Y. J. Lin, P. C. Chen, Z. Yuan, J. Y. Ma and H. T. Chang, *Chem. Commun.*, 2015, **51**, 11983–11986.
- R. Núñez, M. Tarrés, A. Ferrer-Ugalde, F. F. De Biani and F. Teixidor, *Chem. Rev.*, 2016, **116**, 14307–14378.
- J. Poater, C. Viñas, I. Bennour, S. Escayola, M. Solà and F. Teixidor, *J. Am. Chem. Soc.*, 2020, **142**, 9396–9407.
- A. M. Spokoiny, C. W. Machan, D. J. Clingerman, M. S. Rosen, M. J. Wiester, R. D. Kennedy, C. L. Stern, A. A. Sarjeant and C. A. Mirkin, *Nat. Chem.*, 2011, **3**, 590–596.





## ARTICLE

Journal Name

- 54 R. Furue, T. Nishimoto, I. S. Park, J. Lee and T. Yasuda, *Angew. Chemie - Int. Ed.*, 2016, **55**, 7171–7175.
- 55 D. Kodr, C. P. Yenice, A. Simonova, D. P. Saftić, R. Pohl, V. Sýkorová, M. Ortiz, L. Havran, M. Fojta, Z. J. Lesnikowski, C. K. O'Sullivan and M. Hocek, *J. Am. Chem. Soc.*, 2021, **143**, 7124–7134.
- 56 Q. Wang, J. Wang, S. Wang, Z. Wang, M. Cao, C. He, J. Yang, S. Zang and T. C. W. Mak, *J. Am. Chem. Soc.*, 2020, **142**, 12010–12014.
- 57 J. Li, H. Z. Ma, G. E. Reid, A. J. Edwards, Y. Hong, J. M. White, R. J. Mulder and R. A. J. O'Hair, *Chem. - A Eur. J.*, 2018, **24**, 2070–2074.
- 58 X. Kang and M. Zhu, *Chem. Mater.*, 2019, **31**, 9939–9969.
- 59 X. Kang, X. Wei, S. Wang and M. Zhu, *Chem. Sci.*, 2021, **12**, 11080–11088.
- 60 X. Kang, L. Huang, W. Liu, L. Xiong, Y. Pei, Z. Sun, S. Wang, S. Wei and M. Zhu, *Chem. Sci.*, 2019, **10**, 8685–8693.
- 61 H. Yan, F. Yang, D. Pan, Y. Lin, J. N. Hohman, D. Solis-Ibarra, F. H. Li, J. E. P. Dahl, R. M. K. Carlson, B. A. Tkachenko, A. A. Fokin, P. R. Schreiner, G. Gallì, W. L. Mao, Z. X. Shen and N. A. Melosh, *Nature*, 2018, **554**, 505–510.
- 62 T. Baše, Z. Bastl, M. Šlouf, M. Klementová, J. Šubrt, A. Vetushka, M. Ledinský, A. Fejfar, J. Macháček, M. J. Carr and M. G. S. Londesborough, *J. Phys. Chem. C*, 2008, **112**, 14446–14455.
- 63 J. J. Schwartz, A. M. Mendoza, N. Wattanatorn, Y. Zhao, V. T. Nguyen, A. M. Spokoyny, C. A. Mirkin, T. Baše and P. S. Weiss, *J. Am. Chem. Soc.*, 2016, **138**, 5957–5967.
- 64 H. A. Mills, C. G. Jones, K. P. Anderson, A. D. Ready, P. I. Djurovich, S. I. Khan, J. N. Hohman, H. M. Nelson and A. M. Spokoyny, *Chem. Mater.*, 2022, **34**, 15, 6933–6943.
- 65 C. P. Ford, *Coord. Chem. Rev.*, 1994, **132**, 129–140.
- 66 J. Troyano, F. Zamora and S. Delgado, *Chem. Soc. Rev.*, 2021, **50**, 4606–4628.
- 67 C. Zhu, J. Xin, J. Li, H. Li, X. Kang, Y. Pei and M. Zhu, *Angew. Chemie - Int. Ed.*, 2022, **61**, 1–6.
- 68 E. Khatun, A. Ghosh, P. Chakraborty, P. Singh, M. Bodiuzzaman, P. Ganesan, G. Nataranjan, J. Ghosh, S. K. Pal and T. Pradeep, *Nanoscale*, 2018, **10**, 20033–20042.
- 69 S. Perruchas, X. F. L. Goff, S. Maron, I. Maurin, F. Guillen, A. Garcia, T. Gacoin and J. P. Boilot, *J. Am. Chem. Soc.*, 2010, **132**, 10967–10969.
- 70 R. Utrera-Melero, B. Huitorel, M. Cordier, J. Y. Mevellec, F. Massuyeau, C. Latouche, C. Martineau-Corcos and S. Perruchas, *Inorg. Chem.*, 2020, **59**, 13607–13620.
- 71 B. Huitorel, H. El Moll, M. Cordier, A. Fargues, A. Garcia, F. Massuyeau, C. Martineau-Corcos, T. Gacoin and S. Perruchas, *Inorg. Chem.*, 2017, **56**, 12379–12388.
- 72 Q. Benito, X. F. Le Goff, S. Maron, A. Fargues, A. Garcia, C. Martineau, F. Taulelle, S. Kahlal, T. Gacoin, J. P. Boilot and S. Perruchas, *J. Am. Chem. Soc.*, 2014, **136**, 11311–11320.
- 73 B. Huitorel, H. El Moll, R. Utrera-Melero, M. Cordier, A. Fargues, A. Garcia, F. Massuyeau, C. Martineau-Corcos, F. Fayon, A. Rakhmatullin, S. Kahlal, J. Y. Saillard, T. Gacoin and S. Perruchas, *Inorg. Chem.*, 2018, **57**, 4328–4339.
- 74 J. Plešek, S. Hermanek, *Collect. Czech Chem. Commun.*, 1981, **46**, 687–692.
- 75 J. Plešek, Z. Janoušek, S. Hermanek, *Czech Chem. Commun.*, 1978, **43**, 1332–1338.

View Article Online  
DOI: 10.1039/D2SC06578A

Chemical Science Accepted Manuscript





## Supporting Information

### **Carborane-thiol protected copper nanoclusters: Stimuli-responsive materials with tunable phosphorescence**

Arijit Jana, Madhuri Jash, Wakeel Ahmed Dar, Jayoti Roy, Papri Chakraborty, Ganesan Paramasivam, Sergei Lebedkin, Kaplan Kirakci, Sujan Manna, Sudhadevi Antharjanam, Jan Machacek, Monika Kucerakova, Sundargopal Ghosh, Kamil Lang, Manfred M. Kappes\*, Tomas Base\* and Thalappil Pradeep\*

#### **Table of contents**

<b>Items</b>	<b>Description</b>	<b>Page No</b>
<b>1.</b>	Instrumentation	4-8
<b>2.</b>	Computational calculation	8
<b>Table S1</b>	Crystal data and structure refinement for I <sub>9</sub>	9
<b>Table S2</b>	Crystal data and structure refinement for Cu <sub>4</sub> @oCBT	10
<b>Table S3</b>	Atomic coordinates and equivalent isotropic displacement parameters for Cu <sub>4</sub> @oCBT	11
<b>Table S4</b>	Crystal data and structure refinement for Cu <sub>4</sub> @mCBT	12
<b>Table S5</b>	Atomic coordinates and equivalent isotropic displacement parameters for Cu <sub>4</sub> @mCBT	13,14
<b>Table S6</b>	Crystal data and structure refinement for Cu <sub>4</sub> @ICBT	15
<b>Table S7</b>	Atomic coordinates and equivalent isotropic displacement parameters for Cu <sub>4</sub> @ICBT	16
<b>Fig. S1</b>	Photographic images of the synthesis and purification of Cu <sub>4</sub> clusters	17
<b>Fig. S2</b>	Optical and SEM microscopic images of Cu <sub>4</sub> @oCBT crystals. EDS elemental analysis and elemental mapping of the same crystal	17
<b>Fig. S3</b>	Optical and SEM microscopic images of Cu <sub>4</sub> @mCBT crystals. EDS elemental analysis and elemental mapping of the crystal	18
<b>Fig. S4</b>	Optical and SEM microscopic images of Cu <sub>4</sub> @ICBT crystals. EDS elemental analysis and elemental mapping of the crystal	18
<b>Fig. S5</b>	Structural anatomy of Cu <sub>4</sub> S <sub>4</sub> kernel of Cu <sub>4</sub> @oCBT	19
<b>Fig. S6</b>	Structures of Cu <sub>4</sub> @oCBT in three different orientation	19
<b>Fig. S7</b>	ORTEP structure of Cu <sub>4</sub> @oCBT	19
<b>Fig. S8</b>	ORTEP structure of Cu <sub>4</sub> @mCBT	20
<b>Fig. S9</b>	ORTEP structure of Cu <sub>4</sub> @ICBT	20
<b>Fig. S10</b>	Unit cell packing of Cu <sub>4</sub> S <sub>4</sub> unit of Cu <sub>4</sub> @oCBT viewed from different crystallographic axis	21
<b>Fig. S11</b>	Unit cell packing of Cu <sub>4</sub> S <sub>4</sub> unit of Cu <sub>4</sub> @mCBT viewed from different crystallographic axis	21
<b>Fig. S12</b>	Unit cell packing of Cu <sub>4</sub> S <sub>4</sub> unit of Cu <sub>4</sub> @ICBT viewed from different crystallographic axis	22
<b>Table S8</b>	Comparative interatomic bond distance and bond angle of the respective Cu <sub>4</sub> clusters	22
<b>Fig. S13</b>	The MS/MS fragmentation pattern of Cu <sub>4</sub> @oCBT at CE 60. Experimental isotopic distribution patterns of the fragments were matches with theoretical spectrum	23
<b>Fig. S14</b>	The MS/MS fragmentation pattern of Cu <sub>4</sub> @ICBT at CE 60.	24

	Experimental isotopic distribution patterns of the fragments were matches with theoretical spectrum	
<b>Fig. S15</b>	TEM micrographs and EDS elemental mapping of Cu <sub>4</sub> @oCBT	25
<b>Fig. S16</b>	TEM micrographs and EDS elemental mapping of Cu <sub>4</sub> @mCBT	26
<b>Fig. S17</b>	TEM micrographs and EDS elemental mapping of Cu <sub>4</sub> @ICBT	27
<b>Fig. S18</b>	TEM micrographs of Cu <sub>4</sub> @ICBT microcrystals indicating their rhombohedral shape	27
<b>Fig. S19</b>	Combined <sup>11</sup> B{ <sup>1</sup> H} NMR spectra of Cu <sub>4</sub> @oCBT and O <sub>9</sub>	28
<b>Table S9</b>	<sup>11</sup> B{ <sup>1</sup> H} NMR chemical shift data for Cu <sub>4</sub> @oCBT and O <sub>9</sub>	28
<b>Fig. S20</b>	Combined <sup>13</sup> C{ <sup>1</sup> H} NMR spectra of Cu <sub>4</sub> @oCBT and O <sub>9</sub>	29
<b>Fig. S21</b>	Combined <sup>11</sup> B{ <sup>1</sup> H} NMR spectra of Cu <sub>4</sub> @mCBT and M <sub>9</sub>	30
<b>Table S10</b>	<sup>11</sup> B{ <sup>1</sup> H} NMR chemical shift data for Cu <sub>4</sub> @mCBT and M <sub>9</sub>	30
<b>Fig. S22</b>	Combined <sup>13</sup> C{ <sup>1</sup> H} NMR spectra of Cu <sub>4</sub> @mCBT and M <sub>9</sub>	31
<b>Fig. S23</b>	Combined <sup>11</sup> B{ <sup>1</sup> H} NMR spectra of Cu <sub>4</sub> @ICBT and I <sub>9</sub>	32
<b>Table S11</b>	<sup>11</sup> B{ <sup>1</sup> H} NMR chemical shift data for Cu <sub>4</sub> @ICBT and I <sub>9</sub>	32
<b>Fig. S24</b>	Combined <sup>13</sup> C{ <sup>1</sup> H} NMR spectra of Cu <sub>4</sub> @ICBT and I <sub>9</sub>	33
<b>Fig. S25</b>	FT-IR spectra of Cu <sub>4</sub> @oCBT along with the O <sub>9</sub>	34
<b>Fig. S26</b>	FT-IR spectra of Cu <sub>4</sub> @mCBT along with the M <sub>9</sub>	35
<b>Fig. S27</b>	FT-IR spectra of Cu <sub>4</sub> @ICBT along with the I <sub>9</sub>	36
<b>Fig. S28</b>	The calculated IR spectra of Cu <sub>4</sub> @oCBT in gas phase	37
<b>Fig. S29</b>	The calculated IR spectra of Cu <sub>4</sub> @mCBT in gas phase	37
<b>Fig. S30</b>	Raman spectra of Cu <sub>4</sub> @oCBT crystals in comparison with O <sub>9</sub> ligand	38
<b>Fig. S31</b>	Raman spectra of Cu <sub>4</sub> @mCBT crystals in comparison with M <sub>9</sub> ligand	38
<b>Fig. S32</b>	Raman spectra of Cu <sub>4</sub> @ICBT crystals in comparison with I <sub>9</sub> ligand	39
<b>Fig. S33</b>	XPS spectra of Cu <sub>4</sub> @oCBT	39
<b>Fig. S34</b>	XPS spectra of Cu <sub>4</sub> @mCBT	40
<b>Fig. S35</b>	XPS spectra of Cu <sub>4</sub> @ICBT	40
<b>Fig. S36</b>	PL spectra of these clusters in solution and respective crystalline state reveals their CIE nature	41
<b>Fig. S37</b>	Photographs and the respective PL spectra of Cu <sub>4</sub> @oCBT and Cu <sub>4</sub> @mCBT suggesting AIE behavior	41
<b>Fig. S38</b>	Structural variation of Cu <sub>4</sub> @oCBT and Cu <sub>4</sub> @mCBT clusters in solution and crystals	42
<b>Fig. S39</b>	Different types of intermolecular interactions present in Cu <sub>4</sub> @oCBT	42
<b>Fig. S40</b>	Different types of intermolecular interaction present in Cu <sub>4</sub> @mCBT	43
<b>Fig. S41</b>	Different types of intermolecular interaction present in Cu <sub>4</sub> @ICBT	43
<b>Fig. S42</b>	Lifetime decay profile of clusters at 295 K with respective fittings	43
<b>Fig. S43</b>	PL spectra indication oxygen sensitivity of these clusters	44
<b>Fig. S44</b>	Natural transition orbitals for singlet excitation of Cu <sub>4</sub> @mCBT	44
<b>Fig. S45</b>	Natural transition orbitals for singlet excitation of Cu <sub>4</sub> @ICBT	45
<b>Table S12</b>	Calculated excited triplet state energies in eV	45
<b>Table S13</b>	Calculated excited triplet state energies in nm	45
<b>Fig. S46</b>	Structural relaxation of the clusters during intersystem crossing	46
<b>Fig. S47</b>	NTOs of T1 and T1' radiative relaxation of a) Cu <sub>4</sub> @mCBT and b) Cu <sub>4</sub> @ICBT clusters.	47
<b>Fig. S48</b>	Lifetime decay profile of clusters at 5 K with respective fittings	47
<b>Table S14</b>	Assignments of different lattice planes (h k l) of Cu <sub>4</sub> @oCBT	47, 48

<b>Table S15</b>	Assignments of different lattice planes (h k l) of Cu <sub>4</sub> @mCBT	48, 49
<b>Table S16</b>	Assignments of different lattice planes (h k l) of Cu <sub>4</sub> @ICBT	49, 50
<b>Fig. S49</b>	Comparative Raman spectra of Cu <sub>4</sub> @oCBT during mechanical grinding and solvent fuming experiment	51
<b>Fig. S50</b>	Comparative Raman spectra of Cu <sub>4</sub> @mCBT during mechanical grinding and solvent fuming experiment	51
<b>Fig. S51</b>	Differential scanning calorimetry data of Cu <sub>4</sub> @oCBT	52
<b>Fig. S52</b>	Magnified PXRD pattern of Cu <sub>4</sub> @oCBT microcrystalline powder after heating at different temperatures	52
<b>Fig. S53</b>	Differential scanning calorimetry data of Cu <sub>4</sub> @mCBT microcrystals	53
<b>Fig. S54</b>	Magnified PXRD pattern of Cu <sub>4</sub> @mCBT microcrystalline powder after heating at different temperatures	53
<b>Fig. S55</b>	TGA DTG spectra shown less thermal stability of Cu <sub>4</sub> @ICBT in comparison to Cu <sub>4</sub> @oCBT and Cu <sub>4</sub> @mCBT	54
<b>Fig. S56</b>	Differential scanning calorimetry profile of Cu <sub>4</sub> @ICBT	54
<b>Fig. S57</b>	ESI-MS spectrum of <i>ortho</i> -carborane 9-thiol	55
<b>Fig. S58</b>	ESI-MS spectrum of <i>meta</i> -carborane 9-thiol	55
<b>Fig. S59</b>	ESI-MS spectrum of <i>ortho</i> -carborane 12-iodo 9-thiol	56
<b>Fig. S60</b>	Molecular structure and unit cell molecular packing of I <sub>9</sub>	56
<b>Fig. S61</b>	Intermolecular interactions between two I <sub>9</sub> units	57
<b>Fig. S62</b>	Molecular structure and combined unit cell molecular packing of I <sub>9</sub>	57
<b>Fig. S63</b>	UV-vis absorption and ESI-MS spectra of [Cu <sub>18</sub> (DPPE) <sub>6</sub> (H) <sub>16</sub> ] <sup>2+</sup>	58
<b>3.</b>	References	59,60

## 1. Instrumentation

### UV-vis spectroscopy

Solid-state absorption spectra of the NCs (as polycrystalline powders dispersed in perfluoroether oil between two quartz plates) were recorded using an Agilent Cary 5000 UV-Vis-NIR spectrophotometer equipped with a 6-inch integrating sphere. As a standard feature of such apparatus, a photodetector (photomultiplier) is placed directly into the sphere, inside a slit on its bottom. This configuration can be, however, problematic for highly luminescent samples, as is the case with the NCs studied in this work. Namely, UV photons absorbed by the NCs (white powders) are efficiently converted into the green or orange luminescence photons which would be detected by the same photomultiplier, resulting to incorrect absorbance values. In fact, even a 'negative absorbance' can be observed in the UV region, if a photomultiplier has a higher sensitivity to the green/ orange light than to the UV one. To minimize such interference of re-emitted light, the photomultiplier in the sphere was covered in our experiment with a short-pass dielectric filter (Edmund Optics) transmitting light within ca. 240-500 nm and blocking the NCs emission over ca. 510-700 nm. Accordingly, the solid-state absorption spectra were measured within a limited spectral range of 250-490 nm (Figure 4a-c). Absorption spectra in solution were recorded in standard cuvettes using a PerkinElmer Lambda 365 spectrometer in the wavelength range of 200-800 nm.

### Mass spectrometry

Mass spectra of *ortho*-carborane 9-thiol, *meta*-carborane 9-thiol and *ortho*-carborane 12-iodo 9-thiol were recorded using an ion-trap Thermo Scientific LTQ XL mass spectrometer. Mass spectra of all these  $Cu_4$  clusters were measured using Waters Synapt G2Si HDMS instrument. The instrument is equipped with electrospray ionization source, step wave ion transfer optics and a quadrupole mass filter. 1 mM formic acid and cesium acetate were used as a protonation source. Mass spectrum of the nanoclusters were recorded in positive ion-mode. An optimized condition of capillary voltage 3 kV, cone voltage 0 kV, spray current 110 nA, source temperature 50 °C and desolvation temperature 90 °C with gas flow rate of 300 L/h were used for these measurements. Collision energy dependent fragmentation studies were performed upon selecting the particular ion inside the ion mobility cell of the same instrument.

### Photoluminescence

Photoluminescence spectra were measured using Horiba Jobin Yvon Nanolog and Fluorolog-3 spectrometers. The latter instrument was equipped with an optical cryostat based on a closed-cycle helium cryocooler (Cryomex), operating within a temperature range of 5-300 K. Fast freezing of sample solutions and their cooling down was done by inserting a quartz tube with the probe into an optical Dewar filled with liquid nitrogen. All emission spectra were corrected for wavelength-dependent response of the spectrometer and detector (in relative photon flux units).

### **Lifetime and quantum yield**

Luminescence lifetime measurements at ambient temperature were performed using a Fluorolog-3 spectrometer equipped with a cooled TBX-05-C photon detection module (Horiba JobinYvon). The excitation wavelength was 390 nm (SpectraLED-390, Horiba Scientific) and emission wavelength was selected at the maxima of the luminescence emission spectra. The decay curves were recorded in air atmosphere and were fitted to exponential functions by the iterative reconvolution procedure of the DAS6 software (v. 6.8, Horiba Jobin Yvon). The temperature-dependent PL decay in the cryostat was recorded by connecting a photomultiplier to a fast digital oscilloscope (via a 50, 500, 2.500 or 10.000 Ohm load depending on the decay time scale) and using a nsec-pulsed nitrogen laser for excitation at 337 nm. Absolute photoluminescence quantum yields of powder samples were measured at ambient temperature using a Quantaaurus QY C11347-1 spectrometer (Hamamatsu).

### **Infrared spectroscopy**

Perkin Elmer FT-IR spectrometer was used to measure the samples. Each pellet was prepared by mixing 2.0 mg NCs with 20 mg dry KBr.

### **Raman spectroscopy**

Raman spectra were recorded using a CRM-Alpha 300S, WI Tec GmbH confocal Raman microscope, equipped with 532 nm frequency doubled Nd:YAG laser and 632 nm Helium Neon laser.

### **NMR spectroscopy**

Proton decoupled  $^{13}\text{C}$  and  $^{11}\text{B}$  NMR spectra were recorded in its respective deuterated solvents, using a Bruker Avance 500 MHz ( $^{13}\text{C}$ -125 MHz and  $^{11}\text{B}$ -160 MHz) spectrometer. All of the data are processed using Mest-Re Nova NMR software. NMR spectrum for  $\text{Cu}_4@o\text{CBT}$  and  $\text{Cu}_4@i\text{CBT}$  clusters were recorded using  $d_6$ -acetone solvent. All of the carborane ligands and  $\text{Cu}_4@m\text{CBT}$  NMR data were measured using  $\text{CDCl}_3$  (99.99 % pure) solvent.

### **X-ray photoelectron spectroscopy**

X-ray photoelectron spectroscopy were recorded using ESCA probe TPD equipped with polychromatic Mg  $K\alpha$  X ray source ( $h\nu = 1253.6$  eV).

### **Powder XRD**

Powder XRD measurements were performed using a D8 Advance, Bruker instruments using Cu  $K\alpha$  as a X-Ray source ( $h\nu = 8047.8$  eV). Sample drop casted on a glass slide, like a thin film was used for all the PXRD measurements.

## Thermogravimetric analysis

Thermogravimetric (TG) measurements of about 3.5 mg of cluster sample in an alumina crucible were performed using a NETZSCH STA 449 F3 Jupiter instruments equipped with Proteus-6.1.0 software. Both the measurements were performed under nitrogen atmosphere at flow rate of 20 ml/min in the temperature range of 30 to 700 °C with a heating rate of 10 °C/min.

## Single-crystal XRD of Cu<sub>4</sub> clusters

Single crystal X-ray diffraction (SC-XRD) data collection of Cu<sub>4</sub> clusters was performed with Bruker D8 VENTURE single crystal X-ray diffractometer equipped with graphite monochromatic Mo (K $\alpha$ ) ( $\lambda = 0.71073 \text{ \AA}$ ) radiation and PHOTON 100 CMOS detector. The data collection was performed at 296 K for Cu<sub>4</sub>@oCBT and Cu<sub>4</sub>@mCBT and at liquid nitrogen temperature of 200 K for the crystal of Cu<sub>4</sub>@ICBT. The automatic cell determination routine, with 24 frames at two different orientations of the detector was employed to collect reflections for unit cell determination. Further, intensity data for structure determination were collected through an optimized strategy which gave an average 4-fold redundancy. The program APEX3-SAINT (Bruker, 2016) was used for integrating the frames, followed by a multi-scan absorption correction using the program SADABS (Bruker, 2016). The structure was solved by SHELXT-2014 (Sheldrick, 2014) and refined by full-matrix least squares techniques using SHELXL-2018, (Sheldrick, 2018) software package. Hydrogens on all carbon and boron atoms were fixed at calculated positions and refined as riding model with C-H or B-H = 1.10  $\text{\AA}$ , Uiso(H) = 1.2Ueq (C or B).

For, Cu<sub>4</sub>@oCBT crystal data was refined as a two component inversion twin with a BASF value of 0.188. The refinement was converged with an R1 value of 0.051. In this case an alert level B was observed in the IUCR check cif report which is primarily due to disorder in carborane moiety and also due to twinning of the crystal lattice.

In the case of Cu<sub>4</sub>@mCBT, the higher angle reflections are very weak ( $\theta > 23.3^\circ$ ) due to poor resolution of the crystal which caused high Rint value of 0.18 (R1 = 0.098). Five B level alerts were observed in the IUCR check cif report which were explained through validating response form at the end of the corresponding cif file.

For Cu<sub>4</sub>@ICBT, high resolution data is very weak and hence a resolution cut ( $\sim 1.0 \text{ \AA}$ ) was made during data integration. The data was refined as two component inversion twin with BASF value of 0.286. Due to very high thermal and rotational disorder of carborane moieties and also due to poor resolution data, DFIX restraint was applied to their bond distances (a target value of 1.72  $\text{\AA}$ ) to maintain a sensible molecular geometry. Also SIMU restraint was applied to atoms in the carborane moieties with an effective standard deviation of 0.02  $\text{\AA}^2$  to have the same Uij components. The components of the anisotropic displacement parameters in the direction of the bond are restrained to be equal for all non-hydrogen atoms using DELU restraint. The solvent



electron density could not be modelled satisfactorily due to difficulty in locating their position in this low resolution data and hence squeezed using PLATON (version 10719) and the squeeze results are appended in the corresponding cif file. Several attempts were made to collect SC-XRD data at room temperature as well as at low temperatures. This is the best data we could obtain after repeated attempts. Although, it is a low resolution data, the structure is presented here to describe its formation with the support of other experimental findings. A cif check report was made using the service of IUCR in which A and B level alerts were explained at the end of the corresponding cif file as validation response form.

### **SC-XRD of I<sub>9</sub> ligand**

Crystals suitable for single crystal X-ray diffraction were obtained by slow sublimation of I<sub>9</sub> in a sealed ampoule over a few weeks. Single crystal was measured at 95 K on a Supernova four-circles diffractometer equipped with a CCD Atlas S2 detector, using the mirrors-collimated Cu-K $\alpha$  radiation ( $\lambda = 1.54184 \text{ \AA}$ ) from a micro-focus tube and a Cryostream 800 + chiller. The CrysAlis program suite was used for the unit cell determination and data reduction.<sup>1</sup> The crystal structure was solved by charge-flipping using program SUPERFLIP<sup>2</sup> and refined by full-matrix least-squares on F2 using the Jana2020 program package, not yet published successor of Jana2006.<sup>3</sup>

Hydrogen atoms bonded to C and B atoms were discernible in difference Fourier maps and were kept in ideal positions with C–H distance = 0.96  $\text{\AA}$  and B–H distance = 1  $\text{\AA}$ . For all hydrogen atoms, Uiso(H) was set to 1.2Ueq(C/B) of the parent atom. Precise position of the hydrogen atom attached to sulfur in the structure of I<sub>9</sub> was not observed in the difference Fourier map, probably due to multiple possible positions. All non-hydrogen atoms were refined using harmonic refinement. The structure shows two independent molecules per unit cell with a disorder manifested by mixed sulfur and iodine occupancies. Mixed site S/I occupancies 0.768:0.232 for one molecule and 0.933:0.067 for the other molecules per unit cell solved the problems of some atoms showing negative thermal parameters.

In the structure, the residual electron density occurs close to the atoms B<sub>5</sub> and B<sub>11</sub>. These maxima probably correspond to an iodine atom with an occupation of 0.02 and point to possible additional disorder of both molecules. However, boron or carbon atoms with 2% occupation is not possible to observe in the electron density map. Apparently, reliable description of the disorder in is far beyond resolution of our data, although there is no doubt it exists. For these reasons, we did not introduce disorder to the final structure model.

### **Optical imaging**

Optical microscopic images of the crystal were collected in different magnification using LEICA optical microscope equipped with LAS V4.8 software.

## SEM imaging

The SEM measurements were performed using FEI quanta environmental scanning electron microscope (ESEM) at high vacuum mode at operating voltage 30 kV. EDAX spectra and elemental imaging were recorded using the same instruments.

## TEM imaging

Dimension of the nanoclusters were recorded using Transmission electron microscopy, which was recorded using a JEOL 3010 high resolution transmission electron microscope operated at 200 kV. A Gatan multistage CCD camera was used to record the image.

## 2. Computational calculations

The structural, electronic and optical absorption properties of the Cu<sub>4</sub> nanoclusters protected with a monolayer of *ortho*-carborane 9-thiol (O<sub>9</sub>), *meta*-carborane 9-thiol (M<sub>9</sub>) and *ortho*-carborane 12-iodo 9-thiol (I<sub>9</sub>) ligands were computationally studied using density functional theory (DFT) as implemented in grid spaced projector augmented wave (GPAW) software package.<sup>4,5</sup> The effective valence electrons of all the atoms in the considered cluster are described by the PAW set-ups such as Cu (3d<sup>10</sup> 4s<sup>1</sup>), S (3s<sup>2</sup>3p<sup>4</sup>), C (2s<sup>2</sup>2p<sup>2</sup>), B (2s<sup>2</sup>2p<sup>1</sup>) and H (1s<sup>1</sup>). For geometry optimizations, the cluster boundary condition was set by taking the structure in a cubic box and a grid spacing of 0.2 Å was considered for the greater accuracy of real space for electron density inside the cubic box. Further, the convergence criterion to minimize the forces between the atoms in the cluster was to be 0.05 eV/Å, without imposing any symmetry constraints. The PBE (Perdew-Burke-Ernzerhof) exchange-correlation functional was utilized in the calculations as it describes the metal interactions in the cluster.<sup>6,7</sup> The atomic coordinates taken from the crystal structure of Cu<sub>4</sub> cluster were used as a starting point for the geometry optimization. The optimized Cu<sub>4</sub> structures were utilized to calculate the absorption spectra using Gaussian09. Further, the Cu<sub>4</sub> structures were once optimized to investigate the geometrical changes in gas and solvent phases. Solvent effects were modelled by the Polarizable Continuum Model (PCM) with solvent excluding surface, using parameters of dichloromethane for Cu<sub>4</sub>@mCBT, and acetone for Cu<sub>4</sub>@oCBT and Cu<sub>4</sub>@ICBT.<sup>8-10</sup> The IR spectra were calculated for the optimized structures in gas phases from their frequency calculations. All the structures were visualized using visual molecular dynamics (VMD) software.

The excited state emission characteristics were studied using the Gaussian 16 quantum chemistry package<sup>11</sup> within the frame of the Density Functional Theory (DFT) and the Time Dependent DFT (TD-DFT). The hybrid exchange–correlation functional PBE0 by Adamo<sup>12</sup> was used (PBE1PBE in the notation of the Gaussian input) and Los Alamos National Laboratory double-zeta basis LANL2DZ with scalar-relativistic effective core potentials on heavier elements (sulphur and iodine).<sup>13</sup>

**Table S1.** Crystal data and structure refinement for I<sub>9</sub> ligand

Identification code	I <sub>9</sub> ligand
Empirical formula	C <sub>2</sub> B <sub>10</sub> H <sub>10</sub> I S
Formula weight	301.16
Temperature	95 K
Wavelength	1.54184 Å
Crystal system	monoclinic
Space group	P 21/n
Unit cell dimensions	a = 14.1490 (6) Å      α = 90° b = 7.7293 (3) Å      β = 91.659° c = 20.6546 (9) Å      γ = 90°
Volume	2257.88 (16) Å <sup>3</sup>
Z	4
Density (calculated)	1.772 gm/cm <sup>3</sup>
Absorption coefficient	23.481 mm <sup>-1</sup>
F(000)	1128
Crystal size	0.072 x 0.032 x 0.02 mm <sup>3</sup>
Theta range for data collection	2.13 to 37.14°.
Index ranges	-16<=h<=17, -9<=k<=8, -20<=l<=25
Reflections collected	13000
Independent reflections	4635 [R(reflection) = 0.0388]
Completeness to theta = 37.31°	97.9 %
Absorption correction	Empirical Gaussian integration
Max. and min. transmission	0.625 and 0.467
Refinement method	Full-matrix least-squares on F <sup>2</sup>
Data / restraints / parameters	4538 / 0 / 259
Goodness-of-fit on F <sup>2</sup>	1.569
Final R indices [I>2sigma(I)]	R1 = 0.0388, wR2 = 0.0453
R indices (all data)	R1 = 0.0564, wR2 = 0.0485
Absolute structure parameter	0.16 (4)
Extinction coefficient	n/a

**Table S2.** Crystal data and structure refinement for [Cu<sub>4</sub>@oCBT].

Identification code	Cu <sub>4</sub> @oCBT	
Empirical formula	C <sub>8</sub> H <sub>44</sub> B <sub>40</sub> Cu <sub>4</sub> S <sub>4</sub>	
Formula weight	955.23	
Temperature	296(2) K	
Wavelength	0.71073 Å	
Crystal system	Trigonal	
Space group	P3 <sub>1</sub> 21	
Unit cell dimensions	a = 11.4344(6) Å	α = 90°
	b = 11.4344(6) Å	β = 90°
	c = 29.4398(16) Å	γ = 120°
Volume	3333.4(4) Å <sup>3</sup>	
Z	3	
Density (calculated)	1.428 Mg/m <sup>3</sup>	
Absorption coefficient	2.091 mm <sup>-1</sup>	
F(000)	1416	
Crystal size	0.200 x 0.150 x 0.150 mm <sup>3</sup>	
Theta range for data collection	2.922 to 26.057°.	
Index ranges	-14 ≤ h ≤ 13, -14 ≤ k ≤ 14, -36 ≤ l ≤ 36	
Reflections collected	64165	
Independent reflections	4384 [R(int) = 0.0563]	
Completeness to theta = 25.242°	99.6 %	
Absorption correction	Semi-empirical from equivalents	
Max. and min. transmission	0.7453 and 0.6112	
Refinement method	Full-matrix least-squares on F <sup>2</sup>	
Data / restraints / parameters	4384 / 0 / 255	
Goodness-of-fit on F <sup>2</sup>	1.121	
Final R indices [I > 2σ(I)]	R1 = 0.0513, wR2 = 0.1266	
R indices (all data)	R1 = 0.0570, wR2 = 0.1305	
Absolute structure parameter	0.19(4)	
Extinction coefficient	n/a	
Largest diff. peak and hole	1.205 and -0.613 e.Å <sup>-3</sup>	

**Table S3.** Atomic coordinates ( $\times 10^4$ ) and equivalent isotropic displacement parameters ( $\text{\AA}^2 \times 10^3$ ) for  $\text{Cu}_4@o\text{CBT}$ .  $U(\text{eq})$  is defined as one third of the trace of the orthogonalized  $U^{ij}$  tensor.

	x	y	z	$U(\text{eq})$
Cu(1)	0	5122(1)	6667	52(1)
Cu(2)	-61(1)	3393(1)	6038(1)	48(1)
Cu(3)	0	1672(1)	6667	49(1)
C(1)	5803(10)	4668(11)	6190(4)	80(3)
B(10)	5052(13)	3112(16)	5973(6)	89(4)
C(3)	1629(11)	8624(10)	5026(3)	73(3)
C(4)	876(14)	8774(13)	5462(4)	90(4)
B(1)	2607(9)	3069(9)	6067(3)	40(2)
B(2)	3475(10)	4706(10)	6300(3)	50(2)
B(3)	3353(11)	3349(12)	6610(3)	57(2)
B(4)	3485(11)	2215(11)	6228(4)	60(3)
B(5)	3661(12)	2883(12)	5667(4)	62(3)
B(6)	3662(11)	4444(12)	5715(3)	58(3)
B(7)	5193(13)	4455(16)	5670(5)	84(4)
B(8)	5082(12)	5572(12)	6048(5)	68(3)
B(9)	4887(12)	4888(13)	6585(5)	72(3)
C(2)	4867(12)	3354(13)	6528(5)	92(4)
B(11)	-65(10)	6043(10)	5665(3)	46(2)
B(12)	-576(13)	7240(13)	5558(5)	75(4)
B(13)	-643(13)	6166(14)	5115(4)	72(3)
B(14)	779(13)	5943(12)	5176(4)	62(3)
B(15)	1746(11)	6913(10)	5646(3)	53(2)
B(16)	899(12)	7710(11)	5891(4)	62(3)
B(17)	2310(13)	8637(13)	5534(4)	72(3)
B(18)	2160(13)	7535(12)	5102(3)	65(3)
B(19)	803(15)	7101(15)	4774(4)	80(4)
B(20)	-58(16)	7853(15)	5001(5)	87(4)
S(1)	-1112(2)	4535(2)	6036(1)	52(1)
S(2)	725(2)	2030(2)	5972(1)	49(1)

**Table S4.** Crystal data and structure refinement for [Cu<sub>4</sub>@mCBT].

Identification code	Cu <sub>4</sub> @mCBT	
Empirical formula	C <sub>8</sub> H <sub>44</sub> B <sub>40</sub> Cu <sub>4</sub> S <sub>4</sub>	
Formula weight	955.23	
Temperature	296(2) K	
Wavelength	0.71073 Å	
Crystal system	Monoclinic	
Space group	P2 <sub>1</sub> /c	
Unit cell dimensions	a = 11.3989(7) Å	α = 90°
	b = 11.9482(7) Å	β = 91.213(2)°
	c = 32.3144(19) Å	γ = 90°
Volume	4400.1(5) Å <sup>3</sup>	
Z	4	
Density (calculated)	1.442 Mg/m <sup>3</sup>	
Absorption coefficient	2.112 mm <sup>-1</sup>	
F(000)	1888	
Crystal size	0.200 x 0.200 x 0.150 mm <sup>3</sup>	
Theta range for data collection	3.044 to 23.439°.	
Index ranges	-12<=h<=12, -13<=k<=13, -36<=l<=36	
Reflections collected	54022	
Independent reflections	6415 [R(int) = 0.1819]	
Completeness to theta = 23.439°	99.2 %	
Absorption correction	Semi-empirical from equivalents	
Max. and min. transmission	0.7456 and 0.5645	
Refinement method	Full-matrix least-squares on F <sup>2</sup>	
Data / restraints / parameters	6415 / 298 / 505	
Goodness-of-fit on F <sup>2</sup>	1.116	
Final R indices [I>2sigma(I)]	R1 = 0.0986, wR2 = 0.1819	
R indices (all data)	R1 = 0.1808, wR2 = 0.2141	
Extinction coefficient	n/a	
Largest diff. peak and hole	0.484 and -0.429 e.Å <sup>-3</sup>	



**Table S5.** Atomic coordinates ( $\times 10^4$ ) and equivalent isotropic displacement parameters ( $\text{\AA}^2 \times 10^3$ ) for  $\text{Cu}_4\text{@mCBT}$ .  $U(\text{eq})$  is defined as one third of the trace of the orthogonalized  $U^{ij}$  tensor.

	x	y	z	U(eq)
Cu(1)	7455(2)	5278(1)	6964(1)	92(1)
Cu(2)	5347(1)	4301(1)	6816(1)	75(1)
Cu(3)	6138(2)	3468(1)	6103(1)	75(1)
Cu(4)	8236(1)	4472(1)	6211(1)	76(1)
B(7)	8429(14)	850(14)	7774(6)	82(4)
C(2)	8369(14)	1984(13)	8096(5)	102(4)
B(14)	6656(18)	9473(15)	5913(7)	110(5)
C(4)	6700(18)	8215(14)	5648(6)	130(5)
C(6)	7110(30)	2216(19)	4596(7)	183(8)
B(21)	7530(20)	3420(20)	4342(7)	152(7)
C(7)	2472(18)	1206(16)	6679(6)	137(6)
B(35)	1466(16)	902(16)	6330(7)	103(5)
B(1)	7058(15)	2683(15)	8023(5)	84(4)
B(2)	8360(13)	3199(14)	7808(5)	75(3)
B(3)	9108(13)	2043(12)	7662(6)	75(4)
B(4)	7148(14)	869(14)	7476(5)	76(3)
B(5)	7154(15)	1258(14)	7976(6)	82(4)
B(6)	8383(14)	2796(13)	7290(5)	73(3)
C(1)	8424(13)	1325(11)	7271(5)	87(3)
B(8)	6300(15)	1960(13)	7631(5)	79(3)
B(9)	7035(13)	3213(12)	7511(5)	64(3)
B(10)	7093(14)	2048(13)	7173(5)	72(3)
B(11)	6674(15)	7103(14)	5992(6)	96(4)
B(12)	8000(19)	7507(17)	5788(7)	115(5)
B(13)	7960(20)	8964(19)	5743(9)	145(6)
B(17)	6610(20)	9113(18)	6421(7)	127(5)
B(15)	5908(16)	8331(14)	6061(7)	101(5)
B(16)	8743(17)	8365(16)	6155(9)	133(6)
C(3)	7846(17)	9476(13)	6219(7)	144(6)
B(18)	6582(15)	7679(17)	6472(7)	102(4)
B(19)	7913(12)	7203(12)	6306(6)	74(3)

B(20)	7860(20)	8449(16)	6585(8)	123(5)
C(5)	8639(18)	3890(30)	4622(7)	188(8)
B(22)	8978(18)	3120(30)	5049(7)	167(8)
B(23)	8000(20)	2020(20)	5034(6)	141(6)
B(24)	6380(20)	3341(19)	4636(6)	115(5)
B(25)	8540(30)	2480(40)	4588(8)	214(10)
B(26)	8100(20)	4340(20)	5117(7)	133(6)
B(27)	7238(17)	4371(18)	4682(5)	97(4)
B(28)	6609(19)	2493(18)	5073(7)	113(5)
B(29)	7784(13)	3082(12)	5372(5)	63(3)
B(30)	6684(16)	3900(16)	5109(5)	91(4)
B(31)	2390(18)	2643(16)	5868(6)	106(5)
B(32)	3506(18)	1738(16)	5958(7)	112(5)
B(33)	2923(18)	647(15)	6233(9)	131(6)
C(8)	2005(18)	1287(15)	5865(6)	130(5)
B(34)	1203(17)	2132(17)	6120(10)	130(6)
B(36)	1929(15)	3192(16)	6299(8)	120(5)
B(37)	3749(17)	1685(17)	6485(8)	126(6)
B(38)	3415(12)	2972(12)	6263(5)	61(3)
B(39)	2750(20)	2580(20)	6709(6)	132(6)
B(40)	1330(20)	2090(20)	6574(10)	154(7)
S(1)	6254(4)	4557(3)	7402(1)	87(1)
S(2)	4434(3)	4195(3)	6223(1)	76(1)
S(3)	7865(3)	2849(3)	5941(1)	70(1)
S(4)	8729(3)	5962(3)	6549(2)	98(1)

**Table S6.** Crystal data and structure refinement for [Cu<sub>4</sub>@ICBT].

Identification code	Cu <sub>4</sub> @ICBT	
Empirical formula	C <sub>8</sub> H <sub>41</sub> B <sub>40</sub> Cu <sub>4</sub> I <sub>3</sub> S <sub>4</sub>	
Formula weight	1332.91	
Temperature	200(2) K	
Wavelength	0.71073 Å	
Crystal system	Tetragonal	
Space group	P4 <sub>3</sub> 2 <sub>1</sub> 2	
Unit cell dimensions	a = 12.716(3) Å	α = 90.00(3)°
	b = 12.716(3) Å	β = 90.00(3)°
	c = 39.812(8) Å	γ = 90.00(3)°
Volume	6438(3) Å <sup>3</sup>	
Z	4	
Density (calculated)	1.375 Mg/m <sup>3</sup>	
Absorption coefficient	2.884 mm <sup>-1</sup>	
F(000)	2512	
Crystal size	0.200 x 0.150 x 0.120 mm <sup>3</sup>	
Theta range for data collection	3.018 to 19.992°.	
Index ranges	-12 ≤ h ≤ 12, -12 ≤ k ≤ 12, -38 ≤ l ≤ 38	
Reflections collected	33001	
Independent reflections	2991 [R(int) = 0.0566]	
Completeness to theta = 19.992°	99.3 %	
Absorption correction	Semi-empirical from equivalents	
Max. and min. transmission	0.5610 and 0.3783	
Refinement method	Full-matrix least-squares on F <sup>2</sup>	
Data / restraints / parameters	2991 / 578 / 273	
Goodness-of-fit on F <sup>2</sup>	1.082	
Final R indices [I > 2σ(I)]	R1 = 0.1061, wR2 = 0.2772	
R indices (all data)	R1 = 0.1123, wR2 = 0.2841	
Absolute structure parameter	0.29(16)	
Extinction coefficient	n/a	
Largest diff. peak and hole	1.252 and -0.727 e.Å <sup>-3</sup>	

**Table S7.** Atomic coordinates ( $\times 10^4$ ) and equivalent isotropic displacement parameters ( $\text{\AA}^2 \times 10^3$ ) for  $\text{Cu}_4\text{@ICBT}$ .  $U(\text{eq})$  is defined as one third of the trace of the orthogonalized  $U_{ij}$  tensor.

	x	y	z	$U(\text{eq})$
Cu(1)	1638(4)	8362(4)	7500	114(3)
Cu(2)	1800(5)	6377(4)	7173(1)	111(2)
Cu(3)	3742(4)	6258(4)	7500	106(2)
I(1)	3120(2)	8882(2)	6837(1)	101(1)
I(2)	849(6)	4473(5)	7562(2)	141(3)
S(1)	515(9)	7496(11)	7194(2)	115(3)
S(2)	3225(10)	5565(9)	7028(2)	108(3)
B(1)	-590(20)	8660(30)	6617(7)	120(6)
B(2)	480(20)	9460(30)	6707(7)	121(6)
C(1)	-630(20)	8470(20)	6193(6)	124(6)
C(2)	390(20)	9130(20)	6030(7)	125(6)
B(3)	1530(20)	8580(30)	6153(7)	115(6)
B(4)	1160(20)	7570(20)	6420(6)	111(6)
B(5)	-160(20)	7490(30)	6442(7)	118(6)
B(6)	460(20)	7780(20)	6062(7)	119(6)
B(7)	-270(20)	9680(20)	6354(7)	125(6)
B(8)	1100(20)	9760(20)	6329(7)	122(6)
B(9)	1550(20)	8760(30)	6576(7)	115(6)
B(10)	520(20)	8100(30)	6763(6)	114(6)
B(13)	3170(30)	4120(20)	7168(9)	158(7)
B(14)	3370(40)	3670(30)	7569(9)	163(7)
B(11)	2340(30)	3240(30)	6965(9)	165(7)
B(12)	3670(30)	3180(30)	6895(9)	170(8)
C(3)	4170(30)	2180(30)	7134(9)	177(8)
C(4)	3160(30)	1630(20)	7351(9)	177(8)
B(15)	2010(30)	2250(30)	7252(10)	171(8)
B(16)	2950(40)	2040(30)	6947(9)	174(8)
B(17)	4320(30)	3450(30)	7267(10)	169(8)
B(18)	3990(30)	2470(30)	7553(9)	174(8)
B(19)	2660(30)	2530(30)	7623(9)	173(8)
B(20)	2150(30)	3540(30)	7386(9)	165(7)

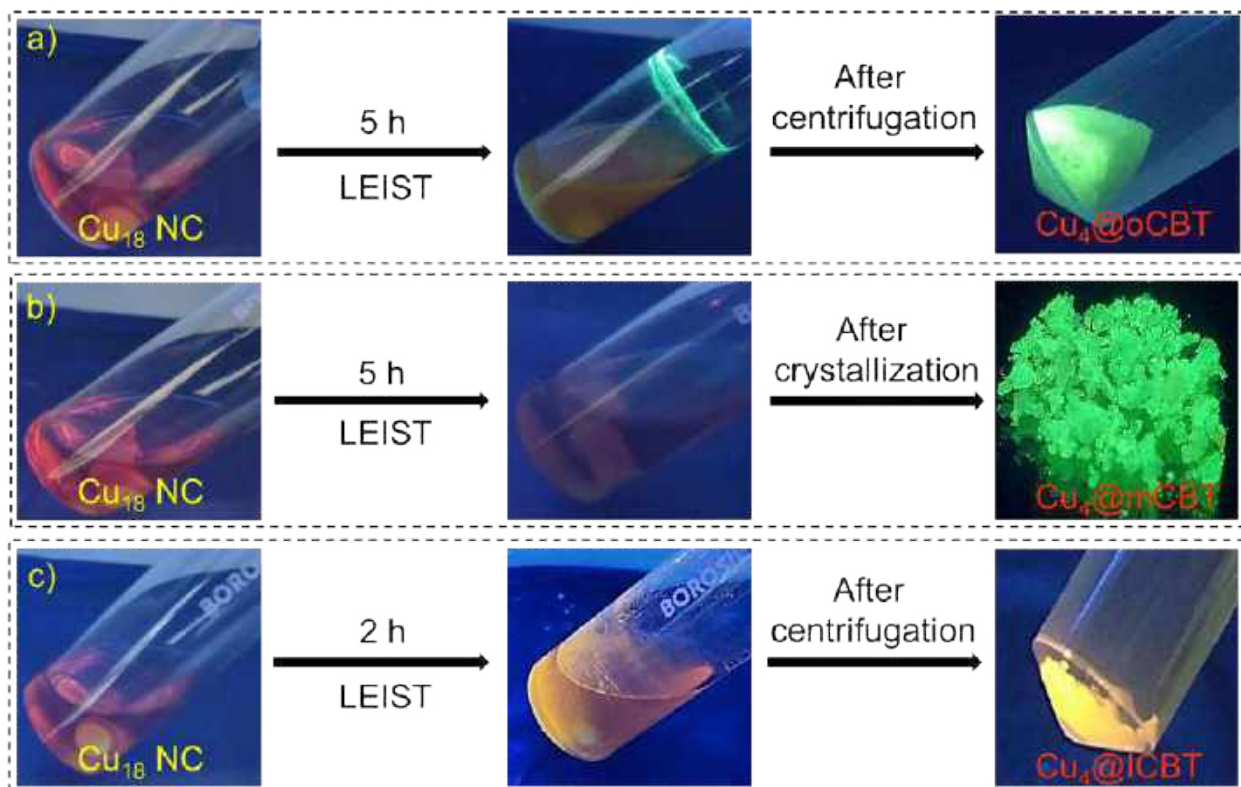


**Fig. S1** Photographic images of the different steps of synthesis and purification of a) Cu<sub>4</sub>@oCBT, b) Cu<sub>4</sub>@mCBT and c) Cu<sub>4</sub>@ICBT, starting from Cu<sub>18</sub>. All of the images were taken under 365 nm UV light.

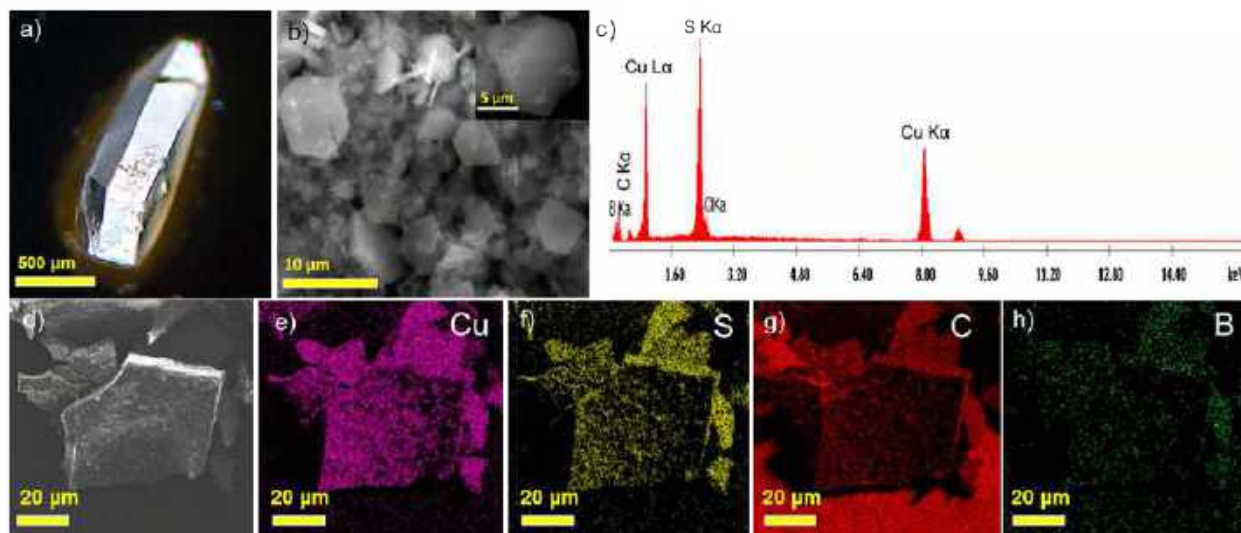


**Fig. S2** a) Optical microscopic image of Cu<sub>4</sub>@oCBT single crystals, b) Large area SEM images of crystals (inset shows magnified image of a single crystal), c) The EDS spectrum of the Cu<sub>4</sub>@oCBT crystals, d-h) the elemental mapping of respective elements present in crystal.

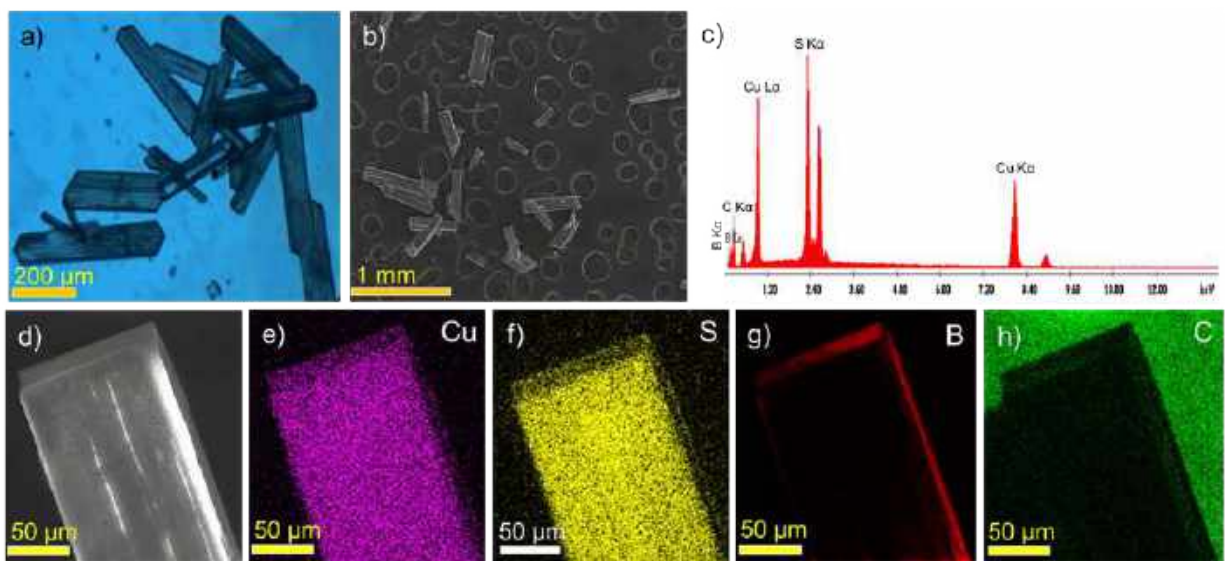


**Fig. S3** a) Optical microscopic image of cuboid crystals of  $\text{Cu}_4\text{@mCBT}$ . b) Large area SEM image of same crystals. c) The EDS spectrum of the crystals have respective elements. d-h) Elemental mapping of the crystal with corresponding elements.

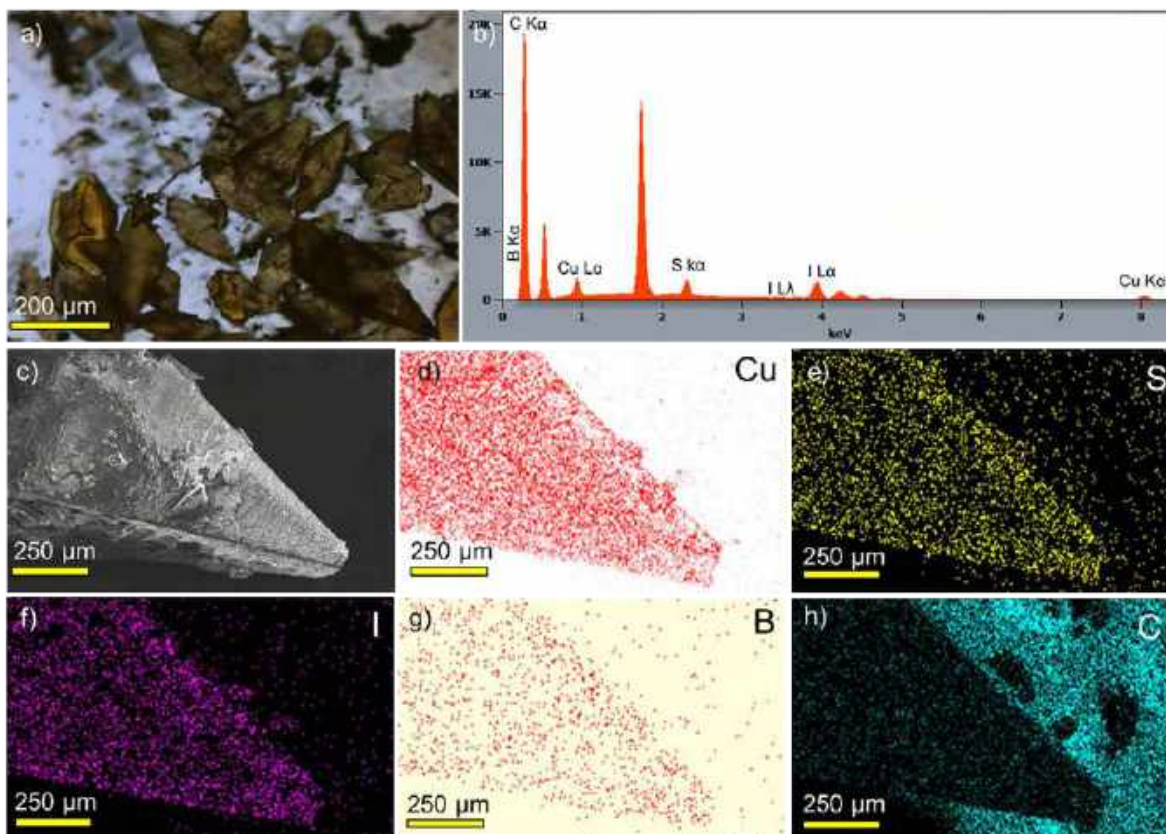


**Fig. S4** a) Optical microscopic image of rhombus crystals of  $\text{Cu}_4\text{@ICBT}$ . b) Large area SEM images for the same crystals. c) The EDS spectrum for the  $\text{Cu}_4\text{@mCBT}$  crystal. d-h) Elemental mapping of the crystal with corresponding its assigned elements.



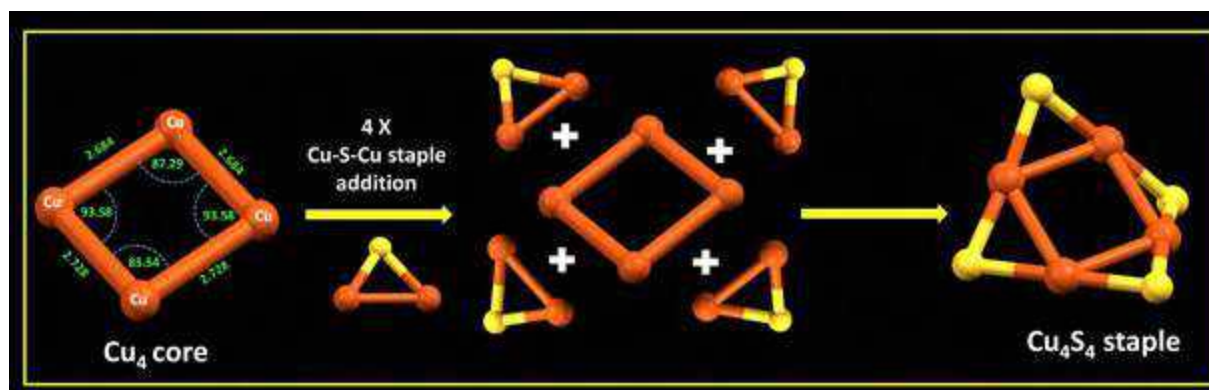


**Fig. S5** Structural anatomy of  $\text{Cu}_4\text{S}_4$  kernel having a square planar  $\text{Cu}_4$  with four 'V-shaped'  $\text{Cu-S-Cu}$  motifs.

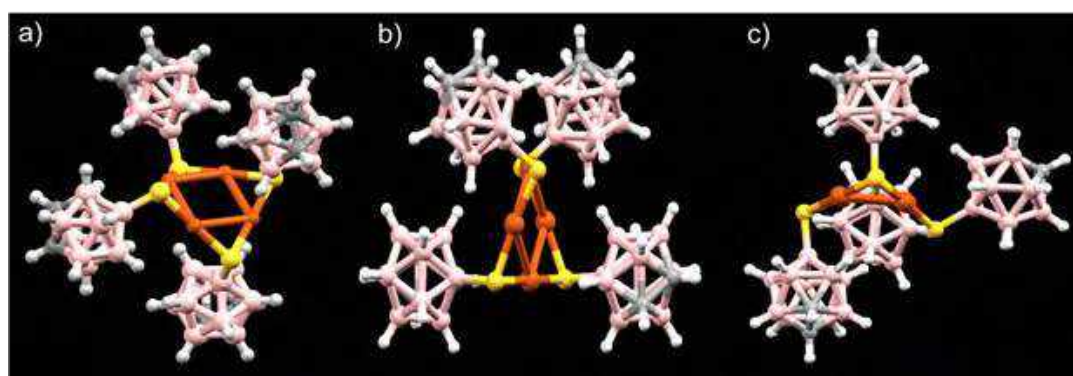


**Fig. S6** a-c) Structures of  $\text{Cu}_4@o\text{CBT}$  in three different orientations showed anti orientation of *ortho*-carborane ligands present in the opposite corner of the cluster.

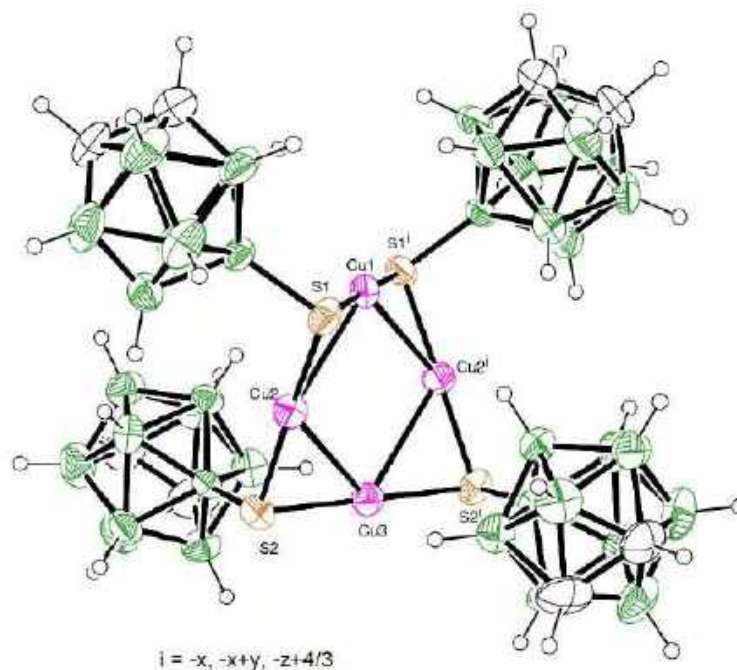


**Fig. S7** ORTEP structure of  $\text{Cu}_4@o\text{CBT}$  having 50% thermal ellipsoid probability.

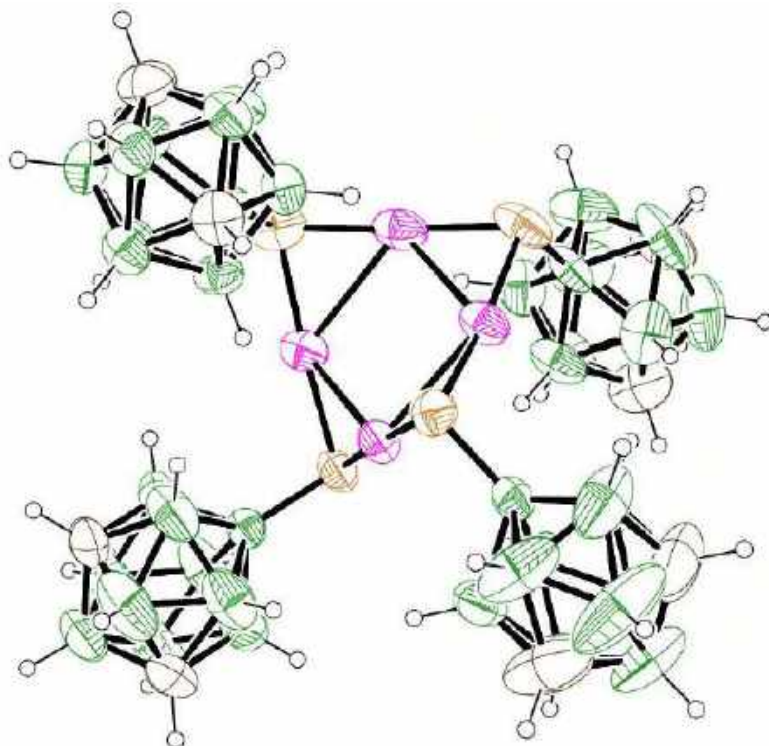


**Fig. S8** ORTEP structure of Cu<sub>4</sub>@mCBT having 50% thermal ellipsoid probability.

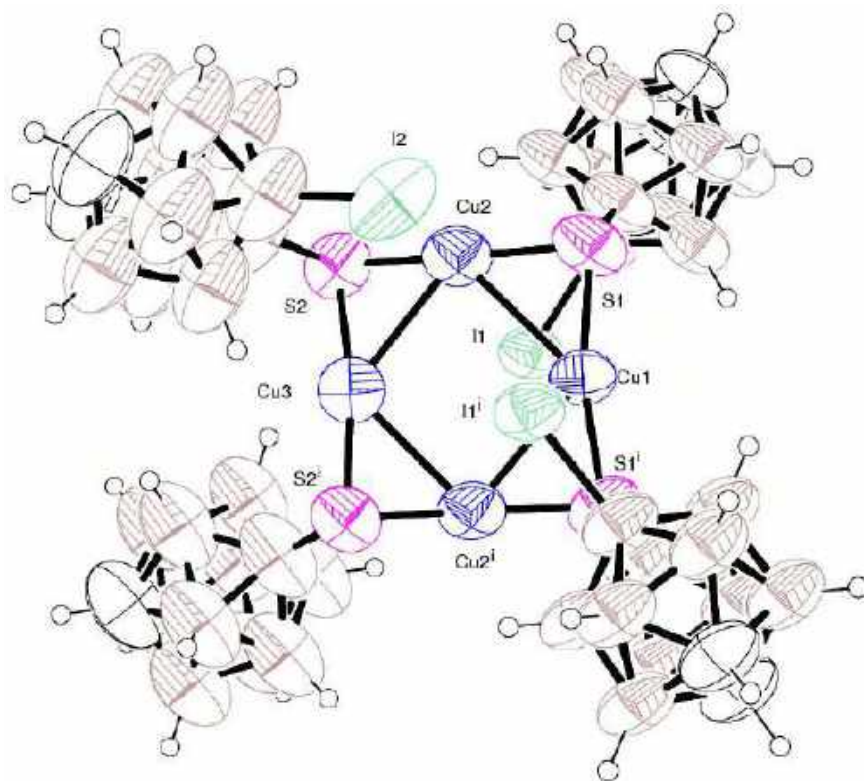


**Fig. S9** ORTEP image of Cu<sub>4</sub>@ICBT having 50 % thermal ellipsoid probability.

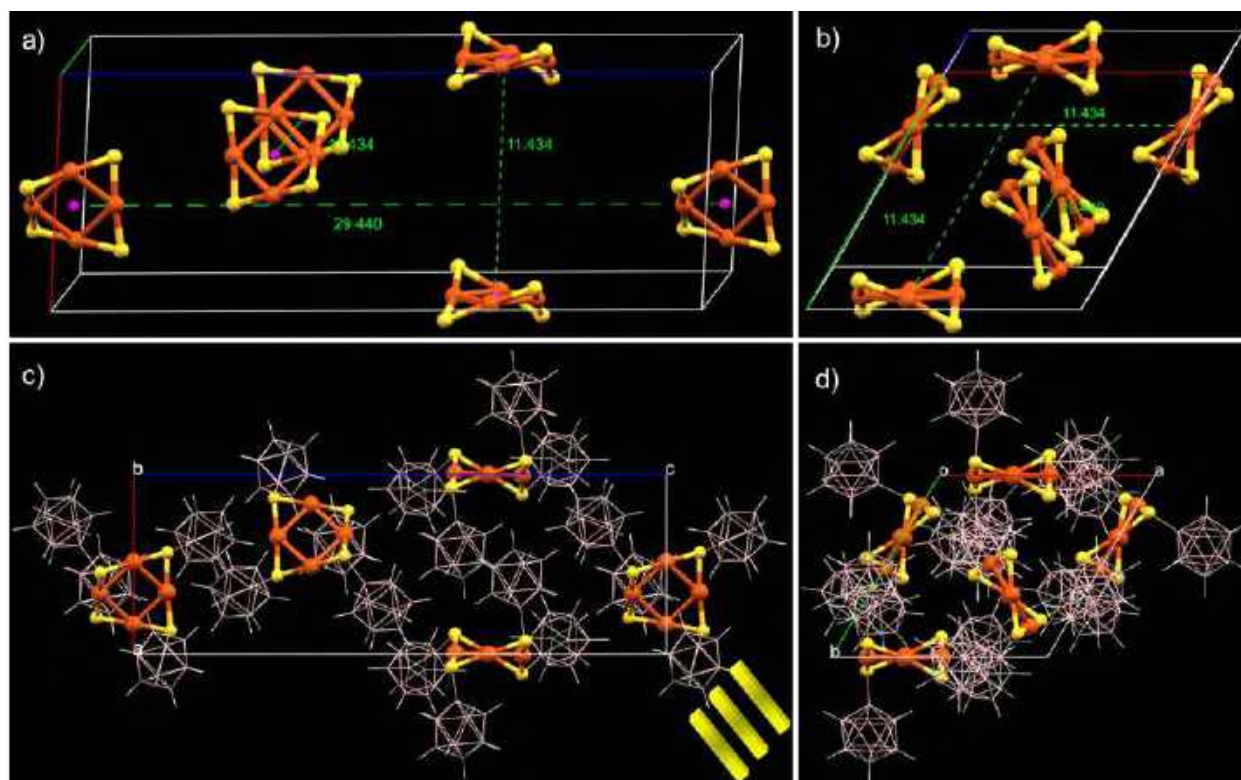


**Fig. S10** Unit cell packing of  $\text{Cu}_4\text{S}_4$  unit of  $\text{Cu}_4@o\text{CBT}$  viewed from a) b and b) c crystallographic axis. The distances between opposite  $\text{Cu}_4\text{S}_4$  centroids are marked here. Unit cell molecular packing along c) b and d) c crystallographic axis.

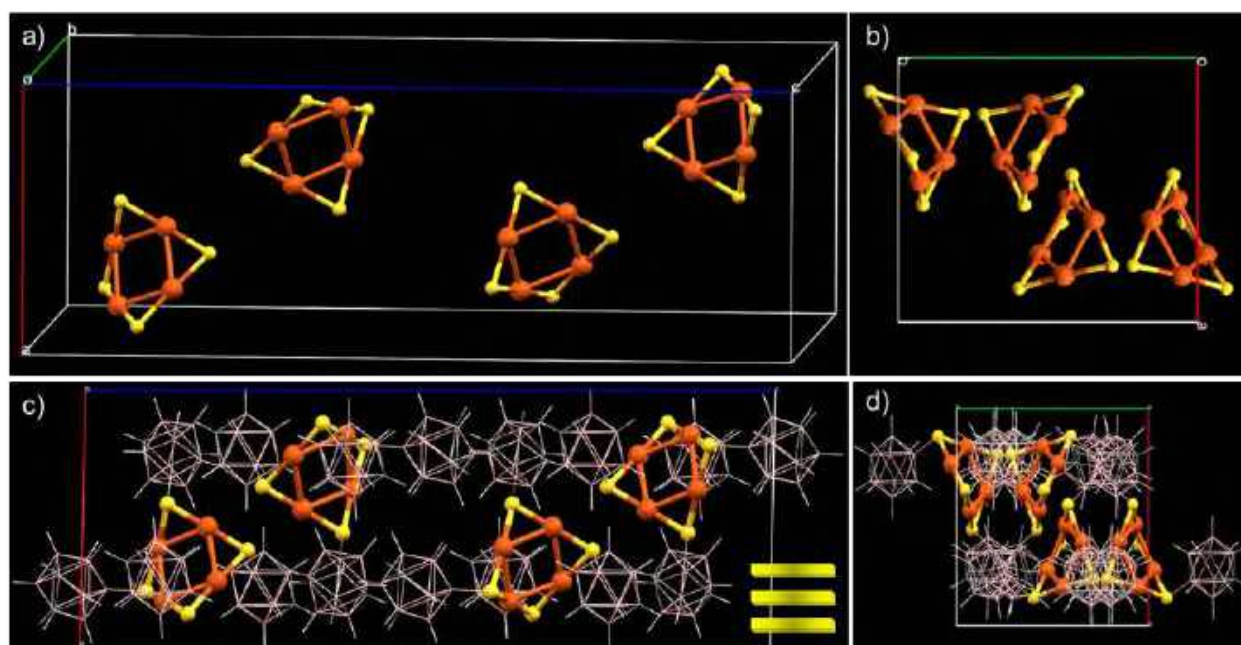


**Fig. S11** Unit cell packing of  $\text{Cu}_4\text{S}_4$  unit of  $\text{Cu}_4@m\text{CBT}$  viewed from a) b and b) c crystallographic axis. Unit cell molecular packing viewed from c) b and d) c crystallographic axis.



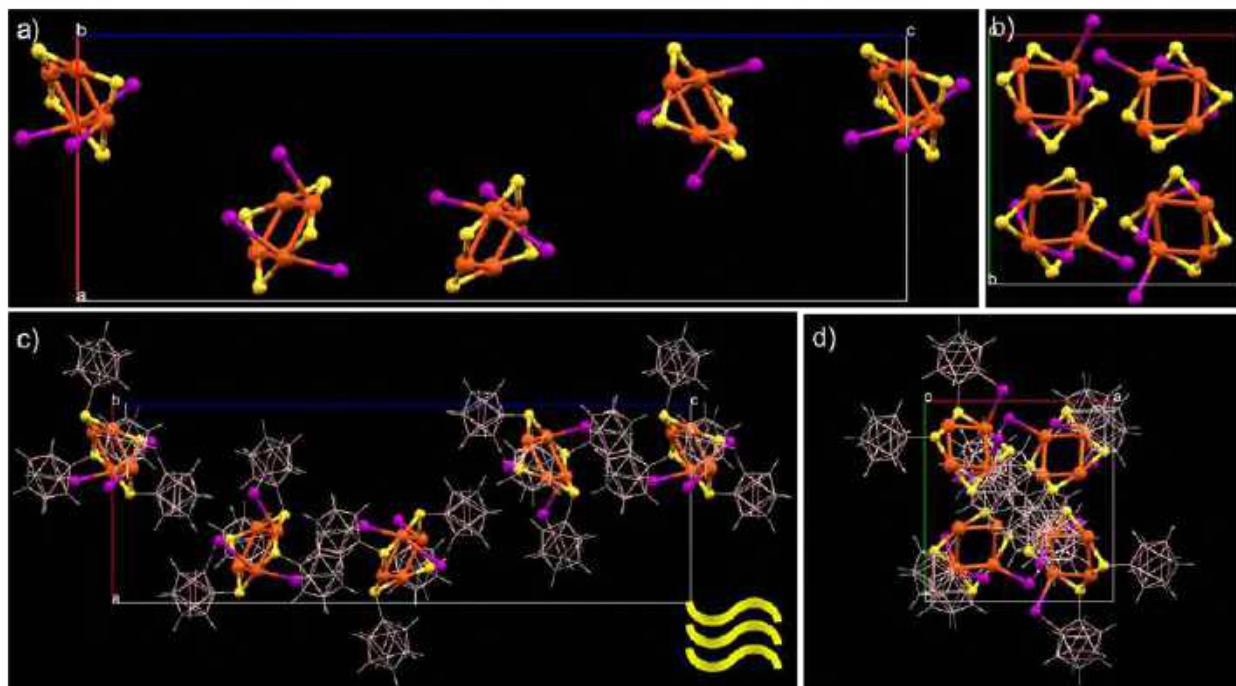


**Fig. S12** Unit cell packing of  $\text{Cu}_4\text{S}_4$  unit of  $\text{Cu}_4@ICBT$  viewed from a) b and b) c crystallographic axis. Unit cell molecular packing viewed from c) b and d) c crystallographic axis.

**Table S8.** Comparative interatomic bond distances and bond angles of the respective  $\text{Cu}_4$  clusters.

Sl. No	Contents	$\text{Cu}_4@oCBT$	$\text{Cu}_4@mCBT$	$\text{Cu}_4@ICBT$
1.	Cu-Cu bond distance	2.68 Å, 2.68 Å, 2.73 Å, 2.73 Å	2.68 Å, 2.71 Å, 2.78 Å, 2.70 Å	2.85 Å, 2.85 Å, 2.80 Å, 2.80 Å
2.	Cu-Cu-Cu bond angle	87.29°, 93.58°, 93.58°, 85.54°	89.75°, 89.91°, 88.17°, 92.11°	84.18°, 94.66°, 96.99°, 84.18°
3.	Cu-S-Cu bond angle	76.58°, 76.58°, 78.13°, 78.13°	76.48°, 76.62°, 80.20°, 77.29°	80.22°, 80.22°, 81.93°, 81.93°
4.	Opposite S-S distance	5.54 Å, 5.54 Å	5.42 Å, 5.49 Å	5.94 Å, 5.94 Å
5.	CB B-S distance	1.88 Å, 1.88 Å, 1.89 Å, 1.89 Å	1.86 Å, 1.91 Å, 1.87 Å, 1.87 Å	1.88 Å, 1.88 Å, 1.92 Å, 1.92 Å
6.	CB-CB centroid distance	7.37 Å, 8.22 Å, 7.37 Å, 9.23 Å	7.54 Å, 7.91 Å, 7.46 Å, 9.24 Å	9.37 Å, 9.06 Å, 7.56 Å, 9.06 Å
7.	Opposite CB-CB centroid distance	9.73 Å, 9.73 Å	9.3 Å, 9.64 Å	10.59 Å, 10.59 Å

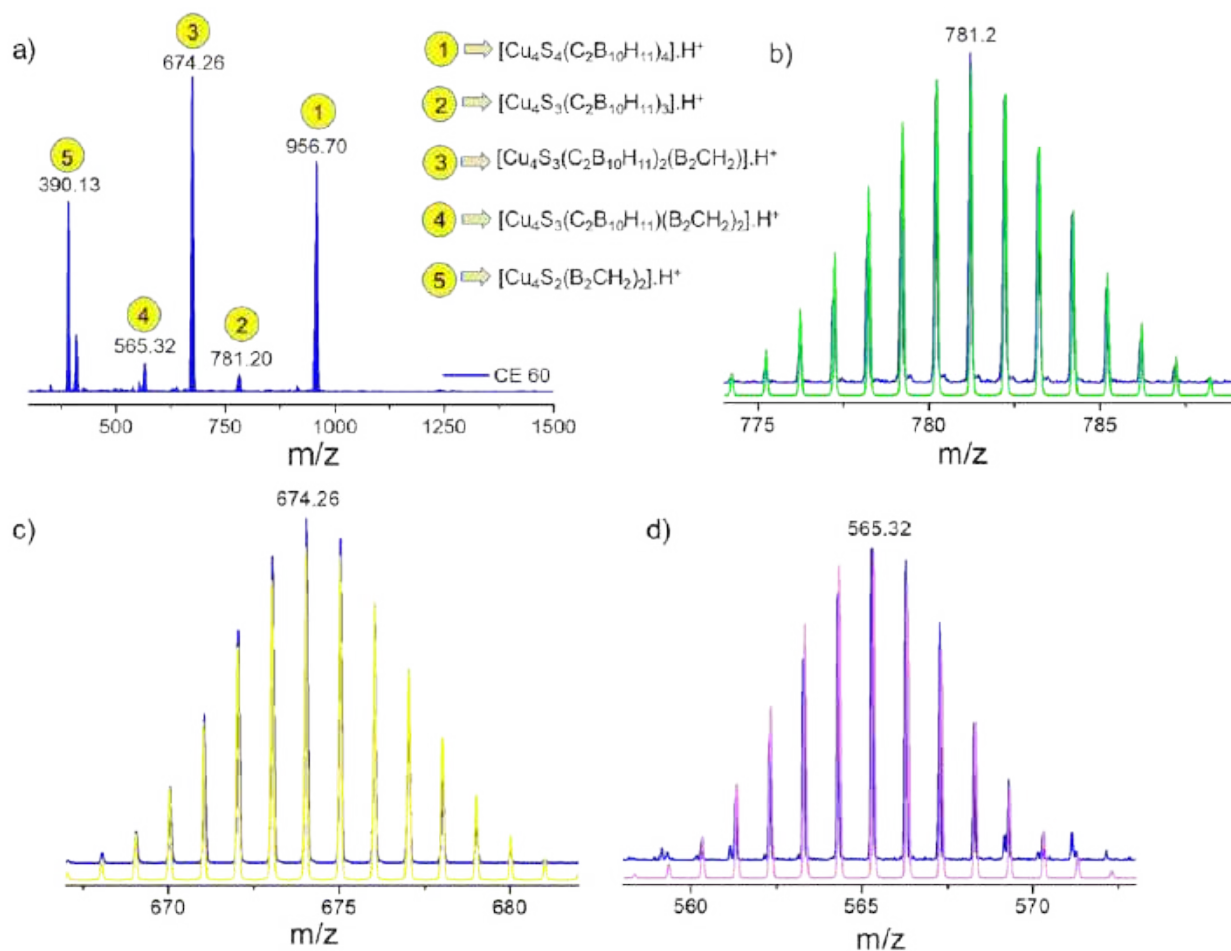


**Fig. S13** a) The MS/MS fragmentation pattern of  $\text{Cu}_4\text{@oCBT}$  at CE 60. Experimental isotopic distribution patterns of the fragments were matches with theoretical distribution of b) 781.20, c) 674.26 and d) 565.32 peaks, respectively.

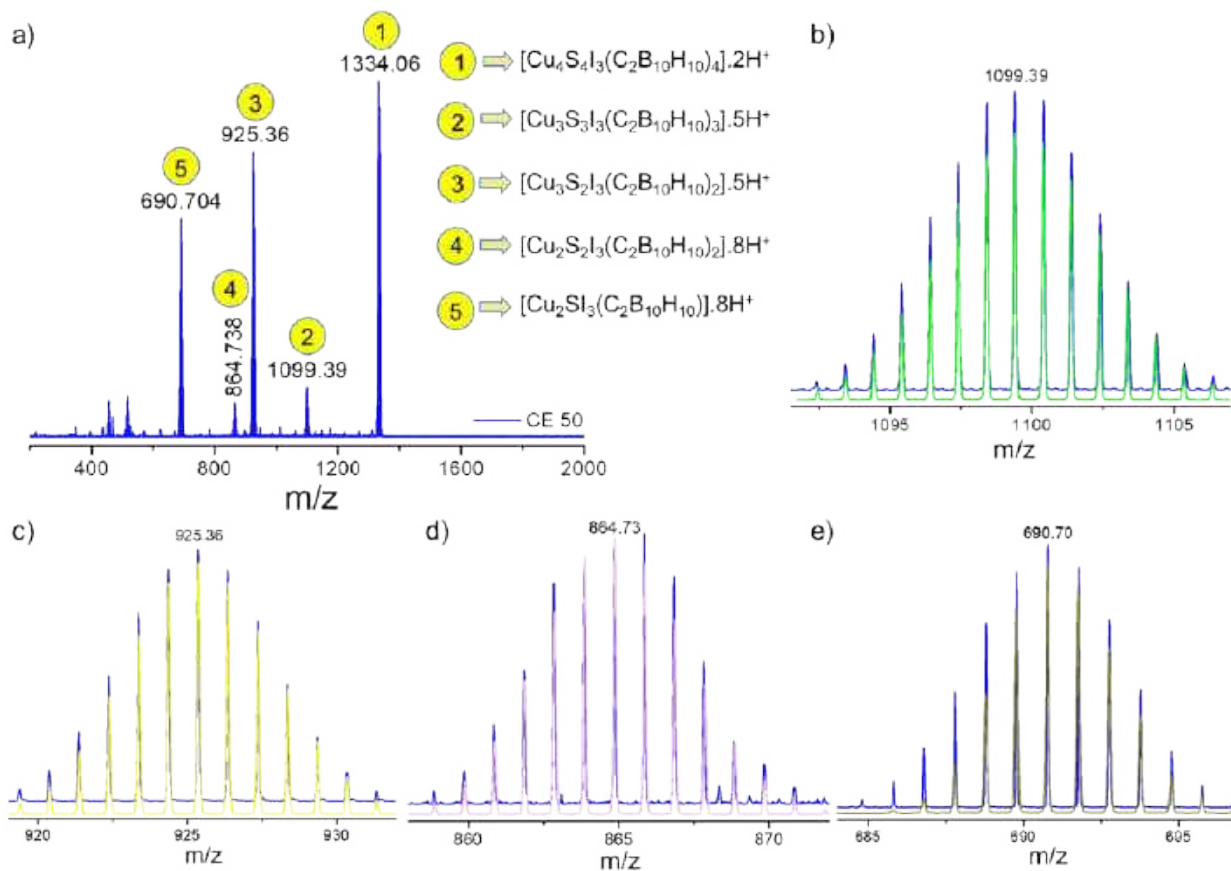


**Fig. S14** a) The MS/MS fragmentation pattern of  $\text{Cu}_4\text{@ICBT}$  at CE 50. Experimental isotopic distribution patterns of the fragments were matches well with theoretical distribution of b) 1099.39, c) 925.36, d) 864.73 and e) 690.70 peaks, respectively.



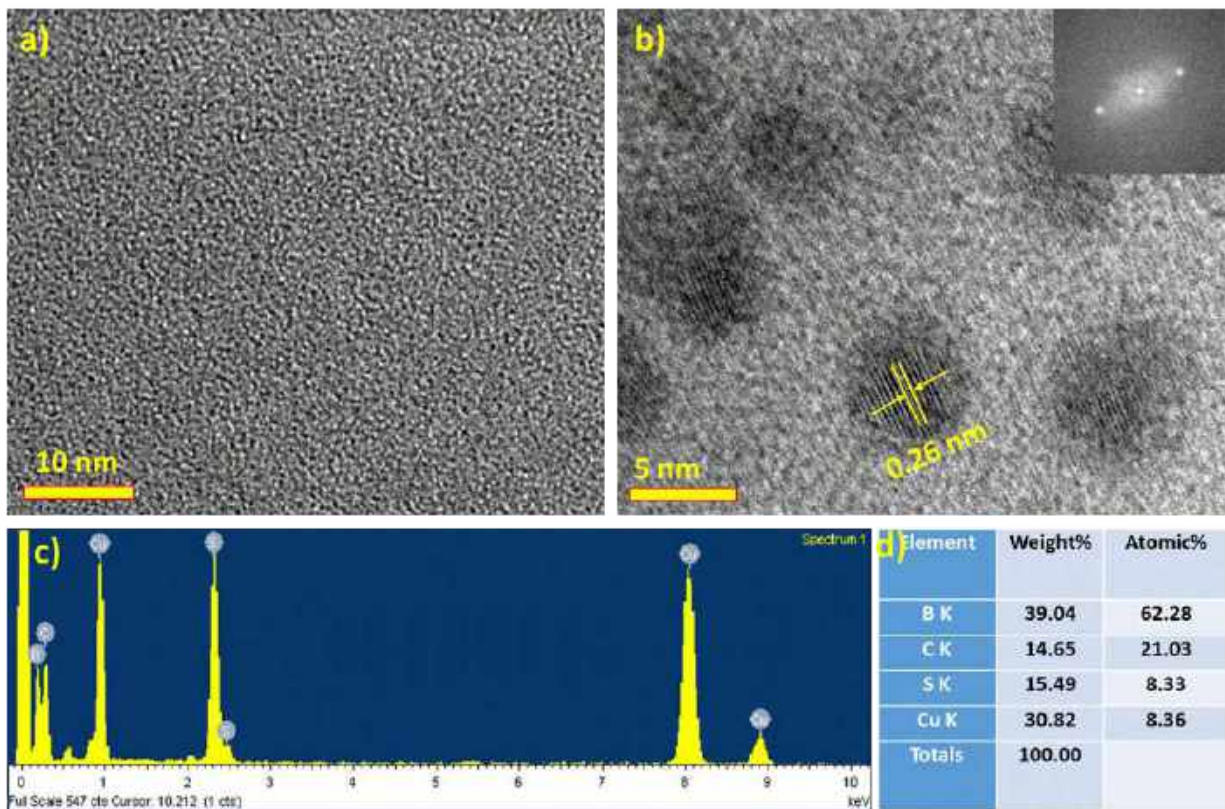


**Fig. S15** a) Large area TEM micrograph of  $\text{Cu}_4@o\text{CBT}$  after 2 min beam exposure, b) HRTEM image after 15 min beam exposure shows the formation of lattice with spacing of 0.26 nm (inset shows the diffraction spots), c) EDS spectral profile of the cluster, d) elemental assignments of the cluster.

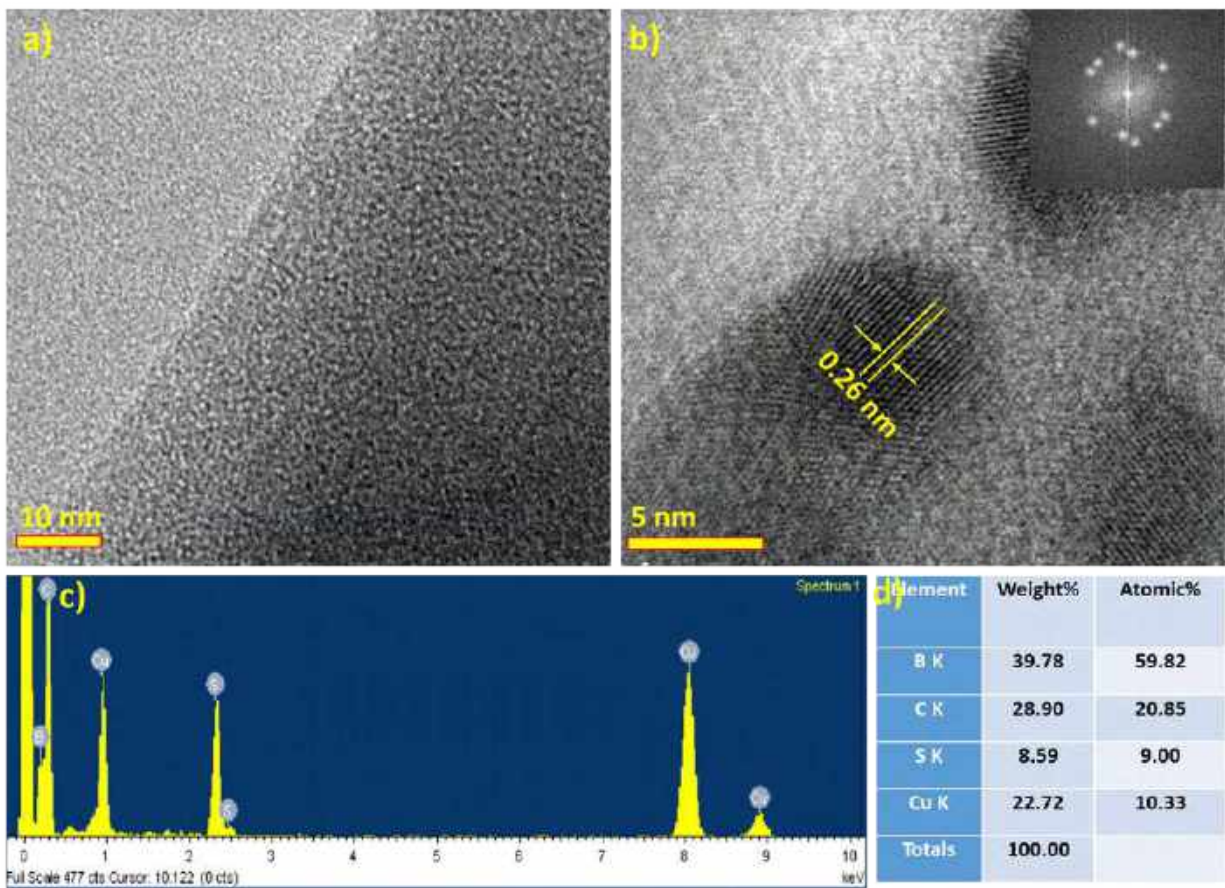


**Fig. S16** a) Large area TEM micrograph of the Cu<sub>4</sub>@mCBT after 2 min beam exposure. b) HRTEM image of the NC after 15 min beam exposure shows the formation of lattice with lattice spacing 0.26 nm ((inset shows the diffraction spots), c) EDS spectral profile of the cluster, d) elemental assignments of the cluster.

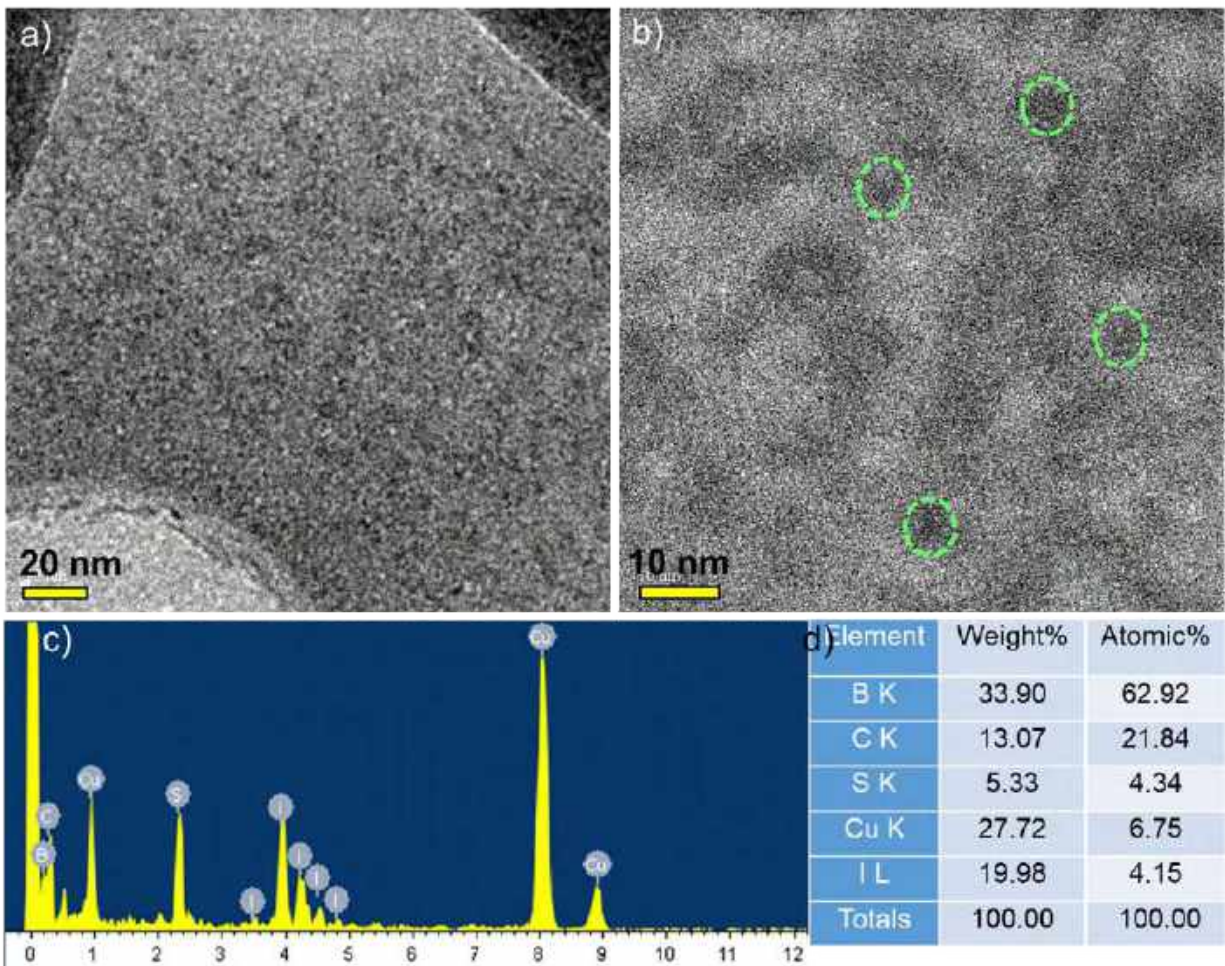


**Fig. S17** a) Large area TEM micrograph of the Cu<sub>4</sub>@ICBT after 2 min beam exposure. b) HRTEM image of the NC after 5 min beam exposure shows the formation of larger particles, c) EDS spectral profile of the cluster, d) elemental assignments of the cluster.

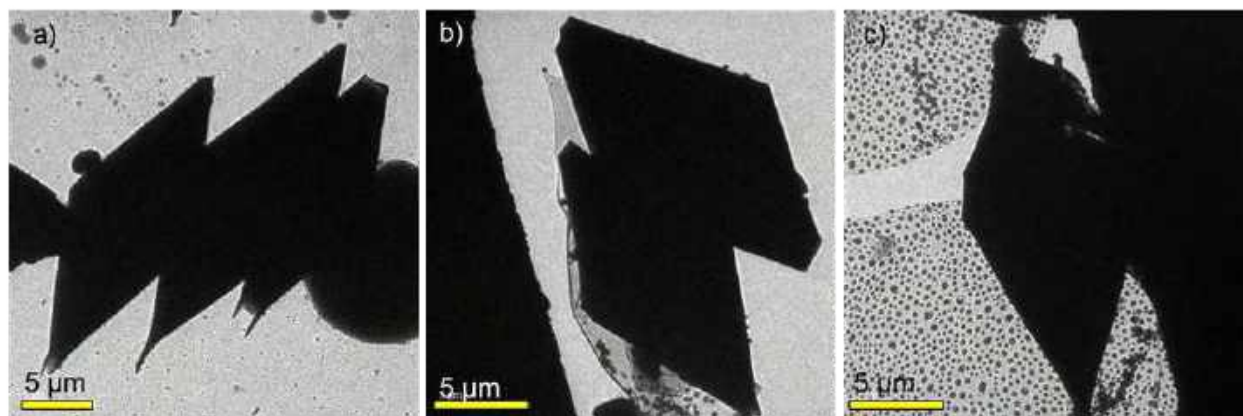


**Fig. S18** TEM micrographs of Cu<sub>4</sub>@ICBT microcrystals indicate their rhombohedral nature. Diluted cluster leads to the fast formation of microcrystalline materials.



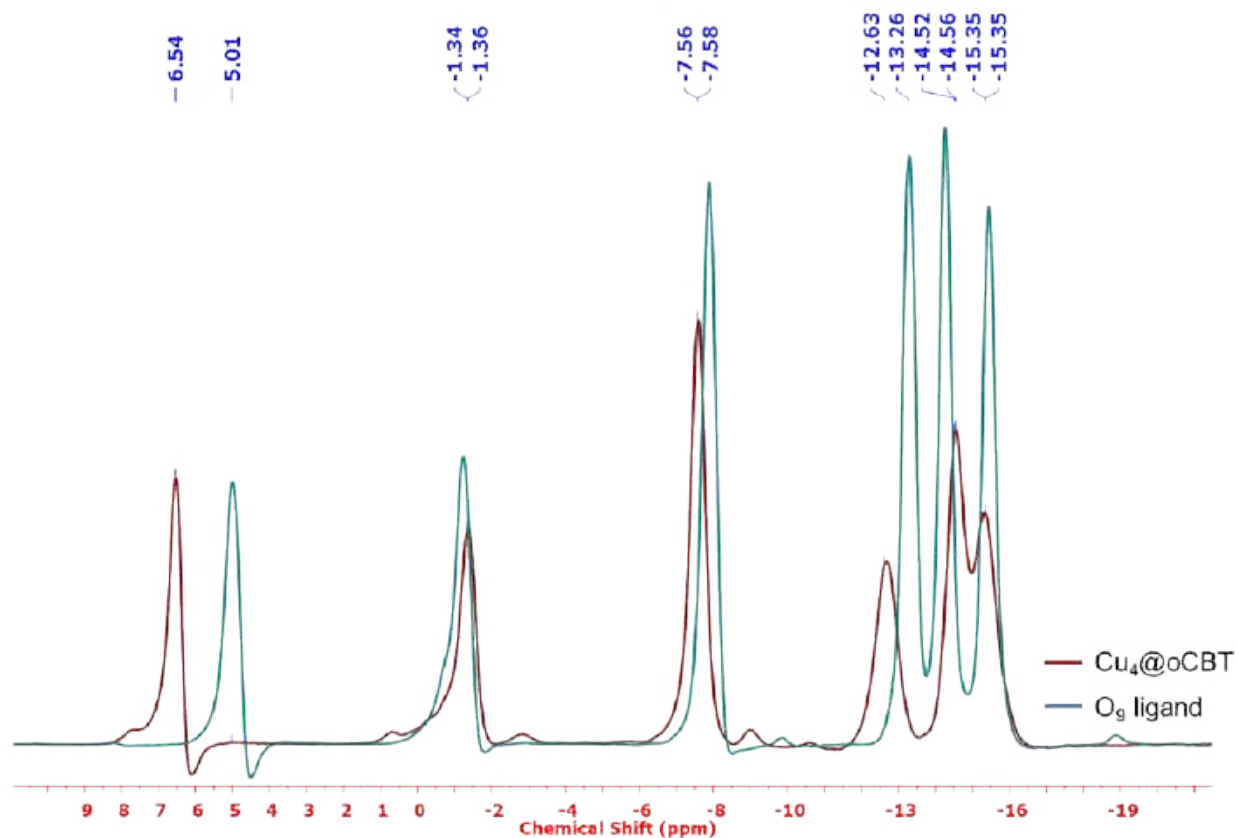


**Fig. S19** Combined  $^{11}\text{B}\{^1\text{H}\}$  NMR spectra of  $\text{Cu}_4@o\text{CBT}$  and  $\text{O}_9$  ligand.

**Table S9.**  $^{11}\text{B}\{^1\text{H}\}$  NMR chemical shift data for  $\text{Cu}_4@o\text{CBT}$  and  $\text{O}_9$  ligand.

Chemical shift (ppm) of $\text{Cu}_4@o\text{CBT}$	Intensity ratio
6.54, -1.36, -7.56, -12.63, -14.56, -15.35	(1:1:2:1:3:2)
Chemical shift (ppm) of $\text{O}_9$ ligand	
5.01, -1.34, -7.58, -13.26, -14.52, -15.35	(1:1:2:2:2:2)

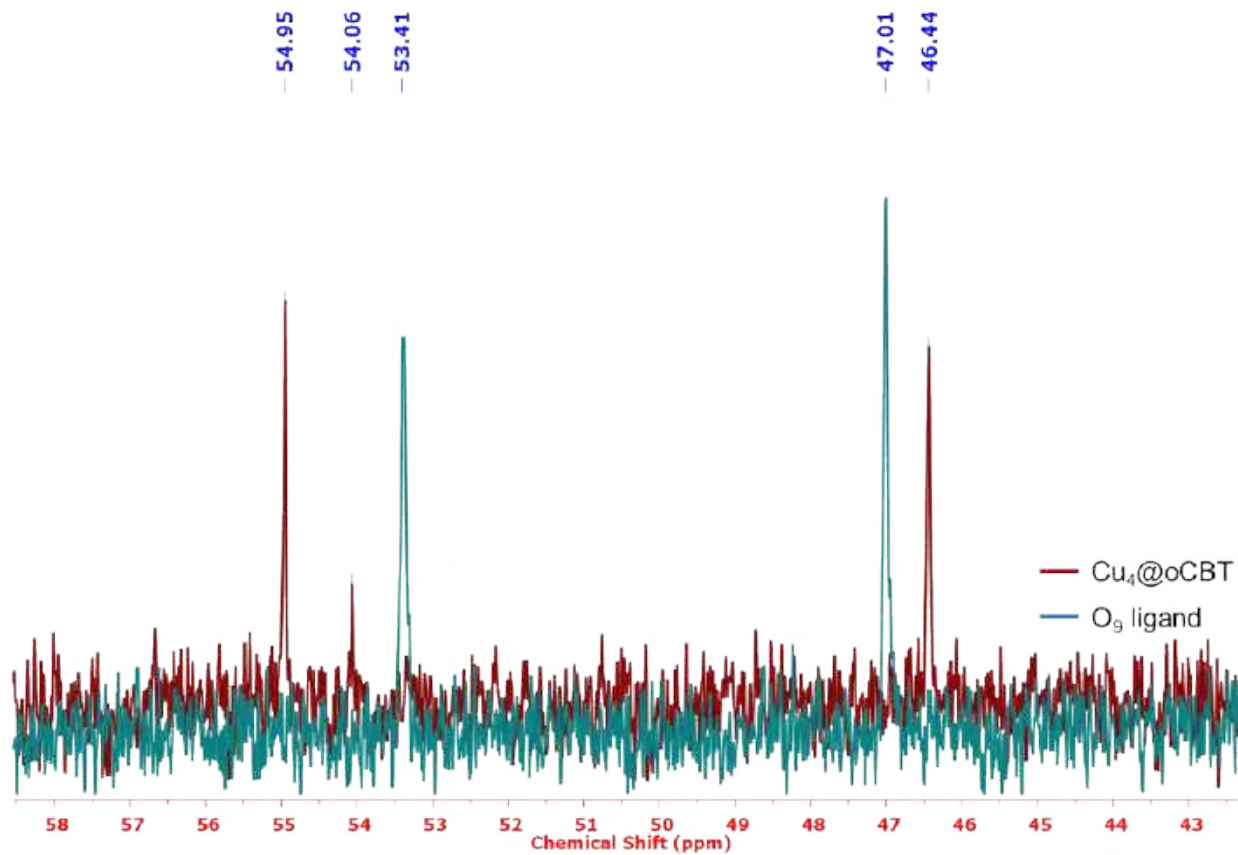


**Fig. S20** Combined  $^{13}\text{C}\{^1\text{H}\}$  NMR spectra of  $\text{Cu}_4@o\text{CBT}$  and  $\text{O}_9$  ligand.  $\delta = 54.06$  ppm is due to solvent impurity.

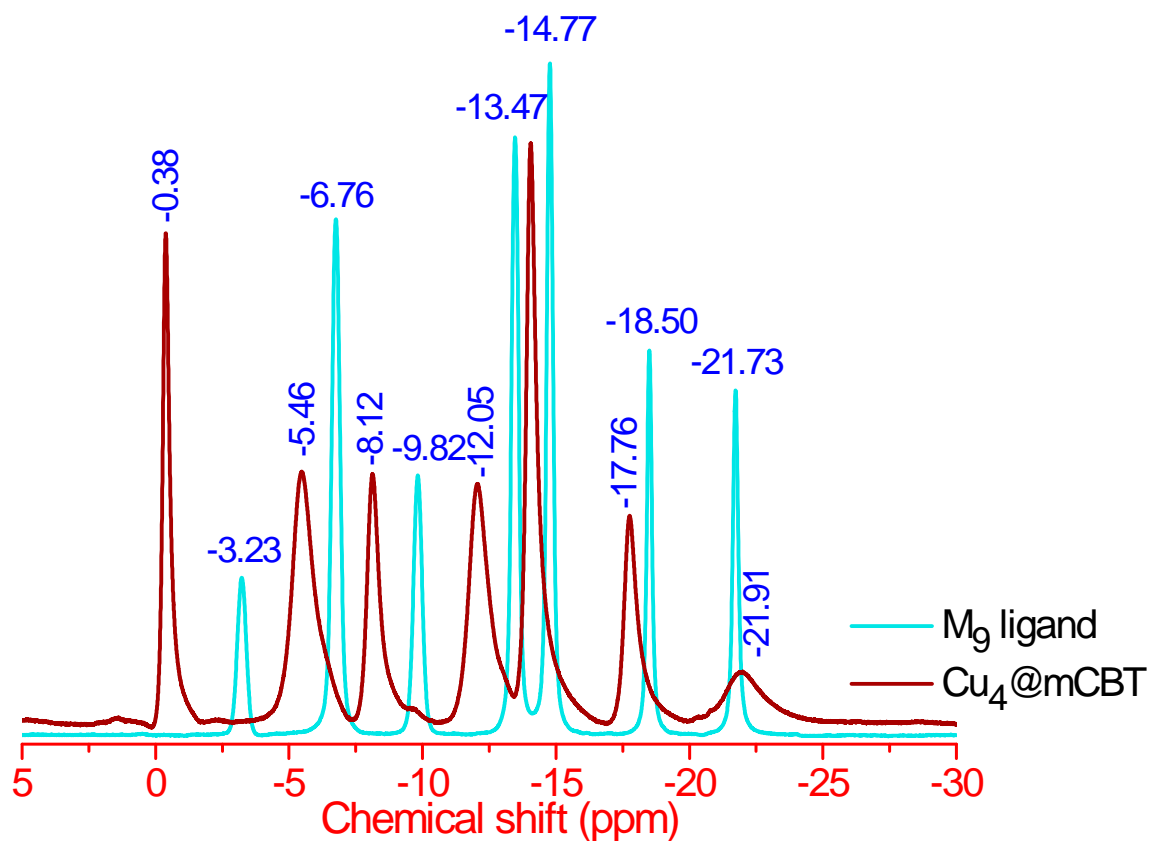


**Fig. S21** Combined  $^{11}\text{B}\{^1\text{H}\}$  NMR spectra of  $\text{Cu}_4@m\text{CBT}$  and  $\text{M}_9$  ligand.

**Table S10.**  $^{11}\text{B}\{^1\text{H}\}$  NMR chemical shift data for  $\text{Cu}_4@m\text{CBT}$  and  $\text{M}_9$  ligand.

Chemical shift (ppm) of $\text{Cu}_4@m\text{CBT}$	Intensity ratio
-0.38, -5.46, -8.12, -12.05, -14.05, -17.76, -21.91	(1:2:1:2:2:1:1)
Chemical shift (ppm) of $\text{M}_9$ ligand	
-3.23, -6.76, -9.82, -13.47, -14.77, -18.50, -21.73	(1:2:1:2:2:1:1)



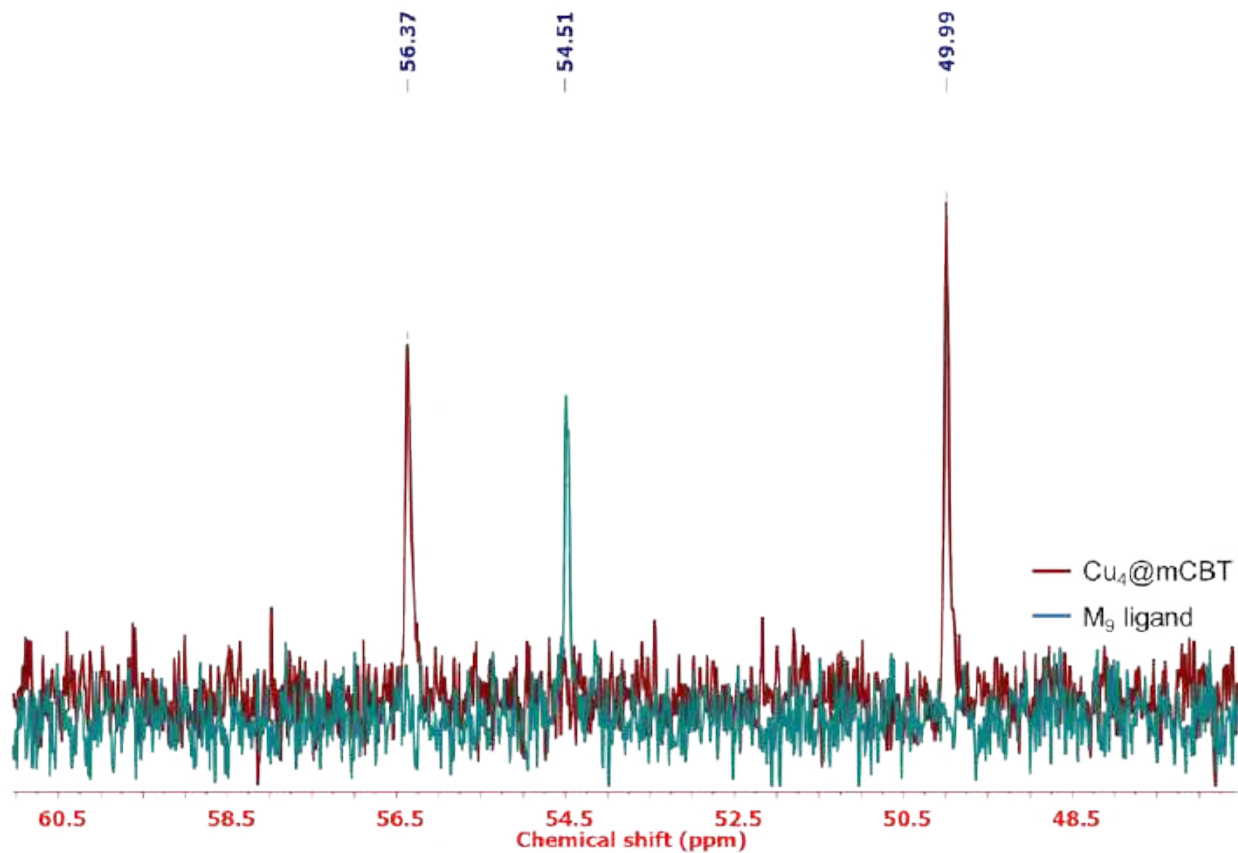


**Fig. S22** Combined  $^{13}\text{C}\{^1\text{H}\}$  NMR spectra of  $\text{Cu}_4@m\text{CBT}$  and  $\text{M}_9$  ligand.

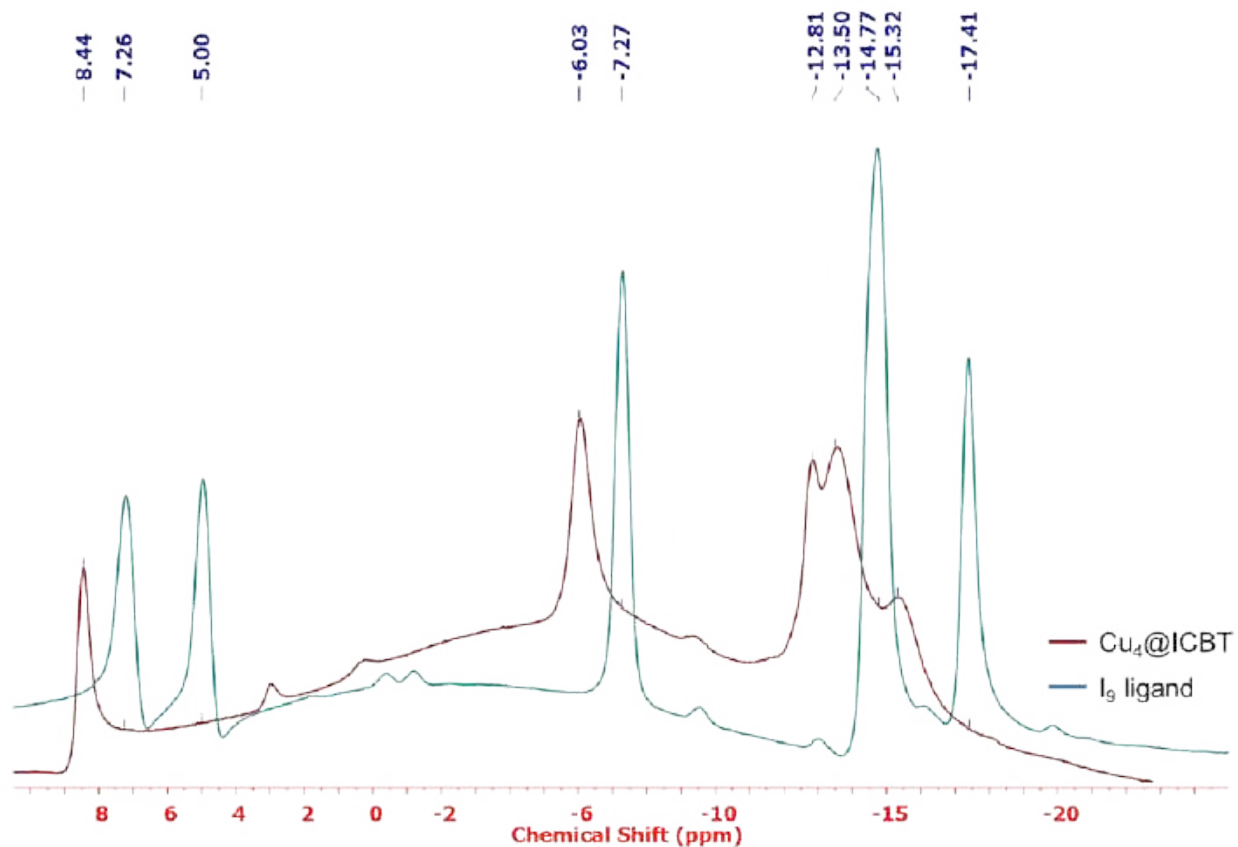


**Fig. S23** Combined  $^{11}\text{B}\{^1\text{H}\}$  NMR spectra of  $\text{Cu}_4\text{@ICBT}$  and  $\text{I}_9$  ligand.

**Table S11.**  $^{11}\text{B}\{^1\text{H}\}$  NMR chemical shift data for  $\text{Cu}_4\text{@ICBT}$  and  $\text{I}_9$  ligand.

Chemical shift (ppm) of $\text{Cu}_4\text{@ICBT}$	Intensity ratio
8.44, -6.03, -12.81, -13.50, -15.32	(1:3:2:3:1)
Chemical shift (ppm) of $\text{I}_9$ ligand	
7.26, 5.00, -7.27, -14.77, -17.41	(1:1:2:4:2)

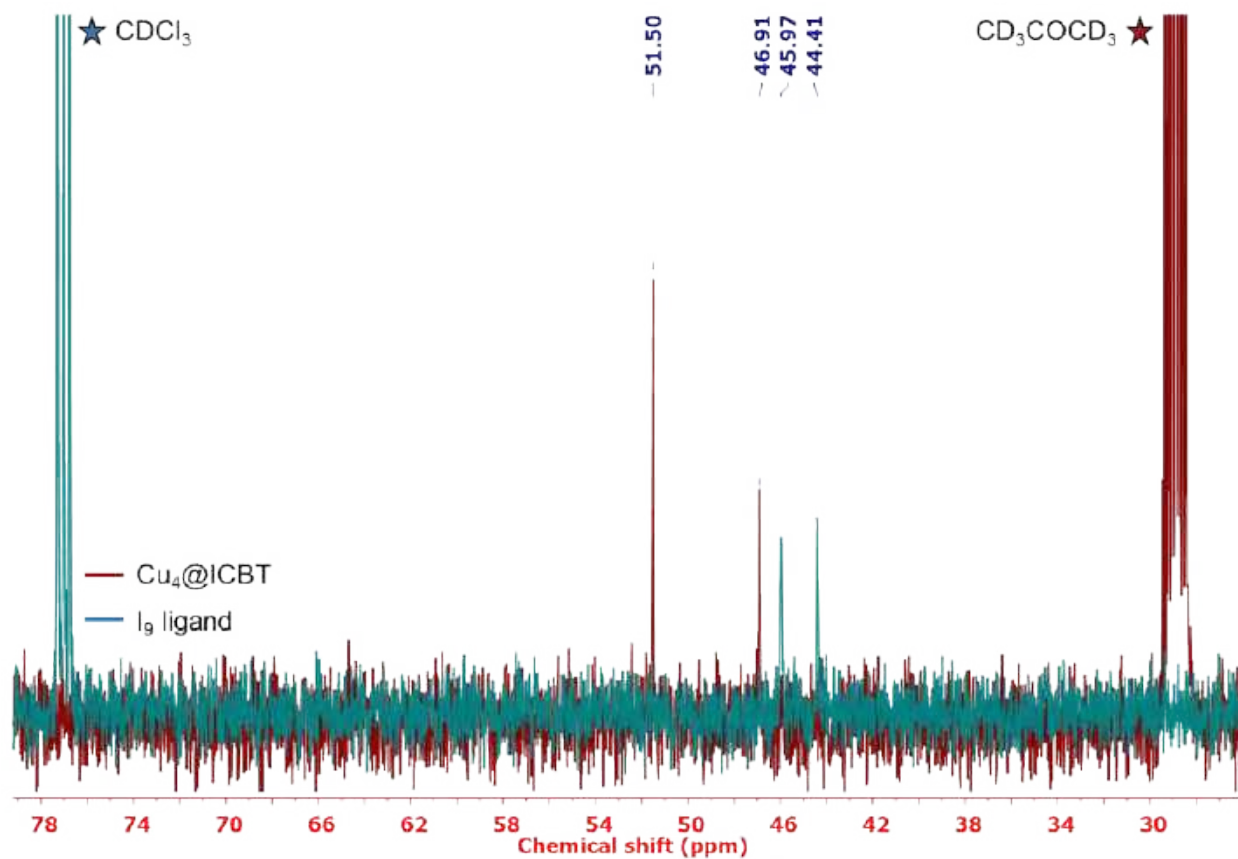


**Fig. S24** Combined  $^{13}\text{C}$   $\{^1\text{H}\}$  NMR spectra of  $\text{Cu}_4@ICBT$  and  $I_9$  ligand. Solvents peaks are marked in the respective spectrum.

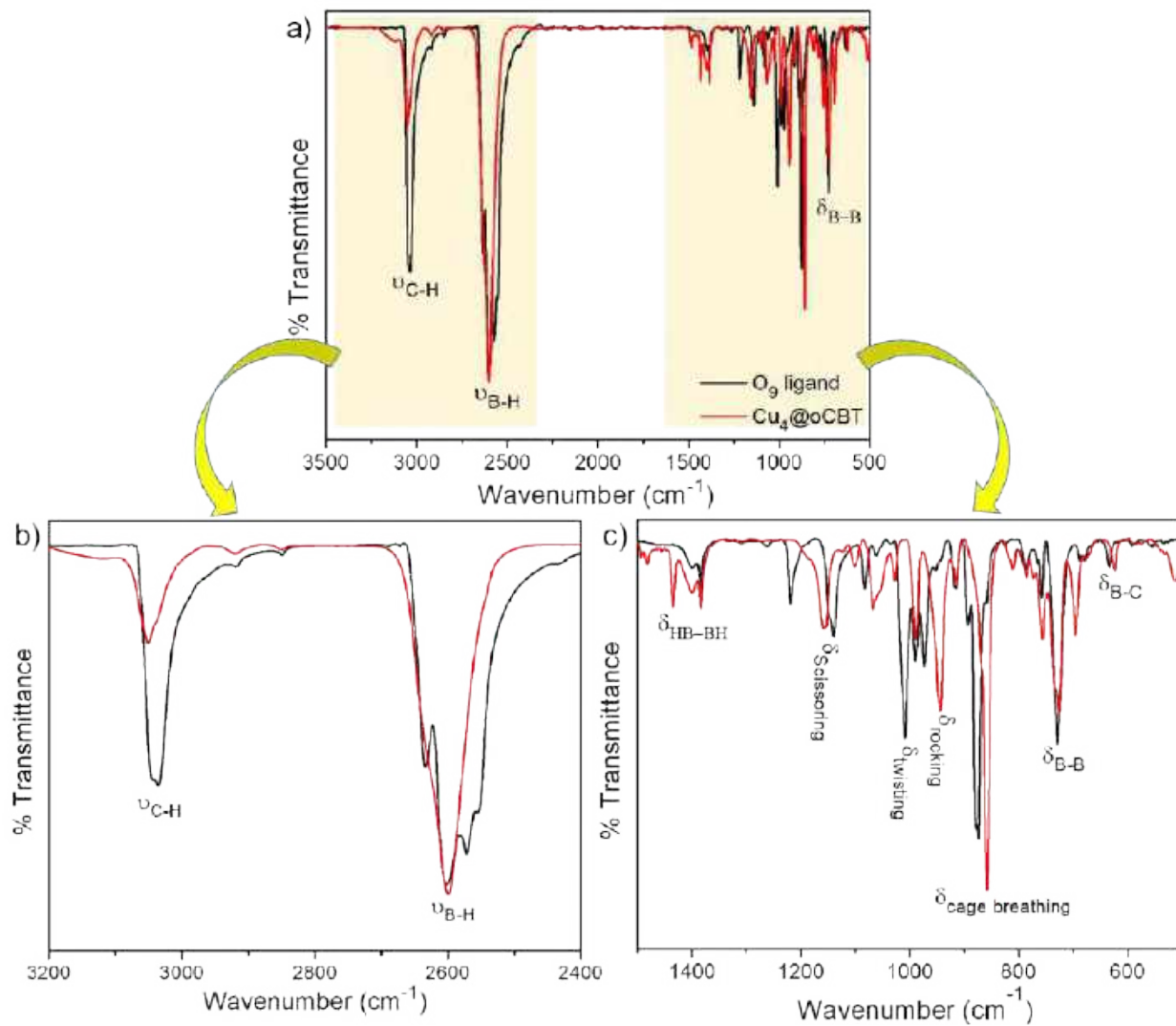


**Fig. S25** a) The full range FT-IR spectra of  $\text{Cu}_4@o\text{CBT}$  along with the  $\text{O}_9$  ligand. b, c) Enlarged view of the spectral regions. Spectral assignments are performed based on the theoretical calculations shown in Fig. S28.

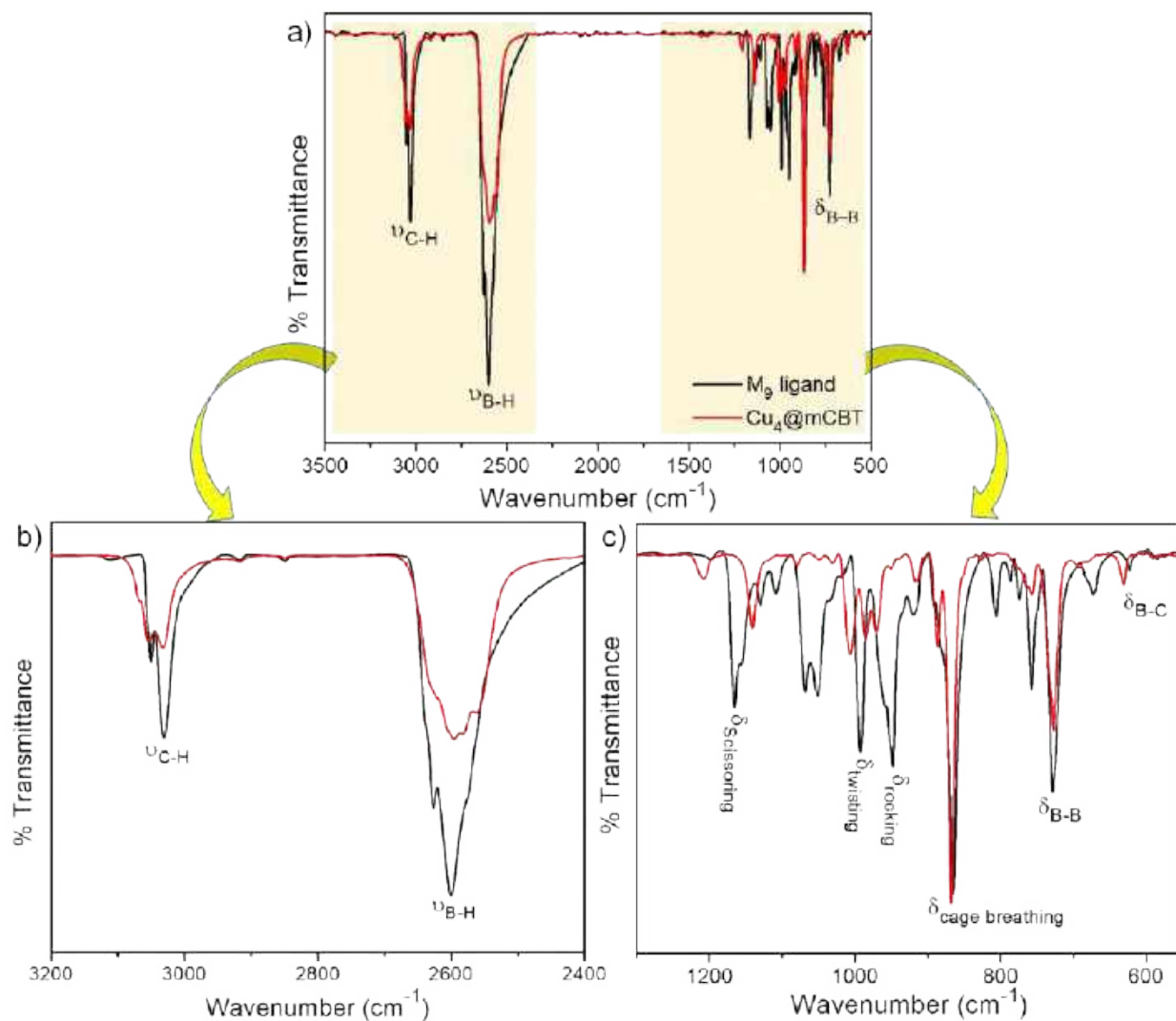


**Fig. S26** a) The full range FT-IR spectra of  $\text{Cu}_4@m\text{CBT}$  along with the  $\text{M}_9$  ligand. b, c) Enlarged view of the spectral regions.

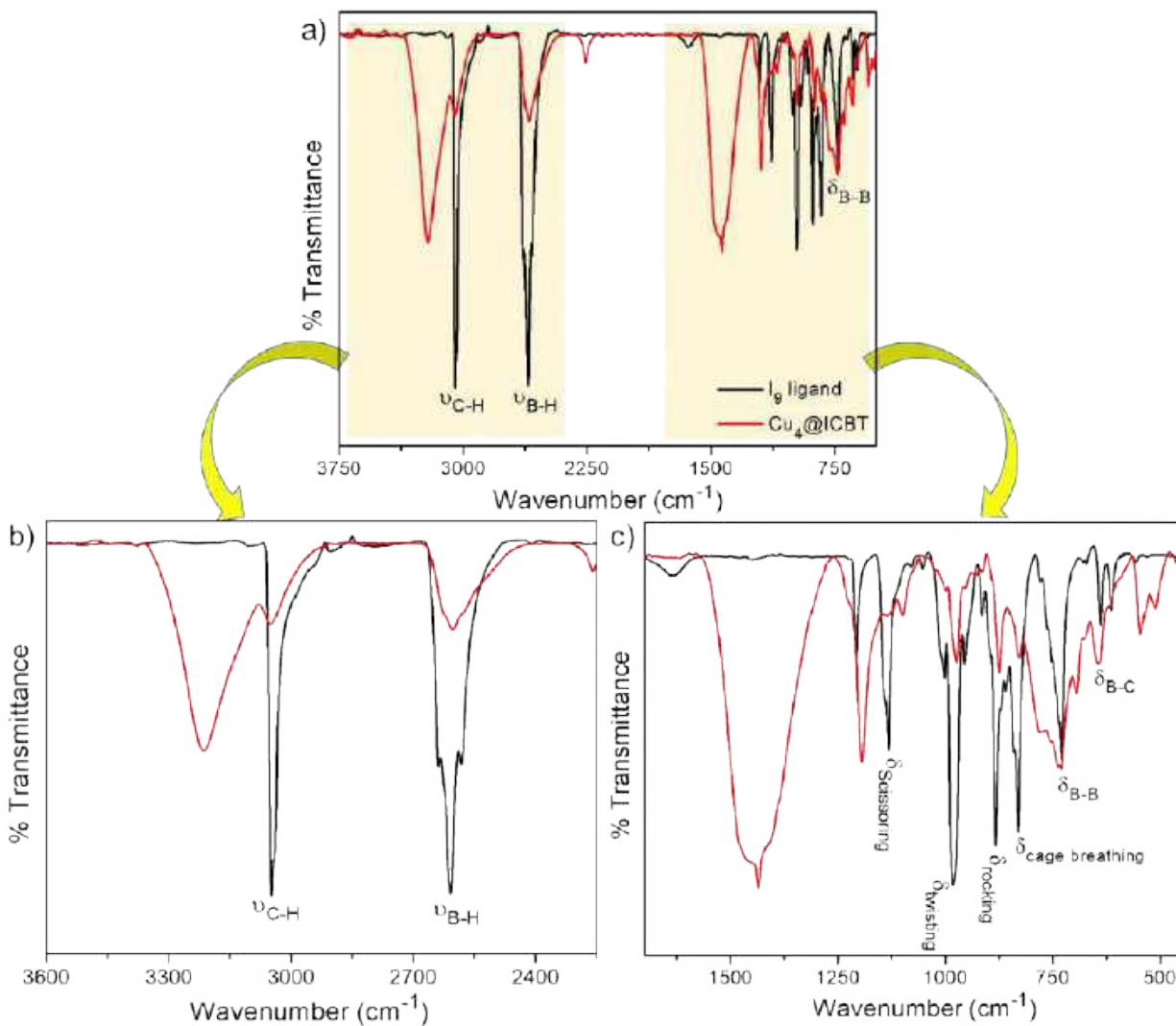


**Fig. S27** a) The full range FT-IR spectra of  $\text{Cu}_4@ICBT$  along with the  $\text{I}_9$  ligand. b, c) Enlarged view of the spectral regions. Peaks of interest are marked here.



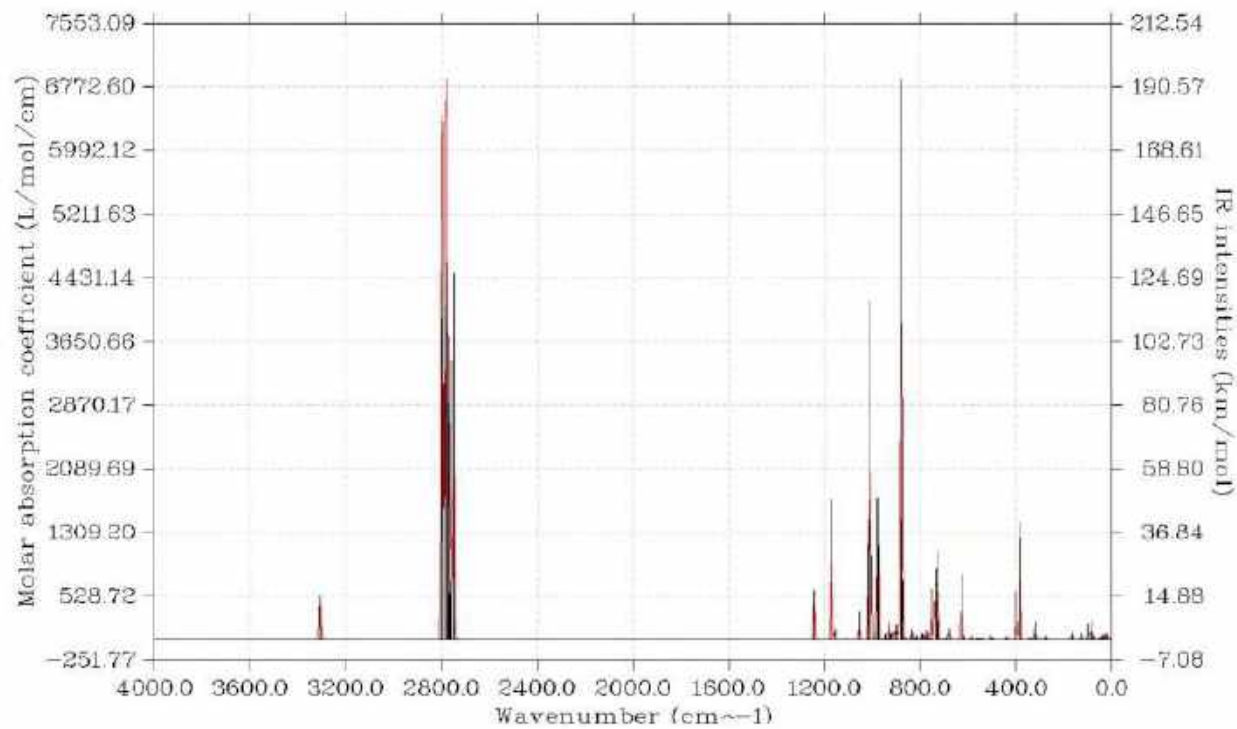


**Fig. S28** The calculated IR spectra of  $\text{Cu}_4@o\text{CBT}$  in the gas phase.

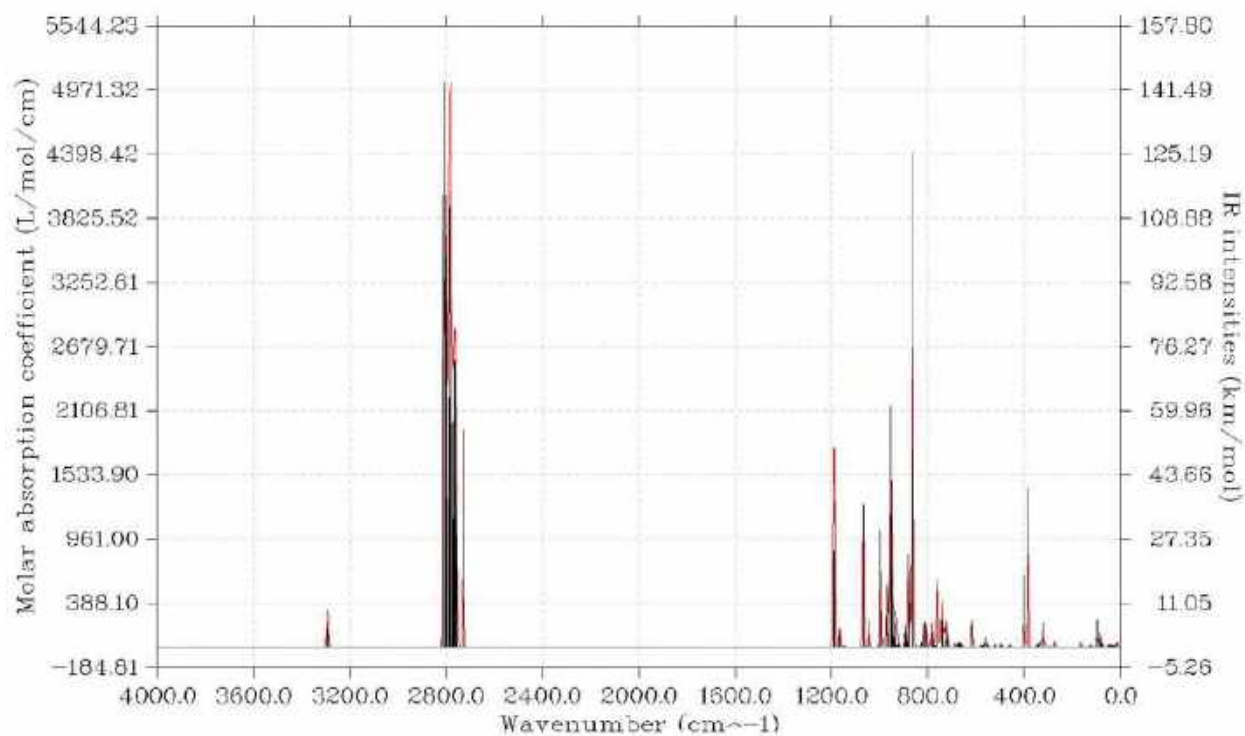


**Fig. S29** The calculated IR spectra of  $\text{Cu}_4@m\text{CBT}$  in the gas phase.

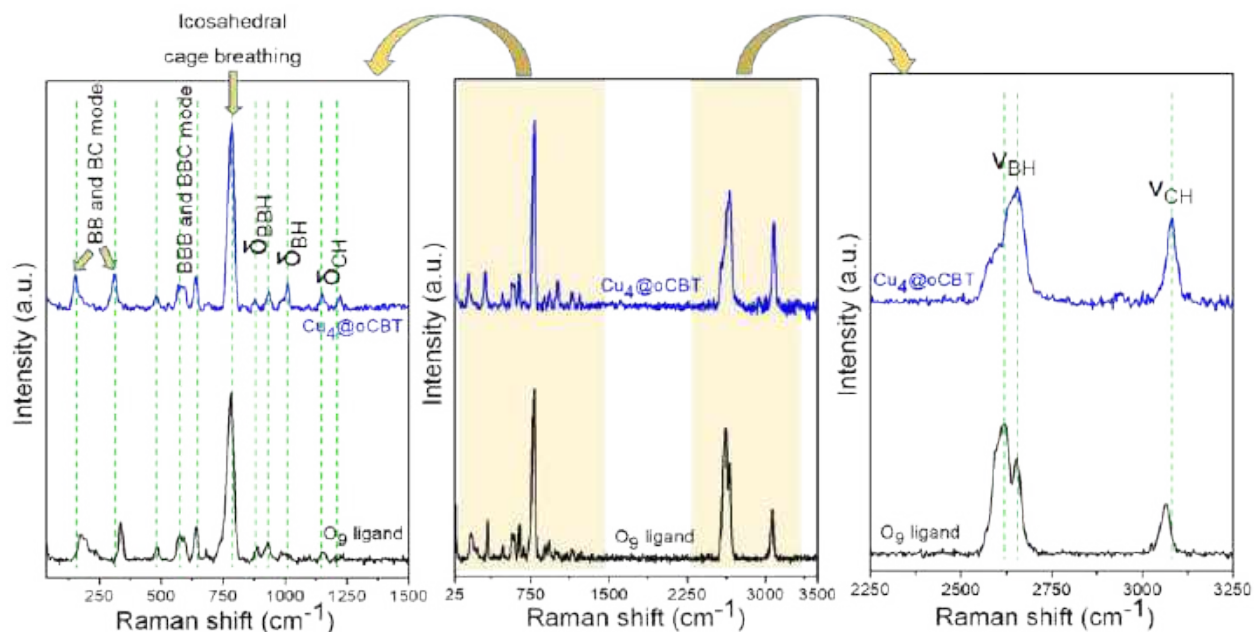


**Fig. S30** Raman spectra of  $\text{Cu}_4@o\text{CBT}$  crystals in comparison with  $\text{O}_9$  ligand. An expanded view with marked peaks shows the variation of carboranes vibrational modes in the cluster. The 532 nm laser was used for these measurements. Spectral assignments are performed following the literature.<sup>14</sup>

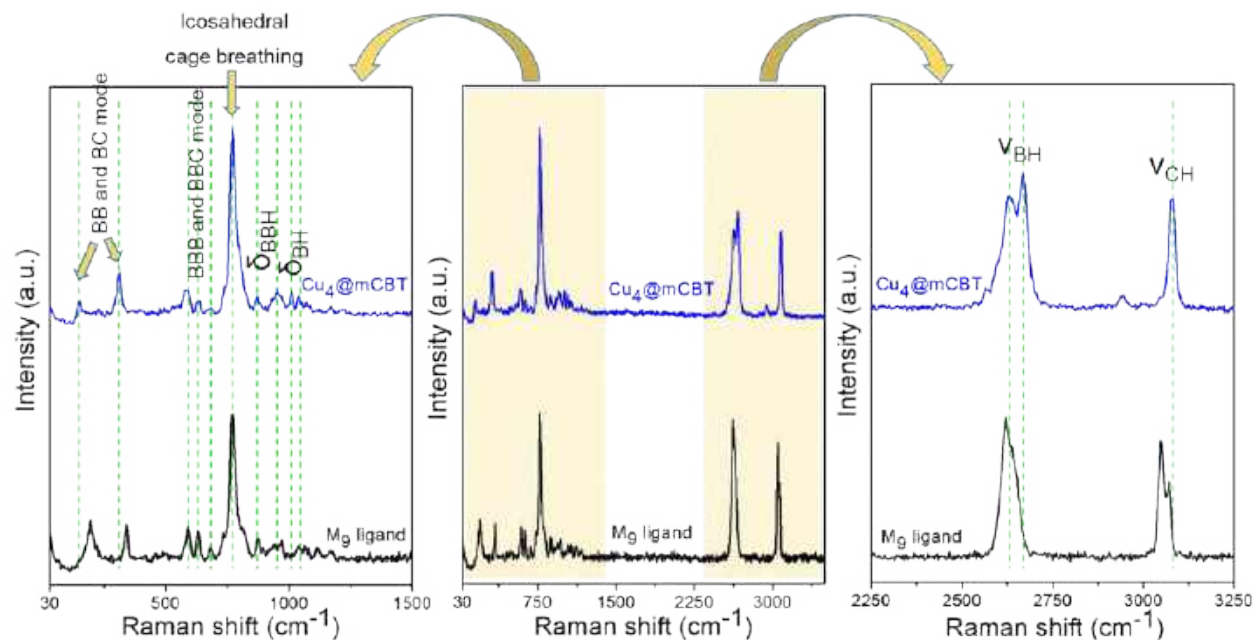


**Fig. S31** Raman spectra of  $\text{Cu}_4@m\text{CBT}$  crystals in comparison with  $\text{M}_9$  ligand. An expanded view with marked peaks shows the variation of carboranes vibrational modes in the cluster. The 532 nm laser was used for these measurements. Spectral assignments are performed following the literature.<sup>14</sup>

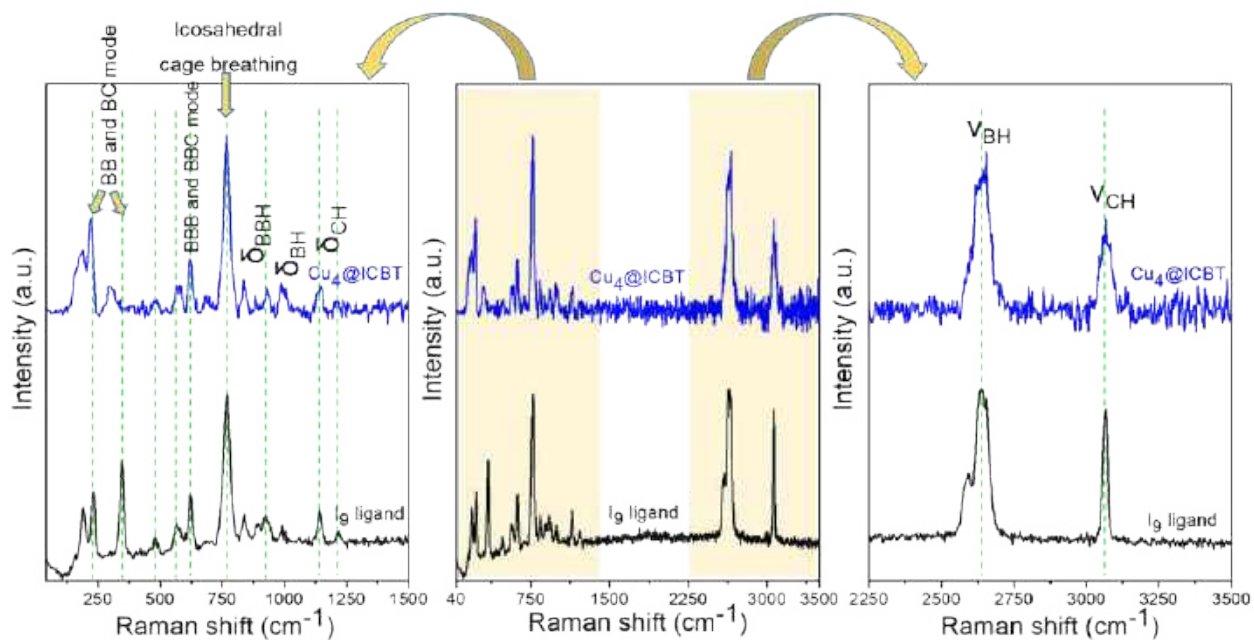


**Fig. S32** Raman spectra of  $\text{Cu}_4\text{@ICBT}$  crystals in comparison with the  $\text{I}_9$  ligand. An expanded view with marked peaks shows the variation of carboranes vibrational features in the cluster. The 532 nm laser was used for these measurements. Spectral assignments are performed following earlier literature.<sup>14</sup>

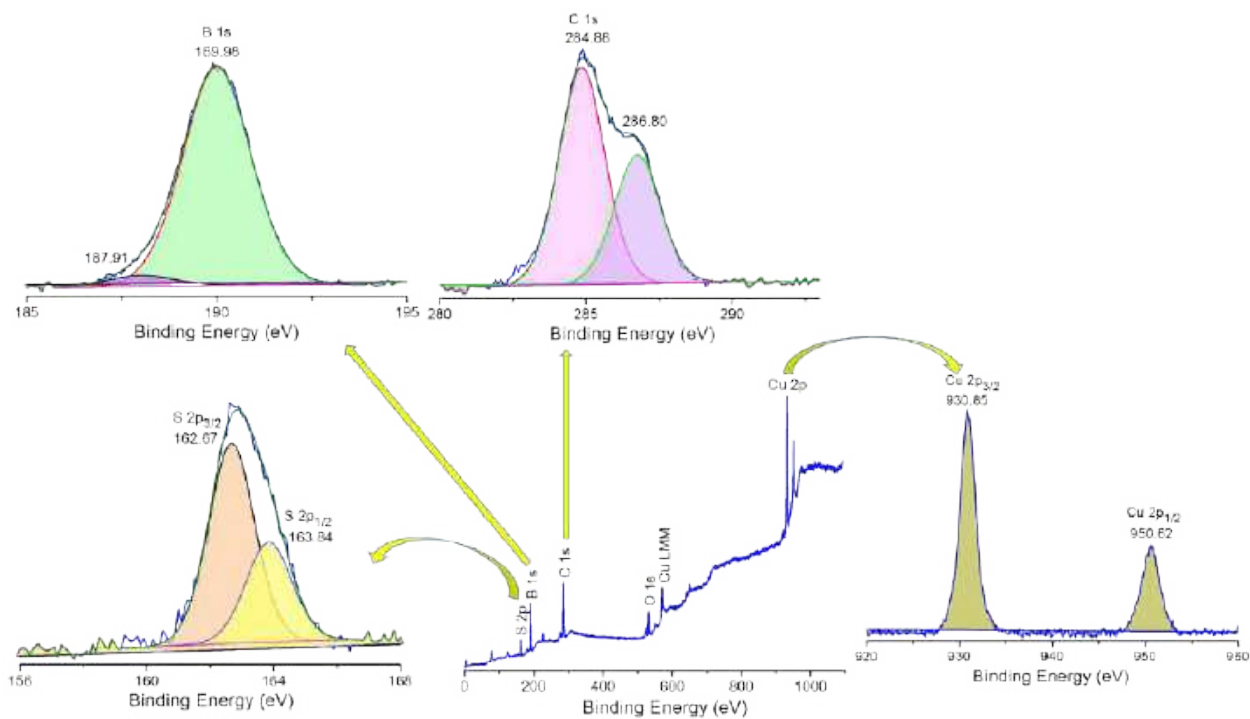


**Fig. S33** XPS spectrum of  $\text{Cu}_4\text{@oCBT}$ . The survey spectrum shows the existence of respective elements. Expanded peak fitting of Cu 2p, S 2p, C 1s and B 1s spectral regions.

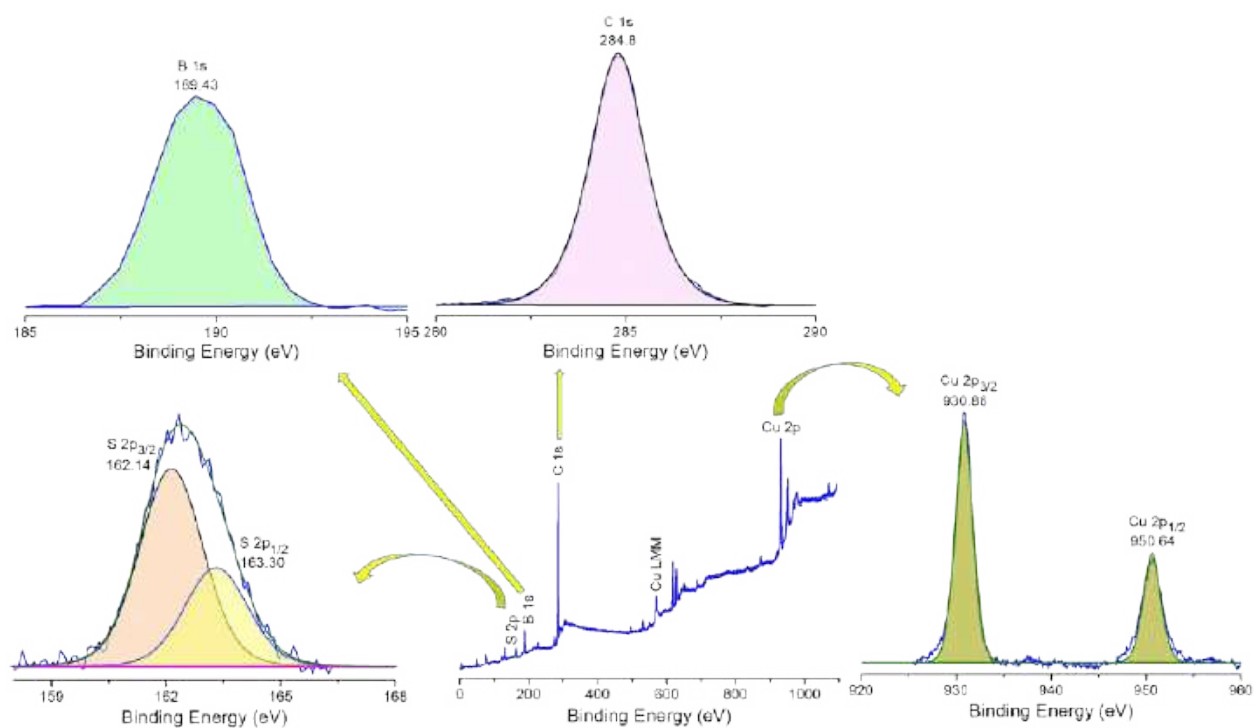


**Fig. S34** XPS spectrum of Cu<sub>4</sub>@mCBT. The survey spectrum shows the presence of respective elements. Expanded peak fitting of Cu 2p, S 2p, C 1s and B 1s spectral regions.

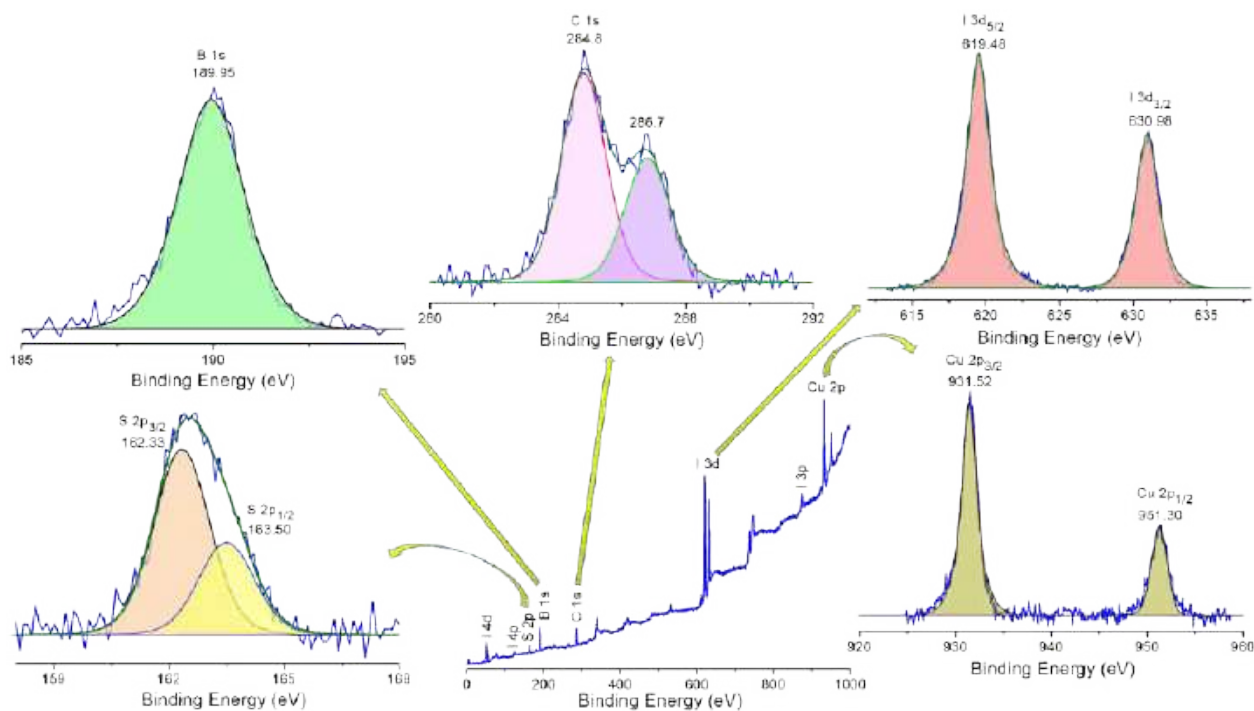


**Fig. S35** XPS spectrum of Cu<sub>4</sub>@ICBT. The survey XPS spectrum shows the presence of respective elements. Expanded peak fitting of Cu 2p, S 2p, I 3d, C 1s and B 1s spectral regions.



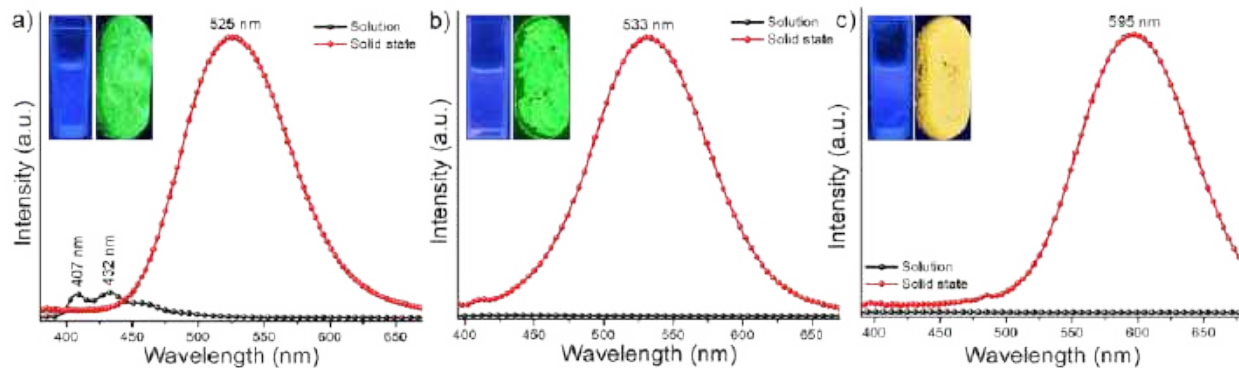


**Fig. S36** Photoluminescence spectra of a) Cu<sub>4</sub>@oCBT, b) Cu<sub>4</sub>@mCBT and c) Cu<sub>4</sub>@ICBT in the solid state as well as their respective solution (inset shows the photographic images of the respective clusters under UV lamp both in solution and in solid state).

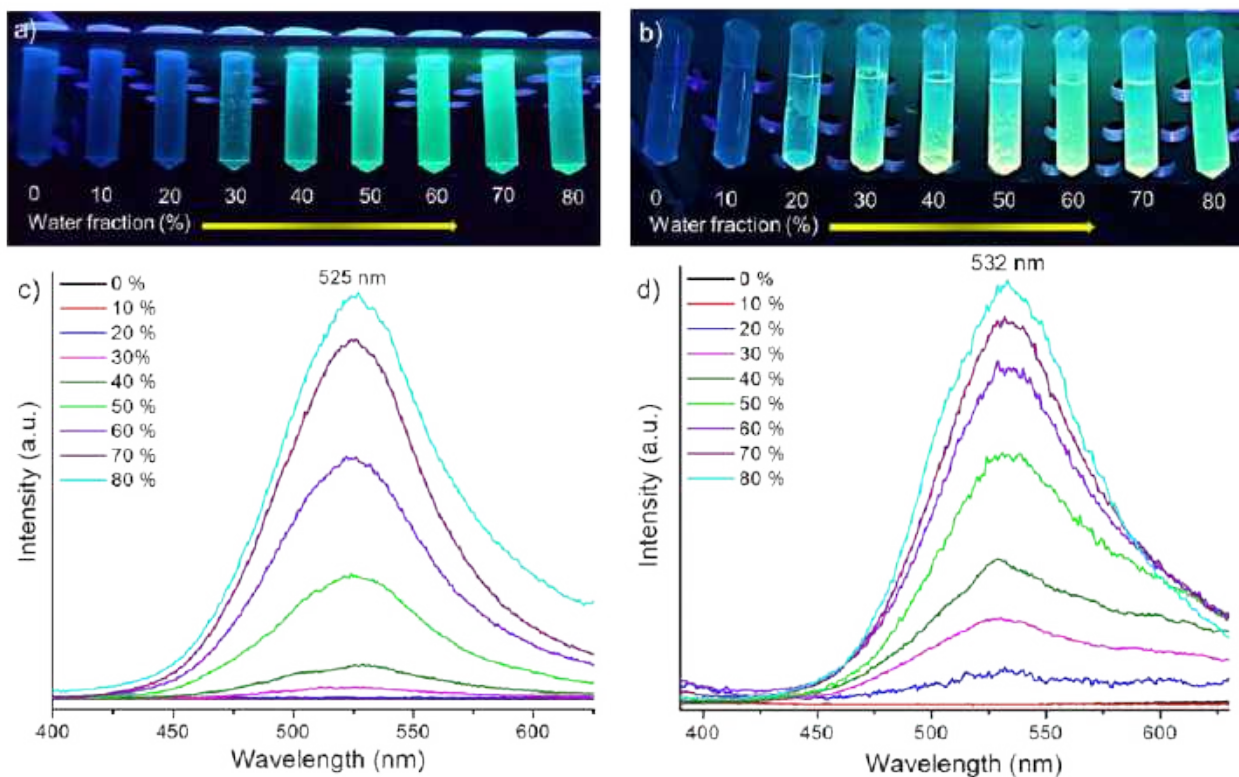


**Fig. S37** Photographs of a) Cu<sub>4</sub>@oCBT and b) Cu<sub>4</sub>@mCBT with varying fraction of water (volume %) indicating AIE behavior of these materials. The respective PL spectra of c) Cu<sub>4</sub>@oCBT and d) Cu<sub>4</sub>@mCBT with varying fraction of water.

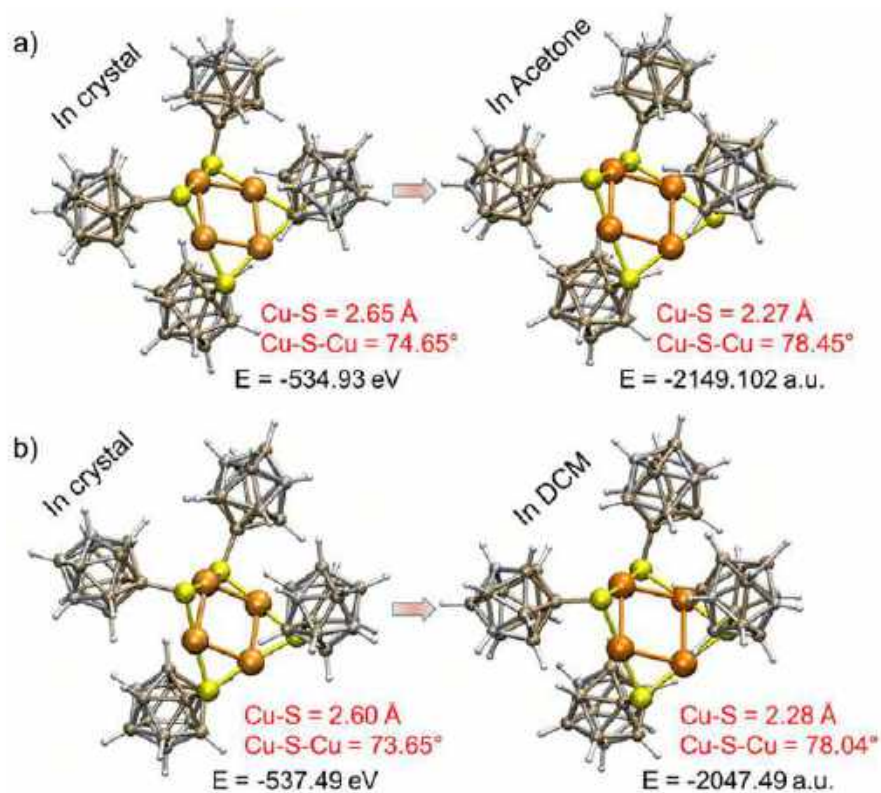


**Fig. S38** Structural variation through DFT studies of d)  $\text{Cu}_4@o\text{CBT}$  and e)  $\text{Cu}_4@m\text{CBT}$  in different states. Shortening of the distance of Cu-S bond and expansion of Cu-S-Cu bond angles were observed of these NCs.

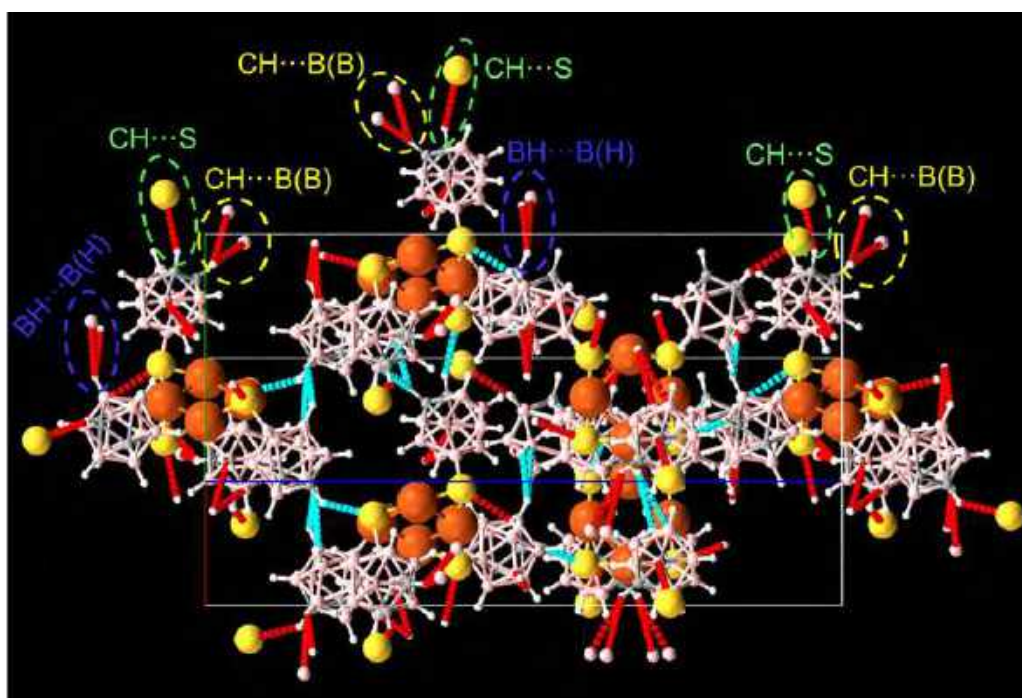


**Fig. S39** Different types of intermolecular interactions *i.e.*, CH-S, BH-BH and CH-BB present in  $\text{Cu}_4@o\text{CBT}$ .



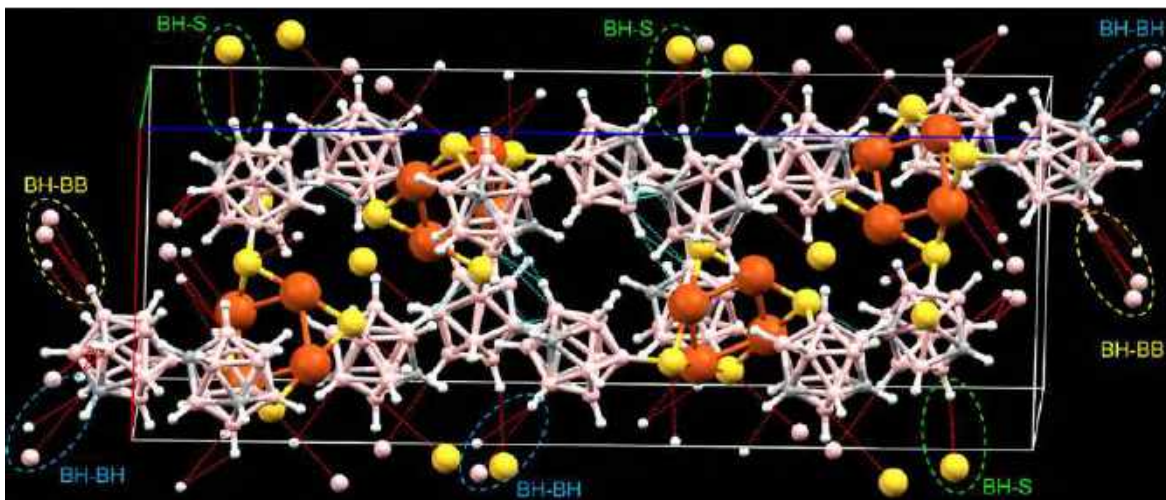


**Fig. S40** Different types of intermolecular interactions *i.e.*, BH-S, BH-BH and BH-BB present in  $\text{Cu}_4@o\text{CBT}$ .

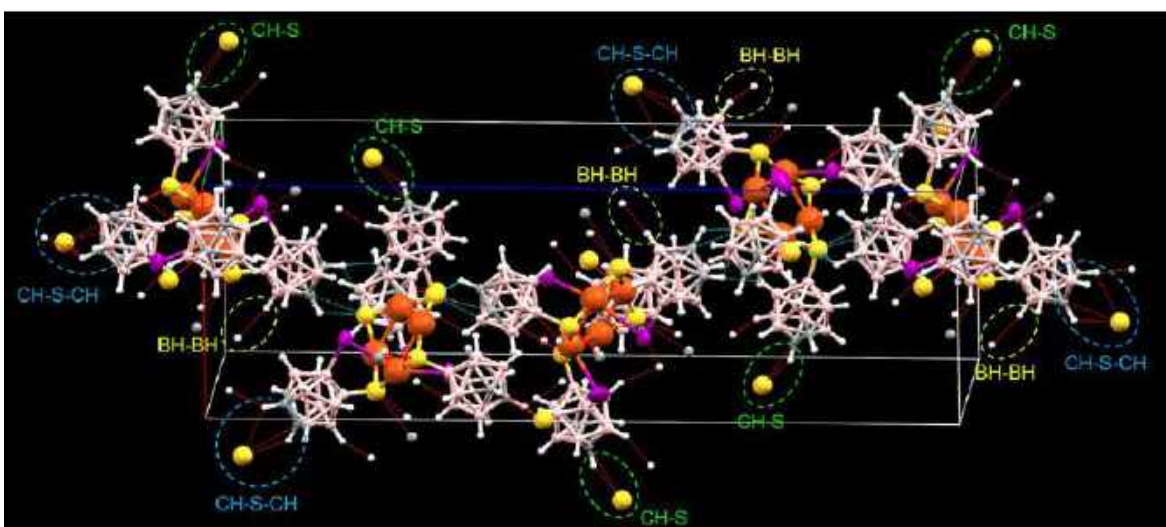


**Fig. S41** Different types of intermolecular interactions *i.e.*, CH-S-CH, BH-BH and CH-S present in  $\text{Cu}_4@i\text{CBT}$ .

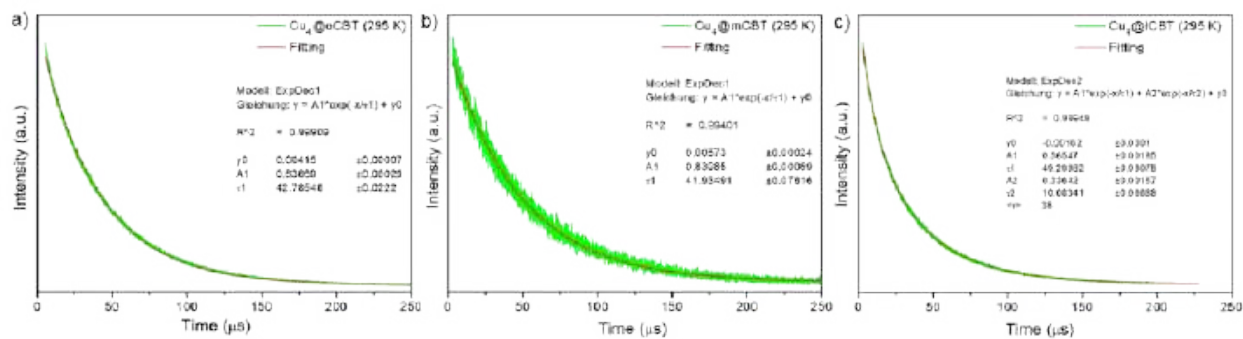


**Fig. S42** Lifetime decay profile of a)  $\text{Cu}_4@o\text{CBT}$ , b)  $\text{Cu}_4@m\text{CBT}$  and c)  $\text{Cu}_4@i\text{CBT}$  at 295 K with respective fittings.

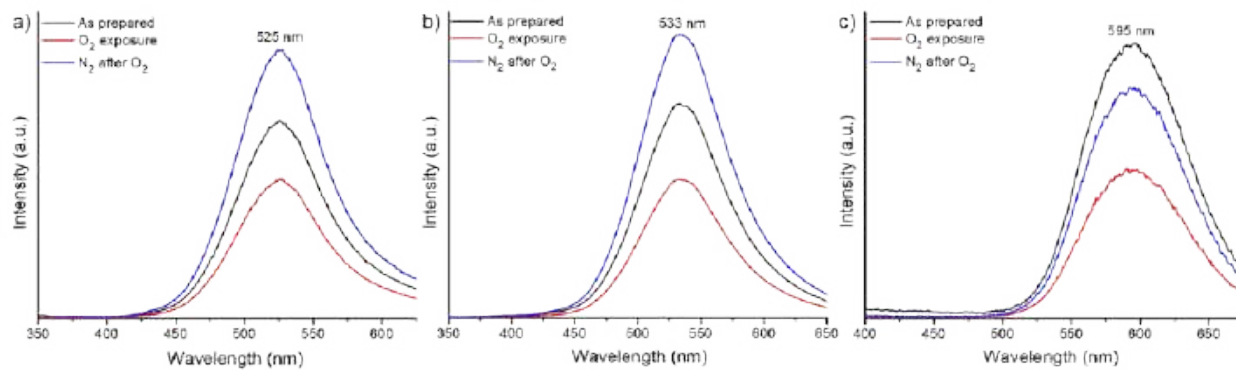


**Fig. S43** PL emission spectra of a)  $\text{Cu}_4@o\text{CBT}$ , b)  $\text{Cu}_4@m\text{CBT}$  and c)  $\text{Cu}_4@i\text{CBT}$  clusters before and after oxygen exposure. Reducing of the intensity upon  $\text{O}_2$  exposure (exposure time 12 h) suggest emission originating from the triplet state. Subsequent emission enhancement upon  $\text{N}_2$  exposure.

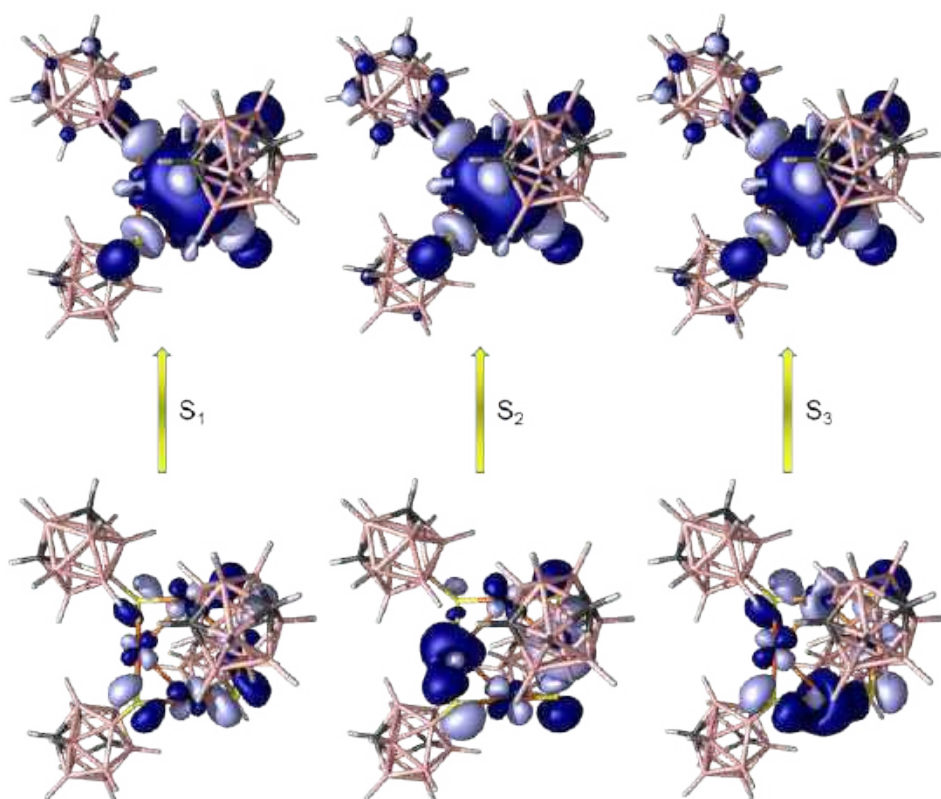


**Fig. S44** Natural transition orbitals for first 3 singlet excitations of  $\text{Cu}_4@m\text{CBT}$ .

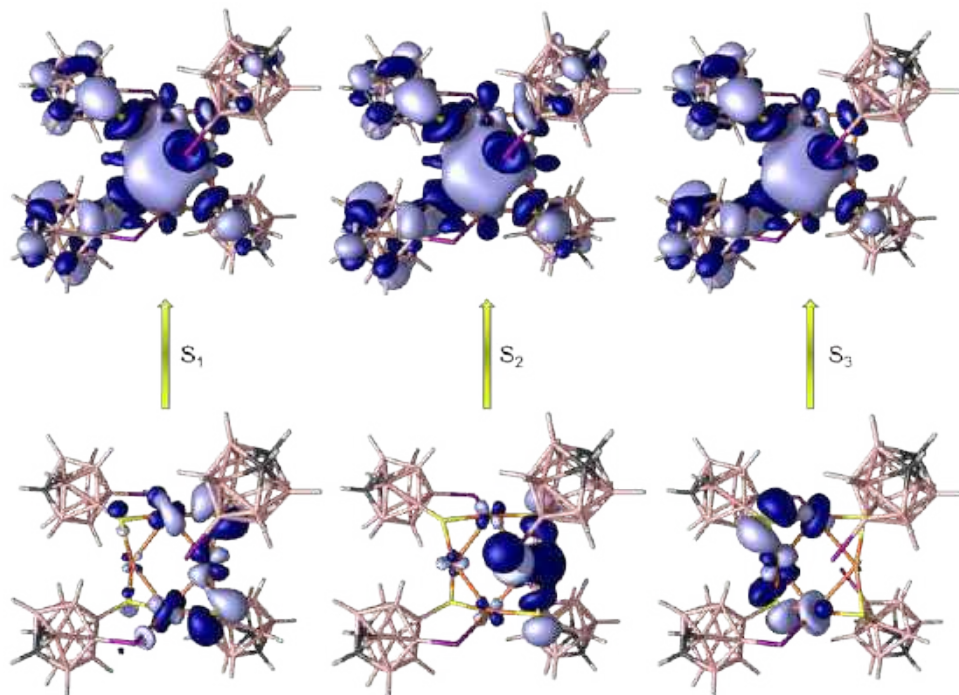


**Fig. S45** Natural transition orbitals for first 3 singlet excitations of  $\text{Cu}_4@ICBT$ .

**Table S12.** Calculated excited triplet state energies of  $\text{Cu}_4$  clusters, in eV.

Cluster	In vacuum ( $T_1$ )	In solution ( $T_1$ )	X-ray geometry ( $T_1$ )	Relaxed triplet ( $T_1'$ )
$\text{Cu}_4@oCBT$	3.89	3.89	4.09	2.35
$\text{Cu}_4@mCBT$	3.90	3.89	4.19	-
$\text{Cu}_4@ICBT$	3.56	3.62	3.82	1.83

**Table S13.** Calculated excited triplet state energies of  $\text{Cu}_4$  clusters, in nm.

Cluster	In vacuum ( $T_1$ )	In solution ( $T_1$ )	X-ray geometry ( $T_1$ )	Relaxed triplet ( $T_1'$ )
$\text{Cu}_4@oCBT$	318.45	318.50	303.19	526.95
$\text{Cu}_4@mCBT$	318.18	318.61	296.08	-
$\text{Cu}_4@ICBT$	361.23	343.88	324.36	679.34

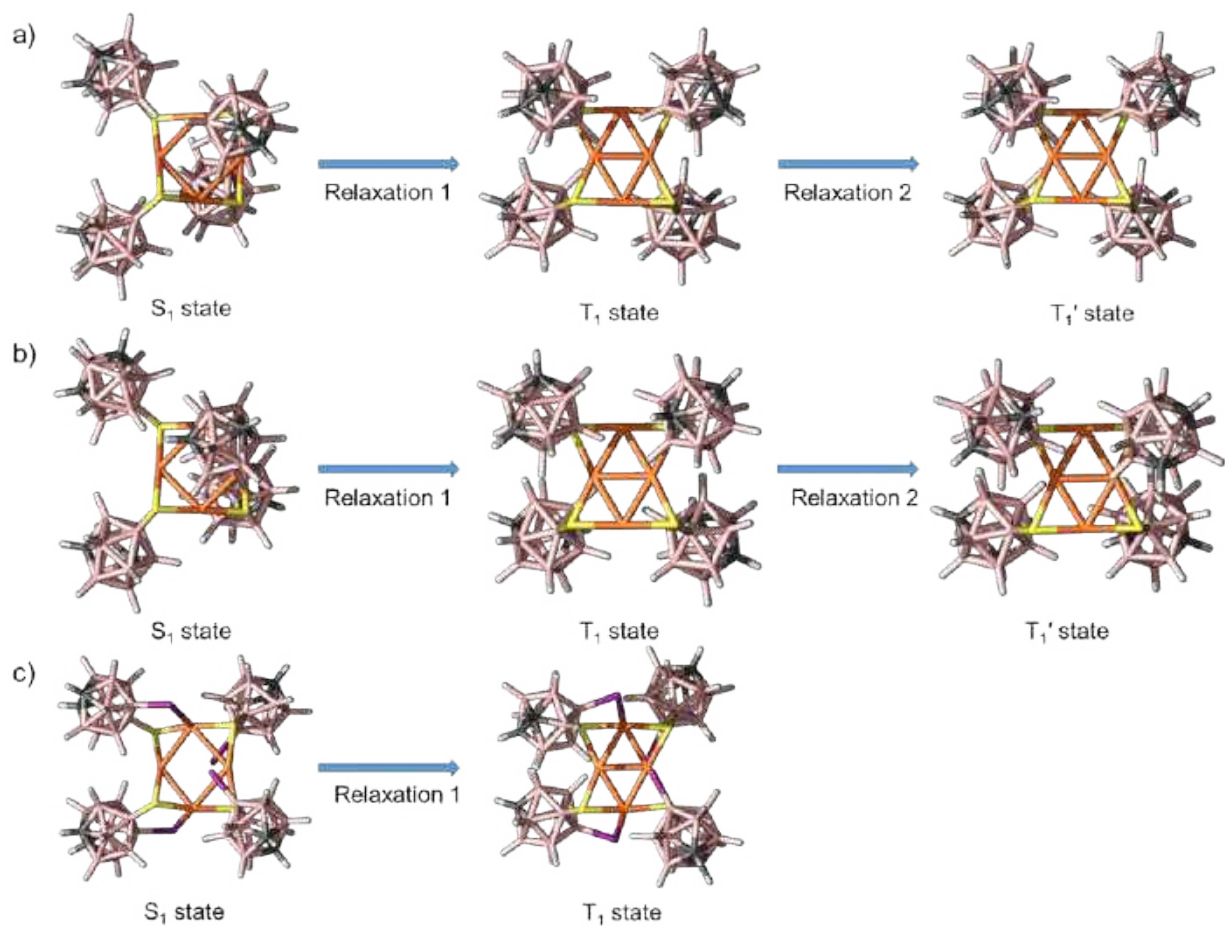


**Fig. S46** Singlet to triplet ( $S_1$  to  $T_1$ ) followed by triplet states ( $T_1$  to  $T_1'$ ) structural relaxations of a)  $\text{Cu}_4$ @oCBT, b)  $\text{Cu}_4$ @mCBT and c)  $\text{Cu}_4$ @ICBT clusters.



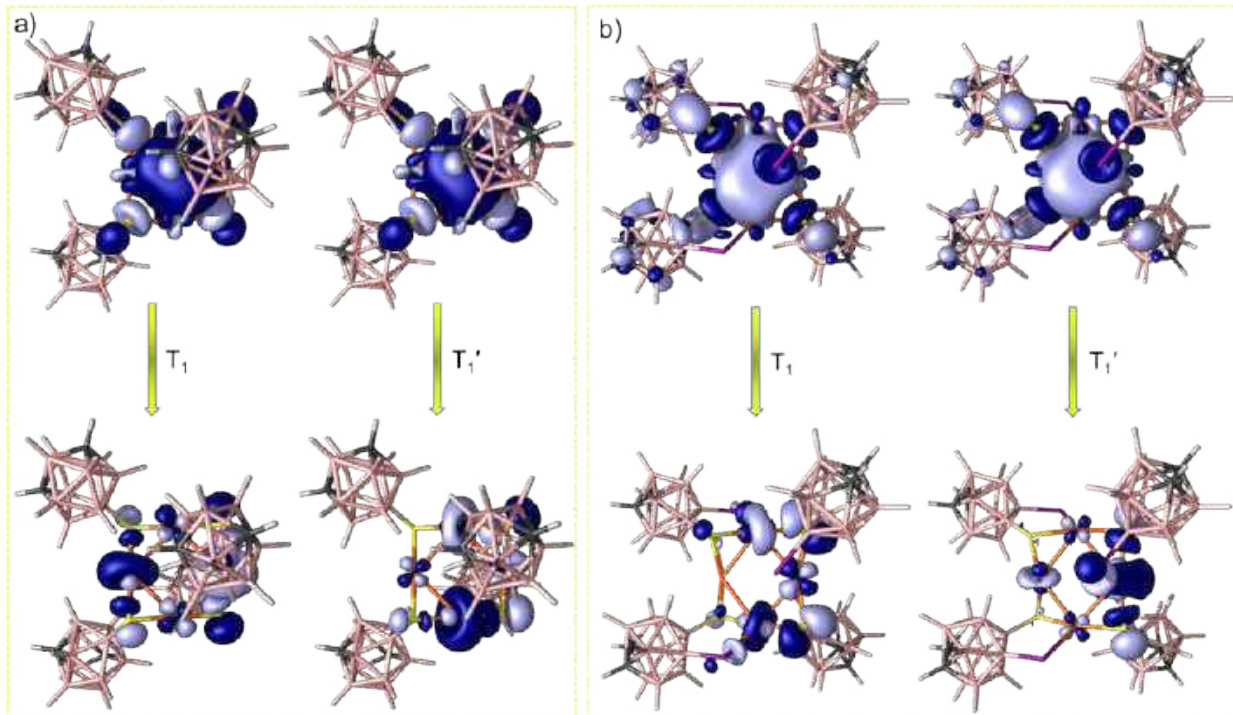


**Fig. S47** NTOs of T1 and T1' radiative relaxation of a) Cu<sub>4</sub>@mCBT and b) Cu<sub>4</sub>@ICBT clusters.

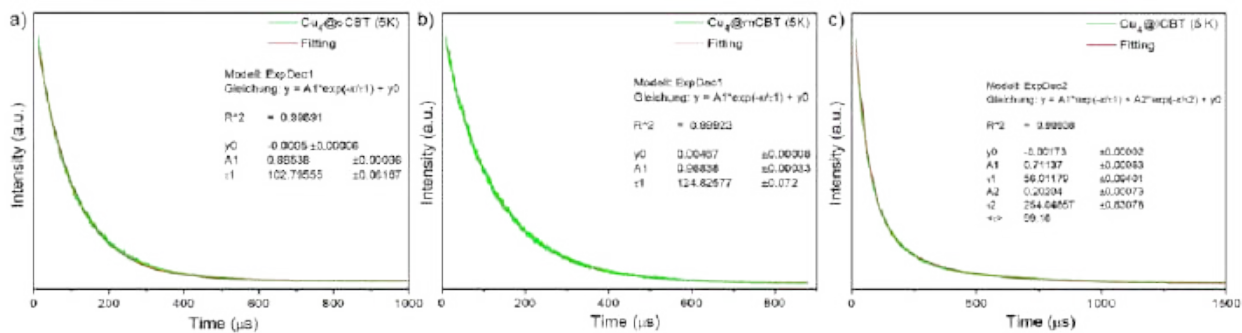


**Fig. S48** Lifetime decay profile of a) Cu<sub>4</sub>@oCBT, b) Cu<sub>4</sub>@mCBT and c) Cu<sub>4</sub>@ICBT at 5 K with respective fittings.

**Table S14.** Assignments of different lattice planes (h k l) of Cu<sub>4</sub>@oCBT through simulated PXRD.

Sl. no	Peak position 2θ (degree)	Lattice plane (h k l)
1	9.001	(0 0 3)
2	9.418	(1 0 1)
3	10.76	(1 0 2)
4	12.687	(1 0 3)
5	14.982	(1 0 4)
6	15.484	(2 -1 0)
7	15.777	(2 -1 1)
8	16.621	(2 -1 2)
9	17.515	(1 0 5)
10	17.912	(2 0 0)

11	18.157	(2 0 1)
12	18.896	(2 0 2)
13	19.65	(2 -1 4)
14	20.075	(2 0 3)
15	22.961	(1 0 7)
16	23.46	(2 0 5)
17	23.758	(3 -1 0)
18	23.89	(2 -1 6)
19	24.523	(3 -1 -2)
20	25.453	(3 -1 -3)
21	25.807	(1 0 8)
22	26.699	(3 -1 -4)
23	27.161	(3 0 1)
24	27.673	(3 0 2)
25	28.230	(3 -1 5)
26	29.638	(3 0 -4)
27	30.001	(3 -1 6)
28	30.234	(2 0 8)
29	31.04	(3 0 5)
30	31.266	(4 -2 0)
31	31.482	(2 -1 9)
32	31.976	(3 -1 7)
33	32.69	(3 0 -6)
34	33.15	(4 -1 2)
35	33.61	(4 -2 4)
36	33.865	(4 -1 3)
37	34.143	(3 -1 8)
38	34.512	(3 0 7)
39	34.846	(4 -1 -4)

**Table S15.** Assignments of different lattice planes (h k l) of Cu<sub>4</sub>@mCBT through simulated PXRD.

Sl. no	Peak position 2θ (degree)	Lattice plane (h k l)
1	5.46	(0 0 2)
2	7.765	(1 0 0)
3	7.881	(0 1 1)
4	9.197	(0 1 2)
5	9.395	(1 0 -2)
6	9.582	(1 0 2)
7	10.723	(1 1 0)
8	11.037	(0 1 3)
9	11.963	(1 1 -2)
10	12.115	(1 1 2)
11	13.413	(1 1 -3)
12	13.611	(1 1 3)
13	15.220	(1 1 -4)
14	15.539	(2 0 0)
15	15.805	(0 2 2)
16	16.986	(1 2 1)



17	17.559	(1 1 5)
18	17.674	(1 2 2)
19	18.059	(1 0 -6)
20	18.353	(1 0 6)
21	18.597	(1 2 -3)
22	18.962	(2 1 -3)
23	19.251	(2 1 3)
24	20.141	(1 2 4)
25	20.633	(2 1 4)
26	21.788	(1 2 5)
27	22.29	(2 1 5)
28	22.982	(0 3 2)
29	23.206	(2 2 3)
30	23.410	(3 0 0)
31	23.816	(1 3 1)
32	24.339	(0 2 7)
33	24.672	(3 1 -1)
34	25.114	(1 3 3)
35	25.779	(3 1 -3)
36	26.104	(3 1 3)
37	26.259	(0 3 5)
38	27.013	(2 2 -6)
39	27.421	(2 2 6)
40	27.801	(2 1 -8)
41	28.64	(2 3 3)
42	29.361	(2 3 -4)
43	30.156	(3 2 4)
44	30.803	(2 3 5)
45	31.05	(0 4 3)
46	31.698	(3 1 7)
47	31.991	(4 0 2)
48	32.183	(1 1 -11)
49	32.706	(3 3 1)
50	32.945	(3 3 -2)
51	33.401	(2 3 -7)
52	33.525	(4 1 3)
53	33.96	(3 0 -9)
54	34.384	(1 3 -9)

**Table S16.** Assignments of different lattice planes (h k l) of Cu<sub>4</sub>@ICBT through simulated PXRD.

Sl. no	Peak position 2θ (degree)	Lattice plane (h k l)
1	7.3	(1 0 1)
2	8.247	(1 0 2)
3	8.879	(0 0 4)
4	9.62	(1 0 3)
5	10.07	(1 1 1)
6	10.79	(1 1 2)

7	11.28	(1 0 4)
8	11.878	(1 1 3)
9	13.11	(1 0 5)
10	13.256	(1 1 4)
11	13.91	(2 0 0)
12	14.85	(1 1 5)
13	15.045	(1 0 6)
14	15.44	(2 0 3)
15	15.56	(2 1 0)
16	16.2	(2 1 2)
17	16.55	(2 0 4)
18	16.95	(2 1 3)
19	17.83	(2 0 5)
20	19.15	(1 0 8)
21	19.32	(2 0 6)
22	20.55	(2 1 6)
23	21.06	(3 0 1)
24	22.089	(3 1 0)
25	22.19	(3 1 1)
26	22.38	(1 1 9)
27	22.53	(3 1 2)
28	22.67	(2 0 8)
29	22.77	(3 0 4)
30	23.09	(3 1 3)
31	23.86	(3 1 4)
32	24.49	(2 0 9)
33	25.23	(3 2 0)
34	25.31	(3 2 1)
35	25.49	(2 1 9)
36	27.321	(2 1 10)
37	28.516	(3 1 8)
38	29.772	(3 2 7)
39	29.958	(2 2 10)
40	31.179	(2 1 12)
41	31.754	(4 2 2)
42	32.436	(3 2 9)
43	32.737	(4 2 4)
44	33.276	(3 1 11)
45	34.294	(3 0 12)

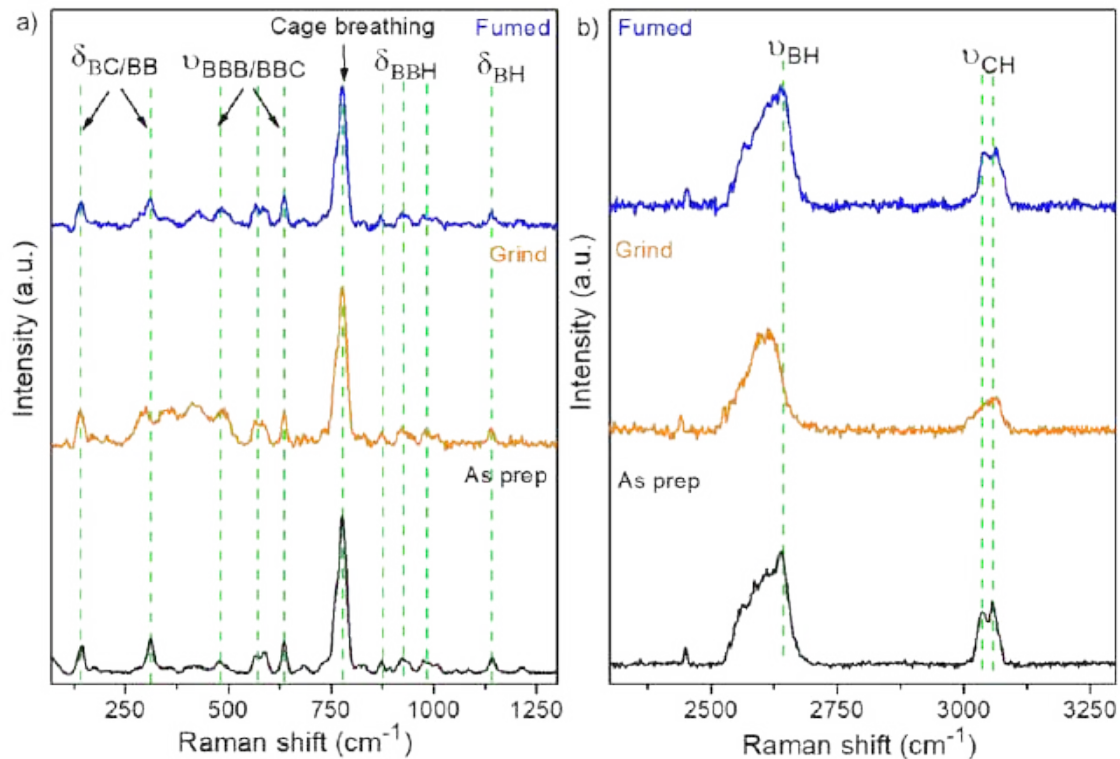


**Fig. S49** Comparative Raman spectra of  $\text{Cu}_4@o\text{CBT}$  during mechanical grinding and solvent fuming experiment.

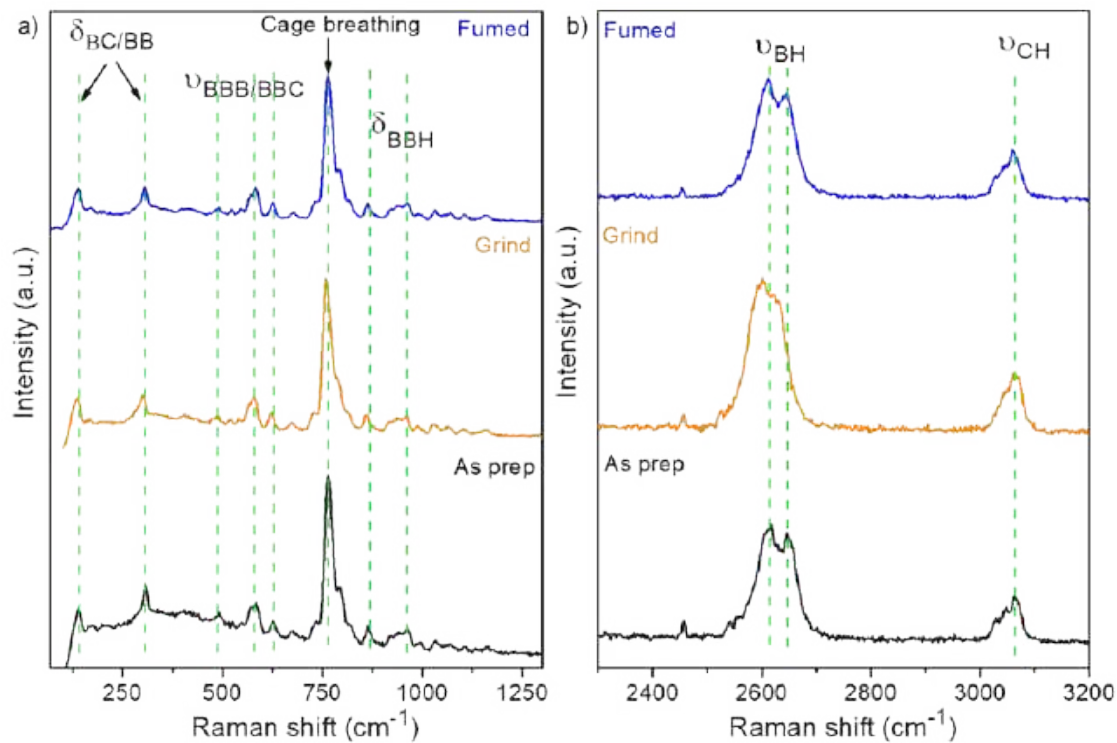


**Fig. S50** Comparative Raman spectra of  $\text{Cu}_4@m\text{CBT}$  during mechanical grinding and solvent fuming experiment.

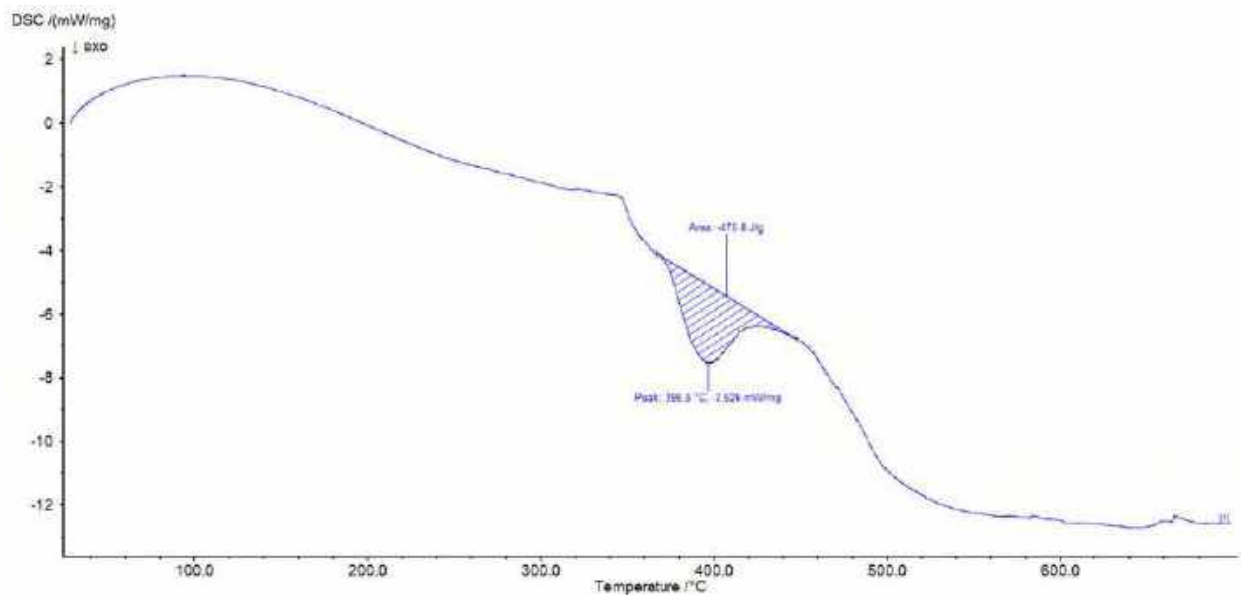


**Fig. S51** Differential scanning calorimetry (DSC) data of Cu<sub>4</sub>@oCBT microcrystals. Data was collected upon heating the sample from 25 to 750 °C. The first exothermic peak at 396.5 °C indicates superior thermal stability of the cluster.

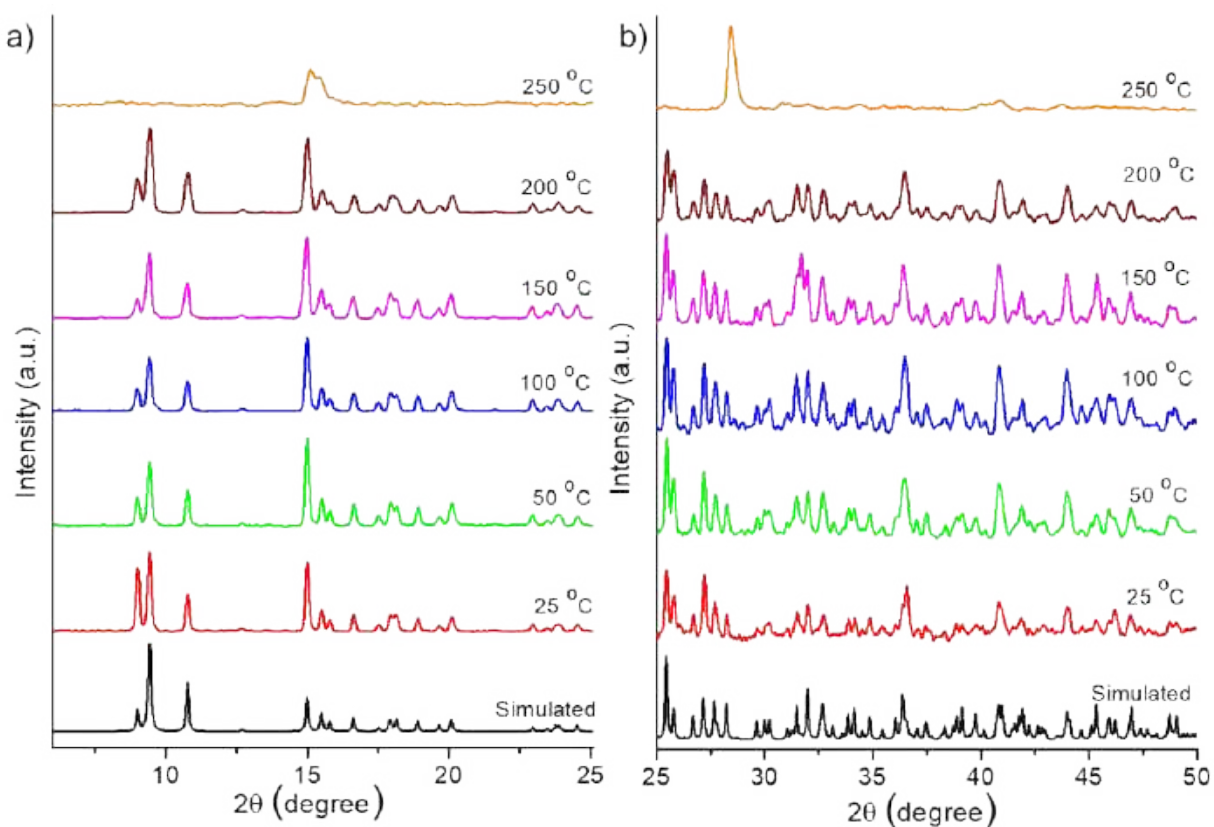


**Fig. S52** Magnified PXRD pattern of Cu<sub>4</sub>@oCBT microcrystalline powder after heating different temperatures at a) 5-25° region and b) 25° to 50° region (3 x magnification). There is no significant change of peak patterns indicating phase stability of the NC upon heating.

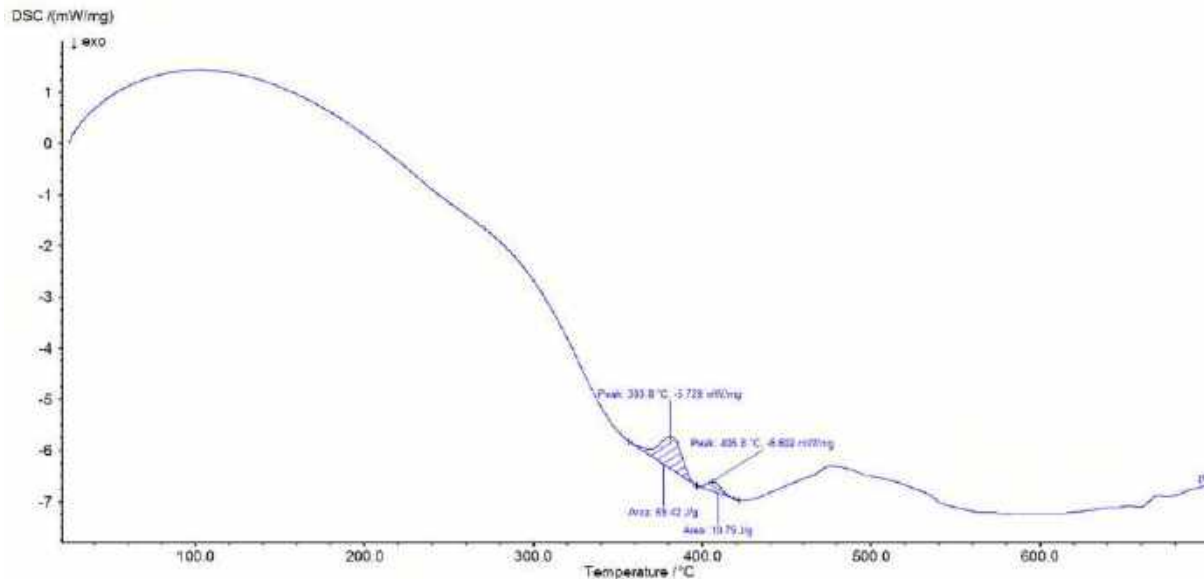


**Fig. S53** Differential scanning calorimetry (DSC) data of  $\text{Cu}_4\text{@mCBT}$  microcrystals. Data was collected upon heating the sample from 25 to 750 °C.

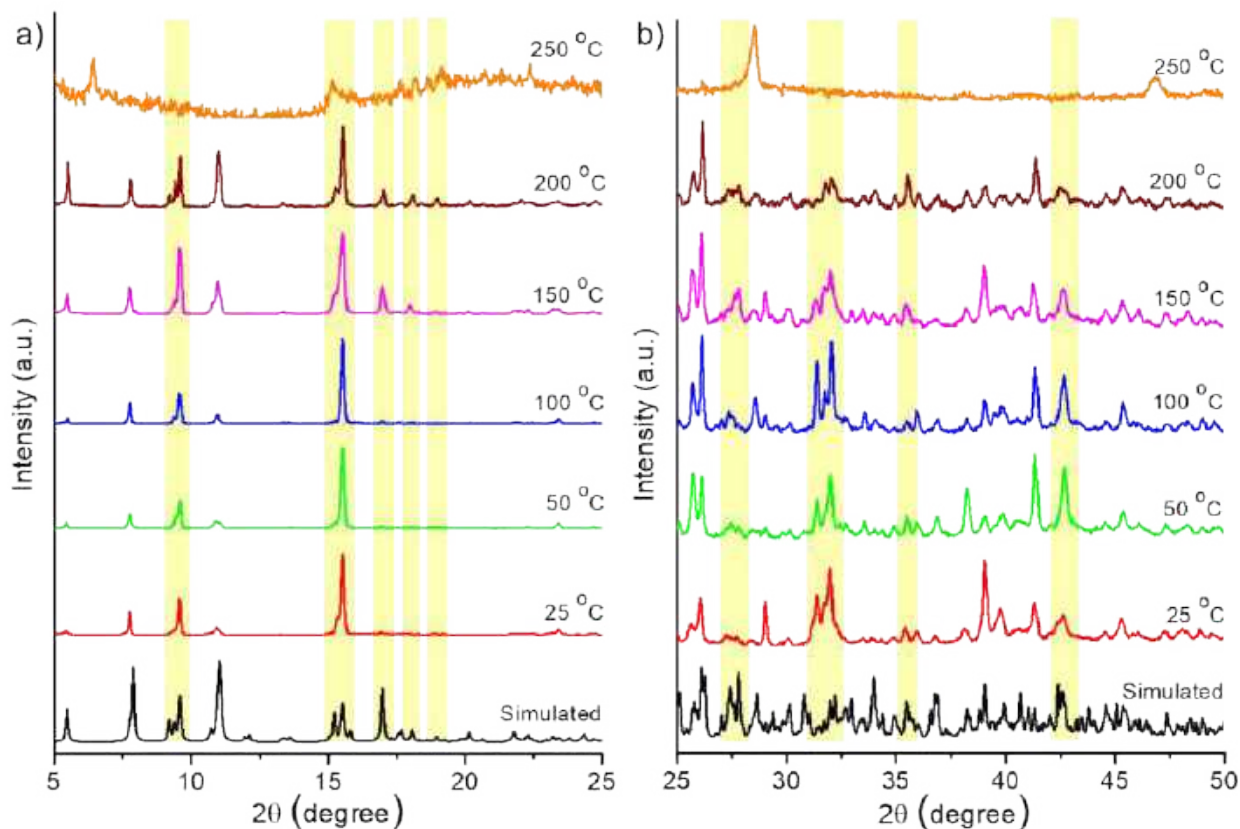


**Fig. S54** Magnified PXRD pattern of microcrystalline  $\text{Cu}_4\text{@mCBT}$  after heating different temperatures at a) 5-25° region and b) 25-50° region (5x magnification). Highlighted peaks indicated the change of the diffraction patterns after 150 °C heating, which indicates temperature-induced structural distortion, which leads to the yellow emission from the sample.

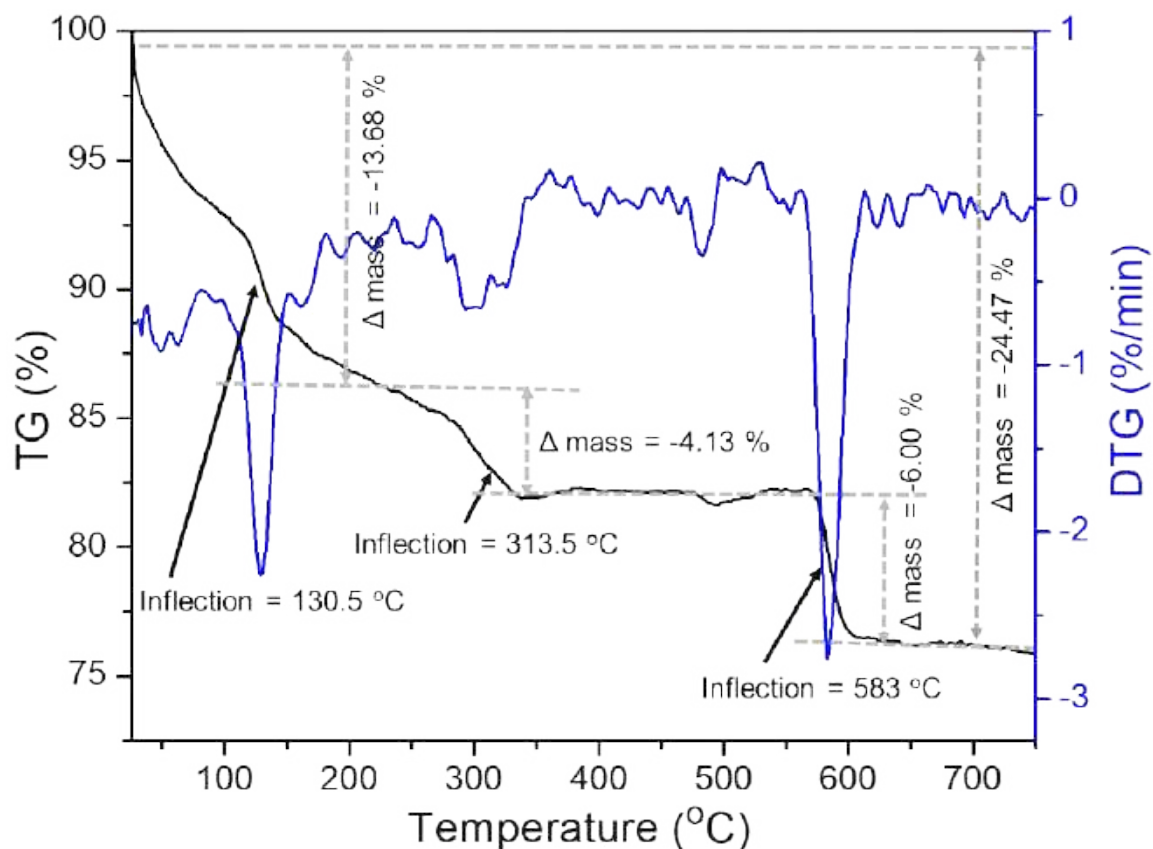


**Fig. S55** TGA DTG spectra showed less thermal stability of Cu<sub>4</sub>@ICBT compared to Cu<sub>4</sub>@oCBT and Cu<sub>4</sub>@mCBT derivatives.

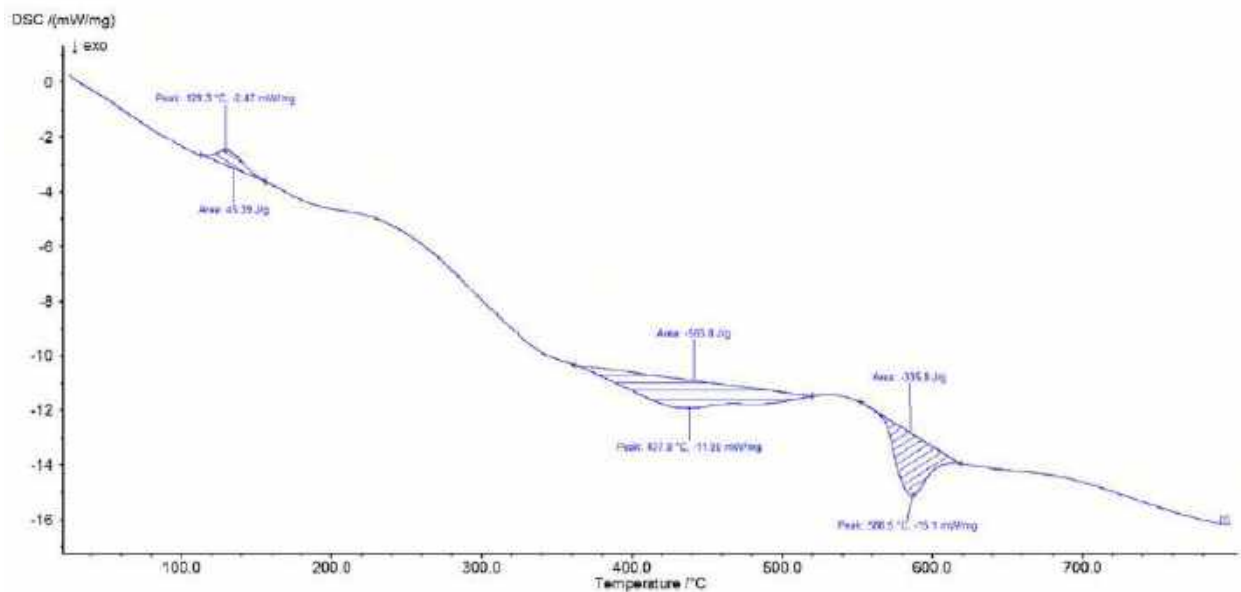


**Fig. S56** Differential scanning calorimetry (DSC) data of Cu<sub>4</sub>@ICBT microcrystals. Spectrum was collected upon heating the sample from 25 to 750 °C. The first endothermic peak at 129 °C indicates lower thermal stability than Cu<sub>4</sub>@oCBT and Cu<sub>4</sub>@mCBT.



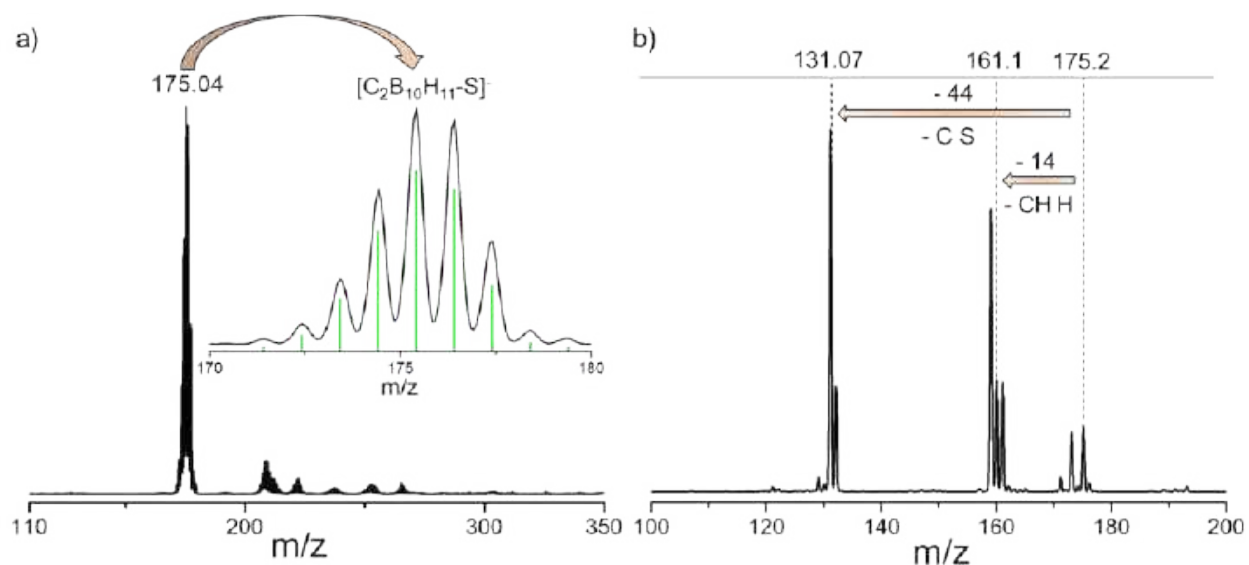


**Fig. S57** a) Negative ion-mode ESI-MS spectrum of *ortho*-carborane 9-thiol ligand. Inset shows isotopic distribution of the experimental spectrum (black), centered at m/z 175.04 matches well with theoretical spectrum (green). b) The MS/MS fragmentation of the molecular ion peak shows the losses of different fragments.

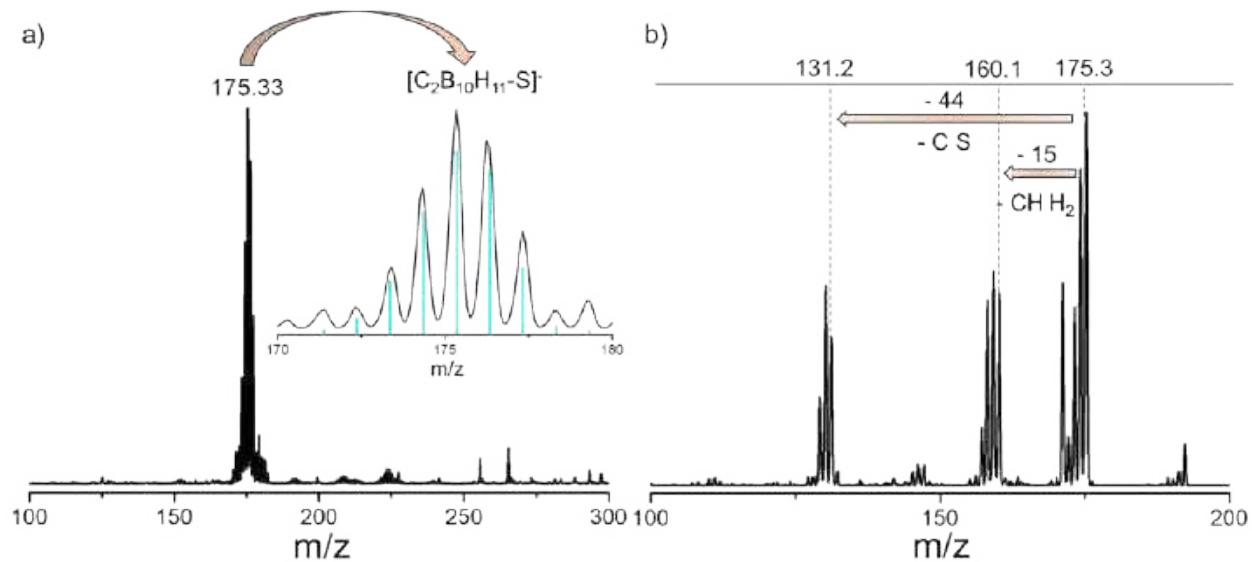


**Fig. S58** a) Negative ion-mode ESI-MS spectrum of *meta*-carborane 9-thiol ligand. Inset shows isotopic distribution of the experimental spectrum (black), centered at m/z 175.33 matches well with theoretical spectrum (cyan). b) The MS/MS fragmentation of the molecular ion peak shows the losses of different fragments from the carborane framework.

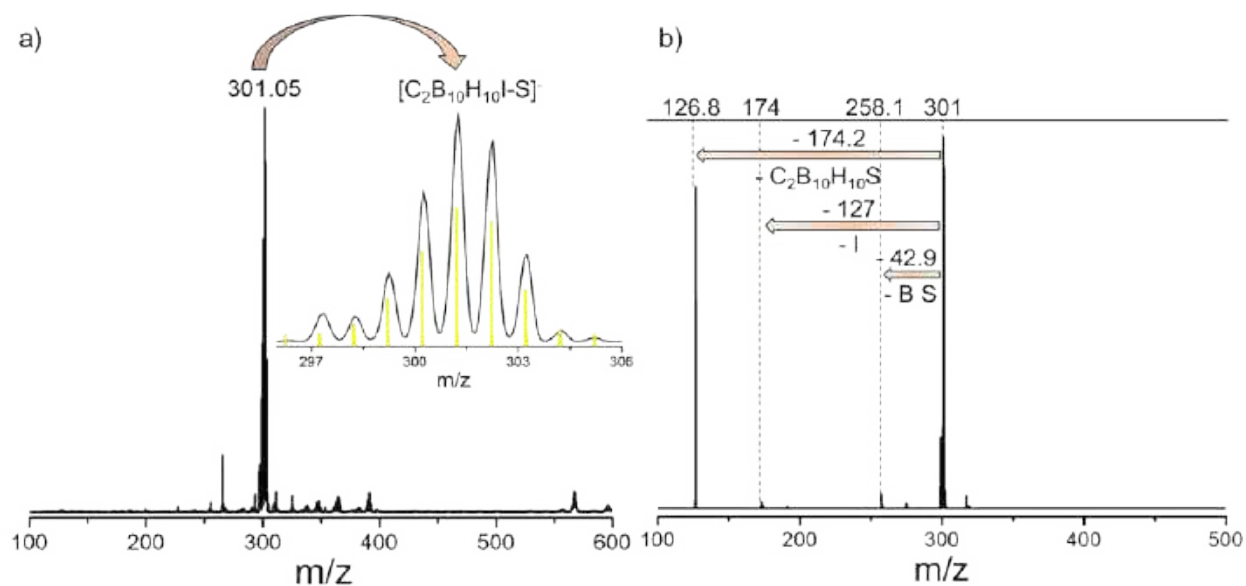


**Fig. S59** a) Negative ion-mode ESI-MS spectrum of *ortho*-carborane 12-iodo 9-thiol ligand. Inset shows isotopic distribution of the experimental spectrum (black), centered at  $m/z$  301.5 with theoretical spectrum (yellow). b) The MS/MS fragmentation of the molecular ion peak shows the losses of different fragments.

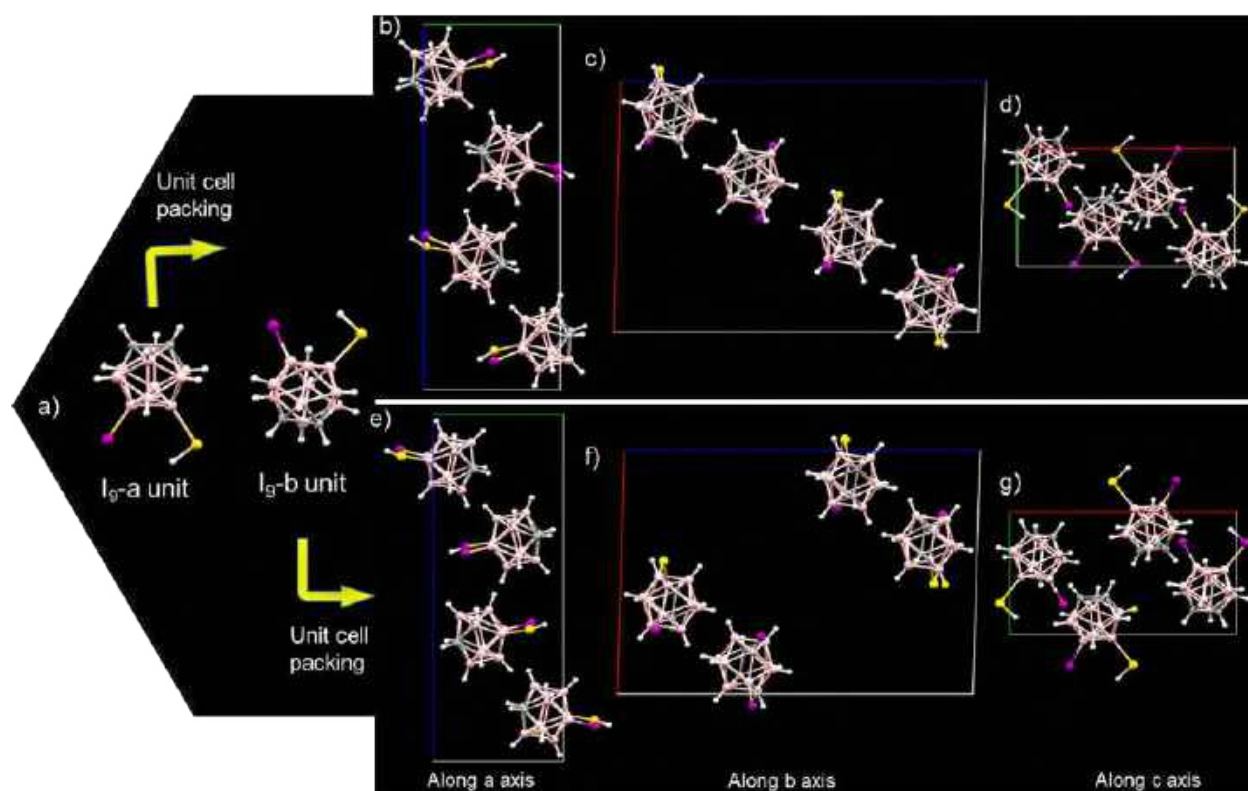


**Fig. S60** a) Molecular structure of  $I_9$  ligand with two different units. Independent unit cell molecular packing of  $I_9$ -a unit viewed from b) a, c) b and d) c crystallographic axis and  $I_9$ -b unit viewed from e) a, f) b and g) c crystallographic axis.

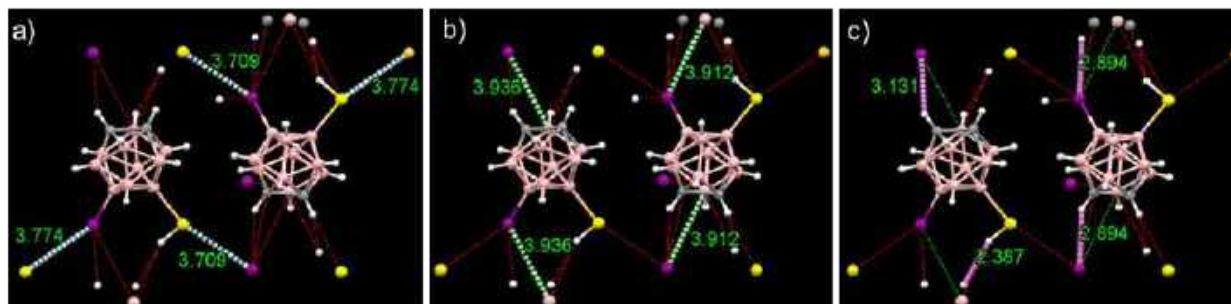


**Fig. S61** Intermolecular interactions between  $I_9$ -a and  $I_9$ -b units. Three short contact interactions *i.e.*, a)  $S \cdots I$ , b)  $I \cdots B$ , c)  $CH \cdots I$  or  $CH \cdots S$  are present between these two units. Interatomic distances are marked here.

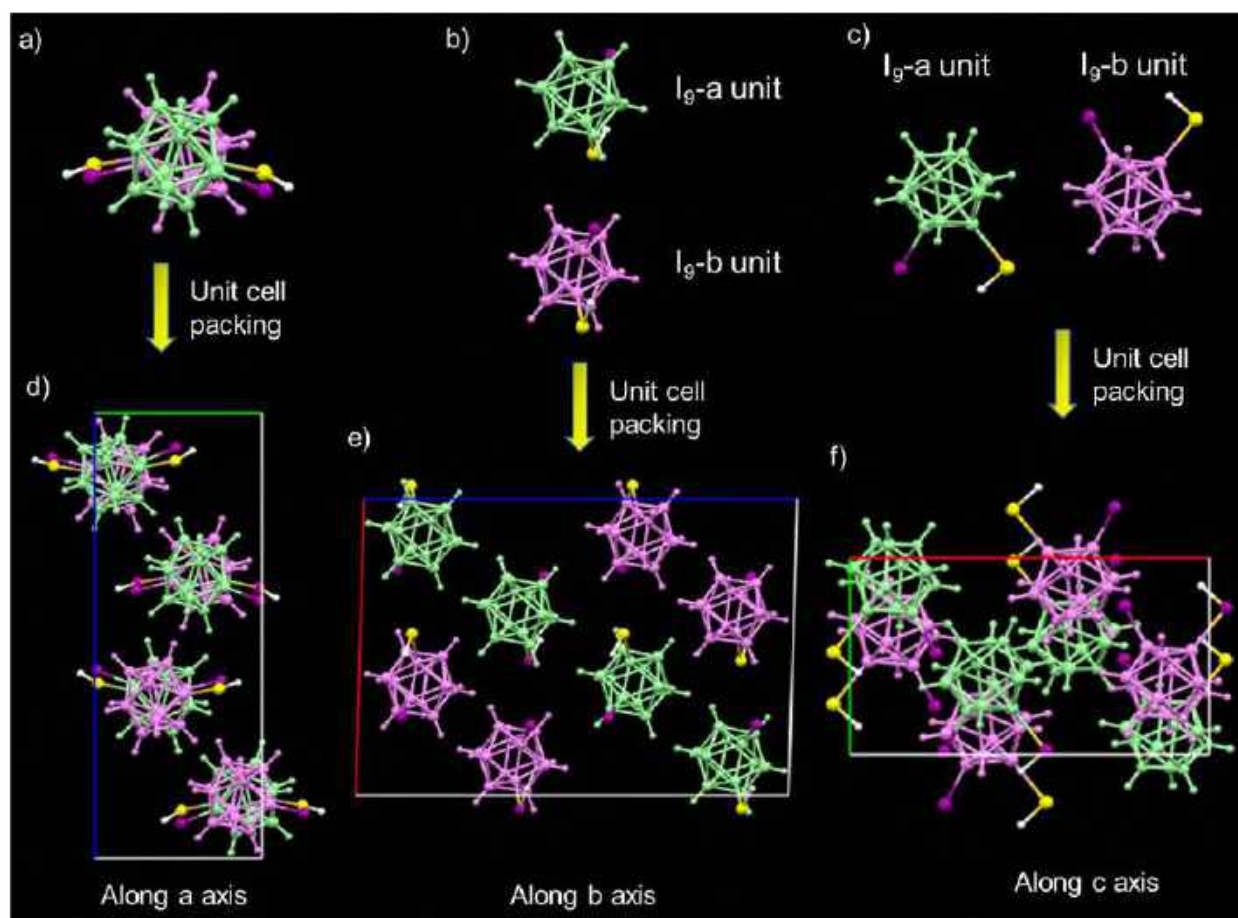


**Fig. S62** Molecular structure of  $I_9$  ligand having two different units viewed from a) a, b) b and c) c crystallographic axis. Combined unit cell molecular packing viewed from d) a, e) b and f) c crystallographic axis.

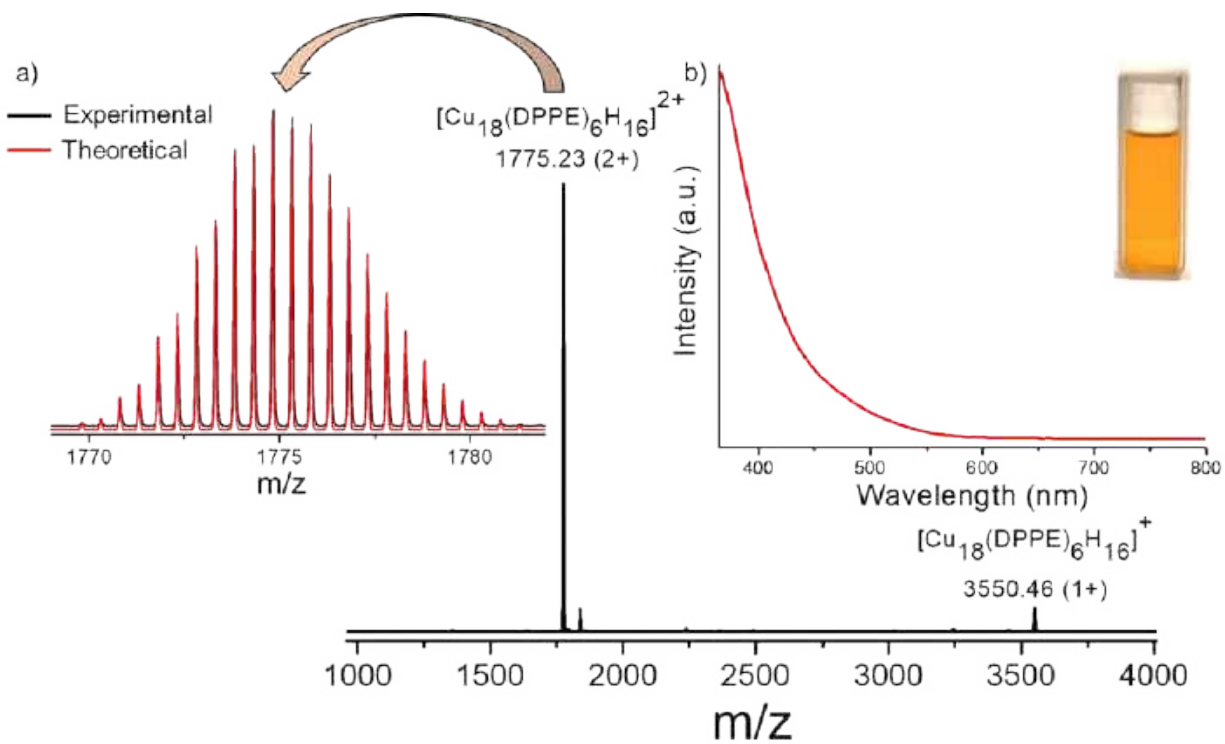


**Fig. S63** Characterizations of the  $[\text{Cu}_{18}(\text{DPPE})_6\text{H}_{16}]^{2+}$ . a) The full range mass spectrum of the NC in positive ion-mode indicates presence of mono and di-cationic species (inset shows exact matching of isotopic distribution of theoretical and experimental spectrum of the di-cationic species), b) UV-vis absorption spectrum of  $\text{Cu}_{18}$  (inset shows the photographic image of the orange colored cluster in DCM).

## References:

- (1) C. C. D. CrysAlis, Xcalibur PX Software, Oxford Diffraction Ltd., Abingdon, Engl. 2008.
- (2) Palatinus, L.; Chapuis, G. SUPERFLIP - a computer program for the solution of crystal structures by charge flipping in arbitrary dimensions. *J. Appl. Cryst.* 2007, **40**, 786-790.
- (3) Petříček, Václav; Dušek, Michal; Palatinus, Lukáš. Crystallographic Computing System JANA2006: General features. *Zeitschrift Für Krist. Mater.* 2014, **229**, 345.
- (4) Mortensen, J. J.; Hansen, L. B.; Jacobsen, K. W. Real-Space Grid Implementation of the Projector Augmented Wave Method. *Phys. Rev. B - Condens. Matter Mater. Phys.* 2005, **71** (035109), 1–11.
- (5) Enkovaara, J.; Rostgaard, C.; Mortensen, J. J.; Chen, J.; Duřak, M.; Ferrighi, L.; Gavnholt, J.; Glinsvad, C.; Haikola, V.; Hansen, H. A.; Kristoffersen, H. H.; Kuisma, M.; Larsen, A. H.; Lehtovaara, L.; Ljungberg, M.; Lopez-Acevedo, O.; Moses, P. G.; Ojanen, J.; Olsen, T.; Petzold, V.; Romero, N. A.; Stausholm-Møller, J.; Strange, M.; Tritsarlis, G. A.; Vanin, M.; Walter, M.; Hammer, B.; Häkkinen, H.; Madsen, G. K. H.; Nieminen, R. M.; Nørskov, J. K.; Puska, M.; Rantala, T. T.; Schiøtz, J.; Thygesen, K. S.; Jacobsen, K. W. Electronic Structure Calculations with GPAW: A Real-Space Implementation of the Projector Augmented-Wave Method. *J. Phys. Condens. Matter* 2010, **22** (253202), 1–24.
- (6) Adamo, C.; Barone, V. Physically Motivated Density Functionals with Improved Performances: The Modified Perdew-Burke-Ernzerhof Model. *J. Chem. Phys.* 2002, **116** (14), 5933–5940.
- (7) Adamo, C.; Barone, V. Toward Reliable Density Functional Methods without Adjustable Parameters: The PBE0 Model. *J. Chem. Phys.* 1999, **110**, 6158–6170.
- (8) Mennucci, B.; Tomasi, J.; Cammi, R.; Cheeseman, J. R.; Frisch, M. J.; Devlin, F. J.; Gabriel, S.; Stephens, P. J. Polarizable Continuum Model (PCM) Calculations of Solvent Effects on Optical Rotations of Chiral Molecules. *J. Phys. Chem. A* 2002, **106**, 6102–6113.
- (9) Cossi, M.; Rega, N.; Scalmani, G.; Barone, V. Energies, Structures and Electronic Properties of Molecules in Solution with the C-PCM Solvation Model. *J. Comput. Chem.* 2003, **24**, 669–681.
- (0) Tomasi, J.; Mennucci, B.; Cammi, R. Quantum mechanical continuum solvation models, *Chem. Rev.*, 2005, **105**, 2999-3093.
- (1) Frisch, M. J.; Trucks, G. W.; Schlegel, H. B.; Scuseria, G. E.; Robb, M. A.; Cheeseman, J. R.; Scalmani, G.; Barone, V.; Petersson, G. A.; Nakatsuji, H.; Li, X.; Caricato, M.; Marenich, A. V.; Bloino, J.; Janesko, B. G.; Gomperts, R.; Mennucci, B.; Hratchian, H. P.; Ortiz, J. V.; Izmaylov, A. F.; Sonnenberg, J. L.; Williams-Young, D.; Ding, F.; Lipparini, F.; Egidi, F.; Goings, J.; Peng, B.; Petrone, A.; Henderson, T.; Ranasinghe, D.; Zakrzewski, V. G.; Gao, J.; Rega, N.; Zheng, G.; Liang, W.; Hada, M.; Ehara, M.; Toyota, K.; Fukuda, R.; Hasegawa, J.; Ishida, M.; Nakajima, T.; Honda, Y.; Kitao, O.; Nakai, H.; Vreven, T.; Throssell, K.; Montgomery, J. A. Jr.; Peralta, J. E.; Ogliaro, F.; Bearpark, M. J.; Heyd, J. J.; Brothers, E. N.; Kudin, K. N.; Staroverov, V. N.; Keith, T. A.; Kobayashi, R.; Normand, J.; Raghavachari, K.; Rendell, A. P.; Burant, J. C.; Iyengar, S. S.; Tomasi, J.; Cossi, M.; Millam, J. M.; Klene, M.; Adamo, C.; Cammi, R.; Ochterski, J. W.; Martin, R. L.; Morokuma, K.; Farkas, O.; Foresman, J. B.; Fox, D. J. Gaussian 16, Revision C.01, *Gaussian, Inc.*, Wallingford CT, 2019.
- (2) Adamo, C.; Barone, V. Toward reliable density functional methods without adjustable parameters: The PBE0 model. *J. Chem. Phys.*, 1999, **110**, 6158-6169.
- (3) a) Dunning, T. H. Jr.; Hay P. J. in *Modern Theoretical Chemistry*, Ed. H. F. Schaefer III, Vol. 3

- (Plenum, New York, 1977), 1-28.
- b) Wadt, W. R.; Hay P. J. Ab initio effective core potentials for molecular calculations – potentials for main group elements Na to Bi, *J. Chem. Phys.*, 1985, **82**, 284-298.
- (14) Leites, L. A. Vibrational Spectroscopy of Carboranes and Parent Boranes and Its Capabilities in Carborane Chemistry. *Chem. Rev.* 1992, **92** (2), 279–323.



Publications with  
other groups

# Strong and Elastic Membranes via Hydrogen Bonding Directed Self-Assembly of Atomically Precise Nanoclusters

Anirban Som, Alessandra Griffo, Indranath Chakraborty, Hendrik Hähl, Biswajit Mondal, Amrita Chakraborty, Karin Jacobs, Päivi Laaksonen, Olli Ikkala,\* Thalappil Pradeep,\* and Nonappa\*

2D nanomaterials have provided an extraordinary palette of mechanical, electrical, optical, and catalytic properties. Ultrathin 2D nanomaterials are classically produced via exfoliation, delamination, deposition, or advanced synthesis methods using a handful of starting materials. Thus, there is a need to explore more generic avenues to expand the feasibility to the next generation 2D materials beyond atomic and molecular-level covalent networks. In this context, self-assembly of atomically precise noble nanoclusters can, in principle, suggest modular approaches for new generation 2D materials, provided that the ligand engineering allows symmetry breaking and directional internanoparticle interactions. Here the self-assembly of silver nanoclusters (NCs) capped with *p*-mercaptobenzoic acid ligands ( $\text{Na}_4\text{Ag}_{44}\text{-pMBA}_{30}$ ) into large-area freestanding membranes by trapping the NCs in a transient solvent layer at air–solvent interfaces is demonstrated. The patchy distribution of ligand bundles facilitates symmetry breaking and preferential intralayer hydrogen bondings resulting in strong and elastic membranes. The membranes with Young's modulus of  $14.5 \pm 0.2$  GPa can readily be transferred to different substrates. The assemblies allow detection of Raman active antibiotic molecules with high reproducibility without any need for substrate pretreatment.

properties.<sup>[1–12]</sup> They are classically prepared using exfoliation, exploiting promoted intralayer bonding over weak interlayer interactions of their 3D counterparts.<sup>[4]</sup> The exfoliation of graphene<sup>[1]</sup> has triggered searches for other covalently interconnected atomically thin 2D nanomaterials, such as transition metal dichalcogenides,<sup>[5]</sup> Mxenes,<sup>[6]</sup> boron nitrides,<sup>[7]</sup> and clays,<sup>[8]</sup> based on exfoliation and delamination,<sup>[9]</sup> molecular beam epitaxy,<sup>[10]</sup> and advanced synthesis.<sup>[11]</sup> In ultrathin 2D nanomaterials, the quantum confinement of electrons in two dimensions opens novel applications, e.g., in flexible optoelectronic devices.<sup>[4,12,13]</sup> Beyond atomic and molecular-level networks, a less studied approach deals with the self-assembly of metal nanoparticles (NPs) to form 2D monolayer membranes, i.e., of nanometric thickness. That this could be relevant, is suggested by the tunable optoelectronic and mechanical properties of self-assembled 2D materials of narrow

size dispersed plasmonic NPs.<sup>[14–17]</sup> However, metal NPs classically suffer from uncontrolled aggregation tendency, polydispersity, and lack of directional interactions.<sup>[18–21]</sup> Additionally, nonspecific bindings and slow diffusion of colloidal-level


## 1. Introduction

Atomically thin 2D nanomaterials have gained immense interest because of their remarkable mechanical and optoelectronic

A. Som, O. Ikkala, Nonappa  
Department of Applied Physics  
Aalto University  
Espoo FI-02150, Finland  
E-mail: olli.ikkala@aalto.fi

A. Griffo, P. Laaksonen, O. Ikkala  
Department of Bioproducts and Biosystems  
Aalto University  
Espoo FI-02150, Finland

A. Griffo, H. Hähl, K. Jacobs  
Department of Experimental Physics  
Saarland University  
66123 Saarbrücken, Germany

 The ORCID identification number(s) for the author(s) of this article can be found under <https://doi.org/10.1002/smll.202201707>.

© 2022 The Authors. Small published by Wiley-VCH GmbH. This is an open access article under the terms of the Creative Commons Attribution License, which permits use, distribution and reproduction in any medium, provided the original work is properly cited.

DOI: 10.1002/smll.202201707

A. Griffo, K. Jacobs  
Max Planck School Matter to Life  
Jahnstraße 29, 69120 Heidelberg, Germany

I. Chakraborty, B. Mondal, A. Chakraborty, T. Pradeep  
DST Unit of Nanoscience and Thematic Unit of Excellence  
Department of Chemistry  
Indian Institute of Technology Madras  
Chennai 600036, India  
E-mail: pradeep@iitm.ac.in

I. Chakraborty  
School of Nano Science and Technology  
Indian Institute of Technology  
Kharagpur 721302, India

Nonappa  
Faculty of Engineering and Natural Sciences  
Tampere University  
Tampere FI-33720, Finland  
E-mail: nonappa@tuni.fi

particles could result in a mixture of different structures rather than the desired homogeneous or precise end-product.<sup>[22,23]</sup> Nevertheless, 2D close-packed arrays of gold nanoparticles, binary superlattices, and nanoparticle–polymer composite arrays have been achieved using evaporation induced assembly, interfacial assembly, binary solvents, antisolvent approach, dip coating, and Langmuir–Blodgett film formation methods.<sup>[24–27]</sup> Still, achieving a combination of precision and reproducibility of self-assembled large-area NP superstructures remains a grand challenge.<sup>[28]</sup>

Recent studies in the literature suggest that the nanoparticle size dispersity, ligand structure, and density hinders the reproducibility, sensitivity, and mechanical properties of NP-based 2D assemblies. Mueggenburg et al. have shown that NP membranes composed of dodecane thiol ligand-capped gold NPs with an average diameter of 9.4 nm show highly scattered elastic modulus with a range of 3–39 GPa.<sup>[29]</sup> The large distribution of elastic modulus is attributed to the uncertainty and compositional differences in membranes made from different nanoparticle batches. The mechanical properties of such membranes strongly depends on the ligand interdigitation and NP packing efficiency. In such systems, the core–core interactions account for less than 10% of the observed overall strength.<sup>[30]</sup> Cheng et al. used a microhole drying method to prepare DNA-capped nanoparticle membranes with inter-nanoparticle distances tunable up to 20 nm and Young's moduli within a narrow range of  $6.49 \pm 1.57$  GPa. However, the observed average moduli values are much less than other NP membranes.<sup>[31]</sup> Gold nanoparticle-based 2D assemblies have been studied for nanoparticle–organic memory field-effect transistors.<sup>[32a]</sup> In such assemblies, the reproducibility of NP density depends on NP size and capping ligands, which in turn affect the device performances.<sup>[32a,b]</sup> Furthermore, the uniform size, density, and inter-nanoparticle distances in monolayers of plasmonic silver nanoparticles have been shown to significantly improve the surface enhanced Raman spectroscopy (SERS) sensitivity and reproducibility.<sup>[17,33–35]</sup> Therefore, there is a need to develop methods for the uniform and reproducible fabrication of precision nanoparticle assemblies.

Atomically precise, monolayer ligand-protected noble metal nanoclusters (NCs) offer tunable size, shape, composition, and oxidation states.<sup>[36]</sup> While a vast number of NCs have been synthesized over the last decade, understanding their structure, optoelectronic properties, catalysis, and biological properties remains the central theme.<sup>[36–38]</sup> NCs are excellent building blocks for well-defined assemblies, composites, and hybrid materials allowing large design flexibility and unique optoelectronic properties.<sup>[39]</sup> Therefore, the next logical step would be the creation of rationally designed assemblies of NCs to attain the desired properties. In their crystalline state, ligand–ligand interactions between the spatially arranged neighboring NCs dictate the packing geometry. Depending on the functionality, these ligands can interact through hydrogen bonding, electrostatic, dipolar,  $\pi$ -stacking, and van der Waals interactions.<sup>[39]</sup> The ability to manipulate such supramolecular forces in detail is the key toward controlling the geometry of the nanocluster assemblies.

Large area monolayer 2D assemblies of NCs with well-defined internal order require a restriction of the NC

crystallization in a particular direction, i.e., symmetry breaking. It has been shown using *para*-mercaptobenzoic acid (*p*MBA)-protected gold NCs ( $\text{Au}_{102}$ -*p*MBA<sub>44</sub>) that symmetry breaking can be achieved by exploiting the anisotropic or patchy hydrogen bonding (H-bonding) ligand distribution.<sup>[40,41]</sup> On the other hand, atomically precise silver NCs have been utilized to achieve hydrogen bonding mediated assembly of tellurium nanowires into 2D cross-bilayer structures,<sup>[42]</sup> and selective encapsulation of plasmonic gold nanorods.<sup>[43]</sup> Liquid–liquid interfaces have also been utilized to create NC 2D assemblies.<sup>[44]</sup> However, precise control over layer thickness and structure in nanoparticle membranes covering a large area and studies on their mechanical properties is still lacking.

Here we report the fabrication of large-area (extending over  $\text{cm}^2$ ) freestanding monolayer membranes of  $\text{Na}_4\text{Ag}_{44}$ -*p*MBA<sub>30</sub> NCs with long-range hexagonally close-packed internal structure. The membranes are prepared by processing at air–water interfaces hosting a transient solvent layer. Specifically, we utilize the selective in-plane growth of the cluster assemblies by facilitating the intralayer H-bonding between the carboxylic acid groups of *p*MBA ligands. The packing of the NCs was analyzed using high resolution transmission electron microscopy (HR-TEM). The ultrathin membranes were also directly deposited across micrometer sized holes. The atomic force microscopy (AFM)-based force spectroscopy showed non-hysteretic elastic deformation upon nanoindentation. The observed Young's modulus of  $14.5 \pm 0.2$  GPa, is significant for a noncovalently interconnected ultrathin membrane of colloidal units. The membranes allow detection of Raman active antibiotics dissolved in water using surface enhanced Raman spectroscopy with high reproducibility, unlike the classic nanoparticles with finite-size distributions and defected structures.

## 2. Results and Discussions

### 2.1. Microscale 2D Colloidal Crystals

We utilized atomically precise silver nanoclusters,  $\text{Na}_4\text{Ag}_{44}$ -*p*MBA<sub>30</sub> (Figure 1a) synthesized according to a reported literature procedure (see Figure S1, Supporting Information, for details).<sup>[45,46]</sup> Formation of  $\text{Na}_4\text{Ag}_{44}$ -*p*MBA<sub>30</sub> was confirmed through UV–vis spectroscopy and ESI mass spectrometry (Figure S2, Supporting Information). The solid state structure of  $\text{Na}_4\text{Ag}_{44}$ -*p*MBA<sub>30</sub> consists of a 32 atom Ag core (concentric icosahedral and dodecahedral Ag atom shells), which is protected by six  $\text{Ag}_2$ -*p*MBA<sub>5</sub> units in an octahedral geometry (Figure 1a).

This arrangement results in the formation of *p*MBA ligand bundles or patches, which break the spherical symmetry. The ligand bundles are classified into L2 (bundle of two) and L3 (bundle of three) *p*MBA groups (Figure 1b), which act as the inter-nanocluster interaction patches to drive the 3D network formation. Incidentally, all the six L2 bundles are located along an imaginary equatorial plane and drive the crystal growth in the lateral dimension (along *ab*-plane). The six L3 bundles are placed above (three) and below (three) the equatorial plane and form H-bonded bridges between the layers (along the *c*-axis). In this way, a single

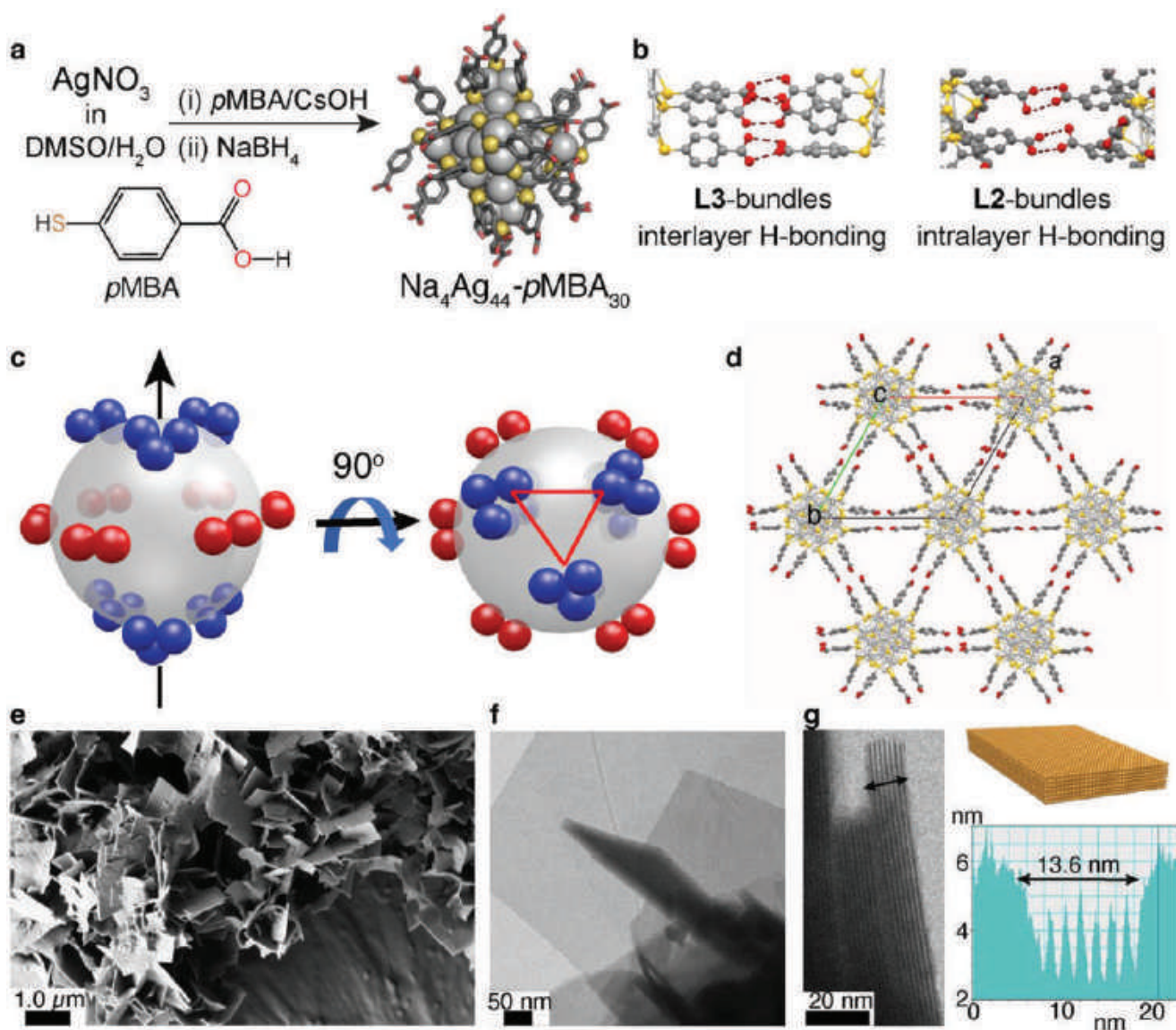


**Figure 1.** Synthesis, patchy ligand distribution, and 2D colloidal crystals. a) Synthesis scheme, and X-ray crystal structure of  $\text{Na}_4\text{Ag}_{44}\text{-pMBA}_{30}$  (CSD entry XIMHOS, hydrogen atoms are not shown for clarity).<sup>[46]</sup> b) Representative L2 and L3 ligand bundles of  $\text{Na}_4\text{Ag}_{44}\text{-pMBA}_{30}$ . c) Schematic representation showing the patchy distribution of L2 (red spheres) and L3 (blue spheres) bundles. The six L2 bundles are located around an imaginary equatorial plane. d) Intralayer packing of the clusters in the crystal structure directed by L2 bundles, showing the possibility of a 2D assembly (see Figure S2d, Supporting Information, for interlayer packing via L3 bundles). e) SEM image of 2D nanosheets of  $\text{Na}_4\text{Ag}_{44}\text{-pMBA}_{30}$  in methanol. f) TEM image of nanosheets. g) TEM image suggests that these nanosheets contain a few layers, as shown in the histogram.

$\text{Na}_4\text{Ag}_{44}\text{-pMBA}_{30}$  is involved in 24 H-bonds ( $6 \times \text{L2}$ ) with clusters from the same layer (Figure 1c). The L3 bundles contribute to 18 inter-nanocluster H-bonds each with clusters from layers above and below, respectively (Figure S2d, Supporting Information).

We envisaged that  $\text{Na}_4\text{Ag}_{44}\text{-pMBA}_{30}$  provides a feasible starting point to create 2D NC superstructures (Figure 1d), as it intrinsically allows a larger number of intralayer H-bonds between the NCs compared to the interlayer bonds. The creation of 2D assemblies of  $\text{Na}_4\text{Ag}_{44}\text{-pMBA}_{30}$  would thus require selectively restricting the formation of interlayer L3 H-bonds to drive the crystal growth along the lateral direction and to limit the growth in the perpendicular direction. Herein we expected that kinetically controlled self-assembly

could be feasible. To test our hypothesis, we first screened solvents to facilitate 2D colloidal crystal growth of  $\text{Na}_4\text{Ag}_{44}\text{-pMBA}_{30}$ , before aiming the monolayer membranes. Thus we found that, when a dispersion of  $\text{Na}_4\text{Ag}_{44}\text{-pMBA}_{30}$  in *N,N'*-dimethylformamide (DMF) was added to methanol (nonsolvent), an immediate precipitation was observed. The scanning electron microscopy (SEM) images of the dispersion revealed the presence of microscopic 2D colloidal crystals (Figure 1e). A closer examination of TEM images revealed that these sheets are, in fact, stacks with a few layer thicknesses (Figure 1f). For example, in Figure 1g the TEM image shows a stack of seven layers (Figure S3c–e, Supporting Information, for HR-TEM images). Therefore, this



strategy offered a certain degree of control on the 2D stacking of  $\text{Na}_4\text{Ag}_{44}\text{-pMBA}_{30}$ . However, precisely controlling the layer thickness and limiting it to a monolayer necessitated identifying more refined strategies.

## 2.2. Freestanding Monolayer Membrane

Self-assembly of molecules at interfaces (air–liquid or liquid–liquid) leading to monomolecular membranes has been investigated extensively for several decades.<sup>[47,48]</sup> Therein Langmuir–Blodgett (LB) processing allows thin membranes of a variety of nanomaterials at the air–water interface taken that they are sufficiently hydrophobic.<sup>[49]</sup> However, the  $\text{Na}_4\text{Ag}_{44}\text{-pMBA}_{30}$  NCs could not be assembled using the LB-processing, as they are dispersible in water. To achieve monolayer membranes, we carried out a systematic study using a series of solvents. When a dispersion of  $\text{Na}_4\text{Ag}_{44}\text{-pMBA}_{30}$  in DMF was added to ethanol, propanol, butanol, and acetone, they all resulted in mesoscale colloidal crystals similar to those in methanol (Figure S3f–i, Supporting Information). Interestingly, a stable dispersion of  $\text{Na}_4\text{Ag}_{44}\text{-pMBA}_{30}$  without immediate precipitation was obtained in 1-pentanol. Exploiting this property, we first dispersed the clusters in 1-pentanol, which was subsequently transferred in a dropwise manner on a water surface (Figure S1, Supporting Information). 1-Pentanol, due to its longer alkyl chain length, has low solubility in water (22 g L<sup>-1</sup>) compared to lower alcohols.

In the literature 1-pentanol has been used as a cosurfactant for stable microemulsion preparation and interface synthesis of gold mesocrystals.<sup>[50]</sup> In our experiment, when a dispersion of  $\text{Na}_4\text{Ag}_{44}\text{-pMBA}_{30}$  in 1-pentanol was placed on the surface of the water, pentanol quickly spreads to form a membrane. The clusters trapped inside this pentanol layer assemble through the formation of H-bonds and float at the air–water interface (Figure 2a). The resulting freestanding  $\text{Na}_4\text{Ag}_{44}\text{-pMBA}_{30}$  membrane can be picked from the air–water interface and transferred onto suitable substrates as shown using a glass coverslip ( $d \approx 1.2$  cm). An immediate transfer of the membrane on to the substrate is better for the stability and to avoid any degradation upon contact with water for longer time. Increased concentration of 1-pentanol in water may also be detrimental for membrane preparation. For example, in a control experiment when  $\text{Na}_4\text{Ag}_{44}\text{-pMBA}_{30}$  in 1-pentanol was added on the surface containing a mixture of 1-pentanol/water (2/75 v/v) resulted in droplets and no film formation was observed (Figure S1, Supporting Information).

The membranes were examined using TEM by transferring them onto TEM grids with lacey, holey, or ultrathin carbon support films. That the membrane extended over micrometer area can be seen in the large area TEM image (Figure 2b). The HR-TEM images, fast Fourier transform (FFT), and inverse fast Fourier transform (IFFT) analysis of the membrane deposited on TEM grid with ultrathin carbon support indicate the well-defined overall hexagonally close-packed (hcp) assembly as well as the membrane is of monolayer thickness (Figure 2c,d). Further analysis of the  $\text{Na}_4\text{Ag}_{44}\text{-pMBA}_{30}$  monolayer membrane revealed an average interparticle distance of 2.33 nm and periodicity of 2.01 nm (Figure 2e).

The UV–vis spectrum of the  $\text{Na}_4\text{Ag}_{44}\text{-pMBA}_{30}$  monolayer membranes showed the same characteristic peaks as observed for the individual solvent dispersed  $\text{Na}_4\text{Ag}_{44}\text{-pMBA}_{30}$  NCs. This suggests that the intrinsic properties of the NCs are retained in the monolayer membranes (Figure 2f,g). However, the absorption peaks turned broader in the monolayer membrane, indicating a possible electronic coupling between the NCs. In the Raman spectrum,  $\text{Na}_4\text{Ag}_{44}\text{-pMBA}_{30}$  monolayer membranes exhibit several peaks ranging from 300 to 1800 cm<sup>-1</sup> of which two strong bands at 1077 and 1584 cm<sup>-1</sup> are due to  $\nu_{12}$  and  $\nu_{8a}$  aromatic ring vibrations (of the pMBA ligands), respectively (Figure 2h; Figure S5a,b, Supporting Information). For comparison, the Raman spectrum of a drop-casted  $\text{Na}_4\text{Ag}_{44}\text{-pMBA}_{30}$  film on a coverslip was taken, which shows a similar spectral pattern. Still, the peaks are better resolved in the case of  $\text{Na}_4\text{Ag}_{44}\text{-pMBA}_{30}$  monolayer membranes. The most intense peak at 1584 cm<sup>-1</sup> was utilized to construct the Raman spectral image (Figure S5c, Supporting Information), which resembles the optical image of the  $\text{Na}_4\text{Ag}_{44}\text{-pMBA}_{30}$  monolayer membrane (Figure S5d, Supporting Information). A few regions show higher intensity (Raman spectra in Figure 2h) because of multilayers at those locations due to the folding or crumpling of  $\text{Na}_4\text{Ag}_{44}\text{-pMBA}_{30}$  monolayer membranes while transferring onto the substrate.

## 2.3. Mechanical Properties of $\text{Na}_4\text{Ag}_{44}\text{-pMBA}_{30}$ Membranes

After a successful demonstration of the feasibility of free-standing  $\text{Na}_4\text{Ag}_{44}\text{-pMBA}_{30}$  monolayer membrane formation, we turned our attention to determine the mechanical properties of the nanometric membranes. The freshly prepared  $\text{Na}_4\text{Ag}_{44}\text{-pMBA}_{30}$  monolayer membrane was transferred onto Quantifoil gold grids with a holey carbon support film, having a hole diameter of 0.6  $\mu\text{m}$  (Figure 3a).

That the freestanding membrane stretched across the holes could be seen from the TEM images (Figure S6, Supporting Information). However, for high magnification imaging, the Quantifoil grids with holey carbon support were not suitable. Therefore, the grids were sputter-coated with platinum before transferring the membranes (see Figure S6c,d, Supporting Information, for TEM image of a pristine sputter-coated grid). The sputter-coated grid allowed for better imaging of  $\text{Na}_4\text{Ag}_{44}\text{-pMBA}_{30}$  monolayer membranes stretched across holey grids (Figure 3b–d; Figure S7, Supporting Information). It is important to note that NCs are inherently electron beam sensitive and, therefore, at higher magnification, beam damage and their aggregation into larger nanoparticles can be observed. The HR-TEM images and IFFT suggests that the monolayer membrane stretched across the hole still incorporated a hexagonal nanocluster assembly (Figure 3d).

AFM measurements showed that the  $\text{Na}_4\text{Ag}_{44}\text{-pMBA}_{30}$  monolayer membranes within the holes were smooth and flat (Figure 3e,f). Height profile images indicate that the monolayer membrane drape over the hole (Figure 3g; Figure S8, Supporting Information). Importantly, the height of various 2D membranes deposited on holey support films has been discussed in the literature.<sup>[51–55]</sup> We used the Quantitative Nanomechanical Measurement-mode of the AFM to obtain the

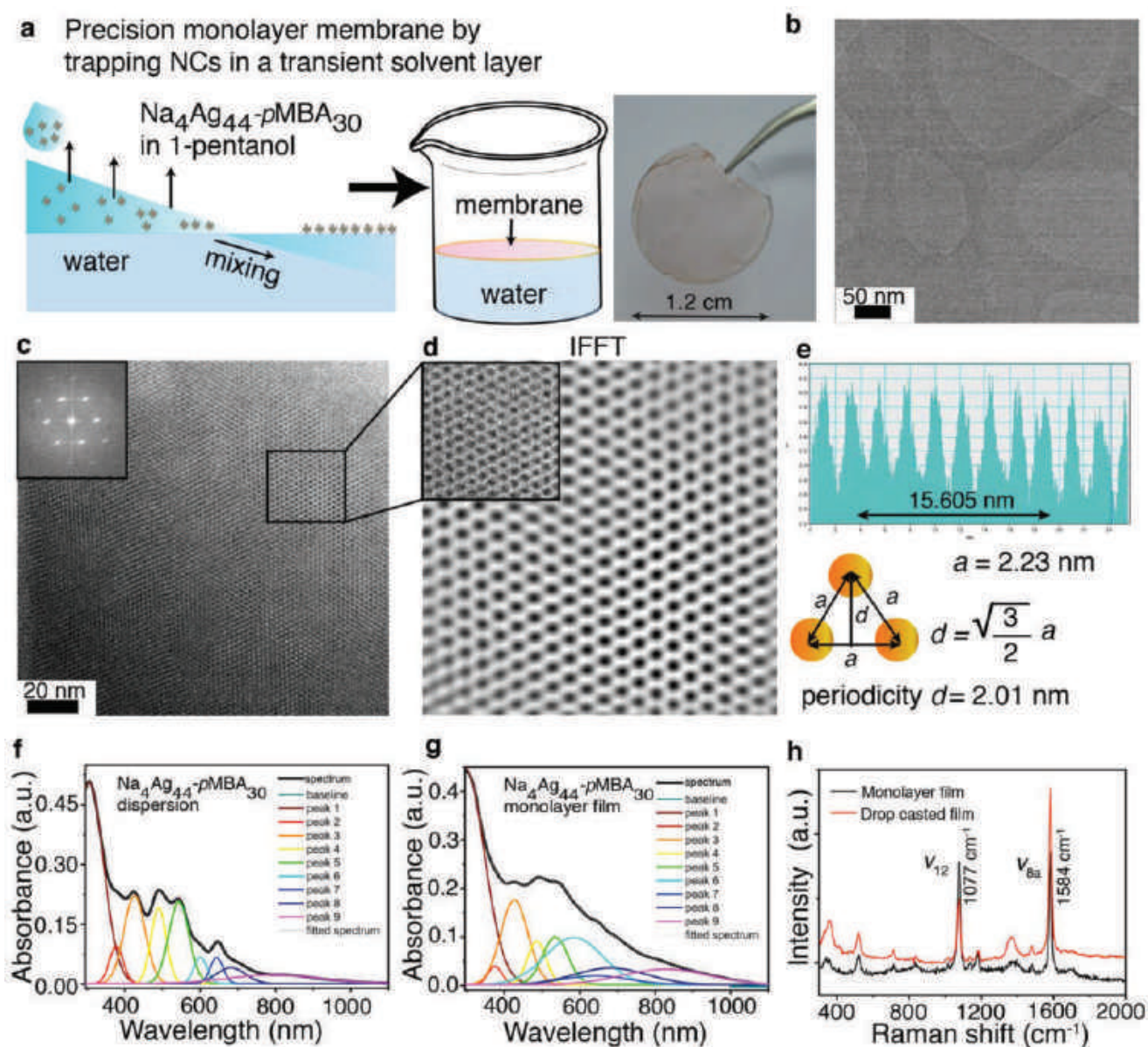


**Figure 2.** Freestanding  $\text{Na}_4\text{Ag}_{44}\text{-pMBA}_{30}$  membranes. a) Schematics showing the formation of the monolayer  $\text{Na}_4\text{Ag}_{44}\text{-pMBA}_{30}$  assembly in a liquid-assisted air–water interface method (left). Large area  $\text{Na}_4\text{Ag}_{44}\text{-pMBA}_{30}$  monolayer membrane transferred onto a microscope coverslip (right). b) TEM image of the monolayer assembly stretched over a lacey carbon support membrane. c) TEM image suggesting the hexagonal packing of  $\text{Na}_4\text{Ag}_{44}\text{-pMBA}_{30}$  NCs (inset shows the FFT). d) IFFT image from the marked area in image c. e) Profile showing the inter-nanoparticle distance and periodicity. f) UV–vis spectrum of  $\text{Na}_4\text{Ag}_{44}\text{-pMBA}_{30}$  in aq. dispersion along with peak fitting. g) UV–vis spectrum of  $\text{Na}_4\text{Ag}_{44}\text{-pMBA}_{30}$  monolayer membrane. h) Raman spectra of  $\text{Na}_4\text{Ag}_{44}\text{-pMBA}_{30}$  monolayer membrane (black) and that of drop-casted  $\text{Na}_4\text{Ag}_{44}\text{-pMBA}_{30}$  dispersion (red) showing the presence of the characteristic bands (see Figure S4, Supporting Information).

correct height of the membrane. In this mode, the contact point is evaluated and used as height information which is hence independent of the force applied by the probe. The obtained “real height” images show that the membrane (rather than recessed) is suspended on the rim of the holes whose height is  $\approx 20 \text{ nm}$  (see the image of the control grid in Figure S10, Supporting Information).

Next, AFM indentation experiments were carried out on freestanding monolayer membranes suspended on grids having a hole radius of  $0.6 \mu\text{m}$ . For the characterization of the

membrane elasticity, force curves were recorded at the center of the holes. A typical trace of the force–displacement curve is presented in Figure 4b. For each sample, several holes covered with the membrane were probed. We observed consistent force–displacement curves for multiple indents on a single spot without breaking the membrane. An increasing force starting from  $10 \text{ nN}$  was applied until the value of  $\approx 16\text{--}18 \text{ nN}$  was reached, which represents the maximum load that the suspended membrane can withstand before breaking (Figure S11, Supporting Information, for additional force–displacement



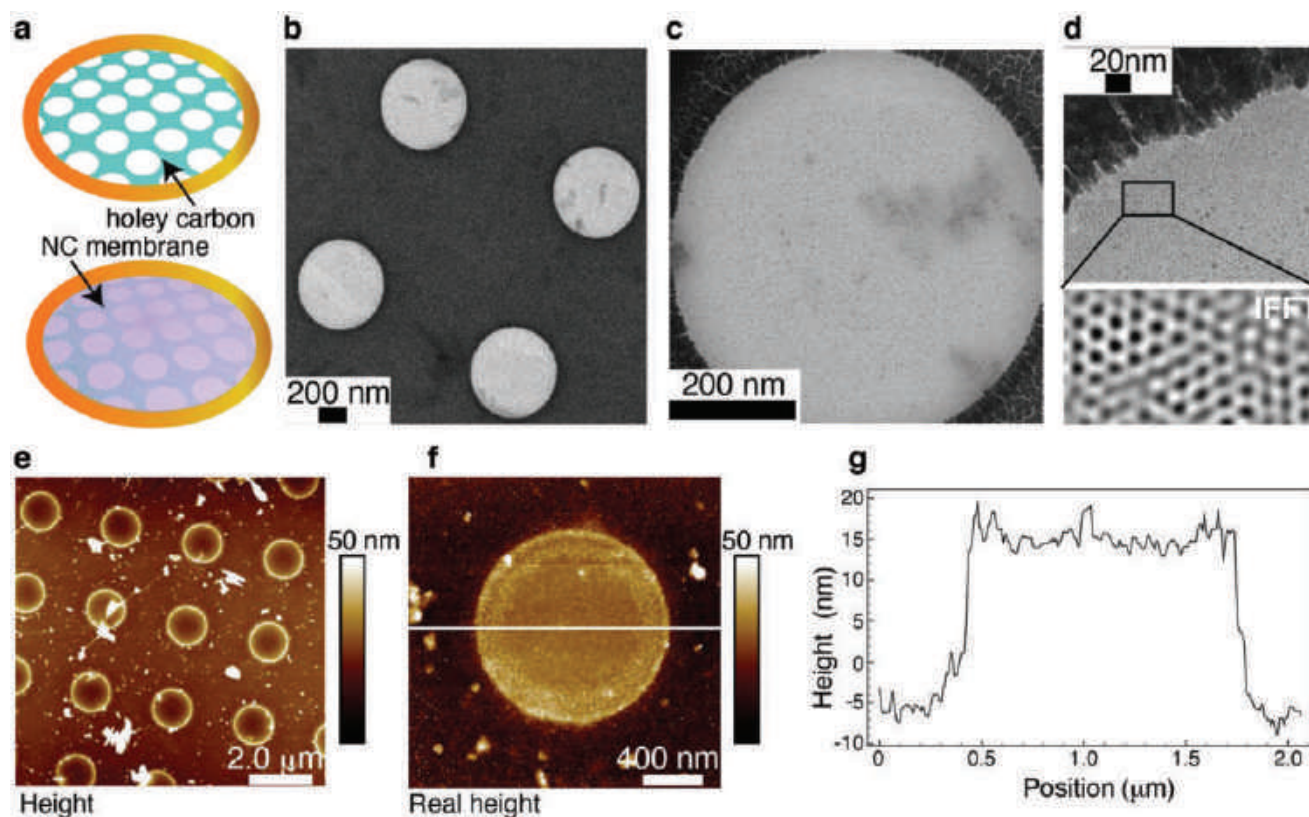


**Figure 3.** TEM and AFM imaging of  $\text{Na}_4\text{Ag}_{44}\text{-pMBA}_{30}$  membranes. a) Schematics showing the deposition of  $\text{Na}_4\text{Ag}_{44}\text{-pMBA}_{30}$  membrane on a gold grid with a holey carbon support membrane. b) TEM image showing cluster monolayers spanned across the holes (Figure S5, Supporting Information, for additional images). c) TEM image of one of the holes showing the cluster membrane being present across the hole. d) High-magnification TEM image and IFFT of the marked area showing hcp array of  $\text{Na}_4\text{Ag}_{44}\text{-pMBA}_{30}$  (note: NCs are sensitive to electron beam). e) Large area AFM height image of the cluster monolayer deposited on a TEM grid. f,g) AFM image of one of the holes, showing the cluster membrane spanned across the hole, and the corresponding height profile.

curves over different covered holes). Figure 4c,d shows the membrane before and after breakage upon a series of indents, respectively. As expected, the higher is the load applied, the deeper is the penetration depth (Figure 4e; Figures S11 and S12, Supporting Information, for additional AFM images and overlap of multiple  $F\delta$  curves, respectively). For small indentations,  $\delta$ , all curves are linear in force,  $F$ . However, when  $\delta$  considerably exceeds the membrane thickness,  $h$ , they turn nonlinear/cubic ( $F \approx \delta^3$ ). At large indentation, the obtained cubic term dominates, allowing to extract Young's modulus,  $E$ .<sup>[31,56]</sup> This is an essential point for the determination of  $E$  (see Equation (1)) since the apparent spring constant,  $k$ , for small  $\delta$ , depends on the prestretch of the membrane that is a priori unknown and cannot be used to determine  $E$  at small indentations. However, the prestretching of the monolayer membranes can be neglected for larger indentations, where the stretching energy dominates.

For homogeneous membranes, the effective  $E$  can be extracted using Equation (1), by analyzing the force curves within the framework of elasticity theory<sup>[57,58]</sup>

$$F = k\delta + \frac{\pi E h}{3R^2} \delta^3 \quad (1)$$

where  $h$  is the membrane thickness,  $R$  is the hole radius,  $\delta$  is the indentation depth, and  $k$  is the spring constant that depends on the prestrain of the membrane and used as a fitting parameter.

The model is applicable for  $\delta/h \gg 1$  and a point-like force. This is the case if the tip diameter is small compared to the hole radius, which is valid only for sharp styluses. The Scanasyt tip used in our measurements has a nominal radius of curvature of 2 nm (maximum nominal value at 12 nm). The tip radius was also estimated by tip qualification measurement and revealed a value of  $\approx 11$  nm, which closely matches the maximum nominal value and is much smaller than the hole radius. The  $E$  values extracted by the fit of the  $F(\delta)$  curves, fall in the range between 10 and 30 GPa as shown in the histograms of Figure 4g with Gaussian distribution centered at  $14.5 \pm 0.2$  GPa. The absence of hysteresis between the loading/unloading curves confirms the elastic nature of the  $\text{Na}_4\text{Ag}_{44}\text{-pMBA}_{30}$  monolayer membrane. At higher applied loads, however, when the membrane is close to the rupture, sometimes a slight hysteretic behavior is observed, indicating probably that the membrane is damaged or stretched irreversibly beyond a yield point, as also reflected by the low prestress values associated. The calculated average values for Young's modulus of  $\text{Na}_4\text{Ag}_{44}\text{-pMBA}_{30}$  membranes fall slightly above the range observed for deformations of

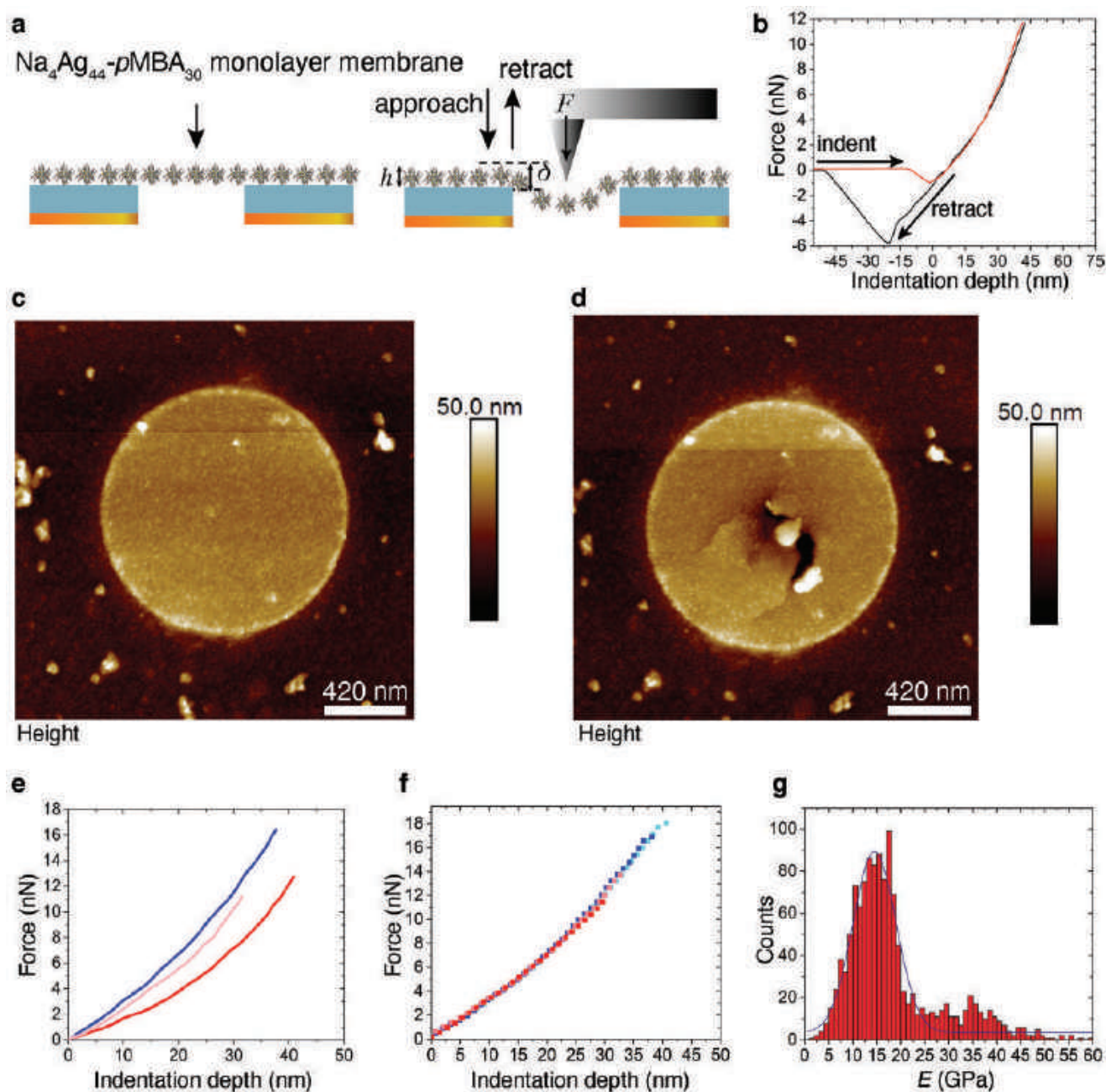


**Figure 4.** AFM measurements. a) A cartoon representation of the membrane deposited on top of the TEM grid and related AFM experimental setup. b) A typical force–displacement curve and the absence of hysteresis suggests the elastic nature of the membrane. c) AFM height image of the membrane before indentation. d) AFM image of the membrane after many indentation cycles at different close spots. e) Overlap of  $F(\delta)$  curves recorded on three different holes covered with membrane. f)  $F(\delta)$  curves recorded on the same spot of a hole covered with membrane by increasing force. g) Histogram reporting the  $E$  modulus value extracted by fitting the  $F(\delta)$  curves.

several larger nanoparticle-based membranes,<sup>[31,32,54,59]</sup> yet, the distribution of the obtained values is much narrower than the wide distribution range (3–39 GPa) of gold nanoparticle membranes reported earlier.<sup>[31]</sup>

The high modulus of  $\text{Na}_4\text{Ag}_{44}\text{-pMBA}_{30}$  membranes can be attributed to the well-defined H-bonded connectivity of nanoparticles and their structural integrity. In contrast to the narrow size dispersed alkanethiol-capped plasmonic nanoparticle

membranes,<sup>[29]</sup> the  $\text{Na}_4\text{Ag}_{44}\text{-pMBA}_{30}$  clusters are atomically precise with covalently bound short and rigid ligands. Therefore, the  $\text{Na}_4\text{Ag}_{44}\text{-pMBA}_{30}$  membranes are devoid of ligand entanglement, a common feature in polymer membranes. Importantly, the solid state structure of  $\text{Na}_4\text{Ag}_{44}\text{-pMBA}_{30}$  shows highly directional H-bonding distances between  $\text{O}\cdots\text{H}$  is 1.54 and 2.6 Å for the  $\text{O}\cdots\text{O}$ , and with the angle  $\angle\text{OHO}$  of 177°.<sup>[43,44]</sup>



## 2.4. Surfaced Enhanced Raman Spectroscopy

Noble metal nanoparticles deposited on functionalized surfaces have been studied in the literature as SERS substrate for detection and monitoring antibiotics.<sup>[60]</sup> Plasmonically coupled metallic nanostructures with ultrasmall ( $\approx 1$  nm or smaller) nanogaps can generate very strong and tunable electromagnetic fields that result in strong SERS signals from Raman dyes in the gap. However, even small changes ( $<1$  nm) in the structure of the coupled plasmonic nanogaps can significantly affect the localization of electrons and thereby, signal intensity in such plasmonically fabricated metamaterials.<sup>[61]</sup> High-yield synthetic strategies with nanometer-level structural control and reproducibility are greatly challenging owing to the inherent polydispersity in the size of nanoparticles. While the existing methods utilize highly sophisticated fabrication methods, we show that the  $\text{Na}_4\text{Ag}_{44}\text{-pMBA}_{30}$  membranes can overcome some of these challenges. Notably, the membrane can be readily transferred to the substrate and require no surface pretreatment to detect the target Raman-active molecules such as amphotericin B (Amp B, see Supporting Information for details). The Raman spectrum of standard Amp B shows the specific bands at  $1559\text{ cm}^{-1}$  corresponding to the C=C stretch due to the hydrophobic polyene domain and at  $1157\text{ cm}^{-1}$ , corresponding to the C–C stretching.<sup>[62,63]</sup> As shown in **Figure 5a**, when Amp B ( $250\text{ }\mu\text{g mL}^{-1}$ ) was drop-casted on  $\text{Na}_4\text{Ag}_{44}\text{-pMBA}_{30}$  film, the peak at  $1157\text{ cm}^{-1}$  emerged.

Besides, the peak at  $1429\text{ cm}^{-1}$  due to the stretching of  $-\text{COO}$  in  $\text{Na}_4\text{Ag}_{44}\text{-pMBA}_{30}$  film suffered a significant blue shift. These spectral features are highly reproducible, as shown using multiple membranes (**Figure S14b**, Supporting Information). Amp B has been detected before using AgNP as the plasmonic entity.<sup>[63]</sup> Here, we show that  $\text{Na}_4\text{Ag}_{44}\text{-pMBA}_{30}$  films can detect as low as  $2.5\text{ }\mu\text{g mL}^{-1}$  of Amp B. Whereas, at this concentration, the characteristic peak was not observed in the case of a similar film containing polydispersed AgNPs (**Figure S14d**, Supporting Information). Thus, as a proof of concept, it is shown that the precision film made of  $\text{Na}_4\text{Ag}_{44}\text{-pMBA}_{30}$  assemblies is more efficient SERS substrate as compared to traditionally used AgNPs.

## 3. Conclusions

Here we showed self-assembly of atomically precise  $\text{Na}_4\text{Ag}_{44}\text{-pMBA}_{30}$  NCs into freestanding elastic membranes with long-range hexagonal intralayer structure over  $\text{cm}^2$ -scale. This was accomplished by utilizing the hydrogen bonding dimerizations between the terminal *p*-mercaptobenzoic acid protecting ligands of the neighboring NCs. The patchy distribution of ligands around the metal core directed preferentially intralayer hexagonal assembly (in the *ab*-plane) and only to a lesser amount interplane hydrogen bonds (in the *c*-direction). Thereby the lateral growth perpendicular to the layers could be limited upon trapping the clusters in a transient solvent layer on the air–water interface facilitating a long-range intralayer structure within the monolayer. TEM imaging indicates an extended hexagonal 2D packing of the  $\text{Na}_4\text{Ag}_{44}\text{-pMBA}_{30}$  NCs in the membrane with a cluster-to-cluster distance of  $2.33\text{ nm}$ . This agrees with the triclinic unit cell parameters *a* and *b* in the 3D  $\text{Na}_4\text{Ag}_{44}\text{-pMBA}_{30}$  X-ray single crystal structure. The membranes could easily be transferred onto various substrates for desired applications. This is an important asset as well-defined colloidal structures have often been achieved upon templating with a specific substrate. On the other hand, the shown freestanding membranes with long-range order are expected to be relevant in applications to combine the mechanical and optoelectronic properties. The membranes behave elastically without any observable hysteresis, and display high Young's modulus of  $14.5 \pm 0.2\text{ GPa}$  (based on the Gaussian distribution center resulting from a set of experiments). Finally, the distinct constituent nanocluster spectral peaks remain observable in the membranes, even if slightly broadened, therefore indicating that the intrinsic properties of the individual NCs are retained in self-assembled membranes. These findings suggest that 2D colloidal materials where ligand capped NCs are bound together by H-bonds could raise unique elasticity and stiffness values, also suggesting to combine with optoelectronic properties of the nanoclusters for future single-electron transistors, metamaterials, and multifunctional devices.

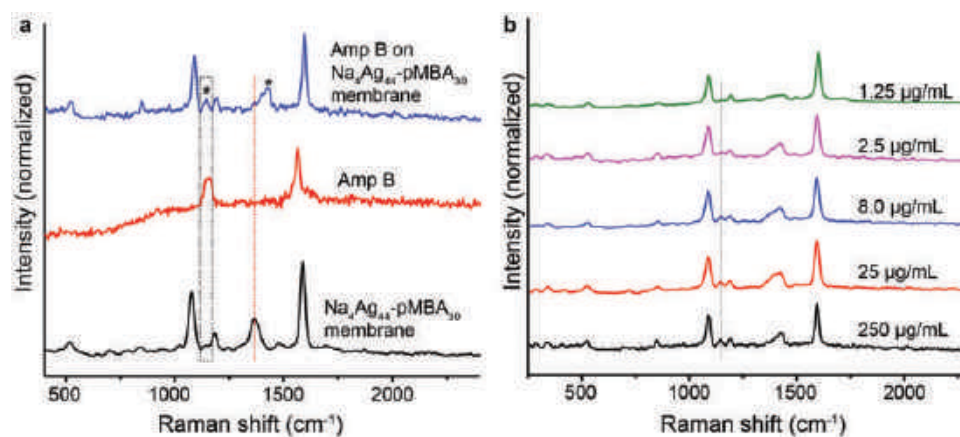


**Figure 5.** Surface enhanced Raman spectroscopy (SERS) measurements. a) Raman spectra of  $\text{Na}_4\text{Ag}_{44}\text{-pMBA}_{30}$  membrane, Amp B, and Amp B ( $250\text{ }\mu\text{g mL}^{-1}$ ) deposited over  $\text{Na}_4\text{Ag}_{44}\text{-pMBA}_{30}$  membrane. b) Variable concentration SERS spectra of Amp B deposited on  $\text{Na}_4\text{Ag}_{44}\text{-pMBA}_{30}$  membrane.

## Supporting Information

Supporting Information is available from the Wiley Online Library or from the author.

## Acknowledgements

The authors acknowledge the support by Academy of Finland Centre of Excellence in Molecular Engineering in Biosynthetic Hybrid Materials (HYBER, 2014-2019), ERC-Advanced Grant (DRIVEN), Photonics Research and Innovation (PREIN) Flagship, Department of Science and Technology, Government of India through Nano Mission, Centre of Excellence on Molecular Materials and Functions, IIT Madras, German Research Foundation (DFG, SFB 1027, Project B1) and Max Planck School Matter to Life supported by the German Federal Ministry of Education and Research (BMBF). This work made use of the Nanomicroscopy Center (Aalto-NMC) premises and the AFM facilities at Aalto University.

## Conflict of Interest

The authors declare no conflict of interest.

## Author Contributions

A.S., A.G., and I.C. contributed equally to this work. A.S., I.C., and N. conceived and carried out the synthesis and characterization. A.S. and N. carried out self-assembly, electron microscopy imaging, ESI mass spectrometry, and Raman spectroscopy measurements. A.G. conceived and carried out the AFM measurements and analyzed the data together with H.H., K.J., and P.L. T.P., O.I., and N. directed the experimental research. B.M. and A.C. performed the synthesis of NCs and membranes for SERS measurements. All authors contributed to preparation of the final manuscript.

## Data Availability Statement

The data that support the findings of this study are available from the corresponding author upon reasonable request.

## Keywords

2D membranes, colloids, nanoclusters, nanoparticle self-assembly, precision nanoparticles

Received: March 17, 2022

Revised: May 9, 2022

Published online: August 1, 2022

- [1] K. S. Novoselov, A. K. Geim, S. V. Morozov, D. Jiang, Y. Zhang, S. V. Dubonos, I. V. Grigorieva, A. A. Firsov, *Science* **2004**, 306, 666.
- [2] X. Peng, L. Peng, C. Wu, Y. Xie, *Chem. Soc. Rev.* **2014**, 43, 3303.
- [3] L. Chen, J. Wen, P. Zhang, B. Yu, C. Chen, T. Ma, X. Lu, S. H. Kim, L. Qian, *Nat. Commun.* **2018**, 9, 1542.
- [4] D. Akinwande, N. Petrone, J. Hone, *Nat. Commun.* **2014**, 5, 5678.
- [5] M. Chhowalla, H. S. Shin, G. Eda, L.-J. Li, K. P. Loh, H. Zhang, *Nat. Chem.* **2013**, 5, 263.

- [6] M. Naguib, V. N. Mochalin, M. W. Barsoum, Y. Gogotsi, *Adv. Mater.* **2014**, 26, 992.
- [7] L. H. Li, Y. Chen, *Adv. Funct. Mater.* **2016**, 26, 2594.
- [8] S. Rosenfeldt, M. Stöter, M. Schlenk, T. Martin, R. Q. Albuquerque, S. Förster, J. Breu, *Langmuir* **2016**, 32, 10582.
- [9] J. N. Coleman, M. Lotya, A. O'Neill, S. D. Bergin, P. J. King, *Science* **2011**, 331, 568.
- [10] J. M. Wofford, S. Nakhaie, T. Krause, X. Liu, M. Ramsteiner, M. Hanke, H. Riechert, J. M. J. Lopes, *Sci. Rep.* **2017**, 7, 43644.
- [11] A. Narita, X.-Y. Wang, X. Feng, K. Müllen, *Chem. Soc. Rev.* **2015**, 44, 6616.
- [12] Q. H. Wang, K. Kalantar-Zadeh, A. Kis, J. N. Coleman, M. S. Strano, *Nat. Nanotechnol.* **2012**, 7, 699.
- [13] F. Xia, H. Wang, D. Xia, M. Dubey, A. Ramasubramanian, *Nat. Photonics* **2014**, 8, 899.
- [14] W. Cheng, N. Park, M. T. Walter, M. R. Hartman, D. Luo, *Nat. Nanotechnol.* **2008**, 3, 682.
- [15] T. Wen, S. A. Majetich, *ACS Nano* **2011**, 5, 8868.
- [16] C. Yu, X. Guo, M. Muzzio, C. T. Seto, S. Sun, *ChemPhysChem* **2019**, 20, 23.
- [17] W. J. Cho, Y. Kim, J. K. Kim, *ACS Nano* **2012**, 6, 249.
- [18] R. Sardar, A. M. Funston, P. Mulvaney, R. W. Murray, *Langmuir* **2009**, 25, 13840.
- [19] S. Zhang, G. Leem, L. Srisombat, T. R. Lee, *J. Am. Chem. Soc.* **2008**, 130, 113.
- [20] C. S. Weisbecker, M. V. Merritt, G. M. Whitesides, *Langmuir* **1996**, 12, 3763.
- [21] V. N. Manoharan, *Science* **2015**, 349, 1253751.
- [22] K. E. B. Doncom, L. D. Blackman, D. B. Wright, M. I. Gibson, R. O'Reilly, *Chem. Soc. Rev.* **2017**, 46, 4119.
- [23] T. J. Woehl, T. Prozorov, *J. Phys. Chem. C* **2015**, 119, 21261.
- [24] T. P. Bignioni, X.-M. Lin, T. T. Nguyen, E. I. Crowin, T. A. Witten, H. M. Jaeger, *Nat. Mater.* **2006**, 5, 265.
- [25] A. Desireddy, C. P. Joshi, M. Sestak, S. Little, S. Kumar, N. J. Podraza, S. Masillac, R. W. Collins, T. P. Bignioni, *Thin Solid Films* **2011**, 519, 6077.
- [26] A. Dong, J. Chen, P. M. Vora, J. M. Kikkawa, C. B. Murray, *Nature* **2010**, 266, 474.
- [27] J. Pang, S. Xiong, F. Jaeckel, Z. Sun, D. Dunphy, C. J. Brinker, *J. Am. Chem. Soc.* **2008**, 130, 3284.
- [28] C. Klinke, *Europhys. Lett.* **2017**, 119, 36002.
- [29] K. E. Mueggenburg, X.-X. Lin, R. H. Goldsmith, H. M. Jaeger, *Nat. Mater.* **2007**, 6, 656.
- [30] A. Raveendran, M.-V. Meli, *ACS Omega* **2017**, 2, 4411.
- [31] W. Cheng, M. J. Campolongo, J. J. Cha, S. J. Tan, C. C. Umbach, D. A. Muller, D. Luo, *Nat. Mater.* **2009**, 8, 519.
- [32] a) F. Alibert, S. Pleutin, D. Guérin, C. Novembre, S. Lenfant, K. Lmimouni, C. Gamrat, D. Vuillaume, *Adv. Funct. Mater.* **2010**, 22, 330; b) F. Alibert, S. Pleutin, O. Bichler, C. Gamrat, T. Serrano-Gotarrendona, B. Linares-Barranco, D. Vuillaume, *Adv. Funct. Mater.* **2012**, 8, 609.
- [33] J. Langer, D. J. de Aberasturi, J. Aizpurua, R. A. Alvarez-Puebla, B. Auguie, J. J. Baumberg, G. C. Bazan, S. E. J. Bell, A. Boisen, A. G. Brolo, J. Choo, D. Cialla-May, V. Deckert, L. Fabris, K. Faulds, F. J. G. de Abajo, R. Goodacre, D. Graham, A. J. Haes, C. L. Haynes, C. Huck, T. Itoh, M. Käll, J. Kneipp, N. A. Kotov, H. Kuang, E. C. L. Ru, H. K. Lee, J.-F. Li, X. Y. Ling, et al., *ACS Nano* **2020**, 14, 28.
- [34] P. Pal, A. Bonyar, M. Veres, L. Himics, L. Balazs, L. Juhasz, I. A. Csarnovics, *Sens. Actuators, A* **2020**, 314, 112225.
- [35] R. X. He, R. Liang, P. Peng, *J. Nanopart. Res.* **2017**, 19, 267.
- [36] a) I. Chakraborty, T. Pradeep, *Chem. Rev.* **2017**, 117, 8208; b) R. Jin, C. Zeng, M. Zhou, Y. Chen, *Chem. Rev.* **2016**, 116, 10346; c) H. Häkkinen, *Nat. Chem.* **2012**, 4, 443.

- [37] a) Y. Li, M. Zhou, R. Jin, *Adv. Mater.* **2021**, *33*, 2006591; b) B. Zhang, J. Chen, Y. Cao, O. J. H. Chai, J. Xie, *Small* **2021**, *17*, 2004381.
- [38] a) T. Kawawaki, A. Ebina, Y. Hosokawa, S. Ozaki, D. Suzuki, S. Hossain, Y. Negishi, *Small* **2021**, *17*, 2005328; b) F. Gao, Q. Yuan, P. Cai, L. Gao, L. Zhao, M. Liu, Y. Yao, Z. Chai, X. Gao, *Adv. Sci.* **2019**, *6*, 1801671; c) L. Gao, Y. Zhang, L. Zhao, W. Niu, Y. Tang, F. Gao, P. Cai, Q. Yuan, X. Wang, H. Jiang, X. Gao, *Sci. Adv.* **2020**, *6*, 1421.
- [39] a) S. Chandra, Nonappa, G. Beaune, A. Som, S. Zhou, J. Lahtinen, H. Jiang, J. V. I. Timonen, O. Ikkala, R. H. A. Ras, *Adv. Opt. Mater.* **2019**, *7*, 1900620; b) J. V. Rival, P. Mymoona, K. M. Lakshmi, Nonappa, T. Pradeep, E. Shibu, *Small* **2021**, *17*, 2005718; c) V. Hynninen, S. Chandra, S. Das, M. Amini, Y. Dai, S. Lepikko, P. Mohammadi, S. Hietala, R. H. A. Ras, Z. Sun, O. Ikkala, Nonappa, *Small* **2021**, *17*, 2005205; d) A. Chakraborty, H. Dave, B. Mondal, Nonappa, E. Khatun, T. Pradeep, *J. Phys. Chem. B* **2022**, *126*, 1842.
- [40] Nonappa, T. Lahtinen, J. S. Haataja, T.-R. Tero, H. Häkkinen, O. Ikkala, *Angew. Chem., Int. Ed.* **2016**, *55*, 16035.
- [41] Nonappa, O. Ikkala, *Adv. Funct. Mater.* **2018**, *28*, 1704328.
- [42] A. Som, I. Chakraborty, T. A. Maark, S. Bhat, T. Pradeep, *Adv. Mater.* **2016**, *28*, 2827.
- [43] A. Chakraborty, A. C. Fernandez, A. Som, B. Mondal, G. Natarajan, G. Paramasivam, T. Lahtinen, H. Häkkinen, Nonappa, T. Pradeep, *Angew. Chem., Int. Ed.* **2018**, *57*, 6522.
- [44] Z. Wu, C. Dong, Y. Li, H. Hao, H. Zhang, Z. Lu, B. Yang, *Angew. Chem., Int. Ed.* **2013**, *52*, 9952.
- [45] A. Desireddy, B. E. Conn, J. Guo, B. Yoon, R. N. Barnett, B. M. Monahan, K. Kirschbaum, W. P. Griffith, R. L. Whetten, U. Landman, T. P. Bigioni, *Nature* **2013**, *501*, 399.
- [46] B. Yoon, W. D. Luedtke, R. N. Barnett, J. Gao, A. Desireddy, B. E. Conn, T. P. Bigioni, U. Landman, *Nat. Mater.* **2014**, *13*, 807.
- [47] J. Zasadzinski, R. Viswanathan, L. Madsen, J. Garnæs, D. K. Schwartz, *Science* **1994**, *263*, 1726.
- [48] K. Ariga, Y. Yamauchi, T. Mori, J. P. Hill, *Adv. Mater.* **2013**, *25*, 6477.
- [49] a) D. H. McCullough, S. L. Regen, *Chem. Commun.* **2004**, 2787; b) K. Ariga, *Langmuir* **2020**, *36*, 7158.
- [50] a) G. Palazzo, L. Carbone, G. Colafemmina, R. Angelico, A. Ceglie, M. Giustini, *Phys. Chem. Chem. Phys.* **2004**, *6*, 1423; b) H. You, Y. Ji, L. Wang, S. Yang, Z. Yang, J. Fang, X. Song, B. Ding, *J. Mater. Chem.* **2012**, *22*, 1998.
- [51] A. Lipatov, H. Lu, M. Alhabeb, B. Anasori, A. Gruverman, Y. Gogotsi, A. Sinitskii, *Sci. Adv.* **2018**, *4*, 0491.
- [52] R. Zhang, V. Koutsos, R. Cheung, *Appl. Phys. Lett.* **2016**, *108*, 042104.
- [53] A. Zandiatashbar, G.-H. Lee, S.-J. An, S. Lee, N. Mathew, M. Terrones, T. Hayashi, C. R. Picu, J. Hone, N. Koratkar, *Nat. Commun.* **2014**, *5*, 3186.
- [54] C. Lee, X. Wei, J. W. Kysar, J. Hone, *Science* **2008**, *321*, 385.
- [55] J. He, P. Kanjanaboos, N. L. Frazer, A. Weis, X.-M. Lin, H. M. Jaeger, *Small* **2010**, *6*, 1449.
- [56] M. Kocun, W. Mueller, M. Maskos, I. Mey, B. Geil, C. Steinemd, A. Janshoff, *Soft Matter* **2010**, *6*, 2508.
- [57] U. Komaragiri, M. R. Begley, J. G. Simmonds, *J. Appl. Mech.* **2005**, *72*, 203.
- [58] K. Tak, W. Shu, G. David, A. Dillard, *Thin Solid Films* **2003**, *425*, 150.
- [59] Y. Wang, H. Chan, B. Narayanan, S. P. McBride, S. K. R. Sankaranarayanan, S. X.-M. Lin, H. M. Jaeger, *ACS Nano* **2017**, *11*, 8026.
- [60] S. J. Clarke, R. E. Littleford, W. E. Smith, R. Goodacre, *Analyst* **2005**, *130*, 1019.
- [61] J.-M. Nam, J.-W. Oh, H. Lee, Y. D. Suh, *Acc. Chem. Res.* **2016**, *49*, 2746.
- [62] R. Miyaoka, M. Hosokawa, M. Ando, T. Mori, H. Hamaguchi, H. Takeyama, *Mar. Drugs* **2014**, *12*, 2827.
- [63] W. V. La Via, J. L. Lambert, M. J. Pelletier, J. M. Morookian, S. J. Sirk, D. Mickiene, T. J. Walsh, M. S. Borchert, *Med. Mycol.* **2006**, *44*, 169.

# Editorials



## Building Pathways to a Sustainable Planet

Cite This: *ACS Sustainable Chem. Eng.* 2022, 10, 1–2

Read Online

ACCESS |



Metrics &amp; More



Article Recommendations

This issue of *ACS Sustainable Chemistry & Engineering* marks the beginning of our 10th year of publication. Throughout the year, this occasion will be recognized by an icon on the cover, which appears for the first time on this issue.

The first 10 years of publication of *ACS Sustainable Chemistry & Engineering* have seen a transformation of our field. As we began publication in 2013, green and sustainable chemistry and engineering was still largely a specialty area. At the time our journal was launched, many in our community had argued for decades that green chemistry and engineering should be embedded throughout the practice of chemistry and engineering. Still, the commonly held view in the scientific community was that while the sustainability of our chemistry and engineering activities was important, it was not yet a critical component of all of our actions. This view has changed significantly in the past decade. Driven by the need for immediate action on climate and a host of other concerns, societies now expect that the practice of science and engineering will be guided by the principles and goals of sustainability. This change is reflected in the growth of our journal and journals that span our field. It is reflected in the direction of research throughout the chemistry and engineering enterprises. It is reflected in the widespread development of products and services that are more sustainable. It is reflected in the calls for sustainability in all aspects of our lives. As a community, our time has come, and our journal can respond, with your help, in a number of important ways.

One way we can respond is to showcase the implementation of sustainability innovations. While many of us will continue to work on fundamental scientific advances and the early stages of technology development, as a journal we will encourage more contributions that describe the commercial level implementation of those advances, highlighting challenges and responses. Implementing solutions quickly will be critical to addressing global energy and environmental challenges. Mapping pathways from lab to market will be an important contribution that our journal can make.

Another way we can respond is to continue to emphasize both qualitative and quantitative scientific assessments of the sustainability of our chemistry and engineering contributions. The use of sustainability metrics has been emphasized in our editorial pages multiple times and is an important criterion considered in our review of manuscripts. The use of sustainability metrics will become increasingly important as scholars new to sustainability look to our publications as models of what constitutes a research contribution to sustainability. We should expect that as sustainable chemistry and engineering becomes mainstream, sustainability claims of various sorts will appear throughout the chemistry and

engineering literature. Our journal should be an exemplar of how we substantiate these claims scientifically, taking entire life cycles into account.

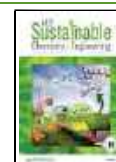
Still another way that we can respond is to highlight the role that sustainability plays in all of the spheres of our lives. We will begin this with editorials addressing the sustainability implications of everyday decisions. These editorials will be written with the audience of you, our current readers, in mind, but also new readers. These new readers may include colleagues that are new to sustainability. They may include researchers from cultures and societies that have been underrepresented in our community. They may include innovators interested in the widespread implementation of the advances described in our journal. They may include the next generation of scientists and engineers attempting to identify a career path that addresses sustainability. We should welcome these additions to our journal's audience, and our editorial pages will include contributions that translate our specialized language for wider audiences. Look for editorials related to sustainability in the workplace, in the home, in product systems, and other topics of broad interest.

Our community's time has come. We are being called to action. It is a complex call with numerous facets, but to make the message simpler, we recall a call to action made by U.S. President John Kennedy in 1961. In leading the United States down a pathway of unprecedented technological innovation, he called on the nation to "commit itself to achieving the goal, before this decade is out, of landing a man on the Moon and returning him safely to Earth". As a community, we should lead and commit ourselves to achieving the goal, before the current decade is out, of building pathways to a sustainable planet.

We welcome your participation in these efforts. That participation could be, as it has always been, through the contribution of manuscripts, through participation in the review process, and through the use of the publications that appear in the journal. It could be through organizing Virtual Special Issues on critical topics or by submitting thought provoking Perspectives, using the process described in our recent editorial.<sup>1</sup> It could also be through membership on our editorial boards; we will have another open call for membership at the end of this year. Finally, it could be

Received: December 19, 2021

Published: January 10, 2022



through inspiring our community. We hope that you have found this editorial inspiring, and the image in Figure 1



**Figure 1.** Earthrise photograph taken aboard the spacecraft Apollo 8 by astronaut Bill Anders (December 1968). Photo courtesy of NASA.

encapsulates this message. Throughout this year, we invite contributions of inspirational images and brief editorials that describe the images. We will feature these images in editorials in our journal. The images might be focused on the challenges we face, might celebrate the diversity of the community that is addressing the challenges, or might illustrate solutions. If you have an idea for artwork and an editorial that describes it, please contact one of the editors to discuss your ideas. We look forward to your creativity. No matter how you may choose to participate, however, we look forward to interacting with you and welcome comments and suggestions.

**David T. Allen**, Editor-in-Chief [orcid.org/0000-0001-6646-8755](https://orcid.org/0000-0001-6646-8755)

**Peter Licence**, Executive Editor [orcid.org/0000-0003-2992-0153](https://orcid.org/0000-0003-2992-0153)

**Bala Subramaniam**, Executive Editor [orcid.org/0000-0001-5361-1954](https://orcid.org/0000-0001-5361-1954)

**Paul T. Anastas**, Chair, Editorial Advisory Board [orcid.org/0000-0003-4777-5172](https://orcid.org/0000-0003-4777-5172)

**D. Julie Carrier**, Associate Editor [orcid.org/0000-0003-3322-4660](https://orcid.org/0000-0003-3322-4660)

**Jingwen Chen**, Associate Editor [orcid.org/0000-0002-5756-3336](https://orcid.org/0000-0002-5756-3336)

**Nicholas Gathergood**, Associate Editor [orcid.org/0000-0002-9398-9799](https://orcid.org/0000-0002-9398-9799)

**Jeannette M. Garcia**, Associate Editor [orcid.org/0000-0002-8336-4592](https://orcid.org/0000-0002-8336-4592)

**Jinlong Gong**, Associate Editor [orcid.org/0000-0001-7263-318X](https://orcid.org/0000-0001-7263-318X)

**Hongxian Han**, Associate Editor [orcid.org/0000-0002-2522-1817](https://orcid.org/0000-0002-2522-1817)

**King Kuok (Mimi) Hii**, Associate Editor [orcid.org/0000-0002-1163-0505](https://orcid.org/0000-0002-1163-0505)

**Bing-Joe Hwang**, Associate Editor [orcid.org/0000-0002-3873-2149](https://orcid.org/0000-0002-3873-2149)

**Andrew Marr**, Associate Editor [orcid.org/0000-0001-6798-0582](https://orcid.org/0000-0001-6798-0582)

**Michael Meier**, Associate Editor [orcid.org/0000-0002-4448-5279](https://orcid.org/0000-0002-4448-5279)

**Audrey Moores**, Associate Editor [orcid.org/0000-0003-1259-913X](https://orcid.org/0000-0003-1259-913X)

**Ryuhei Nakamura**, Associate Editor [orcid.org/0000-0003-0743-8534](https://orcid.org/0000-0003-0743-8534)

**Thalappil Pradeep**, Associate Editor [orcid.org/0000-0003-3174-534X](https://orcid.org/0000-0003-3174-534X)

**Liane Rossi**, Associate Editor [orcid.org/0000-0001-7679-0852](https://orcid.org/0000-0001-7679-0852)

**Bert Sels**, Associate Editor [orcid.org/0000-0001-9657-1710](https://orcid.org/0000-0001-9657-1710)

**Michael K. C. Tam**, Associate Editor [orcid.org/0000-0002-7603-5635](https://orcid.org/0000-0002-7603-5635)

**Lin Zhuang**, Associate Editor [orcid.org/0000-0002-5642-6735](https://orcid.org/0000-0002-5642-6735)

**Julio F. Serrano**, Managing Editor [orcid.org/0000-0002-7803-808X](https://orcid.org/0000-0002-7803-808X)

## AUTHOR INFORMATION

Complete contact information is available at:

<https://pubs.acs.org/10.1021/acssuschemeng.1c08512>

## Notes

Views expressed in this editorial are those of the authors and not necessarily the views of the ACS.

## REFERENCES

- (1) Allen, D. T.; Carrier, D. J.; Chen, J.; Gathergood, N.; Garcia, J. M.; Gong, J.; Han, H.; Kuok (Mimi) Hii, K.; Hwang, B.-J.; James, A. L.; Jha, M.; Licence, P.; Marr, A. C.; Meier, M.; Moores, A.; Nakamura, R.; Pradeep, T.; Rossi, L.; Sels, B.; Subramaniam, B.; Tam, M. K. C.; Zhuang, L.; Serrano, J. F. Expectations for Perspectives in *ACS Sustainable Chemistry & Engineering*. *ACS Sustainable Chem. Eng.* **2021**, *9* (49), 16528–16530.

# Book Chapter

## Chapter 16

# Concepts of Sustainability in Clean Water Technologies

Sritama Mukherjee, Jenifer Shantha Kumar, Ankit Nagar, and Thalappil Pradeep\*

DST Unit of Nanoscience (DST UNS) and Thematic Unit of Excellence (TUE), Department of Chemistry, Indian Institute of Technology Madras, Chennai 600036, India

\*Email: [pradeep@iitm.ac.in](mailto:pradeep@iitm.ac.in)

Water is essential for human survival. Hence, universal access to safe and affordable drinking water is included as one of the Sustainable Development Goals of the United Nations. With increasing global water stress and stricter revised regulations by bodies such as World Health Organization (WHO) and U.S. Environmental Protection Agency (USEPA) for safe drinking water, it is imperative to research efficient water treatment and quality monitoring technologies that are environmentally benign, affordable, and have ease of implementation. In this regard, sustainable nanomaterial-based technologies are capable of delivering real-time solutions cost-effectively using less energy by reducing ecological impact. These technologies are expected to play a significant role in water remediation including potable water treatment, sensing, wastewater desalination, and water harvesting. However, it is crucial to carefully assess the various sustainability criteria for diverse technologies before their large-scale implementation. In this chapter, we discuss a variety of emerging nanomaterial-based treatment and sensing techniques in the scientific literature and in the market, from the concepts of sustainability and their applications to assess clean water technologies using sustainability metrics. Bio-based processes look promising for the future of water purification in terms of effectiveness and environmental safety. Apart from current nanotechnological frontiers in diverse clean water applications, suggestions for future research are also provided.

## Introduction

Out of the total of  $\sim 1.4 \times 10^{18}$  tons of water available on our planet, only 2.5% is fresh water (1). Nearly 69.6% of this freshwater is frozen and not readily accessible for humans. The remaining  $\sim 30.1\%$  is present as underground lakes. The remaining 0.4% of the total freshwater is the most useful portion for humans and it exists mostly on land as lakes, rivers, and swamps and also as atmospheric humidity (2). Globally, more than 700 million people lack access to safe water, particularly in developing countries. Therefore, it has become mandatory to practice water treatment

and reuse as alternatives to reduce the stress on freshwater resources (3). As the quantity of water on the planet is nearly constant and as the human aspirations and consequently the water demand is increasing, concerns of sustainability become apparent on all aspects of clean water.

There lies a huge gap between the demand and supply of this resource due to rising population, climate change, deterioration in water quality, and poor management. Water pollutants are of three types: organic, inorganic, and biological (4). Many of them are toxic and detrimental to humans and ecosystems. As an example, arsenic is one of the most hazardous elements, present in many regions above its permissible limits. Other severely toxic heavy metals are mercury, uranium, lead, chromium, copper, nickel, cadmium, and zinc. In addition, high concentrations of phosphates, selenides, chromates, nitrates, sulfates and oxalates are also hazardous and may also alter the taste of water. Organic contaminants like detergents, hydrocarbons, phenols, pesticides, organo-chlorine compounds and phthalates are known to be toxic. Emerging pollutants comprise pharmaceuticals and personal care products (PPCPs) which do not degrade naturally (5–7). Their sources include household and hospital waters which contain drugs and drug products, packaging, and additives present in detergents. The concentration of PPCPs in water ranges from 0.001 ppb to 1 ppb (5). Therefore, conventional treatment methods used in treatment facilities prove inadequate for such contaminants. Polycyclic aromatic hydrocarbons (PAHs) are another class of water pollutants generated by the combustion of fossil fuels. Because of their low solubility and high affinity for particulates, they are found in low concentrations in water. In potable water, PAHs detected at high concentrations are phenanthrene, pyrene, fluoranthene, and anthracene (8). The microbial contamination of water is often fecal in origin. The main sources of such contamination are water treatment plants, industries and hospitals. The effect of urban activities on the concentration of pathogens has already been established. Natural organic matter (NOM) is one of the principal parameters to understand water quality in such cases and determine the treatment process.

The global population is expected to reach nearly 8.2 billion by 2025 (9). This suggests a dire need to prepare for the current and forthcoming challenges associated with water scarcity. To ensure good public health and hygiene, it is necessary to remove conventional as well as emerging contaminants from water at affordable cost and with less energy, ideally causing no impact to the environment. Conventional methods of purification (Table 1) include adsorption, filtration, ultraviolet irradiation, desalination, disinfection, coagulation, etc., while emerging nanotechnology-enabled methods involve the use of carbon nanocomposites, metal or metal oxide nanoparticles (NPs), nanoporous ceramics, and other nanomaterials.

The past decade has seen a rapid surge in nanomaterials-based water purification approaches. The science of nano-sized materials has resulted in affordable technologies for the removal of emerging pollutants such as arsenic, fluoride, iron, organics, bacteria, nitrates, viruses, etc., found in groundwater, surface water, industrial discharges, and several other sources. Existing treatment technologies have enabled us to achieve practically any desired degree of water quality. For industrial purposes, conventional processes including secondary treatment, filtration, and disinfection processes are sufficient to achieve the required quality of reclaimed water. Nanotechnology-enabled processes, however, have the potential to overcome challenges associated with conventional technologies. These processes are affordable, multifunctional, modular, highly efficient, and require lesser pressure for filtration and enable easy cleaning using back-flushing. They have already been implemented for the removal of sediments, charged particulate matter, bacteria, pathogens and heavy metals (18).

This chapter presents an overview of the recent progress in concepts of sustainability in materials for water purification and associated technologies.

**Table 1. A Summary of Traditional Water Purification Technologies**

<i>Adsorption</i>	<i>Filtration</i>	<i>Electrochemical</i>	<i>Disinfection</i>
Natural adsorbents (10, 11)	Micro-filtration (12)	Electrocoagulation (13, 14)	Chlorination (15)
Synthetic adsorbents (16, 17)	Ultra-filtration (18, 19)	Electroflotation (20, 21)	Chloramination (15)
Biomass adsorbents (22, 23)	Nano-filtration (24)	Electrodeposition (25, 26)	Chlorine dioxide
Agricultural wastes (22, 27)	Reverse Osmosis (RO) (19, 24)	Electrokinetic treatment (28, 29)	Ozonation (15, 30–32)
	Aerogels (33), Chalcogels (34, 35)	Electrooxidation (36, 37)	Ultraviolet radiation (15, 38, 39)
			Pasteurization (40, 41)

## Sustainable Materials and Technologies for Water Purification

Recent developments in nanoscience have provided us with several implementable solutions for removing contaminants from polluted water for producing freshwater. Figure 1 depicts the translation process from lab to market where the first step is the synthesis of nanomaterials at lab scale (circle 1), followed by exploring a phenomenon exhibited by nanomaterials (circle 2), and, beyond the proof-of-concept stage, building nanomaterials-embedded products that are deployed in the field (circle 3).

We group the water purification technologies and water quality sensors into two categories for better discussion, although this classification may not be accurate in some cases: a. being developed and deployed, and b. commercial technologies in water purification.

### Being Developed and Deployed

#### *Water Purification Technologies*

##### Adsorption

The removal capacity of the adsorbents depends on density and porosity of particle and bulk, external surface area, internal surface area, pore size distribution, surface structure, functionalization and operational parameters such as temperature, pH and contact time (48). Various organic and inorganic adsorbents have been developed with engineered nanomaterials (ENMs) for effective removal of environmental pollutants with various molecular sizes, hydrophobicity and speciation behavior (49). These ENMs include carbonaceous materials such as carbon nanotubes and their derivatives, fullerenes, graphenic materials, activated carbon, etc., nanoscale metal and metal oxides of Fe, Ti, Ag, Zr, Zn and so on; magnetic nanoparticles such as those involving Fe, Ni, Co or their oxides and alloys, core-shell nanoparticles, etc. (48, 50)



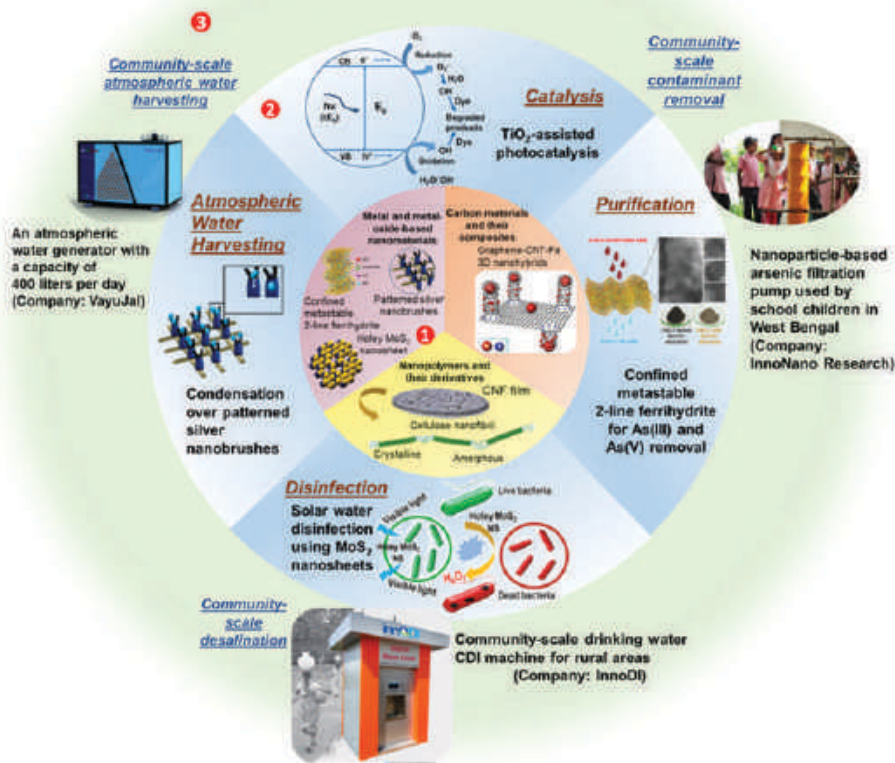


Figure 1. Schematic showing the journey of nanomaterials from lab to market. Circle 1 covers building blocks used to create nanomaterials; circle 2 comprises of phenomena reported using such nanomaterials; and outermost circle 3 shows the implementation of nanomaterials in the form of products that create a societal impact. Pictures having 2-line ferrihydrite in circles 1 and 2 adapted with permission from ref (42). Copyright John Wiley and Sons, 2017. Images containing holey MoS<sub>2</sub> in circles 1 and 2 adapted with permission from (43). Copyright 2018 The Authors. Published by WILEY-VCH Verlag GmbH & Co. KGaA, Weinheim under Creation Commons Attribution 4.0 International License. Image in the bottom section of circle 1 adapted with permission from ref (44) under Copyright 2020, The Author(s) under Creation Commons Attribution 4.0 International License (CC BY license). Schematic illustration of graphene-CNT-Fe (CNT - Carbon Nanotubes) nano hybrid in the innermost circle (44, 45) adapted with permission from ref (45). Copyright American Chemical Society, 2013. Picture of a community-scale CDI machine in the outermost circle adapted with permission from ref (46). Copyright Innodi Water Technologies Pvt. Ltd, 2018. Picture of an atmospheric water generator in the outermost circle adapted with permission from ref (47). Copyright Vayujal Technologies Pvt. Ltd, 2019. The sub-sections following discuss state-of-the-art nanomaterials and related technologies, and their societal impact in the context of clean water.

Composite materials are formed by a combination of the matrix (continuous phase) and reinforced materials (dispersed). Nanocomposites have nanoparticles merged within diverse functionalized materials like multiwall CNTs (MWCNTs), activated carbon, graphene oxide, polymeric or biopolymeric fibers, clays, zeolites, etc. (51) They have advantages over other materials due to their unique characteristics such as high durability, high rigidity, high strength, gas-barrier features, corrosion resistance, low density, and heat resistance. Al<sub>2</sub>O<sub>3</sub>/MWCNTs have been reported to remove Cd<sup>+2</sup> and trichloroethylene from the polluted water, TiO<sub>2</sub>-zeolite nanocomposites are known for the removal of industrial dyes from wastewater (52, 53). AMRIT, acronym for Anion and Metal Removal by Indian Technology, is instrumental in supplying arsenic-free water for over 1.2 million people every day, has new nanostructured materials with large adsorption capacities for arsenite and arsenate ions in water, in field conditions (54). The unprecedented large capacity in field conditions is attributed to the inherent structure of the composite with confined metastable 2-line ferrihydrite in biopolymer cages of chitosan, which allows the creation of effective adsorption sites (42). Similarly, filters composed of noble metal nanoparticle-coated metal oxides remove pesticides from drinking water using nanochemistry (55, 56). That technology has already reached over 7.5 million people by 2016, when implementation data were last collected, reducing pesticide levels from over 20 times the safety standard, present in several parts of India, to concentrations substantially below it (57). Sankar et al. reported an antimicrobial composition consisting of an aluminum oxyhydroxide–chitosan composite with silver particles of 10–20 nm diameter embedded in it (58). Such solutions do not require electricity and are affordable, even for those living in the poorest parts of the world. Adsorbents were made further sustainable by making composites with reinforced micro- and nanocellulose with active nanoscale adsorption sites that showed higher uptake and exceptional mechanical stability (59, 60).

### Membranes

Filtration membranes comprising nano-TiO<sub>2</sub> do not degrade due to fouling and provide high filtration efficiency at a high water flux (61). Nanoporous zeolites, nanoporous polymers, and attapulgite clays have a capacity of binding contaminants up to 100,000 times larger than conventional activated carbon (62). Pure silica particles with an active material's coating are far more effective in removing toxic chemicals and pathogens at affordable costs (63). CNT-based technology has been effective in treating biological pollutants in traditional water treatment plants, thereby solving the problem of keeping treated water biostable in the distribution lines (64). Such membranes have been recognized as promising alternatives to RO membranes and for performing desalination. Mass production of CNT membranes is becoming increasingly cost-effective and is predicted to reach the desalination market in another 5-6 years, as researchers are presently working to reduce the scalability issues associated with the technology (65). Numerous technologies have been investigated as a potential replacement for conventional RO membranes in desalination and water recycling applications. Nanocomposite membranes possess ~1-3 fold more permeability to water with the same rejection as commercial RO membranes and can be multifunctional with antimicrobial and photo-reactive characteristics (66). Nanotechnology-based purification systems are affordable, portable, easy-to-handle, highly efficient, and offer unusually high surface areas. Nanomaterials, such as MoS<sub>2</sub> nanosheets for disinfection, CNF films for biocidal activity, silver nanobrushes for atmospheric water harvesting, and ferrihydrite for heavy metal removal are debuting

commercial applications in the water sector (54). Large-scale production of nanomaterials and their composites are expected to rise due to the demand to produce clean water in both time and energy-efficient manner.

### Capacitive Deionization

Capacitive deionization (CDI), which fundamentally involves making use of an electrical voltage applied between two electrodes for the facile removal of charged ionic species from aqueous solutions is increasingly being considered as a viable solution for water purification which is more energy-efficient than most of the conventional water treatment processes. CDI using nanomaterials that exhibit characteristics such as high specific surface area, high conductivity, fast adsorption/desorption rates, electrochemical stability, resistance to biofilm formation, and easy processability have opened up new possibilities. Research on further modification of CDI technology utilizing ion-exchange membranes has enabled overcoming the operational limitation by eliminating the discharging cycle, enabling self-regeneration, and improving ion adsorption capacity, providing practically unlimited surface area for ion adsorption resulting in up to 80-90% salt removal efficiency with the electrode (67). CDI has multiple advantages over other desalinating processes: (i) the technique works by the process of electroadsorption, and is even more energy-efficient, as it does not require any high-pressure pumps; (ii) as the module works in 0.8–2.0V, it can be combined with solar/wind power and can work in remote areas, where availability of electricity is a major issue; (iii) water rejection is much less, even down to 10%; (iv) carbon particles can withstand much higher temperatures than membranes and can be used for wider applications; and (v) as the device works like a capacitor, energy recovery is possible (68, 69).

### Atmospheric Water Generator

Our planet's hydrological cycle circulates 45,500 billion metric tons (bmt) of water annually (70). Humans are responsible for the consumption of nearly 4000 bmt water every year, much lower than the quantity of water moving in the hydrological cycle (1). Any withdrawal of water from the atmosphere accelerates the hydrological cycle as it reduces the residence time of water in water bodies. Moreover, water consumption for any human activity returns it eventually to freshwater sources. A total of 12,960 bmt of atmospheric water is sufficient to fulfill the water requirements of mankind (71).

Water in the atmosphere exists as fog, clouds and water vapor. Several methods have been explored to harvest all forms of atmospheric water. One of the early attempts includes deployment of twin plastic nets of size  $\sim 28.0 \text{ m} \times 3.6 \text{ m}$  that harvested nearly  $11 \text{ L/m}^2/\text{day}$  from October 1969 until December 1970 in Mariepskop in Mpumalanga, South Africa (72). While such 'passive' water harvesters proved useful, the water generated was insufficient in moderately humid conditions. Therefore, active water harvesting was explored, where atmospheric water generators (AWGs) used the Peltier effect or a refrigeration cycle to bring down the temperature of the surrounding air below its dew point to enable condensation (73). This enabled atmospheric water extraction in highly water scarce regions to overcome the challenges of freshwater transportation of long distances and highly contaminated groundwater and surface water sources. While several commercial products are already serving people today, research continues in the direction of developing energy-efficient condensing surfaces and accessing regions with relative humidity (RH) of less than 40%.

Adsorption-based harvesting has emerged as a promising alternative to condensation-based technologies. While conventional desiccant materials such as zeolites and silica gel absorb humidity, their slow sorption kinetics, low absorption capacity and high energy requirement for regeneration limit them from practical implementation. Several promising alternatives such as metal-organic frameworks (MOFs) possess high surface area and tunable pore size. As an example, a kilogram of  $\text{Zr}_6(\text{OH})_4(\text{fumarate})_6$  has the capacity to harvest 2.8 L/day at 20% RH, thereby encouraging further research on developing molecular materials for water harvesting in deserts (74). Impregnating such MOF NPs into thermo-responsive polymers like poly(*N*-isopropylacrylamide) has enabled harvesting closer to room temperature (30). Current focus is on improving the absorption capacity by introducing hydrophilic ligands in the nanopores, reducing energy requirement for desorption, faster sorption kinetics and cyclic stability for several hundreds of sorption cycles (75). In order to further explore harvesting methods and aspects of designing water generators, readers may consult references (1), (72), and (75).

### Water Quality Sensors

Nanomaterials have been demonstrated to show readable colorimetric, fluorescent, magnetic, electrochemical, and plasmonic responses for water quality parameters and contaminants such as heavy metals, organic and inorganic contaminants, and pathogens. They help in accomplishing high sensitivity, portability, multiplexity, and flexibility in sensors for monitoring the quality of water (76). Several nanomaterials such as nanowires, quantum dots, metal nanoparticles, and carbonaceous nanoparticles are well known to detect various contaminants in water (77–81). Figure 2A shows a colorimetric sensor capable of sub-ppm level detection of fluoride was made with ceria@zirconia core-shell nanoparticles and its color changes from yellow to red, indicating the increasing fluoride concentration in the sample, from 0.1 ppm onwards, even in presence of other interfering ions (76). The results were communicable to the user through a smart phone based application.

Lab on chip sensors and other microfluidic sensors are capable of replacing several conventional lab scale water quality analysis techniques and reducing the chemical reagents consumed in the process (89, 90). A wide range of electrochemical sensors are available for the detection of various ions, molecules, and microbes in water and these sensors are portable, quick, and capable of real-time monitoring of water quality. A stripping voltammetry-based arsenic sensor has been fabricated by Gupte et al., through electrodeposition of  $\text{MnO}_x$  on indium doped tin oxide electrode to achieve a limit of detection (LOD) of 1 ppb  $\text{As}^{3+}$  with high selectivity, as shown in Figure 2B&C (83). Several nanomaterials and nanocomposites are used in electrochemical sensors and they are composed of carbon, metals, noble metals, metal oxides and metal hydroxides.

Nanoclusters are emerging materials for monitoring water quality (91–93). They are of 1–2 nm dimension and differ from more traditional nanomaterials in their molecular behavior and these have proven to be effective in identifying several contaminants in water (91–93). Conventionally, nanomaterials are prepared in solvent systems that are not sustainable and leave toxic residues. Chemically synthesized nanomaterials are also reported to be less biocompatible. Biological methods of nanomaterial synthesis are effective in rendering biocompatibility to such materials though they are time-consuming and have not yet reached an industrial scale even after being known for several decades (94). Nanoclusters have been synthesized using amino acids, proteins, and aptamers, which improved their biocompatibility and various sensing properties have been demonstrated with such

materials (95–97). While bovine serum albumin-protected gold nanoclusters (Au@BSA NCs)-loaded cellulose nanocrystal–alginate hydrogel beads can simultaneously sense and scavenge heavy metal ions (Figure 2D) (84), freestanding luminescent films composed of the quantum cluster, Au<sub>15</sub> could sense Cu<sup>2+</sup> up to 1 ppm (Figure 2G) (86). Techniques like AESD RS (ambient electro spray deposition Raman spectroscopy) enable detecting and characterizing *E. coli* at its lowest concentration of 10<sup>2</sup> CFU/mL as shown in Figure 2E & F (85). Figure 2J shows electrospun polymer nanofibers containing gold nanoclusters used for detecting Hg<sup>2+</sup> in water (88). Au@SiO<sub>2</sub>@Ag<sub>15</sub> mesoflowers were reported to detect less than one zeptomole of TNT (Figure 2H & I) (87). Emerging techniques such as ambient electro spray based synthesis of nanoclusters and nanoparticles provide an opportunity to reduce the solvent and additional reagent requirement for their synthesis (98). Solid-state synthesis of nanoclusters has been demonstrated by Rao et al., proving that nanoclusters can be synthesized more sustainably without the use of solvents as in chemical synthesis methods (99). Sustainable synthesis of sensor materials is an important direction.

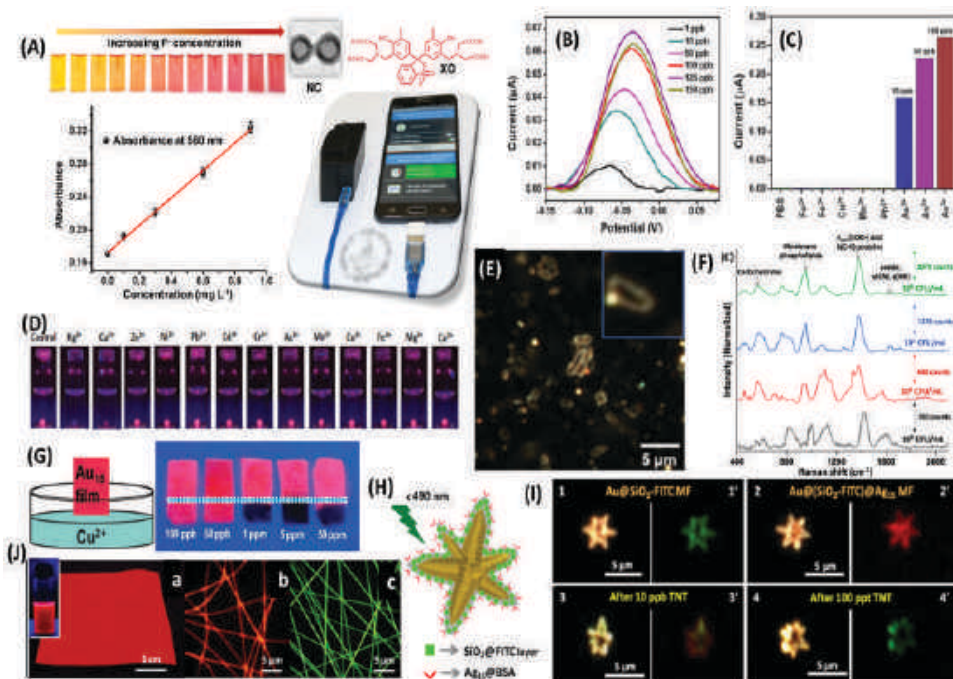


Figure 2. Various sensing methods using nanomaterials for the detection of contaminants such as (A) F<sup>-</sup> adapted with permission from ref (82), Copyright American Chemical Society, 2020; (B) & (C) As<sup>3+</sup> adapted with permission from ref (83), Copyright American Chemical Society, 2019; (D) various heavy metal ions adapted with permission from ref (84), Copyright American Chemical Society, 2016; (E) & (F) *E. coli* adapted with permission from ref (85), Copyright Royal Society of Chemistry, 2019; (G) Cu<sup>2+</sup> adapted with permission from ref (86), Copyright American Chemical Society, 2012; (H) & (I) TNT adapted with permission from ref (87), Copyright Wiley-VCH, 2012; and (J) Hg<sup>2+</sup> adapted with permission from ref (88), Copyright American Chemical Society, 2014 at trace level concentrations, respectively.



Internet of Things (IoT) enables real-time data collection on the quality of water across the water distribution network and at remote locations (100). Gloria et al., have developed an IoT enabled sensor for quantifying the water supplied for irrigation to minimize the wastage of water and the sensor works wirelessly (101).

Though portable sensors have been commercialized for parameters such as pH, TDS, dissolved oxygen, minerals, etc., commercialization of sensors that can detect a wide variety of contaminants and dissolved molecules has not been achieved yet and much research is being carried out for the development of such devices (102). Sensors are available as kits and are mostly based on colorimetric detection (93). Real Tech Inc. has developed UV/VIS LED based real-time water quality sensors which are low cost and capable of detecting chromium, hydrocarbons, nitrates, nitrites, etc. (103). Upcoming sensors are also looked at for properties such as portability, on-line real-time monitoring, reusability, cost-effectiveness, and sustainability.

### Commercial Technologies in Water Purification

The earlier section discussed emerging methods of purification. Here, we will discuss the implementation of emerging methods into commercial water purification technologies and products in the market. While nanomaterials such as CNTs, cellulose-based nanomaterials, MXenes, aquaporins, etc., have shown outstanding performance at the lab scale, several of them have also been successfully mass-produced and translated into products (54). As an example, CNTs are among the widely utilized nanomaterials for purification purposes (104). CNT-based filtration systems are efficient in removing inorganic, organic and biological contaminants from water (105). Globally, companies like GEA Group (106), Inopor (107), Applied Membranes (108), Koch Separation Solutions (109), and Alfa Laval (110) are manufacturing nanomaterials-based membranes in their filtration systems.

Another technology, known as acoustic nanotube technology, invented by NASA, involves the use of acoustics rather than pressure to drive water through CNT nanochannels (111). It consumes less power compared to the conventional pressure-driven systems, enabling operation in remote areas and with support from solar power. The flow of water is not gravity-dependent. This technology is scalable and multiple large-area filters can be integrated into a system.

Recent years have witnessed a surge in the use of photocatalytic technologies for water treatment. As an example, Panasonic came up with a way of binding the photocatalyst  $\text{TiO}_2$  to a commercial adsorbent and a catalyst, zeolite, which allowed the photocatalyst to maintain its inherent active sites and ensure its effective recovery post-treatment and reuse (112).  $\text{TiO}_2$  can mineralize hazardous organics into safe compounds. The photocatalyst can break down pesticides (113), dyes (114), pathogens (115), microbes (116), crude oil (76), and reduce heavy metal ions present in water (81).

Apart from the earlier mentioned nanomaterials which have managed to penetrate the commercial sector, several others have shown promise for translation beyond lab scale. Similar to  $\text{TiO}_2$  NPs, ZnO NPs have shown extraordinary photocatalytic activity and excellent antimicrobial activity in presence of waterborne pathogens (92). Filters coated with Ag NPs are effective in removing pathogens such as *Escherichia coli*, *Shigella dysenteriae*, and *Vibrio cholerae* (91). Zerovalent Fe NPs have a strong reduction potential to oxidize organic dyes, uranyl ion ( $\text{UO}_2^{2+}$ ), phenols and metalloids (93, 94). For practical use, they can be integrated with solid matrices such as activated carbon. Graphene derivatives such as graphene oxide, pristine graphene and reduced graphene oxide



possess remarkable antifouling and photocatalytic properties and are excellent adsorbents (97). Graphene-based membranes with the thickness of a few atoms are known to perform better than conventional polyamide membranes (95). Application of graphene nanomaterials for desalination has been explored extensively (96, 117). Their ion adsorption capacities allow them to effectively remove salts from water. Graphene and its oxide derivatives have also shown antimicrobial properties against microorganisms such as *E. coli* (118), *Staphylococcus aureus* (71, 89), *Candida albicans* (90), etc. Nanocomposites comprising an adsorbing matrix such as SiO<sub>2</sub> and an antiviral TiO<sub>2</sub> coating can inactivate waterborne viruses. Likewise, Ag<sub>2</sub>S@Ag effectively adsorbs dyes from wastewater (119). Membranes comprising metal or metal oxide NPs embedded in a polymeric matrix are effective in removing heavy metals and microbes from water. Detailed literature regarding nanomaterials with potential for commercialization can be found in ref (96) (100).

### **Sustainability in Materials and Technologies: Parameters and Limitations**

Clean water forms the basis of Sustainable Development Goal 6 (SDG 6), established by the United Nations in 2015. The SDG 6 promises to ‘ensure availability and sustainable management of water and sanitation for all’ (120). Under this goal, there are clean water-related targets like (a) access to safe and affordable drinking water for all; (b) improvement in water quality by the decrease in pollution, eliminating or minimizing release of untreated hazardous chemicals and materials, halving the proportion of untreated wastewater and substantially increasing recycling and safe reuse globally; (c) expand international cooperation and capacity-building support to developing countries in water and sanitation-related activities and programs, including water harvesting, desalination, water efficiency, wastewater treatment, recycling and reuse technologies, and so on (121). Material science has acted as an incredibly important catalyst in achieving the aforementioned targets by being the essential ingredient of various manufacturing processes related to water purification technologies. Various clean water applications need materials to scale up at various stages, therefore the study of the environmental footprint of materials and processes on deeper scales becomes essential to be monitored (122, 123). Assessment of the environmental impact of nanomaterials and related technologies has become one of the significant fields in sustainability research that would provide a foundation for pollution reduction and the introduction of cleaner technologies and operations. Studying the manufacturing processes of engineered materials and the development of reactors with the ability to recover and reuse the spent materials have become crucial (53). Advanced analysis, development of clean technologies, and environmental policies can mitigate the environmental burden directly and indirectly.

While nanotechnologies for water purification continue to emerge, an area of intense research has been the toxic effect of nanoparticles. These particles largely differ in their chemical and physical properties compared to the same materials in bulk (micron-scale) forms. Past research indicates that the smaller size of particles causes larger toxicity due to an increase in surface-to-volume ratio upon the decrease in size (51). Another challenge is the tendency of nanoparticles to form aggregates in solution, which have properties entirely different from individual nanoparticles. In this regard, the most widely reported nanomaterials are CNTs and nanoclays as well as those of SiO<sub>2</sub>, AlO<sub>2</sub>, TiO<sub>2</sub>, Au and Ag (124).

Any technology, in order to be sustainable, must address all three components of the sustainability triple bottom line: environmental, economic, and societal. Before employing any nano-enabled technology, it is essential to examine factors including efficiency, cost, product

lifetime, and, also environmental and social impacts. These factors are important for both end-users and industries, and understanding each of these can answer fundamental concerns like the advantages that nanotechnology offers in addressing global water challenges over existing technologies. Clarifications on aspects like safety, stability, regeneration, reuse and disposal aspects of nanomaterials can majorly help in the selection and design of nanomaterials to maximize structure–property–function relationships (125). Scalability is another parameter that needs to be studied for the commercial viability of nano-based technologies. Factors that affect the scalability of nanomaterials include the natural resource availability of the raw material, the cost of extraction and manufacturing, and compatibility with common water treatment infrastructure (126). A study was conducted by Kamali et al. using a multi-criteria decision approach (assisted by a fuzzy-Delphi method) integrating the technical, economic, environmental and social criteria in order to rank the nine treatment processes among the various sewage treatment technologies for processing industrial effluents (53). In this investigation, 17 criteria including technical (i.e., treatment efficiency, ease of implementation, combination possibility, process stability, and health and safety risks), environmental (i.e., biowaste waste generation, the release of chemical substances, CO<sub>2</sub> emission, water reuse potential, and recovery of by-products), economic (i.e., initial investments, maintenance costs, and operating costs), and social (odor impact, noise impact, visual impact, and public acceptance) were considered to rank the studied methods for the treatment of industrial effluents. The study realized membrane-based technologies followed by adsorption, oxidation with nanomaterials and through the Fenton process in the decreasing order of sustainable physicochemical methods for the treatment of industrial effluents. Ren et al. evaluated the social, economic, and environmental sustainability of ceramic filters impregnated with silver nanoparticles for point-of-use (POU) drinking water treatment in developing countries (127). It focused on assessing the cultural acceptability of this treatment among its intended users, understanding the impacts of raw water quality on disinfection performance, and varying materials composition and/or manufacturing techniques to optimize disinfection. The ceramic filters also exhibit better environmental performance than the centralized water system for four of five evaluated life cycle impacts: energy use, water use, global warming potential, and particulate matter emissions (PM10).

About 7% of the global energy production is used to enable the anthropogenic water cycle, which includes drinking water supply and wastewater treatment (128). The energy intensity of a water recycling system is the energy required per volume of raw water for the whole process involving collection/conveyance, treatment, and distribution and usually measured as kWh/m<sup>3</sup> where the energy consumption depends not only on the quantity but also the quality of raw water and the associated mandated standards (129). Energy consumption is a crucial sustainability parameter as it is a significant contributor to climate change and also to the total cost for the water utilities that necessitates to identify effective and efficient ways of reducing energy use and greenhouse gas emissions. One way to achieve these goals is to incorporate renewables sources of energy, particularly solar or wind energy into the operation of water and wastewater treatment plants (130).

## Sustainability Metrics

Sustainability or green metrics is an attempt to quantify the progress toward the broader goal of environmental sustainability by taking a holistic approach (131). Mukherjee et al. calculated the sustainability metrics of ferrihydrite incorporated microcellulose and nanocellulose/PANI nanocomposites for the removal of arsenic and fluoride from water, respectively (59, 60).

Composites for release of essential minerals to purified (often desalinated) water were also considered for similar evaluation by Ravindran et al. (132) All the three materials were assessed by the parameters including mass intensity, solvent intensity, reaction mass efficiency, energy consumption, E-factor, and CO<sub>2</sub> emission (133). To understand the principles behind these parameters, we need to consider two main concepts that are responsible for making any material or process ‘green’: a) efficient utilization of resources (raw materials, energy resources, chemicals, etc.) in the process of manufacture and application of materials, and b) minimize waste generation and use of hazardous solvents and reagents in the manufacture and application of materials. Mass-based metrics such as mass intensity (MI) or reaction mass efficiency (RME) measures the amount of material needed to synthesize the desired product, which takes into account reaction yield, stoichiometry, solvents, and reagents in a reaction mixture (134). Solvent/water intensity involves considering only the solvent or water used in the synthesis. Lesser MI means less reagents and solvent required leading to less solvent waste, reduced capacity and energy requirements, finally resulting in reduced environmental burden and cost. The E-factor is the actual amount of waste produced in the process and takes waste from all auxiliary components, for example, solvent and chemical losses during filtration or washing, into account (133). Energy intensity (EI) is another important parameter that gauges the process efficiency of any manufacturing or application process. Low EI implies a reduction in energy usage that reduces the environmental burden related to power generation, transport, and use, in turn resulting in increased efficiency, shorter processes, milder conditions and cost reduction (135). To study the environmental impact of a process, carbon footprint estimation is essential as it often accounts for direct emissions from the processes that would lead to a contribution toward global climate change (136). Table 2 summarizes various sustainability metrics, their quantitative expression and the corresponding environmental and economic manifestations.

Several tools have been designed to assess the sustainability of (nano)materials and related technologies such as (a) life cycle assessment (LCA) (137), (b) risk assessment (RA) (138), (c) GUIDEnanotool (139, 140), (d) LICARA nanoSCAN (141), (e) Quantitative structure–activity relationships (142), (f) Techno-economic assessment (143), (g) Ashby-based nanomaterial selection (144), (h) fuzzy-Delphi method (53), (i) sustainability metrics (134), and so on, among which LCA and RA have become more established in the literature for nanotechnology assessment, while other tools are trying to adapt themselves for nanomaterials (125). LCA is a systematic method for assessing the potential environmental impacts of products, services and processes across their entire life cycles (145). In the case of nanomaterials, stage of their life cycle, i.e. from the production of the nanomaterials to the products that contain these nanomaterials, use or application of such products and their ultimate end-of-life management/disposal, all of them are considered together is one lifecycle. The LCA methodology, as defined in ISO 14040 (146), comprises four iterative steps: (i) goal and scope definition, (ii) inventory analysis, (iii) impact assessment, and (iv) interpretation. LCA also aims to include a broad range of impact categories, such as climate change, acidification, photochemical ozone formation, human toxicity, ecotoxicity, and resource depletion (137).

Risk assessment (RA) refers to the quantitative and qualitative evaluation of the risk posed to human health and/or the environment by the presence of a particular contaminant or by mixtures of contaminants (147). Risk is defined as the probability of exposure to a hazard, where exposure can be assessed by measuring environmental concentrations or by modeling the environmental fate of a contaminant, yielding a predicted environmental concentration (PEC) (148). Basic ideas related to adverse effects are commonly expressed in terms of laboratory-derived dose–response relationships. There are four main phases of environmental RA; hazard assessment: establishing which hazard

is present; exposure assessment: establishing a predicted environmental concentration (PEC) or predicted daily intake (PDI); effect assessment: establishing critical levels of exposure based on predicted no effect concentration (PNEC) or acceptable daily intake (ADI); and risk characterization: calculating the PEC/PNEC or PDI/ADI quotient (138).

**Table 2. Various Metrics and Their Corresponding Expressions Used for Sustainability Assessment**

<i>Metrics</i>	<i>Environmental manifestation</i>	<i>Economical manifestation</i>	<i>Expression</i>
<i>Mass based</i>			
<i>Mass intensity</i>	Low stoichiometry, catalytic, less solvent need/waste, recyclable	More from less, reduced capacity requirements, reduced cost	$\frac{\text{mass of all reactants used excluding water}}{\text{mass of product}} \text{ kg/kg product}$
<i>Solvent/water intensity</i>			$\frac{\text{mass of all water used}}{\text{mass of product}} \text{ kg/kg product}$
<i>Process efficiency based</i>			
<i>Reaction mass efficiency</i>	Minimal by-product formation, reduced environmental burden	More from less, reduced cost	$\frac{\text{mass of product}}{\text{mass of all reactants}} \times 100\%$
<i>Atom economy</i>			$\frac{\text{mol wt of product}}{\text{sum of mol wts of reactants}} \times 100$
<i>Eco-efficiency based</i>			
<i>E-factor</i>	Recyclable, reusable, renewable	Less emissions, less expenses on waste handling, reduced cost	$\frac{[\text{kg}(\text{raw materials}) - \text{kg}(\text{desired product})]}{\text{kg}(\text{total product including water})}$
<i>Energy consumption</i>	Reduced environmental burden related to power generation, transport, and use	Increased efficiency, shorter processes, milder conditions, reduced cost	$\frac{\text{amount of nonrenewable energy used}}{\text{mass of product}}$ kW*h/kg
<i>Carbon footprint</i>	Reduced greenhouse gases emissions	Process efficiency leads to cost efficiency in long term	GHG $\Sigma$ (production, transportation, sales, distribution, use)
<i>Life cycle assessment</i>	Cradle-to-grave assessment of resources and energy consumption, emissions and fate for production, transportation, sales, distribution, use, and final fate		$\text{A} + \text{B} \xrightarrow{\text{D solvent}} \text{C}$

## Limitations and Prospects

While there has been significant research on safe nanomaterial compositions and production, there is a need to further understand the structure–property–hazard relationships of nanomaterials. Changes in nanomaterial structure and properties can impact toxicity and exposure routes. Nanomaterials are employed in more than 1600 commercial products today, including food. This poses a serious health risk associated with the intake of ENMs (149). Therefore, careful evaluation of these ENMs is required against their hazardous nature. Most of these evaluations are in-vitro studies and use impractically high concentrations. Therefore, in-vivo tests are required at low doses which should be conducted on animal subjects followed by human subjects.

**Economic feasibility:** Given the scenario that water scarcity is more prominent in underdeveloped and developing countries, it becomes vital to develop affordable technologies. As an example, IIT Madras had developed a ferrihydrite nanomaterial that removes arsenic from groundwater at less than 0.14 cents per gallon (144). More such technologies are needed to revolutionize nanomaterials-based purification systems.

**Environmental impact:** For some nanomaterial manufacturing processes, the extraction of precursor materials, especially critical metals, can be environmentally costly and damaging.

Post-treatment water should not have nanomaterials above the acceptable limits. Here there is also an opportunity to improve detection and quantification techniques to be in-line and in real-time to prevent releases to the environment or into drinking water. Accumulation of nanomaterials due to leaching increases their concentration significantly which is a serious health hazard. Although integration of ENMs with water purifiers is a relatively new approach, another emerging problem associated with it is the formation of a pathogenic biofilm on the ENM coating employed in water purifiers.

Better public–private partnerships are needed for establishing guidelines to address the transition from a traditional linear flow of materials in a “take – make –use –dispose” economy to a greener, circular economy. The latter seeks to eliminate waste through the design of products and processes with resource efficiency and suggests recycling. Appropriate sustainability metrics will be an essential component that will emphasize the use of renewable bio-based resources for deriving raw materials and energy.

## Biological Methods in Clean Water: Implications to Sustainability

Biological purification methods prevent the nonbiodegradable polymeric membranes and chemical reagents from ending up in the environment and reduce the by-products such as greenhouse gas emissions due to the energy-intensive water purification processes (150, 151). While most of the chemical methods are capable of separating contaminants from water, biological methods are capable of accumulating and degrading them while producing useful biomass simultaneously. The application of biological treatment methods in clean water has been explored for several centuries and is of great interest to date as they are sustainable, cost-effective, and can generate useful by-products (152). A wide range of contaminants such as heavy metals, hydrocarbons, dyes, toxicants, as well as ions can be removed biologically (152, 153). Also, biological treatment methods do not involve the harmful oxidation, reduction, or disinfection steps as followed in chemical treatments and also eliminate the need for disinfection products that leave unsafe by-products in the purified water (153–155). Biological methods include biosorption, biomaterial based flocculation, and coagulation, biological filtration membranes as well as aerobic and anaerobic wastewater treatment with microbes and plants.

## Biosorbents

Biosorption is a natural way of purifying water through biomaterials and living organisms such as bacteria, fungi, and yeast. They are often derived from industrial and agricultural biowaste. While the synthetic adsorbents are of high cost and nonbiodegradable, they also have problems in the regeneration of the used sorbent materials (156). Table 3 lists a few of the biosorbents and the wide variety of contaminants that can be removed by them.

**Table 3. Some Examples of Biosorbents with High Adsorption Capacity Toward Contaminants**

<i>Biosorbent</i>	<i>Contaminant</i>	<i>Property</i>	<i>Ref.</i>
<i>Oceanobacillus profundus</i> bacterium	Heavy metal	97% removal of Pb at 50 mg/ml	(157)
Waste fungal biomass of <i>Ganoderma lucidum</i>	Heavy metal	93% removal of Pb(II) and 97% for Cd(II)	(158)
Amine-functionalized biosorbent from biogas residue	Nutrients	>82% of nitrate and phosphate removals after 8 cycles of adsorption and desorption	(159)
Extracellular polymeric substances extracted from <i>Klebsiella</i> sp.	Heavy metal	Pb (II) removed at maximum biosorption capacity of 99.5 mg g <sup>-1</sup>	(160)
<i>Pseudomonas alcaliphila</i> NEWG-2 bacterium	Heavy metal	96.60% of Cr <sup>6+</sup> removed at 200mg/ml of Chromium concentration	(155)
Chitosan	PPCPs	Tetracycline adsorption capacity of 93.04 mmol/kg	(161)
Rice straw biochars	PPCPs	Doxycycline and ciprofloxacin adsorption capacity of 8.93 to 108.42 mg/g respectively	(162)
<i>Aspergillus niger</i> fungus pellets	Textile dye	98% for 200 mg L <sup>-1</sup> Acid Orange 56 and Acid Blue 40	(163)

## Biological Water Treatment

Microorganisms are employed for the treatment of wastewater under aerobic or anaerobic conditions depending upon the oxygen requirement of the system.

Microalgae based wastewater treatment: This method is replacing conventional chemical treatments and has been proven to be effective in the treatment of hydrocarbons, surfactants, pharmaceuticals, personal care products, pesticides, plasticizers, flame retardants, and heavy metals (152). Microalgae culture offers the advantage of biomass production which can be used for generating fertilizers, animal feed, liquid fuel, etc. Carbon fixation is a great advantage in such algal biomass production combined with wastewater treatment. Microalgae perform nutrient stripping by consuming nitrogen and phosphorus from wastewater and providing oxygen and useful biomass in return. When grown in co-cultures with bacteria, the microalgae provide them the required oxygen, eliminating the need for external aeration. The microalgae have also been studied to show a reduction of Chemical Oxygen Demand (COD) and Biological Oxygen Demand (BOD) in wastewater and it is important to control these levels as releasing water with high COD and BOD can be harmful to the aquatic organisms. The dry weight of algae obtained after the treatment varies with the algal



species and the growth conditions of the cells. Commonly used species of microalgae for wastewater treatment include *Chlorella vulgaris*, and the choice of the species depends upon the treatment method. Both anaerobic and aerobic treatments are used for the algal treatment of wastewater (164). High rate algal ponds (HRAP) (Figure 3A) are used for increasing the rate of water treatment by microalgae by controlling the lux level and depth of culture (165, 166).

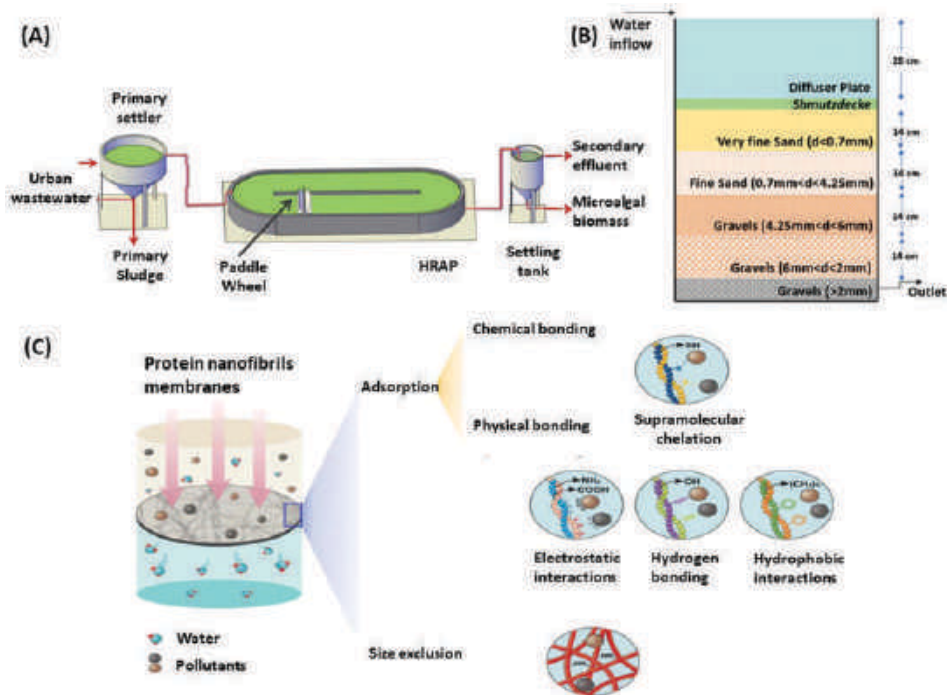


Figure 3. (A) Schematic of a high rate algal pond. Adapted with permission from ref (182). Copyright The Authors, some rights reserved; exclusive licensee MDPI. Distributed under a Creative Commons Attribution License 4.0 (CC BY) <https://creativecommons.org/licenses/by/4.0/>". (B) Schematic of a slow sand filter. Adapted with permission from ref (183). Copyright Elsevier Ltd., 2021 (C) Mechanism of water purification by protein nanofibrils. Adapted with permission from ref (184). Copyright The Authors, some rights reserved; exclusive licensee Nature Research. Distributed under a Creative Commons Attribution License 4.0 (CC BY) <https://creativecommons.org/licenses/by/4.0/>".

## Biological Filtration

Slow sand filtration: Slow sand filters (SSF) are notable biological and environment-friendly filtration techniques that are majorly used in developing countries for the filtration of drinking water (167). They involve naturally formed biofilm on sand particles to reduce the turbidity of water along with the removal of contaminants. The biofilm is termed as a hypogeal layer or schmutzdecke which contains a microbial consortium of bacteria, fungi, algae and protozoa, along with aquatic insect larvae (Figure 3B) (168). The SSF is capable of biodegrading pesticides, micropollutants, pharmaceuticals, and organic pollutants. These living organisms metabolize the contaminants and even reduce the bacterial count by 90-99% and viruses by >70% (167, 169–171). The suspended particles are trapped by the mucilaginous biofilm formed by the microbes. The United States Environmental Protection Agency has recognized this technique and WHO has recommended SSF as the cheapest, simplest and efficient method of water filtration which can be carried out with

local skills and resources available (172, 173). Protein nanofibrils are emerging as sustainable water purification materials which are capable of performing both adsorption and nano-sieving (174). The amino acids present on the protein nanofibrils offer supramolecular chelation to the pollutants in water and the high surface-to-volume ratio of nanofibrils improves their adsorption capacity. Figure 3C shows water purification through protein nanofibrils. Protein nanofibrils can be cost-effectively made by the unfolding, hydrolysis, or aggregation of proteins from industrial waste such as whey and oil cake (174, 175).

## Biomimetic Membranes

**Aquaporins based membranes:** Aquaporins are nature's gift to water purification and desalination industry. They have been applied only for a decade, to manufacture highly efficient and sustainable water filtration membranes (176). Aquaporins, the transmembrane water channel proteins have been selectively transporting water molecules across the cells of living organisms for a billion years (177). Several water purification membranes have been synthesized with Aquaporin incorporation in them following deciphering aquaporin protein structure by Peter Agre in the early 1990s for which he was awarded the Nobel prize (178). The mechanism of water selectivity in aquaporins was achieved by electrostatic interactions between the amino acids in the channels and the channel size (179). Aquaporins are present as tetramers and span the cell membranes such that each monomer forms a water channel transporting  $10^9$  water molecules per monomer per second (Figure 4A) (180). Thus, the productivity (permeability per unit driving force) of aquaporin incorporated membranes is ~80 times higher than that of the commercial RO membranes (181).

Aquaporins have an hourglass shaped channel that is 3 Å in pore size, allowing the water molecules alone to go through, which have a diameter of 2.8 Å while rejecting the solutes and ions present in water (179, 180). The aromatic/arginine (Ar/R) selectivity filter present at the core of the channels ensure selectivity toward water molecules and perform size sieving. The phenylalanine at the core of the filtration channel weakens the water-water hydrogen bond facilitating the transport of water. And the positive charge present on the arginine and histidine sites helps in rejecting the positively charged ions and protons entering the channel (185).

Aquaporin incorporated water filtration membranes offer sub-nanoporous water channels with high water permeability and possess extreme selectivity to water molecules while they block all the other solutes including some volatile contaminants. Aquaporins incorporated membranes have also been demonstrated to be effective in rejecting some neutral species such as urea which makes them applicable even in desalination (186). Initially, aquaporin-based membranes were synthesized with the Aquaporin Z (Aqp Z) proteins extracted from *E. coli* and embedded in lipid bilayers sandwiched by porous support such as cellulose, polysulfone, mica, etc. To improve the stability of the proteins in the membranes, the membrane synthesis has been modified with vesicles containing Aqp Z (Figure 4D) (187). The vesicles were embedded in block copolymers to stabilize the hydrophobic protein system which is much likely to aggregate in the membrane. Aquaporins incorporated membranes have also been demonstrated to be effective in rejecting some neutral species such as urea, which makes them applicable even in desalination (186). These membranes have also been tested at the international space station by NASA to measure their efficacy in space where every drop of moisture is filtered and re-used and the membranes have proven efficient even in the zero gravity conditions and capable of filtering semi volatile components too (188, 189).

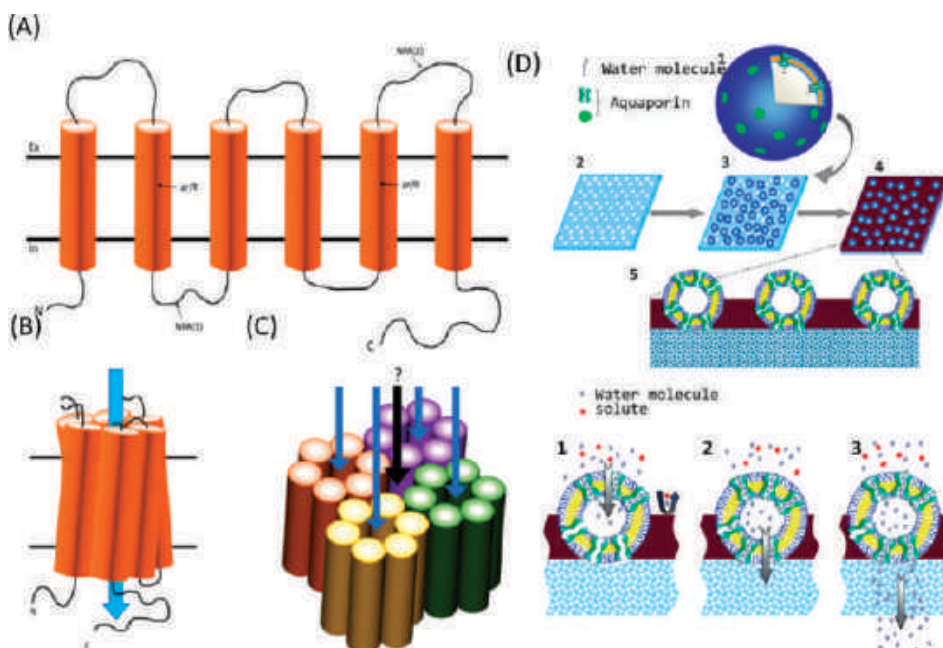


Figure 4. The orientation of aquaporin water channels on the cell membranes. (A) The secondary structure of the aquaporins has six  $\alpha$  helices with the ar/R motif in one of the helices. The aquaporins have three extracellular and two connecting intracellular loops. (B) The monomer of the aquaporins forms a tertiary structure, which has an hourglass shaped water channel. (C) The homotetramer of the monomers carrying a water channel each. The function of the central hole is (marked with a black arrow) is not known. Adapted from ref (190). Copyright Elsevier, 2015. (D) Schematic of the synthesis of aquaporin water purification membrane synthesized by imprinting the Aqp Z polymer vesicles in a porous cellulose substrate. Adapted with permission from ref (191). Copyright The Authors, some rights reserved; exclusive licensee MDPI. Distributed under a Creative Commons Attribution License 4.0 (CC BY).

Such biomimetic membranes are more highly sustainable than their synthetic counterparts as they can work without electricity. This is achieved through the forward osmosis mechanism utilizing just the osmotic potential while the reverse osmosis-based aquaporin membranes fitted at the mouth of taps use the pressure of the incoming water for purification. Such membranes are commercialized by the Danish company Aquaporin A/S for filtration of running tap water using the Aquaporin Inside® technology (192).

## Water Purification Tomorrow

Since ancient times and at present, water purification materials are mostly based on carbon. Egyptians and Sumerians used wood charcoal for water purification in 3750 BC (1). Since its introduction in the 1940s, activated carbon has been an important material in clean water applications. However, carbon has come in various forms in the recent past, like carbon nanotubes, graphene-based materials, and carbon nanofibers, which have been utilized in water treatment for membrane-based separation, disinfection, adsorption, etc. (2). Many new materials are getting into water treatment in the recent past and their integration with carbon will create new opportunities. Materials science for clean water continues to be exciting both for sensing and for treatment.

Today, awareness exists about the optimum concentration of minerals that are safe for consumption in drinking water. Next-generation purification technologies are expected to be

selective in purifying minerals as per the recommended concentration limits, at any input concentration. Along with developing sustainable and safe technologies, it is necessary to ensure that these treatment methods are affordable. Addressing their associated safety concerns will ensure a sustainable water-secure ecosystem.

Internet of things (IoT) has evolved substantially and is already integrated with sensing technologies. Such a wireless network would enable sensing and monitoring of pollutants across water bodies. The next revolution in the water sector is expected to be connected to the Big Data and Artificial Intelligence (AI) revolution. Currently, the water sector essentially witnesses the need to establish water conservation regulations and actions toward a circular water economy (3). Water needs should not only be fulfilled by freshwater resources or water transport, but also through adequately treated wastewater. Wastewater will not only provide clean water, useful residual chemicals and energy but also become a source of data, through wastewater-based epidemiology and associated hydroinformatics. These will add to the improved sustainability of the entire water infrastructure. It would be possible to create a global digital twin of water infrastructure and link it with every aspect of water such as quantity and quality along with their impacts, such as agriculture, health and economy. If this can be done, even nationally, it will add great value to a water-secure world. This presents numerous possibilities for technology development.

Rapid developments in affordable sensing technologies, and quality sensing in remote areas, and virtually omnipresent social media are contributing to the growth of big data in the water sector. This growth is positively influencing water-related governmental regulations. Moreover, the emerging interlink between AI and data science has unraveled new pathways for extracting, organizing, and analyzing data, thus creating possibilities for data-driven innovations. Such knowledge along with policy interventions and management will be the way forward for ensuring water security.

## References

1. Peeters, R.; Vanderschaeghe, H.; Rongé, J.; Martens, J. A. Energy Performance and Climate Dependency of Technologies for Fresh Water Production from Atmospheric Water Vapour. *Environ. Sci. Water Res. Technol.* **2020**, *6* (8), 2016–2034. <https://doi.org/10.1039/D0EW00128G>.
2. Ahuja, S. Overview of Advances in Water Purification Techniques. In *Advances in Water Purification Techniques*; Ahuja, S., Ed.; Elsevier: 2019; pp 1–15. <https://doi.org/10.1016/B978-0-12-814790-0.00001-6>.
3. Prüss-Üstün; A.; Bos, R.; Gore, F.; Bartram, J. *Safer Water, Better Health: Costs, Benefits and Sustainability of Interventions to Protect and Promote Health*, 1st ed.; Sheffer, M., Ed.; World Health Organization: Geneva, 2018.
4. Ali, I.; Aboul-Enein, H. Y. *Instrumental Methods in Metal Ion Speciation*, 1st ed.; CRC Press: Boca Raton, 2006. <https://doi.org/10.1201/9781420019407>.
5. Kunduru, K. R.; Nazarkovsky, M.; Farah, S.; Pawar, R. P.; Basu, A.; Domb, A. J. 2 - Nanotechnology for Water Purification: Applications of Nanotechnology Methods in Wastewater Treatment. In *WATER PURIFICATION Nanotechnology in the Agri-Food Industry*, Vol. 9; Grumezescu, A. M., Ed.; Academic Press: 2017; pp 33–74. <https://doi.org/10.1016/B978-0-12-804300-4.00002-2>.
6. Eregowda, T.; Mohapatra, S. Fate of Micropollutants in Engineered and Natural Environment. In *Resilience, Response, and Risk in Water Systems*; Springer Transactions in Civil and Environmental Engineering; Kumar, M., Munoz-Arriola, F., Furumai, H., Chaminda, T. ,

- Eds.; Springer: Singapore, 2020; pp 283–301. [https://doi.org/10.1007/978-981-15-4668-6\\_15](https://doi.org/10.1007/978-981-15-4668-6_15).
7. Carballa, M.; Omil, F.; Ternes, T.; Lema, J. M. Fate of Pharmaceutical and Personal Care Products (PPCPs) during Anaerobic Digestion of Sewage Sludge. *Water Res.* **2007**, *41* (10), 2139–2150. <https://doi.org/10.1016/j.watres.2007.02.012>.
  8. Mojiri, A.; Zhou, J. L.; Ohashi, A.; Ozaki, N.; Kindaichi, T. Comprehensive Review of Polycyclic Aromatic Hydrocarbons in Water Sources, Their Effects and Treatments. *Sci. Total Environ.* **2019**, *696*, 133971. <https://doi.org/10.1016/j.scitotenv.2019.133971>.
  9. *Worldometer - Current World Population*. <https://www.worldometers.info/world-population/> (accessed July 27, 2021).
  10. Moradeeya, P. G.; Kumar, M. A.; Thorat, R. B.; Rathod, M.; Khambhaty, Y.; Basha, S. Nanocellulose for Biosorption of Chlorpyrifos from Water: Chemometric Optimization, Kinetics and Equilibrium. *Cellulose* **2017**, *24* (3), 1319–1332. <https://doi.org/10.1007/s10570-017-1197-x>.
  11. Asere, T. G.; Stevens, C. V.; Du Laing, G. Use of (Modified) Natural Adsorbents for Arsenic Remediation: A Review. *Sci. Total Environ.* **2019**, *676*, 706–720. <https://doi.org/10.1016/j.scitotenv.2019.04.237>.
  12. Anis, S. F.; Hashaikheh, R.; Hilal, N. Microfiltration Membrane Processes: A Review of Research Trends over the Past Decade. *J. Water Process Eng.* **2019**, *32*, 100941. <https://doi.org/10.1016/j.jwpe.2019.100941>.
  13. Ghernaout, D.; Elboughdiri, N. Electrocoagulation Process Intensification for Disinfecting Water – A Review. *Appl. Eng.* **2019**, *3* (2), 140–147. <https://doi.org/10.11648/j.ae.20190302.20>.
  14. Shahedi, A.; Darban, A. K.; Taghipour, F.; Jamshidi-Zanjani, A. A Review on Industrial Wastewater Treatment via Electrocoagulation Processes. *Curr. Opin. Electrochem.* **2020**, *22*, 154–169. <https://doi.org/10.1016/j.coelec.2020.05.009>.
  15. Pichel, N.; Vivar, M.; Fuentes, M. The Problem of Drinking Water Access: A Review of Disinfection Technologies with an Emphasis on Solar Treatment Methods. *Chemosphere* **2019**, *218*, 1014–1030. <https://doi.org/10.1016/j.chemosphere.2018.11.205>.
  16. Cosgrove, S.; Jefferson, B.; Jarvis, P. Pesticide Removal from Drinking Water Sources by Adsorption: A Review. *Environ. Technol. Rev.* **2019**, *8* (1), 1–24. <https://doi.org/10.1080/21622515.2019.1593514>.
  17. Crini, G.; Lichtfouse, E.; Wilson, L. D.; Morin-Crini, N. Conventional and Non-Conventional Adsorbents for Wastewater Treatment. *Environ. Chem. Lett.* **2019**, *17* (1), 195–213. <https://doi.org/10.1007/s10311-018-0786-8>.
  18. Al Aani, S.; Mustafa, T. N.; Hilal, N. Ultrafiltration Membranes for Wastewater and Water Process Engineering: A Comprehensive Statistical Review over the Past Decade. *J. Water Process Eng.* **2020**, *35*, 101241. <https://doi.org/10.1016/j.jwpe.2020.101241>.
  19. Shi, X.; Tal, G.; Hankins, N. P.; Gitis, V. Fouling and Cleaning of Ultrafiltration Membranes: A Review. *J. Water Process Eng.* **2014**, *1*, 121–138. <https://doi.org/10.1016/j.jwpe.2014.04.003>.
  20. Mohtashami, R.; Shang, J. Q. Electroflotation for Treatment of Industrial Wastewaters: A Focused Review. *Environ. Process.* **2019**, *6* (2), 325–353. <https://doi.org/10.1007/s40710-019-00348-z>.

21. Kolesnikov, V. A.; Il'in, V. I.; Kolesnikov, A. V. Electroflotation in Wastewater Treatment from Oil Products, Dyes, Surfactants, Ligands, and Biological Pollutants: A Review. *Theor. Found. Chem. Eng.* **2019**, 53 (2), 251–273. <https://doi.org/10.1134/S0040579519010093>.
22. Bhatnagar, A.; Sillanpää, M.; Witek-Krowiak, A. Agricultural Waste Peels as Versatile Biomass for Water Purification – A Review. *Chem. Eng. J.* **2015**, 270, 244–271. <https://doi.org/10.1016/j.cej.2015.01.135>.
23. Giannakoudakis, D. A.; Hosseini-Bandegharaei, A.; Tsafrakidou, P.; Triantafyllidis, K. S.; Kornaros, M.; Anastopoulos, I. Aloe Vera Waste Biomass-Based Adsorbents for the Removal of Aquatic Pollutants: A Review. *J. Environ. Manage.* **2018**, 227, 354–364. <https://doi.org/10.1016/j.jenvman.2018.08.064>.
24. Yang, Z.; Zhou, Y.; Feng, Z.; Rui, X.; Zhang, T.; Zhang, Z. A Review on Reverse Osmosis and Nanofiltration Membranes for Water Purification. *Polymers* **2019**, 11 (8), 1252. <https://doi.org/10.3390/polym11081252>.
25. Wang, Y.; Gu, Y.; Li, H.; Ye, M.; Qin, W.; Zhang, H.; Wang, G.; Zhang, Y.; Zhao, H. Electrodeposition of Hierarchically Amorphous FeOOH Nanosheets on Carbonized Bamboo as an Efficient Filter Membrane for As(III) Removal. *Chem. Eng. J.* **2020**, 392, 123773. <https://doi.org/10.1016/j.cej.2019.123773>.
26. Jiao, M.; Zhu, L.; Xie, C.; Zhao, H.; Zhang, C.; Li, Y.; He, Y.; Teng, H.; Han, E. A Novel Electrodeposited Sandwich Electrode with an Efficient Performance in Complex Water Treatment. *Surf. Coatings Technol.* **2021**, 406, 126645. <https://doi.org/10.1016/j.surfcoat.2020.126645>.
27. Romanovski, V. Agricultural Waste Based-Nanomaterials: Green Technology for Water Purification. In *Micro and Nano Technologies, Aquanotechnology*; Abd-Elsalam, K. A., Zahid, M., Eds.; Elsevier: 2021; Chapter 25, pp 577–595. <https://doi.org/10.1016/B978-0-12-821141-0.00013-6>.
28. Gill, R. T.; Harbottle, M. J.; Smith, J. W. N.; Thornton, S. F. Electrokinetic-Enhanced Bioremediation of Organic Contaminants: A Review of Processes and Environmental Applications. *Chemosphere* **2014**, 107, 31–42. <https://doi.org/10.1016/j.chemosphere.2014.03.019>.
29. Wen, D.; Fu, R.; Li, Q. Removal of Inorganic Contaminants in Soil by Electrokinetic Remediation Technologies: A Review. *J. Hazard. Mater.* **2021**, 401, 123345. <https://doi.org/10.1016/j.jhazmat.2020.123345>.
30. Wu, Z.; Abramova, A.; Nikonov, R.; Cravotto, G. Sonozonation (Sonication/Ozonation) for the Degradation of Organic Contaminants – A Review. *Ultrason. Sonochem.* **2020**, 68, 105195. <https://doi.org/10.1016/j.ultsonch.2020.105195>.
31. Mecha, A. C.; Chollom, M. N. Photocatalytic Ozonation of Wastewater: A Review. *Environ. Chem. Lett.* **2020**, 18 (5), 1491–1507. <https://doi.org/10.1007/s10311-020-01020-x>.
32. Yu, G.; Wang, Y.; Cao, H.; Zhao, H.; Xie, Y. Reactive Oxygen Species and Catalytic Active Sites in Heterogeneous Catalytic Ozonation for Water Purification. *Environ. Sci. Technol.* **2020**, 54 (10), 5931–5946. <https://doi.org/10.1021/acs.est.0c00575>.
33. Hasanpour, M.; Hatami, M. Application of Three Dimensional Porous Aerogels as Adsorbent for Removal of Heavy Metal Ions from Water/Wastewater: A Review Study. *Adv. Colloid Interface Sci.* **2020**, 284, 102247. <https://doi.org/10.1016/j.cis.2020.102247>.



34. Scott, S. M.; Hu, T.; Yao, T.; Xin, G.; Lian, J. Graphene-Based Sorbents for Iodine-129 Capture and Sequestration. *Carbon* **2015**, *90*, 1–8. <https://doi.org/10.1016/j.carbon.2015.03.070>.
35. Riley, B. J.; Pierce, D. A.; Chun, J.; Matyáš, J.; Lepry, W. C.; Garn, T. G.; Law, J. D.; Kanatzidis, M. G. Polyacrylonitrile-Chalcogel Hybrid Sorbents for Radioiodine Capture. *Environ. Sci. Technol.* **2014**, *48* (10), 5832–5839. <https://doi.org/10.1021/es405807w>.
36. Särkkä, H.; Bhatnagar, A.; Sillanpää, M. Recent Developments of Electro-Oxidation in Water Treatment — A Review. *J. Electroanal. Chem.* **2015**, *754*, 46–56. <https://doi.org/10.1016/j.jelechem.2015.06.016>.
37. Salmerón, I.; Oller, I.; Malato, S. Electro-Oxidation Process Assisted by Solar Energy for the Treatment of Wastewater with High Salinity. *Sci. Total Environ.* **2020**, *705*, 135831. <https://doi.org/10.1016/j.scitotenv.2019.135831>.
38. Yang, W.; Zhou, H.; Cicek, N. Treatment of Organic Micropollutants in Water and Wastewater by UV-Based Processes: A Literature Review. *Crit. Rev. Environ. Sci. Technol.* **2014**, *44* (13), 1443–1476. <https://doi.org/10.1080/10643389.2013.790745>.
39. Matafonova, G.; Batoev, V. Recent Advances in Application of UV Light-Emitting Diodes for Degrading Organic Pollutants in Water through Advanced Oxidation Processes: A Review. *Water Res.* **2018**, *132*, 177–189. <https://doi.org/10.1016/j.watres.2017.12.079>.
40. Abraham, J. P.; Plourde, B. D.; Minkowycz, W. J. Continuous Flow Solar Thermal Pasteurization of Drinking Water: Methods, Devices, Microbiology, and Analysis. *Renew. Energy* **2015**, *81*, 795–803. <https://doi.org/10.1016/j.renene.2015.03.086>.
41. Zaman, S.; Yeasmin, S.; Inatsu, Y.; Ananchaipattana, C.; Bari, M. L. Low-Cost Sustainable Technologies for the Production of Clean Drinking Water—A Review. *J. Environ. Prot.* **2014**, *05* (01), 42–53. <https://doi.org/10.4236/jep.2014.51006>.
42. Kumar, A. A.; Som, A.; Longo, P.; Sudhakar, C.; Bhuin, R. G.; Gupta, S. S.; Anshup; Sankar, M. U.; Chaudhary, A.; Kumar, R.; Pradeep, T. Confined Metastable 2-Line Ferrihydrite for Affordable Point-of-Use Arsenic-Free Drinking Water. *Adv. Mater.* **2017**, *29* (7), 1604260. <https://doi.org/10.1002/adma.201604260>.
43. Sarkar, D.; Mondal, B.; Som, A.; Ravindran, S. J.; Jana, S. K.; Manju, C. K.; Pradeep, T. Holey MoS<sub>2</sub> Nanosheets with Photocatalytic Metal Rich Edges by Ambient Electrospray Deposition for Solar Water Disinfection. *Glob. Challenges* **2018**, *2* (12), 1800052. <https://doi.org/10.1002/gch2.201800052>.
44. Tavakolian, M.; Jafari, S. M.; van de Ven, T. G. M. A Review on Surface-Functionalized Cellulosic Nanostructures as Biocompatible Antibacterial Materials. *Nano-Micro Lett.* **2020**, *12* (1), 73. <https://doi.org/10.1007/s40820-020-0408-4>.
45. Vadahanambi, S.; Lee, S.-H.; Kim, W.-J.; Oh, I.-K. Arsenic Removal from Contaminated Water Using Three-Dimensional Graphene-Carbon Nanotube-Iron Oxide Nanostructures. *Environ. Sci. Technol.* **2013**, *47* (18), 10510–10517. <https://doi.org/10.1021/es401389g>.
46. *Innodi - Innovative Technologies in Water Treatment*. <http://www.innodi.in/> (accessed July 27, 2021).
47. *VayuJal*. <http://www.vayujal.com/> (accessed July 27, 2021).
48. Teodosiu, C.; Gilca, A. F.; Barjoveanu, G.; Fiore, S. Emerging Pollutants Removal through Advanced Drinking Water Treatment: A Review on Processes and Environmental Performances

- Assessment. *J. Clean. Prod.* **2018**, *197*, 1210–1221. <https://doi.org/10.1016/j.jclepro.2018.06.247>.
49. Qu, X.; Brame, J.; Li, Q.; Alvarez, P. J. J. Nanotechnology for a Safe and Sustainable Water Supply: Enabling Integrated Water Treatment and Reuse. *Acc. Chem. Res.* **2013**, *46* (3), 834–843. <https://doi.org/10.1021/ar300029v>.
50. van der Hoek, J. P.; Bertelkamp, C.; Verliefde, A. R. D.; Singhal, N. Drinking Water Treatment Technologies in Europe: State of the Art – Challenges – Research Needs. *J. Water Supply Res. Technol.* **2014**, *63* (2), 124–130. <https://doi.org/10.2166/AQUA.2013.007>.
51. Peng, Z.; Liu, X.; Zhang, W.; Zeng, Z.; Liu, Z.; Zhang, C.; Liu, Y.; Shao, B.; Liang, Q.; Tang, W.; Yuan, X. Advances in the Application, Toxicity and Degradation of Carbon Nanomaterials in Environment: A Review. *Environ. Int.* **2020**, *134*, 105298. <https://doi.org/10.1016/j.envint.2019.105298>.
52. Li, J.; Huang, Y.; Shao, D. Conjugated Polymer-Based Composites for Water Purification 581. In *Fundamentals of Conjugated Polymer Blends, Copolymers and Composites: Synthesis, Properties, and Applications*; Saini, P., Ed.; Wiley: 2015; pp 518–618. <https://doi.org/10.1002/9781119137160>.
53. Kamali, M.; Persson, K. M.; Costa, M. E.; Capela, I. Sustainability Criteria for Assessing Nanotechnology Applicability in Industrial Wastewater Treatment: Current Status and Future Outlook. *Environ. Int.* **2019**, *125*, 261–276. <https://doi.org/10.1016/j.envint.2019.01.055>.
54. Nagar, A.; Pradeep, T. Clean Water through Nanotechnology: Needs, Gaps, and Fulfillment. *ACS Nano* **2020**, *14* (6), 6420–6435. <https://doi.org/10.1021/acsnano.9b01730>.
55. Nair, S. A.; Pradeep, T. Halocarbon Mineralization and Catalytic Destruction by Metal Nanoparticles. *Curr. Sci.* **2003**, *84* (12), 1560–1564.
56. Sreekumaran Nair, A.; Tom, R. T.; Pradeep, T. Detection and Extraction of Endosulfan by Metal Nanoparticles. *J. Environ. Monit.* **2003**, *5* (2), 363–365. <https://doi.org/10.1039/B300107E>.
57. Sreeprasad, T. S.; Maliyekkal, S. M.; Lisha, K. P.; Pradeep, T. Reduced Graphene Oxide–Metal/Metal Oxide Composites: Facile Synthesis and Application in Water Purification. *J. Hazard. Mater.* **2011**, *186* (1), 921–931. <https://doi.org/10.1016/j.jhazmat.2010.11.100>.
58. Sankar, M. U.; Aigal, S.; Maliyekkal, S. M.; Chaudhary, A.; Anshup, A. A.; Kumar, A. A.; Chaudhari, K.; Pradeep, T. Biopolymer-Reinforced Synthetic Granular Nanocomposites for Affordable Point-of-Use Water Purification. *Proc. Natl. Acad. Sci. U. S. A.* **2013**, *110* (21), 8459–8464. <https://doi.org/10.1073/pnas.1220222110>.
59. Mukherjee, S.; Kumar, A. A.; Sudhakar, C.; Kumar, R.; Ahuja, T.; Mondal, B.; Srikrishnarka, P.; Philip, L.; Pradeep, T. Sustainable and Affordable Composites Built Using Microstructures Performing Better than Nanostructures for Arsenic Removal. *ACS Sustain. Chem. Eng.* **2019**, *7* (3), 3222–3233. <https://doi.org/10.1021/acssuschemeng.8b05157>.
60. Mukherjee, S.; Ramireddy, H.; Baidya, A.; Amala, A. K.; Sudhakar, C.; Mondal, B.; Philip, L.; Pradeep, T. Nanocellulose-Reinforced Organo-Inorganic Nanocomposite for Synergistic and Affordable Defluoridation of Water and an Evaluation of Its Sustainability Metrics. *ACS Sustain. Chem. Eng.* **2020**, *8* (1), 139–147. <https://doi.org/10.1021/acssuschemeng.9b04822>.

61. Bai, H.; Liu, Z.; Sun, D. D. Hierarchically Multifunctional TiO<sub>2</sub> Nano-Thorn Membrane for Water Purification. *Chem. Commun.* **2010**, 46 (35), 6542–6544. <https://doi.org/10.1039/C0CC01143F>.
62. Singer, P. A.; Daar, A. S.; Salamanca-Buentello, F. Harnessing Nanotechnology to Improve Global Equity. *Issues Sci. Technol.* **2005**, 21 (4), 57–64.
63. *Cheap, Clean Drinking Water Purified Through Nanotechnology*; ScienceDaily; Inderscience Publishers: February 26, 2008.
64. Upadhyayula, V. K. K.; Deng, S.; Mitchell, M. C.; Smith, G. B. Application of Carbon Nanotube Technology for Removal of Contaminants in Drinking Water: A Review. *Sci. Total Environ.* **2009**, 408 (1), 1–13. <https://doi.org/10.1016/j.scitotenv.2009.09.027>.
65. Access to Safe Water for the Bottom of Pyramid: Strategies for Disseminating. *Society for Technology and Action for Rural Advancement (TARA)*. 2012. <https://www.gov.uk/research-for-development-outputs/access-to-safe-water-for-the-bottom-of-pyramid-strategies-for-disseminating-technology-research-benefits-first-half-yearly-progress-report> (accessed July 27, 2021).
66. Hoek, E. M. V.; Pendergast, M. T. M.; Ghosh, A. K. Nanotechnology-Based Membranes for Water Purification. In *Micro and Nano Technologies*, 2nd ed.; Street, A., Sustich, R., Duncan, J., Savage, N., Eds.; William Andrew Publishing: Oxford, 2014; Chapter 9, pp 133–154. <https://doi.org/10.1016/B978-1-4557-3116-9.00009-3>.
67. Gupta, S. S.; Islam, M. R.; Pradeep, T. Capacitive Deionization (CDI): An Alternative Cost-Efficient Desalination Technique. In *Advances in Water Purification Techniques*; Ahuja, S., Ed.; Elsevier, 2019; Chapter 7, pp 165–202. <https://doi.org/10.1016/B978-0-12-814790-0.00007-7>.
68. Kumar, R.; Sen Gupta, S.; Katiyar, S.; Raman, V. K.; Varigala, S. K.; Pradeep, T.; Sharma, A. Carbon Aerogels through Organo-Inorganic Co-Assembly and Their Application in Water Desalination by Capacitive Deionization. *Carbon N. Y.* **2016**, 99, 375–383. <https://doi.org/10.1016/j.carbon.2015.12.004>.
69. Islam, M. R.; Gupta, S. S.; Jana, S. K.; Srikrishnarka, P.; Mondal, B.; Chennu, S.; Ahuja, T.; Chakraborty, A.; Pradeep, T. A Covalently Integrated Reduced Graphene Oxide–Ion-Exchange Resin Electrode for Efficient Capacitive Deionization. *Adv. Mater. Interfaces* **2021**, 8 (5), 2001998. <https://doi.org/10.1002/admi.202001998>.
70. Oki, T.; Kanae, S. Global Hydrological Cycles and World Water Resources. *Science* **2006**, 313 (5790), 1068–1072. <https://doi.org/10.1126/science.1128845>.
71. Olivier, J. Fog-Water Harvesting along the West Coast of South Africa: A Feasibility Study. *Water SA* **2004**, 28 (4), 349–360. <https://doi.org/10.4314/wsa.v28i4.4908>.
72. Tu, Y.; Wang, R.; Zhang, Y.; Wang, J. Progress and Expectation of Atmospheric Water Harvesting. *Joule* **2018**, 2 (8), 1452–1475. <https://doi.org/10.1016/j.joule.2018.07.015>.
73. Kim, H.; Yang, S.; Rao, S. R.; Narayanan, S.; Kapustin, E. A.; Furukawa, H.; Umans, A. S.; Yaghi, O. M.; Wang, E. N. Water Harvesting from Air with Metal-Organic Frameworks Powered by Natural Sunlight. *Science* **2017**, 356 (6336), 430–434. <https://doi.org/10.1126/science.aam8743>.
74. Yilmaz, G.; Meng, F. L.; Lu, W.; Abed, J.; Peh, C. K. N.; Gao, M.; Sargent, E. H.; Ho, G. W. Autonomous Atmospheric Water Seeping MOF Matrix. *Sci. Adv.* **2020**, 6 (42), eabc8605. <https://doi.org/10.1126/sciadv.abc8605>.

75. Zhou, X.; Lu, H.; Zhao, F.; Yu, G. Atmospheric Water Harvesting: A Review of Material and Structural Designs. *ACS Mater. Lett.* **2020**, *2* (7), 671–684. <https://doi.org/10.1021/acsmaterialslett.0c00130>.
76. Kwon, S.; Fan, M.; Cooper, A. T.; Yang, H. Photocatalytic Applications of Micro- and Nano-TiO<sub>2</sub> in Environmental Engineering. *Crit. Rev. Environ. Sci. Technol.* **2008**, *38* (3), 197–226. <https://doi.org/10.1080/10643380701628933>.
77. Wang, C.; Yu, C. Detection of Chemical Pollutants in Water Using Gold Nanoparticles as Sensors: A Review. *Rev. Anal. Chem.* **2013**, *32* (1), 1–14. <https://doi.org/doi:10.1515/revac-2012-0023>.
78. S. A., N.; P. B. C., F. Development of a Turn-on Graphene Quantum Dot-Based Fluorescent Probe for Sensing of Pyrene in Water. *RSC Adv.* **2020**, *10* (21), 12119–12128. <https://doi.org/10.1039/C9RA10153E>.
79. Nair, A. N.; Chava, V. S. N.; Bose, S.; Zheng, T.; Pilla, S.; Sreenivasan, S. T. In Situ Doping-Enabled Metal and Nonmetal Codoping in Graphene Quantum Dots: Synthesis and Application for Contaminant Sensing. *ACS Sustain. Chem. Eng.* **2020**, *8* (44), 16565–16576. <https://doi.org/10.1021/acssuschemeng.0c05789>.
80. Huang, Z.; Chen, S.; Wang, Y.; Li, T. Gold Nanoparticle Modified Silicon Nanowire Array Based Sensor for Low-Cost, High Sensitivity and Selectivity Detection of Mercury Ions. *Mater. Res. Express* **2020**, *7* (3), 035017. <https://doi.org/10.1088/2053-1591/ab7d0b>.
81. Gopinath, K. P.; Madhav, N. V.; Krishnan, A.; Malolan, R.; Rangarajan, G. Present Applications of Titanium Dioxide for the Photocatalytic Removal of Pollutants from Water: A Review. *J. Environ. Manage.* **2020**, *270*, 110906. <https://doi.org/10.1016/j.jenvman.2020.110906>.
82. Mukherjee, S.; Shah, M.; Chaudhari, K.; Jana, A.; Sudhakar, C.; Srikrishnarka, P.; Islam, M. R.; Philip, L.; Pradeep, T. Smartphone-Based Fluoride-Specific Sensor for Rapid and Affordable Colorimetric Detection and Precise Quantification at Sub-Ppm Levels for Field Applications. *ACS Omega* **2020**, *5* (39), 25253–25263. <https://doi.org/10.1021/acsomega.0c03465>.
83. Gupte, T.; Jana, S. K.; Mohanty, J. S.; Srikrishnarka, P.; Mukherjee, S.; Ahuja, T.; Sudhakar, C.; Thomas, T.; Pradeep, T. Highly Sensitive As<sup>3+</sup> Detection Using Electrodeposited Nanostructured MnO<sub>x</sub> and Phase Evolution of the Active Material during Sensing. *ACS Appl. Mater. Interfaces* **2019**, *11* (31), 28154–28163. <https://doi.org/10.1021/acsam.9b06023>.
84. Mohammed, N.; Baidya, A.; Murugesan, V.; Kumar, A. A.; Ganayee, M. A.; Mohanty, J. S.; Tam, K. C.; Pradeep, T. Diffusion-Controlled Simultaneous Sensing and Scavenging of Heavy Metal Ions in Water Using Atomically Precise Cluster–Cellulose Nanocrystal Composites. *ACS Sustain. Chem. Eng.* **2016**, *4* (11), 6167–6176. <https://doi.org/10.1021/acssuschemeng.6b01674>.
85. Ahuja, T.; Ghosh, A.; Mondal, S.; Basuri, P.; Jenifer, S. K.; Srikrishnarka, P.; Mohanty, J. S.; Bose, S.; Pradeep, T. Ambient Electro Spray Deposition Raman Spectroscopy (AESD RS) Using Soft Landed Preformed Silver Nanoparticles for Rapid and Sensitive Analysis. *Analyst* **2019**, *144* (24), 7412–7420. <https://doi.org/10.1039/C9AN01700C>.
86. George, A.; Shibu, E. S.; Maliyekkal, S. M.; Bootharaju, M. S.; Pradeep, T. Luminescent, Freestanding Composite Films of Au<sub>15</sub> for Specific Metal Ion Sensing. *ACS Appl. Mater. Interfaces* **2012**, *4* (2), 639–644. <https://doi.org/10.1021/am201292a>.

87. Mathew, A.; Sajanlal, P. R.; Pradeep, T. Selective Visual Detection of TNT at the Sub-Zeptomole Level. *Angew. Chemie Int. Ed.* **2012**, *51* (38), 9596–9600. <https://doi.org/10.1002/anie.201203810>.
88. Ghosh, A.; Jeseentharani, V.; Ganayee, M. A.; Hemalatha, R. G.; Chaudhari, K.; Vijayan, C.; Pradeep, T. Approaching Sensitivity of Tens of Ions Using Atomically Precise Cluster–Nanofiber Composites. *Anal. Chem.* **2014**, *86* (22), 10996–11001. <https://doi.org/10.1021/ac502779r>.
89. Pang, L.; Dai, C.; Bi, L.; Guo, Z.; Fan, J. Biosafety and Antibacterial Ability of Graphene and Graphene Oxide In Vitro and In Vivo. *Nanoscale Res. Lett.* **2017**, *12* (1), 564. <https://doi.org/10.1186/s11671-017-2317-0>.
90. Di Giulio, M.; Zappacosta, R.; Di Lodovico, S.; Di Campli, E.; Siani, G.; Fontana, A.; Cellini, L. Antimicrobial and Antibiofilm Efficacy of Graphene Oxide against Chronic Wound Microorganisms. *Antimicrob. Agents Chemother.* **2018**, *62* (7), e00547-18. <https://doi.org/10.1128/AAC.00547-18>.
91. Mpenyana-Monyatsi, L.; Mthombeni, N. H.; Onyango, M. S.; Momba, M. N. B. Cost-Effective Filter Materials Coated with Silver Nanoparticles for the Removal of Pathogenic Bacteria in Groundwater. *Int. J. Environ. Res. Public Health* **2012**, *9* (1), 244–271. <https://doi.org/10.3390/ijerph9010244>.
92. Dimapilis, E. A. S.; Hsu, C. S.; Mendoza, R. M. O.; Lu, M. C. Zinc Oxide Nanoparticles for Water Disinfection. *Sustain. Environ. Res.* **2018**, *28* (2), 47–56. <https://doi.org/10.1016/j.serj.2017.10.001>.
93. Ottofuelling, S.; Von der Kammer, F.; Hofmann, T. Commercial Titanium Dioxide Nanoparticles in Both Natural and Synthetic Water: Comprehensive Multidimensional Testing and Prediction of Aggregation Behavior. *Environ. Sci. Technol.* **2011**, *45* (23), 10045–10052. <https://doi.org/10.1021/es2023225>.
94. Wang, X.; Zhu, M.; Liu, H.; Ma, J.; Li, F. Modification of Pd–Fe Nanoparticles for Catalytic Dechlorination of 2,4-Dichlorophenol. *Sci. Total Environ.* **2013**, *449*, 157–167. <https://doi.org/10.1016/j.scitotenv.2013.01.008>.
95. Homaeigohar, S.; Elbahri, M. Graphene Membranes for Water Desalination. *NPG Asia Mater.* **2017**, *9* (8), e427–e427. <https://doi.org/10.1038/am.2017.135>.
96. Goh, P. S.; Ismail, A. F. Graphene-Based Nanomaterial: The State-of-the-Art Material for Cutting Edge Desalination Technology. *Desalination* **2015**, *356*, 115–128. <https://doi.org/10.1016/j.desal.2014.10.001>.
97. Fathizadeh, M.; Xu, W. L.; Zhou, F.; Yoon, Y.; Yu, M. Graphene Oxide: A Novel 2-Dimensional Material in Membrane Separation for Water Purification. *Adv. Mater. Interfaces* **2017**, *4* (5), 1600918. <https://doi.org/10.1002/admi.201600918>.
98. Bose, S.; Chatterjee, A.; Jenifer, S. K.; Mondal, B.; Srikrishnarka, P.; Ghosh, D.; Chowdhuri, A. R.; Kannan, M. P.; Elchuri, S. V; Pradeep, T. Molecular Materials through Microdroplets: Synthesis of Protein-Protected Luminescent Clusters of Noble Metals. *ACS Sustain. Chem. Eng.* **2021**, *9* (12), 4554–4563. <https://doi.org/10.1021/acssuschemeng.0c09145>.
99. Rao, T. U. B.; Nataraju, B.; Pradeep, T. Ag9 Quantum Cluster through a Solid-State Route. *J. Am. Chem. Soc.* **2010**, *132* (46), 16304–16307. <https://doi.org/10.1021/ja105495n>.

100. Khan, S. T.; Malik, A. Engineered Nanomaterials for Water Decontamination and Purification: From Lab to Products. *J. Hazard. Mater.* **2019**, *363*, 295–308. <https://doi.org/10.1016/j.jhazmat.2018.09.091>.
101. Glória, A.; Dionisio, C.; Simões, G.; Cardoso, J.; Sebastião, P. Water Management for Sustainable Irrigation Systems Using Internet-of-Things. *Sensors* **2020**, *20* (5), 1402. <https://doi.org/10.3390/s20051402>.
102. *IoT Solution for Water Management*. <https://www.libelium.com/iot-solutions/smart-water/> (accessed July 27, 2021).
103. *Real tech Inc*. <https://realtechwater.com/> (accessed July 27, 2021).
104. Das, R.; Ali, M. E.; Hamid, S. B. A.; Ramakrishna, S.; Chowdhury, Z. Z. Carbon Nanotube Membranes for Water Purification: A Bright Future in Water Desalination. *Desalination* **2014**, *336*, 97–109. <https://doi.org/10.1016/j.desal.2013.12.026>.
105. Smith, S. C.; Rodrigues, D. F. Carbon-Based Nanomaterials for Removal of Chemical and Biological Contaminants from Water: A Review of Mechanisms and Applications. *Carbon* **2015**, *91*, 122–143. <https://doi.org/10.1016/j.carbon.2015.04.043>.
106. *GEA Group*. <https://www.gea.com/en/index.jsp> (accessed July 27, 2021).
107. *Inopor*. <https://inopor.com/en/13-en.html> (accessed July 27, 2021).
108. *Applied Membranes, Inc*. <https://www.appliedmembranes.com/> (accessed July 27, 2021).
109. *Koch Separation Solutions*. <https://www.kochseparation.com/> (accessed July 27, 2021).
110. *Alfa Laval India Private Limited*. <https://www.alfalaval.in/> (accessed July 27, 2021).
111. *Filtering Water with Acoustics Nanotube Technology*. [https://www.nasa.gov/centers/johnson/techtransfer/technology/MSC-24180-1\\_Water-Filtering-Device.html](https://www.nasa.gov/centers/johnson/techtransfer/technology/MSC-24180-1_Water-Filtering-Device.html) (accessed July 27, 2021).
112. Ino, D. *Method for Decomposing Organic Compound Contained in Aqueous Solution*. U.S. Patent Application US20140027387, 2013.
113. Varma, K. S.; Tayade, R. J.; Shah, K. J.; Joshi, P. A.; Shukla, A. D.; Gandhi, V. G. Photocatalytic Degradation of Pharmaceutical and Pesticide Compounds (PPCs) Using Doped TiO<sub>2</sub> Nanomaterials: A Review. *Water-Energy Nexus* **2020**, *3*, 46–61. <https://doi.org/10.1016/j.wen.2020.03.008>.
114. Konstantinou, I.; Albanis, T. TiO<sub>2</sub>-Assisted Photocatalytic Degradation of Azo Dyes in Aqueous Solution: Kinetic and Mechanistic Investigations A Review. *Appl. Catal. B, Environmental* **2004**, *49* (1), 1–14. <https://doi.org/10.1016/j.apcatb.2003.11.010>.
115. McCullagh, C.; Robertson, J. M. C.; Bahnemann, D. W.; Robertson, P. K. J. The Application of TiO<sub>2</sub> Photocatalysis for Disinfection of Water Contaminated with Pathogenic Micro-Organisms: A Review. *Res. Chem. Intermed.* **2007**, *33* (3), 359–375. <https://doi.org/10.1163/156856707779238775>.
116. Laxma Reddy, P. V.; Kavitha, B.; Kumar Reddy, P. A.; Kim, K.-H. TiO<sub>2</sub>-Based Photocatalytic Disinfection of Microbes in Aqueous Media: A Review. *Environ. Res.* **2017**, *154*, 296–303. <https://doi.org/10.1016/j.envres.2017.01.018>.
117. Mahmoud, K. A.; Mansoor, B.; Mansour, A.; Khraisheh, M. Functional Graphene Nanosheets: The next Generation Membranes for Water Desalination. *Desalination* **2015**, *356*, 208–225. <https://doi.org/10.1016/j.desal.2014.10.022>.



118. Perreault, F.; de Faria, A. F.; Nejati, S.; Elimelech, M. Antimicrobial Properties of Graphene Oxide Nanosheets: Why Size Matters. *ACS Nano* **2015**, *9* (7), 7226–7236. <https://doi.org/10.1021/acsnano.5b02067>.
119. Sadovnikov, S. I.; Gusev, A. I. Recent Progress in Nanostructured Silver Sulfide: From Synthesis and Nonstoichiometry to Properties. *J. Mater. Chem. A* **2017**, *5* (34), 17676–17704. <https://doi.org/10.1039/C7TA04949H>.
120. Goal 6: Ensure access to water and sanitation for all. <https://www.un.org/sustainabledevelopment/water-and-sanitation/> (accessed July 27, 2021).
121. Ensure availability and sustainable management of water and sanitation for all. <https://sdgs.un.org/goals/goal6> (accessed July 27, 2021).
122. Beyene, H. D.; Ambaye, T. G. Application of Sustainable Nanocomposites for Water Purification Process. In *Sustainable Polymer Composites and Nanocomposites*; Inamuddin, Thomas, S., Kumar Mishra, R., Asiri, A. M., Eds.; Springer International Publishing: Cham, 2019; pp 387–412. [https://doi.org/10.1007/978-3-030-05399-4\\_14](https://doi.org/10.1007/978-3-030-05399-4_14).
123. Kamali, M.; Costa, M. E.; Aminabhavi, T. M.; Capela, I. Sustainability of Treatment Technologies for Industrial Biowastes Effluents. *Chem. Eng. J.* **2019**, *370*, 1511–1521. <https://doi.org/10.1016/j.cej.2019.04.010>.
124. Borovik, A.; Karanikola, V.; Zucker, I. Platform Selection of Engineered Nanomaterials for Water Decontamination Applications. *Environ. Sci. Nano* **2020**, *7* (12), 3641–3654. <https://doi.org/10.1039/d0en00786b>.
125. Falinski, M. M.; Plata, D. L.; Chopra, S. S.; Theis, T. L.; Gilbertson, L. M.; Zimmerman, J. B. A Framework for Sustainable Nanomaterial Selection and Design Based on Performance, Hazard, and Economic Considerations. *Nat. Nanotechnol.* **2018**, *13* (8), 708–714. <https://doi.org/10.1038/s41565-018-0120-4>.
126. Wickson, F.; Carew, A. L. Quality Criteria and Indicators for Responsible Research and Innovation: Learning from Transdisciplinarity. *J. Responsible Innov.* **2014**, *1* (3), 254–273. <https://doi.org/10.1080/23299460.2014.963004>.
127. Ren, D.; Colosi, L. M.; Smith, J. A. Evaluating the Sustainability of Ceramic Filters for Point-of-Use Drinking Water Treatment. *Environ. Sci. Technol.* **2013**, *47* (19), 11206–11213. <https://doi.org/10.1021/es4026084>.
128. Molinos-Senante, M.; Sala-Garrido, R. Evaluation of Energy Performance of Drinking Water Treatment Plants: Use of Energy Intensity and Energy Efficiency Metrics. *Appl. Energy* **2018**, *229*, 1095–1102. <https://doi.org/10.1016/j.apenergy.2018.08.102>.
129. Paul, R.; Kenway, S.; Mukheibir, P. How Scale and Technology Influence the Energy Intensity of Water Recycling Systems-An Analytical Review. *J. Clean. Prod.* **2019**, *215*, 1457–1480. <https://doi.org/10.1016/j.jclepro.2018.12.148>.
130. Bukhary, S.; Batista, J.; Ahmad, S. An Analysis of Energy Consumption and the Use of Renewables for a Small Drinking Water Treatment Plant. *Water* **2020**, *12*, 28. <https://doi.org/10.3390/w12010028>.
131. Windsor, R.; Cinelli, M.; Coles, S. R. Comparison of Tools for the Sustainability Assessment of Nanomaterials. *Curr. Opin. Green Sustain. Chem.* **2018**, *12*, 69–75. <https://doi.org/10.1016/j.cogsc.2018.06.010>.
132. Jakka Ravindran, S.; Mahendranath, A.; Srikrishnarka, P.; Anil Kumar, A.; Islam, M. R.; Mukherjee, S.; Philip, L.; Pradeep, T. Geologically Inspired Monoliths for Sustainable Release

- of Essential Minerals into Drinking Water. *ACS Sustain. Chem. Eng.* **2019**, *7* (13), 11735–11744. <https://doi.org/10.1021/acssuschemeng.9b01902>.
133. Jiménez-González, C.; Constable, D. J. C.; Ponder, C. S. Evaluating the “Greenness” of Chemical Processes and Products in the Pharmaceutical Industry—a Green Metrics Primer. *Chem. Soc. Rev.* **2012**, *41* (4), 1485–1498. <https://doi.org/10.1039/C1CS15215G>.
134. Sheldon, R. A. Metrics of Green Chemistry and Sustainability: Past, Present, and Future. *ACS Sustain. Chem. Eng.* **2018**, *6* (1), 32–48. <https://doi.org/10.1021/acssuschemeng.7b03505>.
135. Martins, A. A.; Mata, T. M.; Costa, C. A. V.; Sikdar, S. K. Framework for Sustainability Metrics. *Ind. Eng. Chem. Res.* **2007**, *46* (10), 2962–2973. <https://doi.org/10.1021/ie060692l>.
136. Anastas, P.; Eghbali, N. Green Chemistry: Principles and Practice. *Chem. Soc. Rev.* **2010**, *39* (1), 301–312. <https://doi.org/10.1039/b918763b>.
137. Salieri, B.; Turner, D. A.; Nowack, B.; Hischier, R. Life Cycle Assessment of Manufactured Nanomaterials: Where Are We? *NanoImpact* **2018**, *10*, 108–120. <https://doi.org/10.1016/j.impact.2017.12.003>.
138. Guineé, J. B.; Heijungs, R.; Vijver, M. G.; Peijnenburg, W. J. G. M. Setting the Stage for Debating the Roles of Risk Assessment and Life-Cycle Assessment of Engineered Nanomaterials. *Nat. Nanotechnol.* **2017**, *12* (8), 727–733. <https://doi.org/10.1038/NNANO.2017.135>.
139. Linkov, I.; Seager, T. P. Coupling Multi-Criteria Decision Analysis, Life-Cycle Assessment, and Risk Assessment for Emerging Threats. *Environ. Sci. Technol.* **2011**, *45* (12), 5068–5074. <https://doi.org/10.1021/ES100959Q>.
140. Fernández-Cruz, M. L.; Hernández-Moreno, D.; Catalán, J.; Cross, R. K.; Stockmann-Juvala, H.; Cabellos, J.; Lopes, V. R.; Matzke, M.; Ferraz, N.; Izquierdo, J. J.; Navas, J. M.; Park, M.; Svendsen, C.; Janer, G. Quality Evaluation of Human and Environmental Toxicity Studies Performed with Nanomaterials – the GUIDEnano Approach. *Environ. Sci. Nano* **2018**, *5* (2), 381–397. <https://doi.org/10.1039/C7EN00716G>.
141. van Harmelen, T.; Zondervan-van den Beuken, E. K.; Brouwer, D. H.; Kuijpers, E.; Fransman, W.; Buist, H. B.; Ligthart, T. N.; Hincapié, I.; Hischier, R.; Linkov, I.; Nowack, B.; Studer, J.; Hilty, L.; Som, C. LICARA NanoSCAN - A Tool for the Self-Assessment of Benefits and Risks of Nanoproducts. *Environ. Int.* **2016**, *91*, 150–160. <https://doi.org/10.1016/J.ENVINT.2016.02.021>.
142. Lamon, L.; Asturiol, D.; Vilchez, A.; Ruperez-Illescas, R.; Cabellos, J.; Richarz, A.; Worth, A. Computational Models for the Assessment of Manufactured Nanomaterials: Development of Model Reporting Standards and Mapping of the Model Landscape. *Comput. Toxicol.* **2019**, *9*, 143–151. <https://doi.org/10.1016/J.COMTOX.2018.12.002>.
143. Siegert, M.; Sonawane, J. M.; Ezugwu, C. I.; Prasad, R. Economic Assessment of Nanomaterials in Bio-Electrical Water Treatment. In *Advanced Research in Nanosciences for Water Technology*; Prasad, R., Karchiyappan, T., Eds.; Springer: Cham, 2019; pp 1–23.
144. Ashby, M. F. Chapter 10 - Eco-Informed Materials Selection. In *Materials and the Environment*; Ashby, M. F., Ed.; Butterworth-Heinemann: Boston, 2013; pp 275–317. <https://doi.org/10.1016/B978-0-12-385971-6.00010-5>.
145. Visentin, C.; Trentin, A. W. da S.; Braun, A. B.; Thomé, A. Life Cycle Sustainability Assessment of the Nanoscale Zero-Valent Iron Synthesis Process for Application in

- Contaminated Site Remediation. *Environ. Pollut.* **2021**, 268, 115915. <https://doi.org/10.1016/j.envpol.2020.115915>.
146. ISO - ISO 14050:2020 - *Environmental management — Vocabulary*. <https://www.iso.org/standard/75300.html> (accessed July 27, 2021).
147. Van Leeuwen, C. J. General Introduction. In *Risk Assessment of Chemicals*; van Leeuwen, C. J., Vermeire, T. G., Eds.; Springer: Dordrecht, 2007; pp 1–36. <https://doi.org/10.1007/978-1-4020-6102-8>.
148. Sperber, W. H. Hazard Identification: From a Quantitative to a Qualitative Approach. *Food Control* **2001**, 12 (4), 223–228. [https://doi.org/10.1016/S0956-7135\(00\)00044-X](https://doi.org/10.1016/S0956-7135(00)00044-X).
149. Siegert, M.; Sonawane, J. M.; Ezugwu, C. I.; Prasad, R. Economic Assessment of Nanomaterials in Bio-Electrical Water Treatment. In *Advanced Research in Nanosciences for Water Technology*; Prasad, R., Karchiyappan, T., Eds.; Springer International Publishing: Cham, 2019; pp 1–23. [https://doi.org/10.1007/978-3-030-02381-2\\_1](https://doi.org/10.1007/978-3-030-02381-2_1).
150. Elimelech, M.; Phillip, W. A. The Future of Seawater Desalination: Energy, Technology, and the Environment. *Science*. **2011**, 333 (6043), 712–717. <https://doi.org/10.1126/science.1200488>.
151. Guo, Y.; Lu, H.; Zhao, F.; Zhou, X.; Shi, W.; Yu, G. Biomass-Derived Hybrid Hydrogel Evaporators for Cost-Effective Solar Water Purification. *Adv. Mater.* **2020**, 32 (11), 1907061. <https://doi.org/10.1002/adma.201907061>.
152. Matamoros, V.; Gutiérrez, R.; Ferrer, I.; García, J.; Bayona, J. M. Capability of Microalgae-Based Wastewater Treatment Systems to Remove Emerging Organic Contaminants: A Pilot-Scale Study. *J. Hazard. Mater.* **2015**, 288, 34–42. <https://doi.org/10.1016/j.jhazmat.2015.02.002>.
153. Beuckels, A.; Smolders, E.; Muylaert, K. Nitrogen Availability Influences Phosphorus Removal in Microalgae-Based Wastewater Treatment. *Water Res.* **2015**, 77, 98–106. <https://doi.org/10.1016/j.watres.2015.03.018>.
154. Chen, B.; Wang, Y.; Hu, D. Biosorption and Biodegradation of Polycyclic Aromatic Hydrocarbons in Aqueous Solutions by a Consortium of White-Rot Fungi. *J. Hazard. Mater.* **2010**, 179 (1–3), 845–851. <https://doi.org/10.1016/j.jhazmat.2010.03.082>.
155. El-Naggar, N. E.-A.; El-khateeb, A. Y.; Ghoniem, A. A.; El-Hersh, M. S.; Saber, W. I. A. Innovative Low-Cost Biosorption Process of Cr<sup>6+</sup> by *Pseudomonas Alcaliphila* NEWG-2. *Sci. Rep.* **2020**, 10 (1), 14043. <https://doi.org/10.1038/s41598-020-70473-5>.
156. Pyrzyńska, K. Removal of Cadmium from Wastewaters with Low-Cost Adsorbents. *J. Environ. Chem. Eng.* **2019**, 7 (1), 102795. <https://doi.org/10.1016/j.jece.2018.11.040>.
157. Mwandira, W.; Nakashima, K.; Kawasaki, S.; Arabelo, A.; Banda, K.; Nyambe, I.; Chirwa, M.; Ito, M.; Sato, T.; Igarashi, T.; Nakata, H.; Nakayama, S.; Ishizuka, M. Biosorption of Pb (II) and Zn (II) from Aqueous Solution by *Oceanobacillus Profundus* Isolated from an Abandoned Mine. *Sci. Rep.* **2020**, 10 (1), 21189. <https://doi.org/10.1038/s41598-020-78187-4>.
158. Rozman, U.; Kalčíková, G.; Marolt, G.; Skalar, T. Environmental Technology & Innovation Potential of Waste Fungal Biomass for Lead and Cadmium Removal : Characterization, Biosorption Kinetic and Isotherm Studies. *Environ. Technol. Innov.* **2020**, 18, 100742. <https://doi.org/10.1016/j.eti.2020.100742>.
159. Pan, J.; Gao, B.; Song, W.; Xu, X.; Yue, Q. Modi Fi Ed Biogas Residues as an Eco-Friendly and Easily-Recoverable Biosorbent for Nitrate and Phosphate Removals from Surface Water.

- J. Hazard. Mater.* **2020**, 382 (May 2019), 121073. <https://doi.org/10.1016/j.jhazmat.2019.121073>.
160. Wei, W.; Wang, Q.; Li, A.; Yang, J.; Ma, F.; Pi, S.; Wu, D. Biosorption of Pb (II) from Aqueous Solution by Extracellular Polymeric Substances Extracted from *Klebsiella* Sp. J1: Adsorption Behavior and Mechanism Assessment. *Sci. Rep.* **2016**, 6 (July), 31575. <https://doi.org/10.1038/srep31575>.
161. Kang, J.; Liu, H.; Zheng, Y.-M.; Qu, J.; Chen, J. P. Systematic Study of Synergistic and Antagonistic Effects on Adsorption of Tetracycline and Copper onto a Chitosan. *J. Colloid Interface Sci.* **2010**, 344 (1), 117–125. <https://doi.org/10.1016/j.jcis.2009.11.049>.
162. Zeng, Z. W.; Tan, X. F.; Liu, Y. G.; Tian, S. R.; Zeng, G. M.; Jiang, L. H.; Liu, S. B.; Li, J.; Liu, N.; Yin, Z. H. Comprehensive Adsorption Studies of Doxycycline and Ciprofloxacin Antibiotics by Biochars Prepared at Different Temperatures. *Front. Chem.* **2018**, 6 (MAR), 1–11. <https://doi.org/10.3389/fchem.2018.00080>.
163. Li, S.; Huang, J.; Mao, J.; Zhang, L.; He, C.; Chen, G.; Parkin, I. P.; Lai, Y. In Vivo and in Vitro Efficient Textile Wastewater Remediation by *Aspergillus Niger* Biosorbent. *Nanoscale Adv.* **2019**, 1 (1), 168–176. <https://doi.org/10.1039/c8na00132d>.
164. Wollmann, F.; Dietze, S.; Ackermann, J.-U.; Bley, T.; Walther, T.; Steingroewer, J.; Krujatz, F. Microalgae Wastewater Treatment: Biological and Technological Approaches. *Eng. Life Sci.* **2019**, 19 (12), 860–871. <https://doi.org/10.1002/elsc.201900071>.
165. Sutherland, D. L.; Park, J.; Heubeck, S.; Ralph, P. J.; Craggs, R. J. Size Matters – Microalgae Production and Nutrient Removal in Wastewater Treatment High Rate Algal Ponds of Three Different Sizes. *Algal Res.* **2020**, 45, 101734. <https://doi.org/10.1016/j.algal.2019.101734>.
166. Lindberg, R. H.; Namazkar, S.; Lage, S.; Östman, M.; Gojkovic, Z.; Funk, C.; Gentili, F. G.; Tysklind, M. Fate of Active Pharmaceutical Ingredients in a Northern High-Rate Algal Pond Fed with Municipal Wastewater. *Chemosphere* **2021**, 271, 129763. <https://doi.org/10.1016/j.chemosphere.2021.129763>.
167. Elliott, M. A.; Stauber, C. E.; Koksal, F.; DiGiano, F. A.; Sobsey, M. D. Reductions of *E. Coli*, Echovirus Type 12 and Bacteriophages in an Intermittently Operated Household-Scale Slow Sand Filter. *Water Res.* **2008**, 42 (10–11), 2662–2670. <https://doi.org/10.1016/j.watres.2008.01.016>.
168. Campos, L. C.; Su, M. F. J.; Graham, N. J. D.; Smith, S. R. Biomass Development in Slow Sand Filters. *Water Res.* **2002**, 36 (18), 4543–4551. [https://doi.org/10.1016/s0043-1354\(02\)00167-7](https://doi.org/10.1016/s0043-1354(02)00167-7).
169. Saleh, I. A.; Zouari, N.; Al-Ghouti, M. A. Removal of Pesticides from Water and Wastewater: Chemical, Physical and Biological Treatment Approaches. *Environ. Technol. Innov.* **2020**, 19, 101026. <https://doi.org/10.1016/j.eti.2020.101026>.
170. Schijven, J. F.; van den Berg, H. H. J. L.; Colin, M.; Dullemeent, Y.; Hijnen, W. A. M.; Magic-Knezev, A.; Oorthuizen, W. A.; Wubbels, G. A Mathematical Model for Removal of Human Pathogenic Viruses and Bacteria by Slow Sand Filtration under Variable Operational Conditions. *Water Res.* **2013**, 47 (7), 2592–2602. <https://doi.org/10.1016/j.watres.2013.02.027>.

171. Aronino, R.; Dlugy, C.; Arkhangelsky, E.; Shandalov, S.; Oron, G.; Brenner, A.; Gitis, V. Removal of Viruses from Surface Water and Secondary Effluents by Sand Filtration. *Water Res.* **2009**, *43* (1), 87–96. <https://doi.org/10.1016/j.watres.2008.10.036>.
172. Huisman, L.; Wood, F. I. C. E. W. E. ; World Health Organization: Belgium, 1974.
173. *Technologies for Upgrading Existing or Designing New Drinking Water Treatment Facilities*, 1st ed.; CRC Press: Boca Raton, 2017. <https://doi.org/10.1201/9781003073178>.
174. Peydayesh, M.; Mezzenga, R. Protein Nanofibrils for next Generation Sustainable Water Purification. *Nat. Commun.* **2021**, *12* (1), 3248. <https://doi.org/10.1038/s41467-021-23388-2>.
175. Aggarwal, N.; Eliaz, D.; Cohen, H.; Rosenhek-Goldian, I.; Cohen, S. R.; Kozell, A.; Mason, T. O.; Shimanovich, U. Protein Nanofibril Design via Manipulation of Hydrogen Bonds. *Commun. Chem.* **2021**, *4* (1), 62. <https://doi.org/10.1038/s42004-021-00494-2>.
176. Jensen, P. H.; Keller, D.; Hélix-Nielsen, C. *Membrane for Filtering of Water*. U.S. Patent 7,857,978 B2, 2010.
177. Agre, P.; Bonhivers, M.; Borgnia, M. J. The Aquaporins, Blueprints for Cellular Plumbing Systems. *J. Biol. Chem.* **1998**, *273* (24), 14659–14662. <https://doi.org/10.1074/jbc.273.24.14659>.
178. Agre, P. Aquaporin Water Channels (Nobel Lecture). *Angewandte Chemie (International ed. in English)* **2004**, *43*, 4278–4290. <https://doi.org/10.1002/anie.200460804>.
179. Gravelle, S.; Joly, L.; Detcheverry, F.; Ybert, C.; Cottin-Bizonne, C.; Bocquet, L. Optimizing Water Permeability through the Hourglass Shape of Aquaporins. *Proc. Natl. Acad. Sci.* **2013**, *110* (41), 16367–16372. <https://doi.org/10.1073/pnas.1306447110>.
180. Wagh, P.; Escobar, I. C. Biomimetic and Bioinspired Membranes for Water Purification: A Critical Review and Future Directions. *Environ. Prog. Sustain. Energy* **2019**, *38* (3), e13215. <https://doi.org/10.1002/ep.13215>.
181. Abdelrasoul, A.; Doan, H.; Lohi, A.; Cheng, C. H. Aquaporin-Based Biomimetic and Bioinspired Membranes for New Frontiers in Sustainable Water Treatment Technology: Approaches and Challenges. *Polym. Sci. - Ser. A* **2018**, *60* (4), 429–450. <https://doi.org/10.1134/S0965545X18040016>.
182. Vassalle, L.; Sunyer-Caldú, A.; Díaz-Cruz, M. S.; Arashiro, L. T.; Ferrer, I.; Garfí, M.; García-Galán, M. J. Behavior of UV Filters, UV Blockers and Pharmaceuticals in High Rate Algal Ponds Treating Urban Wastewater. *Water* **2020**, *12*, 2658. <https://doi.org/10.3390/w12102658>.
183. Agrawal, A.; Sharma, N.; Sharma, P. Designing an Economical Slow Sand Filter for Households to Improve Water Quality Parameters. *Mater. Today Proc.* **2021**, *43*, 1582–1586. <https://doi.org/10.1016/j.matpr.2020.09.450>.
184. Peydayesh, M.; Mezzenga, R. Protein Nanofibrils for next Generation Sustainable Water Purification. *Nat. Commun.* **2021**, *12* (1), 3248. <https://doi.org/10.1038/s41467-021-23388-2>.
185. Lee, C. S.; Choi, M.; Hwang, Y. Y.; Kim, H.; Kim, M. K.; Lee, Y. J. Facilitated Water Transport through Graphene Oxide Membranes Functionalized with Aquaporin-Mimicking Peptides. *Adv. Mater.* **2018**, *30* (14), 1705944. <https://doi.org/10.1002/adma.201705944>.
186. Kumar, M.; Grzelakowski, M.; Zilles, J.; Clark, M.; Meier, W. Highly Permeable Polymeric Membranes Based on the Incorporation of the Functional Water Channel Protein Aquaporin

- Z. Proc. Natl. Acad. Sci.* **2007**, *104* (52), 20719–20724. <https://doi.org/10.1073/pnas.0708762104>.
187. Xie, W.; He, F.; Wang, B.; Chung, T.-S.; Jeyaseelan, K.; Armugam, A.; Tong, Y. W. An Aquaporin-Based Vesicle-Embedded Polymeric Membrane for Low Energy Water Filtration. *J. Mater. Chem. A* **2013**, *1* (26), 7592–7600. <https://doi.org/10.1039/C3TA10731K>.
188. Volpin, F.; Badeti, U.; Wang, C.; Jiang, J.; Vogel, J.; Freguia, S.; Fam, D.; Cho, J.; Phuntsho, S.; Shon, H. K. Urine Treatment on the International Space Station: Current Practice and Novel Approaches. *Membranes (Basel)*. **2020**, *10* (11), 327. <https://doi.org/10.3390/membranes10110327>.
189. Tommerup, M. B.; Kleinschmidt, K.; Vogel, J.; Flynn, M.; Shaw, H. Testing Aquaporin Inside™ Membrane on the International Space Station – Part II. *47th Int. Conf. Environ. Syst.* **2017**, 152.
190. Tang, C.; Wang, Z.; Petrinić, I.; Fane, A. G.; Hélix-Nielsen, C. Biomimetic Aquaporin Membranes Coming of Age. *Desalination* **2015**, 368, 89–105. <https://doi.org/10.1016/j.desal.2015.04.026>.
191. Halsey, A. M.; Conner, A. C.; Bill, R. M.; Logan, A.; Ahmed, Z. Aquaporins and Their Regulation after Spinal Cord Injury. *Cells* **2018**, *7* (10), 174. <https://doi.org/10.3390/cells7100174>.
192. *Zero powered by AQUAPORIN INSIDE®*. <https://aquaporin.com/products/zero/> (accessed July 27, 2021).



# Patents

## Indian Patents (Granted)

1. Synthesis of highly anisotropic metallic mesostructures, T. Pradeep, Chandramouli Subramaniam, application no. 2262/CHE/2008, dated February 19, 2008, issued as patent no. 392320, dated March 18, 2022.
2. A method for the preparation of immobilized graphene-based composite from asphalt and its application in water purification, T. Pradeep, Theruvakkattil Sreenivasan Sreeprasad, Soujit Sengupta, Mundampra Maliyekkal Shihabudheen, application no. 3863/CHE/2012, dated September 17, 2012, issued as patent no. 393415, dated March 29, 2022.
3. Method for generating different phases of copper sulphide nanostructures using electrospray deposition (ESD) under ambient conditions, T. Pradeep, Arijit Jana, Sourav Kanti Jana, Depanjan Sarkar application no. 201941032379, dated August 9, 2019, issued as patent no. 396273, dated May 5, 2022.
4. Visible detection of quantity of water flow using quantum clusters, T. Pradeep, Annamalai Leelavathi, Mohan Udhaya Sankar, Chaudhary Amrita, Anshup, Thumu Udayabhaskararao, application no. 1521/CHE/2012, dated April 17, 2012, issued as patent no. 401784, dated July 21, 2022.
5. Structure and topology conserving transformations between two archetypal nanoparticles, T. Pradeep, K. R. Krishnadas, Ananya Baksi, Atanu Ghosh, Ganapati

Natarajan application no. 201641034921, dated October 13, 2016, issued as patent no. 405913, dated September 6, 2022.

## Indian Patents (Applied)

1. Method of fabricating a conducting cloth based breath humidity sensor and applications thereof, T. Pradeep, Pillalamarri Srikrishnarka, Dasi Raaga Madhuri, Sourav Kanti Jana, Bobby George, application no. 202241008331, dated February 17, 2022.
2. A selective and efficient process for the extraction of noble metals, T. Pradeep, Md Rabiul Islam, Tanmayaa Nayak, application no. 202241026274, dated May 05, 2022.
3. A method to transform crystalline minerals to nanoparticles by microdroplets, T. Pradeep, B. K. Spoorthi, Pallab Basuri, application no. 202241038282, dated July 7, 2022.
4. A method of cultivating rice without soil for its complete life cycle using nanotechnology, T. Pradeep, T.N.V.K. V Prasad application no. 202241043559, dated July 29, 2022.
5. A method for environmental arsenic detection and public awareness using human cells, T. Pradeep, Tanvi Gupte, application no. 202241049077, dated August 28, 2022.
6. Material and method for sustainable and affordable atmospheric water harvesting, T. Pradeep, Ankit Nagar; Sonali Seth, application no. 202241049229, dated August 29, 2022.

7. Vertically aligned nanoplates of atomically precise  $\text{Co}_6\text{S}_8$  cluster for practical arsenic sensing, T. Pradeep, Anagha Jose, Arijit Jana, Tanvi Gupte, Keerthana Unni, Ankit Nagar, Amoghavarsha R. Kini, B.K. Spoorthi, application no. 202241076581, dated December 29, 2022.

## PCT (Applied)

1. An electrode system based on differential oxidant response for the detection of free chlorine, T. Pradeep, Kamalesh Chaudhari, Tullio Servida, Vishnu V, B. K. Spoorthi, application no. PCT/IN2022/050637, dated July 14, 2022.

# Selected Media Reports



## IIT Madras professor Padma Shri Thalappil Pradeep wins VinFuture Prize for tech to remove arsenic from groundwater

IIT Madras professor Padma Shri Thalappil Pradeep has won the VinFuture Prize, one of the largest ever annual prizes globally, for his low-cost filtration system to remove arsenic from groundwater.

**By India Today Web Desk:** Professor Thalappil Pradeep of IIT Madras bagged the award in one of the four categories of the annual 'VinFuture Prizes'. Nearly 1,000 nominations from 71 different countries were scanned through to choose the winners.

Professor Pradeep received the special prize for 'Innovators from Developing Countries' in recognition of his work on a low-cost filtration device for the removal of heavy metals such as arsenic and others from groundwater.



*IIT Madras professor Padma Shri Thalappil Pradeep has won the VinFuture Prize, one of the largest ever annual prizes globally, for his low-cost filtration system to remove arsenic from groundwater.*

**By India Today Web Desk:** Professor Thalappil Pradeep of IIT Madras bagged the award in one of the four categories of the annual 'VinFuture Prizes'. Nearly 1,000 nominations from 71 different countries were scanned through to choose the winners.

Professor Pradeep received the special prize for 'Innovators from Developing Countries' in recognition of his work on a low-cost filtration device for the removal of heavy metals such as arsenic and others from groundwater.



This could provide access to clean water for hundreds of millions of people who currently live in areas with dirty water.

The VinFuture Prize was presented to Professor T Pradeep from IIT Madras on December 20, 2022, in Hanoi, Vietnam. He now holds the post of Institute Professor in IIT Madras' Department of Chemistry.

### **OTHER AWARDS RECEIVED BY THE IIT MADRAS PROFESSOR**

Professor Pradeep has received numerous awards before, including the Padma Shri, the [Nikkei Asia Prize](#), and the Prince Sultan Bin Abdulaziz International Prize for Water. His innovations are providing clean water to more than 1.2 crore people.

One of the highest annual rewards ever given out globally, the VinFuture Grand Prize is valued at US\$3 million. It also includes three special awards, each worth US\$ 500,000, presented to innovators from developing nations, innovators from women, and innovators who have made remarkable contributions to developing sectors.

### **WHAT THE PROFESSOR SAID**

Professor T Pradeep, while thanking the awards jury said, "This recognises everyone who worked with me, everyone who has been benefited from the work and those who enabled the translation of our work."

"At the same time, I am aware of the huge gap yet to be bridged to deliver clean water to everyone. I hope that this recognition will help in realizing that dream. I thank my institute which gave me everything. I thank my country, which made me stand up," he said.

### **HOW THE AWARD-WINNING TECH WORKS**

Professor Pradeep found sustainable and cheap nanoparticles that can be used to create clean water. The removal of arsenic and other substances by these materials has no effect on the surroundings.

This technique, which makes use of straightforward designs, offers a low-cost way to cleanse groundwater and get it to millions of affected households. This technology is more useful in distant locations because it doesn't need electricity.

### **ABOUT THE VINFUTURE PRIZE**

The largest Vietnamese conglomerate, Vingroup, was founded by Phm Nht Vng, the country's first billionaire, and his wife, Phm Thu Hng. At the foundation of their independent, not-for-profit company is the VinFuture Prize.



## Science

# IIT Madras gets new research centre for frequent wastewater analysis

BL Chennai Bureau | May 9 | Updated On: May 09, 2022



Researchers at a lab in International Centre for Clean Water (ICCW), IIT Madras

Facility to act as an intelligence unit to track and prevent a virus outbreak in its early stages

The Indian Institute of Technology Madras is establishing a new research centre that will test wastewater in a city for indicator organisms and chemicals, and make the data available to the public. The

facility will act as an intelligence unit to track and prevent a virus outbreak in its early stages.

The International Centre for Clean Water (ICCW) is establishing this Wastewater-Based Epidemiology (WBE) research facility and the project is supported with funding of \$1 million by CryptoRelief, an initiative started by Sandeep Nailwal.

The data obtained from various wastewater sources and treatment facilities will be analysed and made available to the public through dashboards. Gradually, this facility will be extended to other parts of India, said a release from IIT Madras.

Crypto Relief is the result of the global crypto community mobilising to help India combat the Covid crisis, and to help it prepare for future outbreaks, the release added.

### RELATED

Why are India's garbage dumpsites burning?





## IIT Madras professor wins international prize

T. Pradeep recognised for his work on making potable groundwater accessible

December 28, 2022 09:42 pm | Updated 09:42 pm IST - CHENNAI

THE HINDU BUREAU

 COMMENTS  SHARE

 READ LATER

Indian Institute of Technology Madras professor T. Pradeep has been awarded the VinFuture Prize for his low-cost filtration system to remove arsenic and other heavy metals from groundwater.

VinFuture prizes are given in four categories annually and the award-winners are selected from around 1,000 nominations from 71 countries and recognise innovators from developing countries. The VinFuture Grand Prize worth \$3 million includes three special prizes, each valued at \$5,00,000 given to women innovators, innovators from developing countries, and innovators with outstanding achievement in emerging fields.

Mr. Pradeep, a professor in the Department of Chemistry, discovered affordable and sustainable nanomaterial that removed arsenic and other material. The method employed simple designs and purified groundwater. The technology does not require electricity.

Mr. Pradeep, who received the award at a ceremony in Hanoi, Vietnam last week, said the award recognised all who worked with him, those who benefited from the work and those who enabled translation of the work. He has been awarded the Padma Shri, Nikkei Asia Prize and Prince Sultan Bin Abdulaziz international prize for water.

# IIT Madras Professor Selected as Laureate of Prince Sultan Bin Abdulaziz International Prize for Water

By: [Education and Careers Desk](#)

Last Updated: JUNE 13, 2022, 12:39 IST



Prof T Pradeep from IIT Madras

Prof. T. Pradeep's Research Group developed environmentally friendly 'water positive' nanoscale materials for the affordable, sustainable, and rapid removal of arsenic from drinking water.

Follow us: [Facebook](#) [Twitter](#) [Instagram](#)  
[Telegram](#) [Google News](#)

**T**he Indian Institute of **Technology** (IIT) Madras Prof Thalappil Pradeep has been selected as the laureate of the 10th edition of the prestigious 'Prince Sultan Bin Abdulaziz International Prize for Water' (PSIPW). He was selected for the Award under 'Creativity Prize' category given for 'breakthrough discovery' in any water-related field.

Prof. T. Pradeep's Research Group developed environmentally friendly 'water positive' nanoscale materials for the affordable, sustainable, and rapid removal of arsenic from drinking water. Prof. Pradeep has been recognized earlier with the Padma Shri, and Nikel Asia Prize, among many others and his technologies are delivering clean water to over 1.2 crore people.

The bi-annual international scientific award was established on 21 October 2002 by Prince Sultan Bin Abdulaziz Al Saud of Saudi Arabia. The prize carries a cash component of \$2,66,000 (Rs. 2 Crore Approx) besides a gold medallion, a trophy, and a certificate.

The awards ceremony will take place on September 12 at the United Nations Headquarters in New York. The award mentions Prof. T. Pradeep's team members - Avula Anil Kumar, Chennu Sudhakar, Sritama Mukherjee, Anshup, and Mohan Udhaya Sankar.

Speaking about this award, Prof. T. Pradeep, Institute Professor, Department of Chemistry, IIT Madras, said, "Clean water is truly a problem of advanced materials. We could contribute to the area in a small way, thanks to our great nation."

Commenting on the future projects, he added, "There is much to do in every area of water such as desalination, humidity harvesting, sensing, and recycling. Our wonderful team is working on each one of them. The area is wide open for all to contribute."

The Prize Council, under the chairmanship of the President of King Saud University Dr. Badran Al-Omar, and under the direction of PSIPW President HRH Prince Khalid Bin Sultan Bin Abdulaziz, approved the winners for the 10th Award (2022) of the Prince Sultan Bin Abdulaziz International Prize for Water (PSIPW) on 5th June 2022.

The 10th Award winners were formally disclosed during the Space and Water Agenda of the 65th Session of the United Nations Committee on the Peaceful Uses of Outer Space (UN COPUOS).

The PSIPW is a leading, global scientific award focusing on cutting-edge innovation in water research. It gives recognition to scientists, researchers and inventors around the world for pioneering work that addresses the problem of water scarcity in creative and effective ways.

Volume 58  
Number 91  
25 November 2022  
Pages 12619–12742

# ChemComm

Chemical Communications

[rsc.li/chemcomm](https://rsc.li/chemcomm)



ISSN 1359-7345



ROYAL SOCIETY  
OF CHEMISTRY

**COMMUNICATION**

Thalappil Pradeep *et al.*

Aggregation of molecules is controlled in microdroplets



# Pradeep Research Group



Current group as on December 30, 2022



## Acknowledgements

Students and  
Collaborators

Funding



सत्यमेव जयते

Department of Science & Technology  
Govt. of India



Science & Engineering Research Board  
Department of Science & Technology  
Government of India



सत्यमेव जयते

GOVERNMENT OF INDIA  
**MINISTRY OF  
MINES**